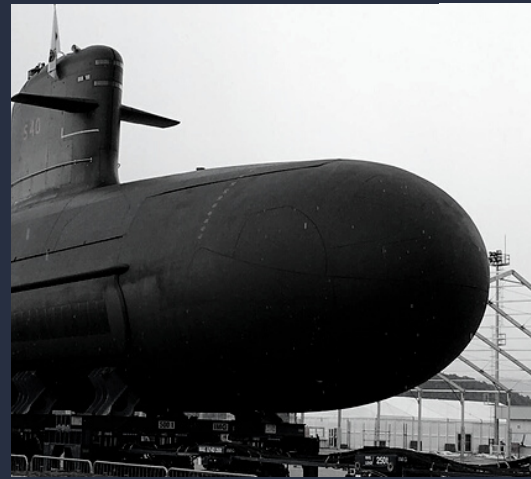VOLUME II

Fundamental Concepts and Models for the Direct Problem

EDITORS: ARIOSTO B. JORGE, CARLA T.M. ANFLOR, GUILHERME F. GOMES, and SERGIO H.S. CARNEIRO

University of Brasilia (UnB)
Post-Graduate Program - Integrity of Engineering Materials

Book Series in Discrete Models, Inverse Methods, & Uncertainty Modeling in Structural Integrity

Volume II

Fundamental Concepts and Models for the Direct Problem

Book Series Editors

Ariosto Bretanha Jorge (leading editor)
Carla Tatiana Mota Anflor
Guilherme Ferreira Gomes
Sergio Henrique da Silva Carneiro

This Book Series is an initiative of the Post-Graduate Program - Integrity of Engineering Materials (PPG-Integridade) of University of Brasilia (UnB)

With the incentive, encouragement and support from

- Latin American Journal of Solids and Structures (LAJSS) (www.lajss.org)
- Brazilian Society of Mechanical Sciences and Engineering (ABCM) (www.abcm.org.br)
- Brazilian Association of Computational Methods in Engineering (ABMEC) (www.abmec.org.br).

Brasília – DF
Open access digital book published by
University of Brasilia Central Library (BCE/UnB)
2022

Edited as an initiative of: Universidade de Brasília
Faculdade do Gama (FGA) / Faculdade de Tecnologia (FT)
Programa de Pós-Graduação em Integridade de Materiais da Engenharia

Address:
Universidade de Brasília, Campus do Gama
Área Especial de Indústria e Projeção – Setor Leste
Prédio UED (Unidade de Ensino e Docência) - 1º Andar
CEP: 72.444-240, Gama - DF, Brasil

Contact: Phone: (+55) (61) 3107-8903 WebSite: http://www.pgintegridade.unb.br/
E-mail pgintegr@unb.br; ctanflor@gmail.com; ariosto.b.jorge@gmail.com

Cataloging-in-Publication (CIP) Data:
Prepared by the librarian at University of Brasilia Central Library (BCE/UnB).

Foreword from FGA / UnB

The engineering sector drives and enables the development of a country. The formation of an engineer allows a technical capacity to evaluate, plan, design, suggest and apply all possible techniques in search of the best construction of a technological equipment. Currently, the engineer must be more and more prepared to solve existing problems in various sectors of society. It is through it that societies grow in search of progress.

The recognition of engineering and the training of new professionals increases every year in Brazil. In the 2000s, the University of Brasília (UnB) went through an expansion process, resulting in the implementation of the new UnB Engineering Campus in the city of Gama (UnB-Gama, FGA). Five new undergraduate courses were created: Aerospace Engineering, Automotive Engineering, Electronic Engineering, Energy Engineering and Software Engineering. The UnB Gama Campus project converges to increase the education level of the Brazilian population, especially in the five areas of engineering activity, all in line with current national public policies, aimed at expanding the population's access to quality higher education in the country.

Following the high quality teaching line, the UnB-Gama campus has the Graduate Program in Integrity of Engineering Materials (PPG-Integridade). The program has the following lines of research: Dynamics and Vibrations, Fatigue, Structural Materials, Biomaterials, Structure Fluid Interaction and Numerical Simulation of the Mechanical Behavior of Materials. This book series is an initiative of PPG-Integridade - UnB, organized as a collaborative work involving researchers, engineers, scholars, from several institutions, universities, industry, recognized both nationally and internationally.

Beside the high technical quality and relevance of the topics covered in the books, this series will enable an essential internationalization of the research currently developed within the University of Brasília. Several authors from different countries also contributed to these books, enabling greater interaction between national and international research groups. This internationalization raises the level of academic education for new professionals in the field of engineering, in addition to more advanced scientific research and technological development.

Additionally, this book series features a strong contribution from the industrial sector. Several professionals from different companies collaborated with the writing of some chapters in the three volumes that make up this series. These initiatives are of great strategic importance, as they allow the grouping of different technical capabilities. On the part of companies in the sector, with knowledge of market demands, and on the part of universities, by adding the technical-scientific knowledge of their team of researchers to the improvement of innovative products and services.

This book should be appreciated by anyone in need of knowledge of Materials Integrity. The completeness of Discrete Modeling and Inverse Methods theory combined with the Uncertainty Modeling in Structural Integrity makes these books mandatory for everybody aiming at Direct and Inverse Problems, including model-based and signal-based inverse problems.

Prof. Dr. Sandro A.P. Haddad, Director
UnB-Gama campus (https://fga.unb.br/)

Foreword from LAJSS

Book Series in Discrete Models, Inverse Methods, & Uncertainty Modeling in Structural Integrity

Book Series editors: Ariosto B. Jorge, Carla T.M. Anflor, Guilherme F. Gomes, and Sergio H.S. Carneiro

This book series represents a commendable effort in compiling the latest developments on three important Engineering subjects: discrete modeling, inverse methods, and uncertainty structural integrity. Although academic publications on these subjects are plenty, this book series may be the first time that these modern topics are compiled together, grouped in volumes, and made available for the community.

The application of numerical or analytical techniques to model complex Engineering problems, fed by experimental data, usually translated in the form of stochastic information collected from the problem in hand, is much closer to real-world situations than the conventional solution of PDEs. Moreover, inverse problems are becoming almost as common as direct problems, given the need in the industry to maintain current processes working efficiently, as well as to create new solutions based on the immense amount of information available digitally these days. On top of all this, deterministic analysis is slowly giving space to statistically driven structural analysis, delivering upper and lower bound solutions which help immensely the analyst in the decision-making process.

All these trends have been topics of investigation for decades, and in recent years the application of these methods in the industry proves that they have achieved the necessary maturity to be definitely incorporated into the roster of modern Engineering tools. The present book series fulfills its role by collecting and organizing these topics, found otherwise scattered in the literature and not always accessible to industry.

Moreover, many of the chapters compiled in these books present ongoing research topics conducted by capable fellows from academia and research institutes. They contain novel contributions to several investigation fields and constitute therefore a useful source of bibliographical reference and results repository.

The Latin American Journal of Solids and Structures (LAJSS) is honored in supporting the publication of this book series, for it contributes academically and carries technologically significant content in the field of structural mechanics.

On behalf of LAJSS,

Prof. Dr. Marcílio Alves (USP), Editor-in-Chief
Prof. Dr. Rogério J. Marczak (UFRGS), Assoc. Editor
Prof. Dr. Pablo A. Muñoz-Rojas (UDESC), Assoc. Editor
Prof. Dr. Marco L. Bittencourt (Unicamp), Assoc. Editor

Latin American Journal of Solids and Structures (LAJSS)
(www.lajss.org)

Foreword from ABCM

The Brazilian Society of Mechanical Sciences and Engineering – ABCM welcomes enthusiastically the publication of the Book Series in Models, Inverse Methods & Uncertainty Modeling in Structural Integrity.

The initiative, undertaken by Prof. Ariosto B. Jorge, Dr. Carla T.M. Anflor, Dr. Guilherme F. Gomes and Dr. Sergio H. S. Carneiro, with the support of the University of Brasília, is received by the scientific community as a valuable contribution to the dissemination of knowledge encompassing the large number of topics covered in the three volumes of the series.

These topics have been judiciously selected to encompass comprehensively the theoretical aspects, modeling techniques and numerical methods related to Structural Integrity, and are presented in a large collection of chapters authored by renowned experts, from both academia and industry. We gladly realize that many members of ABCM have contributed as authors.

Besides the comprehensive and well-articulated content, one distinguishing characteristic of this book series is that it has been conceived to serve both for educational purposes at graduate level and as an information source for researchers and engineering practitioners, which amplifies, to a large extent, its utility. Another relevant feature is that the material is intended to be available to the public in electronic format at no cost, which highlights the generosity of the authors and editors and their commitment to the most fundamental academic principles.

On behalf of the scientific community of the field of Mechanical Sciences and Engineering, ABCM acknowledges the editors and authors of the present book series for their contribution to the progress of Engineering research and education.

Prof. Dr. Domingos Alves Rade
President of ABCM

On behalf of

Brazilian Society of Mechanical Sciences and Engineering (ABCM)
(www.abcm.org.br)

Foreword from ABMEC

The whole range of topics related to Direct & Inverse Problems and Modeling of Uncertainties is substantially associated with the needs of the mechanical, civil, aeronautical/aerospace, nuclear, and naval/oceanic industries. Indeed, they play a core role in industrial renewal, contributing to productivity and competitiveness. Especially taking Brazil into account, this book series, conceived as a comprehensive one that covers these important topics, is very welcome.

These themes are also among the main interests of the Brazilian Association of Computational Methods in Engineering, ABMEC. ABMEC is concerned with the application of numerical methods and digital computers to the solution of engineering problems. Its mission is to promote, foster, and organize activities encompassing the development and use of such computational methods in Brazil.

We are fortunate to have the opportunity to support this book series as a collaborative work that intends to involve scholars from different institutions and researchers from industry, with national and international relevance. We sincerely believe that this work will provide a common forum for discussion, education, and research information transfer between the several subjects concerning computational methods in engineering.

Our congratulations to the editors, professors Ariosto Bretanha Jorge, Carla Tatiana Mota Anflor, Sergio Henrique da Silva Carneiro, Guilherme Ferreira Gomes for this important contribution to the Brazilian engineering.

Prof. Dr. Felício Bruzzi Barros
President of ABMEC

On behalf of

Brazilian Association of Computational
Methods in Engineering (ABMEC)
(www.abmec.org.br)

Acknowledgements

Acknowledgements from the Book Series editors

Personal dedications from the Book Series editors

A personal dedication from Ariosto Bretanha Jorge, leading editor

In my point of view, this Book Series project represents the culmination of a dedicated academic career, in many aspects intrinsically related to the different research topics and areas covered along the three Volumes of the Book Series.

I would like to thank all my co-editors of the Book Series, all the co-authors of the book chapters, and also all the researchers, scholars, students with whom I had the opportunity to share collaborative work throughout my many years along this academic career. I've enjoyed learning a lot from you all!

To you, my sincere thank you!

I would like also to dedicate this project to my wife Daisy, for her love, understanding, and unconditional support, throughout my entire academic career, and to my daughter Elisa and my son Luís Paulo, for their love and support.

To you, my true love and deepest appreciation!

Ariosto

A personal dedication from Carla Tatiana Mota Anflor

I would like to thank my parents, Maria Emilia and Miro (in memoriam), for their love and support during this infinite academic journey.

Special thanks to Professor Ariosto B. Jorge for inviting me to join the Book Series editors team and for being a great advisor until nowadays. Also, sincere thanks to my coleagues Guilherme Gomes and Sergio Carneiro, for their friendship during our editorial working times.

Carla

A personal dedication from Guilherme Ferreira Gomes

To my beloved father Expedito Ferreira Gomes (*in memoriam*).
"Those we love never die, they just leave before us."

Guilherme

A personal dedication from Sergio Henrique da Silva Carneiro

To my wife Lúcia and my children Pedro, Letícia and Matheus, for their love and support.

To my parents Neli and Joaquim (in memoriam) and my brother Luiz, my true roots, my foundation.

To all my students, past and present, graduate and undergraduate, from whom I have learned so much.

To my colleagues in Academia and research institutes, for all the knowledge and wisdom they have shared with me throughout my career.

To the Brazilian Air Force, for the privilege of serving my Country in the company of dedicated and honored men and women.

Sergio

Brasilia, July 15th, 2022.

Table of Contents

Chapter 1

Introduction to the Direct Problem: Materials, Technologies, and Discrete Modeling

Introduction to the Direct Problem: Materials, Technologies, and Discrete Modeling

Ariosto Bretanha Jorge[1a*], Carla Tatiana Mota Anflor[1b],

Guilherme Ferreira Gomes[2] and Sérgio Henrique da Silva Carneiro[1c]

[1]Post-Graduate Program - Integrity of Engineering Materials, University of Brasilia, Brazil. Book series editors. E-mail: ariosto.b.jorge@gmail.com, anflor@unb.br, shscarneiro@unb.br
[2]Mechanical Engineering Institute, Federal University of Itajubá, Itajubá, Brazil. Book series editor. E-mail: guilhermefergom@unifei.edu.br

*Corresponding author. Book series leading editor.

Abstract

This chapter presents an overview of the Book Series in Direct Methods, Inverse Methods and Uncertainty Modeling (of which its Volume I: Model-Based and Signal-Based Inverse Methods has already been published), and a presentation of the current Volume II: Fundamental Concepts and Models for the Direct Problem. The chapter includes an introduction to the different topics in Optimization and Identification Techniques detailed in Volume I, and an introduction to topics related to materials, technologies, and discrete modeling, comprising the several chapters included in this Volume II of the Book series.

1 Book Series in Discrete Models, Inverse Methods, & Uncertainty Modeling in Structural Integrity: overview

The Book series in "Discrete Models, Inverse Methods, & Uncertainty Modeling in Structural Integrity" is an initiative of the Post-Graduate Program - Integrity of Engineering Materials (PPG-Integridade) of University of Brasilia (UnB), organized as a collaborative work involving researchers, engineers, scholars, from several institutions, universities, industry, recognized both nationally and internationally.

This book series is an activity related to the Research, Development & Innovation (R,D&I) Project at UnB, titled: "Technological Demonstration Platform for Inverse Methods and Uncertainty Modeling Integrity of Structures and Components", available at the UnB Central Library (in Portuguese) (Ariosto Bretanha Jorge, 2020).

The Book Series project is comprised by three Volumes:

- Volume I – Model-based and Signal-Based Inverse Methods (Ariosto B. Jorge et al., 2022b)
- Volume II – Fundamental Concepts and Models for the Direct Problem
  - o Part I – Technologies and Materials Modeling
  - o Part II - Discrete Modeling
- Volume III – Uncertainty Modeling: Fundamental Concepts and Models

The different book chapters were elaborated encompassing the relevant project topics, including chapters covering:

- Fundamentals, including topics such as: basic principles, concepts & foundations, for the Direct & Inverse Problems (including model-based and signal-based inverse methods), and for the Modeling of Uncertainties;
- Special Topics, Applications, and Research Review, including topics such as: research review, state-of-the-art & future trend topics, for the Direct & Inverse Problems (including model-based and signal-based inverse methods), and for the Modeling of Uncertainties.

The book chapters were prepared as a collaborative work by researchers, engineers, scholars, involved in research, development and applications in the related areas.

The research areas of interest throughout the book chapters include:

- Modeling of the inverse problem, monitoring & diagnosis / prognosis: models and methods for inverse problems, optimization methods (including techniques such as; multi-objective optimization, topology optimization, evolutionary optimization), Wavelets, Kalman Filter (KF), Particle Filter (PF), Machine Learning (ML), Artificial Intelligence (AI), Data Science (DS), for applications such as Structural Health Monitoring (SHM) (including impedance-based and Lamb Wave-based techniques), Health & Usage Monitoring Systems (HUMS);
- Modeling of the direct problem: mechanics of materials (including metallic materials, composites), structures (including civil, mechanical naval, aeronautical structures) machinery design and mechanical components, fracture mechanics, impact, fatigue, damage tolerance, integrity, mechanical vibrations, dynamics of structures, computational mechanics, including mathematical methods and numerical methods for discrete modeling for continuum mechanics (such as Finite Element Methods (FEM), Boundary Element Methods (BEM), Mesh-Free Methods (MFM));
- Probabilistic methods and modeling of uncertainties: probabilistic methods in engineering, Design of Experiments (DOE), Response Surface Methods (RSM), Risk & Reliability (including structural and system reliability), Uncertainty Modeling (UM) & Uncertainty Quantification (UQ), Bayesian Approaches (BA), stochastic Finite Element approaches (Stochastic FEM, Spectral FEM, Polynomial Chaos), stochastic optimization, meta-modeling (including techniques such as Surrogate Models (SM), Reduced Order Models (ROM)), model Verification & Validation (V&V).

The different models, methods and approaches presented throughout the several chapters in the three Volumes of this Book Series are intended as an introductory presentation of some possibilities of methods that could be used in problems related to integrity of structures and components, and maybe even extended to other engineering areas, as appropriate. The list of models is not unique, and is neither comprehensive nor exhaustive, and the reader is encouraged to look for different possibilities of methods that may be applicable to the particular engineering problem at hand.

A common aphorism, often presented as *"All models are wrong, but some are useful"*, is usually considered to be applicable to scientific models in general, and to statistical models in particular. The aphorism recognizes that statistical or scientific models always fall short of the complexities of reality but can still be of use. The aphorism is generally attributed to the statistician George E. P. Box, although the underlying concept predates Box's writings.

Section 2 presents an overview of Volume I - Model-Based and Signal-Based Inverse Methods, which includes chapters on several Optimization Models and Identification Techniques. An introduction and context is presented, as well as a listing of the chapters included in Volume I.

Section 3 presents an overview of Volume II - Fundamental Concepts and Models for the Direct Problem, which includes chapters distributed in Part I – Technologies and Materials Modeling, and in Part II - Discrete Modeling. An introduction and context is presented, as well as a listing of the chapters included in Volume II.

Section 4 presents some final remarks and acknowledgements.

2 Overview of Volume I

2.1 Model-Based and Signal-Based Inverse Methods – context

The detection, localization, classification and identification of parameters and/or material properties, related to the integrity of structures and components, with and without defects or damages, involves the modeling of inverse problems, as well as an adequate modeling and quantification of the uncertainties involved in the problem.

The formulation of the direct problem, of the inverse problem, and the related uncertainties modeling, needed for an adequate description of the structure and/or the mechanical component, and of its potential defects or damages, involves multidisciplinary modeling techniques, whose understanding and proper application transcends the field of integrity and damage tolerance, being able to serve as a basis for applications, in other contexts or fields.

Among the application problems of interest for inverse methods, one can cite Structural health monitoring (SHM) and Health and Usage Monitoring Systems (HUMS).

The monitoring of structural integrity (SHM) is a competitive technique for damage detection and identification, wherein information is collected online, and compared with an existing database for an undamaged ("healthy") structure. From this comparison, real-time information on the presence of damages can be obtained, including their localization, size, propagation speed, and, ultimately, the remaining operational life of the structural component.

The monitoring of mechanical components (HUMS) is a technique which is being used to follow / accompany the state of the integrity of mechanical systems / components (Health) and to monitor the appearance of indicators of the presence of damage (usage) in dynamic systems, such as rotating components (in engines, for example) and in gearboxes (in mechanical transmission systems, for example). In this case, the comparison is made between vibration signals from the healthy components (accumulated historical data) and from the components being monitored, to identify significant discrepancies in the vibration signals, which could be correlated to specific / particular / known damages.

The scientific challenge of the modeling of inverse problems, as well as of the adequate modeling and quantification of the related uncertainties, in a problem of integrity of structures and components, involves several aspects:

- The modeling of the problems (direct problem, inverse problem, uncertainties) needs to be done, whenever possible, by using more than one technique, for each case being described, in order to implement, for the particular problem at hand, model techniques which are independent, complementary, and/or redundant. Whenever possible, more than one model should be used, for redundancy and/or comparative analysis, especially in the case of unavailability of prior data for the healthy structure and/or component.
- The techniques used for inverse methods may involve:
  i. Optimization techniques, based on multi-objective optimization models, using classical optimization techniques (such as Sequential Quadratic Programming (SQP), BFGS, etc), or evolutionary optimization techniques (such as Genetic Algorithms (GA), Differential Evolution (DE), Sunflower Optimization (SFO), Lichtenberg Algorithm (LA), etc.);
  ii. Identification techniques based on Artificial Intelligence, Machine Learning, Pattern Recognition, Data Science, etc., models (such as identification models based on Artificial Neural Networks (ANN), for example;
  iii. Models based on the Wavelet Transform (continuous Wavelet Transform (CWT), discrete Wavelet transform (DWT), with different types and sizes of the Wavelet window, for example);
  iv. Stochastic models (such as Kalman Filter (KF), Extended Kalman Filter (EKF), Extended Information Filter (EIF), Particle Filter (PF), Least Squares (LS), etc).
- In several situations, the direct models to be implemented may involve different problem physics (Multi-physics Modeling), and multiple scales (Multi-scale Modeling). In such cases, the description for the direct problem may involve coarser global models, and more detailed local models;
- The computational simulations and the experimental / laboratory tests must take into account the additional challenge of properly simulating / representing the local behavior of a complex structure, in the regions of interest, where the defect of damage is expected to be, or is expected to appear. For example, Fracture Mechanics (FM) problems and Damage Tolerance (DT) problems cannot be properly represented by reduced-scale models, as the damaged region must be represented using full-scale models. In these cases, the computational simulations (and also the experimental / laboratory tests) are required to reproduce the situation in the region of the damage using high fidelity local models. Thus, the region of the damage must be modeled in full scale, with the model also representing properly the geometry, the mechanical properties, and the real loading in that local region (loading that is coming from the external loads that were applied in the structure or in the component as a whole).
- In many cases, inverse problems may belong to the category of ill-posed problems, which represents an additional challenge in the modeling of the problem at hand. In these cases, the approach for the inverse method may require additional hypothesis to be made (for problem regularization, for example), or that a meta-modeling approach is adopted (such as surrogate models, reduced order models, etc), replacing the original model by the proper meta-model, and then solving this approximate model for the problem.
- The modeling of inverse problems, such as in the case of SHM and/or HUMS, must take into account the proper modeling of the sensor behavior, and also the uncertainties associated to these sensors, as well as the simultaneous use of multiple,

independent, techniques for monitoring, with different sensors. The optimal sensor positioning, to maximize the Probability of Detection (PoD), may be seen as a topological optimization problem and/or as a stochastic optimization problem.

- The modeling of inverse problems may involve the detection, localization, and identification of parameters and/or material properties (for example, properties such as elasticity modulus, Poisson's ratio, etc), which may vary through time (for example, material degradation thought time) and also along the length of the structure or mechanical component (for example, local changes which may occur in the material properties and / or mechanical properties of a composite plate, due to the debonding between the layers of the composite material).

2.2 Chapter topics in Volume I: presentation

Along Volume I of the Book Series, several topics related to model-based and signal-based methods for inverse problems were presented in the several book chapters, representing the collaborative work from researchers, engineers, scholars, engaged in research, development and applications in the related areas, affiliated to several institutions, universities, industry, and recognized both nationally and internationally.

The book chapters in Volume I of the Book Series were distributed as follows:

- Chapter 1: Introduction to Optimization and Identification Techniques for Model-Based and Signal-Based Inverse Problems (Ariosto B. Jorge et al., 2022a)
- Chapter 2: Overview of Some Optimization and Identification Techniques for Inverse Problems of Detection, Localization and Parameter Estimation (Sousa et al., 2022)
- Chapter 3: An overview of Linear and Non-linear Programming methods for Structural Optimization (Choze, Santos, Jorge, et al., 2022)
- Chapter 4: Overview of Traditional and Recent Heuristic Optimization Methods (Choze, Santos, & Gomes, 2022)
- Chapter 5: Application of Machine Learning and Multi-Disciplinary/Multi-Objective Optimization Techniques for Conceptual Aircraft Design (Mattos et al., 2022)
- Chapter 6: On a Bio-Inspired Method for Topology Optimization via Map L-Systems and Fractone Modeling (Kobayashi, 2022)
- Chapter 7: Fundamentals on the Topological Derivative concept and its classical applications (Carvalho et al., 2022)
- Chapter 8: Ultrasound Obstacle Identification using the Boundary Element and Topological Derivative Methods (Cisilino & Anflor, 2022)
- Chapter 9: Fundamental Concepts on Wavelet Transforms (Erwin Ulises Lopes Palechor et al., 2022)
- Chapter 10: Application of Wavelet Transforms to Structural Damage Monitoring and Detection (Erwin Ulises Lopez Palechor et al., 2022)
- Chapter 11: Inverse Methods using KF, EKF, EIF, PF, and LS Techniques for Detection, Localization, and Parameter Estimation (Myers & Jorge, 2022)
- Chapter 12: Fundamental Concepts for Impedance-based Structural Health Monitoring (Finzi Neto & Moura, 2022)

- Chapter 13: Fundamental Concepts for Guided Lamb Wave-based Structural Health Monitoring (Finzi Neto et al., 2022)
- Chapter 14: Machine Learning and Pattern Recognition: Methods and Applications for Integrity Monitoring of Civil Engineering Structures (Alves et al., 2022)

3 Overview of Volume II

3.1 Fundamental Concepts and Models for the Direct Problem – context

The modeling of the Direct Problem includes disciplines related to:

- Materials Science, Mechanics of Materials (applications to engineering materials, such as metallic materials, composites, biomaterials, etc.), Material Characterization Techniques (Digital Image Correlation (DIC), etc.);
- Modeling & Design of Structures (applications to several Engineering branches such as Mechanical, Aeronautical, Civil, Naval, Ocean & Offshore, Nuclear, Energy, Oil & Gas, etc.);
- Design of Machines and Mechanical Components;
- Manufacturing Technologies and Processes (Additive Manufacturing, etc.)
- Structural & Component Integrity (Fracture Mechanics, Fatigue, Impact, Contact, Damage Tolerance, Inspection, Non-Destructive Testing (NDE), Maintenance, Structural Health Monitoring (SHM), Health and Usage Monitoring Systems (HUMS), etc.);
- Mechanical Vibrations, Acoustics, Structural Dynamics (Data Acquisition, Modal Testing & Modal Analysis Techniques, etc.);
- Computational Mechanics, Mathematical Methods, Numerical Methods (such as Finite Element Methods (FEM), Boundary Element Methods (BEM), Meshless / Meshfree Methods, etc.).

Regarding structural integrity applications, the problem of detecting damage in a structure involves modeling the direct problem, that is, the behavior of that structure in the presence of one or more pre-established damages, of assumed shape and size, and at given locations. This modeling can be done, for example, involving the analysis of the distribution of stresses and strains in parts with cracks, done through a FEM, BEM or Meshless modeling, or by analyzing the distribution of sound waves in this cracked part, emitted by a pre-established source, by means of a FEM, BEM or Meshless modeling.

Regarding component integrity applications, for the problem of detecting faults in dynamic components, experimental vibration data can be acquired from accelerometers conveniently distributed in the vicinity of the components of interest. In this case, there would be no direct problem modeling (the direct model is implicit), as the vibration data would be acquired for the healthy components to be later compared with the vibration data of the defective (with failures) components.

With respect to Direct Problem Modeling, several problems of interest in structural integrity can be modeled as initial value problems and/or boundary value problems. In the case of boundary value problems, not varying in time, there is a valid partial differential equation in the region that represents the problem domain, and valid

boundary conditions at the boundary of this region. In the case of time-dependent initial value problems, there are also valid initial conditions in this domain.

A boundary value problem can be represented by a general equation of type $Au = p$, valid in the domain D, with boundary conditions valid in the boundary ∂D. The complexity of the problem, the geometry of the boundary, the actions (external loads, restrictions on supports) limit the possibilities of analytical solution for this problem, which generates a demand for approximate solutions, such as, for example, through:

- replacement of the differential operator A by an approximate operator A^*. This is the case of the finite difference method, which adopts an algebraic operator A^*, where the derivative at a given point is expressed through the values of the function at points located in a neighborhood of that point, allowing the construction of a system of linear equations, to be solved with the proper application of the initial and boundary conditions;

- replacement of the variable u by an approximate variable u^*, expressed in the form of a linear combination of a set of basic functions. These functions can be polynomial, trigonometric, etc. The coefficients of this linear combination are the components of this approximate solution in the coordinate system represented by these basic functions. When the number of components tends to infinity, the approximate solution u^* tends to the solution u. Among the approximate solutions based on this method, many correspond to methods called "projective", where the equation valid in the domain is projected in an auxiliary subspace of functions, called support functions, and integrated in the domain, with its boundary conditions, using integration by parts. This category of methods includes, among others:
  - o The Finite Element Method (FEM), using an integration by parts and, in each element, the same functions, both for support and for approximation of the variable u, in order to obtain the solution in points of the domain, called nodes, and, by interpolation using these functions, the solution at all other points in the domain;
  - o The Boundary Element Method (BEM), using two integrations by parts and using support functions called fundamental solutions, in order to eliminate the domain integral, leaving only the boundary integrals (also known as boundary integrals). Thus, the solution is initially obtained only at the nodes of the discretized contour. Then, by interpolation, the solution is found at the other points of the contour. Finally, by post-processing, the solution is obtained at any desired point in the domain.

For problems of interest in structural integrity, the finite element method can be efficiently applied to problems in which the domain is inhomogeneous, where the discretization of the elements would already consider this local non-homogeneity.

On the other hand, problems involving domain singularities, such as stress distribution in the vicinity of the crack tip, in fracture mechanics, can be well represented using the boundary element method.

For initial value problems, with variable (in the domain and/or in the frontier) dependent on time, it may need a combination of methods that include the finite difference method, to model the march in time of the variable of interest.

Other numerical methods are also available, such as the Meshless / Meshfree Methods, in which the global system of equilibrium equations is constructed using a node-by-node process, performed in the local domain of each node, and thus there is no need to define *a priori* a mesh of finite elements or a mesh of boundary elements.

For the application of inverse methods in dynamic components, the methodology is based on the comparison of vibration data acquired and stored throughout the life of the components still undamaged, with the most recent vibration data, for the components currently in use, from so that significant changes in the spectrum of acquired signals can be used as a starting point for the detection and identification of damage to these components. In this case, instead of a numerical code for the direct problem, vibration and acoustics data acquisition systems are used, together with structural dynamics, vibration analysis, modal testing & modal analysis techniques.

The direct problem modeling can also include the study of the damage evolution with time (such as, for example, the crack propagation rate), in order to estimate the remaining useful life (safe life) of the structure.

The science and technology behind analyzing structures is not yet mature, and further advancements and research are unnecessary for the basic understanding of structural mechanics phenomena and behavior (design/analysis/test) (Hamm et al., 2021). Some remaining challenges in the structures discipline include many areas still in need of rigorous research to arrive at physics-based methodologies, including: Fracture Mechanics, Composite Materials, New Materials, Manufacturing and Processing Methods, New Applications, Lack of Physics-Based Theories, New Test Methods, Incorporation of Research Advancements, Computational Advances, Multi-Discipline Interactions.

One final note; in the context of philosophy of science, two fundamental issues were pointed out in (Da Costa & French, 2006). One issue concerns the appropriate attitude we should take towards scientific theories - whether we should regard them as true or merely empirically adequate, for example. The other issue concerns the nature of scientific theories and models and how these might best be represented. These two issues together lead us to arguing that theories and models should be regarded as partially rather than wholly true, with issues in terms of belief, theory acceptance, and the realism-antirealism debate.

3.2 Chapter topics in Volume II: presentation

Along this Volume II of the Book Series, several topics related to technologies, materials and discrete modeling for direct problems are presented in the several book chapters, representing the collaborative work from researchers, engineers, scholars, engaged in research, development and applications in the related areas, affiliated to several institutions, universities, industry, and recognized both nationally and internationally.

The book chapters in this Volume II of the Book Series are distributed as follows:

- Chapter 1: Introduction to the Direct Problem: Materials, Technologies, and Discrete Modeling

Part I - Technologies, Structural Integrity & Material Modeling

- Chapter 2: Technologies and Materials Issues Related to Naval and Ocean Engineering
- Chapter 3: New Advances in Thermoplastic Commingled Composites: Processing and Molecular Dynamics
- Chapter 4: The Influence of Weaving Patterns on the Effective Mechanical Response of Reinforced Composites - A Study Through Homogenization
- Chapter 5: Auxetic Structures: Parametric Optimization, Additive Manufacturing, and Applications
- Chapter 6: Additive Manufacturing of Ti-Alloys for Aerospace, Naval and Offshore Applications
- Chapter 7: Review of Low Cycle Fatigue: Issues in Naval and Offshore Engineering
- Chapter 8: Modeling of Damage in Turbine Blades for Large Deformations
- Chapter 9: Stresses on Expansion Joints Used in Penetrations
- Chapter 10: Leak-Before-Break Technology for Piping in Nuclear Industry
- Chapter 11: Fatigue Control in Angra Nuclear Power Plants
- Chapter 12: On the use of Modal Test Data in Inverse Problems: Fundamentals and Applications
- Chapter 13: Application of Deep Learning Techniques for the Impedance-based SHM to the Oil & Gas Industry
- Chapter 14: Noise, Vibration, and Health and Usage Monitoring Systems (HUMS) of Aircraft Dynamic Components
- Chapter 15: On Vibration Analysis and Health and Usage Monitoring Systems (HUMS) of Dynamic Components of Helicopters
- Chapter 16: Model-Based Parameter Identification for Helicopter Main Rotor Balancing and Tracking Using Once-per-Revolution Vibration Data

Part II - Discrete Modeling: Finite Element, Boundary Element, Meshfree Methods

- Chapter 17: Finite Element Method for Structural Integrity Problems
- Chapter 18: An Application of Finite Element Method and Sensitivity Analysis in Structural Dynamics
- Chapter 19: The Boundary Element Method for Potential Problems
- Chapter 20: The Boundary Element Method for Structural Problems
- Chapter 21: The Boundary Element Method for Damage Modeling
- Chapter 22: Application of Roving Mass Technique Associated with Wavelet Transform to Structural Damage Detection and Localization
- Chapter 23: Local Mesh Free Methods in Linear Elasticity and Fracture Mechanics
- Chapter 24: Meshless smoothed point interpolation methods for damage modelling
- Chapter 25: A New Non-Iterative Reconstruction Method for Solving a Class of Inverse Problems

4 Final remarks and acknowledgements

This Chapter presents an overview of the Book Series in Direct Methods, Inverse Methods and Uncertainty Modeling, with focus on:

- The previously published Volume I: Model-Based and Signal-Based Inverse Methods, including an introduction to the different topics in Optimization and Identification Techniques detailed in this Volume I of the Book series;
- This current Volume II: Fundamental Concepts and Models for the Direct Problem, including an introduction to the topics in Materials, Technologies and Discrete Models, presented in this Volume II of the Book series;

This book series is an initiative of the Graduate Program in Integrity of Engineering Materials (PPG-Integridade) at the University of Brasilia (UnB), Brazil (www.pgintegridade.unb.br).

The editors would like to thank PPG-Integridade and UnB for the initiative, incentive and support for this Book Series project.

The book series is organized as a collaborative work involving researchers, engineers, scholars, engaged in research, development and applications in the related areas, affiliated to several institutions, universities, industry, and recognized both nationally and internationally.

The editors are grateful and would like to show their appreciation to all the co-authors of the book chapters, for their participation, dedication, and support.

The book series is published as a digital version, with ISBN provided by UnB, and DOI for each chapter, provided by the Latin American Journal of Solids and Structures (LAJSS) (www.lajss.org).

The scope of the Book series is in the broad areas of interest of LAJSS, and also of the Brazilian Society of Mechanical Sciences and Engineering (ABCM) (www.abcm.org.br) and the Brazilian Association of Computational Methods in Engineering (ABMEC) (www.abmec.org.br).

For increased visibility, these three institutions are encouraging the divulgation of the Book Series project in their websites.

The editors would like to express their appreciation to LAJSS, ABCM and ABMEC, for their incentive, encouragement and support for this Book Series project.

References

Alves, V. N., Cury, A. A., Roitman, N., & Magluta, C. (2022). Machine Learning and Pattern Recognition: Methods and Applications for Integrity Monitoring of Civil Engineering Structures. In Ariosto B. Jorge, C. T. M. Anflor, G. F. Gomes, & S. H. S. Carneiro (Eds.), *Model-based and Signal-Based Inverse Methods* (pp. 502–535). https://doi.org/10.4322/978-65-86503-71-5.c14

Carvalho, F. S. de, Anflor, C. T. M., Jorge, A. B., Cisilino, A. P., & Marczak, R. J. (2022). Fundamentals on the Topological Derivative concept and its classical applications. In Ariosto B. Jorge, C. T. M. Anflor, G. F. Gomes, & S. H. S. Carneiro (Eds.), *Model-based and Signal-Based Inverse Methods* (pp. 269–300). https://doi.org/10.4322/978-65-86503-71-5.c07

Choze, S. B., Santos, R. R., & Gomes, G. F. (2022). Overview of Traditional and Recent Heuristic Optimization Methods. In Ariosto B. Jorge, C. T. M. Anflor, G. F. Gomes, & S. H. S. Carneiro (Eds.), *Model-based and Signal-Based Inverse Methods* (pp. 107–142). https://doi.org/10.4322/978-65-86503-71-5.c04

Choze, S. B., Santos, R. R., Jorge, A. B., & Gomes, G. F. (2022). An overview of Linear and Non-linear Programming methods for Structural Optimization. In Ariosto B. Jorge, C. T. M. Anflor, G. F. Gomes, & S. H. S. Carneiro (Eds.), *Model-based and Signal-Based Inverse Methods* (pp. 65–106). https://doi.org/10.4322/978-65-86503-71-5.c03

Cisilino, A. P., & Anflor, C. T. M. (2022). Ultrasound Obstacle Identification using the Boundary Element and Topological Derivative Methods. In Ariosto B. Jorge, C. T. M. Anflor, G. F. Gomes, & S. H. S. Carneiro (Eds.), *Model-based and Signal-Based Inverse Methods* (pp. 301–330). https://doi.org/10.4322/978-65-86503-71-5.c08

Da Costa, N. C. A., & French, S. (2006). Science and Partial Truth: A Unitary Approach to Models and Scientific Reasoning. In *Science and Partial Truth: A Unitary Approach to Models and Scientific Reasoning*. https://doi.org/10.1093/019515651X.001.0001

Finzi Neto, R. M., & Moura, J. dos R. V. de. (2022). Fundamental Concepts for Impedance-based Structural Health Monitoring. In Ariosto B. Jorge, C. T. M. Anflor, G. F. Gomes, & S. H. S. Carneiro (Eds.), *Model-based and Signal-Based Inverse Methods* (pp. 443–471). https://doi.org/10.4322/978-65-86503-71-5.c12

Finzi Neto, R. M., Rezende, S. W. F. de, & Moura, J. dos R. V. de. (2022). Fundamental Concepts for Guided Lamb Wave-based Structural Health Monitoring. In Ariosto B. Jorge, C. T. M. Anflor, G. F. Gomes, & S. H. S. Carneiro (Eds.), *Model-based and Signal-Based Inverse Methods* (pp. 472–501). https://doi.org/10.4322/978-65-86503-71-5.c13

Hamm, K. R., Imtiaz, K. S., & Raju, I. S. (2021). Some remaining challenges in aerospace structures. *AIAA Scitech 2021 Forum*. https://doi.org/10.2514/6.2021-0574

Jorge, Ariosto B., Anflor, C. T. M., Gomes, G. F., & Carneiro, S. H. S. (2022a). Introduction to Optimization and Identification Techniques for Model-Based and Signal-Based Inverse Problems. In Ariosto B. Jorge, C. T. M. Anflor, G. F. Gomes, & S. H. S. Carneiro (Eds.), *Model-based and Signal-Based Inverse Methods* (pp. 1–7). https://doi.org/10.4322/978-65-86503-71-5.c01

Jorge, Ariosto B., Anflor, C. T. M., Gomes, G. F., & Carneiro, S. H. S. (Eds.). (2022b). *Model-based and Signal-Based Inverse Methods*. https://doi.org/10.4322/978-65-86503-71-5

Jorge, Ariosto Bretanha. (2020). *Technological Demonstration Platform for Inverse Methods and Uncertainty Modeling Integrity of Structures and Components (Plataforma demonstradora tecnológica para métodos inversos e modelagem de incertezas em integridade de estruturas e componentes).* University of Brasilia. https://repositorio.unb.br/handle/10482/39570

Kobayashi, M. H. (2022). On a Bio-Inspired Method for Topology Optimization via Map L-Systems and Fractone Modeling. In Ariosto B. Jorge, C. T. M. Anflor, G. F. Gomes, & S. H. S. Carneiro (Eds.), *Model-based and Signal-Based Inverse Methods* (pp. 237–268). https://doi.org/10.4322/978-65-86503-71-5.c06

Mattos, B. S. de, Bortolete, F. A., Fregnani, J. A. T. G., Jorge, A. B., Alves, W. M., & Cruz, R. V. (2022). Application of Machine Learning and Multi-Disciplinary/Multi-Objective Optimization Techniques for Conceptual Aircraft Design. In Ariosto B. Jorge, C. T. M. Anflor, G. F. Gomes, & S. H. S. Carneiro (Eds.), *Model-based and Signal-Based Inverse Methods* (pp. 143–236). https://doi.org/10.4322/978-65-86503-71-5.c05

Myers, M. R., & Jorge, A. B. (2022). Inverse Methods using KF, EKF, EIF, PF, and LS Techniques for Detection, Localization, and Parameter Estimation. In Ariosto B. Jorge, C. T. M. Anflor, G. F. Gomes, & S. H. S. Carneiro (Eds.), *Model-based and Signal-Based Inverse Methods* (pp. 382–442). https://doi.org/10.4322/978-65-86503-71-5.c11

Palechor, Erwin Ulises Lopes, Silva, R. S. Y. C., Morais, M. V. G. de, Bezerra, L. M., & Jorge, A. B. (2022). Fundamental Concepts on Wavelet Transforms. In Ariosto B. Jorge, C. T. M. Anflor, G. F. Gomes, & S. H. S. Carneiro (Eds.), *Model-based and Signal-Based Inverse Methods* (pp. 331–356). https://doi.org/10.4322/978-65-86503-71-5.c09

Palechor, Erwin Ulises Lopez, Silva, R. S. Y. C., Gomes, G., Morais, M. V. G. de, Bezerra, L. M., & Jorge, A. B. (2022). Application of Wavelet Transforms to Structural Damage Monitoring and Detection. In Ariosto B. Jorge, C. T. M. Anflor, G. F. Gomes, & S. H. S. Carneiro (Eds.), *Model-based and Signal-Based Inverse Methods* (pp. 357–381). https://doi.org/10.4322/978-65-86503-71-5.c10

Sousa, B. S. de, Gomes, G. F., Alexandrino, P. da S. L., Cunha, S. S., & Jorge, A. B. (2022). Overview of Some Optimization and Identification Techniques for Inverse Problems of Detection, Localization and Parameter Estimation. In Ariosto B. Jorge, C. T. M. Anflor, G. F. Gomes, & S. H. S. Carneiro (Eds.), *Model-based and Signal-Based Inverse Methods* (pp. 8–64). https://doi.org/10.4322/978-65-86503-71-5.c02

Part I

Technologies, Structural Integrity & Material Modeling

Chapter 2

Technologies and Materials Issues Related to Naval and Ocean Engineering

Chapter details

Chapter DOI:

Chapter suggested citation / reference style:

Marques, André L. F. (2022). "Technologies and Materials Issues Related to Naval and Ocean Engineering". *In* Jorge, Ariosto B., et al. (Eds.) *Fundamental Concepts and Models for the Direct Problem*, Vol. II, UnB, Brasilia, DF, Brazil, pp. 15–50. Book series in Discrete Models, Inverse Methods, & Uncertainty Modeling in Structural Integrity.

P.S.: DOI may be included at the end of citation, for completeness.

Book details

Book: Fundamental Concepts and Models for the Direct Problem

Edited by: Jorge, Ariosto B., Anflor, Carla T. M., Gomes, Guilherme F., & Carneiro, Sergio H. S.

Volume II of Book Series in:

Discrete Models, Inverse Methods, & Uncertainty Modeling in Structural Integrity

Published by: UnB City: Brasilia, DF, Brazil Year: 2022

Technologies and Materials Issues Related to Naval and Ocean Engineering

André Luís Ferreira Marques

Naval & Nuclear Engineer - Rear Admiral (Naval Constructor) (retired) Brazilian Navy. Affiliations: University of São Paulo (USP), Electrical & Computer Engineering - PhD candidate. Paulista University (UNIP), Electrical Engineering (ICET) - Professor. Green Yellow of Brazil - Data Scientist. Brazil. E-mail: aferreiramarques@uol.com.br

Abstract

The sea routes have been part of the globalization movements and help to shape up the world economy heavily. Seafaring has required different ship types, with specific dimensions, propulsion power and engineering materials. More recently, the defense sector has guided the development of naval and marine technologies, mainly in the underwater branch. With the use of nuclear technology, ships have gained a buster in his autonomy and range, setting other challenges tough. Fire aboard and run aground can happen at different world areas, and no ship seems fully protected against them, although their annual frequency has dimmed in the last half century. All these achievements were possible with a broader application of materials technology and selection properly. In the current energy transition and environment protection enhancement, ship materials reliability has caught more attention of ocean and naval experts, who are now applying Machine Learning and Artificial Intelligence, with wireless digital networks, for ship maintenance and hazard analysis, among others, helping to improve the ship performance, especially the economics and safety.

Keywords: naval engineering, ship structures, advanced materials, ship construction, ship design, screw alloys, materials reliability, mechanical fatigue, ship risk management, hydrogen embrittlement, steel toughness, corrosion.

1 Introduction

1.1 The importance of sea communications

Looking to a photograph of the Earth from the outer space, it is easy to see that most of the planet surface is covered by sea waters, connecting continents, people, and cultures. This characteristic has made feasible manifold routes and improved the exchanged of items, services, and other side assets towards History.

In his book [1], Boxer highlighted the importance of the sea communications in the build-up of Portugal as a maritime sea power. Even with few resources, that nation was able, from the XV to the XVIII Century, to expedite a first full version of the globalization, carrying thousands of tons of any kind of goods and people, discovering new lands and so on. Today, more than ninety percent of the world trade is made by sea [2]. Therefore, sea communications have become more and more vital to mankind.

In a closer example, due to the British naval blockade to France, from 1804 to 1815, the war in Europe took a different shape during the Napoleonic era. In other words, the French Empire could not use sea communications to get key raw materials or goods, from Asia, America, and Africa, and made its actions based on a continental approach exclusively. One of the consequences was the move of the Portuguese Court to Brazil, after the French-Spanish invasion of Portugal, in a change of a central power to a colony in the first time in History. In the end, the naval blockade changed our fate for good in the end, opening new lanes to our country, without any parallel among other former colonies. As an initial remark, the dominance of sea communications makes all the difference between countries and societies, showing aftermaths beyond a naive eyesight.

The ship design and its links with economics & environment issues

The use of sea needs all sorts of boats, ships, ferries, among other kinds of maritime transportation means. The design of ships depends on its general purpose, safety standards, the kind of sea routes and weather conditions to be sailed. In the last decade, the ship casualties and accidents have dimmed hopefully [3]. Equally important, to make it real, ship designers and operators have taken the economic feasibility carefully. Due to shorter profit margins, because of recent economic and logistic transients, the shipping companies look nowadays for more reliable and cheaper ship systems.

In another technical perspective, environmental requirements have been narrowed due to the worse climate effects seen in the last two decades and, thus, the environment impact has received more attention in the ship design process. For instance, the change from fossil fuels to electricity to propel a ship has been considered, together with a deeper recycling planning and action of ship materials, mainly in oil tankers and drilling rigs [4]. The ship safety standards have been raised to a degree preventing fuel, oil or cargo spills into the oceans and further harm to marine species and coastlines [5]. Nonetheless, small incidents and even accidents can take place in any ship.

1.2 Overall preview of the chapter

In this chapter, the connections between materials behavior, such as steel and non-ferrous alloys, and ship design issues will be covered, after a quick overview in the types of ships and their general characteristics. Moving on, construction and manufacturing processes, testing, structural failure, and trends in ship materials selection will be addressed. The chapter reading intends to provide a broad view on how some material aspects impact the ship construction and handling technology. Besides, it may present a spark to the readers to get deeper into the items covered.

2 Development

2.1 Types of ships

As a quick opening, this section deals with the ship technical characteristics to allow a better understanding of their kinds and singularities. Normally, the displacement or weight, is the main parameter, being measured in tons, and helps to cluster a certain ship. The overall dimensions also help to define a ship, such as total length (L), beam (B) and draft (H), expressed in meters. Table 1 summarizes some figures and types of ships.

Table 1: main figures related to each type of ships

Ship type	Length m	Beam m	Draft m	Displacement ton	Max Speed knots
Container ship	400	60	15	250.000	23
Large Oil tanker	400	60	30	500.000	18
Harbor tug	30	10	4	75	10
Line cruiser	250	25	7	70.000	20
Frigate	120	15	4	3.500	27
Naval cruiser	170	17	10	10.000	33
Corvette	80	10	3.5	2.000	25
Aircraft carrier	300	70	11	100.000	30
Nuclear attack submarine	100	12	11	9.000	30

2.2 Vessels versus naval ships

The term 'merchant ship' or 'vessel' refers to the ships used in the general shipping of goods and people in the civilian market, managed by commercial companies, private or state owned. For instance, an oil tanker is a sort of merchant ship (MS) or vessel, the same applicable for ore freighters. On the other hand, the word 'Naval Ship' or simply 'ship' refers to the military or defense application, such as aircraft carriers, attack submarines, troop cargo ships and so on.

In terms of design, naval ships have more strict design criteria, due to the wartime scenario they may find. For example, naval ships are designed to survive to nearby explosions or 'shocks', even nuclear attack, and its fallouts, which is not the case for the merchant ships. In the Brazilian Navy, some ships, like the Niteroi class frigates, can provide shelter for nuclear attacks, due to its specific design. On the other hand, merchant ships are required to have insurance contracts, not only for their cargo but also to themselves. Due to the possibility to be attacked and the need to survive in some extend, the insurances companies do not cover naval ships, as also seen with other defense hardware, otherwise the insurance burden will be too costly and closer to infinity. Figure 1 shows the Frigate F-43 'Liberal' of the Brazilian Navy.

Figure 1: Brazilian Navy Frigate F43 'Liberal [6]

Naval ships have structural shape & painting colors (normally Munsell scale 6.5N grey) related to the requirement to avoid being detected easily. Their system reliability and noisy propagation management are key as well, which is not the case for merchant ships, more focused on the economic feasibility of their operation and ownership. Figure 2 shows the special painting configuration of a naval ship during the Second World War.

Figure 2: special camouflage layout of a US naval vessel in the IIWW [7]

2.2.1.1 Surface ships

Among naval and merchant ships, there is another set called 'surface ships', or those which sail on the sea surface, facing two media (air and water) normally within a wave pattern. Surface ships are the most numerous categories and have a wide range of characteristics. Classic examples of surface ships are oil tankers, general cargo ships, transatlantic ships, trawlers, tugs, and others. They are made of a combination of steel,

wood, and polymeric materials mostly. The larger the surface ship, the heavier its structure. Figure 3 shows a standard large oil tanker.

Figure 3: a typical large oil tanker [8]

2.2.1.2 Submarines

Submarines make part of a special type of ship, due to its ability to dive several times along its operational life. When submerged, the submarine can navigate at higher speeds, in comparison to the condition at surface. This feature comes from the hydrodynamics details, while sailing in a homogeneous mean [9].

Nonetheless, submarine diving requires a safe and reliable set of systems and procedures, making submarines more expensive ships than surface ships, even with heavier displacement. Bottomline, submarines are complex ships, being used more for defense purposes than merchant applications, dealing with fatigue, noisy management, system redundancy, and other technical details, more carefully. As the sea exploration rises, in the search of different sources of raw materials, like minerals and food, civil applications of submarines have been in focus in the last decades. Figure 4 shows the Brazilian Navy submarine S-41 'Riachuelo', which has a conventional propulsion system.

Figure 4: Brazilian Navy S-40 'Riachuelo' submarine [10]

2.2.2 Oil Drilling Rigs

The discovery and exploration of oil sources at the bottom of the oceans has encourage the continuous design and development of oil drilling rigs in the last seventy years. They can be used to prospect and to extract oil to be stored in large oil tankers, being floatable or fixed depending on the application. Their operation requires manifold support systems, such as long mooring lines, support surface ships, among others.

In the energy transition trend, towards an environment with lower carbon signatures, the oil drilling rigs may have different applications, such as to support large ocean mining operations or as rescue bases in key positions in the middle of sea routes. Figure 5 presents a typical oil drilling rig operated for the Brazilian oil company Petrobras. This oil drilling rig is floatable (no structure link to the bottom of the sea) and sails like a vessel or ship. The materials used in its construction belong to the common list found in shipyards and shops dedicated to ships. Even the hardware focused on the oil exploration can use shipping construction materials.

Figure 5: a standard oil drilling rig used for Petrobras [11]

2.2.2.1 Drones

The expansion of the digital technology has motivated the development of unmanned systems, which show less risk for the human operations. Unmanned underwater systems and unmanned ships are a reality more and more, using digital signal processing in large scale with the application of artificial intelligence and machine learning tools. Drones used in maritime applications has been made of advanced polymeric materials, such as carbon and aramid fibers. Equally important, they also use advanced energy management systems, like high-capacity batteries.

Figure 6 helps to catch some details of an underwater drone used for environment surveys.
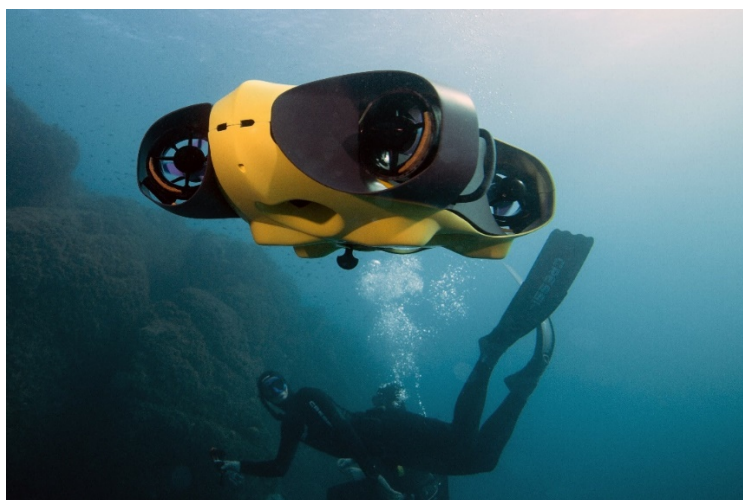
Figure 6: Drone used in underwater environment survey [12]

2.3 Ship general characteristics

As said above, ships can be clustered by its displacement or weight, measured in tons. The L-B-H dimensions have impact in the ship performance, evaluated by ratios, like: L/B, which is related to maneuverability, the B/H (ship stability), L/(displacement)$^{0.33}$ linked to the ship propulsion resistance. Reference [13] has more details about these ratios. These are more individual label for a boat.

For merchant ships the payload capacity and speed are most relevant due to economics. The weapons capacity and its types, autonomy and main purpose define the outline of the naval ships. For instance, the aircrafts (planes, helicopters, and drones) are the main weapons of an aircraft carrier. For strategic submarines, the long-range missiles, with nuclear weapons, are the main military asset.

Another way to categorize a ship is its structural pattern that can be longitudinal or transverse, considering the bow-stern axis. For small boats, there were longitudinal framing as a common sense. Nevertheless, the transverse framing is the current way to build-up the ship structure nowadays. For instance, submarines have circular ring steel structures, with circularity difference smaller than 3%, due to the compression loads while diving.

Figure 7 presents the two patterns of ship structures. Note the set of beams, longitudinal and transverse, making a grid where the spacing depends on the structure design criteria. In the outer part, metal plates close the spaces between the grid points. Bulkheads can be found transversally, segregating blocks and large parts of the ship, providing the longitudinal tightness. For bulkheads, the main structure design load is buckling (compressive loads) of metal sheets. Normally, the keel is the lowest and largest beam, laying longitudinally.
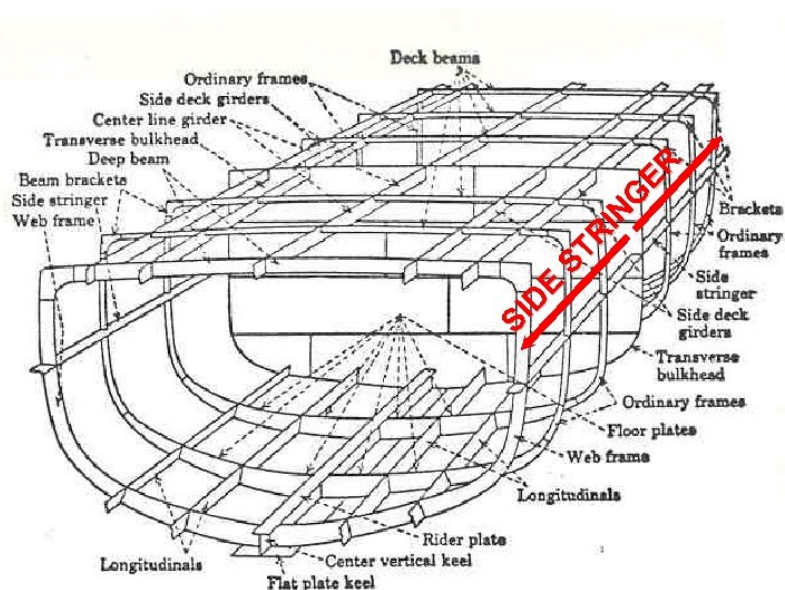
Figure 7: longitudinal and transverse framing patterns of ships [14]

Today ship construction is also based on modules, optimizing the construction schedules, done inside assembling buildings preferably to improve the fabrication quality. Figure 8 shows the assembling of ship structural blocks in a drydock, with tasks being done simultaneously.

Figure 8: Ship modular construction in a shipyard [15]

2.4 Overall ship design criterion

In a broad view, ships are taken as an integration of systems: structures, propulsion, electric, auxiliaries, navigation, and others. These systems are combined according to design techniques also present in the aerospace industry, by the design and review steps, trying to maximize the solutions to the common trade-offs.

In addition, the ship design also considers at its very start the examples done previously, as 'similar or reference' ships, to explore the best answers, practices and experiences achieved.

2.4.1 How a ship is designed

A classical method to design a ship is the convergence or 'spiral' technique. Once the overall technical requirements have been defined, the ship designer starts to define the main dimensions: L, B, H, displacement etc. Following the steps of Figure 9, at the end of each turn, the designer has a set of ship characteristics that differ smaller and smaller from the previous turns, if the design has been properly conducted. Design reviews take place at any moment to confirm this trend and the fulfilment of the technical requirements. For instance, the ship design need to consider different logistic chains, where some chains change more frequently than others, and this feature must be considered in the convergence indicated above.
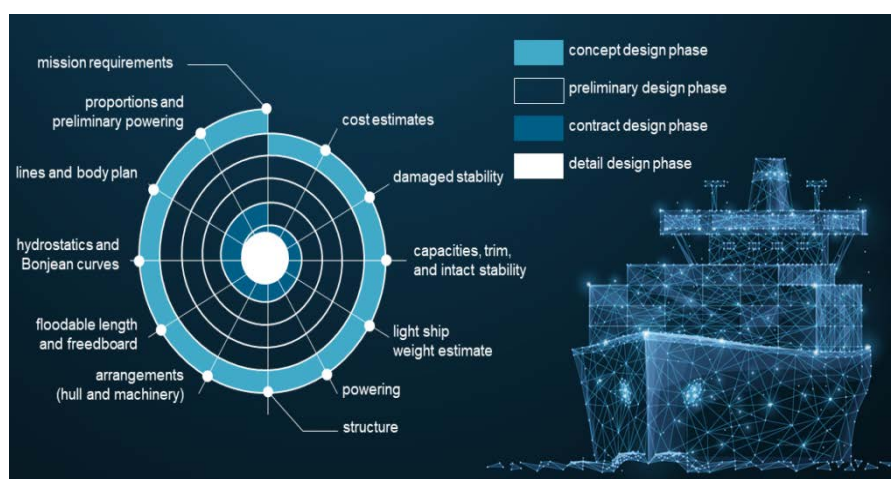
Figure 9: Spiral design scheme for ships [16]

2.4.2 Conceptual, Preliminary and Detailed Design

After receiving the general guidelines from the ship owner, the first stage is the conceptual design, when the design team has convergence of the main initial figures, according to main requirements, the technical rules selected, and the comparison to similar ships. Also in this step, the design team has an order of magnitude of the margins to be considered in the next phases.

Normally, as the design advances, the margins tend to decrease. At the end of the first phase, the line drawing of the ship will be done, allowing to check how the design cope with the stability and safety requirements. Figure 10 presents an example of a line drawing of an oil tanker.
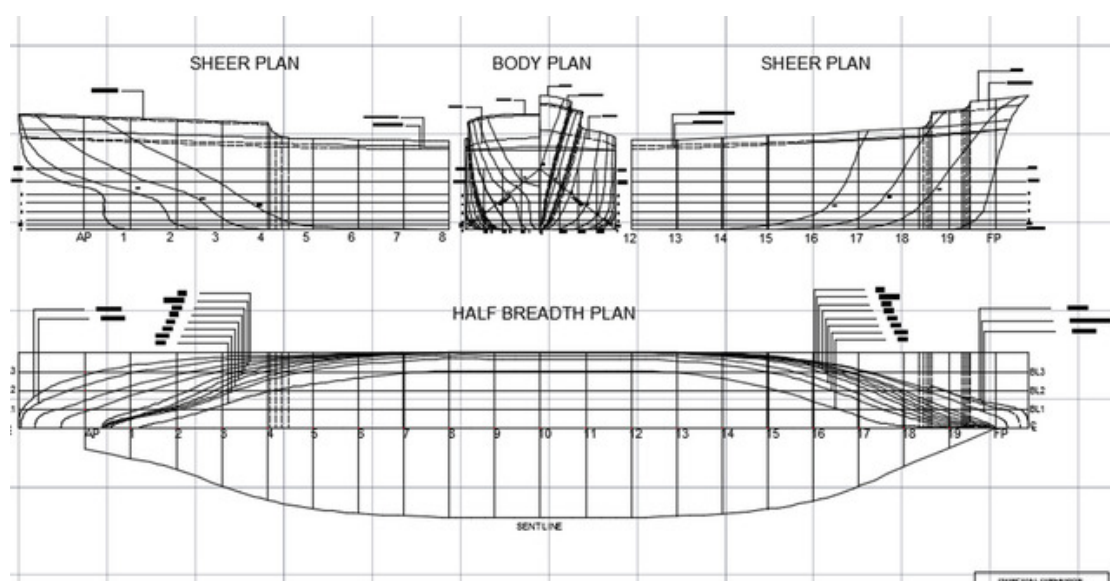
Figure 10: Ship lines or body plan of a cargo ship [17]

The upper part of the drawing shows the longitudinal view cuts of the ship, and, at the middle, there is a transverse view cut where the right side shows the fore section, towards the bow, and the left side the aft part, towards the stern. The lower part of the drawing shows a bird eye´s view and the cuts as horizontal planes, taken vertically.

The application of this drawings aims the determination of manifold ship parameters linked to the stability, the determination of the wet surface, the overall power required and surface and volume estimate to the quantity of metal sheets necessary for the shipyard construction. The drawing also allows to have a better insight of the number of metal blocks to be welded and, consequently, an first ideal about the ship cost.

In the preliminary design, the main systems of the ship have the hardware chosen, with a better figure of dimensions, weight, system performance and other technical features. For instance, the propulsion system will be quite defined in terms of power, fuel consumption, volume required, operational temperature range, brand of motors, size, and shape of the screw and so on.

The structures will have their size, materials selection, layout, weight, and others also defined, indicating the best construction techniques to be taken. In addition, the module construction scheme will be also clearly set. Thus, the approved preliminary design allows the ship owner to sign the construction contract with a shipyard.

The detailed design encompasses the construction steps in deep, defining all the wiring paths across the ship structures and bulkheads, the definition of the all the supports of motors, electric hardware, piping, the whole set of welding drawings and its procedures applicable to each structure, among others. Normally, the shipyard design team takes charge of the detailed design documents. The overall cost of the ship will have a clearer figure so far. The material purchase by the shipyard starts after the contract has been signed, with priority to the long lead items, or those with a long time to be delivered. As soon as the detailed design documents have been approved, the construction itself can start.

Even during the construction, the ship systems are tested, progressively, according to each technical specification. In the end, after the ship launching into the protected waters of the shipyard, the outfitting starts and continues towards the final tests, which take place with ship moored and at sea, before the acceptance by ship owner.

2.4.3 Availability, maintenability, acessability

For a shipping company, as well airlines, the main objective is to keep the transport mean (ship or airplane) in operation, integrated into logistic chains, action that sustain the profit and the business.

To carry on, the ships and auxiliary system must be available as much as possible, requiring constant attention to the maintenance types and all the intelligence behind.

In this matter, all hardware has its own code of maintenance, overhauling and updates, which must be managed by modern digital systems, including the purchase of spares, lubricating oils, inspection services, which now have more drones and robots than in the last decade. Therefore, the data management system handles a set of sensors, now with Internet of Things (IoT), providing blocks of measurements of technical variables along time, or time series.

In parallel, some material techniques also are considered, such as the management of material behavior as a function of time, and one of them is the Fracture Mechanics.

This field takes care to understand how a crack may appear and how it can propagate inside the crystal lattice or other material structures. Since the 50´s, a better knowledge of crack growth has used more and more laboratory testing, searching for the reasons for material failures and how to prevent or mitigate them. The shipping industry considers all this technical endeavor from the mechanical and material engineering fields.

2.4.4 Reliability-centered maintenance

For any main economic goal, profit rules the enterprise planning and execution and, among the strategic view, the maintenance phase demands special attention due to the probability of incidents and accidents, in case of catastrophic breakdowns, which will wind up as extra costs, turning down the profit margin in the end. By the way, it may fall into a vicious turnaround.

Therefore, once the enterprises can predict the maintenance required goals and metrics, as much as possible, the economic feasibility of systems, hardware and even software apply prediction models related to the reliability centered maintenance.

The main objective is to avoid failure and, equally important, to bound the operational associated costs by the early fault detection, as an example. Another task is the monitoring of the vibrations mode, allowing to assess the change in the whole set of natural frequencies, associating them to some specific system optimization in the end.

Most system engineers have in mind to describe the operational limits, and in this endeavor, they need to determine, or state, when a specific item or a set of items must be replaced.

One fair example is the aerospace industry, based on data collected from manifold sources. Accident analysis has provided indications on how a certain item, such as a shaft bearing or pump gasket, may crack down and provoke an accident/failure, after a spilling or initiating event. As a common sense, an incident or accident come from a sum up or combination of small causes, linked sequentially or by other arrangements. The reliability centered maintenance focuses the management of these details, allowing the maximum availability of hardware, system, or their combinations.

Reference [18] presents some insights about the use of Machine Learning or other digital tools for this aim. In that case, a Structural Monitoring System considers the pattern recognition technique, of cracks or other singularities, to assess how safe a structure has been. In a ship, this means to install a set of strain gauges in key spots, building up a strain measuring log, and to compare the results against a certain safety criterion, linked to the structural safety design approach. After some time of operation, the strain pattern will look up different from the start, due to the reasons discussed in previous items above (i.e. fatigue). The reliability centered maintenance approach compares the evolution of the strain pattern against recommend values gathered from laboratory testing, under the scope to avoid failure.

3 Ship & Marine Technology

3.1 Materials for ship construction

In modern shipbuilding industry, several kinds of materials have been used following the development of polymeric and metallic alloys mostly. Steels have dominated the field, where high tensile steel carbon steel (HTS) figures on the top.

Notwithstanding, the first ship built with steel dates from the end of the 18th Century, but the metallurgy processes at that time were more likely to the Middle Ages, when steel or cast iron were used to join ship wood parts as rivets. In the middle of the 19th Century, steel making improved with a more scientific and engineering approach with support of testing laboratories. With the improvement of the electric technology, during the 20th Century, steel making has matured, and welding has been the main technique to joint steel parts.

Nonetheless, Aluminum alloys, Copper-Nickel alloys, as well as carbon fibers, has their own niche. Take the example of the high-performance yachts, sailing with speeds higher than 30 knots (around 55 km/h), combining advanced concepts of aerodynamics and hydrodynamics, alongside an optimized materials selection. It is worth noting the use of several types of wood, combining resistance and lower density, in comparison to the metallic alloys, for specific applications and due to traditional reasons.

Take the example of a medium size aircraft carrier, with the displacement around 9.000 tons, which has almost 7.500 tons of steel (96% carbon and 4% stainless). The other 1.500 tons are composed by 1.100 tons of copper alloys and 400 tons of Aluminum. The small quantity of stainless steel avoids the fabrication cost to reach stratospheric levels.

The key material properties required for general ship hull applications are high strength, corrosion resistance, fatigue resistance and good ductility for fabrication processes. Thinking on the steels, the only answer for this requirement is low carbon alloys. Table 2 presents the most common alloys selected for ship structure applications.

Table 2: Carbon steel alloys for hull structures

Steel Codification	Yield strength min (MPa)	Tensile strength min (MPa)	Elongation (min) (%)	Main composition C-Mn-Si (%)
A	230	450	22	0.22-3.0-0.3
B	230	450	22	0.21-0.6-0.3
D	230	450	22	0.21-0.6-0.3
A32	310	550	22	0.18-1.2-0.4
A36	350	600	21	0.18-1.3-0.4

Take a common steel alloy used in the automotive industry, the HTS has a mechanical strength 5 times higher, while the ductility shows a ratio of 4.

However, when dealing with submarine hull structures, where the safety factor remains around 1.5-1.8, and the fabrication requirements are tighter than those from the surface ships, other alloys are used, known as high strength low alloy (HSLA) or high yield alloy (HY).

In terms of material stress, due to technical requirements, the design of ship structures normally requires staying at most around the elastic yield, with few cases inside the inelastic field of the materials. Some technical rules are based on the Von Mises design criterion, but others are based on the Tresca criterion.

The materials above deal with the main structure of the ships, or the structure responsible for the ship tightness. For inner structures, known as secondary or even tertiary, with a smaller ship tightness impact, other materials may be used, looking for the affordable economics too. Nonetheless, the designer must have attention in the materials compatibility to avoid corrosion stresses, due to "chemical pile" activation.

One famous example are some naval ships, built during the 60´s and 70's, where the main hull used carbon steel plates, but the superstructure was made with Aluminum alloys, taking the concept to reduce the overall displacement. Consequently, some stress corrosion developed forcing costly repair in the end.

Another interesting case is the screw or propeller, where the conditions above are magnified. Summing all of them up, the copper alloy can withstand the intense corrosive effects of saltwater.

As the propellers have special shapes, following helix lines, with varied thicknesses, ductility has a strong importance, alongside the obvious corrosion resistance. Common rotation speeds fall within 60 and 100 rpms, shaping up a low cycle fatigue case.

Cavitation is a phenomenon to prevent during high propeller speeds because it causes erosion due to implosion of vapor bubbles generated on the blades.

The roughness of the blades serve as an initiation spot for the occurrence of cavitation and the blade surface finishing demands a constant attention. The most common propeller materials are shown in Table 3.

Table 3: materials used in ship or submarine propellers

Alloy Codification	Yield strength min (MPa)	Tensile strength min (MPa)	Elongation (min) (%)	Main composition (%)
Cooper-Aluminum	200	500	20	60Cu-2Al-3Mn
Cooper-Aluminum-Nickel	180	500	30	9Al-4Ni-2Fe
Stainless Steel	550	850	15	13Cr-4Ni-0.06C
Sonoston	270	570	25	36Mn-3.5Cu-3Al
Carbon Fiber	3000	4.000	2	---

One of these alloys of special application is the Sonoston, developed in the 60´s with high damping and mechanical strength, for many applications including military ships.

In ship screws, it is not possible to impose external damping appendices, while handling general vibration issues.

One of the solutions is to use alloys such as Sonoston, based on Manganese, with a mechanical damping capacity over 20 times of other metallic alloys.

The Sonoston alloy also shows a ductile fracture profile with temperatures below -100°C.

Stress corrosion crack can be observed, and it turns to be a disadvantage, but with thicker parts and suitable anodic protection, this drawback has been managed satisfactorily [19].

In the nuclear propulsion, the materials selection takes other boundary conditions, due to the radiation effects, higher stress fields and the risk management.

In more than 95% of the nuclear-powered ships, mostly submarines nowadays, the pressurized water reactor (PWR) is used, where the primary circuit operates with pressures around 150 atm, and the secondary circuit (Rankine cycle) works with pressures of 60 atm.

Due to the flow of cooling and neutronic moderator agents (light water), which induces vibration in the nuclear fuel, fatigue resistance plays a key role too.

Moreover, most of the hardware is designed not to be changed during the ship lifespan, closer to 30 years, requiring thus a high reliability and endurance standard.

For instance, the primary circuit pump is designed to last for 30 years or more, dealing with high pressure, transients, and high fatigue cycle.

On the other hand, in the same energy system, the piping also deals with high pressure, transients, but in a lower fatigue cycle.

Table 4 summarizes the key materials used in the primary circuit of a typical PWR reactor for nuclear propulsion.

Table 4: Common materials used in PWR circuits of nuclear propulsion

Hardware	Material	Yield Strength (MPa)	Mechanical Strength (MPa)	Elongation (%)
Reactor Vessel	SA504 or SS304L	200	500	40
Reactor Internals	SS 304/347/316	200	500	40
Fuel Cladding	Zr-4, Zr alloys	380	500	30
Main Pipe	SS 304/316	200	500	40
Steam generator tubes	600MA or 690TT (325 ^{o}C)	220	570	46
Steam generator shell	Low Carbon Steel	300	600	30

To present more details, Figure 11 shows most of the materials used in the primary circuit, which deals with the nuclear fuel elements, and in the secondary circuit, more specific to generate steam and use it to produce propulsion power or electricity.

Note the vertical border line, which separates the two circuits, also showing the containment limits, regarding pressure and nuclear material tightness.

Although the picture shows 'carbon steel' for the pipelines in the secondary circuit, nowadays 'stainless steel' has been used instead.

Due to the technical requirements, few components inside the primary circuit need to be exchanged during the nuclear facility lifespan.

The classical example is the steam generator, the largest item near the border line, which deals with two pressure loads or, approximately, 150 atm in the primary side, and 60 atm in the secondary circuit. It normally shows problems related to corrosion (e.g., stress-corrosion cracking).

In some extent, the pressurizer also may show corrosion issues, normally associated to the two-phase regime (water-steam) operating condition.
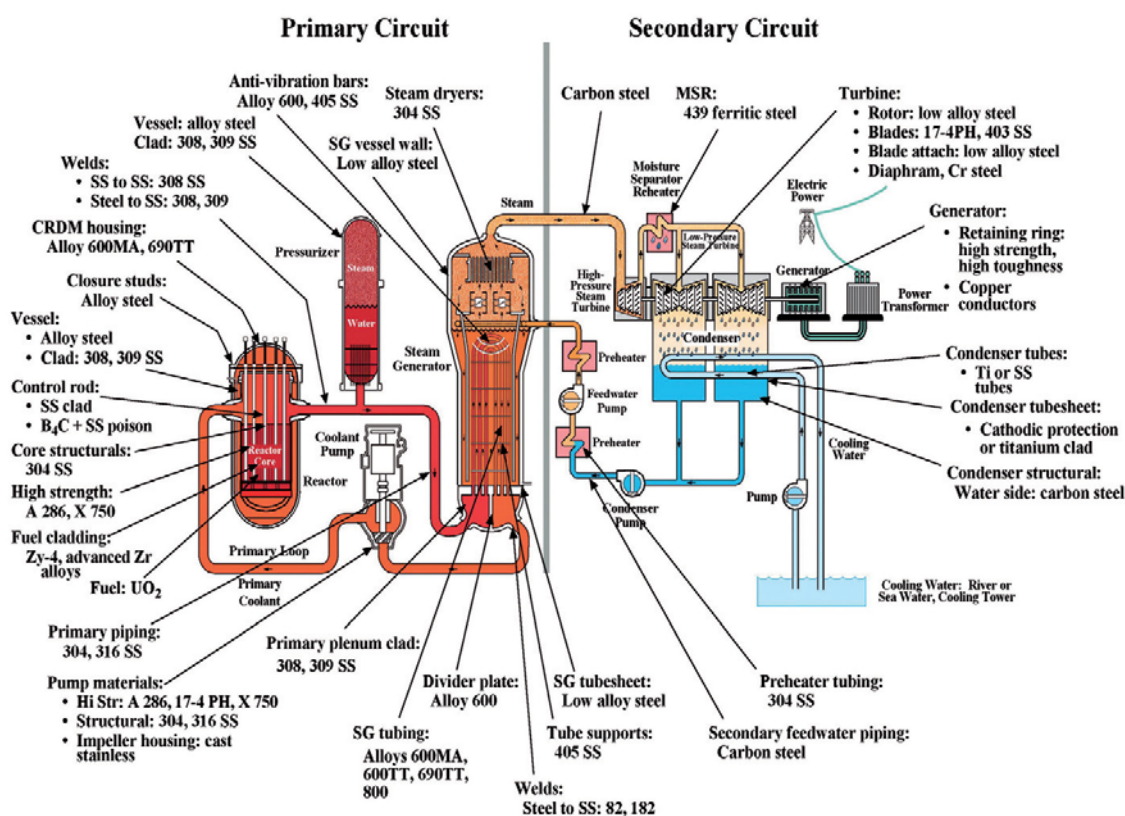
Figure 11: materials among equipment of the primary and secondary circuits [20]

3.2 Ship construction and manufacturing processes

3.2.1 Testing – material characterization

As required by industrial design codes, within the quality control sphere, materials must be checked against their real properties, before allowing their use in fabrication or construction.

In other words, the materials must have its properties within the code range. Thus, material properties are confirmed with the testing of samples.

The American Society of Testing Materials (ASTM) is an example of standard to be considered in this matter, alongside the American Society of Mechanical Engineers (ASME), which focuses the hardware design (e.g., structures, pumps etc.).

Due to reasons related to the safety, reliability and insurance, the material characterization has a high importance, to protect the environment and to avoid huge losses in court disputes.

In the shipbuilding industry, the American Bureau of Shipping (ABS) has its own standards applicable to boats and ships.

Other best-know classification societies are Lloyd´s Register (UK), Det Norske Veritas Germanischer Lloyd (Germany) and Bureau Veritas (France).

For instance, ships with cryogenic or low temperature tanks, for the transport of liquified fuels or special substances, such as acids, the presence of Silicon (Si) in carbon steels must be low and tightly controlled, to avoid brittle failures.

The main material tests applicable to the shipbuilding industry are:
- Chemical composition
- Tensile strength test
- Charpy / Izod test
- Transition temperature test

3.2.2 Welding

Welding is the most common bond process used in ship construction, focusing metallic joints. The Welding Handbook is published by the American Welding Society (AWS) and describes the welding techniques in detail, where the thermal flux management is fundamental for the material properties changes.

During the welding, high heat flux goes throughout the material thickness, making crystal modifications like the heat treatment processes.

In case of a fast cooling of the weld joint, the local material hardness may increase beyond the acceptable levels. Thus, the temperature transient in the weld joint can affect the local mechanical strength and ductility, towards the crack inception and material failure unfortunately.

3.2.2.1 Heat Affected Zone (HAZ)

In the welding processes used in the shipbuilding, due the phenomenon briefly described above, the HAZ is a key factor to be controlled. The American Welding Society (AWS) has technical guidelines on this matter and the HAZ shows its relevance in the hull construction of submarines and reactor pressure vessels. Reference [21] has more data to get deeper.

Figure 12 presents a combination of graphs: on the left-hand side, it shows the steel microstructures developed from the join center position, or the place of the peak temperature.

These microstructures come from different heat transfer pattern and temperature profile as a function of time. On the right-hand side, there is the phase diagram of a typical low carbon steel. The vertical axis shows the temperature, and the horizontal axel has the Carbon concentration (%).

Near the welding joint, there is a set of 5 types of microstructures, which one with different mechanical properties, then with a heterogeneous material profile. This fact must be considered in the mechanical design, to cope with the worst-case scenario for the safety factor. That is the main reason to take heat treatment for welding of thick steel plates, such as the ones present in shipbuilding, to make the material more homogeneous after the welding.

Another solution focuses the use of alloy carbon steel, to handle the lack of homogeneity from the heat flux and temperature distribution.
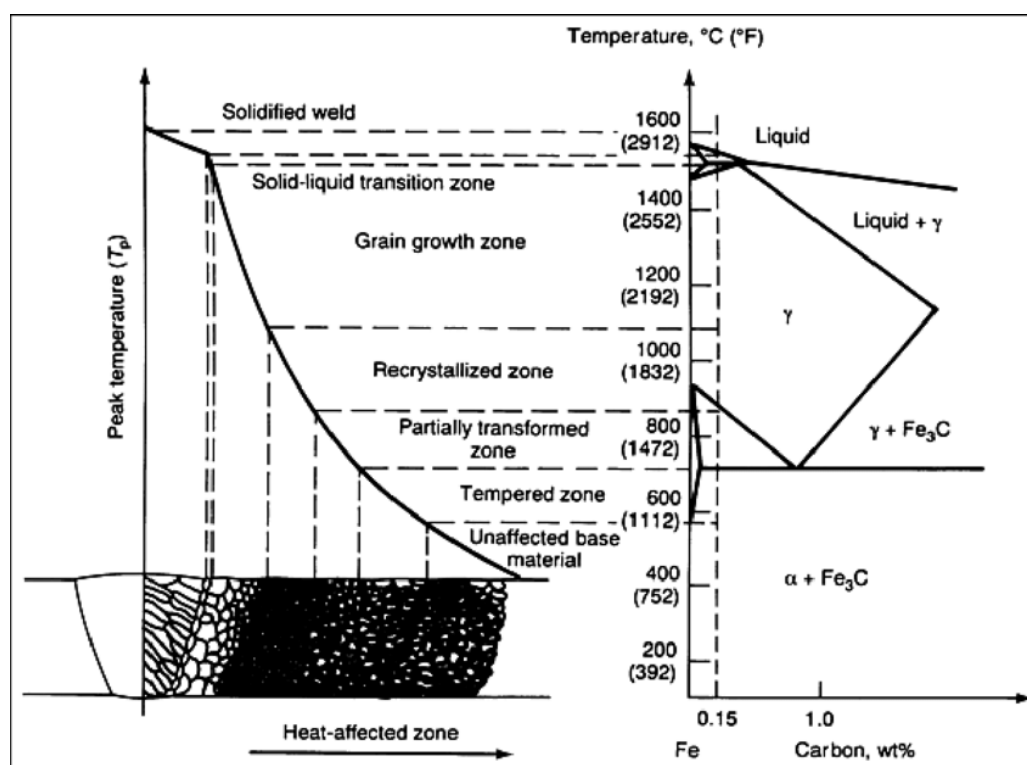
Figure 12: the HAZ typical weld contour [21]

3.2.3 Plate rolling

Most of the steel parts in a ship starts from a plate geometry made with a set of thicknesses and dimensions.

The plates are made in the steel factory by plate rolling, using large cylinders, or rollers, under compression loads on the steel flowing, which is already solid but with temperatures close to the transition threshold, showing a vivid orange reddish color.

This operation sets some residual stresses on the material, after some operations such as quenching, and thus annealing also takes place to handle the final mechanical properties.

3.2.4 Cutting

Prior to any further operation, the steel plates need to be cut into shapes closer to the final geometries required to make up the structural components. In this operation, the steel plates geometries are checked against the optimal scheme to generate the least quantity of material disposal, as also seen in the clothing industry.

Depending on the thickness, several cutting tools can be used, such as gas torch or plasma technology, normally underwater this last one. The main concept is to dim the microstructure are affected by these processes, preserving the material as homogenous as possible. It is worth noting this kind of detail is taken since the preliminary design, allowing dimensions and margins related to the optimization of the whole set of materials.

3.2.5 Bending

As used in mechanical structures of different sizes, the bending process is responsible to produce any sort of curved shapes, mainly in the bow (fore) and stern (aft) ship areas. In addition, bending is used in the resistant hull transition geometries, from the bottom (horizontal) to the main deck (vertical). This shipbuilding application has a strong link with the same applicable in the automotive industry. Normally, the steel plate thickness for the shipbuilding industry remains closer to 2 inches or 50 mm, which must be considered when planning the bend operation. Figure 13 shows the bend structures normally found in oil tankers ships.

Figure 13: Bend plates for oil tanker ships [22]

3.2.6 Machining

In the same fashion of large mechanical structures, machining is quite present for plate preparation to welding. In this case, the notch between two plates must have its shape according to the detailed design. The notch is produced by the machining the two plates. Propulsion shafts are also machined following the detailed design, considering assembling clearances and the softening of sharp corners, to prevent cracks from stress concentration and fatigue.

3.2.7 Metal forming

In some special parts of the ships, with special geometries formats, the metal forming is required, with the application of pressing for instance. The classical case comes from the spheric tanks used to transport liquified substances, such as natural gas, because with this format, the internal stresses are smaller, with lighter structures too. The bow structural hull of submarines is also made by pressing of carbon steel alloys, in small parts to be welded and assembled in the final stage of the manufacturing.

Another example is forging, which is seen for instance in the fabrication of propulsion shafts or assembling bases of heavy hardware, such as the diesel engines for large oil tankers. These engines have peculiar characteristics like large dimensions and weight around tens of tons, using thus just one per ship.

3.2.8 Additive processes

With the technology advance of the polymeric materials, mainly for high tech sailing, additive techniques have been used in the construction of advanced boats, following the aerospace industry trends. Modern outfitting techniques, used for small internal items, can been seen with the use of bonding procedures.

3.3 Main ship systems

As an integration of several hardware, a Work Breakdown System (WBS) helps to present an overall view of the main ship systems. According to Reference [23], the main ship systems are known as:
a) Structures
b) Propulsion
c) Electric
d) Auxiliaries

The ship structures consist of a set of supports and resistant components, requiring monitoring, inspection, and maintenance, like the other systems.

The propulsion components also make a system division because they cover several types of energy management details, using different types of fluids and mechanical parts, and more recently, advanced digital control techniques.

A specific field is dedicated to the electricity, covering subjects as electric motors and generators, automation, switchboards, power converters.

Finally, the auxiliaries take care of all other systems, such as ventilation, air conditioning, hydraulics, steering devices, damage control items.

Additional ship system division may be set, depending on the logistic or management needs.

3.4 Ship structural load profiles

In short words, the main ship structure can be taken as a metallic beam, in a closed profile, being thus a hyperstatic structure. For sea going ships, the main structural load comes from:
• the overall displacement, according to the weight internal arrangement.
• the sea wave patterns, mainly during high seas and storms.
• the propulsion resistance, more significant at high speeds.
• The ship maneuvers, in high angle turns.

In some special cases, specific loads can be observed during the take-off and landing of aircrafts, weapons launching and towing operations, which are kind of common for the naval ships. Specifically, submarines have a more homogenous structure load profile once they go underwater most of the time. The compressive load varies with the diving depth. In general, modern submarines can sail at 300 m deep, corresponding to an external pressure of 30 atm roughly.

3.4.1 Wave loads

The simplest wave configuration faced by the ship structure can be seen in Figure 14, with two cases basically. With the concept said above, the 'ship beam' can have a tension, or compression, distribution leading the main stress profile, due to the buoyancy.
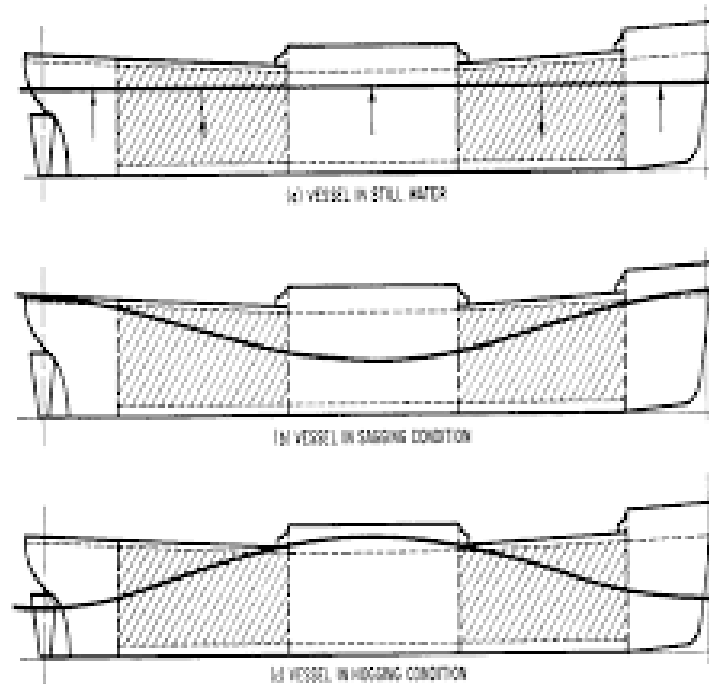
Figure 14: Buoyance wave loads to ship structures [24]

As the buoyance varies along the ship length, according to the wave pattern, the structural stress also changes. In the first picture, the load is equally distributed along the ship length, in a homogeneous fashion, and the structural stress seems quite uniform along the ship length. Nonetheless, as seen on the second picture, the extreme parts of the hull (bow and stern) have more buoyancy and the main hull section (midships) has lower buoyancy. The hull can be taken as bean with tension in the lower part and compression in the upper part. From the last picture, the opposite occurs, alternating the stress profile, typical framework for a fatigue analysis (low cycle).

3.4.2 Other loads

Another way to compute the external load, comes from the water column at every point of the ship structure, which is more relevant in underwater structures, such as submarines, drones and some oil drilling rigs. Winds also represent a key load, mainly for high superstructures, seen in transatlantic ships, figuring around 20.000 m2 or 3 soccer fields, or even more. All the loads above have a transient behavior, varying in time and inducing the fatigue.

3.5 Types of ship structural failures

3.5.1 Corrosion

As the sea environment is rich in Oxygen, with salt and dirty, in some cases, the corrosion process is present to all metal structures of a ship. This feature makes corrosion a constant preoccupation in the shipping industry to prevent stresses beyond the design. As a general guideline, the ship structures have over dimensioned thicknesses to consider lifespans of 30 years or more, even with careful painting and maintenance. Make note that the corrosion product must be taken away, using abrasive methods, which decreases the ship plate thickness. Figure 15 shows a typical corrosion profile present in ship hulls. The reddish spots represent the corrosion at high stage or degradation. The dark lane closer to the water line has marine life accumulation on the hull, also a contributing factor for the corrosion. The vertical black items near the bow are the ship anchors, also experimenting corrosion with middle stage pattern approximately.
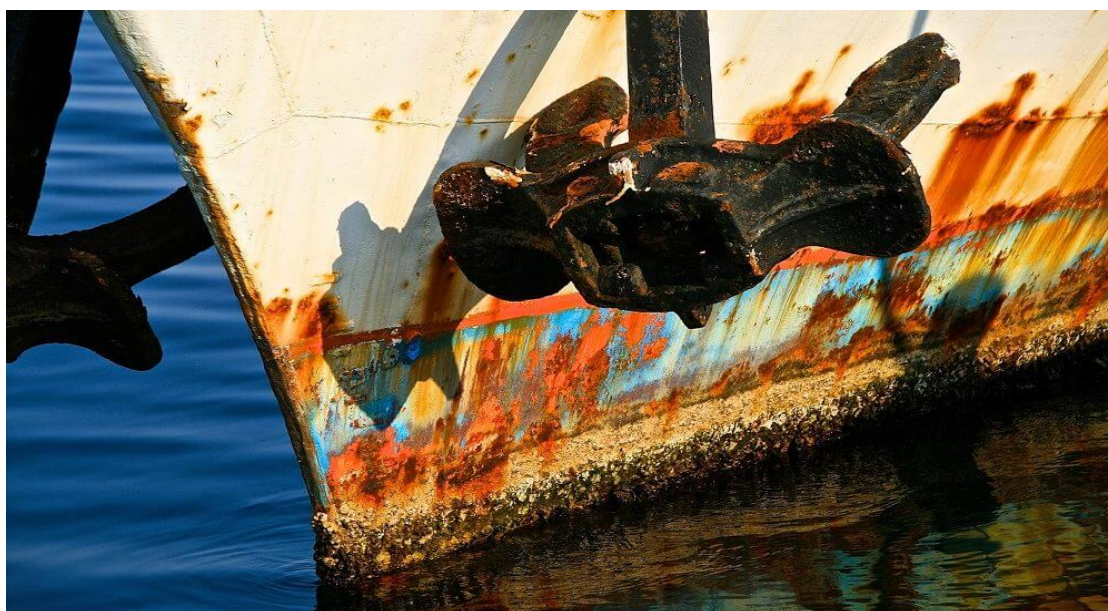
Figure 15: typical hull corrosion stages [25]

3.5.2 Fretting

This kind of failure links between rough surfaces and wear/ corrosion. The wear phenomenon requires a relative motion between surfaces under contact, originating then high levels of roughness, which is one of the sources for cracks, specially at high speeds.

Thus, fatigue can be present under fretting situations too when the fatigue cracks appear at fretting zones. In ships, it is possible to have this failure in rotating parts, such as axles and bearings, due to poor lubrication or maintenance.

As these parts are made of steels, fretting can be confirmed by the presence of pits and fine red dust, on the contact surfaces, which are related to oxides formed during the increasing of wear.

Figure 16 shows some of indications of fretting in a ship propulsion shaft, at the joint flange with screws. On the upper right-hand side, there are nuts and bolts attached to the flange. In the middle, there are two empty holes, showing traces of fretting, pits, and red dust.

The ship shaft is a forged component, machined to handle the geometry changes, like the holes and flanges. Note the light line transition from the horizontal position to the vertical one, where the nuts and bolts are shown. This light transition helps to avoid stress concentration near the shaft joint.

Figure 16: example of fretting in a ship shaft [25]

3.2.3 Fatigue

The ship dynamic load profiles seen in different conditions provoke fatigue failures.

There are two major cases: low cycle and high cycle [26], which need to be taken while composing the structural stress, according to different boundary conditions, such as local load profile, stress concentration, temperature conditions, material composition, welding geometries and so on.

The overview also considers the classic form to address fatigue throughout the evaluation of data from the failure stress against the number of operation cycles.

3.5.3.1 Low-cycle / strain-based fatigue

This situation is observed in the ship main hull, mostly closer to special configurations, normally linked to stress concentration, which happens in welded joints. The low cycle range can be set as lower than 10^4 number of cycles.

Depending on the shape and stress profile, low cycle fatigue may set the material into the plastic regime, which requires a special approach to prevent failure and to forecast the material lifespan.

Reference [27] presents a suitable reasoning to address this low cycle condition. The strain indicator takes the elastic and plastic regimes together, by summing up each contribution.

It also focuses the welding joints as the worst case to be studied, due to the HAZ detected, basing on testing and empiric relations for shipbuilding steels. Figure 17 presents some results related to marine structures low-cycle fatigue. The dots on the upper part of the figure come from mechanical testing, and the order of cycle magnitude is closer to 10.000. It is worth noting the dark points were made with welded specimen of the material, with a lower stress strength, in comparison to the base material.

In the figure two other limit lines are also shown: the elastic strain-life, closer to the fatigue curve, converging to the same stress limit, for higher cycles, and the plastic strain-life, straight down to the end life limit of 105 cycles approximately. The term 'SSC-346' stands for a ship structural committee nr 346, from the US Government (1990), dealing with fatigue characterization of ship fabricated details.
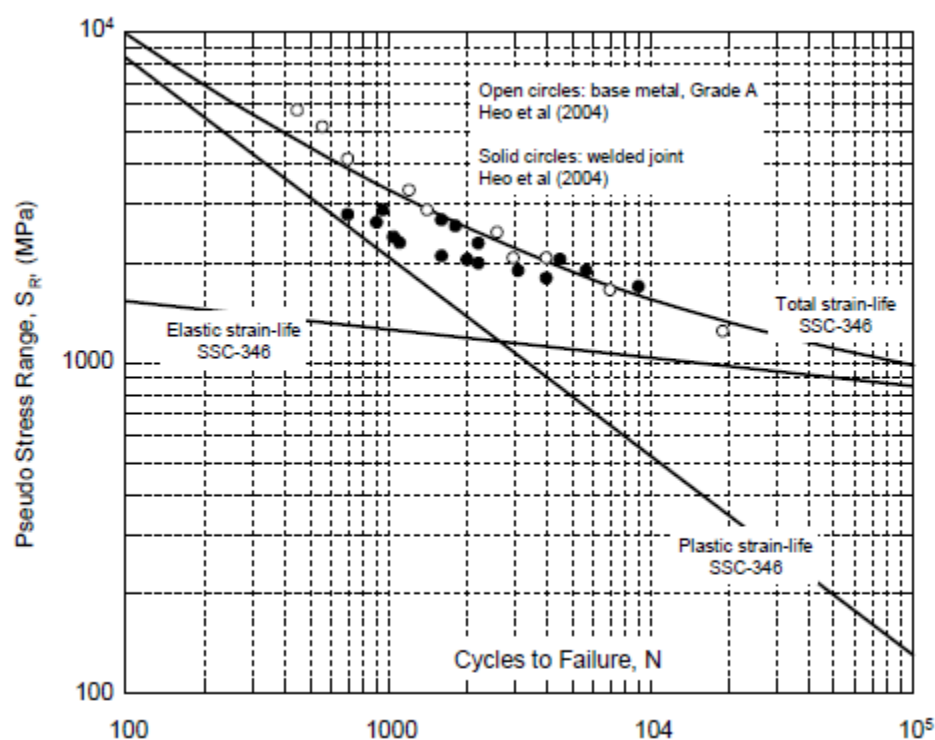
Figure 17: typical strain-based low-cycle fatigue [27]

3.5.3.2 High-cycle / cycle-based fatigue

This case deals with the hardware found in the propulsion systems, like propulsion motors, pumps, air compressors, but it can also be seen in structural items. High cycle fatigue is assumed for work patterns above 10^5 cycles and it is also common to consider a very high cycle fatigue when dealing above 10^7 cycles. Reference [28] covers most of the details related to high cycle fatigue, including the fractography. In a general sense, high cycle fatigue is linked to tough failure mechanisms. Figure 18 shows a comparison of different materials and their behavior under high cycle fatigue, indicating the shipbuilding cases (A36 and other structural steels). Note that the alloy steel 4340 (0.4% of Carbon) exhibits a 100% higher fatigue strength than classical structural steels, and some specimen did not fail at 10^7 cycles or more.
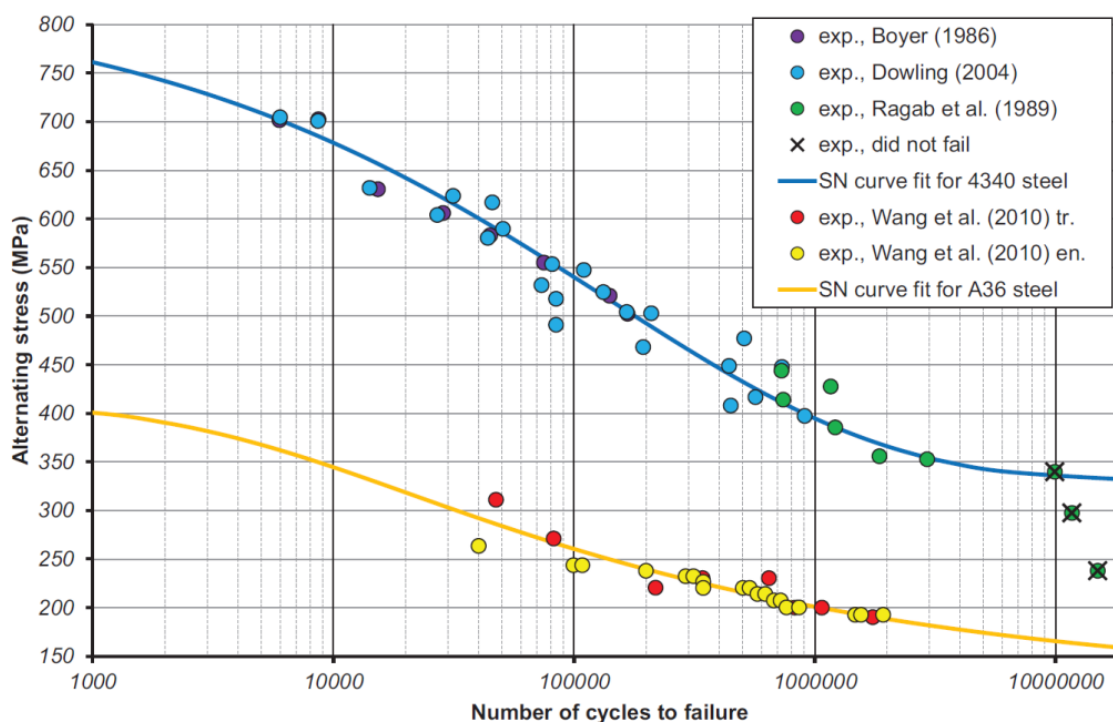
Figure 18: typical high cycle fatigue [28]

3.5.4 Hydrogen embrittlement

Hydrogen is the smallest and lightest atom and thus, as an ion H^+, it can have high mobility throughout crystal planes of metallic materials. Therefore, the diffusion of Hydrogen reveals quite easy when the concentration difference and temperature conditions are present.

As a matter of fact, this diffusion of Hydrogen is reversible consequently and, at room temperatures, it takes order of minutes to happen. In a few words, the presence of Hydrogen produces 'hydrides', which are brittle, inside the crystal lattice (interstitial), inducing the material failure because, when diffused into metallic matrices, this introduces brittle clusters, weakening the material toughness. Three major conditions favor this phenomenon: stress, a Hydrogen source, and the susceptibility of the target material. Note that it is a low temperature phenomenon for steels, which are not affected by Hydrogen embrittlement above of 150°C. All these can be found in ship structures once salt water is a fair source of Hydrogen and other ions.

Figure 19 shows a stress-strain graph (in the middle) and four associated metallography details, regarding the evolution of hydrogen embrittlement, during a effort to use heat treatment as a way to reduce the damage from the phenomenon. In this study, the authors propose to use 'selective laser melting' (SLM) to change the metal structure locally to increase the hydrogen embrittlement resistance. They also propose to carry on a heat treatment (annealing) with the SLM. The idea is to produce materials with the curves in the upper part of the tension test result, rather than the ones in the left lower corner.
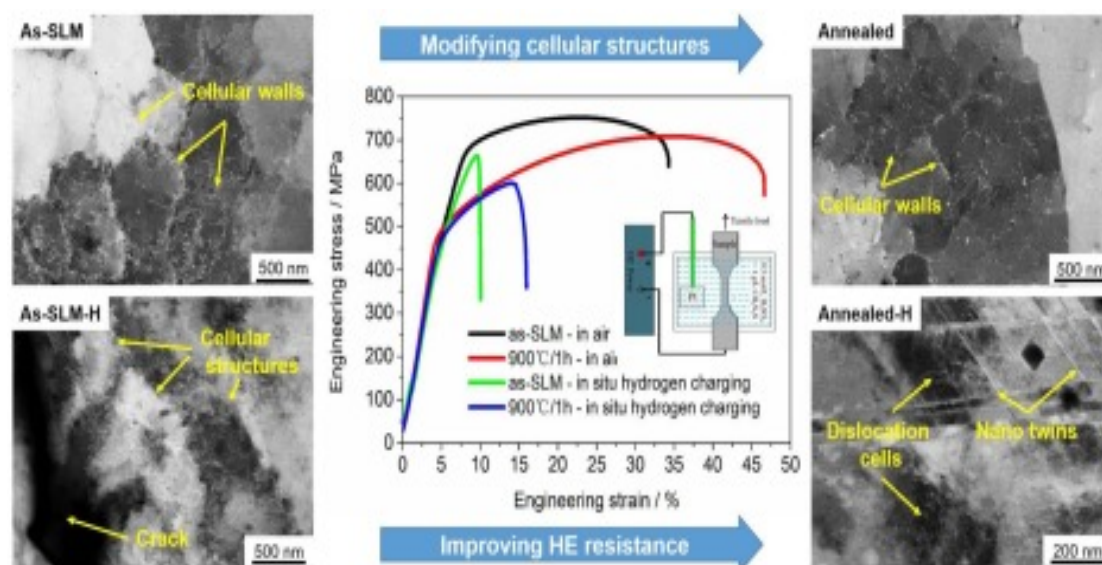
Figure 19: hydrogen embrittlement metallography [29]

During the processing of metal plates at shipyards or factories, the operations of rolling, forming, coating, or cleaning may also introduce Hydrogen as described above, due to poor quality control techniques. The presence of dirty, inadequate, or damp materials in the fabrication line can be a Hydrogen diffusion source, which diffuses due to bad electroplating control. As seen in many industrial applications for high quality welding, the electrodes used in shipyards must have a low Hydrogen content and must be kept at controlled atmosphere (special casing or barns), avoiding moisture or other sources of Hydrogen. Any electric source can also start the Hydrogen diffusion and, therefore, galvanic corrosion needs attention to prevent the phenomenon.

3.5.5 Transition temperature failures

Metallic alloys exhibit a change in their ductility while the operating temperature changes, in direct relation or as the temperature lows so does the ductility. Nonetheless, this modification is not proportion, rather it shows a step profile. The temperature associated to this step start up (down) is called transition temperature. This phenomenon requires attention when dealing with structures facing low operating temperatures, such as cryogenic systems or polar navigation. In short words, above the transition temperature, the metal has a ductile behavior, as the strain follows the load application, as discussed previously. For temperatures below the transition threshold, the failure becomes 'tough' or no pre-sign of crack down can be detected, to avoid the total material collapse. Thus, the transition temperature demands special attention to ensure the suitable operating structure envelope.

3.5.5.1 Liberty ships

These ships were constructed in WWII to transport goods and soldiers between North America and Europe and had a cargo capacity of almost 11.000 ton. Based on a British design, they symbolized a classical example of the huge industrial potential of the USA at that time, mobilizing 18 shipyards and a total of 2700 ships, making 4 ships per day as mean rate.

The American design considered welding in the place of rivets, originally designed by the British. Due to poor quality control actions, the employment of non-skilled workers, and other minor causes, some Liberty ships faced fatal cracks, evaluated as brittle failures.

The North Atlantic Ocean has severe conditions in terms of wave and wind loads, besides lower temperatures during the winter. Therefore, the transition temperature mechanism influenced the material behavior, or temperatures lower than the critical ductile-brittle transition zone.

The same phenomenon was already observed in some ships which operated in the Great Lakes, between Canada and the EUA, once the region shows normally very low temperatures in winter normally. Figure 20 shows of the damaged Liberty ships.
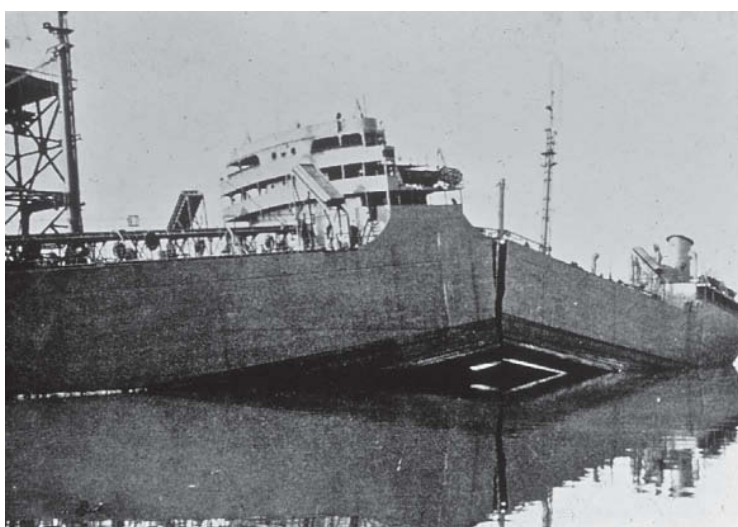
Figure 20: A damaged Liberty ship due to hull cracking [30]

The cracks were originated in regions typically of stress-concentration, such as hatch corners. Additional causes for these failures were overweight and storms beyond the design envelope.

The whole structural design was then redone, widening the space between beams, making the ship less stiff and flexible enough to absorb strain in severe conditions. In addition, the transition temperature of the alloy steel was then dimmed to levels below the North Atlantic harsh conditions.

Figure 21, from the US Naval Research Laboratory [31], shows some technical hints of the importance of the transition temperature on steel alloys, after keeping in mind that above the transition temperature the material will have a ductile behavior, which goes towards a safer way.
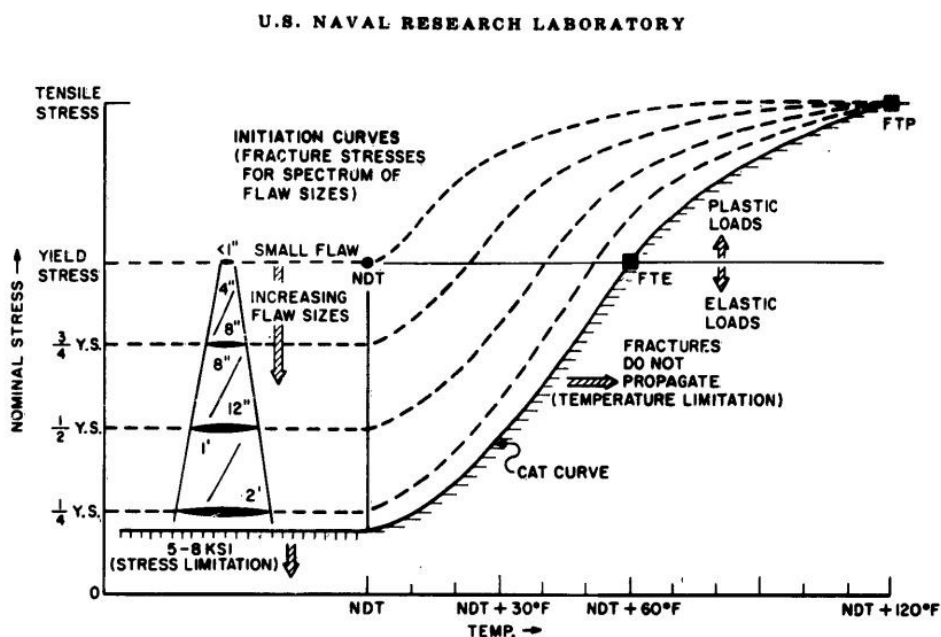
Fig. 9 — Generalized fracture analysis diagram, as referenced by the NDT temperature

Figure 21: the transition temperature curve [31]

The temperatures are represented in the horizontal axis and the nominal tensile testing stresses are shown in the vertical axis. As well known, the Yield stress represents the threshold between the elastic and plastic strain regimes.

Below the transition temperature, the material behavior will close to the tough category, and the higher the tensile load the faster a small crack will propagate (see the upper left corner of the picture), in opposition to a lower the tensile load (lower left corner respectively).

Trends in material selection for ship construction

The herald of an energy transition move indicates the substitution of the fossil fuels in the shipping industry and, consequently, the ship structures and materials already ask for more advance techniques linked to lighter and more reliable structures and systems.

The use of electric power shows to manage a set of advantages when reducing the CO_2 footprint, although further development has been required for the batteries and energy management systems. Nanomaterials have shown a favorable way to be spread into the ship materials sphere, allowing a more precise property build up and selection, mainly to hull paints and covers.

The lighter ship structure will ask for lower propulsion power, for the same payload, and the polymeric materials present an advantage at a large. The development of systems to handle the Hydrogen has its place in the shipping technologies, strengthening the possibilities of the electric ship power. Some ships can burn liquified natural gas (LNG), which is not so environmental aggressive as other fossil fuels, but it requires special safety measures to prevent explosion and fires aboard.

The integration of different power forms, such as screw and modern sails, can save money in time during this transition. For instance, the steel making industry has researched greener ways to operate furnaces and the whole logistic and factory chains, managing the wastes (thermal and material) more carefully (e.g., using more heat recovery techniques). This initiative adds a smaller CO_2 footprint to the shipping industry as well.

3.5.6 Structural reliability

In modern structural design, the use of probability models has increased to save resources, lives and to a better environmental protection, because the data management has improved with the use of larger digital computing engineering. Therefore, the structural reliability has better profiles and continues to be expressed as the complement of the failure probability, or structure reliability equals to (1 – structure failure probability). As a result, structural reliability becomes more and more a design philosophy taking the place of the deterministic methods, being also applicable to the structural maintenance.

The core of the ship structural reliability is to handle the set of uncertainties found in the ship construction, operation, and maintenance. These uncertainties lie on the variability of the material composition, processing (where welding has a main contribution) and degradation (here oxidation/corrosion leads). Due to the large number of factors, it has been a place to use statistic models to predict the material failure, in different orders of math complexity.

As an example, the combination of two different materials, such as steel and Aluminum, or the impact of ice into ships not designed for it put together different approaches when dealing with ship structural reliability. Also worth noting, the use of accelerometers with wireless digital networks grabs data from hot spots to feed up statistical methods, and the Machine Learning and Artificial Intelligence tools to provide a quick overview of the hull reliability.

Another example of material reliability assessment comes from the nuclear material selection aiming the primary circuit conditions, or the materials closer to the nuclear core. To cool down the nuclear fuel elements and to extract the heat produced by the fission reaction chain, light water is used in most of the reactors.

Therefore, the materials will face a water medium under nuclear fluence, measured in terms of number of neutrons per square centimeters (n/cm^2). This last characteristic comes from the integration of the neutron flux ($n/cm^2.s$) over time, where one core can last for say 30 months or more, depending on the nuclear materials selected and actual power profile. During the fission, high energy particles are released from the core and produce heavy impact in the structural materials. The operational and economic performance of a reactor comes from the reactor core performance and its interaction with all the surrounding materials.

Stress corrosion cracking has presented problems in reactor materials reliability, when dealing with alloys such as the 600 and 152, they have a high corrosion resistance tough. These alloys also have a thermal expansion coefficient like the carbon steel, which is the main material of the reactor pressure vessel, and it is advisable to use materials with the same expansion coefficient, to prevent strain or dissimilar deformations due to the temperature.

In the last forty years, these alloys have been used but shown early cracks impeding the reactor economics. The Electric Power Institute (EPRI/USA) has conducted a series of laboratory testing regarding the stress corrosion cracking in pressurized water reactors, mainly to assess what metallic alloys will improve the material reliability.

Even today, the causes of this stress cracking phenomenon have not been understood fully, and the prediction when and where it may occur has been a challenge, although studies have been carried out in weld parts. The most key chemical components have been identified as Carbon and Chromium, both present in the alloys, but also their manufacturing details, residual stresses, and the operational envelope have a significant contribution. To improve the material reactor reliability, the solution was the change for the alloy 690, which is now set for the new designs and replacements.

3.5.7 Risk management

Since its beginning, the shipping industry operates along the insurance market, due to the amount of money involved. The prediction of how things may go wrong takes part of the mathematic techniques used by the insurance companies. They are based on data collected from different sources and time, and generate the probability of an event to happen, which is then linked to the consequences of this event, in terms of money figures.

The multiplication of the probability to happen and the money consequences is called 'risk' in a straight manner. Therefore, different math techniques have been developed to calculate the probability and to assess the consequences, shaping up what is called 'risk management'. The Bayes theorem is instrumental within this whole procedure because it handles the conditional probability, or the probability of something to happen, knowing that another event has already occurred.

In the shipping industry, the risk management has different levels, and it starts a way before the ship operation per se. While studying the shipping routes, based on forecast market requirements, to link ports and cargo terminals, weather data is analyzed as a time series to identify seasonal components, which may be set in terms of wave loads or storms intensity. This analysis will make part of the probability to have a damage hull and all the consequences, in other words to figure out the risk associated to the route.

Another risk involved deals to run aground while entering or exiting some terminals and ports. Shallow waters require constant chart update because sand or bottom obstacles vary in position quite often. Even using port pilots, the probability to run aground exists and, in some cases, can damage the hull drastically. In this case, even with a certain damage extension, a ship may sail under restraint envelopes till to reach a shipyard for repair.

The hull structure and related systems (e.g., ballast control, fire control etc.) must be monitored to evaluate the probabilities involved. For instance, the hull structure is checked in terms of strain evolution (longitudinal and transversally) of the different kind of structural components. This strain evolution makes part of probabilistic models to assess the hull safety, or how close the actual load condition is to the design or licensing limit. As mentioned before, accelerometers and wireless networks also work in data gathering to fill up math algorithms used for risk management.

Unfortunately, fire aboard has a not neglected frequency, as an initiation event for an accident, and thus, the probability of fire and its progression aboard is taken during the risk management. The consequences of a fire while in a port or terminal are different from those in the middle of an ocean.

The risk management takes care to quantify this set of conditions, which impacts the operational costs. Maintenance conditions are also taken by the risk management because some spare parts change may occur on route, depending on the difficult or importance level. Moreover, some repairs are not allowed while on sailing and must be done at a skilled shipyard.

One of the forms to assess the maritime risk is to build up a matrix, considering the levels of severity (impacts) and the probabilities. The impacts may be from 'minor' to 'catastrophic', and the probabilities may be linked to a frequency of occurrence in terms of years.

For instance, an event that has a probability to occur at every 10 million years is less probable than the one to occur at every 100 years. Thus, a matrix can be colored in terms of the acceptance of the risk. Figure 22 shows an example of the risk matrix. The figures shown may vary depending on the accumulated data and operational experience, among other factors. Grounding and collision are the main accidents on the scene, but others exist such as fire and hull failures. The main consequence also regarded is the presence of 'leak', which may or not occur, with odd environmental aftermaths. As a general point of view, the ship must set sail with 'negligible risk' area. The acronym 'ALARP´' stands for as low as reasonably practical.

Figure 22: example of ship accident risk matrix [32]

3.5.7.1 Hazard analysis

The nuclear and petrochemical industries provide good examples of hazard analysis, which are also taken by the shipping case. The handle of dangerous materials, such as acids, fuels, explosive gases, and others demand a chain of safety measures to cope with the risk which is accepted by national safety authorities. For instance, some ships operate with aviation fuel, such as the aircraft carriers. The hazard analysis demands to consider the same provisions set for airports added with those from the naval culture or requirements, to protect people, hardware, and the environment. Normally, aviation fuel vaporizes in conditions different from the crude oil burned in some ship power systems and then it requires different kind of stopping valves, instrumentation, and storage tanks (e.g., due to corrosion).

The hazard analysis classifies the ship areas/conditions into categories linked to the safety measures need to follow the legal framework where the ship is registered or operates. For instance, while in ports, nuclear propulsion ships are required to maintain their nuclear reactors in a hot shutdown condition, which means there is no propulsion power, but only the power necessary to operate their safety systems accordingly. In addition, some auxiliary systems may be required, external to the ship, to provide heat removal from the ship nuclear systems, which is the case of the heating and cooling ventilation systems. Another example of hazard analysis focuses the need to maintain tanks almost full, rather than operating with intermediate levels. In ships, the half level condition normally worsens the ship stability, due to a phenomenon called 'free water' oscillation. Furthermore, depending on the fluid and its temperature, the half level may set an easier vaporization condition, increasing the fire probability.

4 Concluding Remarks

In this chapter, a general view of the ship design was presented, covering its phases and relevant technical issues. The characterization of the ship dimensions and systems, along design drawings and materials application, was described in a progressive way. As the sections of the chapter were presented, the engineering materials field had been expanded in terms of technical figures and details. The focus was to provide a spark to the reader about the variety of topics around the ship materials selection and its evolution, without the pretense explore all the fields in deep. The data presented came from open sources, intending to provide a order of magnitude of the reasoning discussed along the text, and they may be seem as mean values. All topics here shown are under continuous development, mainly the nuclear examples, and more recently the application of Machine Learning and Artificial Intelligence. As a high potential subject for technical improvement, the environmental impact reduction with new fuels and propulsion systems has its place to catch the general attention.

Acknowledgements

References

[1] Boxer, R. 'The Portuguese seaborne empire, 1415-1825'. Hutchinson and Co. Ltd, 1969. ISBN 978-972-44-1602-1.

[2] https://www.oecd.org/ocean/topics/ocean-shipping/#:~:text=The%20main%20transport%20mode%20for,transport%20arteries%20for%20global%20trade, acessed on March 27th 2022.

[3] https://imo.libguides.com/c.php?g=659460&p=4655524, accessed on March 27th 2022.

[4] Foretich, A. Zaimes, G. Hawkins, T. Newes, E. "Challenges and opportunities for alternative fuels in the maritime sector". Maritime Transport Research, Volume 2, 2021, 100033, ISSN 2666-822X, https://doi.org/10.1016/j.martra.2021.100033.

[5] Anish. In Guidelines. Oct 7th 2019. https://www.marineinsight.com/guidelines/fighting-oil-spill-on-ship/. Accessed on March 25th 2022.

[6] https://www.marinha.mil.br/noticias/fragata-liberal-completa-o-41o-aniversario-participando-da-operacao-amazonia-azul-mar-limpo. Accessed on Jan 25th, 2022.

[7] McRobbie, L.R. 'When the British Wanted to Camouflage Their Warships, They Made Them Dazzle'. April, 7th, 2016. https://www.smithsonianmag.com/history/when-british-wanted-camouflage-their-warships-they-made-them-dazzle-180958657/. Accessed on Jan 25th 2022.

[8] https://www.nauticexpo.com/prod/hyundai-heavy-industries/product-31139-447904.html. Accessed on Jan 25th 2022.

[9] https://www.sspa.se/naval-technology/hydrodynamics-submarines. Accessed on Jan 26th 2022.

[10] https://clickpetroleoegas.com.br/en/navy-initiates-proof-of-sea-of-the-submarine-riachuelo/. Accessed on Jan 30th 2022.

[11] https://petrobras.com.br/en/. Accessed on Jan 30th 2022.

[12] Davis, C. "The underwater drone revolution". Underwater Imaging. January, 9th, 2019. https://www.deeperblue.com/the-drones-revolution/. Accessed on Jan 31st 2022.

[13] Britannica, T. Editors of Encyclopaedia. "naval architecture." Encyclopedia Britannica, April 19, 2018. https://www.britannica.com/technology/naval-architecture. Accessed on Jan 20th 2022.

[14] Eyres,D. Bruce, G. Ship Construction (Seventh Edition), 2012. https://www.sciencedirect.com/topics/engineering/longitudinal-framing accessed on Jan 20th 2022.

[15] Eckstein, M. "Navy, Industry Working Through DDG-51 Flight III Detail Design; Draft RFP For Ship Construction Released". https://news.usni.org/2015/11/12/navy-industry-working-through-ddg-51-flight-iii-detail-design-draft-rfp-for-ship-construction-released. Accessed on March, 29th 2022.

[16] Mosedale. E. "Is the ship design spiral holding you back?" https://blogs.sw.siemens.com/simcenter/ship-design-spiral-simcenter/. Accessed on Jan, 25th 2022.

[17] https://www.cadcrowd.com/3d-models/ship-lines-plan-drafting. Accessed on March, 29th 2022.

[18] Salehi, Hadi & Burgueño, Rigoberto. (2018). Emerging artificial intelligence methods in structural engineering. Engineering Structures. 171. 170-189. https://doi.org/10.1016/j.engstruct.2018.05.084.

[19]http://stonemarinepropulsion.com/wp-content/uploads/2021/08/Sonoston-alloy-NL.pdf. Accessed on Jan 30th 2022.

[20] Allen T. Busby, J. Meyer, M. Petti, D." Materials challenges for nuclear systems". Materials Today. Volume 13, Issue 12. 2010. Pages 14-23. ISSN 1369-7021. https://doi.org/10.1016/S1369-7021(10)70220-0.

[21] Jia, L.J. & Ikai, Toyoki & KANG, LAN & Ge, Hanbin & Kato, Tomoya. (2016). Ductile cracking simulation procedure for welded joints under monotonic tension. Structural Engineering and Mechanics. 60. 51-69. https://doi.org/10.12989/sem.2016.60.1.051.

[22] http://www.ourwaysteels.com/steel-plate-rolling.html, webpage. Accessed on Jan 15th 2022.

[23] Koenig, Philip C., and Walter L. Christensen. "Development and Implementation of Modern Work Breakdown Structures in Naval Construction: A Case Study." J Ship Prod 15 (1999): 136–145. https://doi.org/10.5957/jsp.1999.15.3.136.

[24] Brown, J. C., et al. "Measurement of Wave-Induced Loads in Ships at Sea [and Discussion]." Philosophical Transactions: Physical Sciences and Engineering, vol. 334, no. 1634, The Royal Society, 1991, pp. 293–306. http://www.jstor.org/stable/53773.

[25] Dymarski, Czesław. (2009). Analysis Of Ship Shaft Line Coupling Bolts Failure. Journal of Polish CIMAC. 4.

[26] Garbatov, Yordan & Rudan, Smiljko & Gaspar, Bruno & Guedes Soares, Carlos. (2011). Fatigue Assessment of Marine Structures. https://doi.org/10.13140/RG.2.1.3185.0488.

[27] Wang, X, Kang, J, Kim, Y, & Wirsching, PH. "Low Cycle Fatigue Analysis of Marine Structures." Proceedings of the 25th International Conference on Offshore Mechanics and Arctic Engineering. Volume 3: Safety and Reliability; Materials Technology; Douglas Faulkner Symposium on Reliability and Ultimate Strength of Marine Structures. Hamburg, Germany. June 4–9, 2006. pp. 523-527. ASME. https://doi.org/10.1115/OMAE2006-92268.

[28] https://fatigue-life.com/high-cycle-fatigue/. Accessed on March, 29th 2022.

[29] Zhenghong Fu, Bangjian Yang, Kefu Gan, Dingshun Yan, Zhiming Li, Guoqing Gou, Hui Chen, Zhirui Wang,Improving the hydrogen embrittlement resistance of a selective laser melted high-entropy alloy via modifying the cellular structures. Corrosion Science. Volume 190,2021,109695. ISSN 0010-938X. https://doi.org/10.1016/j.corsci.2021.109695.

[30] Arshab, M. 'Liberty Ships Failures'. Metallurgy & Materials Engineering. Dec, 25th, 2015. https://metallurgyandmaterials.wordpress.com/2015/12/25/liberty-ship-failures/. Accessed on Feb 16th 2022.

[31] Rath, B. and DeYoung, D. https://www.tms.org/pubs/journals/jom/9807/rath-9807.html. Accessed on Feb 16th 2022.

[32] Dasgupta, S. in Marine Safety. https://www.marineinsight.com/marine-safety/risk-assessment-for-ships-a-general-overview/. Accessed on March, 25th 2022.

Suggested Reading

A - https://www.academia.edu/41835546/Materials_Selection_in_Mechanical_Design_Fourth_Edition, which is a book on materials selection from Prof. Michael F. Ashby, with several technical charts guiding the selection of different engineering material for real applications.

B - https://www.materials.unsw.edu.au/study-us/high-school-students-and-teachers/materials-shaped-history, which provides an overview of the history evolution of materials processing and its consequences in normal life.A. H. Cheng and D. T. Cheng. Heritage and early history of the boundary element method. Eng. Anal. Bound. Elem., 2005. ISSN 09557997. doi: 10.1016/j.enganabound.2004.12.001.

C - https://lps.library.cmu.edu/ETHOS/article/id/40/, dedicated to the material science history, focusing the technology transitions and its aftermaths.A. H. Cheng and D. T. Cheng. Heritage and early history of the boundary element method. Eng. Anal. Bound. Elem., 2005. ISSN 09557997. doi: 10.1016/j.enganabound.2004.12.001.

D - https://www.nrl.navy.mil/Our-Work/Areas-of-Research/Material-Science-Technology/, where examples of laboratory campaigns are shown to develop defense hardware related to naval affairs.A. H. Cheng and D. T. Cheng. Heritage and early history of the boundary element method. Eng. Anal. Bound. Elem., 2005. ISSN 09557997. doi: 10.1016/j.enganabound.2004.12.001.

E - https://www.sname.org/, a broad site covering manifold shipbuilding and design issues.A. H. Cheng and D. T. Cheng. Heritage and early history of the boundary element method. Eng. Anal. Bound. Elem., 2005. ISSN 09557997. doi: 10.1016/j.enganabound.2004.12.001.

Chapter 3

New Advances in Thermoplastic Commingled Composites: Processing and Molecular Dynamics

New Advances in Thermoplastic Commingled Composites: Processing and Molecular Dynamics

Ricardo M. Di Benedetto [1*], Anderson Janotti[2], Guilherme F. Gomes[3], Antonio C. Ancelotti Junior[4], and Edson C. Botelho[5]

[1]Materials and Technology Department, School of Engineering, São Paulo State University, Guaratingetá, Brazil – ricardo@ntc.eng.br

[2]Department of Materials Science & Engineering, University of Delaware, Newark, USA – janotti@udel.edu

[3]Mechanical Engineering Institute, Federal University of Itajubá, Itajubá, Brazil. NTC – Composite Technology Center – guilhermefergom@unifei.edu.br

[4]Mechanical Engineering Institute, Federal University of Itajubá, Itajubá, Brazil. NTC – Composite Technology Center – ancelotti@unifei.edu.br

[5]Materials and Technology Department, School of Engineering, São Paulo State University, Guaratingetá, Brazil – edson.botelho@unesp.br

*Corresponding author

Abstract

This chapter addresses a current and innovative topic related to thermoplastic commingled composites. Computational molecular dynamics simulations represent a very sophisticated technique for characterizing microstructures, but it is still not widely explored in the area of high-performance thermoplastic polymers. The molecular dynamics technique evaluates the movements of atoms as a function of time and temperature, according to external demands and boundary conditions of the molecular system. Based on thermodynamics, atomistic and classical mechanics theories, molecular dynamics simulations with empirical potentials aim at (i) the development of new polymeric materials, (ii) the optimization of polymer properties, and (iii) the characterization of these materials. The molecular dynamics technique provides a prediction of mechanical and thermal behavior of high-performance polymeric microstructures, reducing the number of tests and experimental practices, which increases the operational cost of engineering projects and the characterization of structural composite materials. Furthermore, this chapter also includes a scientific and technological literature background to demonstrate and highlight the conjuncture between thermal processing parameters, thermal degradation kinetics, processing optimization, thermal and mechanical characterization techniques. It also includes literature and experimental background based on previous studies.

Keywords: Molecular dynamics; thermoplastic commingled composites; thermal consolidation.

1   Introduction

Interatomic potentials are mathematical functions that describe the interaction between pair of atoms or the interaction between groups of atoms, considering the condensed phase or systems with very large number of atoms. From this perspective, computational simulations using molecular dynamics (MD) with empirical potentials have been used to explain and predict the thermal and mechanical behavior of polymeric materials. The atomic microstructure is investigated according to the movements of the atoms in three-dimensional space.

Typically, polymeric materials display amorphous or semi-crystalline structures, which makes it difficult to realistically simulate interatomic movements. The molecular structure of thermoplastic polymers is composed of high entropy thermodynamic systems. This condition limits the precise determination of the positions of atoms in three-dimensional space. The validation of the technique for characterizing high-performance thermoplastic polymers using MD simulations depends on the level of representativeness of the models and the reliability of the theoretical and experimental data.

MD method is based on mathematical calculations of potential energies. The calculations measure the displacement of atoms as a function of time and temperature. Scientific studies with an emphasis on MD of polymeric microstructures are promising and have attracted the attention of researchers and companies, favoring partnerships and technological advances. The use of computer simulations in engineering projects creates opportunities for new scientific work in a continuous and integrated way. Computational analyzes work together with experimental practices, offering support to companies and research centers. In addition to reducing project time and costs, the use of computer simulation provides a competitive advantage in the development of new materials and products.

MD simulations that describe the behavior of thermoplastic materials have been an active research area with great potential for impact in basic and applied research. These simulations can be used to conduct mathematical tests to predict and simulate the material behavior.

2   Theorical Background

2.1 Thermal Processing and Degradation

Commingled yarns are hybrid structures in which two different materials are mixed to form continuous filament tow. This technology provides easier storage and drapability [1], due to the ability of textile preforms to conform to the surface of molds. Thus, thermoplastic commingled materials allow the preform conformation to make a rigid structure [2] under applied temperature and pressure. Thermoplastic commingled composites are versatile materials, recyclable, with high performance and significant manufacturing costs reduction [2]. Focusing on the overall reduction of production costs, the use of thermoplastic commingled composites reduces the weight of components and establishes the best characteristics of geometry, materials, and processing parameters [3].

The processing of thermoplastic composites, however, involves thermo-oxidative degradation of the matrix during consolidation. The thermal degradation directly affects the mechanical properties of the composite structures. Degradation kinetics methodologies determine the limits of temperature and time in which the material can be processed. Friedman's isoconversional kinetic model is an example of how to investigate the matrix thermo-oxidative degradation. Any variation in processing parameters can cause significant changes in the mechanical behavior of these materials [4,5].

Friedman's model [6] calculates the activation energy (E_a), defined as the minimum energy required for chemical reaction. The pre-exponential factor (A_α) is determined by the linearization of the degradation degree rate $\left(\frac{d\alpha}{dt}\right)$, as a function of the temperature inverse $(1/T)$ for each degree of degradation (α). Equation 1 allows for calculating the variation of the rate constant of a chemical reaction with temperature, in which $-\frac{E_a}{RT}$ and lnA_α are equivalent to the line's equation slope and intersection, respectively:

$$ln\left(\frac{d\alpha}{dt}\right) = lnA_\alpha - \frac{E_a}{RT};$$

(1)

Friedman's method correlates the degradation degree as a function of time for a given temperature, according to:

$$\alpha = A_\alpha \exp\left(-\frac{E}{RT}\right)t,$$

(2)

resulting in a time/temperature graph, considering the time and temperature required to provide the softening range of the thermoplastic matrix without reaching its degrees of temperature onset damage degradation [7]. Thermal degradation must be considered when processing thermoplastic composites. To estimate the degree of degradation using Friedman's kinetic model, thermogravimetry (TGA) must be performed with at least three different heating rates.

Darcy's law [8] is a constructive equation used to predict how a viscous fluid is able to impregnate the reinforcing fibers of the composite material [8]. This period can be estimated by the impregnation time t_{imp}. Darcy's law has been used to precisely define the soak time (isothermal), defined in Equations 3 and 4, considering the pressure rate $\frac{dP}{dx}$ constant:

$$u_p = \frac{dx}{dt} = \frac{K}{\eta}\frac{dP}{dx},$$

(3)

$$t_{imp} = \frac{\eta D_p^2}{2KP},$$

(4)

where u_p is the impregnation velocity of the viscous polymer, K is the reinforcing fibers coefficient of permeability, η is the polymer viscosity, $\frac{dP}{dx}$ is the pressure gradient, and D_p is the impregnation distance related to the thickness of the laminate. Figure 1 represents a viscous flow impregnating the reinforcement fibers by external pressure.
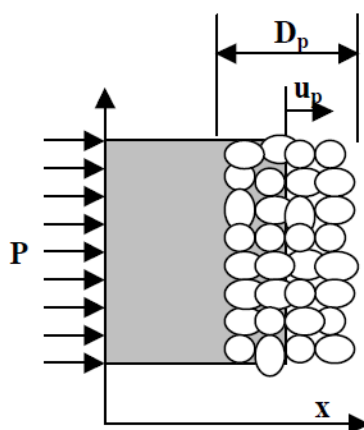
Figure 1: Schematic of impregnation under pressure of the reinforcing fibers by a viscous flow (adapted from [8]).

The determination of the processing pressure is usually obtained empirically. Total consolidation is considered until there are no more detectable defects and voids within the laminate. The consolidation pressure P should be enough to reach these conditions, but not allow the polymer matrix to leak beyond the reinforcement fibers out of the metal matrix. Finally, the viscosity η of the polymeric matrix can be obtained by rheology analysis.

2.2 Statistic Modeling and Soft Computing Techniques

Multiple regression models (MRM) can be used to describe a studied process or a material behavior as a three-dimensional (3D) plane, or response surface. The 3D plane refers to independent explanatory variables such as processing time, temperature, and the target property. Optimizing the thermal processing of thermoplastic commingled composites reduces production costs and optimizes the composite properties.

MRM was developed to predict a mechanical property as a function of (i) thermal and viscoelastic properties of the matrix; (ii) kinetic parameters of degradation, and (iii) consolidation parameters. The regression coefficients β_1 and β_2, (Equations 5 and 6) indicate the variation in the mean response to each unit of the independent variable x_1, when the other variables are kept fixed. Y is the response-dependent variable [9],[10]:

$$\beta_1 = \frac{(\sum x_2^2)(\sum x_1 Y) - (\sum x_1 x_2)(\sum x_2 Y)}{(\sum x_1^2)(\sum x_2^2) - (\sum x_1 x_2)^2} ; \tag{5}$$

the parameter β_2 indicates the variation in the mean response to each unit of x_2, when x_1 is kept constant [9],

$$\beta_2 = \frac{(\sum x_1^2)(\sum x_2 y) - (\sum x_1 x_2)(\sum x_1 y)}{(\sum x_1^2)(\sum x_2^2) - (\sum x_1 x_2)^2}. \tag{6}$$

The least-squares method (LSM) is a statistical technique used to find the best fit for a set of data points, precisely predicting the behavior of dependent variables or responses. Based on the MRM and LSM, the maximum likelihood function L (Equation 7) must be minimized. L represents a function to measure the probability of observing a set of dependent variable values [9–12]:

$$L = \sum_{i=1}^{n} \left(Y_i - \beta_0 + \beta_1 x_{i1} + \beta_2 x_{i2} + \cdots + \beta_p x_{ip} \right)^2. \tag{7}$$

Another important step of the optimization process refers to variable selection, specifically the stepwise method. This statistical tool automatically chooses the best predictive variables to fit regression models. Akaike Information Criterion (AIC) is based on this fit to estimate the likelihood of the MRM to predict or estimate future values. The minimum AIC (Equation 8) defines the variables which were included or removed from the model [13],[14], i.e.,

$$AIC = -2log(L_p) + 2[(p + 1) + 1], \tag{8}$$

where, L_p is the maximum likelihood function and p the number of explanatory variables.

Soft computing techniques including artificial neural networks (ANN) and machine learning offer new prospects to predict the mechanical behavior of thermoplastic commingled composites. Recent studies [15–22] have been used to predict the mechanical behavior of structural composite materials by computational modeling [23]. ANN technique has been applied to improve the behavior of structural composite materials [24], including the design optimization of composite components [25], structural behavior of natural fibers reinforced composite [26], recyclability of

thermoplastics composites [27], and to improve mechanical properties of these materials [28],[29]. Systematic and interactive approaches involving composite materials allow to achieve the ideal characteristics of the material.

ANN has been used to (i) investigate mechanical properties of composite materials, (ii) properties optimization, (iii) understand the effects of manufacturing parameters, and (iv) develop new computational methods for materials characterization. Basically, ANN is a computational system arranged of processing elements operating in parallel, whose function is obtained according to the network structure, the connection strengths, and the processing performed at computing elements or nodes.

In general, a neural network is a processor with a natural tendency for storing experiential knowledge and making it available for practical use. ANN resembles the human brain in two respects: (i) knowledge is acquired through a learning process, and (ii) interneuron connection forces are used to store knowledge [30].

2.3 Initiating molecular dynamics in thermoplastic composites

MD-based on empirical potentials established a new generation of characterization of thermoplastic structures. Essentially, MD is a computer simulation method to analyzes atomic movements and, thus, predict thermal and mechanical behavior of polymeric molecules. The benefits associated with advances in MD for thermoplastic composites are promising and attractive for the science and technology of high-performance composite materials, potentially reducing the material's development time. The main scientific challenge is to establish the atomic and molecular positioning criteria that can contribute to a more realistic result of computer simulations.

MD simulations that describe the behavior of polymeric materials have been an active research area with great potential for impact in basic and applied research. Computational practice is a procedure that uses advanced software to conduct mathematical tests to predict and simulate material behavior.

The innovation proposed consists of the development of analytical models, experimental analyzes, and MD simulations to investigate the thermal and mechanical behavior of polymers. MD simulations will be conducted to evaluate intermolecular movements and investigate the thermal and mechanical behavior of thermoplastic matrices. The literature presents modeling and simulation gaps when thermoplastic composites are involved. This topic has raised great scientific interest because of the practical results: (i) assist decision-making in the selection of polymeric materials, (ii) determine optimal processing parameters, (iii) predict the thermal and mechanical behavior of polymers, and (iv) optimize the performance of thermoplastic commingled structures.

3   Experimental Practices

This topic involves the experimental results consisting of raw material characterization, processing procedures, thermal degradation kinetics, optimization of the material properties, and an initial approach to MD simulations applied to thermoplastic composites.

3.1 Commingled technology

The CF/PA commingled tow combines 37 µm PA yarns into 12k 7 µm carbon fibers, as shown in the SEM micrography in Figure 2.
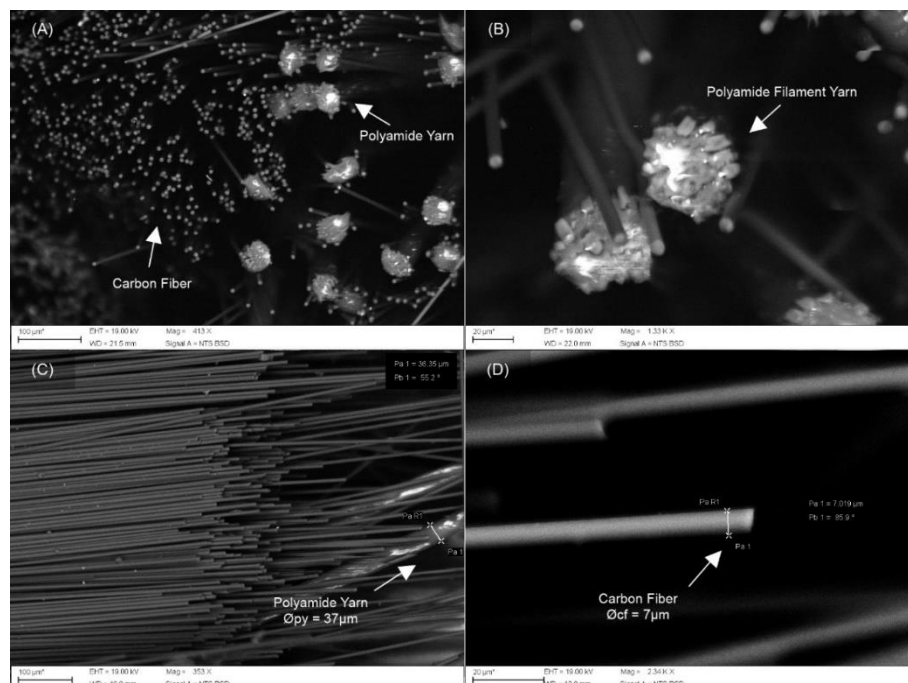
Figure 2: SEM micrography of CF/PA6 commingled tow to measure fibers and yarn diameters (adapted from [7]).

The constituents of CF/PEEK commingled tow are shown in Figure 3. According to the SEM micrography, the material is composed by 12k 7 µm carbon fibers and 26 µm PEEK yarns.
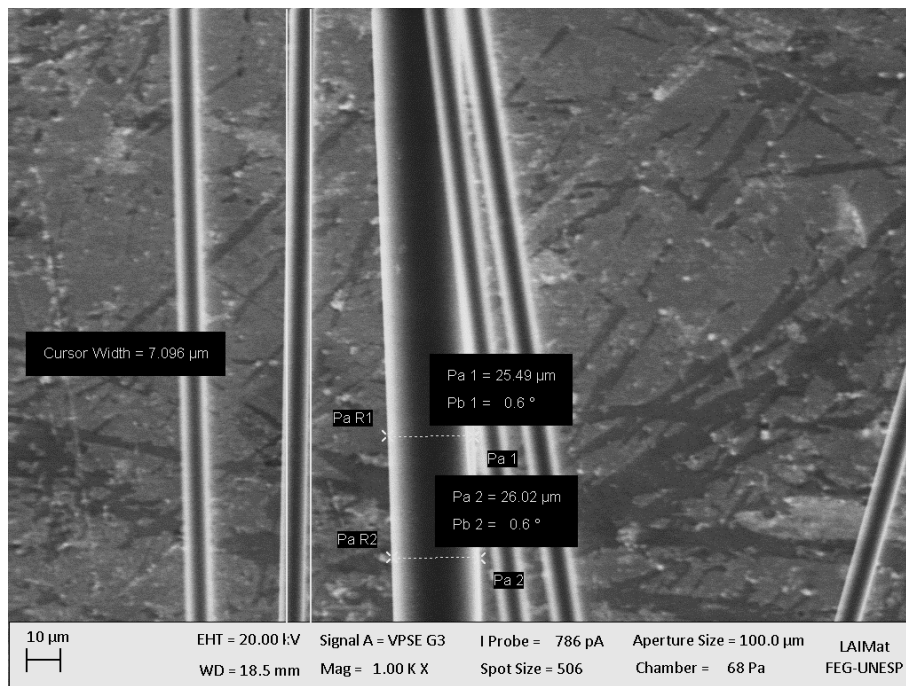
Figure 3: SEM micrography of CF/PEEK commingled tow to measure fibers and yarn diameters (adapted from [31]).

3.2 Thermal analysis

Differential scanning calorimeter (DSC) analysis reveals the phenomena that occur during thermal cycles, and it guides the selection temperatures to process CF/PA commingled composite. The result of DSC analysis is shown in Figure 4.
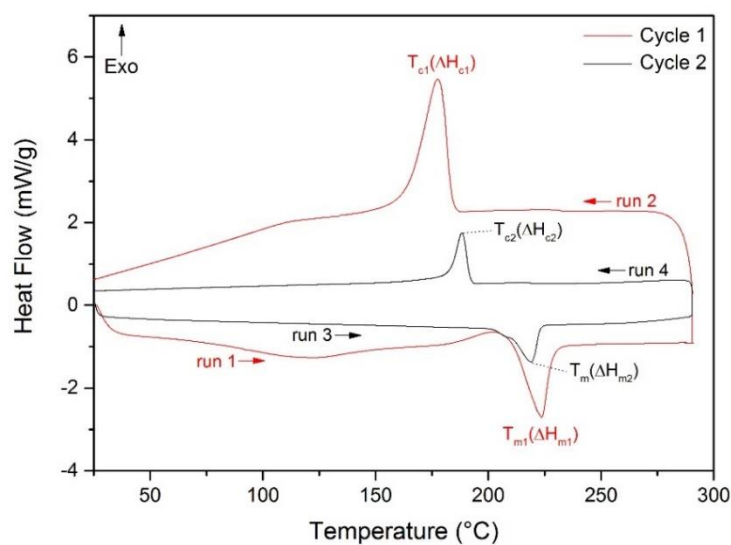
Figure 4: DSC thermal cycles of thermoplastic polymer to reveal endothermic and exothermic peaks associated to melting point and crystallization (adapted from [7]).

The DSC was conducted in two steps. The first cycle erases the thermal history of the sample associated with its previous processing [32]. The second cycle allows the calculation of more accurate values for melting point (Tm) and crystallization temperature (Tc) disregarding the thermal history influence. The melting and crystallization enthalpies, ΔHm and ΔHc, were also identified. To process a thermoplastic commingled composite efficiently the processing cycle should consider the temperatures Tm and Tc and the cooling rate.

The crystallization degree of semicrystalline polymers should be as high as possible to enhance the mechanical and thermomechanical properties of composite structures. Therefore, a low cooling rate favors crystalline structure formation, and it can be calculated by relating ΔHm and ΔHc.

3.3 Degradation Limits

Friedman's isoconversional method allows for the prediction, as a function of time and temperature, of the degree of degradation and establishes the processing window. Graphically, the result of the degradation kinetics study shows the limits of temperature and time in which the composite material should be processed (see Table 1).

Table 1: Thermal degradation kinetics parameters obtained by Friedmann`s isoconversional method.

Material	Temperature, T (°C)		Time, t (min)		Ea (α=0.05) kJ/mol	Molecular Mass (g/mol)
	melt	*onset*	*melt*	*onset*		
PA	220	320	112	4.5	93.70	113
PEEK	338	550	142	12.3	73.26	228

Figure 5 shows the results of the degradation kinetics analysis for the CF/PA6 commingled composite. It reveals the relation between the activation energy E_a and α in (a) and the limits of degradation according to T_p in (b). Figure 6 shows the degradation kinetics analysis of the CF/PEEK commingled composite.

(Intentionally left blank)

(a)   (b)
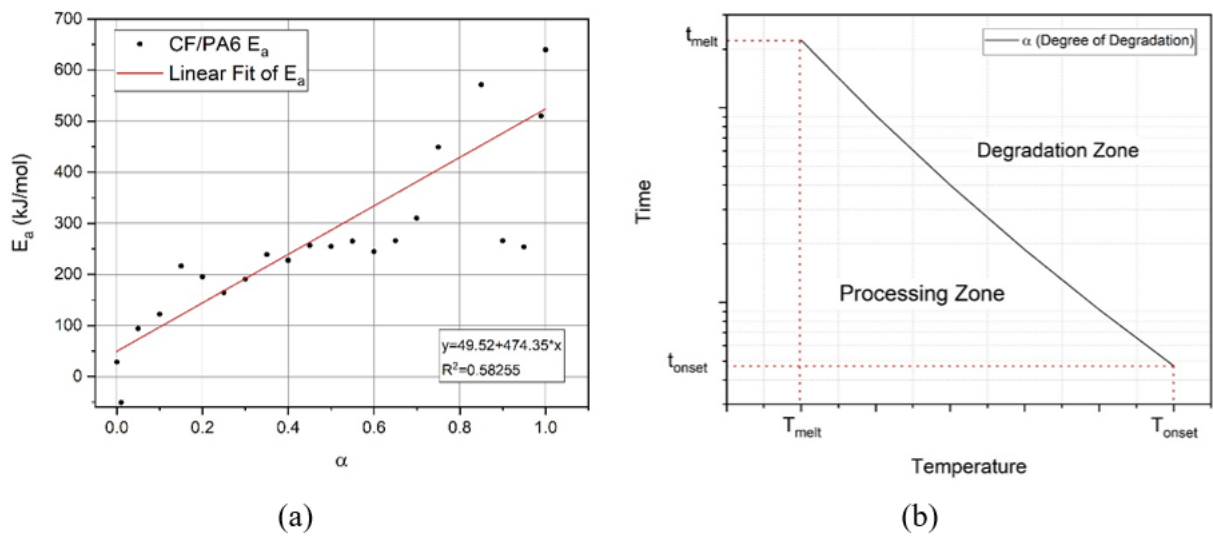
Figure 5: Thermal degradation kinetics analysis for CF/PA6. (a) E_a *versus* α. (b) Thermal degradation limits plot (Adapted from [31])

(a)   (b)
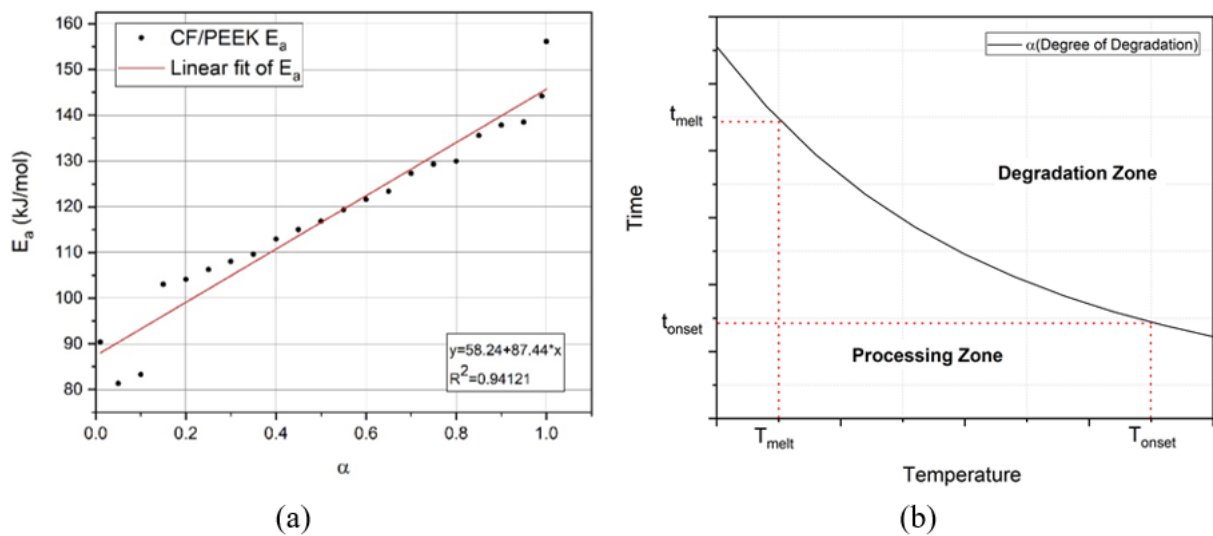
Figure 6: Thermal degradation kinetics analysis for CF/PEEK. (a) E_a *versus* α. (b) Thermal degradation limits plot (adapted from [31]).

3.4 Composite Layup and Processing

The consolidation of thermoplastic commingled composites requires high temperature and pressure. A metallic mold with an integrated heating system can be used to fabricate the composite material as shown in Figures 7 and 8.
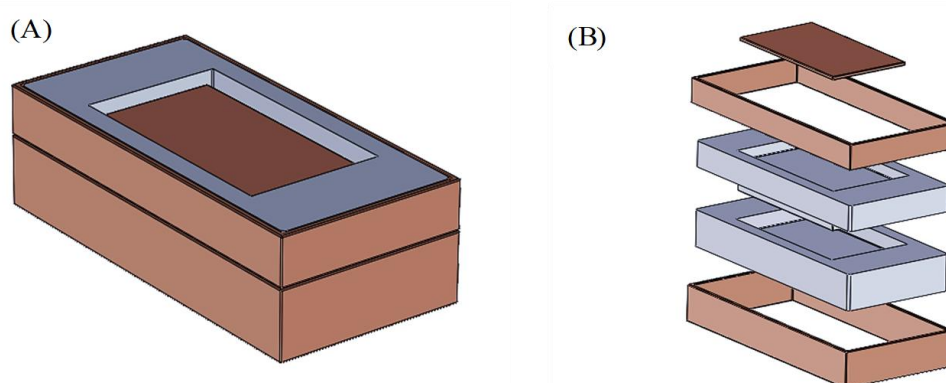
Figure 7: Heating system and metallic mold assembly developed to manufacture the thermoplastic commingled composites. (A) Metallic mold with heating system used to consolidate the materials. (B) Exploded view to show the assembly (adapted from [33]).
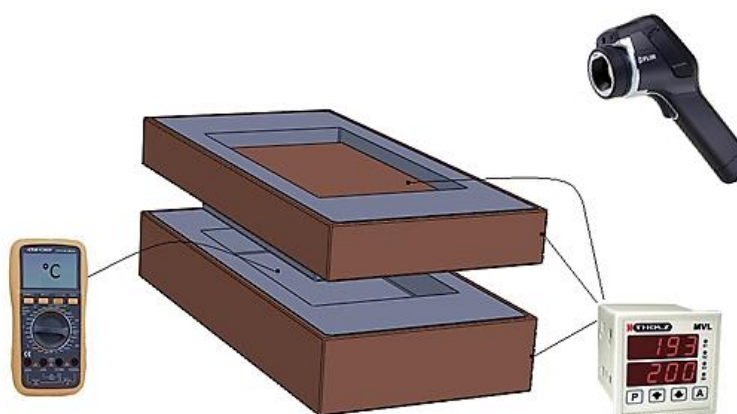
Figure 8: Integrated temperature control and monitoring systems during the thermoplastic composite consolidation.

Next, the thermal processing of the commingled composites was performed. Figure 9 shows the filament winding process and thermal consolidation using the metallic mold with the integrated heating system.
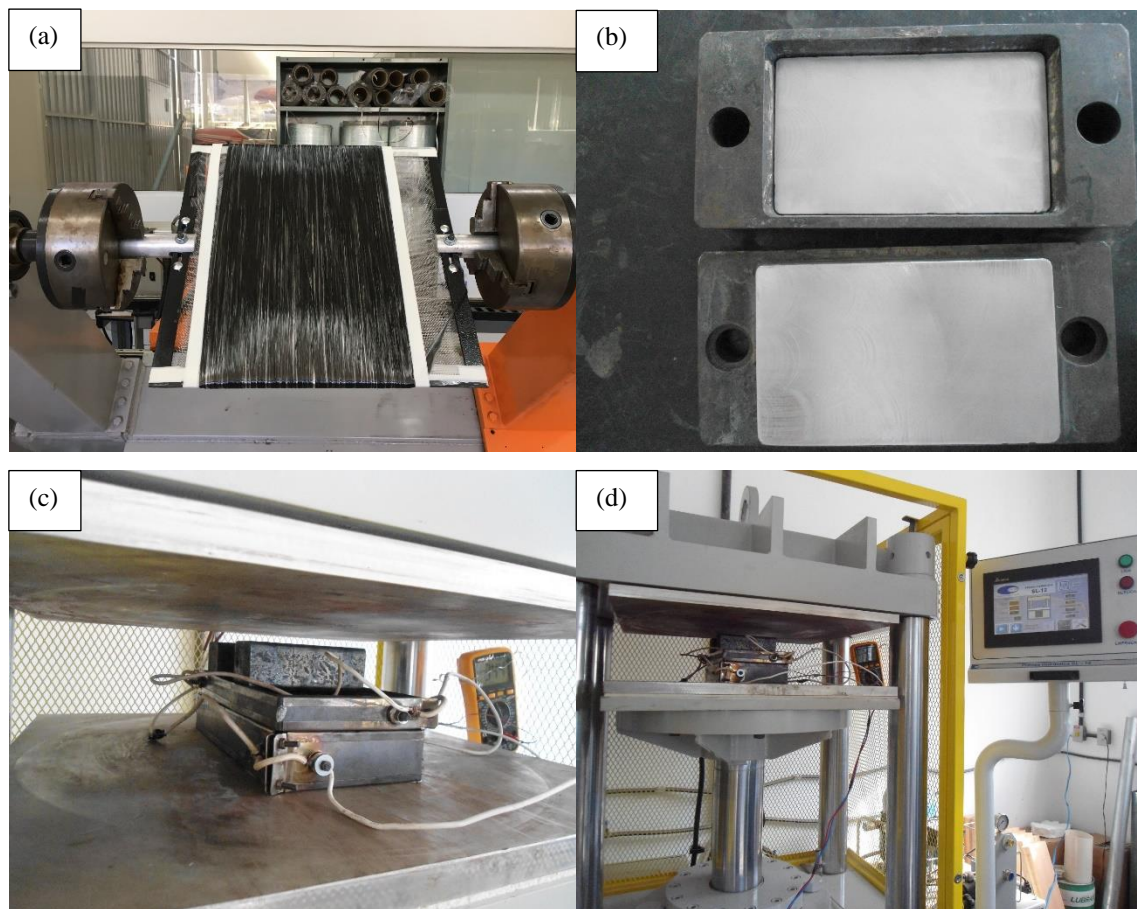
Figure 9: Thermal processing of thermoplastic commingled composites. (a) Filament winding to construct the laminate layers. (b) Metallic mold used to consolidate the composite. (c) Heating system assembly. (d) Hydraulic press used on the commingled composite consolidation (Adapted from [33]**).**

The manufacturing of thermoplastic materials requires a high level of heating control. Thus, the thermal inspection was conducted simultaneously with the consolidation as demonstrated in Figure 10 (a). A specimen of commingled composite with 10 layers (3mm thickness laminate) is shown in Figure 10 (b).

The optimization of the mechanical and thermomechanical properties of commingled thermoplastic composites depends on the appropriate processing cycle that reduces process time and cost, but also guarantees a high degree of crystallinity, mainly because it is associated with the cooling rate.

(a)   (b)
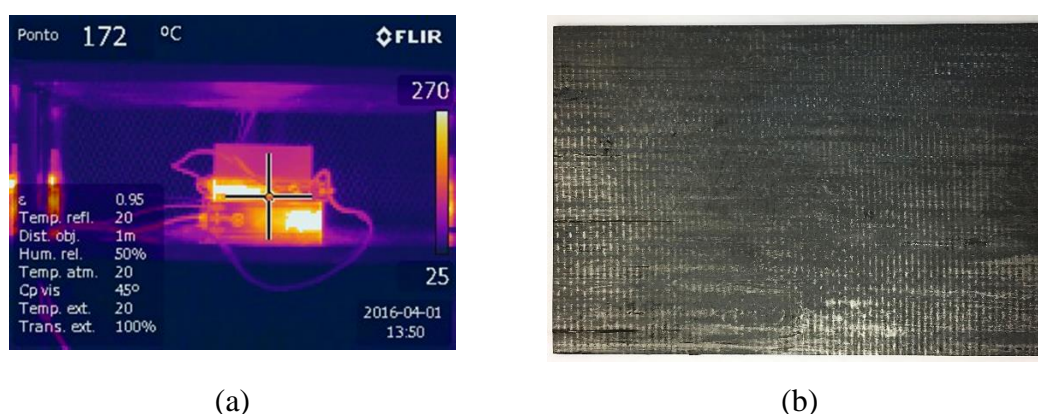
Figure 10: Thermal monitoring during processing of thermoplastic commingled composites. (a) Thermal inspection. (b) 10 layers laminate manufactured.

3.5 Ultrasound Inspection

The ultrasound inspection assessed the quality of the composite by performing a surface scan. This technique ensures a precise quality inspection in which defects, voids, and delamination can be identified. Ultrasonography is also used to determine the minimum consolidation pressure, capable of eliminating all voids and air from the interior of the material, until the total consolidation of the composite has been concluded.

As an example, Figures 11 and 12 present an ultrasound scan using insufficient processing pressure. The presence of voids can be seen, indicating that the pressure used to fabricate the thermoplastic material was insufficient.
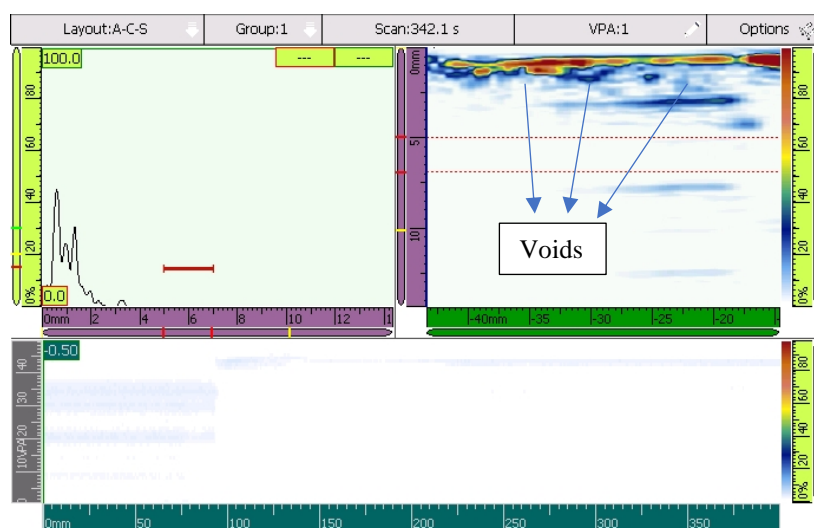
Figure 11: CF/PA ultrasound scan indicating voids in the laminate when insufficient pressure was used.
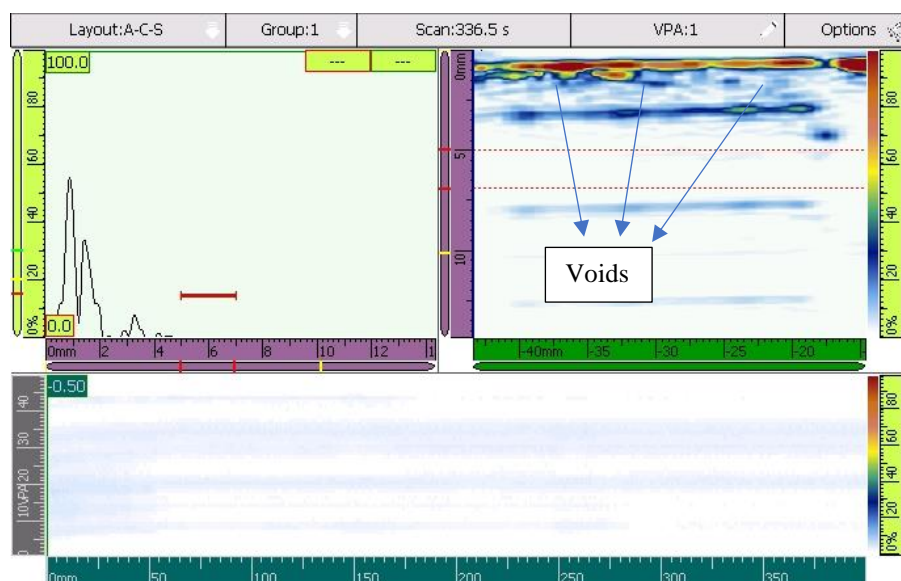
Figure 12: CF/PEEK ultrasound scan indicating voids when insufficient pressure was used.

The presence of voids inside the material represents a high risk of premature failure. This defect is therefore associated with insufficient pressure during consolidation. When the pressure is correctly adjusted to the material, the ultrasound inspection does not show the presence of voids. Figures 13 and 14 are ultrasound inspections with no defects detected in the laminate. It served to determine the pressure P=0.30 MPa that is needed to impregnate the reinforcing fibers by the molten polymer.
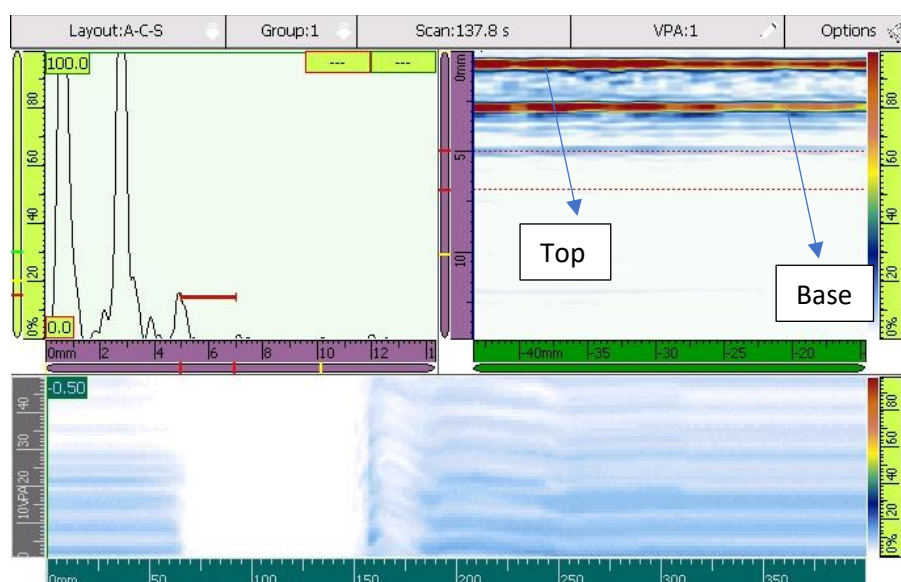
Figure 13: CF/PA ultrasound scan with no presence of defects when an appropriate pressure was used on fabrication.
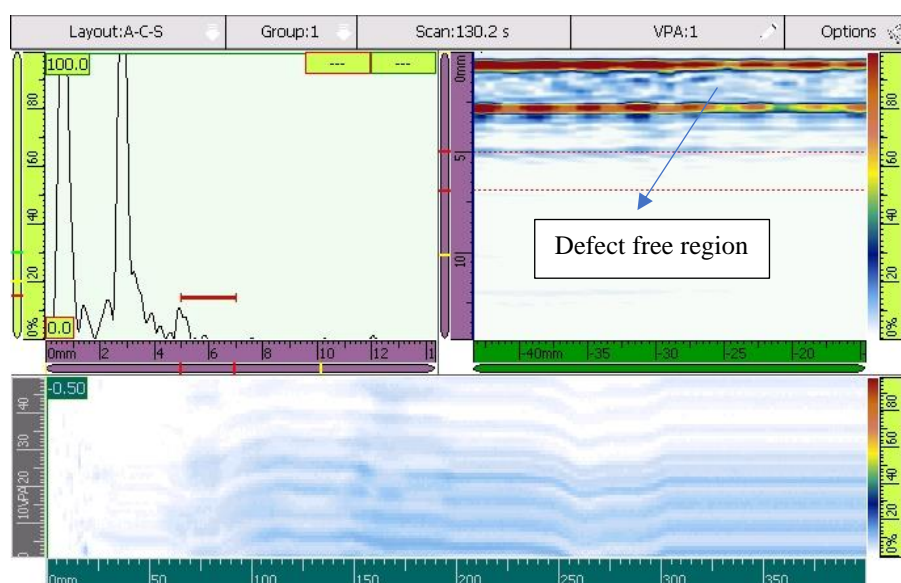
Figure 14: CF/PEEK ultrasound scan with no presence of defects when an appropriate pressure was used on fabrication.

3.6 Statistics and Modeling

3.6.1   Multiple regression and artificial neural network

A multiple regression model was developed to predict a specific property. The impact energy absorption (IEA) capability of thermoplastic commingled composites is an extremely important parameter to guarantee high-performance components. The regression model was obtained in a previous work of Di Benedetto et al. (2019) [34], and can be written as follows (Equation 9):

$$IEA = \ \beta_0 + \beta_1 \left(\frac{-E_a}{ln\left(\frac{\alpha}{A_\alpha}t\right)} \right) + \beta_2 \left(\frac{\nu D_p^2}{2KP} \right); \tag{9}$$

where β_0, β_1, and β_2 are the regression coefficients.

The regression model established a relationship between the degradation limits with the consolidation parameters. As a result, it predicts the IEA capability of commingled composites based on the matrix degradation, the matrix properties, thermal degradation kinetics, and the processing parameters.

Design of experiments (DOE) is a quality tool used to analyze the effect of the processing parameters, polymeric matrix properties, and the thermal degradation kinetics, on the IEA. The data acquisition obtained according to Equation 9 was used as input for the DOE analysis. A Pareto chart is used to evaluate the effect of each variable. The absolute values of the standardized effects are shown as a bar graph. Figure 15 is a Pareto chart of the IEA of thermoplastic commingled composite.
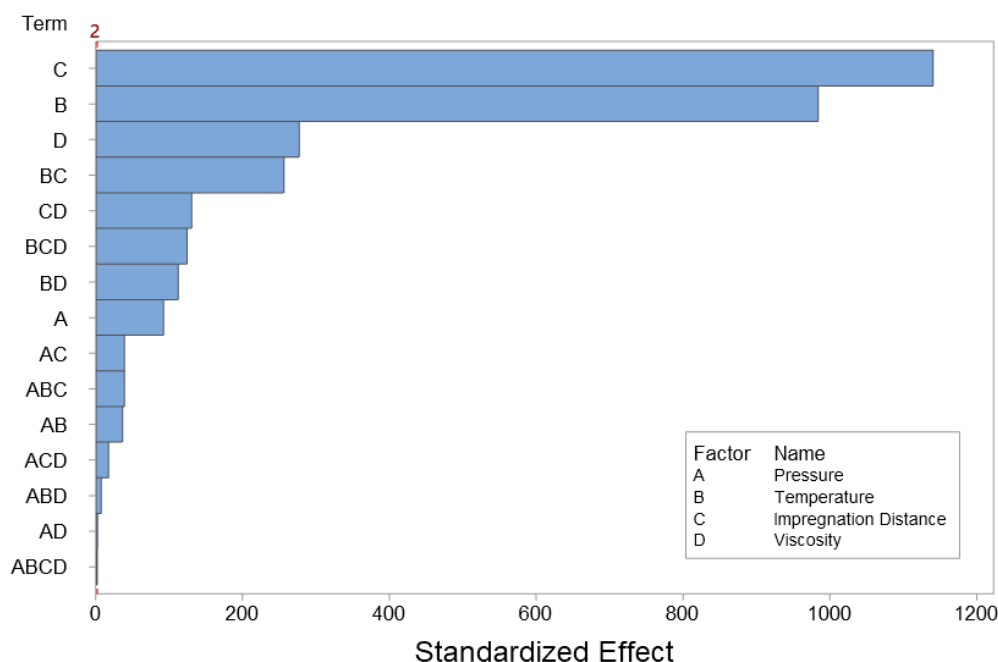
Figure 15: Pareto chart of the standardized effects on *IEA* revealing the level of the effects and its interaction (adapted from [31]).

The Pareto chart exhibits a reference line (t_{calc}=2) to indicate which effects are statistically significant. According to the results in Figure 15, the impregnation distance D_p and temperature T are the independent variables that have stronger effects over IEA. The matrix viscosity v and the interaction between processing temperature T_p and impregnation distance D_p have similar effects on IEA. Lastly, the consolidation pressure P was the variable with less effect compared to the others. No significant effect on IEA was observed in the interaction between all these four parameters.

Another resource of DOE analysis is the surface response plot. This surface indicates how the behavior of the material changes as a function of temperature T_p, pressure P and impregnation distance D_p. The regression model was applied considering a reduction of the impregnation distance as demonstrated by the response surface in the Figure 16.
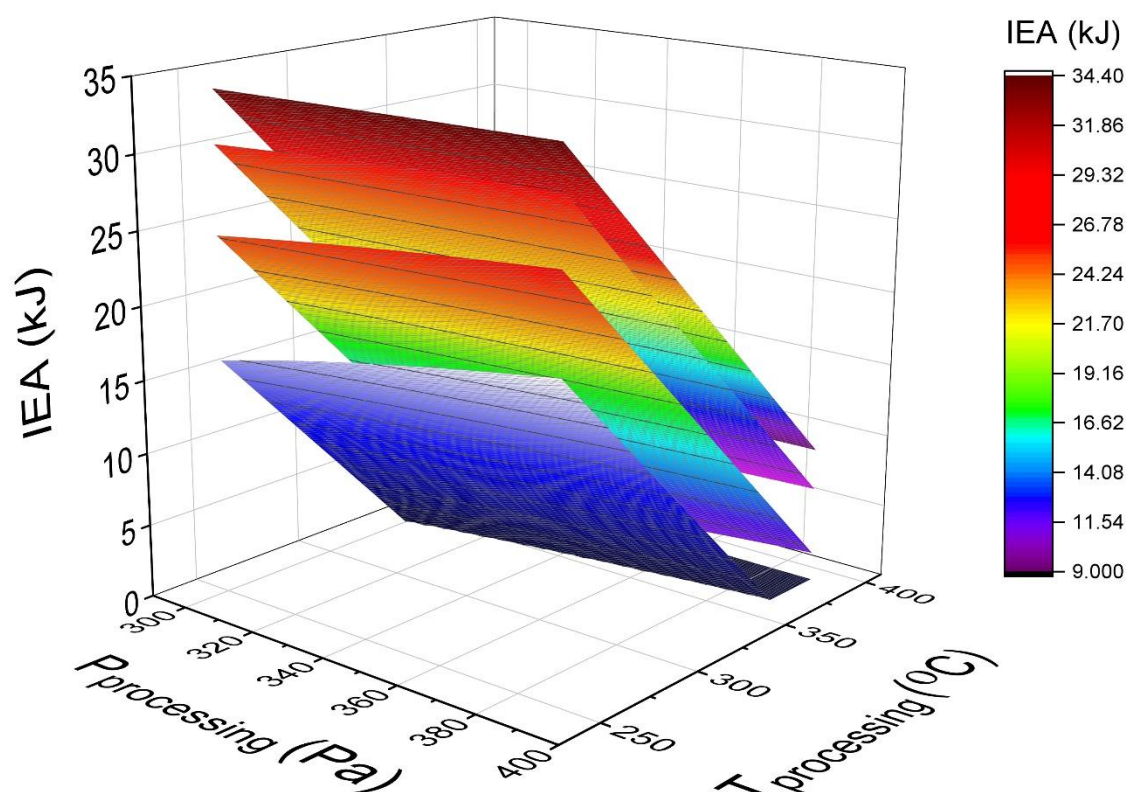
Figure 16: Representative 3D response surface considering the increase of impregnation distance D_p (adapted from [31]).

Technically, the surface response identifies the combination of input variable settings that optimize the IEA response. The optimization corresponds to the combination of P=390Pa, T_p=250°C, D_p=0.3mm, and v=2000Pa.s, which provides the maximum IEA value (36.09 kJ), for example.

The artificial neural network developed by Di Benedetto, et. al (2021) [35] was applied to Carbon Fiber/PA6 and Carbon Fiber/PEEK specimens subjected to a low-velocity impact test (LVI). The goal was to collect data from Equation 9 for the training phase of a neural network. Temperature, pressure, impregnation distance, and viscosity were selected as input variables. The output of the neural network is then targeted focusing on the dynamic impact energy absorption property.

Figure 17 shows the graphical results of the IEA standard as a function of pressure and temperature for fixed values of impregnation and viscosity. Figures 17(a) and (c) show the overlapping experimental results and those obtained by ANN. It turns out that the planes are practically overlapping. Figures 17(b) and 17(d) show the error obtained, that is, the difference between trained (IEATR) and experimental (IEAEXP) data, i.e., IEAE-IEATR. The global difference for the known data from the neural network is of the order of 0.02 kJ (< 1%).
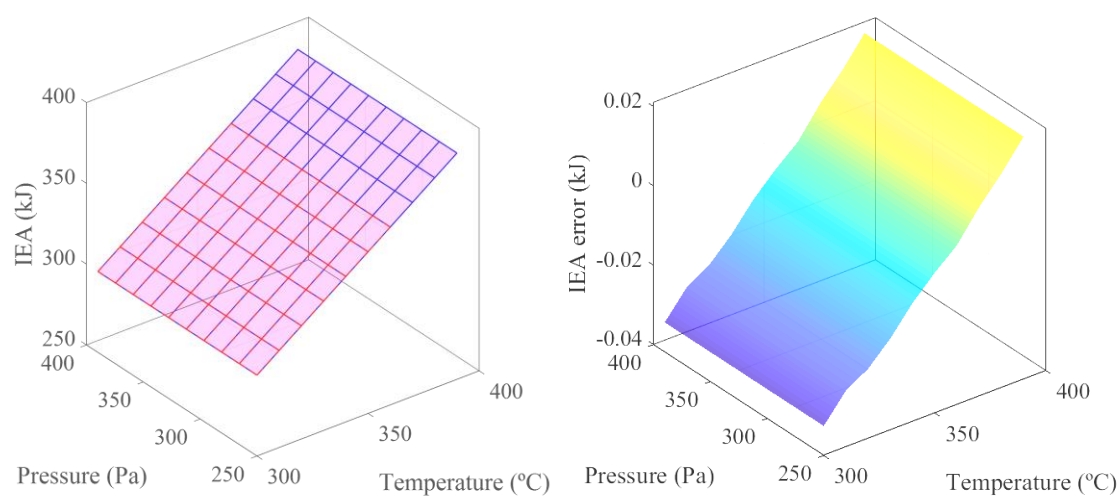
(a) $D_p = 0.0009$; $\nu = 1.4$

(b) Error $D_p = 0.0009$; $\nu = 1.4$
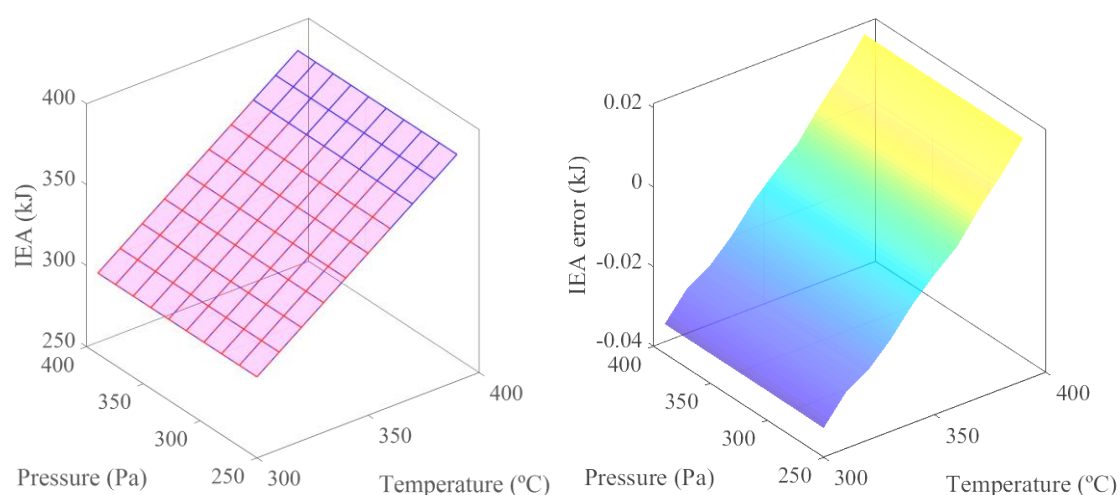
(c) $D_p = 0.0012$; $\nu = 1.4$

(d) Error $D_p = 0.0012$; $\nu = 1.4$

Figure 17: Graphical results of the IEA standard for trained data known

(legend: ━ Experimental ━ ANN) (Adapted from [35]).

Figure 17 reveals an excellent agreement between the modeled and experimental data. Accurate results have been obtained in the testing and validation stages. Therefore, ANN has exceptional predictive abilities that can be used in the development of new thermoplastic composites with desired mechanical impact properties.

3.7 Initiating Molecular Dynamics to Thermoplastic Materials

The application of atomistic molecular dynamics techniques to high-performance polymers depends directly on knowing the conformation of the microstructure. The steric

hindrance defines free axes of rotation of thermoplastic molecules. The challenge of realistically defining the position of atoms imposes specific boundary conditions that during the geometry optimization. Figure 18 is an example of a generic polymeric chain (n=16) and Figure 19 shows the result of the MD simulation.
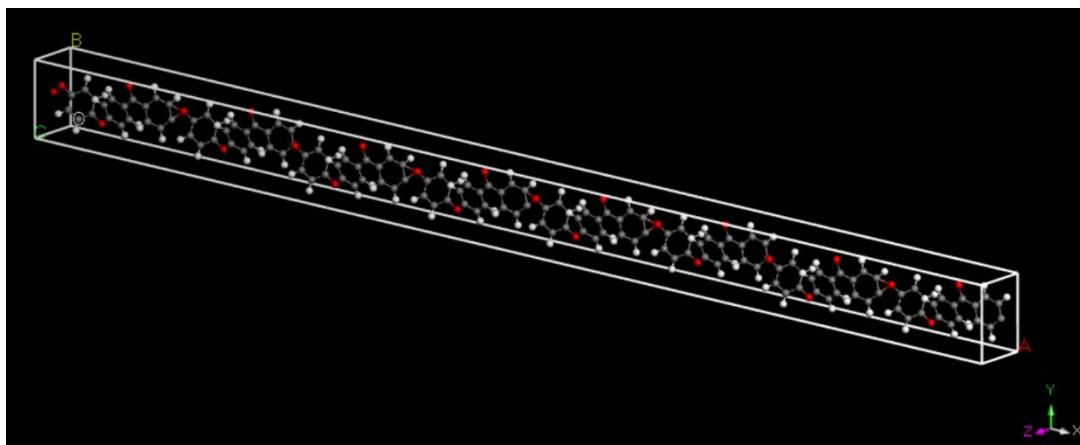
Figure 18: Molecule geometry optimized by MD simulation considering the effect of steric hindrance and distance between atoms.
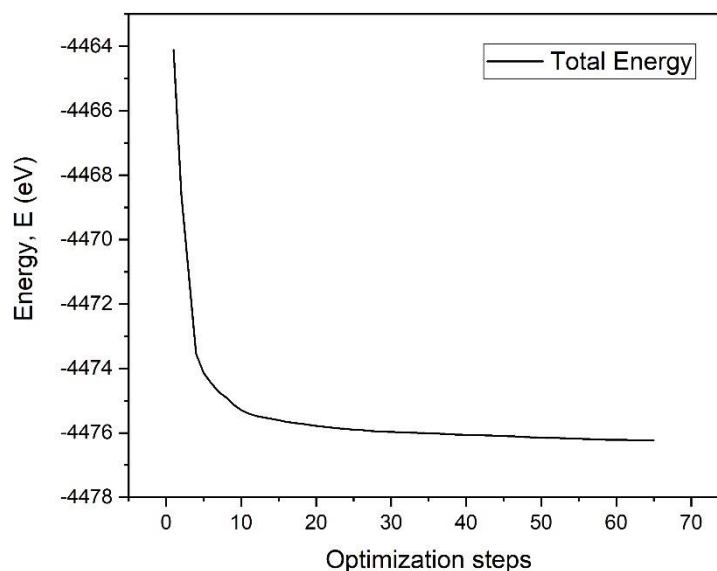
Figure 19: Number of optimization steps in the geometry simulation showing the minimum energy state.

From these results, calculation parameters are established to assemble polymeric macrostructures with better-defined positions in a 3D space. The combination of MD simulation and experimental practices is an innovative approach to high-performance

structural composites. However, for the molecular dynamics technique to work as a sophisticated technique for characterizing thermoplastic polymers, more precise information on the atomistic structure of the composites is a necessary first step.

For this reason, new studies are being carried out to create parameters of molecular positioning in semi-crystalline structures. Therefore, studies are being carried out to create new parameters of molecular positioning in semi-crystalline structures. The goal is to (i) establish a conformation criterion for macromolecular polymers, (ii) identify, in each case, the most stable position of atoms in a polymeric structure through energy and force minimization, and (iii) compare potential energy results for each type of conformation.

4   Conclusion

This chapter addressed a design for characterizing composites. The research stages were described pointing out the most important scientific findings, including a recent review of thermoplastic commingled composites processing and properties.

The combination of Darcy's law and Friedman's isoconversional method proved to be a powerful tool to optimize the performance of thermoplastic composites and, thus, define specific parameters to perform thermal consolidation.

It was concluded that the ANN is an alternative to traditional methods to determine the processing parameters for the manufacturing of commingled composite. The use of an analytical multiple regression model as a new approach of ANN architecture was a promising approach which caused an increase of ANN's reliability to predict composite properties.

Developing a technique for characterizing high-performance polymeric materials by simulating molecular dynamics with empirical potentials is the main objective of our near-future research. New advances in the molecular dynamics of thermoplastic polymers have the potential to contribute to new techniques for characterizing composites, reducing operating costs, optimizing structures and materials, and determining their properties.

References

[1]   WEST, B. P. V.; PIPES, B. P. ; KEEFE, M.; ADVANI SG. The draping and consolidation of commingled fabrics. Compos Manuf 1991;2:10–22.

[2]   EADS. The research requirements of the transport sectors to facilitate an increased usage of composite materials. Part I Compos Mater Res Requir Aerosp Ind 2004:1–20.

[3]   CARRUTHERS, J. J.; KETTLE, A. P.; ROBINSON AM. Energy Absorption Capability and Crashworthiness of Composite Material Structures: A Review. Appl Mech Rev 1998;51:1–15.

[4]   JACOB, G. C.; FELLERS, J. F.; SIMUNOVIC, S.; STARBUCK JM. Energy Absorption in Polymer Composites for Automotive Crashworthiness. J Compos Mater 2002;36:813–50.

[5]   NIKFAR, B.; NJUGUNA J. II International Conference on Structural Nano Composites. IOP Conf. Ser. Mater. Sci. Eng., 2014, p. 1–6.

[6]   FRIEDMAN HL. Kinetics of Thermal Degradation of Char-Forming Plastics from Thermogravimetry. Application to a Phenolic Plastic. J Polym Sci PART C 1964;1:183–95.

[7]   DI BENEDETTO RM, RAPONI OA, JUNQUEIRA DM, ANCELOTTI JUNIOR AC. Crashworthiness and Impact Energy Absorption Study Considering the CF/PA Commingled Composite Processing Optimization. Mater Res 2017;20:792–9.

[8]   SASTRY AM. Impregnation and Consolidation Phenomena. Compr Compos Mater 2000;2:609–22.

[9]   EFROYMSON MA. Multiple regression analysis. New York, NY: John Wiley & Sons; 1960.

[10]   AIKEN, L. S.; WEST SG. Multiple regression: Testing and interpreting interactions. Sage. Newbury Park, CA: 1991.

[11]   AGOSTINELLI C. Robust stepwise regression. J Appl Stat 2002;29:9–16.

[12]   UYANIC, G. K.; GULER N. A Study of Multiple Linear Regression Analysis. Soc Behav Sci 2013;106:234–40.

[13]   AKAIKE H. A new look at the statistical model identification. IEEE Trans

Automat Contr 1974;19:716–23.

[14]   BOZDONGAN H. Model selection and Akaike's Information Criterion (AIC): The general theory and its analytical extensions. Psychometrika 1987;52:345–70.

[15]   MENG, N.; CHUA, Y. J.; WOUTERSON, E.; ONG CPK. Ultrasonic signal classification and imaging system for composite materials via deep convolutional neural networks. Neurocomputing 2017;257:128–35.

[16]   KUMAR, C. S.; ARUMUGAM, V.; SENGOTTUVELUSAMY, R.; SRINIVASAN, S.; DHAKAL HN. Failure strength prediction of glass/epoxy composite laminates from acoustic emission parameters using artificial neural network. Appl Acoust 2017;115:32–41.

[17]   ALLEGRI G. Modelling fatigue delamination growth in fibre-reinforced composites: Power-law equations or artificial neural networks? Mater Des 2018;155:59–70.

[18]   LI, Y.; LEE, T. H; WANG, C.; WANG, K.; TAN, C.; BANU, M.; HU SJ. An artificial neural network model for predicting joint performance in ultrasonic welding of composites. Procedia CIRP 2018;76:85–8.

[19]   PARIKH, H. H.; GOHIL PP. Experimental determination of tribo behavior of fiber-reinforced composites and its prediction with artificial neural networks. Durab. Life Predict. Biocomposites, Fibre-Reinforced Compos. Hybrid Compos., 2019, p. 301–20.

[20]   MARTINEZ, M. J.; PONCE MA. Fatigue damage effect approach by artificial neural network. Int J Fatigue 2019;124:42–7.

[21]   ATTA, A.; ABU-ELHADY, A. A.; ABU-SINNA, A.; SALLAM HEM. Prediction of failure stages for double lap joints using finite element analysis and artificial neural networks. Eng Fail Anal 2019;97:242–57.

[22]   KHAN, A.; KO, D.; LIM, S. C.; KIM HS. Structural vibration-based classification and prediction of delamination in smart composite laminates using deep learning neural network. Compos Part B Eng 2019;161:586–94.

[23]   DI BENEDETTO, R. M.; BOTELHO, E. C.; GOMES, G. F.; JANOTTI, A.; ANCELOTTI JUNIOR AC. FACTORIAL DESIGN MODEL ANALYSIS OF THERMOPLASTIC COMMINGLED COMPOSITES CRASHWORTHINESS. J Thermoplast Compos Mater 2020;1:1–26.

[24] SURESH, S.; KUMAR VSS. Experimental determination of the mechanical behavior of glass fiber reinforced polypropylene composites. GCMM 2014, 2014, p. 632–41.

[25] LEPŠÍK, P.; KULHAVÝ P. DESIGN OPTIMIZATION OF COMPOSITE PARTS USING DOE METHOD. 58th ICMD 2017, 2017, p. 200–5.

[26] FERREIRA, B. T.; SILVA, L. J.; PANZERA, T. H.; SANTOS, J. C.; SANTOS, R. T.; SCARPA F. Sisal-glass hybrid composites reinforced with silica microparticles. Polym Test 2019;74:57–62.

[27] SINGH, R.; KUMAR, R.; RANJAN, N.; PENNA, R.; FRATERNALI F. On the recyclability of polyamide for sustainable composite structures in civil engineering. Compos Struct 2018;184:704–13.

[28] IBRAHIM, Y.; MELENKA, G.; KEMPERS R. Flexural properties of three-dimensional printed continuous wire polymer composites. Mater Sci Technol 2019;35:1471–82.

[29] ALMEIDA, J. H. S.; ANGRIZANI, C. C.; BOTELHO, E. C.; AMICO S. Effect of fiber orientation on the shear behavior of glass fiber/epoxy composites. Mater Des 2015;65:789–95.

[30] ALEKSENDRIC, D.; CARLONE P. Soft Computing in the Design and Manufacturing of Composite Materials. Walthan, USA: Woodhead Publishing; 2015.

[31] DI BENEDETTO, R. M.; JANOTTI, A. J.; GOMES, G. F.; ANCELOTTI JUNIOR, A. C.; BOTELHO EC. Statistical approach to optimize crashworthiness of thermoplastic commingled composites. Mater Today Commun 2022;31:2352–4928. doi:https://doi.org/10.1016/j.mtcomm.2022.103651.

[32] BANNACH, G.; PERPETUO, G. L.; CAVALHEIRO, E. T. G.; CAVALHEIRO, C. C. S.; ROCHA RR. Efeitos da história térmica nas propriedades do polímero pet: um experimento para ensino de análise térmica. Quim Nova 2011;34:1–10.

[33] SOUZA, B. R.; DI BENEDETTO, R. M.; HIRAYAMA, D.; RAPONI, O. A.; BARBOSA, L. C. M.; ANCELOTTI JUNIOR AC. Manufacturing and Characterization of Jute/PP Thermoplastic Commingled Composite. Mater Res J Mater 2017;1:1–8.

[34] DI BENEDETTO RM, BOTELHO EC, GOMES GF, JUNQUEIRA DM,

ANCELOTTI JUNIOR AC. Impact Energy Absorption Capability of Thermoplastic Commingled Composites. Compos Part B Eng 2019;176:1–29.

[35]   DI BENEDETTO RM, BOTELHO EC, JANOTTI A, ANCELOTTI JUNIOR AC, GOMES GF. Development of an artificial neural network for predicting energy absorption capability of thermoplastic commingled composites. Compos Struct 2021;257:113–31.

Chapter 4

The Influence of Weaving Patterns on the Effective Mechanical Response of Reinforced Composites - A Study Through Homogenization

Chapter details

Chapter DOI:

Chapter suggested citation / reference style:

da Rocha, Jonas T., et al. (2022). "The Influence of Weaving Patterns on the Effective Mechanical Response of Reinforced Composites - A Study Through Homogenization". *In* Jorge, Ariosto B., et al. (Eds.) *Fundamental Concepts and Models for the Direct Problem*, Vol. II, UnB, Brasilia, DF, Brazil, pp. 76–119. Book series in Discrete Models, Inverse Methods, & Uncertainty Modeling in Structural Integrity.

P.S.: DOI may be included at the end of citation, for completeness.

Book details

Book: Fundamental Concepts and Models for the Direct Problem

Edited by: Jorge, Ariosto B., Anflor, Carla T. M., Gomes, Guilherme F., & Carneiro, Sergio H. S.

Volume II of Book Series in:

Discrete Models, Inverse Methods, & Uncertainty Modeling in Structural Integrity

Published by: UnB City: Brasilia, DF, Brazil Year: 2022

DOI: https://doi.org/10.4322/978-65-86503-83-8

The Influence of Weaving Patterns on the Effective Mechanical Response of Reinforced Composites - A Study Through Homogenization

Jonas Tieppo da Rocha[1], Tales Vargas de Lisbôa[2] and Rogério José Marczak[3*]

[1]Mechanical Engineering Department, UFRGS, Porto Alegre, Brazil.
E-mail: jonas.tieppo@ufrgs.br
[2]Mechanics and Composite Materials Department, Leibniz Institute of Polymer Research, Dresden, Germany, E-mail: tales-lisboa@ipfdd.de
[3*]Mechanical Engineering Department, UFRGS, Porto Alegre, Brazil.
E-mail: rato@mecanica.ufrgs.br
[*]Corresponding author

Abstract

A study on the influence of the waving patterns on the mechanical response of textile composites is presented. Three typical weaving patterns of industrial interest are explored, as well as a case of cross-ply laminate composite. Homogenization techniques were employed, with the RVE being subjected to well-known displacement and periodic boundary conditions. Owing to the reduced thickness to span ratio usually found in engineering applications of textile composites, we proposed a different set of boundary conditions to disregard repetition along the transverse direction. All boundary conditions were verified to satisfy Hill-Mandel energy equivalence. The engineering constants estimated for the four composites and three sets of boundary conditions are obtained and compared through anisotropy indices and the Frobenius norm of the stiffness. The reduced constitutive tensor, used in thin plate and shell problems, is also derived from their homogenized 3D counterparts and discussed. The strain fields are also investigated for one textile, and the engineering constants were used in a test case to illustrate the weave pattern influence in an actual component.

1 Introduction

Fiber-reinforced composites can be roughly divided into two categories when the size of the fibers and how they are arranged/distributed in the matrix phase are taken into account: (a) particulate, when the fibers are short enough to disregard its geometry and spatial orientation, and (b) fiber-reinforced, when the reinforcement phase is continuous or at least long enough so that its orientation has considerable influence on the overall mechanical behavior of the component. Other sub-categories can be drawn, however,

our interest lies in fiber-reinforced composites or, more specifically, composites built by interlacing bundles of fiber in a repetitive pattern commonly known as textile composites.

In the traditional composite manufacturing processes, fiber-reinforced composites are manufactured by laminating several layers of unidirectional fiber laminae embedded in a pre-impregnated matrix material. The effective properties of the composite can be controlled by changing fiber orientation in a layer, stacking sequence, fiber and matrix material properties, and constituents volume fraction combination. This method of manufacturing is labor-intensive and does not allow transverse (through-the-thickness) fiber reinforcement, resulting in poor interlaminar strength [ming Huang, 2000, Sankar and Marrey, 1997].

As an alternative, textile processes such as weaving, braiding, and knitting can produce larger volumes of material at faster rates. In these techniques, bundles of fiber are interlaced following a specific pattern (fig. 1), then impregnated with a suitable matrix material and cured in a mold to provide the final form. The 2D woven and braided laminae thus manufactured offer increased through-the-thickness and impact resistance properties as a consequence of the bundle interlacing [Mazumda, 2002]. Because the interlocking is in general different in the thickness direction, this kind of structure is sometimes called 2.5D textile structures [Sankar and Marrey, 1997]. These processes allow the manufacturing of complex-shaped components as integral units, reducing or eliminating the use of joints, glues, and fasteners. These advances in manufacturing, however, demand the development of analytical approaches to predict the performance of the components made by these processes.
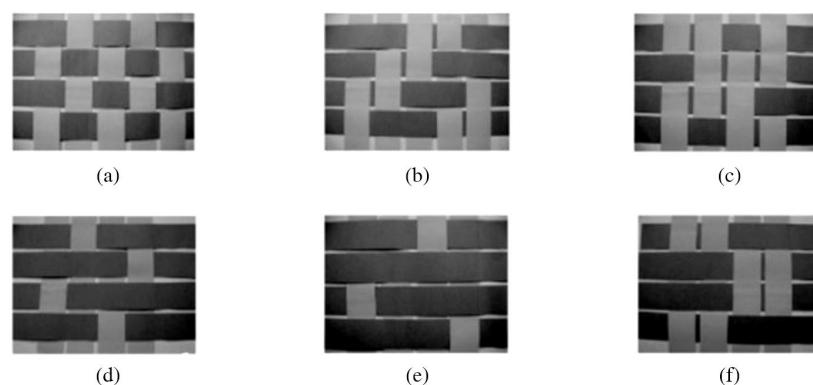
Figure 1: Schematics of woven composites without matrix pockets: (a) plain weave; (b) 2×2 twill weave; (c) 4-harness satin weave; (d) 5-harness satin weave; (e) 8-harness satin weave; (f) basket weave (Dixit and Mali [2013]).

Textile composites which in most ways behave like laminates fall into the category of laminar textiles, while those in which triaxial stresses exist and incorporate weaving along the transverse direction as well. The present study aims at the first category. We re-examine homogenization procedures used to compute the effective (macroscopic) properties of woven composites, as well as the nature of the boundary data which may be assigned to an RVE. The overall effective moduli for linearly elastic RVEs of three common textile composites are thoroughly studied, under a set of uniform boundary traction, linear boundary displacements, and periodic conditions. Special attention is given

to mixed boundary conditions, culminating in a proposal of a new set of boundary conditions to be used with RVE analysis, aiming its usage with thin plate/shell finite element (FEA) or boundary element (BEA) analysis.

Stiffness constitutive relations for 3D elastic as well as their 2D thin-plate counterparts for three types of textile composites are analyzed and compared to available results. Average mechanical constants are retrieved for both cases and discussed. The results show that the differences in the macroscopic behavior caused by inherent mechanisms associated with particular weaving patterns are captured using homogenization, which is very difficult to be distinguished when average field theories are used.

Throughout the text, we assume familiarization with Elasticity Theory, index notation, as well as knowledge of the essentials of homogenization, RVE analysis, and average field theory.

2   Modeling Composites Reinforced by Weave Fibers

The modeling of composites reinforced by woven fabrics can be divided into two methodologies: analytical or numerical. The analytical approaches are usually based on physical measurements of the constituents and possibly ruled by some type of averaging calculation. The importance of analytical solutions lies in their ability to represent the mechanical behavior of the composite and give insights to the project, like bending-extension coupling magnitudes, overall stiffness, and approximated failure loads. However, they are limited if the designer wants to explore more complex constructions of fiber and matrix. Furthermore, most analytical forms are based on the Classical Laminate Theory (CLT). Assumptions of such approach neglect the shear in the thickness direction (out of plane), which makes the analysis incapable of predicting some effects like delamination. Computational methodologies are more powerful, can be extended to non-linear phases, but is generally computer-intensive.

Due to the complex microstructure of woven composites, computational homogenization is commonly used for the estimation of their elastic constants. In the present case, numerical modeling of a RVE is usual because of its ability to capture the effects of complicated textile architectures. If these effects are not precisely represented, the mechanical properties of the textile composite, which serves as input data for analyzing the response of the structural components made from this composite, become compromised.

Ideally, a two-step homogenization approach to predict the effective properties should be used. The first homogenization step (micro-homogenization) deals with determining the effective properties of tows (bundles) from fiber and matrix properties. The second homogenization step (macro-homogenization), is actually used to retrieve the effective properties. In the present work, only the second step will be used, considering that industrial tows used in textile composites are well tested and documented. This approach is by far the most used by researchers in this field. The other important aspect is the type of boundary condition which should be used on textiles, also discussed here.

Therefore, it is clear that the homogenization analysis of thin textile composites has differences if compared to the analysis of a general 3D anisotropic solid, and this is reflected in many important contributions in the literature. Barbero et al. [2006] employed periodic boundary conditions on the homogenization of a plain-weave, comparing the results with experiments and the CLT approach. The results showed an excellent agreement

with the experiments, overcoming the CLT procedure, especially on the effective shear modulus determination. Rao et al. [2008] also applied periodic boundary conditions on the study of the effect of the textile architecture on its mechanical properties. The author also studied the influence of debonding between fibers and the surrounding matrix, by applying a unit-cell along with a cohesive zone model. The approach showed good agreement with experimental results, especially when debonding is considered. Jacques et al. [2014] studied a general application of periodic boundary conditions for textiles and proposed an approach to circumvent the requirement of a periodic mesh by applying constraints on reference nodes along the boundaries of the RVE. Ullah et al. [2019] implemented a complete computational framework for predicting the elastic behavior of 2D and 3D textiles composites. The implementation employed three boundaries conditions types: static uniform boundary conditions, periodic boundary conditions, and uniform traction boundary conditions. Results showed a difference smaller than 5% between the tested boundary conditions and experimental data. Espadas-Escalante et al. [2017] reached a distinct result: the effective elastic results differ for textile composites. In this study, the uniform traction conditions were not adequate to predict E_{11} and E_{22} elastic moduli. The author proposed a set of mixed boundary conditions which were the combination of an out-of-plane traction condition (not necessarily null) and periodic boundary conditions for the plane directions. Results for mixed boundary conditions performed better for E_{11} modulus.

Regardless of the approach employed to predict effective material properties, analytical or numerical, it must be capable of embodying the particular strain field in the repeating cell for each pattern, even when they have the same fiber volume fraction. With average field theories, this will, in general, deliver the same result.

2.1 Analytical approach

Let a point in a three-dimensional medium characterized by its stress-strain state in Voigt notation (Jones [2018]), i.e.:

$$\boldsymbol{\sigma} = \begin{pmatrix} \sigma_{11} \\ \sigma_{22} \\ \sigma_{33} \\ \sigma_{13} \\ \sigma_{23} \\ \sigma_{12} \end{pmatrix} , \qquad \boldsymbol{\varepsilon} = \begin{pmatrix} \varepsilon_{11} \\ \varepsilon_{22} \\ \varepsilon_{33} \\ \varepsilon_{13} \\ \varepsilon_{23} \\ \varepsilon_{12} \end{pmatrix} . \tag{1}$$

The most general constitutive relation between $\boldsymbol{\sigma}$ and $\boldsymbol{\varepsilon}$, with the thermodynamic and tensor symmetry constraints already considered, is the generalized Hooke's law:

$$\boldsymbol{\sigma} = \mathbf{C}\,\boldsymbol{\varepsilon} , \tag{2}$$

where $\mathbf{C}$ contains up to 21 different constitutive constants. Laminated composites generally have a high aspect ratio, allowing to model most structural elements under the simplifications of plate or shell models. Although very limited for industrial applications, plate models reduce the equilibrium equations to the point of obtaining simplified analytical solutions containing essential information regarding the deformation kinematics, like

da Rocha, Jonas T., et al. (2022) Weaving Patterns on Mechanical Response of Composites

pp. 76-119

in-plane and bending stress and strain. For the sake of simplicity, herein we will consider only plate models under the linear elastic regime.

The plate's mid-surface is generally considered as a reference plane, which lies on the (x_1, x_2) plane so that the thickness h is measured through the x_3-axis, $x_3 = [-h/2, +h/2]$. Among the several laminated plate models proposed, most of the analytical solutions are based on Classical Laminate Theory (CLT), which employs the classic thin plate kinematics. Therefore, it is advisable to recall the main Kirchhoff's hypothesis for plates:

1. Transverse normal fibers initially straight and perpendicular to the reference surface remain so after the deformation;

2. Transverse normal fibers inextensible.

As a consequence, transverse shear strains (ε_{13} and ε_{23}) and the transverse normal strain (ε_{33}) are neglected, reducing the number of strains to three. The number of non-null stress follows Hooke's law, except that the transverse normal stress is *ad hoc* assumed zero, characterizing the well-known inconsistency of thin plate theory. The generalized Hooke's law (eq. (2)) now reduces to:

$$
\begin{pmatrix} \sigma_{11} \\ \sigma_{22} \\ \sigma_{12} \end{pmatrix} = \begin{bmatrix} C_{11} & C_{12} & C_{13} \\ C_{12} & C_{22} & C_{23} \\ C_{13} & C_{23} & C_{33} \end{bmatrix} \begin{pmatrix} \varepsilon_{11} \\ \varepsilon_{22} \\ \varepsilon_{12} \end{pmatrix} , \tag{3}
$$

or, for short:

$$
\boldsymbol{\sigma} = \bar{\bar{\mathbf{C}}}\boldsymbol{\varepsilon} , \tag{4}
$$

where $\bar{\bar{\mathbf{C}}}$ corresponds to the reduced constitutive matrix (Jones [2018]).

The plate resultant stresses (stresses by unit length) are evaluated by integrating the local stresses throughout the thickness, resulting in the in-plane (extensional or membrane) and out-of-plane (bending) stresses:

$$
\mathbf{N} = \begin{pmatrix} N_{11} \\ N_{22} \\ N_{12} \end{pmatrix} = \int_h \begin{pmatrix} \sigma_{11} \\ \sigma_{22} \\ \sigma_{12} \end{pmatrix} \mathrm{d}x_3 , \tag{5}
$$

$$
\mathbf{M} = \begin{pmatrix} M_{11} \\ M_{22} \\ M_{12} \end{pmatrix} = \int_h \begin{pmatrix} \sigma_{11} \\ \sigma_{22} \\ \sigma_{12} \end{pmatrix} x_3 \, \mathrm{d}x_3 . \tag{6}
$$

The following additional assumptions are used to include the case of laminated plates (CLT):

3. The laminas are perfectly bonded;

4. Each lamina is linear-elastic and orthotropic;

5. The strain field is continuous through the plate thickness.

In Jorge, Ariosto B., et al. (Eds.) Fundamental Concepts and Models for the Direct Problem, Vol. 2, UnB

81

Now recall that the strain field $\boldsymbol{\sigma}$ of eq. (3) can also be split into its extensional (membrane) and bending parts:

$$\boldsymbol{\varepsilon} = \boldsymbol{\varepsilon}^m + x_3\,\boldsymbol{\kappa} \ , \tag{7}$$

where ε^m accounts for extension/shear deformations while $\boldsymbol{\kappa}$ accounts for curvature changes of the plate. After inserting eq. (7) into eq. (3), the latter can be integrated in the thickness direction – eqs. (5) and (6) (Reddy [2003]), adding the contribution of each lamina. The basic resultant stress-strain of the CLT is then obtained:

$$\begin{pmatrix} \mathbf{N} \\ \mathbf{M} \end{pmatrix} = \begin{bmatrix} \mathbf{A} & \mathbf{B} \\ \mathbf{B} & \mathbf{D} \end{bmatrix} \begin{pmatrix} \boldsymbol{\varepsilon}^m \\ \boldsymbol{\kappa} \end{pmatrix} \ , \tag{8}$$

where $\mathbf{A}$, $\mathbf{B}$, and $\mathbf{D}$ are the extensional, bending-extension coupling, and bending *stiffness* matrices, respectively. The inverse of these coefficients is denoted as $\mathbf{a}^*, \mathbf{b}^*, \mathbf{d}^*$, respectively, whenever *compliance* coefficients are needed. Besides using stress-resultants, eq. (8) must be further distinguished from eq. (3) because it already incorporates Kirchhoff's plate model kinematics, so it will be called ABD-matrix.

2.1.1 Ishikawa and Chou model

One of the first approaches to evaluate analytically the stiffness of woven composites that have been published is the well-known series model presented by Ishikawa [1981], who provided closed-form solutions for the macroscopic coupling coefficients of the $\mathbf{B}$ submatrix. The model is based on Kirchhoff's plate theory as well, and therefore it is an interesting method to be compared to other solutions. Here, the effects of temperature are not considered, although, in the original formulation Ishikawa [1981], the expressions are complete. A simple comparison example is the expressions for the ABD-matrix in eq. (8), in terms of engineering constants for a two-lamina cross-ply plate simulating a plain-weave composite were derived as:

$$A_{11} = A_{22} = h\,\frac{(E_{11} + E_{22})}{2} = h\,\frac{(E_{LL} + E_{TT})}{2\,(1 - v_{LT}v_{TT})} \ , \tag{9a}$$

$$A_{12} = h\,E_{12} = h\,\frac{v_{LT}E_{TT}}{(1 - v_{LT}v_{TT})} \ , \tag{9b}$$

$$A_{66} = h\,E_{66} = h\,G_{LT} \ , \tag{9c}$$

$$B_{11} = -B_{22} = \frac{(E_{11} - E_{22})\,h^2}{8} = \frac{(E_{LL} - E_{TT})\,h^2}{8\,(1 - v_{LT}v_{TT})} \ , \tag{9d}$$

$$D_{11} = D_{22} = \frac{(E_{11} + E_{22})\,h^3}{24} = \frac{(E_{LL} + E_{TT})\,h^3}{24\,(1 - v_{LT}v_{TT})} \ , \tag{9e}$$

$$D_{12} = \frac{E_{66}h^3}{12} = \frac{v_{LT}E_{LL}h^3}{12\,(1 - v_{LT}v_{TT})} \ , \tag{9f}$$

$$D_{66} = \frac{E_{66}h^3}{12} = \frac{G_{LT}h^3}{12} \ , \tag{9g}$$

where L and T are the main material directions of the laminae.

The basic idea of the series model is to neglect the two-dimensional character of the plate and assume a repetitive occurrence of an alternating two-layer beam cell with length $2a$. If the cell is repeated n times, average stress or strain can be retrieved by integration.

Let the model be subjected to a uniform traction $N = (N_{11} \ 0 \ 0)^T$. The average curvature can be evaluated as Ishikawa [1981]:

$$\bar{\kappa}_{11} = \frac{1}{na} \int_0^{na} \kappa_{11} \mathrm{d}x \ . \tag{10}$$

This leads to simple expressions for the average values of the compliance coefficients $\mathbf{a}^*$ and $\mathbf{b}^*$. Considering yet that in a cross-ply laminate, if stacking sequence is inverted the coupling terms change sign, the average curvature is:

$$\bar{\kappa}_{11} = \left(1 - \frac{2}{n}\right) b^*_{11} N_1 \ , \tag{11}$$

implying that the corrected compliance b^w_{11} coefficient for a two-layer weaving composite is:

$$b^{*w}_{11} = \left(1 - \frac{2}{n}\right) b^*_{11} \ . \tag{12}$$

Similar considerations are made for other coefficients, leading additionally to:

$$\begin{aligned} a^{*w}_{11} &= a^*_{11} \ , \\ d^{*w}_{11} &= d^*_{11} \ . \end{aligned} \tag{13}$$

The inversion of the abd-matrix, given by eqs. (12) and (13), generates a corrected ABD-matrix which gives the lower bound of the stiffness:

$$\begin{aligned} D^w_{ij} &= \left\{ d^*_{ij} - \left(1 - \frac{2}{n}\right)^2 b^*_{ik} a^*_{kl} \left(b^*_{lj}\right)^{-1} \right\}^{-1} \ , \\ B^w_{ij} &= -\left(1 - \frac{2}{n}\right) \left(a^*_{ik}\right)^{-1} b^*_{kl} D^w_{lij} \ , \\ A^w_{ij} &= \left(a^*_{ij}\right)^{-1} + \left(1 - \frac{2}{n}\right)^2 \left(a^*_{ik}\right)^{-1} b^*_{kl} D^w_{km} b^*_{mn} \left(a^*_{nj}\right)^{-1} \ . \end{aligned} \tag{14}$$

In order to obtain the corresponding upper bound, the average in-plane stresses can be evaluated considering uniform membrane and bending strains along the length of the model. For instance (Ishikawa [1981]):

$$\begin{aligned} \bar{N}_{11} &= \frac{1}{na} \int_0^n a N_1 \, \mathrm{d}x \\ &= A_{11} \varepsilon^m_{11} + A_{12} \varepsilon^m_{22} + \left(1 - \frac{2}{n}\right) B_{11} \kappa_{11} \ , \end{aligned} \tag{15}$$

and the corrected plate stiffness coefficients follow directly. They represent the stiffness upper bounds:

$$A^w_{ij} = A_{ij} \ ,$$
$$B^w_{ij} = \left(1 - \frac{2}{n}\right) B_{ij} \ ,$$
$$D^w_{ij} = D_{ij} \ ,$$

$$(16)$$

with the coefficients of the right-hand side calculated from eq. (9). Figure 2 shows the upper and lower bounds for b^*_{11} and A_{11} as functions of the repetition frequency. It must be noted that, for a plain-weave, $n = 2$ and the coupling b^*_{11} vanishes.
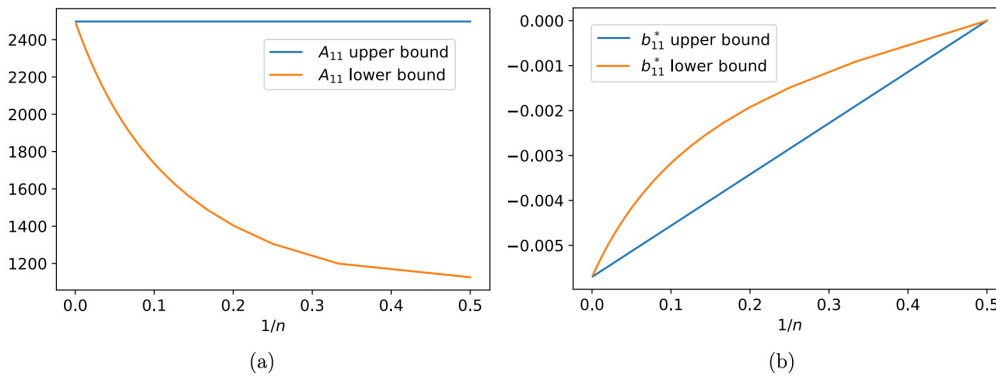
Figure 2: Upper and lower bounds of for (a) A_{11} **and (b)** b^*_{11} **as in Ishikawa [1981].**

2.2 Numerical approach

2.2.1 RVE

The *Representative Volume Element* (RVE) provides a useful tool to relate the microstructure and the overall (or effective) properties of a heterogeneous solid (Nemat-Nasser and Hori [1996], Hill [1963]). RVE-based approaches to classical multi-scale solid mechanics with both macro and micro-scales described in terms of conventional kinematics are very well understood and lie on solid theoretical grounds set in the works of Hill [1972] and Mandel [1998]. Therefore, they constitute a particularly well-suited methodology to be applied in the present context, since the main interest lies in the analysis of the macroscopic linear elastic constitutive relation for a class of composites.

An RVE must structurally represent the whole solid regarding an average value of the property P, that is, it must contain an adequate volume of material (or size D) such as to represent the effective mechanical properties of the material in a statistically homogeneous way, regardless the size of the material features (λ). As an analogy, fig. 3 illustrates a study of the color perception (property P) of an image for varying number of pixels (of size λ) in the RVE of length D sampled from the image. The length D is conventionally equal to the repeating unit cell (RUC) dimension. Nemat-Nasser and Hori [1996] claim that the RVE must include the features which have a first-order impact on the homogenized properties. Therefore, in metallurgical research, for instance, a couple of microns could be considered a micro-scale, and hundreds of microns could be defined as a macro-scale or continuum scale. On the other hand, in composite mechanics, the

RVE should have at least some millimeters to contain enough reinforcements that could capture properly macroscopic properties. In the general case, it is not possible to establish a RUC, hence D can be any real number. By regulating the size of the RVE, is expected that the property P will asymptotically reach a stable value for a computationally acceptable number of RUCs. The solid is therefore homogenized, hence one can apply the right techniques to retrieve its overall properties.

Since the present study is focused on composites whose reinforcement phase of the material is weaved, forming a fabric-like pattern, one could take advantage of the periodic structure, and represent the RVE by a number of RUCs. In this case, the required number of RUCs is relatively low, as it will be shown in the following sections. It is important to note that a homogenization analysis based on RVE is different than what is postulated by the average field theory. The average field theory is based on the physics and experimental definition of the overall properties of heterogeneous solids. In a RVE size analysis, on the other hand, establish relations between the micro-scale and the macro-scale using some sort of multi-scale perturbation technique. The properties will reach asymptotically to a macro value, as illustrated in fig. 3. At this point, the number of heterogeneities categorizes statistically macro-properties, and a procedure can be derived to determine, for example, the engineering constants of the media.
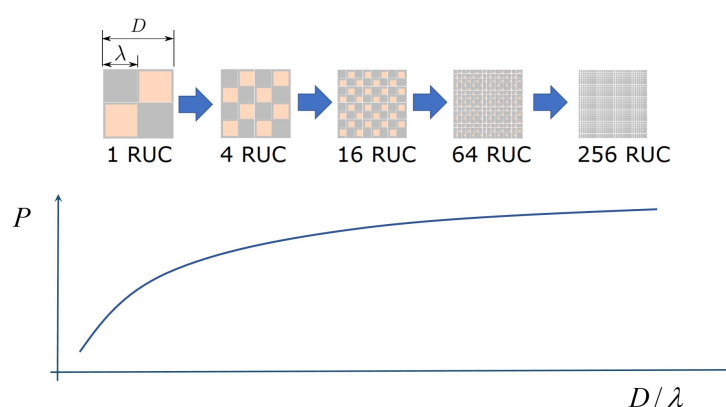
Figure 3: Exemplification of a RVE size and convergence of an overall property P.

2.2.2 Boundary conditions

The boundary conditions imposed on the RVE play a key role in the analysis. They must obey minimum requirements in order to ensure energy equivalence between the average and the local stress and strain states (Nemat-Nasser and Hori [1996]). In most cases, the typical boundary conditions used in RVE analysis fall into three categories: static uniform boundary conditions (SUBC), kinematic uniform boundary conditions (KUBC), and periodic boundary conditions (PBC) (Hazanov and Amieur [1995], Espadas-Escalante et al. [2017]). In this work, an additional type of boundary condition will be proposed, derived from a combination of the others, herein referred to as mixed boundary conditions (MBC).

The aforementioned energy equivalence, also known as the Hill-Mandel Principle of Macro-homogeneity (or just Hill's energy criteria, for short), must be satisfied by all boundary conditions and will be explored in the context of static problems under linear

regime (Hill [1965], Mandel [1998], de Souza Neto and Feijóo [2008]). Denoting the volumetric average as $\langle \cdot \rangle_V$, the macro-stress and macro-strain defined over a material sample are:

$$\langle \sigma_{ij} \rangle_V = \frac{1}{|V|} \int_V \sigma_{ij} \mathrm{d}V \ , $$
$$\langle \varepsilon_{ij} \rangle_V = \frac{1}{|V|} \int_V \varepsilon_{ij} \mathrm{d}V \ . \tag{17}$$

Evidently, σ_{ij} and ε_{ij} are the stresses and strains at a microscopic level, so that Hooke's law must refer to a point $\mathbf{x} \in \mathbf{V}$:

$$\sigma_{ij}(\mathbf{x}) = C_{ijkl}(\mathbf{x})\varepsilon_{kl}(\mathbf{x}) \ . \tag{18}$$

At the macroscopic level, the elastic tensor represents an average constitutive relation in V, and therefore:

$$\langle \sigma_{ij} \rangle_V = \bar{C}_{ijkl} \langle \varepsilon_{kl} \rangle_V \ , \tag{19}$$

where the dependence on the size V is in evidence.

Hill's energy condition requires that the average strain energy density $\langle U \rangle$ is equivalent to both states. By using eqs. (18) and (19), one has, in the absence of stress rates:

$$\langle U \rangle_V = \frac{1}{2} \langle \varepsilon_{ij} C_{ijkl} \varepsilon_{kl} \rangle = \frac{1}{2} \langle \langle \varepsilon_{ij} \rangle_V \bar{C}_{ijkl} \langle \varepsilon_{kl} \rangle_V \rangle \ , \tag{20}$$

or

$$\langle \sigma_{ij} \varepsilon_{ij} \rangle_V = \langle \sigma_{ij} \rangle_V \langle \varepsilon_{ij} \rangle_V \ . \tag{21}$$

Before proceeding into the details of each type of boundary condition, it is important to prove the relationship between $\langle \varepsilon_{kl} \rangle_V$ and the boundary conditions of the SUBC type, i.e.:

$$u_i|_{\partial V} = \varepsilon_{ij}^A x_j \ , \tag{22}$$

where ε_{ij}^A denotes a prescribed constant strain state, and x corresponds to a position vector. From the average strain definition (eq. (17)), we have:

$$\langle \varepsilon_{ij} \rangle_V = \frac{1}{2V} \int_V \left(\frac{\partial u_i}{\partial x_j} + \frac{\partial u_j}{\partial x_i} \right) \mathrm{d}V \ . \tag{23}$$

For generality, let's assume that volume V is composed of two subregions of volume V_1 and V_2 connected by an interface volume $V_1 \cap V_2$, so that $V = V_1 + V_2 + V_1 \cap V_2$ as shown in fig. 4.

Under this volume partition, eq. (23) is rewritten:

$$\langle \varepsilon_{ij} \rangle_V = \frac{1}{2V} \left[\int_V \left(\frac{\partial u_i}{\partial x_j} + \frac{\partial u_j}{\partial x_i} \right) \mathrm{d}V + \int_{V_1 \cap V_2} \left(\frac{\partial u_i}{\partial x_j} + \frac{\partial u_j}{\partial x_i} \right) \mathrm{d}V \right] \ , \tag{24}$$

which can be converted into a boundary-only equation using the divergence theorem:
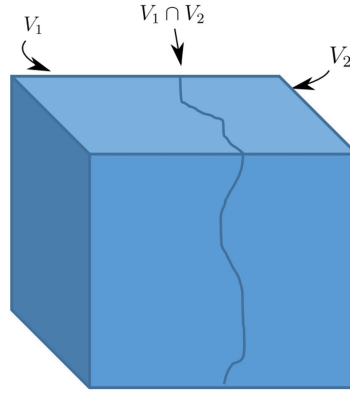
Figure 4: Division of a volume V into three parts.

$$\langle \varepsilon_{ij} \rangle_V = \frac{1}{2V} \left[\int_{\partial V} (u_i n_j + u_j n_i) \, \mathrm{d}A + \int_{\partial V_1 \cap \partial V_2} (u_i n_j + u_j n_i) \, \mathrm{d}A \right] . \qquad (25)$$

Now the boundary condition (eq. (22)) can be imposed, resulting in:

$$\langle \varepsilon_{ij} \rangle_V = \frac{1}{2V} \left[\int_{\partial V} \left(\varepsilon_{ij}^A x_j n_j + \varepsilon_{ij}^A x_i n_i \right) \mathrm{d}A + \int_{\partial V_1 \cap \partial V_2} (u_i n_j + u_j n_i) \, \mathrm{d}A \right] ,$$
$$= \frac{1}{2|V|} \left[\int_V \left(\frac{\partial}{\partial x_j} \left(\varepsilon_{ij}^A x_j \right) + \frac{\partial}{\partial x_i} \left(\varepsilon_{ji}^A x_i \right) \right) \mathrm{d}V + \int_{\partial V_1 \cap \partial V_2} (u_i n_j + u_j n_i) \, \mathrm{d}A \right] ,$$
$$(26)$$

which, after manipulation, simplifies to:

$$\langle \varepsilon_{ij} \rangle_V = \varepsilon_{ij}^A + \frac{1}{2V} \int_{\partial V_1 \cap \partial V_2} (u_i n_j + u_j n_i) \, \mathrm{d}A . \qquad (27)$$

The term $u_i n_j + u_j n_i$ in eq. (27) represents the jump in the displacement field along with the interface between V_1 and V_2. Whenever the volumes are perfectly bonded, the boundary integral terms vanishes, resulting in the equivalence known as *Average Strain Theorem*, written as:

$$\langle \varepsilon_{ij} \rangle_V = \varepsilon_{ij}^A . \qquad (28)$$

2.2.3   Static uniform boundary conditions

Once eq. (28) is demonstrated and proved, it is possible to detail the different boundary condition types. As aforementioned, the Static Uniform Boundary Conditions (SUBC) is established if the displacements on the boundary are described as in eq. (22). Other authors, such as Espadas-Escalante et al. [2017] and Shen and Brinson [2006], alternatively named it Uniform Displacement Boundary Condition, as proposed by Hazanov and Amieur [1995]. Essentially, the SUBC is a kinematically admissible displacement field that creates a homogeneous strain field. For example, if a pure-extension condition is imposed on a cube, such as shown in fig. 5, one writes:

$$\varepsilon^A = \begin{bmatrix} \varepsilon_{11}^A & 0 & 0 \\ 0 & 0 & 0 \\ 0 & 0 & 0 \end{bmatrix} .$$

If the global coordinate system is placed at the cube center, it is trivial to write:

$$u\big|_{\mathbf{x}_i = (a_1, 0, 0)^T} = -u\big|_{\mathbf{x}_i = (-a_1, 0, 0)^T} = \varepsilon_{11}^A a_1 ,$$

where a_1 is the half-length of the cube.
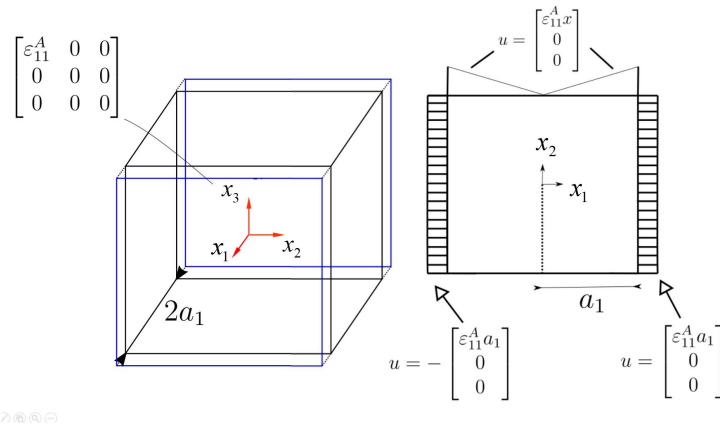
Figure 5: Boundary conditions scheme for the ε_A state.

Now it is necessary to show that Hill's energy condition is satisfied for the boundary condition $u_i|_{\partial V} = \varepsilon_{ij}^A x_j$. The work done by the surface traction t_i on the surface ∂V of the solid is written:

$$\begin{aligned}
\int_{\partial V} u_i t_i \mathrm{d}A &= \int_{\partial V} u_i \sigma_{ij} n_j \, \mathrm{d}A , \\
&= \int_V \frac{\partial}{\partial x_j}\left(u_i \sigma_{ij}\right) \mathrm{d}V , \\
&= \int_V \left(\frac{\partial}{\partial x_j} u_i\right)\sigma_{ij} \, \mathrm{d}V , \\
&= \int_V \varepsilon_{ij} \sigma_{ij} \, \mathrm{d}V .
\end{aligned} \tag{29}$$

Alternatively, one can write:

$$\begin{aligned}
\int_{\partial V} u_i t_i \mathrm{d}A &= \int_{\partial V} \varepsilon_{ij}^A x_j \sigma_{ij} n_j \, \mathrm{d}A , \\
&= \int_V \frac{\partial}{\partial x_j}\left(\varepsilon_{ij}^A x_j\right)\sigma_{ij} \, \mathrm{d}V , \\
&= \int_V \varepsilon_{ij}^A \sigma_{ij} \, \mathrm{d}V .
\end{aligned} \tag{30}$$

One can recall the Average Strain Theorem (eq. (28)) and observe that the resultants of eqs. (29) and eqs. (30) prove the energy equivalence, since:

$$\langle \varepsilon_{ij} \rangle_V \sigma_{ij} \equiv \varepsilon_{ij}^A \sigma_{ij} \ . \tag{31}$$

2.2.4 Periodic boundary conditions

Luciano and Sacco [1998] introduced the evaluation concept of the overall properties of a periodic media subjected to either a mean strain or mean stress field. In a periodic prism $2a_1 \times 2a_2 \times 2a_3$ (see fig. 6), the displacement field on its boundary can be written as:

$$u_i(a_1, x_2, x_3) - u_i(-a_1, x_2, x_3) = 2\varepsilon_{i1}a_1, \forall x_2 \in [-a_2, a_2], \forall x_3 \in [-a_3, a_3] \ , \tag{32a}$$

$$u_i(x_1, a_2, x_3) - u_i(x_1, -a_2, x_3) = 2\varepsilon_{i2}a_2, \forall x_1 \in [-a_1, a_1], \forall x_3 \in [-a_3, a_3] \ , \tag{32b}$$

$$u_i(x_1, x_2, a_3) - u_i(x_1, x_2, -a_3) = 2\varepsilon_{i3}a_3, \forall x_1 \in [-a_1, a_1], \forall x_2 \in [-a_2, a_2] \ . \tag{32c}$$

Equation (32) is known as Periodic Boundary Conditions (PBC). Further details of the derivation of eqs. (32) are omitted in this text. They can be found, however, in Luciano and Sacco [1998]. The micro-strains and micro-stresses within the periodic media are represented by the equations:

$$\varepsilon_{ij}(x_1, x_2, x_3) = \varepsilon_{ij}^0 + \varepsilon_{ij}^p(x_1, x_2, x_3) \ , \tag{33}$$

$$\sigma_{ij}(x_1, x_2, x_3) = \sigma_{ij}^0 + \sigma_{ij}^p(x_1, x_2, x_3) \ , \tag{34}$$

where ε_{ij}^0 and σ_{ij}^0 represent the mean strains and mean stresses, respectively. ε_{ij}^p and σ_{ij}^p are the V-periodic strain and stresses. Those entities are defined by the following expressions:

$$\varepsilon_{ij}^0 = \frac{1}{V} \int_V \varepsilon_{ij}(x_1, x_2, x_3) dV = \langle \varepsilon_{ij} \rangle_V \ , \tag{35a}$$

$$\sigma_{ij}^0 = \frac{1}{V} \int_V \sigma_{ij}(x_1, x_2, x_3) dV = \langle \sigma_{ij} \rangle_V \ , \tag{35b}$$

$$0 = \frac{1}{V} \int_V \varepsilon_{ij}^p(x_1, x_2, x_3) dV \ , \tag{35c}$$

$$0 = \frac{1}{V} \int_V \sigma_{ij}^p(x_1, x_2, x_3) dV \ . \tag{35d}$$

Equations (32) establish a relationship between displacements over opposite faces. Therefore, the displacements are not directly imposed, differently from what eq.(22) proposes. Aiming at their computational implementation, eq.(32a) can be rewritten as:

$$u_i(a_1, x_2, x_3) - u_i(-a_1, x_2, x_3) = \begin{bmatrix} \varepsilon_{11} & \varepsilon_{12} & \varepsilon_{13} \\ \varepsilon_{21} & \varepsilon_{22} & \varepsilon_{23} \\ \varepsilon_{31} & \varepsilon_{32} & \varepsilon_{33} \end{bmatrix} \begin{bmatrix} a_1 \\ 0 \\ 0 \end{bmatrix} \ . \tag{36}$$

The same procedure is applied to eqs. (32b) and (32c) as well. Equation (36) indicates that opposite faces are subjected to the restrictions defined at the center position of each one. They produce, however, ambiguities at vertices and along edges, as they can have over-defined boundary conditions, as clarified by Barbero [2007].

Considering a periodic body like the one depicted in fig. 6, symmetric edges respective to the center of the body must be tied. In order to exemplify future computational implementation, edges parallel to x_3 must respect the following condition:

$$u_i(a_1, a_2, x_3) - u_i(-a_1, -a_2, x_3) = \begin{bmatrix} \varepsilon_{11} & \varepsilon_{12} & \varepsilon_{13} \\ \varepsilon_{21} & \varepsilon_{22} & \varepsilon_{23} \\ \varepsilon_{31} & \varepsilon_{32} & \varepsilon_{33} \end{bmatrix} \begin{bmatrix} a_1 \\ a_2 \\ 0 \end{bmatrix} . \tag{37}$$

And vertices such those lying on $x_i = (a_1, a_2, a_3)$ and $x_i = (-a_1, -a_2, -a_3)$ must be tied by:

$$u_i(a_1, a_2, a_3) - u_i(-a_1, -a_2, a_3) = \begin{bmatrix} \varepsilon_{11} & \varepsilon_{12} & \varepsilon_{13} \\ \varepsilon_{21} & \varepsilon_{22} & \varepsilon_{23} \\ \varepsilon_{31} & \varepsilon_{32} & \varepsilon_{33} \end{bmatrix} \begin{bmatrix} a_1 \\ a_2 \\ a_3 \end{bmatrix} . \tag{38}$$

Analogous equations can be defined for others vertices and edges.
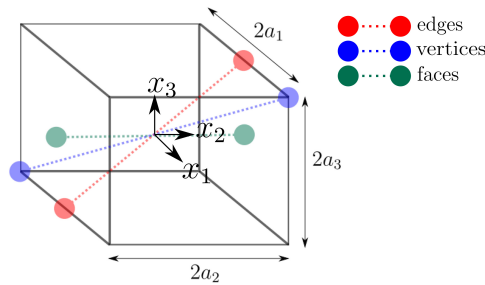
Figure 6: Definition of geometric entities for the periodic boundary conditions scheme.

The satisfaction of Hill's energy condition for this type of boundary condition is not easily found in the literature. For sake of completeness, a short proof can be derived. Hazanov and Amieur [1995], among others, showed that the following equivalence holds:

$$\int_{\partial V} \left(t_i - \langle \sigma_{ij} \rangle n_j \right) \cdot \left(u_i - \langle \varepsilon_{ij} \rangle x_j \right) \mathrm{d}A = 0 \quad \Leftrightarrow \quad \langle \sigma_{ij} \varepsilon_{ij} \rangle_V - \langle \sigma_{ij} \rangle_V \langle \varepsilon_{ij} \rangle_V = 0 \, , \tag{39}$$

which can be transformed in a volume integral as:

$$\frac{1}{V} \int_V \left(\sigma_{ij} - \langle \sigma_{ij} \rangle_V \right) \cdot \left(\varepsilon_{ij} - \langle \varepsilon_{ij} \rangle_V \right) \mathrm{d}V = \langle \sigma_{ij} \varepsilon_{ij} \rangle_V - \langle \sigma_{ij} \rangle_V \langle \varepsilon_{ij} \rangle_V = 0 \, . \tag{40}$$

Inserting eqs. (33) and (34) in eq. (40) and expanding the resultant, one obtains:

$$\frac{1}{V} \int_V \Big(\sigma_{ij}^0 \varepsilon_{ij}^0 - \sigma_{ij}^0 \langle \varepsilon_{ij} \rangle_V - \langle \sigma_{ij} \rangle_V \varepsilon_{ij}^0 + \sigma_{ij}^0 \varepsilon_{ij}^p + \sigma_{ij}^p \varepsilon_{ij}^0 + \sigma_{ij}^p \varepsilon_{ij}^p +$$
$$- \sigma_{ij}^p \langle \varepsilon_{ij} \rangle_V - \langle \sigma_{ij} \rangle_V \varepsilon_{ij}^p + \langle \sigma_{ij} \rangle_V \langle \varepsilon_{ij} \rangle_V \Big) \, dV = \langle \sigma_{ij} \varepsilon_{ij} \rangle_V - \langle \sigma_{ij} \rangle_V \langle \varepsilon_{ij} \rangle_V = 0 \, , \tag{41}$$

and, by canceling out the equivalent terms in eq. (41), one can write:

$$\frac{1}{V} \int_V \sigma_{ij}^p \varepsilon_{ij}^p \, \mathrm{d}V = 0 \ . \tag{42}$$

Another way to see eq. (42) comes up by interpreting it as a simple circular convolution between two periodic signals σ and ε with period V, i.e. $\int_V \sigma \varepsilon \, \mathrm{d}V$ which in this case, results in a function with the same period. Because the signals are symmetric, the convolution must be zero.

2.2.5   Mixed boundary conditions

One of the first applications of Mixed Boundary Conditions (MBC) in the context of the RVE homogenization problem was presented by Hazanov and Amieur [1995], accounting for both traction (p_i) and displacement (u_i) boundary values as follows:

$$\Big(p_i - \langle \sigma_{ij} \rangle_V n_j\Big)\Big(u_i - \langle \varepsilon_{ij} \rangle_V x_j\Big) = 0 \ , \quad \text{on} \quad \partial V \ , \tag{43}$$

therefore, combining sets of KUBC and SUBC. It is important to highlight that this type of boundary condition is limited to elastic materials that show orthotropic symmetry, at most. Any less symmetric material, i.e., monoclinic or triclinic symmetries, would generate coupling stresses that would not respect eq. (43). A great advantage of this approach is to reproduce effectively the boundary conditions from experimental tests, as in Shen and Brinson [2006], which imposed KUBC in faces perpendicular to the loading and SUBC on faces parallel to the loading.

Recently, in a general homogenization scheme proposed by Glüge [2013], the RVE boundary is divided into *n* parts, each one subjected to an average strain $\langle \varepsilon_{ij} \rangle_V$:

$$\langle \varepsilon_{ij} \rangle_V \int_{\partial V_n} x_j n_i dA = \int_{\partial V_n} u_j n_i \, \mathrm{d}A \ . \tag{44}$$

The above equation leads to important remarks:

1. If $n \to \infty$, then $u|_{\partial V} = \varepsilon_{ij}^A x_j$ as in SUBC.

   Proof: The integral drops in (44) and it follows that:

$$\begin{aligned}
\langle \varepsilon_{ij} \rangle_V x_j n_i dA &= u_j n_i dA, \text{ in } \partial V \ , \\
u|_{\partial V} &= \langle \varepsilon_{ij} \rangle_V x_j \ , \\
u|_{\partial V} &= \varepsilon_{ij}^A x_j \ .
\end{aligned} \tag{45}$$

2. If $n \to \infty$, when the faces are mirrored such that $n_i dA^+ = -n_i dA^-$, eq.(44) corresponds to a PBC.

   Proof: Equation (44) is divided into $n_i dA^+$ and $n_i dA^-$, with position vectors $x_j^+ = -x_j^-$, the superscripts meaning opposite sides of an RVE as follows:

$$\begin{aligned}
\langle \varepsilon_{ij} \rangle_V x_j^+ n_i dA^+ + \langle \varepsilon_{ij} \rangle_V x_j^- n_i dA^- &= u_i^+ n_j dA^+ + u_i^- n_j dA^- \ , \\
2\langle \varepsilon_{ij} \rangle_V x_j^+ &= u_i^+ - u_i^- \ .
\end{aligned} \tag{46}$$

   This is equivalent to eq. (32).

3. If $n = 1$, $\partial V_n \to \partial V$, and eq.(44) represents KUBC. Equation (44) then becomes:

$$\langle \varepsilon_{ij} \rangle_V = \frac{1}{V} \int_{\partial V} u_i n_j \, \mathrm{d}A \,, \tag{47}$$

which can be shown to correspond to a homogeneous stress field.

In a study focused on textiles made by Espadas-Escalante et al. [2017], the concept of MBC as a combination of PBC and KUBC is proposed. In the plane directions, the composite is treated as periodic, while in the out-of-plane direction uniform traction is imposed. This allows applying a traction-free condition along the out-of-plane direction, which replicates the plane-stress condition expected in thin structures such as textiles. Emphasis is given to the fact that *"homogenization is highly dependent of boundary conditions' choosing for one layer of textile composite"*. The most important results can be numbered as:

- Differences between SUBC and KUBC on E_{11} homogenization can vary as much as 200%;

- MBC approach asymptotically PBC as the number of layers is increased in a laminate;

- The out-of-plane E_{33} seems to be less sensitive than E_{11} to boundary condition type (differences of 10%);

- The results showed that SUBC and PBC performed better in comparison to experimental results for in-plane mechanical properties.

3 A New Set of Boundary Conditions

The study of Espadas-Escalante et al. [2017] motivated the implementation of a different set of MBC. Since PBC and SUBC deliver better results when compared to experimental data, the basic idea is to mix PBC for the in-plane degrees of freedom and SUBC for the out-of-plane degrees of freedom, trying to extract the best of both sets of boundary conditions. This proposal will be referenced as MBC* along with this chapter.

Considering again a prism $2a_1 \times 2a_2 \times 2a_3$ with a centered coordinate system, the degrees of freedom in the 1-2 directions are specified as proposed by Luciano and Sacco [1998], while for direction 3, SUBC is used. Each face is identified by its relative position: West, East, North, South, Upper, and Lower, as in fig.7. Naturally, for the degrees of freedom in the plane 1-2 the stress and strain fields admit the distribution given by eqs. (33) and (34), repeated below for convenience. No *a priori* assumptions are made for the strain and stress fields along the out-of-plane axis (x_3).

$$\varepsilon_{ij}(x_1, x_2, x_3) = \langle \varepsilon_{ij} \rangle_V + \varepsilon_{ij}^p(x_1, x_2, x_3) \,, \quad \text{for } i = 1, 2 \,, \tag{48a}$$

$$\sigma_{ij}(x_1, x_2, x_3) = \langle \sigma_{ij} \rangle_V + \sigma_{ij}^p(x_1, x_2, x_3) \,, \quad \text{for } i = 1, 2 \,, \tag{48b}$$

$$\int_V \varepsilon_{ij}^p(x_1, x_2, x_3) \, \mathrm{d}V = 0 \,, \tag{48c}$$

$$\int_V \sigma_{ij}^p(x_1, x_2, x_3) \, \mathrm{d}V = 0 \,. \tag{48d}$$
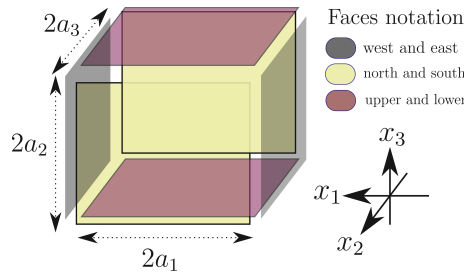
Figure 7: Face notation for the proposed set of boundary conditions.

Therefore, one has on the West and East faces:

$$
\begin{cases}
u_1(a_1, x_2, x_3) - u_1(-a_1, x_2, x_3) = 2\varepsilon_{11}^A a_1 \,, & \forall\, x_1 \in (-a_1, a_1) \,, \\
u_2(a_1, x_2, x_3) - u_2(-a_1, x_2, x_3) = 2\varepsilon_{21}^A a_1 \,, & \forall\, x_2 \in [-a_2, a_2] \,, \\
u_3(a1, x_2, x_3) = -u_3(-a_1, x_2, x_3) = \varepsilon_{3j}^A x_j \,, & \forall\, x_3 \in [-a_3, a_3] \,,
\end{cases}
\tag{49}
$$

and on the North and South faces:

$$
\begin{cases}
u_1(x_1, a_2, x_3) - u_1(x_1, -a_2, x_3) = 2\varepsilon_{11}^A a_2 \,, & \forall\, x_1 \in [-a_1, a_1] \,, \\
u_2(x_1, a_2, x_3) - u_2(x_1, -a_2, x_3) = 2\varepsilon_{21}^A a_2 \,, & \forall\, x_2 \in (-a_2, a_2) \,, \\
u_3(x_1, a_2, x_3) = -u_3(x_1, -a_2, x_3) = \varepsilon_{3j}^A x_j \,, & \forall\, x_3 \in [-a_3, a_3] \,,
\end{cases}
\tag{50}
$$

while on the Upper and Lower faces:

$$
\begin{cases}
u_1(x_1, x_2, a_3) - u_1(x_1, x_2, -a_3) = 2\varepsilon_{11}^A a_2 \,, & \forall\, x_1 \in [-a_1, a_1] \,, \\
u_2(x_1, x_2, a_3) - u_2(x_1, x_2, -a_3) = 2\varepsilon_{21}^A a_2 \,, & \forall\, x_2 \in [-a_2, a_2] \,, \\
u_3(x_1, x_2, a_3) = -u_3(x_1, x_2, -a_3) = \varepsilon_{3j}^A x_j \,, & \forall\, x_3 \in (-a_3, a_3) \,.
\end{cases}
\tag{51}
$$

By analyzing the proposed boundary conditions in terms of the Average Strain Theorem, the volume average is carried out to the boundary by the divergence theorem as follows:

$$
\begin{aligned}
\langle \varepsilon_{ij} \rangle_V &= \frac{1}{|V|} \int_V \varepsilon_{ij} \, \mathrm{d}V \,, \\
&= \frac{1}{2|V|} \int_V \left(\frac{\partial u_i}{\partial x_j} + \frac{\partial u_j}{\partial x_i} \right) \mathrm{d}V \,, \\
&= \frac{1}{2|V|} \int_{\partial V} \left(u_i n_j + u_j n_i \right) \mathrm{d}A \,.
\end{aligned}
\tag{52}
$$

The boundary can be divided into six parts, according to the colored faces of fig. 7:

$$
\partial V = \partial V^e + \partial V^w + \partial V^n + \partial V^s + \partial V^u + \partial V^l
\tag{53}
$$

hence:

$$\langle \varepsilon_{ij} \rangle_V = \frac{1}{2|V|} \left\{ \int_{\partial V^e} \left(u_i^e n_j^e + u_j^e n_i^e \right) \mathrm{d}A + \int_{\partial V^w} \left(u_i^w n_j^w + u_j^w n_i^w \right) \mathrm{d}A + \ldots \right.$$

$$\left. \int_{\partial V^u} \left(u_i^u n_j^u + u_j^u n_i^u \right) dA + \int_{\partial V^l} \left(u_i^l n_j^l + u_j^l n_i^l \right) \mathrm{d}A \right\} , \tag{54}$$

$$= \frac{1}{2|V|} \left\{ \Psi^{w/e} + \Psi^{n/s} + \Psi^{u/l} \right\} .$$

On the West and East faces, noting that $n^e = -n^w$:

$$\Psi^{w/e} = \int_{\partial w/e} \left\{ (u_i^e - u_i^w) n_j^e + (u_j^e - u_j^w) n_i^e \right\} \mathrm{d}A . \tag{55}$$

Noting also that $u_i^e = u_i(a_1, x_2, x_3)$ and $u_i^w = u_i(-a_1, x_2, x_3)$, by using the boundary conditions of eq. (49):

$$\Psi^{w/e} = 2 \int_{\partial w/e} \begin{bmatrix} 2\varepsilon_{11} a_1 \\ 2\varepsilon_{21} a_1 \\ 2\varepsilon_{3i} x_i \end{bmatrix} \begin{bmatrix} n_1^e & n_2^e & n_3^e \end{bmatrix} \mathrm{d}A , \tag{56}$$

and observing that $n^e = \begin{bmatrix} 1 & 0 & 0 \end{bmatrix}$:

$$\Psi^{w/e} = 4 \int_{\partial w/e} \begin{bmatrix} \varepsilon_{11} a_1 & 0 & 0 \\ \varepsilon_{21} a_1 & 0 & 0 \\ \varepsilon_{3i} x_i & 0 & 0 \end{bmatrix} \mathrm{d}A . \tag{57}$$

Since the third line requires a particular approach, one writes it separately. The first step is to split the expression into three integrals, written by:

$$\int_{\partial w/e} \varepsilon_{3i} x_i \mathrm{d}A = \int_{\partial w/e} \left(\varepsilon_{31} a_1 + \varepsilon_{32} x_2 + \varepsilon_{33} x_3 \right) \mathrm{d}x_2 \, \mathrm{d}x_3 ,$$

$$= \varepsilon_{31} a_1 (4 a_2 a_3) + \varepsilon_{32} \left. \frac{x_2^2}{2} \right|_{-a_2}^{a_2} \cdot 2a_3 + \varepsilon_{33} \left. \frac{x_3^2}{2} \right|_{-a_3}^{a_3} \cdot 2a_2 , \tag{58}$$

$$= \varepsilon_{31} a_1 (4 a_2 a_3) .$$

One notices that the last two terms of the second line vanish because $\left. \frac{x_2^2}{2} \right|_{-a_2}^{a_2} = \left. \frac{x_3^2}{2} \right|_{-a_3}^{a_3} = 0$. The eq. (57) can be rewritten as follows:

$$\Psi^{w/e} = \begin{bmatrix} \varepsilon_{11} & 0 & 0 \\ \varepsilon_{21} & 0 & 0 \\ \varepsilon_{31} & 0 & 0 \end{bmatrix} 2|V| , \tag{59}$$

where $|V| = 8 a_1 a_2 a_3$. Taking similar steps fo $\Psi^{n/s}$ and $\Psi^{u/l}$, we arrive at:

$$\Psi^{n/s} = \begin{bmatrix} 0 & \varepsilon_{12} & 0 \\ 0 & \varepsilon_{22} & 0 \\ 0 & \varepsilon_{33} & 0 \end{bmatrix} 2|V| , \tag{60}$$

$$\Psi^{u/l} = \begin{bmatrix} 0 & 0 & \varepsilon_{13} \\ 0 & 0 & \varepsilon_{23} \\ 0 & 0 & \varepsilon_{33} \end{bmatrix} 2|V| \ . \tag{61}$$

Now eqs. (59), (60), and (61) can be inserted into the expression for $\langle \varepsilon_{ij} \rangle_V$ (eq. (54)) and resulting in:

$$\langle \varepsilon_{ij} \rangle_V = \begin{bmatrix} \varepsilon_{11} & \varepsilon_{12} & \varepsilon_{13} \\ \varepsilon_{21} & \varepsilon_{22} & \varepsilon_{23} \\ \varepsilon_{31} & \varepsilon_{32} & \varepsilon_{33} \end{bmatrix} = \varepsilon_{ij}^A \ , \tag{62}$$

which proves that the Average Strain Theorem holds for the eqs. (49)- (51).

In order to verify if this set of boundary conditions complies the Hill's energy condition, one follows the approach introduced by Hazanov and Amieur [1995]. It is worth noting that eq. (39) is automatically satisfied if $u_i = \langle \varepsilon_{ij} \rangle_V x_j$ on ∂V and this is readily verified for u_3. Nonetheless, for the remaining degrees-of-freedom, further investigation must be performed. Firstly, one rewrites eq. (40) for u_1 and u_2, and using the divergence theorem, obtaining (Hazanov and Amieur [1995]):

$$\frac{1}{V} \int_V \left(\sigma_{1j} - \langle \sigma_{1j} \rangle_V \right) \cdot \left((\varepsilon_{1j} - \langle \varepsilon_{1j} \rangle_V \right) dV = 0 \ , \tag{63a}$$

$$\frac{1}{V} \int_V \left(\sigma_{2j} - \langle \sigma_{2j} \rangle_V \right) \cdot \left((\varepsilon_{2j} - \langle \varepsilon_{2j} \rangle_V \right) dV = 0 \ , \tag{63b}$$

$$\int_{\partial V} \left(t_3 - \langle \sigma_{3j} \rangle_V n_j \right) \cdot \left((u_3 - \langle \varepsilon_{3j} \rangle_V x_j \right) dA = 0 \ . \tag{63c}$$

As already mentioned, considering the third equation in eqs. (49)-(51) on any of the boundary surfaces, $u_3 = \langle \varepsilon_{3j} \rangle x_j$ and eq. (63c) vanishes automatically, in view of eq. (62). For u_1 and u_2, the same steps applied to prove Hill's criteria for periodic boundary conditions can be used, along with the stress and strain fields of eq.(48), leading to a similar result of eq. (42) as follows:

$$\frac{1}{V} \int_V \sigma_{ij}^p \varepsilon_{ij}^p \ \mathrm{d}V = 0 \ , \quad i = 1, 2 \ .$$

4 Evaluation of Effective Elastic Properties

The basic procedure to evaluate the effective elastic constants is well known (Zohdi [2002]). Essentially, eq. (19), repeated below for convenience, must be solved for RVE subjects to any of the boundary conditions discussed in the previous sections:

$$\langle \sigma_{ij} \rangle_V = \bar{C}_{ijkl} \langle \varepsilon_{kl} \rangle_V \ . \tag{64}$$

Now if the local stress field $\boldsymbol{\sigma}$ can be numerically calculated through either a FE or a BE analysis, so is $\langle \boldsymbol{\sigma} \rangle_V$, and eq. (64) provides six equations. One way to overcome the insufficient number of equations is by solving the RVE problem for other types of boundary conditions. This will provide the necessary equations to recover all entries of $\bar{\mathbf{C}}$

in the macroscopic constitutive relation of eqs. (64). Given the dimensions of $\bar{\mathbf{C}}$, applying six independent strain states will suffice (see fig. 8):

$$
\varepsilon^1 = \begin{bmatrix} \varepsilon_{xx} & 0 & 0 \\ 0 & 0 & 0 \\ 0 & 0 & 0 \end{bmatrix}, \quad \varepsilon^2 = \begin{bmatrix} 0 & 0 & 0 \\ 0 & \varepsilon_{yy} & 0 \\ 0 & 0 & 0 \end{bmatrix}, \quad \varepsilon^3 = \begin{bmatrix} 0 & 0 & 0 \\ 0 & 0 & 0 \\ 0 & 0 & \varepsilon_{zz} \end{bmatrix},
$$
$$
\varepsilon^4 = \begin{bmatrix} 0 & \varepsilon_{xy} & 0 \\ \varepsilon_{xy} & 0 & 0 \\ 0 & 0 & 0 \end{bmatrix}, \quad \varepsilon^5 = \begin{bmatrix} 0 & 0 & \varepsilon_{xz} \\ 0 & 0 & 0 \\ \varepsilon_{xz} & 0 & 0 \end{bmatrix}, \quad \varepsilon^6 = \begin{bmatrix} 0 & 0 & 0 \\ 0 & 0 & \varepsilon_{yz} \\ 0 & \varepsilon_{yz} & 0 \end{bmatrix}.
$$
$$(65)$$

The final system of linear equations can be derived as:

$$
\begin{bmatrix} \langle \sigma^1 \rangle_{6\times 1} \\ \langle \sigma^2 \rangle_{6\times 1} \\ \langle \sigma^3 \rangle_{6\times 1} \\ \langle \sigma^4 \rangle_{6\times 1} \\ \langle \sigma^5 \rangle_{6\times 1} \\ \langle \sigma^6 \rangle_{6\times 1} \end{bmatrix}_V = \begin{bmatrix} [C]_{6\times 6} & [0]_{6\times 6} & \cdots & \cdots & \cdots & [0]_{6\times 6} \\ [0]_{6\times 6} & [C]_{6\times 6} & [0]_{6\times 6} & \cdots & \cdots & [0]_{6\times 6} \\ \vdots & [0]_{6\times 6} & [C]_{6\times 6} & [0]_{6\times 6} & \cdots & [0]_{6\times 6} \\ \vdots & \vdots & [0]_{6\times 6} & [C]_{6\times 6} & [0]_{6\times 6} & [0]_{6\times 6} \\ \vdots & \vdots & \vdots & [0]_{6\times 6} & [C]_{6\times 6} & [0]_{6\times 6} \\ [0]_{6\times 6} & \cdots & \cdots & \cdots & [0]_{6\times 6} & [C]_{6\times 6} \end{bmatrix} \begin{bmatrix} \langle \varepsilon^1 \rangle \\ \langle \varepsilon^2 \rangle \\ \langle \varepsilon^3 \rangle \\ \langle \varepsilon^4 \rangle \\ \langle \varepsilon^5 \rangle \\ \langle \varepsilon^6 \rangle \end{bmatrix}_V, \quad (66)
$$

where $\langle \sigma^k \rangle$ and $\langle \varepsilon^k \rangle$, $k = 1..6$ are the average stress and strain states in Voigt notation. Equation (66) can be optimized for computational implementation. Starting with the vectorization of each $[C]$ sub-matrix:

$$
[C]_{36\times 1} = [M]^{-1}_{36\times 36} [\langle \sigma \rangle_V]_{36\times 1}, \qquad (67)
$$

with $\mathbf{M} = [\mathbf{M}^1_{ab} \ldots \mathbf{M}^k_{ab}]^T_{k=1..6}$, where k is one of the strain cases in eq.(65), and $\mathbf{M}^k_{ab}$ is the concatenated matrix (6 lines $\times$ 36 columns):

$$
\mathbf{M}^k_{ab} = \begin{cases} \begin{bmatrix} \langle \varepsilon^k \rangle_1 & \langle \varepsilon^k \rangle_2 & \cdots & \langle \varepsilon^k \rangle_6 \end{bmatrix}, & \text{if } a = b \\ \begin{bmatrix} 0 & 0 & 0 & 0 & 0 & 0 \end{bmatrix}, & \text{if } a \neq b \end{cases}, \qquad (68)
$$

or in matrix representation:
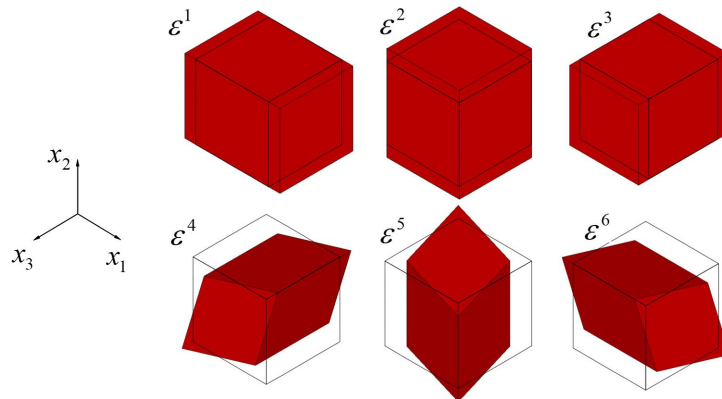
Figure 8: Visualization of the strain states ε^i in eqs. (65) for the particular case of constant strains.

$$\mathbf{M}^k_{ab} = \begin{bmatrix} \langle \varepsilon^k \rangle_{1\times 6} & [0]_{1\times 6} & \cdots & \cdots & \cdots & [0]_{1\times 6} \\ [0]_{1\times 6} & \langle \varepsilon^k \rangle_{1\times 6} & [0]_{1\times 6} & \cdots & \cdots & [0]_{1\times 6} \\ \vdots & [0]_{1\times 6} & \langle \varepsilon^k \rangle_{1\times 6} & [0]_{1\times 6} & \cdots & [0]_{1\times 6} \\ \vdots & \vdots & [0]_{1\times 6} & \langle \varepsilon^k \rangle_{1\times 6} & [0]_{1\times 6} & [0]_{1\times 6} \\ \vdots & \vdots & \vdots & [0]_{1\times 6} & \langle \varepsilon^k \rangle_{1\times 6} & [0]_{1\times 6} \\ [0]_{1\times 6} & [0]_{1\times 6} & [0]_{1\times 6} & [0]_{1\times 6} & [0]_{1\times 6} & \langle \varepsilon^k \rangle_{1\times 6} \end{bmatrix} . \tag{69}$$

Redundant equations can possibly be eliminated to account for the various symmetries of $\bar{\mathbf{C}}$. Alternatively, constraints can be used as well. The engineering constants can now be retrieved by inverting the stiffness matrix obtained by the solution of eq. (67), $\bar{\mathbf{S}} = \bar{\mathbf{C}}^{-1}$ as follows:

$$\bar{\mathbf{S}} = \begin{bmatrix} 1/E_1 & -\nu_{21}/E_2 & -\nu_{31}/E_3 & \eta_{1,23}/G_{23} & \eta_{1,13}/G_{13} & \eta_{1,12}/G_{12} \\ -\nu_{12}/E_1 & 1/E_2 & -\nu_{32}/E_3 & \eta_{2,23}/G_{23} & \eta_{2,13}/G_{13} & \eta_{2,12}/G_{12} \\ -\nu_{13}/E_1 & -\nu_{23}/E_2 & 1/E_3 & \eta_{3,23}/G_{23} & \eta_{3,13}/G_{13} & \eta_{3,12}/G_{12} \\ \eta_{23,1}/E_1 & \eta_{23,2}/E_2 & \eta_{23,3}/E_3 & 1/G_{23} & \mu_{23,13}/G_{13} & \mu_{23,12}/G_{12} \\ \eta_{13,1}/E_1 & \eta_{13,2}/E_2 & \eta_{13,3}/E_3 & \mu_{13,23}/G_{23} & 1/G_{13} & \mu_{13,12}/G_{12} \\ \eta_{12,1}/E_1 & \eta_{12,2}/E_2 & \eta_{12,3}/E_3 & \mu_{12,23}/G_{23} & \mu_{12,13}/G_{13} & 1/G_{12} \end{bmatrix} . \tag{70}$$

4.1 Fiber volume correction

In computational modeling of a textile composite, it is common to allow a thin layer of matrix material on the top and bottom sides of the RVE, as shown in fig. 9). This measure helps to avoid mesh generation issues (see, for instance, Long and Brown [2011]). As a result, the actual fiber volume fraction of the computational model is lowered and the homogenization process is affected. To correct this effect, Barbero's methodology (Barbero et al. [2006]) is followed in this work.

The correction is based on three fiber volume fractions: the overall, the mesoscale, and the tow fraction, denoted as V_o, V_g, and V_s, respectively. V_o is the ratio between the dry fiber volume and total (after curing) composite volume. The V_g measure is defined as the volume occupied by the strands with impregnated resin in the cured composite, or alternatively, in the computational representation of the tows. Finally, V_s is the volume fraction inside the strand. V_s is generally high (larger than 0.8), however, it is hard to be obtained experimentally. Barbero et al. [2006] introduce the following relationships among the volume fractions:

$$V_s = \frac{V_0}{V_g} . \tag{71}$$

V_g is obtained computationally while the V_o is an experiment value expected to be known. Furthermore, Barbero et al. [2006] suggest the following volume fraction correction for the Young modulus:

$$E = \frac{V_g}{V_g^\alpha} E^\alpha ; \tag{72}$$

with the superscript α meaning the value in the FEM model. Aiming at analyzing the stiffness matrix altogether, this correction is applied over the reduced constitutive tensor:

$$\bar{\mathbf{C}} = \frac{V_g}{V_g^\alpha} \, \bar{\mathbf{C}}^\alpha \; . \tag{73}$$

The approach is straightforward and corrects undesired effects on the final homogenized tensor. The issues do not appear in experimental values validation, since only common engineering constants are generally corrected and they are obtained from the main diagonal of the compliance tensor. Thus, caution is advisable when interpreting coupling coefficients. A deeper investigation of this correction and its influence on the stiffness/compliance tensors is out of the scope of this text.
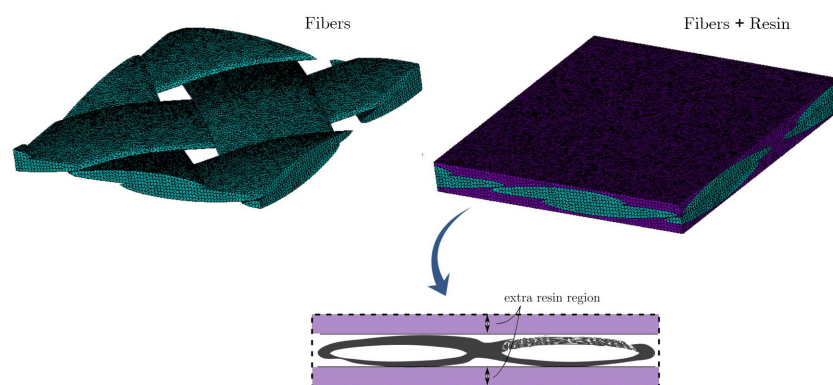
Figure 9: Typical extra layer of resin added by computational tools.

4.2 Principal directions of anisotropy

Rand and Rovenski [2007] introduced a straightforward methodology for defining the principal directions of an anisotropic material based on a bulk modulus tensor and a deviatoric modulus tensor. These are also contractions of the stiffness tensor, and are given by the following definitions:

- Bulk modulus tensor

$$\mathbf{K} = \begin{bmatrix} K_{11} & K_{12} & K_{13} \\ K_{12} & K_{22} & K_{23} \\ K_{13} & K_{23} & K_{33} \end{bmatrix} , \qquad K_{ij} = \sum_{k=1}^{3} S_{ijkk} \; . \tag{74}$$

- Deviatoric modulus tensor

$$\mathbf{L} = \begin{bmatrix} L_{11} & L_{12} & L_{13} \\ L_{12} & L_{22} & L_{23} \\ L_{13} & L_{23} & L_{33} \end{bmatrix} , \qquad L_{ij} = \sum_{k=1}^{3} S_{ikjk} \; . \tag{75}$$

The principal directions of $\mathbf{K}$ coincide with the principal directions of anisotropy of the material. In order to ensure a canonical system, the eigenvalues λ_i^K of $\mathbf{K}$ (or λ_i^L of $\mathbf{L}$) must be ordered $\lambda_3^K > \lambda_2^K > \lambda_1^K$, so that the *strongest* material direction will be oriented in the 3-axis, while the and the weakest remains in the 1-axis. Furthermore, a necessary (but not sufficient) condition for two materials to be considered the same is the invariants of $\mathbf{K}$ and $\mathbf{L}$ being the same. Consequently, the eigenvalues of these tensors can develop a suitable metric to compare the effects of the distinct boundary conditions on the homogenization results. There are a total of six invariants are associated with $\mathbf{K}$ and $\mathbf{L}$ tensors that can be used for expedite comparisons between two anisotropic materials. They are written as follows:

$$
\begin{aligned}
I_1^K &= \lambda_1^K + \lambda_2^K + \lambda_3^K & I_1^L &= \lambda_1^L + \lambda_2^L + \lambda_3^L \\
I_2^K &= \lambda_1^K \lambda_2^K + \lambda_1^K \lambda_3^K + \lambda_2^K \lambda_3^K & I_2^L &= \lambda_1^L \lambda_2^L + \lambda_1^L \lambda_3^L + \lambda_2^L \lambda_3^L \\
I_3^K &= \lambda_1^K \lambda_2^K \lambda_3^K & I_3^L &= \lambda_1^L \lambda_2^L \lambda_3^L
\end{aligned}
$$

5   Numerical Results

In this section, several results obtained through homogenization considering the boundary conditions described in the present chapter will be presented and discussed for a set of selected composites. For each case (composite + boundary condition set), the homogenized stiffness matrix is determined. Some metrics using these tensors are calculated so as to allow a better analysis of the differences that each set of boundary conditions may produce.

In view of the over-determined system of eq. (67) and the numerical nature of its solution, the $\bar{\mathbf{C}}$ tensor may not result perfectly symmetric. This was avoided by enforcing its symmetry before calculating other results, that is:

$$
\bar{\mathbf{S}}^{-1} = \bar{\mathbf{C}} \doteq \frac{1}{2}(\bar{\mathbf{C}}^{\mathrm{T}} + \bar{\mathbf{C}}) \,, \tag{76}
$$

Some indices are determined as a direct comparison among the resulting $\bar{\mathbf{C}}$ would be cumbersome and not quite objective. Therefore, the present work used the following indicators to compare the different stiffnesses:

1. Two anisotropy indices: the universal elastic anisotropy index (A_u), and Zener's anisotropy index (A_z) following Ranganathan and Ostoja-Starzewski [2008];

2. The Frobenius norm of the stiffness matrix;

3. The invariants of $\mathbf{K}$ and $\mathbf{L}$, regarding the principal planes of anisotropy (subsection 4.2);

4. Classical Laminate Theory (CLT) comparison through the reduced constitutive tensor (de Vargas Lisbôa and Marczak [2017]);

The universal elastic anisotropy index (A_u), the Zener's anisotropy index (A_z), and the Frobenius norm (F_r) are calculated as follows:

$$A_u(\bar{\mathbf{C}}) = 5\frac{G^V}{G^R} + \frac{K^V}{K^R} - 6 \; , \tag{77}$$

where

$$
\begin{aligned}
9K_v &= (\bar{C}_{11} + \bar{C}_{22} + \bar{C}_{33} + 2(\bar{C}_{12} + \bar{C}_{23} + \bar{C}_{13}) \; , \\
15G_v &= (\bar{C}_{11} + \bar{C}_{22} + \bar{C}_{33}) - (\bar{C}_{12} + \bar{C}_{23} + \bar{C}_{13}) + 3(\bar{C}_{44} + \bar{C}_{55} + \bar{C}_{66})
\end{aligned} \; , \tag{78}
$$

and

$$A_z(\bar{\mathbf{C}}) = \frac{2\bar{C}_{44}}{\bar{C}_{11} - \bar{C}_{12}} \; , \tag{79}$$

$$F_r(\bar{\mathbf{C}}) = \sqrt{\operatorname{tr}(\bar{\mathbf{C}}\bar{\mathbf{C}})} \; . \tag{80}$$

For comparisons with CLT, eq. (3) is used. Given the kinematic assumptions of thin plate theory and $\sigma_{33} = 0$, a reduction of the 6×6 constitutive tensor can be derived by adjusting the remaining stiffnesses as follows:

$$\bar{\bar{C}}_{ij} = C_{IJ} - \frac{C_{I3}C_{3J}}{C_{33}} \; , \tag{81}$$

where $\{I, J\} = \{1, 2, 6\}$ and $I = i + \max\left(3(i - 2), 0\right)$, the later also valid when upper and lower i are replaced for j. Evidently, $\bar{\bar{\mathbf{C}}} = \bar{\bar{\mathbf{S}}}^{-1}$.

The results section will be divided into two sections. In the first one, one studies a simple $[0/90]_s$ cross-ply laminate and uses the advantage of its simplicity to analyze it under the context of the CLT. In the second section textile composites manufactured with typical weaving will be analyzed and compared with experimental results from the literature [Scida et al., 1998]. In order to calculate A_u, A_z, and F_r from experimental data to be used as reference values, the compliance matrix is calculated from eq. (70) using the measured engineering constants.

The mechanical and the geometric properties of the composites analyzed throughout this section are listed in tables 1 and 2, respectively.

Table 1: Material properties used.

Material	E_{11} (MPa)	E_{22} (MPa)	G_{12} (MPa)	G_{23} (MPa)	ν_{12}	ν_{23}
E-glass	73	73	30.4	30.4	0.2	0.2
Epoxy	3.2	3.2	1.16	1.16	0.38	0.38
Vinylester derakane	3.4	3.4	1.49	1.49	0.35	0.35
E-glass/Vinylester, $V_s = 0.8$	57.5	18.8	7.44	7.26	0.25	0.29
E-glass/Epoxy, $V_s = 0.8$	59.3	23.2	8.68	7.60	0.21	0.32
E-glass/Epoxy, $V_s = 0.75$	55.7	18.5	6.89	6.04	0.22	0.34

Table 2: Geometric properties of the analyzed composites.

Material	E-glass/Vinylester	E-glass/Vinylester	E-glass/Epoxy	E-glass/Epoxy
Weave class	$[0/90]_s$	Plain weave	2/2 twill weave	8-harness satin
Strand width (mm)	0.20	0.60	0.83	0.60
Strand thickness (mm)	0.20	0.05	0.09	0.09
Unit-cell thickness (mm)	0.88	0.10	0.2275	0.18
FVF[†] Strand (V_s)	1.00	0.80	0.75	0.80
Composite (V_o)	0.26	0.55	0.38	0.52
Meso-Scale (V_m)	0.26	0.687	0.507	0.65

[†] Fiber volume fraction

5.1   Cross-ply laminates

In this section, results for the $[0/90]_s$ cross-ply laminate (see figure 10) are discussed. The material and geometric properties used in this case are listed in tables 1 and 2, respectively. Since the geometry of the problem was generated in the TexGen software [Lin et al., 2011, Long and Brown, 2011], the input parameters of TexGen are shown in table 3, for the sake of reproducibility.

Table 3: TexGen weave parameters for the top layers of the $[0/90]_s$ cross-ply laminate.

Material	N. Layers	Warp/Weft Yarns	Yarn Spacing (mm)	Yarn Width (mm)	Fabric. thk.
E-glass/Epoxy	2	5	0.5	0.2	0.4
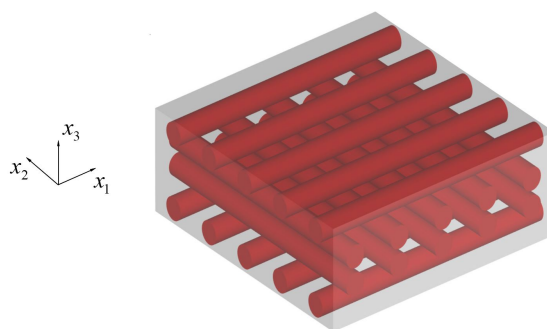
Figure 10: Simplified $[0/90]_s$ cross-ply laminate.

5.1.1   Homogenized stiffness

The $\bar{C}$ matrix evaluated for each case of boundary conditions discussed in sections 2.2.2 and 3, namely SUBC and PBC, will be herein referenced by the corresponding superscripts. The proposed set of mixed boundary conditions described in section 3, MBC*, will be assessed in the context of both, the 3D $\bar{C}$ and thin structures such as plate/shell using $\bar{\bar{C}}$. Therefore, the raw results of the symmetrized stiffness obtained for the cross-ply $[0/90]_S$ laminate are:

$$
\bar{\mathbf{C}}^{SUBC} = \begin{bmatrix}
15525.50 & 3256.47 & 3585.68 & 0.70 & 0.03 & -0.01 \\
3315.44 & 15426.91 & 3612.21 & 0.61 & 0.07 & 0.01 \\
3585.76 & 3485.87 & 9505.93 & 0.35 & -0.03 & -0.01 \\
1.43 & 0.25 & 0.23 & 2307.38 & -0.01 & -0.02 \\
-0.01 & 0.10 & -0.06 & -0.01 & 2671.86 & 0.17 \\
-0.01 & -0.01 & -0.01 & -0.04 & 0.48 & 2508.81
\end{bmatrix}, \qquad (82a)
$$

$$
\bar{\mathbf{C}}^{PBC} = \begin{bmatrix}
15343.92 & 3240.38 & 3527.00 & 0.20 & 0.01 & -0.01 \\
3240.34 & 15334.77 & 3527.50 & 0.18 & 0.00 & 0.01 \\
3526.94 & 3527.50 & 9101.15 & 0.16 & -0.03 & -0.02 \\
0.20 & 0.18 & 0.16 & 1944.53 & 0.01 & -0.00 \\
0.00 & 0.00 & -0.03 & 0.01 & 2255.10 & 0.12 \\
-0.00 & 0.01 & -0.02 & -0.00 & 0.12 & 2255.68
\end{bmatrix}, \qquad (82b)
$$

$$
\bar{\mathbf{C}}^{MBC^*} = \begin{bmatrix}
15351.59 & 3238.43 & 3548.45 & 0.20 & 0.02 & -0.01 \\
3238.39 & 15342.42 & 3548.96 & 0.17 & 0.02 & 0.00 \\
3548.39 & 3548.95 & 9425.97 & 0.15 & -0.03 & -0.03 \\
0.20 & 0.17 & 0.15 & 1944.53 & 0.01 & -0.00 \\
-0.00 & 0.00 & -0.06 & 0.01 & 2352.61 & 0.18 \\
-0.01 & 0.01 & -0.03 & -0.00 & 0.43 & 2306.12
\end{bmatrix}. \qquad (82c)
$$

5.1.2   3D anisotropy and engineering constants

Once the homogenized, matrices given by eqs. (82) are generated, the anisotropy indicators are computed along with the engineering constants for comparison purposes. Table 4 summarizes these calculations for an E-glass/vinylester cross-ply laminate.

Table 4: Cross-ply E-glass/vinylester composite

b.c.	E_{11}	E_{22}	E_{33}	ν_{13}	ν_{12}	A_u	A_z	F_r
SUBC	13.9	13.8	8.15	0.32	0.138	1.53	0.437	25703.14
MBC*	13.8	13.7	8.07	0.32	0.136	1.84	0.388	25414.39
PBC	13.7	13.7	7.76	0.33	0.134	1.94	0.373	25261.47

If the F_r norm is considered, and assuming it can give us at least a weak indication of the composite stiffness, the results in Table 4 shows that:

$$
F_r\left(\bar{\mathbf{C}}^{SUBC}\right) > F_r\left(\bar{\mathbf{C}}^{MBC^*}\right) > F_r\left(\bar{\mathbf{C}}^{PBC}\right) . \qquad (83)
$$

Espadas-Escalante et al. [2017] conducted a similar study with a mixed boundary condition consisting of a combination of the PBC and the uniform traction boundary conditions (UTBC), here referred to as MBC**. The results showed that:

$$
F_r\left(\bar{\mathbf{C}}^{SUBC}\right) > F_r\left(\bar{\mathbf{C}}^{PBC}\right) > F_r\left(\bar{\mathbf{C}}^{MBC^{**}}\right) > F_r\left(\bar{\mathbf{C}}^{UTBC}\right) , \qquad (84)
$$

suggesting that the MBC** combination of UTBC and PBC produced a resulting $\bar{C}$ stiffer than $\bar{C}^{UTBC}$. On the other hand, our MBC* proposal, combining SUBC and PBC, produced a $\bar{C}$ less stiff than $\bar{C}^{SUBC}$. These conclusions highlight that combinations of distinct boundary conditions have the potential to represent better actual stiffness, as these combinations allow the generation of intermediary strain fields, particularly for more complex fiber distributions.

The PBC infers a 3D infinite domain. Despite being valid for large 3D bodies, in textile composites or shell-like geometries this set might not be accurate in the out-of-plane direction. Furthermore, the SUBC imposes a direct strain state along the boundary, which can be seen as an upper bound limit of the elastic properties. Consequently, one expects that the MBC should generate results with intermediary stiffness between the SUBC and the PBC.

Table 5 presents a comparison between the I_i^K and I_i^L for the boundary conditions sets evaluated. As mentioned in section 4.2, a necessary condition to claim that two anisotropic materials behave identically is that their invariants I_i^K and I_i^L must be equal. This implies that the main planes of anisotropy have the same spatial orientation. Table 5 shows clearly that the three sets of boundary conditions generate similar results. The small differences appear to be a consequence of the local strain fields generated in the boundary condition application, which is also reflected in the numerical values of the engineering constants (Table 4).

Table 5: Invariants of K and L for the cross-ply E-glass/vinylester composite.

b.c.	I_1^K	I_2^K	I_3^K	I_1^L	I_2^L	I_3^L
SUBC	6.13×10^4	1.24×10^9	8.30×10^{12}	5.54×10^4	10.1×10^9	6.05×10^{12}
MBC*	6.08×10^4	1.22×10^9	8.10×10^{12}	5.33×10^4	9.35×10^9	5.37×10^{12}
PBC	6.04×10^4	1.20×10^9	7.90×10^{12}	5.27×10^4	9.12×10^9	5.16×10^{12}

A direct comparison of other 3D homogenized compliance entries is presented in Table 6 for completeness. In particular, values for out-of-plane compliance are provided for reference, as these are not commonly found in the literature.

Table 6: Other entries for 3D homogenized compliance

Model	$\bar{S}_{13}$	$\bar{S}_{32}$	$\bar{S}_{63}$	$\bar{S}_{12}$	$\bar{S}_{33}$	$\bar{S}_{66}$
SUBC	$-2.34 \cdot 10^{-5}$	$-2.32 \cdot 10^{-5}$	$-2.67 \cdot 10^{-10}$	$-9.93 \cdot 10^{-6}$	$1.23 \cdot 10^{-4}$	$4.33 \cdot 10^{-4}$
MBC*	$-2.36 \cdot 10^{-5}$	$-2.37 \cdot 10^{-5}$	$-4.79 \cdot 10^{-9}$	$-9.87 \cdot 10^{-6}$	$1.24 \cdot 10^{-4}$	$5.14 \cdot 10^{-4}$
PBC	$-2.44 \cdot 10^{-5}$	$-2.45 \cdot 10^{-5}$	$-5.54 \cdot 10^{-9}$	$-9.77 \cdot 10^{-6}$	$1.29 \cdot 10^{-4}$	$5.14 \cdot 10^{-4}$

5.1.3   2D anisotropy and engineering constants

After reducing the $\bar{C}^{SUBC}$, $\bar{C}^{PBC}$, and $\bar{C}^{MBC*}$ homogenized matrices (eq. (81)), their CLT counterparts are obtained as follows:

$$\bar{\bar{\mathbf{C}}}^{SUBC} = \begin{bmatrix} 14172.94 & 1947.22 & 0.96 \\ 1947.22 & 14101.87 & 0.32 \\ 0.96 & 0.32 & 2307.38 \end{bmatrix} \tag{85a}$$

$$\bar{\bar{\mathbf{C}}}^{MBC^*} = \begin{bmatrix} 14015.78 & 1902.40 & 0.15 \\ 1902.40 & 14006.21 & 0.12 \\ 0.15 & 0.12 & 1944.53 \end{bmatrix} \tag{85b}$$

$$\bar{\bar{\mathbf{C}}}^{PBC} = \begin{bmatrix} 13977.11 & 1873.35 & 0.14 \\ 1873.35 & 13967.55 & 0.12 \\ 0.14 & 0.12 & 1944.53 \end{bmatrix} \tag{85c}$$

It is worth highlighting that the tensor reduction disregards the following entries of the homogenized 3D stiffness matrix due to the kinematic hypotheses of Kirchhoff plate theory:

$$\begin{bmatrix} C_{11} & C_{12} & C_{13} & C_{14} & C_{15} & C_{16} \\ C_{21} & C_{22} & C_{23} & C_{24} & C_{25} & C_{26} \\ C_{31} & C_{32} & C_{33} & C_{34} & C_{35} & C_{36} \\ C_{41} & C_{42} & C_{43} & C_{44} & C_{45} & C_{46} \\ C_{51} & C_{52} & C_{53} & C_{56} & C_{55} & C_{56} \\ C_{61} & C_{62} & C_{63} & C_{64} & C_{65} & C_{66} \end{bmatrix} \tag{86}$$

Consequently, some of the entries in eqs. (82) responsible for the asymmetry are not considered.

It is interesting to note that one can retrieve the effective engineering constants for the composite either from the inverse of eq. (70) combined with any of the eqs. (82) or, alternatively, from the elementary relations of mechanics of composite materials (Jones [2018], Nettles [1994]), fed by the inverses of the eqs. (85). In both cases, the equations are the same, provided the $\{I, J\} \rightarrow \{i, j\}$ index change is performed and the correct matrices are used. Therefore, to retrieve the effective properties from the CLT (reduced) matrices, we have:

$$E_{11} = \frac{1}{\bar{\bar{S}}_{11}} \qquad E_{22} = \frac{1}{\bar{\bar{S}}_{22}}$$
$$G_{12} = \frac{1}{\bar{\bar{S}}_{33}} \qquad \nu_{12} = -\frac{\bar{\bar{S}}_{12}}{\bar{\bar{S}}_{22}} \tag{87}$$

In Table 7, the effective properties are computed from eqs. (87) using $\bar{\bar{S}}_{ij}$ from the inverses (85) are compared. The ROM acronym refers to the values obtained using the rule of mixtures (Jones [2018], Nettles [1994]). It is clear that the different calculations of the reduced stiffness matrix produced a consistent agreement for the elastic moduli. Another comparison of the values in Table 7 is provided in fig. 11, where E_{11} of the various formulations are plotted along with the bounds described in section 2.1.1. One observes that for a cross-ply laminate ($N = 2$) the homogenized values agree with the upper bound of Ishikawa [1981].

Table 7: Effective engineering constants for cross-ply E-glass/vinylester composite.

b.c.	E_{11}	E_{22}	G_{12}	ν_{12}
SUBC	13.90	13.83	2.307	0.1374
MBC*	13.76	13.75	1.945	0.1357
PBC	13.73	13.72	1.945	0.1340
ROM	13.39	13.39	2.05	0.118
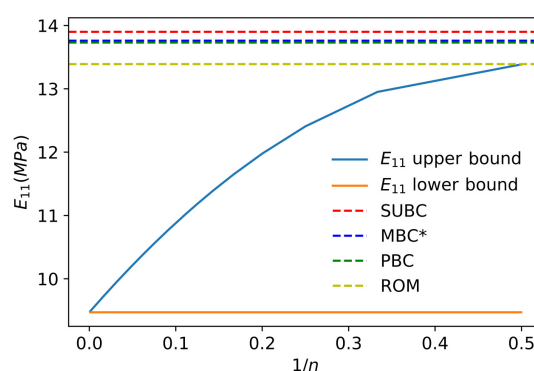
Figure 11: Comparison of the elastic moduli obtained by the various formulations and the bounds proposed by Ishikawa [1981].

5.2 Textile composites

In this section, the homogenization process is conducted for some weave composites typically found in the industry. The geometry was also generated in a commercial textile composites simulation software (TexGen) and the results are compared to experimental and numerical evaluations from literature. Later, the homogenized stiffness matrix is reduced to CLT and also compared. The cases are analyzed and the corresponding fiber volume fractions are:

1. Plain Weave E-glass/Vinylester ($V_s = 0.8$);

2. 2/2 twill weave E-glass/Epoxy ($V_s = 0.75$)

3. 8-Harness Satin Weave E-glass/Epoxy ($V_s = 0.8$)

The weave patterns studied are diagrammed in fig. 12 and the corresponding geometries generated by TexGen are shown in fig. 13. The weaving parameters used to generate these models are listed in Table 8 and were retrieved from Scida et al. [1999]. The stiffness matrices were corrected in order to simulate the real fiber volume fraction of the composite, as described in section 4.1, eq. (73).

Table 8: TexGen input parameters used.

Material	Weave class	Strand width (mm)	Comp. thickness (mm)	Yarn Spacing (mm)	V_g^α	V_g/V_g^α
E-glass/Vinylester	Plain weave	0.6	0.1	0.625	0.589	1.165
E-glass/Epoxy	2/2 twill weave	0.83	0.2275[†]	1	0.498	1.017
E-glass/Epoxy	8-Harness Satin Weave	0.6	0.18	0.8	0.526	1.235

[†] The total thickness of the composite is 0.2275 mm. However, the fabric thickness which is actually inserted in TexGen is 0.18 mm. Hence, the fabric thickness is corrected by adding an additional layer of matrix material.

(a) Plain Weave (b) 2/2 twill weave (c) 8-Harness Satin Weave
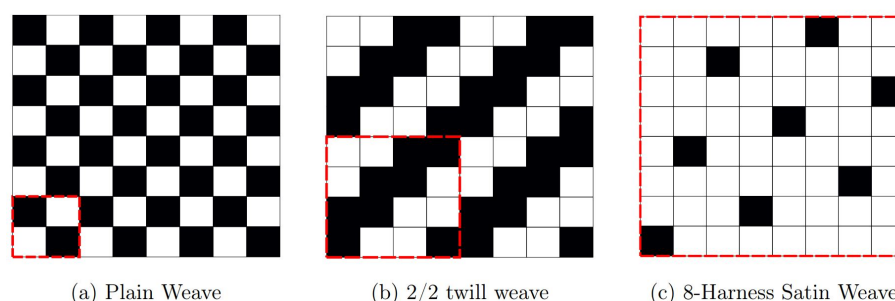
Figure 12: Weave pattern schemes used to generate the three weave composites studied.

(a) Plain Weave (b) 2/2 twill weave (c) 8-Harness Satin Weave
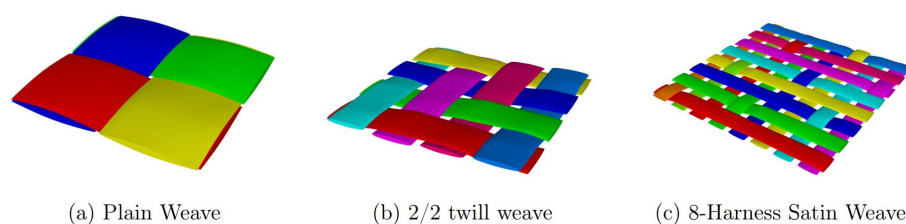
Figure 13: RVE geometries generated for each pattern of Fig. 12.

5.2.1 Homogenized stiffness

In this subsection, the 3D homogenized (non-contracted) stiffness matrix computed for each of the three textile composites will be discussed. For short, they will be distinguished by their names attached to the $\bar{C}$ matrix. They are:

$$\bar{C}_{\text{plain}}^{SUBC} = \begin{bmatrix} 28874.13 & 6117.78 & 6305.27 & -18.19 & -481.47 & 732.65 \\ 6478.04 & 29131.20 & 6312.37 & 759.37 & 1.27 & -4.18 \\ 6305.42 & 5584.47 & 13194.71 & 12.05 & -0.56 & 18.27 \\ -47.26 & 634.76 & 0.54 & 2721.56 & 5.10 & -10.19 \\ -481.44 & -1.84 & -0.59 & 2.74 & 2983.75 & -17.24 \\ 988.30 & -9.13 & 26.10 & -7.48 & -31.46 & 4775.66 \end{bmatrix} \quad (88a)$$

$$\bar{C}_{\text{plain}}^{PBC} = \begin{bmatrix} 28331.60 & 6452.85 & 6197.92 & -30.53 & -457.13 & 957.37 \\ 6453.30 & 28634.90 & 6211.23 & 465.35 & -4.90 & 7.81 \\ 6197.87 & 6210.75 & 13084.94 & 0.92 & -0.58 & 30.03 \\ -30.52 & 465.35 & 0.93 & 2772.56 & 1.67 & -10.37 \\ -457.13 & -4.90 & -0.58 & 1.67 & 2771.43 & -30.76 \\ 957.37 & 7.83 & 30.05 & -10.38 & -30.76 & 4876.75 \end{bmatrix} \quad (88b)$$

$$\bar{C}_{\text{plain}}^{MBC^*} = \begin{bmatrix} 28433.07 & 6382.58 & 6218.58 & -12.93 & -425.32 & 965.06 \\ 6382.95 & 28736.06 & 6231.57 & 540.20 & 1.89 & 2.27 \\ 6218.54 & 6231.17 & 13149.13 & 2.16 & 2.04 & 29.91 \\ -41.71 & 432.58 & -1.67 & 2450.17 & 1.75 & -12.08 \\ -425.34 & 1.89 & 2.02 & 0.84 & 2892.14 & -25.63 \\ 965.06 & 2.27 & 29.92 & -6.21 & -25.63 & 4877.89 \end{bmatrix} \quad (88c)$$

for the plain weave;

$$\bar{C}_{\text{twill}}^{SUBC} = \begin{bmatrix} 22170.91 & 4914.31 & 5076.26 & -5.64 & -194.87 & 289.69 \\ 5192.57 & 22055.12 & 5080.02 & 311.95 & 0.86 & -7.25 \\ 5075.87 & 4633.46 & 10108.11 & 4.63 & 0.37 & 10.33 \\ -17.74 & 261.84 & -0.20 & 2076.20 & 5.42 & -2.96 \\ -194.42 & -2.72 & 0.26 & 2.48 & 2224.88 & -3.69 \\ 418.73 & -12.08 & 15.33 & -1.86 & -10.68 & 3470.17 \end{bmatrix} \quad (89a)$$

$$\bar{C}_{\text{twill}}^{PBC} = \begin{bmatrix} 21837.35 & 5160.93 & 5015.48 & -13.78 & -188.56 & 398.70 \\ 5160.86 & 21993.03 & 5020.53 & 189.97 & 0.77 & -8.24 \\ 5014.96 & 5020.10 & 10029.43 & 0.31 & -0.19 & 15.17 \\ -13.77 & 189.98 & 0.32 & 2090.10 & 2.94 & -3.50 \\ -188.57 & 0.76 & -0.20 & 2.94 & 2089.89 & -9.37 \\ 398.71 & -8.23 & 15.19 & -3.50 & -9.37 & 3504.09 \end{bmatrix} \quad (89b)$$

$$\bar{C}_{\text{twill}}^{MBC^*} = \begin{bmatrix} 21915.77 & 5121.05 & 5028.02 & -6.63 & -178.92 & 402.97 \\ 5120.99 & 22076.02 & 5033.40 & 220.81 & 3.25 & -9.55 \\ 5027.62 & 5033.08 & 10078.52 & 2.14 & 0.85 & 16.21 \\ -18.22 & 180.12 & -0.64 & 1870.07 & 3.05 & -4.16 \\ -178.93 & 3.22 & 0.77 & 2.11 & 2155.16 & -7.72 \\ 402.99 & -9.54 & 16.22 & -1.93 & -7.72 & 3505.08 \end{bmatrix} \quad (89c)$$

for the 2/2 twill weave, and

$$
\bar{\mathbf{C}}_{\text{satin}}^{SUBC} =
\begin{bmatrix}
27304.15 & 5970.20 & 6365.65 & -10.42 & -157.92 & 202.39 \\
6286.58 & 27858.86 & 6370.29 & 239.53 & -0.02 & 4.42 \\
6364.15 & 5909.39 & 12948.78 & 5.73 & -1.05 & 7.11 \\
-17.03 & 179.75 & 0.00 & 2786.00 & 1.67 & -3.91 \\
-157.59 & -0.62 & -0.14 & 0.78 & 2940.36 & -12.73 \\
293.66 & -1.20 & 9.81 & -2.32 & -10.03 & 4159.94
\end{bmatrix}
\tag{90a}
$$

$$
\bar{\mathbf{C}}_{\text{satin}}^{PBC} =
\begin{bmatrix}
26809.47 & 6210.06 & 6264.62 & -11.56 & -158.35 & 269.87 \\
6211.52 & 26985.12 & 6273.02 & 161.25 & -1.54 & 2.28 \\
6259.36 & 6266.59 & 12817.02 & 1.49 & -1.49 & 10.61 \\
-11.37 & 162.08 & 1.63 & 2685.45 & 0.51 & -2.77 \\
-158.34 & -1.56 & -1.54 & 0.51 & 2684.54 & -8.53 \\
269.90 & 2.32 & 10.66 & -2.77 & -8.58 & 3992.46
\end{bmatrix}
\tag{90b}
$$

$$
\bar{\mathbf{C}}_{\text{satin}}^{MBC^*} =
\begin{bmatrix}
26899.39 & 6179.88 & 6285.15 & -15.72 & -151.36 & 274.57 \\
6181.20 & 27078.99 & 6294.05 & 85.15 & 1.01 & 1.05 \\
6281.49 & 6289.15 & 12902.98 & 7.00 & -0.82 & 10.68 \\
-16.82 & 155.13 & -0.10 & 2430.36 & 0.62 & -3.52 \\
-151.82 & 1.04 & 0.11 & 0.46 & 2843.23 & -6.85 \\
274.58 & 1.07 & 10.72 & -0.88 & -6.92 & 3993.26
\end{bmatrix}
\tag{90c}
$$

for the 8-harness satin weave.

5.2.2 3D anisotropy, engineering constants, and comparison with literature

At this point, having the 3D $\bar{\mathbf{C}}$ matrix for each weave pattern as given by eqs. (88)-(90), the effective material properties can be computed, as well as the anisotropy indicators. Without the imposition of any type of constraints, as implemented here, the $\bar{\mathbf{C}}$ matrices are allowed to result fully anisotropic. That is, no effort was made to try to frame the resulting matrices into any specific material symmetry. Tables 9, 10, and 11 list all 9 effective material properties so obtained for the three weave composites under each type of boundary condition, as well as similar values from the literature, when available. In Tables 10 and 11, the starred values come from the analytical calculations of Scida et al. [1999], not experimental values.

Table 12 summarizes the anisotropy indicators for all three weave composites subjected to each of the three boundary conditions studied. Finally, Tables 13, 14, and 15 list the calculations of the invariants of $\mathbf{K}$ and $\mathbf{L}$ for each weave pattern. The effective engineering constants are compiled in Tables 13, 14, and 15 for each textile analyzed.

Table 9: Effective material properties comparison for E-glass/vinylester plain-weave composite.

b.c	E_1	E_2	E_3	G_{12}	G_{23}	G_{31}	ν_{13}	ν_{23}	ν_{12}
SUBC	25.18	25.81	11.06	4.74	2.70	2.97	0.42	0.35	0.13
PBC	24.66	25.12	10.87	4.84	2.76	2.76	0.41	0.41	0.13
MBC*	24.78	25.52	10.92	4.84	2.44	2.88	0.41	0.41	0.13
Barbero et al. [2006]	24.44	24.53	10.25	5.51	3.15	3.16	0.38	0.38	0.13
Scida et al. [1999]	24.8	24.8	8.5	6.5	4.2	4.2	0.28	0.28	0.11

Table 10: Effective material properties comparison for 2/2 twill E-glass woven fabric/epoxy composite.

b.c	E_1	E_2	E_3	G_{12}	G_{23}	G_{31}	ν_{13}	ν_{23}	ν_{12}
SUBC	19.92	19.93	8.29	3.46	2.07	2.22	0.44	0.39	0.13
PBC	18.91	19.10	8.17	3.50	2.01	2.01	0.43	0.43	0.14
MBC*	19.00	19.92	8.21	3.49	1.87	2.15	0.43	0.43	0.13
Scida et al. [1999]	19.2	19.2	10.92*	3.6	3.78*	3.78*	0.305*	0.305*	0.13

Table 13: Invariants of K and L for the plain weave composite.

b.c.	I_1^K	I_2^K	I_3^K	I_1^L	I_2^L	I_3^L
SUBC	1.08×10^5	3.82×10^9	4.36×10^{13}	9.22×10^4	2.76×10^9	2.65×10^{13}
PBC	1.08×10^5	3.79×10^9	4.31×10^{13}	9.09×10^4	2.68×10^9	2.55×10^{13}
MBC*	1.08×10^5	3.80×10^9	4.34×10^{13}	9.08×10^4	2.68×10^9	2.55×10^{13}

Table 14: Invariants of K and L for the 2/2 twill weave composite.

b.c.	I_1^K	I_2^K	I_3^K	I_1^L	I_2^L	I_3^L
SUBC	8.43×10^4	2.32×10^9	2.07×10^{13}	6.99×10^4	1.58×10^9	1.15×10^{13}
PBC	8.43×10^4	2.32×10^9	2.07×10^{13}	6.92×10^4	1.56×10^9	1.12×10^{13}
MBC*	8.44×10^4	2.33×10^9	2.08×10^{13}	6.91×10^4	1.55×10^9	1.12×10^{13}

Table 15: Invariants of K and L for the 8-harness satin weave composite.

b.c.	I_1^K	I_2^K	I_3^K	I_1^L	I_2^L	I_3^L
SUBC	1.06×10^5	3.65×10^9	4.09×10^{13}	8.81×10^4	2.52×10^9	2.32×10^{13}
PBC	1.04×10^5	3.56×10^9	3.95×10^{13}	8.55×10^4	2.38×10^9	2.12×10^{13}
MBC*	1.05×10^5	3.58×10^9	3.99×10^{13}	8.56×10^4	2.38×10^9	2.14×10^{13}

Table 11: Effective material properties comparison for E-glass eight-harness satin weave/epoxy composite.

b.c	E_1	E_2	E_3	G_{12}	G_{23}	G_{31}	ν_{13}	ν_{23}	ν_{12}
SUBC	23.81	24.59	10.65	4.16	2.79	2.94	0.44	0.39	0.13
PBC	23.36	23.54	10.47	3.99	2.69	2.69	0.42	0.42	0.13
MBC*	23.46	23.6	10.54	3.99	2.43	2.84	0.44	0.39	0.13
Scida et al. [1999]	25.6	25.6	15.65*	5.7	5.42*	5.42*	0.283*	0.283*	0.13

Table 12: Anisotropy indicators for the weave composites analyzed.

b.c.	Plain weave			2/2 twill weave			8-harness satin weave		
	A_u	A_z	F_r	A_u	A_z	F_r	A_u	A_z	F_r
SUBC	3.26	0.241	39597	3.24	0.243	34788	3.00	0.263	35800
PBC	3.22	0.253	39081	3.25	0.251	34578	3.05	0.261	35071
MBC*	3.40	0.222	39189	3.43	0.223	34678	3.14	0.235	35183

5.2.3 2D anisotropy and engineering constants

$$\bar{\bar{\mathbf{C}}}_{\text{plain}}^{SUBC} = \begin{bmatrix} 28874.13 & 6297.91 & 6305.35 \\ 6297.91 & 29131.20 & 5948.42 \\ 6305.35 & 5948.42 & 13194.71 \end{bmatrix} \tag{91a}$$

$$\bar{\bar{\mathbf{C}}}_{\text{plain}}^{PBC} = \begin{bmatrix} 28331.60 & 6453.07 & 6197.89 \\ 6453.07 & 28634.90 & 6210.99 \\ 6197.89 & 6210.99 & 13084.94 \end{bmatrix} \tag{91b}$$

$$\bar{\bar{\mathbf{C}}}_{\text{plain}}^{MBC^*} = \begin{bmatrix} 28433.07 & 6382.77 & 6218.56 \\ 6382.77 & 28736.06 & 6231.37 \\ 6218.56 & 6231.37 & 13149.13 \end{bmatrix} \tag{91c}$$

for the plain weave;

$$\bar{\bar{\mathbf{C}}}_{\text{twill}}^{SUBC} = \begin{bmatrix} 22170.91 & 5053.44 & 5076.07 \\ 5053.44 & 22055.12 & 4856.74 \\ 5076.07 & 4856.74 & 10108.11 \end{bmatrix} \tag{92a}$$

$$\bar{\bar{\mathbf{C}}}_{\text{twill}}^{PBC} = \begin{bmatrix} 21837.35 & 5160.93 & 5015.48 \\ 5160.86 & 21993.03 & 5020.53 \\ 5014.96 & 5020.10 & 10029.43 \end{bmatrix} \tag{92b}$$

$$\bar{\bar{\mathbf{C}}}_{\text{twill}}^{MBC^*} = \begin{bmatrix} 21915.77 & 5121.02 & 5027.82 \\ 5121.02 & 22076.02 & 5033.24 \\ 5027.82 & 5033.24 & 10078.52 \end{bmatrix} \tag{92c}$$

for the 2/2 twill weave, and

$$\bar{\bar{\mathbf{C}}}^{SUBC}_{\text{satin}} = \begin{bmatrix} 27304.15 & 6128.39 & 6364.90 \\ 6128.39 & 27858.86 & 6139.84 \\ 6364.90 & 6139.84 & 12948.78 \end{bmatrix} \tag{93a}$$

$$\bar{\bar{\mathbf{C}}}^{PBC}_{\text{satin}} = \begin{bmatrix} 26809.47 & 6210.79 & 6261.99 \\ 6210.79 & 26985.12 & 6269.80 \\ 6261.99 & 6269.80 & 12817.02 \end{bmatrix} \tag{93b}$$

$$\bar{\bar{\mathbf{C}}}^{MBC^*}_{\text{satin}} = \begin{bmatrix} 26899.39 & 6180.54 & 6283.32 \\ 6180.54 & 27078.99 & 6291.60 \\ 6283.32 & 6291.60 & 12902.98 \end{bmatrix} \tag{93c}$$

for the 8-harness satin weave, noting again that the symmetry was enforced before the reduction of the stiffness tensors.

Now the stiffness given in eqs. (91), (92), and (93) can be inverted to easily calculate the engineering constants in order to verify how our results compare with the ones obtained by Scida et al. [1999], as well as the value values obtained using ROM (Jones [2018], Nettles [1994]). The homogenized engineering constants are listed in Tables 16, 17, and 18. It is interesting to note that even properties not directly affected by the reduction $\bar{\mathbf{C}} \to \bar{\bar{\mathbf{C}}}$, such as E_{11}, change their values despite the expression for its evaluation being the same in both, 3D and CLT.

Table 16: Effective engineering constants for the plain weave composite.

b.c.	E_{11}	E_{22}	G_{12}	ν_{12}
UDBC	27.28	27.74	4.75	0.21
PBC	26.61	27.15	4.84	0.22
MBC*	26.76	27.29	4.84	0.22
ROM	27.18	27.18	4.05	0.11
Scida et al. [1999]	24.8 ±1.1	24.8 ±1.1	6.5 ±0.8	0.11 ±0.01

Table 17: Effective engineering constants for the 2/2 twill weave composite.

b.c.	E_{11}	E_{22}	G_{12}	ν_{12}
SUBC	20.96	20.33	3.46	0.22
PBC	20.56	20.76	3.49	0.23
MBC*	20.66	20.87	3.49	0.23
ROM	18.76	18.97	2.48	0.12
Scida et al. [1999]	19.2 ±1.1	19.2 ±1.1	3.6 ±0.1	0.13 ±0.005

Table 18: Effective engineering constants for the 8-harness satin weave composite.

b.c.	E_{11}	E_{22}	G_{12}	ν_{12}
UDBC	25.93	26.48	4.15	0.22
PBC	25.35	25.54	3.98	0.23
MBC*	25.46	25.66	3.99	0.23
ROM	25.74	25.74	3.74	0.12
Scida et al. [1999]	25.6 ± 0.2	25.6 ± 0.2	5.7 ± 0.3	0.13 ± 0.005

Finally, the same exercise made for the cross-ply laminate in fig. 11 can be repeated for all three textile composites, to visualize where E_{11} is placed relative to the analytical bounds described in section 2.1.1. These results are plotted in fig. 14. The textile composites analyzed here (plain, 2/2 twill, and 8-harness satin) do not have the same material/V_o combinations, and therefore the bounds, as well as the value predicted by ROM, are different for each one. It is clear, however, that the difference of moduli for the boundary conditions may reach 3-4%.
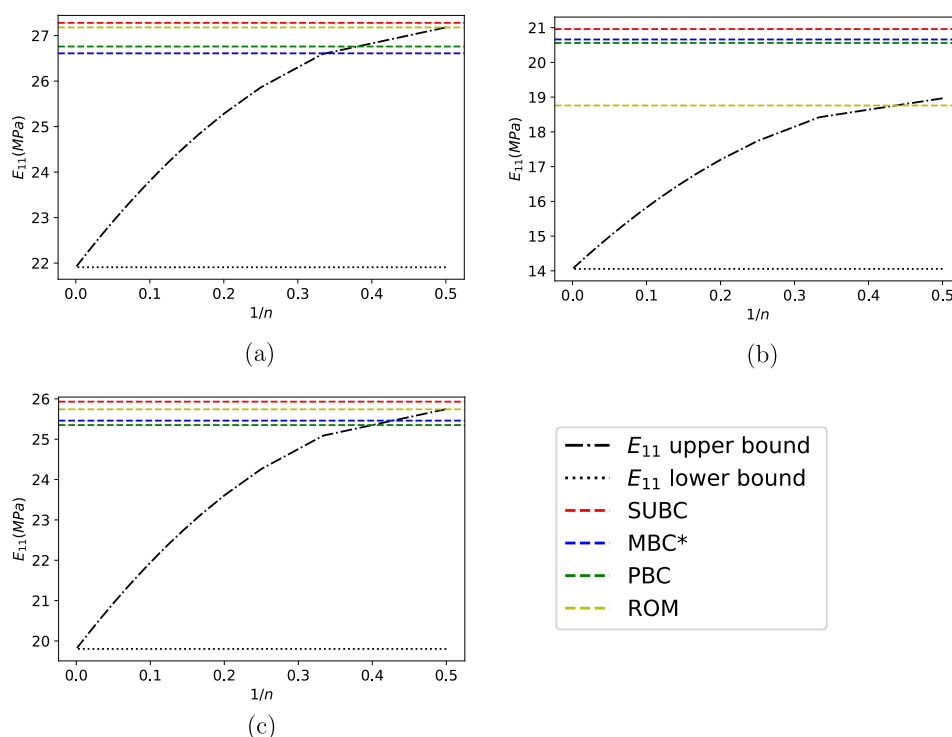
**Figure 14: Comparison of the elastic moduli obtained by the various formulations and the bounds proposed by Ishikawa [1981] for (a) plain weave; (b) 2/2 twill weave, and (c) 8-harness satin weave.**

5.3 Stress and strain fields

In order to provide an idea of how the different weave patterns influence the stress and strain distribution, figs. 15, 16, and 17 show the stress plot of these configurations for

each boundary condition studied under ε^1 strain state. The finite element mesh of the matrix phase is not plotted for clarity. Only the σ_{13} component is shown, but it suffices to evidence how the patterns command differently the deformation mechanism of each composite. Although not shown here, patterns of composite with the same fiber/matrix material composition and fractions will respond differently, and the particularities of each deformation mode cannot be captured by average field theory approaches. RVE homogenization equipped with a proper set of boundary conditions seems to be the only method able to reproduce the internal mechanism created by each particular bundle disposition, and each one reflects differently on the $\bar{C}$ and $\bar{\bar{C}}$ matrices. And as a consequence, on the effective mechanical properties as well. This is further evidenced in figs. 15, 16, and 17 by noting the distinguished stress concentration along the fiber bundles for each type of composite.
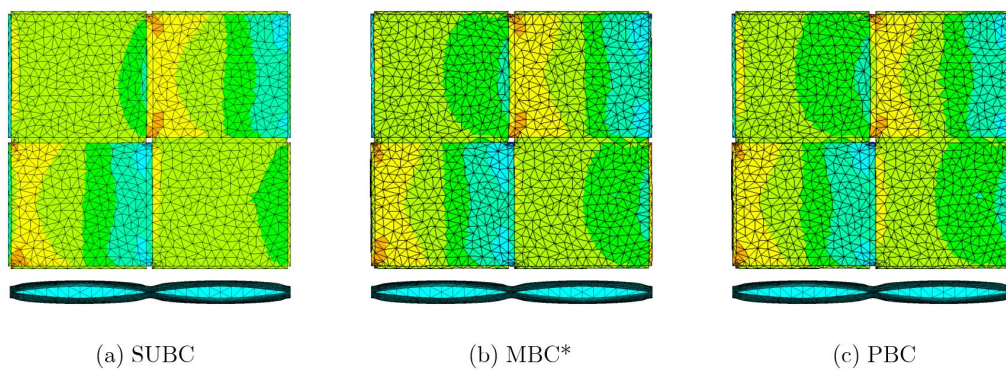
(a) SUBC   (b) MBC*   (c) PBC

Figure 15: σ_{13} **stress/strain response for the plain weave composite under** ε^1 **strain state, for all boundary conditions studied.**

(a) SUBC   (b) MBC*   (c) PBC
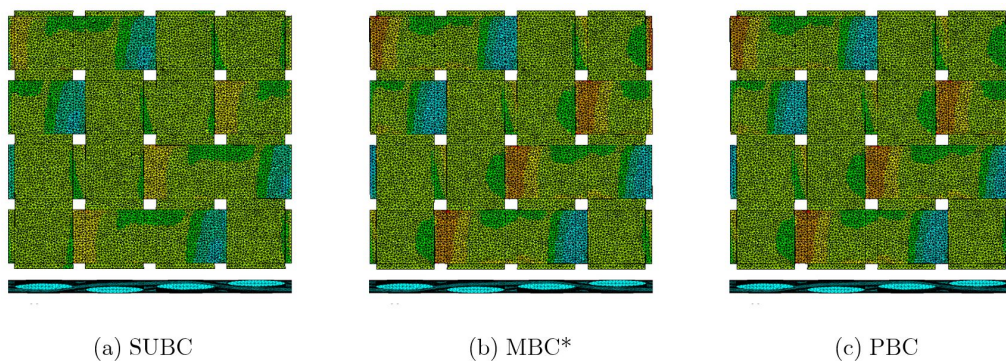
Figure 16: σ_{13} **stress/strain response for the 2/2 twill weave composite under** ε^1 **strain state, for all boundary conditions studied.**
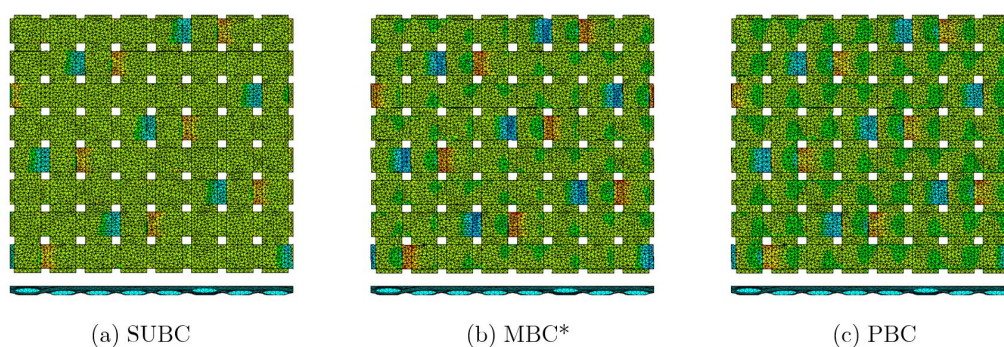
(a) SUBC   (b) MBC*   (c) PBC

Figure 17: σ_{13} **stress/strain response for the plain weave composite under** ε^1 **strain state, for all boundary conditions studied.**

5.4   Overall mechanical response

Aiming at inciting further investigations on the influence of the homogenization and the various boundary conditions on the overall response of a mechanical component, this section presents a simple exercise based on the simulation of a cantilever plate subjected to end moment (Fig. 18). This case emulates a bending-governed problem which can be analyzed using conventional thin plate/shell finite element based on the reduced matrices given in eqs. (91)-(93). The data used for this problem is $L = 300$ mm, $w = 100$ mm, and $h = 1$ mm, with a unit moment at the end, $M = 1$ N mm.

The plots of transverse displacement are shown in figs. 19, 20, and 21 for all three types of textiles studied here. It is evident that the boundary conditions used in the homogenization influence the results, particularly in the case of the 2/2 twill weave. However, the important aspect seems to be the weaving pattern, subject of future investigation, as they could not be compared here due to the difference in material composition, geometry, and fiber fraction of the three textiles studied.
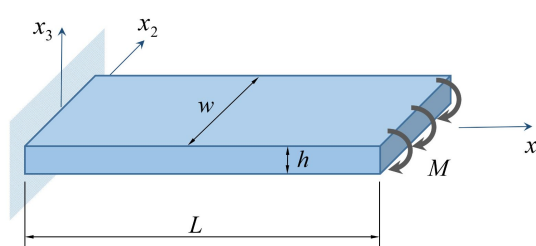
Figure 18: Cantilever plate problem.
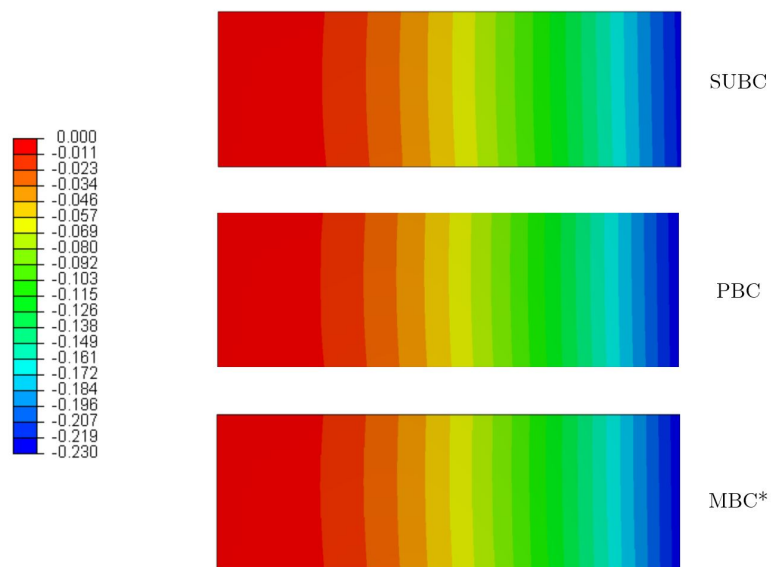
Figure 19: Transverse displacement (u_3) responses of the cantiler plate. Shell finite element results with plain weave properties (91)**.**

Figure 20: Transverse displacement (u_3) responses of the cantiler plate. Shell finite element results with 2/2 twill weave properties (92)**.**

Figure 21: Transverse displacement (u_3) **responses of the cantiler plate. Shell finite element results with 8-harness satin weave properties** (93)**.**

6   Conclusions

This article discussed some numerical modeling possibilities for the retrieval of the homogenized constitutive matrices of composite textiles whose fiber phase is built through weaving patterns of fiber tows embedded in a linearly elastic matrix phase.

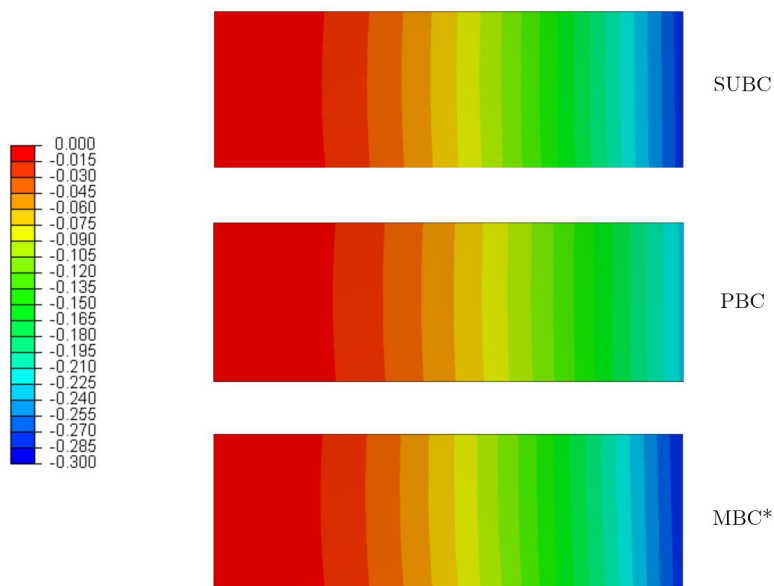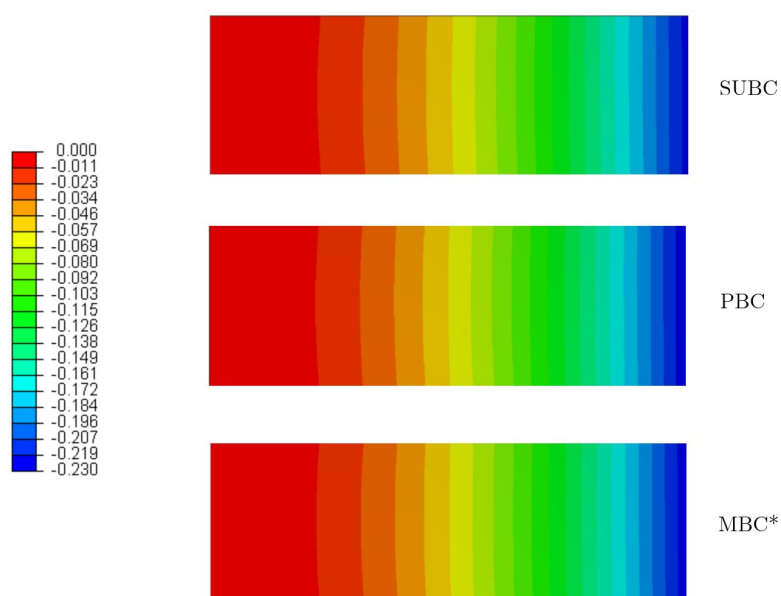Although the essentials of homogenization via RVE analysis are well understood for simple multi-scale analysis, we showed that the boundary conditions imposed on the RVE may have non-negligible reflexes on the results. In particular, repetitive cells may need other sets of boundary conditions than the uniform displacements commonly employed. We also identify that the usual periodic boundary conditions are not suitable for thin textile composites as plates and shells, as the periodic restrictions along the transverse directions are not the same as the in-plane ones. Aiming at such structures, we proposed a new set of mixed boundary conditions and proved that it complies with the Hill-Mandel criteria.

A second aspect explored in the present study refers specifically to the homogenized constitutive matrices used in the modeling of thin structures. In general, these matrices are computed as suggested by the classical laminate theory, departing from the values of the moduli of the constituents. Because the formulas based on the average field theory cannot take into account the specific weaving pattern of each textile, these formulas are not able to distinguish the variations in stiffness that arise from the different types of interlacing. In such cases, a homogenization approach becomes imperative, altogether with a proper set of boundary conditions. A number of anisotropy indicators were used to compare objectively the variations in the stiffness coefficients for each type of boundary condition. We have shown that the methodology used was able to estimate both 3D and 2D constitutive matrices as well as they are compared to each other and to available results.

References

E. Barbero, J. Trovillion, J. Mayugo, and K. Sikkil. Finite element modeling of plain weave fabrics from photomicrograph measurements. *Composite Structures*, 73(1):41–52, 2006.

E. J. Barbero. *Finite element analysis of composite materials*. CRC press, 2007.

E. de Souza Neto and R. Feijóo. On the equivalence between spatial and material volume averaging of stress in large strain multi-scale solid constitutive models. *Mechanics of Materials*, 40:803–811, 2008.

T. de Vargas Lisbôa and R. J. Marczak. A recursive methodology for the solution of semi-analytical rectangular anisotropic thin plates in linear bending. *Applied Mathematical Modelling*, 48:711–730, 2017.

A. Dixit and H. Mali. Modeling techniques for predicting the mechanical properties of woven-fabric textile composites: a review. *Mech. Compos. Mater.*, 49:1–20, 2013.

J. J. Espadas-Escalante, N. P. van Dijk, and P. Isaksson. A study on the influence of boundary conditions in computational homogenization of periodic structures with application to woven composites. *Composite Structures*, 160:529–537, 2017.

R. Glüge. Generalized boundary conditions on representative volume elements and their use in determining the effective material properties. *Computational materials science*, 79:408–416, 2013.

S. Hazanov and M. Amieur. On overall properties of elastic heterogeneous bodies smaller than the representative volume. *International Journal of Engineering Science*, 33(9): 1289–1301, 1995.

R. Hill. Elastic properties of reinforced solids: some theoretical principles. *Journal of the Mechanics and Physics of Solids*, 11(5):357–372, 1963.

R. Hill. A self-consistent mechanics of composite materials. *Journal of the Mechanics and Physics of Solids*, 13(4):213–222, 1965.

R. Hill. On constitutive macro-variables for heterogeneous solids at finite strain. *Proc R Soc Lond A*, 326:131–147, 1972.

T. Ishikawa. Anti-symmetric elastic properties of composite plates of satin weave cloth. *Fibre Science and Technology*, 15(2):127–145, 1981.

S. Jacques, I. De Baere, and W. Van Paepegem. Application of periodic boundary conditions on multiple part finite element meshes for the meso-scale homogenization of textile fabric composites. *Composites Science and Technology*, 92:41–54, 2014.

R. M. Jones. *Mechanics of composite materials*. CRC press, 2018.

H. Lin, L. P. Brown, and A. C. Long. Modelling and simulating textile structures using texgen. In *Advanced Materials Research*, volume 331, pages 44–47. Trans Tech Publ, 2011.

A. Long and L. Brown. Modelling the geometry of textile reinforcements for composites: Texgen. In *Composite reinforcements for optimum performance*, pages 239–264. Elsevier, 2011.

R. Luciano and E. Sacco. Variational methods for the homogenization of periodic heterogeneous media. *European Journal of Mechanics-A/Solids*, 17(4):599–617, 1998.

J. Mandel. *Plasticité Classique et Viscoplasticité*. CISM Lecture Notes No. 97. Springer, 1998.

K. Mazumda, S. *Composites manufacturing: materials, product, and process engineering*. CRC Press, 2002.

Z. ming Huang. The mechanical properties of composites reinforced with woven and braided fabrics. *Composites science and technology*, 60(4):479–498, 2000.

S. Nemat-Nasser and M. Hori. Micromechanics: overall properties of heterogeneous materials, 1996.

A. T. Nettles. NASA-RP-1351 - basic mechanics of laminated composite plates". Nasa ref. publ. 135, NASA Marshall Space Flight Center, 1994.

O. Rand and V. Rovenski. *Analytical methods in anisotropic elasticity: with symbolic computational tools*. Springer Science & Business Media, 2007.

S. I. Ranganathan and M. Ostoja-Starzewski. Universal elastic anisotropy index. *Physical review letters*, 101(5):055504, 2008.

M. V. Rao, P. Mahajan, and R. Mittal. Effect of architecture on mechanical properties of carbon/carbon composites. *Composite Structures*, 83(2):131–142, 2008.

J. N. Reddy. *Mechanics of laminated composite plates and shells: theory and analysis*. CRC press, 2003.

B. V. Sankar and R. V. Marrey. Analytical method for micromechanics of textile composites. *Composites Science and Technology*, 57(6):703–713, 1997.

D. Scida, Z. Aboura, M. Benzeggagh, and E. Bocherens. Prediction of the elastic behaviour of hybrid and non-hybrid woven composites. *Composites science and technology*, 57(12):1727–1740, 1998.

D. Scida, Z. Aboura, M. Benzeggagh, and E. Bocherens. A micromechanics model for 3d elasticity and failure of woven-fibre composite materials. *Composites Science and Technology*, 59(4):505–517, 1999.

H. Shen and L. C. Brinson. A numerical investigation of the effect of boundary conditions and representative volume element size for porous titanium. *Journal of Mechanics of Materials and Structures*, 1(7):1179–1204, 2006.

Z. Ullah, X.-Y. Zhou, L. Kaczmarczyk, E. Archer, A. McIlhagger, and E. Harkin-Jones. A unified framework for the multi-scale computational homogenisation of 3d-textile composites. *Composites Part B: Engineering*, 167:582–598, 2019.

T. Zohdi. Computational modeling and design of new random microheterogeneous materials. *CISM Course Notes*, 1, 2002.

Chapter 5

Auxetic Structures: Parametric Optimization, Additive Manufacturing, and Applications

Auxetic Structures: Parametric Optimization, Additive Manufacturing, and Applications

Matheus B. Francisco[1*], João L. J. Pereira[2],
and Guilherme F. Gomes[3]

[1]Institute of Production Engineering and Management, Federal University of Itajubá, Brazil. E-mail: matheus_brendon@unifei.edu.br
[2]Institute of Mechanical Engineering, Federal University of Itajubá, Brazil. Email: joaoluizjp@gmail.com
[3]Institute of Mechanical Engineering, Federal University of Itajubá, Brazil. Email: guilhermefergom@unifei.edu.br

*Corresponding author

Abstract

This chapter focuses on presenting some concepts about auxetic structures. These models are known to have a negative Poisson's ratio, making them have some improved properties over conventional structures. The auxetics can be constructed with auxetic materials or conventional ones if they adopted the appropriate configuration to generate this behavior. Some configurations (reentrant, double arrowhead, chiral and rotated squares) will be presented in this work and will also be shown the manufacture via 3D printing of auxetic models. The additive manufacturing is a process widely used in the manufacture of auxetics. The application and the optimization of some of these structures will be related. It is expected that at the end of the chapter, the reader will be familiar with auxetic structures.

Keywords: Auxetic Structures; Poisson's ratio; Optimization; Additive Manufacturing; Surrogate Modeling; Design of Experiments.

1 An Overview of Auxetic Structures

The relationship between transversal and longitudinal strain is given by Poisson's ratio. This property is influenced by the atomic density of the materials, that is, the denser the atomic density, the higher its Poisson's ratio tends to be. For example, the Poisson's ratio of gold is higher than that of steel. Furthermore, analyzing some crystalline structures such as centered cubic face (CCF), hexagonal closed packed (HCP), body centered cubic (BCC) and diamond cubic (DC) it is possible to notice that

the structures with higher atomic density also have higher Poisson's ratio, i.e. $v_{fcc} > v_{hcp} > v_{bcc} > v_{dc}$.

The materials or structures that presents negative Poisson's ratio (NPR) are known as auxetics, that is, they expand in the transverse direction when are pulled in the vertical direction. This behavior is different from conventional materials (steel, carbon, rubber, wood) that have to compress in the transverse direction during a longitudinal tensile load to compensate the loss of density. The discovery of auxetic behavior in some materials caused several research to be done seeking to understand its properties, and many things were discovered. However, much research still needs to be done today.

Most of the auxetic materials shown in literature are polymeric, which makes these materials less resistant to mechanical stresses. One way around this problem is to construct structures with conventional materials so that it has auxetic behavior. This is possible because of the configuration in which the structure is constructed, using some unit cells that provide the negative Poisson's ratio, such as: reentrant, double-V, perforated models. Each of these models has its advantages and disadvantages and the choice by one of them is depending on the application of the structure, the tools available for manufacture, the material to be used and so on.

It is also possible to construct composite auxetics using the joining of auxetics and non-auxetics materials for the development of the structure. The great advantage of this technique is to be able to join the properties of two (or more) different materials to arrive at better properties of the model. The research found in literature using these multi-material auxetics can be divided into 4 groups: modification of the lamination angle; produce auxetic structures using auxetic matrix; explore and evaluating the properties of these structures and design and build auxetics composites.

The auxetic models has better performance than conventional ones in several applications, such as more efficient and resistant filters [Quisse et al., 2016], special prosthetic materials [Vinay et al., 2019], improved protective equipment [Duncan et al., 2018] and medical implants of expandable stents [Gat et al., 2015]. The high energy absorption and fracture resistance of the auxetics makes them suitable for defense applications, for example, body armour [Linforth et al., 2020], shock-absorbing equipment [Duncan et al., 2016] and packaging materials [Tomazinziz et al., 2019]. Other's properties of auxetic are the increased shear modulus and indentation resistance [Evans et al., 2000], higher energy absorption capabilities [Scarpa et al., 2003], and better fracture toughness [Lakes and Elms., 1993]. The applications of this type of structure are diverse and many studies have been carried out in recent years covering several areas such as aerospace [Lira et al., 2011] and medical: smart bandages [White, 2009], dilators [Evan et al., 2000], antenna [Gupta and Gupta, 2005], and protective pads [Yang et al., 2016].

Figure 1a shows the application of auxetics in ballistic/fragment impacts [imbalzano et al., 2017]. Military cars are subject to passing through uneven terrain and with fragments of war products. In this way, these cars are subject to various impacts on the bottom and the use of auxetics to absorb energy from these impacts can protect the car and the people who are driving. Figure 1b shows the use of auxetics within a wing profile [Wu et al., 2019]. This can be used to absorb energy and control the level of vibration, for example. Finally, Figure 1c shows a medical application of auxetics [Mir et al., 2014]. It is known that the vascular system of the body shows anisotropic behavior, whereas the conventional coronary stents have isotropic properties. This

results in a mismatch between anisotropic-isotropic properties of the stent and arterial wall, and this in turn is not favorable for mechanical adhesion of the conventional coronary stents with the arterial wall. It is believed that an auxetic coronary stent with inherent anisotropic mechanical properties and negative Poisson's ratio will have good mechanical adhesion with the arterial wall.

(a)

(b)

(c)
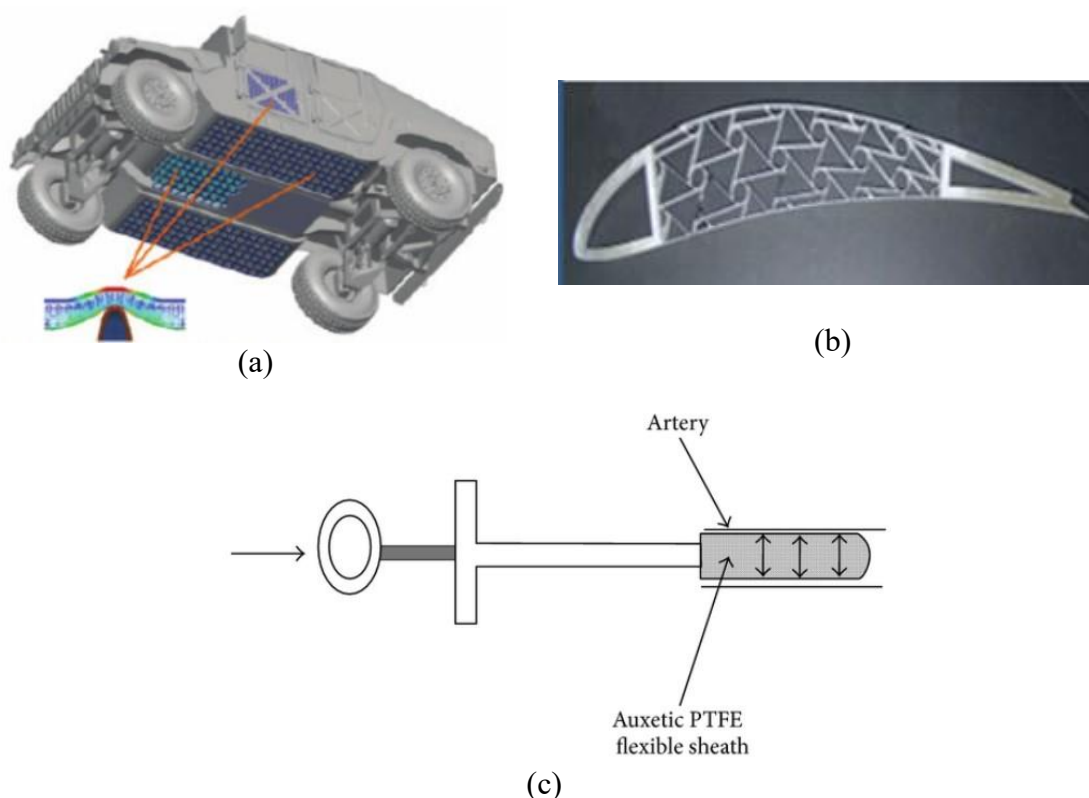
Figure 1: Auxetic application in (a) fragment impact protection [Imbalzano et al., 2017], (b) energy absorption in a wing [Wu et al., 2019] and (c) medical stent [Mir et al., 2014].

1.1 Poisson's ratio in the Mechanic of Materials

The relationship between longitudinal and transverse strain is given by Poisson's ratio (Equation 1). In conventional structures, the deformations have contrary signs, obtaining the positive Poisson's ratio. In auxetics, the strain has the same signal generating NPR.

$$\nu = -\frac{\varepsilon_x}{\varepsilon_z} = -\frac{\varepsilon_y}{\varepsilon_z} \tag{1}$$

where ν is the Poisson's ratio, ε_x, ε_y and ε_z are the strains in the x, y, and z direction, respectively. This property influence on the behavior of the structures and several studies were done to understand the points of improvement and the points of worsening in the model. For example, Guo et al. [2020] studied the deformation behaviors and energy absorption of auxetic lattice cylindrical structures under axial crushing load. The author compared auxetic cylindrical structures with conventional cylindrical structures

to analyze which one had the best performance, concluding that the structures with negative Poisson's ratio had better performance.

The Poisson's ratio of isotropic materials depends of the modulus of elasticity (E), the shear modulation (G) and the bulk modulus (K), as shown in Equation 2 and 3. Combining the Equation 2 and 3, it is possible to find the Equation 4 that represent the relation between G and K. Notice how the Poisson's ratio influences these properties and, consequently, the mechanical performance of these structures. Thus, the study of auxetics is of great importance to the scientific community. It is important to note that for anisotropic materials it is necessary to specify several elastic constants depending on the structural characteristics of the crystal.

$$G = \frac{E}{2(1+\nu)} \tag{2}$$

$$K = \frac{E}{3(1-2\nu)} \tag{3}$$

$$\frac{2G}{3K} = \frac{1-2\nu}{1+\nu} \tag{4}$$

In most known materials, bulk modulus (K) is larger than shear modulus (G). Thus, one can make the implication presented in Equation 5. Moreover, a necessary condition to obtain the NPR is that the shear modulus is larger than the buckling modulus, both of which must be positive. For the G in Equation 2 to be positive, we have that the Poisson's ratio must be greater than -1 and for K to be positive in Equation 3, the Poisson's ratio must be less than 0.5. Thus, the Poisson's ratio varies within this interval and the graph in Figure 2 can be constructed to show the restriction impost in Equation 5.

$$\frac{2}{3} \leq \frac{1-2\nu}{1+\nu} \tag{5}$$
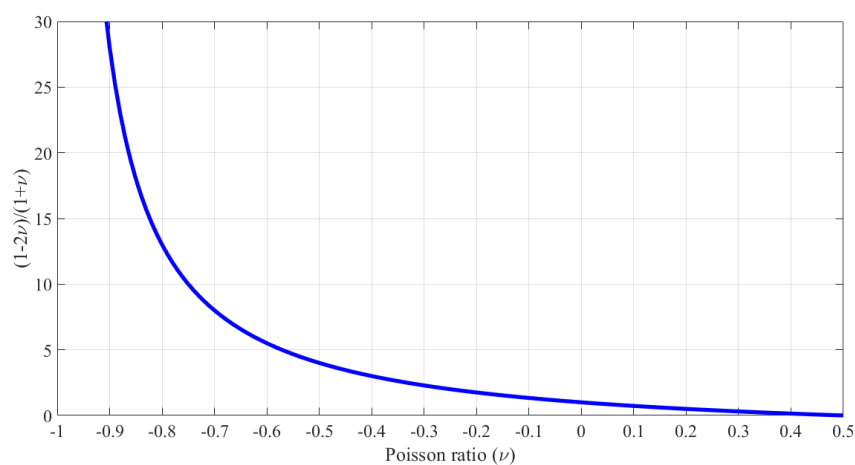
Figure 2: graphical relationship between ν and $\frac{1-2\nu}{1+\nu}$. [Francisco et al., 2021]

The Figure 2 shows that the Poisson's ratio gets smaller and smaller when the $\frac{2G}{3K}$ ratio increases. This ratio tends to infinity when the Poisson's ratio is trending to -1, on the other hand, the Poisson's ratio restriction being less than 0.5 prevents the values G and K to be negative. It is important to remember that this relationship applies to auxetic materials. For auxetic structures, calculations depend on the configuration adopted and the material used. Going further, it is worth remembering that to construct auxetic structures, it can be used auxetic or conventional materials, provided that the correct configuration for the construction of the model is adopted. The focus of this chapter is not to demonstrate the formulas for calculating the Poisson's ratio, but it is important to make it clear that the isotropic or anisotropic behavior of the material has a great influence on this parameter.

1.2 Natural and non-natural auxetic materials and structures

Materials with negative Poisson's ratio can be metallic [Ren et al., 2016], Ceramic [Hu et al., 2020], polymeric [Sahra and Dhanasekar, 2017], composite [Li et al., 2020]. Some examples of natural auxetic material are like α-cristoblaite [Evans et al., 1991], pyrolytic graphite [Voigt et al., 1966], some biological tissues [Lees et al., 1991] and crystalline cellulose [Yao et al., 2016], in a defined form, and α-quartz. While some materials have natural auxetic characteristics, others need to be modified to achieve these characteristics. Foam's materials, for example, exhibit conventional behavior, however, it is possible to obtain auxetic behavior by processing the material in the correct way [Najarian et al., 2018].

Auxetics foams are constructed from the compression of a piece of foam in all three directions and are subjected to temperature above the softening point of the material. After this process, they are removed and cooled to ambient temperature until they are removed from the mold. For polyester foams, Lakes and Roderic [1987] reported that a compression factor between 1.4 and 4 is sufficient to generate auxetic behavior in the structure. On the other hand, for reticulated metal foams, it is not necessary to use high temperatures.

2 Types of Cellular Auxetic Structures

Structures with negative Poisson's ratio can be constructed with conventional materials since the adopted configuration is suitable to generate an auxetic behavior. Some of these settings, which are recognized in literature and have already been used in several articles published around the world, will be shown in this section. However, it is important to note that there are several other existing models.

Additive manufacturing is a great ally in the manufacture of auxetics structures, as these often have complex configurations to be manufactured by conventional processes. Meena and Singamneni [2021] used the 3D printing technique to develop a novel hybrid auxetic structures for improved in-plane mechanical properties. The authors reported that the manufacture of this new part by a process other than 3D printing would make the cost of manufacturing the company unfeasible its production.

Several models have been created over the years through diverse different methodologies, for example: rotational structures [Grima et al., 2016]. , topology optimization [Gao et al., 2019], and taking inspiration from nature [Ren et al., 2018]. Some of the most famous auxetics configurations are re-entrant hexagonal honeycombs

[Liu et al., 2016], double arrowhead honeycomb [Wang et al., 2018], chiral [Zhang et al., 2018]. When additive manufacturing is used to manufacture structures, the print parameters influence the properties of the models. In addition, the material used also has great influence, Johnston and Kazanci [2021] carried out an analysis to know how three different material configurations effect the responses of three different cellular geometries and proved that the material really has great impact structural responses.

2.1 Re-entrant models

Gibson et al. [1982] were the pioneers to study reentrant models, they studied analytically   the   mechanic   properties   of   a   reentrant   structure   and   performed experimental tests to validate the result. The authors developed models representing the mechanical properties of the structure in terms of bending, elastic buckling, and plastic collapse. The reentrant hexagonal model studied is shown in Figure 3. The value of the θ angle that makes the structure to be considered conventional or auxetic, i.e., if θ value is positive, the structure is conventional if the value is negative, there is an auxetic structure.
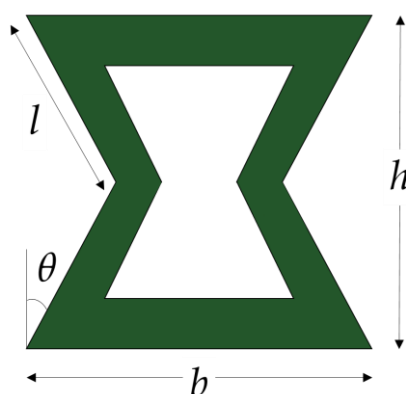
Figure 3: Design parameters of the reentrant auxetic unit cell.

Auxetic structures, in general, are periodic structures, that is, they have a unit cell that repeats itself throughout the model. Thus, you can analyze only one cell and extrapolate the results to the entire structure. Gibson et al. [1982] developed analytical models for the cell shown in Figure 3, the authors considered that each part of the cell can be considered   a   bar and that an external force caused a deformation in the structure. They found Equations 1 to 4 that describe, respectively, modulus of elasticity in the direction of force, modulus of elasticity in the direction transverse to force, Poisson's ratio and the shear modulus of the structure.

$$E_1 = \frac{K_f(\frac{b}{l} + sen\theta)}{hcos^3\theta} \tag{1}$$

$$E_2 = \frac{K_f cos\theta}{h\left(\frac{b}{l} + sen\theta\right) sen^2\theta} \tag{2}$$

$$v_{12} = \frac{sen\theta(\frac{b}{l} + sen\theta)}{cos^2\theta} \tag{3}$$

$$G_{12} = \frac{K_f(\frac{b}{l} + sen\theta)}{h\left(\frac{b}{l}\right)^2 \left(1 + \frac{2b}{l}\right)cos\theta} \tag{4}$$

The v_{21} can be found by the $E_1 v_{21} = E_2 v_{12}$ which is valid when one has the symmetric stiffness matrix. Two considerations were made by Gibson et al. [1982] during the development of the analytic models: bars deform only along their axis with no change in angle and the structure is under stretching efforts in vertical directions. the force exerted due to the applied stress σ_2 is given by Equation 5 and the P component of w that acts along the diagonal bar is given by Equation 6.

$$w = h\cdot(lsin\cdot\theta + b)\ cos\theta \tag{5}$$

$$P = h\cdot\sigma_2\cdot(l\cdot sin\theta + b)cos\theta \tag{6}$$

Knowing that the deformation of the structure is directly proportional to the applied force, we have that $P = K_s\delta$, where K_s is a tension constant. The deformation can be calculated by dividing equation 6 by tension constant, as shown in Equation 7, which, divided by length l, gives the strain given by Equation 8. Moreover, the relationship between the deformation, given by Equation 8, and the stress σ_2 is known as Hooke's law and is given by Equation 9.

$$\delta = \frac{h\sigma_2(lsen\theta + b)cos\theta}{K_s} \tag{7}$$

$$\varepsilon_2 = \frac{h\sigma_2(lsen\theta + b/l)cos\theta}{K_s} \tag{8}$$

$$E_2 = \frac{K_s}{h(lsen\theta + b/l)cos\theta} \tag{9}$$

Gibson et al. [1982] also made the calculations to find the deformation in direction 1, obtaining Equation 10. Thus, it is possible to find the Poisson's ratio by dividing the equation 8 by Equation 10. The Equation 11 shows the model for Poisson's ratio.

$$\varepsilon_1 = \frac{h\sigma_2 sen\theta cos\theta}{K_s} \tag{10}$$

$$v_{12} = -\frac{sen\theta}{sen\theta + \frac{b}{l}}$$

(11)

It is important to note that the Poisson's ratio of this model depends on the parameters θ, b and l. These three parameters are fundamental to define the auxetic behavior of the structure and, consequently, its mechanical properties.

2.2 Double-V models

Larsen et al. [1996] was one of the pioneers studying double arrowhead structures. Auxetic structures are periodic (repeat the same unit cell) and so the study of only one cell is sufficient to understand the behavior of the whole model. The parameters of a double-V cell is shown in Figure 4, It takes 3 cell parameters to build the model: two angles (θ_1 and θ_2) and the length l.
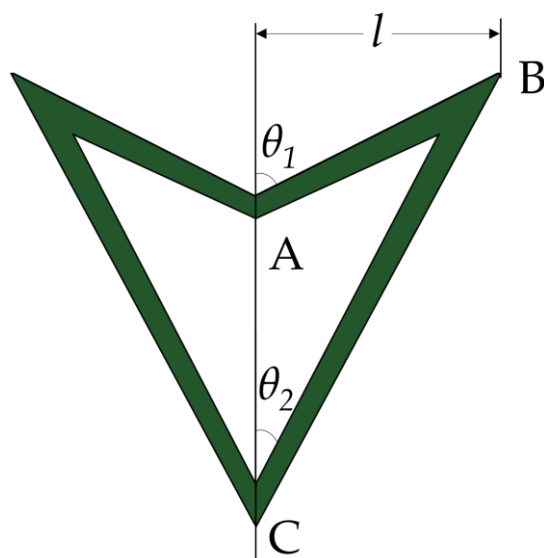
Figure 4: design parameter of the double arrowhead auxetic unit cell.

Qiao and Chen [2014] studied the double-V model analytically. The structure was subjected to a uniform stress σ_∞ which corrects a vertical force equal to $P_a = 2 \cdot \sigma_\infty \cdot lb\cdot$, where b is the dimension out of the plane of the structure. Some boundary conditions were adopted for the development of the analysis: the point C is constrained in all degrees of freedom and the point A is constrained to rotation and horizontal displacement (this implies in a reaction force F_a and reaction moment M_a when σ_∞ is applied). The Equation 12 and 13 shows the normal strains in x and y directions, when u_y^A is the vertical displacement of point A and u_x^B is the horizontal displacement of point B.

$$\varepsilon_y = \frac{u_y^A \cdot sin\theta_1 \cdot sin\theta_2}{l \cdot \sin(\theta_1 - \theta_2)}$$

(12)

$$\varepsilon_x = \frac{u_x^B}{l} \qquad (13)$$

The relationship between equations 12 and 13 gives us the Poisson's ratio that is shown in Equation 14. It is also possible to calculate the modulation of elasticity, as shown in Equation 15 and 16, where E_s is the Young's modulus of the solid material and I is the second moment of inertia.

$$v_{xy} = -\frac{\varepsilon_x}{\varepsilon_y} = \frac{1}{tan\theta_1 \cdot tan\theta_2} \qquad (14)$$

$$E_y = \frac{\sigma_\infty}{\varepsilon_y} = \frac{3E_s I}{bl^3} \alpha(\theta_1, \theta_2) \qquad (15)$$

$$\alpha = -\frac{4(cos\theta_1 - cos\theta_2)}{sin\theta_1 sin\theta_2} - \frac{(cos\theta_1 cos\theta_2 - 1)^2(cos\theta_1 cos\theta_2 - 3)}{sin\theta_1 sin\theta_2(cos\theta_1 - cos\theta_2)} + \frac{(cos\theta_1 cos\theta_2 + 3)(cos\theta_1 cos\theta_2 - 1)}{cos\theta_1 - cos\theta_2} \qquad (16)$$

It is noticed that θ_1 and θ_2 angles have influence on the Poisson's ratio value, the higher the angles, the lower the Poisson's ratio. This is because the angle interferes with the deformation capacity of the structure, that is, depending on the values of θ_1 and θ_2, the structure will be able to deform more or less. Similarly, the angles also affect the modulation of elasticity, in addition, the length l also has influence.

2.3 Rotating squares and Rectangle models

Grima and Evans [2000] were the pioneers studying the rotating squares and rectangle models. The authors verified that this type of structure would have the Poisson's ratio equal to -1. In addition, they developed an analytic study to show the equations that govern the structure. The relationship between the deformation and the stress found by them is shown in Equation 17, being S the compliance matrix of the structure.

$$\begin{vmatrix} \varepsilon_1 \\ \varepsilon_2 \\ \gamma_{12} \end{vmatrix} = \begin{vmatrix} S_{11} & S_{12} & S_{13} \\ S_{21} & S_{22} & S_{23} \\ S_{31} & S_{32} & S_{33} \end{vmatrix} \bullet \begin{vmatrix} \sigma_1 \\ \sigma_2 \\ \tau_{12} \end{vmatrix} \qquad (17)$$

$$S = \begin{vmatrix} \frac{1}{E_1} & \frac{-v_{21}}{E_2} & 0 \\ \frac{-v_{12}}{E_1} & \frac{1}{E_2} & 0 \\ 0 & 0 & 0 \end{vmatrix}$$

The authors also found the equation representing the young modulus of the structure and it is shown in Equation 18, where θ is the angle shown in Figure 5, l is the length of the squares and k_h is the rotational stiffness constant.

$$E_1 = E_2 = \frac{8k_h}{t^2(1 - sin\theta)} \qquad (18)$$
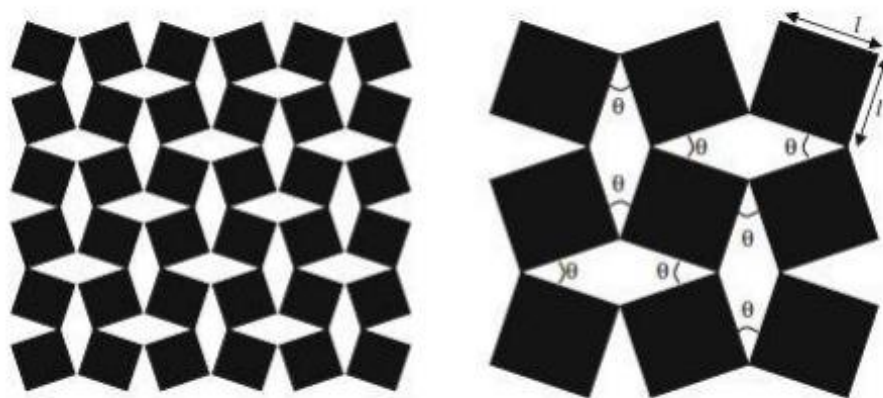
Figure 5: Auxetic model proposed by Grima and Evans: overview and details. [Grima and Evans, 2000]

Grima et al. [2007] continued studies in rotating squares to assess whether semi-rigid structures would also have an auxetic behavior. The authors developed an analytic study based on the model shown in Figure 6. Equations 19-39 shows the behavior of the model.
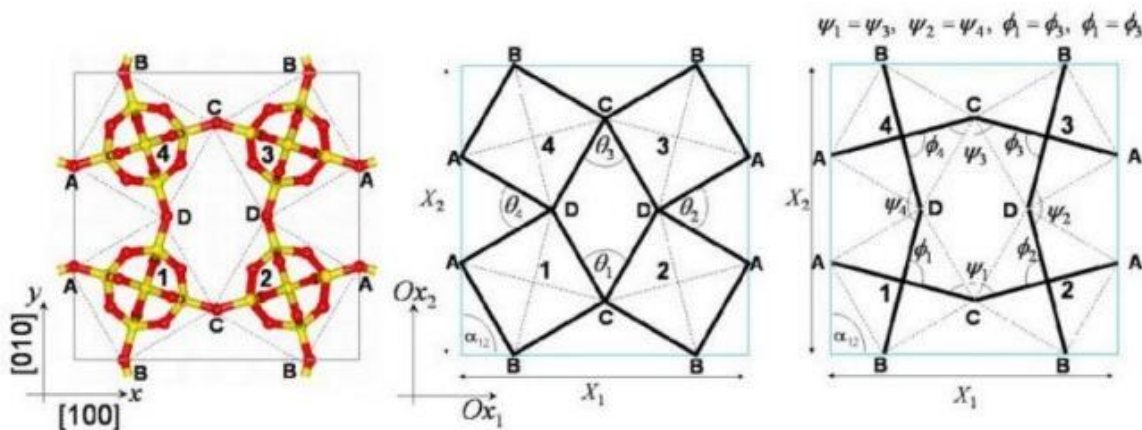
Figure 6: Variables used in the model proposed by Grima et al. [2007]

$$v_{12} = v_{21} = -cotg(\frac{\Psi_1}{2})tan(\frac{\Psi_2}{2})[\,1 + 4(\frac{K_\Psi}{K_\emptyset})]^{-1} \qquad (19)$$

$$E_1 = E_2 = \frac{8K_\Psi(K_\emptyset + 2K_\Psi)}{l_d^2 z(K_\emptyset + 4K_\Psi)} \cdot \frac{sin(\frac{\Psi_2}{2})}{sin(\frac{\Psi_1}{2})cos^2(\frac{\Psi_2}{2})} \qquad (20)$$

$$G_{12} = K_\emptyset \frac{1}{z}[l_d \, sin \, (\frac{\Psi}{2})]^{-2} \tag{21}$$

where l_d is the length of AC or BD (diagonal of the square) in figure 6, the rotational stiffnesis given by K_φ and $K_\emptyset$ that restrain changes to the angles φ and Ø, respectively, and z is the thickness in the third direction of the squares. Thus, it is possible to calculate the Poisson's ratio, the modulus of elasticity and the shear modulation by the following equations:

$$\nu_{12} = \nu_{21} = -[1 + 4(\frac{K_\Psi}{K_\emptyset})]^{-1} \tag{22}$$

$$E_1 = E_2 = \frac{8K_\Psi(K_\emptyset + 2K_\Psi)}{l_d^2 z(K_\emptyset + 4K_\Psi)} \cdot sec^2 \, (\frac{\Psi}{2}) \tag{23}$$

$$G_{12} = \frac{K_\emptyset}{z l_d^2}[sin^2 \, (\frac{\Psi}{2})]^{-1} \tag{24}$$

The off axis elastic moduli at an angle ζ around the third direction are given by Grima et al. [2007] by Equation 25, 26 and 27. where m = cos(ζ) and n = sin(ζ).

$$\frac{1}{E_1^\zeta} = \frac{m^4}{E_1} + \frac{n^4}{E_2} - m^2n^2 \, (2 \cdot \frac{\nu_{12}}{E_1} - \frac{1}{G_{12}}) \tag{25}$$

$$\nu_{12}^\zeta = E_1^\zeta \, [(m^4 + n^4)\frac{\nu_{12}}{E_1} - m^2n^2(\frac{1}{E_1} + \frac{1}{E_2} - \frac{1}{G_{12}}) \tag{26}$$

$$\frac{1}{G_{12}^\zeta} = \frac{m^4 + n^4}{G_{12}} + 2m^2n^2 \, (\frac{2}{E_1} + \frac{2}{E_2} + \frac{1}{G_{12}} + \frac{4\nu_{12}}{E_1}) \tag{27}$$

2.4 Chiral Models

It is said that an object is chiral when there is no possibility of it to be superimposed on its mirrors image. The chiral models rotate when they receive compressive force, causing auxetic behavior to be evidenced. The movement of this type of structure while receiving a load is like what happens with transmissions and crankshaft [Necemer et al., 2020]. Prall and Lakes [1997] studied this type of structure through analytical and experimental analyses for strain in plane. The equations found by then that represent the deformations of the structure are shown in equations 28-30. Furthermore, the parameters used by the authors are shown in Figure 7.

$$e = r \cdot sin\varphi \tag{28}$$

$$e_1 = r \cdot \varphi \cdot cos\theta \tag{29}$$

$$e_2 = r \cdot \varphi \cdot sin\theta \tag{30}$$
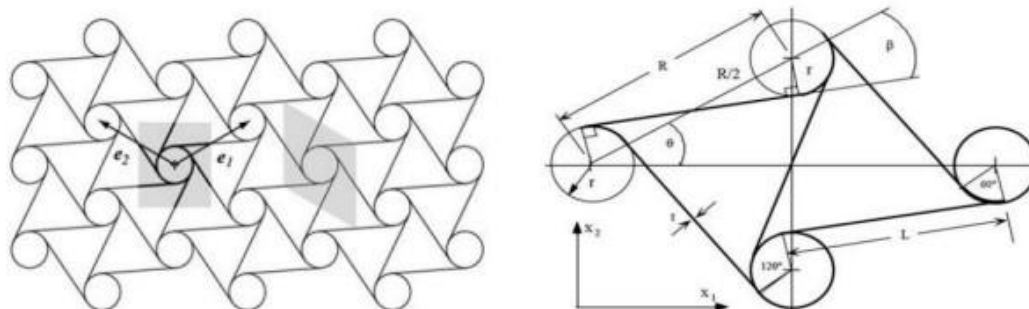
Figure 7: Geometry of a hexagonal chiral lattice. [Prall and Lakes, 1997]

where φ is the angle of applied deformation in the structure. The r·sinφ ~ r·φ can be made because the structure is subjected to small deformations. The Equation 31 shows the calculus of φ by the elementary beam theory, where t is the thickness of the structure, d is the width of the structure, E is the material Young's modulus and T is the applied load in the system.

$$\varphi = \frac{2LT}{Et^3d} \tag{31}$$

The authors concluded that the deformations ε_1 and ε_2 can be given by Equations 32 and 33, respectively. Furthermore, the Poisson's ratio is given by the relationship between the longitudinal and transversal deformed, as shown in Equations 34 and 35.

$$\varepsilon_1 = \varphi \cdot \frac{r}{R} \tag{32}$$

$$\varepsilon_2 = \varphi \cdot \frac{r}{R} \tag{33}$$

$$\nu_{12} = -\frac{\varepsilon_2}{\varepsilon_1} \tag{34}$$

$$\nu_{21} = -\frac{\varepsilon_1}{\varepsilon_2} \tag{35}$$

3 Auxetic Structures in Engineering

This section will be responsible for showing how auxetics structures are used within engineering. For this, it will be shown a way of manufacturing some models and then will be reported on some utilizations of this type of structure. It is important to

note that there are several auxetic models and various applications of these models, it is not possible to exemplify all the possibilities here and only a few will be shown next.

3.1 Fabrication of auxetic models

Auxetic structures usually have a complex shape, which makes it difficult to manufacture. However, the advancement of additive manufacturing has greatly facilitated the development of these structures and has been widely used by many authors around the world. The author of this chapter manufactured three auxetic structures, using 3D printing, to exemplify the construction of these models. The structures that will be shown here were manufactured via 3D printing on the Ultimaker® 2+ printer using Polylactic acid (PLA) filament with a diameter of 1.75mm. The printing temperature and the build plate temperature is equal to 200°C and 60C°, respectively. The print speed, the layer height and the infill density are equal to 55mm/s, 0.4mm and 20%, respectively. Several materials can be used for manufacturing, however, in this section, polylactic acid (PLA) was used which is a polymer widely used for the manufacture of these models .

For the example of this section, it was used the auxetic model shown in figure 3 and 4, respectively. In addition, three auxetics structures were constructed: reentrant tube, reentrant beam, and double-V beam. The initial values of the design parameter for the reentrant beam are equal to 16mm, 8mm and 60° for the base length, oblique length and angle of the unit cell, respectively. Thus, the author adopted seven cells in the horizontal, three in the vertical direction and 30mm of death. The same parameters of the unit cell were used to construct the reentrant tube, the other parameters of the tube are shown in table 1.

Table 1: Design parameter adopted for the tube manufacturing.

Variable	Symbol	Unit	Value
Angle	α	degrees	60
Oblique length	l	mm	8
Horizontal length	b	mm	16
Height of Tube	H	mm	83.2
Diameter of Tube	D	mm	91.68
Height of Cell Unit	h	mm	13.85
N° of horizontal cell	N_c	-	24
N° of vertical cell	N_h	-	6

For the double-V model, the design parameters are shown in Figure 4 (angle θ_1 , angle θ_2 , and oblique length l). The values adopted to build the structure are θ_1 equal to 60°, θ_2 equal to 30° and oblique length l equal to 30mm. Thus, it will be adopted three cells in horizontal and four in vertical direction. All the models were designed in a

software CAD and transferred to the Ultimaker Cura to set the print paramenters. Figure 8 shows the manufacturing process of the three models constructed and the final structure.
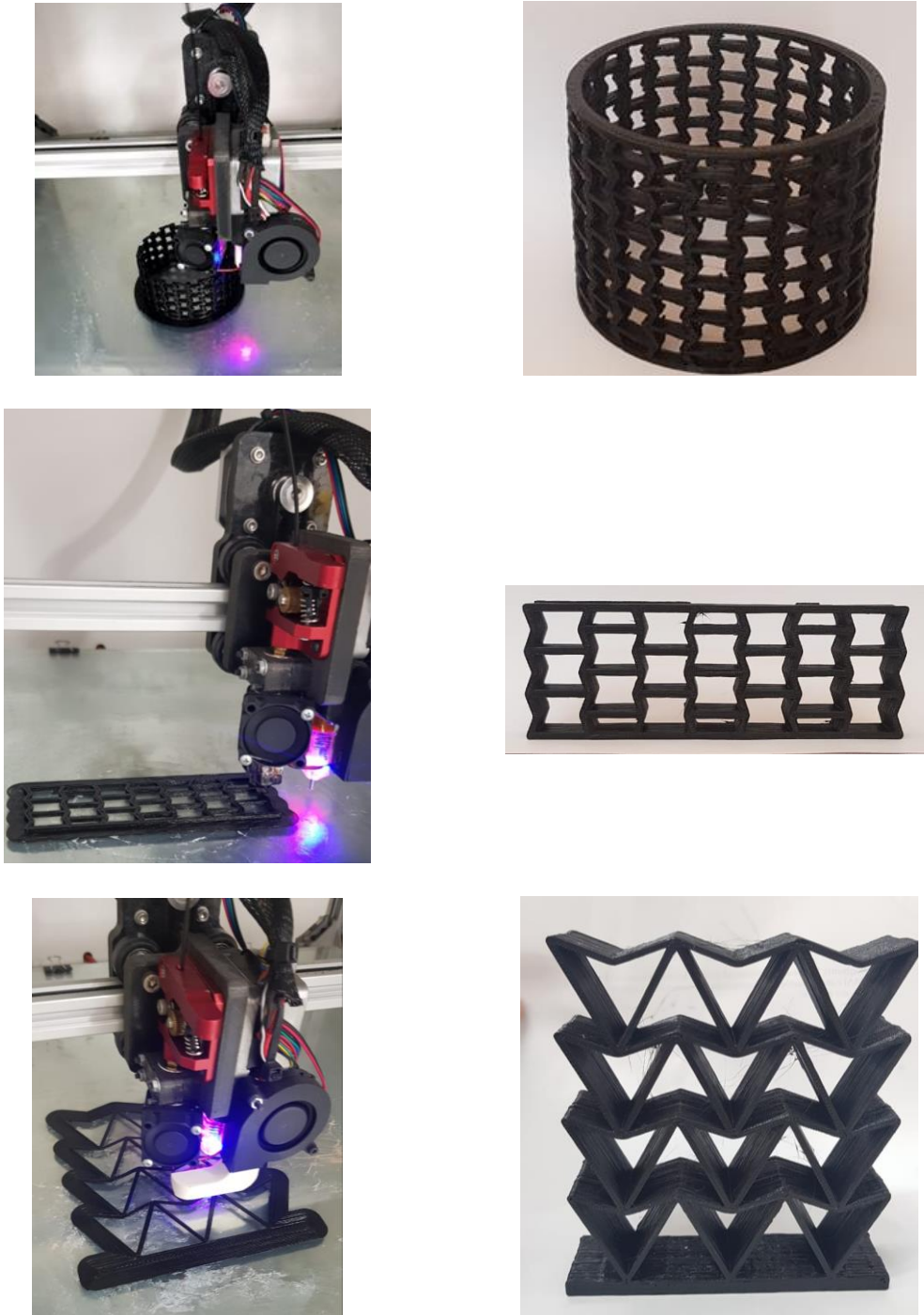
Figure 8: Manufacturing process and the final structures studied in this chapter.

3.1.1 Experimental Results of Auxetic Structures

The three structures proposed in this chapter were subjected to a compression test. Figure 9 shows the compression test carried out on the auxetic tube from the initial

experiment (t=0s) until the end time (t = 140s). The maximum load reached was 3254 N and the mass of the structure is equal to 84.3g. Figure 10 shows the deformation of the part during the experimental test for the reentrant beam, the maximum load obtained by the structure was 12467N and has a mass of 70g. Finally, Figure 11 shows   the deformation of the double-V structure during the compression test, the maximum load reached was 2100N and the mass of the structure was 116g. The table 2 compiles these results.

Table 2: Experimental results of the auxetic structures studied in this chapter.

Structure	Maximum load (N)	Mass (g)	Load-mass ratio (N/g)
Reentrant tube	3254	84.3	38.6
Reentrant beam	12467	70	178.1
Double-V beam	2100	116	18.1

Table 2 shows that the reentrant beam is the structure that gets the major maximum load and is the lightest structure of the three studied. However, the choice for one of them depends on the application and manufacturing process available. Furthermore, further tests should be performed to evaluate other responses together with the maximum compression load supported. It is important to note that all these parts were manufactured using the same printing parameters and the same material.

(INTENTTIONALY LEFT BLANK)
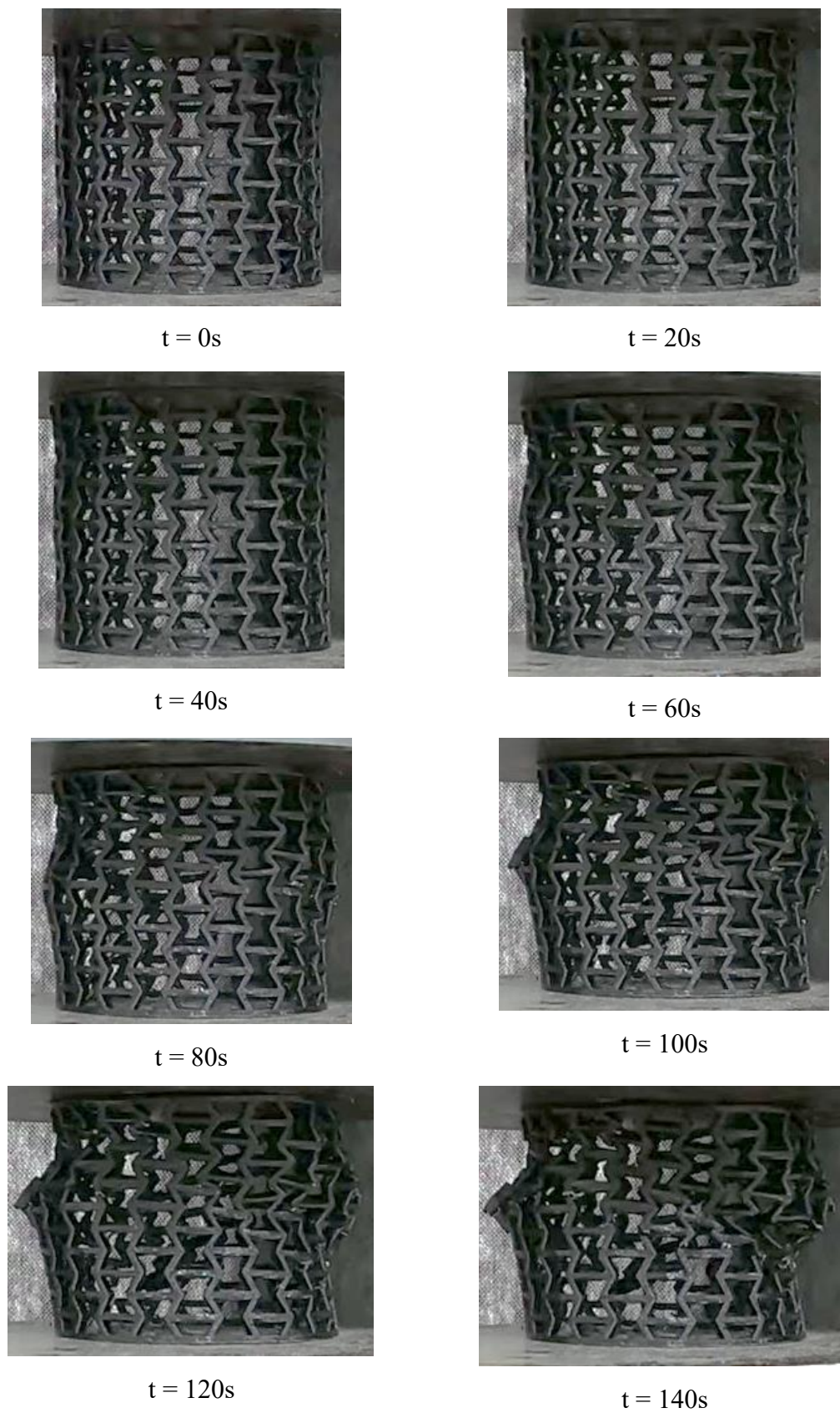
Figure 9: Performance of auxetic reentrant tube in compression tests.

(a) t = 0s

(b) t = 20s

(c) t = 40s

(d) t = 60s

(e) t = 80s

(f) t = 100s

(g) t = 120s

(h) t = 140s
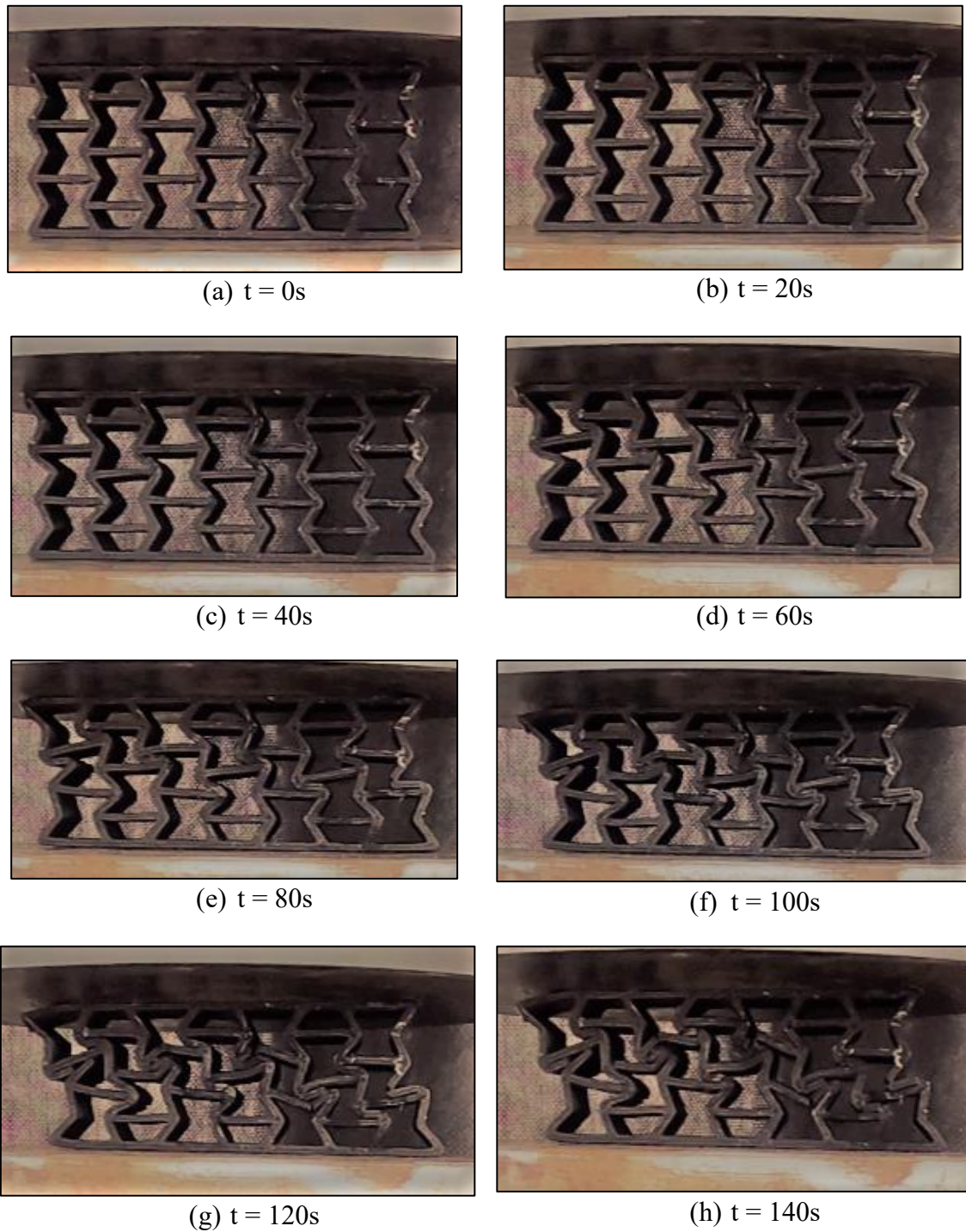
Figure 10: Performance of auxetic reentrant beam in compression tests.

t= 0s

t= 15s

t = 35s

t = 50s

t = 65s

t = 80s

t = 90s

t = 100s
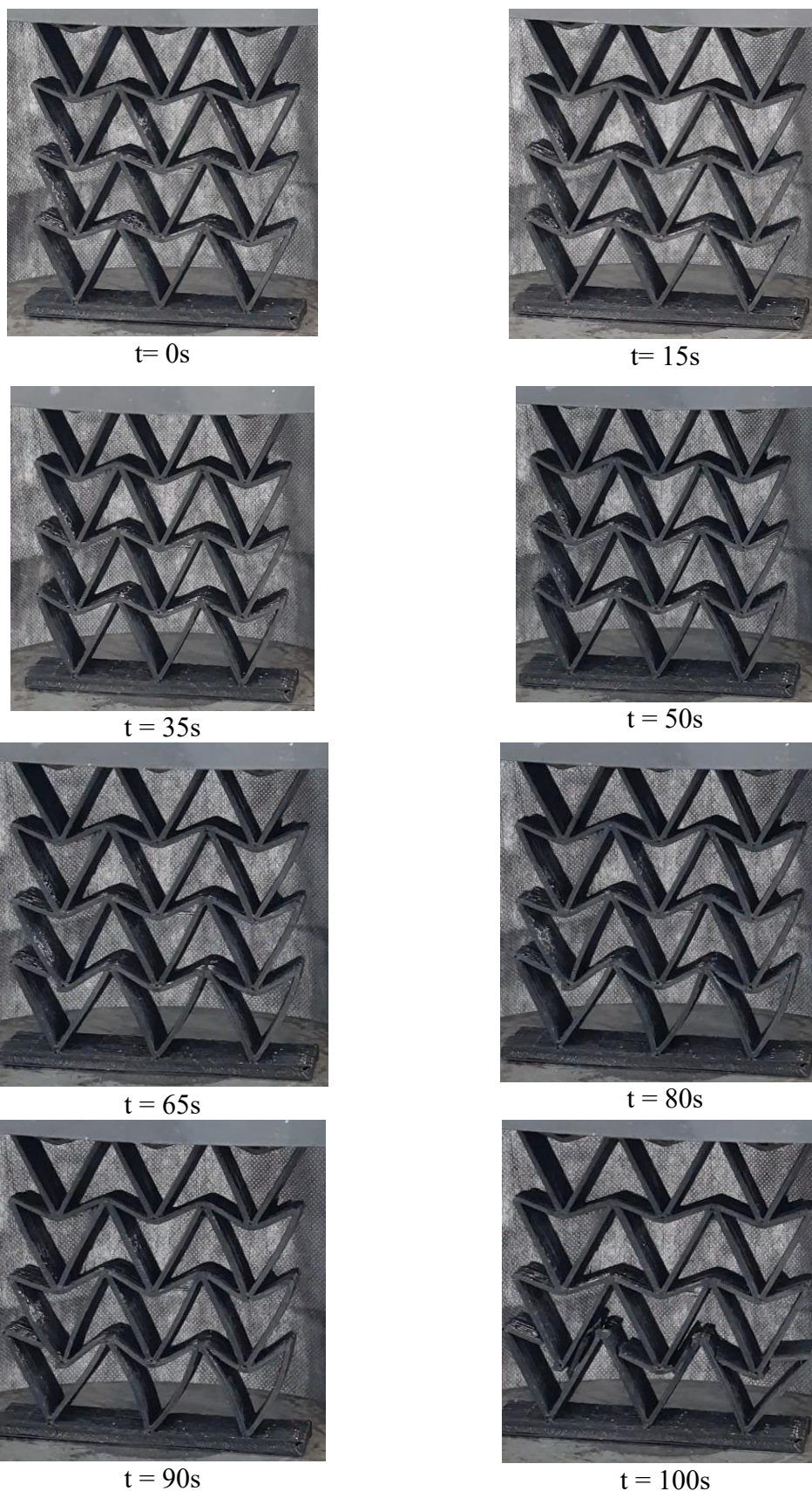
Figure 11: Performance of auxetic double-V beam in compression test.

3.2 Auxetic Structures Applied in Engineering

The idea of applying auxetics structures in engineering is not something recent, as it had its beginning around the 1970s. However, the difficulty of manufacturing these structures caused the studies not to prosper at that time. Today, additive manufacturing has been a great ally of the manufacture of auxetics structures, as it facilitated the manufacture of these models. Thus, several auxetics configurations began to appear and several applications for these models were studied, some of these applications will be shown in this section.

Foser et al. [2018] evaluated whether the use of auxetic foam in sport helmet was feasible. The author's objective was to study whether the use of this foam would improve its linear impact acceleration attenuation. Figure 12 shows the helmet used by the author. Furthermore, the author compared the results of the auxetics model with conventional ones, showing that auxetics have superior performance, i.e., Gadd severity index reduced by 11% for frontal impacts (39.9J) and 44% (24.3J) for side impacts. Thus, it was possible to verify that auxetics structures could be used for protection both in the sports industry and in other areas.

Shah et al. [2022] carried out a finite element analysis of the ballistic impact on auxetic sandwich composite human body armour. The authors analyzed with several different types of projections, comparing the responses of the auxetic structure with conventional structures. The author concluded that the indentation resistance improved with the auxetic armour and deformation in auxetic armor was observed greater for each of the cases when compared to the conventional armor, due to higher energy absorption. Thus, it is perceived that the investment in auxetics structures for protective equipment is valid and very important to improve the safety of current protective equipment.

Figure 12: Foam inserts: (a) foreheads, (b) right side and (c) left side [Shepherd et al., 2020].

The automotive industry is increasingly seeking to build light, comfortable and safe cars. The need for economical cars makes the reduction of their weight one of the main objectives in the design of automobiles. In addition, safety is also a very important item and the construction of a crash box (integral component for ensuring the safety of a car which serves as an energy absorbing member) should cause the car to absorb some of the energy in case of frontal collision during car accidents. Wang et al. [2018] analyze the application of auxetic structures to design jounce bumpers, this study was able to improve the noise, vibration, and harshness performance of the automobile. Zhou et al. [2016] carried out a multi objective optimization of an auxetic structure focused on building a crash box with auxetic structures and improving the collision performance of the car.

Other studies have also been done seeking to optimize the energy absorption of some components to increase car safety. Gao et al. [2018] studied a cylindrical auxetic structure in a novel crash box, compared with conventional models, the auxetic structure has lower peak crushing force and higher energy absorption. Lee et al. [2019] compared auxetic and conventional structures in development of a crash tube, and the performance of auxetic structures was superior to conventional structures. Thus, it can be noted that the use of auxetic structures in protective equipment is of great interest to the world scientific community.

Another much explored feature of auxetic structures is the damping mechanism. Chen et al. [2020] studied the damping mechanism of CFRP three-dimensional double-

arrow-head auxetic structures. The author manufactured the structure in carbon fiber reinforced polymer (CFRP) and submitted it to compressive loading-unloading tests and sine sweep frequency experiments. The author compared the performance of the construction structure with a conventional structure, and the auxetics obtained better results, i.e., excellent comprehensive characteristics of light weight, high specific strength and high damping performance. The structure tested by the author is shown in Figure 13. This better damping capability makes these structures can be applied in conditions that need to reduce the vibration level or reduce vibration transmissibility.
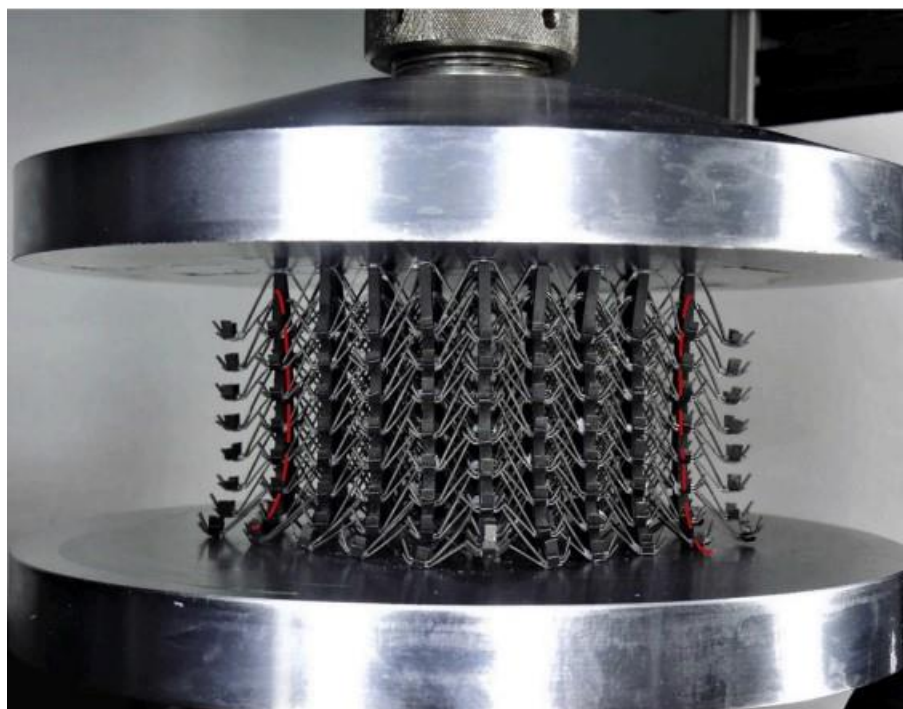
Figure 13: Deformed photograph of the 3D DAH structure during compression. [Chen et al., 2020]

Budarupu et al. [2016] studied the design concepts of an aircraft wing using morphing airfoil with auxetic structures. The authors evaluated the aerodynamic forces that appear on the flight during the flight to use as a contour condition. The advantages of the morphing airfoil with auxetic structure are (i) larger displacement with limited straining of the components and (ii) unique deformation characteristics, which produce a theoretical in-plane Poisson's ratio of − 1. The structure used by the author is shown in Figure 14. It is possible to notice that auxetics structures can be applied in various situations and that their use can generate several advantages over conventional structures.
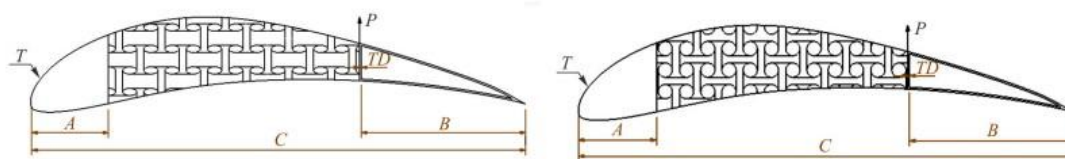
Figure 14: Airfoil with auxetic structure of (a) elliptical cells and (b) circular cells used by Budarupu et al. [2016].

Several other authors have published studies focused on the application of auxetic structures in real problems. Günaydin et al. [2019] used the anti-tetrachiral and reentrant models to study the deformation mechanism of these structures. The authors concluded that the auxetic models have higher performance in crush absorption than conventional ones thanks to its high shear strength, i.e., auxetics have better performance to be applied in automotive bumpers, for example. Figure 15a shows the application studied by Lee et al. [2019] He evaluated the performance of auxetic structures manufactured via additive manufacturing with SUS316L under low impact condition, concluding that these structures have better performance than conventional structures to absorb impact energy.

Figure 15b shows the model of the study conducted by Chang et al. [2017] which aimed to use auxetics structures to protect concrete structures against impact and blast loadings. The authors carried out two experimental tests: drop weight impact and filed blast test. The results showed that the plate made with auxetic structure absorbed 19.1% more energy than the plate built with conventional structures. This work showed the importance of the study of auxetic structures applied to protection systems. Figure 15c shows a new shock absorbing uniaxial graded auxetic damper developed by Al-Rifaie and Sumelka [2019]. The authors conducted several tests and found that this structure is applicable in various situations, such as: blast resistant doors; blast resistant for retrofitting sensitive buildings; elevator (absorbing unexpected crash of elevators or cable failure in multi-story buildings); crash energy absorbing system in motor vehicles front bumpers; and many other possible applications.

Finally, Figure 15d shows the fuselage sections with negative Poisson's ratio structure insert below the cargo floor studied by Wang et al. [2021]. The author studied the use of these structures in the aircraft fuselage to assess the energy absorption capacity during a crash landing. They concluded that these structures have better energy absorption performance than conventional structures and that they have potential in improving the crashworthiness behavior of aircraft.

(a)

(b)

(c)

(d)
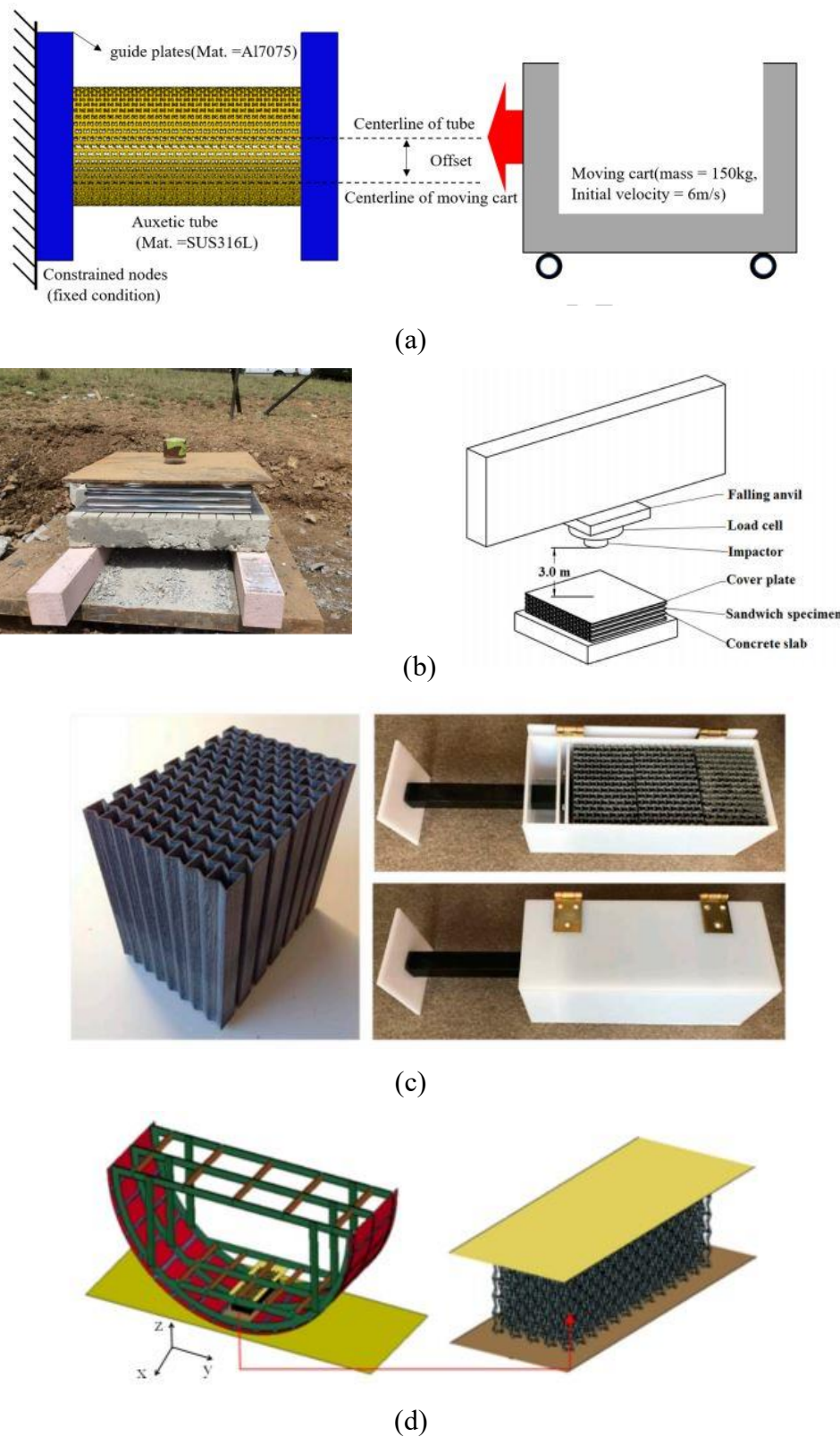
Figure 15: Examples of auxetic applications: (a) automotive bumpers [Lee et al., 2019] (b) protective systems against impact [Chang et al., 2017] (c) shock absorbing [Al-Rifaie and Sumelka, 2019] and (d) aircraft's fuselage [Wang et al., 2021].

4 Optimization of Auxetic Structures

Auxetic structures can be applied in various situations and the optimization of these models for each of the applications is very important. Optimization can be mono objective, when there is only one objective, or multi-objective when you want to optimize multiple responses simultaneously. This second methodology is more real, because the structures are subjected to several loads simultaneously during their operation. In this section, a methodology called parametric optimization will be shown.

4.1 Parametric optimization in Auxetic Structures

Parametric optimization is a methodology used to find the best design variables of a given structure. In this section, we will demonstrate a parametric optimization study of a reentrant beam. For this, we first need to figure out which variables are important to the problem, so that we will use them to get our goal. Thinking of a reentrant cell, equations 1-11 can be used to describe the structure analytically. Moreover, it is perceived by equation 11 that the Poisson's ratio of the structure depends on b (length of the horizontal bar), l (length of the oblique bar) and θ (angle between these bars).

From the moment we find which design variables are important for the analysis, it is necessary to find out in which range is the optimal point. This is a very difficult task and can be done in two ways: using the experience of the designer or doing an exploratory analysis. Generally, when the designer knows very well the behavior of the structure, he can deduce within what range the design parameters can stay to achieve good results. If you do not have this knowledge, exploratory analysis is the best option. Exploratory analysis consists of performing some experiments to find the intervals of the design parameters that best generate results.

In the present study, a reentrant beam was constructed as shown in the compression tests in Figure 10. A numerical model representing the structure was constructed and validated with experimental data. From this, some simulation was performed with different configurations to understand at which intervals we could find the optimal point, so the length of the oblique bar will vary between 6mm to 10mm , the length of the horizontal bar will vary between 14mm to 18mm, and the angle α (α = 90 - θ) will vary between 50° to 70°. From this interval, you can use a statistical technique called response surface methodology to create a series of experiments. The design of experiments and the experimental results are shown in Table 3. The answers of interest are Poisson's ratio (v), Failure load (Q_u), Buckling load (λ), Natural frequency (ω_n) and Mass (M).

Table 3 – Design of experiment considering three manufacturing (design) factors.

Exp.	$\alpha(°)$	$b(mm)$	$l(mm)$	v	$Q_U(N)$	$\lambda(N)$	$\omega_n(Hz)$	$M(g)$
	Variables			Responses				
1	50	14	6	-1,24	19350	101100	342,4	57,42
2	70	14	6	-1,98	18330	110900	332,0	57,42
3	50	18	6	-1,25	17990	133200	320,2	66,42
4	70	18	6	-2,00	16200	129700	294,9	66,42
5	50	14	10	-1,38	7643	32390	125,2	74,70
6	70	14	10	-2,59	7989	44350	146,1	74,70
7	50	18	10	-1,39	9422	37650	132,1	83,70
8	70	18	10	-2,61	8366	45240	137,8	83,70
9	50	16	8	-1,33	13800	58830	202,5	70,56
10	70	16	8	-2,35	9191	67770	204,2	70,56
11	60	14	8	-1,77	12260	60390	204,1	66,06
12	60	18	8	-1,78	12290	62650	193,9	75,06
13	60	16	6	-1,61	17640	104100	356,2	61,92
14	60	16	10	-1,89	8564	39200	134,1	79,20
15	60	16	8	-1,78	12570	62040	199,8	70,56
16	60	16	8	-1,79	12280	60660	195,4	71,22
17	60	16	8	-1,78	12350	60510	195,9	70,77
18	60	16	8	-1,77	12790	63620	203,9	70,35
19	60	16	8	-1,77	12630	62050	199,6	70,78
20	60	16	8	-1,78	12410	60540	195,7	70,99

From the results shown in Table 3 it is possible to find regression models that represent each of the answers of interest. The models are shown in Table 4 and, to verify that these models are reliable, the adjusted R² parameter is analyzed, as shown in table 5.

Table 4: Regression coefficients for fit regression model.

Response	X_1	X_2	X_3	X_1^2	X_2^2	X_3^2	X_1X_2	X_1X_3	X_2X_3	C
M		2,25	4,32							0,066
v	0,0681		0,1385	0,0006		0,0078	0,0059			-2,537
λ	-5297	14153	-48851	47		3264			-1398	343939
ω_n	-3,19	-18,02	-231,2			8,15		0,389	1,809	1589
Q_u	-81,3	-1477	-8769			223,1			176,4	74049

Table 5: Model Summary for fit regression model.

Response	S	R^2 (adj)
M	0,198716	99,92%
ν	0,019170	99,76%
λ	4334,500	97,87%
ω_n	9,363410	98,37%
Q_u	785,6230	95,30%

The Table 5 shows that the adjustment of the data to the models was high, all above 95%, so it can be concluded that the models are representing the data well. Other statistical analyses can be done to verify which factors are important to the model, for example, however this will not be done here, because the focus is to show the process of optimizing an auxetic structure. Thus, the models shown in Table 4 will be used as the objective function of the optimization process and the range of variation of the variables will be the constraints. Equation 36 shows the compression performance optimization design and Figure 16 the Pareto's front for this problem.

$$\min F(X)=\{-Q_u, -\lambda, \nu\}$$

$$\text{subject to:}$$
$$14 \leq b \leq 18 \text{ [mm]}$$
$$6 \leq l \leq 10 \text{ [mm]}$$
$$50 \leq \alpha \leq 70 \text{ [°]}$$

(36)
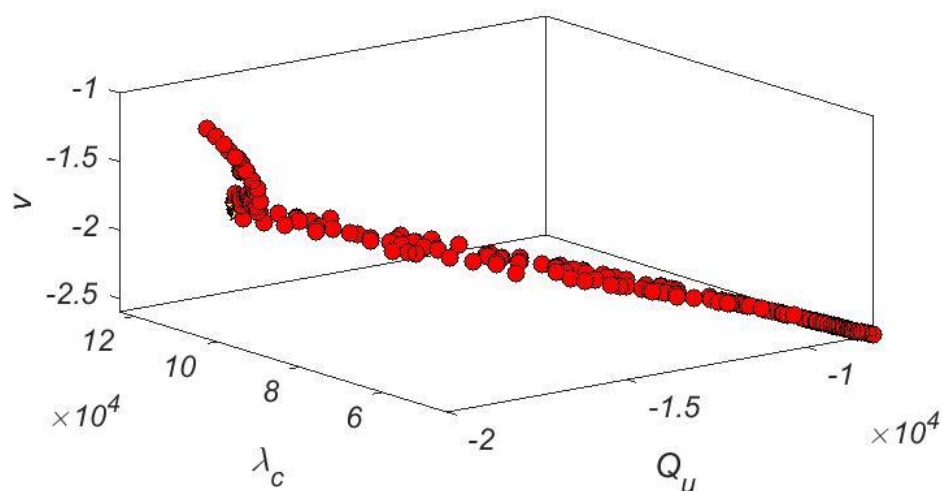
Figure 16: Pareto's front for Poisson's ratio, failure load and critical buckling load of reentrant auxetic beam.

It is perceived by Figure 16 that it is not possible to improve all responses simultaneously, that is, to decrease the Poisson's ratio, both the failure load and the critical buckling load will also decrease. All red dots on the chart are great points and can be chosen. In this work, we used the TOPSIS criterion to decide which point of the chart will be chosen, this criterium choose the point farthest from the worst result and the closest to the best result. The chosen point is shown in Table 6 and Figure 17 shows the optimized structure and the initial structure. The results obtained with this configuration compared to the initial configuration are shown in Table 7.

Table 6 - Optimum configuration for compression performance of reentrant auxetic beam.

Configuration	
θ (°)	70
b (mm)	16
l (mm)	6

(a)   (b)
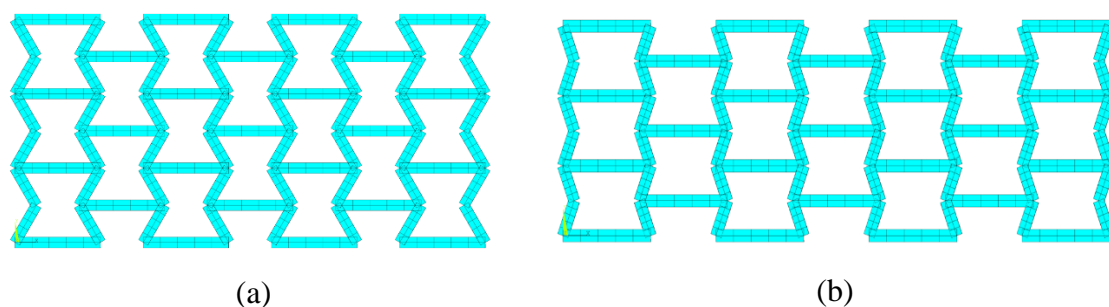
Figure 17: The (a) Initial and (b) optimized reentrant beam structure.

Table 7: Comparison between the initial and the optimized reentrant beam structure results (compression performance).

Response	Initial structure results	Optimized structure results	Improvement
Q_u (N)	12570	17160	26.75%
λ (N)	62040	108500	42.82%
ν	-1.78	-1.99	10.55%
ω_n (Hz)	199.80	312.88	36.14%
M (g)	70.56	61.92	12.24%

Similarly, the model can be optimized to improve the modal performance of the structure. The goal may be to maximize natural frequency and minimize Poisson's ratio and mass. The minimization in this case is to decrease the mass value and to leave the structure with a more pronounced auxetic behavior. The maximization of the natural frequency aims to remove the frequency of the vibration frequency structure of most

mechanical equipment. Thus, optimization can be represented in Equation 37. It is noticed that the restrictions are the intervals defined for each of the variables and Figure 18 shows the Pareto chart for the three responses simultaneously and Table 8 shows the optimal point chosen by the TOPSIS criterion.

$$\min F(X) = \{-\omega_n, v, M\}$$

$$subject\ to:$$

$$14 \le b \le 18\ [\text{mm}]$$

$$6 \le l \le 10\ [\text{mm}]$$ (37)

$$50 \le \alpha \le 70\ [°]$$
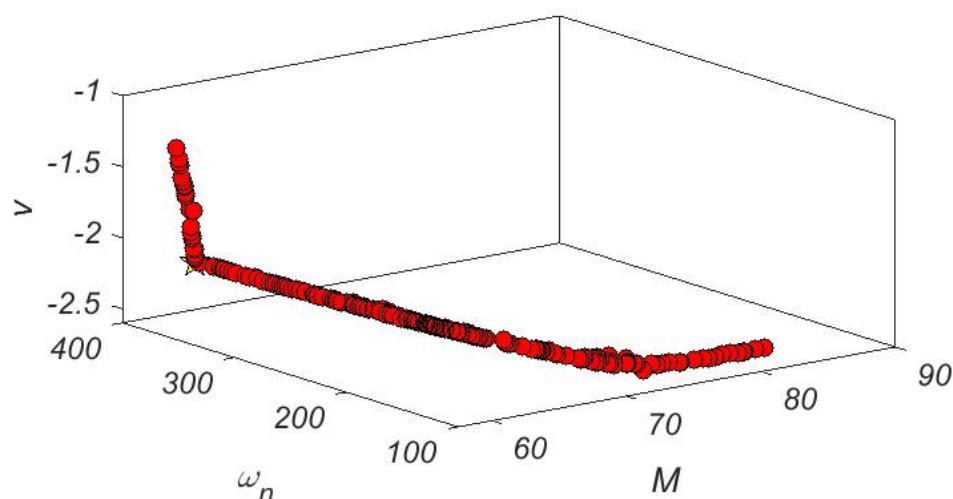
Figure 18: Pareto's front for Poisson ratio, natural frequency, and mass of the reentrant auxetic beam.

Table 8: Optimum configuration for modal performance of reentrant auxetic beam.

Configuration	
θ (°)	70
b (mm)	14
l (mm)	6

It is perceived by figure 18 that it is possible to increase the natural frequency and reduce the mass, as they are inversely proportional parameters. However, this condition implies increasing the Poisson's ratio, as they are conflicting objectives. Thus, by the TOPSIS criterion, the point marked a yellow star was chosen on the chart that corresponds to the point shown in Table 8 and the Table 9 shows the comparison between the initial and the optimized configuration. Figure 19 shows the initial and

optimized structure, while the table shows the comparison of the results between the structures.

(a)   (b)
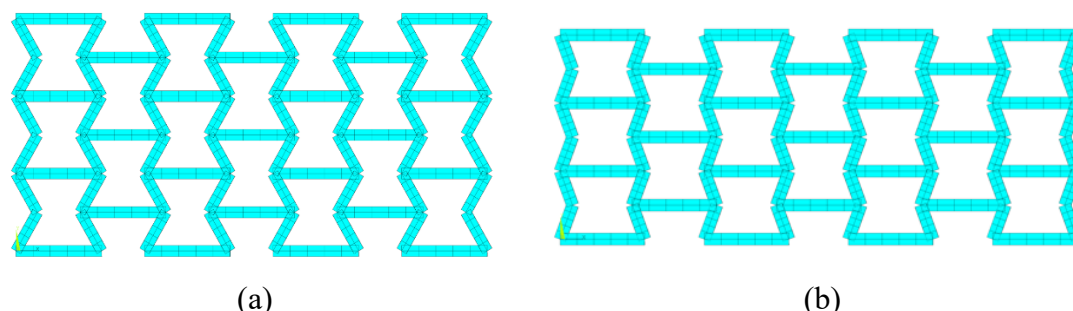
Figure 19: The model of (a) initial and (b) optimized auxetic beam structure for modal performance.

Table 9: Comparison between the initial and the optimized auxetic beam structure results (Modal performance).

Response	Initial structure results	Optimized structure results	Improvement
Q_u (N)	12570	18330	31.42%
λ (N)	62040	110900	44.06%
ν	-1.78	-1.98	10.10%
ω_n (Hz)	199.80	332.10	39.83%
M (g)	70.56	57.42	18.62%

5 Concluding Remarks

The chapter focused on showing the reader what auxetic structures are. It has been reported that these structures have negative Poisson coefficient and that there are several improved properties because of this characteristic. These structures can be constructed with auxetic or conventional materials, and the configuration adopted is fundamental for this behavior. Some unit cells have been shown and the choice to adopt any of them depends on the application of the structure and manufacturing processes available.

This chapter also showed the manufacture of a reentrant girder through additive manufacturing. This process facilitated the development of new structures with negative Poisson coefficient, because it removed the manufacturing difficulty that exists through conventional processes, such as machining, for example. This structure was submitted to a compression test and the results were shown so that the reader has knowledge of the performance of this structure.

Finally, it proved to be a way to optimize an auxetic model, reaching the optimal parameters of structure construction. The results obtained from the optimal model were compared with the initial model to verify the improvement of the structure. This methodology proved very propitious to perform the parametric optimization of

structures with negative Poisson coefficient and the techniques used here can be applied in other structures as well.

Acknowledgements

References

Evans, Ken. and Andrew Alderson. 2000. Auxetic materials: Functional materials and structures from lateral thinking. Advanced Materials, 12(9): 617–628.

Ouisse, M., Collet, M., & Scarpa, F. (2016). A piezo-shunted kirigami auxetic lattice for adaptive elastic wave filtering. Smart Materials and Structures, 25(11), 115016.

Vinay, V. C., & Varma, D. M. (2019). Fabrication and testing of auxetic foams for rehabilitation applications. Journal of the Indian Institute of Science, 1-8.

Duncan, O., Shepherd, T., Moroney, C., Foster, L., Venkatraman, P. D., Winwood, K., ... & Alderson, A. (2018). Review of auxetic materials for sports applications: Expanding options in comfort and protection. Applied Sciences, 8(6), 941.

Gatt, Ruben. Luke Mizzi, Joseph Azzopardi, Keith Azzopardi, Daphne Attard, Aaron Casha, Joseph Brifa and Joseph Grima. 2015. Hierarchical Auxetic Mechanical Metamaterials. Sci. Rep. 5, 246(9):2025–2032. https://doi.org/10.1002/pssb.200982033 35

Linforth, S. J. (2020). Auxetic Armour System for Protection Against Soil Blast Loading (Doctoral dissertation).

Duncan, O., Foster, L., Senior, T., Alderson, A., & Allen, T. (2016). Quasi-static characterisation and impact testing of auxetic foam for sports safety applications. Smart Materials and Structures, 25(5), 054014.

Tomažinčič, D.; Nečemer, B.; Vesenjak, M.; Klemenc, J. Low-cycle fatigue life of thin-plate auxetic cellular structures made from aluminium alloy 7075-T651. Fatigue Fract. Eng. Mater. Struct. 2019, 42, 1022–1036.

K.E. Evans, K.L. Alderson, Auxetic materials: the positive side of being negative, Eng. Sci. Educ. J. 9 (4) (2000) 148–154.

F. Scarpa, L.G. Ciffo, J.R. Yates, Dynamic properties of high structural integrity auxetic open cell foam, Smart Mater. Struct. 13 (1) (2003) 49.

R.S. Lakes, K. Elms, Indentability of conventional and negative Poisson's ratio foams, J. Compos. Mater. 27 (12) (1993) 1193–1202.

C. Lira, F. Scarpa, R. Rajasekaran, A gradient cellular core for aeroengine fan blades based on auxetic configurations, J. Intell. Mater. Syst. Struct. 22 (9) (2011) 907–917.

L. White, Auxetic foam set for use in smart filters and wound dressings, Urethanes Technol. Int. 26 (4) (2009) 34–36.

Gupta, N., & Gupta, K. M. (2005, March). Metamaterial and auxetic hybrid composite antennas. In antenna technology: small antennas and novel metamaterials, 2005. IWAT 2005. IEEE international workshop on (pp. 414-417). IEEE. 36

C. Yang, H.D. Vora, Y.B. Chang, Evaluation of auxetic polymeric structures for use in protective pads, ASME 2016 International Mechanical Engineering Congress and Exposition, Am. Soc. Mech. Eng., 2016, (pp. V009T12A066-V009T12A066).

Imbalzano, G., Tran, P., Ngo, T. D., & Lee, P. V. (2017). Three-dimensional modelling of auxetic sandwich panels for localised impact resistance. *Journal of Sandwich Structures & Materials*, *19*(3), 291-316.

Wu, W., Hu, W., Qian, G., Liao, H., Xu, X., & Berto, F. (2019). Mechanical design and multifunctional applications of chiral mechanical metamaterials: A review. *Materials & Design*, *180*, 107950.

Mir, M., Ali, M. N., Sami, J., & Ansari, U. (2014). Review of mechanics and applications of auxetic structures. *Advances in Materials Science and Engineering*, *2014*.

Lakes, Roderic. 1987. Foam structures with a negative Poisson's ratio, Science, 235: 1038– 1040.

Zahra, T., & Dhanasekar, M. (2017). Characterisation of cementitious polymer mortar– Auxetic foam composites. Construction and Building Materials, 147, 143-159.

Ren, X., Shen, J. H., Ghaedizadeh, A., Tian, H. Q., & Xie, M. (2016). Numerical simulations of 3D metallic auxetic metamaterials in both compression and tension. In Applied Mechanics and Materials (Vol. 846, pp. 565-570). Trans Tech Publications Ltd.

Li, T., Liu, F., & Wang, L. (2020). Enhancing indentation and impact resistance in auxetic composite materials. Composites Part B: Engineering, 198, 108229.

Hu, J. S., Wang, B. L., Li, J. E., & Wang, K. F. (2020). Thermal shock resistance behavior of auxetic ceramic honeycombs with a central crack or an edge crack. Ceramics International.

Evans, K.E.; Nkansah, M.A.; Hutchinson, I.J.; Rogers, S.C. Molecular network design. Nature 1991, 353, 124.

Voigt, W. Lehrbuch der Kristallphysik; Vieweg+Teubner Verlag: Wiesbaden, 1966;

Lees, C.; Vincent, J.F.V.; Hillerton, J.E. Poisson's ratio in skin. Biomed. Mater. Eng. 1991. 37 [53] Yao, Y. T., Alderson, K. L., & Alderson, A. (2016). Modeling of negative Poisson's ratio (auxetic) crystalline cellulose I β. Cellulose, 23(6), 3429-3448.

Najarian, F., Alipour, R., Rad, M. S., Nejad, A. F., & Razavykia, A. (2018). Multi-objective optimization of converting process of auxetic foam using three different statistical methods. Measurement, 119, 108-116.

MEENA, Kusum; SINGAMNENI, Sarat. Novel hybrid auxetic structures for improved inplane mechanical properties via additive manufacturing. Mechanics of Materials, v. 158, p. 103890, 2021.

Alderson, A., & Evans, K. E. (2001). Rotation and dilation deformation mechanisms for auxetic behaviour in the α-cristobalite tetrahedral framework structure. Physics and Chemistry of Minerals, 28(10), 711-718.

Gao, J., Xue, H., Gao, L., & Luo, Z. (2019). Topology optimization for auxetic metamaterials based on isogeometric analysis. Computer Methods in Applied Mechanics and Engineering, 352, 211-236.

Ren, X., Shen, J., Tran, P., Ngo, T.D., Xie, Y.M., 2018. Design and characterisation of a tunable 3D buckling-induced auxetic metamaterial. Mater. Des. 139, 336 – 342.

Liu, W., Wang, N., Luo, T., Lin, Z., 2016. In-plane dynamic crushing of re-entrant auxetic cellular structure. Mater. Des. 100, 84–91.

Wang, X., Wang, B., Wen, Z., Ma, L., 2018. Fabrication and mechanical properties of CFRP composite three-dimensional double-arrow-head auxetic structure. Compos. Sci. Tech., 164, 92- 102.

Zhang, H., Luo, Y., Kang, Z., 2018. Bi-material microstructural design of chiral auxetic metamaterials using topology optimization. Compos. Struct. 195, 232-248.

Grima, J.N., Missi, L., Azzopardi, K.M., Gatt, R., 2016. Auxetic perforated mechanical metamaterials with randomly oriented cuts. Adv. Mater. 28, 385-389.

JOHNSTON, Ross; KAZANCI, Zafer. Analysis of additively manufactured (3D printed) dualmaterial auxetic structures under compression. Additive Manufacturing, v. 38, p. 101783, 2021.

Gibson, L.J., The mechanics of two-dimensional cellular material, proceedings of the royal Society of London series A – mathematical physical and engineering Science 382:25 (1982)

Larsen, U. D., Signund, O., & Bouwsta, S. (1997). Design and fabrication of compliant micromechanisms and structures with negative Poisson's ratio. *Journal of microelectromechanical systems*, *6*(2), 99-106.

Qiao, J. X., & Chen, C. Q. (2015). Impact resistance of uniform and functionally graded auxetic double arrowhead honeycombs. *International Journal of Impact Engineering*, *83*, 47-58.

J.N. Grima, K.E. Evans, Auxetic behavior from rotating squares, J. Mater. Sci. Lett. 19 (2000) 1563–1565, https://doi.org/10.1023/A:1006781224002.

Grima JN, Zammit V, Gatt R, Alderson A, Evans KE (2007) Auxetic behavior from rotating semirigid units. Phys Status Solidi B 244(3):866–882

Nečemer, B., Glodež, S., Novak, N., & Kramberger, J. (2020). Numerical modelling of a chiral auxetic cellular structure under multiaxial loading conditions. Theoretical and Applied Fracture Mechanics, 107, 102514

D. Prall, R. Lakes, Properties of a chiral honeycomb with a Poisson's ratio of –1, Int. J. Mech. Sci. 39 (1997) 305–314, https://doi.org/10.1016/j.jpeds.2009.04.058.

Foster, L., Peketi, P., Allen, T., Senior, T., Duncan, O., & Alderson, A. (2018). Application of auxetic foam in sports helmets. Applied Sciences, 8(3), 354.

Shah, I. A., Khan, R., Koloor, S. S. R., Petrů, M., Badshah, S., Ahmad, S., & Amjad, M. (2022). Finite Element Analysis of the Ballistic Impact on Auxetic Sandwich Composite Human Body Armor. *Materials*, *15*(6), 2064.

Shepherd, T., Winwood, K., Venkatraman, P., Alderson, A., & Allen, T. (2020). Validation of a Finite Element Modeling Process for Auxetic Structures under Impact. physica status solidi (b), 1900197.

Wang, Y., Zhao, W., Zhou, G., Gao, Q., & Wang, C. (2018). Optimization of an auxetic jounce bumper based on Gaussian process metamodel and series hybrid GA-SQP algorithm. *Structural and Multidisciplinary Optimization*, *57*(6), 2515-2525.

Zhou, G., Ma, Z. D., Li, G., Cheng, A., Duan, L., & Zhao, W. (2016). Design optimization of a novel NPR crash box based on multi-objective genetic algorithm. *Structural and Multidisciplinary Optimization*, *54*(3), 673-684.

Gao, Q., Zhao, X., Wang, C., Wang, L., & Ma, Z. (2018). Multi-objective crashworthiness optimization for an auxetic cylindrical structure under axial impact loading. *Materials & design*, *143*, 120-130.

Lee, W., Jeong, Y., Yoo, J., Huh, H., Park, S. J., Park, S. H., & Yoon, J. (2019). Effect of auxetic structures on crash behavior of cylindrical tube. *Composite Structures*, *208*, 836-846.

Budarapu, P. R., YB, S. S., & Natarajan, R. (2016). Design concepts of an aircraft wing: composite and morphing airfoil with auxetic structures. *Frontiers of Structural and Civil Engineering*, *10*(4), 394-408.

Francisco, M. B., Pereira, J. L. J., Oliver, G. A., Roque da Silva, L. R., Cunha Jr, S. S., & Gomes, G. F. (2021). A review on the energy absorption response and structural applications of auxetic structures. *Mechanics of Advanced Materials and Structures*, 1-20.

Wang, T., An, J., He, H., Wen, X., & Xi, X. (2021). A novel 3D impact energy absorption structure with negative Poisson's ratio and its application in aircraft crashworthiness. *Composite Structures*, *262*, 113663.

Günaydın, K., Eren, Z., Kazancı, Z., Scarpa, F., Grande, A. M., & Türkmen, H. S. (2019). In-plane compression behavior of anti-tetrachiral and re-entrant lattices. *Smart Materials and Structures*, *28*(11), 115028.

Lee, W., Jeong, Y., Yoo, J., Huh, H., Park, S. J., Park, S. H., & Yoon, J. (2019). Effect of auxetic structures on crash behavior of cylindrical tube. *Composite Structures*, *208*, 836-846.

Qi, C., Remennikov, A., Pei, L. Z., Yang, S., Yu, Z. H., & Ngo, T. D. (2017). Impact and close-in blast response of auxetic honeycomb-cored sandwich panels: experimental tests and numerical simulations. *Composite structures*, *180*, 161-178.

Al-Rifaie, H., & Sumelka, W. (2019). The development of a new shock absorbing Uniaxial Graded Auxetic Damper (UGAD). *Materials*, *12*(16), 2573.

Chapter 6

Additive Manufacturing of Ti-Alloys for Aerospace, Naval and Offshore Applications

Chapter details

Chapter DOI:

Chapter suggested citation / reference style:

Mendoza, Michael Y., et al. (2022). "Additive Manufacturing of Ti-Alloys for Aerospace, Naval and Offshore Applications". *In* Jorge, Ariosto B., et al. (Eds.) *Fundamental Concepts and Models for the Direct Problem*, Vol. II, UnB, Brasilia, DF, Brazil, pp. 154–183. Book series in Discrete Models, Inverse Methods, & Uncertainty Modeling in Structural Integrity.

P.S.: DOI may be included at the end of citation, for completeness.

Book details

Book: Fundamental Concepts and Models for the Direct Problem

Edited by: Jorge, Ariosto B., Anflor, Carla T. M., Gomes, Guilherme F., & Carneiro, Sergio H. S.

Volume II of Book Series in:

Discrete Models, Inverse Methods, & Uncertainty Modeling in Structural Integrity

Published by: UnB City: Brasilia, DF, Brazil Year: 2022

DOI: https://doi.org/10.4322/978-65-86503-83-8

Additive Manufacturing of Ti-Alloys for Aerospace, Naval and Offshore Applications

Michael Y. Mendoza[1*], Leonel Leonardo Delgado - Morales[2], and Victor Contreras Palma[3]

[1*]Institute of Naval Architecture and Ocean Engineering, Universidad Austral de Chile,
E-mail: michael.mendoza@uach.cl
[2]Institute of Design and Industrial Methods, Universidad Austral de Chile, Chile.
E-mail: leonel.delgado@uach.cl
[3]Institute of Naval Architecture and Ocean Engineering, Universidad Austral de Chile.
E-mail: victor.palma@uach.cl
*Corresponding author

Abstract

Titanium alloys are well-known by their excellent corrosion resistance and high strength-to-weight ratio. The aerospace industry has been taking advantage of those properties and enhancing them with novel manufacturing techniques such as Additive Manufacturing (AM). However, the naval and offshore industry has very limited use of those benefits. This is mainly due to technical limitations such as small-scale parts and low deposition rates of the most common AM processes. This work presents a review of the state-of-the-art in AM and its applications, in which relevant publications related to this important area of investigation are considered. Initially, titanium is described as the main alloy. The Laser Engineered Net-Shape (LENS^{TM}), Electron Beam Additive Manufacturing (EBAM$^@$) and Wire Arc Additive Manufacturing (WAAM) processes are presented. Given that WAAM offers potential solutions for size and deposition rates with design challenges and new materials for component fabrication, at the end of the chapter, applications from the naval and offshore areas where this method is used are shown.

Keywords: Titanium alloys; additive manufacturing; naval and offshore industry; aerospace components; WAAM

1 Introduction

Titanium alloys are recognized by their excellent mechanical and chemical properties such as excellent corrosion resistance, good fatigue performance and low modulus (high flexibility). Several examples of Ti-alloys applications are aircraft components, automotive, chemical processing equipment, biomedical industries and more recently in naval applications. During titanium processing, an inert atmosphere or vacuum is required, and this condition among others becomes titanium a material of high cost. Therefore, certain applications have limitations to use this material

(Lütjering and Williams [2007]). To justify the inherent cost of titanium, features and characteristics of novel techniques as additive manufacturing (AM) need to be deeply understood to take advantage of the processing methods and the resultant material properties.

Additive manufacturing of titanium alloys has several applications as mentioned before. However, the focus has been in the aerospace industry and more specifically for military applications. A common limitation for AM is the part size. Most AM techniques focus on small processing chambers to produce small parts. The naval industry is characterized by large-size components, but it has been working gradually to use parts made by AM (Ziółkowski and Dyl [2020]). The global market is increasing the use of additive manufacturing technology and the titanium demand. Figure 1 shows the US market projection until 2028. Therefore, it is important to understand material processing conditions, microstructure, and performance correlation (Londono [2019]).
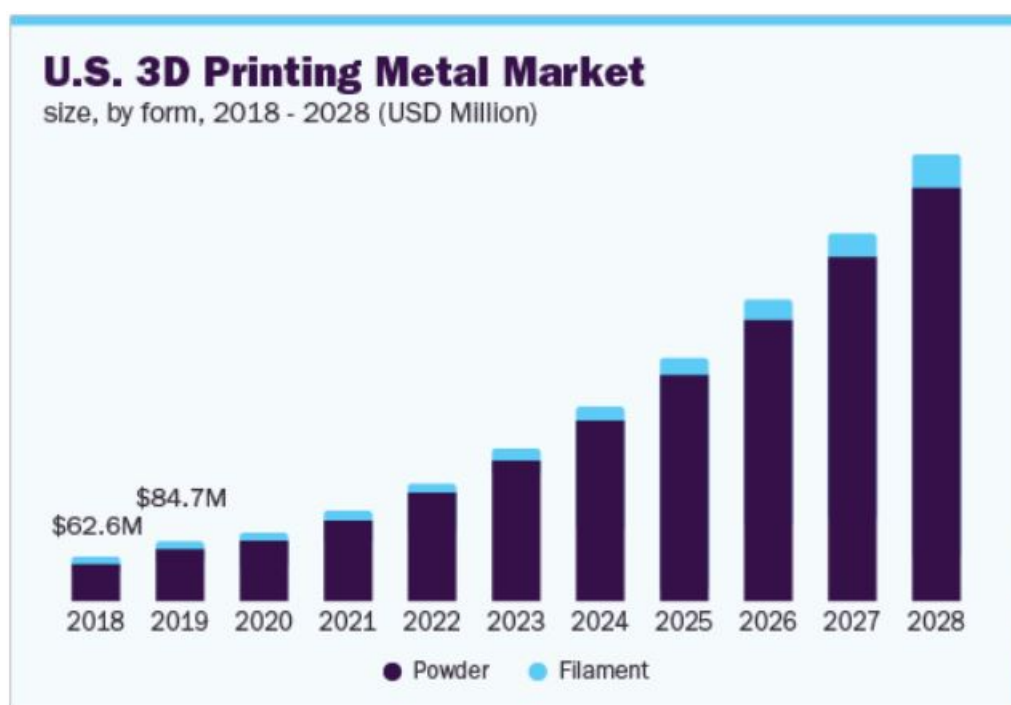
Figure 1: U.S. AM Metal Market (Grand View Research Inc [2021])

This chapter discusses additive manufacturing technology in general and focuses on laser engineered net-shape (LENS**TM**), electron beam additive manufacturing (EBAM[@]) and wire arc additive manufacturing (WAAM). Titanium alloys will be the main material, but other materials will be also analyzed. The discussion will also include specific applications on aircraft, naval and offshore components.

2 Titanium Alloys

Elemental titanium is hexagonal closed packaged structure (HCP) also known as α phase. $P6_{3/mmc}$ is the space group symmetry with number 194. As an allotropic metal, titanium transforms at 882°C to body-centered cubic structure (BCC) also known as β phase. $Im\bar{3}m$ is the space group symmetry with number 229 (Lütjering and Williams [2007]). Figure 2 shows those 2 crystal structures with lattice parameters and the most close-packed slip planes.

The α phase has a c/a ratio of 1.587 which is lower than the ideal of 1.633. It makes the prism slip planes more packed than the basal slip planes. The β phase to the right of Figure 2 shows a
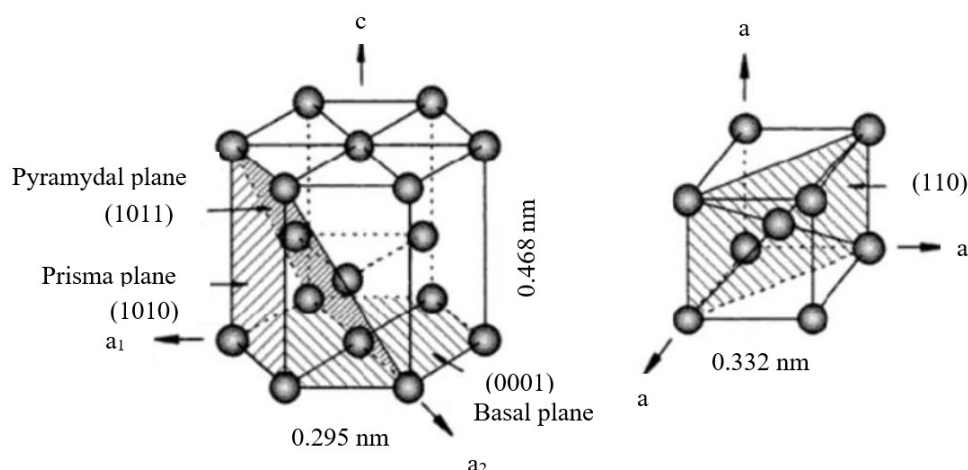
Figure 2: Crystal structure of phase (left) and β phase (right) (Londono [2019])

lattice parameter of 0.332 nm which is at 900°C (Lütjering and Williams [2007]). The Youngâ modulus in single crystals of α is from 100 Gpa with a stress axis perpendicular to the c-axis and 145 Gpa with a stress axis parallel to the c-axis. This fact shows the high elastic anisotropy of pure titanium at room temperature. The Youngâs modulus in single crystals of β phase can not be measured due to the instability of that phase at room temperature. The β phase can be stable at room temperature just by addition of alloying elements (Londono [2019])

2.1 Alloying elements

The purpose to add another element to titanium is to stabilize either α phase or β phase. This is achieved by changing the position of the α/β transformation temperature. Figure 3 shows schematic diagrams of the most common alloying elements of titanium. Al, O, N and C are α stabilizers. It means they rise the α/β transformation temperature. Al is the most common α stabilizer due to its high solubility. Oxygen content can affect the strength of titanium and it is used to define different grades of commercially pure (CP) titanium. Other elements as B and Ge can stabilize α phase, but their solubilities a lower and can form intermetallic compounds (Lütjering and Williams [2007]). The alloying elements that stabilize β phase can be isomorphous which means they are miscible at all compositions or eutectoid that basically means they are not miscible at all compositions and can form other phases. Examples of β isomorphous stabilizers are V and Mo. Vanadium being used in the most common Ti-alloy Ti-6Al-4V.

Fe, Cr and Si are common β eutectoid stabilizers. There are some other elements as Zr and Sn that are considered neutral. α titanium alloys are common in the chemical and processes industry where corrosion resistance and ductility are required. On the other hand β titanium alloys are largely utilized in biomedical applications due to their biocompatibility and low modulus (Chen et al. [2020]). However, it is important to mention that most of the commercial alloys are multicomponent. Ti-6Al-4V is the best example of a multicomponent alloy and it is known as the âworkhorseâ of the titanium industry with more than 50% of the total titanium usage of the world (Inc [2022]).

2.2 Alloy classification

Titanium alloys are classified based on the metallurgy. In other words, it is based on the final microstructure. There are alpha (α), near alpha, alpha + beta ($\alpha+\beta$) and beta (β) titanium alloys.
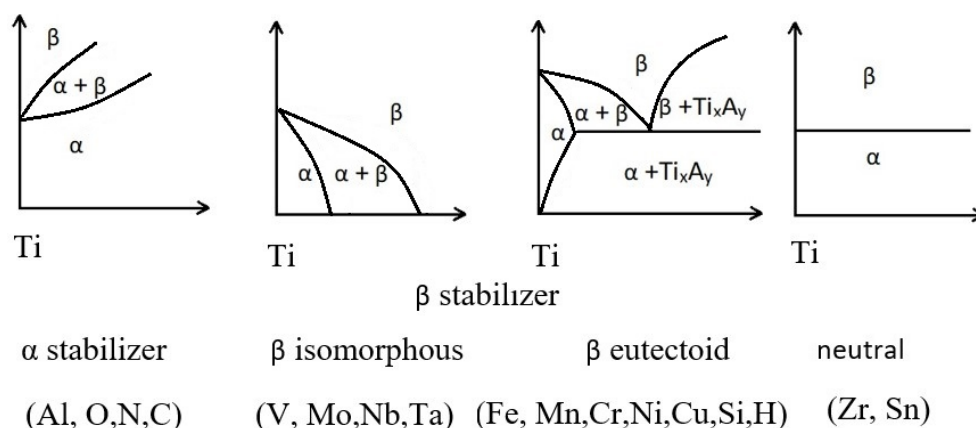
Figure 3: Schematic alloying elements effect on titanium (Lütjering and Williams [2007])

Each different microstructure offers different properties for different specific applications. Alpha and near alpha alloys have low and medium strength, which increases with the addition of interstitial elements or impurities such as Oxygen, Nitrogen or Carbon (Londono [2019]). The ASTM classify the commercially pure titanium alloys by CP Grade 'X'. Where the grade is a number that indicates the oxygen content 0.18 wt% to 0.4 wt% for grades from 1 to 4 (NeoNickel [2022]). Table 1 shows the classification of titanium alloys with some examples.

Table 1: Commercial titanium classification

Titanium Classification	Titanium Grades
Alapha (α)	CP Grades 1,2,3,4
Near - alapha (α)	Ti-5Al-2.5Sn, Ti-3Al-2.5V
Alapha + Beta ($\alpha+\beta$)	Ti-6Al-4V, IMI 685, IMI 834, Ti-811
Beta (β)	Beta 21S, Beta C, Ti-6246, Beta CEZ

The near-alpha alloys are mostly alpha, but with small amount of beta phase (2-5 vol.%) (Lütjering and Williams [2007]). These alloys are as alpha good for corrosion resistance applications, but the small amount of beta phase controls the recrystallization of α grains upon annealing. The $\alpha + \beta$ alloys have both phases, but β is present in a larger proportion than in the near α alloys. These alloys are heat treatable which means higher strength and hardness than α or near α alloys. However, creep strength and cold formability are not as good as for α alloys. These alloys are also classified by their microstructure into fully lamellar, equiaxed and bi-modal. The detailed description of those microstructures can be found in (Lütjering and Williams [2007]). Finally, β alloys are rich in β phase and are heat treatable to reach very high strength. However, fatigue strength and ductility in the heat-treated condition are low. Alloys such as Beta 21S and Beta C are mostly used in aerospace applications.

3   Additive Manufacturing

In general terms, additive manufacturing (AM) can be defined as a process where a heat source melts added material to a substrate. The heat source is in relative motion respect to the substrate to build the computer aid designed shape of the deposition. In Figure 4, common heat sources

are presented (e.g., laser, electron beam and plasma). Also, all feedstocks are showed (e.g., wire, powder bed and powder blown) Collins [2003].
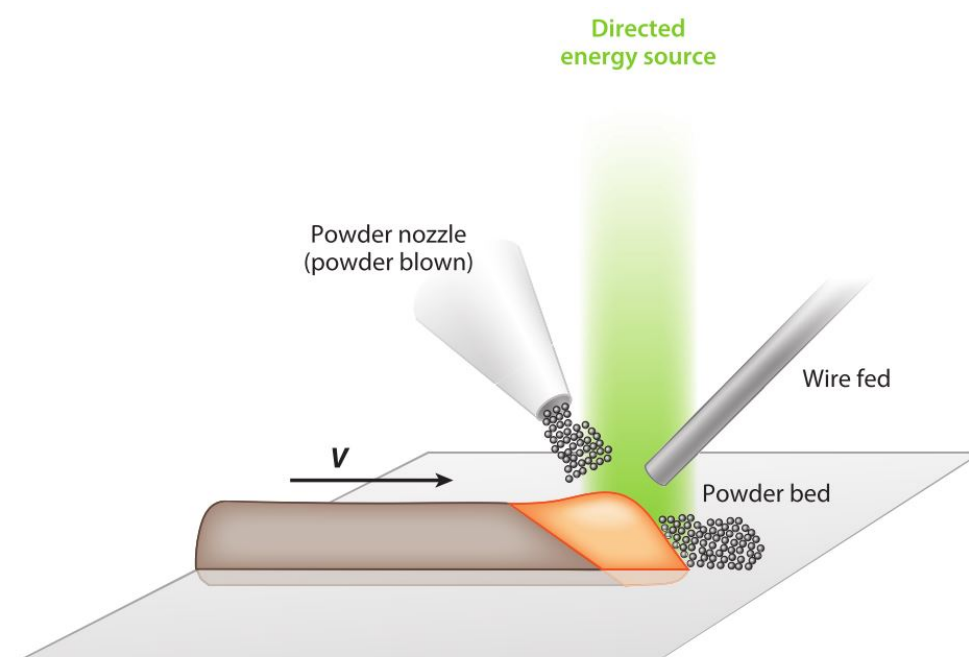
Figure 4: Schematic one pass of AM (Adapted from Collins [2003])

In addition, AM systems can be defined by the atmosphere where the process is occurring (e.g., inert gas, vacuum, and gas shield). AM technology has a strong influence on material properties due to the processing conditions such as heat source power, atmosphere, deposition speed among others. The microstructure is defined by heat transfer, fluid dynamics, phase transformations and the thermophysical properties of the material. Knowing the microstructure evolution in AM is very important to determine the properties of the material (Mendoza et al. [2019]). AM is a process that involves a condition that is far from thermodynamical equilibrium due to the rapid solidification. This factor leads to a lower solute partitioning compared with other manufacturing techniques (Collins et al. [2016]).There are several studies regarding the microstructure evolution of AM (Thijs et al. [2010] and Kriczky et al. [2015]). Some other studies have been focus on the molten pool modeling to predict the experimental microstructure evolution Peyre et al. [2008] and Rolchigo et al. [2017]). AM offers the research advantage of produce graded compositions within the same sample. This is achieved by using elemental powder blends in a system with multiple hoppers (Collins [2003] and Gong et al. [2017]).

The grain size in any microstructure is important for the resultant mechanical properties. There are many efforts to study the effect of alloying elements on grain size (Bermingham et al. [2008]). In 2001, a model was developed to predict the grain size refinement based on constitutional under-cooling and nucleant particles (Easton and St. John [2001]). Alloying elements such as boron (B) (Bermingham et al. [2008]) and beryllium (Be) (Bermingham et al. [2009]) acting as good grain refiners. All these efforts were focused on casting titanium alloys, but the fundamentals were extrapolated to additive manufacturing on titanium alloys for alloying elements such as molybdenum (Mo) (Mendoza et al. [2019]) and tungsten (W) (Mendoza et al. [2017]). More recent research revealed the grain refiner power of lanthanum oxide (La_2O_3) (Ng et al. [2022]) and an hydrogenation treatment on wire arc additive manufacturing (WAAM) (Xiaolong et al. [2022]).

Texture in additive manufacturing has been reported by many researchers in several alloys,

including Ti-alloys (Banerjee et al. [2006]). Build orientation can affect the mechanical properties as reported by Simonelli (Simonelli et al. [2014]). In addition, many researchers have demonstrated how the processing parameters of additive manufacturing such as energy density or travel speed determine the microstructure (Hrabe and Quinn [2013]). In the classical understanding of solidification in AM, a <001> growth direction has been reported to be parallel to the maximum gradient of temperature (Mendoza Londono [2016]). This preferential direction on solidification (i.e., texture) creates the intrinsic anisotropy of some additive manufactured Ti-alloys. However, the common columnar microstructure in AM can be modified to equiaxed by the addition of alloying elements (Collins et al. [2016]) or by further heat treatments (Qi et al. [2021]).

4   Laser Engineering Net-Shaping (LENS^TM)

In 1997, this technology was licensed by Optomec Inc. It was originally developed by Pratt Whitney and Sandia National Laboratories (Mudge and Wald [2007]). The heat source in this technique is a laser and the regulated flow of mass is controlled by a powder feed system. Argon gas atmosphere is used as protection and keeps oxygen content lower than 10 ppm in the glove box (Obielodan and Stucker [2012]). Several advantages of this technique include less machining required to the final component, it can repair or manufacture new components and different elements can be used at the same time (e.g., compositionally graded parts) (Mendoza Londono [2016]). Figure 5 shows the typical process lay-out.
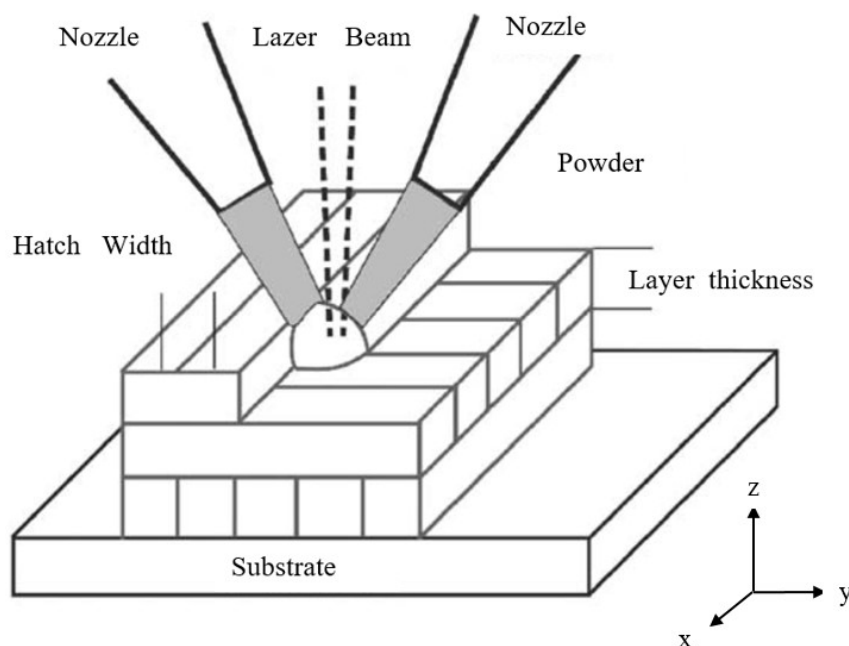
Figure 5: Schematic representation of LENS^TM process (Collins [2003])

In 2001 was reported the thermodynamic enthalpy of mixing as a key factor determining the compositional homogeneity and microstructure Schwendner et al. [2001]. Laser power and hatch width are LENS^TM parameters that can be modified independently to control the resultant microstructure of the deposited material. However, it was previously and conveniently demonstrated that all LENS^TM parameters are related to the total contribution of input energy. Therefore, travel speed, laser power, hatch width and layer thickness can be represented by a single term called

energy density Sears [2002]. This term can be used to understand the resultant mechanical properties of the deposited material. In fact, at certain level of energy density the deposited material or component will show equivalent mechanical properties to a conventionally forged material of the same composition Collins [2003]. As an example the critical energy density for IN 690 N2 is 165 Wh/in^3 Sears [2002]. Timetal 21S (also known Beta-21S) is a β type titanium alloy with composition Ti-15Mo-2.7Nb-3Al-0.2Si in Wt.%. 15Mo was replaced by 9.4Cr which is the equivalent amount required to stabilize β phase in the same proportion than the 15Mo. Cr was selected because its enthalpy of mixing (Δ Hmix) with titanium is -32 kJ/mol compared with -16 kJ/mol for Ti-Mo. This replacement of alloying element demonstrated that the total input energy (energy density) can be altered by the enthalpy of mixing. In this specific case the higher exothermic enthalpy of mixing of Ti-Cr reduced the critical energy density by $\sim$ 3kJ/in^3 Collins [2003].

4.1 Discontinuities in LENS$^{\text{TM}}$ deposits

Very acceptable processing parameters on LENS$^{\text{TM}}$ have been determined by trial-and-error approach. However, several work has been done to establish the relationship between the resultant microstructure of deposited material and the processing parameters Kobryn et al. [2000] This understanding is very important for the process control and design. Discontinuities include porosity, lack of fusion between layers and unmelted particles. Porosity is caused by entrapment of gas from either the powder feed system or from the powder particles. The porosity reported is nearly spherical in shape and did not have any preferential location Kobryn et al. [2000].In general terms, the porosity will decrease inasmuch the power increases and it is related with the fact that more power is more energy available to melt the same amount of powder. However, a reduction of porosity because of a higher travel speed is not as intuitive as for the power supply. The explanation reported Kobryn et al. [2000] for this behavior is the reduction of delivered powder due to the augmented travel speed.

The entrapped gas bubbles come from the powder system or the powder itself as mentioned before. However, a very high input energy on a small area of material can produce a keyhole Courtois et al. [2014]. This physics phenomena results in a very deep and narrow shape of the molten pool and that shape makes more difficult to gas bubbles to escape from the solidification front. High levels of input energy can also contribute to molten pool instabilities and create spheroidization of the liquid metal, also known as balling effect Gu et al. [2013]. This balling effect can induce more porosity Attar et al. [2014]. Figure 6 shows a pore in a SEM image (a) and a schematic molten pool with entrapped gas bubbles (b).

Lack of fusion between layers is due to not enough energy to melt the previously deposited layer or the substrate for the first layer. This can be caused by low energy density or an excessive powder feed rate Liu et al. [2021]. It is also known that the substrate acts as a heat sink and according to Kobryn et al. thin substrates dissipate heat faster than thick substrates. This condition leads to thin substrates to show more lack of fusion compared to thick substrates (Kobryn et al. [2000]).

As mentioned at the beginning of this section all processing parameters in LENS$^{\text{TM}}$ can be represented by the energy density term (Collins [2003]). This term is defined by Equation 1. Here ρ is the laser power, ν is the travel speed, $t_{thickness}$ is the layer thickness or spacing and $t_{thickness\ width}$ is the distance between passes (Mendoza et al. [2017]). The energy density is proportional with the grain width on the columnar morphology in LENS$^{\text{TM}}$ depositions. Higher energy density values will produce larger molten pools, which in turn implicates lower cooling rates (Mendoza et al. [2017]). Figure 7 shows this trend for the Ti-W system.

$$\rho_{energy} = \frac{p}{\nu \cdot t_{thickness} \cdot t_{thickness\ width}}. \tag{1}$$
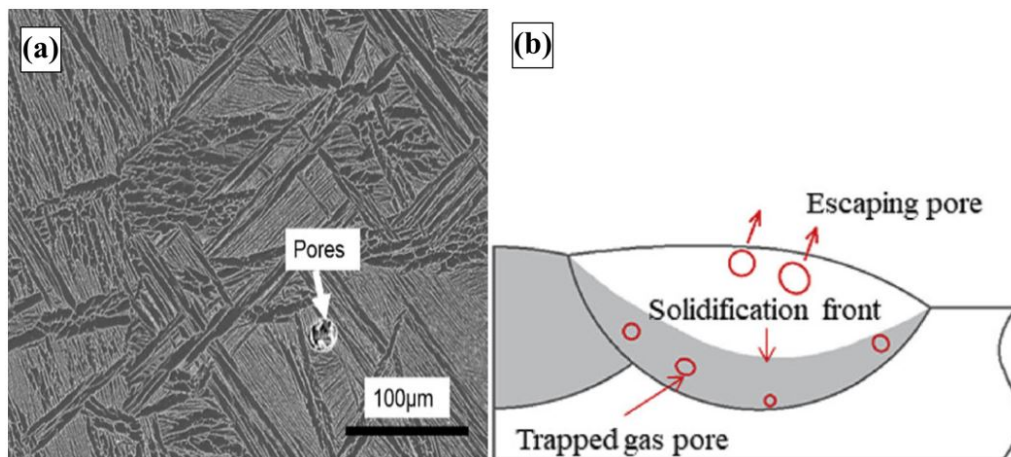
Figure 6: Pore in a Ti-alloy (a) and pores in molten pool (adapted from (Liu et al. [2021])
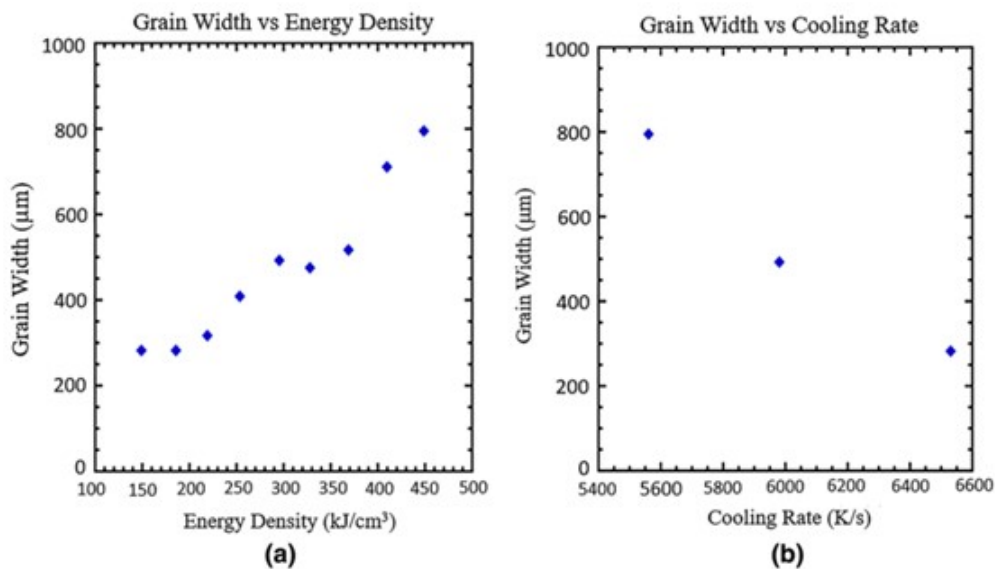
Figure 7: Grain width trend with energy density (a) and cooling rate (b) (Mendoza et al. [2017])

The energy density is a critical manufacturing factor for the homogeneity and resultant properties of any AM deposition. There are other examples on how the energy density can determine not just the grain size, but also the porosity, lack of fusion and in some cases unmelted particles. Backscatter electron micrographs in Figure 8 show large field view of the xz plane of two different energy densities (high and low) depositions made using LENS$^{\text{TM}}$ technology for a fixed composition of Ti-15Mo Mendoza et al. [2019]. By these two images, the sample with energy density of 7.4 MJ/in^3 (8b) shows less unmelted particles, less lack of fusion and a very high compositional homogeneity. On the other side, the sample with energy density of 2.4 MJ/in^3 (8a) shows a lack of fusion in almost all layers and in some cases as large as 500 μm. The unmelted particles of Mo are easy to visualize in the backscatter electron micrographs because the average atomic mass determines the contrast on those images. Therefore, the brighter regions are Mo rich zones and darker gray regions are rich in titanium.
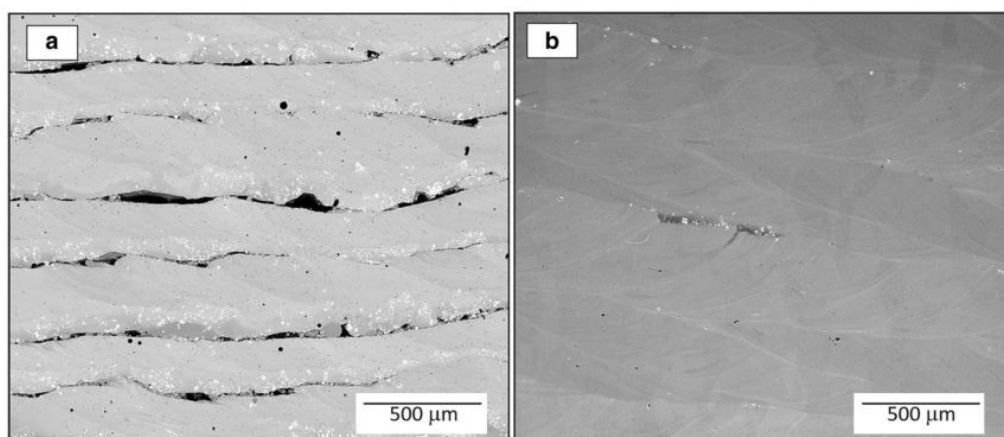
Figure 8: Micrographs of Ti-15Mo at 2.4 MJ/in^3 (a) and 7.4 MJ/in^3 (b) (Mendoza et al. [2019])

4.2   Residual stress

Dwell times between individual layer deposition is very common technique in additive manufacturing to allow additional colling time. The accumulation of residual stress in AM has several similarities with the welding process since both are a layer-by-layer deposition. In 1997, it was reported that reducing input energy leads to a lower workpiece distortion in welding Michaleris and DeBiccari [1997]. Later in 2003, it was reported that pre-heating the weld region can reduce the net distortion Deo and Michaleris [2003]. In a similar manner for additive manufacturing, pre-heating the bulk substrate can lead to a reduction of the residual stress and total distortion on the deposited material Jendrzejewski et al. [2004]. Additive manufacturing involves the deposition of multiple layers to build a component in larger dimensions compared to welding or laser cladding. Therefore, dwell times and path planning are important factors to determine the resultant residual stress and workpiece distortion. Decreasing dwell time between passes reduces the residual stress in deposited Co-based Stellite SF6 alloy Jendrzejewski and Śliwiński [2007]. Different position paths affect the residual stress and distortion in AISI 1117 C- Mn steel Nickel et al. [2001] and in AISI 316 austenitic stainless steel Mercelis and Kruth [2006].

In a more recent work in additive manufacturing, the dwell time and material selection were studied Denlinger et al. [2015]. In-situ measurements of temperature and distortion were performed in Ti-6Al-4V, and Ni-Cr-Mo solid solution strengthened Inconel[@]625. This research work also compared one alloy with a solid-state allotropic transformation (Ti-6Al-4V) and another one that does not (Inconel[@]625). Three different dwell times were used with the same input energy for both alloy systems Denlinger et al. [2015]. This study showed that increasing the dwell time to allow additional cooling time resulted in a reduction of residual stress in Inconel[@]625. However, for the Ti-6Al-4V alloy, increasing the dwell time resulted in an augmented level of residual stress. Figure 9 shows the above-mentioned trend.

There are two main mechanism for the residual stress accumulation in additive manufacturing. The first mechanism is thermal stress due to the strong gradient of temperature between subsequent layers of deposition. These temperature gradients generate residual stress in the vertical direction predominantly. The second mechanism is the phase transformation due to solidification, and it has a preferential residual stress generation in the horizontal direction. In addition, additive manufactured Ti-6Al-4V at certain critical energy density value suffers a solid phase transformation. This transformation from β phase to a martensitic α' phase also induce residual stress on the deposited material Yakout et al. [2020].
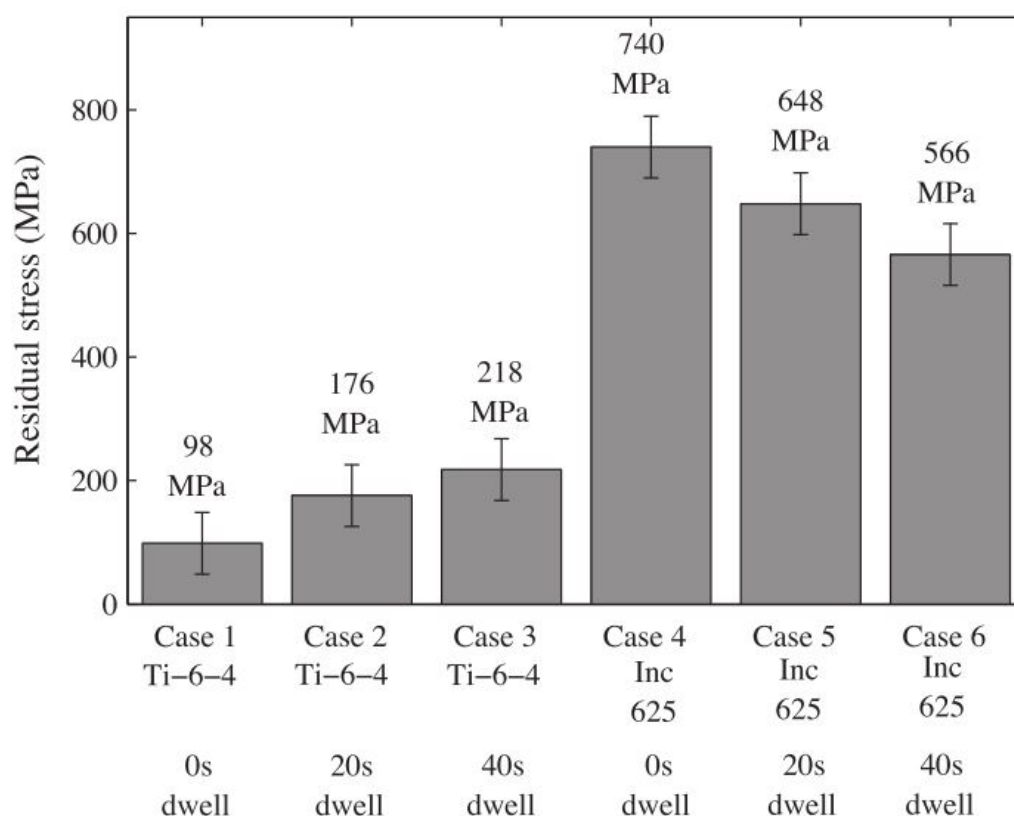
Figure 9: Variation of residual stress with dwell time for 6 cases (Denlinger et al. [2015])

In 2021, researchers worked on a study where the laser power and travel speed were fixed to evaluate the influence of laser scan strategies on residual stress. Four different strategies were used with 2 continues over the sample and the other 2 using small islands with alternating patterns Strantza et al. [2021]. They found very large residual stresses on the order of $1/2$ to $3/4$ of yield strength of additive manufactured Ti-6Al-4V with a concept laser equipment. The non-continuous or island strategies resulted in more residual stress specially at the extreme edges of the deposited material. On the other hand, a reduction of the residual stress was observed in the continuous scan strategy with a rotation of $90°$C per layer. They suggest Strantza et al. [2021] that scan strategies allowing faster cooling rates are responsible for higher residual stress on deposited material. In addition, in the island strategy, those near to the edges show even faster colling rates producing even more residual stress.

4.3 Grain size, morphology, and texture

In additive manufacturing in general, the heat source melts the incoming material. For the LENS[TM] specific case, the laser melts the powder metal creating a molten pool on a substrate. This molten pool experiences a very rapid colling of 104-106 K/s Strantza et al. [2021]. This unique condition leads to a unidirectional solidification of columnar grains (prior β grains for Ti-alloys). The substrate is acting as a strong heat sink promoting the vertical growth. Therefore, the columnar grains are a result of epitaxial growth from the bottom of the molten pool in direct contact with the substrate. Several examples of columnar grains are Ti-Mo system Mendoza et al. [2019] Ti-6Al-4V system Kelly and Kampe [2004] and Ti-Cr system Zhang et al. [2010]. Figure 10 shows an optical

micrograph of a columnar morphology of a LENS$^{\textbf{TM}}$ Ti-W sample.

Figure 10: Optical micrograph of Ti-6W alloy.

Equiaxed grains are also observed in AM deposited material. Normally, they develop at the top region of deposition. This phenomena occurs because the substrate acting as a heat sink at the bottom is less effective at the top. Unmelted particles at the top surface and the lower temperature gradient induce nucleation of new grains (Liu et al. [2021]). The columnar to equiaxed transition (CET) can also be achieved by a β annealing treatment after deposition (Zhu et al. [2015]) or adding alloying elements among others (S.Tamirisakandala et al. [2005]).

Regarding adding alloying elements to transform the morphology from columnar to equiaxed and reduce the grain size, there are many research publications about the topic. Many of them are focus on cast alloys and not in additive manufacturing. However, the factors affecting the grain size such as inoculants, cooling rates and compositional effects can be considered in AM. Recent work on grain refinement was considering the effect of the growth restriction factor as a thermodynamic parameter defining grain size. Equation 2 defines the growth restriction factor Q, where m is the slope of the liquidus line, c_0 is the solute concentration and k is the partition coefficient.

$$Q = mc_0(k-1) = \frac{d\Delta T_c}{df_s}. \tag{2}$$

The differential term to the right is expressing the concept of the growth restriction factor as the rate of development of constitutional supercooling (ΔT_c) relative to the rate of solid development (f_s). Boron (B) acting as a grain refiner was reported on Ti-6Al-4V and Ti-6242 (S.Tamirisakandala et al. [2005]). Similar studies applying the growth restriction factor of boron reported same results on as-cast commercially pure titanium (Bermingham et al. [2008]). The refiner power of boron was also noted in the review paper by Collins et al. analyzing the boron modified TNZT alloy (Collins et al. [2016]). The explanation for this phenomena is that boron

solute is rejected in front of the solid-liquid interface. That boron rich region is undercooled and restricts the growth of any preexistent nuclei and promotes the activation of new nuclei.

Based on solute contributions and nuclei effects on grain size Easton & St. John developed a semi-empirical relationship to assess the grain refinement on Al and Mg alloys (Easton and St. John [2001]). The general relationship is expressed in Equation 3:

$$d = a + \frac{b}{Q}, \tag{3}$$

where d is grain diameter, a is the y-intercept defined in Equation 4, b is the slope defined in Equation 4 and Q is the already defined growth restriction factor:

$$a = \frac{1}{(\rho \cdot f)^{1/3}} \tag{4}$$

$$b = b_1 + \Delta T_n, \tag{5}$$

in Equation 4, ρ is the density of nucleant particles and f is the activated fraction of particles. This equation shows that a is inversely proportional to the maximum number of activated nuclei. For Equation 5, the term ΔT_n is the necessary undercooling to activate nucleation and b_1 is a constant. Therefore, the slope b basically represents the undercooling necessary to activate nucleation, higher values of b lead to lower potency of nuclei. Easton & St. John demonstrated the applicability of this concepts (equation) on Al and Mg alloys. However, ulterior studies (Banerjee et al. [2006]) demonstrated the extended applicability of the same concepts on Ti-alloys. All this work was based on as-cast Ti-alloys. Only in 2017, Mendoza et al. reported that despite the out of thermodynamical equilibrium condition of AM, it is possible to predict in some degree the grain refiner power of alloying elements by utilizing these concepts on additive manufacturing and more specifically of LENS$^{\text{TM}}$ technology on titanium alloys (Mendoza et al. [2017]). Figure 11 shows three backscatter micrographs of average compositions of 5, 13 and 25 pct on the Ti-W system. The features in all micrographs are very similar with prior β grains with alpha laths inside the grains. However, the grain size was clearly reduced by the tungsten (W) additions (Mendoza et al. [2017]).
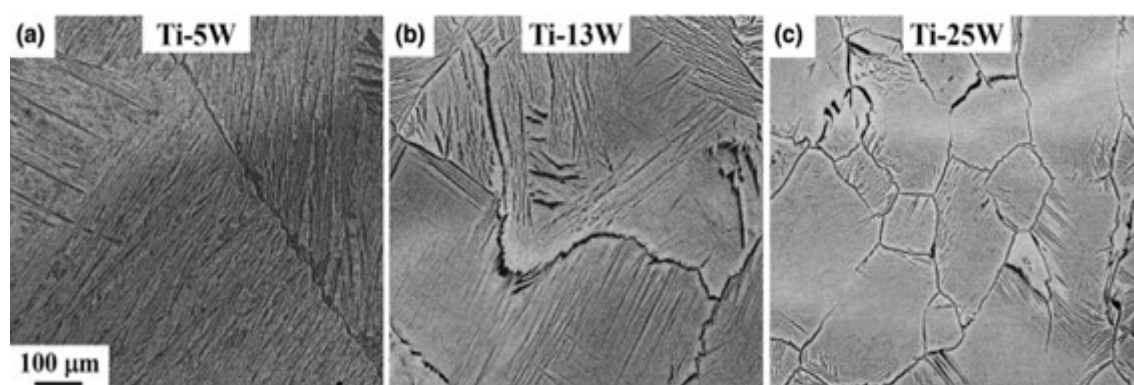
Figure 11: Backscatter micrographs of Ti-W system (Mendoza et al. [2017])

These results summarize the grain refiner power of tungsten as an alloying element with a high growth restriction factor of about 22.6 C_0. Later in 2019, same authors applied the same concept in AM with an alloying element with a very low growth restriction factor of 6.5C_0 (molybdenum). Figure 12 shows backscatter micrographs of a compositional gradient sample deposited with LENS$^{\text{TM}}$ at locations of 0.9, 2.8 and 8.2 wt.% of Molybdenum (Mo). In this case, the prior

β grain size of the titanium alloy was not reduced by the Mo additions and the morphology was in fact columnar over the entire sample. These two higher (Ti-W) and lower (uTi-Mo) bound scenarios of grain refiners based on growth restriction factor sggest the applicability of the thermodynamical concepts on additive manufacturing.
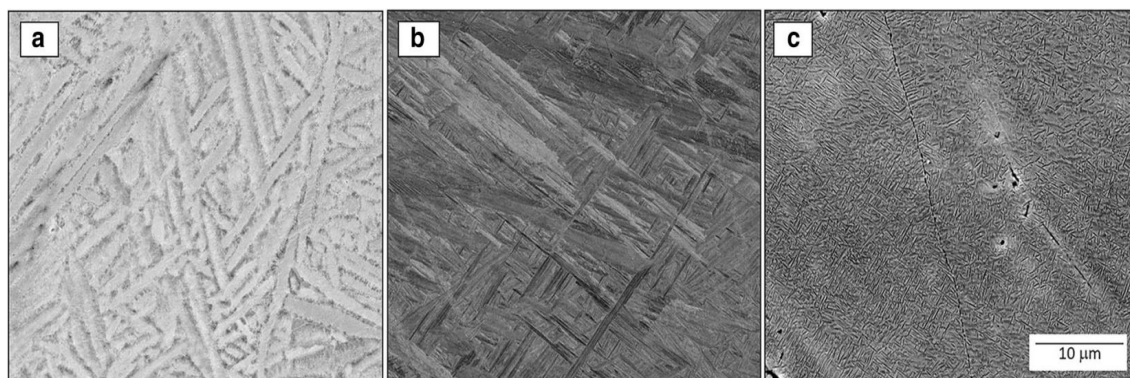
Figure 12: Backscatter micrographs of Ti-Mo System (Mendoza et al. [2019])

Tedman et al. worked with powder additions of W, Mo and Nb to assess their efficacy as nucleant particles in titanium alloys. The samples were deposited using wire arc additive manufacturing (WAAM), a technology that will be described in a further section in this chapter. They found that particles surviving the melting process are acting as potent nucleation points for β crystals. The alloying elements acting as inoculants suffer partial dissolution and enrich the surrounding liquid. That solute enrichment raised the equilibrium liquidus temperature and lead to preferential crystal growth or solidification upon the surface once the cooling process starts (Tedman-Jones et al. [2019]). They call that process as âdissolutional supercoolingâ which basically applies the same concept of constitutional undercooling at the solidification front analyzed previously in the Ti-W system (Mendoza et al. [2019]). They call that process as âdissolutional supercoolingâ which basically applies the same concept of constitutional undercooling at the solidification front analyzed previously in the Ti-W system (Mendoza et al. [2019]). Other efforts were focus on evaluating grain size and morphology for three different Ti-alloy systems. The idea was to compare non-growth restricting solutes or nucleant particles in a Ti-6Al-4V alloy, containing growth restricting solutes, but non-nucleant particles in a Ti-3Al-8V-6Cr-4Mo-4Zr alloy and the last system was containing all the previous growth restricting solutes and including nucleant particles in a Ti-3Al-8V-6Cr-4Mo-4Zr + La_2O_3. The results on first system were large grain size and a combination of columnar and equiaxed grain morphology. The second system refined the grain size by 55% but did not show a significant columnar to equiaxed transition (CET). However, the last system with the La_2O_3 additions (nucleant particles) refined the grain size over 85% and produced a clear zone of equiaxed grains at the top of each layer (Bermingham et al. [2019]).

In 2022, efforts to improve the understanding of solute and nucleant particles were focus on aluminum alloys, but using alloying elements as Si, Cu and Ni (Tan et al. [2022]). They concluded that despite the rapid solidification in AM, a high enough solute concentration is still necessary to create the constitutional undercooling which in turn induce heterogenous nucleation (grain refinement). In addition, it was demonstrated that additions of strong nucleant particles as lanthanum hexaboride (LaB6) (Tan et al. [2022]) and high melting point yttria (Y_2O_3) particles (Wang et al. [2021]) highly increases th$_2$e grain refinement in their AM depositions.

Regarding texture, there is a large number of researchers reporting the <001> texture which is concordant with the greatest temperature gradient in the vertical direction (z axis). Ni based alloy IN738LC made by selective laser melting shows the characteristic <001> texture (Kunze et al.

[2015]). It is also the case for Ti-alloys (Qiu et al. [2015]). However, additions of Zn, Mg and Ti in cubic systems as Al-alloys can deviate the <001> texture to be <110> (Collins et al. [2016]). In a more recent approach for an additive manufactured Ti-6Al-4V study, it was demonstrated that the scanning strategy can modify texture and microstructure (Quintana et al. [2020]). This phenomena could be related to different thermal cycles allowing different cooling rates affecting solidification and texture.

5 Electron Beam Additive Manufacturing (EBAM$^{@}$)

Electron beam additive manufacturing technique is a metal 3D printing process launched by Sciaky Inc. in 2009. The system uses an electron beam as the heat source and a wire is fed into the electron beam to create the molten pool in a vacuum chamber. The vacuum chamber is a requirement for the electron beam and also provides a non-reactive environment for the deposition of high purity materials (Mendoza Londono [2016]). In general, wire feed systems as EBAM$^{@}$ are suitable for large-scale volumes due to its high deposition rates (Frazier [2014]). This technique can produce high quality structures, up to 19 inches length, made of Titanium, Nickel-based alloys, and tantalum among others in days (Inc [2022]). The original purpose to develop EBAM$^{@}$ was for aerospace applications. However, it is now beneficial for a wide range of industries and applications where reducing cost and time is top priority. Some examples of EBAM$^{@}$ applications are Oil & gas equipment, turbine blades for energy production, medical equipment, industrial pump components and marine propulsion. Figure 13 shows a schematic view of the EBAM$^{@}$ technology. A unique advantage of EBAM$^{@}$ is the dual wire feed system that allows to combine two different metals or alloys to create a specific custom alloy. In addition, it is also possible to change the mixture ratio of the wire feed to create a graded part as in LENS^{TM}. After the part is completed, a heat treatment, machining and final inspection is performed. (Inc [2022]).
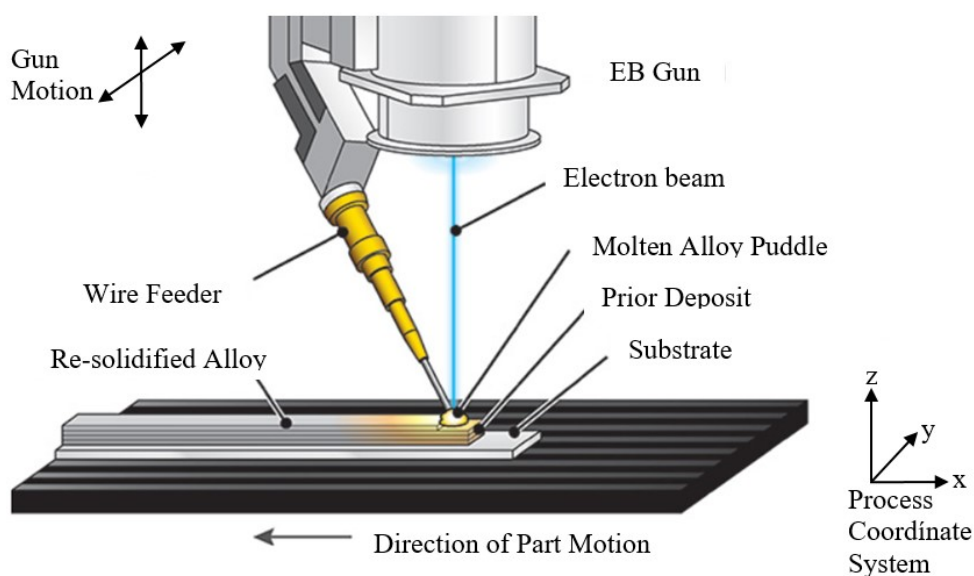
Figure 13: Schematic view of the EBAM$^{@}$ technology (Inc [2022])

Discontinuities in EBAM$^{@}$ are similar as in LENS^{TM} including porosity and lack of fusion between layers. However, porosity is less, and unmelted particles are not present because EBAM$^{@}$ does not operate with powder. Wire systems have higher deposition rates which represents deposition of larger objects that are ideal for large mechanical systems as air frame structures or aircraft

engines. It can be equipped with multiple nozzles with different metals in a single electron beam gun to create custom alloys.

Regarding the residual stress in electron beam additive manufacturing, it is governed by temperature gradients and phase transformations during solidification as described in section 4.2. In EBAM$^@$, the deposition rate is higher compared with LENS^{TM} which leads to lower dwell time. The direct implication of less time between layers was described as material dependent as illustrated in Figure 9 comparing Ti-6Al-4V with Inconel$^@$625 in section 4.2. Grain size, morphology and texture is equivalent to the described in section 4.3 for LENS^{TM}, but due to the larger scale volume and speed of deposited material, it needs to consider different thermal cycles. Hayes et al. shows a good example of microstructure features under EBAM$^@$ (Hayes et al. [2017]).

In general, both technologies are applying the same principles with small differences that can affect the resultant properties of the deposited material. It is important to mention that on average, AM-Grade Ti-6Al-4V powder is 141% more expensive than the AM-Grade Ti-6Al-4V wire. The use of metallic powder also represents a higher safety concern because breathing in fine particles, such as titanium or nickel, can be harmful (Inc [2022]).

6   Wire Arc Additive Manufacturing (WAAM) and Marine Applications

As described in section 1, titanium and its alloys are used due to their excellent corrosion resistance in aerospace, chemical and power plants among other industries, but it is generally used little to build ships. In 2002, Nippon Steel corporation completed all-titanium ships in cooperation with shipbuilders (Kimura et al. [2002]). The critical question is how additive manufacturing and specifically titanium alloys can contribute to marine or naval applications. The industrial marine environment is dominated by complex and ever larger components when compared with other industries (e.g., aerospace industry). It is also a harsh and corrosive environment for systems such as offshore platforms and various ship classes (Strickland [2016]). Wire arc additive manufacturing (WAAM) is another AM technique with additional capabilities to manufacture large-scale components. WAAM has a much higher deposition rate than other AM techniques (e.g., LENS^{TM} and EBAM$^@$) making it suitable for marine applications (Wang et al. [2012]). In this section, wire arc additive manufacturing technique is described with an emphasize in marine applications.

6.1   Wire arc additive manufacturing

This is a metallic 3D printing machine, where metallic wires are the feeding material, and the heat source is an electric arc. The protective environment depends on the type of arc welding. The original idea of WAAM was in 1925 with a simple arc welding to deposit ornaments (Ralph [1925]). After about one century of development, WAAM becomes suitable for new applications. In this process a wire is fed into an electric arc and melted with the substrate or the previous deposited layer. The efficiency of the material is near to the 100% because there is not powder handling and not unmelted particles. The cost associated with WAAM is around one order of magnitude less when compared with laser-based powder processes. Discontinuities in WAAM are basically the same as those in EBAM$^@$), considering that both techniques are using a wire feedstock. The high deposition rate of WAAM allows the manufacture of very large-scale components. However, some drawbacks such as low density due to violent melt pool interaction, poor surface quality and less dimensional accuracy (Rosli et al. [2019]). Figure 14 shows a WAAM system integrated with a MIG/MAG at the welding institute (TWI). In addition, due to the size and speed of depositions the dwell time is less between layers, and it has been reported with different effects on residual stress depending on material (section 4.2). However, due to the large heat source, a high tensile residual stress might be induced (Lin et al. [2021]). The WAAM systems can be divided into three main

systems and a fourth one designed for titanium alloys. In general, they are based in traditional welding methods such as gas metal arc welding (GMAW), gas tungsten arc welding (GTAW) and plasma arc welding (PAW). Robotic welding systems are the based to integrate these three simple configurations (Lin et al. [2021]). The selection of material and welding technology are driven by the user application. For instance, if quality and process stability are a priority, GTAW should be preferred over GMAW. On the other hand, GMAW is preferred if the priority is high deposition rate (Cunningham et al. [2018]). However, the PAW system offers good quality and high deposition rate, but with higher initial cost. Several metals and alloys have been used for WAAM process such as steels, stainless steel, nickel-based alloys, aluminum alloys and titanium alloys. The last alloys system has superior properties (Lin et al. [2021]) and is the focus of attention for metals in additive manufacturing in different industries such as aerospace, military and weapons, marine and shipbuilding. However due to the high cost of titanium, the applicability is limited in several industries.

6.1.1   GMAW based WAAM system

Gas metal arc welding is a welding process where an electric arc is created between the substrate (workpiece metal) and the electrode (consumable wire). The wire is fed continuously and melted in a molten pool protected by a shielding gas (e.g., argon helium etc.). The Figure 15 shows the configuration of the GMAW-WAAM integrated system. The current and voltage are the key parameters to control the GMAW-WAAM system because it controls the input energy. Due to the nature of the heat source high thermal inputs are received by the wire and substrate. This leads to unwanted deformations resulting in dimensional tolerances of ± 1 mm (Prado-Cerqueira et al. [2017]). In order to remove the non-suitable surface finish, the company FRONIUS GmbH patented the cold metal transfer technique (CMT) (Office) [2022]). In CMT, the current intensity and voltage are controlled to transfer metal to the molten pool and retracting the electrode at very short intervals to produce a clean, splatter-free deposition. The process integrates the movement and deposition of material in four phases described in detail by (Prado-Cerqueira et al. [2017]).

6.1.2   GTAW based WAAM system

Gas tungsten arc welding is a process where a non-consumable tungsten electrode provides the heat, and an independent wire is fed to produce the deposited material in the molten pool. In this technique the wire feed orientation has a strong influence on the transfer material and quality of the deposit. Front, back and side feeding are normally used, but front feeding is the regular orientation for Ti-alloys and Fe-Alloys (Shen et al. [2016]). Figure 16 shows the configuration of GTAW-WAAM system. This configuration has a gas lens to guarantee the shielding gas is in laminar flow to reduce oxidation. It is very important for titanium alloys due to the high reactivity with oxygen at high temperatures. Normally, a tracing shielding device is used to protect titanium alloys and that will be discussed in a subsequent section (Pan et al. [2018]).

GTAW-WAAM has the capability to manufacture compositionally graded materials as with (LENS[TM]) or (EBAM[@]) technologies (Shen et al. [2016]). For this objective, two different wire-feed systems can provide different metals or alloys to the molten pool. The deposited material composition can be controlled by adjusting the wire-feed rate independently just as in blown powder systems. Preheating the substrate and placing suitable tracing shielding help to control the interlayer temperature and reduce oxidation, especially critical for titanium alloys (Pan et al. [2018]).

Figure 14: WAAM system used at TMI (Office) [2022])

6.1.3   PAW based WAAM system

Plasma arc welding is a process where a plasma is used to transfer an electric arc to a work piece or parent material. Then the metal to be welded is melted by the intense heat generated by the electric arc. Plasma is defined as a gas that was heated to a very high temperature and ionized to make it electrically conductive (Mannion and Heinzman [1999]). The torch in PAW has a tungsten electrode with a copper nozzle for the plasma. They create a pilot arc that is transferred to the metal to be welded. The arc energy in plasma welding can reach three times the GTAW (Pan et al. [2018]).

   Plasma gases are usually argon, and the torch system has also a secondary gas source that can be helium, hydrogen, and argon to play the shielding role. The distance from workpiece to the
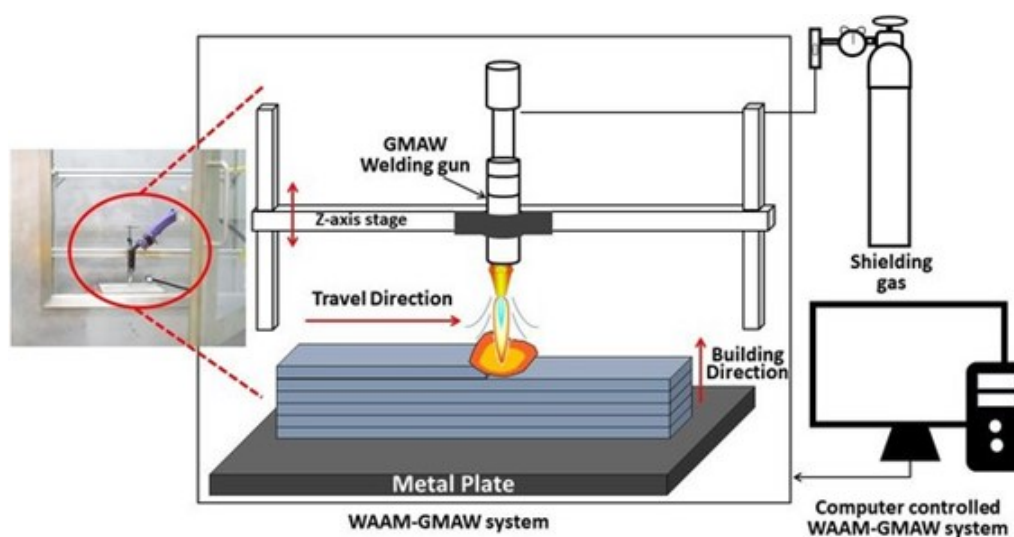
Figure 15: Schematic GMAW-WAAM integrated system (Rosli et al. [2019])
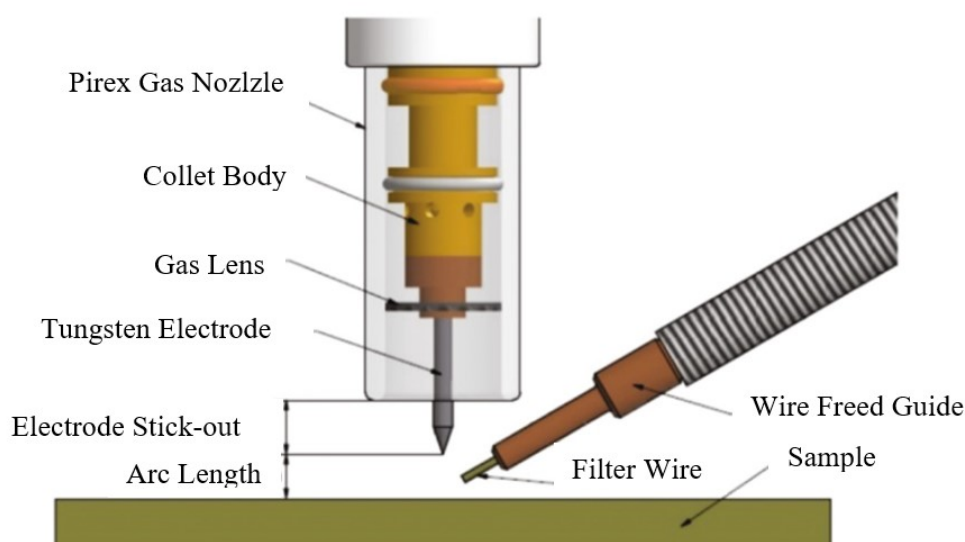
Figure 16: Schematic GTAW-WAAM integrated system (Pan et al. [2018])

tungsten electrode tip (stand-off distance) is not as critical as in GTAW due to the cylindrical and focus arc shape of PAW (Mannion and Heinzman [1999]). Therefore, the arc transfer is gentle and consistent to produce high quality deposits of material. The stability of the electric arc reduces the arc wander effect which is a deflection of the arc that can lead to lack of fusion imperfections (Mannion and Heinzman [1999]). The Table 2 shows a basic comparison of these three WAAM systems.

6.2 WAAM systems to manufacture titanium-alloy components

As mentioned in section 6.1.2 Titanium and its alloys are very reactive with oxygen at elevated temperatures. Several researchers reported severe oxidation on WAAM Ti-based components (Bermingham et al. [2018]). That reactivity produces oxides that embrittle the deposited mate-

Table 2: Comparison of WAAM systems (Lin et al. [2021])

WAAM systems	Deposition rate (kg/h)	Stability	Cost	Heat input	Thermal efficiency
GMAW-based	3-4	Splash	Low	High	84%
GTAW-based	1-2	Good	Low	Low	67%
PAW-based	2-4	Good	High	High	47%

rial, making the WAAM system not very suitable for Titanium alloys. To prevent oxidation on titanium some researchers have been used a closed chamber filled with inner gas (Alonso et al. [2019]). However, the chamber adds several limitations to the manufacturing process. First, the chamber restricts the size of the components to be smaller than the chamber itself. The robot arm movement is also restricted which affects the direction and rate of deposition. Therefore, the use of chambers to manufacture titanium alloys is not very practical for large-scale or ultra-large-scale parts as required for the naval industry (Lin et al. [2021]).

To eliminate the closed chamber requirement several efforts, propose the use of tracing shielding devices (Lin et al. [2021]). This device is usually fixed to the torch and provides a focalized distribution of inert gas to cover only the latest deposited region to prevent the oxidation. Figure 17 shows trace shielding designs for the basic WAAM systems. The tracing shielding device has been a custom-made feature added only to fit specifical needs in a particular application.
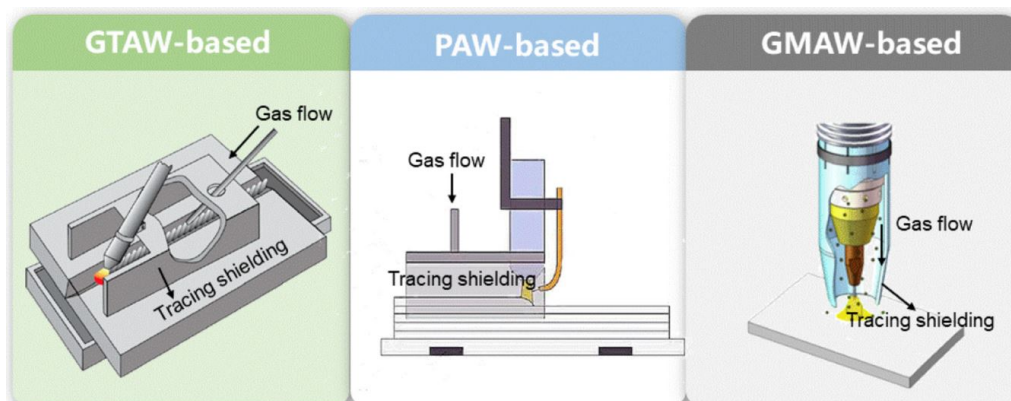
Figure 17: Tracing shielding design for WAAM (Lin et al. [2021])

The grains size as described in section 4.3 with (LENS^{TM}) deposits is governed by epitaxial growth which is inherent to any AM technique. In this case, several hybrid WAAM systems have been designed to promote grain refinement on titanium alloy deposits (Lin et al. [2021]). Martina et al. proposed one of those hybrid-WAAM systems with a preheating of deposited layer during the deposition of the next layer. This modification resulted in a good refinement of the prior β grains and a columnar to equiaxed transition (CET). This custom-adapted process is named inter-pass rolling (IRWAAM) (Martina et al. [2015]).

6.3   Naval and Offshore applications

Titanium is considered an optimal material for the excellent corrosion resistance in sea water. However, due to cost and other manufacturing considerations it is not widely used in the naval and offshore industry. During more than 50 years offshore steel structures were designed with corrosion allowance and not considering for a real corrosion protection (Kimura et al. [2002]). In 1997, the only corrosion allowance idea is abandoned and new methods to offer certain degree of corrosion protection are proposed. The titanium-clad steel covering on the piers (splash and tidal

zones) of the Trans-Tokyo Bay (TTB) (i.e., Aqua-Line) was one of the first corrosion protection methods implemented on offshore infrastructure (Kimura et al. [2002]). Covering existing steel pipe piles with 0.5 mm thick titanium sheet has been a work performed for many years at Nippon Steel Nagoya works. Shipyards in Japan use titanium to manufacture several parts such as exhaust cooling pipes, mufflers, fire-fighting sea water guide pipes and valves, ladders, shafts and propellers due to corrosion resistance or weight reduction (Kimura et al. [2002]).

The naval industry is characterized by a very specific operating conditions of equipment and machinery. For instance, ships have unique operational requirements of reliability and safety. The original equipment manufacturer or local authorities imposed quantity and type of spare parts to be on board (Kostidi and Nikitakos [2018]) for safety reasons. Spare parts inventory is necessary to avoid or reduce breakdowns or ship downtime. If a damage in the ship appears, the spare part needs to be used to continue normal operation. However, if the spare part is not in stock, a request needs to be sent to the land office. From this perspective additive manufacturing could be used on board to manufacture spare parts on demand, reducing the spare part inventory and consequently the cost.

In 2015, the container shipping company MAERSK reported the installation of 3D printers (AM) on board to fabricate spare parts (Kostidi and Nikitakos [2018]). In addition, the US navy has implemented the installation of 3D printers (AM) for afloat manufacturing of spare parts (Strickland [2016]). The benefits from this approach can improve operational efficiency in areas of spare parts and tooling. However, there are some technical concerns regarding the static environment that those AM techniques require for quality of deposited or printed material (Strickland [2016], Kostidi et al. [2021]).

Queguineur et al. made an evaluation of wire arc additive manufacturing (WAAM) on large-scale components for naval applications (Queguineur et al. [2018]). Their objective was to study the processing parameters optimization associated with the mechanical properties of stainless steel (AISI 316L) and copper-aluminum alloy (Cu-8Al-2Ni-2Fe) with a GMAW-WAAM system. They demonstrated that GMAW-WAAM technology is an alternative to cast products for the naval industry in terms of mechanical and corrosion results for the AISI 316L. The Cu-Al alloys showed a slight decrease in mechanical behavior compared with as cast products (Queguineur et al. [2018]). However, this result only represents that further research needs to be addressed to better implement AM technology in naval applications.

The current use of additive manufacturing or 3D printing in the naval industry, is limited to auxiliary components for ships. Those components or spare parts are engines, heat exchangers, valves, pumps and propellers (BAYRAMOÄLU et al. [2019]). In Netherlands, the association of RAMLAB, Promarin, Autodesk, Bureau Veritas and Damen shipyard manufactured the worldâs first-class 3D-printed ship propeller, named as WAAMpeller. Figure 18 shows the successful implemented WAAMpeller by RAMLAB. The WAAMpeller has a diameter of 1.3 m, weight of 180 kg and was manufactured to drive a Stan Tug 1606 (Ziółkowski and Dyl [2020]. The whole manufacturing process was supervised and certified by Bureau Veritas. The used material was an aluminum, nickel, and bronze alloy.

A recent effort on AM propeller was reported to use a numerical approach to design a hollow blade that was also fabricated to correlate the optimization process (Muller et al. [2019][2019]). The process of producing a hollow blade is very difficult to conventional foundry process and offers the option to control thickness in different sections of the hollow blade (See Figure 19). This concept could lead to a reduction of initial raw material and an augmented hydrodynamic performance compared with solid propellers (Muller et al. [2019][2019]).

The study reported an improvement of the hydrodynamic performance by reducing cavitation and mass reduction of 23% in air and 36% in water (Muller et al. [2019] [2019]). Other benefits presented were the reduction of underwater radiated noise at higher frequencies where cavitation

Figure 18: WAAMpeller (BAYRAMOÄLU et al. [2019])

Figure 19: Hollow blade (Muller et al. [2019] [2019])

is the main contributor. In the offshore industry, marine risers are often subjected to structural and functional requirements. The failure of those components can imply severe environmental

and economic impacts. Marine risers are subjected to corrosion attack due to hydrogen sulphide, Chlorides, and carbon di-oxide gases. At the same time, they are also under continuous environmental loads; wind, waves, current, ice, and impacts. Because of the above, the innovation in conventional design of the marine risers is a challenge because of the increase of the water depth on offshore production, especially in sensitive zones as the weld on the thick forged ends, counterbored riser pipe, and cladding along with the critical locations, e.g. of susceptible zones can be observed in Figure 20.
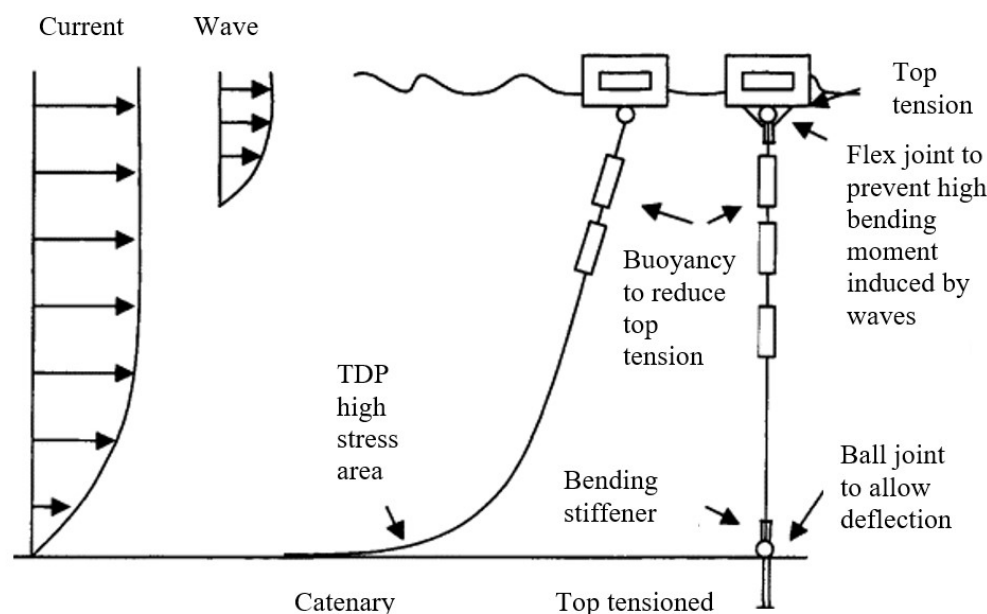
Figure 20: Example of tensions of risers at top and bottom, and external enviromental loads(Bai and Bai [2005])

Among those, the risers in some cases must withstand pressures over 20,000 psi (137,89 MPa) and temperatures exceeding 176°C. Sandwich composite risers can be an alternative to those challenges, but delamination can be a threat to their use under the combination of thermal and mechanical loads. Under high temperature and pressure effects (HTHP) thermal stresses occur at the metal and ceramics bonding interface due the differences of their thermal expansion, this can lead to a crack formation and delamination in the interface. Functionality Graded Materials (FGM) are designed to overcome this damages because they possess no distinct material interfaces. FGM´s are produced by several AM techniques, the WAAM technique was used in the work of Chandrasekaran et al. [2022], where a test specimen was produced composed by Duplex stainless steel and Carbon Manganese Steel as can be observed in Figure 21.

This composition is chosen based on the functional requirements without compromising the strength criteria. Tension test, and X-Ray computed Tomography analysis where performed. The X-Ray Computed Tomography showed that the WAAM process is acceptable for part fabrication. From the mechanical properties, it is seen that the yield and ultimate strengths of FGM are higher by 11.16% and 24.75%, respectively, in comparison with that of the standard X52 steel used in marine risers. The toughness, strength ratio, and ductility ratio are also higher for the FGM samples, while Modulus of Elasticity and Poisson´s ratio values are in the same range as X52 steel. Other potential application is the case of offshore wind applications, where the same benefits of WAAM technique can be applied to overcome monopile residual stress derived from corrosion-fatigue, improving by this technique the fatigue life (Ermakova et al. [2019]).
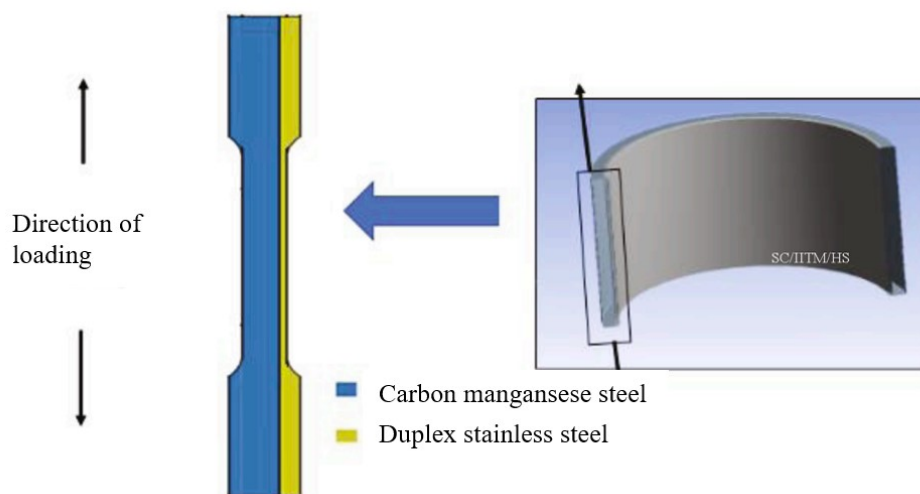
Figure 21: Sectional view showing the region where the mechanical properties are determined (along the longitudinal axis of the FGM marine riser), Chandrasekaran et al. [2022]

7   Concluding Remarks

Additive manufacturing techniques (i.e., 3D printing) are growing in different industries. However, the Naval and Offshore industry is characterized as conservative to changes and the major development of AM has been in the aerospace and automotive sectors. The knowledge generated by those sectors and the most recent implementation of that technology in the naval and offshore industry can reveal the benefits and challenges. WAAM and titanium alloys for the those industry is still a new topic and there are several technical challenges such as oxidation protection, distortion control and static environment. Regarding ship propellers and offshore systems such as risers and offshore wind platforms there is a wide opportunity to explore materials and design in WAAM systems to reduce cost and improve hydrodynamic and mechanical performance.

Acknowledgements

References

U. Alonso, F. Veiga, A. Suárez, and T. Artaza. Experimental investigation of the influence of wire arc additive manufacturing on the machinability of titanium parts. *Metals*, 10(1):24, 2019. ISSN 2075-4701.

H. Attar, M. Calin, L. C. Zhang, S. Scudino, and J. Eckert. Manufacture by selective laser melting and mechanical behavior of commercially pure titanium. *Materials Science and Engineering: A*, 593:170–177, 2014. ISSN 09215093. doi: 10.1016/j.msea.2013.11.038.

Y. Bai and Q. Bai. Chapter 22 - Design of Deepwater Risers. In Y. Bai and Q. Bai, editors, *Subsea Pipelines and Risers*, chapter 22, pages 401–412. Elsevier Ltd., elsevier s edition, 2005. ISBN

9780080445663,. doi: https://doi.org/10.1016/B978-008044566-3.50024-5. URL https://www.sciencedirect.com/science/article/pii/B9780080445663500245.

R. Banerjee, S. Nag, S. Samuel, and H. L. Fraser. Laser-deposited Ti-Nb-Zr-Ta orthopedic alloys. *J Biomed Mater Res A*, 78(2):298–305, 2006. ISSN 1549-3296 (Print) 1549-3296 (Linking). doi: 10.1002/jbm.a.30694. URL http://www.ncbi.nlm.nih.gov/pubmed/16637044.

K. BAYRAMOÄLU, K. D. KAYA, S. YILMAZ, B. GÖKSU, and B. MURATO. Utilization of 3D Printing Technologies in Marine Applications. In *4th International Congress on 3D Printing (Additive Manufacturing) Technologies and Digital Industry*, 2019.

M. J. Bermingham, S. D. McDonald, K. Nogita, D. H. St. John, and M. S. Dargusch. Effects of boron on microstructure in cast titanium alloys. *Scr. Mater.*, 59(5):538–541, 2008. ISSN 13596462. doi: 10.1016/j.scriptamat.2008.05.002.

M. J. Bermingham, S. D. McDonald, D. H. StJohn, and M. S. Dargusch. Beryllium as a grain refiner in titanium alloys. *J. Alloys Compd.*, 481(1-2):L20–L23, 2009. ISSN 09258388. doi: 10.1016/j.jallcom.2009.03.016.

M. J. Bermingham, J. Thomson-Larkins, D. H. St John, and M. S. Dargusch. Sensitivity of Ti-6Al-4V components to oxidation during out of chamber Wire+ Arc Additive Manufacturing. *Journal of Materials Processing Technology*, 258:29–37, 2018. ISSN 0924-0136.

M. J. Bermingham, D. H. StJohn, J. Krynen, S. Tedman-Jones, and M. S. Dargusch. Promoting the columnar to equiaxed transition and grain refinement of titanium alloys during additive manufacturing. *Acta Materialia*, 168:261–274, 2019. ISSN 1359-6454.

S. Chandrasekaran, S. Hari, and M. Amirthalingam. Functionally graded materials for marine risers by additive manufacturing for high-temperature applications: Experimental investigations. *Structures*, 35(December 2021):931–938, 2022. ISSN 23520124. doi: 10.1016/j.istruc.2021.12.004. URL https://doi.org/10.1016/j.istruc.2021.12.004.

L.-Y. Chen, Y.-W. Cui, and L.-C. Zhang. Recent development in beta titanium alloys for biomedical applications. *Metals*, 10(9):1139, 2020.

P. Collins. The influence of the enthalpy of mixing during the laser deposition of complex titanium alloys using elemental blends. *Scr. Mater.*, 48(10):1445–1450, 2003. ISSN 13596462. doi: 10.1016/s1359-6462(03)00081-2.

P. C. Collins, D. A. Brice, P. Samimi, I. Ghamarian, and H. L. Fraser. Microstructural Control of Additively Manufactured Metallic Materials. *Annu. Rev. Mater. Res.*, 46(1):63–91, 2016. ISSN 1531-7331 1545-4118. doi: 10.1146/annurev-matsci-070115-031816.

M. Courtois, M. Carin, P. Le Masson, S. Gaied, and M. Balabane. A complete model of keyhole and melt pool dynamics to analyze instabilities and collapse during laser welding. *Journal of Laser Applications*, 26(4):42001, 2014. ISSN 1938-1387. doi: 10.2351/1.4886835.

C. R. Cunningham, J. M. Flynn, A. Shokrani, V. Dhokia, and S. T. Newman. Invited review article: Strategies and processes for high quality wire arc additive manufacturing. *Additive Manufacturing*, 22:672–686, 2018. ISSN 2214-8604.

E. R. Denlinger, J. C. Heigel, P. Michaleris, and T. A. Palmer. Effect of inter-layer dwell time on distortion and residual stress in additive manufacturing of titanium and nickel alloys. *Journal of Materials Processing Technology*, 215:123–131, 2015. ISSN 0924-0136.

M. Deo and P. Michaleris. Mitigation of welding induced buckling distortion using transient thermal tensioning. *Science and technology of Welding and Joining*, 8(1):49–54, 2003. ISSN 1362-1718.

M. Easton and D. H. St. John. A Model of Grain Refinement Incorporation Alloy Constitution and Potency of Heterogeneous Nucleant Particles. *Acta Mater.*, 49:1867–1878, 2001.

A. Ermakova, A. Mehmanparast, and S. Ganguly. A review of present status and challenges of using additive manufacturing technology for offshore wind applications. *Procedia Structural Integrity*, 17:29–36, 2019. ISSN 24523216. doi: 10.1016/j.prostr.2019.08.005. URL `https://doi.org/10.1016/j.prostr.2019.08.005`.

W. E. Frazier. Metal Additive Manufacturing: A Review. *J. Mater. Eng. Perform.*, 23(6):1917–1928, 2014. ISSN 1059-9495 1544-1024. doi: 10.1007/s11665-014-0958-z.

X. Gong, S. Mohan, M. Mendoza, A. Gray, P. Collins, and S. R. Kalidindi. High Throughput Assays for Additively Manufactured Ti-Ni Alloys Based on Compositional Gradients and Spherical Indentation. *Integrating Materials and Manufacturing Innovation*, 2017. ISSN 2193-9772. doi: 10.1007/s40192-017-0100-9. URL `https://doi.org/10.1007/s40192-017-0100-9`.

D. D. Gu, W. Meiners, K. Wissenbach, and R. Poprawe. Laser additive manufacturing of metallic components: materials, processes and mechanisms. *International Materials Reviews*, 57(3): 133–164, 2013. ISSN 0950-6608 1743-2804. doi: 10.1179/1743280411y.0000000014.

B. J. Hayes, B. W. Martin, B. Welk, S. J. Kuhr, T. K. Ales, D. A. Brice, I. Ghamarian, A. H. Baker, C. V. Haden, D. G. Harlow, H. L. Fraser, and P. C. Collins. Predicting tensile properties of Ti-6Al-4V produced via directed energy deposition. *Acta Materialia*, 133:120–133, 2017. ISSN 13596454. doi: 10.1016/j.actamat.2017.05.025.

N. Hrabe and T. Quinn. Effects of processing on microstructure and mechanical properties of a titanium alloy (Tiâ6Alâ4V) fabricated using electron beam melting (EBM), part 1: Distance from build plate and part size. *Mater. Sci. Eng*, 573:264–270, 2013.

S. Inc.   Make Metal Parts Faster   Cheaper with EBAM® Metal 3D Printing Technology., 2022.   URL `https://www.sciaky.com/additive-manufacturing/electron-beam-additive-manufacturing-technology`.

R. Jendrzejewski and G. Śliwiński. Investigation of temperature and stress fields in laser cladded coatings. *Applied Surface Science*, 254(4):921–925, 2007. ISSN 0169-4332.

R. Jendrzejewski, G. Śliwiński, M. Krawczuk, and W. Ostachowicz. Temperature and stress fields induced during laser cladding. *Computers structures*, 82(7-8):653–658, 2004. ISSN 0045-7949.

S. M. Kelly and S. L. Kampe. Microstructural evolution in laser-deposited multilayer Ti-6Al-4V builds: Part I. Microstructural characterization. *Metallurgical and Materials Transactions*, 35 (6):1861, 2004. ISSN 1073-5623.

K. Kimura, K. Kinoshita, K. Tokuno, and H. Shimizu. Application of titanium to construction, civil engineering and ocean development. *Nippon Steel Technical Report*, pages 6–10, 2002. ISSN 0300-306X.

P. A. Kobryn, E. H. Moore, and S. L. Semiatin. The effect of laser power and traverse speed on microstructure, porosity, and build height in laser-deposited Ti-6Al-4V. *Scripta Materialia*, 43 (4):299–305, 2000. ISSN 1359-6462.

E. Kostidi and N. Nikitakos. Is it time for the maritime industry to embrace 3d printed spare parts? *TransNav: International Journal on Marine Navigation and Safety of Sea Transportation*, 12 (3), 2018. ISSN 2083-6473.

E. Kostidi, N. Nikitakos, and I. Progoulakis. Additive Manufacturing and Maritime Spare Parts: Benefits and Obstacles for the End-Users. *Journal of Marine Science and Engineering*, 9(8): 895, 2021.

D. A. Kriczky, J. Irwin, E. W. Reutzel, P. Michaleris, A. R. Nassar, and J. Craig. 3D spatial reconstruction of thermal characteristics in directed energy deposition through optical thermal imaging. *Journal of Materials Processing Technology*, 221:172–186, 2015. ISSN 09240136. doi: 10.1016/j.jmatprotec.2015.02.021.

K. Kunze, T. Etter, and J. Grässlin. Texture, anisotropy in microstructure and mechanical properties of IN738LC alloy processed by selective laser melting (SLM). *Mater. Sci. Eng. A*, 620: 213–222, 2015.

Z. Lin, K. Song, and X. Yu. A review on wire and arc additive manufacturing of titanium alloy. *Journal of Manufacturing Processes*, 70:24–45, 2021. ISSN 1526-6125.

Z. Liu, B. He, T. Lyu, and Y. Zou. A Review on Additive manufacturing of titanium alloys for aerospace applications: directed energy deposition and beyond Ti-6Al-4V. *Jom*, 73(6):1804–1818, 2021. ISSN 1543-1851.

M. Y. M. Londono. *On the Influence of Microstructural Features of Linear Friction Welding and Electron Beam Additive Manufacturing Ti-6Al-4V on Tensile and Fatigue Mechanical Properties*. Thesis, 2019. URL `https://dr.lib.iastate.edu/handle/20.500.12876/31927`.

G. Lütjering and J. C. Williams. *Titanium*. Springer, 2007. ISBN 3540730362.

B. Mannion and J. Heinzman. Plasma arc welding brings better control. *Tooling Prod*, 5:29–30, 1999.

F. Martina, P. A. Colegrove, S. W. Williams, and J. Meyer. Microstructure of interpass rolled wire+ arc additive manufacturing Ti-6Al-4V components. *Metallurgical and Materials Transactions A*, 46(12):6103–6118, 2015. ISSN 1543-1940.

M. Y. Mendoza, P. Samimi, D. A. Brice, B. W. Martin, M. R. Rolchigo, R. LeSar, and P. C. Collins. Microstructures and Grain Refinement of Additive-Manufactured Ti-xW Alloys. *Metallurgical and Materials Transactions A*, 48(7):3594–3605, 2017. ISSN 1073-5623 1543-1940. doi: 10.1007/s11661-017-4117-7.

M. Y. Mendoza, P. Samimi, D. A. Brice, I. Ghamarian, M. Rolchigo, R. LeSar, and P. C. Collins. On the role of composition and processing parameters on the microstructure evolution of Ti-xMo alloys. *BMC Chemistry*, 13(1), 2019. ISSN 2661-801X. doi: 10.1186/s13065-019-0529-3.

Mendoza, Michael Y., et al. (2022)Additive Manufacturing TiAlloys Aerospace,Naval,Offshore

pp. 154-183

M. Y. Mendoza Londono. *Molten pool modeling, microstructure and grain refinement in Ti-alloys*. Thesis, 2016.

P. Mercelis and J. Kruth. Residual stresses in selective laser sintering and selective laser melting. *Rapid prototyping journal*, 2006. ISSN 1355-2546.

P. Michaleris and A. DeBiccari. Prediction of welding distortion. *Welding Journal-Including Welding Research Supplement*, 76(4):172s, 1997. ISSN 0043-2296.

R. P. Mudge and N. R. Wald. Laser engineered net shaping advances additive manufacturing and repair. *Welding Journal-New York-*, 86(1):44, 2007. ISSN 0043-2296.

P. Muller, G. Rückert, and P. Vinot. On the benefits of metallic additive manufacturing for propellers. In *Sixth International Symposium on Marine Propulsors smp'19, Rome, Italy*, number May, 2019.

NeoNickel. Titanium Titanium Alloy CategorisationNo Title, 2022. URL https://www.neonickel.com/technical-resources/general-technical-resources/titanium-titanium-alloy-categorisation/.

C. H. Ng, M. J. Bermingham, L. Yuan, and M. S. Dargusch. Towards β-fleck defect free additively manufactured titanium alloys by promoting the columnar to equiaxed transition and grain refinement. *Acta Materialia*, 224:117511, 2022. ISSN 1359-6454.

A. H. Nickel, D. M. Barnett, and F. B. Prinz. Thermal stresses and deposition patterns in layered manufacturing. *Materials Science and Engineering: A*, 317(1-2):59–64, 2001. ISSN 0921-5093.

J. Obielodan and B. Stucker. Characterization of LENS-fabricated Ti6Al4V and Ti6Al4V/TiC dual-material transition joints. *The International Journal of Advanced Manufacturing Technology*, 66(9-12):2053–2061, 2012. ISSN 0268-3768 1433-3015. doi: 10.1007/s00170-012-4481-9.

T. L. H. Office). WIRE ARC ADDITIVE MANUFACTURING (WAAM)., 2022. URL https://www.twi-global.com/technical-knowledge/job-knowledge/arc-based-additive-manufacturing-137.

Z. Pan, D. Ding, B. Wu, D. Cuiuri, H. Li, and J. Norrish. Arc welding processes for additive manufacturing: a review. *Transactions on intelligent welding manufacturing*, pages 3–24, 2018.

P. Peyre, P. Aubry, R. Fabbro, R. Neveu, and A. Longuet. Analytical and numerical modelling of the direct metal deposition laser process. *J. Phys. D: Appl. Phys.*, 41(2):25403, 2008. ISSN 0022-3727 1361-6463. doi: 10.1088/0022-3727/41/2/025403.

J. L. Prado-Cerqueira, J. L. Diéguez, and A. M. Camacho. Preliminary development of a wire and arc additive manufacturing system (WAAM). *Procedia Manufacturing*, 13:895–902, 2017. ISSN 2351-9789.

M. Qi, S. Huang, Y. Ma, S. S. Youssef, R. Zhang, J. Qiu, J. Lei, and R. Yang. Columnar to equiaxed transition during β heat treatment in a near β alloy by laser additive manufacture. *Journal of Materials Research and Technology*, 13:1159–1168, 2021. ISSN 2238-7854.

In Jorge, Ariosto B., et al. (Eds.) Fundamental Concepts and Models for the Direct Problem, Vol. 2, UnB

181

C. Qiu, G. A. Ravi, and M. M. Attallah. Microstructural control during direct laser deposition of a β-titanium alloy. *Materials Design*, 81:21–30, 2015. ISSN 02613069. doi: 10.1016/j.matdes. 2015.05.031.

A. Queguineur, G. Rückert, F. Cortial, and J. Y. Hascoët. Evaluation of wire arc additive manufacturing for large-sized components in naval applications. *Welding in the World*, 62(2):259–266, 2018. ISSN 1878-6669.

M. J. Quintana, M. J. Kenney, P. Agrawal, and P. C. Collins. Texture analysis of additively manufactured Ti-6Al-4V deposited using different scanning strategies. *Metallurgical and Materials Transactions A*, 51(12):6574–6583, 2020. ISSN 1543-1940.

M. R. Rolchigo, M. Y. Mendoza, P. Samimi, D. A. Brice, B. Martin, P. C. Collins, and R. LeSar. Modeling of Ti-W Solidification Microstructures Under Additive Manufacturing Conditions. *Metallurgical and Materials Transactions A*, 48(7):3606–3622, 2017. ISSN 1073-5623 1543-1940. doi: 10.1007/s11661-017-4120-z.

N. A. Rosli, M. R. Alkahari, F. R. Ramli, S. Mat, and A. A. Yusof. Influence of process parameters on dimensional accuracy in GMAW based additive manufacturing. *Proceedings of Mechanical Engineering Research Day 2019*, 2019:7–9, 2019. ISSN 9672145659.

K. I. Schwendner, R. Banerjee, P. C. Collins, C. A. Brice, and H. L. Fraser. Direct laser deposition of alloys from elemental powder blends. *Scr. Mater.*, 45(10):1123–1129, 2001. ISSN 1359-6462.

J. W. Sears. The Effects of Processing Parameters on Microstructure and Properties of Laser Deposited PM Alloy 690N2 Powder. Report LM-02K021, Lockheed Martin Corporation, Schenectady, NY 12301 (US), 2002.

C. Shen, Z. Pan, D. Cuiuri, J. Roberts, and H. Li. Fabrication of Fe-FeAl functionally graded material using the wire-arc additive manufacturing process. *Metallurgical and Materials Transactions B*, 47(1):763–772, 2016. ISSN 1543-1916.

M. Simonelli, Y. Y. Tse, and C. Tuck. Effect of the build orientation on the mechanical properties and fracture modes of SLM Tiâ6Alâ4V. *Materials Science and Engineering: A*, 616:1–11, 2014.

S.Tamirisakandala, R. B. Bhat, and J. S. Tiley. Grain refinement of cast titanium alloys via trace boron addition—. *Scr. Mater*, 53(12):1421–1426, 2005.

M. Strantza, R. Ganeriwala, and B. Clausen. Effect of the scanning strategy on the formation of residual stresses in additively manufactured Ti-6Al-4V, 2021. URL `https://www.grandviewresearch.com/industry-analysis/3d-metal-printing-market#.`

J. D. Strickland. Applications of additive manufacturing in the marine industry. *Proceedings of PRADS2016*, 4:8th, 2016.

Q. Tan, Y. Yin, A. Prasad, G. Li, Q. Zhu, D. H. StJohn, and M.-X. Zhang. Demonstrating the roles of solute and nucleant in grain refinement of additively manufactured aluminium alloys. *Additive Manufacturing*, 49:102516, 2022. ISSN 2214-8604.

S. N. Tedman-Jones, S. D. McDonald, M. J. Bermingham, D. H. StJohn, and M. S. Dargusch. A new approach to nuclei identification and grain refinement in titanium alloys. *Journal of Alloys and Compounds*, 794:268–284, 2019. ISSN 0925-8388.

L. Thijs, F. Verhaeghe, T. Craeghs, J. V. Humbeeck, and J.-P. Kruth. A study of the microstructural evolution during selective laser melting of Tiâ6Alâ4V. *Acta Mater.*, 58(9):3303–3312, 2010. ISSN 13596454. doi: 10.1016/j.actamat.2010.02.004.

F. Wang, S. Williams, P. Colegrove, and A. A. Antonysamy. Microstructure and Mechanical Properties of Wire and Arc Additive Manufactured Ti-6Al-4V. *Metall. Mater. Trans. A*, 44(2): 968–977, 2012. ISSN 1073-5623 1543-1940. doi: 10.1007/s11661-012-1444-6.

X. Wang, L.-J. Zhang, J. Ning, S. Li, L.-L. Zhang, and J. Long. Hierarchical grain refinement during the laser additive manufacturing of Ti-6Al-4V alloys by the addition of micron-sized refractory particles. *Additive Manufacturing*, 45:102045, 2021. ISSN 2214-8604.

C. Xiaolong, L. Zulei, G. Yanhua, S. Zhonggang, W. Yaoqi, and Z. Lian. A study on the grain refinement mechanism of Ti-6Al-4V alloy produced by wire arc additive manufacturing using hydrogenation treatment processes. *Journal of Alloys and Compounds*, 890:161634, 2022. ISSN 0925-8388.

M. Yakout, M. A. Elbestawi, and S. C. Veldhuis. A study of the relationship between thermal expansion and residual stresses in selective laser melting of Ti-6Al-4V. *Journal of Manufacturing Processes*, 52:181–192, 2020. ISSN 1526-6125.

Y. Z. Zhang, C. Meacock, and R. Vilar. Laser powder micro-deposition of compositional gradient TiâCr alloy. *Materials Design*, 31(8):3891–3895, 2010. ISSN 02613069. doi: 10.1016/j. matdes.2010.02.052.

Y. Zhu, X. Tian, J. Li, and H. Wang. The anisotropy of laser melting deposition additive manufacturing Tiâ6.5 Alâ3.5 Moâ1.5 Zrâ0.3 Si titanium alloy. *Materials Design*, 67:538–542, 2015. ISSN 0261-3069.

M. Ziółkowski and T. Dyl. Possible applications of additive manufacturing technologies in shipbuilding: a review. *Machines*, 8(4):84, 2020.

Chapter 7

Review of Low Cycle Fatigue: Issues in Naval and Offshore Engineering

Chapter details

Chapter suggested citation / reference style:

Morales, Leonel L. D., et al. (2022). "Review of Low Cycle Fatigue: Issues in Naval and Offshore Engineering". *In* Jorge, Ariosto B., et al. (Eds.) *Fundamental Concepts and Models for the Direct Problem*, Vol. II, UnB, Brasilia, DF, Brazil, pp. 184–208. Book series in Discrete Models, Inverse Methods, & Uncertainty Modeling in Structural Integrity.

P.S.: DOI may be included at the end of citation, for completeness.

Book details

Review of Low Cycle Fatigue: Issues in Naval and Offshore Engineering

Leonel Leonardo Delgado-Morales[1*], Victor Contreras Palma[2],
Jian Gu[3], and Ernesto Molinas[4]

[1]Institute of Design and Industrial Methods, Universidad Austral de Chile, Chile.
E-mail: leonel.delgado@uach.cl
[2]Institute of Naval Architecture and Ocean Engineering, Universidad Austral de Chile,
Chile. E-mail: victor.palma@uach.cl
[3]China Ship Scientific Research Center Wuxi, China. E-mail: gujian@cssrc.com.cn
[4]ACQUATOOL Consultoría, Fortaleza, Brazil.E-mail: ernestomolinas@gmail.com
*Corresponding author

Abstract

Fatigue can be understood as a process of progressive localized plastic strain that occurs in a material subject to cyclic stresses and strains at high stress concentration locations, whose concentration can cause cracks and culminate in the material's fracture. The fatigue process begins with the appearance of the crack, later on with growth, and finally propagation. The study of this phenomenon can be divided into the function of the material life in low and high cycle fatigue, but some studies address problems in the ultra-low and high number of cycles. This chapter addresses aspects of low cycle fatigue, as it is a relatively unexplored area and for which there are few references. Therefore, the main objective of this text is to describe the main aspects of low cycle fatigue, presenting diverse applications and potential problems in the context of fatigue behavior of materials. For this contribution, a review of the technical literature will be presented, considering relevant publications in the last decade. The text overview considers experimental and numerical aspects, fatigue damage, fracture behavior, thermomechanical fatigue, as well as real cases describing how a low-cycle fatigue problem can be defined and the way to approach it through the use of engineering tools found in the literature. Even though the low-cycle fatigue approach and analysis technique covers all engineering, the purpose of this chapter will be on marine and ocean engineering. Several cases described in the reviewed works will be addressed, where problems related to welded structures, turbines, pipelines, risers, mooring chains, floating systems, and wind platforms are presented, situations related to marine and offshore equipment will also be described, showing how low cycle fatigue can present itself in the various situations above, considering that low-cycle fatigue problems can cause structures to fracture, which could consequently cause serious injuries to life and marine environment. At the end of the chapter, potential applications and problems where this phenomenon can appear will be presented.

Keywords: Low Cycle Fatigue, Review, Potential problems

1 Introduction

In the context of mechanical engineering and the study of material fractures, the assessment of the fatigue phenomenon becomes fundamental. Fatigue can be found in countless situations, from traditional problems of component failures in aircraft, vessels, onshore and offshore systems, civil structures, piping systems and various equipment. Fatigue-related problems can be approached from an experimental or numerical point of view (Beesley et al. [2017]; Han et al. [2018]; Li et al. [2021]), depending on the technological resources and infrastructure available for the study. Fatigue fracture can be produced from mechanical failures, related to the type of loading or for other reasons, such as metallographic defects, temperature effects, corrosion, among others (Sharifi et al. [2016]); Hou et al. [2021]); Lee et al. [2020]; Li et al. [2021]; Jiang and Yang [2020]; Orlando et al. [2021]; Zhang et al. [2021]; Gemilang et al. [2021]).

The fatigue phenomenon can be described as a process of plastic strain, which is located in certain regions of the material and progresses along the rupture surface, when a material is subjected to localized strain and cyclic stresses, with the strain concentration it can cause cracks and culminate in the fracture of the material, requiring the presence of three factors simultaneously: dynamic stresses, tractive stresses and plastic strain (Jia and Ge [2019]). It is possible to affirm that the fatigue process starts with the appearance of the crack (onset or nucleation), later on it propagates (appearance of typical marks â beach lines) and finally the rupture. In general, the study of this phenomenon can be divided as a function of material life in low and high cycle fatigue.

The main motivation for the production of this work is to be able to gather scientific contributions related to low cycle fatigue in a concentrated way, material that can become a source of research for students and researchers interested in the subject. The identification of phenomena related to fatigue problems in naval structures, naval systems and artifacts, equipment, among others, as well as the description of how to approach the problems and all this described in a single text, was also an inspiration and a challenge for the authors.

The pricipal objective of the text is to carry out a literature review, describing the state of the art in the context of studies related to low cycle fatigue, which have been published in recent decades in high-impact scientific vehicles. Identifying applications from different areas of knowledge, experimental and numerical methodologies as well as procedures are also objectives of this chapter.

The bibliographical research is based on an exploratory search, in which works published from the 2010s until the present time were considered, the articles have been resumed in Table 1, which address different aspects and applications where low cycle fatigue is present. The research sources are mostly scientific articles published in highly relevant scientific journals that address topics related to: welded join, risers problems and wind turbines, among others. The texts were analyzed chronologically, making a description of their contents, identifying the main aspects, mainly methodological aspects, technical support and laboratory infrastructure (in the case of experimental work), techniques and procedures adopted, as well as the results obtained. An item was also structured with a description of potential problems which can be addressed through the use of low cycle fatigue.

As a final product, a friendly text was obtained, which addresses the issues in a clear and direct way, based on friendly writing, maintaining scientific rigor. This text can become a source of research for students and researchers, especially those starting in this area of knowledge and who need to find information related to the topic in a concentrated way in a single source.

2   Research related to Low Cycle Fatigue - LCF

Research on Low Cycle Fatigue (LCF) focuses on works done from 2010 until the present. Since the topic of fatigue encompasses a vast number of cases, the specific objective of this book is related to the phenomenon presented only in naval structures and systems. We can distinguish different types of research in LCF, some of the most characteristic are described below:

Ligaj and Szala [2012] proposed calculation formulas in high and low cycle ranges of different metal alloys, those formulations consist of three methods expressed from stress, strain and a hybrid method (Stress-strain). They performed comparative analyzes of C45 steel, using loading programs; two-level and multi-level. The problems analyzed by the researchers finds applications on the analysis of naval structures and increases the ranges of analysis methods found in the previous literature.

Wahab et al. [2013], proposed the use of Continuum Damage Mechanics (CDM) theory for the analysis of high and low cycle fatigue. Then they apply this theory to a simple case such as two plates joined using resin and to a friction fatigue problem, those problems were modeled in ANSYS with the objective of predicting the fracture initiation time. The low cycle fatigue initiation model is based on accumulation of plastic deformation, while for high cycle it is based on the release of energy by plastic deformation.

Benoit et al. [2014] presented an experimental system that includes the effect of temperature at the beginning of the fatigue fracture in low cycle problems, the analysis uses stainless steel as material containing 18% Cr and welded test bodies. The study is used image correlation analysis to obtain the deformation gradient of the test bodies. The analysis of the results were complemented with the use of finite element analysis tools and observation of the fractured surfaces. Finally, they proposed an energy model of micro-fracture growth.

Sharifi et al. [2016] presented a three-dimensional analysis of a low cycle problem found in the cylinder head of an internal combustion engine, the fracture initiatives in the accommodation of the intake and exhaust valves. The study focuses on simulating the durability tests of the failed component, as well as the evaluation of the fatigue of low cycle.The analyses consider five operating speeds of the engine, 750, 1650, 2075, 2350 and 2600 rpm. The cylinder head is exposed to multi-axial cyclic loads. Low cycle failure theories such as critical plane theory and accumulated damage are used to predict the fatigue. Numerical models corroborated that the problem can be analyzed as an LCF phenomenon. The analyses founded that the sector where the valves are accommodated to the cylinder head, which are exposed to high temperatures during engine operation, are the critical areas prompt to LCF.

Amirinia and Sungmoon Jung [2017] studied the buffeting response from three hurricane turbulence models which generated LCF damage in turbine tip blade and tower, this work is described in section four. Hamidi Ghaleh Jigh et al. [2019] studied an aluminum foam subjected to compression by means of the finite element method using representative volumetric elements, together with the above, a series of experiments were carried out applying static loads that caused localized plastic deformation, which leads to low cycle fatigue. This made possible to develop an algorithm that calculate the low cycle fatigue models. The material used was aluminum AA6101-T6, the static load experiments were carried out according to the ISO 13314 standards. The numerical results were compared with the experimental results.

Lee et al. [2020] worked on the study of LCF in offshore oil pipelines caused by external loads. Most of the damage in pipelines occurs in the weld bands, where are presented geometric discontinuities. Along with this, external offshore loads such as currents, swells, and platform movements can cause significant plastic deformation and fractures in a low cycle fatigue regime. ASME 2007 Div. 2 adopts S - N curve for joint fatigue evaluation, in this work were carried out an extension methodology of the S - N curve to evaluate the LCF. However, there is a limitation when

describing the behavior of materials when they leave the elastic range of the material because most of the materials in engineering exhibit hardening or softening when subjected to cyclical loads. In this work, they propose an optimized prediction method which was validated with real fatigue data obtained from welds belonging to pipelines used in the industry. It should be noted that this book presents a new problem that could generate Low cycle Fatigue in this type of structure.

Gemilang et al. [2021] studied fatigue phenomenon in anchor chains of offshore platforms, the authors proposed that the traditional system of S - N curves does not really predict the fatigue life behavior of these chains. In this way, they propose a fatigue criterion based on critical multiaxial planes for anchoring chains that considers the damage produced by cyclical plasticization and medium load effects. To develop these criteria, they used finite element models of the critical points of the chains to obtain the multiaxial critical plane. The results are correlated by the conventional fatigue curves. As a case study, the simulation of the mooring chains of an FPSO was used, which shows that the effect of medium tension load significantly reduces the fatigue life of the mooring chains, while the effect of plasticity inducing damage is more limited. The fatigue damage using the proposed technique is significantly higher than the traditional approach using the S - N curves.

There are more complex systems to be analyzed in the naval area, this is the case of offshore wind turbines, as the case analyzed by Xu et al. [2021], which studied the bearing system to support the Nacelle of a 5MW offshore wind turbine, these systems are subjected to aerodynamic and hydrodynamic loads at the same time. Load analysis used time domain series of velocity values to establish the loads for which this component is subjected in an offshore wind turbine, various algorithms (Gumbel's algorithm, rainflow counting algorithm and S - N curves) are used to generate fatigue life load damage. To complete the study, he compared these loads for six types of supports: Onshore, monopile, ITI System(details about this system can be found in Jonkman and Matha [2011]), Tension Leg Platform (TLP), Spar and Semi-submersible. The results of the study show that the dynamics of the wind turbine is directly related to the bearing that allows the Yaw movement of the Nacelle and also that the subcomponents must be taken into consideration for this type of calculation since they also may present low cycle fatigue problems.Another problem present in naval and offshore systems are probabilistic loads, represented by irregular and / or âstrangeâ waves, for this reason a probabilistic study of low cycle fatigue becomes an interesting problem to be studied.

In Song et al. (2021) CDM combined with the cyclic plasticity model is used to evaluate the Low Cycle Fatigue failure of a 10CrNi3MoV steel and its undermached welding. Numerical analysis using the finite element method and supported by ABAQUS is performed. The results make it possible to estimate the fatigue life for both the base material and the undermached welding.

The work of Jiang et al. [2022] presents a model of low cycle fatigue life (ProbLCF-VA), to describe the dispersion of the initiation of fractures by LCF in homogeneous materials subjected to cyclic or random loads. This model can be implemented to estimate probabilistic cumulative damage for a given load history consisting of variable cyclical loads, or to predict the probabilistic onset of the LCF crack, if distributional estimate of a random load spectrum are available. The proposed model describes certain predominant effects such as the interaction of loads and the contributions of small cycles, which are very commonly observed in fatigue tests with cyclic loads of variable amplitude but which can hardly be described by other models with physical and mathematical fundaments.

As well as the previous cases there are other studies that illustrate low cycle fatigue, the following table aims to classify the different types of approaches of the studies in LCF to date (See Table 1).

Table 1: Description of revised works

Author	Year	Research type	Material	Experimental Loads involved in Study
Ligaj and Szala [2012]	2012	Analytical	C45 Steel	-
Wahab et al. [2013]	2013	Analytical - FEA	-	-
Benoit et al. [2014]	2014	Experimental	18% Cr Steel	Thermal and mechanical
Sharifi et al. [2016]	2016	Analytical - FEA	-	-
Beesley et al. [2017]	2017	Experimental	18% Cr Steel	Thermal and mechanical
Amirinia and Sung-moon Jung [2017]	2017	Analytical	Structural Compo-nents(Composite fiberglass materi-als)	Mechanical
Cahís et al. [2018]	2018	Analytical - FEA - Experi-mental	PC-r5, PC-r45 Steels	Mechanical
Hamidi Ghaleh Jigh et al. [2019]	2019	FEA - Experimental	PC-r5, PC-r45 Steels	Mechanical
Jiang and Yang [2020]	2020	Experimental	AH32 steel	Mechanical
Lee et al. [2020]	2020	Analytical - Experimental	API 5L X65 pipeline Steel-Sainless Steel 304	Mechanical
Zhang et al. [2021]	2021	Experimental	Steel with JQMG50-6 welding wire	Mechanical
Xu et al. [2021]	2021	Analytical - FEA	QT-800	Dynamical Aero/Hydrodynamic
Shaohu et al. [2021]	2021	Analytical - FEA - Experi-mental	PC-r5, PC-r45 Steels	Mechanical Internal pres-sure and bending
Orlando et al. [2021]	2021	FEM-Experimental-Time do-main measurement	-	Dynamical, non-stationary and stationary
Gemilang et al. [2021]	2021	Experimental - FEA	R4 steel grade for simulation	Dynamical, hydrodynamic
Song et al. [2021]	2021	Experimental - FEA	10CrNi3MoV steel and its undermatched weldments	Mechanical
Hou et al. [2021]	2021	Experimental	K4750 Ni-Based superalloy	Thermo Mechanical
Jiang et al. [2022]	2022	Analytical	-	Mechanical

3   Fundamental concepts and categories of fatigue

Situations involving fatigue are highly complex and require a deep understanding of the cause of the failure, in the case of naval artefacts and offshore structures, other variables appear that make the problem even more difficult to be addressed. One way to predict fatigue failure is to carry out the life estimate while still designing mechanisms or components. The main methods of studying fatigue are the stress life method (S - N) and the strain life method ($\varepsilon - N$). A brief description of these methods is provided below. The stress life method is the oldest and most used, indicated for high cycle fatigue where the deformation is predominantly elastic. It is based on the stress curve versus the number of cycles of the component, considering the fatigue life to total failure. In general is used the Basquin equation for description of fatigue life. (Equation 1) Cui [2002]

$$\sigma_a = \frac{E \cdot \Delta\varepsilon_e}{2} = \sigma'_f \cdot (2N_f)^b, \tag{1}$$

where E represent Young's modulus, $\Delta\varepsilon_e$ is the elastic strain, σ'_f is the fatigue strength coefficient, N is the number cycles to failure, b is the fatigue strength exponent.

J. Kohout [2001] proposed an expression to describe fatigue for low and high number of cycles, the function has the following form (Correia et al. [2017]):

$$\sigma = \sigma_\infty \left[\frac{N + \mathbf{B}}{N + \mathbf{C}}\right]^b, \tag{2}$$

where a and b are Basquin paranmeters, σ_∞ is the fatigue limit, $\mathbf{B}$ (Equation 4) is the number of cycles corresponding to the intersection of the tangent line of the finite life region and the horizontal asymptote of the ultimate tensile strength, and $\mathbf{C}$ (Equation 5) is the number of cycles corresponding to the intersection of the tangent line of the finite life region and the horizontal asymptote of the fatigue limit Correia et al. [2017]. An equivalent equation when considering the ultimate tensile (σ_1 strength) is:

$$\sigma = \sigma_1 \left[\frac{1 + N/\mathbf{B}}{1 + N/\mathbf{C}}\right]^b, \tag{3}$$

$$\mathbf{B} = \beta \cdot \mathbf{C}, \tag{4}$$

$$\mathbf{C} = 10^7 \cdot \frac{1 - \alpha}{\alpha - \beta}. \tag{5}$$

The expressions for α and β are defined as:

$$\alpha = \left(\frac{\sigma_c}{\sigma_\infty}\right)^{1/b}, \tag{6}$$

$$\beta = \left(\frac{\sigma_1}{\sigma_\infty}\right)^{1/b}, \tag{7}$$

where is σ_c is the fatigue limit for a pre-defined number of cycles (10^7).

On the other hand, the strain life method is more complex, indicated for low and high cycle fatigue, with plastic and elastic strains. It is based on the strain life curve by the number of cycles of the component, considering the fatigue life until crack nucleation. The contributions of elastic and plastic strains are shown in the following equations:

$$\frac{\Delta\varepsilon_e}{2} = \frac{\sigma'_f}{E} \cdot (2N_f)^b, \tag{8}$$

$$\frac{\Delta\varepsilon_p}{2} = \varepsilon'_f \cdot (2N_f)^c. \tag{9}$$

Where $\Delta\varepsilon_e$ is the elastic strain amplitude, ε'_f is the fatigue strength coefficient, E is the elastic modulus, N_f is the number of cycle to failure, $\Delta\varepsilon_p$ is the plastic strain amplitude, ε'_f represents the fatigue ductility coefficient, b is the fatigue strength exponent and c is the fatigue ductility exponent Correia et al. [2017], Cui [2002].

Combining Equation 8 and 9 and considering the superposition of elastic and plastic resistance, an expression is obtained to estimate life in the high and low cycle ranges:

$$\frac{\Delta\varepsilon_T}{2} = \varepsilon_a = \frac{\Delta\varepsilon_e}{2} + \frac{\Delta\varepsilon_p}{2} = \frac{\sigma'_f}{E} \cdot (2N_f)^b + \varepsilon'_f \cdot (2N_f)^c. \tag{10}$$

When the effects of mean stress or mean strain are included, the following equation is used:

$$\frac{\Delta\varepsilon}{2} = \frac{(\sigma'_f -) \cdot (2N_f)^b}{E} + \varepsilon'_f \cdot (2N_f)^c, \tag{11}$$

where σ_m is the mean stress, being positive for tensile values and negative for compressive values.

3.1   Fatigue failure categories

Fatigue failure found in engineering materials is a direct function of the type of load and conditions under which the phenomenon occurs. Sharma et al. [2020] presents a classification of the types of fatigue failure that happens in materials used in engineering (See Figure 1).
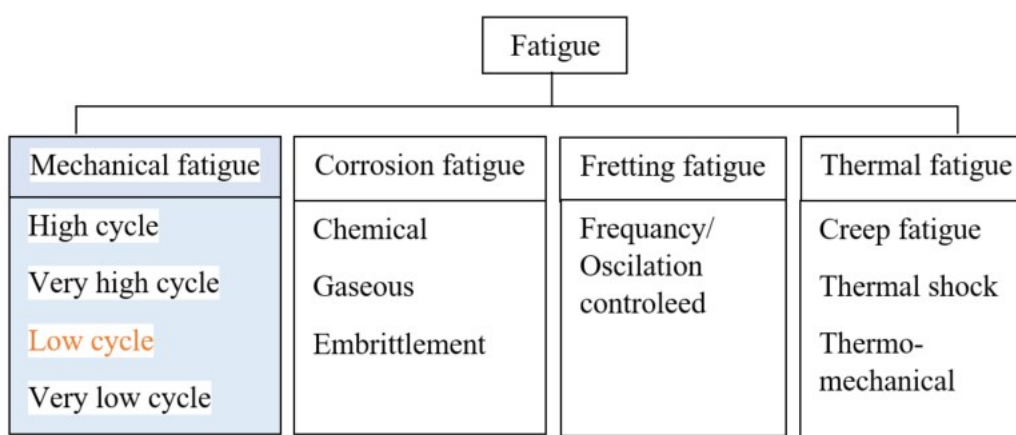
Figure 1: Types of fatigue failure (Adapted from Sharma et al. [2020])

Considering the classification of mechanical fatigue, Neville and Sachs [2020] present three categories, High Cycle Fatigue (HCF), Low Cycle Fatigue (LCF) and Very Low Cycle Fatigue (VLC). A brief description of these categories is given below. The High Cycle Fatigue (HCF) occurs when failure takes more than 10^4 cycles. According to the literature, constituting a significant percentage of all fatigue failures. Components or mechanisms that suffer fatigue failures in this category can take more than 10^5 cycles, in some cases reaching hundreds of millions of cycles from the beginning of application of force to the final failure. Situations in which high cycle fatigue failure occurs are common in several areas of engineering and are widely addressed in the literature. Low Cycle Fatigue (LCF) is when the failure takes less than 10^4 cycles, in general, this type of failure presents itself in a range around 25 cycles from the initial application of force to the final failure. Failures in this category are not very common in industrial equipment, from the point of view of stresses, it can be seen to involve situations in which loads are significantly higher than high cycle failures. Very Low Cycle Fatigue (VLC) occurs less than 10 cycles after charging begins. On the other hand, there are indications that the applied force was slightly less than the force causing the failure. Very High Cycle Fatigue (VHCF) is can be found in situations where the fatigue life is greater than 10^7 cycles. Industrial equipment failures in this category are not very common, however the phenomenon is seen more often than low-cycle fatigue cases. This category has very particular aspects, which differ from HCF and LCF, especially regarding plastic strain levels. The term âinfinite lifeâ is usually used when a component has such a long fatigue life that it will not fail due to this phenomenon. In carbon steels, the number of cycles considered as infinite life must be greater than 10^6. On the other hand, finite life means that the component will fail due to fatigue in a certain number of cycles. Figure 2 shows a schematic figure with the ranges of the categories described.
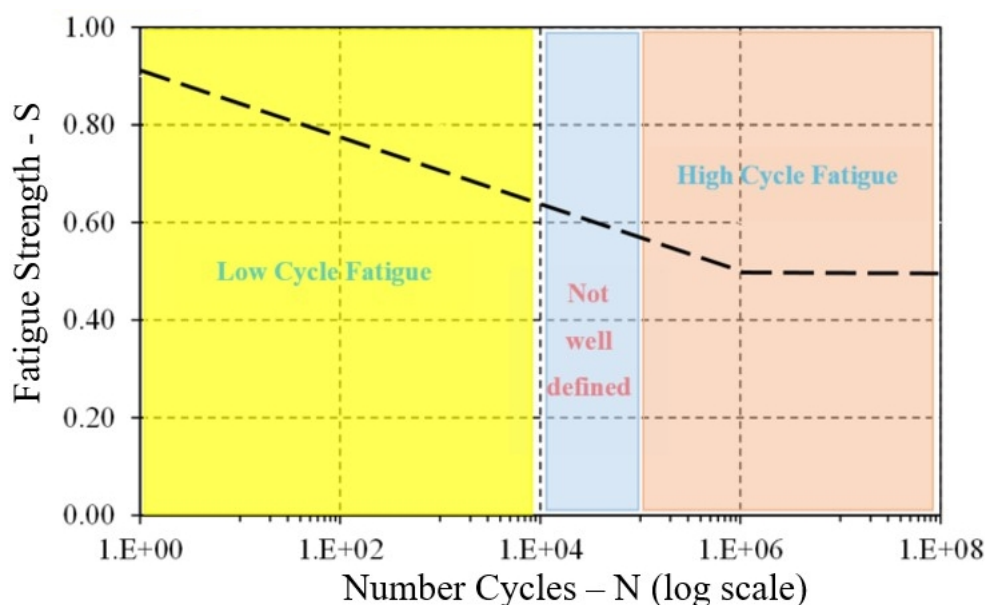
Figure 2: General ranges of fatigue stress cycles (Adapted from Neville and Sachs [2020])

4   Description of Low Cycle Fatigue problems in offshore engineering

This section presents a description of specific jobs in the context of offshore engineering to which low cycle fatigue is applied. The contribution made by Amirinia and Sungmoon Jung [2017] is described, in which the problem of a wind turbine is addressed. Another work described is the publication by Gemilang et al. [2021], where the problem of estimating the life of mooring chains of an FPSO is investigated and finally the paper by Song et al. [2021], where the problem of predicting the life of an undermached welding is studied.

One of the concerns in some structural analyses in LCF are the effect of climate change over offshore structures, specially because the increment of hurricane events in places where offshore wind turbines are installed or future develoment of OWT projects could be implemented. LCF analysis can be evaluated to determine the structural integrity during this extreme events, the work of Amirinia and Sungmoon Jung [2017] adress this issue, where three hurricane turbulence models where considered to describe the energy amount which can affect the turbine during those short periods.

Those wind turbulence spectrums are described as a superposition of eddies. Big eddies, which represent small wave numbers or low frequencies, supply the most energy content of the turbulent flow. In contrast, small eddies with high wave numbers in high frequencies dissipate the gained energy. The three models are:

Kaimal model (Kaimal et al. [1972]):

$$\frac{nS_u}{\sigma_u^2} = \frac{21.6f}{(1+33f)^{5/3}}.$$ (12)

Model A:

$$\frac{nS_u}{\sigma_u^2} = \frac{1}{\beta} X \frac{p_1 f^2 + p_2 f + p_3}{f^3 + q_1 f^2 + q_2 f + q_3}.$$ (13)

Where $\sqrt{\beta} = \sigma/u^*$ is the turbulence radio, u^* represents the friction velocity, and q_i and p_i are

constants proposed by Yu et al. [2008].

Model B:

$$\frac{nS_u}{\sigma_u^2} = \frac{16.66f}{1.72 + 237.24f^{5/3}}. \tag{14}$$

Where $f = nz/Uz$ is the normalized frequency, n is the frecuency, S_u is the spectral density of the longitudinal velocity fluctuation at height z, and σ is the standar deviation of longitudinal velocity fluctuation.

The effect of those models where studied over the structure at the tower and blade of the wind turbine.Buffeting response over the cited components is the main studied effect in this work.

The Buffetting load can be defined as the dynamic amplification of the structural response of the turbulent component of the wind and the impulsive action of periodic gusts (A. Pipinato [2022]).

Wind load on the wing turbine tower is given by:

$$F_{wind(z,t)} = \begin{bmatrix} \vec{f}_{D(z)} \\ \vec{f}_{L(z)} \\ \vec{M}_{a(z)} \end{bmatrix} + \begin{bmatrix} f_{D(z,t)} \\ f_{L(z,t)} \\ M_{a(z,t)} \end{bmatrix} = \vec{f} + B_f v + C_{ac}\dot{r} + K_{ae}r. \tag{15}$$

Where $\vec{f} = [f_D(z,t), f_L(z,t), M_a(z,t)]^T$ are quasi-static forces $B_f v$ are Buffeting forces,$C_{ac}\dot{r}$ and $K_{ae}r$ are self exited forces, u and w are longitudinal and and lateral fluctuating parts of the wind, r and $r\hat{A}$ are structural position and velocity vectors.

$$v(z,t) = [u/U w/U]^T. \tag{16}$$

and

$$\vec{f} = [\vec{f}_D(z), \vec{f}_L(z), \vec{M}_\alpha(z)]^T. \tag{17}$$

The therm $B_f v$ in the Equation 15 denotes the buffeting force and can be expressed as:

$$B_f(z)v(z,t) = \frac{\rho U^2 D}{2}[2X_{Du}\vec{C}_D u(t) + (C_D - \vec{C}_L)X_{Dw}W(\tau)]. \tag{18}$$

Due to wind fluctuations the therms u and w can be expressed as the convolution integrals:

$$B_f(z)v(z,t) = \frac{\rho U^2 D}{2}\int_{-\infty}^{t} I_{Du}(t-\tau)u(\tau) + I_{Dw}(t-\tau)w(\tau)d\tau. \tag{19}$$

Where I_{Du} and I_{Dw} are the aerodynamic impulse functions in along wind and across wind directions respectively. The effects over the tower and blade tip of the three models for different wind speeds can be described in figure 3 A and B, which describes the moments at those sections.

Those moments generated displacements as can seen in figure 4 A and B. With the above information the low cycle fatigue analyses can be adressed, indicating very large loads in a short period.The fatigue load over the structure can be represented as Miners Rule:

$$DI = \sum_{i=1}^{j} \frac{n_i}{N_i}. \tag{20}$$

$$\epsilon_a = \epsilon_{a,e} + \epsilon_{a,p} = \frac{\sigma_f}{E}(2N_f)^b + \epsilon_f(2N_f)^c. \tag{21}$$

Here the equation represents the LCF in the wind turbine steel tower. The LCF can affect the fiberglass material of the blade structure, conventional test-load method and simplified load stress method are the most common fatigue models for blades, the Coffin Mason ϵ-N curve describes the LCF fatigue load during hurrican at 5 A and B for fiberglass.
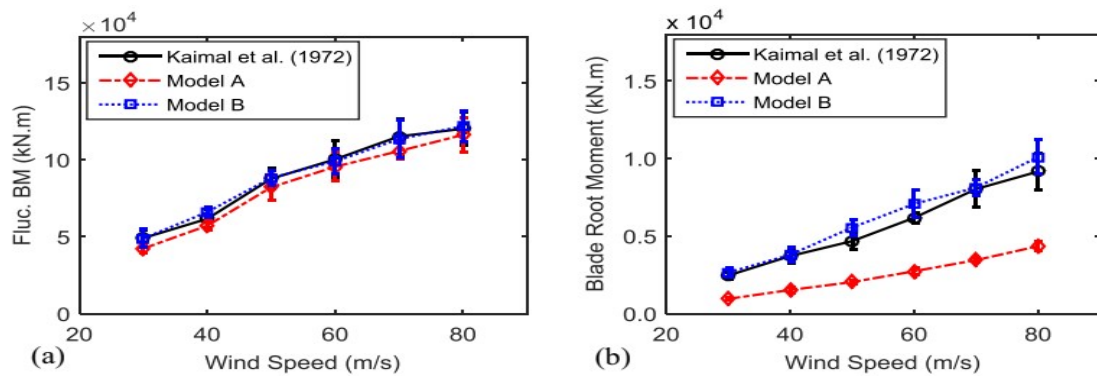
Figure 3: Mean of maximum (a) tower buffeting fore-aft base moments and (b) blade root edge-wise buffeting moment for different wind speeds at 10 m height (Amirinia and Sungmoon Jung [2017])
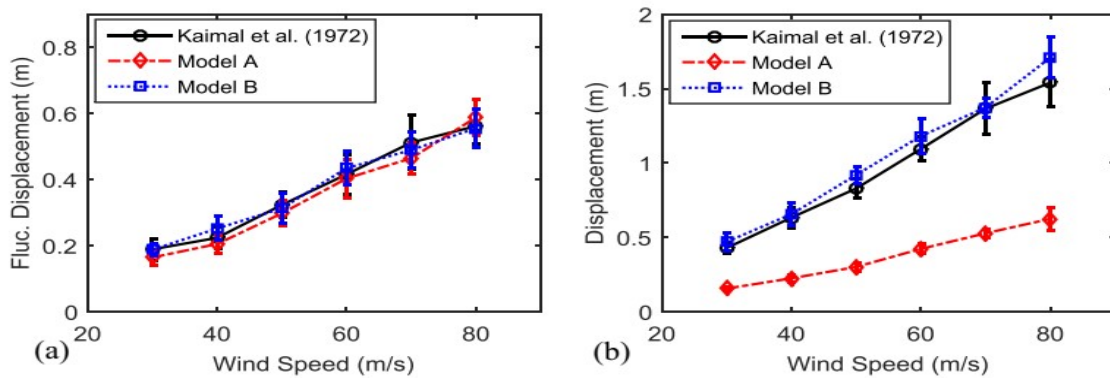
Figure 4: Mean of maximum (a) tower tip buffeting displacements and (b) blade tip displacements for different wind speeds at 10 m height(Amirinia and Sungmoon Jung [2017])
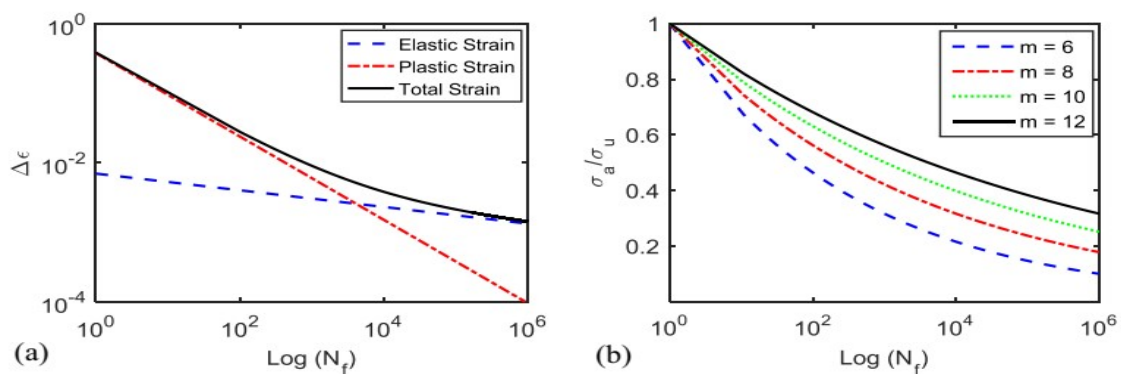

Figure 5: (a) Coffin-Manson ϵ-N curve and (b) fiberglass σ-N curve (Amirinia and Sungmoon Jung [2017])

Since the mean wind speeds and turbulence intensities of various models were identical, the mean load and accordingly the mean damage index caused by fatigue were almost the same; however, different turbulence spectrums resulted in different damage indices in buffeting responses. Authors considered 2 h of hurricane load on the wind farm location, and presented tower base

buffeting damage indices, where the spectrums Model A and Model B have average 53% smaller and 12% larger damage indices compared to Kaimal (Kaimal et al. [1972]) models.Also, the authors shows the blade root damage indices for different wind speeds and hurricane categories where spectrum Model A and Model B resulted in 96% smaller and 24% larger damage indices compared to Kaimal (Kaimal et al. [1972]) model.

Finally the authors stated that further Research is needed to address lateral fluctuation components of Model B and investigate the responses such as tower side to side moment, blade flap-wise moments, and damage indices correlated with lateral components.

In Gemilang et al. [2021]) low cycle fatigue is addressed, applied to an offshore mooring chain. In the study, a multiaxial fatigue approach was carried out, since the effects of the stress-strain state are neglected in a traditional approach, as is the case with the (S - N) method. The chain geometry was defined in accordance with the requirements stipulated by the International Association of Classification Societies (IACS), using R4 steel grade material for its manufacture. The numerical solution, using the Finite Element Method (FEM), was carried out with the aid of the commercial software ABAQUS, being modeled the problem in a simplified way, taking advantage of the symmetry presented by the geometry of the chain. The model called Mono-Rampi, based on bilinear isotropic hardening to derive the mechanical properties of the material, is developed. From the model, it is possible to establish a prediction of the elastoplastic behavior of the material, through a stress-strain curve, as shown in the Figure 6.
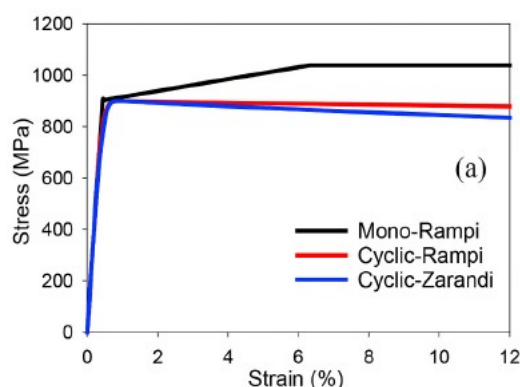
Figure 6: Stress strain curve for bilinear monotonic material model under monotonic loading (Gemilang et al. [2021])

To evaluate the cyclic behavior of the material, the Chaboche constitutive model in linear is used, based on combined isotropic-kinematic hardening, which allows to obtain the behavior of the material for low cycle fatigue. The material response is shown in Figure 7.

To achieve the objectives of the study, the fatigue model based on the critical plane, proposed by Smith-Watson-Topper (SWT) was used. In this method, the fatigue damage is assessed directly in terms of local strains and stresses under progressive loading cycles. The SWT model can be written as follows:

$$SWT = \sigma_{n,max} \frac{\Delta \epsilon_n}{2},\tag{22}$$

where *SWT* is the damage parameter, $\sigma_{n,max}$ is the maximum normal stress and $\Delta \epsilon_n$ is the normal strain range perpendicular to the critical plane during one cycle.

From Equation 23, a relationship is established which allows estimating the life until failure of the material. The formula based on the SWT model has the following form:
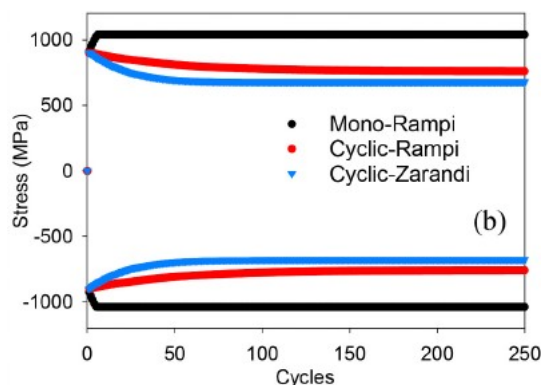
Figure 7: Evolution of the stresses with the number of cycles for Chaboche cyclic material model under cyclic loading (Gemilang et al. [2021])

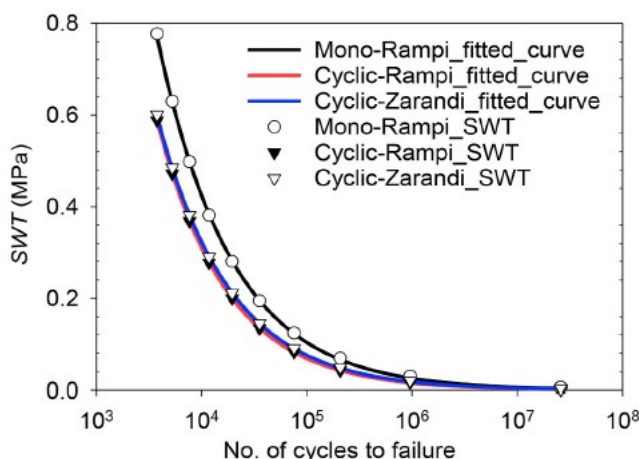$$SWT = A_1 N_f^{a_1} + A_2 N_f^{a_2}, \qquad (23)$$

where N_f represent the number of cycles to failure, the constants A_1, A_2, a_1, a_2 are material characteristic, determined by calibration tests from experimental data.

Figure 8: Fatigue life of mooring chains for the SWT (Gemilang et al. [2021])

Gemilang et al. [2021] perform simulations to estimate loads of the mooring line of an FPSO, in a given configuration, for different sea conditions. They make a prediction of low cycle fatigue life, considering the critical plane, the effects of cyclic plasticity and the mean load.

In the work by Song et al. [2021] Continuous Damage Mechanics combined with the cyclic plasticity model is used to evaluate the Low Cycle Fatigue failure of a 10CrNi3MoV steel and its undermached welding. The investigation takes an experimental and numerical approach, using the constitutive Lemaitre-Chaboche model with kinematic hardening. Hysteresis loops are obtained, evaluating the evolution of the maximum and minimum stress, as well as the accumulative plastic strain per cycle for different stress levels obtained. The material used in the investigation was quenched and tempered, and the V-groove joints were fabricated using the Single Pulse Gas Metal Arc (SPGMAW) welding process. Cylindrical specimens were used, which were subjected to a heat treatment to eliminate potential residual stresses. Tests were carried out to estimate the Low Cycle Fatigue (LCF) life, for which an Instro testing machine equipped with strain gauges

was used. The commercial program of Finite Element Analysis (FEA) ABAQUS, was used for the numerical analysis, being implemented a routine to describe the yield surface, considering nonlinear isotropic and kinematic hardening. The yield surface can be represented by the following expression:

$$f(\sigma - \alpha) = \sqrt{\frac{3}{2}(S - \alpha^{dev})) : (S - \alpha^{dev})}, \tag{24}$$

where, σ is the stress tensor, α^{dev} is strands for the deviatoric part of the back stress tensor and S is the deviatoric stress tensor.

Song et al. [2021], establish that the evolution of damage, under cyclic loading, can be measured through the variation of the Young's modulus, for this a relationship between elasticity, plasticity and damage is proposed, through the following expressions:

$$D_i = 1 - \frac{E_i}{E'}, \tag{25}$$

where, D_i represents the ith cycle, E' is the initial Youngâs modulus, and E_i is the apparent Youngâs modulus of the ith cycle.

$$D_i = 1 - \frac{\Delta w_i}{\Delta w_0}, \tag{26}$$

where Δw_i the apparent hysteresis energy density of the ith cycle, Δw_0 is the hysteresis energy density after cyclic softening.

The initiation of damage for ductile materials subjected to LCF is related to the cyclic hysteresis energy which can be represented as follows:

$$N_0 = c_1 \cdot \Delta w_0^{c_2}, \tag{27}$$

where N_0 refers to the number of cycles of the damage initiation and Δw_i is the hysteresis energy density of the stabilized cycle. The parameters c_1, c_2 are the material constants, which are fitted from the experimental tests. The linearized Equation 27 can be written as:

$$log(N_0) = c_2 log(\Delta w_0) + log(c_1), \tag{28}$$

here, N_0 stands for the numbers of the cycle before hysteresis loop stabilization according to experimental data.

Another important aspect to be described is the damage evolution, in this study a relationship based on the plastic hysteresis energy density is proposed, represented by the following equation:

$$\frac{dD}{dN} = \frac{c_3 \Delta w^{c_4}}{L}, \tag{29}$$

where Δw is the average of the plastic hysteresis energy density of the stabilized cycle. The constants c_3 and c_4 represent the material properties. L is the characteristic length associated with an integration point.

Analogously to the initiation of damage, it is possible to obtain the parameters c_3 and c_4, through the following expression:

$$log(N_e) = log(\frac{L}{c_3} \Delta D) - c_4 log(\Delta w). \tag{30}$$

After obtaining the constants c_3 and c_4, by means of a curve fitting, it is possible to obtain a final fatigue life equation

$$N_f = c_1 \cdot \Delta w_0^{c_2} + \frac{L}{c_3 \cdot \Delta w^{c_4}} \cdot \frac{1}{(1 - c_4)}. \tag{31}$$

The comparisons of the experimental and numerical results of the first hysteresis cyclic stress–strain curves of 0.6% and 0.8% are shown in Figure 9 for the metal base and Figure 10 for undermatched welds. The stable hysteresis loop at half-life cycle from the strain range from 0.6% to 1.2% for base metal and weldments is presented in Figure 11. The fatigue life prediction performed by Song et al. [2021] can be seen in the Figure 12.
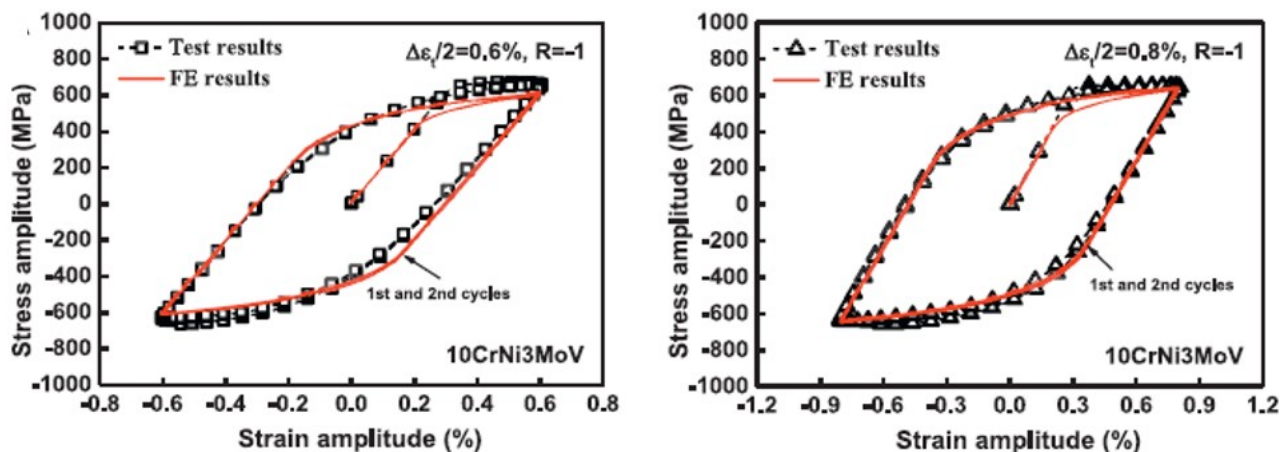
Figure 9: Experimental and simulation comparisons for metal base (10CrNi3MoV steel) (Adapted from Song et al. [2021])
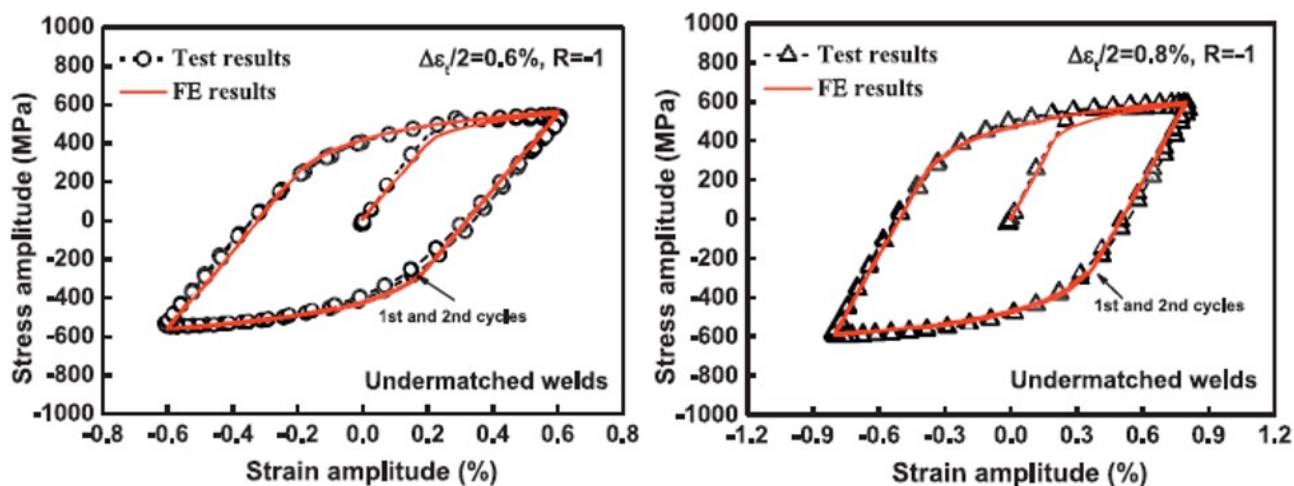
Figure 10: Experimental and simulation comparisons for undermatched welds (Adapted from Song et al. [2021])

5   Identification of new potential problems in Low Cycle Fatigue

One of the main purposes of this review is search for novel problems related to LCF in Ocean Engineering, two cases are described above, this work doesn't intend to give a solution, the authors are working in the analyses of those issues and pretend to give more details in future works.
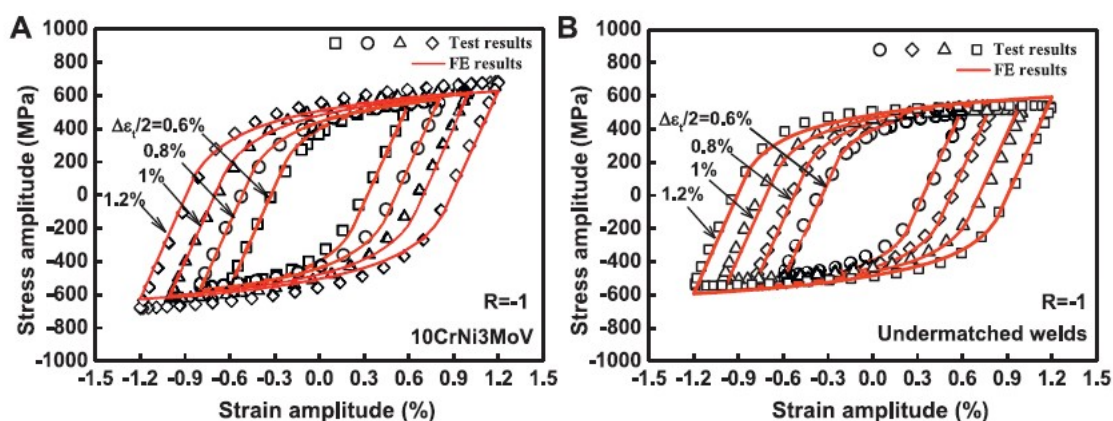
Figure 11: Experimental data and simulation results of hysteresis loops at the half-life cycle for specimens (Adapted from Song et al. [2021])
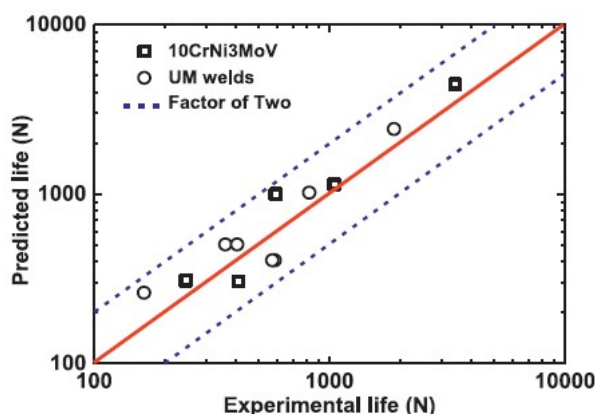
Figure 12: Fatigue life prediction of different materials (Adapted from Song et al. [2021])

5.1 Problem for an Offshore structure: Internal Oceanic Waves (IOW)

The potential problems associated to LCF in offshore systems are intrinsically dependent on the characteristics of oceanic environment forcings. In this context, (IOW) represent the most energetic high-frequency event in coastal oceans, as well as in ocean basins. The amplitude of typical IOWs can reach tens of meters, acting as an important generation mechanism for currents and turbulence (Pomar et al. [2012]). The IOWs develop in the density gradient of the permanent thermocline, the lower limit of the oceanic mixture layer.

The main generating mechanism of these waves is the tidal current excitation over the deep oceanâs density structure. For this reason, they are commonly called internal tides (Apel et al. [1995]). Oceanic thermoclines occur at varying depths (usually between 20 and 600 m), with density gradients of the order of 10^{-2} to 10^{-3} $kg/m^3/m$, generating Brunt-Väisälä periods of the order of 100 to 300 s. The combination of high fundamental periods with low vertical velocity gradients means that the Richardson numbers of these environments can frequently exceed the unit by far.

The interactions between the moving thermocline and the topographic irregularities of the continental shelf can cause resonant effects or the eventual break of internal tides. This gives rise to another type of oscillatory phenomenon, with frequencies close to those of Brunt-Väisälä waves,

so-called internal solitary waves (ISWs). ISWs are characterized by being nonsinusoidal and nonlinear and by presenting themselves in the form of isolated groups of complex shape, generated periodically according to the internal tides. These groups generally present 3 to 12 ISWs with decreasing amplitudes (Apel [2002]), as described in Figure 13. Garrett and Munk [1979] provide an extensive review of the physical properties of internal oceanic waves.
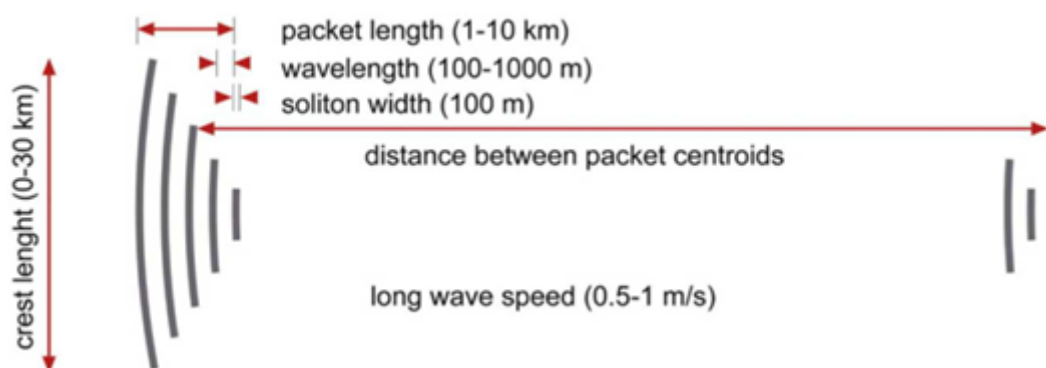
Figure 13: Typical horizontal dimensions associated to the groups of ISWS (Apel [2002])

Unlike internal tides, ISWs generate short waves (wavelengths varying from 10^2 to 10^3 m) that sharply alter the free-surface roughness, allowing their detection by Synthetic Aperture Radar (SAR) satellite images. In Figure 14 Jackson and Apel [2004] illustrate how widely distributed this phenomenon is, being especially relevant in regions where the existence of expressive astronomical tides and extensive continental shelfs are combined.
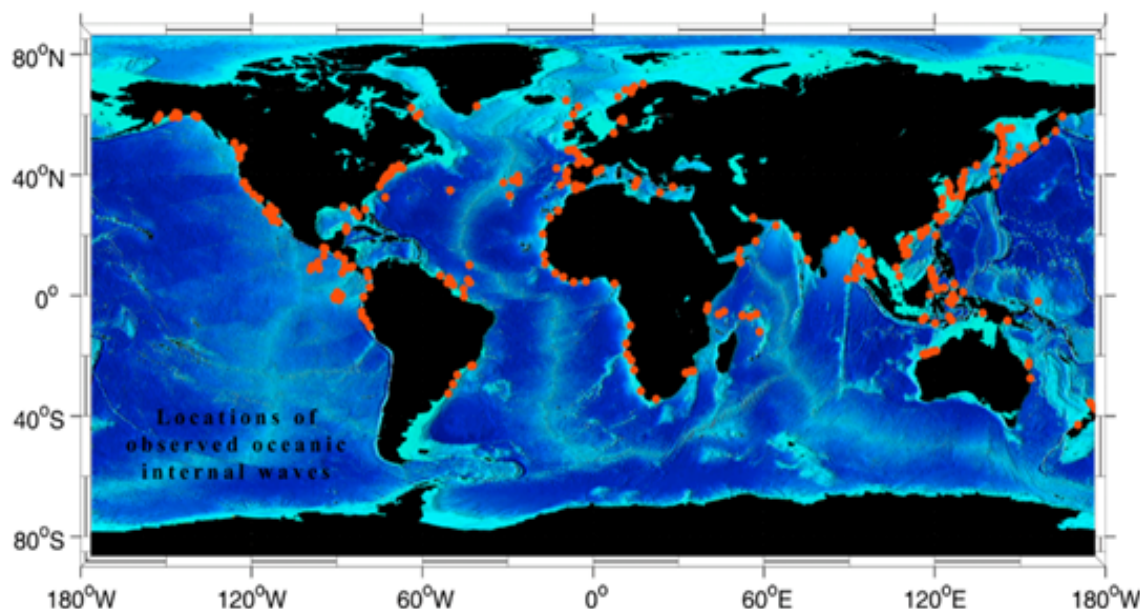
Figure 14: Localization of observed OIW and ISW making use of SAR satellite images(Jackson and Apel [2004])

In the sense of achieving a better understanding about the formation and propagation of ISWs packets, as well as to describe its vertical velocity structure, computational fluid dynamics technics represent a powerful tool. Figures 15 were obtained using a set of computational models developed

under the Delft3D platform in the works of Molinas [2020] and Molinas et al. [2020] and represent a hypothetical situation that resembles the typical characteristics of the ISWs packets that are formed on the Amazon continental shelf (a worldwide hotspot for this phenomenon). Figure 15 (panel A) illustrates the surface signature of two consecutive ISWs packets moving away from their formation zone in the shelf break (propagation to the right). The panel B of the same figure highlights the crests and troughs of the nine ISW that form the packet to the left in the panel A.

Figure 16 shows the vertical structure of the horizontal currents associated to the passage of one these ISWs packets. In comparison with Figure 15, it is important to notice that every water surface crest in Figure 15 corresponds to a thermocline trough in Figure 16 (black lines represent isopicnal surfaces). Antagonistic behaviors occur above and below the pycnocline.
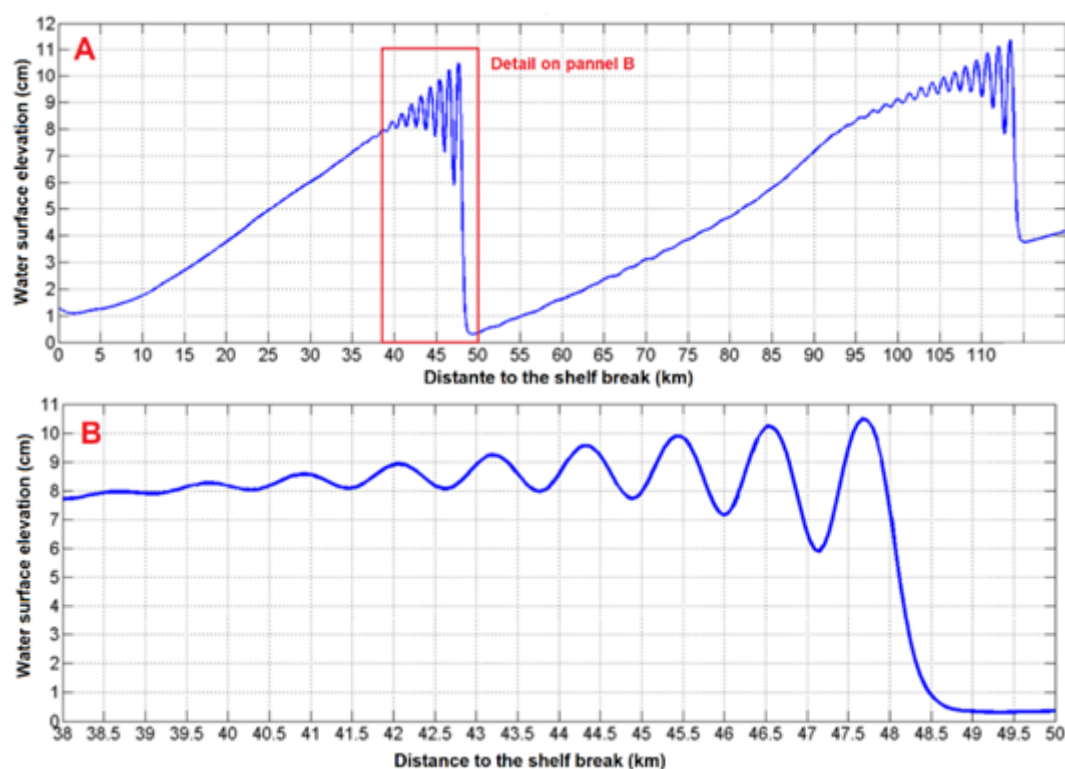
Figure 15: Surface signature of the passage of two consecutive ISWS packets (Molinas [2020] and Molinas Molinas et al. [2020])

In the upper layer (0 to 140 m depth), water surface crests (pycnocline troughs) correspond to regions where the horizontal currents achieve their maximum velocities (up to 40 cm/s in the first wave of the packet), coinciding with the direction of wave propagation. Water surface troughs (pycnocline crests), for instance, represent regions of minimum velocities, still in the direction of wave propagation but with intensities below 10 cm/s.

In the bottom layer (140 to at least 600 m depth), water surface crests (pycnocline troughs) correspond to regions of minimum horizontal currents, achieving values of -10 cm/s, thus in the opposite direction of wave propagation. Water surface troughs (pycnocline crests), for instance, represent regions of local maximum velocities, still in the direction of wave propagation but with intensities in the order of 10 cm/s.

This complex 2DV patterns of oscillatory horizontal velocities area capable of generating major load on structures, especially in what concerns LCF, in the case of risers, flexibles, and mooring systems those waves can potentially produce phenomenon associated to Vortex Induced Vibration (VIV). In general, what we expect is the generation of nearly 10 cycles per semidiurnal
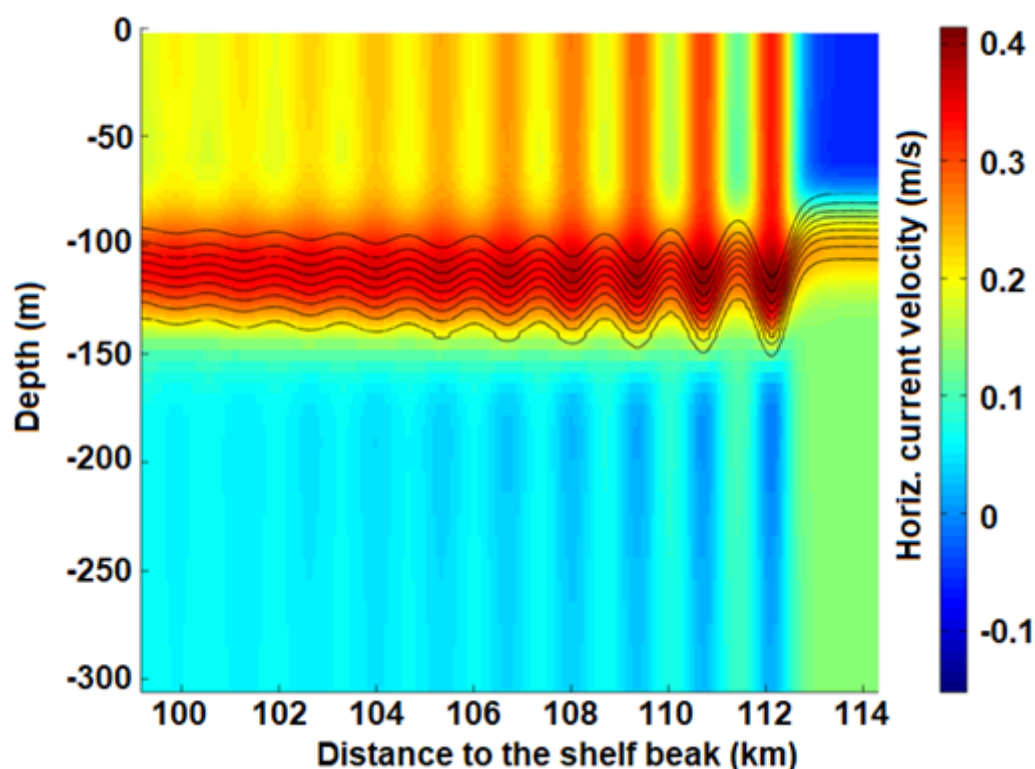
Figure 16: 2DV structure of the horizontal current velocities associated to the passage of a ISWS packet (Molinas [2020] and Molinas et al. [2020]).

tide, what would represent a basis of 7,300 cycles per year or more than 200,000 cycles if we consider a 30-year lifetime for a structure.

5.2   Problem for an Offshore structure: fatigue damage at the touchdown

In ocean engineering, various risers are crucial in the oil and gas (O&G) production systems, conveying the multi-phase flows from the seabed to the floating platform. As a result, the marine risers often need to suffer from complex excitations, including the wave-frequency (WF) responses and low-frequency (LF) drift of the vessel, vortex-induced motion (VIM), and VIV. In addition, the seabed and internal flows could also impact the behavior of the riser. Therefore, there would be plenty of sources for fatigue damage of risers. The fatigue damage at the touchdown zone (TDZ) of the steel catenary riser (SCR) is critical and has recently been paid much attention.

As the O&G exploitation steps into deeper water, the application of SCR becomes wider due to its excellent combined performances of reliability and economy. However, as illustrated in Figure 16, the touchdown point (TDP) between the riser and seabed is found to be more susceptible to appear stress concentration which leads to fatigue damage. According to the subsea survey by remote operating vehicles (ROV), the trench will be generated beneath the SCR with a depth of several riser diameters due to the riser-soil interaction.

Langner Langner [2003] investigated this self-trenching phenomenon of an SCR at the TDP of soft seafloor. By comparing the fatigue damages with rigid seafloor, the curved trench was found to reduce the fatigue risk at the TDP. The riser-soil interaction model, Randolph and Quiggin [2009] proposed a non-linear hyperbolic function to model the seabed resistance forces due to the penetration. With such a function, the high stiffness on reversal forces due to the small cyclic displacements, and the asymptotic behavior with limiting penetration and uplift resistance, can be

captured in the analysis of riser-soil interaction.

To deal with the conventional linear soil model, Hejazi and Kimiaei [2016] introduced the âequivalent linear soil stiffnessâ instead of the complex and time-consuming nonlinear riser-soil interaction model. The stress ranges corresponding to different SCRs were compared between the proposed linear soil model with equivalent stiffness and the nonlinear soil model. A simplified hyperbolic formulation of the equivalent linear stiffness was provided, which was noted insufficient in considering abundant geometrical parameters, irregular motions at different sea states, and trench formation. To improve the efficiency, Qu [2015] proposed a simplified approach to deduce the dynamic responses of the SCR by the dynamic amplification factors (DAFs). Meanwhile, the performance of this approach was found dependent on the fitness of DAF evaluation. Therefore, sensitivity studies were conducted to provide quantitative guidance in estimating DAFs and other parameters.

In view of the limitations of linear riser-soil interaction (RSI) model, many research determined to develop the nonlinear RSI model. Wang et al. (Song et al. [2021], Wang et al. [2013]) introduced a TDZ element into the riser-soil interaction simulation to improve the accuracy of the fatigue analysis at the TDZ.

The influences of seabed stiffness, soil suction forces, mudline shear strength and trench depth were investigated on the fatigue damage, applying the linear hysteretic riser-soil interaction model with TDZ element. As a result, the large seabed stiffness and mudline shear were found harm to the fatigue life of the SCR, while the large soil suction and trench depth were found in favor of the fatigue life. Later, Wang et al. [2013] conducted a large-scale model test of a truncated SCR, where the two-dimensional (2D) in plane motion was imposed at the upper truncated point of the SCR and its impacts on the fatigue damage were investigated.

In the tests, both the in-plane and out-of-plane VIV was induced by the 2D motion, while their influences on the fatigue damage were found dependent on the amplitude and period of the motion. Three critical locations of maximum fatigue damage were concluded by the model tests, namely the TDP, upper sag-bend and top of the SCR.

Similarly, Yuan et al. [2021] carried out experiments to investigate the riser-soil interaction at the TDZ, considering the VIV of the SCR. Both the length and depth of the trench was shown to enlarge with severe heave excitation, while the heave level had less influence on the trench location. Meantime, the VIV was exhibited to make the trench depth growing more smoothly. To predict the fatigue damage of SCR coupling with in-line (IL) and cross-flow (CF) VIV, Wang et al. [2014] further established a time domain approach based on the Euler-Bernoulli equation with empirical hydrodynamic coefficients input.

The previous mentioned (Wang et al. [2015]) riser-soil interaction model was adopted in the simulations which investigated the effects of IL and CF VIV on the fatigue damage of the SCR along the TDZ. Regarding the impacts of trench formation on fatigue damage in the TDZ, Shiri [2014] revealed that the final fatigue damage was independent on the order of the applied waves and the number of the applied wave cycles, given initially created trench. Also, the peak fatigue damage was no longer controlled by the maximum shear force once a trench was created initially.

Substantially, the fatigue of SCR is caused by the cyclic elastic-plastic-damage of the structure. To investigate the constitutive behavior of a next-generation SCR material, i.e. X100Q, Devaney et al. [2018] employed experimental and numerical methods, respectively, which captured the two-stage fatigue damages, namely the early-stage microcracking damage and the secondary damage accumulation. Integrating the low-Cycle fatigue (LCF) and high-Cycle fatigue (HCF) models, the effects of strain range on the damage evolution was predicted successfully.

Also, the interdependency was revealed between the material degradation induced by fatigue damage and the cyclic plasticity at the weld for a range of load cases. To clarify the influences of trench on fatigue damage at the TDP, Shoghi and Shiri [2019] investigated the dependency of

fatigue damage on the variable TDZ in the trench, due to the low-frequency drift of the vessel using both analytical and numerical approaches. The peak fatigue damage was found decreased in the far offset zone (FOZ), while increased in the near offset zone (NOZ), as illustrated in Figure 17.
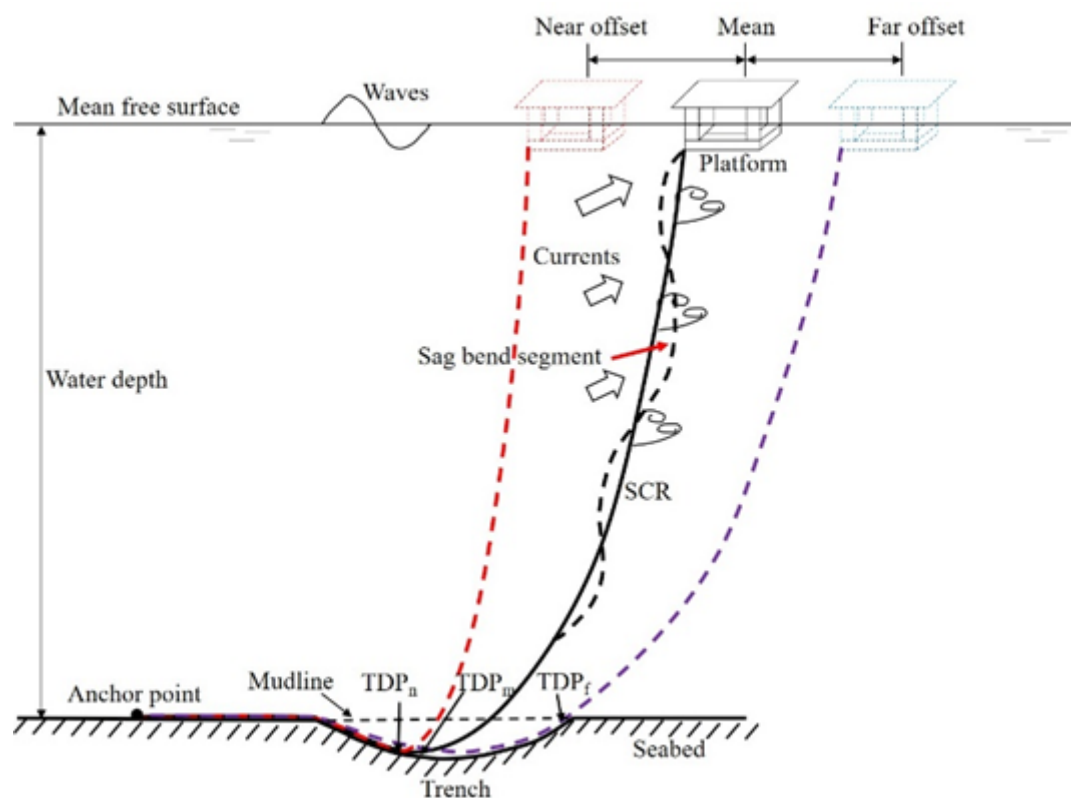
Figure 17: The schematic view of the SCR considering soil-riser interaction

Also, the fatigue damage variation due to the trench effect was found dependent on the direction of the predominant fatigue sea states and the low-frequency excursion of the vessel.

6   Concluding Remarks

This chapter presents an updated compilation of works related to Low Cycle Fatigue and its application in the context of naval and offshore engineering. A series of contributions published in important scientific journals and relevant congress proceedings were described. The text was structured in a friendly way and an easy-to-understand language so that it can contribute, especially for researchers who wish to start studies in the context of Low Cycle Fatigue. Furthermore, a review of theoretical aspects was carried out, fundamentally softening numerical and experimental aspects. The identification of potential problems related to Low Cycle Fatigue, in the context of offshore structures, were presented, in order to encourage the investigation and approach of these and other issues related to the main theme of the text.

Fatigue failure of marine structures can cause catastrophic social,environmental, and economic damage. Studying novel problems related to LCF in naval and offshore structures can avoid potential accidents and improve safety in those systems. Future works aim to study the potential of IOWs effects on naval and offshore structures, especially risers, umbilical, and mooring systems.

Acknowledgements

References

A. Pipinato. *Innovative Bridge Design Handbook*. Elsevier, 2nd editio edition, 2022. ISBN 9780128235508.

G. Amirinia and Sungmoon Jung. Buffeting response analysis of offshore wind turbines subjected to hurricanes. *Ocean Engineering*, 141(April):1–11, 2017. ISSN 00298018. doi: 10.1016/j. oceaneng.2017.06.005.

J. Apel. *Atlas of Oceanic Internal Solitary Waves*. 2002.

J. Apel, Ostrovsky, S. L.A., and Y.A. Internal solitons in the ocean. The Journal of the Acoustical Society of America 98. *The Journal of the Acoustical Society of America*, 98(2863â2864), 1995.

R. Beesley, H. Chen, and M. Hughes. A novel simulation for the design of a low cycle fatigue experimental testing programme. *Computers and Structures*, 178:105–118, 2017. ISSN 00457949. doi: 10.1016/j.compstruc.2016.09.004. URL http://dx.doi.org/10. 1016/j.compstruc.2016.09.004.

A. Benoit, L. Rémy, A. Köster, H. Maitournam, and F. Oger. Experimental investigation of the behavior and the low cycle fatigue life of a welded structure. *Materials Science and Engineering A*, 595:64–76, 2014. ISSN 09215093. doi: 10.1016/j.msea.2013.11.082. URL http://dx. doi.org/10.1016/j.msea.2013.11.082.

X. Cahís, E. Simon, D. Piedrafita, and A. Catalan. Core behavior and low-cycle fatigue estimation of the Perforated Core Buckling-Restrained Brace. *Engineering Structures*, 174(June):126–138, 2018. ISSN 18737323. doi: 10.1016/j.engstruct.2018.07.044.

J. A. F. O. Correia, P. Raposo, M. Muniz-calvente, S. Blasón, G. Lesiuk, A. M. P. D. Jesus, P. M. G. P. Moreira, R. A. B. Calçada, and A. F. Canteli. A generalization of the fatigue Kohout-VeËchet model for several fatigue damage parameters. *Engineering Fracture Mechanics*, 185: 284–300, 2017. ISSN 0013-7944. doi: 10.1016/j.engfracmech.2017.06.009. URL https: //doi.org/10.1016/j.engfracmech.2017.06.009.

W. Cui. A state of the art review on fatigue life prediction methods for metal structures. *Marine Science annd Technology*, 2002.

R. J. Devaney, P. E. O. Donoghue, and S. B. Leen. Experimental characterisation and computational modelling for cyclic elastic-plastic constitutive behaviour and fatigue damage of X100Q for steel catenary risers. *International Journal of Fatigue*, 116(February):366–378, 2018. ISSN 0142-1123. doi: 10.1016/j.ijfatigue.2018.06.032. URL https://doi.org/10.1016/j. ijfatigue.2018.06.032.

C. Garrett and W. Munk. Internal waves in the ocean. *Annu. Rev. Fluid Mech.*, 11(1):339–369, 1979.

G. M. Gemilang, P. A. Reed, and A. J. Sobey. Low-cycle fatigue assessment of offshore moor-ing chains under service loading. *Marine Structures*, 76(August 2020):102892, 2021. ISSN 09518339. doi: 10.1016/j.marstruc.2020.102892. URL https://doi.org/10.1016/j.marstruc.2020.102892.

B. Hamidi Ghaleh Jigh, H. Hosseini-Toudeshky, and M. A. Farsi. Low cycle fatigue analyses of open-celled aluminum foam under compressionâcompression loading using experimental and microstructure finite element analysis. *Journal of Alloys and Compounds*, 797:231–236, 2019. ISSN 09258388. doi: 10.1016/j.jallcom.2019.05.158. URL https://doi.org/10.1016/j.jallcom.2019.05.158.

C. Han, X. Qu, Y. Ma, and D. Shi. Experimental and Numerical Study of Fatigue Damage Assess-ment under Combined High and Low Cycle Loading. *Shock and Vibration*, 2018, 2018. ISSN 10709622. doi: 10.1155/2018/9045658.

R. Hejazi and M. Kimiaei. Equivalent linear soil stiffness in fatigue design of steel catenary risers. *Ocean Engineering*, 111:493–507, 2016. ISSN 0029-8018. doi: 10.1016/j.oceaneng.2015.11.027. URL http://dx.doi.org/10.1016/j.oceaneng.2015.11.027.

K. Hou, M. Ou, M. Wang, X. Hao, Y. Ma, and K. Liu. Low cycle fatigue and high cycle fa-tigue of K4750 Ni-based superalloy at 600 Â°C: Analysis of fracture behavior and deformation mechanism, 2021. ISSN 09215093.

S. V. J. Kohout. A new function for fatigue curves characterization and its multiple merits. 1123 (00), 2001.

C. Jackson and J. Apel. *An atlas of internal solitary-like waves and their properties*. 2004.

L. J. Jia and H. Ge. *Ultra-low-cycle fatigue failure of metal structures under strong earth-quakes. Chapter 2 Stress-strain behaviors in large plastic strain ranges under monotonic load-ing*. 2019. ISBN 978-981-13-2660-8. URL http://link.springer.com/10.1007/978-981-13-2661-5.

W. Jiang and P. Yang. Experimental studies on crack propagation and accumulative mean strain of cracked stiffened plates under low-cycle fatigue loads. *Ocean Engineering*, 214(February): 107744, 2020. ISSN 00298018. doi: 10.1016/j.oceaneng.2020.107744. URL https://doi.org/10.1016/j.oceaneng.2020.107744.

Z. Jiang, Z. Han, and M. Li. A probabilistic model for low-cycle fatigue crack initiation under vari-able load cycles. *International Journal of Fatigue*, 155(September 2021):106528, 2022. ISSN 01421123. doi: 10.1016/j.ijfatigue.2021.106528. URL https://doi.org/10.1016/j.ijfatigue.2021.106528.

J. M. Jonkman and D. Matha. Dynamics of offshore floating wind turbines â analysis of three concepts. *Wind Energy*, (January):557–569, 2011. doi: 10.1002/we.442.

J. C. Kaimal, Y. Izumi, and O. Coté. Spectral characteristics of surface-layer turbulence. pages 563–589, 1972.

C. G. Langner. Offshore Technology Conference 2003. In *Fatigue Life Improvement of Steel Catenary Risers due to Self-Trenching at the Touchdown Point*, Houston, 2003.

J. H. Lee, P. Dong, and M. H. Kim. Low-cycle fatigue evaluation for girth-welded pipes based on the structural strain method considering cyclic material behavior. *International Journal of Naval Architecture and Ocean Engineering*, 12:868–880, 2020. ISSN 20926790. doi: 10.1016/j.ijnaoe.2020.08.005. URL https://doi.org/10.1016/j.ijnaoe.2020.08.005.

Z. Li, J. Li, Z. Chen, J. Guo, Y. Zhu, and Y. Luo. Experimental and computational study on thermo-mechanical fatigue life of aluminium alloy piston. *Fatigue and Fracture of Engineering Materials and Structures*, 44(1):141–155, 2021. ISSN 14602695. doi: 10.1111/ffe.13342.

B. Ligaj and G. Szala. Comparative analysis of fatigue life calculation methods of C45 steel in conditions of variable amplitude loads in the low-and high-cycle fatigue ranges. *Polish Maritime Research*, 19(4):23–30, 2012. ISSN 12332585. doi: 10.2478/v10012-012-0037-z.

E. Molinas. *Marés internas e dinâmica sedimentar na plataforma continental amazônica.* PhD thesis, Federal University of Rio de Janeiro., 2020.

E. Molinas, J. Carneiro, , and S. Vinzon. Internal tides as a major process in Amazon continental shelf fine sediment transport. *Marine Geology*, 430(106360), 2020.

W. Neville and P. Sachs. *Practical Plant Failure Analysis.* 2020. ISBN 9781138324114.

A. Orlando, L. Pagnini, and M. P. Repetto. Structural response and fatigue assessment of a small vertical axis wind turbine under stationary and non-stationary excitation. *Renewable Energy*, 170:251–266, 2021. ISSN 0960-1481. doi: 10.1016/j.renene.2021.01.123. URL https://doi.org/10.1016/j.renene.2021.01.123.

L. Pomar, M. Morsilli, P. Hallock, and B. Bádenas. Internal waves, an under-explored source of turbulence events in the sedimentary record. *Earth Sci.*, 111(1):56–81, 2012.

L. M. Qu. *EStimating the Fatigue Damage of Steel Catenary Risers.* PhD thesis, 2015.

M. Randolph and P. Quiggin. Non-linear Hysteretic Seabed Model For Catenary Pipeline Contact. In *International Conference on Ocean, Offshore and Artic Engineering 2009, Honolulu, USA, OMAE2009-79259*, 2009.

L. Shaohu, Z. Hao, X. Hui, and G. Quanquan. A new theoretical model of low cycle fatigue life for coiled tubing under coupling load. *Engineering Failure Analysis*, 124(February):105365, 2021. ISSN 13506307. doi: 10.1016/j.engfailanal.2021.105365. URL https://doi.org/10.1016/j.engfailanal.2021.105365.

S. M. H. Sharifi, H. Saeidi Googarchin, and F. Forouzesh. Three dimensional analysis of low cycle fatigue failure in engine part subjected to multi-axial variable amplitude thermo-mechanical load. *Engineering Failure Analysis*, 62:128–141, 2016. ISSN 13506307. doi: 10.1016/j.engfailanal.2016.01.003.

A. Sharma, M. C. Oh, and B. Ahn. Recent Advances in Very High Cycle Fatigue Behaviour of Metals and Alloys- A Review, 2020.

H. Shiri. In fl uence of seabed trench formation on fatigue performance of steel catenary risers in touchdown zone. *Marine Structures*, 36:1–20, 2014. ISSN 0951-8339. doi: 10.1016/j.marstruc.2013.12.003. URL http://dx.doi.org/10.1016/j.marstruc.2013.12.003.

R. Shoghi and H. Shiri. Modeling touchdown point oscillation and its relationship with fatigue response of steel catenary risers. *Applied Ocean Research*, 87(March):142–154, 2019. ISSN 0141-1187. doi: 10.1016/j.apor.2019.03.010. URL `https://doi.org/10.1016/j.apor.2019.03.010`.

W. Song, X. Liu, J. Xu, Y. Fan, D. Shi, F. Yang, X. Xia, F. Berto, and D. Wan. Low-Cycle Fatigue Life Prediction of 10CrNi3MoV Steel and Undermatched Welds by Damage Mechanics Approach. *Frontiers in Materials*, 8(April):1–15, 2021. ISSN 22968016. doi: 10.3389/fmats.2021.641145.

M. A. Wahab, I. Hilmy, and R. Hojjati-Talemi. On the use of low and high cycle fatigue damage models. *Key Engineering Materials*, 569-570:1029–1035, 2013. ISSN 16629795. doi: 10.4028/www.scientific.net/KEM.569-570.1029.

J. Wang, S. Fu, R. Baarholm, J. Wu, and C. Martin. Fatigue damage of a steel catenary riser from vortex-induced vibration caused by vessel motions. *Marine Structures*, 39:131–156, 2014. ISSN 0951-8339. doi: 10.1016/j.marstruc.2014.07.002. URL `http://dx.doi.org/10.1016/j.marstruc.2014.07.002`.

K. Wang, H. Xue, and W. Tang. Time domain prediction approach for cross-flow VIV induced fatigue damage of steel catenary riser near touchdown point. *Elsevier*, 43:166–174, 2013. ISSN 0141-1187. doi: 10.1016/j.apor.2013.09.003. URL `http://dx.doi.org/10.1016/j.apor.2013.09.003`.

K. Wang, W. Tang, and H. Xue. Time domain approach for coupled cross- fl ow and in-line VIV induced fatigue damage of steel catenary riser at touchdown zone. *Marine Structures*, 41 (800):267–287, 2015. ISSN 0951-8339. doi: 10.1016/j.marstruc.2015.02.004. URL `http://dx.doi.org/10.1016/j.marstruc.2015.02.004`.

J. Xu, S. Benson, and B. Wetenhall. Comparative analysis of fatigue life of a wind turbine yaw bearing with different support foundations. *Ocean Engineering*, 235(October 2020):109293, 2021. ISSN 0029-8018. doi: 10.1016/j.oceaneng.2021.109293. URL `https://doi.org/10.1016/j.oceaneng.2021.109293`.

B. Yu, A. Gan, and F. J. Masters. Hurricane Wind Power Spectra , Cospectra , and Integral Length Scales. pages 411–430, 2008. doi: 10.1007/s10546-008-9316-8.

Y. Yuan, M. Zheng, H. Xue, and W. Tang. Nonlinear riser-seabed interaction response among touchdown zone of a steel catenary riser in consideration of vortex-induced vibration. *Ocean Engineering*, 227(August 2020):108891, 2021. ISSN 0029-8018. doi: 10.1016/j.oceaneng.2021.108891. URL `https://doi.org/10.1016/j.oceaneng.2021.108891`.

W. Zhang, L. Zeng, P. Gardoni, and X. Qi. Experimental investigation and low-cycle fatigue behavior of I-shaped steel bracing members with gusset plate connections. *Thin-Walled Structures*, 162(February):107593, 2021. ISSN 02638231. doi: 10.1016/j.tws.2021.107593. URL `https://doi.org/10.1016/j.tws.2021.107593`.

Chapter 8

Modeling of Damage in Turbine Blades for Large Deformations

Chapter details

Chapter DOI:

Chapter suggested citation / reference style:

Azlam, Özgür (2022). "Modeling of Damage in Turbine Blades for Large Deformations". *In* Jorge, Ariosto B., et al. (Eds.) *Fundamental Concepts and Models for the Direct Problem*, Vol. II, UnB, Brasilia, DF, Brazil, pp. 209–230. Book series in Discrete Models, Inverse Methods, & Uncertainty Modeling in Structural Integrity.

P.S.: DOI may be included at the end of citation, for completeness.

Book details

Modeling of Damage in Turbine Blades for Large Deformations

Ozgur Aslan[1*]

[1]Atilim University, Department of Mechanical Engineering, 06830, Ankara, Turkey.
E-mail: ozgur.aslan@atilim.edu.tr

[*]Corresponding author

Abstract

This chapter presents a comprehensive framework for the numerical modeling of crack crowth in single crystal turbine blades with thermal barrier coatings for large deformations. The first part presents a generalized numerical model where phase transformation is coupled with mechanics for the life-time estimation of thermal barrier coating (TBC) systems. That framework considers the oxidation induced stresses generated in a TBC which is the prime factor that can lead to failure. The second part considers the behavior of the substrate material which is a single crystal where a thermodynamically consistent constitutive model based on micromorphic continua is presented in order to simulate the regularized fatigue crack growth.

Keywords: turbine blade ; damage mechanics; cleavage, large deformations

1 Introduction

The inlet temperature of a jet engine determines its performance. Higher temperatures provides increased power and improved efficiency. In that sense, the turbine section of the engine where the highest temperatures are read is under severe thermo-mechanical loads and the life time estimation of its components such as turbine blades is of great importance. Mechanical properties of single crystals are strongly anisotropic and nonlinear. The cooling systems on the turbine such as thermal barrier coatings and cooling holes bring certain complexity to the constitutive and numerical modeling.

Depending on its service temperature and substrate material, modern turbine blades may come both with or without a coating. A TBC mainly serve as a protective system against extreme temperatures in order to improve the lifetime of the substrate material which is generally a single crystal superalloy. Since the performance of the gas turbines improves by increasing inlet temperature, a significant amount of research has been conducted focusing on the development of coated systems (Jones [1996]). Deposited on the surface of a substrate material, a TBC system is composed of two layers; a layer bonding the top-coat material to the metallic substrate and a protective top-coat (DeMasi-Marcin et al. [1990]). The top-coat (TC) material is usually a ceramic based material deposited on the bond-coat (BC), which provides the thermal insulation property to the system. In this work, the top-coat is assumed to be produced by electron beam physical vapor deposition (EB-PVD) method providing a structurally more flexible protective ceramic layer
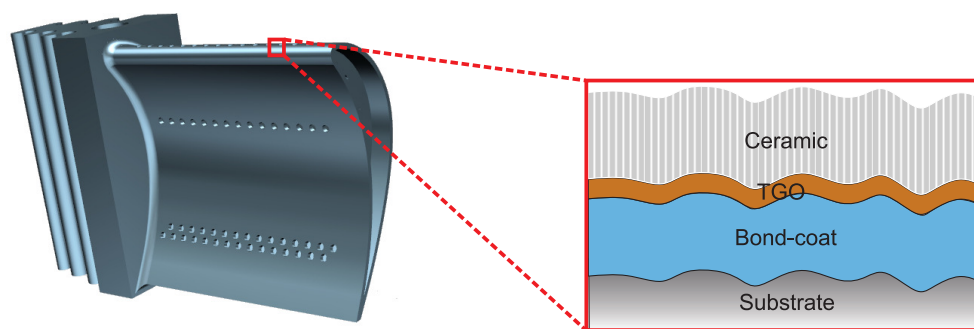
Figure 1: Gas turbine blade with TBC where a thermally grown oxide is developed in the structure.

due to the porous and columnar microstructure. That morphological structure further provides high strain compliance which improves the resistance of the coatings against failure and spallation (Vaidyanathan et al. [2000]).The metallic bond-coat acts as an intermediate layer which provides bonding and decreases the material mismatch in the case of thermal expansion. During the service life a third layer is generated between TC and BC due to the oxidation of the BC which is called thermally grown oxide (TGO) (Fig. 1). That extra layer is formed due to the chemical reaction created by inward transportation of oxygen anions and outward transportation of aluminium cations from BC. Due to the significant change in the volume of the oxide, internally high stresses are generated between BC and TC, which act as the prime failure mechanism of the TBC systems (Miller [1995]).

Considering TGO as a growing new phase in the TBC system, numerical modeling of the whole structure includes coupling of various phenomena. This multiphysics nature involves mechanical, chemical and thermal processes. There are several attempts in the literature where the growth of the TGO is modeled as a new phase in the system (Chang et al. [1987] Cheng et al. [1998] He et al. [2000, 2003] and Xu et al. [2003]). Lately, failure of the system due to chemo-thermo-mechanical nature of the problem is also studied for finite deformations (Evans et al. [2008] Ammar [2010], Loeffel et al. [2013] and Al-Athel et al. [2013]). Considering the growth of TGO, this works follows the theoretical framework presented in the authors previous modeling attempt where phase transformation is coupled with mechanics is developed for the life-time estimation of TBC systems and a modified version of the Allen-Cahn type phase field approach (Sait et al. [2020]). Despite the advances made in the simulation of the oxide growth and oxidation-induced stresses in the structure, less progress is made in modeling the damage evolution and failure simulation of TBCs. In that sense, this work introduces the continuum damage mechanics into the coupled model where a strain based damage variable is defined which directly contributes to the stretching tensor.

Considering the substrate material as a single crystal superalloy, modeling of anisotropic behavior and complex microstructure becomes essential. Apart from the TBC systems where crack initiation and the local failure of the TBC systems can be considered as the end of life time, investigation of crack propagation is more important for the substrate, since a crack may develop but not advance around a cooling hole. Therefore consideration of crack growth modeling becomes a necessity. In single crystals cracking is observed on slip systems in specific crystallographic planes following an intense shear activity under monotonic or cyclic loading conditions (Aslan et al. [2011]). In the literature, there are many modeling attempts where damage localization takes place on crystallographic planes coupled with inelastic deformations (Flouriot et al.,Parisot et al., Musienko and Cailletaud). However, conventional strain based approaches are not able to capture mesh independent localised crack thickness, since a material length scale is not introduced to cap-

ture the size-dependent phenomenon. At this front, initial modeling attempts introduces a length scale is in the plasticity theory (Aifantis [a,b]). The proposed approach is further extended in several works (de Borst and Muhlhaus, de Borst et al., Borst and Pamin [1996]) and established as so-called gradient plasticity theories (Engelen et al., Geers [a,b]). The author of this chapter also contributed this field introducing micromorphic approach to damage mechanics in several works (Aslan and Forest [2009], Aslan et al. [2011], Aslan and Bayraktar [2020],Aslan and Bayraktar [2021]). This chapter further develops the gradient damage approach for finite strains and presents the capability of the model for crack growth.

All the presented theories within the chapter are implemented for the commercial finite element program Abaqus/Standard by writing a user-element subroutine (UEL).

2 Numerical Modeling of TBCs

2.1 Kinematics

Considering a continuous and smooth function $\mathbf{x} = \boldsymbol{\chi}(\mathbf{X}, t)$ which maps the motion of a material point of body B from reference configuration denoted by $\mathbf{X}$ to the spatial point $\mathbf{x}$ of the configuration at time t; the deformation gradient, the velocity, the velocity gradient and the Jacobian read the following:

$$\mathbf{F} = \nabla\boldsymbol{\chi}, \quad \mathbf{v} = \dot{\boldsymbol{\chi}}, \quad \mathbf{L} = \text{grad}(\mathbf{v}) = \dot{\mathbf{F}}\mathbf{F}^{-1}, \quad J = \det\mathbf{F} \tag{1}$$

Following The Kröner's decomposition (Kröner [1959]), the deformation gradient can be decomposed multiplicatively as

$$\mathbf{F} = \mathbf{F}^e\mathbf{F}^i \tag{2}$$

where $\mathbf{F}^e$ represents the elastic distortion which includes the stretch and rotation and $\mathbf{F}^i$ is the inelastic distortion due to plasticity and damage. Then the velocity gradient is decomposed in the following form.

$$\mathbf{L} = \mathbf{L}^e + \mathbf{F}^e\mathbf{L}^i\mathbf{F}^{e-1} \tag{3}$$

where,

$$\mathbf{L}^e = \dot{\mathbf{F}}^e\mathbf{F}^{e-1}, \quad \mathbf{L}^i = \dot{\mathbf{F}}^i\mathbf{F}^{i-1} \tag{4}$$

The right polar decomposition of $\mathbf{F}^e$ gives,

$$\mathbf{F}^e = \mathbf{R}^e\mathbf{U}^e \tag{5}$$

where $\mathbf{U}^e$ is right stretch tensor and $\mathbf{R}^e$ is rotation tensor . The right elastic Cauchy-Green tensor is defined as,

$$\mathbf{C}^e = (\mathbf{U}^e)^2 = \mathbf{F}^{eT}\mathbf{F}^e \tag{6}$$

For the strain measure Hencky's strain is adopted,

$$\mathbf{E}^e = \ln(\mathbf{U}^e) \tag{7}$$

Following the decomposition given in equation (2), the Jacobian can also be decomposed as,

$$J = J^eJ^i, \quad J^e = \det\mathbf{F}^e > 0, \quad J^i = \det\mathbf{F}^i > 0. \tag{8}$$

The elastic and inelastic stretching and spin tensors are,

$$\mathbf{D}^e = \operatorname{sym}\mathbf{L}^e, \quad \mathbf{D}^i = \operatorname{sym}\mathbf{L}^i \tag{9}$$

$$\mathbf{W}^e = \operatorname{skew}\mathbf{L}^e, \quad \mathbf{W}^i = \operatorname{skew}\mathbf{L}^i \tag{10}$$

and the plasticity is assumed as irrotational

$$\mathbf{W}^i = 0 \tag{11}$$

The rate of inelastic deformation gradient would be

$$\dot{\mathbf{F}}^i = \mathbf{D}^i \mathbf{F}^i \tag{12}$$

The total stretching tensor can be decomposed additively into its elastic, and inelastic parts:

$$\mathbf{D} = \mathbf{D}^e + \mathbf{D}^i \tag{13}$$

Eq. (13) is further formulated separately for each layer which considers the plasticity and damage in the inelastic part. Inelastic stretching tensor can be split additively as follows:

$$\mathbf{D}^i = \mathbf{D}^s + \mathbf{D}^p + \mathbf{D}^d \tag{14}$$

where $\mathbf{D}^s$ introduces the volumetric swelling, $\mathbf{D}^p$ is due to the viscoplastic deformation and $\mathbf{D}^d$ represents the stretching due to damage. Following the work of Sait et al. [2020] the swelling $\mathbf{D}^s$ due to oxidation is defined as,

$$\mathbf{D}^s = \dot{\phi}\mathbf{S} \tag{15}$$

where ϕ is the variable for phase field, defining the TGO as a new phase, and $\mathbf{S}$ is the volumetric swelling strain tensor defined using normal, β_l, and inplane, β_t, growth parameters and $\mathbf{n}$ is the surface normal to the interface profile as follows.

$$\mathbf{S} = \beta_l \mathbf{n} \otimes \mathbf{n} + \beta_t(\mathbf{1} - \mathbf{n} \otimes \mathbf{n}) \tag{16}$$

$\mathbf{D}^p$ is composed of inelastic stretching of the bond-coat and the TGO in the interface:

$$\mathbf{D}^p = (1 - \phi)\mathbf{D}_{bc}^p + \phi\mathbf{D}_{ox}^p \tag{17}$$

where $\mathbf{D}_{bc}^p$ and $\mathbf{D}_{ox}^p$ are plastic stretching tensors for BC and the TGO respectively. For both the oxide and the bond-coat material ($i = bc, ox$) the plastic stretching is
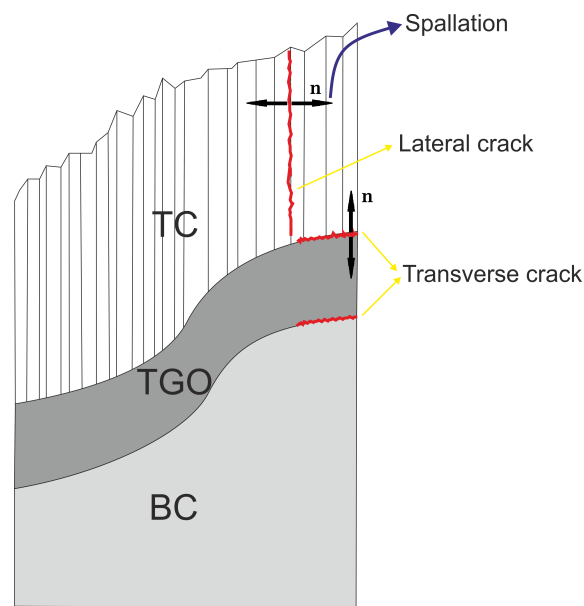
$$\mathbf{D}_i^p = \sqrt{\frac{3}{2}}\mathbf{N}^p \dot{\bar{\varepsilon}}_i^p \tag{18}$$

where the plastic flow direction is determined from,

$$\mathbf{N}^p = \frac{\mathbf{D}_i^p}{|\mathbf{D}_i^p|} \tag{19}$$

and the evolution equation for $\dot{\bar{\varepsilon}}_i^p$

$$\dot{\bar{\varepsilon}}_i^p = \dot{\varepsilon}_0 \langle \frac{\bar{\sigma} - Y_i}{S_i} \rangle^{1/m} \tag{20}$$

Figure 2: Lateral and transverse cracks in the system and spallation of the top-coat due to coalescence of the cracks.

where $\dot{\varepsilon}_0$ is the reference strain rate, Y is the plastic threshold, m is the rate sensitivity parameter and $\bar{\sigma}$ is equivalent stress which is going to be defined in the next section. In the same spirit; the damage stretching is defined as

$$\mathbf{D}^d = \dot{\bar{\varepsilon}}^d \mathbf{N}^d \tag{21}$$

where $\dot{\bar{\varepsilon}}^d$ and $\mathbf{N}^d$ are the equivalent damage strain rate and damage flow direction respectively and,

$$\mathbf{N}^d = \mathbf{n} \otimes \mathbf{n} \tag{22}$$

Considering the experimental observations in the literature (Walter et al. [2000a]), the damage is accumulated in the interface region and also in the columnar structure of the top coat (see Fig.2). Therefore, an opening mode of fracture where $\mathbf{n}$ is a predefined unit vector normal to the damage plane is adopted. Finally evolution equation for the damage variable can be chosen similar to plasticity as

$$\dot{\bar{\varepsilon}}^d = \dot{\varepsilon}_0 \langle \frac{\bar{\sigma}^d - Y^d}{S^d} \rangle^{1/m} \tag{23}$$

2.2   Balance Equations

The presented model considers several physical phenomena bringing new degrees of freedoms and balance equations which are strongly coupled. Neglecting inertial effects in the body, the balance of linear momentum can be expressed as,

$$\mathrm{Div}(\mathbf{T}_R) + \mathbf{b} = 0 \tag{24}$$

where $\mathbf{T}_R$ and $\mathbf{b}$ are the 1st Piola-Kirchhoff stress tensor and the body force vector respectively. The first Piola stress becomes,

$$\mathbf{T}_R = J\mathbf{T}\mathbf{F}^{-T} \tag{25}$$

The Mandel stress is defined in the intermediate configuration as,

$$\mathbf{M}^e = \mathbf{C}^e\mathbf{T}^e \tag{26}$$

The second Piola stress can be expressed as,

$$\mathbf{T}^e = \mathbf{F}^{e-1}\mathbf{F}^{e-T}\mathbf{M}^e \tag{27}$$

Finally, the Cauchy stress can be computed using the equation below.

$$\mathbf{T} = J^{-1}\mathbf{F}^e\mathbf{M}^e\mathbf{F}^{eT} \tag{28}$$

In this study, the moving phase is modelled as variation of a continuous model proposed by Allen-Cahn, which is an extension of the Cahn-Hilliard model (Cahn and Hilliard [1958]) used for the description of two-phase domains. Thermodynamical considerations of the approach is presented in the previous work (Sait et al. [2020]) and shall be excluded here for the sake of clarity.

For the normalized concentration of species c (for $0 \le c \le 1$) and the modified phase field ϕ (for $0 \le \phi \le 1$) balance equations are defined as,

$$\dot{c} = \text{Div}\big(\mathcal{M}\nabla(\frac{\partial\psi_0(c,\phi,\mathbf{E}^e)}{\partial c})\big) \tag{29}$$

$$\beta\dot{\phi} = \text{Div}(\boldsymbol{\alpha}\nabla\phi) - \frac{\partial\psi_0}{\partial\phi} \tag{30}$$

where ψ_0, $\mathcal{M}$, $\boldsymbol{\alpha}$ and β represent the free energy density, the mobility tensor, a tensorial and a scalar phase field parameter, respectively. Additionally, an auxiliary equation is defined with a scalar parameter π which provides the gradient of $\text{tr}(\mathbf{E}^e)$ term that takes place in the coupled equations.

$$P = \pi\text{tr}(\mathbf{E}^e) \tag{31}$$

where P is the auxiliary field variable, and $\mathbf{E}^e$ is the elastic strain tensor.

2.3   Specialization of the Constitutive equations

Following the Allen-Cahn definition of total free energy density, ψ is given by,

$$\psi(\Phi) = \psi_0(\Phi) + \frac{1}{2}\nabla\phi.(\boldsymbol{\alpha}\nabla\phi) \tag{32}$$

Considering the isotropy of the material, the free energy density can be defined in terms of $\Phi(\mathbf{E}^e, \nu, c, \phi, \nabla\phi)$ (see Sait et al. [2020]) and a specific form of free energy density as a combination of mechanical and phase field parts for isothermal analysis can be written as,

$$\psi_0(\Phi) = \psi^M(\phi, \mathbf{E}^e) + \psi^\phi(\phi, c) + \psi^P(\phi, \mathbf{E}^e, c) \tag{33}$$

with mechanical part of the free energy density defined as,

$$\psi^M(\phi, \mathbf{E}^e) = G(\phi)|\mathbf{E}^e|^2 + \frac{1}{2}[K(\phi) - \frac{2}{3}G(\phi)]\text{tr}(\mathbf{E}^e)^2 \tag{34}$$

Considering $G(\phi)$ and $K(\phi)$ as the shear and the bulk modulus of the two phase material. Their dependency on the phase field parameter is chosen as a linear function:

$$K(\phi) = K_{bc}(1 - \phi) + K_{ox}\phi \tag{35}$$

$$G(\phi) = G_{bc}(1 - \phi) + G_{ox}\phi \tag{36}$$

The phase field part is adopted from Kim et al. [1998],

$$\psi^\phi(\phi, c) = \phi^2(3 - 2\phi)\psi_1(c) + [1 - \phi^2(3 - 2\phi)]\psi_2(c) + \chi\phi^2(1 - \phi)^2 \tag{37}$$

$$\psi_i(c) = \frac{1}{2}k_i(c - c_i)^2 \quad (i = 1, 2) \tag{38}$$

where c_1 and c_2 are the maximum and minimum normalized concentration of species in the domain and k and χ are material phase parameters. The coupled term in the free energy density is formulated as,

$$\psi^P(\phi, \mathbf{E}^e, c) = -c_{max}K(\phi)P(c - c_0) \tag{39}$$

here c_{max} reads the maximum oxygen concentration in the alumina (see Grimes and Lagerlo [1998]).

Using the free energy function, following state relations can be derived:

$$\mathbf{T}^e = 2\frac{\partial\psi(\Phi)}{\partial\mathbf{C}^e}, \quad \eta = -\frac{\partial\psi(\Phi)}{\partial\nu}, \quad \mu = \frac{\partial\psi(\Phi)}{\partial c}, \quad \boldsymbol{\mathcal{E}} = \frac{\partial\psi(\Phi)}{\partial\nabla\phi}, \quad \mathcal{P} = \frac{\partial\psi(\Phi)}{\partial\phi} - \mathbf{M}^e : \mathbf{S} \tag{40}$$

with thermodynamic force $\mathcal{P}$ and energetic constitutive response function $\tilde{A}$.

$$\tilde{A}(\Phi) = -\frac{\partial\psi(\Phi)}{\partial\phi} \tag{41}$$

$$\tilde{A}(\Phi) = (3\phi - 2)(\psi_1 - \psi_2) - 2\chi\phi(1 - \phi)(1 - 2\phi) - (K_{ox} - K_{bc})(c - c_0)c_{max}P \tag{42}$$

$$\boldsymbol{\mathcal{E}} = 2(\boldsymbol{\alpha}\nabla\phi) \tag{43}$$

$$\mathcal{P} = \mathbf{M}^e : \mathbf{S} + \tilde{A}(\Phi) \tag{44}$$

where λ is the lamé constant and $\mathbf{1}$ is the identity tensor. The chemical potential μ can be calculated from the free energy function as:

$$\mu = k_1(c - c_1)\phi^2(3 - 2\phi) + k_2(c - c_2)(1 - \phi^2(3 - 2\phi)) - c_{max}K(\phi)P \tag{45}$$

Mandel Stress $\mathbf{M}^e$, thermodynamic force $\tilde{A}(\Phi)$, $\mathcal{E}$ and $\mathcal{P}$ can derived in the following form,

$$\mathbf{M}^e = 2G\mathbf{E}^e + \lambda\mathrm{tr}(\mathbf{E}^e)\mathbf{1} \tag{46}$$

The deviatoric part of the Mandel Stress becomes,

$$\mathbf{M}^e_0 = \mathbf{M}^e - \frac{1}{3}\mathrm{tr}(\mathbf{M}^e)\mathbf{1} \tag{47}$$

The plastic flow direction $\mathbf{N}^p$ is assumed to be colinear to the Mandel stress $\mathbf{M}^e$ and codirectional for both phases.

$$\mathbf{N}^p = \frac{\mathbf{M}^e_0}{|\mathbf{M}^e_0|} \tag{48}$$

The equivalent tensile stress is defined as,

$$\bar{\sigma} = \sqrt{\frac{3}{2}}|\mathbf{M}^e_0| \tag{49}$$

In a similar fashion, equivalent damage stress can be determined from the projection of the Mandel stress:

$$\mathbf{N}^d = \frac{\mathbf{M}^e}{|\mathbf{M}^e|} \tag{50}$$

$$\bar{\sigma}^d = |\mathbf{n} \cdot \mathbf{M}^e \cdot \mathbf{n}| \tag{51}$$

The material softening due to damage evolution is satisfied from the decay of the threshold values. A generalized form is provided below:

$$Y(\bar{\varepsilon}^d) = Y_0 - g(\bar{\varepsilon}^d) \tag{52}$$

here Y_0 is the initial value for the plastic or damage threshold and g is a softening function depending on $\bar{\varepsilon}^d$. In this work, for the sake of simplicity, a linear softening is adopted for both plastic and damage thresholds and the g function reads:

$$g(\bar{\varepsilon}^d) = H\bar{\varepsilon}^d \tag{53}$$

where H is the softening modulus. Above framework is also adopted for topcoat where $\phi = 0$ at all times which boils down the model into an elastoviscoplastic response with damage softening. Note that damage normal vector $\mathbf{n}$ is defined as normal to the sinusoidal interface for bond coat and normal to the columnar structure for the top coat (see Fig.2.).

2.4   Numerical Results and Discussion

Implementation of the model is carried out by using User Element subroutine (UEL) in ABAQUS software. Two-dimensional quadrilateral elements with four nodes and bi-linear shape functions are implemented for the plane-strain analysis. A total of five degrees of freedom (displacement (u_1 and u_2), the normalized concentration of species (c), the phase field variable (ϕ) and the mechanical coupling term P) are defined implemented at the element level.

Fig. 3. presents the numerical model problem analysed for the diffusion-deformation problem. The geometry is a two-layer solid medium created with a 150μm top-coat and a bond-coat with equal thicknesses. The problem is assumed to be isothermal at 1200^oC. The phase field and

Table 1 - Model Parameters

|	TC (EB-PVD)	BC (FeCrAlY)	TGO (Al_2O_3)	Unit
G	15.68×10^3	92.31×10^3	132.0×10^3	MPa
K	19.27×10^3	200.0×10^3	273.0×10^3	MPa
S_α	7.0×10^1	5.0×10^2	1.0×10^3	MPa
S_0	2.0×10^1	-	-	MPa
h	9.0×10^3	-	-	MPa
m	0.25	0.4	0.4	-
$\dot{\varepsilon}_0$	0.5×10^{-10}	1×10^{-4}	1×10^{-4}	-
$\mathcal{M}_{22}$	2×10^{-17}	2×10^{-17}	2×10^{-17}	$m^5.s.mol/J$
$\boldsymbol{\alpha}_{22}$	3.62×10^{-7}	3.62×10^{-7}	3.62×10^{-7}	J/m
β	0.95×10^6	0.95×10^6	0.95×10^6	J/m^3
χ	3.92×10^{-1}	3.92×10^{-1}	3.92×10^{-1}	-
k_1, k_2	6.0×10^3	6.0×10^3	6.0×10^3	$J/mol.m^3$
c_1	0.14	0.14	0.14	-
c_2	0.90	0.90	0.90	-
β_l	-	-	1.4×10^{-1}	-
β_t	-	-	1.6×10^{-3}	-
c_{max}	-	-	0.8×10^5	mol/m^3
π	C -	-	1×10^{-1}	-
Y	1.55×10^2	8.2×10^2	8.2×10^2	MPa
H	-1×10^3	-1×10^3	-1×10^3	MPa
$\dot{\varepsilon}_0$	1×10^{-4}	1×10^{-4}	1×10^{-4}	-
m	0.2	0.2	0.2	-

the concentration variables are set as $\phi = 1$ and $c = 0.92$ at the top line and $\phi = 0$ and $c = 0.12$ at the bottom. No flux boundary condition is applied on the left and right edges of the medium.A hyperbolic tangent transition function is defined for the interface and 2μm transition length is chosen for the hyperbolic tangent transition function. This length is in accordance with the mesh sizes in the interface region of our finite element model (see Kim et al. [1998] and Ammar et al. [2009]). Mechanical boundary conditions are as shown in Fig. 3. The right boundary is constrained to remain vertical to mimic the continuity of the sinusoidal pattern in the system. The mesh used has a minimum size of 0.5μm as concluded in the previous work (see Saeidi et al. [2018]). The material parameters used in the analysis are presented in Table 1.

Figure 4. presents growing TGO as a new phase after 100 hours of oxidation. The growing oxide layer creates high internal stresses which cause plasticity and damage. As it is clearly shown in Figure 5. damage evolution takes place both in TC and BC. Since the damage is confined within in the damage plane, crack propagation is parallel to the columns of ceramic top coat and it is along the interface in the TGO region. Apart from damage strain, the internal compressive stress also causes plastic deformation in TC, TGO and BC regions (see Fig. 6.). Those numerical results are in good agreement with the literature (Tortorelii et al. [2003] and Walter et al. [2000b]).
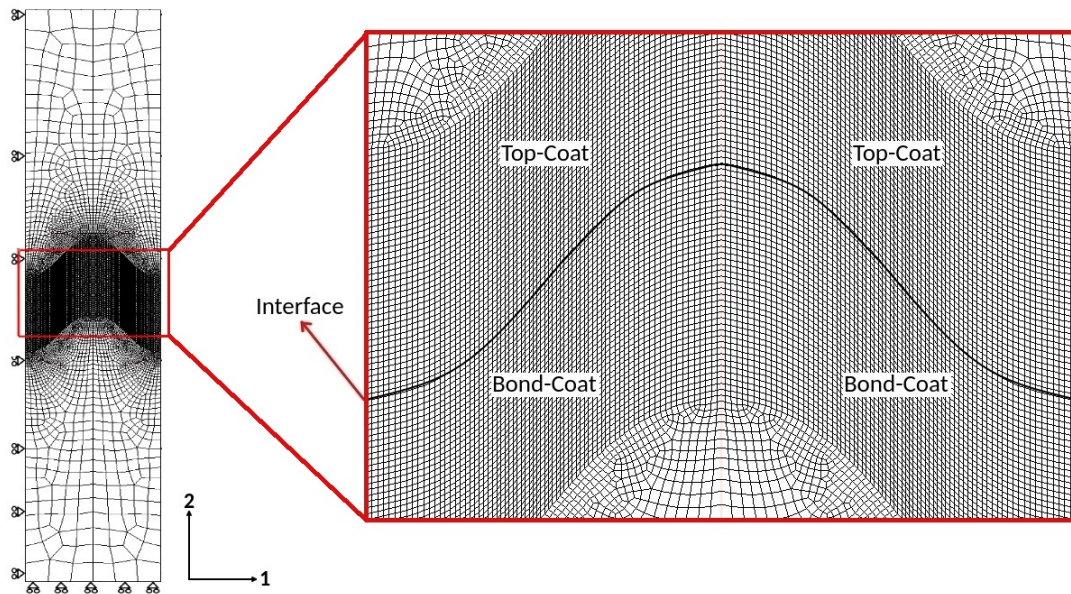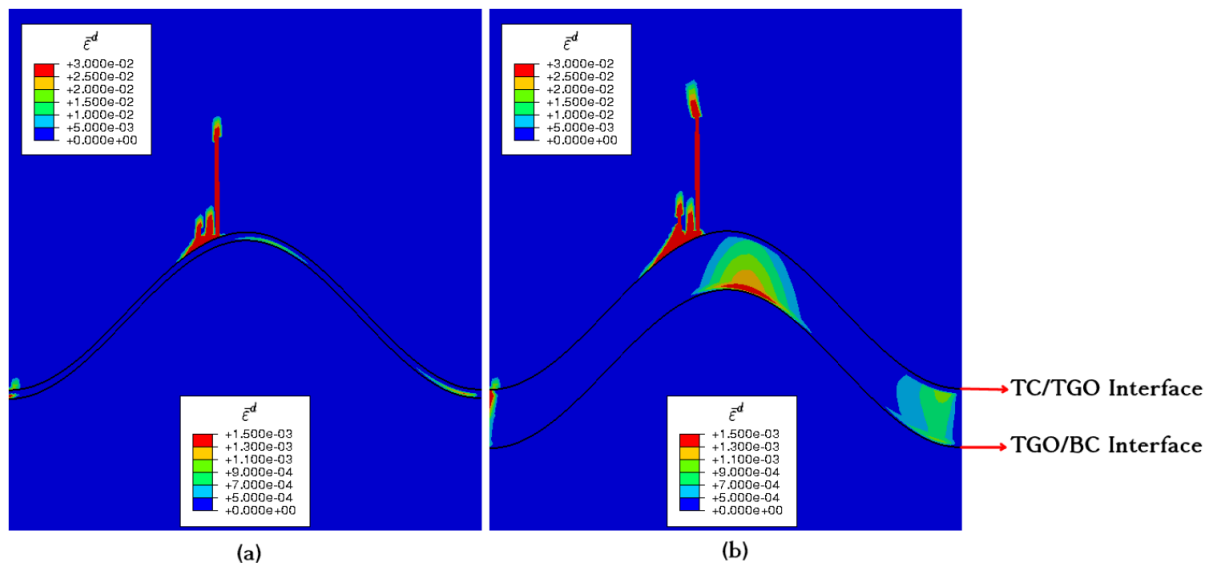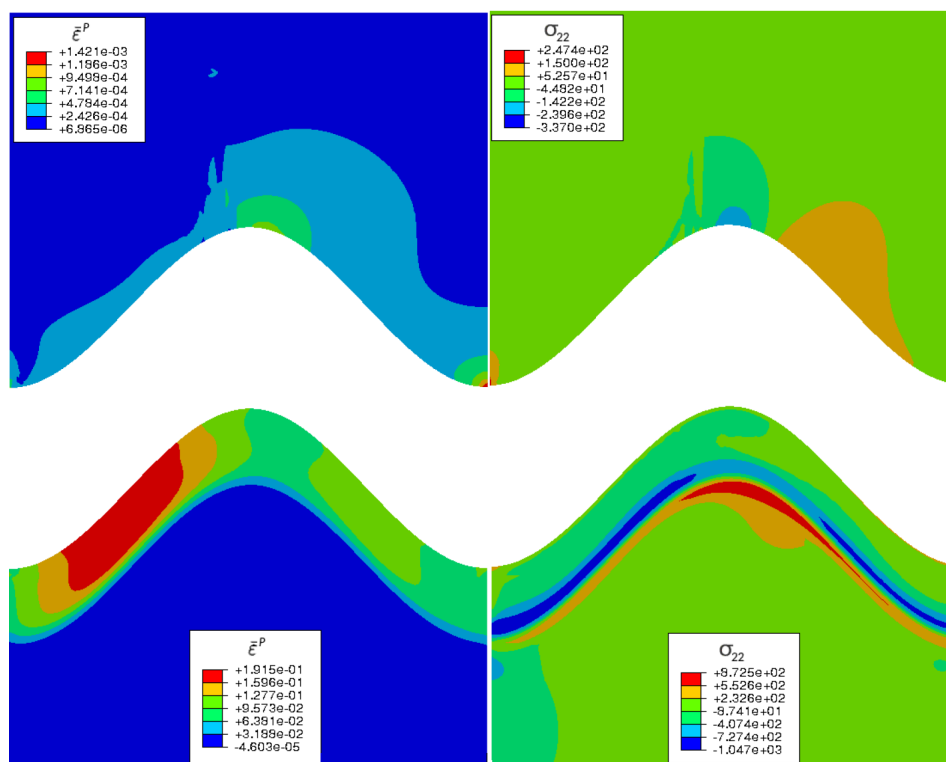
Figure 3: Finite element model of the model problem and mechanical BCs.
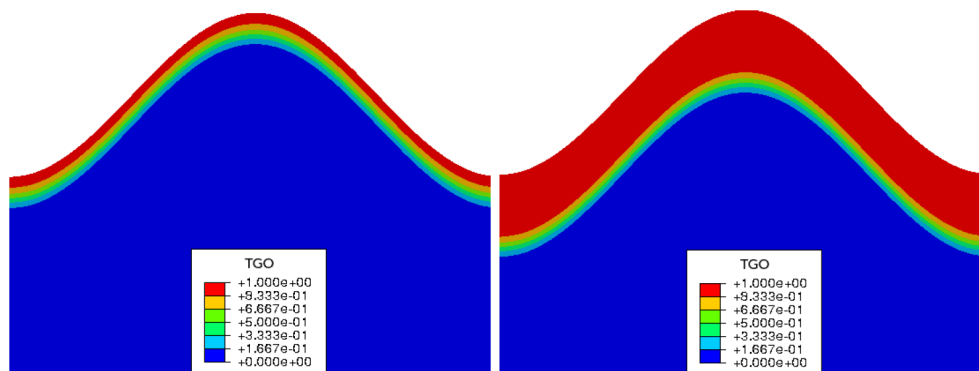
Figure 4: Maps for growing TGO as a new phase. After 10 hrs (left), 100 hrs. (right)

Figure 5: Maps for accumulated damage on TC and BC, after 10 hours (left), 100 hours. (right)

Figure 6: Distribution of accumulated plastic strain and stress in vertical direction for TC and BC
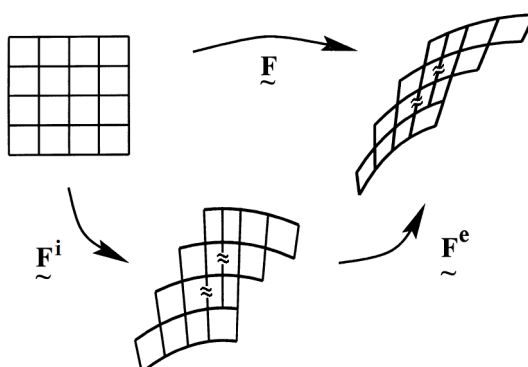
3 Modeling of Crack Growth for Single Crystals

3.1 Kinematics

Considering the same configuration presented in section 2.1, elastic and inelastic part which constitutes the plastic deformation and damage in a crystal can be expressed as follows:

$$\mathbf{F} = \mathbf{F}^e \mathbf{F}^i \tag{54}$$

Figure 7 represents such a deformation for inital and final configurations for a crystal.

Figure 7: Decomposition of the deformation gradient.

However, for the sake of simplicity and the clarity of the proposed theory, the plastic part of the deformation gradient is neglected throughout this work. Then the deformation gradient reads

$$\mathbf{F} = \mathbf{F}^e \mathbf{F}^d \tag{55}$$

$\mathbf{F}^d$ represents the local deformation due to damage generated in the material. Note that $\mathbf{F}^d$ is invariant with respect to rigid body motions that are carried by $\mathbf{F}^e$. In the view of Eq. (3) and (4), the velocity gradient can be decomposed in the following form:

$$\mathbf{L} = \mathbf{L}^e + \mathbf{F}^e \mathbf{L}^d \mathbf{F}^{e-1} \tag{56}$$

where,

$$\mathbf{L}^e = \dot{\mathbf{F}}^e \mathbf{F}^{e-1}, \quad \mathbf{L}^d = \dot{\mathbf{F}}^d \mathbf{F}^{d-1} \tag{57}$$

and the jacobian can also be decomposed as

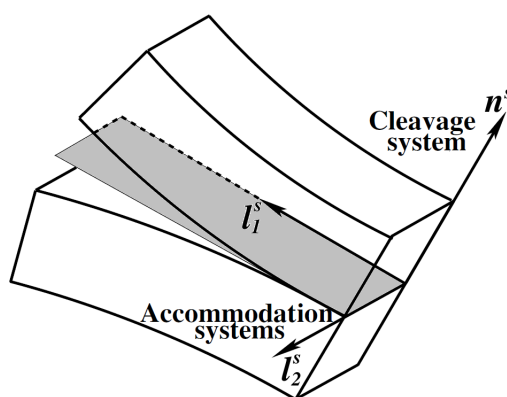$$J = J^e J^d, \quad J^e = \det \mathbf{F}^e > 0, \quad J^d = \det \mathbf{F}^d > 0. \tag{58}$$

The elastic and inelastic stretching and spin tensors are

$$\mathbf{D}^e = \mathrm{sym}\mathbf{L}^e, \quad \mathbf{D}^d = \mathrm{sym}\mathbf{L}^d \tag{59}$$

$$\mathbf{W}^e = \mathrm{skew}\mathbf{L}^e, \quad \mathbf{W}^d = \mathrm{skew}\mathbf{L}^d \tag{60}$$

and damage evolution is assumed irrotational,

$$\mathbf{W}^d = 0 \tag{61}$$

Figure 8: Schematic representation of the cleavage and two accommodation systems to be associated to the crystallographic planes.

the rate of inelastic deformation gradient would be

$$\dot{\mathbf{F}}^d = \mathbf{D}^d \mathbf{F}^d , \quad \mathbf{F}^d(\mathbf{X}, \mathbf{0}) = \mathbf{1} \tag{62}$$

The damage stretching tensor is defined as

$$\mathbf{D}^d = \sum \dot{\delta}_s \mathbf{N}_s^d , \tag{63}$$

where $\dot{\delta}_s$ is the damage rates initiated at each damage system which is a scalar internal variable and $\mathbf{N}_s^d$ is the damage flow direction tensor.

The damage evolution is a combination of following crystallographic contributions:

$$\dot{\mathbf{F}}^d \mathbf{F}^{d-1} = \mathbf{D}^d = \sum_{s=1}^{N_{planes}^d} \dot{\delta}_c^s \underline{\mathbf{n}}^s \otimes \underline{\mathbf{n}}^s + \dot{\delta}_1^s \underline{\mathbf{n}}^s \otimes \underline{\mathbf{l}}_1^s + \dot{\delta}_2^s \underline{\mathbf{n}}^s \otimes \underline{\mathbf{l}}_2^s \tag{64}$$

where $\dot{\delta}_c^s$ $\dot{\delta}_1^s$ and $\dot{\delta}_2^s$ are the strain rates for mode I, mode II and mode III crack growth, respectively and N_{planes}^d stands for the number of damage planes which are fixed for a given crystal structure. The direction of the cleavage damage is defined by the opening δ_s of crystallographic cleavage planes with the normal vector $\underline{\mathbf{n}}^s$. Other damage systems must be introduced for the inplane accommodation along orthogonal directions $\underline{\mathbf{l}}_1^s$ and $\underline{\mathbf{l}}_2^s$, (Fig. 8) and they are only activated if the cleavage damage is initiated. Finally, three damage criteria associated to one cleavage and two accommodation systems take the following form:

$$f_c^s = |\underline{\mathbf{n}}^s \cdot \mathbf{M}^e \cdot \underline{\mathbf{n}}^s| - Y^s \tag{65}$$

$$f_i^s = |\underline{\mathbf{n}}^s \cdot \mathbf{M}^e \cdot \underline{\mathbf{l}}_i^s| - Y^s \quad (i = 1, 2) \tag{66}$$

where Y is the damage threshold and the scalar damage is simply the accumulation of damage generated in all systems.

$$\dot{d} = |\dot{\delta}_c^s| + |\dot{\delta}_1^s| + |\dot{\delta}_2^s| \tag{67}$$

The correspond equivalent stresses projected on to the damage system becomes:

$$\bar{\sigma}_s = \mathbf{M}^e : \mathbf{N}^s \tag{68}$$
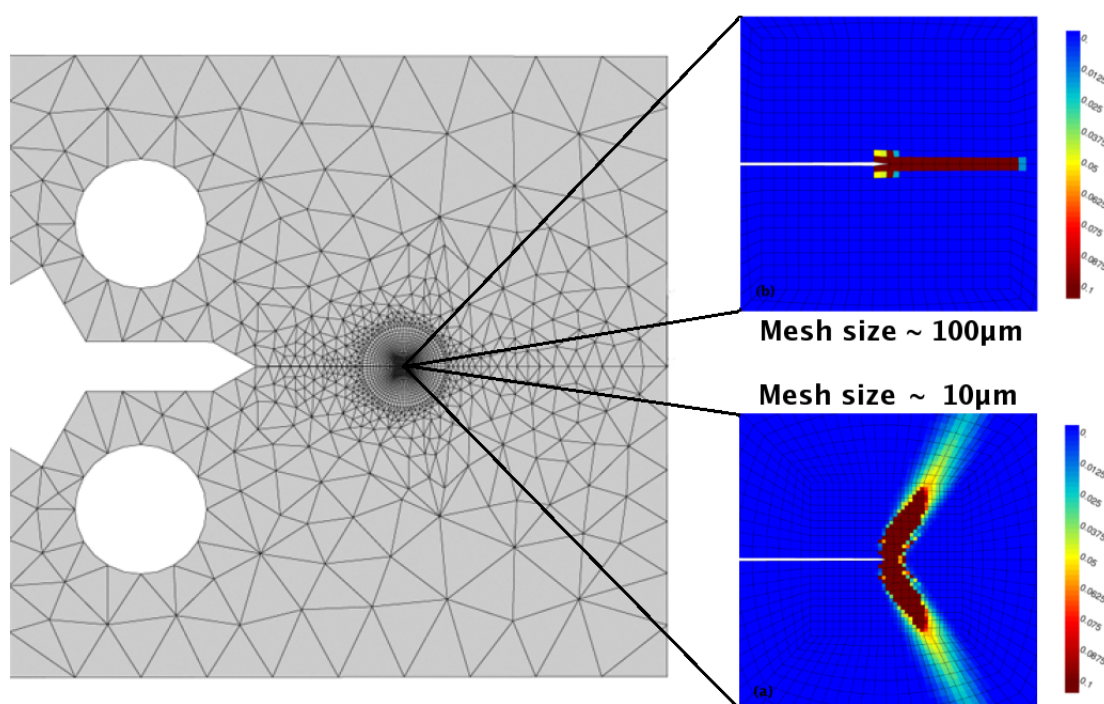
Figure 9: Mesh dependency observed in crack growth simulation of a CT specimen.

$$\mathbf{N}^s_c = \underline{\mathbf{n}}^s \cdot \mathbf{M}^e \cdot \underline{\mathbf{n}}^s \quad , \quad \mathbf{N}^s_i = \underline{\mathbf{n}}^s \cdot \mathbf{M}^e \cdot \underline{\mathbf{l}}^s \tag{69}$$

Finally, the scalar damage rate is defined as

$$\dot{d} = \sum |\dot{\delta}_s| \tag{70}$$

Considering the damage flow similar to Eq. (23), (52) and (53), damage in a single crystal based on slip systems can be fully modelled. However, it clearly shown in the literature that such an approach creates mesh dependent results and the ellipticity is lost and the problem becomes ill posed when localisation starts (Aslan and Forest [2009], Aslan et al.). Figure 9. shows such a mesh dependent solution for different mesh sizes yielding different localization bands.

In order to eliminate such a dependency, regularization of the damage fields is required. In that perpective, micromorphic approach will be introduced into the model in the next section.

3.2   Micromorphic Variable $^\chi d$

Following the work of the work of Aslan and Forest (Aslan and Forest [2009]), the micromorphic counterpart of the damage variable d is chosen as $^\chi d$ for the purpose of mathematical regularization as an additional kinematical degree of freedom. $^\chi d$ is defined as a positive valued scalar variable which constitutes a subset of micromorphic continuum named as microdamage continuum. The details of the theory and thermodynamical considerations are deeply discussed by Aslan and Bayraktar [2020] and Aslan and Bayraktar [2021].

In the scope of this work the free energy is taken as a quadratic potential as a function of elastic strain, $\mathbf{E}^e$, damage, d, microdamage, $^\chi d$ and its gradient, $\nabla\,^\chi d$.

$$\psi(\mathbf{E}^e, d, {}^\chi d, \nabla\,^\chi d) = \mu|\mathbf{E}^e_0|^2 + \frac{1}{2}\kappa(tr\mathbf{E}^e) + \frac{1}{2}B(d - {}^\chi d)^2 + \frac{1}{2}\beta|\nabla\,^\chi d|^2 \tag{71}$$

Where μ, κ, B and β are positive material constants. Following Aslan and Bayraktar [2020] and applying the method of virtual power, a generalized balance equation can be derived as follows:

$$\text{Div } \underline{\mathbf{b}} = \beta \Delta^{\chi} d \tag{72}$$

where b is the generalized traction which yields into the Helmholtz equation:

$$^{\chi}d - \frac{\beta}{B}\Delta^{\chi}d = d \tag{73}$$

Finally the modified damage criterion for linear softening becomes:

$$Y(d) = Y_0 + B(d - {}^{\chi}d) - Hd \tag{74}$$

The semianalytical solution for Eq.73 is sinusoidal with a wave length of

$$\omega = l\sqrt{\frac{H}{(B-H)}} \tag{75}$$

where

$$l^2 = \frac{\beta}{B} \tag{76}$$

### 3.3 Numerical Results and Discussion

As presented in the previous section implementation of the model is carried out by using User Element Subroutine (UEL) in ABAQUS software with same element properties with one exception that in addition to the displacement degrees of freedom (u_1 and u_2), microdamage variable $^{\chi}d$ is defined as a nodal degree of freedom of the finite element formulation. The parameters used in the simulations are provided in Table 2.

As a 2D regularization example, a plate under uniaxial tension with a horizontal cleavage plane is investigated (see Fig. 10.). In order to trigger localization, an initial geometric defect is created on the left edge and a displacement boundary condition is applied in order to create tension. The wave length of the localisation band is manipulated by the varying values of β. FEA results show that localization path is in good agreement with with the orientation of the cleavage plane and the size of the localization band is controlled by l in Eq. (75)

Figure 10. also demonstrates the mesh independency of the size of the damage band with a constant parameter set with varying mesh densities. Results clearly show the successful regularization and mesh independency.

Similar regularized damage bands can be obtained on a rotated plane. In order to demonstrate the capability of the model a 2D block with a the cleavage plane oriented at 25 degrees from the horizontal axis is analysed with a central defect. FEA results show that localization path is successfully matching with the orientation of the predefined cleavage plane and the size of the localisation band is also successfully controlled throughout the crack (see Fig. 11).

As a final example, the CT specimen shown in Figure 9 is simulated with the regularized model. With a changing β parameter, the damage band is managed to be controlled for a growing crack under monotonic loading (see Figure 12.). The same example is also adopted for a cyclic loading case (see Figure 13.) where the model shows a great potential to simulate crack bifurcation and branching seen in the experiments done by Marchal [2006].
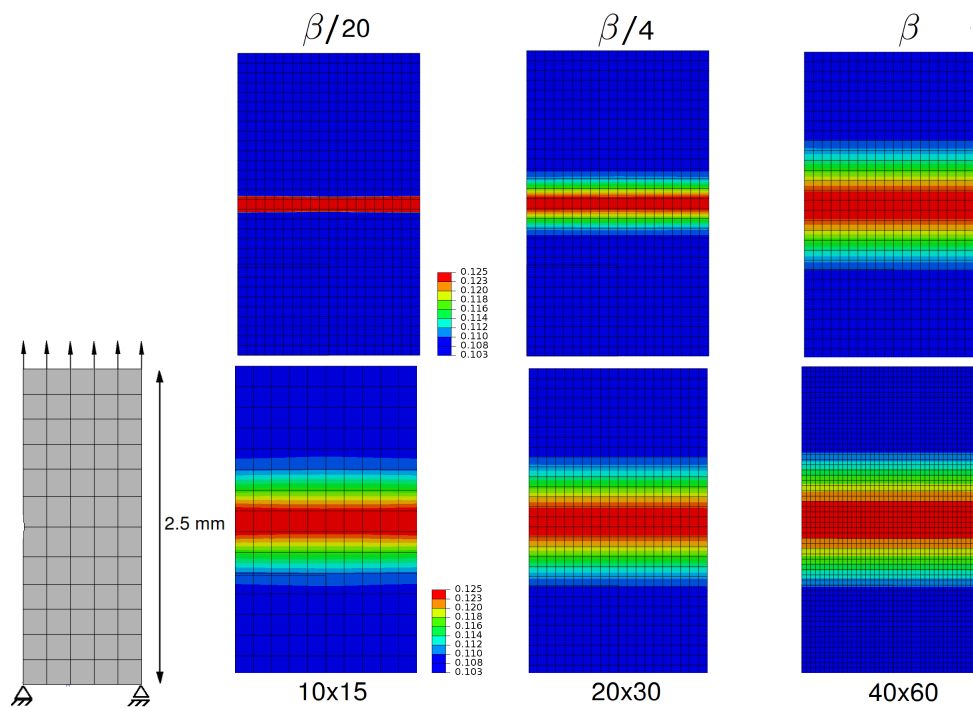
Figure 10: Regularized damage bands in varying sizes manipulated by the parameter β.
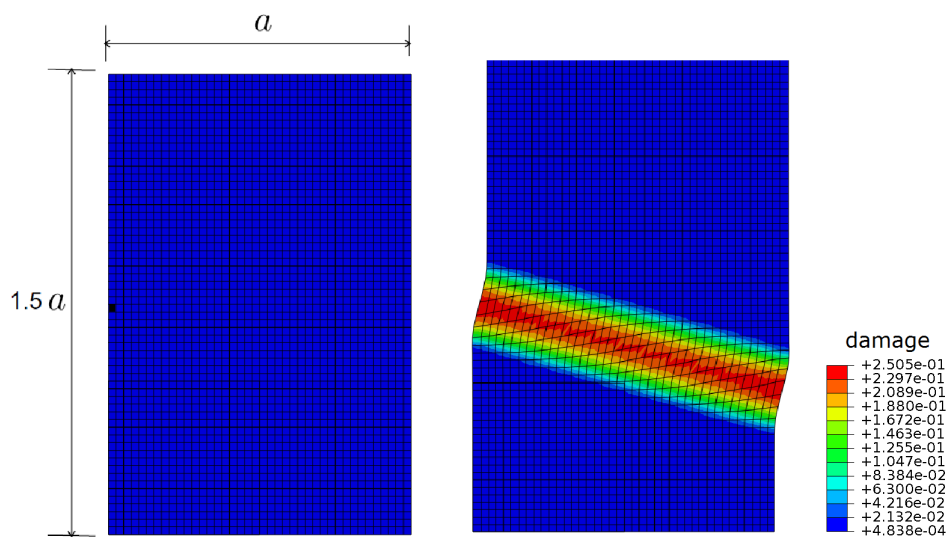
Figure 11: Regularized damage fields for a $^{o}25$ rotated damage plane.

Table 2 - Model parameters for regularized damage model

μ (Pa)	κ (Pa)	β (Pa)	B (Pa)	Y_0 (Pa)	H (Pa)
70.0E9	150.0E9	1.8E3	6.0E9	200.0E6	1.0E9
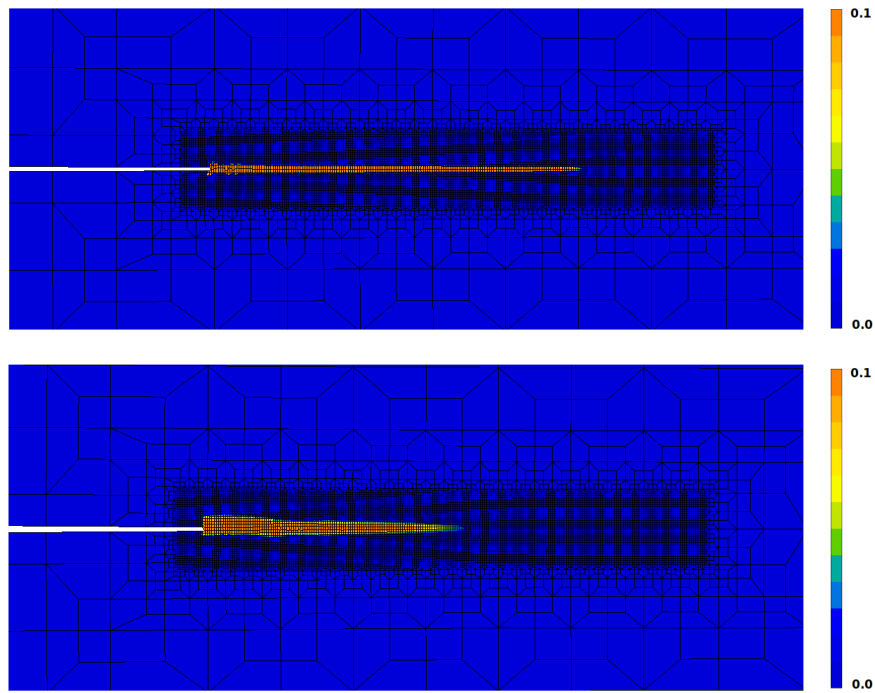
Figure 12: Regularized crack growth in a CT specimen for β (top) and 2β (bottom). Field variable d
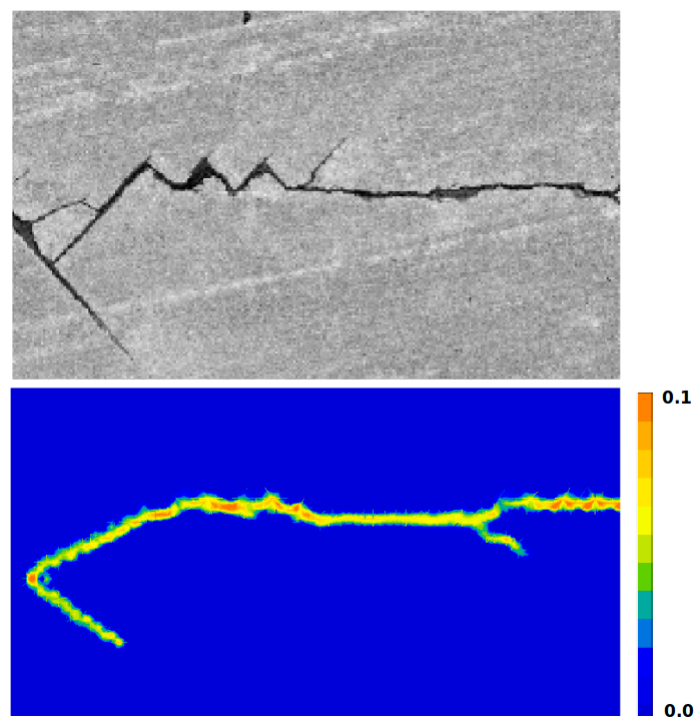
Figure 13: Qualitative comparison between the successive crack bifurcations in a CT specimen (Marchal, 2006) and the numerical simulation showing the crack bifurcation and branching through 111 planes. Field variable d.

4   Concluding remarks

In this chapter a comprehensive framework for the numerical modeling of damage in single crystal turbine blades with thermal barrier coatings for large deformations is presented. In the first part a finite element based phase-field model coupled with damage mechanics in the finite strain framework for oxidation of TBC systems is demonstrated. The phase field approach and mechanics are fully coupled within the model, where the thermodynamic consistency is also ensured. Presented numerical results show that the successful coupling of oxidation and mechanics where damage is initiated by internally generated stress due to the growing oxide. The proposed damage model for TBC systems is able to capture crack growth both in TC and BC in accordance with the experimental results demonstrating a great potential for predicting the lifetime of TBC systems.

The model proposed for single crystal substrate is specifically adopted to capture the damage initiation and propagation on the predefined slip planes of the crystallographic structure. The mesh dependency of the model is eliminated through the implementation of micromorphic theory. Presented numerical results demonstrate that the proposed approach is suitable for large deformations and can provide damage initiation and growth in various orientations. Definition of damage planes in accordance with the crystallography of the material enables the model to simulate crack bifurcations and branching observed in the experiments in the literature.

Acknowledgements

References

E. C. Aifantis. On the microstructural origin of certain inelastic models. *J. Eng. Mat. Technol*, 1984, a.

E. C. Aifantis. The physics of plastic deformation. *Int. J. Plast*, 1987, b.

K. Al-Athel, K. Loeffel, H. Liu, and L. Anand. Modeling decohesion of a top-coat from a thermally-growing oxide in a thermal barrier coating. *Surface and Coatings Technology*, 222: 68–78, 2013. ISSN 02578972. doi: 10.1016/j.surfcoat.2013.02.005.

K. Ammar. Modelling and simulation of phase transformation-mechanics coupling using a phase field method Kais Ammar l ' École nationale supérieure des mines de Paris Spécialité Â≪ Sciences et Génie des Matériaux Â≫ Modelling and Simulation of Phase Transformation-Mec. 2010.

K. Ammar, B. Appolaire, G. Cailletaud, F. Feyel, and S. Forest. Finite element formulation of a phase field model based on the concept of generalized stresses. *Computational Materials Science*, 45(3):800–805, 2009. ISSN 09270256. doi: 10.1016/j.commatsci.2008.09.015. URL http://dx.doi.org/10.1016/j.commatsci.2008.09.015.

O. Aslan and E. Bayraktar. A large-deformation gradient damage model for single crystals based on microdamage theory. *Applied Sciences*, 10(24), 2020. ISSN 2076-3417. doi: 10.3390/ app10249142. URL https://www.mdpi.com/2076-3417/10/24/9142.

O. Aslan and E. Bayraktar. Analytical solutions of model problems for large-deformation micromorphic approach to gradient plasticity. *Applied Sciences*, 11(5), 2021. ISSN 2076-3417. doi: 10.3390/app11052361. URL `https://www.mdpi.com/2076-3417/11/5/2361`.

O. Aslan and S. Forest. Crack growth modelling in single crystals based on higher order continua. *Computational Materials Science*, 45(3):756–761, 2009. ISSN 09270256. doi: 10.1016/j. commatsci.2008.09.016.

O. Aslan, S. Quilici, and S. Forest. Numerical modeling of fatigue crack growth in single crystals based on microdamage theory. *Int. J. Damage. Mech*, 2011:681–705.

O. Aslan, N. M. Cordero, A. Gaubert, and S. Forest. Micromorphic approach to single crystal plasticity and damage. *International Journal of Engineering Science*, 49(12):1311–1325, 2011. ISSN 00207225. doi: 10.1016/j.ijengsci.2011.03.008. URL `http://dx.doi.org/10. 1016/j.ijengsci.2011.03.008`.

R. D. E. Borst and J. Pamin. Some Novel Developments in Finite Element Procedures for Gradient-Dependent Plasticity. *International Journal*, 39(December 1994):2477–2505, 1996. ISSN 1097-0207. doi: 10.1002/(SICI)1097-0207(19960730)39:14⟨2477::AID-NME962⟩3.0. CO;2-E.

J. W. Cahn and J. E. Hilliard. Free Energy of a Nonuniform System. I. Interfacial Free Energy. *The Journal of Chemical Physics*, 28(2):258–267, 1958. ISSN 0021-9606. doi: 10.1063/1.1744102. URL `http://aip.scitation.org/doi/10.1063/1.1744102`.

G. C. Chang, W. Phucharoen, and R. A. Miller. Behavior of thermal barrier coatings for advanced gas turbine blades. *Surface and Coatings Technology*, 30(1):13–28, 1987. ISSN 02578972. doi: 10.1016/0257-8972(87)90004-1.

J. Cheng, E. Jordan, B. Barber, and M. Gell. Thermal/residual stress in an electron beam physical vapor deposited thermal barrier coating system. *Acta Materialia*, 46(16):5839–5850, 1998. ISSN 13596454. doi: 10.1016/S1359-6454(98)00230-4.

R. de Borst and H. B. G. d. p. f. a. Muhlhaus. and algorithmic aspects. *Int. J. Numer. Meth. Eng*, 1992.

R. de Borst, L. J. Sluys, H. B. Muhlhaus, and J. Pamin. Fundamental issues in finite element analysis of localization of deformation. *Eng. Comput*, 1993.

J. T. DeMasi-Marcin, K. D. Sheffler, and S. Bose. Mechanisms of Degradation and Failure in a Plasma-Deposited Thermal Barrier Coating. *Journal of Engineering for Gas Turbines and Power*, 112(4):521–526, 1990. ISSN 0742-4795. doi: 10.1115/1.2906198.

R. A. B. Engelen, M. G. D. Geers, and F. P. T. Baaijens. Nonlocal implicit gradient enhanced elasto-plasticity for the modelling of softening behaviour. *Int. J. Numer. Meth. Eng*, 1996.

A. G. Evans, D. R. Clarke, and C. G. Levi. The influence of oxides on the performance of advanced gas turbines. *Journal of the European Ceramic Society*, 28(7):1405–1419, 2008. ISSN 09552219. doi: 10.1016/j.jeurceramsoc.2007.12.023.

S. Flouriot, S. Forest, G. Cailletaud, A. K"oster, L. Remy, B. Burgardt, et al. Strain localization at the crack tip in single crystal ct specimens under monotonous loading: 3d finite element analyses and application to nickel-base superalloys. *Int. J. Fract*, 2003.

M. G. D. Geers. Finite strain logarithmic hyperelasto-plasticity with softening: a strongly non-local implicit gradient framework. *Comput. Methods in Appl. Mech. Eng*, 1996, a.

M. G. D. Geers. On the role of moving elastic-plastic boundaries in strain gradient plasticity. *Model. Simul. Mater. Sci. Eng*, 2007:7723–7746, b.

R. W. Grimes and K. P. D. Lagerlo. THE DEFECT CHEMISTRY OF SAPPHIRE (a -Al 2 O 3). 46(16):5689–5700, 1998.

M. Y. He, A. G. Evans, and J. W. Hutchinson. Ratcheting of compressed thermally grown thin films on ductile substrates. *Acta Materialia*, 48(10):2593–2601, 2000. ISSN 13596454. doi: 10.1016/S1359-6454(00)00053-7.

M. Y. He, J. W. Hutchinson, and A. G. Evans. Simulation of stresses and delamination in a plasma-sprayed thermal barrier system upon thermal cycling. *Materials Science and Engineering A*, 345(1-2):172–178, 2003. ISSN 09215093. doi: 10.1016/S0921-5093(02)00458-6.

R. Jones. Thermal barrier coatings. In K. H. Stern, editor, *Metallurgical and Ceramic Protective Coatings*, page 194. Chapman & Hall,, London, 1996. ISBN 9789401071710. doi: 10.1533/9780857090829.2.115.

S. G. Kim, W. T. Kim, and T. Suzuki. Interfacial compositions of solid and liquid in a phase-field model with finite interface thickness for isothermal solidification in binary alloys. *Physical Review E - Statistical Physics, Plasmas, Fluids, and Related Interdisciplinary Topics*, 58(3): 3316–3323, 1998. ISSN 1063651X. doi: 10.1103/PhysRevE.58.3316.

E. Kröner. Allgemeine Kontinuumstheorie der Versetzungen und Eigenspannungen. *Archive for Rational Mechanics and Analysis*, 4(1):273–334, 1959. ISSN 00039527. doi: 10.1007/BF00281393.

K. Loeffel, L. Anand, and Z. M. Gasem. On modeling the oxidation of high-temperature alloys. *Acta Materialia*, 61(2):399–424, 2013. ISSN 13596454. doi: 10.1016/j.actamat.2012.07.067.

N. Marchal. Crack-tip stress strain fields in single crystal nickel-base superalloys at high temperature under cyclic loading. PhD thesis, Ecole des Mines de Paris . 2006.

R. a. Miller. Thermal barrier coatings for aircraft engines: History and directions. *Journal of Thermal Spray Technology*, 6(1):35–42, 1995. ISSN 1059-9630. doi: 10.1007/BF02646310.

A. Musienko and G. Cailletaud. Simulation of inter and transgranular crack propagation in polycrystalline aggregates due to stress corrosion cracking. *Acta Mater*, 2009.

R. Parisot, S. Forest, A. Pineau, F. Nguyen, X. Demonet, and J.-M. D. a. Mataigne. and damage mechanisms of zinc coatings on galvanized steel sheets, part ii: Damage modes. *Metall. Mater. Trans*, 2003.

F. Saeidi, E. Gurses, and O. Aslan. A Numerical Approach to Simulate Oxidation in Thermal Barrier Coatings. In *Reference Module in Materials Science and Materials Engineering*, pages 1–7. Elsevier Ltd., 2018. ISBN 9780128035818. doi: 10.1016/B978-0-12-803581-8.11194-4. URL https://linkinghub.elsevier.com/retrieve/pii/B9780128035818111944.

F. Sait, E. Gurses, and O. Aslan. Modeling and simulation of coupled phase transformation and stress evolution in thermal barrier coatings. *International Journal of Plasticity*, 134:102790, 2020. ISSN 0749-6419. doi: https://doi.org/10.1016/j.ijplas.2020.102790. URL `https://www.sciencedirect.com/science/article/pii/S0749641920300656`.

P. F. Tortorelii, K. L. More, E. D. Specht, B. A. Pint, and P. Zschack. Growth stress - Microstructure relationships for alumina scales. *Materials at High Temperatures*, 20(3):303–310, 2003. ISSN 09603409. doi: 10.1179/mht.2003.036.

K. Vaidyanathan, M. Gell, and E. Jordan. Mechanisms of spallation of electron beam physical vapor deposited thermal barrier coatings with and without platinum aluminide bond coat ridges. *Surface and Coatings Technology*, 133-134:28–34, 2000. ISSN 02578972. doi: 10.1016/S0257-8972(00)00891-4.

M. E. Walter, B. Onipede, and C. Mercer. Resulting From Isothermal and Thermocyclic Exposure of a Thermal Barrier Coating. *Journal of Engineering Materials and Technology*, 122(3):333–337, 2000a.

M. E. Walter, B. Onipede, W. Soboyejo, and C. Mercer. Microstructural Features Resulting From Isothermal and Thermocyclic Exposure of a Thermal Barrier Coating . *Journal of Engineering Materials and Technology*, 122(3):333–337, 03 2000b. ISSN 0094-4289. doi: 10.1115/1.482805. URL `https://doi.org/10.1115/1.482805`.

T. Xu, M. Y. He, and A. G. Evans. A numerical assessment of the durability of thermal barrier systems that fail by ratcheting of the thermally grown oxide. *Acta Materialia*, 51:3807–3820, 2003. ISSN 13596454. doi: 10.1016/S1359-6454(03)00194-0.

Chapter 9

Stresses on Expansion Joints Used in Penetrations

Chapter details

Chapter DOI:

Chapter suggested citation / reference style:

P.S.: DOI may be included at the end of citation, for completeness.

Book details

Stresses on Expansion Joints Used in Penetrations

Rodolfo Suanno[1*], José Eduardo Maneschy[2]

[1]Stress Analysis Department - DAN.T, Eletrobras Eletronuclear – Rio de Janeiro, Brazil. E-mail: rsuanno@eletronuclear.gov.br/rsuanno@gmail.com
[2]JEM Consultoria. E-mail:emanesc@gmail.com

*Corresponding author

Abstract

During the 8th outage of the Angra 2 power plant, the expansion joints of the containment penetration JMK05D0201 (LCQ50) were found distorted. The cause was an inadvertent over pressurization made during monthly tests to verify the set pressure. To leave the damaged expansion joint installed, Eletronuclear conducted an elastic-plastic analysis which has demonstrated its integrity. Eletronuclear decided to keep it in place and cover it with an expansion joint designed to resist all loads predicted in the original design specification. This new design is a two-sided (bipartite) bellows with longitudinal field welds. This chapter presents the fatigue and stress analysis of the bipartite overlapping expansion joints considering the loads defined in the design specification.

Keywords: expansion joints; stress analysis; fatigue, mechanical penetrations.

1 Introduction

In nuclear power plants expansion joints, also known as bellows, are frequently mounted in penetrations of the metal containment whose function is to maintain the sealing of the reactor building in case of an accident due to loss of primary refrigerant (LOCA – Loss of Coolant Accident). The joints are designed to absorb the pressure stresses and thermal displacements from the heating and cooling that occur during the operation of the systems where they are installed. The project also includes other loads, such as pressure tests, seismic movements, and LOCA.

During the Angra 2 outage held in 2010, the penetration expansion joints JMK05D0201 (LCQ50) were found distorted, as shown in Figure 1. The cause of the observed deformation was excessive over-pressurization that was inadvertently imposed on the joints during the tests performed periodically to verify their water tightness. As this request was not foreseen, compression instability and subsequent buckling, known in the specialized literature as squirm, of the part occurred.

The evaluations carried out by the construction and engineering teams concluded that replacing the distorted joints with new ones would be extremely complex. Thus, Eletronuclear decided to leave them in service, and install another expansion joint overlapping each of them, designed to resist the same loads specified in the original design. The new configuration, installed in 2011, is a double joint, formed by two similar pieces, connected using a longitudinal weld performed during its assembly in the field.

Reactor Building (UJA)   Annulus (UJB)

Metal Containment
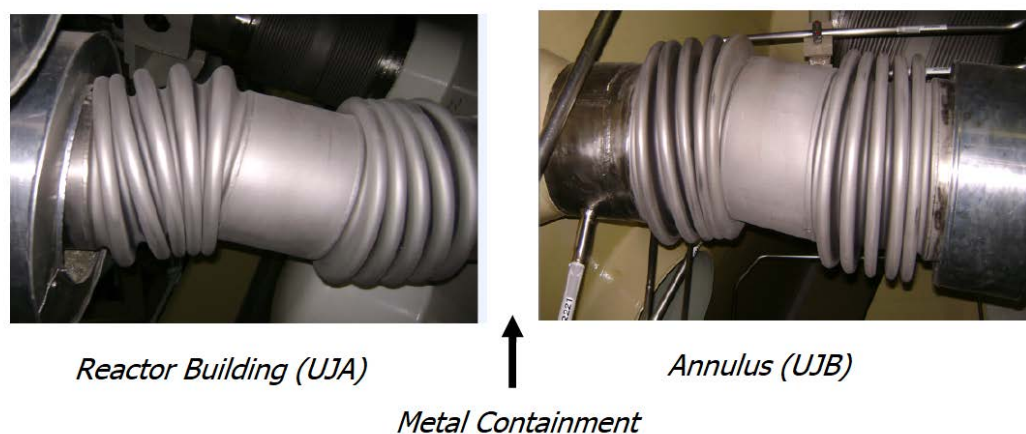
Figure 1 - Distorted penetration expansion joints (LCQ50) of the steam generator purge system

The expansion joints under study belong to the steam generator purge system (LCQ). In each of its loops, this system has two joints connected to the penetration (or nozzle) of the containment shell, one on the side of the reactor building, the UJA, and the other in the annulus, the UJB observed in Figure 2 and 3. A fixed point inside the containment isolates the pipe joints from the purge system. As the double pipe, called the guard pipe, which protects containment in case of breakage of the process line, is fastened directly at the fixed point, there is no load transfer generated by the movements of the containment to the pipe.

In this work, the stress and fatigue analysis is carried out to demonstrate that the configuration with the overlapping joint is adequate from the structural point of view. The evaluation is made by comparing the permissible limits of the codes and standards with the values calculated using loads of the original design, which are the internal pressure and thermal displacements in normal/abnormal operating conditions, the pressure during periodic tests, and displacements caused by LOCA and during the earthquake of safe shutdown plus burst pressure wave. In the present case, the ASME code Section III Subsection NB, and the standard AD-2000/B13 were adopted for stress and fatigue checks, respectively.

The stresses and deformations were determined by the finite element method, with the analyses made in ANSYS and conducted in an elastic regime for the operation load cases, and elastoplastic for tests and accidents. The model uses shell elements to simulate the joint, the tube between the bellows, and the double guard pipe. Contact elements are used to simulate the interaction between bellows.
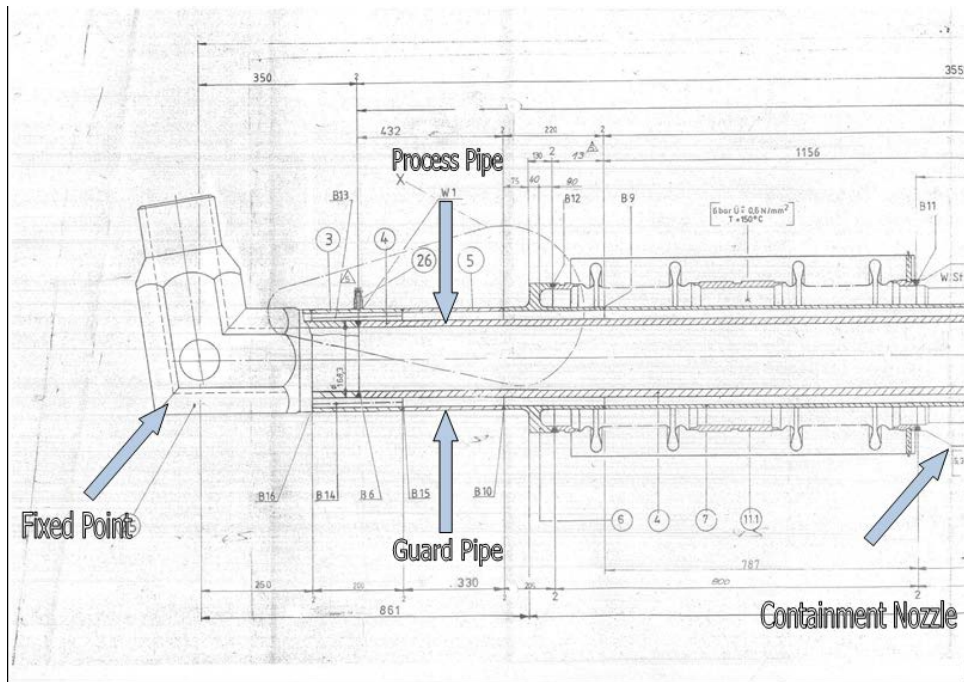
Figure 2- Penetration of the steam generator purge system (UJA building)
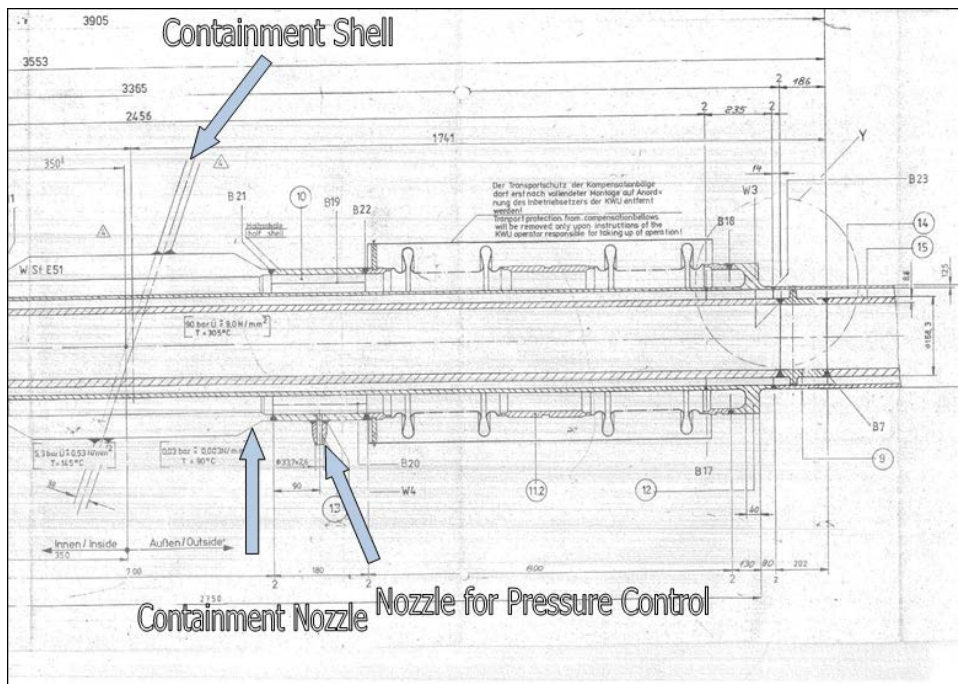
Figure 3- Penetration of the steam generator purge system (UJB building)

2 Original and overlapping expansion joint

The original configuration of the JMK05D0201 penetration expansion joint is universal, with one layer, without reinforcement, five convolutions in each bellow, and consisting of two joints connected by a cylindrical section tube, as illustrated in Figures 4 and 5. The joint was built to specification and manufactured from stainless steel X10CrNiNb18 9 (1.4550).
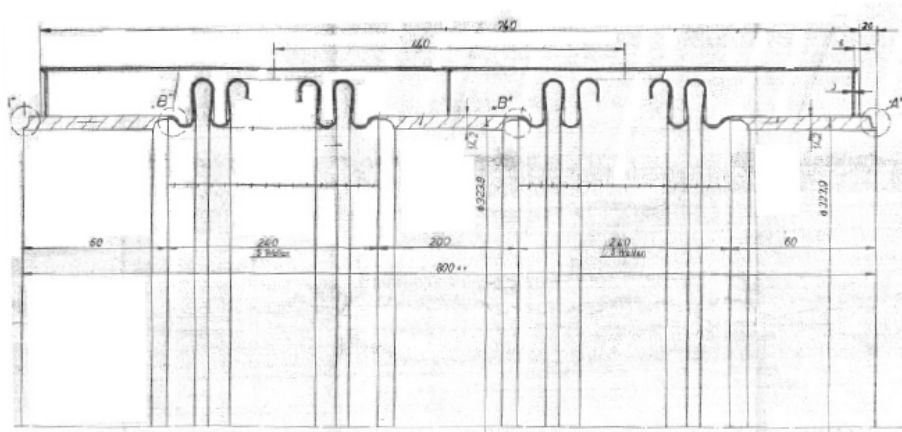
Figure 4- Original expansion joint
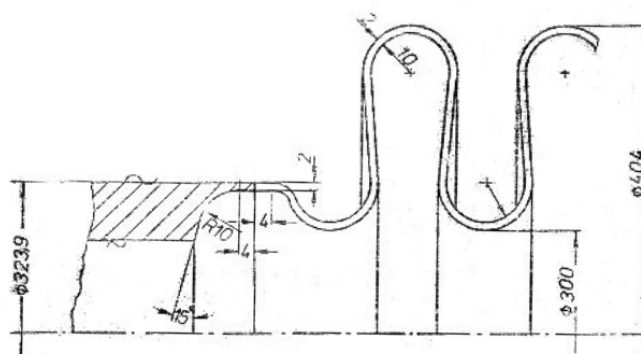
Figure 5 – Original expansion joint. Convolution geometry detail (dimensions in mm)

The overlapping expansion joint is bipartite, consisting of two identical half parts, which are connected by longitudinal welding made during assembly in the field. The representations in Figure 6 show the geometric details of the piece. The specifications, standards, and material for its manufacture are the same as the original joint.

3 Finite element model

As mentioned in Section 1, in each loop of the steam generator purge system there are two expansion joints, one attached to the inner side of the containment in the reactor building (UJA), and on the outside side, in the annulus (UJB). The loads on the joints are the internal pressure between them and the guard pipe, the thermal displacements of operation transmitted by the guard pipe, and the movements imposed by the containment nozzle during tests and accidents. For all these loadings the influence of the flexibility of the region between the fixed point and the expansion joint is negligible. Consequently, only one of them will be modeled since the interest is on the stresses acting in the expansion joint and guard pipe in the overlapping region.
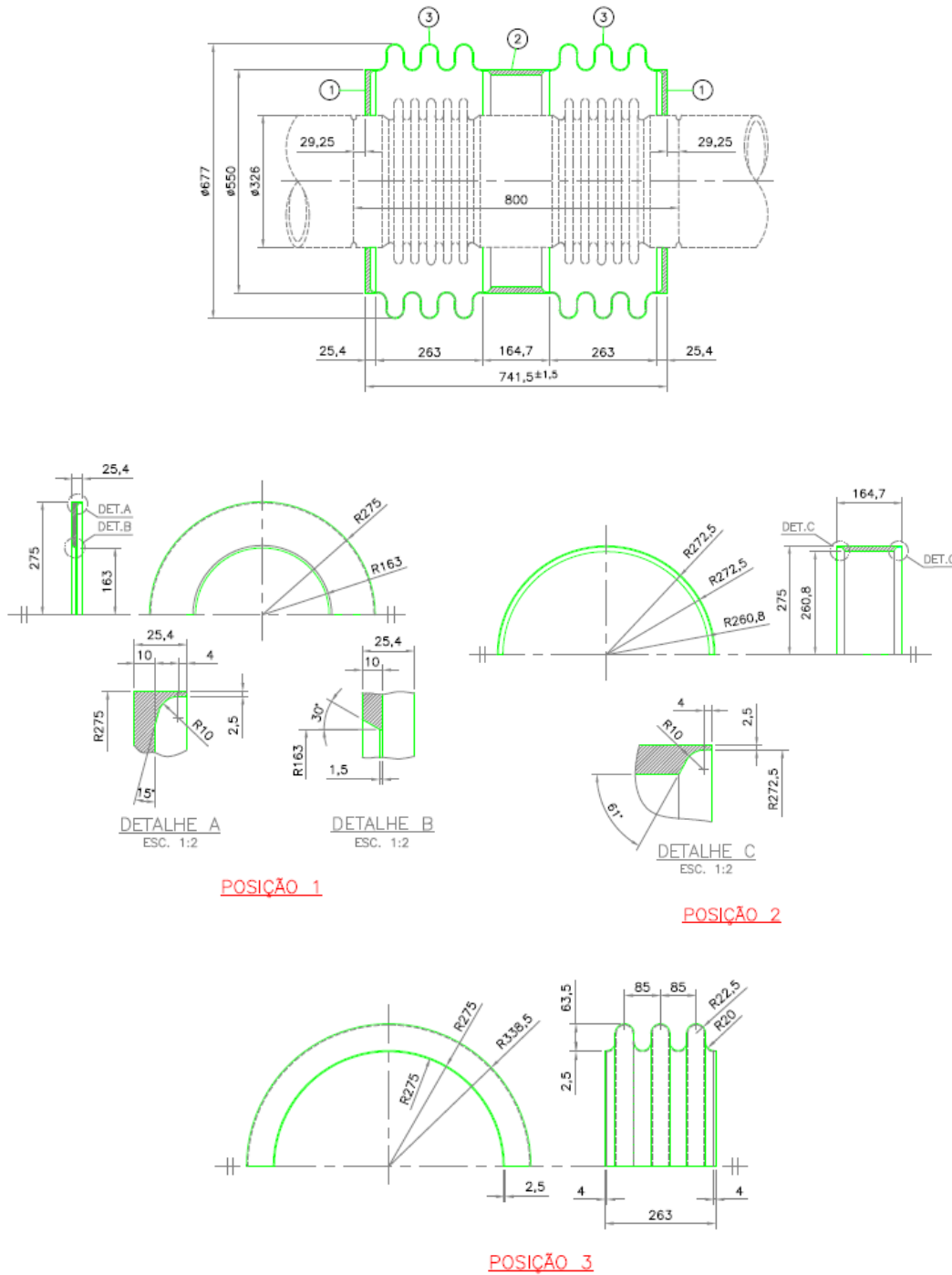
Figure 6 - Overlapping expansion joint (dimensions in mm)

Two finite element models were developed, one to simulate the original joint alone and the other to represent the original joint plus the overlapping. The expansion joint and guard pipe are modeled by SHELL281 shell elements (quadratic interpolation function) of the ANSYS program. By simplification, the part of the guard pipe that extends from

the expansion joint to the supports (fixed point on one side and containment nozzle on the other), is modeled with PIPE16 beam elements. The transition between the shell and beam elements that simulate the continuity of the guard pipe is done with rigid elements. Finite element models for both configurations are shown in Figures 7 through 11.
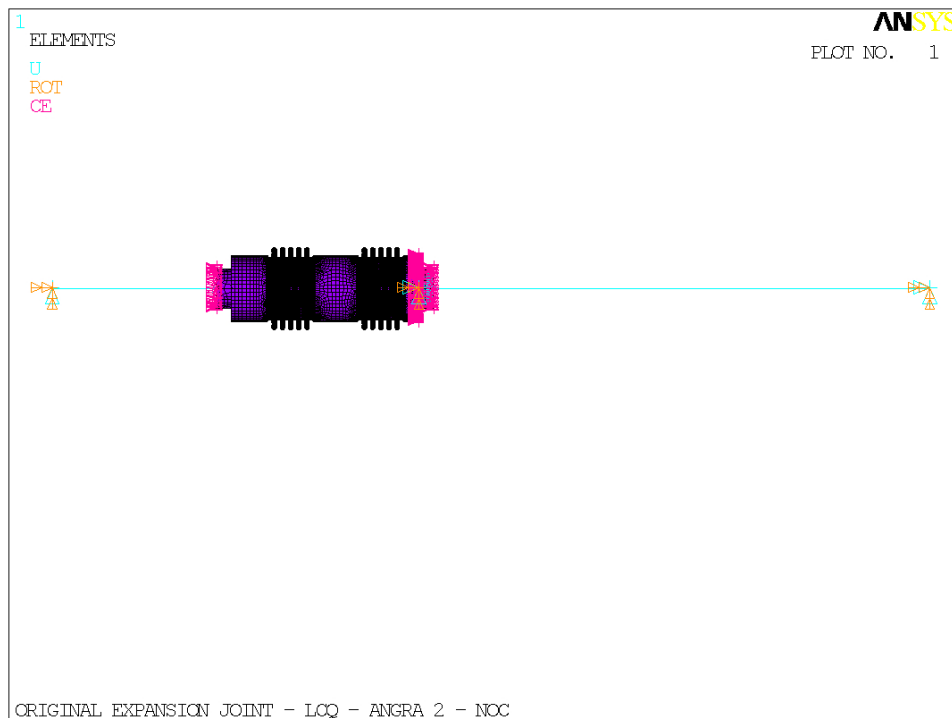
Figure 7- Original expansion joint
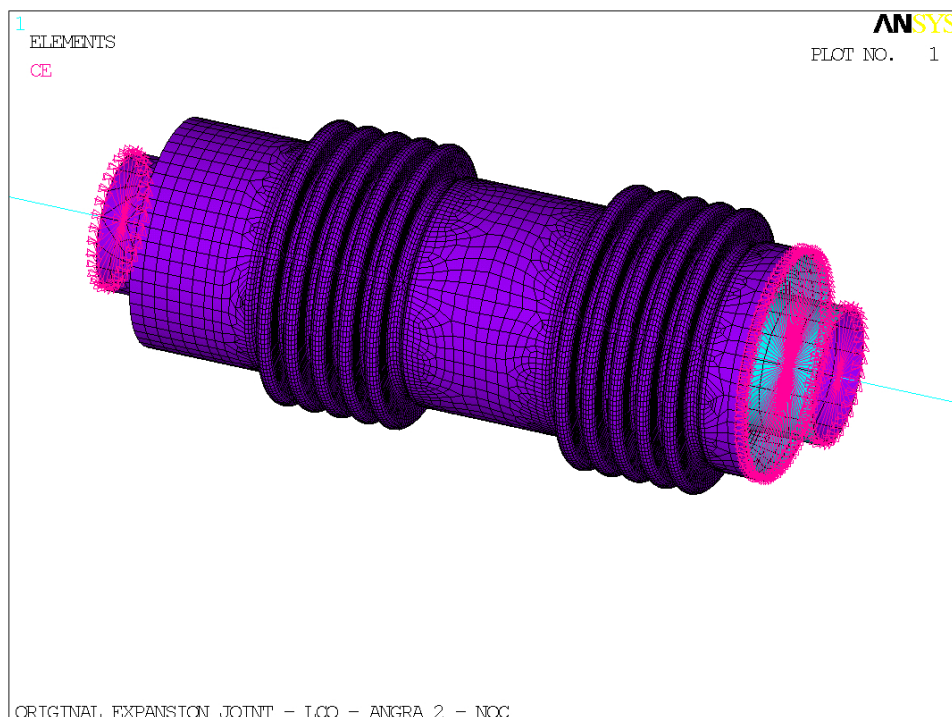
Figure 8- Original expansion joint. The transition between shell and bar elements with rigid elements
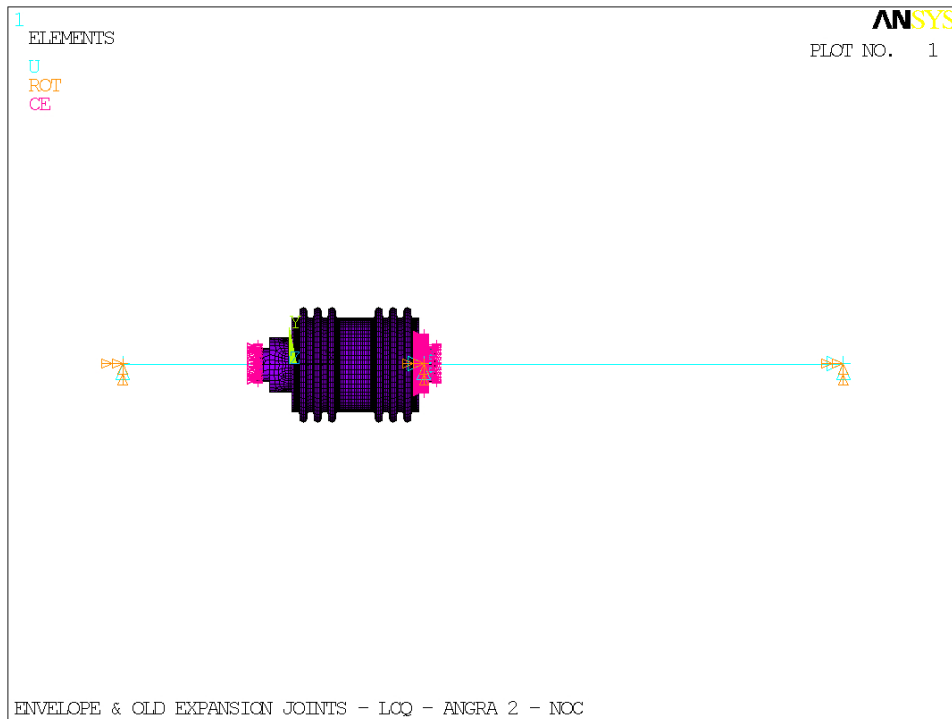
Figure 9- Original and overlapping expansion joints
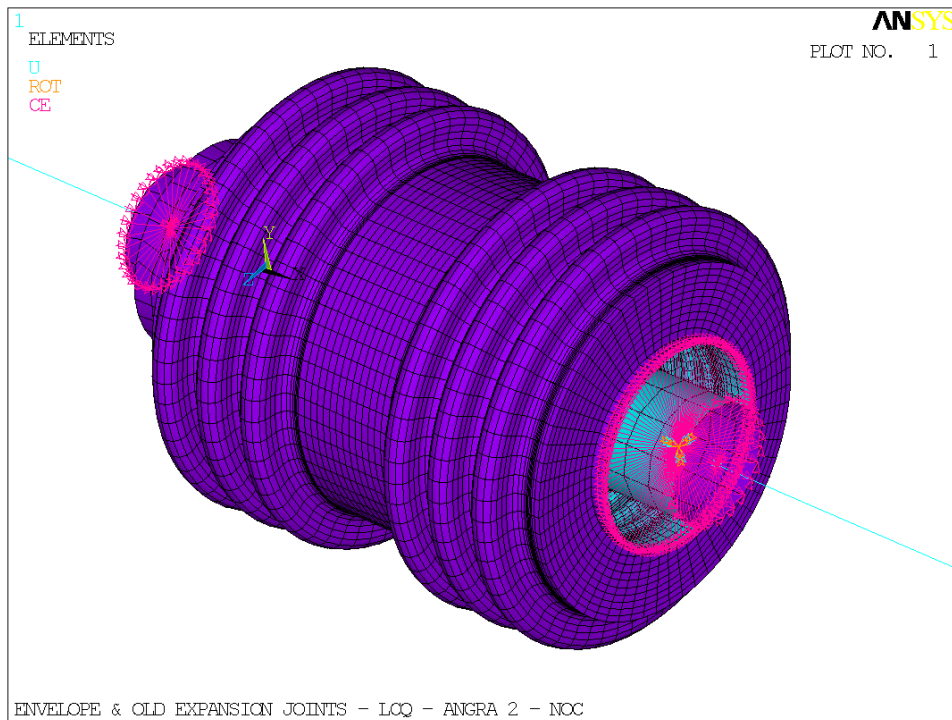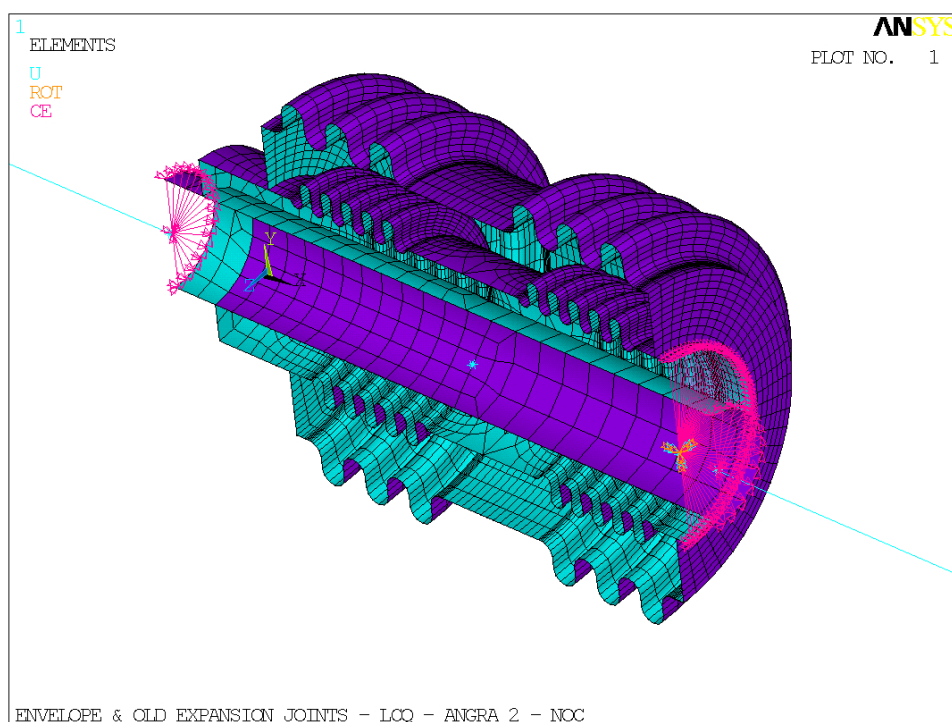
Figure 10 – Original expansion joint and overlapping joint (general and sectional views). The transition between shell and bar elements with rigid elements
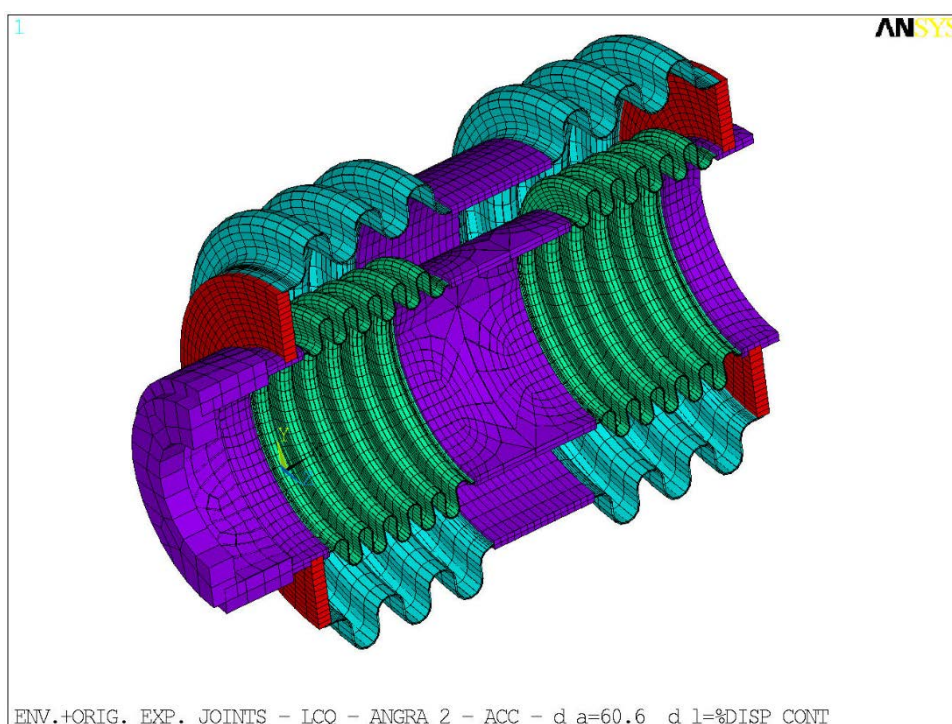
Figure 11- Sectional view and thickness of the original and overlapping expansion joints

3.1 Material properties

The original and overlapping joints are constructed with stainless steel X10CrNiNb18 9 (1.4550). The mechanical properties obtained from DIN 17440 07/85 and MTS 107.01.R2 for the various operating temperatures are shown in Table 1, with R_m tensile

strength, $R_{p0.2}$, and $R_{p1.0}$ the yield limits at 0.2% and 1.0% of strain, S_m the intensity of design stresses as defined in the ASME Code, E the modulus of elasticity and α the coefficient of thermal expansion.

Table 1 - Properties of steel X10CrNiNb18 9 (1.4550)

Temperature	Rm	Rp 0.2	Rp 1.0	Sm	E	α
(°C)	(MPa)	(MPa)	(MPa)	(MPa)	(MPa)	x10⁻⁶ (°C⁻¹)
20	510	205,00	240,00	160,00	2,00000E+05	16
30	-	201,50	236,38	157,58	1,99250E+05	16
80	-	184,00	218,25	145,50	1,95500E+05	16
116	-	173,80	206,20	137,47	1,92720E+05	16

The stress versus strain curve for elastoplastic analysis is determined by the Ramberg-Osgood equation, whose plastic portion is given in the form

$$\frac{\varepsilon}{\varepsilon_o} = \alpha \left(\frac{\sigma}{\sigma_o}\right)^n \qquad (1)$$

with σ the actual stress, σ_o the reference stress, usually the yield limit, ε and ε_o the actual and reference plastic deformations, this last equal to σ_o/E. The α and n parameters are material constants obtained by the best adjustment of the real stress-strain curve obtained from the tensile test.

The stress-strain relationships for the material with the characteristics of Table 1 at temperatures of 30°C, 80°C, and 116°C are shown in Figure 12.
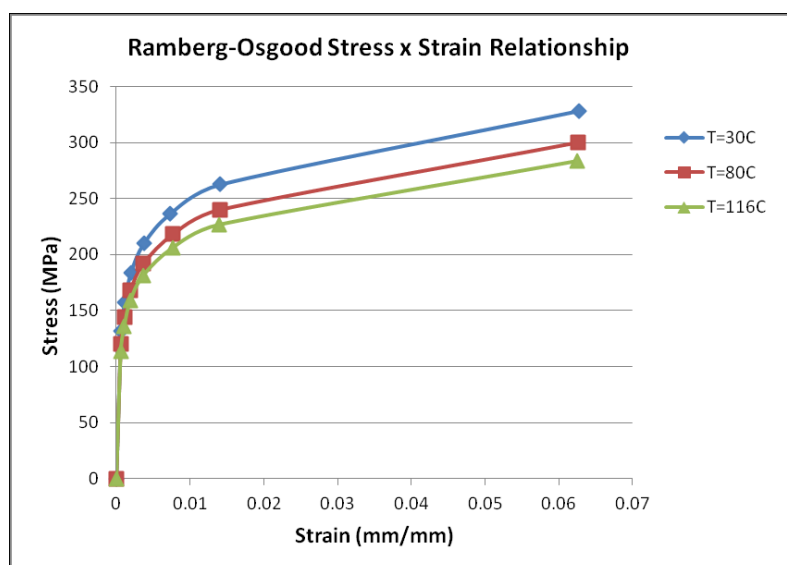
Figure 12 – Stress-strain curves for steel X10CrNiNb18 9 (1.4550)

3.2 Boundary conditions

Because the expansion joint located in the reactor building is anchored at both ends, one at the fixed point and the other welded on containment, Figure 2, movements are prevented in all directions. In the annulus, the joint is welded to containment at one end and guided (free axial displacement) through the auxiliary building on the other, Figure 3. The anchors are modeled as shown in Figure 13, which shows rigid elements coupled to the nodes of the shell elements at one end of the expansion joint to a node at the central axis of the model, which is clamped in all directions.
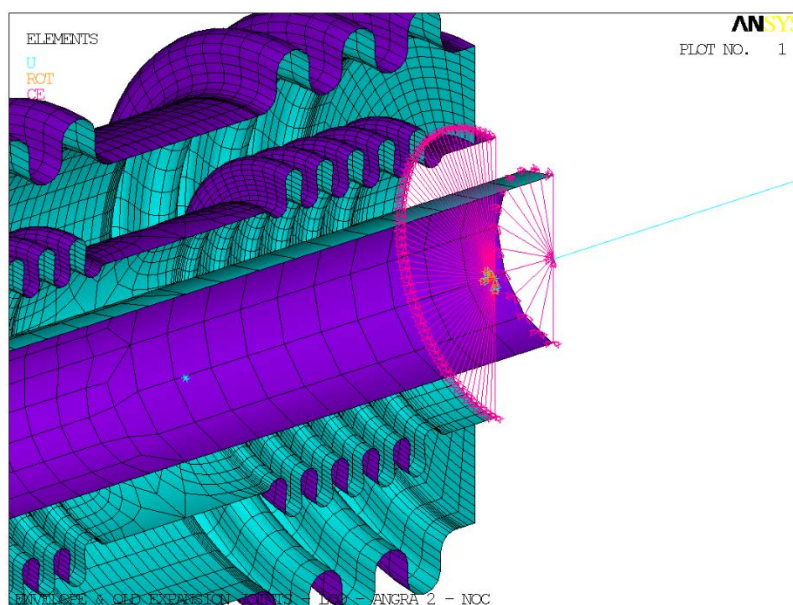
Figure 13 - Restrictions to displacements representing the anchorage in penetration in the containment

3.3 Basic loads

The load cases for the analysis of the expansion joint are the same as the original joint design and are shown in Table 2. Thermal displacements in the joint associated with the operating levels (B1+B2) are imposed by the guard pipe each time the purge system enters service. For the other levels, which depend on the movements of the containment during the pressure tests or accident events, the loading is defined by the axial and lateral displacements transmitted by penetration.

Table 2 - Description of load cases

Classification	Level	Loading Cases Description
Operation	B_1, B_2	1- Envelope normal operation/upset
Test	P	1-First Containment test
		2-Periodic Leak Tightness Containment test
Fault	S	1- LOCA corresponding to the highest pressure
		2- LOCA corresponding to the highest temperature
		3- Earthquake − SSB (SSE+BWP) − Safe Shutdown Earthquake + Burst Pressure Wave

Table 3 summarizes data taken from IWKA reports, and represents all load cases considered, inside (UJA-reactor building) and outside (UJB-annulus building) containment, in the original design of the expansion joints. The columns list for each load level the temperature, pressure range (pi=inside pressure, po=outside pressure), axial (δa), and lateral (δl) displacements respectively. The highlighted rows represent the envelope loading conditions for each load case. It is important to note that the load case P1 (First Containment Integrity and Leakage test) will not be considered in this

analysis because it is performed only at the commissioning phase of the plant and therefore will not be repeated.

Table 3 – Load cases for the expansion joints

	T (C)	Cicles	UJA (Reactor Building)				UJB (Annulus Building)			
			p (bar)		δa (mm)	δl (mm)	p (bar)		δa (mm)	δl (mm)
			po	pi			po	pi		
B1+B2	80	3312	-0.005	3.0	-3.1	0.0	0.0	3.0	12.8	0.0
P1	30	1	6.2	0.0	-7.3	12.2	0.0	0.0	-39.6	22.6
P1	30	1	6.2	0.0	39.6	7.3	0.0	0.0	7.3	12.2
P2	30	15	0.5	0.0	-19.0	1.8	0.0	0.0	-21.5	1.8
P2	30	15	0.5	0.0	-21.5	0.9	0.0	0.0	19.0	0.9
S1	80	1	4.6	3.0	44.0	16.8	0.0	3.0	-34.0	16.8
S2	116	1	2.2	3.0	60.6	8.4	0.0	3.0	-49.8	8.4
S3	80	3	-0.005	3.0	0.0	0.5	0.0	3.0	0.0	0.5
S3	80	3	-0.005	3.0	5.9	0.5	0.0	3.0	15.6	0.5

The internal pressure for the original expansion joint is considered applied in the volume between the expansion joint and the guard pipe. For the overlapping expansion joint the internal pressure is applied in the volume between the overlapping expansion joint and the guard pipe once this case considers that the original expansion joint is no longer tight, and the overlapping expansion joint will perform its function. Table 4 shows the envelope loading conditions for the joints located in the reactor building and annulus.

Table 4 – Envelope Loading Conditions for each load case for the expansion joints

	T (C)	p	δa (mm)	δl (mm)
B1+B2	80	3.005(i)	12.8	0
P2	30	0.5(o)	-21.5	1.8
S1	80	4.6(o)	44	16.8
S2	116	3.0(i)	60.6	8.4
S3	80	3.005(i)	15.6	0.5

4 Results of the analysis

The methodology adopted here is to apply the loadings from the original design to the two finite element models, one for the original expansion joint and the other for the overlapping plus original joint. Thus, one can compare the stresses and deformations of each case and, from there, evaluate the changes that the modification introduces in the design configuration.

The elastic linear analysis for the operating conditions (B1+B2) is conducted assuming two load cases acting separately: i) internal pressure; ii) thermal displacement transmitted by the guard pipe. The respective stress intensities, calculated by the Tresca criterion, are determined along the path shown in Figure 14, created to represent important quantities in the two finite element models.

The stress intensity due to internal pressure in both models is calculated for the upper (TOP), middle (MIDDLE), and lower (BOTTOM) fibers, the first case is presented in

Figure 15. The meridional and circumferential stresses in a convolution are obtained in these three fibers, with the result for the upper fiber indicated in Figure 16.

The stress intensity for the upper fiber caused by the thermal displacement induced by the guard pipe for the operating condition (B1+B2) is illustrated in Figure 17, with the meridional and circumferential stresses in a convolution presented in Figure 18. Additionally, Figure 19 shows the stress intensity and deformations for thermal displacement along with a convolution for the overlapping plus original expansion joint.

An elastoplastic analysis is performed for the other loading conditions (Test-P2, LOCA-S1 and S2, and SSB-S3). The stresses and deformations in the two finite element models are obtained by simulating the properties of steel in the plastic phase with Eq. (1) and considering the material properties of Table 1.

First, the stress intensity for the upper, middle, and lower fibers for the two models in the P2-Test condition is calculated. According to Table 4, initially, the external pressure of 0.5 bar is applied and then the displacements of the containment in the axial and lateral directions, whose values are 21.5 mm and 1.8 mm, respectively. The meridional and circumferential stresses for the fibers along a convolution path and their strains (total and plastic strains) are also determined. Because of the available space, the results are shown in the table in the next section and are not plotted.

Figure 20 shows the stress intensity in the three fibers for the LOCA-S1 load case (maximum external pressure). According to Table 4, the internal pressure of 3.0 bar is applied, then the external pressure of 4.6 bar, and, finally, the axial and lateral displacements of the containment, equal to 44.0 and 16.8 mm, respectively. The meridional and circumferential stresses for the fibers along a convolution are indicated in Figure 21 and the total and plastic deformations in these directions are shown in Figure 22.
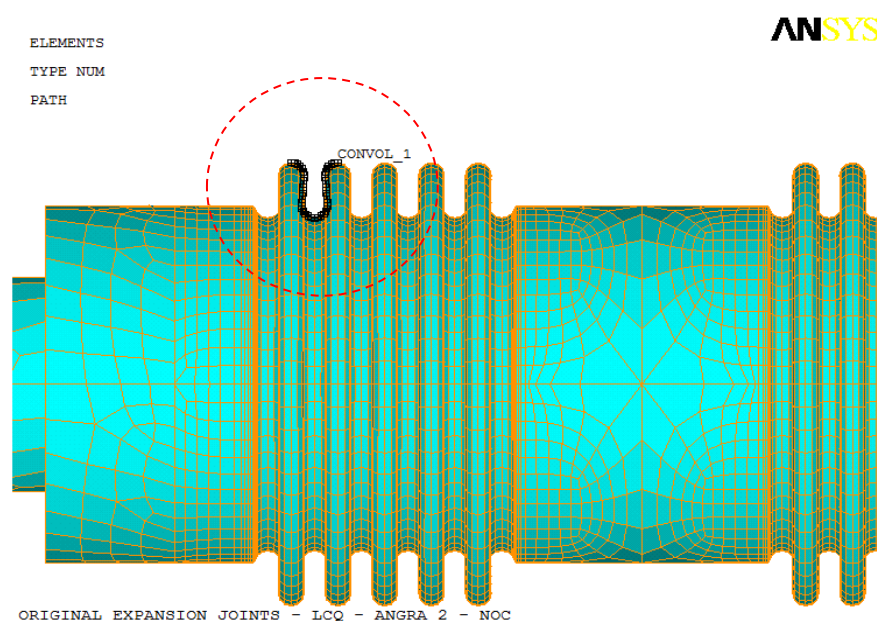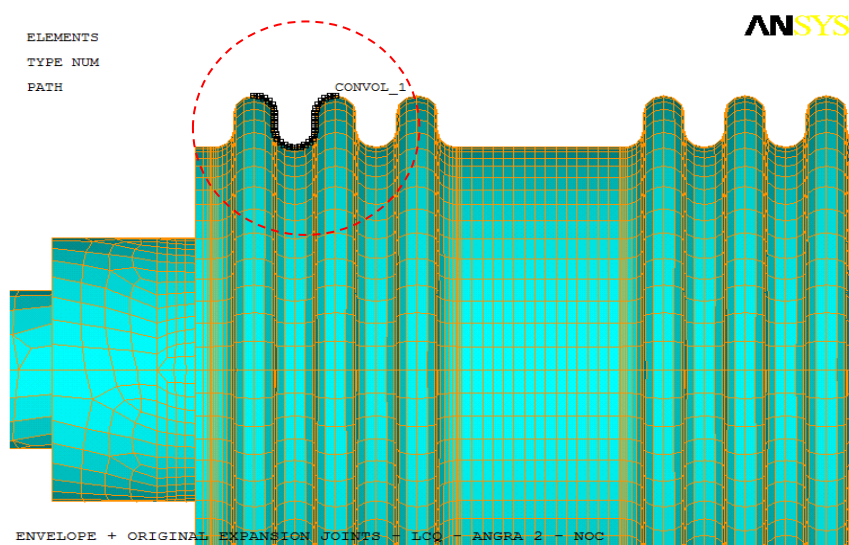
Figure 14 – Path (CONVOL_1) used to represent the meridional and circumferential stresses

The determination of the stress intensity, meridional and circumferential stresses, and total and plastic strains for the LOCA-S2 load case (maximum temperature) is made initially with the application of the internal pressure of 3.0 bar and then with axial displacements of 60.6 mm and lateral displacements of 8.4 mm imposed by containment. These same amounts are found for the SSB-S3 case when the safe shutdown earthquake and pressure waves (SSE+BPW) are superimposed. First, the internal pressure of 3.005 bar is applied, and then the displacements of the containment in the axial directions, equal to 15.6 mm, and lateral, equal to 0.5 mm. The results are in the tables shown in the next section.
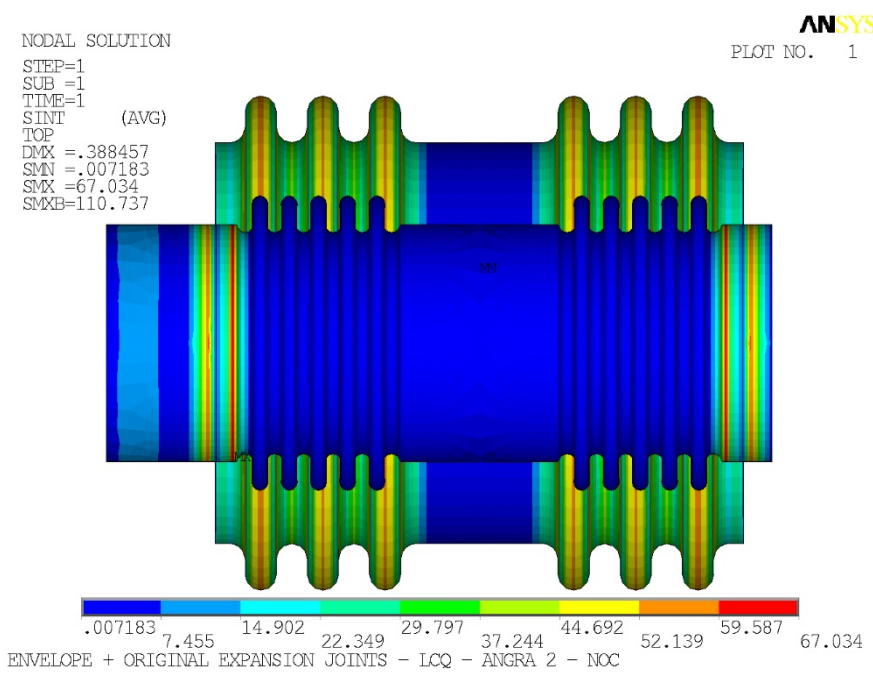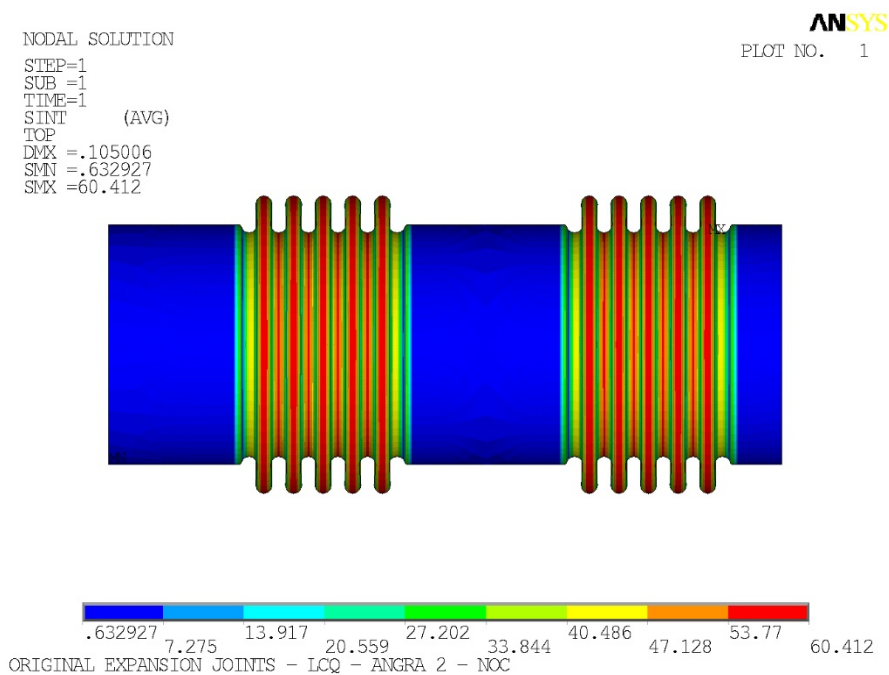
Figure 15– Original & Overlapping + Original Expansion Joints- Stress Intensity –TOP – Load case B1+B2 – Internal Pressure
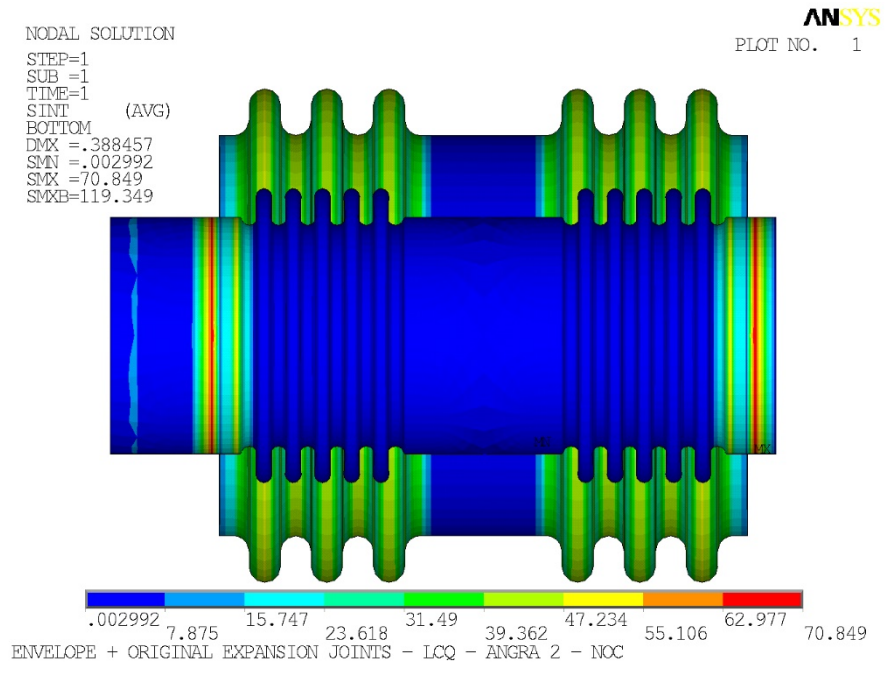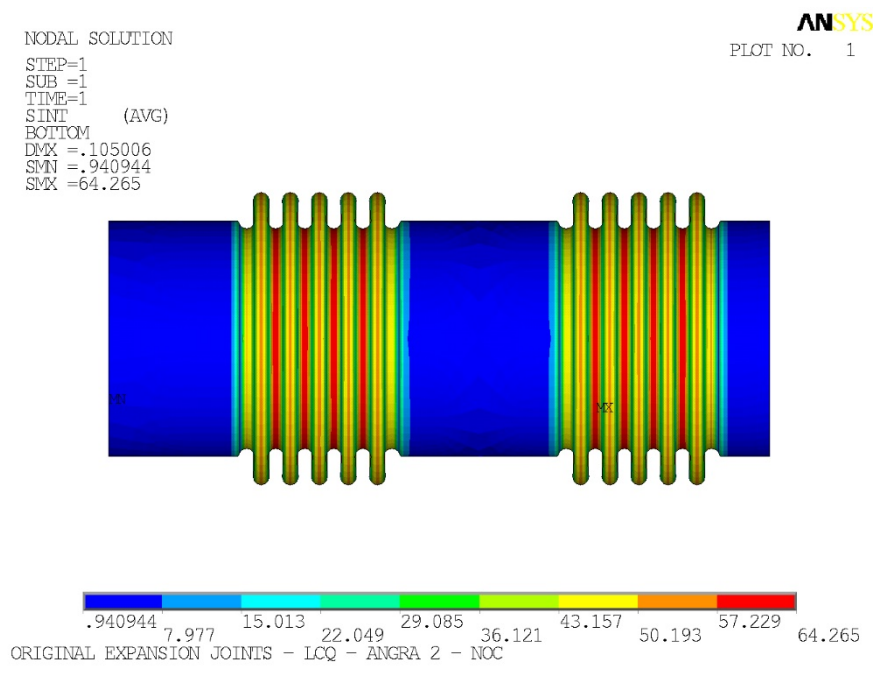
Figure 16– Original & Overlapping + Original Expansion Joints - Stress Intensity –BOTTOM – Load case B1+B2– Internal Pressure

Figure 17– Original & Overlapping + Original Expansion Joints - Meridional and Circumferential Stress – TOP – Load case B1+B2– Internal Pressure
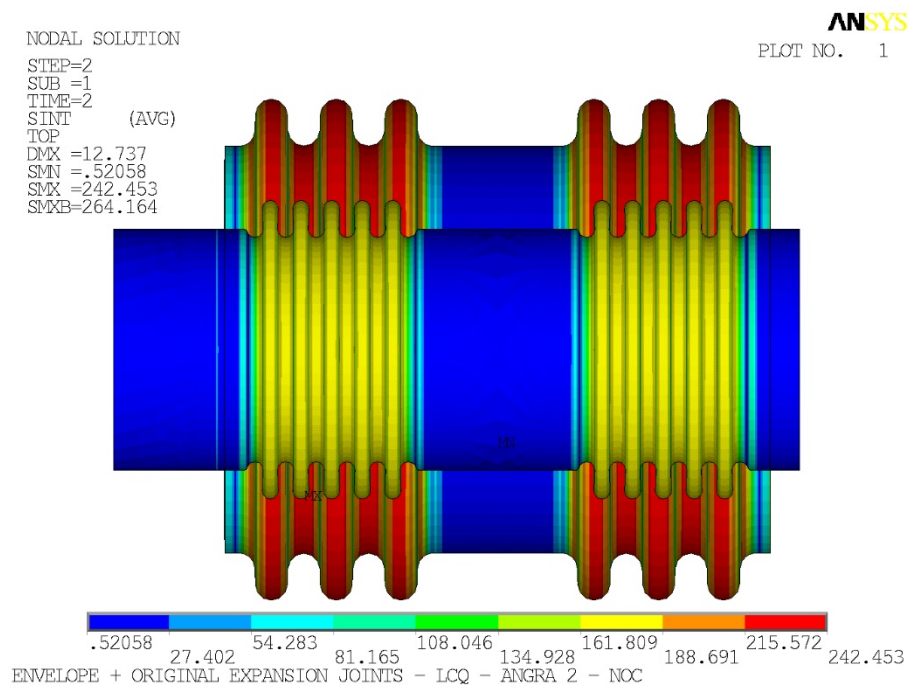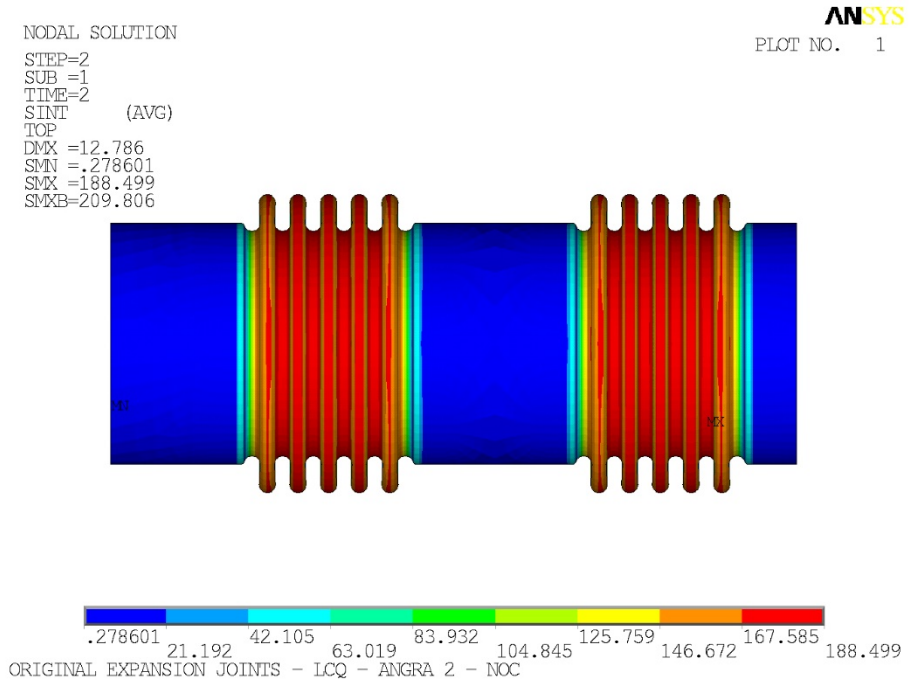
Figure 18– Original & Overlapping + Original Expansion Joints- Stress Intensity –TOP – Load case B1+B2 – Thermal Displacement
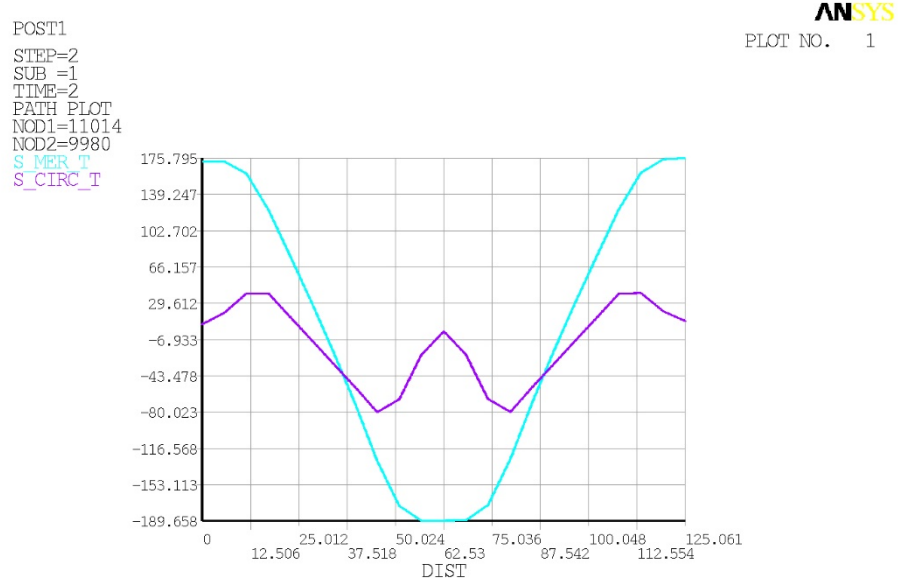
ORIGINAL EXPANSION JOINTS - LCQ - ANGRA 2 - NOC
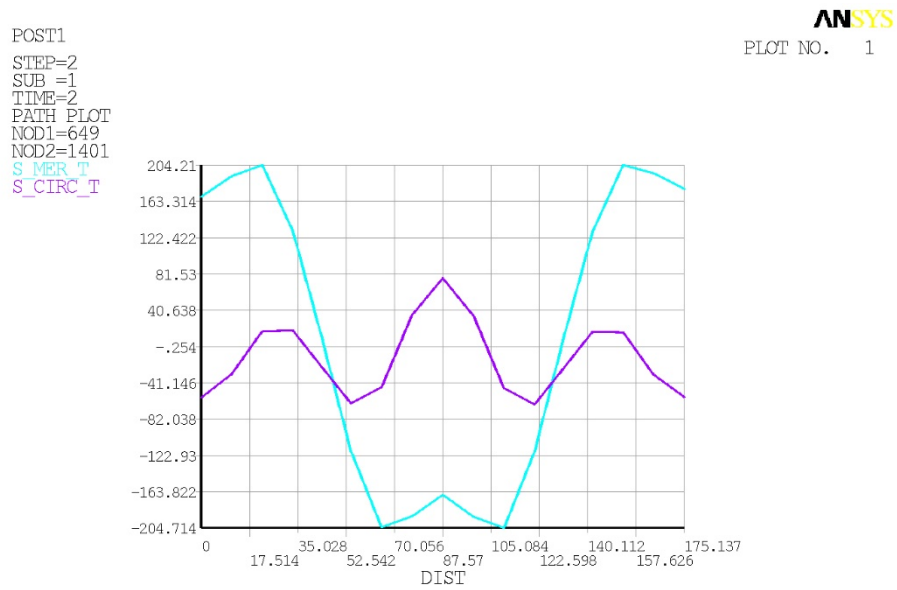
ENVELOPE + ORIGINAL EXPANSION JOINTS - LCQ - ANGRA 2 - NOC

Figure 19– Original & Overlapping + Original Expansion Joints - Meridional and Circumferential Stress – TOP – Load case B1+B2– Thermal Displacement
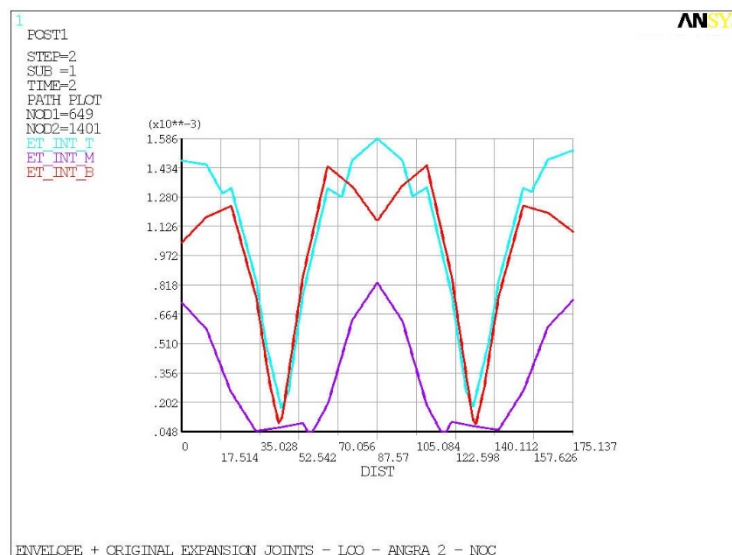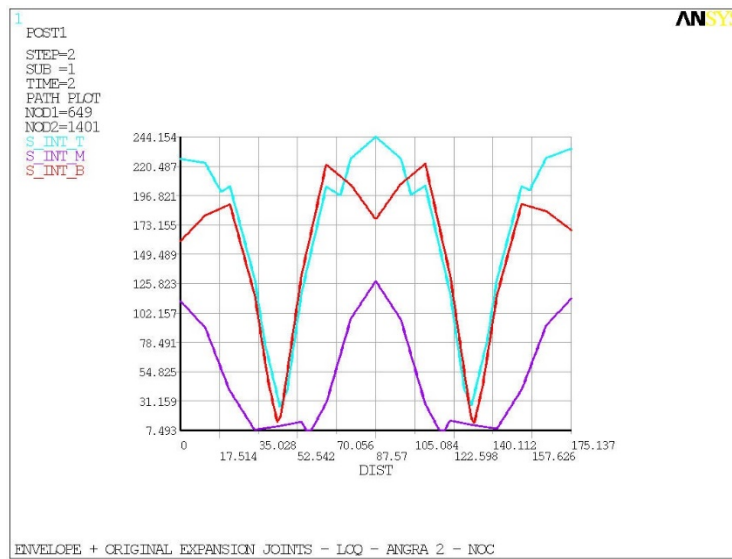
Figure 20– Overlapping + Original Expansion Joints - Stress Intensity and Strain Intensity – TOP, MIDDLE, BOTTOM – Load case B1+B2– Thermal Displacement
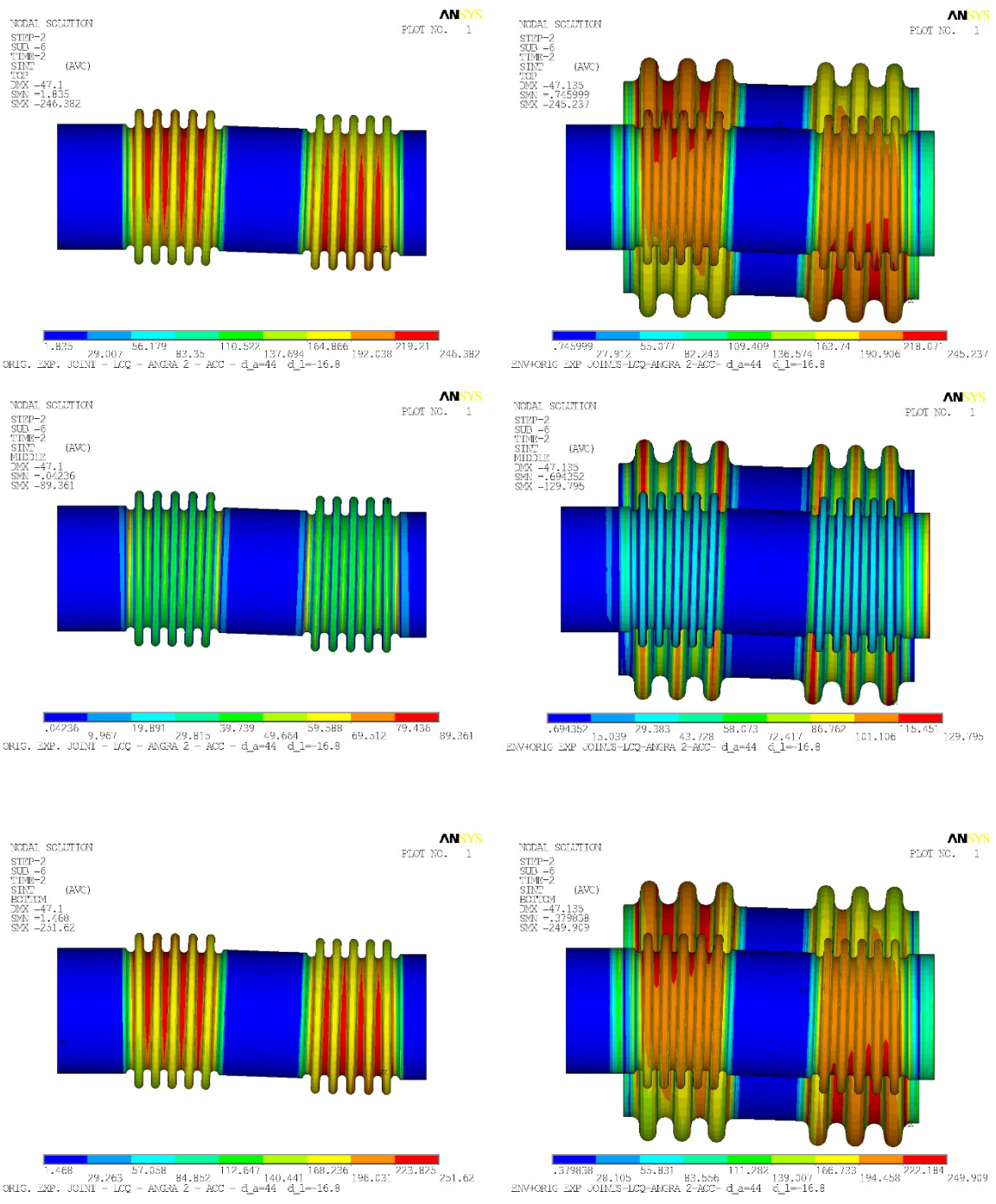
Figure 21– Original & Overlapping + Original Expansion Joints - Stress Intensity– TOP, MIDDLE & BOTTOM – Load case S1 – Internal Pressure Followed by External Pressure + Containment Axial and Lateral Displacements
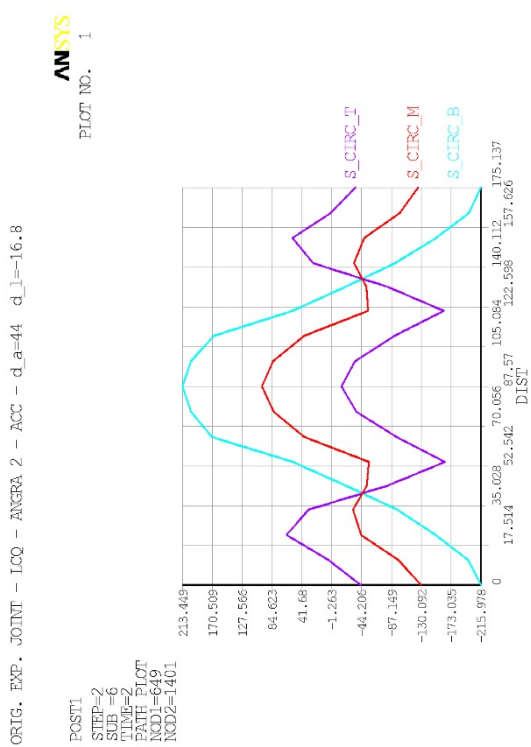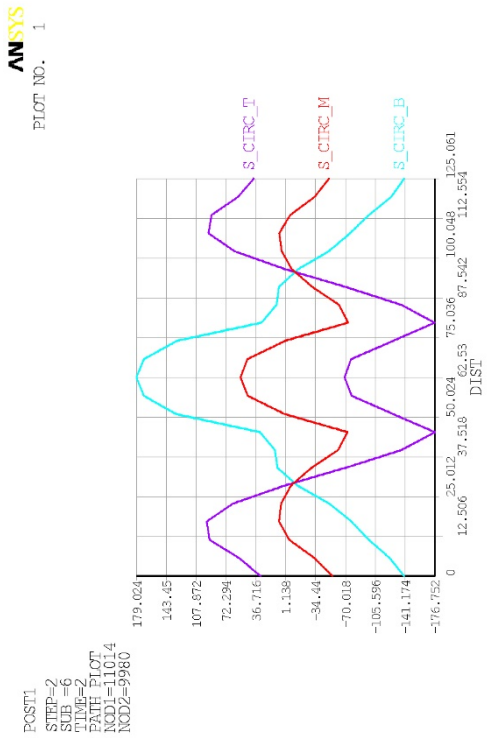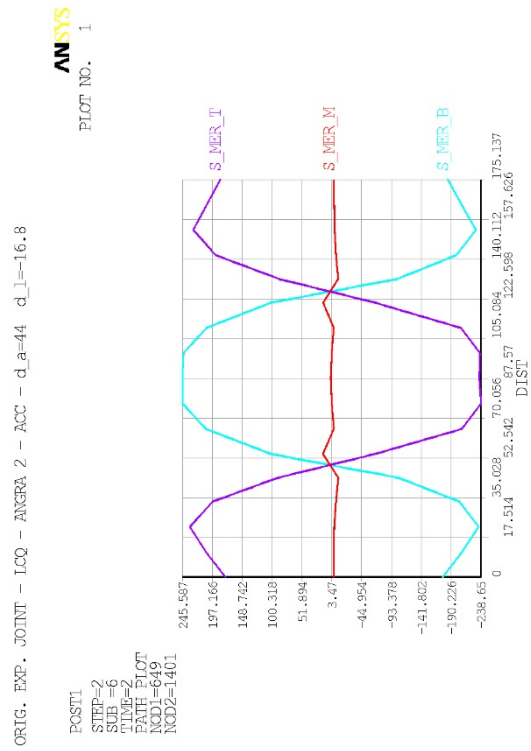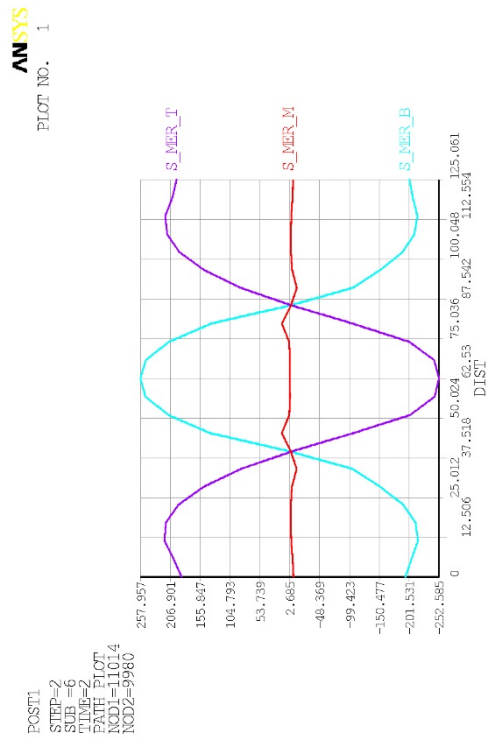
Figure 22– Original & Overlapping + Original Expansion Joints - Circumferential and Meridional Stresses– TOP, MIDDLE & BOTTOM – Load case S1 – Internal Pressure Followed by External Pressure + Containment Axial and Lateral Displacements
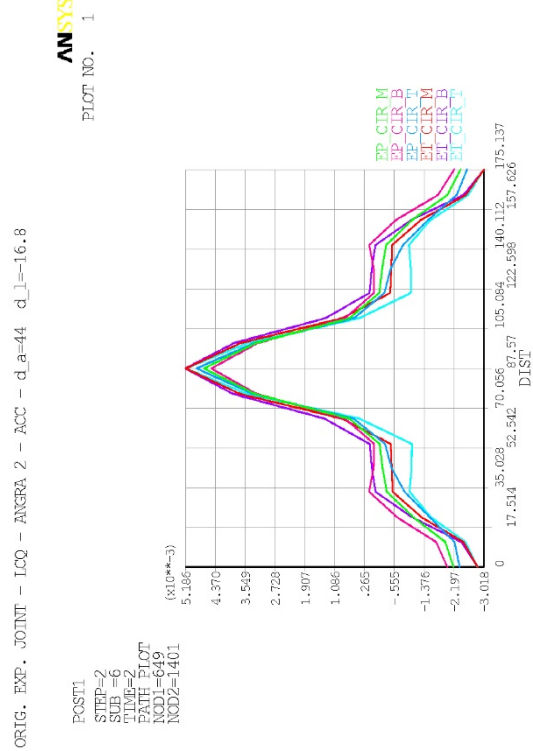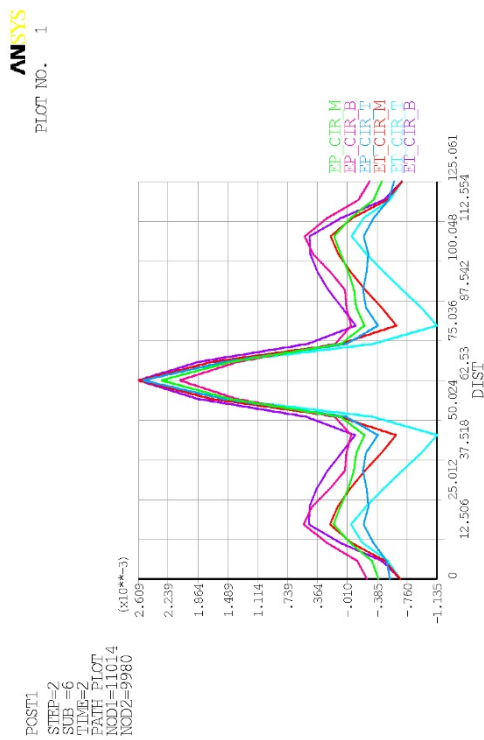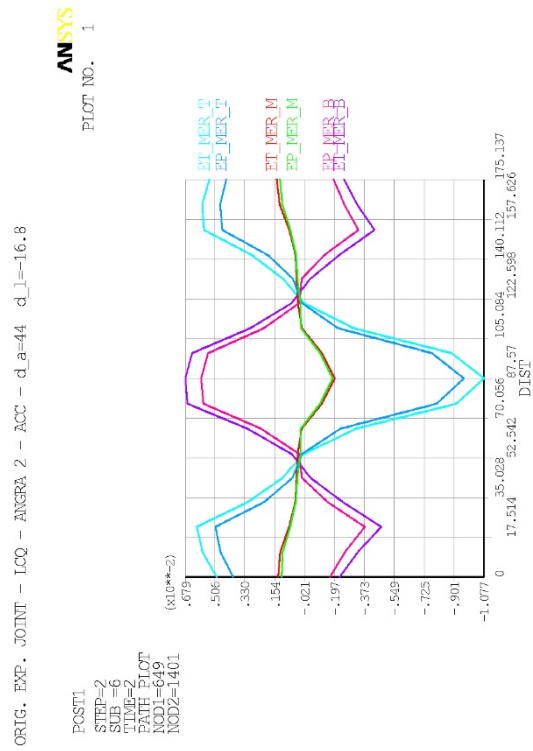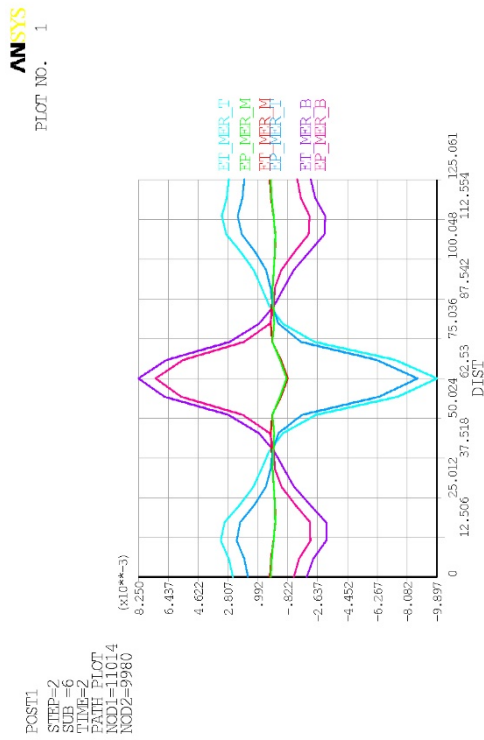
Figure 23– Original & Overlapping + Original Expansion Joints - Circumferential and Meridional Total Strains and Plastic Strains– TOP, MIDDLE & BOTTOM – Load case S1 – Internal Pressure Followed by External Pressure + Containment Axial and Lateral Displacements

5 Stress and fatigue analysis

The stress analysis of the overlapping expansion joint for the operation case (B1+B2) was performed considering the rules of the ASME Code Section III NB-3200. Although this type of verification has not been adopted for the original joint, since the usual is to design it according to the criteria of AD- 2000/B13, here we opted for detailed stress analysis. This alternative gave greater consistency to the structural design of the new piece and facilitated its approval with regulatory agencies in Brazil and Germany. For the other load cases, the qualification of the overlapping joint was by comparison between the results found in its analysis and the original joint.

Expansion joints are used to add flexibility to piping systems. They must withstand internal pressure and, at the same time, be able to absorb, for example, thermal movements. The latter are typically in the form of axial deflections or rotations and, in some cases, lateral displacements at the extremities. Because displacements depend on the number of times the system heats up and cools, the joint should be designed against fatigue.

Joints when requested by internal pressure are subjected to circumferential and meridional stresses. These stresses are called primary, a term used by the ASME code to describe the stresses arising from the external loading, which must satisfy the equilibrium conditions, and which are not self-limiting, that is, once a limit value is reached, plastic flow or collapse occurs. Primary stresses differ from secondary stresses, which in turn have their magnitude reduced as the piece deforms. As secondary stresses are self-limiting, they cause fatigue but do not contribute to the fracture.

In general, expansion joints are analyzed in an elastic regime, even when subjected to high stresses. This is possible because a significant portion of the stresses are secondary and therefore can exceed the yield limit without material failure. The fatigue curves of the ASME Section III code, for example, show values that exceed yield resistance and are therefore deformation curves versus the number of cycles. Thus, although the stress calculated in the elastic regime is not real, it serves as a measure of the strain imposed on the component.

Tables 5 through 10 summarize the results for each of the load cases analyzed in the previous section. The terms that appear in the columns of the tables are identified as:

S_CIR_MAX	Maximum circumferential stress (MPa)
S_CIR_MIN	Minimum circumferential stress (MPa)
S_MER_MAX	Maximum meridional stress (MPa)
S_MER_MIN	Minimum meridional stress (MPa)
S_INT_MAX	Maximum stress intensity (MPa)
ET_CIR_MAX	Maximum circumferential total strain (%)
ET_CIR_MIN	Minimum circumferential total strain (%)
ET_MER_MAX	Maximum meridional total strain (%)
ET_MER_MIN	Minimum meridional total strain (%)
ET_INT_MAX	Maximum total strain intensity (%)
EP_CIR_MAX	Maximum circumferential plastic strain (%)
EP_CIR_MIN	Minimum circumferential plastic strain (%)
EP_MER_MAX	Maximum meridional plastic strain (%)
EP_MER_MIN	Minimum meridional plastic strain (%)

Table 5 – Summary of the Maximum/Minimum Circumferential and Meridional Stresses, Maximum Stress and Strain Intensity for Load case B1+B2 - Internal Pressure

	ORIGINAL EXPANSION JOINT			
	S_CIR_MAX(MPa)	S_CIR_MIN(MPa)	S_MER_MAX(MPa)	S_MER_MIN(MPa)
TOP	20.711	-5.62	61.824	-57.003
MID	15.228	-6.924	3.588	-4.077
BOT	29.509	-25.246	57.044	-65.747
	S_INT_MAX(MPa)	ET_INT_MAX(%)		
TOP	61.824	0.04		
MID	16.22	0.011		
BOT	65.747	0.043		

	OVERLAPPING+ORIGINAL EXPANSION JOINT			
	S_CIR_MAX(MPa)	S_CIR_MIN(MPa)	S_MER_MAX(MPa)	S_MER_MIN(MPa)
TOP	23.598	7.716	57.902	-54.606
MID	26.635	-0.529	3.891	-3.833
BOT	42.859	-16.611	55.725	-50.12
	S_INT_MAX(MPa)	ET_INT_MAX(%)		
TOP	62.501	0.041		
MID	26.963	0.018		
BOT	55.725	0.036		

Table 6 – Summary of the Maximum/Minimum Circumferential and Meridional Stresses, Maximum Stress and Strain Intensity for Load case B1+B2 - Thermal Displacement

	ORIGINAL EXPANSION JOINT			
	S_CIR_MAX(MPa)	S_CIR_MIN(MPa)	S_MER_MAX(MPa)	S_MER_MIN(MPa)
TOP	39.819	-80.091	175.795	-189.658
MID	58.382	-42.908	3.969	0.507
BOT	115.547	-94.224	197.516	-170.681
	S_INT_MAX(MPa)	ET_INT_MAX(%)		
TOP	190.481	0.124		
MID	58.382	0.038		
BOT	197.516	0.128		

	OVERLAPPING+ORIGINAL EXPANSION JOINT			
	S_CIR_MAX(MPa)	S_CIR_MIN(MPa)	S_MER_MAX(MPa)	S_MER_MIN(MPa)
TOP	76.667	-65.608	204.21	-204.714
MID	127.792	-109.596	8.858	4.174
BOT	178.917	-161.994	222.42	-189.968
	S_INT_MAX(MPa)	ET_INT_MAX(%)		
TOP	244.154	0.159		
MID	127.792	0.083		
BOT	222.42	0.145		

Table 7 – Summary of the Maximum/Minimum Circumferential and Meridional Stresses and Strains for Load case P2

	ORIGINAL EXPANSION JOINT			
	S_CIR_MAX(MPa)	S_CIR_MIN(MPa)	S_MER_MAX(MPa)	S_MER_MIN(MPa)
TOP	109.12	-57.001	197.901	-199.475
MID	41.275	-54.978	1.248	-5.916
BOT	123.347	-139.8	201.49	-207.454
	ET_CIR_MAX(%)	ET_CIR_MIN(%)	ET_MER_MAX(%)	ET_MER_MIN(%)
TOP	0.041	-0.057	0.2	-0.191
MID	0.041	-0.057	0.019	-0.02
BOT	0.041	-0.057	0.151	-0.162
	EP_CIR_MAX(%)	EP_CIR_MIN(%)	EP_MER_MAX(%)	EP_MER_MIN(%)
TOP	0.033	-0.042	0.106	-0.098
MID	0.021	-0.03	0.013	-0.015
BOT	0.009	-0.018	0.068	-0.079

	OVERLAPPING+ORIGINAL EXPANSION JOINT			
	S_CIR_MAX(MPa)	S_CIR_MIN(MPa)	S_MER_MAX(MPa)	S_MER_MIN(MPa)
TOP	85.529	-35.008	193.348	-194.055
MID	92.504	-111.072	2.866	-8.799
BOT	177.763	-189.879	199.447	-203.317
	ET_CIR_MAX(%)	ET_CIR_MIN(%)	ET_MER_MAX(%)	ET_MER_MIN(%)
TOP	0.112	-0.135	0.233	-0.239
MID	0.112	-0.135	0.05	-0.052
BOT	0.111	-0.135	0.145	-0.16
	EP_CIR_MAX(%)	EP_CIR_MIN(%)	EP_MER_MAX(%)	EP_MER_MIN(%)
TOP	0.08	-0.093	0.142	-0.144
MID	0.066	-0.08	0.037	-0.039
BOT	0.051	-0.068	0.069	-0.085

Table 8 – Summary of the Maximum/Minimum Circumferential and Meridional Stresses and Strains for Load case S1

	ORIGINAL EXPANSION JOINT			
	S_CIR_MAX(MPa)	S_CIR_MIN(MPa)	S_MER_MAX(MPa)	S_MER_MIN(MPa)
TOP	95.2	-176.752	216.864	-252.585
MID	54.979	-73.253	16.233	-9.503
BOT	179.024	-140.07	257.957	-216.651
	ET_CIR_MAX(%)	ET_CIR_MIN(%)	ET_MER_MAX(%)	ET_MER_MIN(%)
TOP	0.258	-0.114	0.324	-0.99
MID	0.26	-0.07	0.027	-0.082
BOT	0.261	-0.07	0.825	-0.316
	EP_CIR_MAX(%)	EP_CIR_MIN(%)	EP_MER_MAX(%)	EP_MER_MIN(%)
TOP	0.255	-0.06	0.227	-0.871
MID	0.232	-0.044	0.02	-0.075
BOT	0.209	-0.029	0.721	-0.22

	OVERLAPPING+ORIGINAL EXPANSION JOINT			
	S_CIR_MAX(MPa)	S_CIR_MIN(MPa)	S_MER_MAX(MPa)	S_MER_MIN(MPa)
TOP	63.697	-164.054	233.535	-238.65
MID	99.05	-129.686	17.622	-7.141
BOT	213.449	-215.978	245.587	-234.766
	ET_CIR_MAX(%)	ET_CIR_MIN(%)	ET_MER_MAX(%)	ET_MER_MIN(%)
TOP	0.516	-0.301	0.613	-1.077
MID	0.517	-0.302	0.143	-0.199
BOT	0.519	-0.302	0.68	-0.473
	EP_CIR_MAX(%)	EP_CIR_MIN(%)	EP_MER_MAX(%)	EP_MER_MIN(%)
TOP	0.488	-0.255	0.503	-0.959
MID	0.467	-0.237	0.124	-0.186
BOT	0.447	-0.22	0.587	-0.376

Table 9 – Summary of the Maximum/Minimum Circumferential and Meridional Stresses and Strains for Load case S2

	ORIGINAL EXPANSION JOINT			
	S_CIR_MAX(MPa)	S_CIR_MIN(MPa)	S_MER_MAX(MPa)	S_MER_MIN(MPa)
TOP	86.096	-153.483	223.175	-227.011
MID	57.223	-42.412	10.927	-0.473
BOT	168.3	-150.65	230.614	-223.124
	ET_CIR_MAX(%)	ET_CIR_MIN(%)	ET_MER_MAX(%)	ET_MER_MIN(%)
TOP	0.215	-0.134	0.613	-0.753
MID	0.216	-0.134	0.066	-0.08
BOT	0.217	-0.134	0.593	-0.481
	EP_CIR_MAX(%)	EP_CIR_MIN(%)	EP_MER_MAX(%)	EP_MER_MIN(%)
TOP	0.208	-0.134	0.508	-0.644
MID	0.186	-0.112	0.06	-0.072
BOT	0.165	-0.09	0.499	-0.389

	OVERLAPPING+ORIGINAL EXPANSION JOINT			
	S_CIR_MAX(MPa)	S_CIR_MIN(MPa)	S_MER_MAX(MPa)	S_MER_MIN(MPa)
TOP	54.912	-134.506	221.804	-217.793
MID	111.14	-92.424	8.216	-1.778
BOT	210.961	-199.017	222.535	-220.61
	ET_CIR_MAX(%)	ET_CIR_MIN(%)	ET_MER_MAX(%)	ET_MER_MIN(%)
TOP	0.482	-0.376	0.838	-0.893
MID	0.483	-0.376	0.195	-0.202
BOT	0.484	-0.376	0.567	-0.481
	EP_CIR_MAX(%)	EP_CIR_MIN(%)	EP_MER_MAX(%)	EP_MER_MIN(%)
TOP	0.444	-0.35	0.729	-0.786
MID	0.425	-0.328	0.18	-0.186
BOT	0.407	-0.306	0.481	-0.395

Table 10 – Summary of the Maximum/Minimum Circumferential and Meridional Stresses and Strains for Load case S3

	ORIGINAL EXPANSION JOINT			
	S_CIR_MAX(MPa)	S_CIR_MIN(MPa)	S_MER_MAX(MPa)	S_MER_MIN(MPa)
TOP	43.084	-89.158	156.929	-162.339
MID	44.265	-35.463	4.853	-1.946
BOT	110.502	-93.911	172.046	-160.585
	ET_CIR_MAX(%)	ET_CIR_MIN(%)	ET_MER_MAX(%)	ET_MER_MIN(%)
TOP	0.038	-0.026	0.116	-0.14
MID	0.038	-0.026	0.012	-0.013
BOT	0.039	-0.026	0.115	-0.092
	EP_CIR_MAX(%)	EP_CIR_MIN(%)	EP_MER_MAX(%)	EP_MER_MIN(%)
TOP	0.025	-0.015	0.04	-0.061
MID	0.017	-0.009	0.008	-0.008
BOT	0.008	-0.003	0.044	-0.024

	OVERLAPPING+ORIGINAL EXPANSION JOINT			
	S_CIR_MAX(MPa)	S_CIR_MIN(MPa)	S_MER_MAX(MPa)	S_MER_MIN(MPa)
TOP	29.829	-68.497	157.956	-158.092
MID	91.725	-80.838	7.851	-3.891
BOT	153.62	-143.882	167.866	-160.582
	ET_CIR_MAX(%)	ET_CIR_MIN(%)	ET_MER_MAX(%)	ET_MER_MIN(%)
TOP	0.087	-0.073	0.147	-0.152
MID	0.087	-0.073	0.031	-0.03
BOT	0.088	-0.073	0.109	-0.093
	EP_CIR_MAX(%)	EP_CIR_MIN(%)	EP_MER_MAX(%)	EP_MER_MIN(%)
TOP	0.05	-0.042	0.069	-0.076
MID	0.042	-0.032	0.021	-0.02
BOT	0.033	-0.023	0.045	-0.03

The permissible stresses for case B1+B2 are obtained from Table 1 and the stress limits for the corresponding temperature are those of ASME code Section III NB-3200, [1], shown in Table 11.

Table 11 – Admissible Stress for Primary and Secondary stresses

Stress Category	Admissible Stress (MPa) T=80°C
P_m = Primary Membrane	S_m=145.50
P_L+P_b = Primary Local + Bending	1.5 S_m=218.25
P+Q = Primary + Secondary	3.0 S_m=436.50

The current stresses calculated according to ASME Section III NB-3200 and the respective stress limits are compared in Table 12. It is observed that the primary and secondary stresses meet the criteria of the code.

Table 12 – Comparison between Primary and Secondary Acting Stress and Admissible Stress

Stress Category	Acting Stress (MPa) Original expansion joint	Acting Stress (MPa) Original expansion joint	Admissible Stress (MPa) T=80°C
P_m	16.2	27.0	S_m=145.50
P_L+P_b	65.7	62.5	1.5 S_m=218.25
P+Q	197.5	244.1	3.0 S_m=436.50

In fatigue analysis, only the operating conditions (B1+B2) are considered, since the number of cycles for the other conditions (P1, P2, S1, S2, S3) is very low. The stresses due to internal pressure and thermal displacements were obtained by elastic analysis and are shown in Tables 5 and 6.

Fatigue analysis is performed based on effective total strain range curves versus cycles obtained by numerous tests conducted by joint manufacturers. The AD-2000/B13 establishes the correlation

$$N = \left(\frac{10}{2.\varepsilon_{ages}}\right)^{3.45} \quad \text{for } 500 \leq N \leq 10^6 \tag{2}$$

where N is the number of cycles to failure and ε_{ages} is the strain. The allowable number of N_{allow} cycles is

$$N_{allow} \leq \frac{N}{S_L} \quad \text{with } S_L = 5.0 \tag{3}$$

Where S_L is a safety factor adopted for cases in which there are no fatigue test results in the installed joint, as is the situation of Angra 2.

From Table 6 the maximum total deformation intensity is $2\varepsilon_{ages}$=0.159%. As the longitudinal weld of the overlapping joint was manufactured during assembly in the field, an additional safety factor of 4 is employed. By replacing these values in the previous formula, we reach the allowable number of stress cycles N_{allow} equal to 2686 cycles.

It is noted that the calculated number is much higher than expected to occur during the remaining life of the plant. The qualification of the modified configuration for the other load cases (Test-P2, LOCA-S1 and S2, and SSB-S3) was made by comparing the results obtained for the models with the original joint and those with the overlapping joint.

Tables 7 to 10 show that even if there is an increase in plastic strain for the new configuration, these values are close to 1%, with a total strain value equal to 1.077% (load case S1).

6 Conclusions

This chapter presents the stress and fatigue analysis of the modification performed in the original expansion joint of the Angra 2 steam generator purge system. The amendment, which consisted of installing an overlapping joint capable of resisting all originally planned loads, was adopted to circumvent the problems arising from replacing the deformed joint with a new one.

Two finite element models were developed, one to simulate the original joint and the other to represent the original plus the overlapping joint. The analyses were performed under an elastic regime for the operation condition (internal pressure and thermal displacements) and elastoplastic for the test and accident cases (earthquake and LOCA).

The overlapping joint was qualified for the operation loads (B1+B2) comparing the current stresses with the limits of the ASME Code Section III NB-3200. For fatigue analysis, the AD 2000/B13 procedure was followed. For the other requests (Test-P2, LOCA-S1 and S2, and SSB-S3) the structural qualification was made by comparing the results of both models, using the value of the calculated plastic deformation.

References

ASME Section III Rules for Construction of Nuclear Power Plant Components, ASME B&P Vessel Code, American Society of Mechanical Engineers. New York, 2010.

AD 2000-MerkBlatt B13 - Single-ply bellows expansion joints.

ANSYS 12.1® - User manual.

DIN 17440 07/85 Stainless steels; technical delivery conditions for plates, hot-rolled strip, wire rods, drawn wire, bars, forgings, and semi-finished products.

MTS 107.01.R2 – Material Test Sheet

IWKA reports 501.02-300155/300156 – Bellows Design

Ramberg, W.; W. R. Osgood. Description of Stress-Strain Curves by Three Parameters. NACA TN 402, National Advisory Committee for Aeronautics, 1943.

Kraftwerk Union, Angra 2 BRA 011RSB Rohrdurchfuhrung Auslegungsblatt fur Kompensatoren ABK, V 245/134/82, Seite 13.1/13.2.

Suanno, R., Fatigue and Stress Analysis of the Bipartite Overlapping Expansion Joints of the Containment Penetration JMK05D0201 (LCQ50) – Eletronuclear internal report BQ/2/LCQ50/110114

Suanno, R., Maneschy, J.E., Francioni, M., Stress Analysis of the Bipartite Overlapping Expansion Joints of the Containment Penetration – Angra 2. Proceedings of the ASME 2012 Pressure Vessels & Piping Division Conference, PVP2012-78840, Toronto, Ontario, Canada.

Chapter 10

Leak-Before-Break Technology for Piping in Nuclear Industry

Leak-Before-Break Technology for Piping in Nuclear Industry

José Eduardo Maneschy

JEM Consultoria. E-mail:emanesc@gmail.com

Abstract

Leak-Before-Break (LBB) concept is applied in the nuclear industry to eliminate from the piping design the postulated guillotine breaks. The adoption of this technology allows to design mechanical component and supports without the high dynamic loads which results from the pipe rupture. This chapter shows how thermo-hydraulics, material science, and elastic-plastic fracture mechanics are employed to apply the LBB technology to eliminate rupture from a large primary loop piping.

Keywords: LBB; guillotine break; fracture mechanics; leak rate

1 Problem Description

The concept of leak-before-break (LBB) in piping has been used in the nuclear industry since the mid-1980s. The basic idea of the LBB is to perform an analysis to demonstrate that leakage through a circumferential crack (or flaw) is detected by the leakage monitoring system and the plant is shutdown before the unstable crack growth. The LBB demonstration involves some engineering disciplines, highlighting thermo-hydraulics, materials science, and fracture mechanics.

Historically, the LBB concept was developed to eliminate double-ended guillotine break loss-of-coolant accident (LOCA) from the structural design. LOCA is postulated to occurs in primary loop piping and other high energy lines, those with operating temperature or pressure greater than 200°F or 275 psig, respectively. Once the LBB is demonstrated these ruptures are excluded from the design basis and the dynamic stresses resulting from LOCA are not considered in the structural analysis of the mechanical components. As a result, it is no longer necessary to design the reactor vessel internals and nozzles, primary loop equipment and supports, and piping against these dynamic loads.

Another advantage of applying LBB is that pipe-whip restraints and jet-impingement shields, both required to protect critical equipment from the dynamic effects of the postulated rupture, could be removed. As the costs of these protection elements are high, and in some cases their existence makes it difficult or even impossible to inspect components in service, the removal or non-installation of these restraints and shields is

highly desirable not only for economic reasons, but also, to reduce the radiation dose received by maintenance personnel.

The most common approaches to apply LBB are those based on the J/T methodology or on the limit load theory. The two mandatory technical references for LBB analysis in Brazil and U.S. are NUREG-1061 [1984] and SRP 3.6.3 [1987]. In 2007, SRP 3.6.3 was issued with no significant change in calculation procedures compared to the original edition. LBB is demonstrated when all requirements in these documents are met.

In this chapter, the LBB concept is used to eliminate from the design of the primary loop the postulated guillotine break. In Figure 1, the segment of one reactor coolant loop piping (the hot leg) is schematically represented with a circumferential crack in the region adjacent to the weld, subject to axial loads P and moment M resulting from normal operating (pressure, deadweight, and thermal expansion) and accident conditions (basic design earthquake, DBE). The geometric characteristics of the pipe are the outside diameter, D_o, equal to 33.9 inches and the thickness, t, of 2.45 inches, which is manufactured from SA-351 CF8A cast stainless steel. The weld is constructed with stainless steel SFA-5.4 (SMAW for filler) and SFA-5.9 (GTAW for root pass).
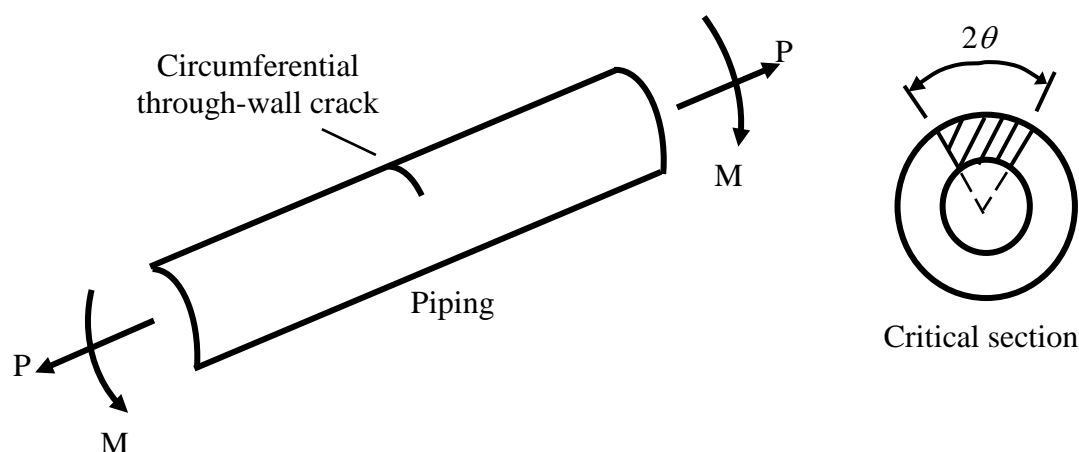
Figure 1: Segment of the pipe and section where the break is postulated

2 Step-by-Step or the Application of LBB

As established in NUREG 1061 and SRP 3.6.3, to demonstrate the LBB requirements are met, the following seven steps are considered:

1 - Show that the piping is not susceptible to degradation in service such as high or low cycle fatigue, stress corrosion cracking, erosion, damage caused by water hammer, etc. An assessment must be prepared to demonstrate that the integrity of the piping during plant lifetime will not be affected by any type of degradation.

2 - Obtain the tensile and fracture properties of the base and weld metals, given by the stress and strain curve and the *J*-integral *versus* crack extension (J-R) curve), both estimated using the actual information of the piping materials or, in the absence of these, in similar data found in the literature. The properties are established assuming that the material is thermally aged, that is, its original characteristics are modified (reduced toughness) by the effect of the operating temperature.

3 - Determine the loads (axial force and moment) for leak rate analysis and crack stability. In the first case algebraic combination is used for normal operating loads. The crack stability check is performed with the sum of the absolute values of the normal operating and accident (DBE) operating loads.

4 - Postulate the through-wall circumferential flaw in the section of the piping with the highest stress in conjunction with the most unfavorable tensile and fracture material properties. Several sections of piping must be analyzed because the critical location is not always the point of the highest stress.

5 - Multiply by 10 the leakage monitoring system capability. Typically, plants have monitoring systems that detect leaks of less than 1.0 gpm (gallon per minute) in no more than one hour.

6 - Perform leak rate analysis for cracks subject to normal operating loads. In this step, the flaw under this condition will open and produce the leakage detected by the monitoring system. The leakage crack size is multiplied by 2.0.

7 - Use elastic-plastic fracture mechanics based on the J/T method to verify if the previously obtained crack is stable under normal operating combined with accident loads. If this requirement is met the guillotine break will not occur. Alternatively, depending on the toughness of the material, the analysis may be conducted by limit load theory.

The safety coefficients for leakage (10, step 5) and crack size (2, step 6) aim to cover the uncertainties inherent in the formulations used in the calculation of the leakage crack size (step 6) and critical crack size (step 7).

The main aspects of LBB that is covered in this chapter are crack stability analysis (step 7), material characterization (step 2) and leakage analysis (step 6).

3 Crack Stability Analysis

In LBB applications the circumferential through-wall flaw is subject to extreme stresses in which the normal operating and accident loads are superimposed. In this condition, as the plastification level is expressive, the analysis is carried out in an elastic-plastic regime. Depending on the toughness of the material, the J/T approach, developed in NUREG/CR-3464 [1983], is the most used technique for checking the crack stability. The analysis using the limit load theory is described in Section 6.

J-integral and tearing modulus *T* are quantities that represent the potential for crack extension. When applied *J* is smaller than J_{Ic}, defined as *J* at flaw initiation, crack growth does not occur. On the other hand, when *J* is equal to or greater than J_{Ic}, stable tearing is initiated. In this situation, the J/T method is adopted to determine when the defect becomes unstable, that is, the instant associated with the pipe rupture. The correlation between the *J* and *T* is

$$T = \frac{dJ}{da} \frac{E}{\sigma_f^2} \tag{1}$$

with *dJ* the increase in *J* to an amount of crack extension *da*, σ_f the flow stress, assumed as the average between the yield and ultimate strength of the material, S_y, and S_u,

respectively, and E is the modulus of elasticity. The crack instability occurs when the applied tearing modulus is greater than the material tearing modulus T_{mat},

$$T > T_{mat} \tag{2}$$

with T_{mat} obtained experimentally.

The J-integral, the parameter that indicates the driving force that extends the crack, is calculated using the General Electric and Electric Power Research Institute (GE/EPRI) scheme. The total value of J is the sum of the elastic J_e and plastic J_p components. For pipe with circumferential through-wall flaw subject to combined axial load P and moment M, Zahoor [1989] defines the following equations

$$J_e = f_t \frac{P^2}{4Rt^2E} + f_b \frac{M^2}{R^3t^2E} \tag{3a}$$

$$J_p = \alpha\sigma_o\varepsilon_o R(\pi-\theta)\left(\frac{\theta}{\pi}\right)h_l\left(\frac{P}{P_o}\right)^{n+1} \tag{3b}$$

with R the mean radius of the pipe and t the thickness, θ half-angle of flaw (in radians) illustrated in Figure 1, P_o the reference load, assumed the value in which the pipe section is fully plastic, and α and n the constants of the Ramberg-Osgood stress and strain curve, written as

$$\frac{\varepsilon}{\varepsilon_o} = \frac{\sigma}{\sigma_o} + \alpha\left(\frac{\sigma}{\sigma_o}\right)^n \tag{4}$$

with σ and ε true stress and strain, σ_o the reference stress, usually assumed the yield stress, and ε_o the reference strain, equal to σ_o/E.

The correction factors f_t and f_b are functions of crack size and type of load; the dimensionless function h depends on the component and crack geometry, type of load, and constant n from the Ramberg-Osgood equation. Values of f_t, f_b, and h, shown in Figure 2, are found in Zahoor [1989].

To determine the applied tearing modulus, T, two solutions are calculated for J. One, with flaw length a, and other with $a+\Delta a$, where $\Delta a=R\Delta\theta$ and $\Delta\theta$ commonly assumed to be 0.01θ. Thus, from Equation (1)

$$T = \frac{J_{a+da} - J_a}{\Delta a}\frac{E}{\sigma_f^2} \tag{5}$$

4 Material Properties

Fracture properties are given in terms of the J-R curve, which indicates the materials resistance to stable crack growth. The correlation between the J-integral of the material, J_{mat}, and the crack extension, Δa, is expressed as
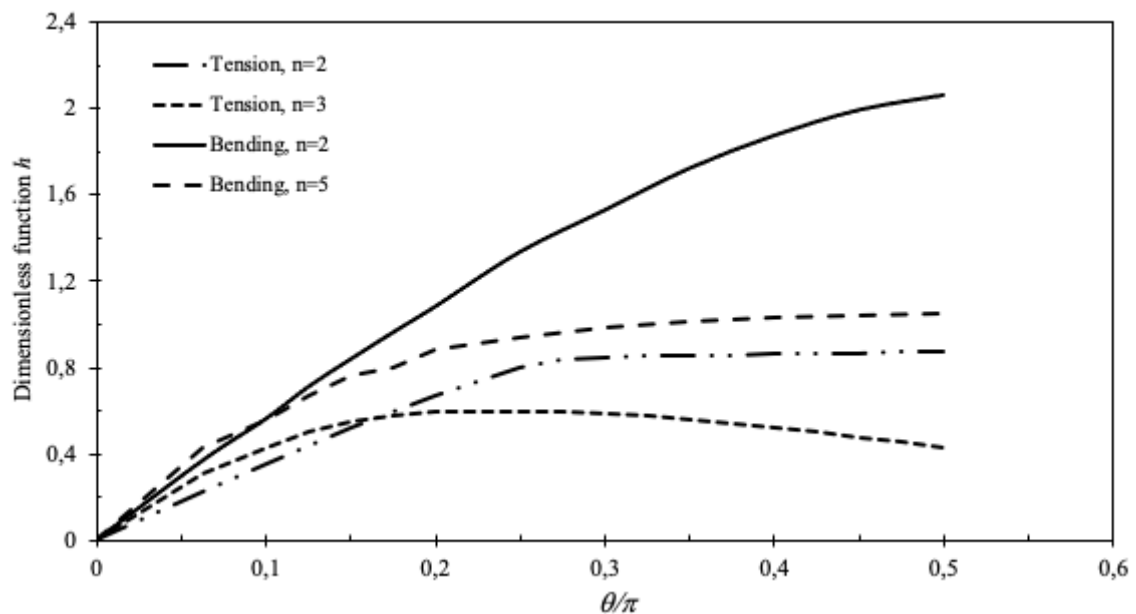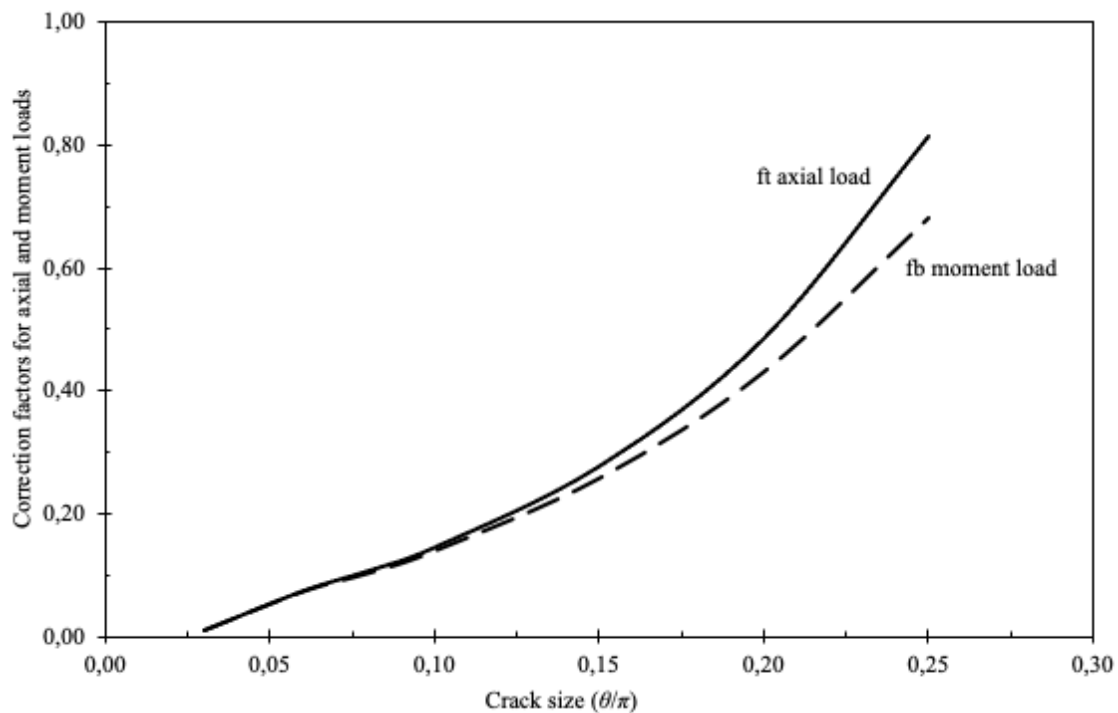
Figure 2: Values of f_t, f_b, and h as a function of through-wall circumferential crack

$$J_{mat} = c\Delta a^m \tag{6}$$

with c and m constants obtained by experiments. Instability is achieved when the J increase exceeds the corresponding increase in toughness. This establishes the ductile failure criterion (ductile tearing failure mode) as $T > T_{mat}$, where the materials tearing modulus is, as in Equation (1),

$$T_{mat} = \frac{dJ_{mat}}{da} \frac{E}{\sigma_f^2} \tag{7}$$

The properties of base metals and welds of the pipe analyzed in this chapter consider the fracture toughness modeled by Equation (6), with the data from the J-R curves shown in Table 1 and represented in Figure 3. All information are for thermally aged materials available in NUREG/CR-4513 [1994] for base metal and NUREG/CR-6428 [1996] for weld.

Table 1 – Fracture properties for aged material (minimum values)

	J_{Ic} in-lb/in^2	c in-lb/in^2	m
Base metal (SA 351-CF8A)[1]	1500	5660	0.34
Weld metal (stainless steel)[2]	228	3813	0.64

[1] Properties at 550°F   [2] Properties at 617°F
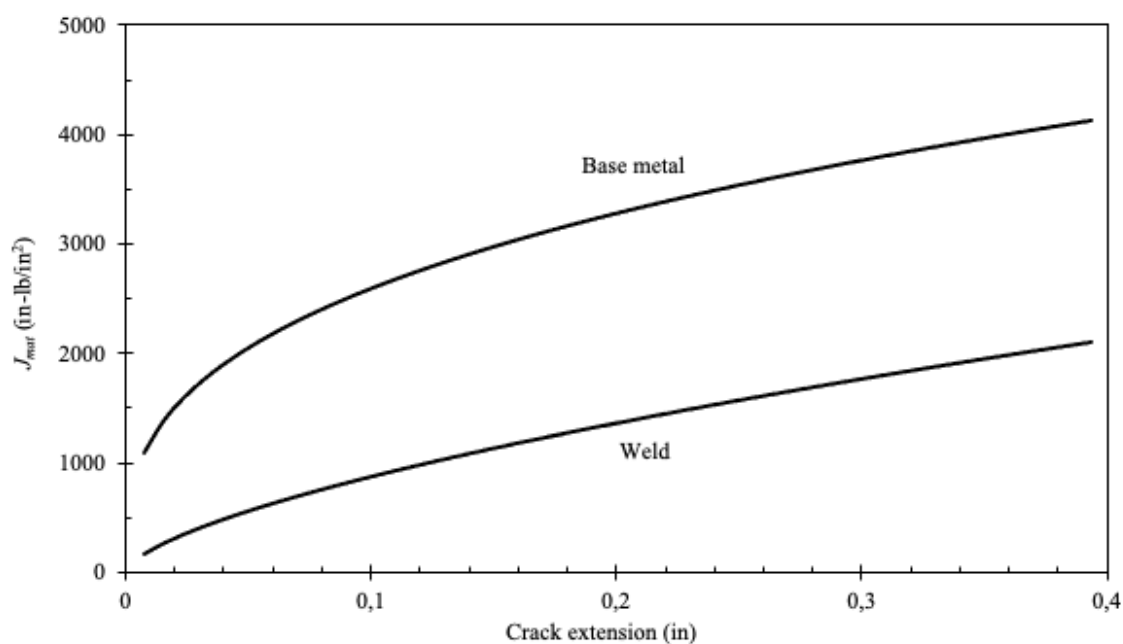
Figure 3: J-R curve for aged material (minimum values at 550°F)

The GE/EPRI scheme requires, in addition to fracture properties, that the stress and strain curve of the material be represented by the sum of the elastic and plastic deformation portions given by the Ramberg-Osgood as presented in Equation (4). Values from this curve are shown in Table 2 and in Figure 4. As in the previous case, the properties are for thermally aged materials and were taken from the NUREG/CR-6142 [1994] and NUREG/CR-4513 [1994].

Table 2 – Tensile properties for aged material

	E ksi	σ_o ksi	S_u ksi	α	n
Base metal (min.)[1]	24940	21.78	64.82	1.28	5.9
Base metal (avg.)[1]	24940	25.80	79.86	0.45	5.9
Weld metal (min.)[2]	25215	47	60	-	-

[1] Properties at 550°F (SA 351-CF8A)   [2] Properties at 617°F (stainless steel)
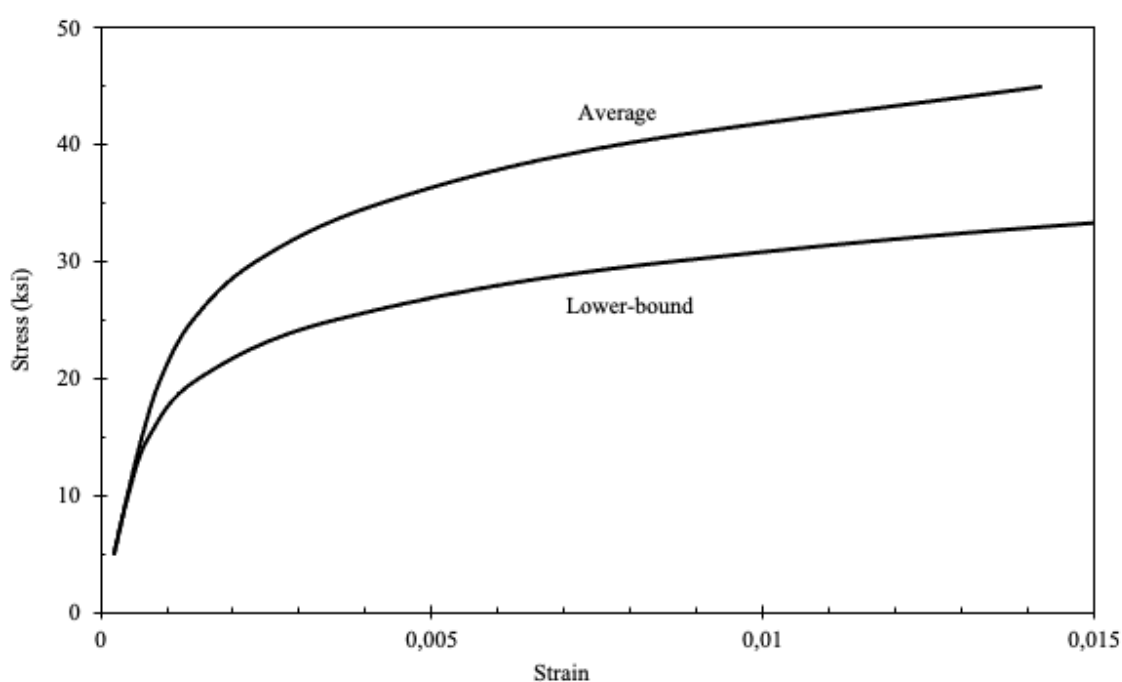
Figure 4: Stress and strain curve for aged material (SA 351-CF8A at 550°F)

5 Leak Rate Analysis

In accordance with step 6 of Section 2 of this chapter, the LBB application requires that a correlation be established between the flow rate, Q, and the through-wall crack size, θ/π, for the piping under normal operating loads. Based on this result it is determined the crack that will open to produce a leakage capable of being detected by the plant monitoring system.

Leak rate is obtained by two analyses, the first using elastic-plastic fracture mechanics to calculate the crack opening area, COA. Once COA is found, thermo-hydraulic analysis is performed to determine leak rate through the crack.

Several computer programs are available for leak rate analysis. Among them, SQUIRT, from the U.S. Nuclear Regulatory Commission (NRC), PICEP owned by EPRI, and proprietary softwares developed by reactor vendors such as Westinghouse, Framatome, and Mitsubishi. The PICEP [1992] is widely used for LBB applications in the nuclear industry and is adopted in the present analysis.

In PICEP, the conditions for the fluid are subcooled water, saturated or superheated steam, with leak rate dependent on pressure, temperature, and on the morphology of the crack (e.g., surface roughness, straight or sinuous flow path, friction factor). The PICEP leak rate model is based on the Henry-Fauske equations [1970; 1971] for the two-phase fluid through long channels. The program calculates the crack tip opening displacement, COD, using the GE/EPRI scheme. The implemented formulas for COD are compilations of the solutions obtained by the finite element method for axial loads, pure bending, and for the combination between them [Zahoor 1989]. The crack area through which leakage occurs is estimated by assuming elliptical, diamond, or circular shaped openings when viewed from the pipe surface. Analytical and experimental results suggest that the ellipse shape is the most suitable for LBB applications.

The PICEP was validated by comparing its results with those of numerous experiments carried out by the NRC (NRC Degraded Piping Program) and EPRI in the U.S., and by others in Canada, Italy, and Japan. In addition, PICEP results were compared with those provided by software such as the mentioned SQUIRT.

For the leak rate analysis, thermo-hydraulic conditions related to the normal operation of the plant are used. The behavior of the material is represented by the Ramberg-Osgood equation, Equation (4), with its properties given in terms of the average values. This is a conservative option because it leads to leaks that produce larger crack opening angles.

Following step 5 of Section 2, the normalized crack length, θ / π, is obtained with the minimum detectable leakage from the monitoring system (e.g. 1.0 gpm) multiplied by 10. The use of this safety factor minimizes any errors that may be introduced into the model adopted to characterize the crack.

6 Example

In this study, the LBB is verified for a pipe subjected to the loading shown in Table 3. The postulated through-wall circumferential flaw is in the base metal, in one of the critical sections, which were selected from the material properties and stresses acting on the pipe. The values of P and M in Table 3 are given by the structural analysis of the piping, with P being the axial reaction forces, including the pressure load, and M is the applied moment, calculated as the square root of the sum of squares of each of the bending and torsion moments. Leakage analysis combines pressure, weight, and thermal loads by the algebraic sum. Stability analysis combine these loads plus DBE by the absolute sum.

Table 3 – Loads at piping critical section

Leakage analysis		Stability analysis	
P (kips)	M (in-kips)	P (kips)	M (in-kips)
1500	18713	1838	21327

For the leak rate analysis, it is assumed that the through-wall circumferential flaw is caused by fatigue and has an elliptical shape. In this type of degradation, the crack is straight along the entire pipe thickness. PICEP recommends that leakage and flaw morphology be characterized by surface roughness equal to 0.00157 inches, pressure loss coefficient of 0.61, and the ratio of crack inlet area to exit area be 1.0. Initial fluid conditions are subcooled water, internal pressure of 2250 psia, and temperature of 620°F. Average material properties are given in Table 2 and normal operating loads (pressure, weight, and thermal) in Table 3.

The result for the leak rate analysis in terms of the flow rate, Q, and the half-normalized flaw angle, θ/π, is represented in Figure 5 for the base metal at one critical location.

Leakage monitoring systems installed in the plants have the sensitivity to measure flow rates above 0.01 gpm, with 1.0 gpm being the typical number for LBB applications. From step 5 of Section 2, the leakage crack size is found using a safety factor of 10. Thus, with 10 gpm on the curve in Figure 5, θ/π is equal to 0.0695 (12.5 degrees).

In LBB applications, several sections of piping must be analyzed, as the largest θ/π does not necessarily occur where the stresses for the normal operating condition are the highest. This is because the lower the stress, the higher the crack size to maintain constant flow. Consequently, loads lower than those for P and M in Table 3 produce a curve more to the right than shown in Figure 5 which, for a fixed value of Q (e.g., 10 gpm), allows to obtain θ/π greater than 0.0695. Furthermore, other factors, such as the toughness of the material, influence the result and only a complete analysis determines the most critical section.

For the stability analysis, and according to step 6 of Section 2, the leakage crack size associated with the detectable leak rate ($\theta/\pi = 0.0695$) is multiplied by 2.0. Therefore, the stability is verified for θ/π equal to 0.139. In this example, by hypothesis, applied J is greater than J_{Ic}, and thus the crack extension occurs. The J/T method is implemented with the minimum material properties from Tables 1 and 2 and with the combination of normal operating and accident loads (pressure, weight, thermal, and DBE) from Table 3.

With Equations (3) and information from Zahoor [1989], the total value of J is equal to 607.9 in-lb/in2. From Equation (1) the applied T is 3.02. Combining Equations (6) and (7), the material tearing modulus, T_{mat}, is equal to 26. As T is smaller than T_{mat}, the flaw postulated in the SA 351-CF8A base metal is stable, that is, the failure by ductile tearing does not occur. The graphical representation of the method is in Figure 6.

Considering now the flaw is in the stainless steel weld and is subjected to the loads from Table 3 and conditions identical to those in the previous example. Although the flaw is in the weld, the tensile properties of the base metal control fracture. This, θ/π, applied J, and T remain the same (the values of J and T in the weld are smaller than in the base metal). The only changes are in the fracture properties of the materials, Table 1 and Figure 3, now those from the weld. Using the same calculation procedure, the T_{mat}, is equal to 28. As T is smaller than T_{mat}, the flaw postulated in the stainless steel weld is stable, with a safety coefficient slightly higher than that of the case of crack in the base metal. The results for both cases are shown in Table 4.
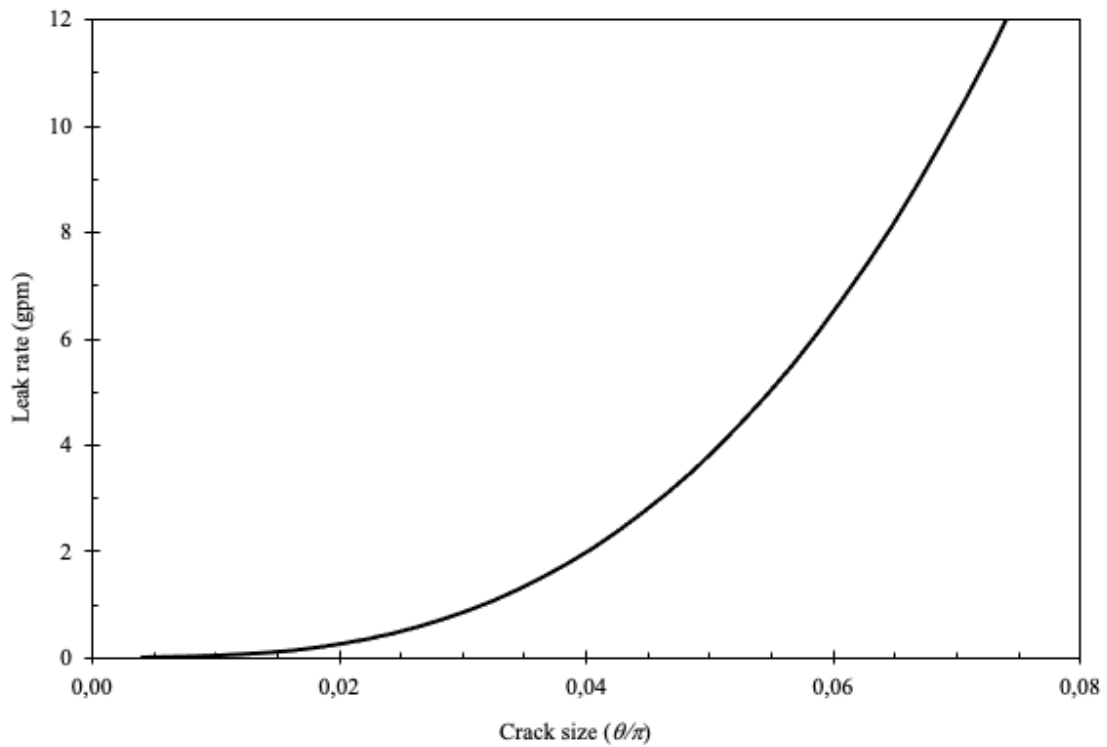
Figure 5: Leakage and through-wall crack size in the base metal
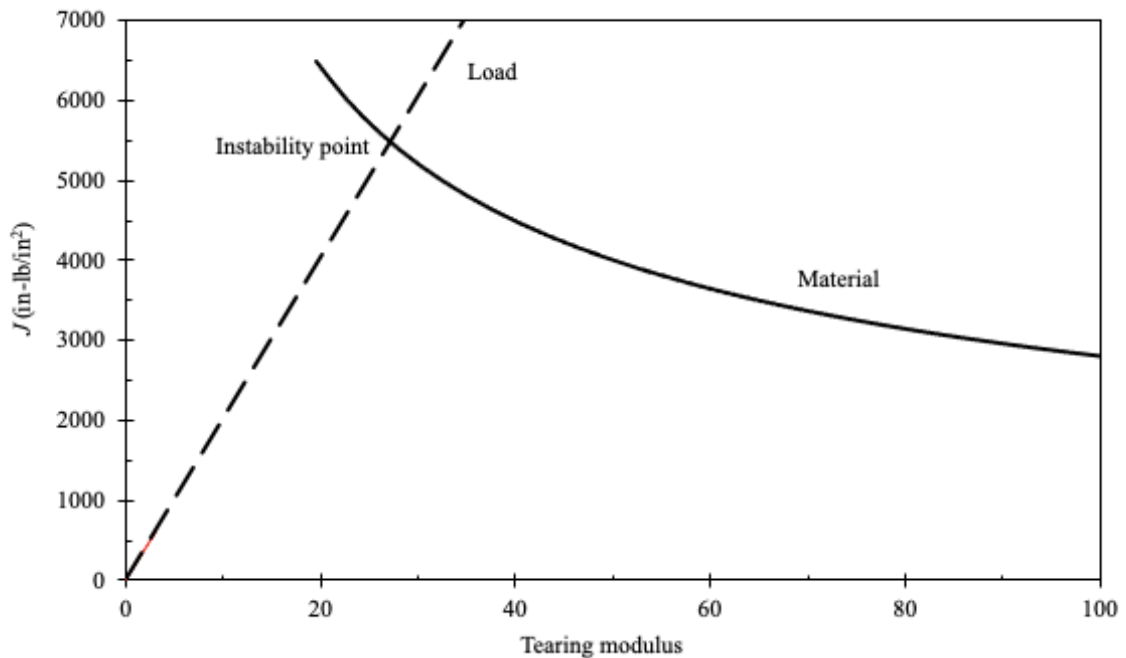
Figure 6: Analysis of crack stability in the base metal (θ/π =0.139)

Table 4 – Crack stability analysis (J/T method)

Through-wall crack location	T	T_{mat}	$\dfrac{T_{mat}}{T}$
Base metal	3.02	26	8.6
Weld metal	3.02	28	9.3

Another aspect of LBB that should be discussed is that when the toughness of base and weld metals are very high, it is mandatory to verify whether the failure can occur by a mechanism other than ductile tearing. One possibility to investigate is plastic collapse, a situation in which the straight section of the pipe becomes completely plastic before fracture. The appropriate theory for this analysis is the limit load.

The limit load theory considers that failure occurs when the stress due to external loads on the section is equal to the flow stress, σ_f. This indicates that the toughness of the material is high enough to ensure that the failure mode is controlled by tensile properties. A detailed description of the analytical procedure to determine the critical crack length based on the limit load theory is available in the ASME code XI Appendix C (2010). The basic equations are

$$M_o = 2\sigma_f R^2 t \left[2\sin\beta - \sin\theta \right] \tag{8}$$

$$\beta = \frac{\pi}{2}\left[1 - \frac{\theta}{\pi} - \frac{P_m}{\sigma_f} \right] \tag{9}$$

with β, the angular location of the neutral axis in the cracked pipe, whose original position is changed by the presence of the crack, and P_m and M_o being the membrane stress and moment applied at the time of plastic collapse. The other quantities have already been defined.

The stability analysis is conducted with the minimum tensile properties of Table 2 and the normal operating loads combined with the accident loads shown in Table 3. To find the critical crack size a spreadsheet is used to solve Equations (8) and (9) simultaneously. The results for the base and weld metals are presented in Table 5, where the leakage crack size and critical flaw size are compared. Since the ratio between these quantities is greater than 2.0, step 6 of Section 2 is met and failure by plastic collapse does not occur.

Table 5 – Crack stability analysis (limit load method)

Through-wall crack location	θ/π_Q Leakage crack size	θ/π_{cr} Critical crack size	$\dfrac{\theta/\pi_{cr}}{\theta/\pi_Q}$
Base metal	0.0695	0.366	5.3
Weld metal	0.0695	0.412	5.9

As the numbers in Tables 4 and 5 show, the margins for limit load are smaller than those of the J/T method and, in this situation, the most likely failure mode is plastic collapse.

These results agree with what exist in most practical situations, in which for LBB applications in stainless steel pipes, whose toughness is high, the crack stability is controlled by plastic collapse (limit load theory). If, on the other hand, the steel is ferritic, or even austenitic operating at temperatures where the toughness may not be as elevated (about 300°F), the stability is controlled by the ductile tearing (J/T method).

7 Further Remarks

The LBB procedure described in this chapter follows NRC documents originally published in the mid-1980s. Nevertheless, the basis established at that time remains valid for recent LBB applications, as are noticed for several plants in U.S., such as Surry 1 and 2 in 2019, D.C. Cook 1 and 2 in 2018, and Turkey Point 3 and 4 in 2018. In Brazil, Angra 1 adopted the same LBB procedure for the reactor coolant loop primary piping in 2010, and for the accumulator and surge lines, predicted to be implemented in 2022.

Although no modifications have been made to the calculation procedures, further refinements should be incorporated to demonstrate the feasibility of LBB. Some of these refer to the use of programs to determine leak rate considering a) probabilistic simulations or realistic models of the crack morphology; b) inclusion of dynamic effects and/or cyclic loads in the characterization of materials; and b) effects of residual stress in the calculation of crack opening displacement [Rahman 1997] and [NUREG/CR-6765 2001].

It should be noted that from the early 2000s, when primary water stress corrosion cracks (PWSCC) were detected in the Alloy 82/182 bimetallic weld that connect the ferritic components with those fabricated with stainless steel, the LBB procedures started to consider other important aspects, mainly those related to the leak rate analysis. For example, the leakage crack size for PWSCC at Alloy 82/182 weld calculated using the default values from PICEP is 28% greater than the number determined for fatigue. However, published data from 2003 provides a higher value for the crack size, with the crack half-angle for PWSCC 69% greater than the value obtained for the fatigue case. The discrepancy is explained by differences in the morphology of the cracks, which in case of PWSCC have lower surface roughness and sinuous path, as opposed to fatigue, which are straight through the thickness. In NUREG/CR-6765 [2001] and in Rudland et. al. [2003] there is a detailed description of how to include the effects of these parameters in the analyses.

As a result, in cases where LBB is applied to dissimilar metal welds the PWSCC crack size associated with detectable leakage is larger than that determined for fatigue. For the same conditions as the example shown here, the size of the circumferential through-wall crack postulated for the stability is θ/π equal to 0.235, against 0.139, the number calculated for fatigue.

In step 1 of Section 2 it is stated that NUREG 1061 and SRP 3.6.3 requires that the piping candidate to LBB should not be susceptible to degradation, such as PWSCC. In nuclear plants it is demonstrate that the integrity of the piping during lifetime is not affected by the PWSCC if a mitigative measure is implemented. The choice of the

industry are repairs, as those named mechanical stress improved process (MSIP) or structural weld overlay (SWOL), both adopted to provide a PWSCC resistant barrier to the Alloy 82/182 original welds. These mitigative repair process are applied to convert tensile residual stress in the inside surface of these welds into compressive residual stress field, thereby minimizing the probability to have initiation or propagation of PWSCC at the Alloy 82/182 material.

LBB can also be conducted in the form of boundary analysis curves approach. In this cases curves which correlate loads under normal operating and accident conditions are obtained to meet the required crack stability margin for specified leak rate, pipe, and material. Data presented in this format is very convenient during early plant design when the results of the piping layout is still preliminary, or stress analysis are not yet known. Later in the design phase, with P and M available, it is easy to verify for which combinations of the stresses the LBB is demonstrated. An example of boundary analysis curves in terms of the normal operating stress, σ_{op}, and maximum stress $\sigma_{op}+\sigma_{DBE}$, the superposition of normal and accident (DBE) stresses, involves the following steps:

a) For a stress under normal operating condition calculate the leak rate Q and crack size θ/π_Q curve. Repeat this analysis for various σ_{op} values;

b) If the plant monitoring system detects 1.0 gpm, and considering the margin of 10, obtain, for each level of σ_{op}, the leakage crack size for 10 gpm. Repeat this step to generate the curve σ_{op} and θ/π_Q;

c) For a value of the stress under normal and accidental operating conditions use the limit load method to calculate the critical crack size. Repeat this analysis for various stress values to obtain the curve correlating the maximum stress $\sigma_{op}+\sigma_{DBE}$ and θ/π_{cr};

d) Combining steps b) and c), and with θ/π_Q equal to half of θ/π_{cr}, determine the envelope curve σ_{op} and $\sigma_{op}+\sigma_{DBE}$.

Figure 7 schematically represents each of the previous steps and illustrates how the envelope curve for LBB validation is obtained. A numerical example is in Figure 8, which is a bounding analysis curve for a 12 inches pipe diameter, 1.312 inches thickness, forged stainless steel SA-376 TP316, operating at 653°F and 2235 psig. LBB is demonstrated if the normal operating and maximum stresses, determined from the piping stress analysis, and represented by the various points σ_{op} and $\sigma_{op}+\sigma_{DBE}$, as presented in the figure, fall below or at the curve.

8 Conclusions

The example shows an application in the nuclear industry of LBB for a piping, the hot leg from the primary loop. The pipe is fabricated with a cast stainless steel, and it is assumed that the postulated through-wall circumferential crack caused by fatigue is located at the base metal or weld.

For each crack, two types of analyses are performed: a) leak rate analysis; and b) crack stability analysis. In the first case, the crack size associated with the detectable leak rate
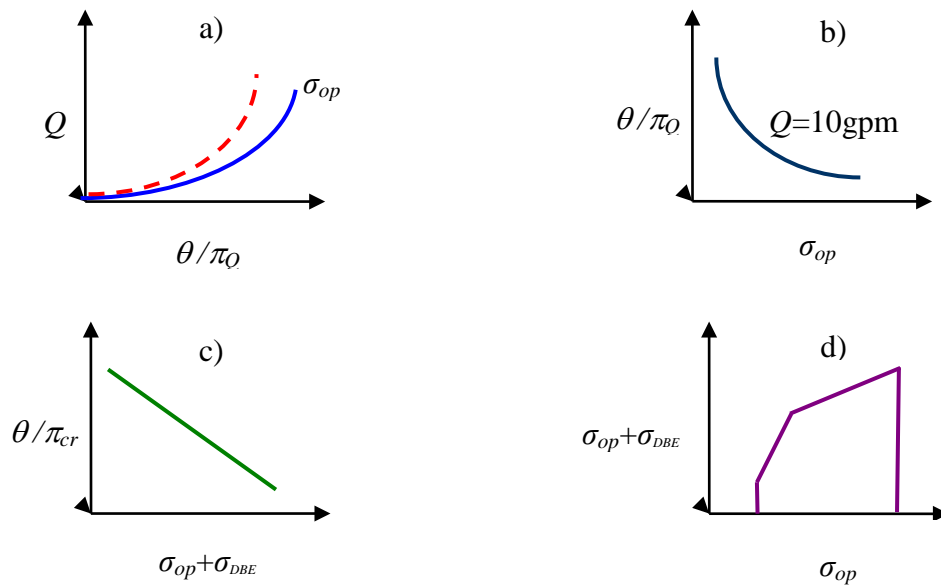
Figure 7: Schematic representation to determine the boundary analysis curve
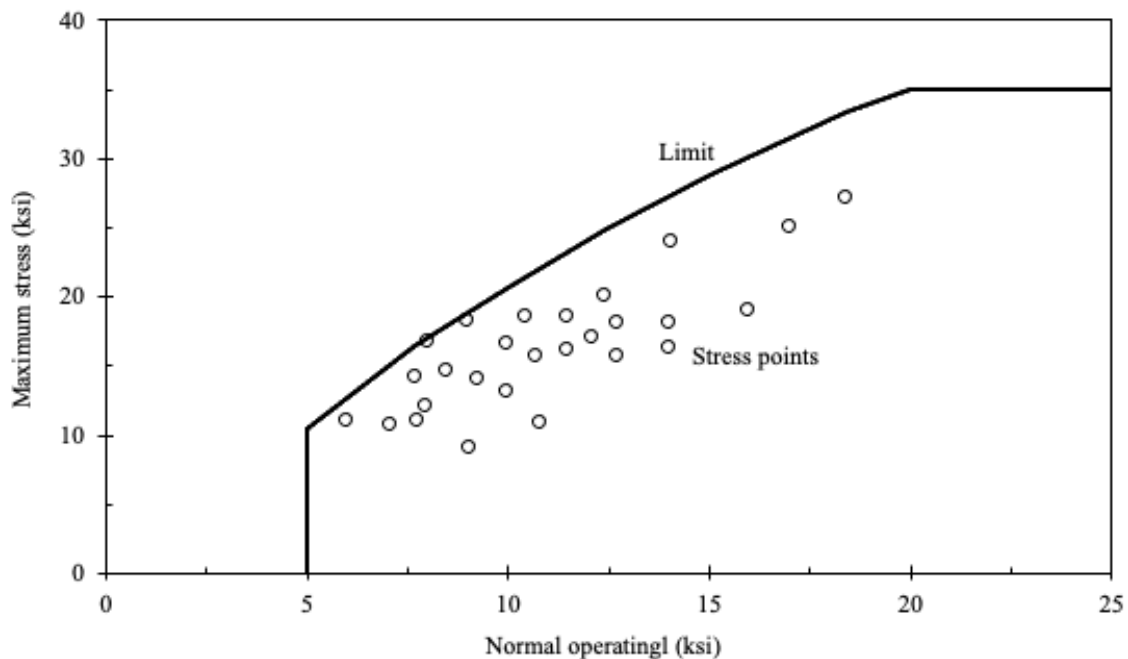
Figure 8: Typical boundary analysis curve for LBB validation

is obtained. Once this size is determined, the stability of the crack is verified, using the J/T method (ductile tearing) or the limit load theory (plastic collapse).

As the toughness of materials from the primary loop piping is high, the most frequent failure mode is plastic collapse. However, for cracks in ferritic or austenitic steels where toughness is reduced by thermal aging, failure by ductile tearing is more likely, especially with the system operating close to 300°F.

When the feasibility of LBB is demonstrated, postulated break loads (LOCA) are eliminated from the design basis. The advantage of LBB is that components such reactor vessel internals and nozzles, primary loop equipment and supports, and piping need not to be designed to withstand LOCA loads. As an added benefit, pipe-whip restraints, and jet-impingement shields, both installed to protect critical equipment from the dynamic effects of the postulated breaks, are not necessary.

References

ASME American Society of Mechanical Engineers. ASME Boiler and Pressure Vessel Code. New York, 2010.

A. Zahoor. Ductile Fracture Handbook. NP-6301-D Research Project, Electric Power Research Institute, 1989.

D. Rudland, R. Wolterman, G. Wilkowski, and R. Tregoning. Impact of PWSCC and Current Leak Detection on Leak-Before-Break, Presentation from NRC Conference on Vessel Head Penetration Inspection, Cracking, and Repairs, September 29 - October 2, 2003.

EPRI. Leak-Before-Break Evaluation for PWR Alloy 82/182, Materials Reliability Program, MRP-140, Report 1011808, Electric Power Research Institute, November 2005.

NUREG. Evaluation of Potential for Pipe Breaks, NUREG-1061 Volume 3, US Nuclear Regulatory Commission (NRC), 1984.

NUREG. The Application of Fracture Proof Design Methods Using Tearing Stability Theory to Nuclear Piping Postulating Circumferential Through-Wall Cracks, NUREG/CR-3464, US Nuclear Regulatory Commission (NRC), 1983.

NUREG. Estimation of Fracture Toughness of Cast Stainless Steels During Thermal Aging in LWR Systems, NUREG/CR-4513R1, ANL-93/22, US Nuclear Regulatory Commission (NRC), 1994.

NUREG. Effects of Thermal Aging on Fracture Toughness and Charpy-Impact Strength of Stainless Steel Pipe Welds, NUREG/CR-6428, ANL-95/47, US Nuclear Regulatory Commission (NRC), 1996.

NUREG. Tensile-Property Characterization of Thermally Aged Cast Stainless Steels, NUREG/CR-6142, ANL-93/35, US Nuclear Regulatory Commission (NRC), 1994.

NUREG. Development of Technical Basis for Leak-Before-Break Evaluation Procedures, NUREG/CR-6765, US Nuclear Regulatory Commission (NRC), 2001.

PICEP. Pipe Crack Evaluation Program (Revision 4), NP-3596-SR, Electric Power Research Institute (EPRI), 1992.

R.E. Henry and H. K. Fauske. The Two-Phase Critical Flow of One-Component Mixtures in Nozzles and Short Tubes, Journal of Heat Transfer, American Society of Mechanical Engineers Transactions, 1971.

R.E. Henry. The Two-Phase Critical Discharge of Initially Saturated ou Subcooled Liquid, Nuclear Science and Engineering, 41, p. 337, 1970.

SRP. Leak-Before-Break Evaluation Procedures, Draft Standard Review Plan 3.6.3, Federal Register Vol. 52 No. 167, August 26, 1987.

SRP. Leak-Before-Break Evaluation Procedures, NUREG-0800, Standard Review Plan 3.6.3, US Nuclear Regulatory Commission (NRC), 2007.

Westinghouse. Leak-Before-Break Evaluation of the AP1000 Piping, Appendix 3B, AP1000 Design Control Document, Westinghouse, 2007.

Chapter 11

Fatigue Control in Angra Nuclear Power Plants

Chapter details

Chapter DOI:

Chapter suggested citation / reference style:

P.S.: DOI may be included at the end of citation, for completeness.

Book details

Fatigue Control in Angra Nuclear Power Plants

Miguel Cisternas[1*]

[1]Stress Analysis Department – DAN.T, ELETRONUCLEAR, Brazil.
E-mail: mcister@eletronuclear.gov.br / miguelc2308@gmail.com

*Corresponding author

Abstract

The fatigue control of Nuclear Power Plants (NPP) operating in Brazil is performed through different procedures. In a first analysis, the occurrence of thermal transients is observed. If an unspecified transient occurs, a detailing of the event is carried out with the aim of reducing it to design values. At the same time, an automatic transient monitoring system will show the consequences of the transient that has occurred, as well as fatigue monitoring at selected locations. The Angra NPP were designed to operate during a period of 40 years of service. It should be noted that the Angra NPP is expected to operate for another 20 years of service. The new 60-year operational limits can be obtained by following the United States Nuclear Regulatory Commission (USNRC) regulations or through German standards (KTA). Fatigue control at Angra NPP is done by controlling the number of transients and/or the cumulative fatigue usage factor (CUF), not necessarily in that order.

Keywords: Thermal Stratification; Fatigue Monitoring; EAF Environmentally Assisted Fatigue; Fen Environmental Correction Factor; TLAA Summary from NUREG and KTA

1 Introduction

Fatigue analysis is performed to ensure the safe operation of components subject to cyclic transients, such as those generated by events where temperature changes occur (heating/cooling, safety injection, etc.), and are known as design transients.

The design transients were obtained by defining a conservative occurrence for the magnitude and frequency of most events expected to occur in a Nuclear Power Plant. A catalog of allowable design limits for 40 years of operation was provided by the NSSS Vendor (Nuclear Steam Supply System).

Based on these events, the fatigue analyzes obtain the so-called cumulative fatigue usage factor (CUF), whose limit corresponds to 1.0. It is considered that values greater than 1.0 would be the beginning of a crack in the material of the pipes and components and it is intuitive to realize that if the number of observed design transients is less than the allowable limit, the CUF will not be exceeded.

At the Angra NPP, an automatic event counting system is used and employs the operating parameters generated (temperature, pressure, flow, valve position, pump

condition, etc.) by the existing instrumentation in the plant, and through appropriate algorithms, and based on the actual transients that have occurred, calculate the cumulative fatigue usage factor at a specific location.

The Angra NPP were designed to operate during a period of 40 years of service (40 Years of Operation). However, the Angra NPP should operate for additional periods of 20 years of service. This new period is known as 60-Year Transient Projected Cycles.

In the 1980´s, it was discovered in Japan that the fatigue life that occurs in severe environments could be reduced.

New tests carried out at the Argonne National Laboratory (ANL), O.K. Chopra and A. Sather [1990], showed that the fatigue effects in a water environment, at the nominal temperature at full power, are significantly greater than the effects of fatigue in air environment, where the fatigue curves were developed.

The Angra NPP use the fatigue curves of the ASME III code [1989] and also the German standards, Nuclear Safety Standards Commission (KTA) [1996]. The current design fatigue curves of the ASME Code were based primarily on strain–controlled fatigue tests of small polished specimens at room temperature in air.

Using the current version of the ASME code requires the application of a penalty, which was called Environmental Fatigue Correction Factor (Fen), detailed in NUREG-1801, Rev. 2 [2010]. It should be noted that this penalty reduces fatigue life as it increases the cumulative fatigue usage.

Thus, to compensate for the increase in the CUF, which is limited to 1.0, the fatigue analyzes must necessarily be revised. After reviewing the analyses, new transient limits should be considered as admissible values. An example of this threshold reduction is the Plant Heat up event, with a reduction from 200 (40 years of operation) to 150 (60-year transient projected cycles).

The procedures applied at the Angra NPP to control fatigue are presented next.

Operational Transient Monitoring Transient data observed through thermocouples installed on the external surface of the pipes	**Automated Fatigue Monitoring** Using data from the operational parameters generated by the existing instrumentation in the plant

Permissible Cycle Limits

Fatigue correction factor used in life extension projection of a Nuclear Power Plant - Summary of the use of NUREG and KTA rules

2 Operational Transient Monitoring

2.1 Observation of Operational Temperature Transients and Thermal Stratification Phenomenon

Temperature transients that occur during the operation of a Nuclear Power Plant are observed through thermocouples installed on the external surface of the pipes, in various cross sections, M. Cisternas [2009].

Two typical thermocouple configurations are used in Angra NPP:

Single Configuration

Angular position T2 (90°)

Angular position T1 (270°)

Full Configuration

Angular position T5 (90°)

Angular position T4 (45°)

Angular position T3 (0°)

Angular position T2 (315°)

Angular position T1 (270°)
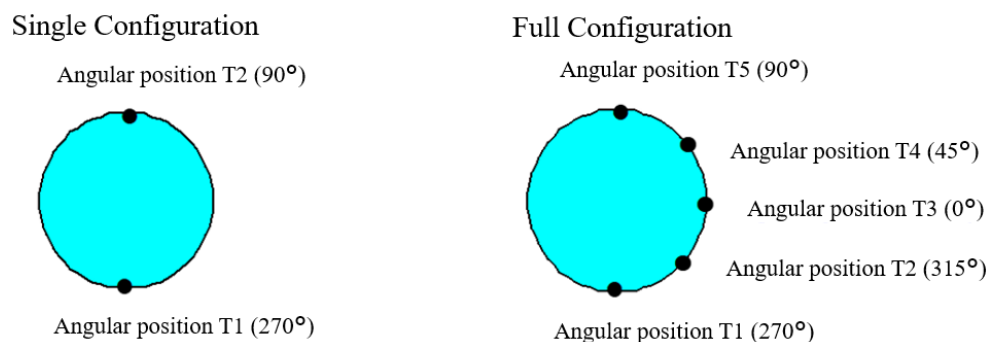
Figure 1: Typical configurations of thermal monitoring

The temperature difference between the hot water (top) and cold water (bottom) in a piping is known as thermal stratification (Figure 2).

Hot Water

Pipe

T_{HOT}

T_{COLD}

Stratified Pipe

Cold Water
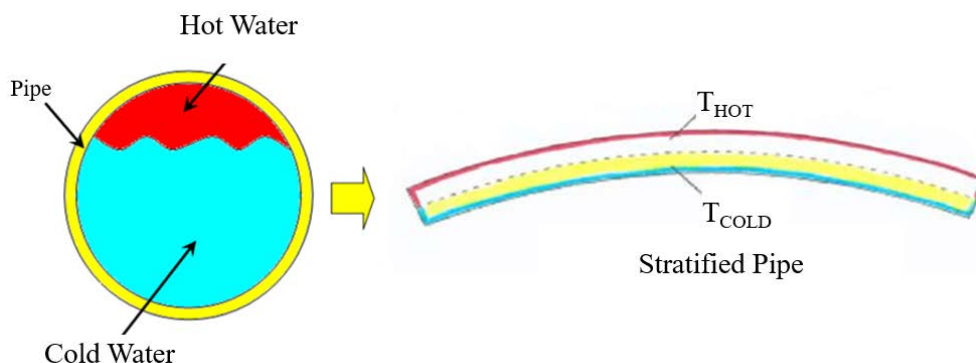
Figure 2: Thermal stratification

Thermal stratification can be divided into three types:

a) Global Stratification: Global bending effects in the piping system that can produce modified piping thermal expansion moments remote from the regions affected by the stratification. That is, can produce pipe bending and can cause the piping to exceed the thermal displacements considered in the original design.

b) Local stresses at the region of stratification related to there being a non-linear stress distribution around the circumference of a piping system. That is, local stratification causes an increase in thermal stresses on the tube wall and a consequent reduction in fatigue life.

c) Transient and / or steady through wall stress (currently defined by ΔT_1 and ΔT_2 in the code). These stresses would also not be uniform around a piping system for stratified conditions. This item will be detailed in section 3.2

2.2 Temperature Stratification in the Hot-Leg of the Reactor Coolant Line at the Angra NPP

Temperature stratification occurs in the hot-leg of the Reactor Coolant Line (RCL) during normal operation due to the outsurge flow of the hot water of the Pressurizer into the Hot Leg of the RCL.

Thus, it is important to know the behavior of temperatures inside the pipe.

At the Angra NPP, thermal stratification is observed through thermocouples installed on the external surface of the pipes.

Data acquisition is performed by a software, FieldChart Novus Version 2.0.3.1. [2013], that allows to display the data in digital and graphic format, in batches or in real time, and in real time trend and historic trend views. The software allows to zoom, superimpose and link graphs, and print or export all data.

Figure 3 shows Hot Leg location.
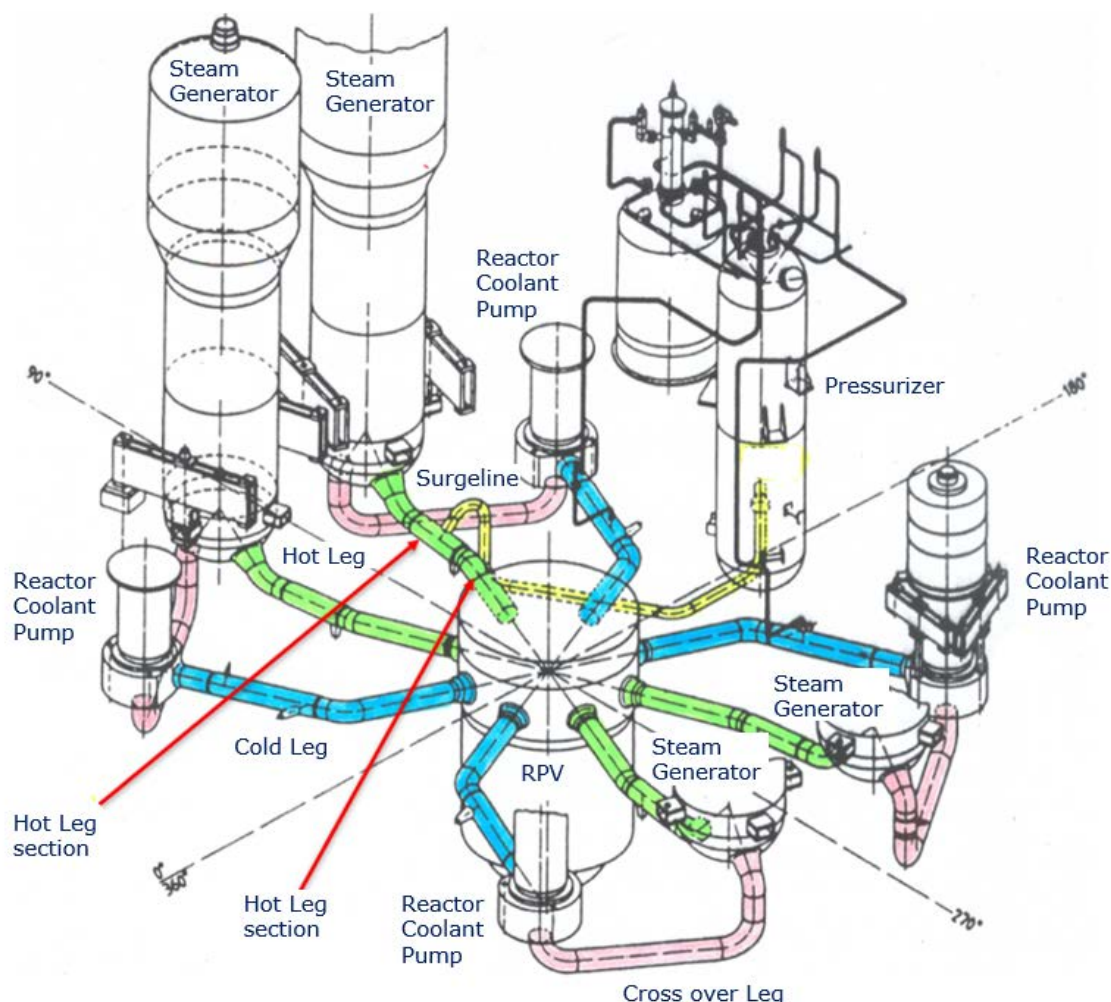
Figure 3: Hot leg location

Figure 4 shows temperature data for a section of the hot leg of the Reactor Coolant Line, located next to the Pressurizer Surgeline.
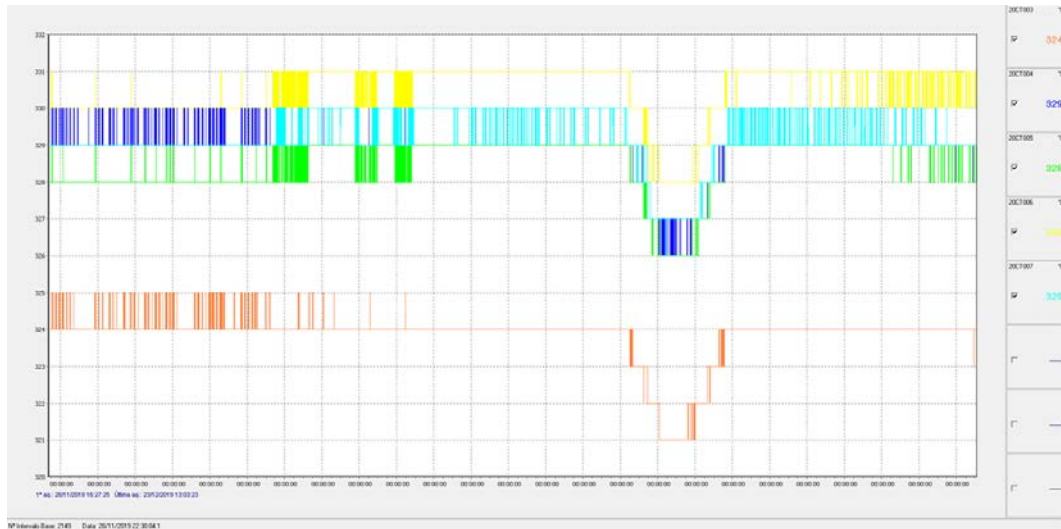
Figure 4: Data temperature at Hot Leg Location

Figure 5 shows temperature of the thermocouples installed on the external surface of the pipe.
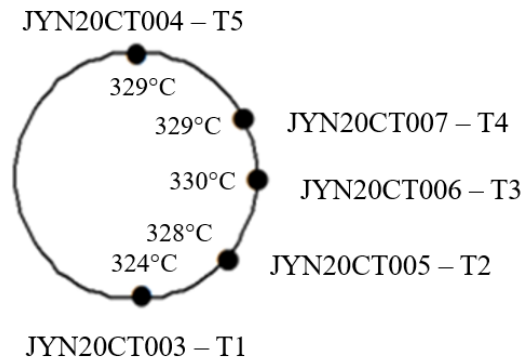
Figure 5: Temperature on the external surface of the pipe at hot leg location

Figure 6 shows the internal points where the temperature is unknown. The transfer of temperatures from the external surface to the internal points of the pipe is carried out using the Boundary Elements Method, M. Cisternas at al. [1987].
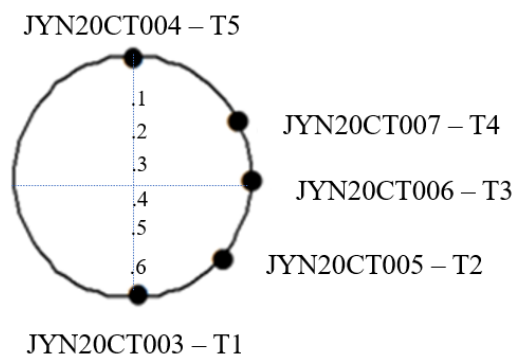
Figure 6: Internal points of the pipe where the temperature is unknown

Table 1 shows the temperature in the internal points using the Boundary Elements Method.

Table 1: Temperature in the Internal Points using the Boundary Elements Method.

```
INTERNAL POINTS

     R               Z              POTENTIAL (U)

   0.00000        343.52000         329.06112
   0.00000        263.59000         329.13072
   0.00000         56.52000         329.11331
   0.00000        -56.52000         328.76312
   0.00000       -263.59000         326.85224
   0.00000       -343.52000         325.49331
```

Note: The expected value in normal plant operation is around 325.1 °C. This shows that the tube working stratified, presents values observed above those expected in normal plant operation.

The current Section–III design fatigue curves of the ASME Code [1989], were based primarily on strain–controlled fatigue tests of small polished specimens at room temperature in air. The Angra NPP use the fatigue curves of the project following this methodology, which correspond to the ASME III code, year 1989 and also to the German standards, Nuclear Safety Standards Commission (KTA) [1996].

The ASME Code fatigue evaluation procedures are described in NB-3600, "Piping Design," and NB-3200, "Design by Analysis". For each stress cycle or load set pair, an individual fatigue usage factor is determined by the ratio of the number of cycles anticipated during the lifetime of the component to the allowable cycles. Fatigue design curves defines the allowable number of cycles as a function of applied stress amplitude.

The CUF is the sum of the individual usage factors, and ASME Code Section III requires that at each location the CUF must not exceed 1.

2.3 Effects of Thermal Stratification

The effects of stratification are considered by determination of piping bending moments due to stratification and by calculating additional local stresses due to a non-linear temperature difference across the pipe diameter.

In a stratified section, there may be stresses developed even if the piping section is free to expand. The nonlinear top-to-bottom temperature distribution in a pipe produces a non-uniform stress distribution around the pipe circumference. The stresses have the same characteristics as a non-linear through wall stress distribution in that they will not result in gross thermal displacement of the piping system and contribute only to fatigue. If a piping program is being used to perform stress analysis, this additional stress may be transformed on equivalent ΔT_1.

The additional stresses due to through wall thermal gradients should also determine for each loading condition. Thermal transients produce large ΔT_1 and ΔT_2 stresses, and gross structural discontinuities T_a - T_b axial stress that shall be considered. However, there can be also be some through-wall temperature differences that occur with steady stratification that cannot be neglected.

Once these moments, piping parameters and / or local stresses are determined, the piping fatigue analysis can proceed using the methods commonly used for piping analysis. The code allowable for primary stress intensities should be unaffected by thermal loading. The service Level A/B stress intensity ranger shall be evaluated per NB-3650 of section III of the ASME code. Eletronuclear uses Finite Element Program KWUROHR and Finite Element Program PIPESTRESS. More detailed analysis may be conducted using the rules of NB-3200, where the stresses at multiples locations around the circumference of a component may be considered. Eletronuclear uses Finite Element Program ANSYS.

2.4 Temperature Gradients ΔT_1 And ΔT_2 and Range of Average Temperature on Gross Structural Discontinuities Ta (Tb)

The temperature distribution in the radial thickness of the pipe varies from the inner surface to the outer surface. This variation in temperature or distribution along the radial thickness of the tube is known as the thermal gradient. Figure 7 shows a temperature distribution t as a function of the radial thickness a:
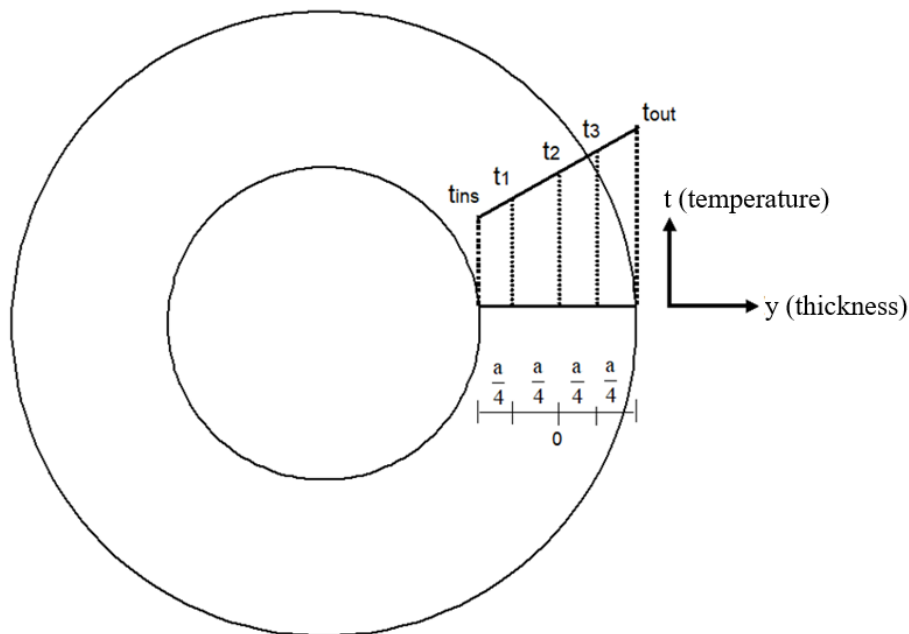
Figure 7: Temperature distribution in the thickness of the pipe

According to the ASME III code, the thermal gradient can be decomposed into three different parameters, ΔT_1, ΔT_2 and T_a-T_b, where ΔT_1 represents the temperature difference between the outer surface and internal tube, based on an equivalent linear distribution:

$$\Delta T_1 = \frac{12}{a^2} \int_{-a/2}^{a/2} y\, t(y)\, dy \tag{1}$$

$$\Delta T_1 = -\frac{5}{8} t_{ins} - \frac{3}{4} t_1 + \frac{3}{4} t_3 + \frac{5}{8} t_{out} \tag{2}$$

ΔT_2 represents the temperature difference between the surface and the equivalent linear distribution:

$$\Delta T_2 = \text{Maximum} \begin{cases} \left| t_{out} - T_{Avg} \right| - \dfrac{|\Delta T_1|}{2} \\ \left| t_{ins} - T_{Avg} \right| - \dfrac{|\Delta T_1|}{2} \\ 0 \end{cases} \tag{3}$$

T_a-T_b or Ta (Tb) represents the average temperature on the tube wall:

$$T_{Avg} = \frac{1}{a} \int_{-a/2}^{a/2} t(y)\, dy \tag{4}$$

$$T_{Avg} = \frac{t_{ins}}{8} + \frac{t_1}{4} + \frac{t_2}{4} + \frac{t_3}{4} + \frac{t_{out}}{8} \tag{5}$$

2.5 Contribution of Thermal Stratification in ASME NB-3653.2

- No terms are added in equation 10 of ASME NB-3653.2.

- Term added in Equation 11 of ASME code NB-3653.2, Structural Integrity Associates, 2008.

$$E\,\alpha\,|\Delta T_3| \tag{6}$$

Where:

$E\alpha$ = modulus of elasticity (E) times the mean coefficient of thermal expansion (α), both at room temperature

$|\Delta T_3|$ = Top Temperature - Bottom Temperature

2.6 Contribution of Thermal Stratification in ASME NB-3200

- No contribution to the term S_n = primary + secondary stress intensity; Equivalent to value calculated by equation 10 of ASME NB-3653.2.

- Contribution is added to term S_P = peak stress intensity; Equivalent to value calculated by equation 11 of ASME NB-3653.2.

2.7 Unspecified thermal stratification in the Main Feedwater line of the Angra Nuclear Power Plant

The occurrence of unspecified thermal stratification was observed in the Main Feedwater line (figure 8) of the Angra NPP.
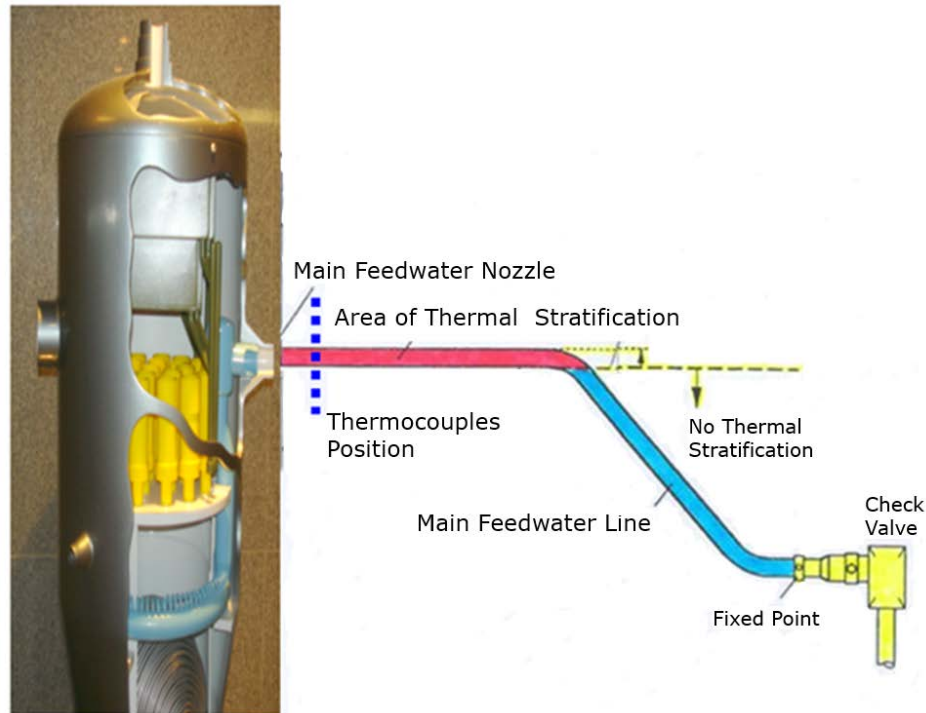
Figure 8: Main feedwater line of Angra NPP

Figure 9 shows a graph with the temperature values observed in the thermocouples installed in the Main Feedwater line of the Steam Generator, M. Cisternas [2009].
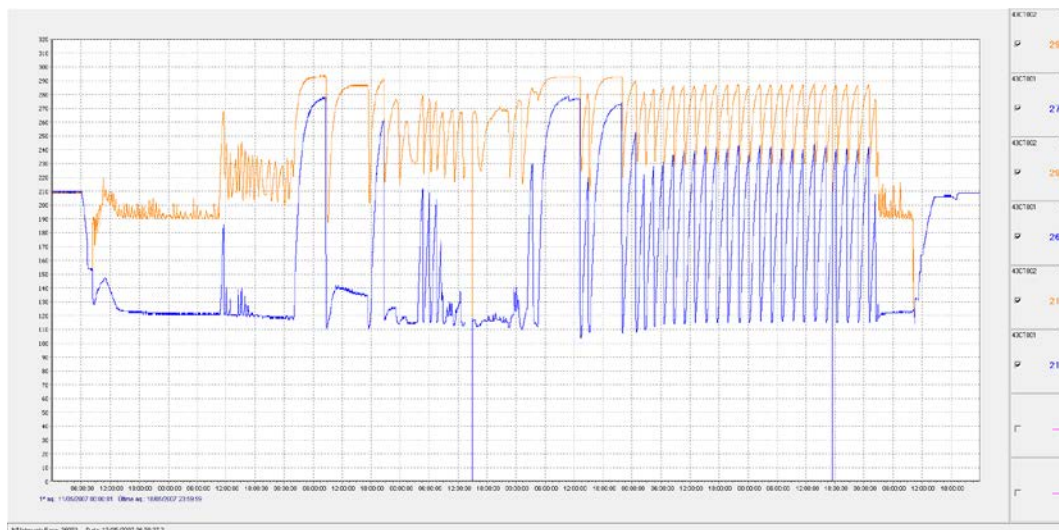
Figure 9: Temperatures observed in a cross section of the main feedwater line

Note: Observed temperature transients are not included in the NSSS vendor transient catalog with the same frequency and magnitude.

2.8 Evaluation of Plant Data

During the Start-up or Reactor Trip (no cooldown) of a Nuclear Power Plant, the supply of steam generators occurs at low feedwater mass flow rates, and significant stratification of fluid temperatures in the steam generator feedwater nozzles has been detected. This stratification leads to undesired temperature gradients which in turn lead to strain and hence stress in the nozzle material. This all contributes to accelerated fatigue and possible shortening of the life of the component. For this reason, it has become necessary to change the feeding procedure to reduce thermal loading on the steam generator feedwater nozzles.

After observing unexpected temperatures, it is necessary to perform an evaluation of the plant data. At least three distinct regions can be seen;

  - Near constant temperature difference

  - Near constant mean temperature difference with mild fluctuations, and

  - Fluctuations and increase in temperature difference coupled with fluctuations in mean absolute temperature

The three distinct regions can be seen in figure 10:
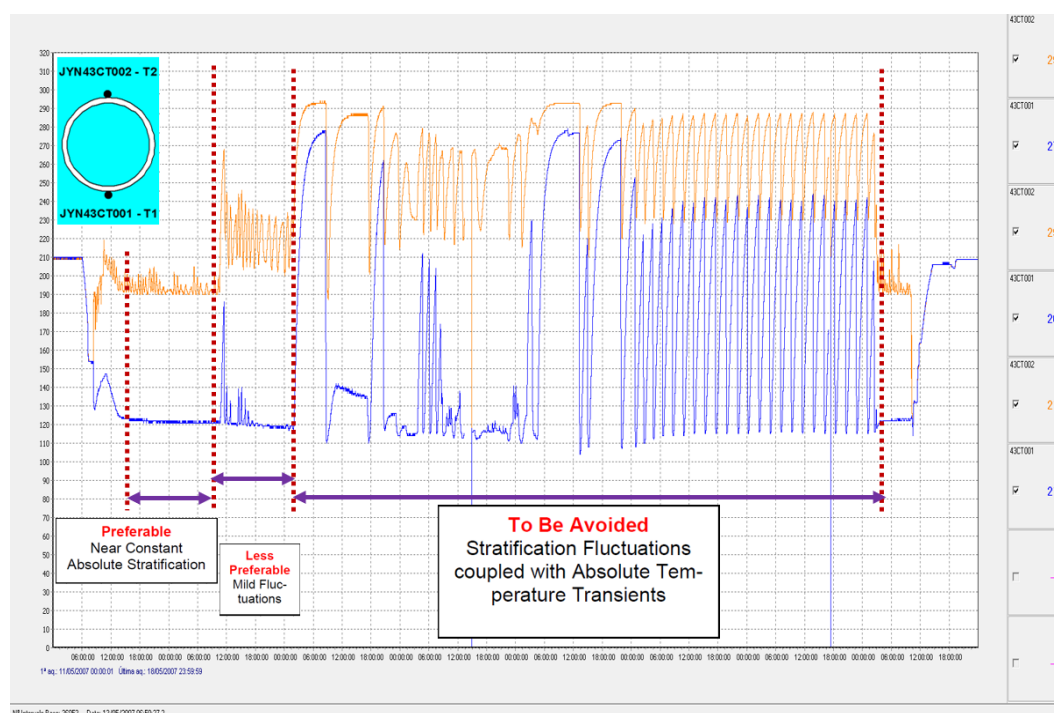
Figure 10: Evaluation of plant data

If stratification is present, it is preferable that the temperature difference remains as small and constant as possible. Fluctuations in temperature differences result in fluctuations in strains, stresses and finally fatigue.

Change the feeding procedure: Continuous feeding rather than intermittent feeding is preferable. A constant and inevitable stratification temperature difference in the main feedwater line during Start up or Reactor Trip (no cooldown) is to be expected.

Impact on pipes and components: Needs to be investigated.

2.9 Verification of the Occurrence of Thermal Stratification Phenomenon

In 1988, the USNRC (Nuclear Regulatory Commission) issued bulletin 88-08 advising about the occurrence of thermal stratification in lines connected to the Reactor Coolant Lines (RCL) of Nuclear Power Plants. In addition, bulletin 88-11 notifies that the Pressurizer Surge line should include thermal stratification loading in the fatigue analysis to verify for unexpected thermal movements that could cause the closing of the gap between the surge line and the supports provided against pipe whip restraints.

Many plants started commercial operation or were conceived before 1988, and only new reactors were designed to prevent this new load case. The other plants, had a high cost to include the thermal stratification loading, as a case of normal operation.

The following figure 11 shows the Angra NPP primary circuit, Finite Element Program, KWUROHR system [2014].
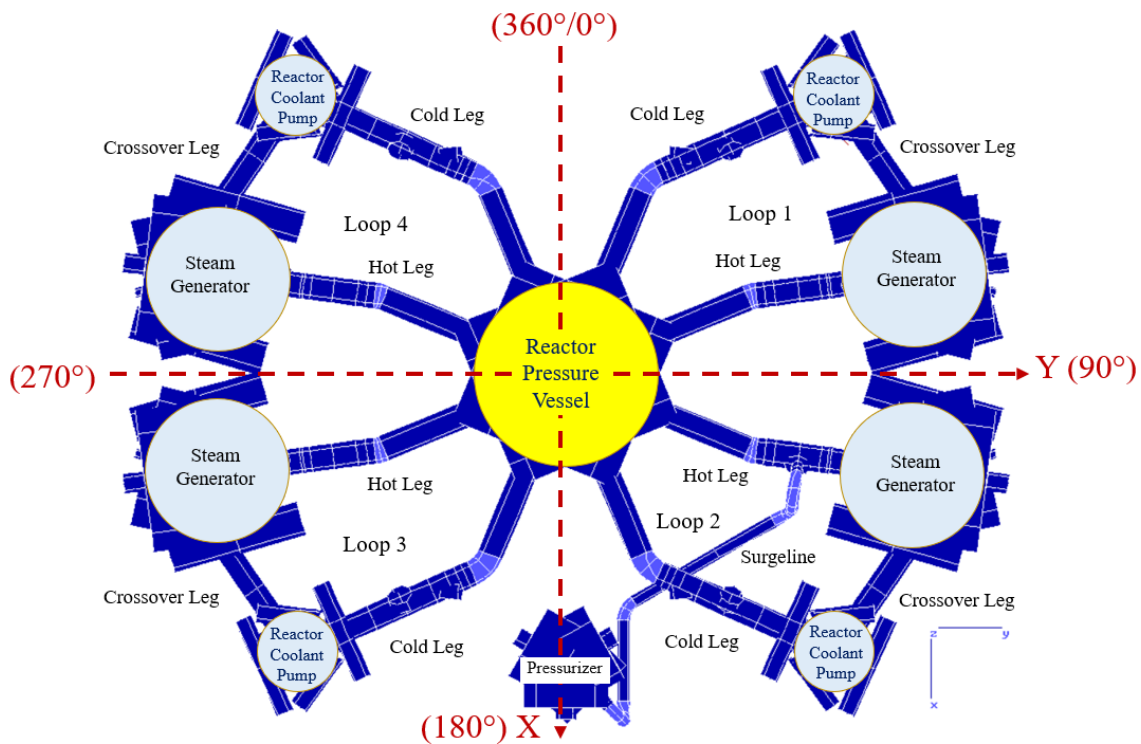
Figure 11: Angra Nuclear Power Plant primary circuit

Unexpected temperature transients were observed in loops 1 and 4 of the Main Feedwater line. In this chapter, the analysis will be concentrated on loop 4.

The displacement of the nozzle of loop 4, where it is connected to the Main Feedwater line, was obtained from the thermal analysis of the Angra NPP Reactor Coolant Line (RCL).

Figure 12 presents the finite element model of Angra NPP Reactor Coolant Line:
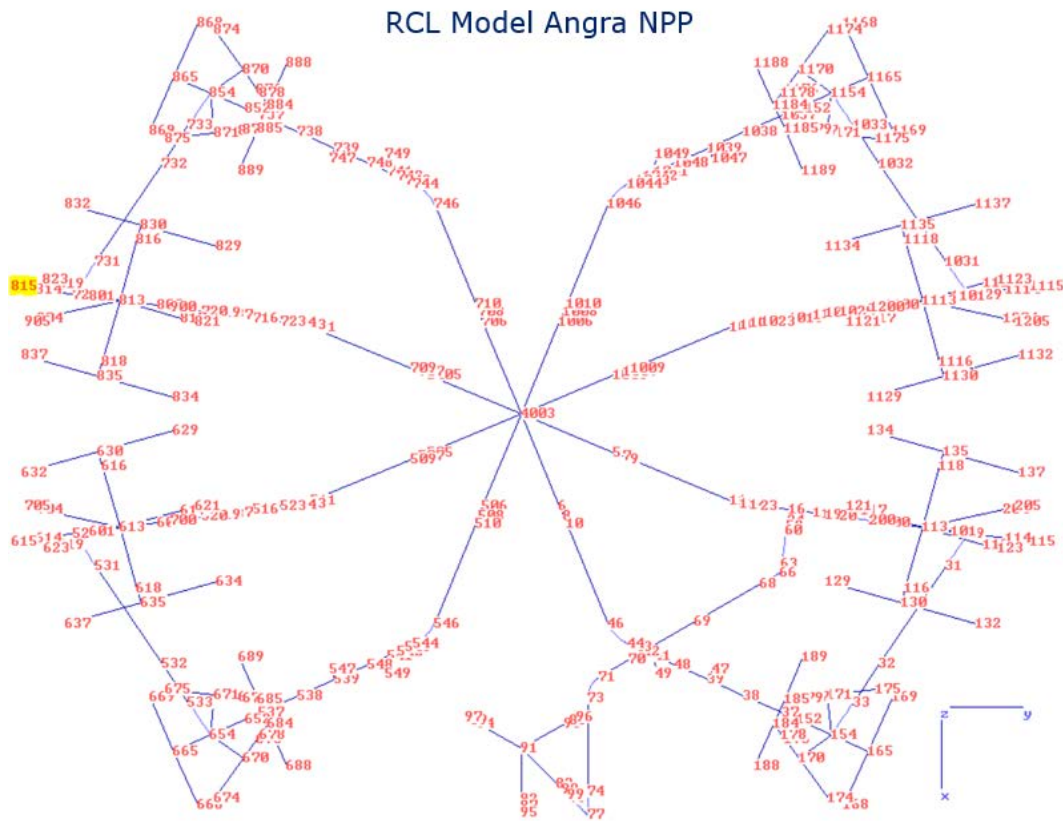
Figure 12: Finite element model of Angra NPP RCL

The results of the displacements of the connection between the nozzle of the Steam Generator loop 4 (nodal point 815) and the Main Feedwater line, obtained from the primary circuit model, are presented below in table 2:

Table 2: Displacement of the nozzle RCL/main feedwater line at loop 4 of Angra NPP.

```
DISPLACEMENTS and ROTATIONS at Fittings   (Individual Load Cases and Superpositions)
                                 Local Coordinate-System with Rotation-No. :
Load Case              Category      u        v        w        uu       vv       ww
                                ------------ mm ------------   ---------- mrad ----------
-------------------------------------------------------------------------------------
Operation                          41.83    -4.22    60.52    -0.23    -1.30     0.00
-------------------------------------------------------------------------------------
Nodal Pt.  :  815
```

The GAP adopted by the NSSS vendor for the installation of the Pipe Whip Restraints type support was 41 mm.

However, the finite element model that includes the main feedwater line shows that a higher value would be needed, and is shown in Figure 13.
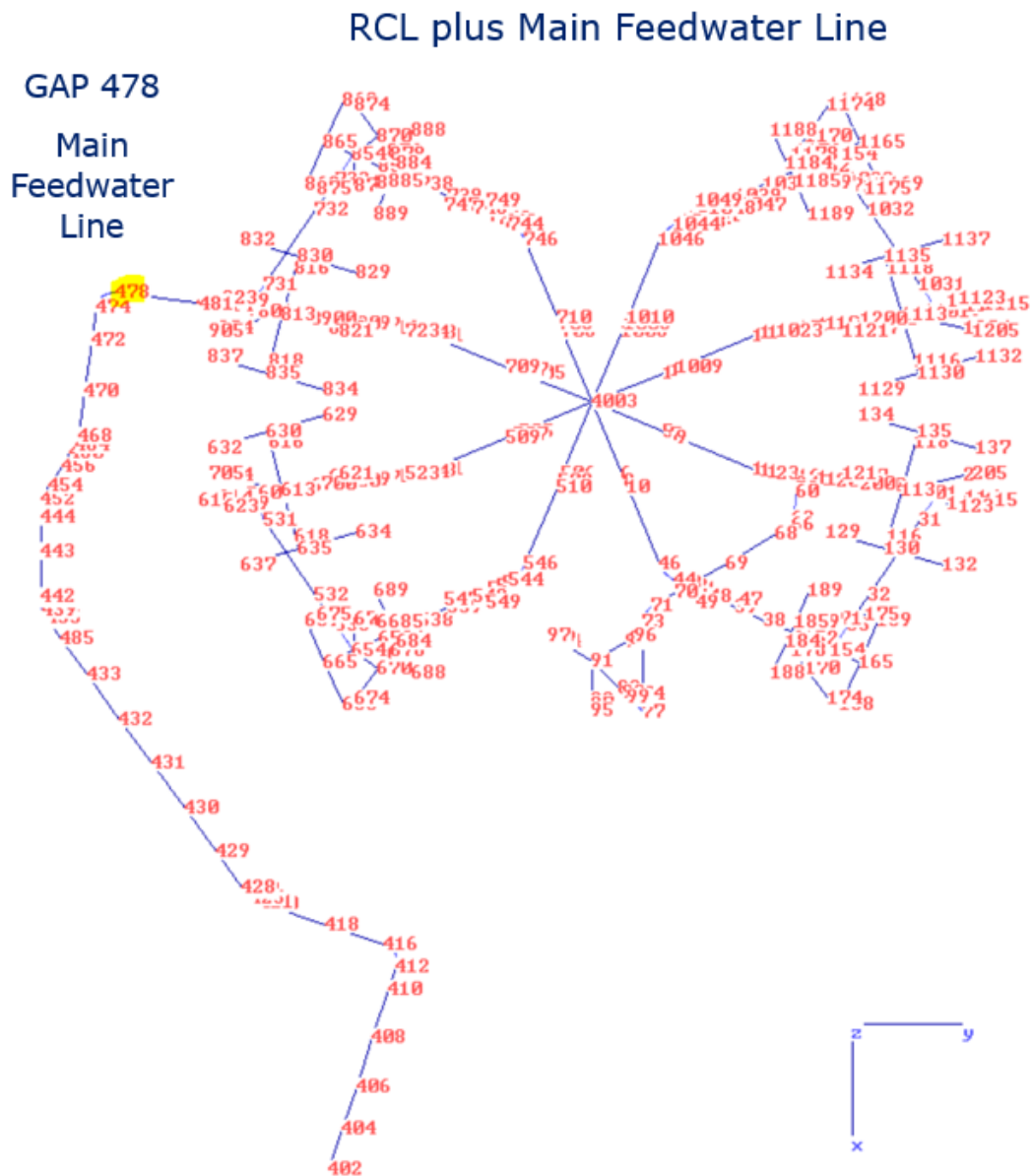
Figure 13: Finite element model of Angra NPP to RCL plus main feedwater line

The results of the displacements of the nodal point 478 of the Main Feedwater line besides Pipe Whip Restraints location are presented below in table 3:

Table 3: Displacement of the nodal point 478 of the main feedwater line.

```
DISPLACEMENTS and ROTATIONS at Fittings  (Individual Load Cases and Superpositions)
                        Local Coordinate-System with Rotation-No. :
Load Case          Category       u          v          w         uu         vv         ww
                                ----------- mm -----------     --------- mrad ---------
-------------------------------------------------------------------------------------------
Operation                         53.68       1.79      52.26      -6.24       5.05       4.24
-------------------------------------------------------------------------------------------
Nodal Pt.  :   478
```

The Angra Steam Generator including the connection to the Main Feedwater line are presented in figure 14, that shows the location of the Pipe Whip Restraints (PWR) support:
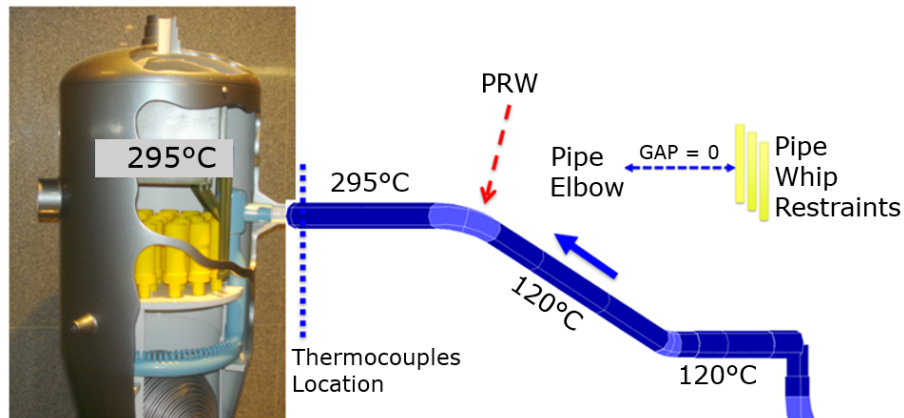
Figure 14: Pipe whip restrain location

After detecting unexpected temperature transients in the Main Feedwater line, the pipe and nozzle inspections were performed. Tests were also carried out with penetrating liquid at the welds. No damage to the pipe and nozzle welds were identified. Figure 15 shows inspection of the Pipe Whip Restraints (located on the wall) of the Main Feedwater line.

Figure 15: Inspection in main feedwater line and pipe whip restrain support

Figure 16, shows the top view of the original configuration of the Pipe Whip Restraints (PWR) support.
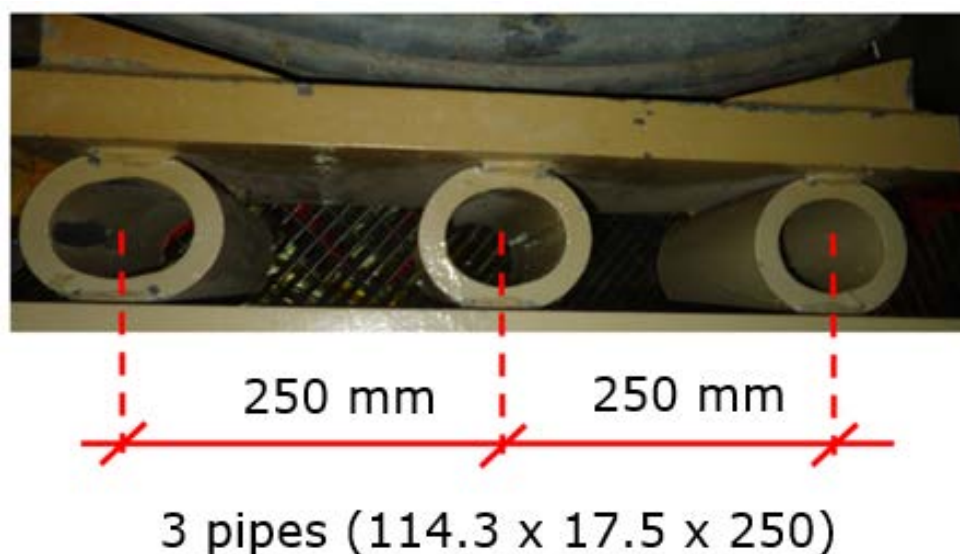
Figure 16: original configuration of the pipe whip restraints

Inspection of Pipe Whip Restraints showed that they had been affected by excessive movement of the Main Feedwater line.

In other words, the GAP between the line and the wall, where the PWR is located, has closed, causing a permanent deformation of the PWR-type support. The same effect was seen in another loop.

Figure 17 shows the top view of the Pipe Whip Restraints with permanent deformations.

Figure 17: deformed pipe whip Restraints (top view)

Finding: For this discovery, in Angra NPP, Pipe Whip Restrains supports installed beside the Main Feedwater line may be characterized as similar to bulletin 88-08.

A Comparison of deformed structure x Stress analysis with the ANSYS finite element system, [2017], considering stress distribution for 20 mm displacement is presented in figure 18, W. Menezes [2018].
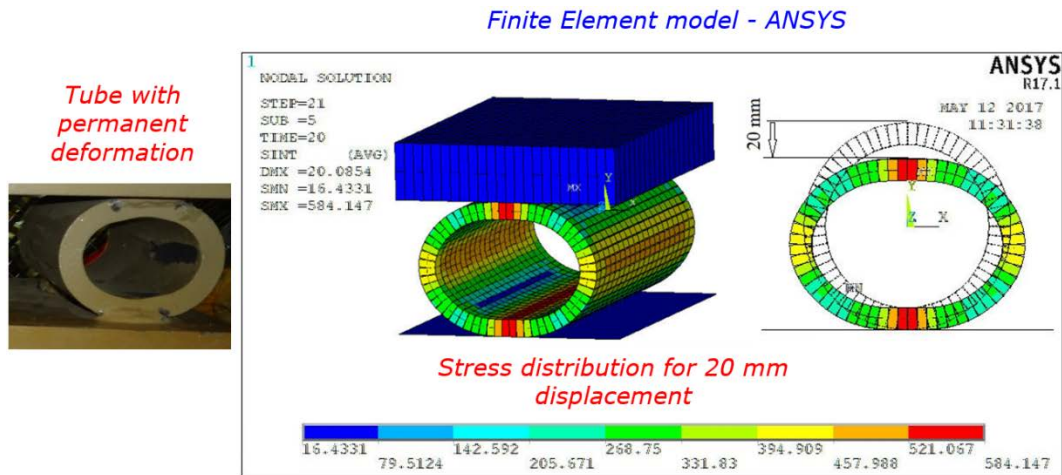
Figure 18: Deformed structure (Ovalization) x ANSYS model

In the cold shutdown mode of operation, the observed GAP is approximately 30 mm as shown in figure 19.

Figure 19: Top view of PWR in cold mode

Summary:

  a) Actual GAP plus deformed model by Ansys = 50 mm.

  b) Theoretical GAP required by calculation is 53 mm

  c) The last inspection accomplished that the PWR was not fully deformed.

Conclusion: There was still energy in the pipeline trying to move towards the PWR.

Note: This location was not included in the check of support clearances performed during first hot and cold plant conditions.

Solution: Is required a Pipe Whip Restraints support with smaller dimensions, so that the Main Feedwater line does not have movement restrictions when it is in operation.

The new adopted Pipe Whip Restraints support is shown below in figure 20, W. Menezes [2018].
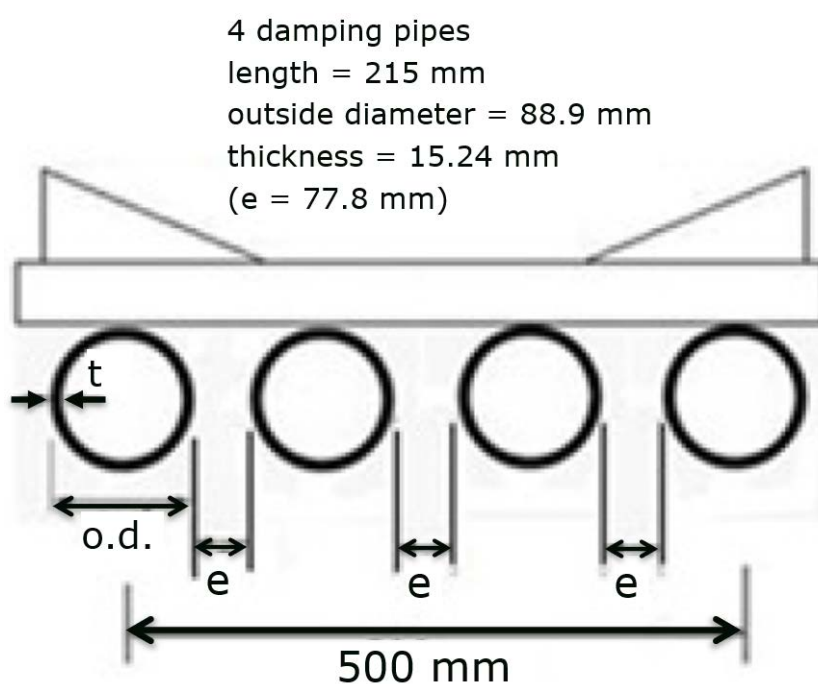
Figure 20: New pipe whip restraints

It can be noted that at Angra NPP, the phenomenon of thermal stratification was not included in the transient catalog provided by the NSSS vendor, with the magnitude that was observed. Therefore, the Main Feedwater line had to change the operating mode to reduce the number of monitored transients.

3 Automated Fatigue Monitoring

3.1 Fatigue Monitoring System in Angra NPP

An automated fatigue monitoring system is used to track the fatigue condition of Angra nuclear power plants over time.

The fatigue monitoring system performs an incremental analysis, in that all results are cumulative, reflecting all input files processed since monitoring began. As each new data file is input and processed, the results are updated to reflect the entire input history. This approach imitates the fatigue behavior of plant components, which gradually accumulate fatigue usage as they experience the various events and transients that occur during plant life.

The fatigue monitoring system allows to review the fatigue status of the plant, from the start of monitoring to the current date, in terms of plant cycles and fatigue usage factors. The staff of the plant can also sharpen focus down to a particular plant event or transient, to investigate the cause of each increment of usage. The fatigue monitoring system database for each plant unit maintains an extensive history of plant data and other computed parameters, to provide system engineers with the data they need to evaluate unusual transients or to justify alternate fatigue evaluations.

3.2 Automated Cycle Counting (ACC)

Automated Cycle Counting (ACC) analyzes the Angra NPP input data to recognize patterns, and uses those patterns to identify when recordable plant events occur. Each time an event is identified, the fatigue monitoring system records all the relevant parameters and stores it in the List of Events. It is possible also maintain the list by manually adding, editing, or deleting events.

The fatigue monitoring system is able to correctly model and analyze fatigue for all known types of Angra NPP under a wide range of operating procedures and Tech-Spec requirements, FSAR, [2020].

3.3 Plant Operating Data

The fatigue monitoring system requires data collected by plant instrumentation devices and are listed below, C. Carney et al. [2001]:

- Piping and components temperature
- Piping and components pressure
- Valve position (Open/Closed)
- Pump status (Stop/Run)
- Component flow
- Nuclear Power
- Component signal (Off/On)
- Component level (0 to 100%)
- Reactor Trip signal (normal/TRIP)
- Manual Reactor Trip signal (normal/TRIP)
- Turbine Trip signal (normal/TRIP)
- Manual safety injection signal (Off/On)

3.4 Cycle Counting Summary

The fatigue monitoring system performs the identification, recording and monitoring of traceable plant events. The cycle counting summary shows automated cycle counting events occurred during a report period (based on the events' end times).

The following reactor coolant system transients are automatically monitored in Angra NPP:

- Accumulator safety injection

- Auxiliary spray during cooldown

- Control rod drop

- High head safety injection

- Inadvertent reactor coolant system depressurization

- Inadvertent safety injection

- Inadvertent Auxiliary spray

- Large step load decrease with steam dump

- Loss of load

- Loss of power

- Operating basis earthquake

- Pressurizer cooldown

- Partial loss of reactor coolant flow

- Primary side hydrostatic test

- Primary side leakage test

- Plant heat up and cooldown

- Residual heat removal operation during cooldown

- Reactor trip from full power

      Case A - with no inadvertent cooldown

      Case B - with cooldown and no safety injection actuation

      Case C - with cooldown and safety injection actuation

- Refueling

- Step load increase and decrease of 10 percent of full power

- Turbine roll test

- Unit loading and unloading between 0 and 15 percent of full power

Automated Cycle Counting of the fatigue monitoring system identify a new event whenever the event's initiation conditions are met. Once an event is identified, it will track the values for any output parameters until the termination conditions occur. At that time, it records the event in the List of Events, then returns to looking for the next initiation.
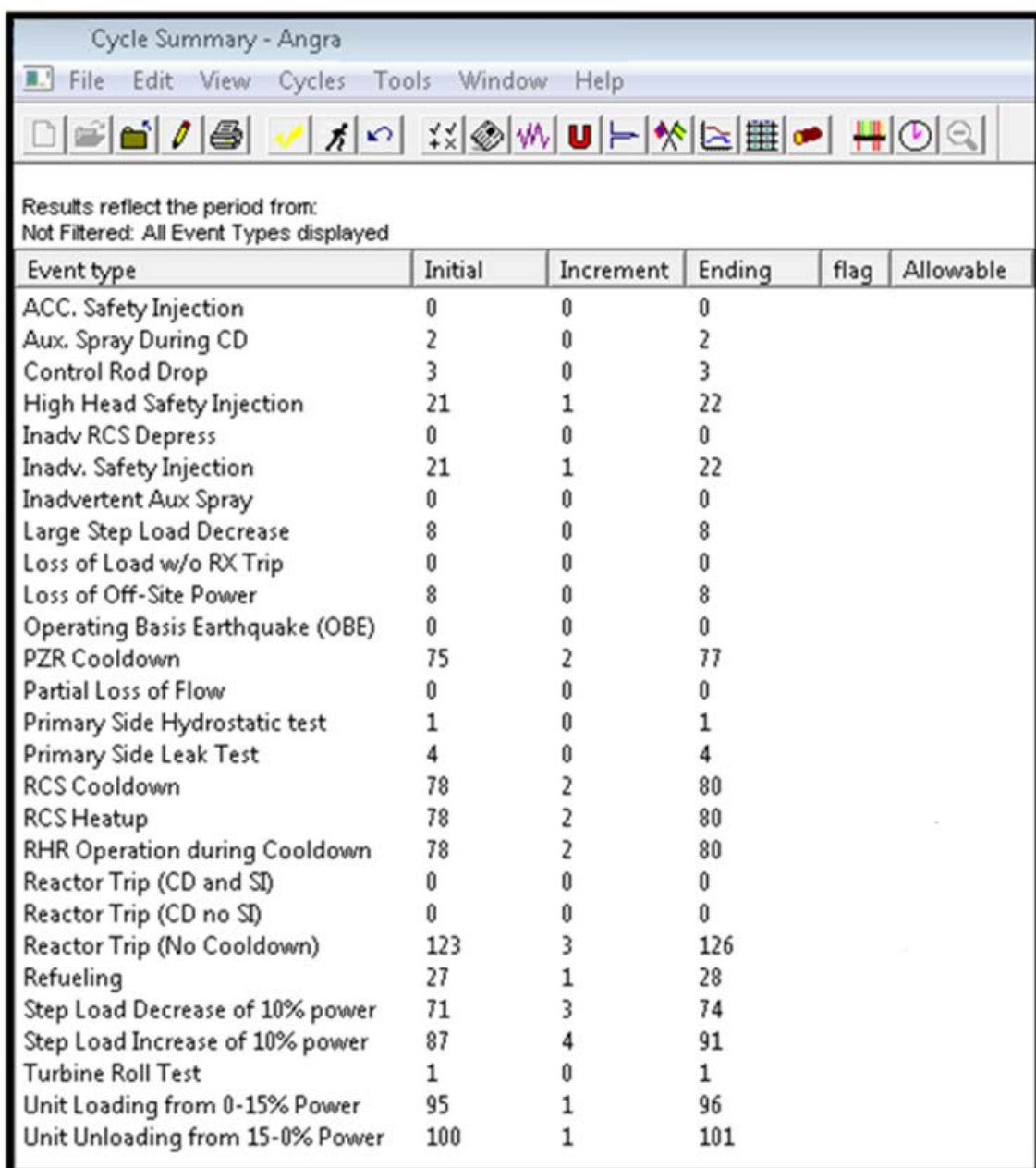
Some events are manually accounted for by a plant administrative procedure. However, it must be ensured that the event in fact occurred. Some events that did not actually occur can increase the number of events. A classic example is plant heat up, which is stopped before reaching the nominal temperature condition.

The logic of the automatic cycle counting procedure uses a threshold value for the Reactor Coolant Lines temperature values in the events plant heat up and cooldown.

These two events are not counted if the average temperature difference of the Reactor Coolant Line between the previous temperature of the event and the current temperature is ΔT ≤ 83 °C, that is, for the accounting of the heating event, the difference of average temperature of the Reactor Coolant Line between the previous temperature of the event and the temperature current must be above 83°C and must remain above this value for at least 5 minutes.

An example of the Angra NPP Cycle Summary is shown in Table 4.

Table 4: Example of transient cycle summary.

Cycle Summary - Angra
File   Edit   View   Cycles   Tools   Window   Help

Results reflect the period from:
Not Filtered: All Event Types displayed

Event type	Initial	Increment	Ending	flag	Allowable
ACC. Safety Injection	0	0	0		
Aux. Spray During CD	2	0	2		
Control Rod Drop	3	0	3		
High Head Safety Injection	21	1	22		
Inadv RCS Depress	0	0	0		
Inadv. Safety Injection	21	1	22		
Inadvertent Aux Spray	0	0	0		
Large Step Load Decrease	8	0	8		
Loss of Load w/o RX Trip	0	0	0		
Loss of Off-Site Power	8	0	8		
Operating Basis Earthquake (OBE)	0	0	0		
PZR Cooldown	75	2	77		
Partial Loss of Flow	0	0	0		
Primary Side Hydrostatic test	1	0	1		
Primary Side Leak Test	4	0	4		
RCS Cooldown	78	2	80		
RCS Heatup	78	2	80		
RHR Operation during Cooldown	78	2	80		
Reactor Trip (CD and SI)	0	0	0		
Reactor Trip (CD no SI)	0	0	0		
Reactor Trip (No Cooldown)	123	3	126		
Refueling	27	1	28		
Step Load Decrease of 10% power	71	3	74		
Step Load Increase of 10% power	87	4	91		
Turbine Roll Test	1	0	1		
Unit Loading from 0-15% Power	95	1	96		
Unit Unloading from 15-0% Power	100	1	101		

The control of cycles in accounted events is carried out through limits of alarm and related actions. In general, all locations have Cumulative Usage Factor (CUF) below the design limits. Controlling cycles in accounted events allows you to ensure that no site exceeds the limits of the cumulative fatigue usage provided for in the original design.

Output results must be reviewed and modified as necessary to correct errors in the numbers of cycles or usage factors calculated by fatigue monitoring system. These errors occur when the plant computer outputs are modified to produce some event logic in order to perform required surveillance testing, thus indicating transients that did not actually happen. An example of an erroneous event is when a Reactor Shut down (TRIP) signal is generated without a corresponding reduction in power.

This event should be excluded from data files and the fatigue monitoring system should be run again in order to update the results. If data is lost during generation of the data files so than an actual transient is not included, then this transient must be manually input into fatigue monitoring system.
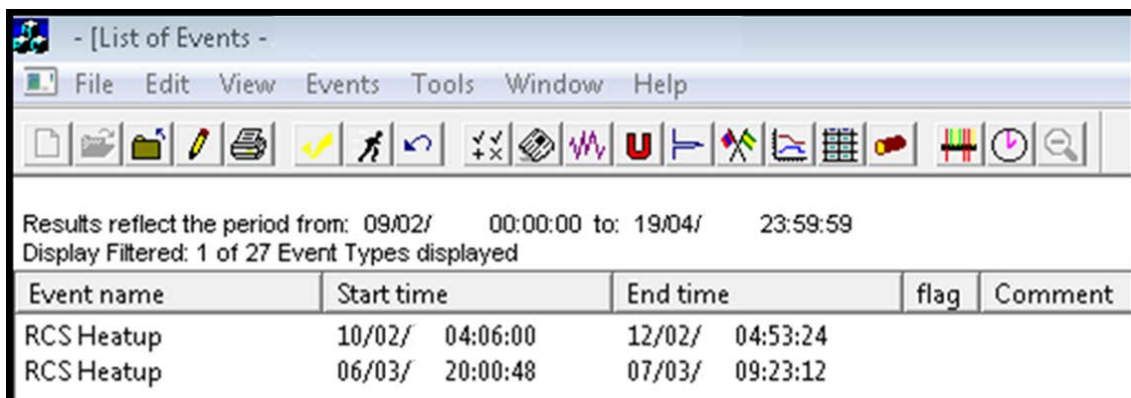
With the fatigue monitoring system, it is possible to review the fatigue status of the plant, from the start of monitoring to the current date, in terms of plant cycles and fatigue usage factors. It is possible also sharpen focus down to a particular plant event or transient, to investigate the cause of each increment of usage. The fatigue monitoring system database for the Nuclear Power Plant maintains an extensive history of plant data and other computed parameters, to provide system engineers with the data they need to evaluate unusual transients or to justify alternate fatigue evaluations (such as partial cycle counts, although this is not licensed in Angra NPP).

3.5 List of Events

The List of Events shows a list of all recorded plant events over a given period of time (the report period). The event record includes the starting date/time and the duration of the event.

Example of List of Events that occurred during a Plant heat up are shown in Table 5.

Table 5: List of events for reactor coolant line heat up during a plant cycle.
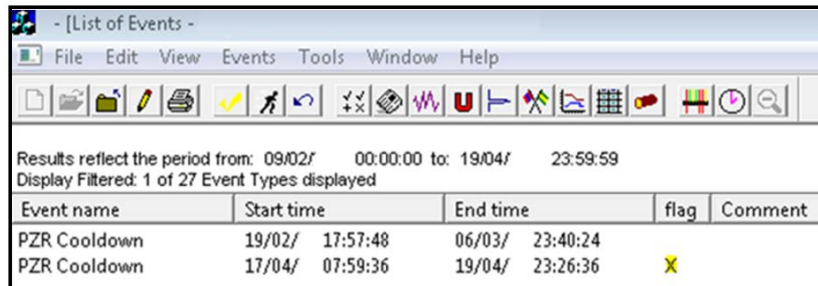
3.6 Verification of Warning Displays in a List of Events Table

If any device exceeds the plant's operating limits, a warning will be activated.

In this case the index flag will be activated with the letter X. This can be seen in table 6.
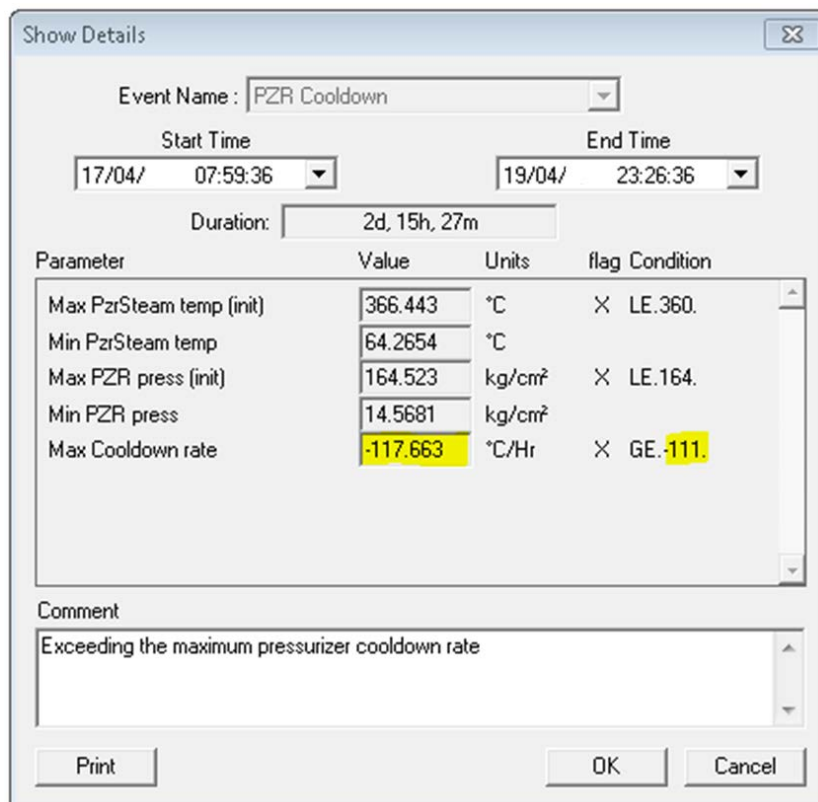
Table 6: List of events for pressurizer cool down during a plant cycle.

Example of event details showing the X-activated flag are shown in table 7.

Table 7: Details list of events.

The details presented in table 7 for a Pressurizer event, shows the fatigue monitoring system verifying the cooling rate every 30 continuous minutes (rate using a 30-minute running average), from a preset value (360°C) to the temperature considered as steady-state (below 65.6°C). Below the stationary value, it is considered that there is no metal fatigue. This class of data allows the fatigue monitoring system verify design parameters with values presented by plant instrumentation during a cycle or event.

3.7 Fatigue Monitoring in Selected Locations - Cycle-Based Fatigue

Fatigue monitoring in selected locations is performed using the Cycle-Based Fatigue (CBF) methodology that utilizes the compiled Automated Cycle Counting event list to compute fatigue usage for monitored fatigue locations based on event patterns.

In Angra there are 2 types of Cycle-Based Fatigue locations:

    a) Per-Cycle (CBPC).
    b) Event Pairing (CBEP)

3.7.1 Per-Cycle Usage (CBPC)

In the Per-Cycle Usage locations, a specific fatigue usage increment is associated with each type of event. This usage increment can either be a fixed amount for all events of a given type, or it can be a "partial-cycle" usage based on one or more of the event's recorded parameters. The total fatigue usage for each CBPC location is the sum of the individual usage increments of all of the recorded events in the Event List.

In Angra NPP some locations were analyzed using the Per Cycle Method (CBPC), which were chosen due to the high Cumulative Usage of Fatigue (CUF) presented in the original project. These locations perform fatigue control through the occurrence of one of the transients 1 to 27 listed in Table 3. Figures 16 and 17 shows locations CBPC.

The location shown in figure 21, monitors fatigue usage factor in the pipe weld to check valve in the safety injection line.
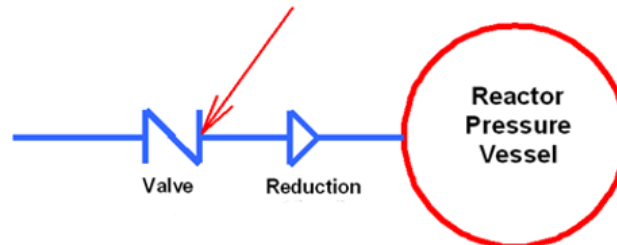
Figure 21: Location SI_VALVE - safety injection line - austenitic stainless steel

The location shown in figure 22, monitors CUF on the pressurizer spray line Tee.
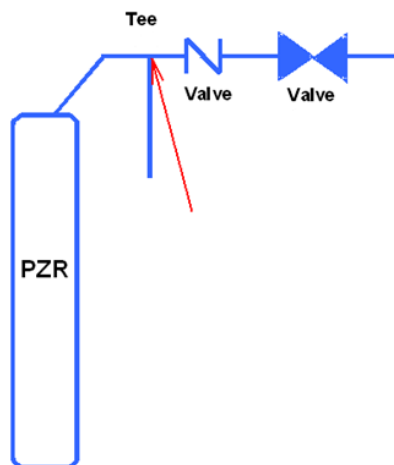
Figure 22: Location PZR_TEE - pressurizer spray line tee - austenitic stainless steel

3.7.2 Event Pairing (CBEP)

For the Event Pairing method, each type of event is associated with a set of transients (that is, stress states) at the monitored location. Then, a pair-usage table is derived, giving the fatigue usage that would result from each possible pair of transients. Note that many transient pairs produce no significant usage, so these pairs are not included in the pair-usage table. To compute the fatigue usage, all events are reduced to their component transients, which are then counted. The transients are paired, highest-usage pairs first, and the usage for that pair is counted. Then the paired transients are removed, and the process continues with the next lower non-empty pair of transients. At the end, any unmatched transients are counted using the highest-usage pair which contains that transient.

In Angra NPP other locations were analyzed using the Event Pairing Method (CBEP) methodology, which increases the factor of accumulated fatigue usage whenever a predefined pair of load cases occurs. Figure 18 shows locations CBEP.

Figure 23 shows two fatigue monitoring locations type CBEP. One is the Residual Heat Removal Tee to the Accumulator Line (nodal point 138) and the other is the Accumulator Line Cold Leg Nozzle (nodal point 212), M. Cisternas [2012].
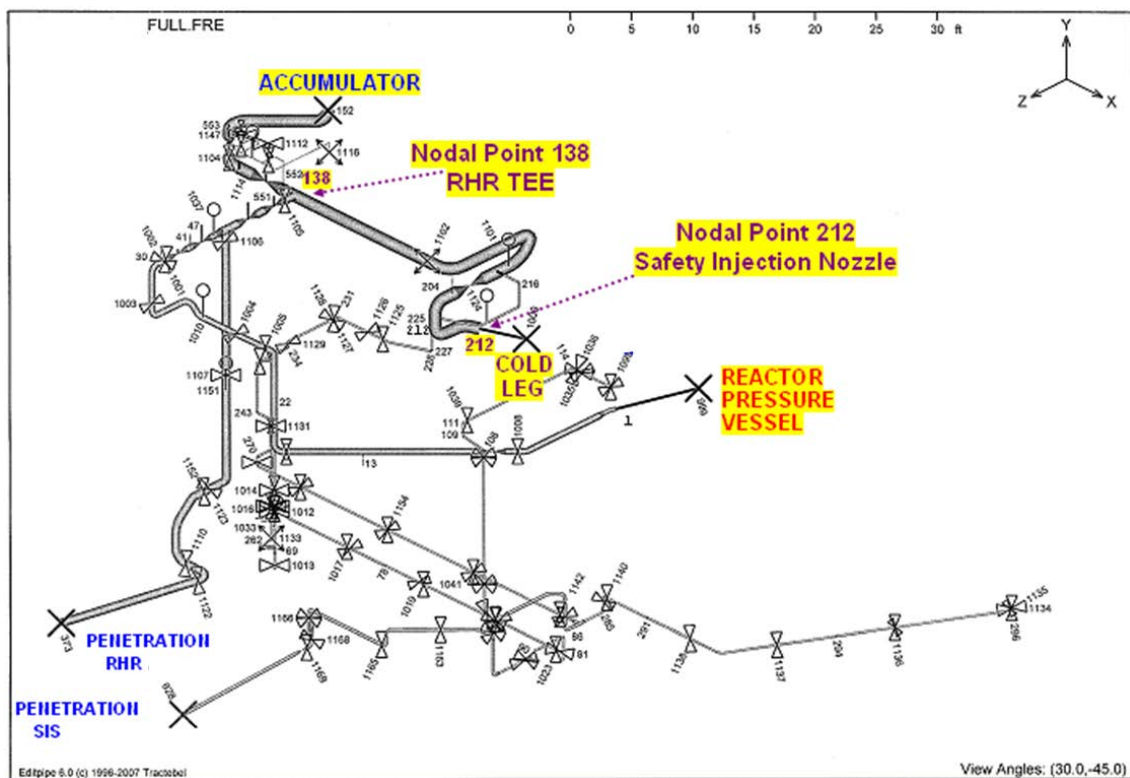
Figure 23: Locations RHRTEE and ACSI - austenitic stainless steel

The location shown in figure 24, monitors fatigue usage factor at both of the Reactor Pressure Vessel outlet nozzles.
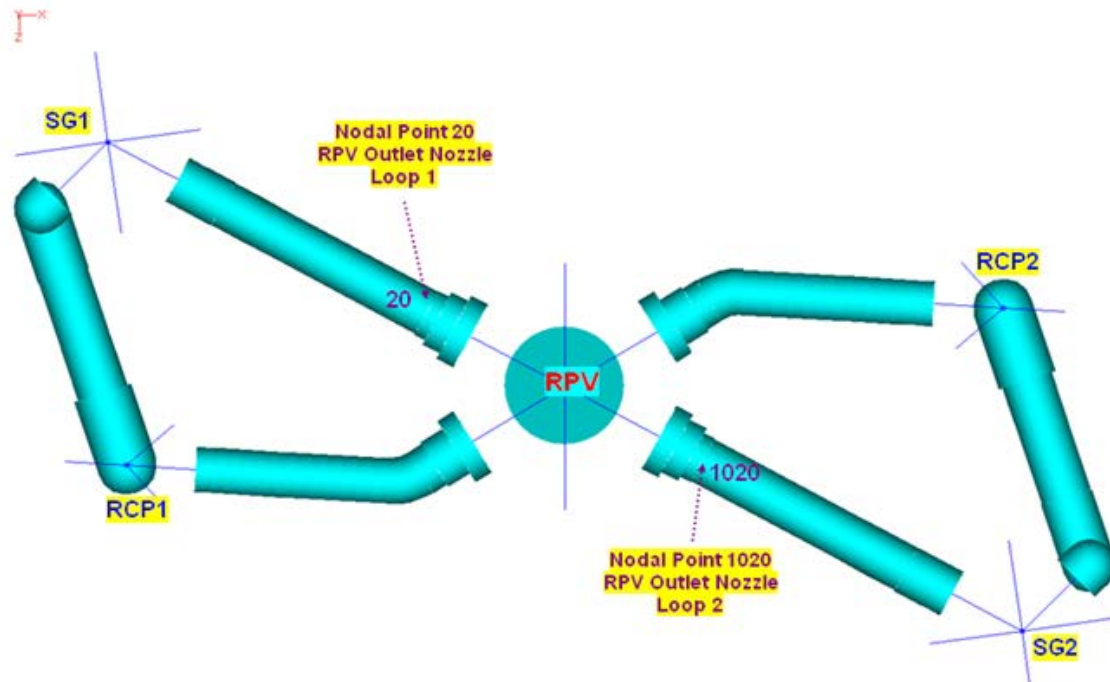
Figure 24: Reactor vessel outlet nozzles - ferritic steels

The location shown in figure 25, monitors fatigue usage factor at both of the Reactor Pressure Vessel inlet nozzles.
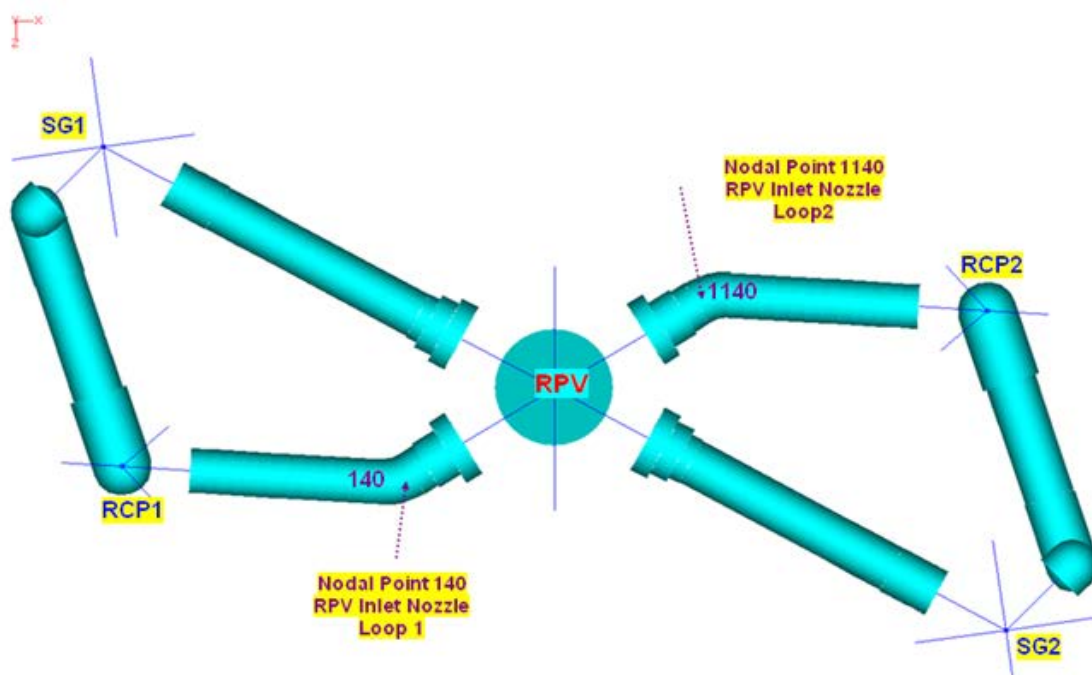
Figure 25: Reactor vessel inlet nozzles - ferritic steels

3.8 Summary of Cumulative Fatigue Usage Factors

The fatigue monitoring system in nuclear power plant components based on actual plant data are performed in some selected locations. Actual plant transients generally cause stress cycling that is typically less severe than that computed in the original design analysis. The use of a fatigue monitoring system can show that accumulated fatigue usage is much less than would be expected, based on consideration of design transients. The potential economic benefits derived from accurate cumulative usage factor assessment through the use of a fatigue monitoring system can be significant with regard to component life extension. Direct benefit is also provided in the areas of plant operation and maintenance throughout plant operating life.

Cumulative Fatigue Usage (CUF) is the measure of accumulated damage underwent by a component due to cyclic stresses.

The fatigue monitoring system performs an incremental analysis, in that all results are cumulative, reflecting all input files processed since monitoring began. As each new data file is input and processed, the results are updated to reflect the entire input history. This approach imitates the fatigue behavior of plant components, which gradually accumulate fatigue usage as they experience the various events and transients that occur during plant life.

An example with cumulative fatigue usage factor in selected locations, showing the maximum value where redundant locations exist are shown in Table 8.

Table 8: Example of cumulative usage factors.

Fatigue Type: Low Cycle
Results reflect the period from:
Not Filtered: All Locations displayed

Location	Type	Initial U	Increment	Ending U	Allowable
ACSI	CBEP	0.01618	0.00041	0.01659	1.00000
PZR_TEE	CBPC	0.66880	0.00380	0.67260	1.00000
RHRTEE	CBEP	0.00234	0.00006	0.00240	1.00000
RPVI	CBEP	0.02222	0.00074	0.02296	1.00000
RPVO	CBEP	0.07968	0.00222	0.08190	1.00000
SI_VALVE	CBPC	0.01254	0.00060	0.01313	1.00000

The Stress and fatigue analysis engineer evaluates the significance of the transient cycle counts. Any transient behavior beyond the design basis may indicate the need to monitor additional locations for fatigue and to modify operations to minimize piping or component fatigue.

3.9 Projection of Cumulative Fatigue Usage (CUF) Location

The design limit on fatigue assumes that the starting point of a crack occurs when the Cumulative Fatigue Usage Factor reaches the value 1.0.

Figure 26 shows the projection of the cumulative fatigue usage factor for 40-year operating life of the plant for location Pressurizer Tee (PZR_TEE) of table 7.
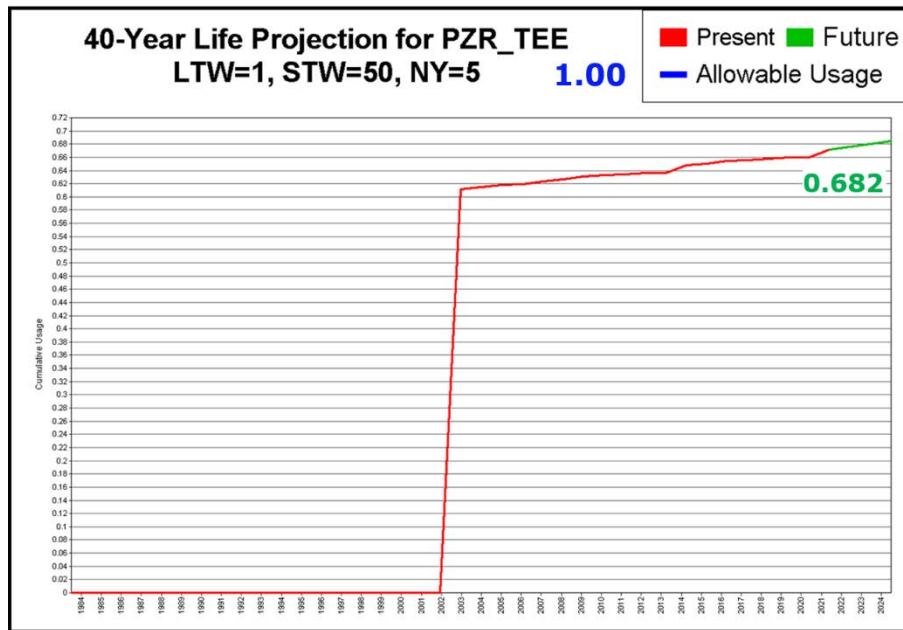
Figure 26: Location pressurizer tee (PZR_TEE) – 40-year life projection

Figure 27 shows the CUF projection for 60 years of operation.
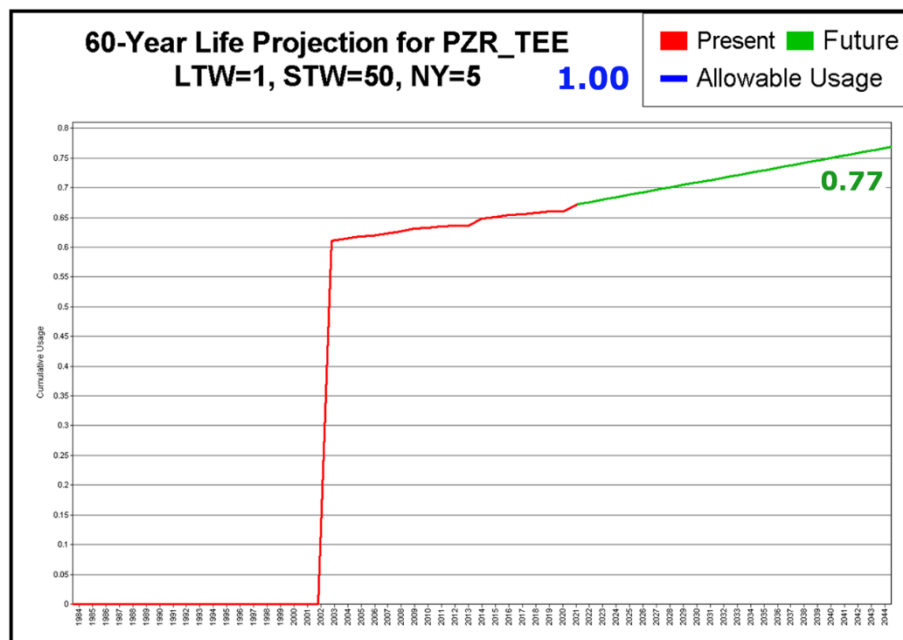
Figure 27: Location pressurizer tee (PZR_TEE) – 60-year life projection

4 Permissible Cycle Limits

4.1 Permissible Cycle Limits for the Planning of 60 Years of Operation

The Angra NPP were designed to operate during a period of 40 years of service (40 Years of Operation). However, the Angra NPP should operate for additional period of 20 years of service. This new period is known as 60-Year Transient Projected Cycles.

A catalog of allowable design limits for 40 years of operation was provided by the NSSS Vendor (Nuclear Steam Supply System). Limits for 60 years of operation can be obtained following the rules of the U.S. Nuclear Regulatory Commission (USNRC), or through the German standards, Nuclear Safety Standards Commission (KTA).

Currently, in the nuclear industry, there is no uniform procedure of rules and techniques to be used to obtain the limits for 60 years of operation.

To cover the possible environmental influence on fatigue resistance, plants that follow USNRC procedures, such as Angra 1 NPP, are subject to the so-called Environmentally Assisted Fatigue (EAF). In this case, there is an environmental penalty arising from tests carried out at the Argonne National Laboratory (ANL), which showed that the effects of fatigue in a water environment, at nominal temperature at full power, are significantly greater than the effects of fatigue in an air environment, in which the current fatigue curves of the ASME code were developed. Note that this penalty reduces fatigue life as it increases the accumulated fatigue usage factor. Basically, it consists of the assumption that the number of cycles allowed in the Reactor is subject to the considered environment. That is, it depends on the operating temperature, oxygen concentration and deformation rate of the materials used. The environmental correction factor (Fen) is defined through a mathematical formula, which has been continuously updated. Selected locations in NUREG/CR-6260 [1995], need to apply the Fen penalty.

For Austenitic materials, NUREG/CR-5704 (Effects of Light Water Reactor Coolant Environments on Fatigue Design Curves of Austenitic Stainless Steels) [1999], gives a maximum value for Fen equal to:

$$Fen = 15.3485$$

In general, the value calculated using "ANSYS" finite element systems, after great computational effort using refined models, presents an average value around:

$$Fen = 5.0.$$

For Ferritic materials, NUREG/CR-6583 (Effects of LWR Coolant Environments on Fatigue Design Curves of Carbon and Low-Alloy Steels) [1998], gives a maximum value for Fen equal to:

$$Fen = 2.4547.$$

The Fen penalty is applied directly to the CUF factor (Cumulative Fatigue Usage Factor), that is:

$$CUF_{60\text{-}YEAR} = F_{en} \times CUF_{40\text{-}YEAR}$$

Alternatively, both NUREG/CR-5704 and NUREG/CR-6583 may be replaced by NUREG/CR-6909 (Effect of Light Water Reactor Coolant Environments on the Fatigue Life of Reactor Materials) [2007], requiring the use of new fatigue curves.

In other words, there is still no consensus on the applied formulations. The fatigue analyzes that follow this procedure are called TLAA analyses, which are analyzes whose validity is limited by the time or cycles of use (Time-Limited Aging Analysis).

On the other hand, for plants that follow German Safety Standards, such as Angra 2, the German KTA standard also presented rules in case the environmental effects cannot be excluded, as in the event projection for 60 years of operation, and are presented Next:

    a) KTA 3201.4 [2010], describes the following rules:

In projecting events for 60 years of operation, the number of allowable transients must be reduced until reaching the following limits for the cumulative fatigue usage factor (CUF), which will be considered as fixed values:

> CUF = 0.2 for Austenitic stainless steel.
>
> CUF = 0.4 for Ferritic steels (carbon steel and low alloy steels).

    b) KTA 3211.2 [2013], describes the following rules:

In projecting events for 60 years of operation, the number of allowable transients must be reduced until reaching the following limits for the cumulative fatigue usage factor (CUF), which will be considered as fixed values:

> CUF = 0.4 for Austenitic and Ferritic materials.

The values adopted for CUF as being 0.2 or 0.4 depending on the standard, are called attention threshold, and correspond to 60 years of plant operation.

The definition of attention thresholds reflects the current state of knowledge of environmental influences. This state of knowledge must evolve further in the future, and the decision will be made on the basis of this new basis and at the level of attention thresholds of the KTA standard or, if necessary, its omission will be decided.

Table 9 next presents a summary of the use of rules from NUREG and KTA for transient projections for 60 years of operation:

Table 9: Fatigue correction factor - summary of the use of rules from NUREG and KTA.

NUREG		KTA	
NUREG/CR-5704 (1999-04)	NUREG/CR-6583 (1998-02)	KTA 3201.4 (2010-11)	KTA 3211.2 (2013-11)
Austenitic	Ferritic	Austenitic and Ferritic	Austenitic and Ferritic
Effects of LWR Coolant Environments on Fatigue Design Curves of Austenitic Stainless Steels	Effects of LWR Coolant Environments on Fatigue Design Curves of Carbon and Low-Alloy Steels	Components of the Reactor Coolant Pressure Boundary of Light Water Reactors Part 4: In-service Inspections and Operational Monitoring	Pressure and Activity Retaining Components of Systems Outside the Primary Circuit Part 2: Design and Analysis
Fatigue Life Correction Factor = Fen CUF 60-YEAR = Fen x CUF		Cumulative Usage Factor = CUF	
Austenitic Fen = 15.3485 (Fen maximum) Fen ~ 5 (Fen calculated)	Ferritic Fen = 2.4547	Austenitic Limit = CUF = 0.2 (Fen = 5)	Austenitic Limit = CUF = 0.4 (Fen = 2.5)
		Ferritic Limit = CUF = 0.4 (Fen = 2.5)	Ferritic Limit = CUF = 0.4 (Fen = 2.5)

Summary for Ferritic materials:

For the accounting of the number of transients occurring in Ferritic materials, the use of attention threshold is very similar if obtained using NUREG rules or the German KTA standard. That is:

Adopting KTA for Ferritic materials implicitly means using Fen = 2.5000

Adopting NUREG for Ferritic materials means using Fen = 2.4547

Summary for Austenitic materials:

For the accounting of the number of transients occurring in Austenitic materials, the use of attention threshold is very similar if obtained using NUREG rules after a long computational effort or the German KTA standard. That is:

Adopting KTA for Austenitic materials implicitly means using Fen = 5.0

Adopting NUREG for Austenitic materials means using Fen ~ = 5.0

(After great computational effort using refined models)

Application of the rules to obtain the CUF for 60-year transient projected cycles

Table 10 shows the cumulative fatigue usage factor (CUF) for 60 years of operation, using the results output shown in table 8.

Table 10: Cumulative fatigue usage factor for 60 years of operation.

System or Component	Location	Material	$CUF_{40\text{-}Year}$ (Table 8)	Environmental Correction Factor F_{en} (Maximum threshold)	$CUF_{60\text{-}Year}$ (Projected)	Warning threshold (60% $CUF_{60\text{-}Year}$)
Accumulator Safety Injection Line	(ACSI)	Austenitic	0.01659	15.3485	0.25463	0,60000
Pressurizer Spray Line	(PZR_TEE)	Austenitic	0.67260	N/A	0.77000[1,2]	0,60000
Residual Heat Removal Line	(RHRTEE)	Austenitic	0.00240	15.3485	0.03684	0,60000
Cold Leg Nozzles	(RPVI)	Ferritic	0.02296	2.4550	0.05637	0,60000
Hot Leg Nozzles	(RPVO)	Ferritic	0.08190	2.4550	0.20106	0,60000
Safety Injection Line	(SI_VALVE)	Austenitic	0.01313	N/A	0.02400[1,2]	0,60000

[1] It is not a selected location defined in NUREG/CR-6260, so it only needs to make projections for 40 and 60 years of operation considering the limit for $CUF \leq 1.0$ (Figures 26 and 27).

[2] Projection for 60 years of operation performed by a fatigue monitoring system.

Conclusion: In general, the methodology used by NUREG when compared to the methodology used by the German KTA standard to address the environmental-assisted fatigue problem seems to lead to similar values, after great computational effort using refined models.

The use of fixed value penalties (NUREG and KTA for Ferritic materials and KTA for Austenitic materials) can reduce costs and avoid creating very refined models.

The employ of the maximum NUREG threshold value for Austenitic materials, should preferably be used in fatigue control of selected locations, which make use of automatic systems.

References

O.K. Chopra and A. Sather. NUREG/CR-5385, ANL-89/17, Argonne National Laboratory, Initial Assessment of the Mechanisms and Significance of Low-Temperature Embrittlement of Cast Stainless Steels in LWR Systems. 1990.

Code ASME Boiler and Pressure Vessel Code Section III, Division 1, Subsections NB, NC and ND. 1989.

KTA 3201.2. Nuclear Safety Standards Commission, Components of the Reactor Coolant Pressure Boundary of Light Water Reactors. Part 2: Design and Analysis. 1996.

NUREG-1801 Rev. 2. Generic Aging Lessons Learned (GALL) report. 2010.

FieldChart Novus Version 2.0.3.1. Help Manual for FieldChart Novus®. 2013.

M.A.C. Cisternas, J.F.C. Telles and W.J. Mansur. Potential Problems Involving Axisymmetric Geometry and Arbitrary Boundary Conditions by the Boundary Element Method, BETECH 87, Computational Mechanics Institute, Southampton. 1987.

M. Cisternas. Thermal Stratification Monitoring in Angra 2 NPP, Brazil, Nuclear Plant Fatigue Applications Workshop, Charlotte, NC. 2009.

Finite Element Program KWUROHR, Version_10.0.0. 2014.

Finite Element System ANSYS, Version_R17.1. 2017.

W. Menezes, Dynamic analysis of Pipe Whip Restraints considering the reduction of the outer diameter of the damping pipes. ELETRONUCLEAR Report. 2018.

Angra Final Safety Analysis Report, FSAR. 2020.

C. Carney, J. A. Hofmann, C. R. Limpus. User's Manual for FatiguePro Fatigue Monitoring System, Version 3.0, EPRI, Palo Alto, CA. 2001.

Finite Element System PIPESTRESS, Version 3.6.2. 2009.

M. Cisternas. Accumulator System to RCL and Safety Injection System to RPV – Loop 1. Class 1 Snubber Reduction Program. ELETRONUCLEAR Report. 2012.

NUREG/CR-6260, INEL-95/0045. Idaho National Engineering Laboratory, Application of NUREG/CR-5999 Interim Fatigue Curves to Selected Nuclear Power Plant Components. 1995.

NUREG/CR-5704, ANL-98/31. Argonne National Laboratory, Effect of LWR Coolant Environments on Fatigue Design Curves of Austenitic Stainless Steels. 1999.

NUREG/CR-6583, ANL-97/18. Argonne National Laboratory, Effect of LWR Coolant Environments on Fatigue Design Curves of Carbon and Low-Alloy Steels. 1998.

NUREG/CR-6909, ANL-06/08. Argonne National Laboratory, Effect of LWR Coolant Environments on the Fatigue Life of Reactor Materials. 2007.

KTA 3201.4. Components of the Reactor Coolant Pressure Boundary of Light Water Reactors. Part 4: In-service Inspections and Operational Monitoring. 2010.

KTA 3211.2. Pressure and Activity Retaining Components of Systems Outside the Primary Circuit. Part 2: Design and Analysis. 2013.

Structural Integrity Associates, Inc, "Approach for Evaluation of Piping Affected by Stratification and Thermal Cycling", AFD-03-028. 2008.

Chapter 12

On the use of Modal Test Data in Inverse Problems: Fundamentals and Applications

Chapter details

Chapter DOI:

Chapter suggested citation / reference style:

P.S.: DOI may be included at the end of citation, for completeness.

Book details

On the use of Modal Test Data in Inverse Problems: Fundamentals and Applications

Guilherme F. Gomes[1*], Sergio H. S. Carneiro[2],

Carlos E. S. Cesnik[3], and Ariosto B. Jorge[4]

[1]Mechanical Engineering Institute, Federal University of Itajubá (UNIFEI), Brazil.
E-mail: guilhermefergom@unifei.edu.br
[2]Aerospace Engineering Course, FGA, University of Brasilia (UnB), Brazil.
E-mail: shscarneiro@gmail.com
[3]Aerospace Engineering Department, University of Michigan - Ann Arbor (U-M), USA.
E-mail: cesnik@umich.edu
[4]Post-Graduate Program - Integrity of Engineering Materials, University of Brasilia
(UnB), Brazil. E-mail: ariosto.b.jorge@gmail.com

[*]Corresponding author

Abstract

In the past few decades, modal testing has become a major technology for determining, improving and optimizing dynamic characteristics of engineering structures in different fields, with emphasys (but not limited to) mechanical, civil, and aeronautical/aerospace engineering. One of the great advantages of using modal tests is related to their experimental practicality. This practical advantage leads to its strong use in inverse methods, or commonly known as inverse modal-based problems. An inverse problem based on modal parameters can be formulated basically using i) natural frequency, ii) damping factor or loss factor and iii) mode shapes. Other metrics can also be used from the composition of these 3 main responses, such as modal strain energy, inverse FRF and many others. Inverse modal-based identification through optimization algorithms are particularly emphasized. The methods discussed here are mainly elaborated by the evaluation of modal data due to the great potential of application. This chapter discusses the use of computational and intelligent techniques for parameter identification using modal responses. The content in this paper aims to help engineers and researchers find a starting point in developing a better solution to their specific structural problems, either by inverse methods, pattern recognition, or intelligent signal processing.

Keywords: Modal Testing; Experimental Modal Analysis; Parameter Estimation; Inverse Problems.

1   Introduction and Context

The field of modal testing is quite extensive and, to be mastered, it is necessary to integrate knowledge from different engineering fields: vibration measurements, signal processing and structural analysis, including the necessary mathematical background. This Chapter does not intent to address in detail all aspects of experimental modal analysis, but only to familiarize and give the most important concepts and recent application in inverse problems to the reader. For a more comprehensive understanding of the topics covered, the novice researcher may rely on the vast classical books on the field, such as the theoretical foudations of vibration analysis found in Meirovitch [2010] and Inman [2013] or the fundamentals of modal testing, such as Silva and Maia [1999], Ewins [2000], Fu and He [2001] and Avitabile [2017].

According to Aster et al. [2012], the formulation of direct and inverse problems may be seen as an attempt to better understand physical phenomena in general by means of mathematical models, assuming that the underlying physical concepts are adequately understood. The idea is to relate physical parameters characterizing a model $\mathbf{m}$ to a set of data $\mathbf{d}$ by means of an operator G, such that

$$G(\mathbf{m}) = \mathbf{d}. \tag{1}$$

The model $\mathbf{m}$ may be understood as a set of physical parameters and relations; the data $\mathbf{d}$ may be a function of time and/or space, or may be a collection of discrete observations. The operator G can take on different forms, depending on the chosen approach. It can be an ordinary differential equation (ODE), or partial differential equation (PDE), or systems of ODE/PDE. In other cases, G may be a linear or nonlinear system of algebraic equations. This terminology is not a consensus between mathematicians and other scientists. The former usually refer to $G(\mathbf{m}) = \mathbf{d}$ as the model and $\mathbf{m}$ as the set of parameters, while the latter call G the forward operator and $\mathbf{m}$ the model. Without loss of generality, the second terminology is adopted hereafter.

The *forward* problem, or *direct* problem, is the process of obtaining $\mathbf{d}$ given $\mathbf{m}$, which usually involves solving ODEs or PDEs, solving a system of linear or nonlinear algebraic equations, evaluating integrals or even applying numerical algorithms when an explicit form of the operator G is not available. On the other hand, the *inverse* problem is to find $\mathbf{m}$ given $\mathbf{d}$, which can be, in most cases, a much more complex endeavor than solving the associated direct problem. Solution existence, solution uniqueness ant instability of the solution are some of the issues that arise when dealing with inverse problems and that must be carefully addressed. For further information in the topic of inverse problems in strtuctural integrity problems, ranging from basic theoretical background to advanced applications, the reader is encouraged to consult the first volume of the present Book Series (Jorge et al. [2022]).

In this context, modal testing may be seen as an inverse problem in itself, when one focus on the process of identifying a useful dynamic model from measured data. The identified model may be a set of estimated Frequency Response Functions (FRFs) or, more frequently, a set of modal parameters, such as natural frequencies, damping factors and natural mode shapes, which can be used in adequate sets of ODE, PDE or algebraic equations in order to describe the dynamic behavior of the modeled system. Once obtained, the described modal data can, in turn, be used in several applications as *models* in direct/forward problems or as *data* in inverse problems.

The relevance and broad range of the use of modal data in engineering investigations in general, and in structural integrity problems in particular, is the main motivation for the present chapter. The fundamental concepts that are necessary for a basic understanding of the topic are briefly reviewed. Additionally, a selection of recent applications of the use of modal data in structural integrity problems is presented and discussed. The authors hope that the present chapter may provide the reader with the basic tools and information to further studies in the field, taking advantage of a comprehensive list of classical and recent literature for each relevant topic.

2   Overview and Philosophy of Modal Testing

Since the late 1970s, according to Fu and He [2001], modal analysis has increasingly become a major technology in the quest for determining, improving and optimizing dynamic characteristics of engineering structures. A very interesting historical overview of the first 30 years of developments in the field may be found in Brown and Allemang [2007]. Not only has the topic *modal testing* been recognized in mechanical and aerospace engineering, but modal analysis has also encountered profound applications for civil and building structures, bio-mechanical problems, acoustical instruments, transportation and nuclear plants, among others.

In the same way, according to Ewins [2000], since the very early days of awareness of structural vibration, experimental observations have been necessary for the major objectives of *i*) determining the nature and extent of vibration response levels in operation and *ii*) verifying theoretical models and predictions of the various dynamic (vibration) phenomena. There is also a third requirement, which is, *iii*) identifying the essential material properties under dynamic loading, such as damping capacity, friction and fatigue endurance. One of the major requirements of the subject of modal testing is a thorough integration of three components:

- The theoretical basis of vibration;

- Accurate measurement of vibration;

- Realistic and detailed data analysis.

Equally important, in summary, modal analysis is the process of determining the inherent dynamic characteristics of a system in forms of natural frequencies, damping factors and mode shapes, and using them to formulate a mathematical model for its dynamic behavior. The formulated mathematical model is referred to as the modal model of the system and the information for the characteristics are known as its modal data (Fu and He [2001]). Modal analysis embraces both theoretical and experimental techniques. The theoretical modal analysis anchors on a "spatial model" of a dynamic system comprising its mass, stiffness and damping properties. These properties may be given in forms of partial differential equations. Modern finite element (FE) analysis empowers the discretization of almost any structural system and hence has greatly enhanced the capacity and scope of theoretical modal analysis. On the other hand, the rapid development over the last two decades of data acquisition and processing capabilities has given rise to major advances in the experimental realm of the analysis, which has become known as modal testing.

Figure 1 depicts the theoretical and experimental vibration routes previously discussed (Covioli [2021]). On the theoretical path, the relevant geometrical and material properties of the system are the main input for the creation of the so-called "spatial model", most frequently a FE numerical discretization of a complex structure that combines several different continuous elements. This numerical representation in physical coordinates can be transformed through the solution of an algebraic eigenproblem into a model consisting of the natural frequencies and mode shapes of the system, which is referred to as the "modal model". From the modal model it is possible to efficiently obtain response functions in the time domain or in the frequency domain, allowing for a wide range of simulations of the dynamic behavior of the system when submitted to the envelope of excitations that will occur during its operation.
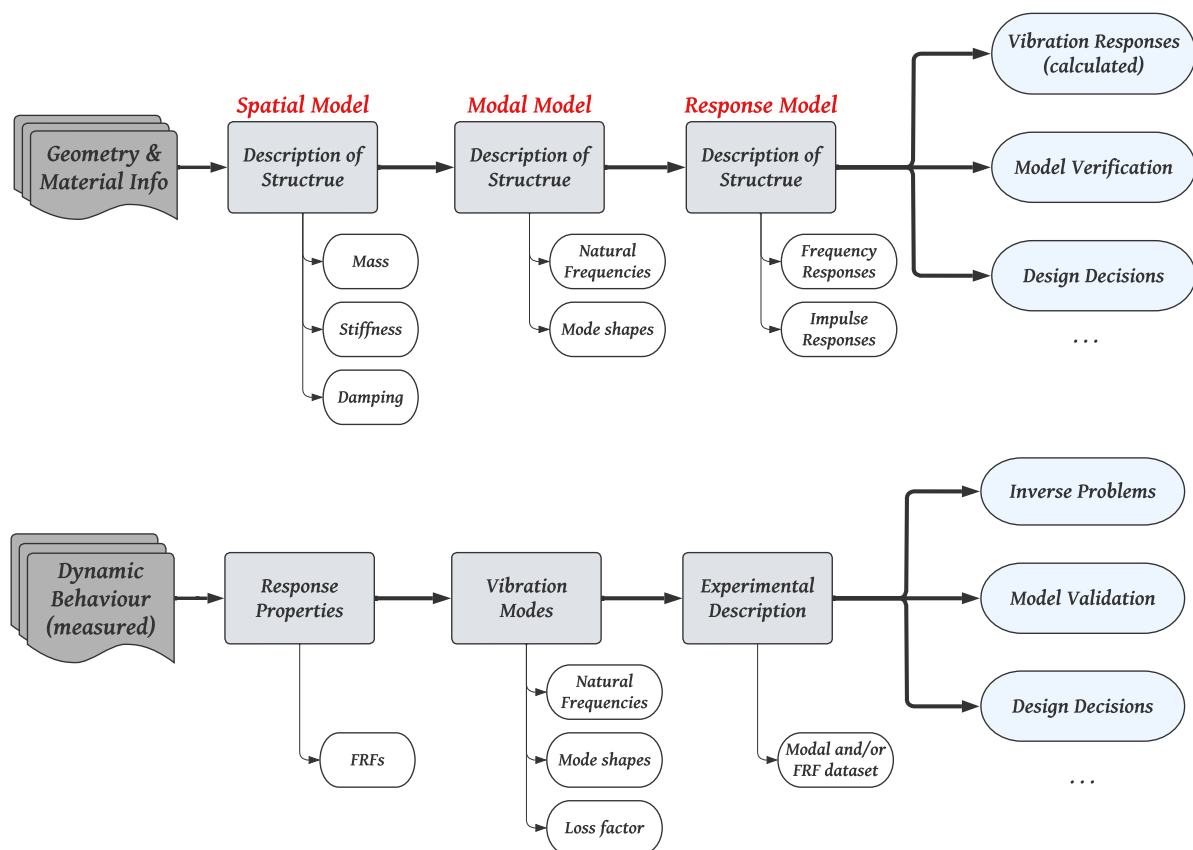
Figure 1: Vibration analysis route : (a) theoretical ; (b) experimental (adapted from Covioli [2021]).

On the experimental path, the starting point is the measurement of the dynamic behavior of the structure when conveniently excited. Signal acquisition and processing of the excitation forces[1] and vibration responses (most frequently accelerations or velocities of selected points of the structure) are the input data for the identification steps that follow.

---

[1]It is possible to perform modal tests without the measurement of the excitation forces, relying solely on the measurement of vibration responses. This is particularly useful when investigation systems in its

Response functions are then obtained and used to feed modal parameter extraction algorithms, resulting in an experimental modal model representing the vibration modes of the structure. Now, the dynamic behavior of the structure is described by a set of identified natural frequencies, modal damping factors and natural mode shapes. The experimental modal parameters, together with a simplified geometrical model of the measured degrees of freedom, constitute the experimental description of the system.

There is a range of complex and relevant problems in engineering that make use of modal data to solve a specific inverse problem, such as: numerical model updating and tuning, detection and identification of damage, identification of mechanical properties, force identification, and sensor optimization problems. The great advantage of using modal data is due to the amount and quality of global information intrinsic to the structure. This chapter is focused on discussing the use of modal data in order to solve a general inverse problem as well as discussing the peculiarities of selected applications.

3　The Frequency Response Function

Most of the parameter identification techniques and algorithms used in Modal Testing to obtain the modal parameters are based on a previous identification of at least one (usually several) FRFs of the system under investigation. Therefore, some basic definitions and equations involved in the modal identification methodology based on FRFs are briefly reviewed.

3.1　Frequency Response Function - SDOF systems

Some mechanical and structural systems can be idealized as Single Degree of Freedom (SDOF) systems. The theory for an SDOF system forms the basis for the analysis of a system with more than one degree of freedom (DOF). It also provides physical insight into the vibration of a structural system. We will use the SDOF system shown in Figure 2 that has a mass, a spring and a damper with either viscous or structural (hysteretic) damping.

For a harmonic force $f(t) = F(\omega)e^{j\omega t}$, the response of the system is another harmonic function $x(t) = X(\omega)e^{j\omega t}$ where $X(\omega)$ is a complex amplitude. Substituting into the equations of motion for viscous damping models, we can derive the ratio of the displacement response and the force input as:

$$H(\omega) = \frac{X(\omega)}{F(\omega)} = \frac{1}{k - \omega^2 m + j\omega c} \tag{2}$$

Briefly, the frequency response function is a transfer function that describes dynamic structural physical behavior (displacement, velocity or acceleration) as a ratio, in the frequency domain, to the input force. FRF depends on the intrinsic structural characteristics

---

operational environment. The procedure is usually called *Operational Modal Analysis*(Avitabile [2017], Covioli [2021]).
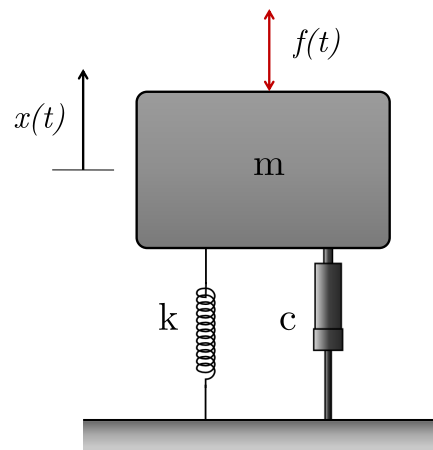
Figure 2: Single degree of freedom (SDOF) system

of mass, stiffness, damping and also the boundary condition (supports and bonds). Figure 3 shows the general idea of the FRF.
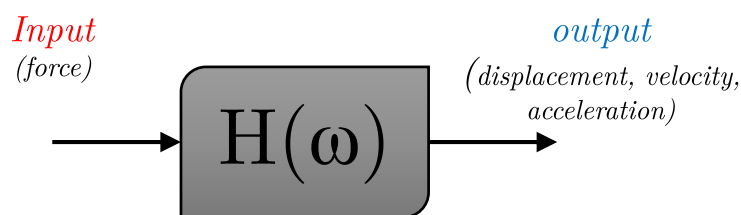
Figure 3: Frequency response function

The ratio written in therms of the dynamic displacement shown in Equation 2, often denoted as $\alpha(\omega)$, is defined as the *compliance* FRF of the system. Although defined as the ratio of the force and response, the FRF is independent of them. When damping is zero, the complex FRF function is relegated to a real function. The FRF is the main function on which modal analysis will depend. Although in theory the FRF is dictated only by the system, in reality the accuracy of measured FRF data is critical to the success of modal analysis.

The system FRF can also be represented in terms of the velocity or the acceleration of the mass. By replacing the displacement response $X(\omega)$ with velocity $\dot{X}(\omega)$ and acceleration $\ddot{X}(\omega)$, types of FRFs can be defined, usually called, respectivelly, as *mobility* ($Y(\omega)$) and *accelerance* $A(\omega)$) functions. The three functions may be written as

$$\alpha(\omega) = \frac{X(\omega)}{F(\omega)} = \frac{1}{k - \omega^2 m + j\omega c}, \tag{3}$$

$$Y(\omega) = \frac{\dot{X}(\omega)}{F(\omega)} = \frac{j\omega}{k - \omega^2 m + j\omega c}, \tag{4}$$

and

$$A(\omega) = \frac{\ddot{X}(\omega)}{F(\omega)} = \frac{-\omega^2}{k - \omega^2 m + j\omega c}. \tag{5}$$

It is clear that the three types of FRFs, $\alpha(\omega)$, $Y(\omega)$, and $A(\omega)$, are easily interchangeable. All three are complex functions of frequency. Their amplitudes follow:

$$|A(\omega)| = \omega|Y(\omega)| = \omega^2|\alpha(\omega)| \tag{6}$$

The phase difference among them remains constant at any frequency:

$$\theta_{A(\omega)} = \theta_{Y(\omega)} + \frac{\pi}{2} = \theta_{\alpha(\omega)} + \pi \tag{7}$$

The reciprocals of the three FRFs of an SDOF system also bear useful physical significance and are sometimes used in modal analysis. They are respectively known as Dynamic Stiffness (Eq. 8), Mechanical Impedance (Eq. 9) and Dynamic Mass (Eq. 10).

$$\frac{1}{\alpha(\omega)} = \frac{force}{displacement} \tag{8}$$

$$\frac{1}{Y(\omega)} = \frac{force}{velocity} \tag{9}$$

$$\frac{1}{A(\omega)} = \frac{force}{acceleration} \tag{10}$$

There are benefits to displaying the FRF in these different formats where some physical conclusion can be made, depending on the specific application. All of these responses are mathematically related (as seen in Equations 3 to 5) so by calculating one FRF, any of the other representations can be determined. In this sense, Figure 4 illustrate the different types of direct and inverse input/output FRF.
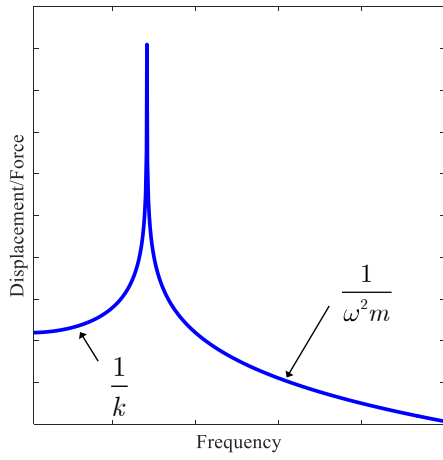
(a) Compliance
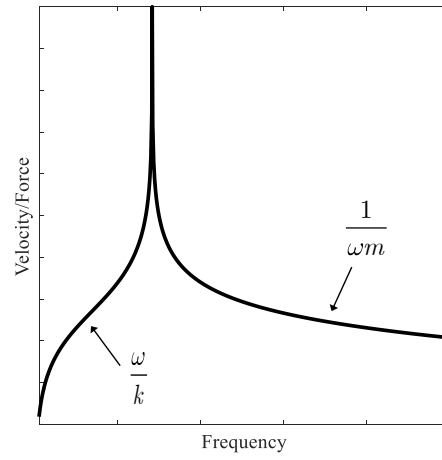
(b) Mobility
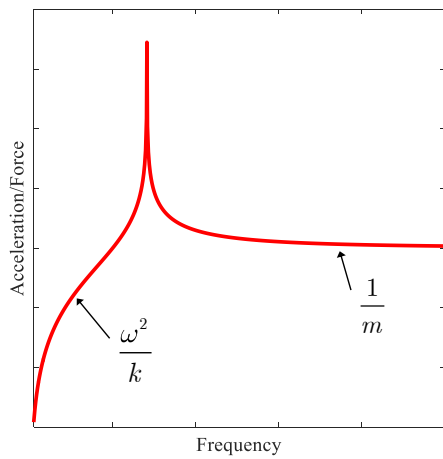
(c) Accelerance
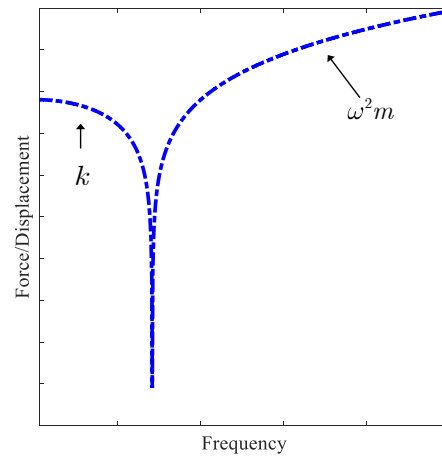
(d) Dynamic Stiffness
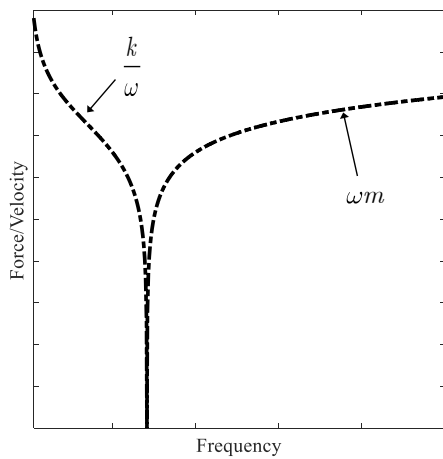
(e) Mechanical Impedance
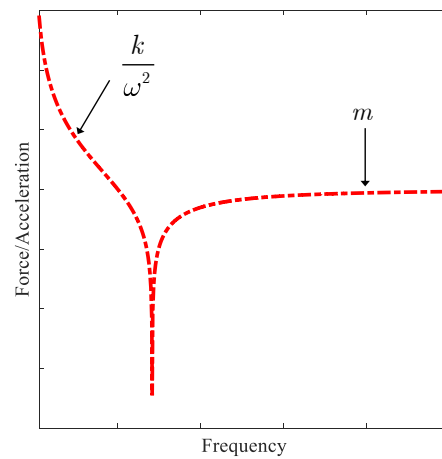
(f) Dynamic Mass

Figure 4: The direct and inverse frequency response functions.

Graphical display of an FRF plays a vital role in modal analysis. A different graphical display highlights different information an FRF carries. Since experimental modal analysis often relies on curve fitting of FRF data, sound understanding of FRFs in graphical forms is imperative. In the following, we will show that even for the FRF of an SDoF system which seems to be analytically simple and trivial, much insight about the function can be gained by studying it in various forms of graphical display. We will use first the receptance FRF to begin our exploration of the graphical display. Since the receptance FRF is a complex function of frequency, it is impossible to fully display it using merely one two-dimensional plot. A three-dimensional plot of a receptance FRF of a typical SDoF system is shown in Figure 5.
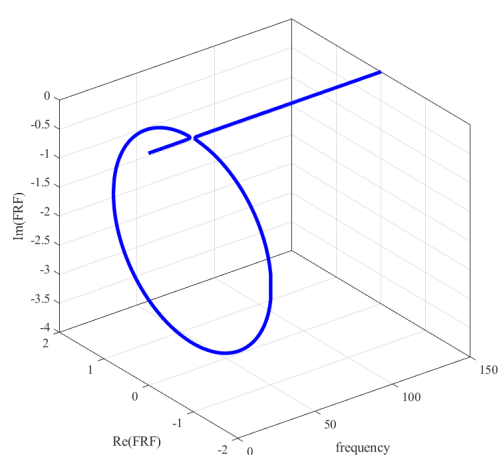
(a) A three-dimensional plot of an FRF
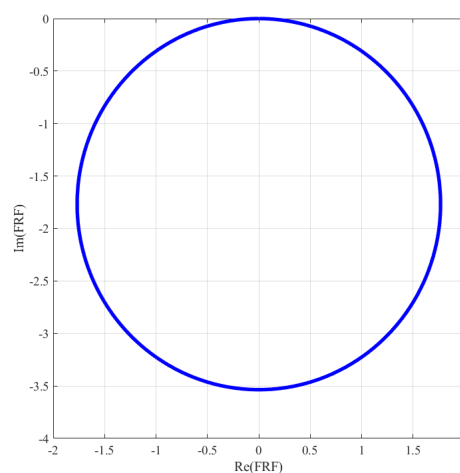
(b) Nyquist plot of an FRF
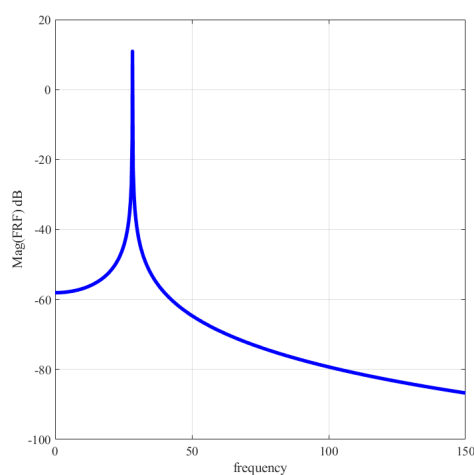
(c) Magnitude of an FRF

Figure 5: An overview of FRF for SDOF system.

3.2   Frequency Response Function - MDOF systems

Next, a multiple degree of freedom system (MDOF) is considered. Similarly to the SDOF case, the equations of motion for a MDOF system can be derived assuming the following simplifications (Avitabile [2017]):

- the mass and or inertia properties of the system are modeled as lumped quantities

- the spring forces (or moments) are proportional to displacement (angular displacement).

- the damping forces (or moments) are proportional to linear velocity (or angular velocity).

Additionally, the derivation is restricted to the case where the physical properties are time invariant. Under these assumptions, the equations of motion for a N degree of freedom linear, time-invariant system can be written in matrix form as

$$[M]\{\ddot{x}(t)\} + [C]\{\dot{x}(t)\} + [K]\{x(t)\} = \{F(t)\}, \tag{11}$$

where $[M]$ is the mass matrix $(N \times N)$, $[C]$ is the damping matrix $(N \times N)$, $[K]$ is the stiffness matrix $(N \times N)$, $F(t)$ is the forcing vector $(N \times 1)$ and $x(t)$ is the vector $(Nx1)$ of displacements. These equations constitute the "spatial model", in the form of system of ODEs, which are usually coupled in the physical coordinates $x(t)$.

It is important to notice that, in structural dynamic problems, matrices $[M]$ and $[K]$ are quite often obtained from a finite element model. Matrix $[C]$ is usually introduced as a representation of localized damping devices in mechanical systems, as, for example, vehicle suspension systems, physical joints in multibody systems and other very specific mechanical problems. However, the damping matrix $[C]$ is seldom available for general, distributed parameter structural problems. The damping characteristics of such systems are introduced in the models from previous heuristic knowledge or, more frequently, from vibration experiments such as modal testing.

The Frequency Response Functions associated to Equation 11 may be also written in matrix form as $[H(\omega)]$, an $(N \times N)$ complex symmetryc matrix given by:

$$[H(\omega)] = \left(-\omega^2 [M] + j\omega [C] + [K]\right)^{-1}, \tag{12}$$

where each individual term in matrix $[H(\omega)]$, denoted by $H_{rs}(\omega)$, represents the FRF related to the response at coordinate r due to an excitation acting on coordinate s of the structural system.

The representation of the system FRFs in Equation 12, despite its simplicity, may be computationally prohibitive for real-life, large structural models, which are easily obtained nowadays with the available FE modeling tools. A much more efficient approach is to introduce a change of coordinates intended to decouple the equations of motion - the *modal analysis* approach, presented in the following paragraphs (the time-dependency of the variables may be occasionally omitted for clarity).

The starting point is the equation for the free vibration of the undamped MDOF system, expressed by

$$[M]\{\ddot{x}\} + [K]\{x\} = \{0\}. \tag{13}$$

Assume that the response $x(t)$ is harmonic and has the general form

$$\{x(t)\} = \{X\} e^{j\omega t}, \tag{14}$$

where $\{X\}$ is an (Nx1) vector of time-independent complex response amplitudes. Substituting (14) into (13), we arrive at the algebraic eigenvalue problem

$$\left([K] - \omega^2 [M]\right) \{X\} = 0. \tag{15}$$

The eigensolution of Eq.(15) yields N pairs of associated eigenvalues and eigenvectors, ω_r^2 and $\{X_r\}$, which are the natural frequencies (squared) and mode shapes of the system. The mathematical process of the eigensolution can be performed by means of direct and indirect techniques. For smaller matrices, the direct techniques decompose the set of equations to get all of the eigenvalues and eigenvectors. However, for complex structures, when the matrices get larger, as is the case for the large finite models, then indirect, iterative numerical techniques are used.

Due to the symmetric nature of the system matrices, the eigenvalues and eigenvectors are real quantities. Each eigenvector $\{X_r\}$ is a vector with N real quantities that are only defined in relative terms, i.e, the direction of the vector is well defined, but not its magnitude. It is useful to represent the eigenvectors by their mass-normalized version $\{\phi_r : //www.overleaf.com/project/629239a6de6fa1d13e3e226bht\}$, imposing the normalization (Eq. 16).

$$\{\phi_r\}^T [M] \{\phi_r\} = 1 \tag{16}$$

The orthogonality properties of the eigenquantities with respect to the system matrices may now be written as shown in Eq. 17.

$$[\Phi]^T [M] [\Phi] = [I] \tag{17}$$

and

$$[\Phi]^T [K] [\Phi] = \lceil \omega_r^2 \rfloor, \tag{18}$$

where $[\Phi]$ is the *modal matrix*, in which each column is a mass-normalized mode shape, and $\lceil \omega_r^2 \rfloor$ is a diagonal matrix of the squared natural frequencies.

The orthogonality properties are useful to uncouple the system equations. Defining a coordinate transformation

$$\{x(t)\} = [\Phi] \{q(t)\}, \tag{19}$$

and substituting into Eq. (13) leads to

$$\{\ddot{q}(t)\} + \lceil \omega_r^2 \rfloor \{q(t)\} = \{0\}. \tag{20}$$

Hence, the coordinate transformation leads to a set of uncoupled equations, corresponding to N independent undamped SDOF systems that can be solved separately.

In general, the damping matrix is not diagonalized by the coordinate transformation and the equations of motion for the damped system will remain coupled. However, under the useful assumption that the damping is *proportional*, i.e., the damping matrix $[C]$ can be written as a linear combination of $[M]$ and $[K]$, the damping matrix can also be diagonalized as

$$[\Phi]^T [C] [\Phi] = \lceil 2\zeta_r \omega_r \rfloor, \tag{21}$$

where ζ_r is the modal damping ratio for mode r. Next, take Eq. (19) into Eq. (11) and pre-multiply by $[\Phi]^T$, resulting in

$$\{\ddot{q}(t)\} + \lceil 2\zeta_r \omega_r \rfloor \{\dot{q}(t)\} + \lceil \omega_r^2 \rfloor \{q(t)\} = [\Phi]^T \{F(t)\} . \tag{22}$$

Equation (22) is the basis for a much more efficient forced response analysis of the original coupled damped MDOF system, now represented by N independent damped SDOF equations in the so-called modal coordinates $\{q(t)\}$. Also, it will lead to a more useful formulation of the system FRFs, more suitable for the development of parameter identification algorithms. After the necessary mathematical manipulation steps, the MDOF system FRFs can now be written as

$$H_{rs}(\omega) = \sum_{k=1}^{N} \frac{A_{rs(k)}}{\omega_k^2 - \omega^2 + 2j\zeta_k \omega \omega_k}, \tag{23}$$

with

$$A_{rs(k)} = \{\phi_k\}_r \{\phi_k\}_s , \tag{24}$$

where $\{\phi_k\}_r$ is the real entry at coordinate r of mode shape k.

Figure 6 depicts a typical FRF of a MDOF system, illustrating the contributions of each single mode, combining the terms in the summation shown in Equation (23).
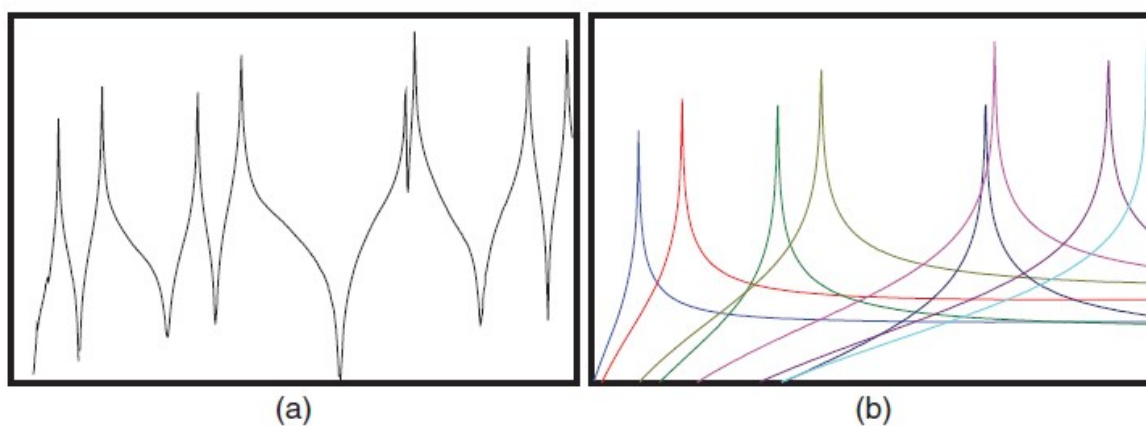
Figure 6: Typical FRF for a MDOF system : (a) "summed" FRF ; (b) individual mode contributions (Avitabile [2017]).

Complementary, Figure 7 shows the FRF plots for a multiple degree of freedom (MDOF) system. In this specific case, the numbers of modes in the shown frequency range are $N = 3$.
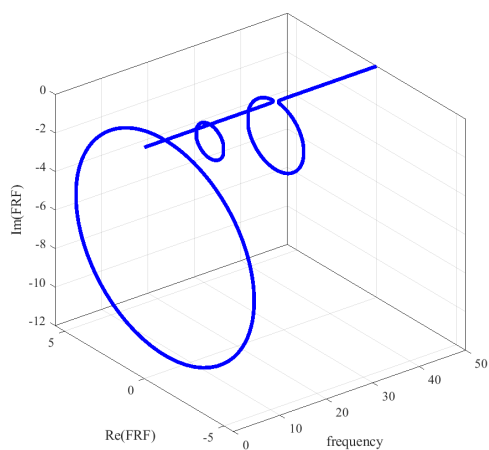
(a) A three-dimensional plot of an FRF
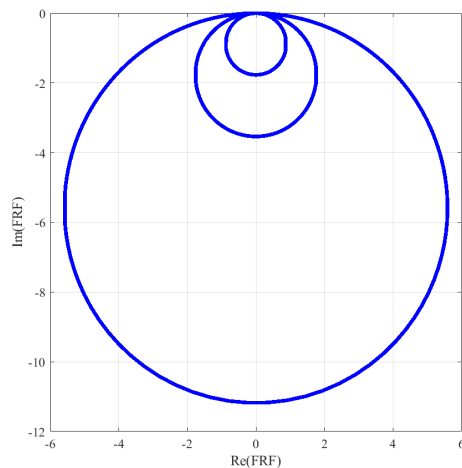
(b) Nyquist plot of an FRF
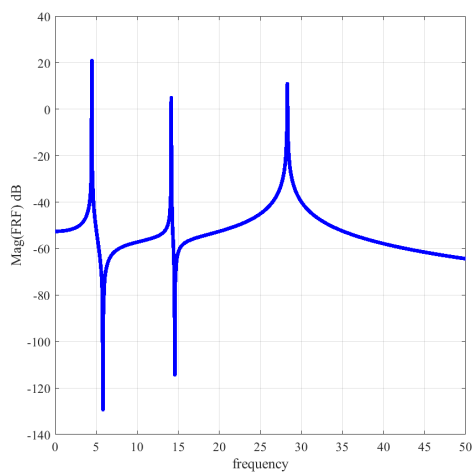
(c) Magnitude of an FRF

Figure 7: An overview of FRF for MDOF system.

Such a three-dimensional plot is complete because it shows the true face of an FRF. It is, however, difficult to be used especially for modal analysis where characteristics such as resonance need to be visually available. From Figure 5, we can see that the 3-D plot, when projected to the frequency-real plane, becomes the real part of the FRF. Likewise, its projection to the frequency-imaginary plane gives the imaginary part of the FRF and that to the real-imaginary plane is the Nyquist plot. These plots (and their variations) highlight different aspects of the FRF. The need to investigate an FRF from a 2-D graphical manifestation gives rise to a number of different graphical presentations of it.

The wide range of modal parameter estimation strategies and algorithms developed over the years rely on some mathematical representation of the system FRFs similar to the one presented in Eq. (23). Slightly different derivations are needed, for instance, when considering more general damping models, which may result in complex mode shapes. Depending on the complexity of the modal test performed, the amount and quality of the acquired data, and the level of details of the desired modal model, one can choose identification procedures ranging from simple curve fitting for individual peaks in Fig. (6), circle fitting of Nyquist plots, line fitting of a broader frequency band including several modes or, for more complex demands, detailed algorithms that might include several FRFs for different excitation points and different measurement locations. The next section discusses some of the issues involved in the experimental identification of FRFs for modal parameter extraction.

3.3 Comments on the Experimental Identification of FRFs

To obtain experimental FRFs with good quality for a successful modal parameter estimation, several aspects of the modal testing procedure have to be carefully taken into account (Akers et al. [2020]). First, a thorough test planning must be conducted, including topics such as test objectives, selection of frequency range of interest, selection of measurement and excitation coordinates, selection of excitation devices and methods (impact or shaker, for example), selection of measurement transducers, definition of support points and apparatus, among others. It is very useful, whenever possible, to create a simplified theoretical/numerical model for preliminary simulations that can greatly facilitate the test planning process.

During the execution of the modal testing tasks, data acquisition and signal processing issues are of paramount importance. The setup of all electronic devices and connections that constitute the excitation and response measurement chains must be carefully and regularly inspected, to ensure that no extraneous influences are contaminating the acquired data. A good understanding of the basics of signal processing theory is also necessary. Issues such as sampling rates, windowing, filtering, averaging, coherence, etc. must be thoroughly considered. This knowledge is essential for the acquisition of data that is potentially free of the effects of spurious noise and data acquisition undesired phenomena, such as leakage and aliasing. For more detailed information on modal test planning and excecution, see Ewins [2000], Fu and He [2001], Peeters et al. [2004] and Avitabile [2017].

Once a set of good quality FRFs is available, it is time for the parameter estimation step. In theory, the FRFs of a MDOF system constitute a square (NxN) matrix of functions. In practice, however, only a limited number of functions is available. Therefore, it

is important to make sure that the correct estimation technique is chosen for the case at hand.

Figure (8) illustrates an schematic classification of parameter estimation methods based on the fitting of the available FRFs. A local approach may be sufficient for smaller problems, using one FRF at a time to estimate natural frequencies, damping ratios and the amplitude of the mode shape for the corresponding coordinate. It is important to notice that the local method does not rely on a single FRF, since it would be impossible to estimate mode shapes. The local stands for analyzing one FRF at a time and combining the results in the end of the process. The global approach includes a set of FRFs obtained at different locations from a single excitation point. In this case, a "column" of the FRF matrix is fed to the estimation algorithm, resulting in the simultaneous estimation of the natural frequencies, damping factors and mode shapes. The polyreference approach is and extension of the global approach. Now, the algorithm can deal with data originated from two or more excitation points. Complex and sophisticated tests may be conducted with simultaneous multi excitation. It is more common, however, to obtain different columns of the FRF matrix in distinct test runs. Care must be taken to make sure that the same test conditions are reproduced for all the data acquisition runs.

$$[H(\omega)]=$$

(a)   **(b)**   **(c)**
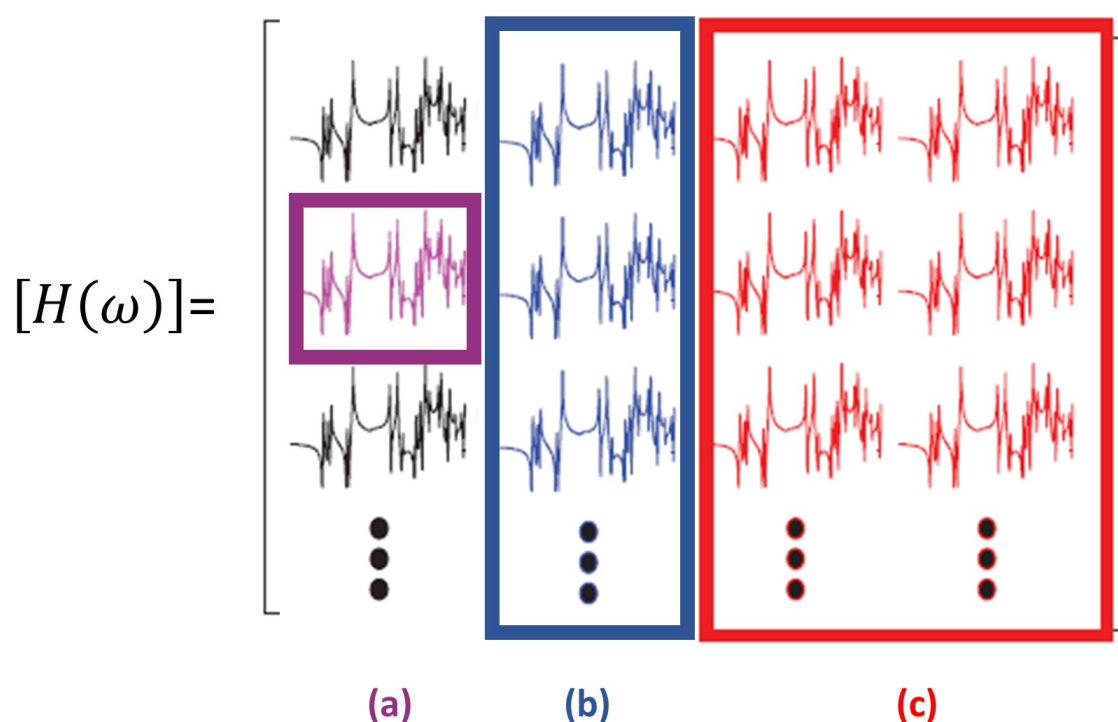
Figure 8: Classification of modal parameter extraction aproaches: (a) Local curvefitting ; (b) Global curvefitting; (c) Polyreference curvefitting (adapted from Avitabile [2017]).

Another important aspect to be considered during the parameter estimation step is related to modal density - the number of peaks in a given frequency band - and damping levels. Modes that are too close to each other may pose difficulties to less sophisticated estimation methods. When damping levels are high, it is sometimes impossible

to distinguish two modes of close natural frequencies. Figure (9) schematically illustrates this very relevant point. The lower frequency mode in (a) is clearly isolated and a SDOF based method may be successful in estimating the modal parameters with good quality. However, the two peaks marked in (b) will certainly demand a more detailed, MDOF estimation algorithm. Two of the most popular methods found in the literature and implemented in commercial Modal Analysis software are the Least Square Complex Exponential method and the PolyMAX method (Avitabile [2017]).

(a)   **(b)**
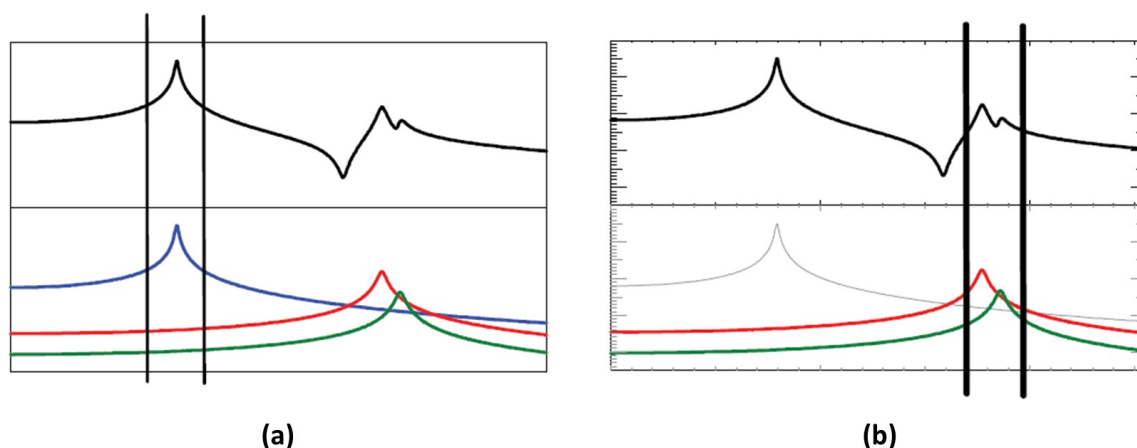
Figure 9: Effect of mode spacing in estimation strategy : (a) SDOF curvefitting ; (b) MDOF curvefitting; (adapted from Avitabile [2017]).

The topics discussed in the present section are obviously only a glimpse on the subject, intended to motivate the reader to a more detailed look at the comprehensive literature referenced at the end of the chapter. As a final comment about practical considerations of a modal testing, it is important to register that the execution of an experimental modal analysis campaign appears to be a challenge only suited for seasoned experimentalist with hundreds of lab hours in his/her résumé. This is certainly true for large complex structures, usually demanding a multidisciplinary team of professionals to get the job done within the required time and quality constraints (Carneiro et al. [1992]. However, a dedicated novice researcher can obtain very rewarding results with smaller problems, more typical in academic research.

4   Inverse Modal Problems

Nowadays, many researches have been focused on the development of several metrics based on the characteristics of static and dynamic (mainly) responses of mechanical systems. An inverse problem is a general strategy or methodology that is used to convert observed measurements into information about a physical object or system in which we are interested (Jorge et al. [2022]). There are several advantages to using modal data in inverse problems, since modal data usually reflect both global and local structural conditions with relevance (Gomes et al. [2018a], Magacho et al. [2021]).

An inverse problem based on modal parameters can be formulated basically using i) natural frequency, ii) damping factor or loss factor and iii) mode shapes. Additional

formulations based on FRF and derived from direct responses such as modal curvature, energy and others are also widely used today. Modal parameters such as natural frequency are values that have a significant amount and quality of global structural information whereas mode shapes are more sensitive to local disturbances. The correct combination of these responses, depending on the formulation and application in question, can lead to reliable and accurate results in the identification of parameters.

Figure 10 briefly shows the general process of an inverse problem. Usually the experimental tests are carried out in order to extract the modal properties (natural frequencies, damping factors and mode shapes). These properties will feed the formulation of an inverse problem that is usually accomplished by minimizing an objective function. This objective function can be the norm (or error) between results measured and calculated by the optimizer. The importance of using optimization techniques, which play a fundamental role in the problem of parameter identification, is also noteworthy. Table 1 shows a list of the main types of objective functions used in most of the research work found in the literature.
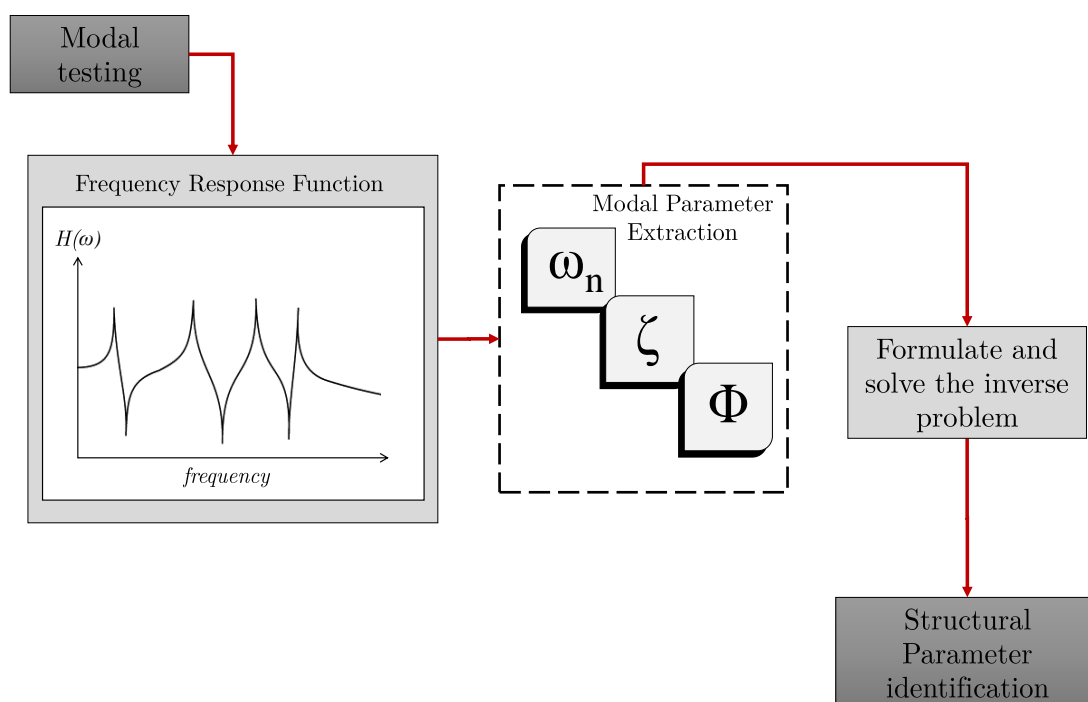
Figure 10: A general flowchart of modal based inverse problems.

In general, the most relevant, discussed applications and source of attention for several engineers and researchers are: damage detection and identification, sensor placement optimization (Gomes et al. [2019a], Gomes et al. [2020]), property identification, structural optimization (by maximizing the fundamental natural frequency) and identification of vibration forces. In this section, a brief discussion of the main contributions to each theme will be made, as well as the advantages and peculiarities of each formulation.

Table 1: Systematic review of the parameters used in optimization in damage detection.

Author	Algorithm	Objective Function
Friswell et al. [1998]	GA	$J = \sum_{j=1}^{r} \left(\frac{\delta\omega_{mj} - \delta\omega_{aj}}{\delta\omega_{mj}} \right)^2 + \sum_{j=1}^{r} (\phi_{mj} - \phi_{aj})^T (\phi_{mj} - \phi_{aj})$
Yong and Hong [2001]	GA	$J = \sum_{i=1}^{nm} \left\{ \left[\left(\frac{\lambda_i(\alpha) - \lambda_i^0}{\lambda_i^0} \right)^A - \left(\frac{\lambda_i^D - \lambda_i^U}{\lambda_i^U} \right)^E \right]^2 + \left[(\phi_{ij}(\alpha) - \phi_{ij}^0) - (\phi_{ij}^D - \phi_{ij}^U) \right]^2 \right\}$
Jafarkhani and Masri [2011]	CMA	$J(\alpha) = \sum_{i=1}^{n} \left[\left(\frac{f_i^e - f_i^a}{f_i^a} \right)^2 + \left(1 - \frac{|\phi_i^{e^T} \phi_i^a|^2}{(\phi_i^{e^T} \phi_i^e)(\phi_i^{a^T} \phi_i^a)} \right) \right]$
Nanda et al. [2012]	PSO	$J = \sqrt{ \frac{1}{n} \sum_{i=1}^{n} \left(\left(\frac{f_i^m}{f_i^c} \right) - 1 \right)^2 }$
Mohan et al. [2013]	PSO	$J = \frac{1}{N} \sum_{q=1}^{N} \left(\sum_{a=1}^{R} \sum_{p=1}^{M} \frac{|H_{ak}(\omega_p, \alpha) - H_{ak}^m(\omega_p)|}{max(H_{ak}^m(\omega_p))} \right)$
Suveges [2016]	DE	$J = \sum_{i=1}^{n} \left[(\sigma_{ix}^{sim} - \sigma_{ix}^{cal})^2 + (\sigma_{iy}^{sim} - \sigma_{iy}^{cal})^2 \right]$
Cha and Buyukozturk [2015]	GA	$J = \sum_{i=1}^{ms} \sum_{i=1}^{el} |\Phi_i^{dT} K_j \Phi_i^d - \Phi_i^{sT} K_j \Phi_i^s|$
Braun et al. [2015]	ACO	$J = \sum_{j=1}^{N} \sum_{i=1}^{N_t} \left[x_j^{Mod}(K, t_i) - x_j^{Exp}(K, t_i) \right]^2$
Gomes et al. [2016a]	GA	$J = \sqrt{ \frac{1}{N} \sum_{i=1}^{n} \left(1 - \frac{\omega_i^d}{\omega_i(\overrightarrow{X})^c} \right)^2 }$
Gomes et al. [2016b]	GA	$J = \sqrt{ \frac{1}{N} \sum_{i=1}^{n} \left(1 - \frac{\omega_i^{real}}{\omega_i(\overrightarrow{X})^{model}} \right)^2 } + \sum_{i=1}^{n} \left(\ddot{x}^{real} - \ddot{x}^{model} \right)^2$
Vo-Duy et al. [2016]	DE	$J = \sum_{i=1}^{nm} \frac{||\Phi_i^d - \Phi_i^d(x)||}{||\Phi_i^d||}$

4.1   Structural Health Monitoring Problems

The damage can be seen as a change in the geometric or physical properties of a material. A structure, in the presence of a damage, will have a mechanical behavior (parameter) that will not resemble an intact structure. These parameters are directly affected by the variation in the physical (modal) properties of the structure (mass, rigidity and damping). When all is said in done, damage may cause local changes in the mass and/or stiffness of the structure and, as an outcome, alter its attributes.

The structural monitoring by itself does not find the solution to structural problems, however, according to Worden et al. [2009], if it is used in conjunction with the development of new computational technologies and mathematical tools, it opens the possibility of solving optimization problems associated with Structural Health Monitoring (SHM) and finding the best solution.

According to Sohn et al. [2003], many damage detection methods reviewed attempt to identify damage by solving an inverse problem, which often requires the construction of analytical models. This reliance on an earlier expository model, which is regularly unverifiable and not completely approved with test information, makes these methodologies less alluring for specific applications.

There are various damage indicators (Gomes et al. [2018b]). Several are constructed from vibration data, either in the time and/or frequency domain. These indicators have proved to be efficient, but there are still areas that need to be improved. Many indicators present sensitivity problems, need a reference state and do not present the probability of detecting false alarms, reducing their reliability.

According to Gopalakrishnan et al. [2011], the SHM methodology offers a complete platform to predict failures before they occur, for this, it is necessary that some properties of the structure under study are provided and the configuration and detection parameters are established, it should also be indicated if the monitoring will be done in part or continuous time. The SHM methodology, once proven reliable, contributes to the premature detection of damages that have led to the collapse of the structure and is an indicator for the scheduling of preventive actions. The field of application of this technique varies from civil structures of the aeronautics and space industry. Some of the main advantages of the SHM application are: i) to minimize the time of application of maintenance actions and stops due to serious failures, ii) the information collected provides valuable data that can be used to adjust the structure mode of operation or even to optimize the design in future improvements and, iii) allow a reconditioning of maintenance actions based on operating and performance conditions and not in periodic maintenance actions, that (probably) may be unnecessary.

Damage is the main cause of structural failure and occurs frequently in mechanical structures. In recent decades, special attention has been given to methods of detecting damage at an early stage to avoid sudden failure of structural components. More specifically, the monitoring of structural integrity based on the vibration of structures has been the focus of attention of many researchers in order to obtain efficient tools of great importance for the civil, aeronautical and mechanical engineering communities. In addition, many research fronts have been focused on the development of reliable damage indicators that allow, in addition to detecting damage, identifying it in terms of location.

One of the first published studies of relevance was developed by Adams et al. [1978]. The authors have developed a non-destructive method of assessing structural integrity

based on vibration measurements. It was shown that the vibration measurements made in the structure (receptance function) can be used, together with a suitable theoretical model (reference), to indicate the location and magnitude of damage, in a one-dimensional model.

At the same time, Cawley and Adams [1979] realized that a certain state of damage can be generated by a reduction in stiffness or by an increase in structural damping. Changes in stiffness, whether local or distributed, lead to changes in the natural frequencies of the structure in question. Further, since the stress distribution across a vibrating structure is non-uniform and is different for each of the natural frequencies, any localized damage would affect each mode individually and differently, depending on the particular location of the damage. Thus, the measurement of modal data of a structure in two or more stages of its life offers the possibility of locating damages in the structure. If a set of dynamic responses is measured before the structure is in service, measurements of those responses can be used to determine if the structure still meets certain operational criteria.

Several researchers develop strategies based on inverse problems in order to identify damage to mechanical structures. The great advantage of using modal data is due to the ease of experimental tests in loco and the quality of the data. Natural frequency data is poorly sensitive to climate change and external factors. In addition, natural frequencies are able to extract the overall structural situation with quality, being a good metric for detecting (whether or not there is damage). However, damage identification strategies can be improved with the aid of vibration modes. Mode shapes are more sensitive to local structural variations. However, mode shapes are sensitive to external noise. A good damage identification strategy can make use of modal parameters combined with the aid of advanced signal processing and acquisition techniques.

In summary, the development of an efficient structural monitoring technologies aims to provide safety and cost savings. However, the number of practical applications of these technologies is still finite. This is mainly due to the complexity of possible damage scenarios and the high performance requirements of the identification methods employed. The study discussed in this section refers mainly to the relationship between these two aspects, in order to reach a specific level of maturity.

4.2   Sensor Placement Optimization

The basic problem of fault and damage detection is to deduce the existence of damage to a structure from measurements made on distributed sensors. It is known that the quality of these measurements, that is, the quality of the structural monitoring, is largely dependent on where the sensors are located in the structure. Cost and practicality issues prevent the instrumentation of all points of interest in the structure and lead to the selection of a smaller set of measurement sites (Barthorpe and Worden [2009], Gomes and Pereira [2020]). The objective of this study is to indicate the problem of sensor placement optimization (SPO) and to describe some methods that have been investigated for its solution besides proposing an alternative optimization of the optimal positioning of these sensors. The following discussion focuses on sensor optimization techniques based on the dynamic structure.

Traditionally, a successful sensor distribution has been heavily dependent on the knowledge and experience of those conducting experimental tests. Practical methods, for example, by choosing sites close to anti-knots of low-frequency vibration modes, are combined

to create coherent sensor distributions (Barthorpe and Worden [2009]). However, for a lot of the times, a single mode of vibration does not have enough information on a damaged structural state, being necessary the use of a set of modes. Therefore, a distribution in the anti-nodes would not be feasible for a predefined number of sensors.

According to the theory discussed in (Barthorpe and Worden [2009]), the objective of sensor positioning can be stated as the need to select a subset of measurement locations from a large finite set of locations, so as to represent the system with the highest possible accuracy using a limited number of degrees of freedom accessible. This can be seen as a three-step decision process:

- Number of sensors - How many sensors need to be placed in the structure to allow a satisfactory dynamic test?

- Sensor positioning optimization - Where should these sensors be located to obtain more accurate data?

- Evaluation - How can the performance of different sensor configurations be measured?

In general, on the first aspect, the minimum requirement for the system to be observable is that the number of sensors required can not be less than the number of modes to be identified, with an upper limit usually imposed by the cost or availability of the equipment. The second aspect is the area that has attracted the most interest. For the limited number of available sensors, the problem is the development of a suitable sensor positioning performance measurement to be optimized and the selection of an appropriate method. Some approaches require a single calculation to be performed, some are iterative, and many others take the form of an objective function to which an optimization technique must be applied. The third and last aspect includes several possibilities for evaluating the performance of chosen sensor sets. In this work, preferably the positioning item will be approached, where a pre-defined number of sensors will be fixed.

In addition, the sensor placement issue attracts a lot of attention from academia and industry, especially due to the growing number of large instrumented monitoring structures over the last decade. This is due in part to economic reasons, to the high cost of data acquisition systems (sensors and their supporting instruments), partly because of the limitations of structural accessibility (Rao et al. [2014]).

The set of degrees of freedom measured in most large structures, usually the shifts of the low frequency modes, provide enough information to describe the dynamic behavior of a structural system with sufficient accuracy to allow its structural state and/or modifications determined in an effective manner. Thus, the fundamental problem is how many and which degrees of freedom must be considered in the process of structural identification. To solve this problem, economic factors that require a limited number of sensors to be placed in accessible locations in the actual structure (Rao and Anandakumar [2007]) should be duly taken into account. Still, according to Rao and Anandakumar [2007], it is crucial that the sensors are located in the most advantageous locations. Otherwise incomplete modal properties will be measured and an accurate assessment of structural health monitoring will be impossible.

Figure 11 shows a general flowchart of a SPO process using an inverse problem. The flowchart starts with numerical structural modeling (discretizing the largest amount of

DOF possible). After obtaining the model, a given objective function J is chosen in order to be minimized/maximized. The optimization of this function can be performed using different algorithms (gradient-based or gradient-free) depending on the complexity of the SPO problem. If a given stop criterion is satisfied, the optimal layout of the N predefined sensors is obtained.
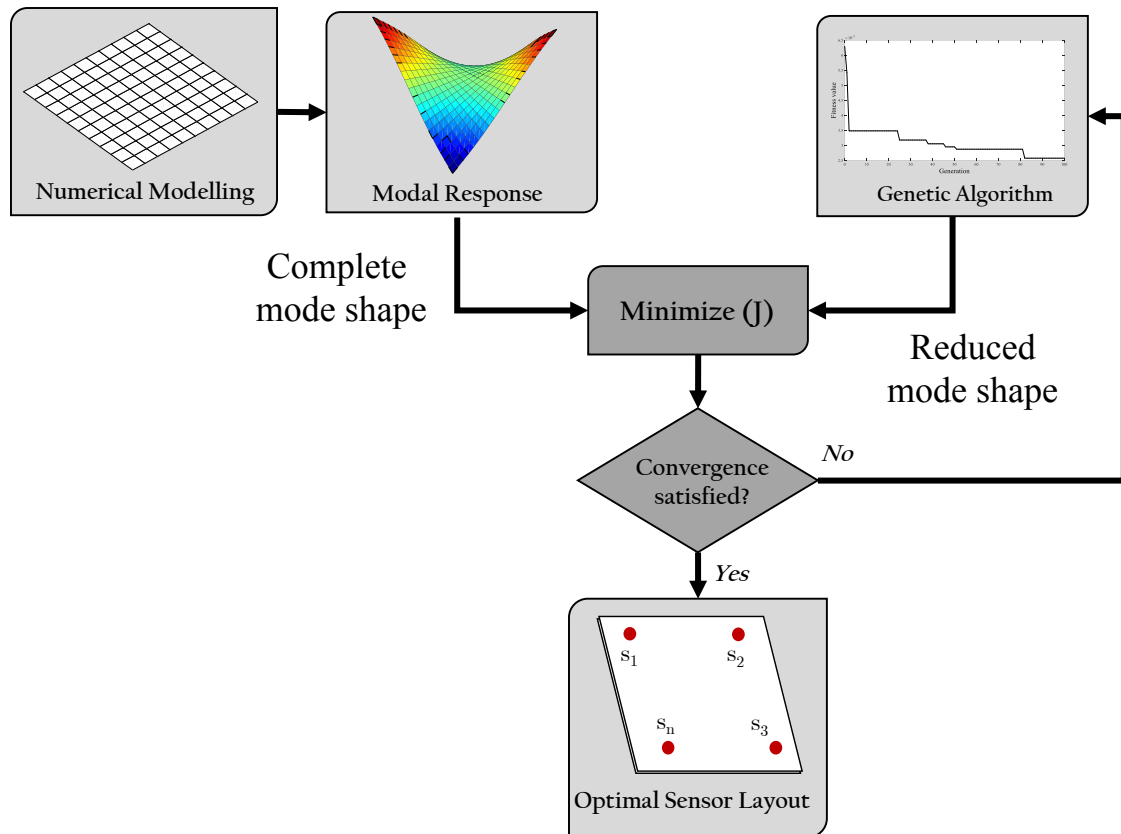
Figure 11: General methodology for SPO based mode shape.

4.3 Identification of Material Properties

Modal responses can also be part of formulating inverse problems in terms of identifying properties. This theme has great relevance because it allows non-destructive (vibration) tests to be conducted in place of traditional destructive tests (such as tensile, compression, bending tests, etc.). In addition to the identification of unknown properties, this formulation strategy can also be used to update and adjust experimental-numerical models.

Modal testing has the potential to provide the basis for rapid, inexpensive characterization of both elastic and viscoelastic properties of composites for design and manufacturing. Knowledge of elastic properties is, of course, required in design, but measurement of elastic properties during manufacturing offers the potential for improvements in quality control as well (Gibson [2000]).

The strategy of identifying mechanical properties by means of an inverse modal problem has its importance in isotropic materials. However, its great justification occurs in

composite materials. The behavior of composite structural systems in which parameters are variable or not perfectly known is still a challenging problem. The most available models to investigate the behavior of composite structures assume an effective homogenized set of material properties. These models fail to capture the true behavior of the wide variety of such structures exhibit significant inherent uncertainty in material parameters (Sepahvand and Marburg [2014]).

In addition, according to Gibson [2000], not only does the material property characterization add to the cost of manufacturing, but the complexity of the test procedures and the test equipment is such that small and medium-sized composite fabrication shops generally have to rely on outside testing laboratories to do the characterization. Such a separation of the manufacturing and testing functions precludes an on-line evaluation of the properties, which is needed for optimization and control of the manufacturing process.Ideally, the composite characterization system should be fast, inexpensive and capable of providing feedback.

5 The Use of Modal Data in Inverse Problems

The central thought for vibration-based damage detection is that damage causes a modification in the mass, stiffness and damping structural matrix. These modifications will also cause recognizable changes in modal properties (natural frequencies, modal damping, and mode shapes). In this section, some classical and modern methodologies based on vibration signals will be described and discussed. Modal experimental analysis is an efficient tool to detect and identify damages, especially delamination in composite materials.

5.1 Natural Frequency-Based Methods

The presence of damage or structural deterioration causes changes in the natural frequencies in the structure. The most useful damage-finding methods (based on dynamic tests) are probably the ones that use changes in resonance frequencies (natural frequencies), because they are easy to obtain and are reliable metrics. Lifshitz and Rotem [1969] present what may have been the first article to propose damage detection through vibration measurements. They analyze the change in the dynamic modules, which may be related to the frequency change, indicating structural damage.

The effect of delamination on the natural frequencies of laminated composite beams has been investigated by Valdes and Soutis [1999]. The use of vibration at higher frequencies allows the identification of delamination occurrence. Additional setups can be also used in addition with modal frequency data. Ling et al. [2004] developed fiber-optic sensors to measure natural frequency in composite structures. The advantage of using fiber-optics is that they can be incorporated in laminated composites structures allowing real-time damage detection. LeBlanc et al. [1992] described how a network of embedded optical fibers could be used to detect and monitor damage (in particular, impact damage) within composites.

Also, as stated by Negru et al. [2015], transversal cracks in composite structures affect their stiffness as well as the natural frequency values. For a given crack, irrespective of its depth, the frequency drop ratio of any two transverse modes is similar (de Assis and Gomes [2021]). This permitted separating the effect of damage location from that of its

severity and to define a Damage Location Indicator as a function of the square of the normalized mode shape curvatures, according to the authors.

Natural frequencies are good damage metrics, not only for delamination, but also for impact analysis. Velmurugan and Balaganesan [2011] studied the natural frequency and damping factors before and after impact as well the effect of damage on natural frequency and damping factors. It was shown that natural frequencies increase with the impact velocity.

5.2   Damping-Based Methods

According to Cao et al. [2017], typical dynamic properties refer to modal parameters: natural frequencies, mode shapes, and damping (or loss factor). Among these parameters, natural frequencies and mode shapes have been investigated extensively for their use in inverse problems such as damage characterization. Equally important, the use of damping as a dynamic property to represent structural damage has not been comprehensively elucidated, primarily due to the complexities of damping measurement and analysis. Furthermore, with advances in instrumentation and analysis tools, the use of damping as index (or objective function) becoming a focus of increasing attention in the modal-based inverse problems (especially for SHM community).

The main advantage of damping property is that damping has greater sensitivity for characterizing damage than natural frequencies and mode shapes in various applications, but damping-based damage identification is still a research direction "in progress" and is not yet well resolved (Cao et al. [2017]). According to Curadelli et al. [2008], damping is a promising damage indicator in structural health monitoring because it has more sensibility to damage than the natural frequency

Structural damping can be identified in both the time domain and frequency domain responses. The main methodologies to damping identification are: *i)* half-power (-3dB) method, *ii)* SDOF time response adjustment, *iii)* Circle fit in Nyquist plot, *iv)* logarithmic decrement method, *v)* Ibrahim time domain method, *vi)* wavelet transform, *vii)* Hilbert transform and many others.

From previous discussion, it can be noted that, whereas damping could be assumed negligible in free vibration analysis, it plays a crucial importance in forced response and must be quantified. In general, the overall damping of a system (SDOF or MDOF) is usually the most difficult parameter to obtain (Adams and Askenazi [1999]). Table 2 shows some selected representative damping ratios.

Among all damping models, viscous damping is most widely used because of its convenience in structural design. In fact, the viscous damping hypothesis has a serious drawback. The energy loss per cycle depends on the frequency; however, this result is inconsistent with many experimental results (Chopra, 2001). Another damping assumption, hysteretic damping, can more accurately describe the energy dissipation. Although it is difficult to translate the hysteretic damping mechanism into the time domain, it is promising to use the hysteretic damping assumption in the frequency domain (Pu et al. [2019]).

Apart from the shifts of the natural frequencies a change takes place also for the damping of the structure. Modal damping ratios would include the hysteretic damping resulting from non lnear phenomena and yielding of the structural members. Hence, damping ratios are very sensitive indices of the extent of inelastic deformation that takes place during

Table 2: Damping constants values for different systems (Adams and Askenazi [1999]).

System	Damping Ratio (ζ)
Metals (in elastic range)	<0.01
Continuous metal structures	0.02 to 0.04
Metal Structure with joints	0.03 to 0.07
Aluminum/Steel transmissions lines	~ 0.0004
Small diameter piping systems	0.01 to 0.02
Large diameter piping systems	0.02 to 0.03
Auto shock absorbers	~ 0.30
Rubber	~ 0.05
Large buildings during earthquakes	0.01 to 0.05
Prestressed concrete structures	0.02 to 0.05
Reinforced Concrete Structures	0.04 to 0.07

physical structural disturbance (Kouris et al. [2017]).Equally important, according to Sehgal and Kumar [2021], in many fields, damping identification provides more sensitive approach to characterize structural damage compared to natural frequencies and modal assurance criterion (MAC) values, but damping-based identification of structural damage needs to be explored further.

In the SHM field, according to Souza et al. [2019], several damage identification approaches are based on computational models, and their diagnostics depend on the set of modelling hypotheses adopted when building the model itself. Among these hypotheses, the choice of appropriate damping models seems to be one of the key issues. Normally, damping models may not provide an increase of knowledge of some unknown parameters when damping rates are lower than 1%. Equally important, real modal properties or real FRF data without considering damping will cause failure to detect the real damages. It is well known that damping mechanism in a real structure is very complicated, and it remains the least-known aspect compared with stiffness and mass. However, the damping correction in a damage detection or FEM updating study will improve the physical parameter detection accuracy (Pu et al. [2019]).

5.3 Mode Shape and Mode Curvature-Based Methods

In addition to the eigenvalues, the eigenvectors (vibration modes) are fundamental and important data in the evaluation of damages in composite materials. In general, natural frequencies are excellent data to detect damage; that is, whether or not there is structural damage. The evaluation of the modes of vibration is more local; that is, these data allow the detection of the location of damage. Fu et al. [2016] presented a two-step approach based on modal strain energy (MSE) and response sensitivity analysis to identify local plate damage. The local damage was simulated by a reduction in modulus of elasticity. The important point is that a method to weaken the "neighborhood effect" has been proposed to reduce false alarms in the location of damages, as these are one of the major challenges facing the SHM community today. Numerical examples were then conducted to illustrate the efficiency of the proposed method, and thus, damages could be success-

fully identified even under the effect of measurement noise. There are some other new developments on the two-step approach or modal strain energy that can be seen in the studies of Hu et al. [2006], Yang et al. [2016] and Moradipour et al. [2015].

Under this approach, Hu and Wang [2009] and Hu and Wu [2009] showed the detection of surface cracks in a laminate using the modal strain energy method. First, the properties of the material were unknown and were obtained using an inverse method through finite element analysis and experimental modal analysis. Modal displacements were used to calculate the modal deformation energies and a damage index was defined by the authors employing the fractional modal deformation energy of the laminate before and after the damage. Consequently, the damage indices obtained from global and local measurements were able to locate the surface crack in the laminate. In this proposed method, only a few modes of vibration were required, and the authors concluded that the method has a relatively low cost and flexibility in measurement, allowing a non-destructive evaluation and feasibility of real-time detection in laminated structures.

It is also noted that Zhang et al. [2013] presented a new method of detecting damage to plates based on the curvature of the frequency shift surface (FSS). Unlike other vibration properties commonly used as vibration modes that may present low accuracy in practice, the proposed method was used as a way to overcome this problem. In addition, it has been found that local damage will only cause local change in FSS, which can be considered an abnormality, since the curvature of the FSS of an intact plaque is smooth, according to the assumption that intact plaque structures are often homogeneous. Compared with traditional methods, the method proposed by the authors has been shown to be more sensitive and accurate in identifying damage.

Techniques based on vibrations and modal data, although they have existed for some decades, are still widely used to the present day. Manoach et al. [2017] presented a time domain method based on Poincaré maps of the motion of a beam subjected to harmonic loading. The proposed damage index is based on the Poincaré maps of the forced response of the healthy and damaged structures. Numerical and experimental results confirmed that the Poincaré map-based method can be successfully used to detect and locate damage. Yang et al. [2017b] presented a Chebyshev pseudo spectral modal curvature formulation for damage detection in beam-like composite structures. The proposed method was developed to overcome the wrap-around problem of the Fourier spectral modal curvature and the authors stated that the damage detection performance is better than the Fourier. Similar results can also be seen in the research of Yang et al. [2017d], Yang et al. [2017c] and Yang et al. [2017a]. Recently Yang et al. [2018] dealt with the problem of vibration health monitoring based on Poincare map method, which has been numerically and experimentally verified as an effective tool in damage assessment. The authors concluded that the performance of the Poincare maps method depends on the selection of excitation, also stated by Yang et al. [2017e].

Mode shapes and their corresponding spatial derivatives can also be used in the formulation of inverse methods for damage assessment using local/global modal strain energy information. Domingues et al., Domingues [2019] investigated the applicability of this approach in detecting and localizing damage areas in aluminun-aluminum honeycomb sandwich panels used in the constructions of the first Brazilian Geostationary Satellite. The method combines a tuned FE model of the structural element, which provides the stiffnes matrix of the undamaged system, and the experimental natural frequencies and

mode shapes of the potentialy damaged panel, obtained from a modal testing procedure. The method showed very promising results, successfully identifying stifness variations as small as 5% in regions of the order of 10 % the total area of the panel.

A nondestructive identification method for composite beams damage was explored by He et al. [2017]. The authors based their work on the curvature mode difference (CMD) as damage index. By combining experimental modal analysis with finite element simulation, the authors were capable of detecting and identifying damage sites. Similarly, Zhou et al. [2018] studied curvature mode shapes for damage identification in laminated composite plates. Numerical simulations demonstrate that the Continuous Wavelet Transform (CWT) is more sensitive to damage identification. Indeed, finite element simulation can be considered as very powerful tool in SHM systems. Some related works using FEA and SHM damage detection problems can be seen in Alaimo [2018], Chronopoulos [2018], Manoach et al. [2017] and Kefal et al. [2017]

5.4　No-Baseline Methods in Inverse Problems

Many methods used by the SHM community need to know the *a priori* condition or structural response of an intact or healthy structure and then, with continuous monitoring, be able to detect damage from changes in a known signal. This strategy works very well and has been used to this day. On the other hand, new methods that do not need a baseline (no-baseline methods) have been emerging.

Trendafilova et al. [2015] presented a Vibration-Based Structural Health Monitoring (VSHM) technique which is developed and applied for delamination assessment in composite laminate structures. The work suggests that the mutual information is a measure for nonlinear signal cross correlation. The mutual information between two signals measured on a vibrating structure is suggested as a damage metric and its application for the purposes of damage assessment is discussed and compared to the application of the traditional linear signal cross-correlation. The authors modeled the damage as a local stiffness reduction (delamination modeling) and stated that the developed damage metric is efficient for the purposes of delamination diagnosis in a composite laminate beam. The same results for laminated plates can be seen in the work of Garcia et al. [2015]. Going further, in the same context, Garcia and Trendafilova [2014] introduced a methodology for structural vibration analysis and vibration-based monitoring which utilizes a special type of Principal Components Analysis (PCA), known as Singular Spectrum Analysis (SSA). The method was applied in a composite laminate beam based on the decomposition of the frequency domain structural variation response using new variables, the Principal Components (PCs). Experimental results demonstrated that different damage scenarios can be clustered and clearly distinguishable.

Due to the above, other unconventional methods making use of structural dynamics are proposed by some researchers (Bovsunovsky [2018]; Park and Oh [2018]; Tributsch and Adam [2018]; Yin et al. [2017]; Abdeljaber et al. [2017]; Zhang et al. [2017]; Souza and Nóbrega [2017]; de Azevedo et al. [2017]). It is clear that there is a need in the development of effective structural monitoring techniques so that the safety and integrity of the composite structures can be improved. Qiao et al. [2007] evaluated dynamic-based damage detection techniques for laminated composite plates using intelligent piezoelectric materials and modern instrumentation such as the Scanning Laser Vibrometer (SLV). The study, aimed at the detection of delamination, made use of the measurements of the

curvature of the modes of vibration, measured indirectly and directly. The implementation of the algorithm by the authors was successful in the detection of laminated plate delamination, demonstrating that the dynamic-based damage detection approach using curvature is a viable technique for the monitoring of composite structures.

Equally important, Viglietti et al. [2018] presented studies on free vibration analysis of some aircraft composite structures with a tapered shape which were analyzed using a 1-D Carrera Unified Formulation (CUF) model, considering different types of damage. The authors' results demonstrated that their approach provided an accurate solution for the free vibration analyses of complex structures and is able to predict the consequences of a global or local failure of a structural composites component.

5.5   Hybrid Methods

As discussed in the previous paragraphs, natural frequencies are excellent overall damage detection metrics while vibration modes are excellent local metrics for identification. Methods that implement both data can be considered more robust and in some cases, more efficient.

In the face of this reality, in recent years, several research fronts have been joining efforts to design better damage rates based on modes of vibration, since these are more effective in locating structural damage. Citing a similar case, Kim et al. [2003] pointed to a methodology to locate and non-destructively estimate the size of damage in structures, for which only some natural frequencies or some modes of vibration are available. First, the authors devised a method of natural frequency-based damage detection. An algorithm was then developed to locate damages by alterations in natural frequencies, being able to estimate crack size from frequency disturbances. Next, a method of damage detection based on vibration modes is described. Both methods are evaluated for several numerically simulated damage scenarios, for which two natural and mode shapes are generated from finite element models. The results of the analyses indicated that the two methods correctly located the damage, but the methodology based on the modes presented greater precision in the identification of cracks.

A hybrid technique proposed by Lopes et al. [2006] was able to identify delamination in composite plates. The damage was identified using a technique that the measured curvature differences before and after impact damage and also natural frequencies. Based on the hybrid technique presented, it was possible to identify internal damage on a laminated composite plate. Equally important, Gomes et al. [2016b] and Gomes [2016] applied an inverse optimization problem in order to detect and identify circular holes and delamination in CFRP plates. The cost function in the optimization procedure was a built in function of natural frequencies and mode shapes. The authors realized that when greater importance (weight) is given to the portion of the mode of vibration, better results are obtained. In fact, as discussed in this review, modes of vibration are better at identifying damages while natural frequencies are more robust and are excellent detection metrics (whether or not there is damage).

Eraky et al. [2015] proposed a procedure based on comparison of modal strain energy for different structural conditions from a damage index (DI). The DI was constructed based on modal data from natural frequencies and mode shapes, respectively. It was noticed that both the experimental and numerical results showed good agreement in identifying damages in flexural structural elements. In the same way, Owolabi et al. [2003]

measured changes in the first three natural frequencies and corresponding amplitudes of the measured acceleration frequency response function were used as a damage detection scheme in beams. Since the frequencies and amplitudes depend on the crack depth and location, these values can be uniquely determined by an inverse problem, thus identifying the damage location. Related research can be found in the literature about damage detection in composite materials using hybrid methods (Qiao et al. [2007]; Ručevskis et al. [2009]; Fox [1992]; Zhang et al. [2010]; Ashory et al. [2017]).

5.6   Frequency Response Function-Based Methods

In addition, safety and economic aspects are the main motivations for increasing research on the monitoring of structural integrity. Since the damage changes the dynamic characteristics of a structure, its modal properties (natural frequencies, damping and modes of vibration), several techniques based on experimental modal analysis have been developed in recent years. Not only are natural frequencies used as damage metrics, but also the use of frequency response functions (FRF) are widely explored by several researchers. As an example, the FRF curvature method was proposed by Sampaio et al. [1999], based only on measured data without the need for any modal identification. In the authors' work, the method was described theoretically and compared to two, more referenced methods in the literature. The results showed that the FRF curvature method obtained good results in the detection, localization and quantification of damages, although this last item still needs more attention. Its main advantage is its simplicity. From FRF measurements, LeBlanc et al. [1992] evaluated the damage effects on changes in the peaks of FRFs. The authors stated that, based on correct FRF analysis, FRF can accurately determine damage levels from the natural frequency and damping levels.

Many current methods for identifying structural damage, such as Genetic Algorithm (GA) and intelligent methods such as artificial neural networks (ANNs) are often implemented on the basis of some measured data and a large number of simulation data of structural vibration responses (Gomes et al. [2019b],Ribeiro Junior et al. [2020],Junior et al. [2021],Junior et al. [2022]). Therefore, Yan et al. [2006] emphasized that the establishment of a precise and efficient dynamic model for a structure is an important precondition. The authors presented an improved modeling method based on modifying the stiffness matrix of the element at the position of structural damage using a modifying coefficient. The influence of the position of structural damage and boundary conditions on the coefficient of modification for structural damage was verified, and for this the authors made use of FRF and natural frequencies. The stiffness matrix can be used in two different contexts. On the one hand, it is used in Finite Element Modelling (FEM) describing a part of the equation system that has to be solved. On the other hand, it describes material parameters in Hooke's law of elasticity where the relation between mechanical stress and strain is given (also known as stiffness tensor).

6   Final Remarks

In summary, this Chapter is focused on the discussion of the use of inverse problems as main strategy for parameter identification in structural systems. Basically, three direct answers can be used to formulate the inverse problem. Natural frequencies are more robust data that give global structural information and little local sensitivity. On the other

hand, damping and mode shapes are responses with a greater amount of local information, however, more sensitive to noise. The quality of the inverse problem formulation also depends on the quality of the experimental test and also on the identification algorithms (gradient-based or gradient-free). Finally, inverse methods using modal data have a wide range of application and are under continuous development and improvement where new metrics and methodologies are developed.

References

O. Abdeljaber, O. Avci, S. Kiranyaz, M. Gabbouj, and D. J. Inman. Real-time vibration-based structural damage detection using one-dimensional convolutional neural networks. *Journal of Sound and Vibration*, 388:154–170, 2017.

R. Adams, P. Cawley, C. Pye, and B. Stone. A vibration technique for non-destructively assessing the integrity of structures. *Journal of Mechanical Engineering Science*, 20 (2):93–100, 1978.

V. Adams and A. Askenazi. *Building better products with finite element analysis*. Cengage Learning, 1999.

J. C. Akers, K. D. Otten, J. W. Sills, and C. E. Larsen. Modern modal testing: A cautionary tale. In *Proceedings of 37th IMAC, Volume 8, Topics in Modal Analysis & Testing*, pages 1–8. Springer, 2020.

A. Alaimo. Numerical and experimental study of a shm system for a drop-ply delaminated configuration. *Composite Structures*, 184:597–603, 2018.

M.-R. Ashory, A. Ghasemi-Ghalebahman, and M.-J. Kokabi. An efficient modal strain energy-based damage detection for laminated composite plates. *Advanced Composite Materials*, pages 1–16, 2017.

R. C. Aster, B. Borchers, and C. H. Thurber. *Parameter Estimation and Inverse Problems â 2nd ed.* Academic Press, Elsevier, 2012.

P. Avitabile. *Modal testing: a practitioner's guide*. John Wiley & Sons, 2017.

R. J. Barthorpe and K. Worden. Sensor placement optimization. *Encyclopedia of structural health monitoring*, 2009.

A. Bovsunovsky. Estimation of efficiency of vibration damage detection in stepped shaft of steam turbine. *Electric Power Systems Research*, 154:381–390, 2018.

C. E. Braun, L. D. Chiwiacowsky, and A. T. Gomez. Variations of ant colony optimization for the solution of the structural damage identification problem. *Procedia Computer Science*, 51:875–884, 2015.

D. L. Brown and R. J. Allemang. The modern era of experimental modal analysis. *Sound and Vibration*, 41(1):16–33, 2007.

M. Cao, G. Sha, Y. Gao, and W. Ostachowicz. Structural damage identification using damping: a compendium of uses and features. *Smart Materials and Structures*, 26(4): 043001, 2017.

S. H. S. Carneiro, H. S. Teixeira Jr, R. Pirk, and J. Arruda. Modal survey of the Brazilian launch vehicle. In SEM, editor, *Proc. 10th Int. Conference on Modal Analysis*, pages 942–948, 1992.

P. Cawley and R. Adams. The location of defects in structures from measurements of natural frequencies. *The Journal of Strain Analysis for Engineering Design*, 14(2): 49–57, 1979.

Y.-J. Cha and O. Buyukozturk. Structural damage detection using modal strain energy and hybrid multiobjective optimization. *Computer-Aided Civil and Infrastructure Engineering*, 30(5):347–358, 2015.

D. Chronopoulos. Calculation of guided wave interaction with nonlinearities and generation of harmonics in composite structures through a wave finite element method. *Composite Structures*, 186:375–384, 2018.

J. V. Covioli. *Developments in reverse engineering and testing of airborne structures*. PhD thesis, University of Rome La Sapienza, 2021.

R. Curadelli, J. Riera, D. Ambrosini, and M. Amani. Damage detection by means of structural damping identification. *Engineering Structures*, 30(12):3497–3504, 2008.

F. M. de Assis and G. F. Gomes. Crack identification in laminated composites based on modal responses using metaheuristics, artificial neural networks and response surface method: a comparative study. *Archive of Applied Mechanics*, 91(10):4389–4408, 2021.

H. D. de Azevedo, P. H. de Arruda Filho, A. M. Ara, N. Bouchonneau, J. S. Rohatgi, R. M. de Souza, et al. Vibration monitoring, fault detection, and bearings replacement of a real wind turbine. *Journal of the Brazilian Society of Mechanical Sciences and Engineering*, 39(10):3837–3848, 2017.

A. C. Domingues. Identificação de dano em estruturas aeroespaciais leves utilizando o método da energia de deformação modal. Dissertação de mestrado, University of Brasília, 2019.

A. C. Domingues, C. T. M. Anflor, and S. H. S. Carneiro. Damage identification in light panels with orthotropic properties using modal strain energy. In *Proceedings of the COngreso Iberoamericano de Ingeniería Mecánica*.

A. Eraky, A. M. Anwar, A. Saad, and A. Abdo. Damage detection of flexural structural systems using damage index method–experimental approach. *Alexandria Engineering Journal*, 54(3):497–507, 2015.

D. J. Ewins. *Modal testing: theory, practice and application.* 2 edition, 2000.

C. Fox. The location of defects in structures-a comparison of the use of natural frequency and mode shape data. In *10th International Modal Analysis Conference*, volume 1, pages 522–528, 1992.

M. Friswell, J. Penny, and S. Garvey. A combined genetic and eigensensitivity algorithm for the location of damage in structures. *Computers & Structures*, 69(5):547–556, 1998.

Y. Fu, J. Liu, Z. Wei, and Z. Lu. A two-step approach for damage identification in plates. *Journal of Vibration and Control*, 22(13):3018–3031, 2016.

Z.-F. Fu and J. He. *Modal analysis*. Elsevier, 2001.

D. Garcia and I. Trendafilova. A multivariate data analysis approach towards vibration analysis and vibration-based damage assessment:: Application for delamination detection in a composite beam. *Journal of Sound and Vibration*, 333(25):7036–7050, 2014.

D. Garcia, R. Palazzetti, I. Trendafilova, C. Fiorini, and A. Zucchelli. Vibration-based delamination diagnosis and modelling for composite laminate plates. *Composite Structures*, 130:155–162, 2015.

R. F. Gibson. Modal vibration response measurements for characterization of composite materials and structures. *Composites science and technology*, 60(15):2769–2780, 2000.

G. Gomes, S. Cunha Jr., and A. Ancelotti Jr. Structural damage localization in composite plates using finite element method and optimization algorithm. *Australian Journal of Basic and Applied Sciences*, 10(14):124–131, 2016a.

G. Gomes, S. Cunha Jr., A. Ancelotti Jr., and M. Melo. Damage detection in composite materials via optimization techniques based on dynamic parameters changes. *International Journal of Emerging Technology and Advanced Engineering*, 6(5):157–166, 2016b.

G. F. Gomes. *Detecção de Danos Estruturais em Material Compósito Laminado via Método de Otimização e Parâmetros Dinâmicos*. Dissertação de mestrado, UNIVERSIDADE FEDERAL DE ITAJUBÁ, 2016.

G. F. Gomes and J. V. P. Pereira. Sensor placement optimization and damage identification in a fuselage structure using inverse modal problem and firefly algorithm. *Evolutionary Intelligence*, 13(4):571–591, 2020.

G. F. Gomes, F. A. de Almeida, S. S. da Cunha, and A. C. Ancelotti. An estimate of the location of multiple delaminations on aeronautical cfrp plates using modal data inverse problem. *The International Journal of Advanced Manufacturing Technology*, 99(5): 1155–1174, 2018a.

G. F. Gomes, Y. A. D. Mendéz, S. S. da Cunha, and A. C. Ancelotti. A numerical–experimental study for structural damage detection in cfrp plates using remote vibration measurements. *Journal of Civil Structural Health Monitoring*, 8(1):33–47, 2018b.

G. F. Gomes, F. A. de Almeida, P. da Silva Lopes Alexandrino, S. S. da Cunha, B. S. de Sousa, and A. C. Ancelotti. A multiobjective sensor placement optimization for shm systems considering fisher information matrix and mode shape interpolation. *Engineering with Computers*, 35(2):519–535, 2019a.

G. F. Gomes, F. A. de Almeida, D. M. Junqueira, S. S. da Cunha Jr, and A. C. Ancelotti Jr. Optimized damage identification in cfrp plates by reduced mode shapes and ga-ann methods. *Engineering Structures*, 181:111–123, 2019b.

G. F. Gomes, J. A. S. Chaves, and F. A. de Almeida. An inverse damage location problem applied to as-350 rotor blades using bat optimization algorithm and multiaxial vibration data. *Mechanical Systems and Signal Processing*, 145:106932, 2020.

S. Gopalakrishnan, M. Ruzzene, and S. Hanagud. Application of the finite element method in shm. In *Computational Techniques for Structural Health Monitoring*, pages 157–175. Springer, 2011.

M. He, T. Yang, and Y. Du. Nondestructive identification of composite beams damage based on the curvature mode difference. *Composite Structures*, 176:178–186, 2017.

H. Hu and J. Wang. Damage detection of a woven fabric composite laminate using a modal strain energy method. *Engineering Structures*, 31(5):1042–1055, 2009.

H. Hu and C. Wu. Development of scanning damage index for the damage detection of plate structures using modal strain energy method. *Mechanical Systems and Signal Processing*, 23(2):274–287, 2009.

H. Hu, B.-T. Wang, C.-H. Lee, and J.-S. Su. Damage detection of surface cracks in composite laminates using modal analysis and strain energy method. *Composite structures*, 74(4):399–405, 2006.

D. Inman. *Engineering Vibrations, International Edition*. Pearson Education Limited, 2013. ISBN 9780273785217. URL https://books.google.com.br/books?id=PPuoBwAAQBAJ.

R. Jafarkhani and S. F. Masri. Finite element model updating using evolutionary strategy for damage detection. *Computer-Aided Civil and Infrastructure Engineering*, 26(3): 207–224, 2011.

A. B. Jorge, C. T. M. Anflor, G. F. Gomes, and S. H. S. Carneiro, editors. *Model-based and Signal-Based Inverse Methods*, volume 1 of *Discrete Models, Inverse Methods, Uncertainty Modeling in Structural Integrity*. University of Brasília, 2022.

R. F. R. Junior, I. A. dos Santos Areias, and G. F. Gomes. Fault detection and diagnosis using vibration signal analysis in frequency domain for electric motors considering different real fault types. *Sensor Review*, 2021.

R. F. R. Junior, I. A. d. S. A. Methodoly, M. M. Campos, C. E. Teixeira, L. E. B. da Silva, and G. F. Gomes. Fault detection and diagnosis in electric motors using 1d convolutional neural networks with multi-channel vibration signals. *Measurement*, page 110759, 2022.

A. Kefal, A. Tessler, and E. Oterkus. An enhanced inverse finite element method for displacement and stress monitoring of multilayered composite and sandwich structures. *Composite Structures*, 179:514–540, 2017.

J.-T. Kim, Y.-S. Ryu, H.-M. Cho, and N. Stubbs. Damage identification in beam-type structures: frequency-based method vs mode-shape-based method. *Engineering structures*, 25(1):57–67, 2003.

L. A. S. Kouris, A. Penna, and G. Magenes. Seismic damage diagnosis of a masonry building using short-term damping measurements. *Journal of Sound and Vibration*, 394:366–391, 2017.

M. LeBlanc et al. Impact damage assessment in composite materials with embedded fibre-optic sensors. *Composites Engineering*, 2(5-7):573–596, 1992.

J. M. Lifshitz and A. Rotem. Determination of reinforcement unbonding of composites by a vibration technique. *Journal of Composite Materials*, 3(3):412–423, 1969.

H.-Y. Ling, K.-T. Lau, and L. Cheng. Determination of dynamic strain profile and delamination detection of composite structures using embedded multiplexed fibre-optic sensors. *Composite structures*, 66(1-4):317–326, 2004.

H. Lopes, J. Santos, R. Guedes, and M. Vaz. A hybrid technique for damage detection on laminated plates. *Photomechanics 2006*, 2006.

E. G. Magacho, A. B. Jorge, and G. F. Gomes. Inverse problem based multiobjective sunflower optimization for structural health monitoring of three-dimensional trusses. *Evolutionary Intelligence*, pages 1–21, 2021.

E. Manoach, J. Warminski, L. Kloda, and A. Teter. Numerical and experimental studies on vibration based methods for detection of damage in composite beams. *Composite Structures*, 170:26–39, 2017.

L. Meirovitch. *Fundamentals of vibrations*. Waveland Press, 2010. ISBN 1478609656.

S. Mohan, D. K. Maiti, and D. Maity. Structural damage assessment using frf employing particle swarm optimization. *Applied Mathematics and Computation*, 219(20):10387–10400, 2013.

P. Moradipour, T. H. Chan, and C. Gallage. An improved modal strain energy method for structural damage detection, 2d simulation. *Structural Engineering and Mechanics*, 54 (1):105–119, 2015.

B. Nanda, D. Maity, and D. K. Maiti. Vibration based structural damage detection technique using particle swarm optimization with incremental swarm size. *International Journal Aeronautical and Space Sciences*, 13(3):323–331, 2012.

I. Negru, G. Gillich, Z. Praisach, M. Tufoi, and N. Gillich. Natural frequency changes due to damage in composite beams. In *Journal of Physics: Conference Series*, volume 628, page 012091. IOP Publishing, 2015.

G. Owolabi, A. Swamidas, and R. Seshadri. Crack detection in beams using changes in frequencies and amplitudes of frequency response functions. *Journal of sound and vibration*, 265(1):1–22, 2003.

H. S. Park and B. K. Oh. Damage detection of building structures under ambient excitation through the analysis of the relationship between the modal participation ratio and story stiffness. *Journal of Sound and Vibration*, 418:122–143, 2018.

B. Peeters, G. Lowet, H. Van der Auweraer, and J. Leuridan. A new procedure for modal parameter estimation. *Sound And Vibration*, 38(1):24–29, 2004.

Q. Pu, Y. Hong, L. Chen, S. Yang, and X. Xu. Model updating–based damage detection of a concrete beam utilizing experimental damped frequency response functions. *Advances in Structural Engineering*, 22(4):935–947, 2019.

P. Qiao, K. Lu, W. Lestari, and J. Wang. Curvature mode shape-based damage detection in composite laminated plates. *Composite Structures*, 80(3):409–428, 2007.

A. R. M. Rao and G. Anandakumar. Optimal placement of sensors for structural system identification and health monitoring using a hybrid swarm intelligence technique. *Smart materials and Structures*, 16(6):2658, 2007.

A. R. M. Rao, K. Lakshmi, and S. Krishnakumar. A generalized optimal sensor placement technique for structural health monitoring and system identification. *Procedia Engineering*, 86:529–538, 2014.

R. F. Ribeiro Junior, F. A. de Almeida, and G. F. Gomes. Fault classification in three-phase motors based on vibration signal analysis and artificial neural networks. *Neural Computing and Applications*, 32(18):15171–15189, 2020.

S. Ručevskis, M. Wesolowski, and A. Čate. Vibration-based damage identification in laminated composite beams. *Scientific Journal of Riga Technical University. Construction Science*, 10(10):100–112, 2009.

R. Sampaio, N. Maia, and J. Silva. Damage detection using the frequency-response-function curvature method. *Journal of Sound and Vibration*, 226(5):1029–1042, 1999.

S. Sehgal and H. Kumar. Damage and damping identification in a structure through novel damped updating method. *Iranian Journal of Science and Technology, Transactions of Civil Engineering*, 45(1):61–74, 2021.

K. Sepahvand and S. Marburg. Identification of composite uncertain material parameters from experimental modal data. *Probabilistic Engineering Mechanics*, 37:148–153, 2014.

J. M. M. Silva and N. M. M. Maia, editors. *Modal Analysis and Testing*. Kluwer Academic Publishers, 1999.

H. Sohn, C. R. Farrar, F. M. Hemez, D. D. Shunk, D. W. Stinemates, B. R. Nadler, and J. J. Czarnecki. A review of structural health monitoring literature: 1996–2001. *Los Alamos National Laboratory*, 2003.

M. Souza, D. Castello, N. Roitman, and T. Ritto. Impact of damping models in damage identification. *Shock and Vibration*, 2019, 2019.

P. R. Souza and E. G. O. Nóbrega. An effective structural health monitoring methodology for damage isolation based on multisensor arrangements. *Journal of the Brazilian Society of Mechanical Sciences and Engineering*, 39(4):1351–1363, 2017.

J. M. C. Suveges. *Estudo Acerca da detecção de danos em estruturas via método de otimização.* Dissertação de mestrado, Universidade Federal de Itajubá, 2016.

I. Trendafilova, R. Palazzetti, and A. Zucchelli. Damage assessment based on general signal correlation. application for delamination diagnosis in composite structures. *European Journal of Mechanics-A/Solids*, 49:197–204, 2015.

A. Tributsch and C. Adam. An enhanced energy vibration-based approach for damage detection and localization. *Structural Control and Health Monitoring*, 25(1), 2018.

S. D. Valdes and C. Soutis. Delamination detection in composite laminates from variations of their modal characteristics. *Journal of sound and vibration*, 228(1):1–9, 1999.

R. Velmurugan and G. Balaganesan. Modal analysis of pre and post impacted nano composite laminates. *Latin American Journal of Solids and Structures*, 8(1):9–26, 2011.

A. Viglietti, E. Zappino, and E. Carrera. Free vibration analysis of locally damaged aerospace tapered composite structures using component-wise models. *Composite Structures*, 192:38–51, 2018.

T. Vo-Duy, V. Ho-Huu, H. Dang-Trung, D. Dinh-Cong, and T. Nguyen-Thoi. Damage detection in laminated composite plates using modal strain energy and improved differential evolution algorithm. *Procedia Engineering*, 142:182–189, 2016.

K. Worden, W. Staszewski, G. Manson, A. Ruotulo, and C. Surace. Optimization techniques for damage detection. *Encyclopedia of Structural Health Monitoring*, 2009.

Y. Yan, L. Yam, L. Cheng, and L. Yu. Fem modeling method of damage structures for structural damage detection. *Composite Structures*, 72(2):193–199, 2006.

Z. Yang, X. Chen, M. Radzienski, P. Kudela, and W. Ostachowicz. A fourier spectrum-based strain energy damage detection method for beam-like structures in noisy conditions. *Science China Technological Sciences*, 60(8):1188–1196, 2017a.

Z.-B. Yang, X.-F. Chen, Y. Xie, and X.-W. Zhang. The hybrid multivariate analysis method for damage detection. *Structural Control and Health Monitoring*, 23(1):123–143, 2016.

Z.-B. Yang, M. Radzienski, P. Kudela, and W. Ostachowicz. Damage detection in beam-like composite structures via chebyshev pseudo spectral modal curvature. *Composite Structures*, 168:1–12, 2017b.

Z.-B. Yang, M. Radzienski, P. Kudela, and W. Ostachowicz. Fourier spectral-based modal curvature analysis and its application to damage detection in beams. *Mechanical Systems and Signal Processing*, 84:763–781, 2017c.

Z.-B. Yang, M. Radzienski, P. Kudela, and W. Ostachowicz. Two-dimensional chebyshev pseudo spectral modal curvature and its application in damage detection for composite plates. *Composite Structures*, 168:372–383, 2017d.

Z.-B. Yang, Y.-N. Wang, H. Zuo, X.-W. Zhang, Y. Xie, and X.-F. Chen. A robust poincare maps method for damage detection based on single type of measurement. In *Journal of Physics: Conference Series*, volume 842, page 012001. IOP Publishing, 2017e.

Z.-B. Yang, Y.-N. Wang, H. Zuo, X.-W. Zhang, Y. Xie, and X.-F. Chen. The fourier spectral poincare map method for damage detection via single type of measurement. *Measurement*, 113:22–37, 2018.

T. Yin, Q.-H. Jiang, and K.-V. Yuen. Vibration-based damage detection for structural connections using incomplete modal data by bayesian approach and model reduction technique. *Engineering Structures*, 132:260–277, 2017.

X. Yong and H. Hong. A genetic algorithm for structural damage detection based on vibration data. In *Proc. 19th International Modal Analysis Conference*, pages 1381–1387, 2001.

W. Zhang, J. Li, H. Hao, and H. Ma. Damage detection in bridge structures under moving loads with phase trajectory change of multi-type vibration measurements. *Mechanical Systems and Signal Processing*, 87:410–425, 2017.

Y. Zhang, L. Wang, S. T. Lie, and Z. Xiang. Damage detection in plates structures based on frequency shift surface curvature. *Journal of Sound and Vibration*, 332(25):6665–6684, 2013.

Z. Zhang, K. Shankar, M. Tahtali, and E. Morozov. Vibration modelling of composite laminates with delamination damage. In *proceedings of 20th International Congress on Acoustics, ICA*, 2010.

J. Zhou, Z. Li, and J. Chen. Damage identification method based on continuous wavelet transform and mode shapes for composite laminates with cutouts. *Composite Structures*, 191:12–23, 2018.

Chapter 13

Application of Deep Learning Techniques for the Impedance-based SHM to the Oil & Gas Industry

Application of Deep Learning Techniques for the Impedance-based SHM to the Oil & Gas Industry

Stanley W. F. Rezende[1*], José dos Reis V. Moura Jr[2],

José Waldemar da Silva[4], Diogo S. Rabelo[3], Quintiliano S. S. Nomelini[4],

Roberto M. Finzi Neto[1], Carlos A. Gallo[1], Julio E. Ramos[5]

[1] Post-Graduate Program – Mechanical Engineering, Federal University of Uberlandia, Brazil. e-mail: stanley_washington@ufu.br; finzi@ufu.br; gallo@ufu.br
[2] Post-Graduate Program – Modeling and Optimization, Fed. University of Catalao, Brazil. e-mail: zereis@ufcat.edu.br
[3] Post-Graduate Program – Industrial Engineering, Fed. University of Goias, School of Sciences and Technology, Aparecida de Goiania, Brazil. e-mail: diogo.rabelo@ufg.br
[4] Faculty of Mathematics - Federal University of Uberlandia, Brazil, e-mail: zewaldemar@ufu.br; quintiliano.nomelini@ufu.br
[5] Petrobras, Petroleo Brasileiro S.A., R&D Center (CENPES), Brazil. e-mail: julio.ramos@petrobras.com.br

*Corresponding author

Abstract

This chapter presents some basic concepts about some fundamental Deep Learning techniques currently used in the data processing. Next, the use of these techniques to aid decision-making in Electromechanical Impedance-based Structural Health Monitoring (ISHM) is presented. Initially, using a CNN to classify structural damage in specimens is evaluated, eliminating the need for temperature compensation. Then, an LSTM network prediction model of the evolution of an accelerated corrosive process (HCl acid) in specimens is presented. Finally, a model based on CNN is carried out as a case study of thickness loss in a real fuel storage tank plate.

Keywords: Deep Learning; Impedance-based Structural Health Monitoring; Oil and Gas Industry

1. Introduction

Human beings use several types of mechanical structures daily to carry out their tasks. These structures, when in operation, are susceptible to failure due to wear conditions, fatigue, or impacts of their mechanical components (Moura Jr and Steffen Jr [2006], Rezende, Barella and Moura Jr [2020]). Therefore, for such facilities to perform their activities correctly, the failures present in the mechanical system must be identified and repaired promptly, which makes integrity monitoring processes a critical aspect nowadays (Palomino *et al.* [2011], Eleftheroglou *et al.* [2018], Ghazvineh *et al.* [2021]).

In addition, it is known that incorrect identification of the presence of damage can have serious economic and safety consequences (Ghazvineh *et al.* [2021]). In this sense, the maintenance of systems considered critical becomes even more fundamental, and, consequently, different inspection and damage assessment techniques have been researched in recent years. These monitoring and inspection techniques now make up the so-called Structural Health Monitoring (SHM) (Zhao *et al.* [2011], Melville *et al.* [2018], Gulgec, Takáč and Pakzad [2019], Rastin, Ghodrati Amiri and Darvishan [2021]).

SHM formulations and methods, in general, aim to provide or improve issues such as safety, operability, minimization of maintenance and repair costs, logistical efficiency, and increase in useful structural life, among others (Moura Jr and Steffen Jr [2006]). For this, SHM methods commonly employ different types of software and hardware to characterize the systems under study, acquire and manage monitoring data, and evaluate, in the long term, these systems' environmental and operational conditions (Melville *et al.* [2018], Gulgec, Takáč and Pakzad [2019], Rastin, Ghodrati Amiri and Darvishan [2021]).

When a structure's degradation process is continuously monitored, its maintenance can be planned predictively rather than periodically, thus reducing associated costs and avoiding unnecessary system downtime (Eleftheroglou *et al.* [2018]). Therefore, this situation requires adopting a damage identification process with rapid prognostic capacity. For certain types of structures, it is necessary to evaluate the integrity and functioning conditions of the system in real-time (Zhao *et al.* [2011], Rastin, Ghodrati Amiri and Darvishan [2021]).

The electromechanical impedance-based SHM method (ISHM), in this context, presents itself as a promising technology to reduce structural risks and maintenance costs. This condition, in turn, is given by the ease that this method offers in its implementation and the possibility of integration with advanced data processing techniques (Moura Jr and Steffen Jr [2006], Leucas [2009], Palomino *et al.* [2011], Na and Baek [2018], Nomelini *et al.* [2021]).

In ISHM, piezoelectric transducers are usually integrated into the mechanical structures. Later, an electronic circuit becomes responsible for monitoring the variation of the electrical impedance of each chip. This procedure is carried out over a wide range of excitation frequencies (usually greater than 30kHz) (Moura Jr and Steffen Jr [2006], Leucas [2009], Na and Baek [2018], Rezende, Barella and Moura Jr [2020]).

As each piezoelectric transducer is mechanically coupled to the structure under investigation, variations in the electrical impedance values suggest a possible presence of structural damage (Nomelini *et al.* [2021]). However, to make a correct measurement of structural failure the method needs a large volume of data for evaluation, which causes a significant increase in the complexity of the abstraction process (Palomino *et al.* [2011], Silva *et al.* [2018], Rezende [2021]).

Due to this increase in computational complexity, recent SHM studies have sought to reconcile integrity monitoring methods with innovative and functional tools for pattern abstraction and classification (Verstraete *et al.* [2017], Ghazvineh *et al.* [2021]). The use of pattern abstraction techniques in the monitoring data sets aims to delimit a causal relationship between the different integrity states of the structures under study (Gulgec, Takáč and Pakzad [2017]). Thus, once the response behavior of the

system is assimilated, it is possible to detect promptly the existence of variations in this behavior, which indicate a possible presence of damage in such structures (Palomino *et al.* [2011], Melville *et al.* [2018]).

In this sense, it should be noted that interpreting the acquired data is more important than collecting the monitoring information. Therefore, pattern abstraction and classification techniques used in conjunction with SHM methods must have high detection power and precision, factors that must still be achieved together with rapid data processing (Gulgec, Takáč and Pakzad [2017], Freitas, Jafelice and Silva [2021], Rastin, Ghodrati Amiri and Darvishan [2021]).

Furthermore, data acquisitions performed during the processing of a given structure can easily contain thousands of pertinent information and, in this way, different types of tasks and operations can also be performed on them, such as damage level regression, classification of the kind of failures and anomaly detection in the monitored system (Barella [2021], Rezende *et al.* [2020]).

Therefore, to elucidate the practical execution of some of these tasks in the daily context of the SHM, in this chapter, three possible aspects of integration between the deep learning (DL) models and the monitoring method based on electromechanical impedance will be evaluated. For this, two neural architectures, namely CNN and LSTM, will be implemented in the following sections of this chapter. Different practical tests will be carried out to identify the presence and severity of failures in mechanical structures.

At first, a binary damage classification task in aluminum beams will be performed, analyzing the sensitivity of the combination of the CNN network and ISHM technique concerning environmental changes in the data acquisition stage. Then, with the LSTM architecture, a model will be developed to predict the level of corrosion in steel beams, which is caused by hydrochloric acid wear, also helping diagnose the structural life of this type of system.

The third and last experiment will be developed to identify (by the CNN network and ISHM method) the structural health conditions of a damaged tank plate (by grinding), thus determining the level of thickness reduction in the region of interest of the coupled PZT sensor.

Encouraging results were obtained by carrying out the previously mentioned experimental tests. Thus, it becomes possible to verify the employability of deep learning models (more specifically, the CNN and LSTM models) in support of the diagnosis of structural failures in mechanical systems.

That said, and to make the theoretical and practical foundation of this chapter clearer and more concise, it was subdivided into sections as follows: initially, in Section 1, the importance of SHM studies was discussed, in addition to pointing out the need to use of machine learning (ML) and DL models in support of the structural health monitoring methods.

In Section 2, the concepts of machine learning and deep learning are deepened, and then the theoretical formulations of the required techniques are presented separately in their subsections. Section 3, on the other hand, focuses on the applications and results obtained in different case studies. Finally, Section 4 highlights the positive aspects of

the methodology used and describes the conclusions that could be inferred throughout the chapter.

2. Machine Learning and Deep Learning Overview

Machine learning (ML) is a subarea of Artificial Intelligence (AI) focused on developing techniques and computational algorithms capable of extracting features in today's most varied problems (Provost and Kohavi [1998], Freitas, Jafelice and Silva [2021]).

In general, machine learning algorithms are based on creating a programmable inference model, in which, from sampled data, a predictive answer is obtained. In this way, such algorithms automatically find more valuable representations of the data, mapping unknown relations in the space of hypotheses (Verstraete *et al.* [2017], Rezende *et al.* [2020]).

Thus, the learning process in ML is performed inductively, where response patterns are automatically defined through experiences already observed by the mathematical model. Consequently, the main challenge is to formulate intermittent problems where a list of mathematical rules is not easily measurable (Freitas, Jafelice and Silva [2021]).

Some conceptions of AI, previously used to solve complex problems, were based on characteristics specified by human operators, who were also responsible for delimiting all types of knowledge used by the computer. However, a limitation of this type of approach is the difficulty in determining what kinds of features are needed for the abstraction process (Liang, Guixi and Hongyan [2015], Rezende [2021]).

On the other hand, ML techniques eliminate the need to formally define which characteristics the classifier should use through a hierarchical representation of concepts. Thus, knowledge is obtained through experience, enabling the computer to make predictions and classifications of complex ideas by abstracting more straightforward concepts.

In this sense, artificial neural networks (ANNs) have stood out as one of the main ML techniques, contributing at the same time to the development of several areas of knowledge (Menezes *et al.* [2009], Barros, Morais and Fernandes [2017], Gulgec, Takáč and Pakzad [2017], Mhatre *et al.* [2017], Sharma and Singh [2017], Cofre-Martel *et al.* [2019]). Its efficiency is mainly due to the way data processing is performed, in which the applied operations are particularly close to those performed by the human brain (Komijani *et al.* [2017], Melville *et al.* [2018]).

While other machine learning approaches use a series of logical blocks to execute the learning process, ANNs operate on a parallel network of nodes. These nodes are responsible for locally processing the abstracted information and, later, through a training algorithm, their response outputs are optimized to obtain the best resolution of the practical problem (Komijani *et al.* [2017]).

It should be noted that no neural architecture is equally applicable to all types of problems found in the literature. Thus, various ANNs have been developed over time, some of which are convolutional (CNN) and recurrent models (such as the LSTM network).

However, most neural architectures are composed of a series of processing units (called artificial neurons) distributed in groups (named layers) in the form of a chain. Thus, as each neural layer is a combined function of the predecessor layer, an ANN's assertiveness also depends on the number of layers used (Komijani *et al.* [2017], Rezende [2021]).

When an ANN is composed of three or more processing layers, it is characterized as a deep neural network, and its application comprises the so-called deep learning (DL) (Chen, Li and Sanchez [2015], Yu *et al.* [2015], Blanco *et al.* [2019]).

In the deep learning approach, the levels of representation of the data are used to follow a hierarchical flow; that is, the high-level characteristics are obtained exclusively through the composition of lower levels, which specialize in a specific type of information (Gulgec, Takáč and Pakzad [2017]).

For this, deep learning models usually require large volumes of data and a high amount of hidden layers for abstraction. As a result, a high computational cost is also required, with data processing often being performed on the computer's graphics unit (Yu *et al.* [2015], Gulgec, Takáč and Pakzad [2019]).

It should be noted that the topic of deep learning is an aspect of machine learning (Figure 1), which has gained significant importance in recent years, mainly due to its ability to solve problems that were not treatable until then; one of them being structural integrity monitoring (Verstraete *et al*. [2017]). Figure 1 presents the arrangement and relationships between the different tasks and areas involved in the context of ML and DL.
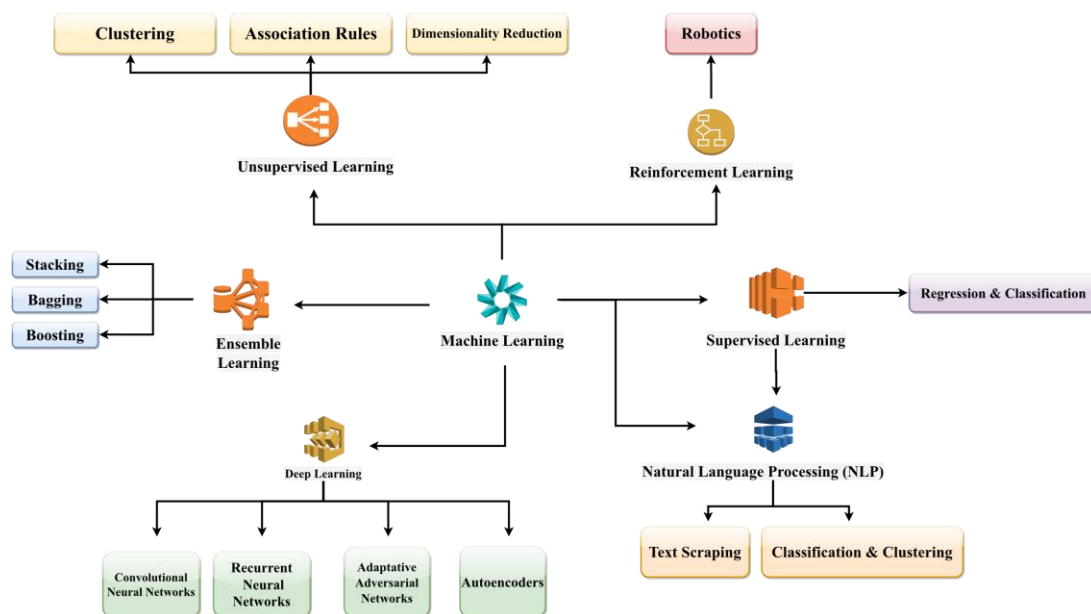
**Figure 1: Association between the main tasks in machine and deep learning.
Source: Adapted from Trekhleb and Xie [2022].**

As shown in Figure 1, several machine learning methods and models are available in the literature that is usable for the most varied types of engineering problems, one of which is identifying the presence of damage in mechanical structures (Verstraete *et al*. [2017]).

Furthermore, DL models represent only a tiny portion of the entire set of models and techniques available. However, existing models have been widely used in several studies, such as natural language processing, computer vision, and automatic sample generation (Portsev and Makarenko [2018], Abdoli, Cardinal and Koerich [2019], Rezende [2021]).

From a general point of view, the objective of using a more significant number of layers in neural models is to increase the abstraction capacity of the data, which are evaluated from different perspectives, to condense better and associate the relationships between the inputs and outputs of the model of the system. Then, with the formulation of the neural model, it is then possible to infer, for example, the future behavior of the structures under study. This procedure is carried out from data not yet verified by the model (Rezende *et al.* [2020]).

2.1. Convolutional Neural Architecture

Convolutional Neural Networks (CNNs) are examples of deep learning models whose procedural formulation is inspired by some areas of the human visual cortex. These regions, called local receptive fields, are responsible for activating different neurons to perform the resource abstraction process and, through their overlap and specific selection, identify patterns of information present in the data (Chen, Li and Sanchez [2015], Albawi, Mohammed and Al-Zawi [2017], Gulgec, Takáč and Pakzad [2019]).

As a rule, CNNs architectures can be composed in different ways, associating different types of neural layers. In which at least one of them, the mathematical operation of convolution is applied and which, in turn, is responsible for the network abstraction capacity (Gulgec, Takáč and Pakzad [2017], Indolia *et al.* [2018], Agarwal *et al.* [2021]).

The convolution operation adopted by a convolutional layer is made from a sliding data window, commonly called a kernel, which is constituted by a mesh of synaptic weights and passes through all the inputs of the evaluated layer. This slippage and abstraction procedure is done to highlight the main local features of each dataset (Ghazvineh *et al.* [2021]).

For this, CNNs assume that in the topology of the experimental data, the values of closer indices are much more correlated than the values of distant indices. This ideal, in turn, can be considered the main factor that justifies the intense application of the convolution technique in images, audio, and other types of vector sets (Chen, Li and Sanchez [2015]).

Furthermore, it should be noted that each convolutional layer of a CNN may contain several abstraction kernels to improve the patterns of available information. The results achieved by each abstraction filter, on the other hand, generate a map of resulting features, which is used as input for the following constituent layers of the network (Chen, Li and Sanchez [2015]).

Figure 2 outlines a general representation of the CNN topology, considering a one-dimensional impedance signal (impedance amplitude only) as input to the model.
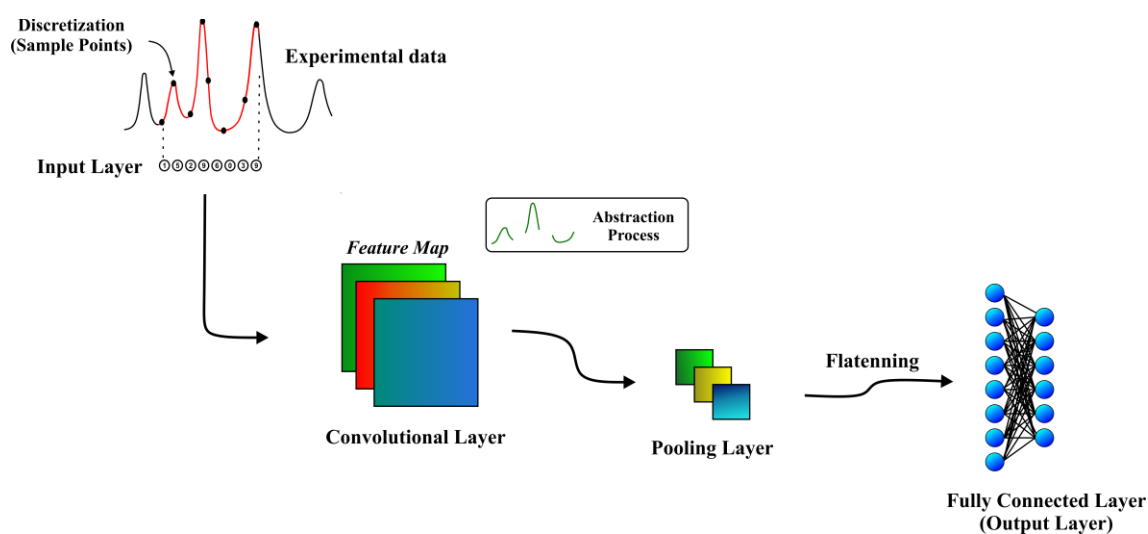
Figura 2: Topologia geral de uma rede convolucional unidimensional.
Source: Adapted from Rezende *et al.* [2020].

As can be seen from the image, we arrive at a feature map of the layer's input values due to applying the convolutional layer. This map, in turn, represents a template of the main characteristics observed in the input data about a given abstraction filter. However, due to the convolution process itself, some concepts intrinsic to this type of process are also present and significantly influence the result of the network; they are the value of stride, padding, and the sharing of free parameters (Chen, Li and Sanchez [2015]).

The stride defines the sliding relationship between the abstraction kernel and the input data vector. Therefore, this parameter is directly linked to the final sensitivity of the feature map. On the other hand, the padding ratio represents the number of zeros added at each end of the input vector to guarantee the mathematical balance of the process. Therefore, these two parameters, i.e., stride and padding, are significantly crucial for the proper functioning of the network.

At the same time, the sharing of free parameters occurs through the transmission of the values of the synaptic weights to other regions of the feature map. This transmission results from the linear displacement between the abstraction cores and the evaluated dataset. Such sharing produces a preliminary reduction in the parameters to be adjusted by the network, which also becomes of particular interest during the model training phase (Rezende [2021]).

Also, since CNNs are generally used to process high-dimensional data, it makes sense to use subsampling layers between their convolution layers. These pooling layers (Figure 2), in turn, are intended to synthesize the information previously abstracted by the convolutional layers, thus employing another reduction in the observed dimensionality without, however, the considerable loss of information necessary for the problem (Rezende *et al.* [2020]).

In the literature, several types of functions can be used in the subsampling step of the pooling layer. Among these functions, we can mention the value choice: maximum, average, and Euclidean norm, among others. However, they aim to represent the analysis region in a single numerical value, transmitted to the next layer through a reduced feature map (Chen, Li and Sanchez [2015], Ghazvineh *et al.* [2021]).

After the synthesis performed by the last pooling layer of the convolutional model, the output values of this layer are fully connected to a new feedforward model, which is responsible for classifying and defining the possible general outputs of the network (Agarwal *et al.* [2021]). A feedforward model is given with a set of neural layers, whose neurons in each layer are fully connected to neurons in its successor layers. Thus, the processing flow follows in a single direction, allowing the identification of patterns observed instantly through the current dataset.

Based on the configuration of practical problems, the output of a neural network must be designed according to the type of problem to be addressed, which can then be given through deterministic data (discrete values) or the degree of belonging to a group (continuous values). Therefore, the final dimensionality of the fully connected layers of a CNN must also be adjusted for this purpose.

It should also be noted that to make the connection between the last pooling layer and the first fully connected layer, a flattening sublayer is used between these two layers to maintain the mathematical and computational integrity of the problem. Such an event stems from the fact that the dimensionality achieved by the feature map resulting from the pooling layer is given as a two-dimensional matrix. However, the input of a feedforward model must be exclusively a one-dimensional vector. Consequently, an adjustment must be made to allow the algebraic operations performed by the network to be completed (Agarwal *et al.* [2021], Ghazvineh *et al.* [2021]).

Once the neural architecture to be used is formulated, its training process begins, which in this case takes place as a supervised learning process. Thus, throughout the synaptic weights' adjustment process, patterns of ideal responses are presented together with the input data groups of the network, and, through a whole process of backpropagation, the network parameters are reevaluated to reduce the errors returned (Gulgec, Takáč and Pakzad [2017]).

In this sense, it is noteworthy that, as CNN networks are Feedforward, they have only one property of immediate reasoning: information is acquired over time by modifying synaptic weights. As a result, all information processed by each layer is associated only with current input values rather than previously processed data by the network.

2.2. Long Short-Term Memory Architecture

In short, to characterize a dynamic system, the analysis of its behavior under current conditions is not enough since its previous state usually influences its current state. In this context, feedforward neural architectures do not always become applicable, as they only have a direct relationship between the current input of the network and its respective output (Bispo [2018]).

This condition of unidirectional input-output transmission performed by feedforward networks makes it impossible to process new information based on resources already processed by ANN. Therefore, such networks can be characterized only as immediate reasoning networks. Short-term memory resources are not present, and the learning process is achieved only by carrying out the entire process of training the synaptic weights (Rezende [2021]).

Thus, based on this principle, it is necessary to add to the ANNs some changes in their topology, which allow them to store a temporal relation of their previous states for their current evaluation. Among the various possible modifications, two stand out: delays in entering the network and the recurrence process.

Delays in the entry of an ANN consist of time-dependent samples, which are composited together with their previous states. Thus, with the application of the delay technique, only the set of inputs is changed, and the ANN architecture remains of the feedforward type, which facilitates its implementation process. However, this adaptation alternative is only applicable in medium-complexity systems. For high-complexity systems, internal structures of state changes are required, which is achieved by applying recurrence between the neurons of an ANN.

Therefore, the recurrence property in an ANN is given by the presence of cycles between its processing units; that is, the output of a neuron of the nth layer is used as input for a neuron of a lower-level layer or the layer itself, assigning feedback to the architecture that will serve as a short-term memory engine (Le et $al.$ [2019]).

Figure 3 exemplifies the recurrence property in an artificial neural network, this effect being used both about different layers and the feedback of the same layer.
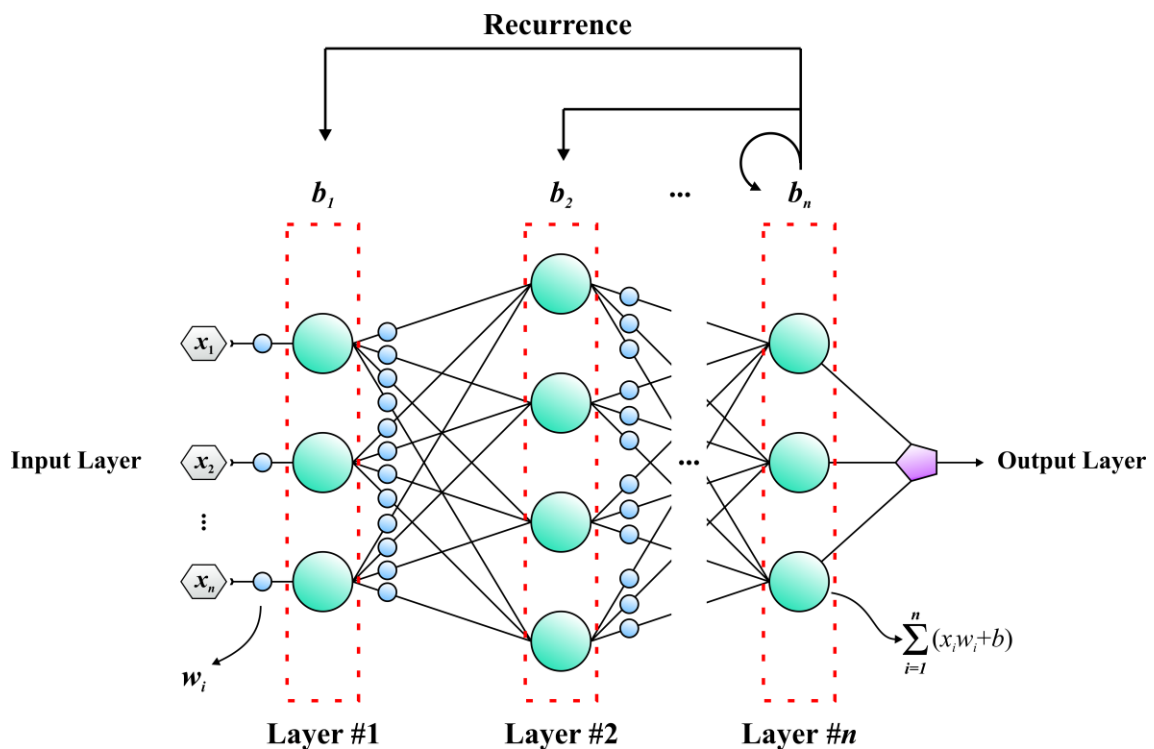
Figure 3: Exemplification of a recurrent neural network.

The practical effect of recurrence in ANNs is to streamline the neural models over time, causing the observed features to flow in both propagation directions and, at the same time, being able to abstract new information through parameters already measured. When a neural network is built with feedback neurons, it is called a Recurrent Neural Network (RNN) and is characterized as a feedback topology (Le et $al.$ [2019], Rezende [2021]).

This short-term memory resource obtained by RNNs makes this type of neural architecture instrumental for many kinds of real applications. However, in practical terms, such models still have some disadvantages when evaluated on large datasets (with unlimited time windows), as their training process can become significantly complex and slow.

Thus, in the quest to improve the temporal processing limit reached by RNNs, about the amount of information kept in their short-term memory, two problems with the gradient descent calculation emerged in deep learning studies. The first, called Exploding Gradient Descendent, refers to an instability imposed on the synaptic weights of the network throughout its training process. This instability, caused by the accumulation of errors evaluated in large chains of layers, can cause some of the values of the synaptic weights to cancel out for the initial layers. In contrast, others become considerably large, and thus the prediction made by the model is affected.

The second problem, called Vanishing Gradient Descendent, is the inability of assimilation by the network for significant temporal dependencies; that is, the gradient values used in the error correction cancel out for the first-time parcels, and the training process ends up not working as expected (Hochreiter and Schmidhuber [1997], Zhao *et al.* [2016], Sherstinsky [2020]).

To effectively solve these two problems that occur with gradient descent when a large volume of sequential data is evaluated, computer scientists Sepp Hochreiter and Jürgen Schmidhuber introduced, in 1997, a new model of recurrent neural network called Long Short-Term Memory (LSTM) (Hochreiter and Schmidhuber [1997], Rezende [2021]).

The LSTM architecture is an example of a feedback network that can retain information for a more significant amount of network inputs, evaluated during the neural training process. The error flow calculated during the same processing is kept constant by including special units in its characteristic neurons. These units are popularly known as gates.

The gates of an LSTM allow the neural network to assertively adjust its synaptic weights while truncating the gradient when information is no longer needed. Such a procedure symbolizes a form of forgetfulness on LSTM, which avoids canceling certain parts of its training process.

Like all RNN architectures, LSTM networks can memorize some information about their previous states over time. However, it should be noted that the LSTM architecture manages to learn and control the time this information remains during the training process, working to create a much more efficient long-term memory mechanism than a normal RNN. This attribute is obtained through one of the gates of the LSTM neurons called forget gate (Le *et al.* [2019]).

In general, neurons (also known as memory cells or blocks) of an LSTM network are composed of 3 gates: the forget gate, the input gate, and the output gate. They all have an activation function to control the information that flows in each direction of the cell, thus enabling its schematization, according to Figure 4.
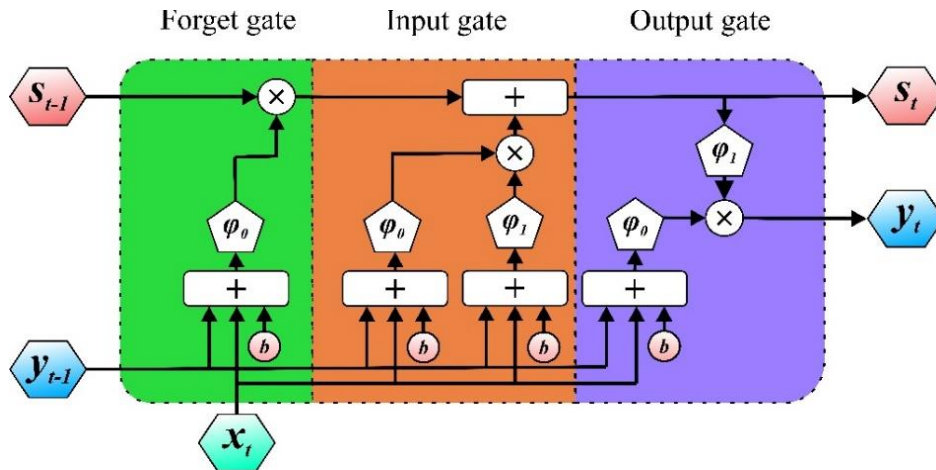
Figure 4: Representation of a memory cell of an LSTM network.
Source: Adapted from Rezende [2021].

As mentioned, the forget gate controls which information will be kept by the LSTM cell. Consequently, also responsible for eliminating unnecessary information from previous states, which contributes to the network learning process. For this purpose, three inputs are presented to the unit, which are: a current input vector (x_t), a previously hidden state vector (s_{t-1}), and an output vector of the previous layer cell (y_{t-1}). Each vector is multiplied by its respective weight matrix and added to the bias (which is responsible for compensating and dimensionalizing the input values in the activation function of this gate) (Yan [2016], Rezende [2021]).

After the usual propagation calculation inside the forget gate, the result is passed through a binary activation function (φ_0), where output 0 represents a forgetting process of the evaluated data, and output 1 means the correctness of the information for future use.

The input gate, on the other hand, is responsible for updating the LSTM cell at the current time, this procedure being based on the cell input values at time t and its previous hidden state s_{t-1} (measured by the forget gate). In this way, the flow of information within this unit is controlled according to equation 1,

$$s_t = \varphi_0(W_0 \cdot [y_{t-1}, x_t] + b) \cdot (s_{t-1} + \varphi_1(W_1 \cdot (y_{t-1}, x_t) + b)) \qquad (1)$$

where φ_0 and φ_1 are generally nonlinear functions and W_i are weight matrices evaluated in each part of the cell structure. In the literature, the sigmoid and TanH functions are commonly used to represent the components φ_0 and φ_1, respectively.

The output (y_t) of the LSTM cell is obtained through the output gate, which uses a sigmoidal function to determine which of the state values will be remembered for the measurement of its final response. These values are then multiplied to a readjustment (exercised by applying a TanH function on the hidden state of cell s_t), to generate the output for the next cell (Yan [2016], Rezende [2021]).

A long-term memory neural network comprises several processing cells layered to form the LSTM architecture. This neural network model has been widely applied in recent years, mainly in treating natural language and time series analysis, thus justifying its evaluation in the present chapter.

3. Experimental Case Studies

3.1. Application of CNN for Temperature Variation Problems

To facilitate understanding the implementation of a CNN in python language and already introducing it in the context of monitoring the structural integrity, the classification of the electromechanical impedance signatures of three geometrically identical aluminum beams (500x38x3.2mm).

Therefore, each structure was monitored under two different integrity conditions (with and without damage) and at three acquisition temperatures (0ºC, 10ºC, and 20ºC). Thus, the experimental conditioning adopted here aims to verify the ability to detect damage in structures subject to temperature variation using the CNN architecture.

The acquisition of impedance signatures was performed using a PZT transducer (20mm in diameter by 1mm in thickness) coupled 100mm away from one of the ends of each analyzed structure. The damage simulation was performed by adding mass to the three structural systems (three nuts ranging from 0.6-2.2g glued 380mm away from the PZT adhesive). Figures 5.a and 5.b show the three aluminum beams used and the imposed damage conditions.

a) Structural Systems (Aluminum Beams + PZTs Insert).

b) Mass addition damage conditions.

Figure 5: Structures used as the object of study.
Source: From Rezende *et al.* [2020].

They were submitted to a boundary condition (single support) to analyze the structures correctly. In this sense, polystyrene foams were used to minimize the influence of noise during the acquisition phase.

Environmental conditions can cause minor changes in the electromechanical impedance signatures during the acquisition process. Thus, in the literature, efforts have been made to minimize possible errors in structural prognosis (Afshari [2012], Rabelo *et al.* [2017a], Rabelo *et al.* [2017b] and Tsuruta *et al.* [2017]).

In this investigation, to delimit and control the three different temperature levels, a climatic chamber of the Platinous EPL-4H series was used, which is available at the LMest laboratory of the Mechanical Engineering course at the Federal University of Uberlandia. Figure 6 illustrates the climate chamber model used in this case study.

Figure 6: Platinous EPL-4H Climatic Chamber.
Source: From Barella [2021].

The Platinous EPL-4H series climate chambers are based on BTHC (Balanced Temperature and Humidity Control), employing a thermodynamic balance to control temperature parameters. The operating volume of the model used is approximately $900L$ (100x100x$90cm$) and can handle the temperature from a range of -35ºC to 180ºC.

For the construction, training, and validation of the CNN model, 20 electromechanical impedance signatures were collected for the baseline state (pristine condition of the structure) and 80 signatures for the damaged state, thus totaling 900 samples for evaluation (300 for each of the beams).

The frequency range used in acquiring impedance signatures was 68-77*kHz* with a step of 4.5*Hz* and 2000 sample points. It is also worth mentioning that the frequency band used was chosen through a trial-and-error process to subsidize a predominance of the random search optimization method.

The random search optimization method was applied to the set of electromechanical impedance signatures to delimit the best scanning range for identifying the presence of damage among the pre-chosen frequency portion. This procedure was based on the methodology imposed by Bento [2017], which uses the RMSD damage metric as a comparison of the best frequency range to be monitored.

Thus, with the application of the random search optimization method, the frequency range chosen became 71*kHz* to 75*kHz*, with a total of 888 sample points. The averages of the impedance signatures can be seen in Figure 7.
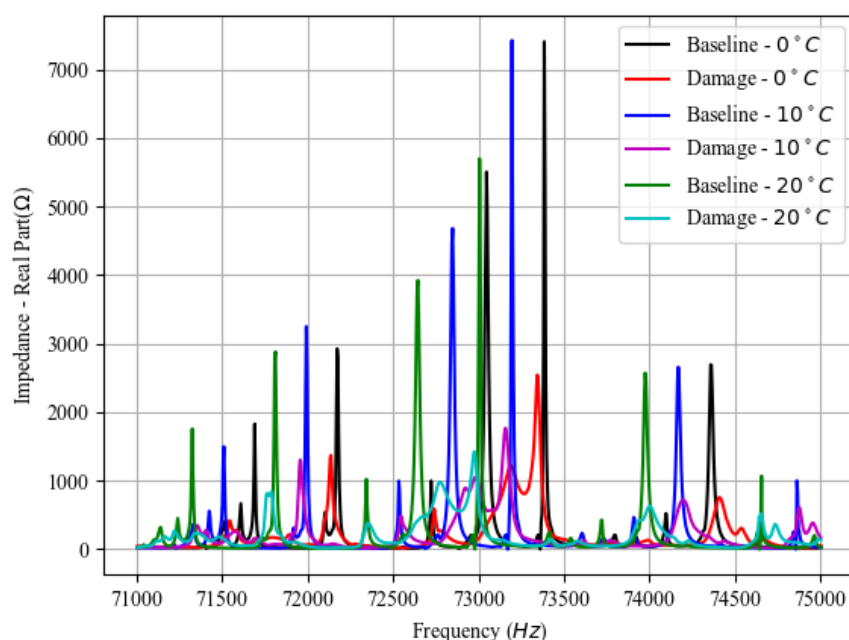
Figure 7: Means of the impedance signatures of each evaluated group.
Source: From Rezende *et al.* [2020].

To define the best CNN architecture for the problem in question, the type and dimensions of the input data used in the network must be identified. Electromechanical impedance signatures are two-dimensional vectors, where we have the electromechanical impedance signals in the frequency domain. Such a phenomenon can be modeled, in this way, by a 2D-CNN using its two parameters. However, if we consider a standardized frequency range for all samples evaluated, another one-dimensional approach can still be performed, using only the impedance values measured in the transducer.

Because the samples considered are measured in the same frequency range (71-75*kHz*), one-dimensional analysis of electromechanical impedance signatures will be employed using a 4-layer 1D-CNN architecture. Thus, the topology used will comprise a convolutional layer, a pooling layer (MaxPooling type), and two fully connected layers, as shown in Figure 8.

Input Layer	input:	$[i_{sample}, 888, 1]$
	output:	$[i_{sample}, 888, 1]$

Layer #1: *Conv*1D	input:	$[i_{sample}, 888, 1]$
	output:	$[i_{sample}, 652, 100]$

Layer #2: *Maxpooling*1D	input:	$[i_{sample}, 652, 100]$
	output:	$[i_{sample}, 326, 100]$

1st Adjustement: *Dropout*	input:	$[i_{sample}, 326, 100]$
	output:	$[i_{sample}, 326, 100]$

Sublayer: *Flatten*	input:	$[i_{sample}, 326, 100]$
	output:	$[i_{sample}, 32600]$

Layer #3: *Dense*	input:	$[i_{sample}, 32600]$
	output:	$[i_{sample}, 10]$

Layer #4: *Dense*	input:	$[i_{sample}, 10]$
	output:	$[i_{sample}, 2]$

2nd Adjustement: *Dropout*	input:	$[i_{sample}, 2]$
	output:	$[i_{sample}, 2]$

**Figure 8: Convolutional neural architecture implemented in the experiment.
Source: From Rezende *et al.* [2020].**

It is worth noting in Figure 8 that the steps called "1st Adjustment", "Sublayer" and "2nd Adjustment" were not included in the count of the layers used since these, by their purpose, apply only one preset to the set of synaptic weights. Furthermore, the dimension i_{sample} represents the batch size of samples evaluated during iteration i of the training phase (although each of these samples is processed separately to adjust the synaptic weights of the network) (Rezende *et al.* [2020]).

To initialize the construction of the convolutional neural network model in python, one must initially import the TensorFlow library into the system's memory and stabilize and stack the first layer (input) of the CNN model. This process can be performed by executing the commands below:

```
>> import tensorflow as tf
>> input = tf. keras.layers.Input(shape=(888,1))
```

All sampling points of the electromechanical impedance signatures were used in this contribution. In this way, the developed inference system adds more degrees of freedom, which provides greater reliability to the classification method.

To introduce the full extent of the impedance signatures in the CNN model, an input layer with 888 neurons was implemented. Thus, each sampling point has its respective input neuron, enabling the convolution between the electromechanical impedance signatures and the abstraction filters.

As a next step in constructing the input layer, the other convolutional and pooling layers must be alternately stacked to the CNN model to elaborate the network architecture to be developed.

Altogether, there are three types of convolutional layers previously implemented in the Keras package: *Conv1D*, *Conv2D*, and *Conv3D*. However, all kinds of convolutional layers perform the same mathematical functions and processes, differing only in the number of dimensions in which the data is convoluted (Rezende [2021]).

The only one-dimensional analysis will be applied to the electromechanical impedance signatures. Therefore, for the implementation of the network, a 1D convolutional layer with 100 abstraction filters was used, where each filter had a dimension of 237 randomly chosen synaptic weights.

The implementation of the convolutional layer developed in this section followed the TensorFlow formulation in the python IDE:

```
>> net_cnn = tf.keras.layers.Conv1D(filters=100, kernel_size=237,
                            strides=1, padding='valid',
                            use_bias=True,
                            activation='relu')(input)
```

where the parameters given to the function are, respectively, the number of filters used for convolution, the length of the abstraction kernel, the linear displacement of the kernel, the type of padding, the use of bias in the convolutional layer, and the activation function used.

The displacement between the abstraction kernels and the input data was assigned as step 1 to evaluate all possible sample points for the convolution process. However, the padding action (valid) was not attributed since the extreme data of the signatures used were already null.

After having performed all the convolutions of the input signals by the convolutional layer, an activation function of the *ReLu* type was applied to its feature maps. The purpose of using this function is to normalize the results of each feature map, thus allowing only the propagation of positive values of the output data of the predecessor layer.

It is worth mentioning that all parameters used in modeling the convolutional layer were chosen to analyze a better portion of the signals used, which are specifically dependent on each case under investigation.

Still, due to the application of the parameters mentioned above, it can be seen in Figure 8 a reduction of 26% in the amount of data to be evaluated by the pooling layer.

This paradigm contributes to its computational cost and helps the classification method's abstraction and data separability.

On the other hand, coupling a section layer to a CNN model depends mainly on the type of function imposed by this same layer, thus varying between the maximum or medium value of each subregion of the characteristics map.

In this work, the pooling layer adopted in the CNN model used only order two filters to abstract the impedance characteristics, keeping only the highest value reached for each of the analyzed areas of the feature map. In this way, only 50% of the input data from the pooling layer will be propagated for consecutive layers.

The python function used for coupling the pooling layer in the CNN model is given as follows:

```
>> net_cnn = tf.keras.layers.MaxPool1D(pool_size=2)(net_cnn)
```

where the only parameter provided to the function is the inspection window dimensionality, which corresponds to the size of the feature map subregion to be evaluated.

Two other adjustment sublayers were implemented to couple the fully interconnected layers to the CNN model, one for dropout and the other for flattening. Such an application aims to computationally adjust the response data of the pooling layer so that they are used as input to the feedforward model.

Due to the significant dimensionality of the output data from the pooling layer, two fully connected layers were added to the classification model. The first dense layer was implemented with ten neurons to allow a reduction in the adjustable parameters of the last layer, which in turn is responsible for the network response output.

The CNN architecture implemented in this contribution aims to catalog the impedance signatures in two states, with and without damage. In this way, the response layer of the model has only two neurons, whose outputs represent the probability of belonging, respectively, to the classes with damage (activation of the second neuron) and without damage (activation of the first neuron).

For the output layer to respond to the probability of each sample belonging to a specific group, the *Softmax* logistic function was used in the fully connected layers. This function performs input data distribution, classifying them according to their similarity with the pre-delimited target classes (Chollet [2017]). Thus, the configuration of the parameters used to implement the fully connected layers is given as follows:

```
>> net_cnn = tf.keras.layers.Dropout(0.2)(net_cnn)
>> net_cnn = tf.keras.layers.Flatten()(net_cnn)
>> net_cnn = tf.keras.layers.Dense(units=10, activation='softmax') (net_cnn)
>> net_cnn = tf.keras.layers.Dense(units=2, activation='softmax') (net_cnn)
```

After the neural topology is developed, the storage and construction of the CNN model with the optimization parameters and adjustment of the synaptic weights must be carried out. Such parameters define how the training algorithm will access and regulate the accessible attributes of the implemented model and delimit the loss function used to identify the error absorbed by the network.

To build a CNN model using the TensorFlow library, type the following commands in the python IDE:

```
>> model = tf.keras.models.Model(input, net_cnn)
>> optimizer = tf.keras.optimizers.RMSprop(learning_rate=0.001, rho=0.8)
>> loss_function = tf.keras.losses.BinaryCrossentropy()
>> model.compile(optimizer= optimizer, loss=loss_function, metrics=['accuracy'])
```

The "Model" function performs the sequencing and construction of the neural layers that make up the network. This process is based on pre-defined tensors. The "Compile" function, on the other hand, configures the neural architecture training and learning processes, delimiting the loss function and the optimization method according to the parameters provided to it.

In this experiment, the *Binary Crossentropy* loss function and the RMSprop (*Probabilistic Root Mean Square*) optimization method are used since they exhibit good efficiency in classification problems. Still, in this section, it is worth noting that the learning rate (η) and the gradient decay factor (ρ) were defined by carrying out previous experiments since they directly influence the performance of the neural training process (Rezende [2021]).

After executing the entire process of building and configuring the CNN model, the network training and learning stage starts. The model is adjusted according to the training samples and target values. To train a CNN in python, we used the fit function, as shown below:

```
>> history = CNN.fit(training_samples, target_training, batch_size=2, epochs=40)
```

The total epochs for training and the number of samples needed to update the synaptic weights (batch size) are also given to this method. The fit history of the synaptic weights is then stored in a data structure for further analysis, such as verifying the learning curve and measuring the accuracy achieved.

It is noteworthy that a CNN model was built and trained for each beam structure individually to enable the prediction of structural damage. Thus, from the 300 impedance signatures for each model, 30 random samples were removed for testing, and the remaining 270 samples were considered to train and build the previously described model.

As mentioned, during the training process, the *Binary Crossentropy* loss function was used to verify the response accuracy of the networks. All models achieved a loss function of about 0.221, representing a slight difference between the result and the target groups related to the complexity of the problem.

Subsequently, the RMSprop optimization algorithm calculated the adjusted weights of each network. At the end of this stage, the accuracies were approximately 85.74%, 89.40%, and 95% for beam structures #1, #2, and #3, respectively.

After adjusting the weights, the trained networks were evaluated using the test samples as input to the models. Thus, each model had ten runs for all 30 samples in the batch. As a result, all three models obtained different degrees of probability of damage detection. Figures 9.a, 9.b and 9.c show a histogram of all tests performed.
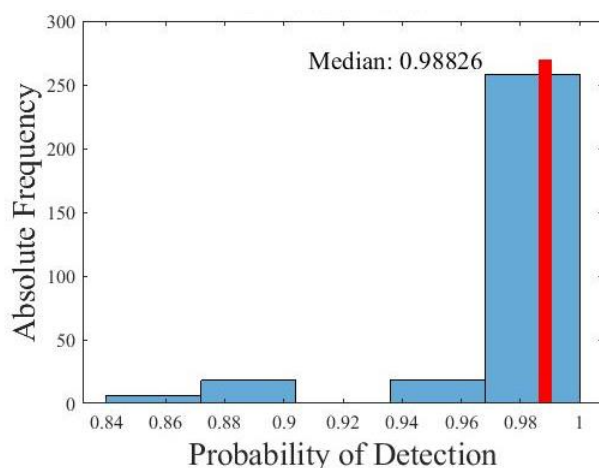
a) Test results for structure #1.
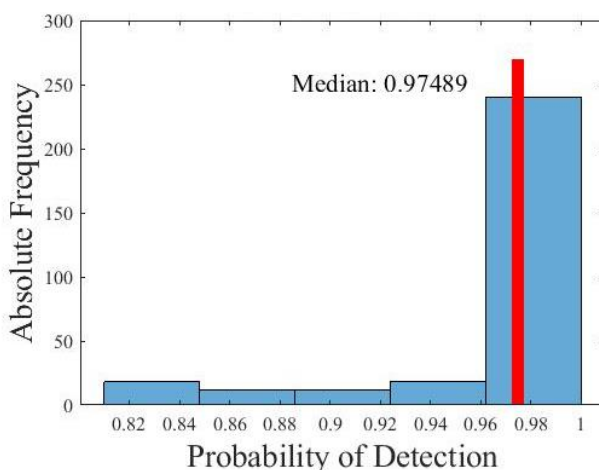
b) Test results for structure #2.
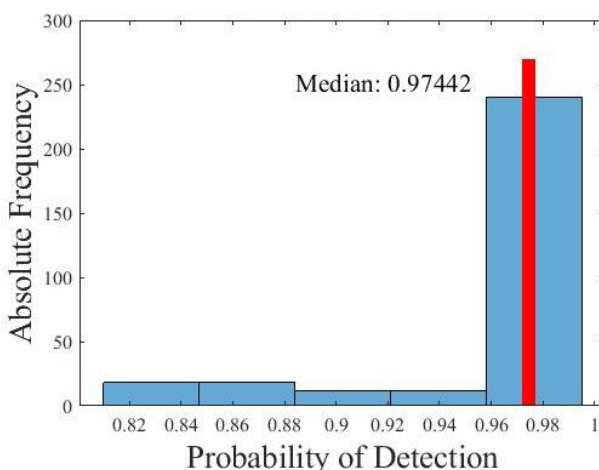
c)   Test results for structure #3.

Figure 9: Histogram with the test results imposed on each model.
Source: From Rezende *et al.* [2020].

According to Figure 9.a, the probability of detection of damage by the first CNN model (structure #1) varies from 84% to 100%. This graph includes all assessed

integrity conditions (baseline and damage) in the test. Since the distribution of results does not follow a normal distribution, its median (which is a better parameter for comparing groups) is evaluated, reaching 98.83%.

Figure 9.b illustrates the histogram for the model of structure #2, and similar results were obtained for the second model, with a probability of detection of damage from 81% to 100%, with a median of 97.49%. Finally, the last histogram presents the probability of damage detection for the third model (structure #3), ranging from 81% to 100%, with a median of 97.44%.

In this initial evaluation, all the developed CNNs models reached a probability of damage detection greater than 97%, meaning a good damage classification capacity for the three structures used. Thus, it is worth mentioning that, although the model used in this section is simple (composed of only one convolutional layer and pooling), the results achieved are favorable to the application of this deep learning technique in the electromechanical impedance SHM method.

Also, since environment temperature is very relevant for the impedance-based SHM technique, changing the amplitudes of its electromechanical impedance signatures, this specific result demonstrates the ability of models to separate damage and primitive signatures, regardless of temperature, being very relevant to the proposed methodology.

3.2. Application of LSTM for Corrosion Problems

In contrast, to execute the implementation process of an LSTM network in Python language, two geometrically identical steel beams ($300x50x3.2mm$) were considered under controlled corrosive action. This experimental condition was formulated to verify alterations in the impedance signatures resulting from the corrosion process of the structures, analyzing the progression of severity in them.

Thus, the experimental design adopted here aims to verify the ability to predict the magnitude of structural failures in steel beams subjected to hydrochloric acid (HCL) corrosion using the LSTM architecture.

The acquisition of impedance signatures was performed using a PZT transducer ($30mm$ in diameter by $2mm$ in thickness) coupled $50mm$ away from one of the ends of each analyzed structure.

To properly evaluate the two steel beams under similar corrosion conditions, all measurements took place with the specimens in the bi-supported form, with contoured regions (cradles) being delimited for the subsequent application of acid in each of the structures separately. Figure 10 shows the beams used in the experimental procedure adopted in this section.
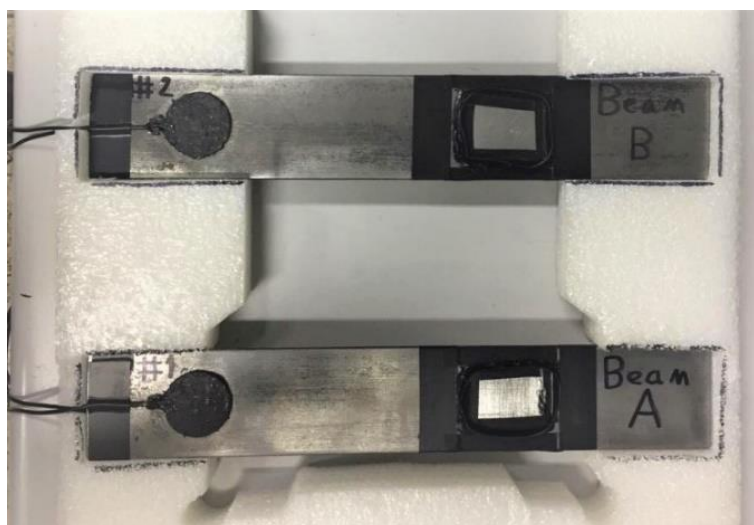
Figure 10: Steel beams used in the HCL corrosion experiment.
Source: From Rezende [2021].

The region (cradle) of HCL application in each structure was defined with a dimension of 32*mm* wide by 44*mm* long, positioned 150*mm* away from its respective PZT adhesive. The concentration of acid used is 36.5%. Its application in each structure was carried out by dripping, which allowed a better optimization of the acquisition process concerning other forms of application present in the literature, such as corrosive mist application.

The order of collection of impedance signatures and application of HCL acid in the monitored structures was defined according to Table 1, in which 30 measurements of impedance signatures were collected for each evaluated severity set, thus totaling 240 samples (120 referring to each of the beams) for the construction of the neural model.

Table 1: Sequencing of collections and integrity groups evaluated in the implementation of the experiment.

Measurement	Application of HCL Acid	Integrity Status Assessed
#1	–	Baseline
	Yes	
#2	–	Damage #1 (24*h* after the 1st Application)
	Yes	
#3	–	Damage #2 (24*h* after the 2nd Application)
#4	–	Damage #3 (48*h* after the 2nd Application)

As can be seen, four levels of integrity of the evaluated structures were considered: an untouched condition of the steel beams (baseline) and three other conditions after partial corrosion of the material by applying HCL acid.

Then, the impedance signatures were monitored in a frequency range of 30-100kHz, with a step of 10.02Hz and 6980 sample points, each calculated with 512 means.

All experiments with the specimens were carried out in an environment enclosed by grids but subject to the external environment, providing variations in temperature and humidity in the monitored beams. Such a formulation was carried out to approximate the experimental tests to the real operating conditions of this type of structure. Thus, it should be noted that the changes in the impedance signatures evaluated may depend both on the characteristics of the progressive corrosion process and the environmental conditions (temperature and noise) of the acquisition phase.

Thus, to minimize the effects of temperature variation on the impedance signatures, a temperature compensation algorithm known as the Effective Frequency Displacement Method by Correlation Analysis was applied, making minor adjustments (horizontal and vertical) in the impedance signatures to maximize the correlation coefficient between the evaluated signal groups (Rabelo *et al.* [2017b]).

After compensating for the effects of temperature variation on the impedance signatures, the RMSD damage metric was implemented to construct the LSTM neural model further. This metric index was used as input to the neural model due to its ability to identify the progression of damage severity better and allow the mutual application of delay and recurrence techniques.

Figures 11.a and 11.b show the impedance signatures and metric index groups before and after temperature compensation.

In the present case study, a two-layer LSTM model (Figure 12) will be used to predict the severity of corrosion in the monitored structures, using only the values of the RMSD damage metric as input to the neural model.

The use of this formulation stems from the fact that, in corrosion problems, the level of structural severity obtained by calculating the damage metrics tends to increase over time, allowing the use of such values in the modeling of the phenomenon. Thus, given the above, the neural architecture used will be composed of only one LSTM layer and a fully connected layer expressed according to Figure 12.

Millstein [2018] highlighted that the modeling of a neural network using the Keras package is performed through the sequencing of tensor layers, in which prototype functions are stacked to build the neural architecture. Thus, the modeling used in this case study followed the same formulation presented in the previous section for the input and fully connected layers, varying only their respective implementation parameters.

As for the recurrence process, an LSTM layer with 120 memory cores was used, in which its activation functions φ_0 (cell activation) and φ_1 (recurrence function) were defined according to the following command:

```
>> net_cnn = tf.keras.layers.LSTM(units=120,
                        activation='tanh',
                        recurrent_activation='sigmoid',
                        use_bias=True)
```
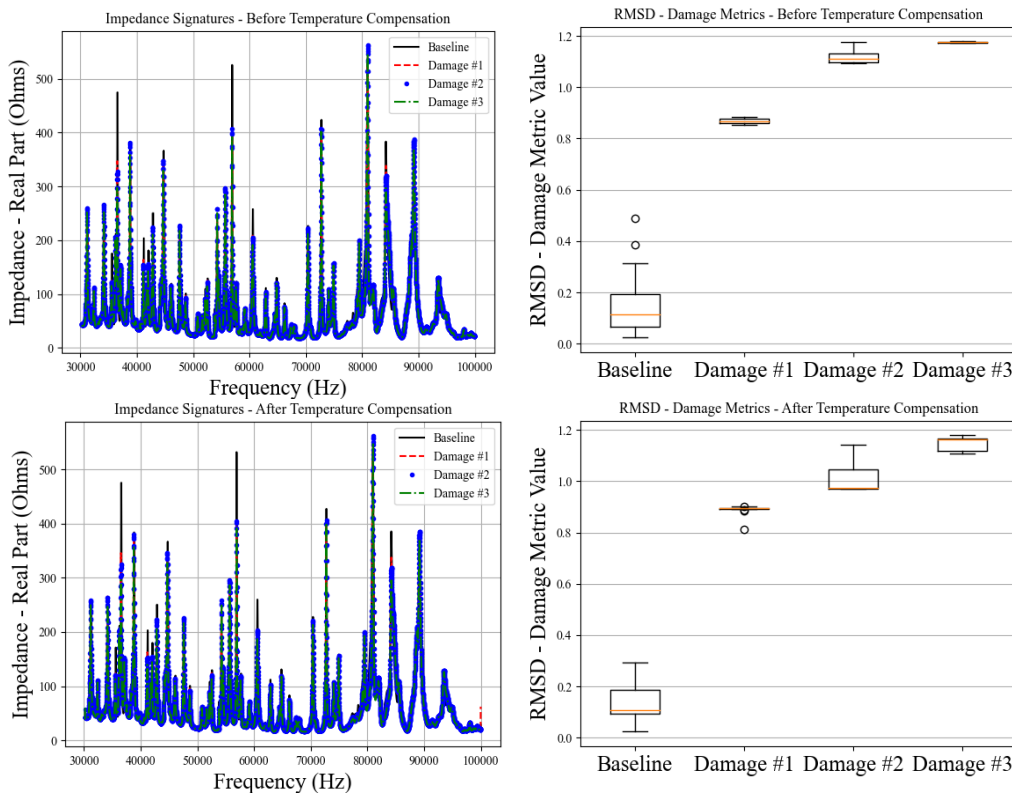
a) Structure #1
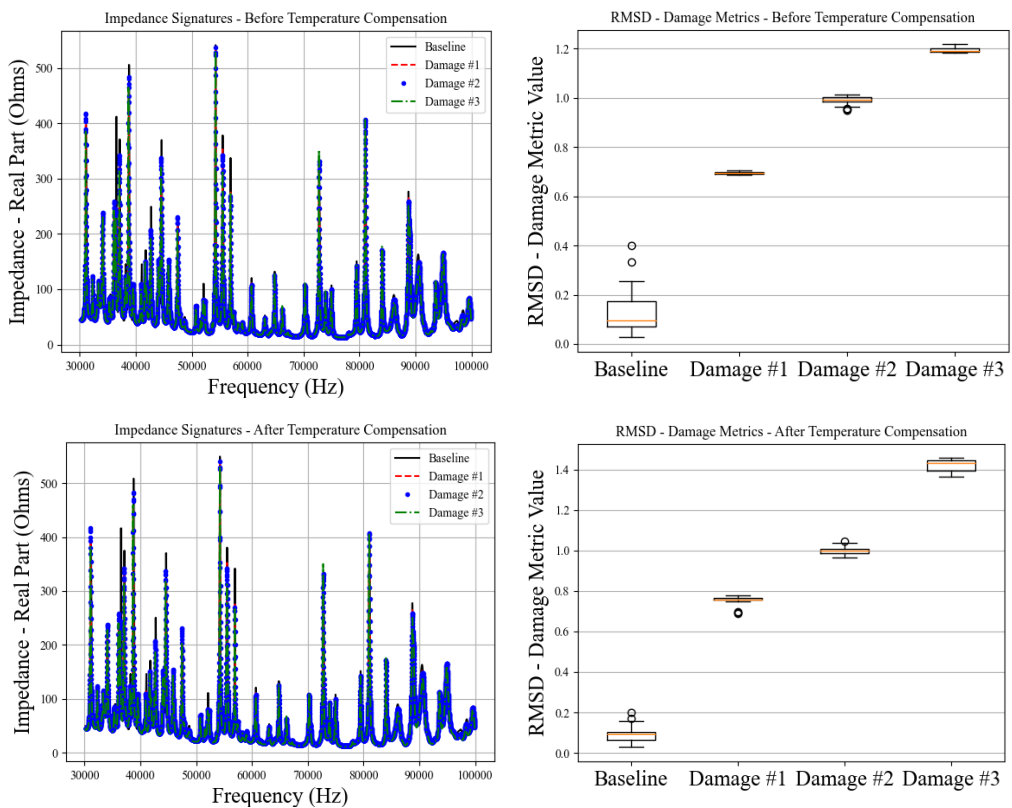
b) Structure #2

Figure 11: Averages each severity level's impedance signatures and their respective RMSD metric values.

Source: From Rezende [2021].
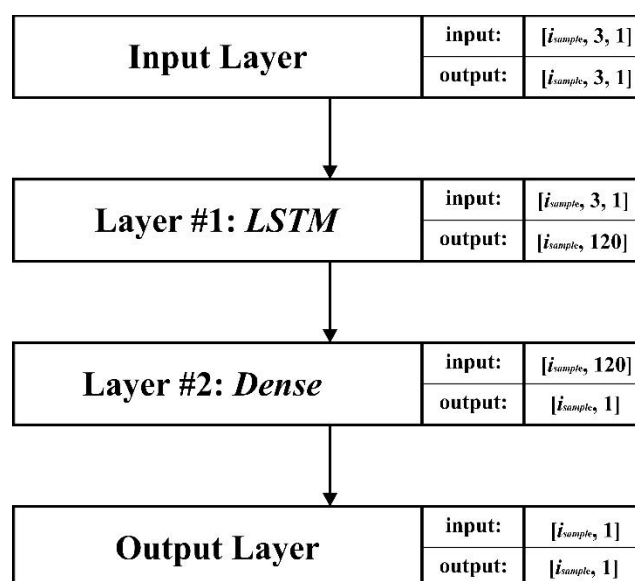
Figure 12: LSTM neural architecture implemented in the experiment.
Source: From Rezende [2021].

As a result of the present case study being evaluated as a regression problem, the RMSE loss function and the optimization method known as Adam was used to configure the neural model, as they present a better efficiency when compared to other methods and procedures available (Gulli and Pal [2017]).

It is also worth noting that an LSTM model was built and trained for each beam structure separately to validate the methodology imposed in this contribution. Thus, of the 120 metric values of each model, 48 sequential samples were removed for testing, and the remaining 72 samples were considered to train and build the previously described neural model.

Furthermore, it is worth mentioning that both the delay and recurrence techniques (provided by the formulation of the LSTM model) were applied jointly to the data group evaluated. However, to introduce the delay technique in the present experimental process, it was used for each forecast point and its respective previous units of the series, which caused a reduction in the number of points to be incorporated in the construction of the model. Thus, considering a delay level $j=3$, the final number of points to be used in the model are 45 values for testing and 69 samples for training the network.

As mentioned, during the training process, the RMSE function was used to verify the response accuracy of the networks. All models achieved a loss function of about 0.0109, representing a slight difference between the expected result and the target values related to the complexity of the problem.

After the error calculation, the optimization algorithm used (*Adam*) adjusted the synaptic weights of each network. At the end of this stage, the accuracy was approximately 90.42% and 90.22% for beam structures #1 and #2.

The trained networks were tested for the efficiency of the test samples after the local parameters of each model had been adjusted. As a result, the accuracy of each model in predicting the structural severity of each surveyed beam varied.

The comparison between the expected results and the actual values of each beam is presented in Figures 13.a and 13.b, and it can be observed that the modeling used in this contribution was able to achieve a high level of precision in terms of structural severity prediction in beams subjected to the corrosive action of hydrochloric acid. For model test data *nº1*, this accuracy was 96.1%, and for model test data *nº2*, it was 92.68%.

a) **Structure #1**

b) **Structure #2**
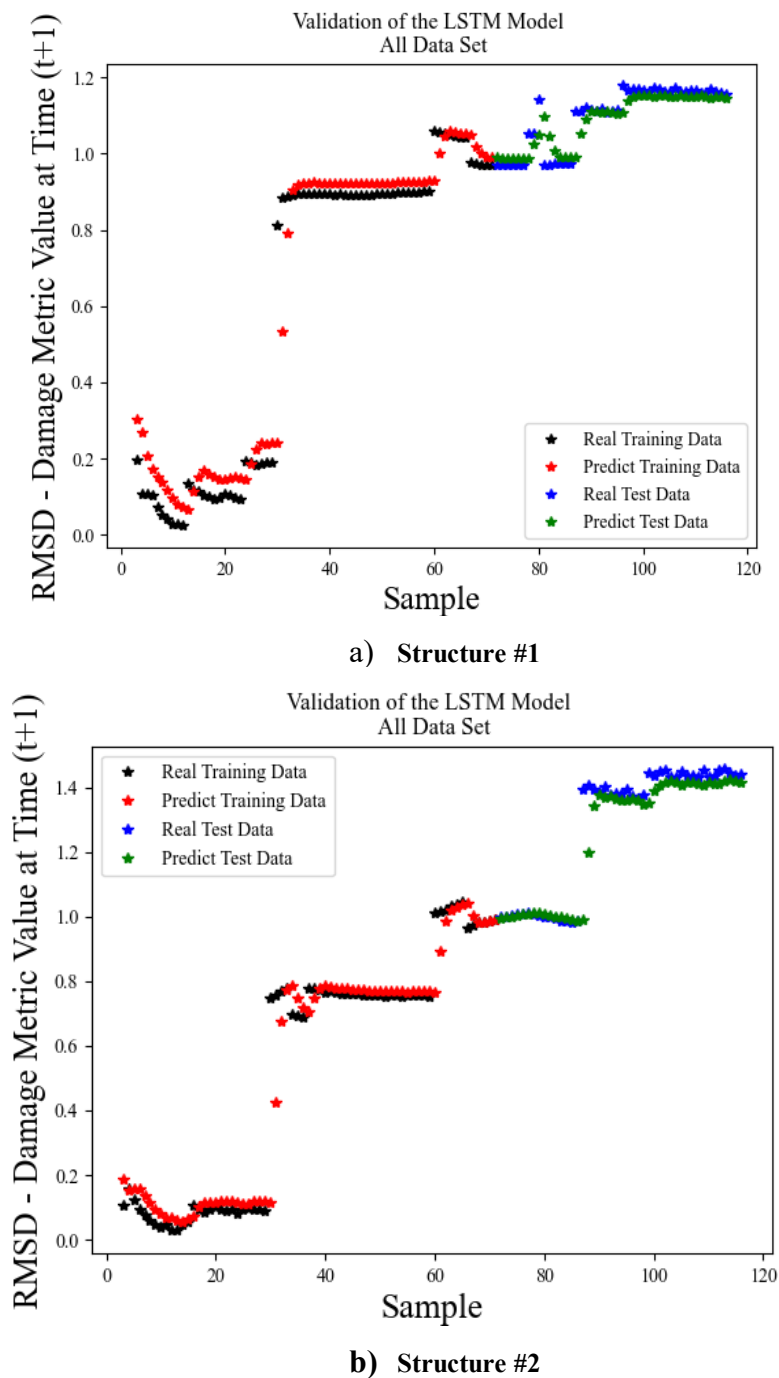
Figure 13: Relationship between the data provided by the LSTM neural models and the pre-delimited target values.
Source: From Rezende [2021].

Consequently, despite the simple LSTM architecture used in this section (containing only one recurring layer), the results were also beneficial for using the technique in conjunction with the SHM method via electromechanical impedance.

2.3. CNN Application for Monitoring Machined Tank Plates

An iron plate-like structure was used as a host system to carry out the third case study of this contribution. At the same time, successive thickness reductions by grinding part of the material were considered the method of artificial damage. Figure 14.a shows the support/structure set used in the present case study, and Figure 14.b shows the application regions of the piezoelectric sensors and the insertion site of the imposed fault.

a) Experimental bench

b) Top view of the structure used

Figure 14: Experimental configuration adopted in the thickness loss study.

As seen in the previous image, three piezoelectric sensors (30mm in diameter) were inserted in the region of interest, equidistant from the area to be ground, restricted by an external diameter of 60mm. However, to simplify the present case study, only PZT-1 impedance signatures will be considered for the next steps of the damage classification process.

Thus, once the instrumental configuration to be adopted throughout the experiment was delimited, a total of 4 conditions of the structural integrity of the plate

under study were evaluated, that is, the initial condition of the plate (integral state) and another three monitoring configurations resulting from material thickness reduction by the plate metal grinding.

In this sense, for each state of structural integrity considered, 30 repetitions of impedance signatures were measured to allow the later use of the CNN architecture in damage classification. In addition, the plate thickness levels in the region of interest were also measured (in a total of 15 repetitions) using ultrasonic tests. Table 2 presents the thickness relationships acquired in each of the repetitions of the ultrasound tests for each state of structural integrity monitored on the plate.

Table 2. Monitored plate thickness measurements in each considered health state.

	Baseline	Damage #1	Damage #2	Damage #3
Measurement #1	5.39	3.65	1.35	1.64
Measurement #2	5.53	3.61	1.97	1.44
Measurement #3	5.53	4.08	2.26	1.38
Measurement #4	5.61	4.30	2.53	2.11
Measurement #5	5.39	4.25	2.06	1.83
Measurement #6	5.65	3.91	2.19	1.71
Measurement #7	5.48	4.04	2.03	1.77
Measurement #8	5.59	3.82	2.07	1.57
Measurement #9	5.35	3.82	2.69	2.19
Measurement #10	5.44	3.65	3.44	2.19
Measurement #11	5.48	3.61	2.50	1.67
Measurement #12	5.50	3.62	2.54	2.07
Measurement #13	5.39	3.52	2.17	1.83
Measurement #14	5.54	3.61	1.57	1.64
Measurement #15	5.57	3.44	1.58	1.64
Average value	5.50	3.80	2.20	1.78
% of thickness	100	69.1	40.0	32.4
Class	1	2	3	4

As can be seen, different levels of material thickness were considered for each state of integrity. These changes, in turn, reflect on electromechanical impedance signatures. Thus, through statistical and mathematical methods, it is possible to infer reliable information about the usability conditions of the structure, making it possible to estimate its useful life and reduce costs and ensure better levels of safety.

A 5-layer 1D-CNN architecture was then implemented in the present case study to verify the CNN topology's sensitivity in identifying and classifying damage due to the loss of machined material. Therefore, the neural model used here was based on a deep neural network composition, being given by an input layer, a convolutional layer, a pooling layer (of the Max Pooling type), and two other fully connected layers (which are to the 3rd hidden layer and the network output layer). Figure 15 presents a schematic of the neural topology used in the tests in this section.
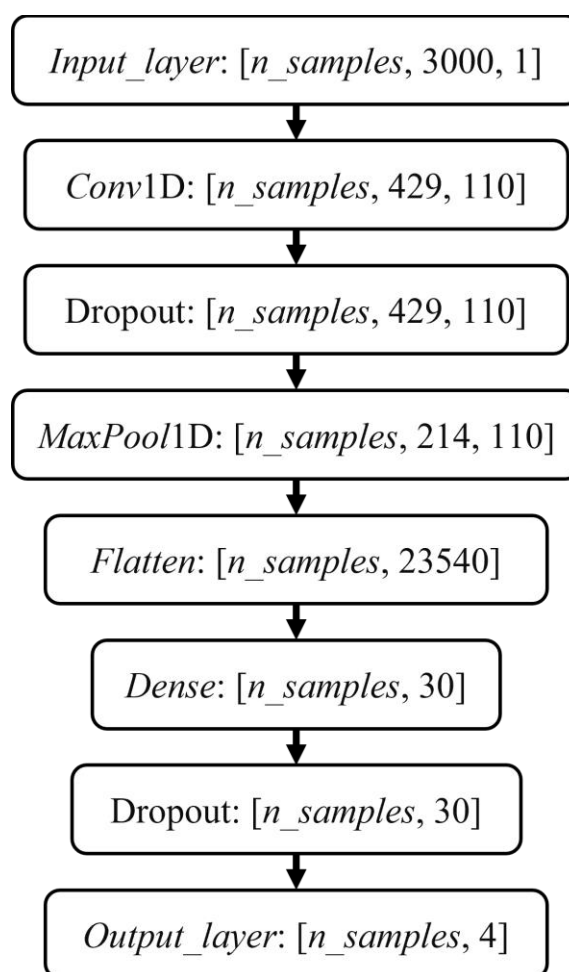
Figure 15: Convolutional neural architecture used in this case study.

It is worth mentioning that, as in the previous problem, the dropout and flattening steps were also not considered in the counting of these neural layers, as they only serve as data manipulation and processing functions during the training phase. Furthermore, it should be noted that all sampling points of the impedance signatures were again considered as input to the CNN architecture, which, in addition to introducing more degrees of freedom to the problem under study (providing more realistic modeling of the observed problem) it also avoids the need to define in advance the unique characteristics of the structure so that its integrity conditions can be identified, making the model responsible for this purpose.

The input layer of the network, in this sense, was formulated with 3000 synaptic neurons, each one representing a specific frequency point of the impedance signature. Then, a *Conv1D* layer was developed with 110 abstraction filters (kernels) and later coupled to the model. Each abstraction filter in this last layer was composed of 200 synaptic weights randomly chosen, and its construction process was like the architecture of the first case study.

For the convolution process, the displacement between the abstraction kernels and the model input data was assigned as step 7 to abstract the main parts of the impedance signal separately. This abstraction reduced 85.7% of the input data,

converting them into a representative vector of 429 sample points for each abstraction filter.

As for the pooling layer of this section, size two kernels were also used, thus keeping only the highest value of each subregion of the data observed in each feature map. Therefore, only 50% of the layer's input data is propagated to consecutive layers, introducing a second reduction of the observed dimensionality (converting each signal into a representative vector of 214 sample points).

After the pooling layer, two other fully connected layers were inserted into the neural network architecture so that the first dense layer was responsible for filtering the data (converting the 23540 input values of the layer into only 30 significant points), and the second layer was responsible for processing them and later defining the network output.

Bearing in mind that the present case study aims to identify and classify the different states of the structural integrity of a machined iron plate system (with loss of material by grinding). In this way, the output of the considered model was attributed through a fully connected layer (of 4 synaptic neurons). Each layer neuron represented the probability that the sample in question belongs to a specific output class (Table 2).

Therefore, to ensure that the output layer responds to the probability that each impedance signature belongs to a group, the softmax logistic activation function was also used in the present case study, with the optimizer model and the loss function equally given the experiment in Section 3.1 of this chapter.

Then, to verify the generalization capacity of the developed neural model (concerning the evaluation and prediction of new impedance data), the set of signals monitored during the instrumentation phase was separated into two subsets of signals, being one for training the network (containing 125 randomly chosen signatures) and the other (including the remaining 55 signatures) for testing and validating the network.

Therefore, considering that the choice of each signature belonging to each set was made at random, the formulation of these sets was characterized by being unbalanced about the evaluated classes. Hence, the number of samples considered in each category is not proportional during the training stage. Thus, although the situation described implies a greater complexity in the processing of the model (since it makes it more sensitive to specific characteristics of the impedance signatures), it brings it closer to the real conditions of its operation since, in concrete monitoring situations, the symmetrical acquisition of signals for the different observed states is not always feasible.

In addition, during the training phase, a cross-entropy loss function was applied to the network responses to verify their accuracy in the target values. At the same time, Adam's algorithm (Adaptive Moment Estimation) adjusted the synaptic weights of the network for each iteration. The characteristic curve of the loss function values (whose final value is 0.000965) obtained in this step and the precision values (whose absolute value is 1) are also measured in Figure 16.
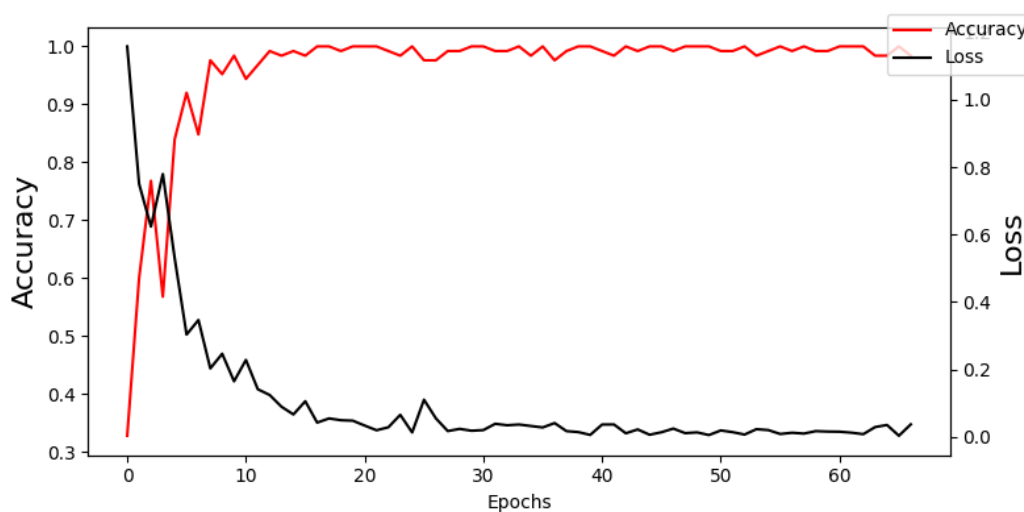
Figure 16: Loss and accuracy function achieved during the 1D-CNN neural network training process.

In Figure 16, when the model reaches the 30th epoch, the adjustment of the synaptic parameters of the network is almost negligible since the magnitude of the observed error is significantly tiny (≈ 0). Thus, even if in the training configurations of the convolutional neural network used, the number of predefined epochs was 1000, the *EarlyStopping* procedure was applied already in the 67th epoch, thus interrupting the training process and, subsequently, avoiding a possible condition of overfitting of the model.

As the last approach to be adopted in the present case study, the neural model developed here was then evaluated for its effectiveness through the confusion matrix, which compares the values predicted by the model and the target values already known from the structure integrity states. In this sense, Figure 17 compares the values predicted by the model and the pre-established target values for the same, both about the training and test sets.

From the above, it can be observed that the model developed is totally sensitive to the integrity classes imposed in the present case study, reaching 100% of accuracy for all the foreseen conditions, both concerning the training and the test set.

Thus, based on what has been exposed in this section, one can verify the efficiency and sensitivity of convolutional neural models in monitoring the structural integrity in iron plate-like structures. The damage condition is still given as reducing the thickness level of material used.

Furthermore, jointly evaluating the results of Sections 3.1 and 3.3, it can be inferred that the use of the 1D-CNN architecture in support of the SHM method based on electromechanical impedance becomes of great applicability, allowing with a certain level of precision, the delimitation of the states of the structural integrity of the evaluated systems, independently of the environmental and operational conditions applied to the experiment during the stage of acquisition of the monitoring signals.
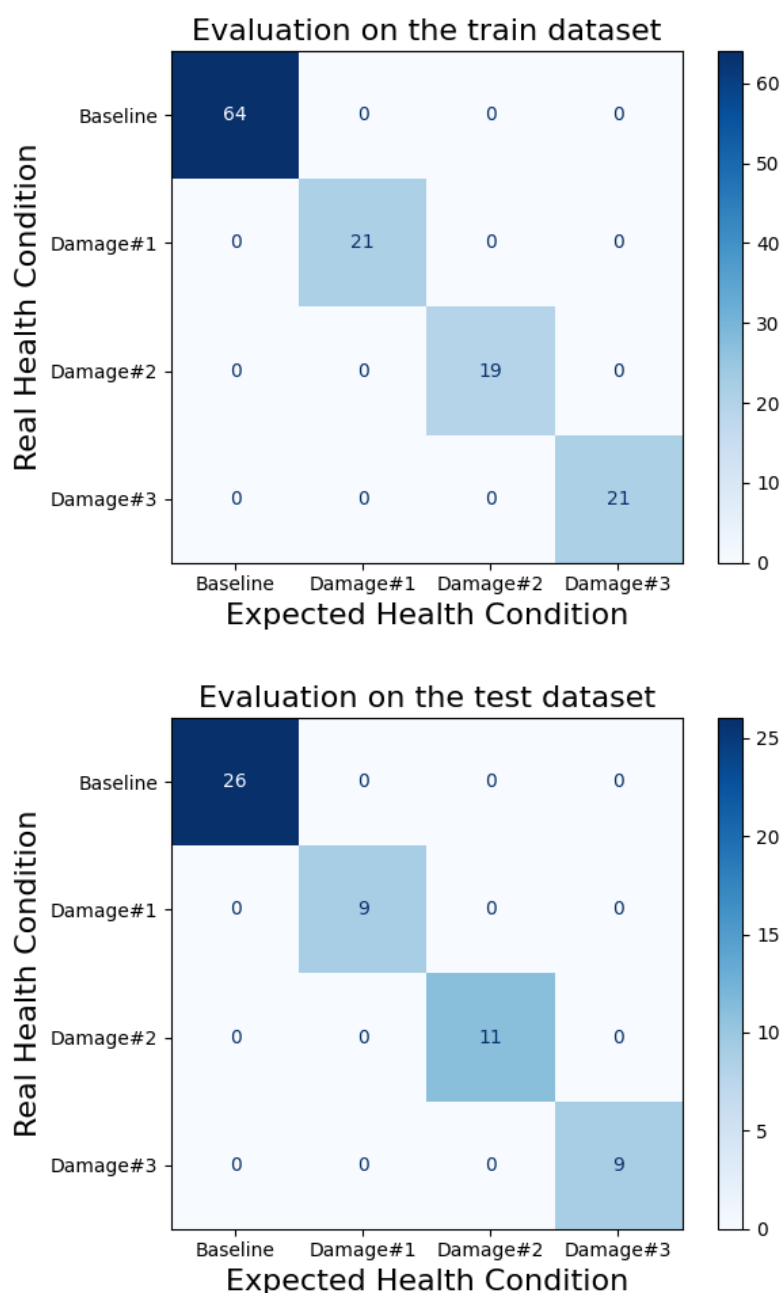
Figure 17: Confusion Matrix of the values predicted by the model in the thickness reduction experiment.

4. Final Remarks

As noted in the previous sections, deep learning models have great flexibility and the ability to represent complex physical phenomena. A peculiarity was observed in the use of CNN, specifically in classifying types of damage in structures due to the lack of a usual pre-processing of the data for temperature compensation. This is expected since Machine Learning techniques present demands of previous feature engineering tasks, unlike Deep Learning techniques that use mechanisms to explore relationships between features, eliminating data pre-processing steps. Still, in the exploratory set using the LSTM networks, it was possible to use these complex relationships to predict a complex

phenomenon such as corrosion in metals. In the final case study, using a plate extracted from a real fuel storage tank, it was possible to present the monitoring of the evolution of the loss of thickness, one of the main problems of corrosive wear explored by the oil and gas industry in this structural type.

Acknowledgments

References

S. Albawi, T. A. Mohammed and S. Al-Zawi. Understanding of a convolutional neural network. *International Conf. on Engineering and Technology* (ICET) (IEEE) pp. 1–16. 2017.

S. Abdoli, P. Cardinal and A. L. Koerich. End-to-end environmental sound classification using a 1d convolutional neural network. *Expert Syst. Appl.* 136 252–63. 2019.

M. Afshari. Vibration-and Impedance-based Structural Health Monitoring Applications and Thermal Effects. *Ph.D. thesis — Virginia Tech*, 2012.

A. Agarwal, A. Agrawal, V. Meruane and K. S. Sangwan. Development of a Machine Learning-Based Model for Damage Detection, Localization and Quantification to Extend Structure Life. *Procedia CIRP*, v. 98, p. 199-204, 2021.

B. P. Barella. Machine learning modeling applied to structural health monitoring systems. (In Portuguese: Modelagem com aprendizado de máquina aplicada aos sistemas de monitoramento de integridade estrutural). *156 f. Master's thesis, Modeling and Optimization, Federal University of Goias, Brazil. 2021.*

W. K. P. Barros, D. S. Morais and M. A. C. Fernandes. Skin cancer detection with artificial neural networks (In Portuguese: Detecção de câncer de pele com redes neurais artificiais). In: *XIII Congresso Brasileiro de Ciências da Computação*. [S.l.: s.n.], 2017.

J. P. M. Bento *et al.* Frequency range optimization by the use of ACO and BCO methods in the impedance-based SHM. In: *24th ABCM International Congress of Mechanical Engineering*. 10.26678/ABCM.COBEM2017.COB17-1363: COBEM, 2017.

T. D. Bispo. LSTM Architecture for Cross-Lingual Hate Speech Classification English-PtBR. (In Portuguese: Arquitetura LSTM para Classificação de Discursos de Ódio Cross-Lingual Inglês-PtBR). *Master's thesis, Computer Science/Smart Computing, Federal University of Sergipe*, *Brazil*. 2018.

A. H. Blanco, B. H. Flores, B. Tomás and B. N. Colorado. A systematic review of deep learning approaches to educational data mining. *Complexity*, *Hindawi*, v. 2019, 2019.

Z. Chen, C. Li and R. V. Sanchez. Gearbox fault identification and classification with convolutional neural networks. *Shock and Vibration*, v. 2015, 2015.

F. Chollet. Deep Learning with Python. [S.l.]: New York, NY, USA: *Manning Publications Co.*, 2017.

S. Cofre-Martel, P. Kobrich, E. Lopez Droguett and V. Meruane. Deep convolutional neural network-based structural damage localization and quantification using transmissibility data. *Shock and Vibration*, Hindawi, v. 2019, 2019.

N. Eleftheroglou, D. Zarouchas, T. Loutas, R. Alderliesten and R. Benedictus. Structural health monitoring data fusion for in-situ life prognosis of composite structures. *Reliability Engineering & System Safety*, v. 178, p. 40-54, 2018.

F. A. Freitas, R. M. Jafelice and J. W. Silva. A new data normalization approach applied to the electromechanical impedance method using adaptive neuro-fuzzy inference system. *J Braz. Soc. Mech. Sci. Eng.* 43, 475 (2021). https://doi.org/10.1007/s40430-021-03186-z

S. Ghazvineh, G. Nouri, S. H. H. Lavassani, V. Gharehbaghi and A. Nguyen. Application of 2-D Convolutional Neural Networks for Damage Detection in Steel Frame Structures. *arXiv preprint arXiv:2110.15895*, 2021.

N. S. Gulgec, M. Takáč and S. N. Pakzad. Structural damage detection using convolutional neural networks. In: *Model validation and uncertainty quantification, Volume 3. Springer, Cham*, p. 331-337. 2017.

N. S. Gulgec, M. Takáč and S. N. Pakzad. Convolutional neural network approach for robust structural damage detection and localization. *Journal of Computing in Civil Engineering, American Society of Civil Engineers*, v. 33, n. 3, p. 04019005, 2019.

A. Gulli and S. Pal. Deep learning with Keras. [S.l.]: *Packt Publishing Ltda*, 2017.

S. Hochreiter and J. Schmidhuber. Long short-term memory. Neural computation, *MIT Press*, v. 9, n. 8, p. 1735–1780, 1997.

S. Indolia, A. K. Goswami, S. P. Mishra and P. Asopa. Conceptual understanding of convolutional neural network-a deep learning approach. *Procedia Computer Science.* 132 679–88. 2018.

H. Komijani, S. Rezaeihassanabadi, M. R. Parsaei and S. Maleki. Radial basis function neural network for electrochemical impedance prediction at presence of corrosion inhibitor. *Periodica Polytechnica Chemical Engineering*, v. 61, n. 2, p. 128-132, 2017.

X. H. Le, H. V. Ho, G. Lee and S. Jung. Application of long short-term memory (LSTM) neural network for flood forecasting. *Water, Multidisciplinary Digital Publishing Institute*, v. 11, n. 7, p. 1387, 2019.

L. F. Leucas. Use of electromechanical impedance and Lamb waves techniques to identify damage in structures with rivets. (In Portuguese: Utilização das técnicas de impedância eletromecânica e ondas Lamb para identificação de dano em estruturas com rebites). 80 *f. Master's thesis, Mechanical Engineering. Federal University of Uberlândia, Brazil,* 2009.

W. Liang, L. Guixi and D. Hongyan. Dynamic and combined gestures recognition based on multi-feature fusion in a complex environment. *The Journal of China Universities of Posts and Telecommunications, Elsevier*, v. 22, n. 2, p. 81–88, 2015.

J. Melville, K. S. Alguri, C. Deemer and J. B. Harley. Structural damage detection using deep learning of ultrasonic guided waves. In: *AIP Conference Proceedings. AIP Publishing LLC*, 2018. p. 230004.

F. C. D. Menezes, K. P. S. O. Rodriguez Esquerre, R. D. A. Kalid, A. Kiperstok, M. C. D. O. Matos and R. Moreira. Artificial neural networks applied to the clotting process. (In Portuguese: Redes neurais artificiais aplicadas ao processo de coagulação). *Engenharia Sanitaria e Ambiental, SciELO Brasil*, v. 14, n. 4, p. 449–454, 2009.

S. M. Mhatre *et al*. A review paper on artificial neural network: A prediction technique. *International Journal of Scientific and Engineering Research* (IJSER), v. 8, p. 2229–5518, 2017.

F. Millstein. Convolutional neural networks in python: Beginner's guide to convolutional neural networks in python. *CreateSpace Independent Publishing Platform, North Charleston,* SC, USA, 2018.

J. R. V. Moura Jr and V. Steffen Jr. Impedance-based Health Monitoring for Aeronautic Structures using Statistical Meta-modeling. *Journal of Intelligent Material Systems And Structures*, v. 17, p. 1023-1036, 2006.

W. S. Na and J. Baek. A review of the piezoelectric electromechanical impedance-based structural health monitoring technique for engineering structures. *Sensors*, v. 18, n. 5, p. 1307, 2018.

Q. S. S. Nomelini, J. W. Silva, C. A. Gallo, R. M. Finzi Neto, J. R. V. Moura Jr and J. E. Ramos. Statistical Process Control (SPC) of Damage Metrics in the Impedance-based Structural Health Monitoring. *Revista Brasileira de Biometria*, v. 39, p. 7-24, 2021.

L. V. Palomino, J. R. V. Moura Jr, K. M. Tsuruta, D. A. Rade and V. Steffen Jr. Impedance-based health monitoring and mechanical testing of structures. *Smart Structures and Systems*, v. 7, p. 15-25, 2011.

R. J. Portsev and A. V. Makarenko. Convolutional neural networks for noise signal recognition *IEEE XXVIII International Workshop on Machine Learning for Signal Processing* (MLSP). 2018

F. Provost and R. Kohavi. Glossary of terms. *Journal of Machine Learning*, v. 30, n. 2-3, p. 271–274, 1998.

D. S. Rabelo, V. Steffen Jr, R. M. Finzi Neto and H. B. Lacerda. Impedance-based structural health monitoring and statistical method for threshold-level determination applied to 2024-t3 aluminum panels under varying temperature. *Structural Health Monitoring, SAGE Publications Sage UK: London, England*, v. 16, n. 4, p. 365–381, 2017a.

D. S. Rabelo, K. M. Tsuruta, D. D. Oliveira, A. A. Cavalini Jr, R. M. Finzi Neto and V. Steffen Jr. Fault detection of a rotating shaft by using the electromechanical impedance method and a temperature compensation approach. *Journal of Nondestructive Evaluation, Springer*, v. 36, n. 2, p. 25, 2017b.

Z. Rastin, G. Ghodrati Amiri and E. Darvishan. Unsupervised structural damage detection technique based on a deep convolutional autoencoder. *Shock and Vibration*, v. 2021, 2021.

S. W. F. Rezende, J. R. V. Moura Jr, R. M. Finzi Neto, C. A. Gallo and V. Steffen Jr. Convolutional neural network and impedance-based SHM applied to damage detection. *Engineering Research Express*, v. 2, n. 3, p. 035031, 2020.

S. W. F. Rezende, B. P. Barella, J. R. V. Moura Jr. Damage Identification of Vehicle Brake Disks by the use of Impedance-Based SHM and Unsupervised Machine Learning Method. *International Journal of Advanced Engineering Research and Science*, v. 7, p. 324-330, 2020.

S. W. F. Rezende. Deep Learning Techniques Applied to Electromechanical Impedance-based Structural Health Monitoring Method. (In Portuguese: Técnicas de aprendizado profundo aplicadas ao monitoramento de integridade estrutural por impedância eletromecânica). 2021. 143 *f. Master's thesis,   Modeling and Optimization, Federal University of Goias, Brazil.* 2021.

P. Sharma and A. Singh. Era of deep neural networks: A review. In: *IEEE. 8th International Conference on Computing, Communication and Networking Technologies* (ICCCNT). [S.l.], 2017. p. 1–5.

A. Sherstinsky. Fundamentals of recurrent neural network (RNN) and long short-term memory (LSTM) network. *Physica D: Nonlinear Phenomena, Elsevier*, v. 404, p. 132306, 2020.

R. B. Silva, F. I. Ferreira, F. G. Baptista, P. R. Aguiar, R. S. Ruzzi, H. B. Hubner and E. C. Bianchi. Electromechanical impedance (EMI) technique as alternative to monitor workpiece surface damages after the grinding operation. *The International Journal of Advanced Manufacturing Technology*, v. 98, n. 9, p. 2429-2438, 2018.

O. Trekhleb and L. Xie. Homemade Machine Learning - Interactive Machine Learning Experiments, GitHub. Available at: https://github.com/trekhleb/homemade-machine-learning#machine-learning-map. Accessed on: 03/06/2022, at 14:00.

K. M. Tsuruta, D. S. Rabelo, C. G. Guimarães, A. A. Cavalini Jr, R. M. Finzi Neto and V. Steffen Jr. Electromechanical impedance-based fault detection in a rotating machine by using an operating condition compensation approach. In: *International Society for Optics and Photonics. A Tribute Conference Honoring Daniel Inman*. [S.l.], 2017.

D. Verstraete, A. Ferrada, E. L. Droguett, V. Meruane and M. Modarres. Deep learning enabled fault diagnosis using time-frequency image analysis of rolling element bearings. *Shock and Vibration*, v. 2017, 2017.

S. Yan. Understanding LSTM and its Diagrams. ML Review: Machine Learning Research, Projects and Educational Materials. 2016. Available at: https://medium.com/mlreview/understanding-lstm-and-its-diagrams-37e2f46f1714.

W. Yu, F. Zhuang, Q. He and Z. Shi. Learning deep representations via extreme learning machines. *Neurocomputing*, *Elsevier*, v. 149, p. 308–315, 2015.

X. Zhao, R. L. Royer, S. E. Owens and J. L. Rose. Ultrasonic Lamb wave tomography in structural health monitoring. *Smart Materials and Structures*, v. 20, n. 10, p. 105002, 2011.

R. Zhao, J. Wang, R. Yan and K. Mao. Machine health monitoring with LSTM networks. In: *IEEE. 10th International Conference on Sensing Technology* (ICST). [S.l.], 2016. p. 1–6.

Chapter 14

Noise, Vibration, and Health and Usage Monitoring Systems (HUMS) of Aircraft Dynamic Components

Chapter details

Chapter DOI:

Chapter suggested citation / reference style:

Cruz, Alejandro R., et al. (2022). "Noise, Vibration, and Health and Usage Monitoring Systems (HUMS) of Aircraft Dynamic Components". *In* Jorge, Ariosto B., et al. (Eds.) *Fundamental Concepts and Models for the Direct Problem*, Vol. II, UnB, Brasilia, DF, Brazil, pp. 386–450. Book series in Discrete Models, Inverse Methods, & Uncertainty Modeling in Structural Integrity.

P.S.: DOI may be included at the end of citation, for completeness.

Book details

Book: Fundamental Concepts and Models for the Direct Problem

Edited by: Jorge, Ariosto B., Anflor, Carla T. M., Gomes, Guilherme F., & Carneiro, Sergio H. S.

Volume II of Book Series in:

Discrete Models, Inverse Methods, & Uncertainty Modeling in Structural Integrity

Published by: UnB City: Brasilia, DF, Brazil Year: 2022

Noise, Vibration, and Health and Usage Monitoring Systems (HUMS) of Aircraft Dynamic Components

Alejandro Rios Cruz[1]   Ariosto B. Jorge[2]   Bento S. de Mattos[1*]

Ronaldo V. Cruz[1]

[1]Instituto Tecnológico de Aeronáutica. E-mail: alejandro.cruz@ga.ita.br, bmattos@ita.br; ronaldoc@ita.br
[2]Post-Graduate Program - Integrity of Engineering Materials, University of Brasilia, Brazil. E-mail: ariosto.b.jorge@gmail.com

*Corresponding author

Abstract

This work is concerned with vibrations and noise in helicopters and turbofan engines. An overview of current and under research techniques to improve the detection of faulty components and Health and Usage Monitoring Systems (HUMS) tools are addressed in this book chapter. An overview of noise theory and existing sources in aircraft is carried out. Some applications with hybrid methods to measure the impact and extension of noise generated, by the landing gear, ice probes, and slatted-airfoil configurations are shown and discussed. Traditionally, system prognostics and health management (PHM) depend on sufficient previous knowledge of critical components degradation process to predict the remaining useful life (RUL). However, accurate physical or expert models are not applicable in most cases. The present work shows an example of how to predict engines' remaining useful life (RUL) by utilizing deep convolutional neural networks (CNNs). CNN is more often utilized for classification and computer vision tasks. The advantage of a deep learning approach is that the user does not need manual extraction or selection of features for models to predict RUL. Moreover, there is a need for pre-existing knowledge of machine health prognostics or signal processing to develop a deep learning-based RUL prediction model. The example uses NASA's Turbofan Engine Degradation Simulation Data Set (C-MAPSS). The data set contains run-to-failure time series for four diverse sets, which were simulated with combinations of operational conditions and fault modes. This example uses only one data set, which is further divided into training and test subsets. In addition, relevant noise sources in transport aircraft and rotorcraft are discussed. A turbofan engine code and another to predict the airframe noise of transport airplanes are employed in a multi-disciplinary design and optimization framework (MDO) to design a 78-seat airliner.

Keywords: noise, vibration in aircraft, health, and usage monitoring system, turbofan engine, convolutional neural network

1. Causes and effects of vibration in dynamic components

1.1 Rotorcraft

The study of the causes and effects of vibrations in dynamic components has become a continuous task for manufacturers of helicopters, engines, and transmission gears. Excitations come from all the possible sources of tan helicopters like main/tail rotors, engines, and transmissions. Vibrations may affect equipment performances and even cause some failures in the short term.

The FAR regulations concerning vibration safety on the helicopter can be summarized in the following way (1):

- §29.251 Vibrations:

  "Each part of the rotorcraft must be free from excessive vibration under each appropriate speed and power conditions"

- §29.1301d Function and installation:

  "Each item of installed equipment must function properly when installed"

- §29.1309a Equipment, systems, and installations:

  "The equipment, systems, and installations whose functioning is required by this subchapter must be designed and installed to ensure that they perform their intended functions under any foreseeable operating condition"

- §29.571 Structural fatigue: this paragraph is not under Dynamics and Vibration responsibility but Structure. Some objectives of equipment assessment:

  - Ensure that vibration does not affect the equipment's performance
  - Prevent vibration-related failures (dynamic fatigue phenomena)
  - Show compliance with FAR 29.251

There is a quest to implement techniques for minimizing the effects of these vibrations and early detection of their impact on the useful life of aircraft components. The usual measures to mitigate or reduction of vibration causes are suppression, absorption, reduction, isolation, or active/passive control of vibrations, or a combination of these techniques. As a result of all these efforts, several maintenance techniques have been developed, to be employed by the aircraft operator, which can be divided into two groups: reduction of the vibration levels and analysis of vibrations.

Vibration reduction techniques available for the helicopter operators focus on the adjustment of the blade track of the main and tail rotors, and/or in the correction of any imbalance present in these rotors, as well as any imbalance present in some specific dynamic components of the aircraft, such as gearboxes, main and tail rotor drive shafts, oil cooler fans, etc.

In a subsequent step, the user should concentrate his efforts on the vibration analysis, which consists in obtaining the aircraft vibration signature, i.e., the survey of the values of vibration amplitude versus frequency, carried out in pre-established locations and flight conditions, utilizing accelerometers and analyzers that directly provide a fault spectrum in the frequency domain.

The records of vibration signatures, duly filed, will form a vibration database of each aircraft type, which will be used as a starting point for the assessment of the vibration levels of a particular aircraft at a certain time of its useful life, allowing the detection, location, and identification of problems or defects, even when they are still incipient. Thus, vibration analysis would become an important predictive maintenance tool to monitor the wear and fatigue of components and reduce maintenance costs.

The reduction of vibrations found in helicopters has, among others, the objectives of (2):

a) Reduce the probability of failures in structural components before they reach their life limit. Such components have an estimated life, considering a certain magnitude of cyclic loads, acting on them. In this way, considering that there is a direct relationship between the vibration level of the structure and the cyclic loads acting, a high level of vibration shows that the structural components of the helicopter are being subjected to efforts beyond those estimated in its design and, consequently, present a high probability of in-service fatigue failures.

b) Minimize the effects of tiredness and fatigue on the crew. Prolonged and repeated exposure to vibrations of different frequencies, amplitudes, and directions can cause various types of aggressions that essentially consist of headaches, tinnitus, general malaise, feeling of drowsiness, general weakness, irritability, a reduction in the will and the ability to concentrate, a reduction in reflexes, a psychic depression as well as fatigue of the eyes and ears. Depending on their intensity and persistence, these disturbances can decisively contribute to pilot fatigue and helicopter accidents.

Each system of a helicopter generates vibration at a specific frequency and amplitude. Despite the main rotor rotating at a constant angular speed, it induces vibrations in many helicopter systems and subsystems. The analysis of vibrations parameters enables the mapping of the nodes and anti-node locations (Figure 2). At each rotor cycle about its axis, the loads caused by the rotor provoke cycled stresses on other systems. If a weight m is added to a determined system, it radically alters the vibration characteristics of that system. Put differently, the balanced mass shall alter the system's natural frequency to the same frequency of excitement. This way, the resonator cancels out the system's vibration.

To better explain the characteristics of the combination of masses and springs a system of two degrees of freedom is taken as an example. A system is defined as having two degrees of freedom when two coordinates are required to describe the motion. This type of system will also have two eigenfrequencies and two normal modes of vibration which, in turn, refer to the relationship between the amplitudes of the two coordinates for each corresponding eigenfrequency.

Free vibration, when subjected to an initial condition, will generally be the superposition of the two normal modes of vibration. However, if a forced harmonic vibration occurs with a given excitation frequency, the amplitude of each of the two coordinates will tend to a maximum at the two proper frequencies.

These characteristics are understood through the example presented in Figure 1. In this spring-mass system, which is used as a vibration absorber in helicopters, k_2 and m_2 are adjusted about the frequency of the exciting force, in such a way that the movement of the main mass m_1 (point B) is reduced to zero (3).

In fact, in Figure 1(b), it can be seen that:

1. for the interval $0 < \Omega < \Omega_A$, the two bodies are moving in phase with the excitation, as the two maximum amplitudes are positive. For frequencies close to 0, the displacements of the two masses are slightly different, depending on the stiffness and mass parameters. However, for $\Omega \cong \Omega_A$, the maximum amplitudes of the two masses tend to infinity. Therefore, Ω_A corresponds to the natural frequency of the 1st normal mode of vibration, which is related to the in-phase motion of the masses;

2. for the interval $\Omega_A < \Omega < \Omega_C$, the two bodies initially move in phase (but in opposition to phase with the excitation), since the two maximum amplitudes are negative, inverting the phase (a maximum amplitude positive and one negative) from $\Omega \cong \Omega_B$;

3. for the interval $\Omega_C < \Omega < \infty$, the two bodies move out of phase symmetrically, so that m_2 and m_1 are, respectively, in-phase and in phase opposition with the excitation. For $\Omega \cong \Omega_C$, the maximum amplitudes of the two masses tend to infinity, and then Ω_C corresponds to the natural frequency of the 2nd normal mode of vibration (masses in phase opposition).

It can also be verified that the amplitude X_1 will be null, when $\Omega = \Omega_B$, but, under these conditions, the absorber mass will be submitted to an amplitude $X_2 = -{F_0}/{k_2}$, since the mass-spring system k_2 and m_2 oppose each other to the disturbing force.
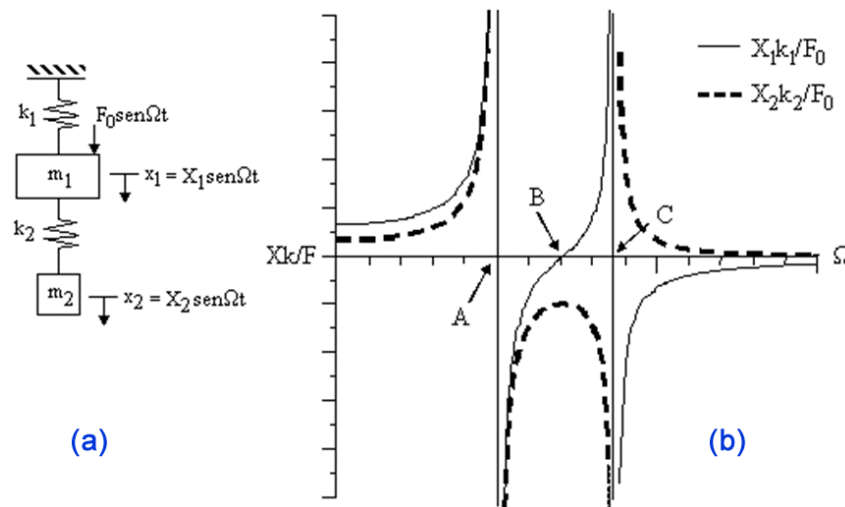
Figure 1: System with two degrees of freedom (3)

The spring-mass combination enables the development of resonators to mitigate vibration. The number of resonators and their location shall be determined to reduce the vibration amplitude to an acceptable minimum. Regarding the reduction of vibration levels suffered by the helicopter crew, some resonators are placed under the pilot and co-pilot seats (Figure 3) to mitigate vertical vibrations from the main rotor. In this case, the resonators are adjusted to mitigate the $nb\Omega$, where n is an integer number representing a multiple of the fundamental frequency of the rotor assembly, b is the number of the blades, and Ω is the rotation frequency of the main rotor. All harmonics will be transmitted to the fuselage but the first one will cause vibration with higher amplitudes.

The multiples of the fundamental frequency (2Ω, 3Ω, 4Ω, etc.) will cause noise and the amplitudes of their vibrations will be considerably lower (3).
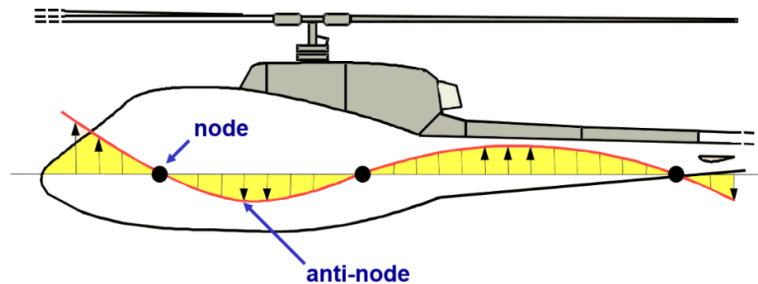
Figure 2: Vertical vibration amplitudes with no cabin resonators (adapted from (4))
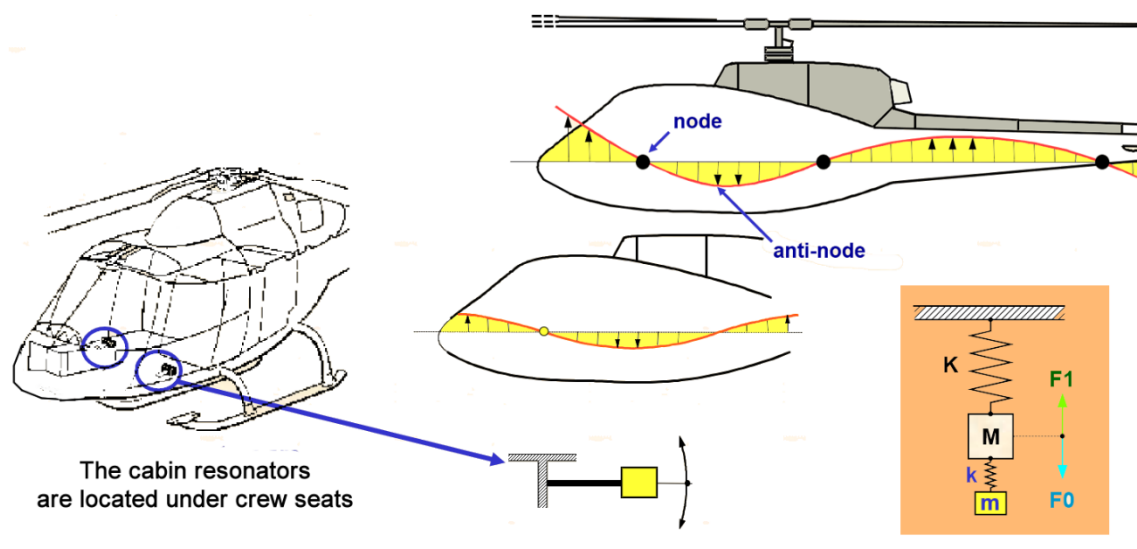
Figure 3: The addition of resonators reduces the vibration amplitude [Adapted from (4)]

The rule of thumb for blade weight and aerodynamic adjustment is that all the blades must be strictly identical in the spanwise sense (same weight and same weight distribution) and aerodynamically (same airfoil geometry). If so, there would be no problems and the rotor would then find flawless functioning. On the contrary, the rotor is unbalanced when the loads are not equal on all the blades. The rotation then induces periodical load variations generating vibrations, whose amplitude depends on the blade load differences.

Rotor blades must be statically and dynamically balanced. Regarding static balance, the blades should have the same static moment, defined as the product of the blade weight (W) and the lever arm, the distance of CG from the rotor axis. Balance weights are properly installed at the blade tips to obtain equal static moments. The weights modify both the blade weight and the blade CG location, i.e. its static moment.

The distance (d) between the CG. and the center of the lift induces a twisting moment, which deforms the blade and therefore the lift that is generated. As consequence, stresses are generated. One requirement for dynamic balance is that the distance (d) be the same for all blades to produce the same twisting moment. This condition is satisfied by adding blade tip balance weights at the front and rear of the airfoil (Figure 4). These weights move the chordwise CG. to adjust the distance (d).
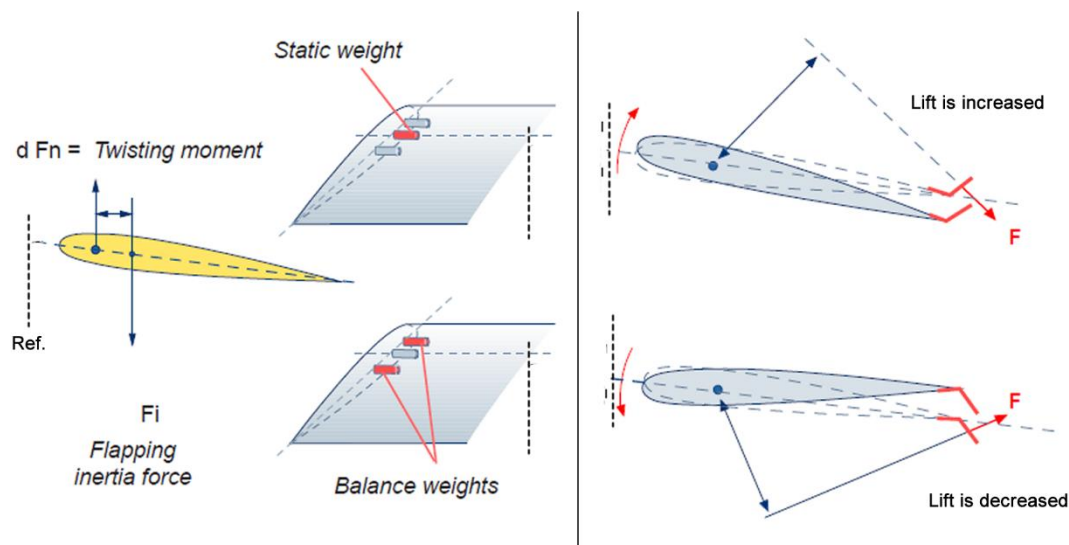
Figure 4: Dynamic balancing (5)

1.2 Turbofan and turboshaft engines

Turbofan engines find widespread use in commercial transport due to their advantage of higher performance and lower noise. The noise reduction for this kind of engine comes from combinations of changes to the engine cycle parameters and low noise design features.

During normal operation, airliners are steadily sending small packages known as ACARS (Aircraft Communication Addressing and Reporting System) to ground stations. Information is transmitted to orbiting satellites that relay the data to ground stations. Each package of messages is limited in size, but it is possible to send considerable measurements taken from the aircraft data computer and engine controllers.

The full authority digital engine (or electronics) control (FADEC) is a system consisting of a digital computer, called an electronic engine controller (EEC) or engine control unit (ECU), and its related accessories that control all aspects of aircraft engine operation. However, FADEC's main objective is to guarantee that the engine works within a prescribed operation envelope, lengthening this way its useful life. The fan speed is the parameter used to define the engine thrust. The FADEC controls the fan speed for the required thrust based on pressure altitude, temperature, and Mach number.

During take-off and cruise phases, information packages are always transmitted. Health Monitoring embedded systems acquire a lot of data (Big data), among them, meaningful indicators, and context information. Typically, information such as N2 (High-Pressure engine speed), EGT (Exhaust Gas Temperature), and FF (Fuel Flow) but also PS3 (static pressure after compressor) and T3 (temperature after compressor) and all associated context data are transmitted (6). Those last measurements give information about the compressor's behavior and help to differentiate compressor degradation from that of the turbine (6).

Helicopter jet engines consist of two stages. The first stage includes a compressor, combustion chamber, and turbine, and resembles the design of a traditional fixed-wing engine. This assembly is followed by the second stage, which is a free turbine, which must rotate at a constant angular speed. The second stage is coupled to the transmission system.

Engine turbines and compressors rotate at very high speeds and must be perfectly balanced for a flawless operation. Problems like disk cracks, blade cracks, and broken blades typically produce unbalanced rotation and are uncovered by monitoring vibration energy at the frequencies corresponding to the compressor and turbine rotating speeds.

Engine performance is gradually degraded throughout its lifetime. Performance must not be allowed to drop below a safe threshold. The engine condition is determined by measuring which engine temperature is required to deliver a given torque or thrust.

2. Health Usage Monitoring System for helicopters (HUMS)

HUMS stands for Health and Usage Monitoring System. Such a system is a common component on board modern helicopters. A helicopter counting with a HUMS experiences improvement in safety, comfort, and easier maintenance. Safety is improved due to the detection of abnormal and dangerous vibration levels. This allows the anticipate detection of cracks, misalignment, unbalance, and corrosion of shaft, bearings, and gears before they fail. Another HUMS benefit is the decrease of maintenance workload because a faulty component can be easily pinpointed. Maintenance becomes less expensive because on-condition maintenance can be then established for many components. From collected HUMS data it is possible to proceed with rotor balance, avoiding a specific technical flight to perform that task. More comfort is possible thanks to better tuning of the aircraft thanks to HUMS data.
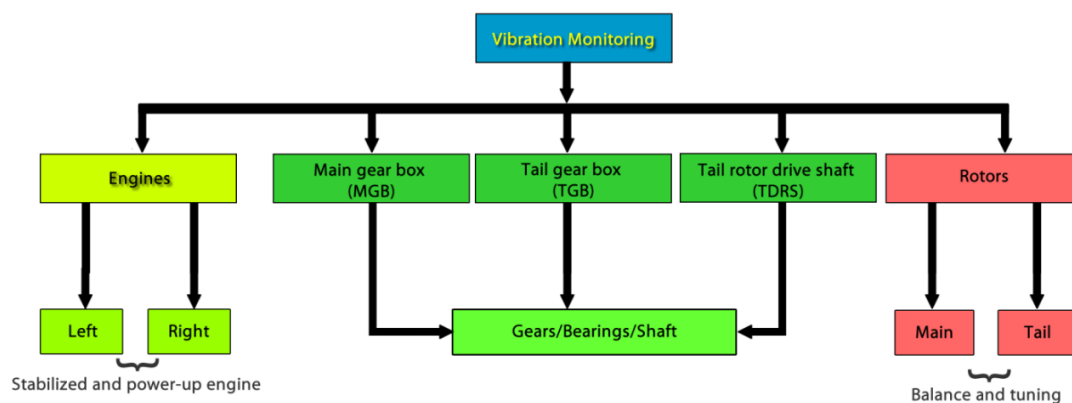
Figure 5: Typical helicopter components being monitored by health and usage monitoring systems (7)

The physical parameters that are measured by accelerometers are

- Displacement: x(t)

- Speed: $v(t) = \frac{dx}{dt}$

- Acceleration: $\gamma(t) = \frac{d^2x}{dt^2}$

Accelerometers utilize the piezoelectric properties to generate a time-domain signal. The health of mechanical components is estimated by the computation of trends and trend analysis by statistical analysis and deep learning tools. To detect anomalies in the functioning of components some analysis requires the Fast Fourier Transform (FFT) to be applied to time-domain a signal. FFT is the graph representation of harmonics in the frequency domain. Figure 6 shows a sound record in a helicopter cabin in its transformation in the frequency domain.

Accelerometers have not changed very much over time. The velometer is an accelerometer with an amplification & integration circuit built into each sensor's base (8). These additional parts ensure the signal is amplified and integrates the basic electrical output from the accelerometer (8). It then converts the direct measurement into a corresponding velocity signal or displacement reading, usually inches per second. In general terms, a velometer produces a more linear response over a far vaster frequency window than that of a basic accelerometer. It tends to be notably efficient at the medium frequency band.

The parameters which may be monitored by health and usage monitoring systems are extensive and may depend to some degree upon the precise engine/gearbox/rotor configuration. Table 1 contains a summary of some helicopter mechanical systems defects and their related indicators in the frequency domain.

Listed below some acquisition parameters together with the rationale for their use.
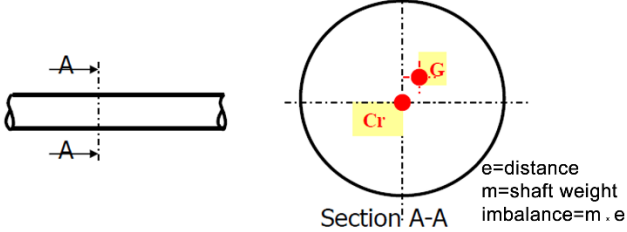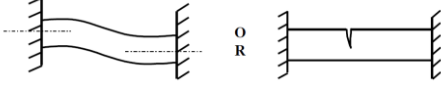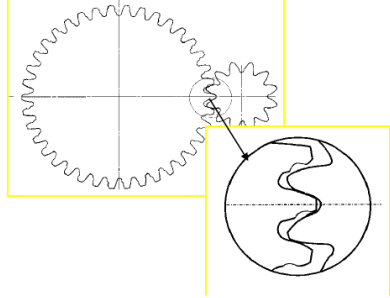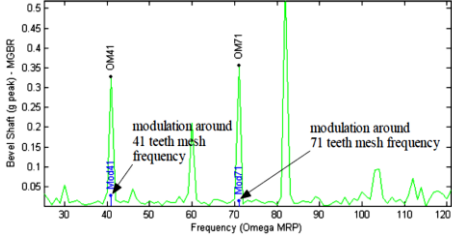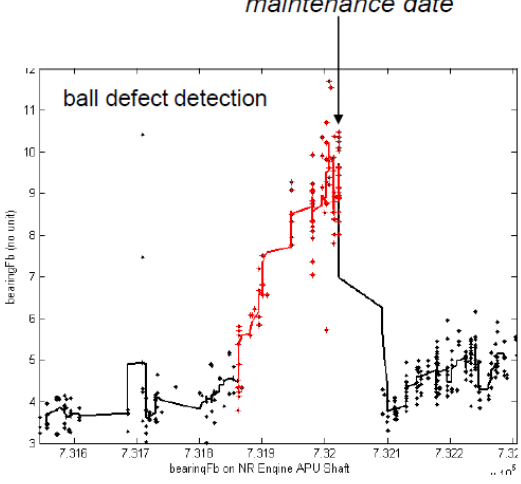
- Speed probes and tachometer generators: the measurement of speed is of great importance to ensure that a rotating component does not exceed limits with the risk of being overstressed.
- Temperature measurement: exceeding temperature limits or a rate of increasing temperatures is often a warning of a major component or system failure.
- Pressure measurement: a tendency to over-pressure or low pressure may be an indication of obstruction or a loss of vital system fluids.
- Acceleration: higher acceleration readings than normally recorded may indicate component overstress or an abnormal wear occurrence. The use of low-cycle fatigue algorithms may indicate blade fatigue which could result in blade failure.
- Particle detection: metal particle detection may indicate higher than normal metal composition in an engine or gearbox oil system resulting from abnormal or excessive wear of a bearing which certainly will fail.
- Signal oscillation: cause may be a defective sensor or a mechanical issue with gears. By building a space state plot of a correlation $\dot{R}(x, y) * R(x, y)$ the origin of oscillation can be determined.
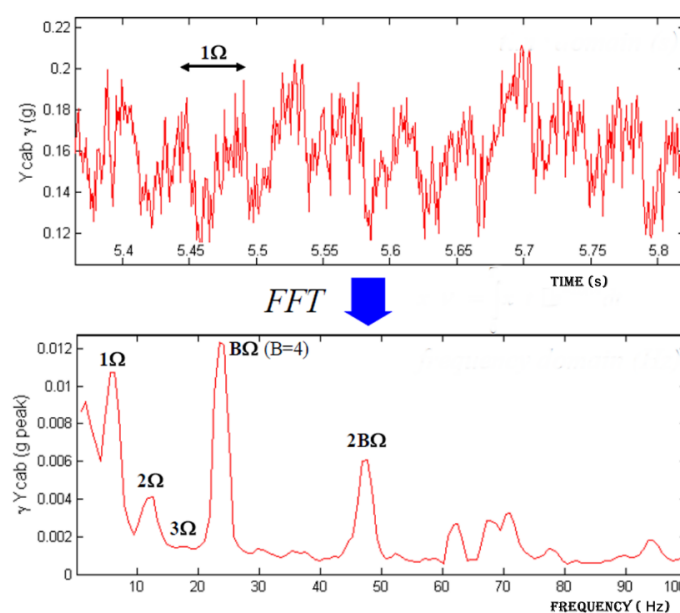
Figure 6: Direct FFT from the raw signal (B means the number of rotor blades, Ω is the rotor rotation) (7)

Table 1: Indicators in the frequency domain (7)

Frequency	Defects	Illustration
1Ω is the rotation frequency of the monitored rotor (or shaft)	imbalance, the result of torque loss, part damaging as crack	
2Ω is twice the rotation frequency of the monitored shaft or rotor	shaft misalignment, shaft cracks, rotor track (RTB)	
$x\Omega$ is the mesh frequency for gears	Gear tooth damage and weariness	
$Modx$ is the amplitude of meshing frequency sideband gears	Gear cracks or hub cracks	
F_i, F_e, F_b, and F_c (bearing indicators)	Bearing damages detection and location	

3. Noise

3.1 General considerations and physics

Noise pollution represents one of the main challenges to the aeronautical community due to the absolute necessity to reduce the noise exposure of the areas adjacent to airports or heliports. It is known that the noise exposure to the crew and especially the passengers and the people around landing and take-off areas represents a great issue.

Aircraft noise can cause community annoyance and has a large impact on people's health. There are records of restlessness in sleep, poor school performance, and increased risk of cardiovascular disease in people living in the vicinity of airports (9).

In some airports, noise restrains air traffic operations. The Frankfurt-am-Main Airport has introduced innovative noise abatement procedures. Respite periods are one of the measures brought about by the successful Dedicated Runway Operations (DROps) project. DROps operations gave affected communities scheduled breaks from aircraft noise at night or during the early morning hours (10). After this, the Alliance for Noise respite periods initiative to develop noise respite periods came into force. Many companies are part of the project and trial operations for noise respite periods started on 23 April 2015. This measure aimed to provide noise stoppage in combination with the six-hour nighttime curfew from 23:00 to 05:00 at the Frankfurt Airport. This affected some communities lying under approaches and departure routes (10).

The sound is a hearing sensation generated by a short time fluctuation of pressure. The sound mechanisms are emission (Figure 7), propagation, and reception.
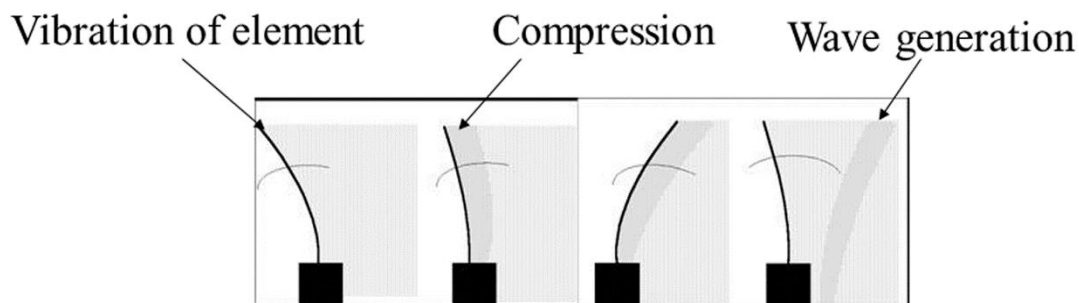
Figure 7: Emission of sound: no vibration, no sound (7)

The human ear does not have the same sensitivity to all frequencies. It is most sensitive at frequencies between 2 kHz and 5 kHz, and least sensitive at high and low frequencies, as illustrated in Figure 8. The long exposure to main rotor frequencies impacts instrument reading capability and causes fatigue and loss of control capacity.

Noise generated by aircraft is a particular case, as it has a wide variable spectrum and a transient intensity-time relationship. For this reason, special rating scales have been developed, which are based on sound annoyance rather than sound intensity, and which contain factors that consider special spectral characteristics and sound persistence. The intensity considered in this case is not the physical one, but the one that our ears perceive. Many other units, such as the dBA, were developed to assess the more general impact of present day-to-day noise and are associated with intensity. The Perceived Noise Level (PNL, which has the PNdB unit) and effective perceived noise (Effective Perceived Noise Leve - EPNL, which has the EPNdB unit) scales are related to the annoyance caused by

aircraft. However, the effective perceived noise level is a complex unit, so the use of dBA is more common to measure aircraft noise in some uses, including airport restrictions, where it is important that monitoring is as simple as possible. possible, and that is comparable with other sounds.

The human ear is sensitive to the timeframe it is exposed to incoming sound waves. The following pressure level is used to measure the exposure to sound

$$L_{eq} = 10 \, log \left(\frac{1}{T_0} \sum_i 10^{L_{Ai}/10} \Delta t_i \right) \tag{1}$$

where T_0 is a reference timespan (day, month, year) and L_{Ai} is dB(A) level during the period Δt_i

The following criterium is used to measure the effects of sound exposure on health (11):

$L_{eq} < 38 \, dB(A)$ *Sleep: keep quality*

$L_{eq} = 65 \, dB(A)$ *Office: strong discomfort, tired feeling*

$L_{eq} > 85 \, dB(A)$ *Workshop: risk of deafness increases with years of exposure*
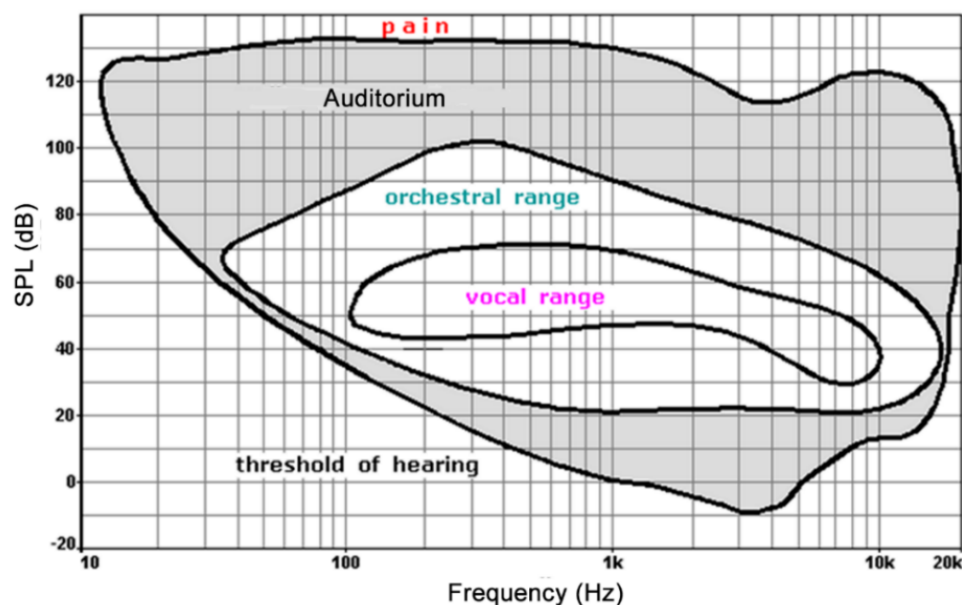
Figure 8: Human sound perception is highly dependent on frequency (11)

The main noise sources found in transport airplanes are shown in Figure 9 and Figure 10. Aircraft systems also generate noise: flight control actuators, auxiliary power units, air cycle machines, and others. Windows, gaps, rain gutters, handgrips, antennas, and skin ripples contribute to the thickening of the boundary layer and therefore increase airframe noise.

 Thanks to the advances in technology and the utilization of high-bypass turbofan engines the engine-generated noise has been reduced considerably. Thus, the noise generated by high-lift devices and landing gear has recorded a percentual increase at the landing and approach flight phases.
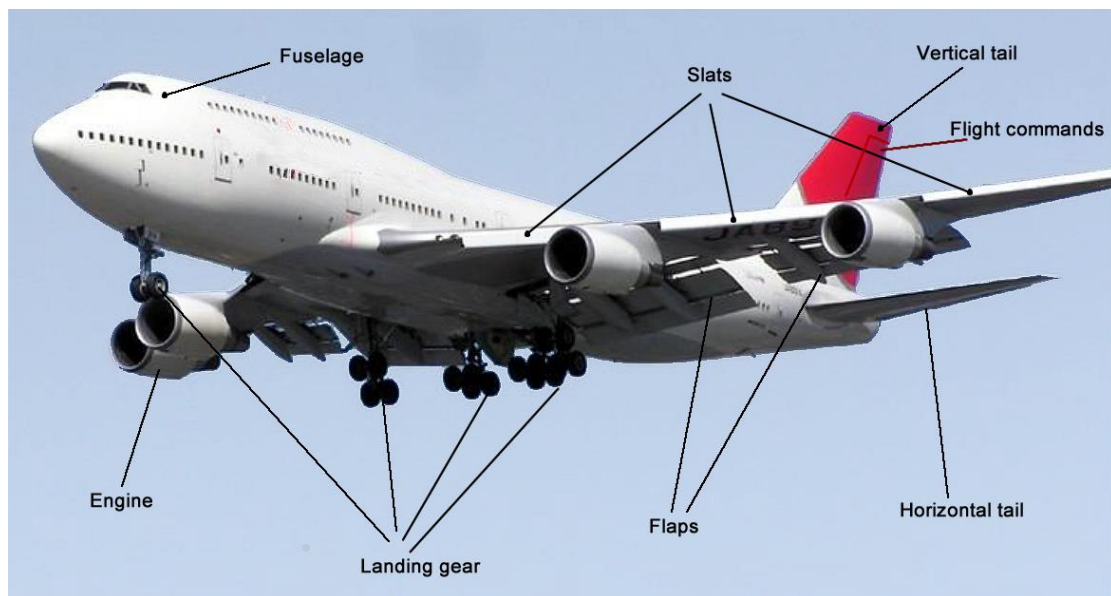
Figure 9: Airplane noise sources (12) [Edition of a public domain photo]

Airplane noise sources are normally divided into two basic groups: engine noise and airframe-generated noise. Each of these two groups is further divided into its components as shown in Figure 10 The noise of each of these components can be analyzed according to its origins as follows. Fan and compressor noise originates essentially from pressure fluctuations and interactions due to the airflow over rotating components. They are composed of **(12)**:

- Noise emitted from the fan or compressor inlet duct:

  - Broadband noise.
  - Discrete-tone noise.
  - Combination of tone noise.

- Noise emitted from the fan discharge duct:

  - Broadband noise.
  - Discrete-tone noise.

- Engine core noise originates from:

  - The process of combustion.
  - Flow around internal obstructions.
  - Scrubbing of the duct walls.
  - Local temperature fluctuations.
  - Flow throughout the turbine.
  - Turbine-blade and blade-stator interactions.
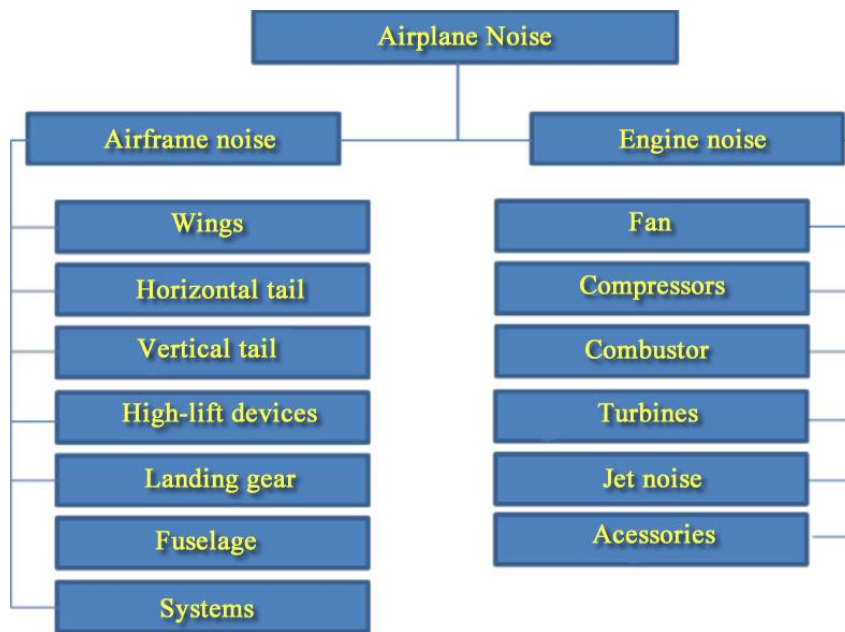
Figure 10: Airplane noise breakdown (12)

Figure 11 illustrates the procedure to calculate the effective perceived noise generated by a flying aircraft from widespread and known parameters.
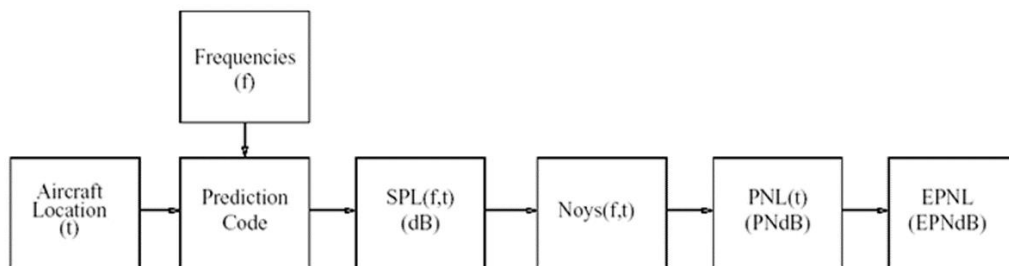
Noys: Adds weight to noise at frequencies considered more "annoying"

PNL: Combination of noys values, independent of frequency

EPNL: PNL corrected for spectral irregularities and duration

DNL: 24-hour averaged noise levels around airport

Figure 11: Calculating the effective perceived noise

It is important to differentiate sound pressure level (SPL) from sound power level (SWL). "Sound power or acoustic power is the rate at which sound energy is emitted, reflected, transmitted, or received, per unit time" (13). SPL depends on the distance and position/location of the source and the environment itself. Ambient, reflections on surrounding surfaces, and absorbing materials will influence the reverberation, sound propagation, as well as damping of the sound. Its unit of measurement is dB. SPW is not dependent on distance, position, or environment. This reveals a very important difference between both parameters. Indeed, SWL is a theoretical concept, and it is not directly measurable. Thus, a determined noise source presents the same sound power independent of its location and it provides a direct comparison between two sound sources.

At low frequencies, the absence of effective acoustic absorption materials requires the search for satisfactory alternative solutions for noise control, such as the application of reactive devices. The acoustic characteristics of reactive silencers are determined only by their geometric shape (without the use of acoustic absorption materials). These devices are designed in such a way as to let a fluid pass by greatly reducing its sound energy. As an example, one can mention compressor silencers, automotive engine exhausts, etc.

The principle of these silencers is based on the reflection of the waves to the source, that is, the waves, when passing through the silencer, find a change in the acoustic impedance of the medium, for a very large or very small value. Then, a small portion of the energy propagates through the silencer and most of the energy is reflected in the source. These silencers are economical and have a low-pressure loss of the loaded fluid.

3.2 Computational aeroacoustics

Only the hybrid or acoustic analogy methods method for the analysis of noise generation is addressed in this section. Here, the flow solution is decoupled from sound propagation. In this approach, the computational domain is split into different regions, such that the governing acoustic or flow field can be solved with different numerical techniques. There is a need for two numerical solvers: a dedicated Computational fluid dynamics (CFD) tool; and an acoustic solver. The flow field is then used to calculate the acoustical sources. Both steady-state and transient fluid field solutions can be used.

There are methods based on a known solution of the acoustic wave equation to compute the acoustic far-field of a sound source. Because a general solution for wave propagation in the free space can be written as an integral over all sources, these solutions are categorized as integral methods. The acoustic sources must be known from some different computations such as a finite element simulation of a moving mechanical system or a CFD simulation of the sources in a moving medium. The integral is taken over all sources at the retarded time (source time), which is the time at that the source is sent out the signal, which arrives now at a given observer position.

All integral methods cannot account for changes in the speed of sound or the average flow speed between source and observer position as they use a theoretical solution of the wave equation. When applying Lighthill's theory **(14)** to the Navier Stokes equations, volumetric sources can be obtained, whereas the other two analogies provide far-field information based on a surface integral. Acoustic analogies are cost-effective in terms of computational efforts, as the known solution of the wave equation is used. One observer distant from the source takes as long as one very close observer. Common for the application of all analogies is the integration over many contributions, which may lead to additional numerical problems because there is addition/subtraction of many large numbers with a result close to zero. In addition, when applying an integral method, usually, the source domain is limited somehow.

Lighthill acoustic analogy

The equation of Lighthill can be derived from the mass and momentum conservation principles (14). The intent is to evolve towards a wave equation in which the acoustic source terms are explicitly present. In this derivation, the absence of mass sources in the domain is assumed. The mass and momentum equations are then given by

$$\frac{\partial p}{\partial t} + \frac{\partial u_i}{\partial x_i} = 0 \tag{2}$$

$$\frac{\partial \rho u_i}{\partial t} + \frac{\partial u_i u_j}{\partial x_i} = \frac{\partial \sigma_{ij}}{\partial x_j} + f_i \tag{3}$$

where σ_{ij} is the stress tensor comprising the viscous stresses τ_{ij} and the static pressure is represented by p. The body force in the i-direction is given by f_i.

For a Newtonian fluid, the viscous stress tensor can be written in terms of viscosity and the gradient of the velocity field as stated in Eq. 4

$$\sigma_{ij} = \tau_{ij} - \delta_{ij}p \tag{4}$$

$$\tau_{ij} = \mu \left[\frac{\partial u_i}{\partial x_j} + \frac{\partial u_j}{\partial x_i} - \frac{2}{3} \frac{\partial u_i}{\partial x_i} \delta_{ij} \right] \tag{5}$$

If the time derivative of the mass equation and the divergence of the momentum equation are taken, these equations can be combined to obtain Equation (6). By linearizing the pressure and the density and subtracting the term $c_0^2 \frac{\partial^2 \rho'}{\partial x_i x_i}$ from both sides, (6) can be rewritten as (7). The linearization is carried out around the uniform free-field pressure and density. This is only valid for very small perturbations on the free field conditions, which is the case in general acoustics.

$$\frac{\partial^2 \rho}{\partial t^2} = \frac{\partial^2 (\sigma_{ij} + \rho u_i u_j)}{\partial x_i \partial x_j} - \frac{\partial f_i}{\partial x_i} \tag{6}$$

$$\frac{\partial^2 \rho'}{\partial t^2} + c_0^2 \frac{\partial^2 \rho'}{\partial x_i \partial x_i} = \frac{\partial^2 T_{ij}}{\partial x_i \partial x_j} - \frac{\partial f_i}{\partial x_i} \tag{7}$$

On the left-hand side, the wave equation is obtained for the perturbation of the density, with $\rho' = \rho - \rho_0$, where ρ_0 is a reference value in a medium at rest for density. In this equation, the right-hand side contains the acoustic source terms. The last term is the contribution of body forces. The T_{ij} is referred to as Lighthill's stress tensor and is given by

$$T_{ij} = \rho u_i u_j - \tau_{ij} + (p' - c_0^2 \rho')\delta_{ij} \tag{8}$$

The three terms of Lighthill's stress tensor that are responsible for the production of sound are:
* $\rho u_i u_j$ related to non-linear convective forces
* τ_{ij} viscous forces
* $(p' - c_0^2 \rho')\delta_{ij}$ is related to the deviation from isotropic conditions

The term $P_{ij} = p'\delta_{ij} - \tau_{ij}$ is the stress tensor that includes viscous stresses and $p' = p - p_0$ is the acoustic pressure, with p_0 taken as a reference value.

For turbulent flows, the viscous term in the Lighthill's stress tensor will be small and T_{ij} can be approximated by $T_{ij \approx} \rho u_i u_j$. Furthermore, if the Mach number is sufficiently small the density ρ can be replaced by the ambient value ρ_∞, resulting in the following equation for the acoustic density fluctuations

$$\frac{\partial^2 \rho'}{\partial t^2} + c_0^2 \frac{\partial^2 \rho'}{\partial x_i \partial x_i} = \rho_\infty \frac{\delta^2 u_i u_j}{\partial x_i \partial x_j} \tag{9}$$

Method of Ffowcs Willians and Hawkings

The Ffowcs Williams-Hawkings (FWH) equation represents an extension of the original work of Lighthill on the aerodynamically generated sound and governs the noise generated by a moving body immersed in a fluid. It is derived from the fundamental conservation laws of mass and momentum, expressed in terms of generalized functions, by representing the presence of the body as a *discontinuity* in the computational domain. These equations will reduce the computational expense in comparison to the solution of Curle's analytical solution (15).

The Ffowcs Williams and Hawkings wave equation can be derived from the Navier-Stokes equations. The idea of this derivation is to force every variable to be zero inside a predefined volume. To achieve this, the wave equation should be modified in such a way that it is valid in the whole flow domain. This way the free field Green's functions can be applied to the inhomogeneous wave equation in the entire domain. This manipulation is done by multiplying the Navier-Stokes equations by the Heaviside step function. This function has the following properties.

$$\begin{array}{l} H(f) = 0 \; for \; f < 0 \\ H(f) = 1 \; for \; f > 0 \end{array} \tag{10}$$

This implies that f < 0 inside the body and f > 0 outside the body therefore in the fluid domain. The function f is a function of the *x*-coordinate. Now let control volume be denoted by *V*, enclose the solid body, and denote the surface of the volume by *S*. Then function f must be chosen such that

$$\begin{array}{l} f(x) < 0 \; if \; x \in V \\ f(x) = 0 \; if \; x \in S \\ f(x) < 0 \; if \; x \notin V \end{array} \tag{11}$$

Now the Navier-Stokes equations are multiplied by the Heaviside function. This way the equations apply to the fluid domain and the variables inside the control volume are zero.

$$H(f) \left[\frac{\partial p}{\partial t} + \frac{\partial u_i}{\partial x_i} \right] = 0 \tag{12}$$

$$H(f) \left[\frac{\partial \rho u_i}{\partial t} + \frac{\partial}{\partial x_j} \{ \rho u_i u_j - \sigma_{ij} \} \right] = 0 \tag{13}$$

Combining these two equations and using the isotropic relation $dp = c_0^2 d\rho$, we obtain the Ffowcs Williams and Hawkings equations given by

$$\frac{1}{c_0^2} \frac{\partial^2 p'}{\partial t^2} - \frac{\partial^2 p'}{\partial x_i \partial x_i} = \frac{\partial^2}{\partial x_i \partial x_j} \{ T_{ij} H(f) \} - \frac{\partial}{\partial x_i} \{ [\sigma_{ij} n_j + \rho u_i (u_n - v_n)] \delta(f) \}$$
$$+ \frac{\partial}{\partial t} \{ [\rho v_n + \rho (u_n - v_n)] \delta(f) \} \tag{14}$$

Here u is the velocity of the fluid and v is the velocity of the surface. For both velocities the subscript i indicates the direction of the velocity and subscript n indicates the normal component. The $\delta(f)$ is the Dirac delta function, which appears from the gradient of the Heaviside function. In Eq. 14 again the sources of sound can be identified. The first term is the contribution by the quadrupoles in the volume as represented by the Lighthill stress tensor. The other two terms are due to the distribution on the control surface because the $\delta(f)$ is zero except at the surface, $f = 0$.

In the Fluent code (16), the contribution of the volume integral is neglected. This means that the quadrupole contribution of the Lighthill stress tensor is automatically excluded from the calculation. We end up with Eq. 15.

$$\frac{1}{c_0^2}\frac{\partial^2 p'}{\partial t^2} - \frac{\partial^2 p'}{\partial x_i \partial x_j} = -\frac{\partial}{\partial x_i}\{[\sigma_{ij}n_j + \rho u_i(u_n - v_n)]\delta(f)\} + \frac{\partial}{\partial t}\{[\rho v_n + \rho(u_n - v_n)]\delta(f)\} \qquad (15)$$

The result is quite simple. The first source term is often called the loading term because it represents the sound generated by the forces on the body. The second term is referred to as the thickness noise, which is related to the time-dependent fluctuation of the surface.

In the result presented in Eq. 15, the integration surface is of big importance. The surface should be chosen in such a way that it is valid to neglect the contribution of the Lighthill stress tensor. For flows with dominant acoustic regions, like the slat cove, this integration surface must enclose the region, so the contributions are considered. For low Mach number flows it is valid to exclude the Lighthill stress tensor, see Pan (17).

If the surface is chosen as the surface of the solid body, which is of course impermeable and non-moving, the relation for the sound production is further simplified to Eq. 16. As can be seen the forces of the fluid on the body are the acoustic sources.

$$\frac{1}{c_0^2}\frac{\partial^2 p'}{\partial t^2} - \frac{\partial^2 p'}{\partial x_i \partial x_j} = -\frac{\partial}{\partial x_i}[\sigma_{ij}n_j\delta(f)] \qquad (16)$$

Earlier reports, like Singer et al. (18), show that taking an off-body surface does not directly imply that the acoustic results will be better, even though an improved model is the case. Flow fluctuations on the body may dissipate and disperse numerically by the CFD computation before reaching the off-body surface. This will be verified with the cylinder test case by performing a simulation with an on-body integration surface and an off-body integration surface.

Eq. 17 can now be calculated using free field Green's functions in the same way as Curle's solution. The result is the pressure fluctuation generated by the unsteady forces.

$$p'_L(x,t) = \frac{1}{4\pi c_0}\iint_S \frac{(x_i - y_i)n_i\partial\sigma_{ij}(y, t_e)}{R^2 \partial t_e} \qquad (17)$$

where the subscript L denotes the pressure perturbation produced by the loading term.

3.3 Application of noise calculation in design and analysis cases

The cylinder and airfoil-slatted configuration analyses presented in this Section were performed by Tijmen Ton and Dennis van Putten during their internship program at Instituto Tecnológico de Aeronáutica.

Cylinder validation case

The flow over a cylinder with a diameter d = 1.9 cm was calculated. The flow is characterized by a freestream velocity of U_∞ = 69.19 m/s at standard sea-level conditions (19), which results in a Reynolds number of about Re_d = 90,000. All simulations of the present work were performed on a PC running a Windows operational system and fitted with an AMD® Athlon™ 64 4000+ (2.42 GHz) processor and 2 GB RAM.

A discussion about the aerodynamic and aeroacoustic validation quantities is part of the content of this case. Then the results of the comparative simulations are presented. At the end of this Section, the results of the best simulation will be presented in more detail and some conclusions will be drawn regarding the follow-up simulations. The time step of the simulations was 5 x 10^{-6} and the total time was 0.2 s.

To perform a qualitative analysis of the results, some appropriate flow quantities must be chosen to use as comparative tools. These quantities must be easily accessible and comparable. Even more important is that good experimental data about them must be available. In the next sections, this is discussed for both the aerodynamic and aeroacoustic aspects of the problem. The raw Sound Pressure Level (SPL) data obtained with Fluent is a noisy signal. This data is smoothed using a locally weighted least squares quadratic polynomial technique which is robust in the sense that is resistant to outliers. The same technique is used for smoothing the Fast Fourier Transformation (FFT) of the raw C_l data. The smoothed data is used to obtain the validation quantities. The aeroacoustic data is sampled from receiver 1, the upper microphone (Figure 12).
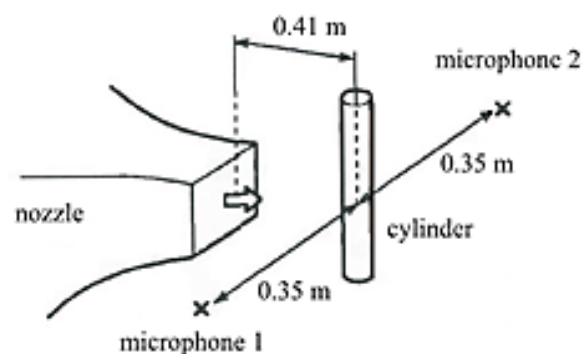
Figure 12: Experimental set-up by van der Kooi (20)

The aerodynamic flow properties that will be used to qualify the simulation results are the mean drag coefficient C_d, root-mean-square (RMS) drag coefficient $C_{d'}$, the mean lift coefficient C_l, the RMS lift coefficient $C_{l'}$ and the Strouhal number St. These quantities are defined by

$$C_d = \frac{D}{q_\infty d} \qquad C_{d'} = \frac{D'}{q_\infty d} \qquad C_l = \frac{L}{q_\infty d} \qquad C_{l'} = \frac{L'}{q_\infty d} \qquad St = \frac{f_s d}{U_\infty} \qquad (18)$$

In Figure 13, the drag coefficient of a circular cylinder is given for a wide range of Reynolds numbers. As can be seen, the Reynolds region of our interest lies in a plateau of nearly constant C_d = 1.2.
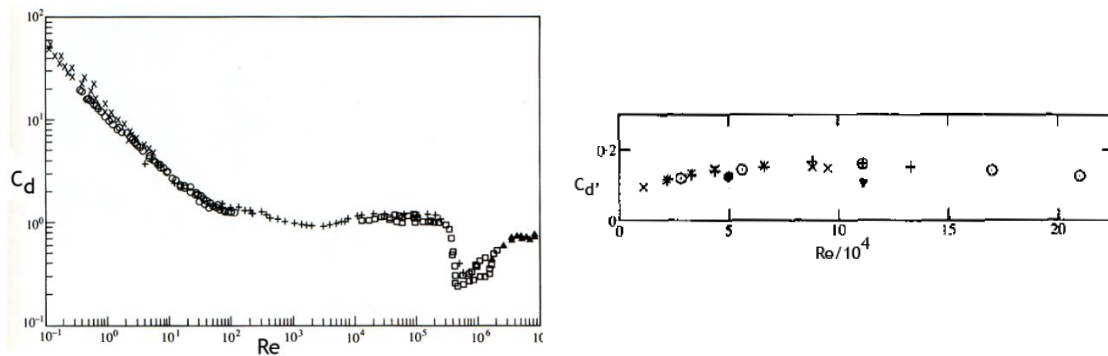
Figure 13: At left, drag coefficient vs. Reynolds number for a circular cylinder. At right, RMS drag coefficient function of Reynolds number (19)

The experimentally determined value of $C_{d'}$ can be found in Figure 12, which was presented by West (21). The reference value for $Re_d = 90,000$ is then $C_d' \approx 0.18$.

Regarding the flow over the cylinder, the mean lift coefficient is zero for obvious reasons. Experimental research on the time-varying lift of cylinder flow has focused on determining the RMS of the lift fluctuations. Despite a lot of efforts, however, researchers have yet not been able to agree on the correct value for $C_{l'}$ *(Re)*. In Figure 14, which is taken from Norberg (22), we consider $C_{l'} \approx 0.45 - 0.6$ for the current case under study.

The vortex shedding Strouhal number can be found in Figure 14 to be $St_{vs} \approx 0.19$. The figure was taken from Norberg (22).
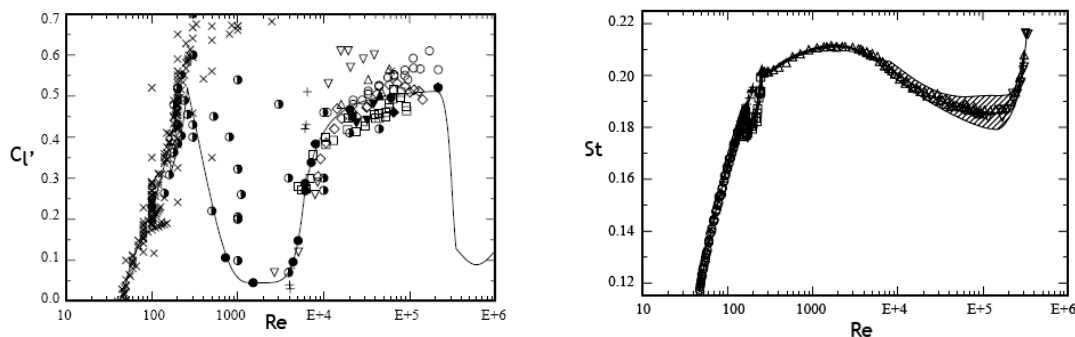
Figure 14: At left, RMS lift coefficient as a function of Reynolds number. At right, Strouhal number as a function of Reynolds number (19)

The aeroacoustic property of interest is the Sound Pressure Level (SPL) at some defined receiver locations. In the simulations, these locations were chosen to replicate the setup used by van der Kooi (20), which is depicted in Figure 12. Van der Kooi measured the SPL of a smooth cylinder at several Reynolds numbers. His results are displayed in Figure 15. The 73 m/s line corresponds to a $Re_d = 100,000$. The properties of most interest are the peak SPL and the Strouhal number St_{ps} at which this occurs. The interpolated peak SPL for $Re_d = 90,000$ is found to be around 107 dB at $St \approx 0.21$.
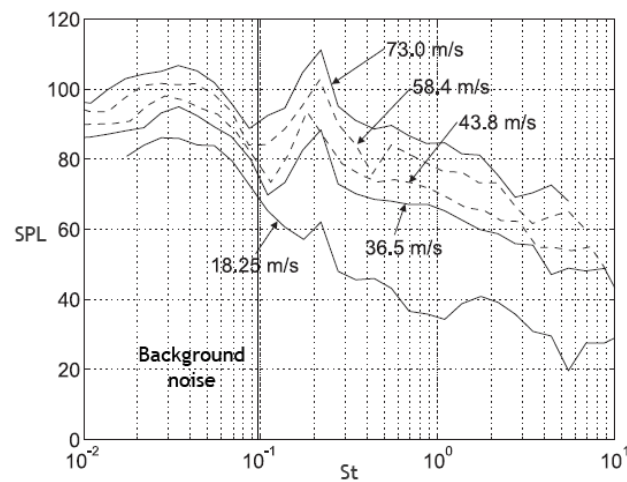
Figure 15: Sound Pressure Level as a function of Strouhal number (19)

Table 2: Summary of reference values (BM) for the benchmark cases (19)

Parameter	Value
C_d	1.2
$C_{d'}$	0.18
C_l	0
$C_{l'}$	0.45-0.60
St_{vs}	0.19
SPL (dB)	107
St_{ps}	0.21

The main conclusion from the literature study was that the influence of the SGS models on the results is quite small. To get some hands-on experience with the performance of the models it was however decided to make a comparison, nonetheless. When using the LDK model, the authors were not able to achieve convergence of the subgrid kinetic energy transport equation involved with this model. Therefore, this model was omitted from further use. All simulations were run with Interactive Time Advancing (ITA) time stepping and SIMPLEC pressure-velocity coupling. In the ITA scheme, within a given timestep, all the equations are solved in a blockwise loop until the convergence criteria for all equations are met. Thus, advancing the solution by one timestep normally requires several global iterations. With the iterative scheme, the non-linearity of the individual equations and couplings between equations are fully accounted for, eliminating the splitting error, which is caused by the segregation of the equations. This is usually overkill because the overall solution accuracy is limited by the time discretization error.

In Table 3, the results of the comparison are displayed. The differences between the results are not large. All models and Smagorinsky seem to overpredict the magnitude of the vortex shedding, because of which all values are slightly higher. Specially the fluctuation coefficients $C_{d'}$ and $C_{l'}$ are quite drastically overestimated. The agreement with the benchmark values is not fine. WALE and LDS are to be around 30% more expensive. The shedding frequency and the SPL are quite well approximated by the WALE simulation. Thus, WALE is used for all other simulations performed in this study.

Table 3: Comparison of SGS models (19)

Parameter	BM	Smagorinsky	LDS	WALE
C_d	1.20	1.486	1.433	1.525
C_d'	0.18	0.3409	0.3407	0.4555
C_l	0	0.0559	-0.0009	0.0007
C_l'	0.45-0.60	1.344	1.127	1.131
St_{vs}	0.19	0.2363	0.2258	0.1860
St_{ps}	0.21	0.2420	0.2253	0.2039
SPL [dB]	107	112.6	111.1	109.4
CPT [s]		1.07	1.37	1.35

One of the most important aspects of numerical analyses is the mesh characteristics. To evaluate the impact of mesh refinement on results three meshes were used in the calculations. The influence of wall treatment on the result is also investigated. The results of the normal grid simulation (which employs wall function) are compared to those obtained using finer meshes, which ought to resolve the full boundary layer structure. The simulations are denoted as coarse, intermediate, and fine. All simulations were performed with Non-Interactive Time Advancing (NITA) time stepping and the WALE SGS model. The NITA scheme performs a single global iteration per timestep. There are sub-iterations performed on the segregated equations within each time step, but the outer iteration (velocity-pressure iteration) is performed just once, hence the term *non-iterative*. This approach effectively drives the splitting error to the time discretization error, and it is nonzero. It must be noted that this method is only applicable for incompressible or flow with negligible compressible effects, which is the case of the present problem. The great advantage of the NITA method is the considerable decrease in computing time. Some sources give examples of a reduction in computational expense of 75% when using NITA instead of ITA. The results are displayed in Table 4 below.

Table 4: Results for different mesh sizes. BM is the reference value (19)

Parameter	BM	Coarse	Intermediate	Fine
C_d	1.20	1.202	0.6015	0.9788
C_d'	0.18	0.2902	0.1162	0.2332
C_l	0	0.0012	0.0352	0.0473
C_l'	0.45-0.60	0.9001	0.6232	0.9534
St_{vs}	0.19	0.2045	0.3027	0.2463
St_{ps}	0.21	0.2222	0.3038	0.2424
SPL [dB]	107	110.4	110.4	109.2
CPT [s]		0.55	0.51	1.78

The results of the finer meshes are somewhat disappointing. The finest mesh gives better results than the intermediate one but is in no way better than the coarsest mesh. In the intermediate case, two different vortex shedding frequencies could be distinguished. The true physical vortex shedding is not captured properly in this simulation. As observed by Piomelli (23) and Templeton (24) the near-wall vortical structures are of a very small scale, but dynamically important. SGS models are found to be incapable of capturing the correct physics associated with these small structures. This means excessively fine grid

resolutions must be adopted when using this so-called *solve-to-wall* approach. Refining the grid in a wall-normal direction creates cells with a bad aspect ratio, which in LES is found to give bad results. This means that all directions must be refined, because of which the necessary resolution approaches that of a full DNS simulation. In both the fine mesh simulations Fluent adopts the *solve-to-wall* approach, although the resolution is not nearly as high as necessary to capture the correct physics. This is probably the main reason for the failure of the finer mesh simulations. The wall-modeling technique used in conjunction with the coarse grid seems to perform adequately and will therefore be adopted in the other more complex cases. It should be noted that the comparison of CPT between the coarse and finer grids is not representative, because the structure of the grids (and their qualities, which influence convergence) differs somewhat. It is however clear that in the case the meshes are structurally comparable, a lower number of cells results in a lower expense.

This section will investigate the influence of the integration surface used in conjunction with the Ffowcs Williams and Hawkings Equation (Eq. 17). The mesh and integration surfaces used for the simulations were discussed previously. The results of the simulations are displayed in Table 5 below. Because the only difference between the simulations is found in the acoustics, only these quantities are given.

Table 5: Comparison of integration surface (19)

Parameter	BM	On-cylinder	Off-cylinder
St_{ps}	0.21	0.2087	0.2087
$SPL\ [dB]$	107	106.4	106.2

It appears that the assumption that the sound generated in the off-body region is negligible is indeed valid in this case. The choice of integration surface hardly alters the outcome. This is not the case for the slatted-airfoil configuration and will be discussed later.

The results presented here are the best ones (Table 6 and Table 7). Excellent visualization of the vortex shedding behavior is formed by a filled contour plot of the velocity magnitude, as given in Figure 16. The vortex shedding character is visible from the low/high-velocity pairs which indicate an alternating sequence of clockwise rotating vortices shedding from the upper side and counterclockwise rotating vortices that are shedded by the lower side.

Table 6: Aerodynamic coefficients for the circular cylinder (19)

Parameter	BM	NITA
C_d	1.20	1.202
C_d'	0.18	0.2902
C_l	0	0.0012
C_l'	0.45-0.60	0.9001
St_{vs}	0.19	0.2045

The SPL spectrum produced by this simulation is displayed in Figure 17. The included experimental data was obtained from an interpolation of the 73.0 m/s and 58.4 m/s datasets of van der Kooi to correct deviating Reynolds number. The agreement with the experimental data is very good. The peak SPL and its corresponding Strouhal number are predicted well. The global deviation is however around 12 dB, which is considerable.

Table 7: Aeroacoustics results for the circular cylinder (19)

Parameter	BM	NITA
St_{ps}	0.21	0.2222
SPL [dB]	107	110.4
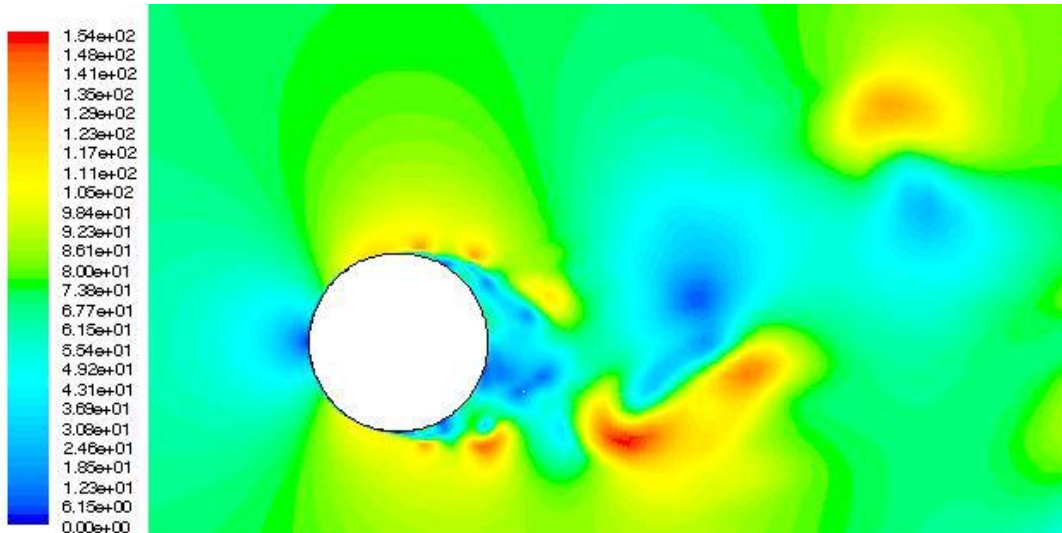
Figure 16: Contours of velocity magnitude @ time = 4.66 x 10^{-1} s. Simulation using NITA and WALE (19)
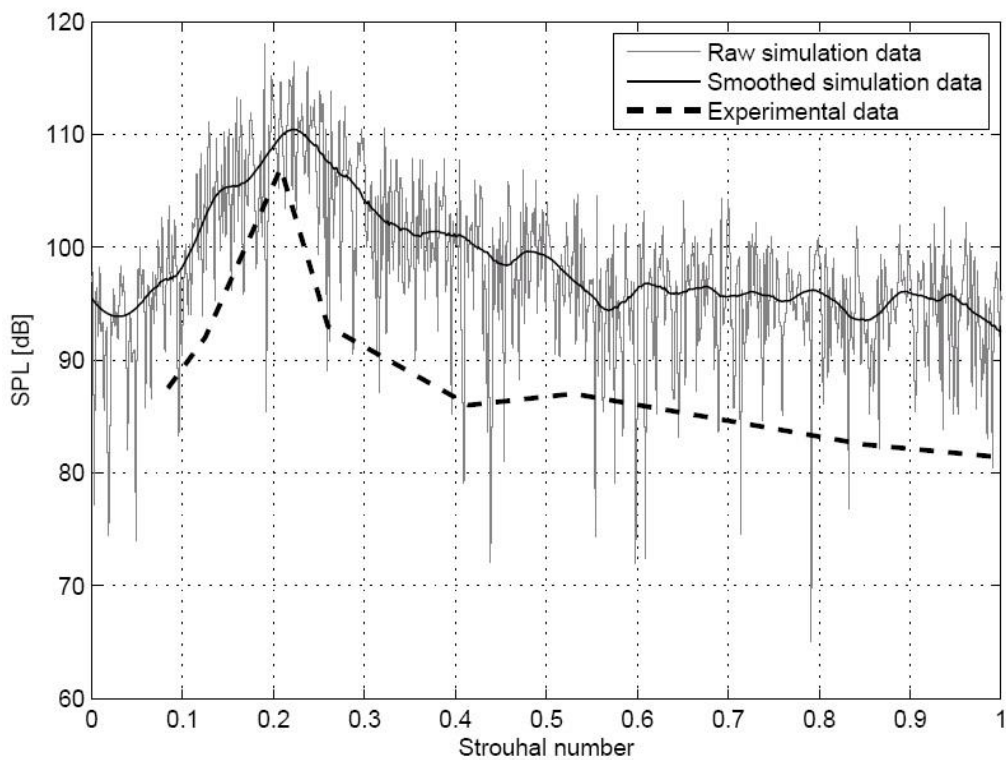
Figure 17: Sound pressure level at receiver 1 (19)

Airfoil with deflected slat

Most airframe noise is broadband in nature, with some low-frequency tones with low-frequency tones associated with cavities and discontinuities. Solid-body interaction with fluid may be related to the dipole noise source (25). In the quadrant where the slat noise is most present, the jet noise dominates. However, considering the low-noise signature of new generations of high by-pass turbofan engines, the slat noise may become the major contributor in this quadrant.

The flow over a deflected slat configuration is considerably complex and is characterized by a vortex in the slat cove region (Figure 18). One approach to reduce the noise caused by the deflected slat is to evaluate it with different horizontal and vertical separations to the main component of the airfoil and then utilize a surface response method to obtain the best configuration. However, techniques to reduce the noise level must consider the requirements of ice protection and the maximum lift coefficient provided by the slat.

The noise-generating mechanisms of slats are (25):

- Unsteady flow separation at the cusp of the slat
- Unsteady mass fluctuations in the slot
- Unsteady motions of the vortex in the slat cove region
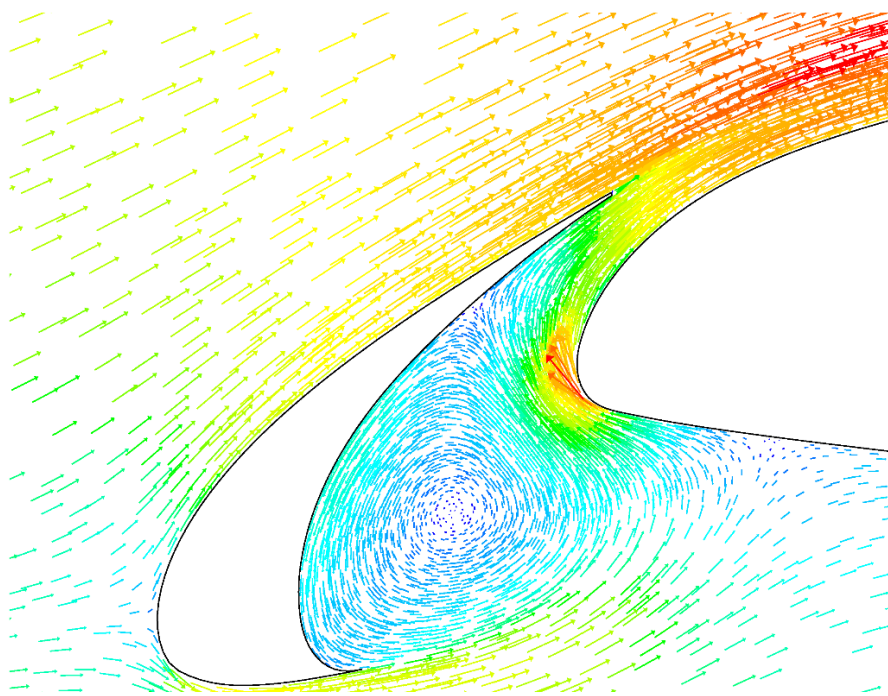
Figure 18: Navier-Stokes flow over a slat configuration showing a strong vortex behind the slat. The picture also allows for the inference of the location of the stagnation points on the slat and main airfoil ($M_\infty = 0.30, \propto = 0^o$)

An acoustic analogy is employed for the noise prediction of a slatted-airfoil configuration (19). The flow was simulated using Large Eddy Simulation (LES) approach and the acoustic propagation is successively calculated with the Ffowcs Williams and Hawkings method (26). For the LES a relatively fine mesh is required. The time step must be limited due to the acoustical calculation, and the spectrum was calculated for the whole audible range (20-20,000 Hz).

The geometry and computational domain of the high-lift airfoil are shown in Figure 19 and Figure 20. As can be seen in Figure 20, the slat and the slot region are bounded by the dashed line, representing a surface used for the computation of sound radiation. A report of Andreou (27) is used for validation of a numeric run that employed the Fluent code (16). The aeroacoustic measurements are done on the tunnel floor by an array of microphones. The vertical distance between the microphone array and the wing was 0.6 m. The use of two different arrays resulted in measurement with a frequency range between 2 kHz and 20 kHz. The validation of the simulation was performed in this bandwidth. The acoustical emission outside this bandwidth will be discussed as well. Especially the contribution in the audible range will be looked at.

Three measurements were performed at α = 6º, 10º, and 16º. Ref. (27) does not only discuss the aeroacoustics of the configuration but also provides important aerodynamic data. The acquired data was corrected due to the perturbation caused by wind-tunnel walls, wake vortex sheet hitting the wind tunnel, and blockage of the model that was tested.
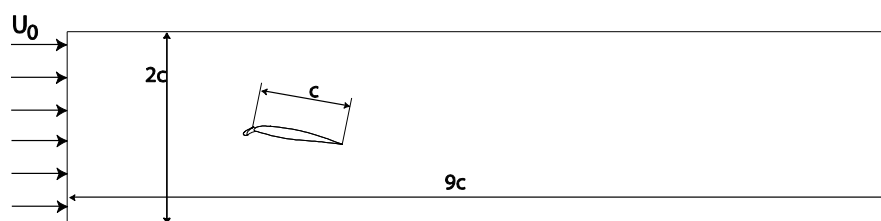
Figure 19: Computational domain for the airfoil slatted configuration (19)
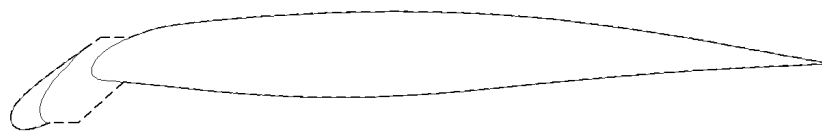
Figure 20: Airfoil configuration being investigated (19)

The report by Andreou focuses on the determination of the sources of sound. The setup with the microphone array can pinpoint the sources of sound. Figure 21 shows the experimental data for different frequencies at an angle of attack of 6º. The leading and trailing edge of the airfoil is indicated by the thick black lines. The slat is the main contributor to the noise generation of the overall configuration.
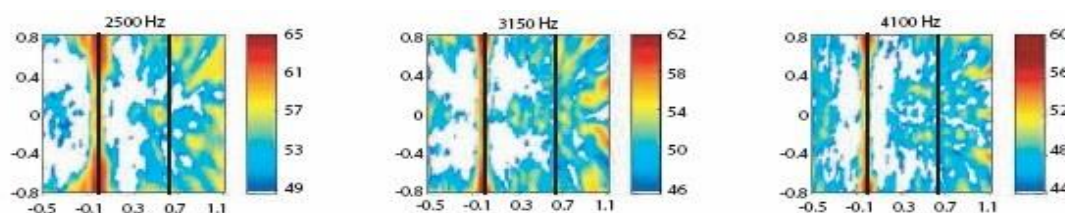
Figure 21: Sound pressure pattern for α = 6º (27)

The source location can also be determined with Fluent (16). This is done by plotting the source dipole strength on the surface of the slat and airfoil. Integrating this term over the surface will give the contribution of all the sources on the surface to a specified observation point. The source dipole strength is given in Figure 22 for α = 6º. The slat, the slot, and the leading-edge region of the main wing are the main sources of sound. The dipole strength on the upper surface of the main wing is not measured in the experiments and therefore is not shown in Figure 23. The source dipole strength for the case of 16º angle of attack is very strong at the upper surface. This indicates that there is a lot of noise

radiation upwards, which was unfortunately not tested in the wind tunnel. Also, the sound pressure level at the tunnel floor was measured in the experiment. Our corresponding acoustic simulation was performed with eight receivers at the lower tunnel floor, with the receivers 0.1 m apart. SPL was calculated at these receiver points. It was found that there is not a significant difference between the receivers. Therefore, the sound pressure level of the receiver below the slat is used for the comparison. In Figure 23 the experimental SPL data is given for different angles of attack.
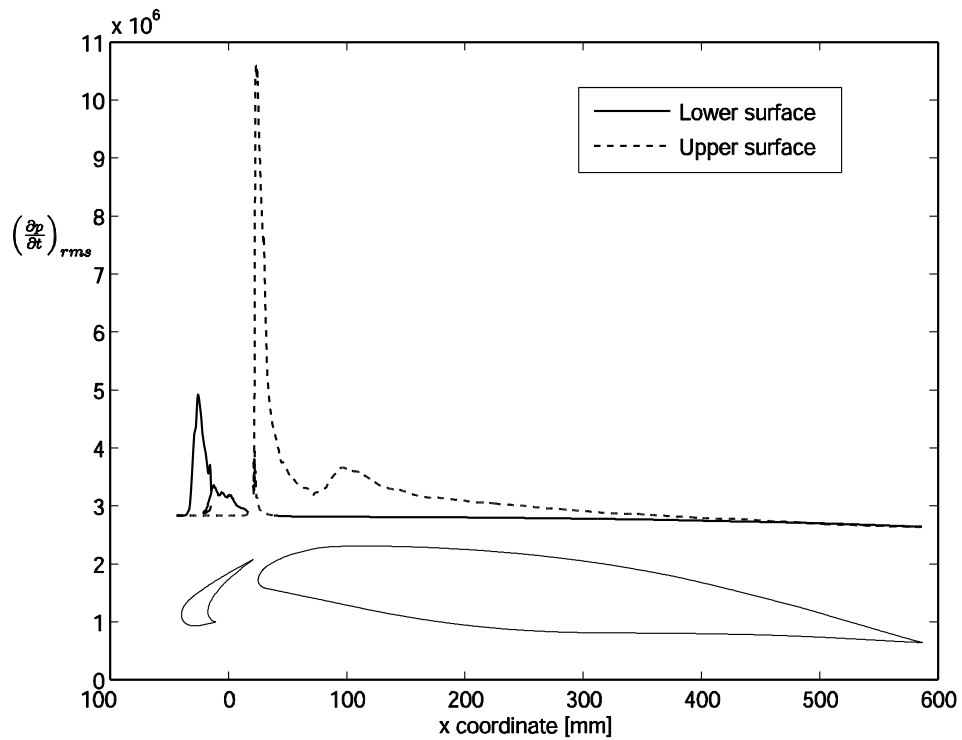
Figure 22: Source dipole strength along airfoil surface (α=6º) (19)
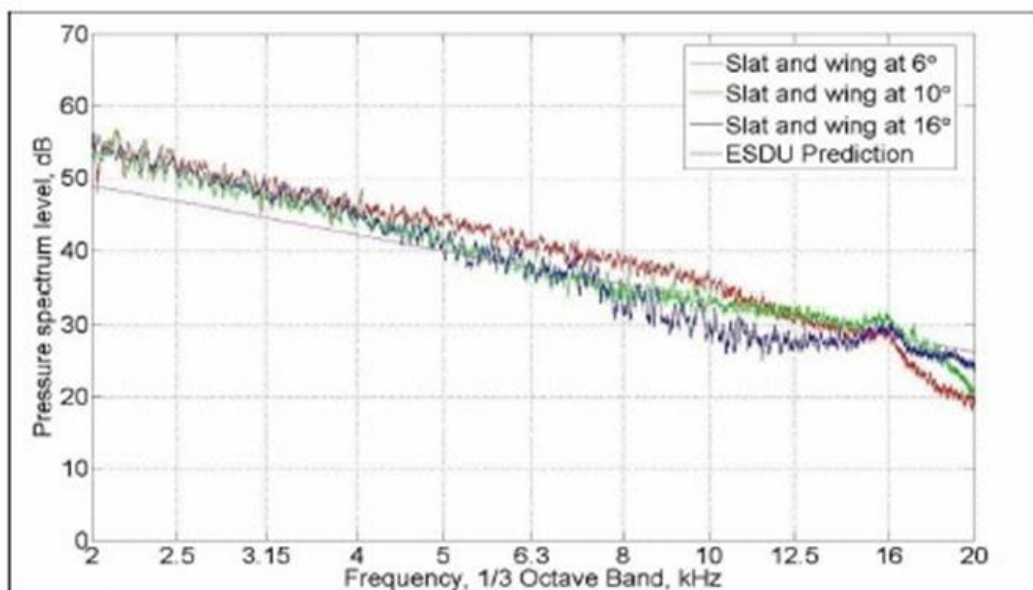
Figure 23: Experimental SPL for α = 6º, 10º, and 16º (27) (19)

The SPL over the frequency that was obtained with the numerical simulation is given in Figure 24. By using a weighted least squares method, the data is smoothed. In Figure 24, the dashed line is a regression of the experimental data, given in Figure 23. Depending on the frequency, the simulation overestimates the SPL from 5 up to 10 dB, so this result can be considered still satisfactory. The trend and specific peak frequencies must be captured properly, and the overall tendency was captured well up to a frequency of about 10 kHz. The decrease in accuracy in the high-frequency region may be accounted for by the mesh size. Literature on this topic states that often the smallest wavelength is resolved with denser meshes, specifically a refinement by a factor of about two is required, demanding a large mesh. To keep the computational expense at a reasonable level, the refinement was only applied to the slot region, because this region is the major source of the noise. The results of this simulation are shown in Figure 24.

(a) Initial grid   (b) Refined grid
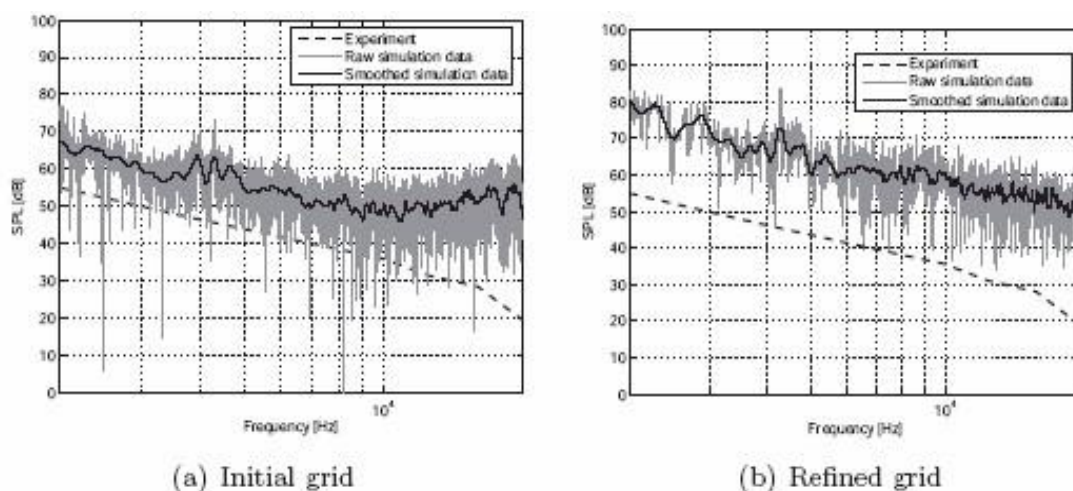
Figure 24: Experimental and computed SPL data for $\alpha = 6^\circ$ (19)

According to Figure 24, the results obtained with the finer grid are not better than those with the coarser mesh. In the low-frequency region, the simulation lacks accuracy. Despite this, the trend was better captured with the finer grid, but this is just an effect of the increased SPL deviation at low frequencies. We can therefore conclude that refining only the slot region is not enough to increase the accuracy of the sound emission prediction. The refining must be extended towards the source surfaces and especially to the lower surface of the slat. It is believed that refinement in these regions will increase the accuracy, and additional simulations are needed to support this claim.

The integration surface is introduced to capture more of the physics of the problem and to obtain a better simulation of the sound production. In the benchmark case, it is proven that for the cylinder the results did not differ much. For the simulation of the slatted-airfoil configuration, two integration surfaces were used to calculate the sound emission. The results of this calculation are shown in Figure 25. For these simulations, the refined grid was used to avoid dissipative effects in the slot region. The use of two separate integration surfaces which are at a close distance is physically not realistic. In the region between the surface, reflection plays a dominant role, but it is not accounted for by the method of Ffowcs Williams and Hawkings. By enclosing this whole reflective region, this problem is avoided, and reflection is considered. The on-body surface is indeed found to perform somewhat worse when looking at the trend line, as can be seen in Figure 25.

(a) On-body integration surface   (b) Off-body integration surface
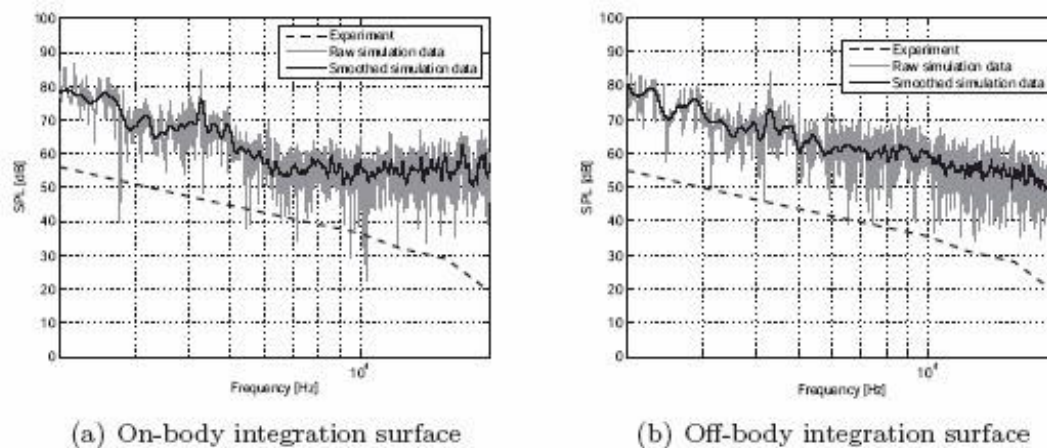
Figure 25: Sound generation from different integration surfaces (19)

In the experiment carried out by Andreou, only the frequencies between 2 kHz and 20 kHz were measured. However, the trend of the numerically obtained SPL shows that low frequencies are most dominant in the spectrum. From an engineering point of view, the bandwidth of interest extends to the low frequencies up to 20 Hz. The simulation was run long enough to also capture even lower frequencies; these results are shown in Figure 26. The region left out of the measurements of Andreou is indeed very interesting. Especially the region between 200 Hz and 1 kHz has a relatively high SPL. This region diminishes when the angle of attack is increased. This phenomenon can be ascribed to the boundary layer instability and the vortex shedding initiated from the instability at the lower slat surface. It only occurs at low angles of attack as will be clarified in the aerodynamic section.
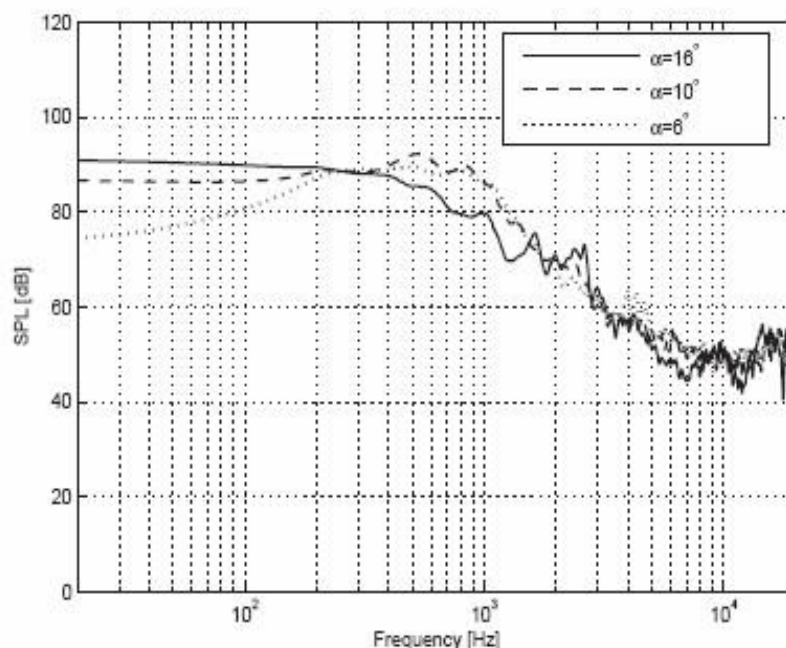
Figure 26: SPL for all angles of attacks in the audible range (19)

The same phenomenon causes the high source dipole strength on the lower slat surface, as shown in Figure 22. The instability in the boundary layer causes pressure fluctuations on the surface, which translates to sound emission. As the angle of attack is raised the boundary layer instability will occur at the upper surface of the slat.

The source dipole sound is caused by the instability of vortex formation in the boundary layer. These instabilities can be visualized by plotting the pressure distribution in the flowfield at a certain instant in time. This distribution is given in Figure 27 as the relative pressure deviation from the freestream pressure. The instability occurs at the upper surface of the main element. These fluctuations were also visible in the source dipole strength plot in Figure 22. There is also a large recirculation area visible in the slot. This region is affected by shear stress which originates from the slat trailing-edge flows.
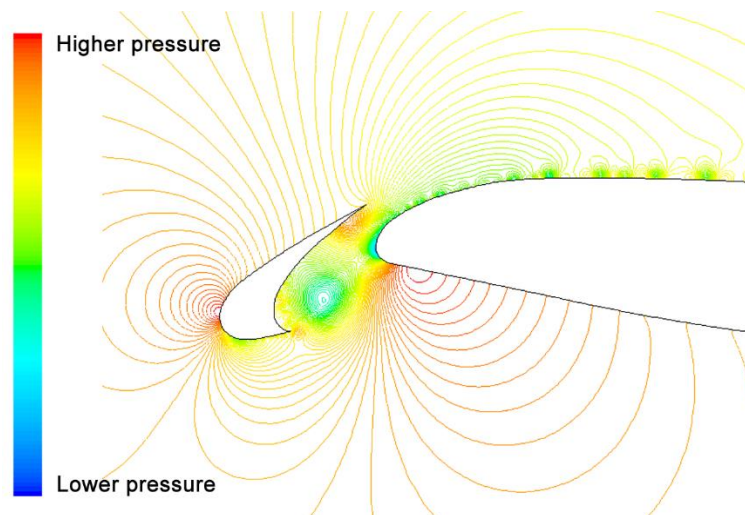
Figure 27: Iso-pressure isobar lines for α = 6º (19)

The boundary layer separation on the slat can be related to the pressure distribution on the surface. If the pressure gradient is negative the flow is accelerated, and the boundary layer will be stretched. This damps the instability and prevents the separation of the boundary layer. On the other hand, if the pressure gradient is positive, separation can occur and therefore the pressure coefficient gives a good estimation for boundary layer separation. For one instant in time the pressure coefficient along the surface is given in Figure 28. The pressure fluctuation on the lower surface of the slat is also clearly visible. Again, these results comply very well with the results found before. For graphical purposes, the slat geometry given in the Figure is stretched and does not comply with the real geometrical dimensions.
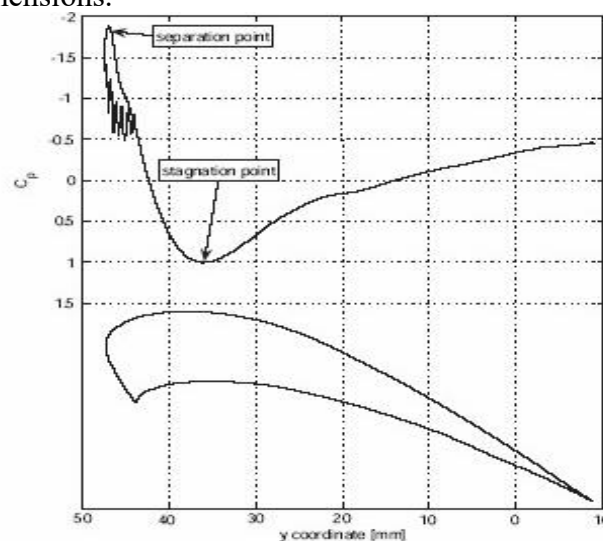
Figure 28: C_P Distribution on slat surface (α = 6º) (19)

The same can be done for the main element. Here the instability occurs at the upper surface. The pressure fluctuations are present over the whole upper surface (Figure 29). The wavelength of the fluctuations increases when traveling towards the trailing edge. This indicates that small eddies are generated near the leading edge and are convected with the flow while increasing in size. As stated before, the scale of the eddies is roughly proportional to the wavelength of the sound radiation. This means that the emission near the leading edge is relatively high-frequent and near the trailing edge low frequent. The scales of the eddies can be visualized using iso-pressure contours. This is done in Figure 30. On the lower surface a negative, or adverse, the gradient is maintained over almost the whole surface, except for the region from half the chord length up to the trailing edge. Here the pressure shows some harmonic oscillations around a nearly constant value. These fluctuations are however very small. They are caused by small eddies that are shedded from the point where the geometry changes suddenly and convected along the surface.
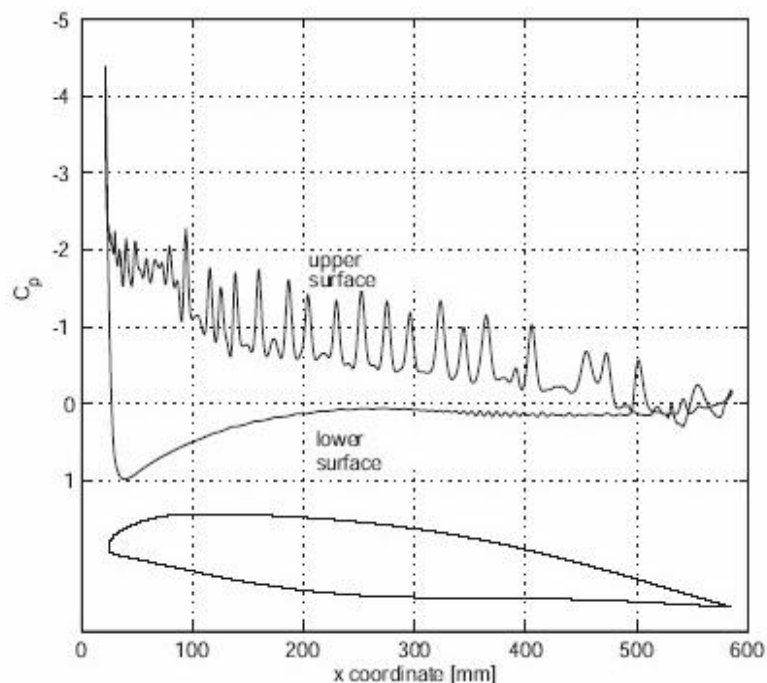
Figure 29: C_P distribution on the main element at $\alpha = 6^\circ$ (19)
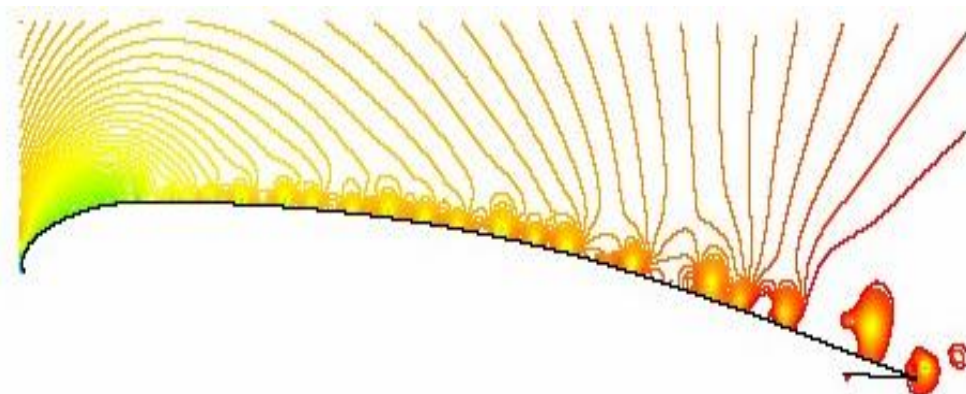
Figure 30: Iso-pressure contours on the main element at $\alpha = 6^\circ$ (19)

Landing gear of a long-haul airplane configuration

White noise consists of a simultaneous combination of sounds of all frequencies. The adjective white is used to describe this type of noise in analogy to the functioning of white light, given that this is obtained through the combination of all chromatic frequencies. Proudman (28), using the analogy of light waves with acoustics, derived a formula for the acoustic power generated by isotropic turbulence without mean flow. More recently, Lilley (29) again derived the formula but this time accounting for the delay time difference which was neglected in Proudman's original derivation. Both derivatives gave an acoustic power yield acoustic power due to the unit volume of isotropic turbulence (in W/m^3). Equation summarizes the relationship between acoustic power and flow variables:

$$P_A = \alpha \rho_0 \left(\frac{u^3}{l}\right)\frac{u^5}{a_0^5} \tag{19}$$

where u and l are the turbulence velocity and length scales, respectively, and $\boldsymbol{a_0}$ is the speed of sound. The parameter α in Equation 19 is a constant. In terms of k and ε, Equation 19 can be rewritten as

$$P_A = \alpha_\epsilon \rho_0 \epsilon M_t \tag{20}$$

with

$$M_t = \frac{\sqrt{2k}}{a_0} \tag{21}$$

Ansys Fluent (30) uses the above model to compute the acoustic power level in dB

$$L_P = 10\, log\left(\frac{P_A}{P_{Ref0}}\right) \tag{22}$$

A CFD simulation for an airplane similar in configuration to the A340 was carried out with Ansys Fluent (30). Some characteristics of this CFD run

- Freestream Mach number of 0.14 and 3° angle of attack.
- Fluent's density-based implicit algorithm was chosen to run the simulation.
- A realizable k-ε turbulence model with standard wall treatment was employed. Corrections for curvature and compressibility were considered.
- The airplane analyzed was modeled with main and nose landing gear extended, including some doors at the open position.
- Airplane geometry and initial surface mesh were generated with the open-source code Sumo (31).
- The final computational mesh is comprised of 7,923,665 tetrahedra.
- Mesh adaptations were performed to smooth absolute gradient values and keep the y^+ parameter within reasonable values.

Contours of surface acoustic power [dB] can be seen in Figure 31 for the main landing gear and the entire aircraft. the corner of the landing gear compartment generates considerable noise. Rounding off this edge would certainly contribute to a significant reduction in the noise level. The downstream pair of wheels is a considerable source of noise, as it receives the flow that was decelerated and separated from the front ones. Figure 32 Shows streamlines colored by velocity magnitude released in front of the main landing gear. The flow is highly disturbed by the front wheels and other cylindrical parts of the landing gear assembly.
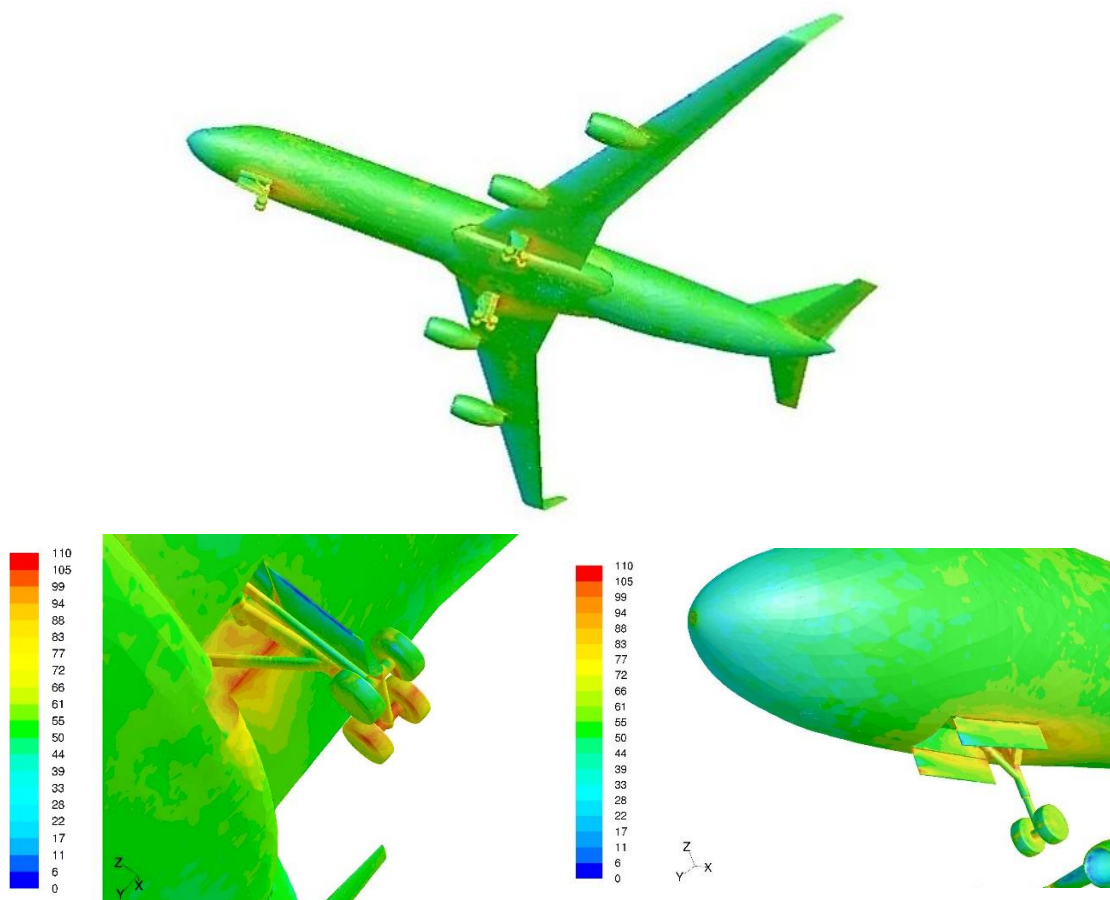
Figure 31: Contours of surface acoustic power level [dB]

The bogie incidence relative to the fuselage centerline (Figure 9 and Figure 32), as already present in many aircraft configurations, contributes to the noise reduction because a part of the wake originating on the front wheels does not impinge on the wheels located downstream. This arrangement also contributes to less mechanical vibration in the landing gear assembly. Cao et al. (32) studied the effect of the bogie pitch angle on the structural design during touchdown. Their results indicate that the overload of main landing gear, drag force, and maximum stress decrease as the initial bogie angle increases. However, the total force of the snubber increases when the initial truck angle increases. Increasing the initial bogie pitch angle at touchdown increases structural robustness (32).
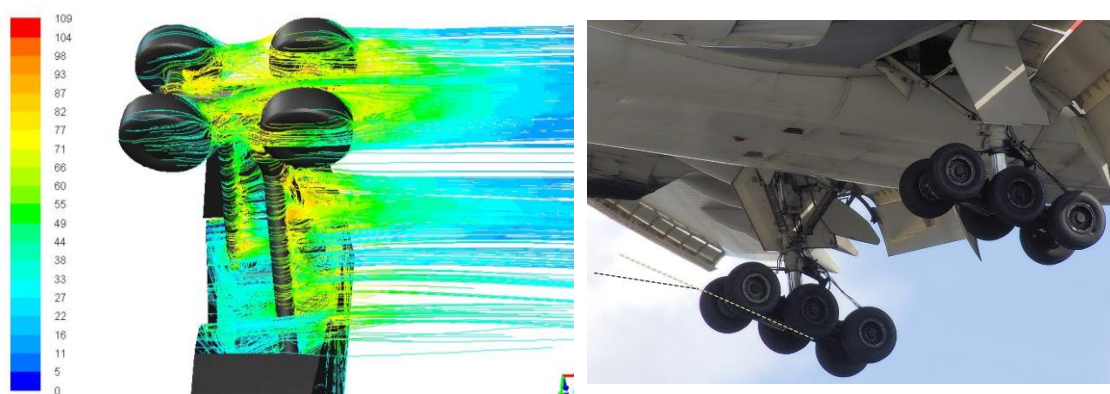
Figure 32: *Left* **- Streamlines close to the main landing gear of the four-engine airplane. Colors are related to acoustic power level [dB]** ($M_\infty = 0.14, \propto= 3^o$)**.**
***Right* - Misalignment of wheels pairs (Photo: Adrian Pingstone, public domain)**

Ice detector

The front fuselage of airplanes must accommodate flight instruments, primary flight control, and the nose landing gear. Externally, it hosts several probes that are vital for the safety of the flight such as angle of attack sensor, total temperature probe, Pitot tubes, and ice detectors.

As ice accretes on the vibrating probe (Figure 33), the nominal natural frequency is reduced due to the ice mass. Reduction of the probe frequency below a predetermined threshold causes changes in a reference signal and the system is then activated, thus causing the protected surfaces to be deiced.

Most ice that builds up on aircraft surface owes its constitution to droplets with a size between 15 and 50 μ. An aircraft certificated to fly into known icing conditions can sustain flight in stratus-type clouds with droplet Median Volume Diameters (MVD) up to 40 μ; and flight in cumulus clouds with droplet MVDs up to 50 μ. Larger droplets present greater inertia, and their trajectories may depart significantly from the streamlines around the aircraft. As a result, larger droplets adhere to larger parts of the aircraft surface and are more likely to strike behind ice-protected surfaces. Supercooled Large Droplets (SLD) can be up to 4000 μ in diameter and, despite icing certification limitations, accidents, and incidents in SLD conditions have been documented, especially following sustained flight in freezing drizzle or freezing rain.
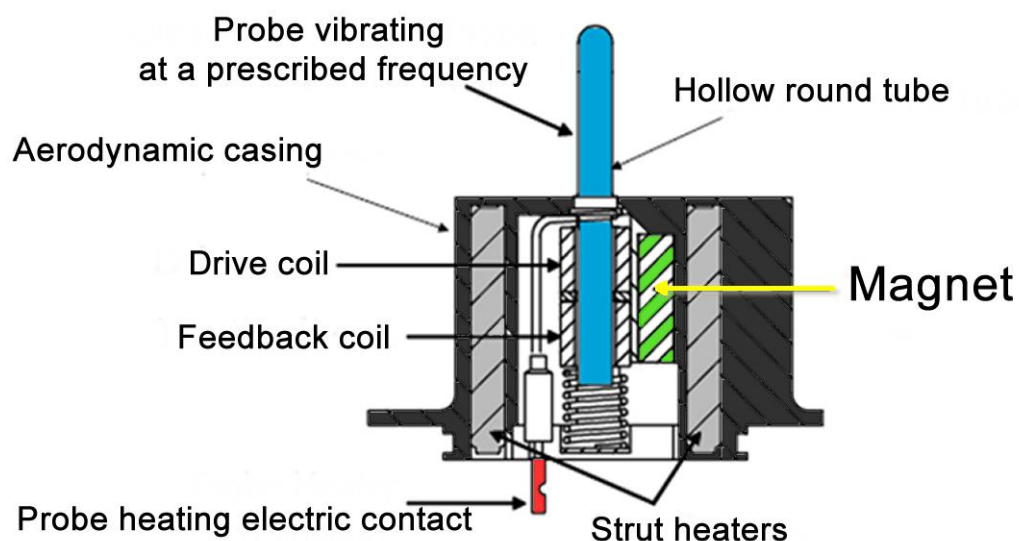
Figure 33: Magnetostrictive ice detector

Navier-Stokes simulations were carried out with the Ansys Fluent code (16) for a 55-seat airliner configuration, which was designated ITA55ADV. Fluent's realizable *k-ε* turbulence model and standard wall functions were employed in this simulation The computational model is not symmetric, with one ice probe placed only on the port side of the front fuselage in the position labeled P2 (Figure 34). This approach intends to measure the impact of the probe on the SWL, comparing the distribution on this side with the flow calculated on the starboard side, which is free from probes. Figure 34 also displays the triangular surface mesh employed in the calculation. The spatial mesh was adapted to lower velocity and pressure gradients and to keep the y+ values within reasonable values.
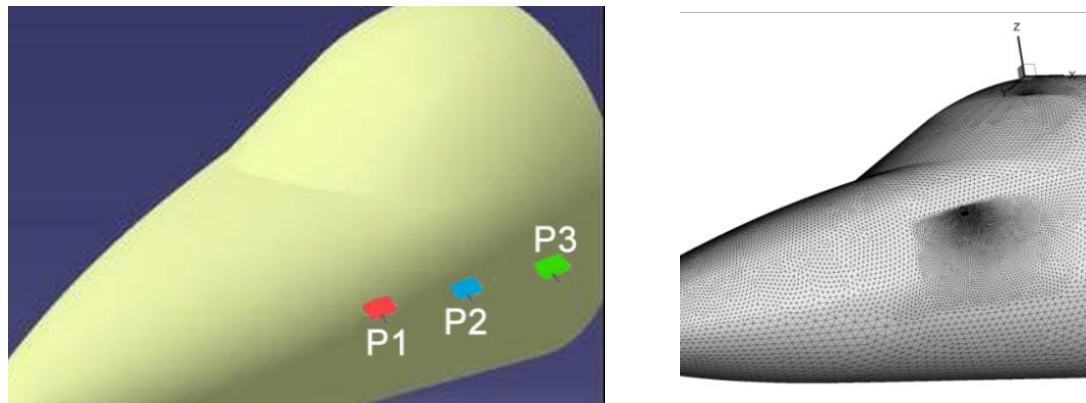
Figure 34: *Left* - **Locations chosen for placement of the ice detector.** *Right* – **Initial surface mesh in the ice-detector region generated for the P2 ice-detector configuration**

A CFD calculation was performed at freestream conditions with $M_\infty = 0.40$ and $\alpha = 3°$. The results show that, besides the logic separation behind the cylindrical part of the probe, the flow also separates at the trailing edge of the P2 configuration according to the Navier-Stokes simulation performed with Fluent (Figure 35). The rounded trailing edge of the basis of the probe is not suited to keep the flow attached (Figure 36), namely at higher Mach numbers. Naturally, the flow behind the probe's cylindrical part is also separated for all conditions in the airplane's flight envelope. The maximum Mach number over the ice detector obtained from the CFD run was found to be as high as 0.89. Comparatively, the fuselage and wings recorded 0.58 as the highest Mach number on these surfaces.
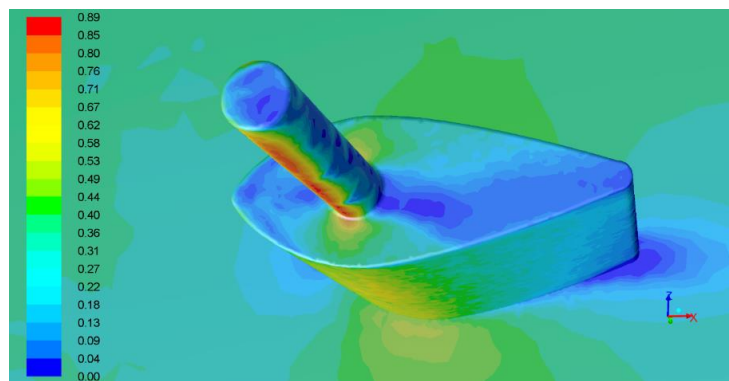
Figure 35: Mach number contours on the ice detector and its neighborhood
($M_\infty = 0.40$, $\alpha = 3°$)
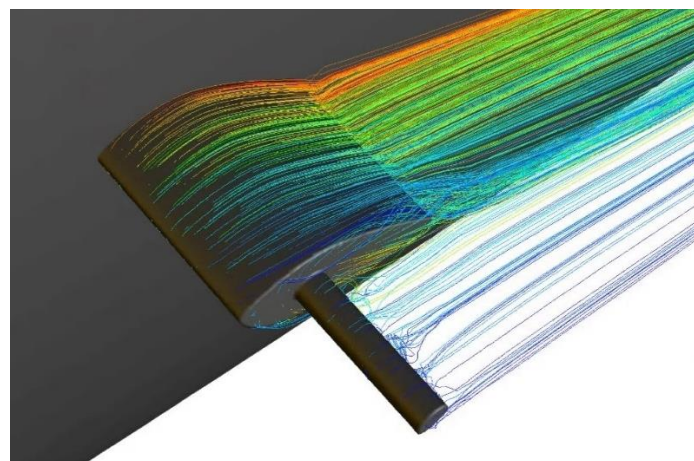
Figure 36: Streamlines ($M_\infty = 0.40$, $\alpha = 3°$)

Figure 37 shows regions where the surface power level was calculated to be higher than 100 dB. It is noticeable the great impact of the ice probe is producing considerable noise. The shape of the fuselage surface over cockpit the accelerates the flow there and causes a thickening of the boundary layer and consequently an increase in the broadband noise. However, the region affected by the ice detector is much larger. This CFD run leads to two important conclusions:

1. It is important to consider aerodynamics and noise in the design of ice probes to avoid flow separation and high accelerated flow over the probe.
2. There are many probes at the front fuselage of airliners, so the combined noise generated by them is considerable and affects mainly the cockpit crew.
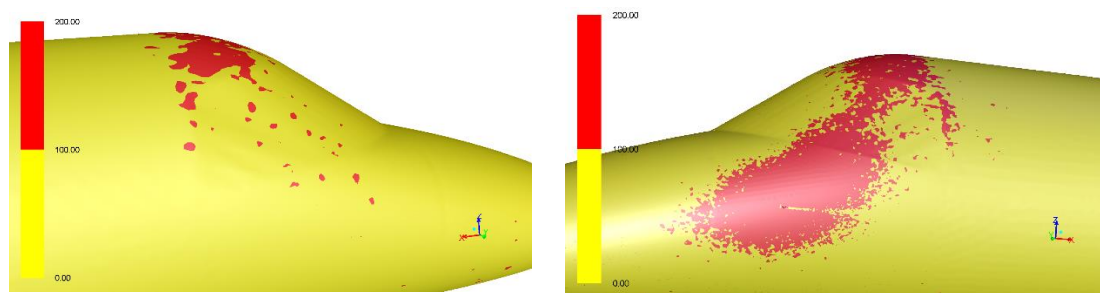
Figure 37: Surface power level above 100 dB reveals that the ice probe is a considerable source of noise

3.4 Some remarks about helicopter noise

In terms of helicopter noise sources, the main sources are the rotor, anti-torque, engines, gearbox, depending on flight condition, transmission gear, and are illustrated in Figure 38. The typical noise sources in helicopters can be summarized as

- Turbulent boundary layer noise.
- Engine noise.
- Heating and ventilation noise.
- Main/tail rotor noise.
- Fan noise.

In a short review of the noise sources generated by the helicopter and connected to the present study, it is worth mentioning the thickness noise which is caused by the blade periodically displacing air during each revolution and is dependent only on the shape and motion of the blade. Generally, the thickness noise propagates in the plane of the rotor as well as the high-speed impulsive noise. In addition, the loading noise is another type of noise source which influences the inside-cabin noise. The noise generated due to the loading on the blade is directed below the rotor and is caused by the acceleration of the force distribution on the air around the rotor blade passing through it. Another important contribution is that of the blade vortex interaction directed down and rearward. It occurs when a rotor blade passes within proximity of the shed tip vortices from a previous blade. The rotor noise sources are depicted in Figure 39.

Figure 38: Helicopter noise sources

Rotating blades emit two distinctly different types of acoustic signatures (33): tone or harmonic noise which is caused by periodic sources with a period linked to a rotation cycle; and broadband noise which is a random, nonperiodic signal caused by the flow-blade interaction.

Helicopter main rotors typically present a rotating frequency between 3 and 7 Hz, depending on the aircraft configuration and performance. The main vibrations caused by the rotors in the structure vary between 3 and 22 Hz, while tail rotors and other accessories rotate at higher frequencies. The most annoying noise for humans is that originated at the tail rotor due to its higher frequency which coincides with the band to which the human ear is most sensitive (34). A method to separate the main rotor noise from that originating from the tail rotor of a helicopter in flight was applied by Farassat and Morris (35). A two-dimensional Fourier analysis method was used, whereas the two-dimensional spectral analysis method is initially applied to artificial signals. This initial analysis provided an idea of the characteristics of the two-dimensional autocorrelations and spectra. Data from a helicopter flight test were then analyzed using data from a 2D-microphone array. Two test aircraft were employed, a Boeing MD902 Explorer NOTAR and a Sikorsky S-76, the latter fitted with a four-bladed tail rotor.
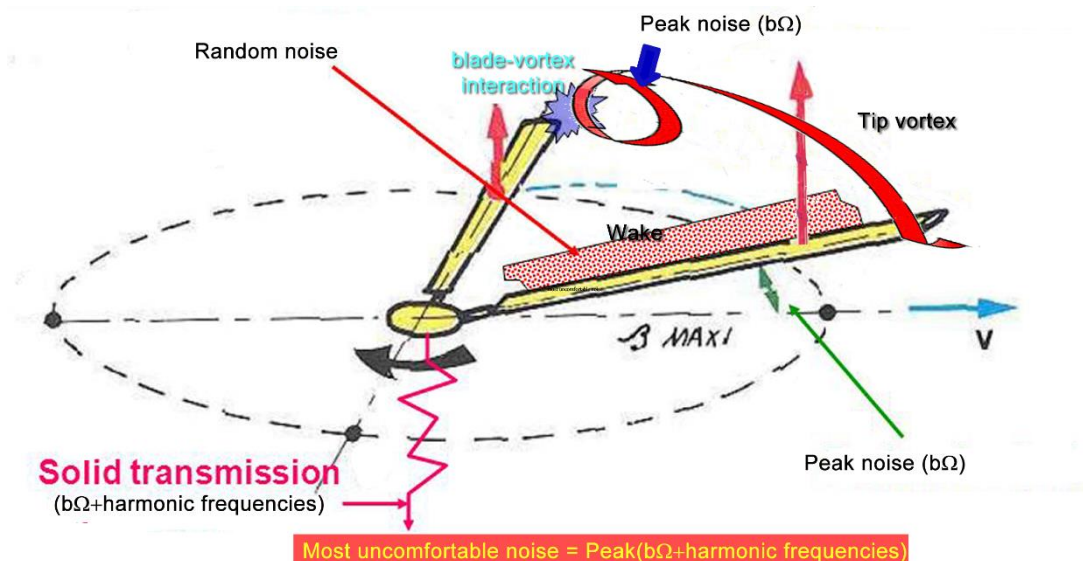
Figure 39: Rotor noise sources [Adapted from Ref. (11)]

The contributions to the internal noise of major helicopter components are summarized in Figure 40. The pressure level is practically linearly decreasing when the frequency is increasing on a logarithmic scale,
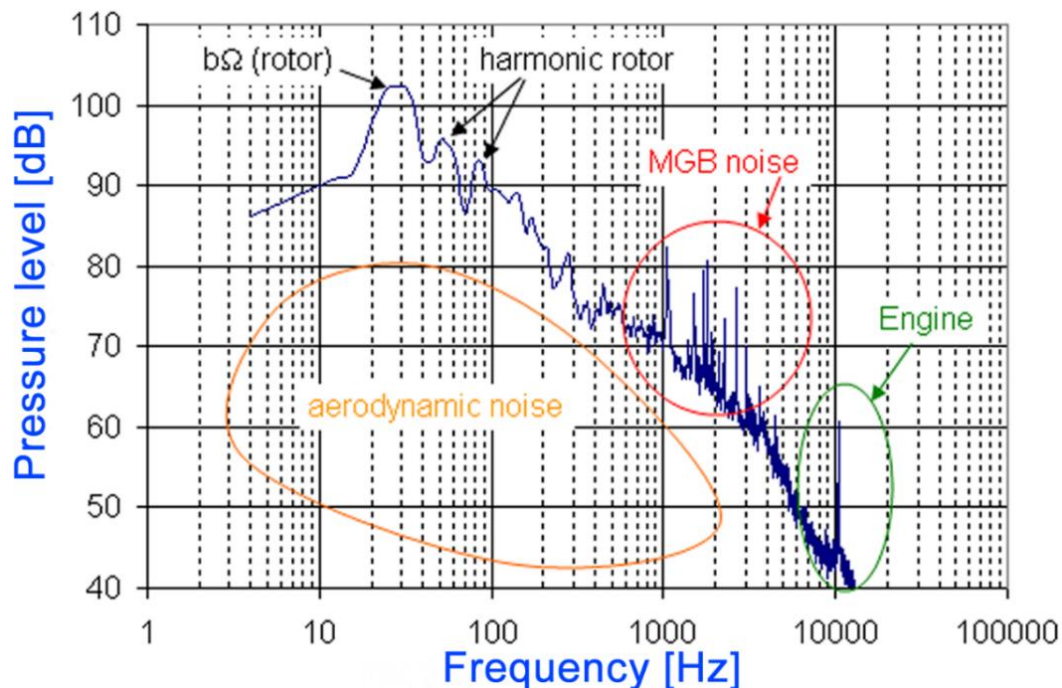
Figure 40: Internal noise mapping (11)

As seen in Figure 39 gearbox is also a major source of noise in helicopter cabins. Several studies address transmission designs by targeting noise reduction (36). The production of gear noise is basically due to the meshing forces acting on the gear teeth. The shape variation of the teeth during their operational cycle will produce sound waves or, in other words, noise (Figure 41). If the forces acting on teeth are reduced, the generated noise will follow this trend. The two main approaches for helicopter transmission are the modification of the tooth shape and contact ratio.

The contact ratio has a strong influence on stiffness. Depending on which part of the toot the contact takes place, the bending stiffness may vary substantially (Figure 42).

Helical gears, as compared to spur gears, typically produce lower noise levels. The helicoidal angle has a strong influence on the overlap ratio (Figure 43):

$$\epsilon_\beta = \frac{b \tan(\beta)}{p} \tag{23}$$

By raising the parameter ϵ_β, the meshing stiffness decreases, and therefore the noise generated by the gears follows suit.

Li et al. proposed a methodology of fault diagnosis combining vibration and sound signals from gears (37). According to them, the two kinds of signals complement each other, which is beneficial for fault diagnosis. However, there is a limitation of the signal source and sensor in assessing the gear state under different working conditions.
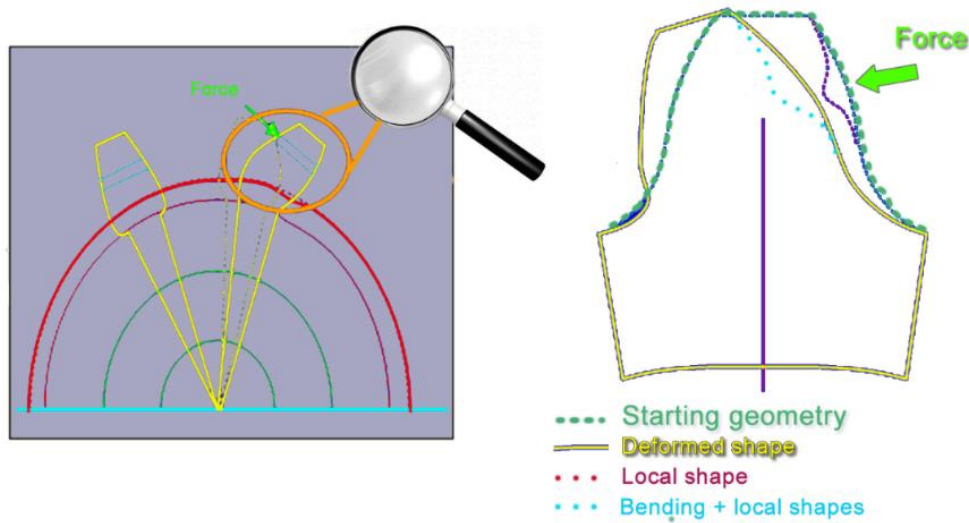
Figure 41: Gear deformation due to loading (11)
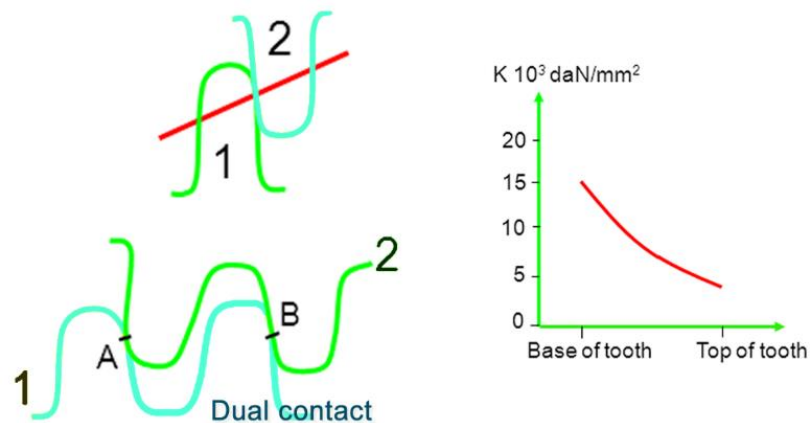
Figure 42: Variation of the bending stiffness according to the contact point (11)

While helical gears provide some degree of noise reduction, their use also generates a thrust load which must be dealt with in the design of the overall system, especially the support bearings, gear blank design, and housing structure (36). Double helical gears cancel the thrust loads from each helix within the gear blank, providing this way relief from the net thrust issue (36).
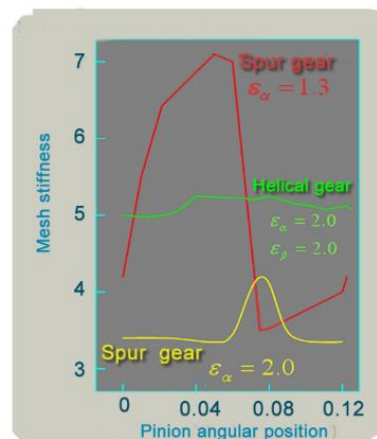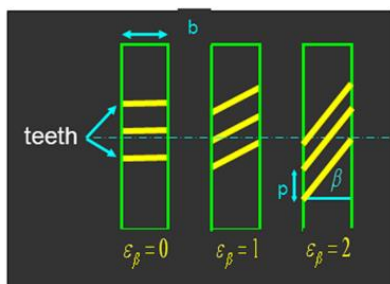
Figure 43: Helical gear (11)

3.5 Turbofan engines

Overview

Interaction of tone and broadband noise mechanisms are found in a multi-blade row propulsor application (Figure 44). Broadband noise is produced by the interaction of airflow with a solid surface, as is the case of a wake from a rotor interacting with a stator. Broadband noise is defined as noise that has a flat spectral density distribution.

Regions of separated flow produce a considerable noise, and the flow separation must be contained as far as possible. These regions can be even found on airplanes in steady-level flight. An example of this is the regions downstream of anti-collision lights, ice detectors, and knobs.

Aeroacoustics measurements are vital for providing validation data for the development of computational aeroacoustics codes (38). The main sources of noise in turbofan engines are as follow:

i.   Rotor self-noise which is significant even with clean inflow and no duct boundary layer includes Gutin tones, thickness noise, tones and broadband sound generated by the interaction of the rotor with upstream flow distortion, and tones and broadband sound generated by the interaction of the rotor wakes with downstream bodies and trailing-edge broadband noise.

ii. The interaction of the rotor with the inlet boundary layer is affected by rotor tip clearance.

iii. An unsteady nonuniformity in the tip-duct gap rotating at a fraction of the fan speed, at least when tip clearance and loading are both large.

iv. Stator-generated noise is significantly affected by propagation through the upstream rotor fan which consists of interaction tones and broadband noise with the shed rotor turbulent wakes and stator trailing-edge noise.
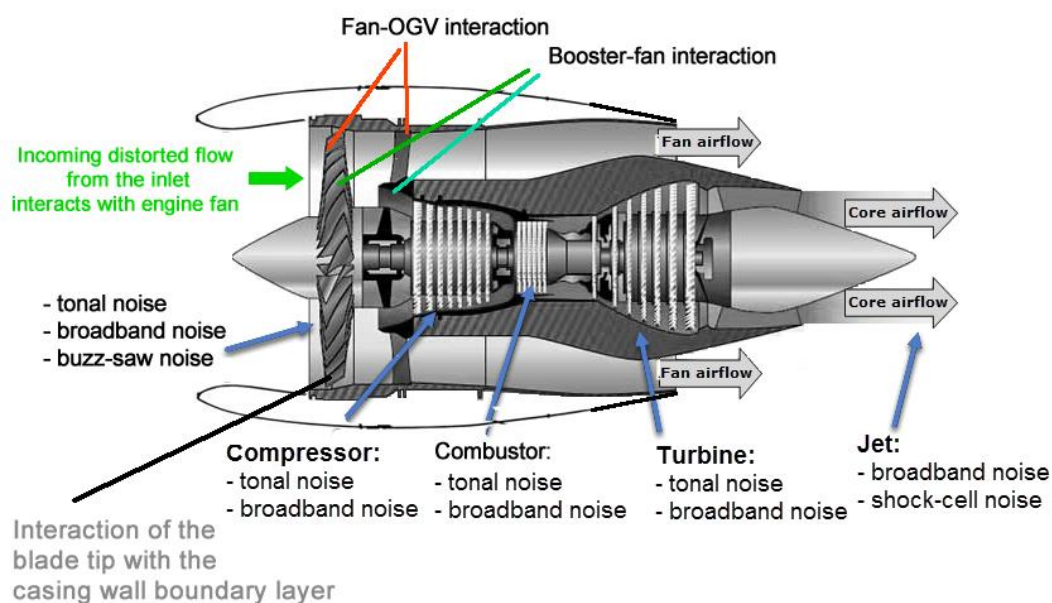
Figure 44: Turbofan engine noise sources (OGV means outlet guide vane)

Example of noise prediction

A computational tool for noise prediction generated by conventional turbofan engines was developed by Muraro in his master's program (39). The tool was based on several methods described in a batch of NASA TM-X reports. Each of those reports addressed some specific component of the engine such as the inlet, fan (40), core (41), turbine, and nozzle (42). The tool was written in MATLAB® language. The following baseline data were considered as an exemplification of noise prediction and a comparison with the results of Refs. (43) (44) is provided. Table 8 shows the ambient and position of the airplane fitted with the engine considered in the present noise estimation example (43).

Table 8: General parameters for noise estimation methods comparison (39)

Parameter	Value	Unit	Description
ΔT_{ISA}	0	ºC	Temperature variation in comparison to ISA
H	0	m	Altitude
P_0	101,325	Pa	Ambient static pressure
ρ_0	1.225	kg/m³	Ambient density
V_0	87	m/s	Ambient velocity or flight velocity
M_0	0.26	-	Ambient Mach number or flight Mach number
θ	50	degree	Directivity angle
ϕ_f	0	degree	Azimuth angle
r	538	m	Distance between the source and the observer

Fan noise

The following parameters (Table 9) are considered for the estimation of the fan noise.

Table 9: Engine parameters for fan noise comparison (39)

Parameter	Value	Unit	Meaning
$\dot{m}_{fan}$	385	kg/s	Fan mass flow rate
PR_{fan}	1.53	-	Fan pressure ratio
η_{fan}	0.9	-	Fan efficiency
D_{fan}	1.6	m	Fan diameter
rpm_{fan}	5,233	rpm	Fan revolutions per minute
$(M_{TR})_D$	1.17	-	M_{TR} value in the fan design point
n_{rotor}	22	-	Number of fan rotor blades
n_{stator}	50	-	Number of fan stator blades
RSS	200	%	Fan rotor/stator spacing

Additionally, there must be informed if the engine has inlet guide vanes and if there are inlet flow distortions. The program results are shown in Figure 45, together with the results from the applet and the ESDU methodology for comparison. The ESDU results are plotted two times, one with the original ESDU method, and another with the Heidmann method (40), the same used in the NASA report. A Java applet for the prediction of noise generated by turbofan engines was some time ago available on the Website of the TU Berlin and it served as a comparison basis. Amado's program results are very similar to the ones obtained by the ESDU results with the NASA method. The difference at higher frequencies can be credited to atmospheric damping, which is not considered in the ESDU method.

However, the applet results are very lower than the programs. This is probably because the applet uses the ESDU own methodology. The difference at higher frequencies is again due to the atmospheric damping.
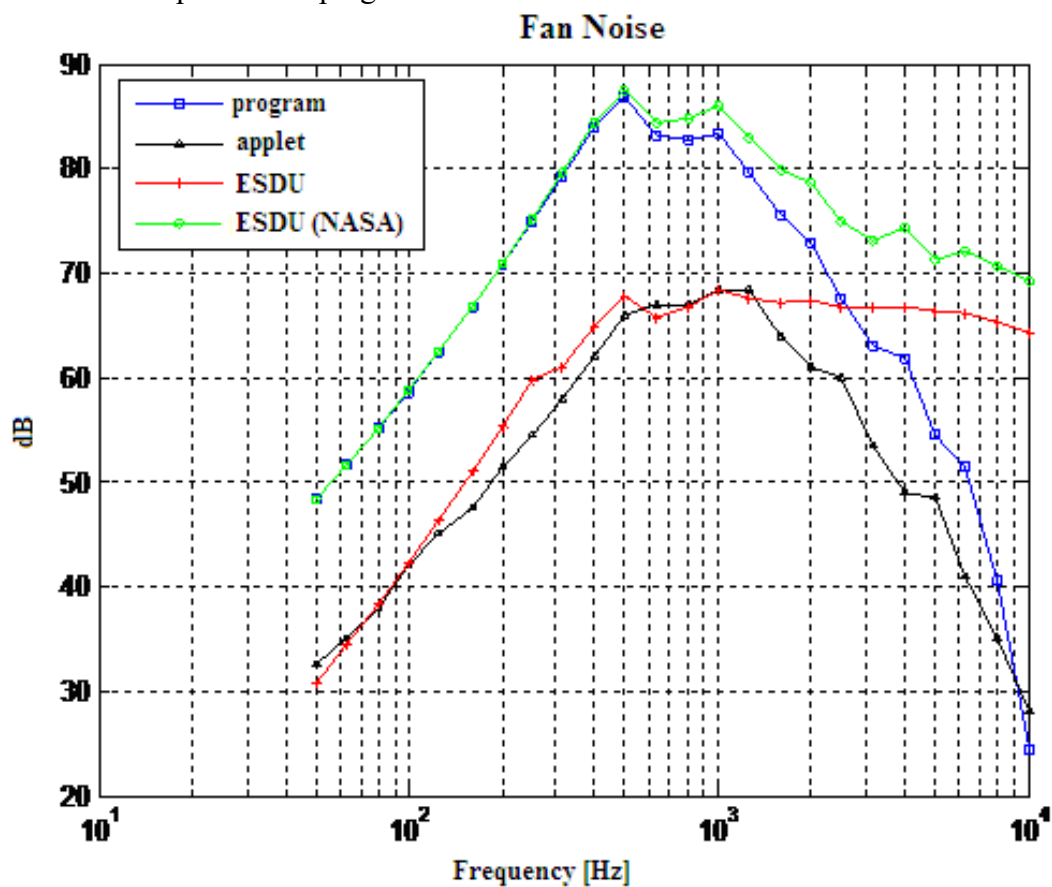
Figure 45: Comparison between the fan noise generated by the program, by the applet, and by the ESDU (39)

Combustion chamber noise

There are 4 parameters needed for the noise prediction generated by the combustion chamber:

Table 10: Engine parameters for combustion chamber noise comparison (39)

Parameter	Value	Unit	Meaning
$\dot{m}_{chamber}$	157	kg/s	Chamber mass flow rate
$T_{entrance}$	844	℃	Air temperature at the chamber entrance
T_{exit}	1,676	℃	Air temperature at chamber exit
$P_{entrance}$	3,000,000	Pa	Air pressure at the chamber entrance

The results are shown in Figure 46, together with the results from the applet and the ESDU.
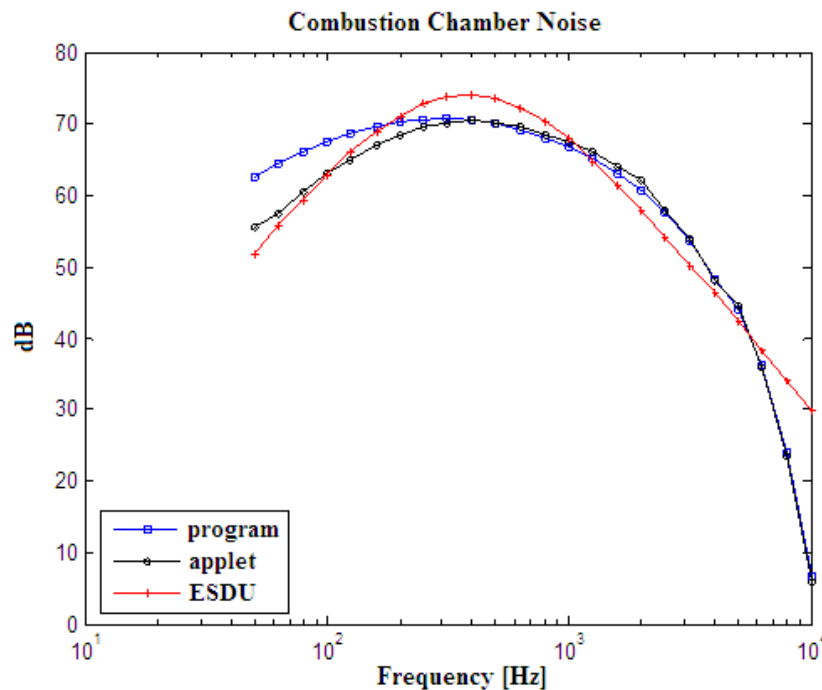
Figure 46: Comparison between the combustion chamber noise results obtained by the program, the applet, and the ESDU (39)

The program results are very close to the applet results, and only show some difference in lower frequencies. The ESDU results are also very similar to the program's, however, since the ESDU method considers a $10.\log_{10}\left(\dfrac{\rho_0 c_0 W_{ref}}{4\pi.p_{ref}^2}\right)$ factor, that is equal to -10.8 dB at the simulation conditions, the results are lower, and the ESDU plot in Figure 46 has this factor value-added.

Turbine noise

For the turbine noise estimation, the following parameters are required:

Table 11: Engine parameters for turbine noise comparison (39)

Parameter	Value	Unit	Meaning
$\dot{m}_{turbine}$	157	kg/s	Turbine mass flow rate
$rpm_{turbine}$	5,233	rpm	Turbine revolutions per minute
$M_{TR\,turbine}$	0.5	-	Mach number at turbine tip
$n_{rotorturbine}$	50	-	Number of turbine rotor blades
$RSS_{turbine}$	50	%	Turbine rotor/stator spacing

The program results are shown in Figure 47 below, together with the applet results for comparison. As it can be seen, both graphics are very close, showing that the program has a good correspondence.
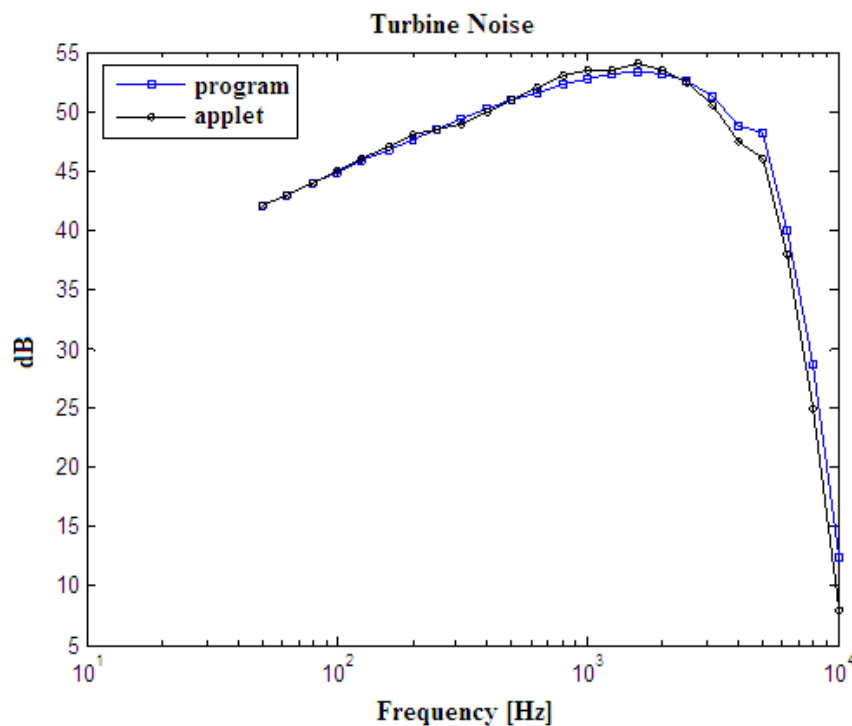
Figure 47: Comparison between the turbine noise results obtained by the program and the applet (39)

Jet noise

Jet noise is caused by a mixture of hot air with the surrounding air. Temperature and velocity gradients can significantly influence the nature of the turbulence, and hence the noise generated. Lighthill (14) proposed the following equation for the power irradiated by the gas exhaustion:

$$P = k \frac{\rho_{jet}}{\rho_{air}} A \frac{V^8}{V_{sound}^5} \tag{24}$$

In Eq. 24, ρ_{jet} e ρ_{air} are the jet and ambient density, respectively; V and V_{sound} are the flow speed and sound speed, respectively; A is the nozzle area, and k is a proportionality constant.

For the estimation of the last part of the engine noise, several velocities, densities, areas, and temperatures are needed (Table 12).

Table 12: Engine parameters for jet noise comparison (39)

Parameter	Value	Unit	Meaning
A_{jet}	0.85	m²	Jet area
h_{gap}	0.15	m	Gap distance
A_{bypass}	2.399	m²	Bypass area
V_{jet}	447	m/s	Jet velocity
V_{bypass}	298	m/s	Bypass velocity
T_{jet}	786	ºC	Jet temperature
T_{bypass}	88	ºC	Bypass temperature
ρ_{jet}	0.22	kg/m³	Jet density
ρ_{bypass}	0.976	kg/m³	Bypass density

Additionally, it is necessary to inform if the nozzle is circular or plug. The results for the applet and the program with a circular nozzle are shown in Figure 48, while Figure 49 shows the results with the plug nozzle. In the two situations, the program has very good results compared to the applet, although with the plug nozzle a small difference can be seen in lower frequencies.
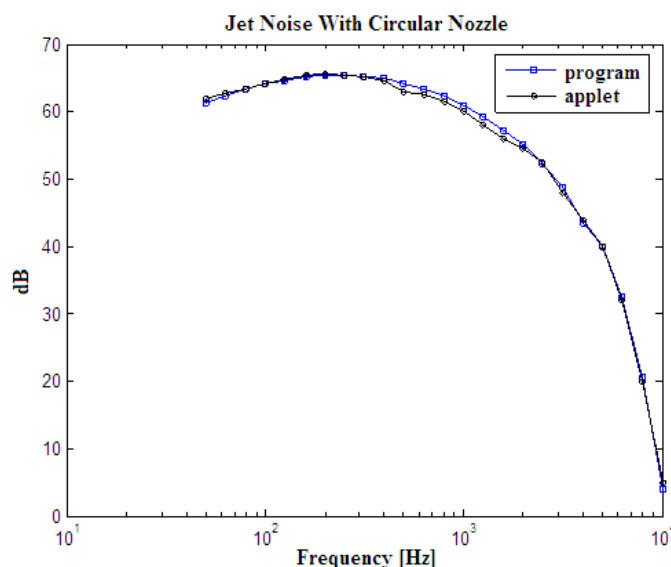
Figure 48: Comparison between the jet noise results with circular nozzles obtained by the program and the applet (39)
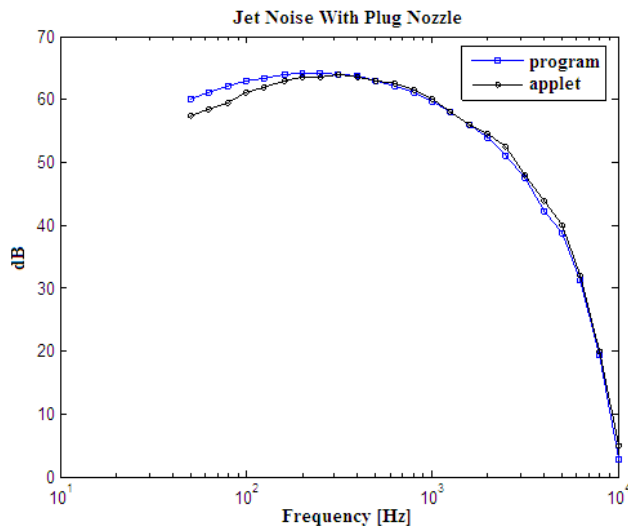
Figure 49: Comparison between the jet noise results with plug nozzles obtained by the program and the applet (39)

By lowering the jet exhaust velocity, the jet noise will be reduced, typically. Some more recent engines like the GE-90 employ this approach by using the engine cycle to extract energy from the engine core and reduce the mixed velocity of the core and fan ducts (38). It is highly desirable to reduce the jet noise without changing the engine cycle, indeed a very challenging problem. In 1996, a jet noise reduction concept using "chevron nozzles" was tested at NASA that reduces the jet noise by mixing the core and bypass flows in a way that reduces low frequency mixing noise from highly turbulent flows (40). This approach is employed in the engines of the B787 airliner.

3.6 Transport airplane optimization with noise constraints

An optimization with noise constraints was carried out for the design of a 78-seat airliner. Some characteristics of this simulation:

- Only twinjet configurations were considered.
- Some FAR rules are set as constraints: missed approach climb gradient, climb gradient in 2nd segment, rate of climb at service ceiling, and others.
- Design variables are set for wing planform and engine definition.
- The turbofan engine model (45) presents five design variables.
- Turbofan noise model according to Ref. (39); airframe noise by Ref. (46).
- The maximum lift coefficient is estimated by the critical section methods.
- Direct Operating Cost (DOC) and Maximum Takeoff Weight (MTOW) are the two objectives.
- Artificial neural networks were employed for the estimation of aerodynamic coefficients (47).
- Range of 2,200 nm with 78 passengers.
- Stabilizers were designed according to controllability and stability criteria (48).
- The genetic algorithm NSGA-II was used as an optimizer.

Figure 50 shows the results of the optimization run. There, 804 airplane configurations were analyzed, of which 279 could properly be sized and did not violate any constraints. Another graph containing the wing aspect ratio and area of the individuals analyzed in the optimization run is shown in Figure 51. Only three airplane configurations composed the Pareto front, which resulted in a line almost parallel to the DOC axis, i. e., the MTOW of the Pareto members differ by a small amount.
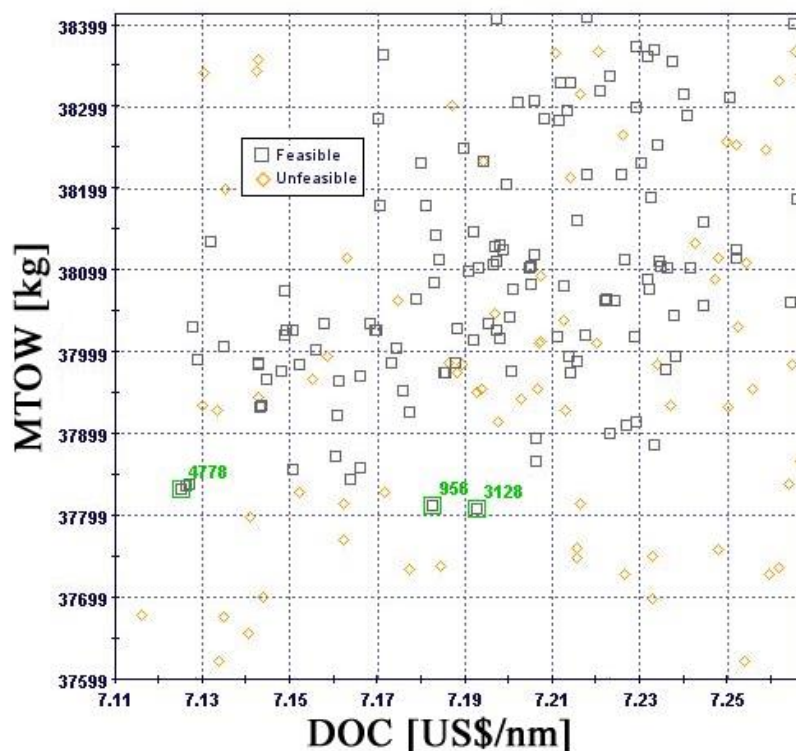
Figure 50: Pareto and dominated individuals of the optimization run for the design of a 78-seat airliner
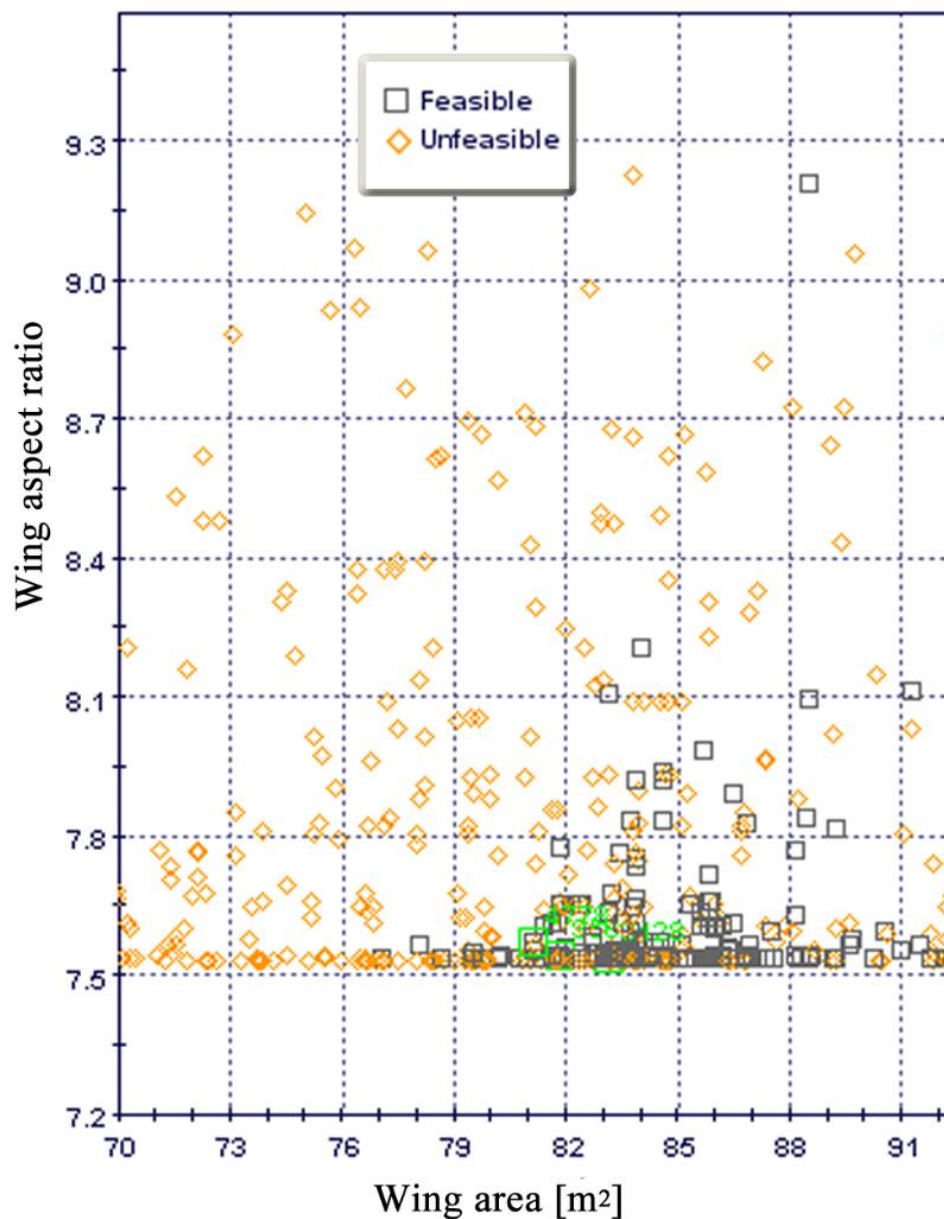
Figure 51: Wing aspect ratio and area of individuals analyzed in the optimization run

Table 13 presents a comparison of characteristics among two E175 versions (AR and LR) to those from three configurations that resulted from the design optimization task. The range for the mission with 78 pax mission was performed at 35,000 ft for the Embraer airplanes and 40,000 and 41,000 ft for the optimized configurations. The thrust provided by the CF34-8E engines of the E175 versions does not enable them to cruise at higher altitudes than 35,000 ft taking off with MTOW, according to the aircraft model employed in the present computations.

The flyover noise (posed as a constraint) was considerably reduced when compared to those from the E175 versions, but the sideline noise (no constraint established) increased approximately by 1 dB.

Table 13: Specifications of the optimally designed 78-seat airliner compared to those of two E175E1 versions. All airplanes present a service ceiling of 41000 ft (49) (50) (51)

	E175 LR	E175 AR	ID 956	ID 4778	ID 3128
Range (MTOW, LRC, 78 Pax, ISA, 100 nm alternate, 45 min loiter) [nm]	2,000[+, 1]	2,200[+, 2]	2,200[†]	2,200[†]	2,200[†]
Maximum operating Mach number	0.82	0.82	0.84	0.84	0.84
Takeoff field length (MTOW, sea level, ISA) [m]	1,724	2,244	2,000	2,000	2,000
Landing field length (MLW, sea level, ISA) [m]	1,259	1,261	1,259	1,259	1,259
BOW [kg]	21,870	21,890	**21,708**	21,830	21,785
MTOW [kg]	38,790	40,370	37,812	37,832	**37,808**
Max. usable fuel [kg]	9,428	9,428	9,187	9,007	9,421
Wing quarter-chord sweepback angle	23.5	23.5	26.63	27.48	27.25
Wing reference area [m^2]	72.72	72.72	82.07	**81.37**	78.53
Wing aspect ratio	8.6	8.6	7.50	7.54	7.50
Fuselage width [m]	3.01	3.01	2.84	2.84	2.84
Engine by-pass ratio	5.00	5.00	5.69	5.27	5.54
Engine overall pressure ratio	28.50	28.50	30.57	31.85	29.37
Fan pressure ratio	1.9	1.9	1.60	1.64	1.65
Static takeoff thrust (Sea level, ISA) [lb]	14,200	14,200	14,902	15,017	14,706
Time to climb to initial or final cruise altitude [min]	18[1]	18[2]	26.3[3]	25.7[4]	24.8[3]
Flyover noise (EPNL)	84.4[*]	85.9[*]	78.8	79.0	**78.6**
Sideline noise (EPNL)	91.9[*]	91.9[*]	**93.0**	93.1	**93.0**
DOC [US$/nm]	-	-	7.183[β]	7.126[β]	7.194[β]
[1,2]FL350 [3]FL400 [4]FL410 / [+] TOW of 38,790 kg / [†] MTOW, 200 nm alternate + 45 min loiter					
[*] Reference (50) / β fuel at US$ 2.387/gallon					

4. Estimation and prediction with convolutional neural networks

4.1 Overview

There are various types of neural networks, which are used for diverse applications and data types. For example, recurrent neural networks are frequently utilized for natural language processing and speech recognition whereas multilayer perceptron networks are frequently utilized for parameter identification (47).

Multilayer-perceptron and other ANNs operating on raw images do not scale well as the image size increases, lacking accuracy (52). For example, consider a color image with 64×64 pixels with a red, green, and blue channel. This results in a total of 64×64×3 inputs to that network, which apparently can be handled. However, if 256×256-pixel images are in place, the total number of inputs and weights would jump to 196,608. For an ANN with multiple hidden layers with a varying number of nodes per layer, these parameters can demand unacceptable training times and unsatisfactory accuracy (52).

Convolutional neural networks (ConvNets or CNNs) are more often utilized for classification and computer vision tasks (53). CNN represents the local features by convolution kernels to solve the problem of high-dimension data.

Manual feature extraction methods to identify items in images demands considerable computational power. By using CNNs a more scalable approach to image classification and object recognition tasks is possible. The CNN methodology is based on utilization of concepts and ideas from linear algebra, specifically matrix multiplication (convolution operation), to identify patterns. Besides finding patterns in images to recognize objects, faces, and scenes, CNNs can also be quite effective for classifying signal data such as audio records, HUMS measuraments, and other time series. One important application of CNN is on autonomous vehicles, which require intensive processing for object recognition.

CNNs embody multilayer perceptrons neural networks ins their structure (47). Multilayer perceptrons usually are fully connected networks, that is, neurons placed in one layer are connected to all other neurons in both the preceding and the following layer. CNNs have three main types of layers (54):
- Convolutional layer
- Pooling layer
- The fully connected layer

The convolutional layer is the first layer of a convolutional network. Convolutional layers can be followed by additional convolutional layers, but a fully connected layer must be the last one. With each layer, the CNN increases in its complexity, identifying greater portions of the image. Earlier layers focus on simple features, such as colors and edges. As the image data progresses through the layers of the CNN, it starts to recognize larger elements or shapes of the object until it finally identifies the intended object.

Convolutional layer characteristics

The convolutional layer is the main part of a CNN. It requires a few components, which are input data, a filter, and a feature map. However, the convolutional layers are where high-demanding computational processing takes place.

Convolution is a mathematical operation on two functions (*f* and g) that produces a third function (*f*g*) that expresses how the shape of one is modified by the other. In practice, the convolution theorem is used to design filters in the frequency domain. The convolution theorem states that the convolution in the time domain equals the multiplication in the frequency domain.

To illustrate the application of a convolutional operation, consider an image sharpening. Taking four times the current pixel and subtracting the neighbors from it results in a sharpened image (Figure 52).

Another example considers a color image where the input consists of a matrix of 3D pixels. This means that the input will have three dimensions, height, width, and depth, which correspond to RGB layers in an image.

The feature capture of a CNN consists of a two-dimensional array where weights are stored. This represents only a portion of the image. The filter size (width and height) can be specified that also determines the size of the receptive field. In Figure 53, a 3x3 matrix was employed. The filter is then applied to an area of the image, and a convolutional operation is then carried out between the input pixels and the filter. This operation, a dot product, is then stored in an output array. This process is repeated until the entire image is processed. The final output from the series of dot products from the input and the filter is known as a feature map or kernel matrix (54).
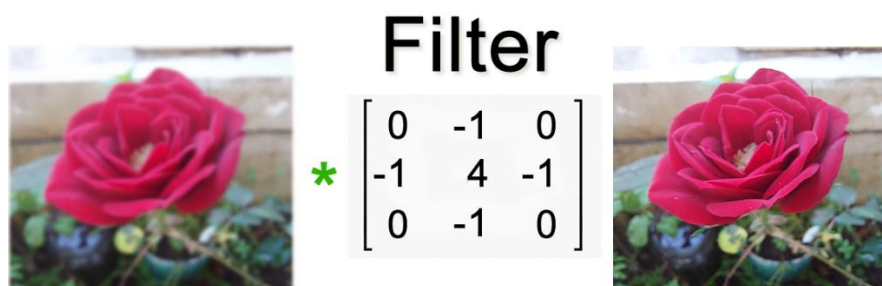
Figure 52: Example of image sharpening
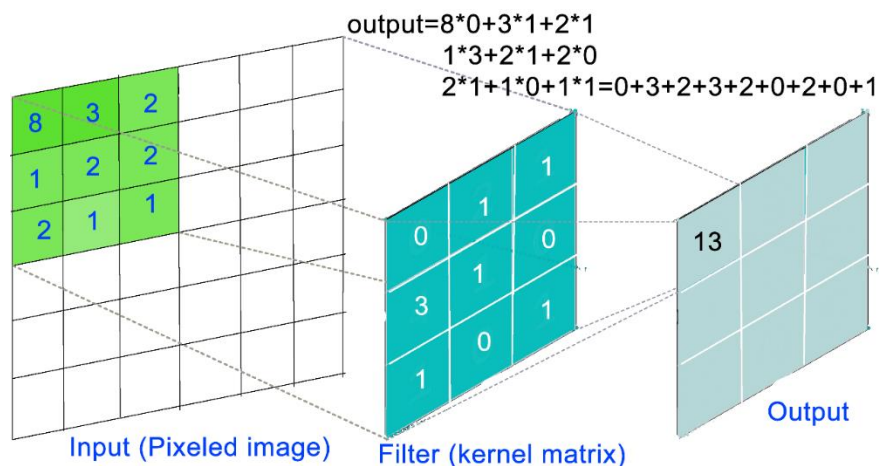
Figure 53: Feature mapping of the color image example [Adapted from (54)]

As can be seen in the image in Figure 53, each output value in the feature map does not have to connect to each pixel value in the input image but it only needs to connect to the receptive field, the area of filter application. Since the output array does not need to map directly to each input value, convolutional (and pooling) layers are commonly referred to as *partially connected* layers.

The weights in the feature detector remain fixed as it moves along the image, which is also known as parameter sharing. Parameters, like the weight values, are modified during the training of the network, which can be performed by backpropagation and optimization algorithms such as gradient descent ones.

Three parameters affect the size of the output, and they must be set before training of a neural network starts (54) (55):

- The *number and size of filters* affect the profundity of the output, so the number of feature maps is directly related to this parameter.
- *Zero-padding* is usually used when the filters do not fit the input image. This sets all elements that fall outside of the input matrix to zero, producing a larger or equally sized output. It must be specified whether to use padding.
- *Stride* is the distance or pixels that the kernel moves over the input matrix. While stride values of two or greater is rare, a larger stride yields a smaller output.
- *Output depth:* This parameter controls the number of neurons in a convolutional layer, which is connected to the same region in the input layer (55).

After each convolution operation, a CNN applies a Rectified Linear Unit (*ReLU*) transformation to the feature or constituent map, conferring non-linear characteristics to the model. The *ReLU* activation operation performs a nonlinear threshold operation, where any input value less than zero is set to zero. This operation is equivalent to

$$f(x) = \begin{cases} x, x > 0 \\ 0, x \leq 0 \end{cases} \tag{25}$$

ReLU allows for faster and more effective training by mapping negative values to zero and keeping positive values active and only the activated features are carried forward into the next layer (56).

As described in the preceding paragraphs, another convolution layer can follow the initial convolution layer. When this happens, the structure of the CNN can become hierarchical as the later layers can see the pixels within the receptive fields of prior layers. As an example, it is required to determine whether an image contains a car or not (Figure 54). The usual approach is to consider the car as a sum of parts. It is comprised of an engine, transmission, wheels, doors, instrumentation et cetera. Each part of the car makes up a lower-level pattern in the neural net, and the combination of its parts represents a higher-level pattern.
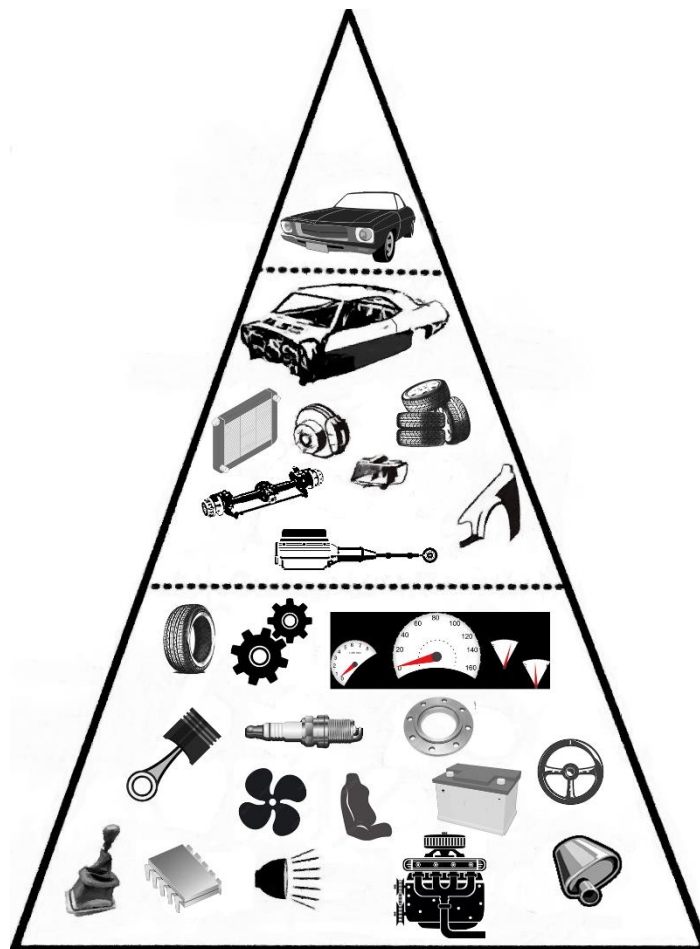
Figure 54: Hierarchy within the CNN [Adapted from (54)]

Ultimately, the convolutional layer converts the image into numerical values, allowing the neural network to interpret and extract relevant patterns.

Pooling Layer

Pooling layers reduce the dimensionality of the problem, lowering the number of parameters present in the input data. Like the convolutional layer, the pooling operation applies a filter across the whole input, but here the filter does not have any weights. Instead, the kernel applies an aggregation function to the values within the receptive field, populating the output array. While a lot of information is lost in the pooling layer, it also has several benefits for CNN. They help to reduce complexity, improve efficiency, and limit the risk of overfitting. There are two common types of pooling in popular use: max and average.

Fully connected layer

Pixel data of the input image are not directly connected to the output layer in partially connected layers. However, in the fully connected layer, each node in the output layer connects directly to a node in the previous layer.

This layer performs the task of classification based on the features extracted through the previous layers and their different filters. While convolutional and pooling layers tend to use *ReLu* functions, FC layers usually leverage a *softmax* activation function to classify inputs appropriately, producing a probability from 0 to 1.

Convolutional neural networks applications

Convolutional neural networks power image recognition and computer vision tasks. Computer vision is a field of artificial intelligence (AI) that enables computers and systems to derive meaningful information from digital images, videos, and other visual inputs, and based on those inputs, it can act. This ability to provide recommendations distinguishes it from image recognition tasks. Some common applications of this computer vision today can be seen in:

- *Marketing*: photo tagging in social media.
- *Maintenance*: gear fault diagnosis. Monitoring and diagnosis are important means to detect and eliminate mechanical faults in real-time or to proceed with preventive maintenance (37).
- *Healthcare*: thanks to machine learning in radiology diseases can be now easily diagnosticated.
- *E-commerce*: Visual search has been incorporated into some e-commerce platforms with the introduction of methodic purchases and data-driven personalized advertising.
- *Automotive*: While the age of driverless cars has not quite emerged, the underlying technology has started to make its way into automobiles, improving driver and passenger safety through features like lane line detection.

4.2 Examples of CNN application for the prediction and forecasting of time-series

CNN-RNN combination

Time series forecasting is an important area of machine learning and in recent years has been the main topic of research in a wide range of sectors such as engineering, energy, finance, and health among others.

This example presents a combination of a CNN with a recurrent neural network (RNN) to predict a function dependent on time-based known values for previous months. The application was developed by H. Sanchez (57).

The CNN is tailored for feature extractions while an RNN has proved its ability to predict values in sequence-to-sequence series. At each time step, the CNN extracts the main features of the sequence while the RNN learns to predict the next value on the next time step (57).

The size of the input of the sequence is lagged by n-months thus the RNN expects an input size of n-months cases to yield the prediction of the next month; one step ahead.

This example used a sine-type distribution with decreasing amplitude over time. The training and the net parameters need further tuning. Fine-tuning is performed by using Bayesian optimization. The observed data was split into training and testing. 90% of the data is used for training and 10% for testing. It is useful to reserve a small portion of the data for validation purposes thus the convergence progress can be closely checked. In this example, the validation data has been ignored.

To improve the convergence process, it is recommended to standardize the data or normalize the data. In this example the data is standardized. The data can be normalized by several normalization algorithms by using *normalize* the function of MATLAB® but the normalization parameters need to be recorded to further de-normalize or convert the data to its generic values.

Monitoring the convergence training process is always useful (Figure 55). By plotting various metrics during training, the user can learn how the training is progressing. For example, it is possible to determine if and how quickly the network accuracy is improving, and whether the network is starting to overfit the training data.
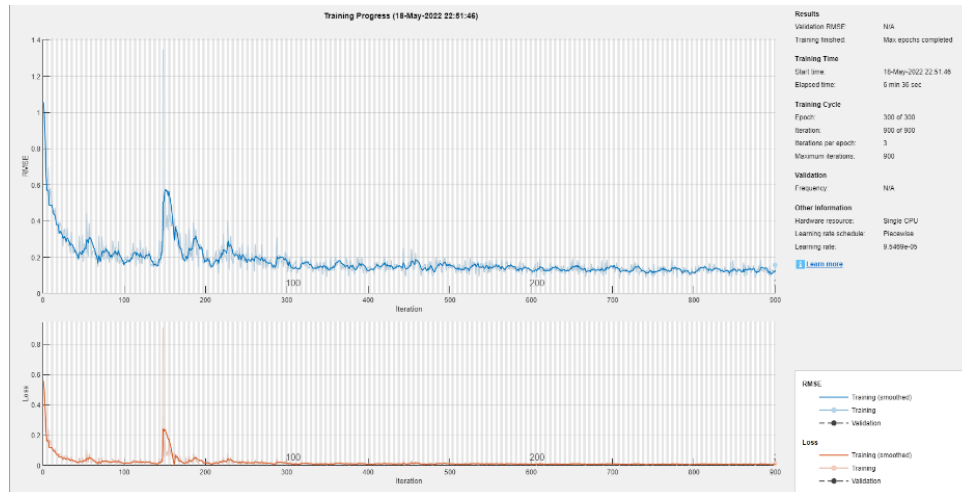
Figure 55: Convergence log of the hybrid ANN for the prediction of time-series

The time series and forecasted with the trained network values are compared in Figure 56 and Figure 57. The simple correlation (Eq. 26) between the testing and the predicted value is also shown in Figure 56.

$$sMAPE = \frac{1}{2} \frac{mean(Y_{predicted} - Y_{test})}{abs(Y_{predicted}) - abs(Y_{test})} \qquad (26)$$

Figure 58 shows the correlation between predicted and observed data and contains. For an ideal prediction capability, the regression curve of the predicted sample should merge with the target line crossing the origin.
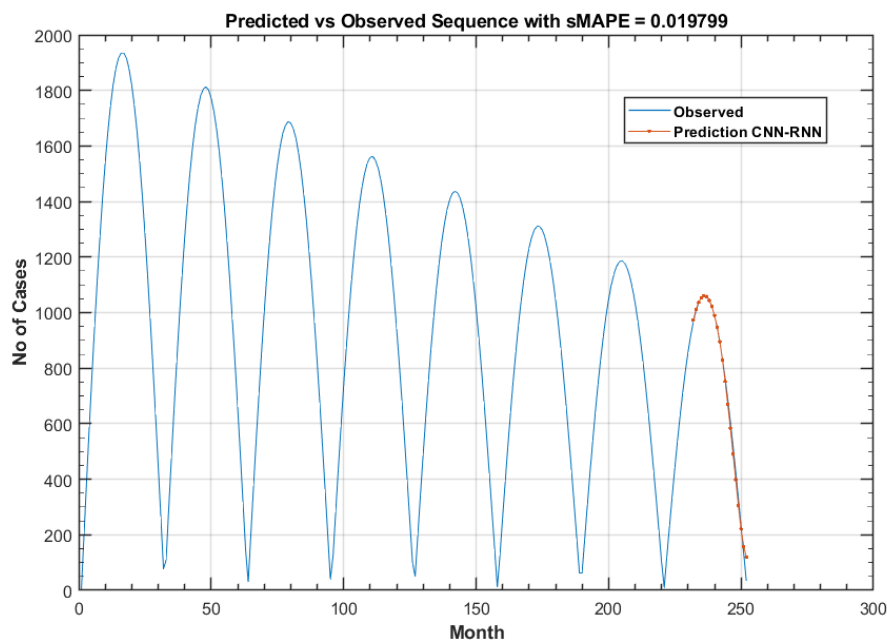
Figure 56: Distribution selected for analysis and its part that was selected for forecasting
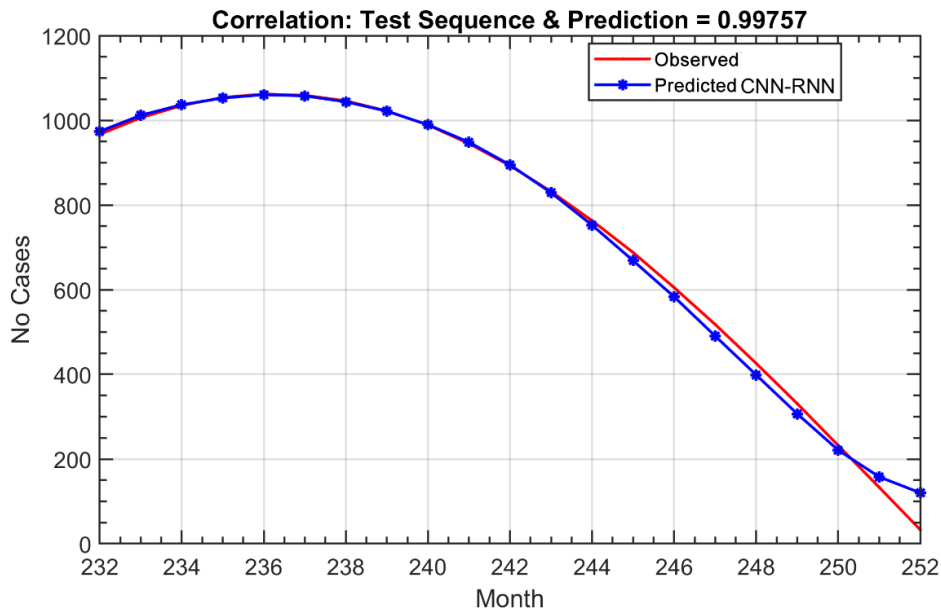
Figure 57: Predicted vs observed sequence for sinusoid-type time series
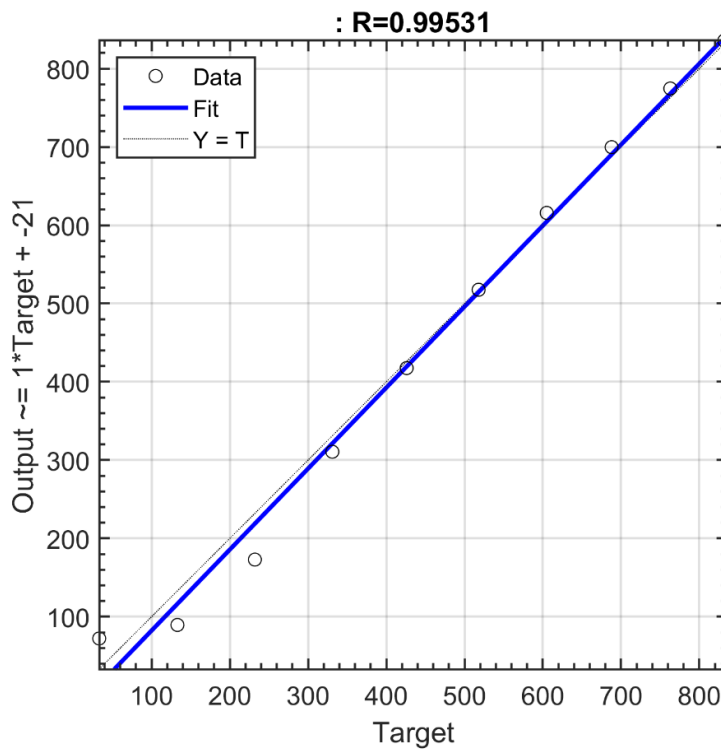
Figure 58: Correlation between predicted and observed data

Historic data concerning the West Texas Intermediate (WTI) price for crude oil is freely available by U.S. Energy Information Administration (58). The WTI Price evolution from January 1986 until April 2022 is shown in Figure 59. Utilizing the same methodology utilized in the previous example, which consists of five convolutional layers and a single fully connected one, the prediction capacity for the last batch of data is shown in Figure 59 and Figure 60. In this case, the hybrid CNN is working as a surrogate model for the crude oil price over time.
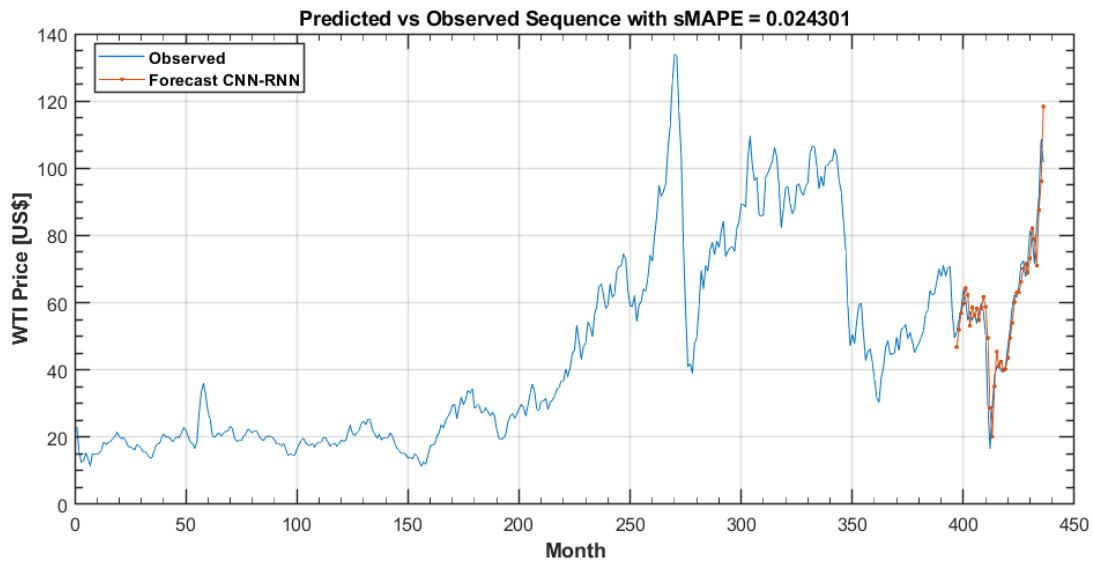
Figure 59: oil data series and prediction capability of the CNN-RNN combination
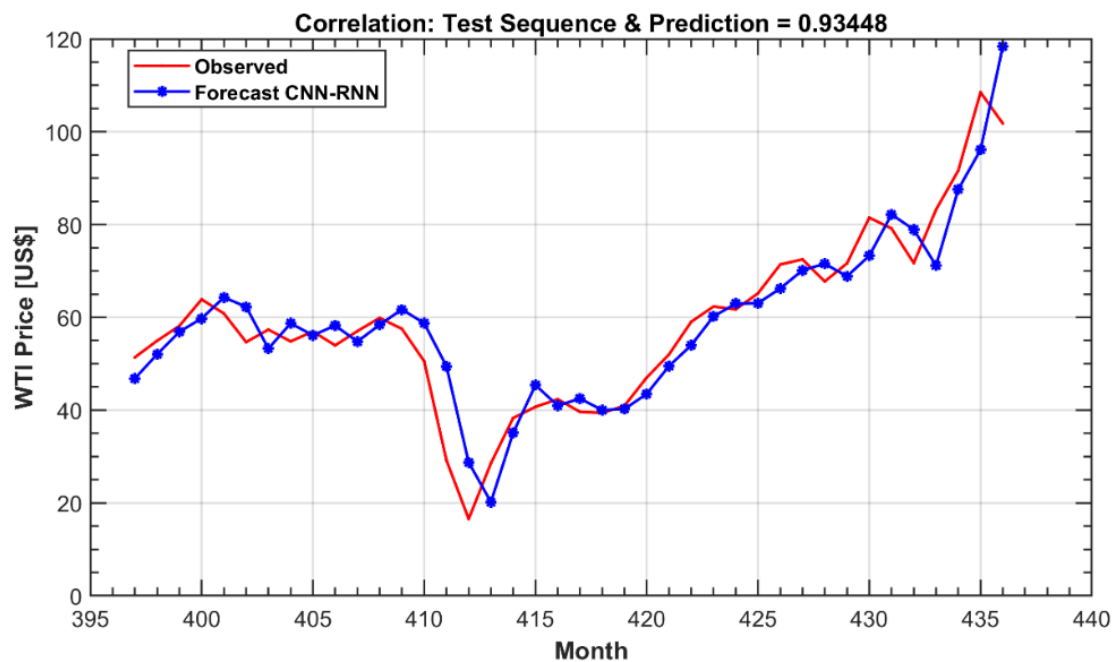
Figure 60: Close-up of the observed and predicted WTI price by the CNN-RNN combination

Non-stationary time series

Despite the good results with the two data sets shown before, these sets contain nonstationary data. Thus, the hybrid RNN does not work very well to proceed with forecasting. However, for other data sets such as stock data, it is recommended to transform the data stationary and then apply the method described before.

The Auto-Regressive Integrated Moving-Average (ARIMA) model was developed by Box-Jenkins (59). This model has been successfully applied in several situations, with emphasis on the forecast of econometric time series.

The ARIMA model establishes the prediction of the future value of a variable with the use of a temporal correlation structure (autocorrelation). This model consists of estimating a variable from a linear function, through several historical observations, considering its random errors.

The difference between exponential smoothing models and ARIMA is that the former is based on describing the trend and seasonality in the series, while the latter is based on autocorrelations present in the data.

The structure of time series data presents a big challenge for researchers and users, considering that traditional regression approaches do not yield valid results. Uncorrelated residuals are a key assumption of many regression methods. Models that fail to account for autocorrelation will have correct parameter estimates, but incorrect standard errors.

The identification steps involve fitting the autoregressive component (variable "p"), the moving average component of the ARIMA model (variable "q"), as well as any required differing to make the time series stationary or to remove seasonal effects (variable "d"). Together, these user-specified parameters are called the order of ARIMA.

The formal specification of the model will be ARIMA (p,D,q), where

- p — Nonseasonal autoregressive polynomial degree nonnegative integer
- D — Degree of nonseasonal integration nonnegative integer
- q — Nonseasonal moving average polynomial degree nonnegative integer

The first step in model identification is to ensure the process is stationary. Stationarity can be checked with a Dickey-Fuller Test. In statistics, the Dickey-Fuller test tests the null hypothesis that a unit root is present in an autoregressive time series model. The alternative hypothesis is different depending on which version of the test is used but is usually stationarity or trend-stationarity (60). Any non-significant value under model assumptions suggests a non-stationarity. The process must be converted to a stationary process to proceed by differencing the time series using a lag in the variable and removing seasonality effects.

After a developed model is properly considered to be stationary and adjusted such that there is no information in the residuals, a forecasting task can then take place. Forecasting assesses the performance of the model against concrete data. The usual approach now is to split the time series into two parts, utilizing the first part to fit the model and the second half to check performance. Usually, the utility of a specific model or the utility of several classes of models to fit actual data can be assessed by minimizing a value like a root mean square.

To proceed with the forecast of WTI oil price using the data from Figure 59 the regARIMA MATLAB® command was initially employed (61). This creates a stationary regression model of the oil-price time series. If the errors have an autocorrelation structure, then it is possible to specify models for them.

A seasonality parameter is required by the regARIMA command, and it exerts a great influence on the results. After the model is created, another step involves its rework by using the ARIMA errors of the previous step. This rework also encompasses the use of the distribution of the innovations to build the likelihood function. Finally, forecast responses of the regression model with ARIMA errors are performed.

Figure 31 shows a forecast with ARIMA data regularization that is compared to the last 200 registers of the WTI oil price. This period, i. e., this part of the data set was never employed in the creation of the regression models. This result represents the best match obtained by adjusting the seasonality parameter. in Figure 32, the area of interest was augmented. The overall trend of the price evolution was satisfactorily captured, but the plunge seen in Figure 32, was in some way anticipated.
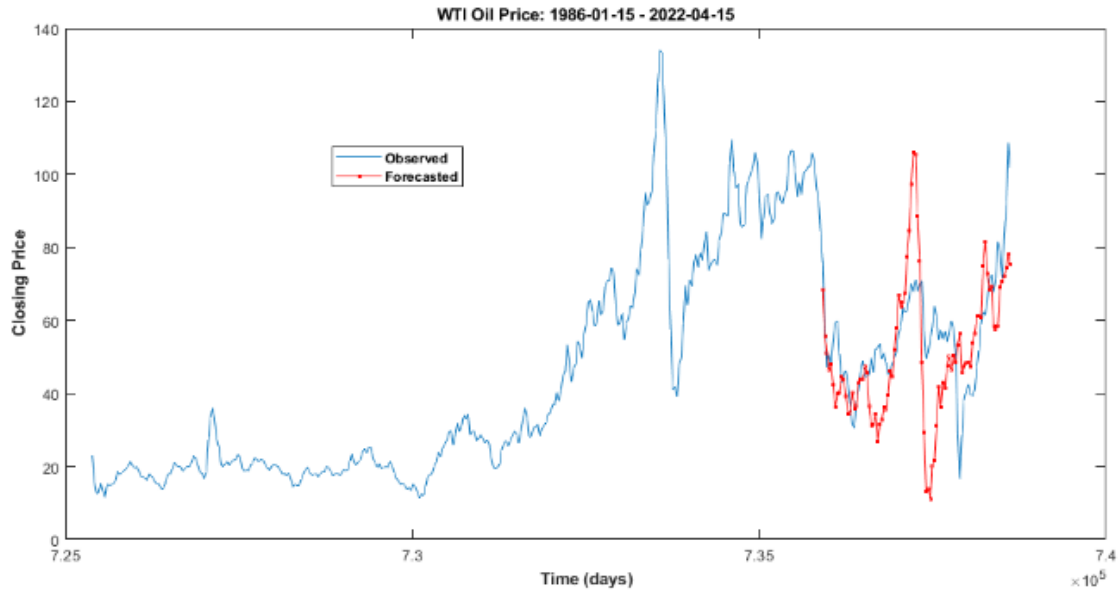
Figure 61: Oil price forecast
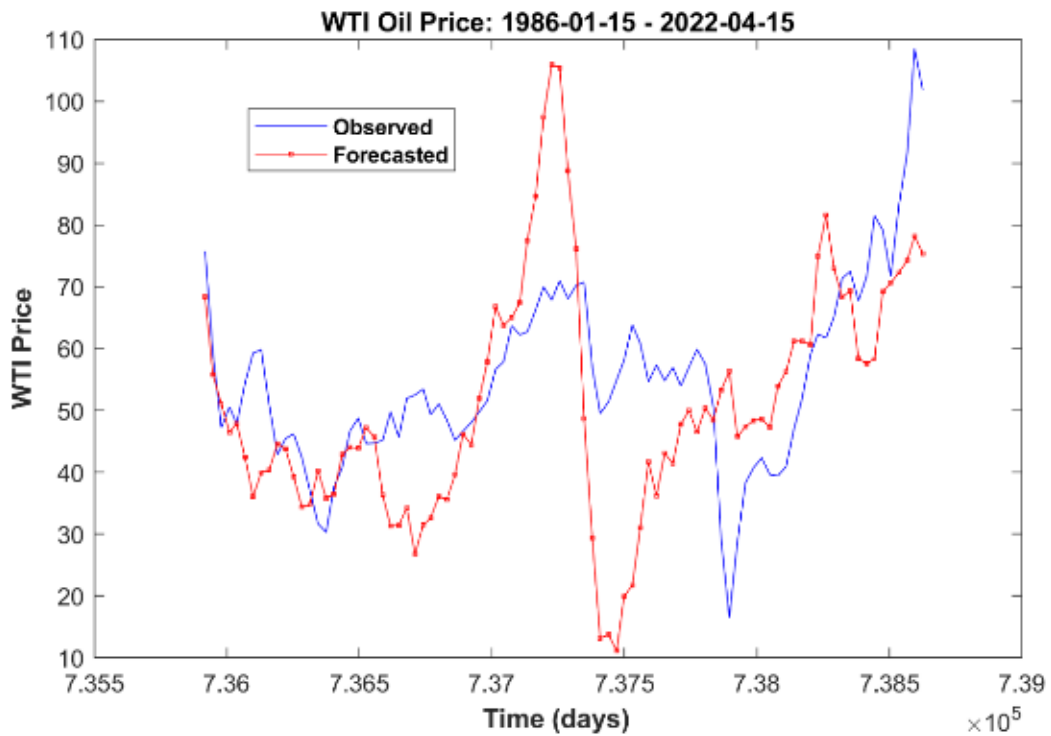
Figure 62: Oil price forecast in detail

4.3 Remained useful life of a turbofan engine

The remaining useful component life (RUL) is given in units of time (e.g., hours or cycles); end-of-life can be subjectively determined as a function of operational thresholds that can be measured. These thresholds depend on user specifications to determine safe operational limits.

Prognostics is currently at the core of systems health management. Reliably estimating remaining life holds the promise of considerable cost savings (for example by preventing unscheduled maintenance and by increasing equipment usage) and operational safety improvements. Remaining life estimates provide decision-makers with information that allows them to improve operational characteristics (like usage) which in turn may prolong the life of the component. It additionally allows companies to account for upcoming maintenance and set in motion a logistics process that supports a seamless transition from defective equipment to a fully operative one. Aircraft engines and structures, helicopter gearboxes, power plants, etc. are some of the typical examples of these types of equipment.

There is a lack of run-to-failure data sets for prognostics based on data. In most cases, real-world data contain fault signatures but no or little data capture fault evolution until failure (62). However, progress has been recorded. Khan and Yairi (63) studied the utilization of deep learning tools, such as, convolutional neural networks (CNNs), and recurrent neural networks (RNNs) in prognosis and health management.

Saxena et. al (62) describe how damage propagation can be modeled within the modules of aircraft gas turbine engines. They built response surfaces for all sensors by using a thermodynamical model for the engine as a function of variations of flow and efficiency of its components. An exponential rate of change for flow and efficiency loss was imposed for each data set, starting at a randomly chosen initial deterioration set point. The rate of change of the flow and efficiency denotes an otherwise unspecified fault with an increasingly worsening effect. The rates of alteration of the faults were constrained to an upper threshold but were otherwise chosen randomly. Damage propagation was allowed to continue until a failure criterion was reached. A health index was defined as the minimum of several superimposed operational margins at any given time instant. The failure criterion is reached when the health index equals zero. The output of the model obtains the cycles of the measurements, typically available from aircraft jet engines.

The prominent advantage of a deep learning approach is that there is no practical necessity for manual feature extraction or selection to use in a customized model to predict RUL. In addition, no prior knowledge is required of equipment health prognostics or signal processing to adequately develop a deep learning-based RUL prediction model.

The remained part of this section shows how to predict the RUL of turbofan engines by using deep convolutional neural networks, based on an example made available by Mathworks, Inc (64) (65). This example utilizes the Turbofan Engine Degradation Simulation Data Set (C-MAPSS) (66). The data set was compressed into a single file that can be freely downloaded from the NASA Website. It contains run-to-failure time-series data regarding four different sets (FD001, FD002, FD003, and FD004), corresponding to tests carried out under different combinations of operational conditions and fault modes. The present application uses only the FD002 data set, which is further divided into training and test groups. The training group contains simulated time-series data for 260 engines.

Each engine contains 21 sensors whose values are recorded at a given instance in a continuous process. Therefore, the sequence of recorded data varies in length and corresponds to a full run-to-failure instance. The test group contains 259 partial series and corresponding values of the remaining useful life at the end of each sequence.

The available data from NASA files present 26 columns of numbers, separated by spaces. Each row is a data record taken during a single operational cycle, and each column represents a different variable:

- Column 1 — Unit number
- Column 2 — Elapsed time
- Columns 3–5 — Operational conditions
- Columns 6–26 — Measurements of 21 sensors

Figure 63 shows some information extracted from the FD002 data set, which contains a failure related to a degradation of the high-pressure compressor. Initially, a verification procedure concerning the variability of some data is carried out and if there are small changes over time this data is discarded (64). Here, it is properly processed and sorted the data in a sequence format, with the first dimension being representative of the number of selected features and the second dimension representing the length of the time sequence. A convolutional layer composes a set with a normalization layer followed by an activation one, this combination being tailored for feature extraction. The fully connected layers and regression layer are used at the last stage of the network to estimate the RUL value and provide the output figure.
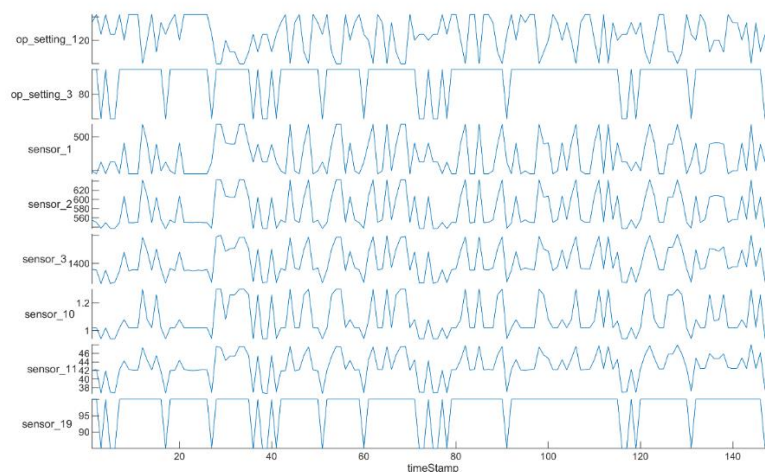
Figure 63: Some data of NASA's Turbofan Engine Degradation Simulation Data Set

The chosen CNN architecture applies a 1-D convolution along the time sequence direction only. Therefore, the order of features has no impact on the training, and only trends for each feature at a time are considered (64).

The CNN consists of five consecutive sets of a convolution 1-d, batch normalization, and a *ReLU* layer, with increasing filter size and number of filters as the first two input arguments to the convolution layer followed by two fully connected layers with 100 neurons each and a dropout layer with a dropout probability of 0.5. Since the network predicts the RUL of the turbofan engine, there is just a single output in the fully connected layer as the last layer of the network. Figure 64 provides a good overview of the network architecture.
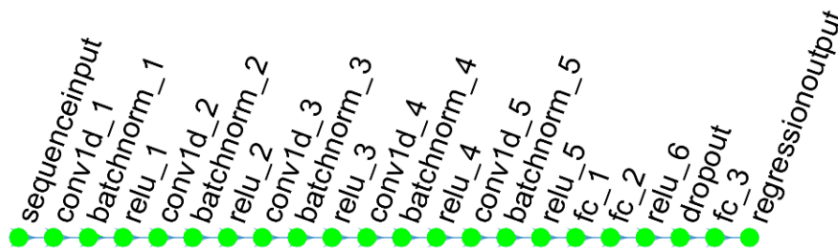
Figure 64: CNN architecture

The calculation of the root mean squared error (RMSE) across all time cycles of the test sequences provides rightful information to analyze how well the network performs on the test data.

The capability of the network predictor to perform throughout the given sequence of data in the test engines can be inferred from the comparison shown in Figure 65. The degradation process is represented by a combination of straight lines. The predicted RUL against the true RUL of a best case prediction reveals a 12-cycle difference concerning the prediction by the CNN and the test data at the fianl stage of this analysis. In general, the agremeent with test data is very good according to Figure 65. However, the CNN prediction of RUL is lower along the some part of period analyzed. In addition, each time this example is run, different results are obtained (Figure 66).
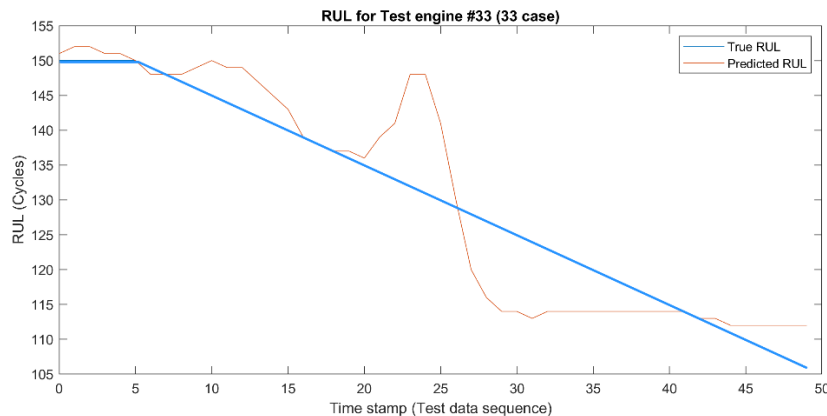
Figure 65: Best prediction case
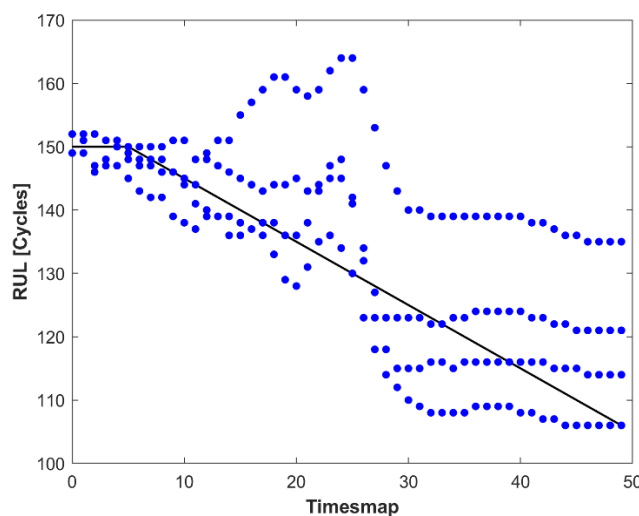
Figure 66: variability of RUL predictions for engine no. 33

5. Conclusions

The Chapter addressed some relevant noise and vibration issues related to transport aircraft and rotorcraft. An example of an application for noise estimation of turbofan engine components showed excellent agreement with two other methods. This approach jointly with another for estimation of airframe noise was employed in an MDO framework for the optimal design of a 78-seat airliner. The flyover noise was posed as a constraint and was effectively reduced for the individuals in the Pareto front when compared to a reference airplane.

From the CFD runs described in the present work, suggestions to lower the noise power level generated by main landing gear arrangements and sensors placed in front fuselages of transport aircraft are provided.

The forecast of the crude oil price by the regularization of non-stationary time series was carried out and the results can be considered acceptable.

A methodology to predict remained useful life of turbofan engines was described and applied to real data made available by NASA. The methodology utilizes convolutional neural networks and there is no need to manually extract features from data.

Acknowledgments

References

1. **Inquiété, Guillaume.** *Offset Brazil: Dynamics and Vibrations - Equipment Qualification.* Marignane : Eurocopter, 2012.
2. **Jorge, A. B.** *Fault detection system of a helicopter rotor from the vibration level (Systeme de Detection de Defauts d'un Rotor d'Helicoptere a Partir du Niveau Vibratoire.* Toulouse : ENSICA, 1992.
3. **Cruz, Ronaldo Vieira.** *Fundamentos da Engenharia de Helicópteros e Aeronaves de Asas Rotativas.* São José dos Campos : ITA, 2022. Apostilha de PRJ-91.
4. **Certain, Bernard, et al.** *Offset Brazil: Vibrations and Ressonance.* [Powerpoint Presentation] Marignane : Eurocopter Test Flight Department, 2012.
5. **Eurocopter.** *THM AS 350B3 Squirrel: Mechanics Instruction Manual.* [PDF] Marignane : Eurocopter, 2010.
6. **Lacaille, J., et al.** Turbofan Engine Monitoring with Health State Identification and Remaining Useful Life Anticipation. *International Journal of Condition Monitoring.* 2, 2015, Vol. 5.
7. **Morel, H.** *Brazil Offset: Dynamics/Health & Monitoring System.* [Powepoint Presentation] Marignane : Eurocopter, 2012.
8. **Rotor & Wing Aviation Services.** Rotor Blade Balancing – Rotor Track & Balance (RTB) & Helicopter Vibration. *Helicopter Rotor Blade Balancing – Tools, Techniques & Education.* [Online] Rotor & Wing Aviation Services, 2022. https://www.rwas.com.au/rotor-track-and-balance-rtb/.
9. **Basner, Mathias, et al.** Aviation Noise Impacts: State of the Science. *Noise&Health.* 2017, Vol. 41.
10. **Mauel, Stefan.** Frankfurt Airport Pioneers Active Noise Abatement. *International Airport Review.* [Online] Russel Publishing Limited, 2015. https://www.internationalairportreview.com/article/20017/frankfurt-airport-pioneers-active-noise-abatement/.
11. **Roulois, G.** *Offset Brazil: Internal Noise.* Marignane : Eurocopter, 2012.

12. **Magalhães, P. E. and Mattos, Bento Silva.** Environmental Aspects of Airplane Design. *Conceptual Design of Green Transport Airplane.* Sharjah : Bentham Science Publishers, 2018, p. 436.

13. **Wikipedia, The Free Encyclopedia.** Sound Power. *Wikipedia.* [Online] Wikipedia, The Free Encyclopedia, 2022. https://en.wikipedia.org/wiki/Sound_power.

14. **Lighthill, Michael James.** On Sound Generated Aerodynamically I. General Theory. *Proceedings of the Royal Society of London Series A.* 1952, Vol. 211.

15. **Rienstra, S. and Hirschberg, A.** An Introduction to Acoustics. [Online] 2021. https://www.win.tue.nl/~sjoerdr/papers/boek.pdf.

16. **Fluent, Inc.** *Fluent 6.2 User Manual.* New Hampshire : Fluent, Inc., 2005.

17. **Pan, Y. S.** Perturbation Solution of the Navier-Stokes Equations and its Relation to the Lighthill-Curie . *Journal of the Acoustical Society of America.* 1975, Vol. 58.

18. *In Computational Aeroacoustic Analysis of Slat Trailing-Edge Flow.* **Lockard, D., Brentner, K. and Singer, B.** Bellevue : %th AIAA/CEAS Aeroacoustics Conference, 1999. AIAA-99-1802.

19. *Aeronoise of a Slatted-Airfoil Configuration.* **Ton, T. A., et al.** Reno : 46th AIAA Aerospace Sciences Meeting and Exhibit, 2008. AIAA 2008-0014.

20. **van der Kooi, J. T.** *An Experimental Study of Aolean Tones and Trailing-edge Noise.* Twente : Master Thesis, University of Twente, 2006.

21. **West, G. S.** Measurements of Fluctuation Pressures and Forces on a Cylinder in the Reynolds Number Range 104 to 2.5 x 105. *Jounal of Fluids and Structures.* 1993, Vol. 7.

22. **Norberg, C.** Fluctuating Lift on Circular Cylinder: Review and New Measurements. *Journal of Fluids and Structures.* 2003, Vol. 17.

23. *Large-Eddy Simulation: Present state and future perspectives.* **Piomelli, U.** Reno : 36th AIAA Aerospace Sciences Meeting and Exhibit, 1998. AIAA 098-0534.

24. **Templeton, Jeremy, Wang, Meng and Moin, Parviz.** Towards LES Wall Models Using Optimization Techniques. *Researchgate.* [Online] 2002. https://www.researchgate.net/publication/251501476_Towards_LES_wall_models_using_optimization_t echniques.

25. **Antoine, Nicolas.** *Aircraft Noise Overview.* Stanford, CA : Aircraft Design & Aerodynamic Group, Stanford University, 2000.

26. **William, Ffowcs and Hawkings, J.** Sound Generation by Turbulence and Surface in Arbitrary Motion. *Phil. Trans. Roy Soc. London.* 1969, Vol. 264.

27. *In Aeroacoustic Study of Airfoil Leading Edge High-Lift Devices.* **Andreou, C., Graham, W. and Shin, H.** Cambridge, MA : 27h AIAA/CEAS Aeroacoustics Conference, 2006. AIAA 2006-2515.

28. **Proudman, I.** The Generation of Noise by Isotropic Turbulence. *Proc. Royal Society.* 114, 1952.

29. **Lilley, G. M.** *The radiated noise from isotropic turbulence revisited.* Hampton, VA : NASA, 1993. CR-93-75.

30. **Ansys, Inc.** Ansys Fluent R15 Tutorial Guide. *Absys Fluent.* [Online] 2013. https://vdocument.in/ansys-fluent-tutorial-guide-r-15.html.

31. **Larosterna.** Sumo: Open Source Mesher. *larosterna Products.* [Online] larosterna, 2017. https://www.larosterna.com/products/open-source.

32. **Cao, Xin, Yuhong, Jia and Jiajie, Tian.** Research on Landing Impact Characteristic of Multi-wheel Bogie Landing Gear's Truck. *International Journal of Aerospace System Engineering.* 2015, Vol. 2.

33. **Glegg, Stewart and Davenport, William.** Open Rotor Noise - Tone and Broadband noise. *Tone Noise.* [Online] ScienceDirect, 2022. https://www.sciencedirect.com/topics/engineering/tone-noise.

34. **Deaconu, Marius, et al.** Helicopter Inside Cabin Acoustic Evaluation: A Case Study - IAR Puma 330. *International Journal of Environment Research and Public Health.* September 2021, pp. 1-14.

35. *Two-dimensinal Fourier Transform Analysis of Helicopter Flyover Noise.* **Farassat, Odylin and Morris, J. Philip.** 55th Annual Forum of the American Helicopter Society : American Helicopter Society, 1999.

36. **Oswald, Fred B., et al.** *Influence of Gear Design on Gearbox Radiated Noise.* Washington, D.C. : NASA Lewis Research Center, 1994. TM-106511.

37. **Yu, Liya, et al.** Gear Fault Diagnosis through Vibration and Acoustic Signal Combination Based on Convolutional Neural Network. *Information.* 2020, Vol. 11.

38. **Huff, Dennnis.** *Noise Reduction Technologies for Turbofan Engines.* Cleveland : NASA/TM—2007-214495, 2007.

39. *Noise Estimation of Installed Turbofan Engines.* **Muraro, Daniel A.** São José dos Campos : 2009 Brazilian Symposium on Aerospace Eng. & Applications, 2009. 3rd CTA-DLR Workshop on Data Analysis & Flight Control.

40. **Heideman, M. F.** *Interim Prediction Method for Fan and Compressor Source Noise.* Cleveland : NASA Lewis Research Center, 1979. p. 68p. TM-X-71763.

41. **Huff, R. G., Clark, B. J. and Dorsch, R. G.** *Interim Prediction Method for Low Frequency Core Engine Noise.* NASA. s.l. : NASA Lewis Research center, 1974. p. 25p. TM-X-71627.

42. **Stone, J. R.** *Interim Prediction Method for Jet Noise.* NASA. s.l. : NASA Lewis Research Center, 1974. TM-X-71618.

43. **Schmid, Michael.** *Entwicklung eines Programmmoduls zur Prognose des Lärms von Strahltriebwerken im Flugzeugvorentwurf.* Berlin : Technische Universität Berlin, Studienarbeit, 2001.

44. **ESDU.** *Computer-based estimation procedure for single-stream jet noise.* s.l. : ESDU 98019, 1998.

45. *The Best Suited Airliner for an Existing Airline Network.* **Siqueira, L., Mattos, B. S. and Loureiro, V.** Palm Springs : 50th AIAA/ASME/ASCE/AHS/ASC Structures, Structural Dynamics, and Materials Conference, 2009. AIAA Paper 2009-2206.

46. *Conceptual optimal design of environmentally friendly airliners: a review of available methodologies and their integration into a consistent framework for everyday use.* **Magalhães, P. E. and Mattos, Bento Silva.** Dallas : 16th AIAA/ISSMO Multidisciplinary Analysis and Optimization Conference, 2015. AIAA 2015-3358.

47. **Secco, Ney and Mattos, Bento Silva.** Artificial neural networks to predict aerodynamic coefficients of transport airplanes. *Aircraft Engineering and Aerospace Technology.* March 2017, pp. 211-230.

48. **Mattos, Bento Silva and Secco, Ney Rafael.** An Airplane Calculator Featuring a High-Fidelity Methodology for Tailplane Sizing. *Journal of Aerospace Technology and Management.* 2013, Vol. 5, pp. 371-386.

49. **EMBRAER Commercial Aviation.** Embraer 175 Performance. [Online] 2018. https://www.embraercommercialaviation.com/wp-content/uploads/2017/02/Embraer_spec_175_web.pdf.

50. **EASA.** *Type-Certificate Data Sheet for Noise for ERJ 170.* s.l. : EASA, 2016. p. 14 of 27. EASA.IM.A.001.

51. **GE Aviation.** CF34-10E - GE Aviation. [Online] October 2018. https://www.geaviation.com/bga/engines/cf34-engine.

52. **Rosebrock, Adrian.** Convolutional Neural Networks (CNNs) and Layer Types. *pyimagesearch.* [Online] Pyimagesearch, 2021. https://pyimagesearch.com/2021/05/14/convolutional-neural-networks-cnns-and-layer-types/.

53. **Krizhevsky, Alex, Sutskever, Ilya and Hinton, Geoffrey.** ImageNet Classification with Deep Convolutional Neural Networks. *Communications of the ACM.* 2017, Vol. 60, 6, pp. 84-90.

54. **IBM.** Convolutional Neural Networks. *IBM Cloud Education.* [Online] IBM, October 2020. https://www.ibm.com/cloud/learn/convolutional-neural-networks.

55. **Asthana, Meghna.** Layers of a Convolutional Neural Network. *Analytics Vidhya.* [Online] Analytics Vidhya, March 2020. https://medium.com/analytics-vidhya/layers-of-a-convolutional-neural-network-168daddd2dd1.

56. **Mathworks, Inc.** Convolutional Network. *Mathworks.* [Online] Mathworks, Inc., 2022. https://www.mathworks.com/discovery/convolutional-neural-network-matlab.html.

57. **Sanchez, H.** Time Series Forecasting Using Hybrid Convolutional Neural Network - Recurrent Neural Network. *Matlab File Exchange.* [Online] Mathworks, Inc., 2002. https://www.mathworks.com/matlabcentral/fileexchange/91360-time-series-forecasting-using-hybrid-cnn-rnn?s_tid=srchtitle. 91360.

58. **U.S. Energy Information Administration.** Petroleum & Other Liquids. *U.S. Energy Information Administration.* [Online] May 2022. https://www.eia.gov/petroleum/reports.php#/T1288. Excel Worksheet.

59. **Box, George and Jenkins, Gwilym.** *Time Series Analysis: Forecasting and Control.* San Francisco : Holden-Day, 1970.

60. **Wikipedia, The Free Encyclopedia.** Dickey–Fuller Test. [Online] Wikipedia, The Free Encyclopedia, 2022. https://en.wikipedia.org/wiki/Dickey%E2%80%93Fuller_test.

61. **Mathworks, Inc.** regARIMA class. *Matlab User Guide.* [Online] Mathworks, Inc., 2022. https://www.mathworks.com/help/econ/regarima-class.html.

62. *Damage propagation modeling for aircraft engine run-to-failure simulation.* **Saxena, Abhinav, et al.** s.l. : International Conference on Prognostics and Health Management, PHM , 2008.

63. **Khan, S. and Yairi, T. S.** A Review on The Application of Deep Learning in System Health Management. *Mechanical Systems and Signal Processing.* 2018, Vol. 107.

64. **Mathworks, Inc.** Remaining Useful Life Estimation Using Convolutional Neural Network. *Mathworks.* [Online] Mathworks, 2022. https://www.mathworks.com/help/predmaint/ug/remaining-useful-life-estimation-using-convolutional-neural-network.html.

65. **Li, Xiang, Ding, Qian and Sun, Jian-Qiao.** Remaining Useful Life Estimation in Prognostics Using Deep Convolution Neural Networks. *Reliability Engineering & System Safety.* 2018, Vol. 172.

66. **NASA Ames.** Turbofan engine degradation simulation data set . *Dashlink.* [Online] NASA, 2022. https://ti.arc.nasa.gov/tech/dash/groups/pcoe/prognostic-data-repository/#turbofan.

Chapter 15

On Vibration Analysis and Health and Usage Monitoring Systems (HUMS) of Dynamic Components of Helicopters

On Vibration Analysis and Health and Usage Monitoring Systems (HUMS) of Dynamic Components of Helicopters

Ariosto B. Jorge[1*], Ronaldo V. Cruz[2], Bento S. de Mattos[2], and Rafael de A. González[3]

[1]Post-Graduate Program - Integrity of Engineering Materials, University of Brasilia, Brazil. E-mail: ariosto.b.jorge@gmail.com
[2]Instituto Tecnológico de Aeronáutica, Brazil. E-mail: bmattos@ita.br; ronaldoc@ita.br
[3]Naval Studies Coordination Center in São Paulo, Brazilian Navy, Brazil. E-mail: rafaelgonzalez.eng@gmail.com

*Corresponding author

Abstract

This chapter presents a compilation of the research work done by the authors and collaborators on the topics of vibration analysis and Health and Usage Monitoring Systems (HUMS) of dynamic components of helicopters, comprising: i) an introduction to helicopter vibration; ii) a discussion and details of vibration analysis techniques for helicopter rotors and dynamic components, from the point of view of the operational user and the technical maintenance of the helicopter; iii) a discussion and details on vibration-based Health and Usage Monitoring Systems (HUMS) philosophy in the predictive maintenance of helicopters, from the point of view of history and evolution of the market; architecture; benefits, disadvantages, limitations; certification challenges; and application perspectives; and iv) a discussion on vibration-based HUMS of dynamic components of helicopters, focused on results and discussions done during the Offset Program of Transfer of Technology in HUMS of the helicopter EC-725, a program involving AIRBUS HELICOPTERS, HELIBRAS, UNIFEI, and ITA. The latter includes, in particular: 1) some discussion and details of the M'ARMS system; 2) its evolution towards the MOD45 indicator; 3) a case study of electrical/signal errors in the vibration acquisition system (accelerometers, cables, etc) with a proposed error indicator; and 4) a finite element modeling of a typical coupling between two sections of a tail drive shaft.

Keywords: helicopter rotor vibration; vibration analysis; HUMS – Health and Usage Monitoring Systems, helicopter dynamic components

1. Vibration analysis and HUMS in dynamic components: chapter outline and introduction to helicopter vibration

This chapter concentrates on a discussion of vibration analysis techniques and the use of a framework of Health and Usage Monitoring Systems (HUMS) for helicopter dynamic components.

Some helicopter vibration reduction techniques focused on balancing and tracking the helicopter rotors are discussed in a separate chapter, concentrated on model-based parameter identification for balancing and tracking a helicopter's main rotor using once-per-revolution vibration data.

1.1 Section content

Subsection 1.2 presents an introduction to helicopter vibration.

Section 2 presents a discussion and details of vibration analysis techniques for helicopter rotors and dynamic components, from the point of view of the operational user and the technical maintenance of the helicopter.

Section 3 presents a discussion and details on vibration-based Health and Usage Monitoring Systems (HUMS) philosophy in the predictive maintenance of helicopters, from the point of view of history and evolution of the market; architecture; benefits, disadvantages, limitations; certification challenges; and application perspectives.

Section 4 presents a discussion on vibration-based HUMS of dynamic components of helicopters, focused on results and discussions done during the Offset Program of Transfer of Technology in HUMS, a program involving AIRBUS HELICOPTERS, HELIBRAS, UNIFEI, and ITA.

Section 5 presents some concluding remarks.

1.2 Introduction to helicopter vibration

This section is based on class notes materials for the courses "Foundations of Helicopter and Rotary Wing Engineering", ITA [1], and "Flight Test Course - vibration theory", PEV, DCTA (Gomes & Cruz, 2008).

All helicopters shake due to rotary sources, such as the rotors, transmission gears, engines, and several other dynamic components. The main causes of the vibration can be understood by remembering some basic concepts about oscillatory movements.

A body must satisfy two conditions to oscillate: it must be able to store potential energy (which means an elastic behavior) and it must be able to have kinetic energy (which means to have mass and velocity). Therefore, oscillation represents the continuous exchange of kinetic and potential energy.

A motion that repeats itself after an equal interval of time T, called the period of the oscillation, is called periodic motion, and the reciprocal $f = {}^1\!/_T$ is known as the frequency. The simplest form of periodic motion is the harmonic motion, which can be obtained, for example, by the movement of a mass coupled to spring without the action of external forces, acting in a vacuum, as shown in Figure 1.
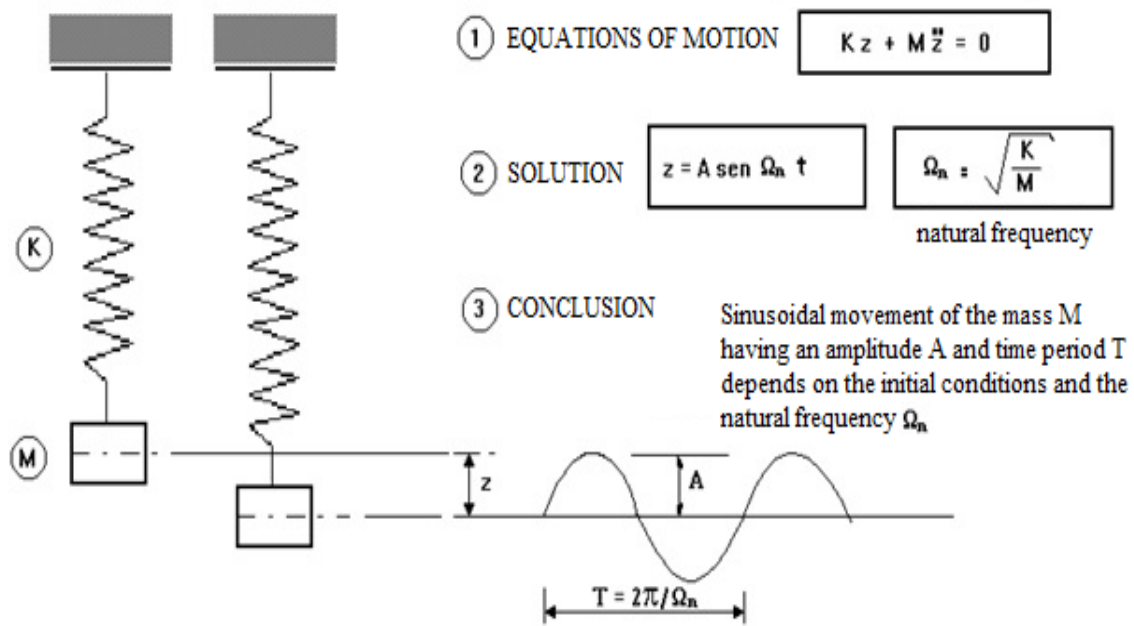
Figure 1: Free Vibration (Adapted from [2])

In this simplified system, the spring has negligible weight concerning the mass *M* and has a stiffness constant *K*. Disregarding the damping of the air, this mass-spring system is conservative and, therefore, the total energy of the system is constant and can be determined by the sum of kinetic energy E_c and potential energy E_p.

When the mass M is displaced from the equilibrium position and then released, sinusoidal oscillations will occur around the equilibrium position of the system according to the equation $z = A \sin \Omega_n t$, where Ω_n is the natural frequency of the spring-mass system in rad/s ($\Omega = 2\pi f$), A is the amplitude of motion and f is the frequency in Hz. Also, if the total energy of the system is constant, the energy equation can be applied between two instants of sinusoidal motion. Thus, if 1 is the static equilibrium position with maximum kinetic energy and 2 is the maximum mass displacement and, therefore, the maximum potential energy, we have, equating both terms, that:

$$\frac{1}{2}KA^2 = \frac{1}{2}MV_{máx}^2 = \frac{1}{2}M(\Omega_n A)^2 \Rightarrow \Omega_n = \sqrt{\frac{K}{M}} \qquad (1)$$

Equation (1) allows us to obtain the natural frequency of the system as a function of its stiffness and mass. However, helicopter vibrations originated from periodic external forces. The system presented in Figure 2 represents an example of harmonically excited vibration, where the upper end of the spring is connected to a base of an eccentric shaft that excites the system with an amplitude X and a frequency Ω.

1) Equation of Motion for Undamped Forced Vibration

$$k(z-x) + M\ddot{z} = 0$$

$$kz + M\ddot{z} = kX\,\mathrm{sen}(\Omega t)$$

2) Solution $z = Z\,\mathrm{sen}(\Omega t)$
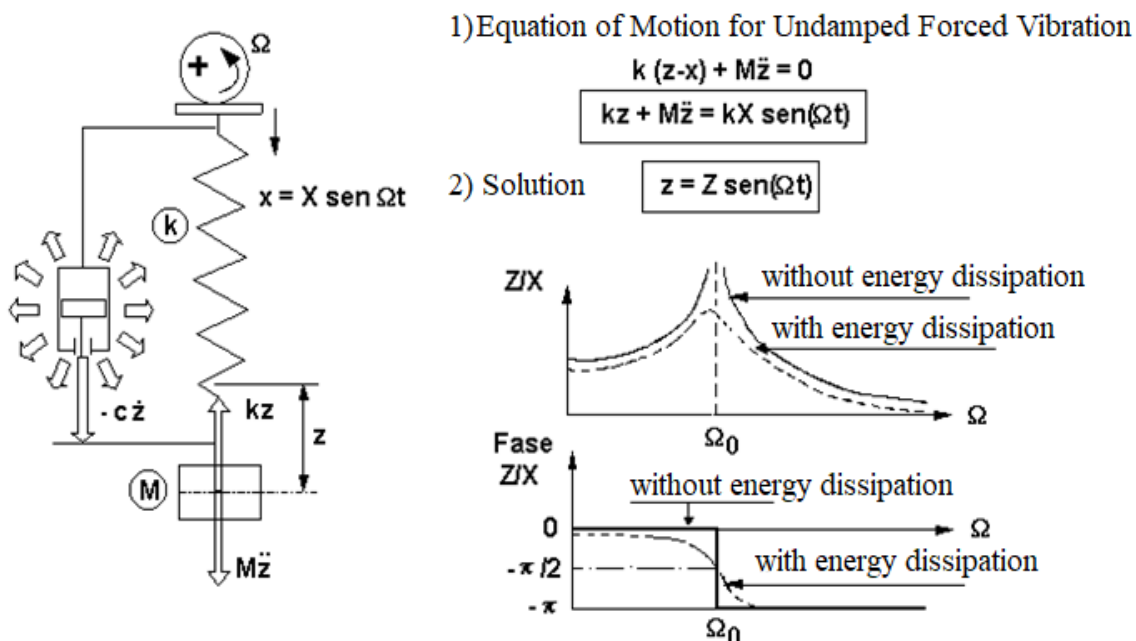
Figure 2: Harmonically excited vibration for damped and undamped systems
(Adapted from [2])

If the rotor speed of that axis is slow, the mass M follows the movement of the base. This means that the mass oscillates with the frequency forced by the eccentric, and both are in phase. If the rotor speed increases, the amplitude passes, in the case of an undamped system, to infinity at the natural frequency of the system. This is the so-called resonant frequency, where there is still a phase inversion. Continuing to increase the speed, the amplitude tends to zero as the excitation frequency approaches infinity, while the mass oscillates in phase opposition regarding oscillatory excitation force.

Introducing viscous damping into the mass-spring system of Figure 2 considerably modifies the response. Its effect is basically to dissipate the energy of the system and, consequently, reduce the oscillation amplitude. This is the basic principle of a helicopter vibration damper. Some examples of vibration dampers are the landing gear dampers and the main rotor lead-lag dampers. Their main functions are to dissipate energy to avoid a catastrophic phenomenon known as ground resonance, an auto-excited instability that occurs when the frequency of the blade lead-lag regressive mode coalesces with a frequency of a fuselage mode on the ground.

Other devices used by helicopter manufacturers to reduce the amplitude of oscillation are vibration isolators and vibration absorbers. Ref. [3] presents a comprehensive analysis of both kinds of vibration controls. Regarding the vibration absorbers, they consist of another mass-spring system attached to the original mass that needs to reduce its vibration amplitude. Therefore, they constitute a two-degree-of-freedom system as shown in Figure 3.
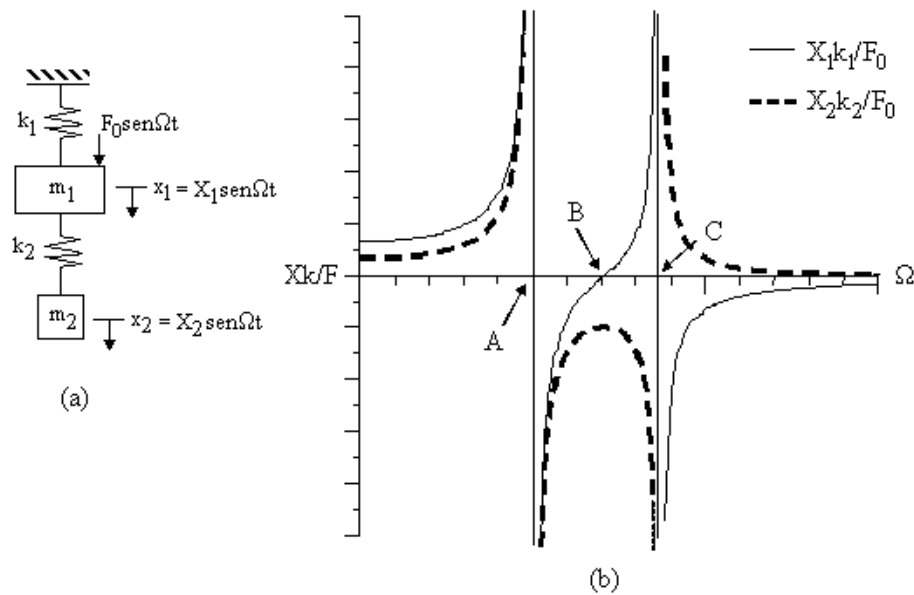
Figure 3: Two-degree-of-freedom system (Adapted from [2])

This type of system has two normal vibration modes: the first mode corresponds to the main mass and the attached absorber mass movement in phase; while the second one consists of a movement of both masses in opposite phases. Each mode has its natural frequency. If there is no external harmonic force acting over the two-degree-of-freedom system, the resulting motion, after an initial excitation, will be the superposition of both normal modes of vibration. However, if there is an external harmonic force acting over the system, the resulting forced harmonic vibration frequency will be the same as the applied external force.

A helicopter vibration absorber has k_2 and m_2 tuned to match the frequency of the external force to be absorbed, which will be the frequency $b\Omega$, where b is the number of blades and Ω is the main rotor speed.

As shown at point B in Figure 3, the attached absorber mass will vibrate at the same frequency $b\Omega$ but in the opposite phase of the external harmonic force. Consequently, the movement of the main mass m_1 is reduced to zero. It should also be noted from Figure 3 that:

a) for the interval $0 < \Omega < \Omega_A$, m_1 and m_2 move in phase with the external harmonic force, once both amplitudes vibrations are positive. For frequencies close to 0, both movements of the bodies are slightly different, depending on the stiffness and mass parameters; however, for $\Omega \approx \Omega_A$, the maximum amplitudes of both masses tend to infinity. Therefore, Ω_A corresponds to the natural frequency of the 1st normal mode of vibration related to the in-phase motion of the masses;

b) for the interval $\Omega_A < \Omega < \Omega_C$, m_1, and m_2 initially move in phase but in opposite phase with regarding the external harmonic force since both maximum amplitudes are negative. Increasing Ω, it will be observed that the bodies start moving in opposite phases from $\Omega \approx \Omega_B$; and

c) for the interval $\Omega_C < \Omega < \infty$, m_1 and m_2 move symmetrically out of phase, so that m_2 and m_1 are, respectively, in-phase and in opposite phase with the external harmonic force. For $\Omega \approx \Omega_C$, the maximum amplitudes of both masses tend to infinity, and then Ω_C corresponds to the natural frequency of the 2nd normal mode of vibration related to opposite phase motions of the masses.

There are several examples of helicopter vibration absorbers. Some of them, such as the cabin resonators and the main rotor vibrator absorber of the Squirrel AS350 helicopter (Figure 4) utilize a physical spring so that it is tuned to one frequency and is effective only over a narrow band of frequencies. Considering the nominal rotor speed of 390 rpm, the $b\Omega$ frequency tuned is 19.5 Hz. Changing rotor speed, the effectiveness of this device is reduced significantly.

(a) Vibrator absorber   (b) Cabin Resonator
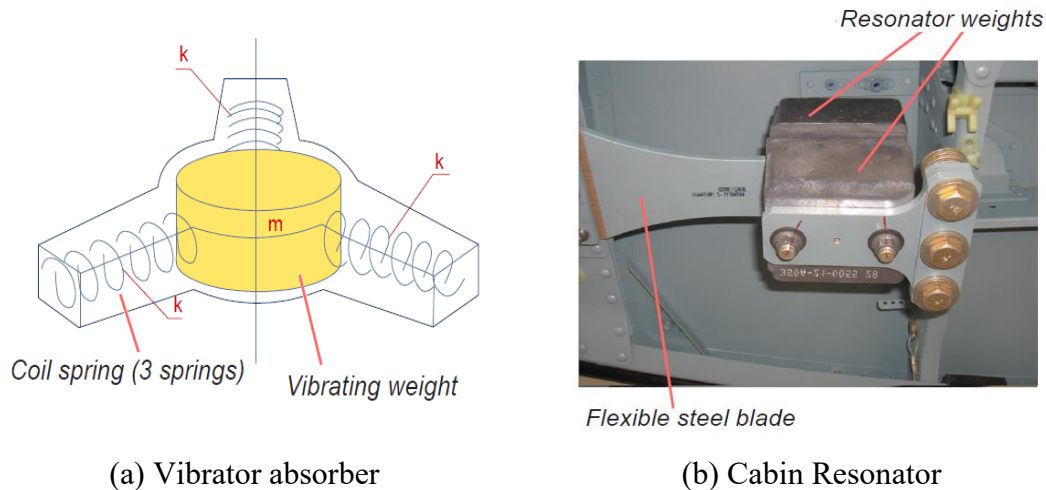
Figure 4: Vibration Absorbers of the Squirrel AS350
[adapted from (EUROCOPTER, 2010)]

Other helicopter vibration absorbers such as the centrifugal pendulums of the BK-177 and the bifilar weights of the UH-60 "Black Hawk" (Figure 5) replace the physical spring with a centrifugal spring. So, using the centrifugal force, the main gain of those absorbers is that they are automatically tuned to $b\Omega$, considering any rotor speed.
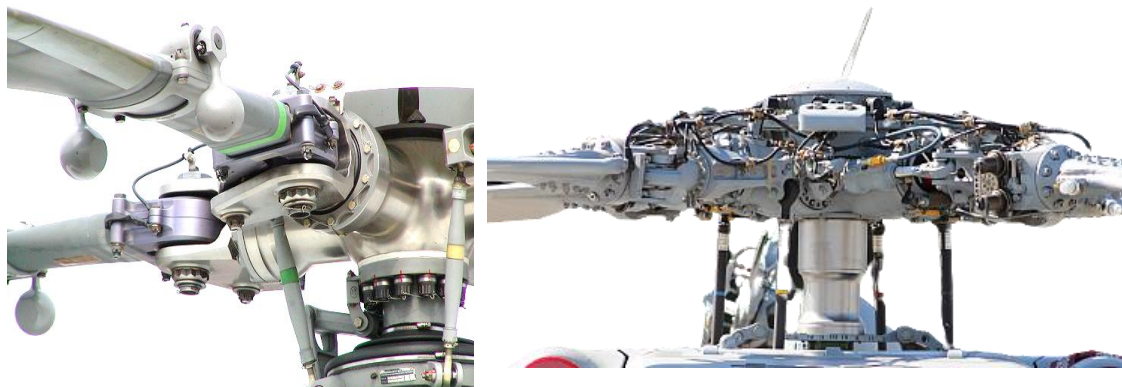
(a) Kawasaki / Eurocopter BK117 centrifugal pendulums [adapted from (JGSDF Camp Akeno Airshow, 2002)]

(b) Black Hawk bifilar absorber (Photo and editing: B. Mattos)

Figure 5: Examples of helicopter vibration absorbers

Vibration absorbers need to be tuned to match the frequency $b\Omega$ of the helicopter's main rotor. It is important to pay attention that lower frequency values mean higher vibration amplitudes, so the main rotor is the main source of helicopter vibration, and much lower frequencies vibration must be reduced.

Considering that the external harmonic forces acting on the blade are cyclic, their effects can be decomposed into the sum of sines and cosines harmonically related, in other words, their forces correspond to frequencies multiples of the rotor speed (1Ω, 2Ω, 3Ω, and successively), in a Fourier series. For the case of the helicopter main rotor, the forced vibrations on the blades are in frequencies multiples of the fundamental frequency Ω (mainly 1Ω). This characteristic requires special attention during blade design, once each blade has many flapping, lead-lag, and torsion elastic modes, as shown in Figure 6. The position of those natural frequencies concerning the harmonic excitation determines the increase or attenuation of the forces applied to the main rotor blades.

It can be noted that 1st Torsion Mode coincides with the 5th harmonic excitation at rotor speeds closer to 7 Hz.

Solution: Stiffen up the blade to increase the 1st Torsion Mode. The natural frequencies must be different from the harmonic excitation at nominal rotor speed.
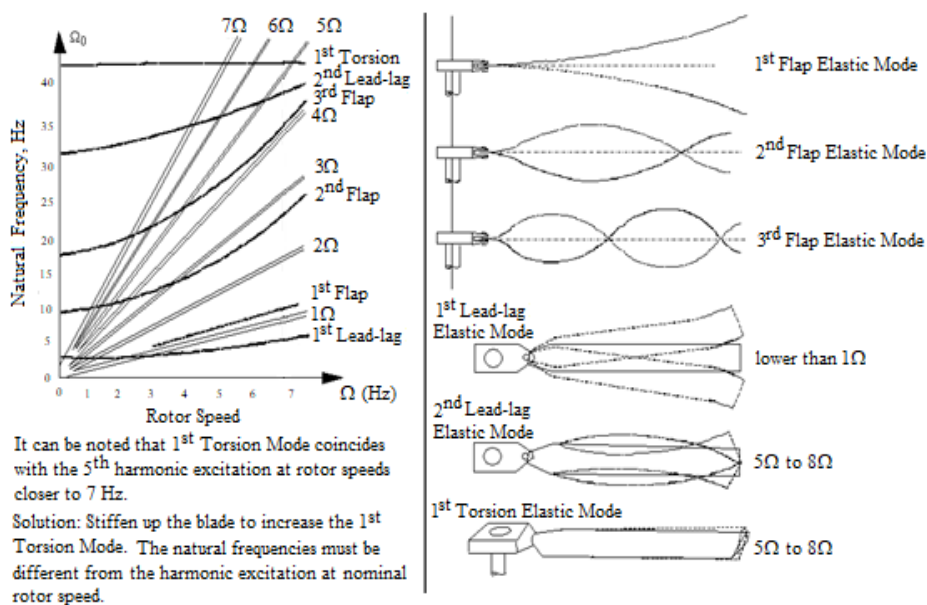
Figure 6: Main Blade Elastic Modes (Adapted from [1])

Furthermore, it should be observed that the aeroelastic coupling of the rotor blades can also cause some instabilities, such as flap/lead-lag instability, pitch/lead-lag instability, flutter, and stall flutter at high blade angles of attack, which also provokes the increased of the vibration levels and the blade loads.

For that reason, the natural frequencies of elastic modes must be separated from each other and also from the harmonic excitation frequencies of the blades at the nominal rotor speed.

This is a design criterion, therefore, if necessary, the manufacturer adds mass or changes the stiffness of the blades to move their natural frequencies away from the excitation harmonics, at least, according to [4], up to typically 4Ω or 5Ω for single-rotor helicopters and up to 6Ω or 8Ω for tandem helicopters.

Such efforts acting on the blades are transmitted to the main rotor hub that works like a filter exciting the fuselage vertically and horizontally at frequencies multiples of the number of the blades, $nb\Omega$, where n is an integer number.

Ref. [5] presents such mathematical deduction for both vertical and horizontal forces transmitted to the fuselage. However, some simplified models can also be used to explain how the main rotor hub acts example for the 1Ω and 2Ω flap excitation as shown in Figure 7.
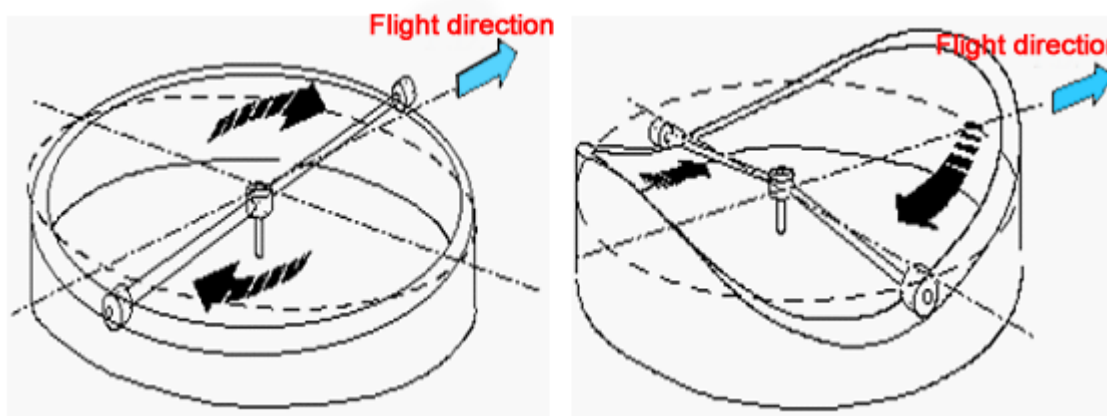
(a) 1st Harmonic Excitation – Flap 1Ω (b) 2nd Harmonic Excitation – Flap 2Ω

Figure 7: Graphical Representation of Flap Excitation (Adapted from [2])

For the 1Ω in flapping, there is a complete oscillation in one rotation of the rotor (Figure 7a). it means there is a maximum vertical displacement at $\psi_P = 180^o$, a minimum at $\psi_P = 0^{o,}$ and zeros at $\psi_P = 90^o$ and 270°, where ψ_P is the blade azimuth position, counted from the position furthest from the flight direction (FD indicated in Figure 7).

As shown in Figure 7a, the two-blade rotor will have one of its blades on a crest and the other one, diametrically opposite, in a depression.

Therefore, the main rotor hub displacement will be zero, in the vertical direction, as long as the trajectory of the blades is the same. For that reason, a two-blade rotor doesn't transmit vertical vibration at 1Ω frequency to the fuselage, if its blades are correctly tracked.

For the 2Ω in flapping motion, there are two complete oscillations in one rotation of the rotor (Figure 7b). This means that there are maximum vertical displacements at $\psi_P = 0^o$ and 180°, minimum at $\psi_P = 90^o$ and $270^{o,}$ and zeros at $\psi_P = 45^o$, 135°, $225^{o,}$ and 315°.

One can conclude that the two-blade rotor will always present vertical displacements that add up.

Therefore, a two-blade rotor will transmit vertical vibration at 2Ω frequency to the fuselage, even if the rotor is perfectly tracked. That is a non-correctable vibration, thus the structure will be excited along the vertical axis at frequencies nbΩ (mainly bΩ).

Another important helicopter vibration feature is related to the horizontal vibration, which is similar to the movement of a sieve. In this case, the structure will be excited along the longitudinal and lateral axes with frequencies (n + 1)Ω and (n - 1)Ω, provided that (n + 1) and (n – 1) are multiples of the number of the blades.

Thus, for a two-blade rotor (b = 2), a horizontal force at 3Ω frequency (n = 3) will transmit forces at 2Ω (m = 1) and 4Ω (m = 2) to the fuselage.

For a three-blade rotor (b = 3), *m* will not be an integer and, therefore, a horizontal force at 3Ω frequency will not transmit forces to the fuselage.

Table 1 presents the oscillatory forces that are transmitted to the fuselage as well their harmonic excitation frequencies as a function of the number of blades.

Table 1: Main Rotor Vibration Transmitted to the Fuselage

	HARMONIC EXCITATION FREQUENCIES ON THE BLADES	MAIN ROTOR VIBRATION FREQUENCIES TRANSMITTED TO THE FUSELAGE		
		$b = 2$	$b = 3$	$b = 4$
VERTICAL EFFORTS AT FLAP HINGE	1Ω	-	-	-
	2Ω	2Ω	-	-
	3Ω	-	3Ω	-
	4Ω	4Ω	-	4Ω
	5Ω	-	-	-
HORIZONTAL EFFORTS AT LEAD-LAG HINGE	1Ω	2Ω	-	-
	2Ω	-	3Ω	-
	3Ω	2Ω and 4Ω	-	4Ω
	4Ω	-	3Ω	-
	5Ω	4Ω and 6Ω	6Ω	4Ω

This table is only valid if the rotor blades are at the same trajectory and perfectly balanced. Otherwise, vibration amplitudes at frequencies of 1Ω, 2Ω, and 3Ω, successively, will appear in the fuselage. That vibration can be reduced utilizing balancing and tracking of the main rotor. This table answers the question about absorbers tuning to match the frequency $b\Omega$. While frequencies different from $nb\Omega$ are correctable by balancing and tracking, multiple frequencies of the number of blades are uncorrectable. For that reason, those frequencies, and especially $b\Omega$, are the focus of helicopter manufacturers to reduce the vibration level in the fuselage.

Indeed, the vibration at a particular point of the helicopter depends on the fuselage's response to the efforts transmitted by the main rotor hub at frequencies multiple of the number of blades. Many helicopter manufacturers and research centers made use of software to obtain modal shapes and their respective frequencies to calculate the fuselage response. Some of them have already been published, such as the NASTRAN (NASA Structural Analysis). An example is shown in Figure 8 for the AS 330.
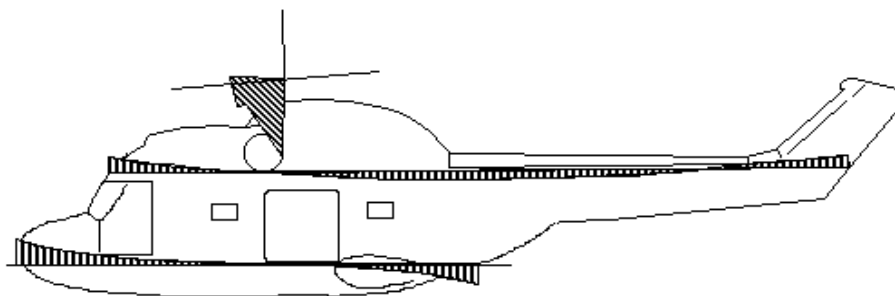
Figure 8: Typical AS 330 dynamic response, longitudinally excited by the rotor hub ($4\Omega = 17,4$ Hz) (Adapted from [2])

This sort of analysis allows designing the structure in such a way that the nodal points (zero amplitude vibration points) are positioned along the fuselage where it's desirable to have the lowest vibration level. This can be done utilizing mass and rigidity adjustments, as well as using vibration absorbers as previously discussed.

Unfortunately, such fuselage regions can change a lot due to different loadings and determined flight conditions. For that reason, flight tests under certain specified conditions are required to confirm the accuracy of the computer model and to certify the helicopter according to paragraph 251 (Vibration) of 14 CFR Part 27 [6] and Part 29 [7], which requires that the helicopter not to be subjected to excessive vibration in all approved flight envelope.

2. Vibration analysis techniques for helicopter rotors and dynamic components

This section is based on the article of Jorge & Torres Filho [8], first presented at "XI Simpósio de Segurança de Aviação da MB", SIPAERM, 1989, Rio de Janeiro, RJ, Brazil.

2.1 Vibration in dynamic components: causes and effects

The study of the causes and effects of vibrations in dynamic components has become a continuous task for manufacturers of aircraft, helicopters, engines, transmission gears, and dynamic components in general, to implement techniques for minimizing the effects of these vibrations, either by suppression, absorption, reduction, isolation, or active/passive control of vibrations, or a combination of these techniques. As a result of this study, several maintenance techniques have been developed, to be employed by the aircraft user, which can be divided into two groups: reduction of the vibration levels and analysis of vibrations.

The vibration reduction techniques available for helicopter users are concentrated, in the first step, in the correction of the trajectory traveled by the blade tips (adjustment of the blade "track") of the main and tail rotors, and/or in the correction of any imbalance present in these rotors, as well as any imbalance present in some specific dynamic components of the aircraft, such as gearboxes, main and tail rotor drive shafts, oil cooler fans, etc.

In a subsequent step, the user should concentrate his efforts on the vibration analysis, which consists in obtaining the aircraft vibration signature, i.e., the survey of the values of vibration amplitude versus frequency, carried out in pre-established locations and flight conditions, utilizing accelerometers and analyzers that directly respond the frequency domain. The records of vibration signatures, duly filed, will form a vibration database of each model aircraft, which will be used as a starting point for the assessment of the vibration levels of a particular aircraft at a certain time of its useful life, allowing the detection, location, and identification of problems or defects, even when they are still incipient. Thus, vibration analysis would become an important predictive maintenance tool, to monitor the wear and fatigue of components, to obtain a reduction in maintenance costs.

The statement of the problem, at the user level, in these two steps, is detailed below. In addition to vibration reduction and analysis techniques, some details of the equipment used for these purposes are described, as well as some prospects for the future.

2.2 Objectives of the vibration Reduction

The vibration reduction has the objectives:

a) Reduce the probability of failures in structural components during their useful life, which considers a certain magnitude of cyclic loads, acting on them. Because there is a direct relationship between the vibration level of the structure and the cyclic loads acting, a high level of vibration shows that the structural components of the helicopter are being subjected to efforts beyond its design envelope and, consequently, present a high probability of in-service fatigue failures;

b) Minimize the effects of tiredness and fatigue on the crew. Prolonged and repeated exposure to vibrations of different frequencies, amplitudes, and directions can cause various types of aggressions that essentially consist of headaches, tinnitus, general malaise, feeling of drowsiness, general weakness, irritability, a reduction in willingness to work, concentration deficit, slower reflexes, a psychic depression as well as fatigue of the eyes and ears. These disturbances, depending on their intensity and persistence, can decisively contribute to helicopter accidents.

From a mechanical point of view, the human body is a complex structure with viscoelastic tissue supplemented by bone tissue. The human body can be considered as a system composed of masses, springs, and dampers. Thus, each region or organ of the body will have a resonant frequency, at which that region or organ will shift or deform more than the other parts of the body, being, therefore, more sensitive to external or excitatory vibrations at that frequency. The resonant frequencies of the human body vary in the following ranges:

- 4 to 8 Hz - chest (internal) and abdomen
- 11 to 15 Hz - spine and joints
- 11 to 25 Hz – skull
- 40 to 60 Hz - rib cage (rib and muscles)

Frequencies between 15 and 30 Hz cause a reduction in visual acuity when the crewmember's gaze is fixed on an immobile object at infinity. This reduction is even more pronounced if the object is fixed but close to the pilot, such as an indicator on the instrument panel.

On the other hand, vibrations transmitted to the pilot through his feet (by the pedals) and the seat, at frequencies between 8 and 15 Hz, combined with the vices of position or posture that the pilot assumes to control the aircraft, can bring spinal trauma, such as injuries to intervertebral discs or herniated discs, for example.

By way of illustration, helicopter main rotors typically rotate between 3 and 7 Hz, depending on the aircraft, and the main vibrations perceived in the structure vary between 3 and 22 Hz, while tail rotors and other accessories rotate at higher frequencies.

c) Improved weapon firing accuracy. Limitations in the use of weaponry can also occur, as the vibrations may make the helicopter an inefficient weapons platform, both from the point of view of directional stability of the machine guns and rockets, as well as from the fact that vibrations in the auxiliary weapons equipment, such as the gun shooting sights, or the guided missile tracking sights can make their use impractical; and

d) Reduce breakdowns in helicopter avionics and electromechanical items. Such breakdowns are caused by friction between internal components or by their fatigue. As a rule of thumb, an estimate of 50% of helicopter breakdowns may be due to problems related to fuselage vibrations.

2.3 Causes of vibration in helicopter rotors and other dynamic components

The most common causes for the occurrence of vibration can be categorized into two groups, depending on the possibility of the operator acting to eliminate or minimize the efforts that caused the vibration:

a) Unavoidable causes:

- the variable aerodynamic forces resulting from the cyclic movement of the blades, necessary to allow translational flight. It is found that such forces predominantly induce vibrations at the multiple frequencies of the aircraft's main rotor rotation times the number of blades, that is, for a 4-blade helicopter with a main rotor rotation speed of 340 RPM (5.7 Hz), the cyclical variation of the pitch of this rotor blades will cause efforts that will induce vibrations in the frequencies of 22.8 Hz, 45.6 Hz, 91.2 Hz, etc., in the aircraft. These efforts increase with the aircraft's translational speed;

- centrifugal forces resulting from the variation in the position of the CG of the rotor set, resulting from the flapping motion of the blades, are necessary to maintain translational flight. The resulting vibration occurs in the plane of the rotor, at the rotation frequency of the main rotor; and

- aerodynamic forces arise from the airflow from the rotors, acting on the helicopter fuselage, or from turbulence and gusts on the aircraft.

b) Avoidable causes

- unbalance of rotating parts and rotors: unbalance always exists, to a greater or lesser degree, in any set or rotating part and is characterized by vibration that occurs once per rotation as shown in Figure 9.
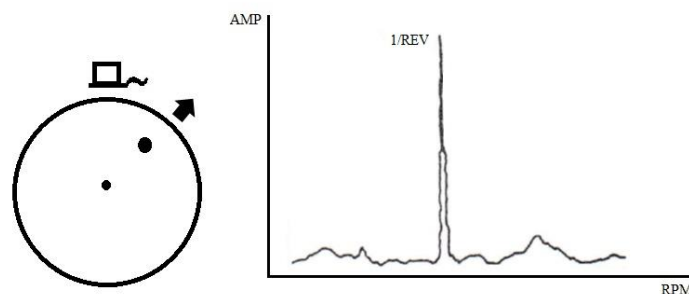
Figure 9: Unbalance of rotating parts and rotors (Adapted from [8])

Imbalance occurs when the center of mass of the rotating body is different from, or farther from, the center of rotation of that body. If the center of mass and the center of rotation are equal, the system is said to be balanced. As the center of rotation cannot be moved, the solution is to move the center of mass, adding weights in opposition to the inertia force produced by the imbalance, which is of the form given by Equation (2):

$$F = M.\,r.\,W^2 \tag{2}$$

where:

F = Force produced by unbalance
M = Mass of the set
r = Radius (radial position of the center of mass)
W = Angular Velocity

Vibration at the frequency of once per revolution is not always due to unbalance but could be indicative of another problem (such as mechanical backlash). The characteristics of unbalance are:

- the vibration occurs at the frequency of once per revolution;
- the phase is stable. For example, if we are trying to balance a tail rotor that exceeds established vibration limits and the phase indication is not stable, this could be an indication of mechanical clearances rather than unbalance; and
- the amplitude of vibration increases with increasing rotational speed.

I.   Misalignments of couplings and bearings

Vibration in an axis due to misalignment is usually intense at a frequency of twice the rotational speed, and the highest levels are in the longitudinal direction of that axis. Misalignment can be of two types:

1. Pre-stress in a bent shaft or improperly bedded bearing; and
2. Deviation of axis centerlines.

Flexible couplings increase the ability to tolerate misalignment, however, they are not the solution to more serious alignment problems.

The longitudinal vibration phase measured at one end of a bi-supported shaft will be 180 degrees out of phase with that measured at the other end of that shaft, provided that the shaft is operating below its natural frequency, as shown in Figure 10.
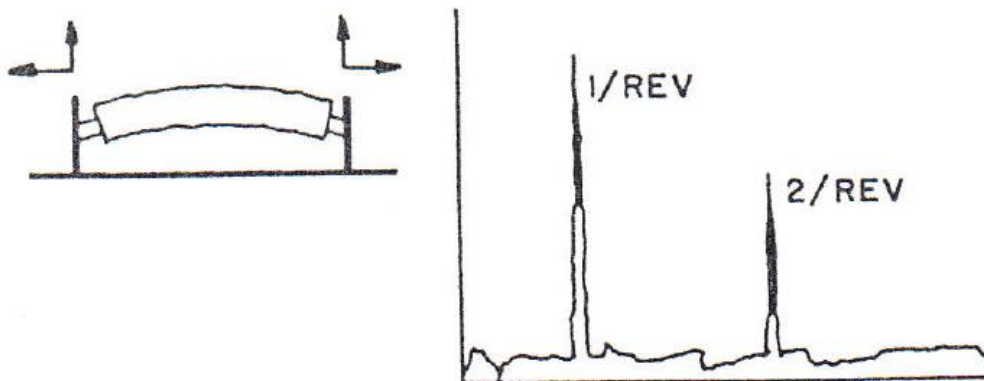
Figure 10: Misalignment of a shaft (Adapted from [8])

This relationship can be used to differentiate misalignment from unbalance, which produces in-phase longitudinal vibration at both ends of the shaft.

This test cannot be used in vertical or lateral directions, as the phase of unbalance varies with its type. It is interesting to note that:

a) Machine dynamics affect phase readings, so the phase difference of vibration in the vertical direction may not be exactly 180 degrees, but may vary between 150 and 200 degrees; and
b) The orientation of the transducers that will capture the vibration is important. These transducers must be placed in the same direction, at both ends of the shaft. If this is not possible, they can be placed pointing one to each side, remembering that now the phase difference between them will be 0 degrees.

I.   Worn, eccentric, or damaged gears.

One of the frequencies associated with gear problems is the so-called "gear mesh", which is equal to the number of teeth times the speed of rotation of the gear. High vibration rates at the gear mesh frequency are common and therefore must be compared with average values taken as a reference to detect the existence of a possible problem. Figure 11 shows a typical spectrum of gear mesh.
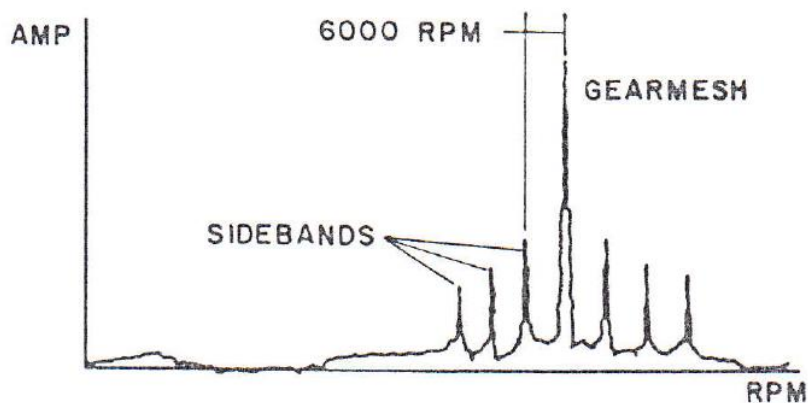
Figure 11: Gearmesh typical spectrum (Adapted from [8])

Sidebands around the gear mesh frequency are usually caused by small eccentricities or backlash in the gears. High levels of vibration at the rotation speeds of the sidebands are a good indicator that there is a problem with the gear. Identifying problems in gears, and examining vibration spectra is a difficult task, as it depends on the resolution of the analyzing equipment used, therefore, this problem identification technique must be used in conjunction with oil analysis, swarf detectors, and monitoring of the temperature of the gear oil.

II.   Looseness in the fixing of components, or mechanical clearances.

Mechanical clearances almost always result in a large number of harmonics in the vibration spectrum. The harmonics (1, 2, 3, etc times the fundamental rotational speed) that characterize the backlash are the result of impulses and truncation (limitation) of the component's response. Figure 12 shows the typical vibration caused by a backlash, both in the time domain (Amplitude versus Time) and the spectrum in the frequency domain (Amplitude versus Frequency).
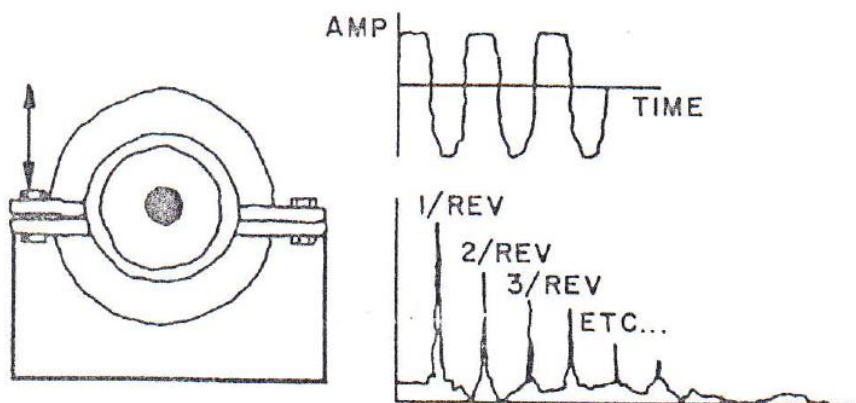
Figure 12: Mechanical backlash vibration (Adapted from [8])

The truncation of the top of the sine wave seen in the time domain is what causes harmonics to appear in the vibration spectrum.

Warped shafts present a situation where the backlash does not result in many harmonics because the truncation is dampened by the warping and the resulting vibration is essentially one time per revolution.

III.   Other causes such as:

1. defective shock absorbers;
2. damaged housing bearings;
3. little lubrication in rotating elements; and
4. displacement of panels.

Balancing dynamic components

The procedures may vary according to the aircraft involved and are provided for in the maintenance manuals for each system, set, or accessory of interest. Thus, for a particular aircraft, the manufacturer may have considered it important to perform the task of balancing the main gearbox oil cooling system fan shaft, while for another aircraft, the balancing of the transmission shaft for the tail rotor may have been considered more important.

It is important to keep in mind that not all shaft problems are due to unbalance. So, if, for example, we add balancing masses and the vibration level does not drop, the shaft may be misaligned or warped, and adding mass will not correct this problem, putting even more stress on the bearings on that shaft. The best solution will be to correct this misalignment, and even replace the shaft, if appropriate.

The clearance in certain components of the aircraft can change the rigidity of the structure, bringing the frequencies of the dynamic loads acting on the structure closer to the natural frequencies of the fuselage. As an example of this situation, one can verify that, in the case of the WG-13 Lynx helicopter, the excessive clearance of the upper mast bearing in its seat in the main gearbox causes an increase in the amplitude of the vibration at the fundamental frequency of the main rotor.

2.4 Vibration analysis in dynamic components of helicopters

Vibration analysis objectives

1. Detect defects in mechanical components (slacks, wear of bearings, gears, misalignments, lack of lubrication) before catastrophic damage to the assembly occurs;
2. Detect structural problems in the aircraft (cracks, loosening of screws and rivets) before catastrophic failures occur;
3. Assist in the diagnosis of breakdowns in mechanical components, indicating the subcomponents of abnormal behavior;
4. Allow maximum utilization of components subject to wear and fatigue, removing them for overhaul only when there is evidence of failure (predictive maintenance), rather than at scheduled time intervals (preventive maintenance).
5. Plan repairs or replacement of components, consequently increasing the quality of repairs, reducing operating costs, and allowing an ordering, in time, of the needs for replacement parts.

Theoretical foundations of vibration analysis

It can be shown that a periodic motion can be represented by a summation of sinusoidal functions, which in turn, represented in the form Amplitude X Frequency, constitute the frequency spectrum of that movement. Figure 13 illustrates a periodic motion, plotted in the time domain and the frequency domain.
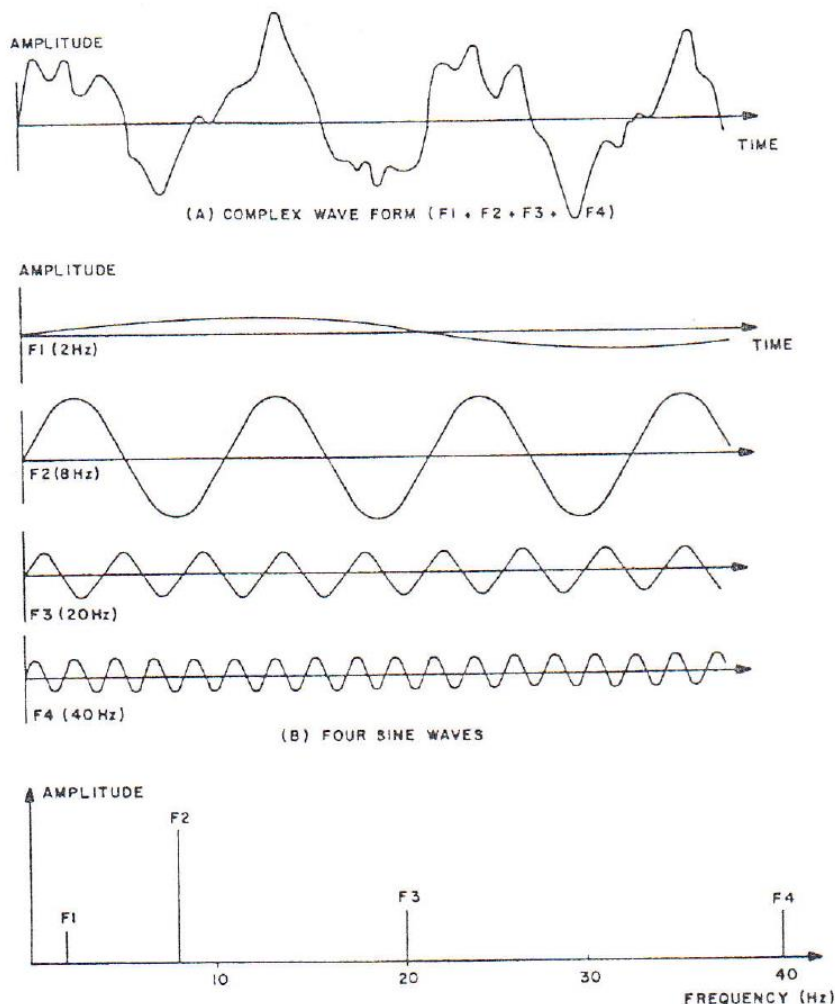
Figure 13: Periodic Motion (time domain and frequency domain) (Adapted from [8])

One must note that forced vibrations occur at the frequency of the external forces causing them, and consequently, a large amplitude of vibration at a certain frequency of the spectrum can be related to the possible causing force. Therefore, the tracking or monitoring of the frequency spectrum of components allows the detection of the beginning of anomalies in components and the determination of their origin.

In the case of helicopters, some manufacturers provide a frequency order sheet that allows locating the possible cause of any discrepancy in the frequency spectrum, obtained by sensing specific points on the helicopter's fuselage.

The transmission of vibrations along the structure of the aircraft is a function of the distribution of mass and stiffness along with the structure. Vibration spectra different than expected or high amplitudes at a certain frequency without an apparent reason can mean changes in structure characteristics, such as loose rivets and screws, cracks, etc.

A practical example of vibration analysis for a helicopter

Figure 14 shows a vibration signature card, obtained with the "Scientific Atlanta model 2521" analyzer for an SH3-A helicopter, where the vibration amplitude at 8099 BPM is very high.
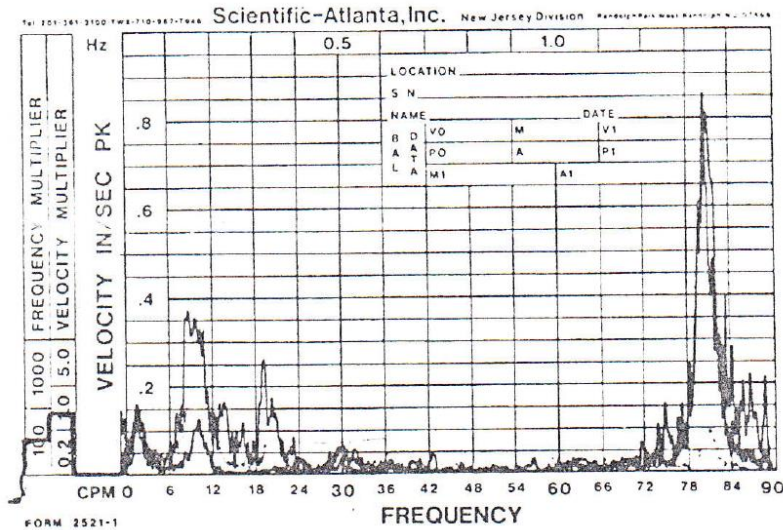
Figure 14: Vibration signature of a helicopter on the ground, with a problem at 8099 rpm (Adapted from [8])

The research of possible causes was done with the help of the "H-3 Troubleshooting Chart". We had, among others: "Generator Adapter broken/deteriorated".

After some research, it was found that the number 2 generator adapter was cracked, a problem that had not yet been discovered during normal aircraft maintenance. After replacing this adapter, the spectrum was as shown in Figure 15, where one can see that the vibration at 8099 RPM was drastically reduced. As it is a high frequency for the sensitivity of the human body, the problem was only detected with the help of the analyzer, not being felt by the crew when in flight.
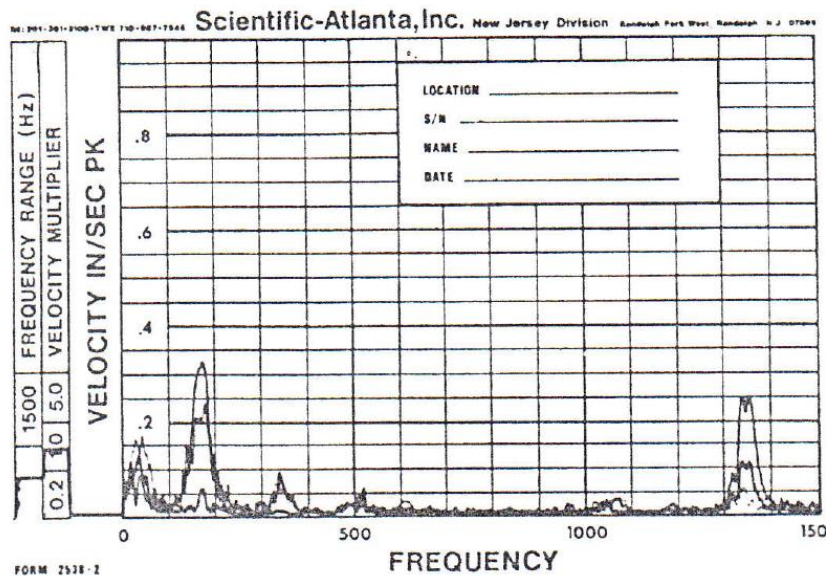
Figure 15: Vibration signature of the helicopter, after changing the generator adaptor (Adapted from [8])

Outline of a vibration analysis program for a helicopter fleet

a) The program consists of all aircraft having their vibration signatures registered and archived for the formation of a vibration database, to have data to compare the vibration signature of an aircraft at a certain time of its useful life (for example aircraft with 500 hours flown; aircraft after overhaul; aircraft after SDLM (Standard depot-level maintenance); aircraft after major structural repair or after an accident, etc) with:

- the vibration average of the different aircraft of the same model, to verify how this aircraft behaves concerning all the others;

- the same aircraft at a previous time, to investigate the possible degradation of the vibration state of the aircraft with use.

b) Aircraft vibration signature records must be obtained:

- only after having been eliminated, or minimized, as far as possible, avoidable vibrations once-per-revolution of the main and tail rotors, by the use of vibration reduction techniques;

- for the flight conditions foreseen for the aircraft, trying to keep the flight parameters as constant as possible;
- with the accelerometers fixed in the positions provided for in the aircraft manuals; and

- usually at pre-established periods or after major maintenance inspections, overhauls, major structural repairs, accidents, etc.

c) After obtaining the cards with the aircraft vibration signature, a data reduction is performed, which consists in obtaining average values of vibration amplitudes, to be used as a source of future comparison. These values are calculated using statistical sampling criteria for each type or model of aircraft, for each flight condition, for each of the frequencies, predicted to be the most significant in terms of vibration problems in the aircraft, and for each of the directions of interest (vertical, lateral, and longitudinal).

For each flight of an aircraft of a particular model, each vibration amplitude value will be compared with the average value existing in the corresponding table, and the evaluation of the results will be made by pre-established criteria, reaching conclusions about the maintenance actions that must be undertaken or not.

Thus, if the vibration amplitude value, at a particular frequency, is considered:

- Good, it means that there is no action to be undertaken;

- Regular, means that the vibration level at that frequency is already in the "Marginal" range, and some maintenance must be programmed (in any equipment which could be somehow related to this vibration frequency) as soon as possible, and greater attention must be paid to secondary indications (as, for example, visual inspection of the equipment involved, analysis of lubricating oil or hydraulic fluid, when applicable, to try to detect particles or debris, etc); and

- High, means that, before the next flight of the aircraft, maintenance troubleshooting must be carried out, according to the appropriate manual for each aircraft.

d) As the vibration of the aircraft is an eminently random phenomenon, one must redouble the attention when finding a vibration value, only, in "High", because this value can just be the result of a single event of turbulence that was registered by the accelerometer, not being, therefore, a vibration of the aircraft itself.

The following guidelines should be followed, as far as possible, to have more solidly based conclusions:

- if the vibration is "High" at a certain frequency in a given flight condition, check if it is also "High" or "Marginal" at the same frequency in other flight conditions; if it is, the need for troubleshooting is consolidated; if not, it could be a problem of turbulence or any other effect that has masked the measurement, generating the need for a better evaluation;

- whenever there are doubts about the intensity of vibration obtained, or if the result obtained indicates the need for replacement or repair of a large component, a new vibration analysis should be carried out to collect more data and be able to obtain more accurate and reliable results; and

- in parallel with the vibration analysis, one should seek to collect as much data as possible, as well as information that may be useful, such as the "life" in hours of the components involved, their last replacement, relevant maintenance information, information on contamination of lubricating oil, hydraulic fluid, etc., when applicable.

e) The evaluation of the results can also be done, in parallel, by comparison with the maximum vibration foreseen in existing international standards on the subject. Thus, as long as there are no average results calculated for a certain model of aircraft, or these average results are not judged sufficiently reliable, or if another criterion for evaluating their vibrations is desired, we can adopt internationally disseminated evaluation criteria. These criteria can be qualitative, such as the "Cooper Harper" scale, or quantitative, such as, for example, those described in the following standards:

- MIL-H-8501A, General Requirements for helicopter flying and ground handling qualities;
- MIL-STDTD-810D, environmental test methods, and engineering guidelines;
- AvP 970, Design Requirements for Aircraft for the RAF and RN, volume 3: rotorcraft design requirements; and
- DEF STAN 00-970, volume 2, chapter 501, vibration and internal noise.

Some remarks on vibration analysis in dynamic components of helicopters

The problem of vibrations in helicopters is considerably more complex than what exists in airplanes, as the helicopter experiences cyclic a variation of aerodynamic loads that cause strong vibrations in the structure, and which currently can only be mitigated by the use of heavy vibration absorbers, insulators, dampers along the fuselage or dynamic decoupling between rotor and fuselage (and also some active systems, currently in the prototype phase or with limited application).

However, until a type of aircraft is obtained that allows translational and hovering flights to be carried out more efficiently (such as V-22 Osprey) this is one of the prices that one has to pay for the use of the helicopter in his entire flight envelope, which is unique.

The existing vibrations in the fuselage of helicopters entail a higher maintenance cost, reduce crew performance, and may even compromise flight safety by the possibility of causing fatigue failures in structural components. It remains for operators to know the causes of the phenomenon and, using existing equipment, reduce the vibration levels of their helicopters to the lowest possible value. Vibration analysis techniques, however, appear as a possible way out of the problems of high maintenance costs and reduced flight safety, as they may allow monitoring the operating conditions of all helicopter components, allowing the installation of reliable programs of predictive maintenance.

Future perspectives: the HUMS for dynamic components of helicopters

The scope of the computer-based HUMS for dynamic components of helicopters typically may include vibration analysis, balancing, and rotor tracking equipment, equipped with computer-based expert systems (artificial intelligence).

Such equipment must present the capacity to be operated by personnel without knowledge of vibrations, to provide the best possible correction of balance and track of rotors, and to analyze vibration spectra, indicating eventual problems and their causes.

In terms of helicopter design, the equipment installed on board may include active systems to nullify vibrations considered "unavoidable". These systems act, through the blades, on the excitation forces, generating a new set of aerodynamic forces that, added to the existing one, cancels the structural vibrations at certain points of the helicopter.

HUMS systems enable continuous monitoring of vibrations, allowing the almost unlimited use of components subject to wear and fatigue, with the assurance that any start of a defect will be detected, and the component will be replaced promptly before catastrophic failure occurs in the assembly. These HUMS systems may also help to reduce or even eliminate the need for periodic replacement or removal of components for overhaul.

The available HUMS equipment can be coupled to onboard computers, as well as to central computer stations on the ground (transmitting their vibration information either online and/or offline), for monitoring and continuous analysis of the information collected. Thus, the comparison with established limits can be done on board or offline, by land-based computers, which can analyze the records obtained in flight.

3 Vibration-based Health and Usage Monitoring Systems (HUMS) philosophy in the predictive maintenance of helicopters

This section is based on the article of González & Donizeti [9], first presented at "XII SIGE - Simpósio de Aplicações Operacionais em Áreas de Defesa", 2010, São José dos Campos, SP, Brazil. XII SIGE, 2010, and on excerpts from the master's thesis [10], for the Post Graduate Program in Mechanical & Aeronautical Engineering at ITA, São José dos Campos, Brazil, 2012.

3.1 Introduction

HUMS (Health and Usage Monitoring Systems) were initially developed for large-size helicopters, such as the one used in offshore activity, being one of the types of condition monitoring systems, commonly called Health Monitoring Systems (HMS), that also consider helicopter employment parameters. Aligned to the philosophy of predictive maintenance, the HUMS actions propose to guarantee continued airworthiness and reduce operating costs through diagnostics forecasting (early diagnosis) and fault prognosis that increase reliability, from the treatment of data collected by algorithms dedicated to increasingly expanded functions and integrated into other subsystems. This collected data for the prediction of failures comes from vibration sensors, such as accelerometers, permanently installed in the fuselage and/or in dynamic components and/or in engines, with different vibration levels corresponding to various helicopter operating conditions. The research effort is also justified by the potential of HUMS to improve flight safety through their proposal to guarantee the replacement of components always before their failures.

This section aims to present an introduction to predictive maintenance for helicopters and a brief qualitative summary of these HUMS systems, segmented into history and evolution of the market; architecture; benefits, disadvantages, limitations; certification challenges; and application perspectives.

The condition monitoring systems, or HMS, were initially developed to improve safety on commercial airplanes. Currently, in this sector, the analysis of information collected by some operating companies that belong to the quality assurance program of their flight operations – FOQA (Flight Operational Quality Assurance), from which potentially dangerous trends in operation and use of components can be identified, even allowing to point out the need for training.

Efforts to develop a particular type of HMS, also considering usage parameters such as the count of operating cycles/time and flight data records (FDR) and exceeding recommended limits (torques and speeds), focused on rotary-wing aircraft, lead to the condition monitoring systems known as HUMS (Health and Usage Monitoring Systems). In this case, in addition to following the degradation of dynamic components (engines and power systems; landing gear; gearboxes and transmission shafts; structural cells) and to the rotor tuning (rotor balance and blade tracking), there are also the benefits of the registration of the performance and the indication of exceeding operational limits, which may significantly compromise the life expectancy of a component. For this purpose, the HUMS relies on a variety of sensors (mainly accelerometers for vibration data collection) by integrating a so-called data acquisition system, which can even include both voice and flight data recorder functions (CVR and FDR).

This data can be processed simultaneously with the flight (on board the aircraft or at a ground station via data cards, provided they are properly interpreted, modify (anticipate/postpone) the required maintenance schedule as well as the crew's operational actions even before the next landing.

Complete systems such as HUMS are expected to perform acquisition, analysis, communication, and storage of data from sensors permanently monitoring critical items and, therefore, are expected to be essential to flight safety, aiming to limit the risk of human and/or material damage to an acceptable level, as defined from Risk Assessment strategies.

In this context, one must note many rotating and critical systems acting on helicopters, a peculiarity whose effects are classified as catastrophic events in the category of the severity of defects (aircraft and human lives). Thus, the vibration magnitude monitoring technology for the detection of associated faults arises from the demand for early diagnostics and effective predictions. And so the HUMS has expanded its acceptance as a strategy aligned with the effectiveness of the maintenance philosophy and, nowadays, has been used as a complementary method to ensure continued airworthiness, defined as guaranteeing the certified level of safety throughout the life cycle of operation of the product (aircraft and/or its systems), as stated in aeronautical regulations, such as, for example, the RBAC 01 from ANAC [11].

3.2 An introduction to predictive maintenance for helicopters

From the point of view of safety and continued airworthiness, aeronautical maintenance is known as an activity of inspection, review, repair, cleaning, conservation, or replacement of parts of an aircraft and its components [11].

Helicopter operating costs are extremely high mainly due to maintenance (24%) and insurance (29%) costs, given the relevant civil and legal liabilities, as well as the perceived levels of danger associated with society [12]. So, as for maintenance costs, they are around a quarter of the total cost of operation [13].

There are compelling prospects for reducing both the consolidation of predictive maintenance and its results in aviation safety and reliability.

Each efficient maintenance program implies the adoption of elements of three types of philosophy that reflect the acquired technological capacity: corrective maintenance; preventive maintenance and predictive maintenance.

Corrective Maintenance is the oldest and most common until the 1950s. It is a reactive fault management technique, expensive because it usually involves major repairs and inopportune times. It emerged when the performance data deficiency of the components involved was mastered. On the surface, the idea of being less costly is conveyed, but the costs increase due to production losses (loss of profits) and the resulting secondary damage, in addition to excessive time to remedy the problem; however, it is useful when sudden failure does not threaten production, such as a drinking fountain, for example. It applies to items classified in the manual as Condition Monitoring – replacement is recommended only in case of discrepancies. Also, the fail-safe design concept allows for corrective, effective, and timely maintenance to be carried out at more favorable times and conditions, such as in major overhauls, allowing much greater tolerances for cracks, a clear practical advantage in areas that are commonly difficult to access.

Preventive Maintenance establishes the second generation. It is based on the predictability of operational behavior, acquired from experimental and statistical observations, and imposed by restrictions on certification specifications that are more suited to the risk peculiarities of the aeronautical activity. For the first time, these conditions were created for proactive maintenance and anticipating failures. In the general context, it includes all maintenance management programs triggered by time, such as operating hours and/or cycles of the items (counted by landing, engine shutdown, etc.), in which they are removed. There may be situations in which they are still usable at the moment of replacement, and there may be also some cases, undesirable ones, in which they may be replaced only after they fail. They are discarded via recording "scrap" or mutilation to avoid unintentional reapplication based on manufacturers' performance projections. It is a highly conservative position, with the disadvantage of wasting time and material by replacing an item with an appreciable useful life when one could act more frequently than necessary. For a machine that could still operate satisfactorily for a longer time, stopping it just for a check does not seem reasonable. It is worth reflecting that opening/closing increases the probability of introducing human factor errors. On the other hand, one should not wait for a breakdown to be corrected, and, therefore, the best solution is to intervene at the ideal moment.

Predictive Maintenance is based on measurements (which must be representative and consistent) of the actual conditions of the equipment on a continuous and periodic basis, according to the criticality level of the item. But some measurements are unfeasible, and imprecise, while some components have a low replacement cost, such as replacing the lubricating oil, for example. In this case, vibration is a vital parameter to define the dynamic conditions of rotating machines. The Predictive Maintenance Philosophy was first born in the analysis of lubricating oil implemented by American Naval Aviation in the 1950s. From there it spread, establishing itself as the third generation from the 1960s onwards, bringing new paradigms to the maintenance logistics function.

The industry continues to evolve in technology, motivated by the relentless search for financial results associated with operational efficiency, which depends on safety and availability. In this sense, as it allows for a better understanding of the dynamics of the phenomena involved, mastery of manufacturing processes, as well as the ability to measure and process evidence of performance, this methodology for having the aircraft at hand has advanced (from the Latin "manutention": the action of holding in the hand): the philosophy based on the condition. As techniques have become more sensitive, failure predictions give way to condition changes, keeping failure at bay.

Predictive Maintenance is positioned as a philosophy that, unlike the reactive doctrine of Corrective Maintenance, is proactive to unpredictable failures to increase the reliability and safety of operation. Based on component condition and integrity, rather than time/life cycle, it identifies the tendency to future failure according to some deviation from the standard of thermal, acoustic, and vibratory quantities (mainly in helicopters), which reveal the known behavior of the system. One can mention the following issues:

- oil spectrometric analysis;
- ferrography (as part of Tribology - investigation of friction wear);
- analysis of particles in hydraulic fluid;
- thermographic analysis;
- noise analysis;
- and vibration analysis (the most important parameter in the case of helicopters).

It is the philosophy most associated with computational resources – it is based on the trend graph (curve) and spectral analysis (if an increase beyond the tolerable is detected). The experience accumulated in the database facilitates the association of each frequency for the diagnosis of each type of failure.

Trends of the fourth generation of these quality tools have recently emerged, characterized by the application of continuous monitoring systems associated with systems for supervising failures. These systems are equipped with signal analysis algorithms (Fast Fourier Transform – FFT, and/or Wavelet, and/or Hilbert), and/or artificial intelligence techniques (Artificial Neural Networks – ANN and/or neuro-fuzzy systems, among others), to provide the diagnosis and prognosis of incipient failures. In search for higher reliability, there is Reliability Centered Maintenance - RCM, which has become popular for its methodologies such as FMEA (Failure Mode and Effect Analysis), FTA (Fault Tree Analysis), and Probabilistic Risk Analysis - PRA. For Root Cause Failure Analysis, see [14].

3.3 Historical developments and market evolution of HUMS

The nature of the aircraft maintenance tasks being performed reflects the technological capacity acquired through time. In the early days of aviation, reactive maintenance prevailed, due to the lack of performance data of the components involved. In this case, no maintenance action was necessary, until a failure occurred, featuring a low level of safety and high costs, both direct (major repairs) and indirect (unavailability). Considering the peculiarities of the risk in an aeronautical activity, the specifications of the related certification processes became more restrictive over time, leading to advances in manufacturing processes that create more reliable items. The predictability of their behavior, acquired from the experimental observations and operating statistics, created conditions for proactive maintenance procedures, anticipating failures. The first one, based on time/operation cycles, was established under a preventive philosophy.

In this situation, each component is replaced according to previous appointments, according to its design concept being fail-safe, Safe Life, or Damage Tolerance. Thus, for decades, high-cost components were removed and discarded, based on manufacturers' performance projections. Several times, this removal could have happened well before the component was unusable and sometimes this removal may have happened only after the failure of the component. In the relentless pursuit of efficiency of operation (and, obviously, on the financial results associated with it), dependent on safety and availability, the industry continued to evolve in technology. With a better understanding of the dynamics of the phenomena involved, a mastery of the manufacturing processes, as well as with the ability to measure and process evidence of performance, progress has been made in yet another methodology of "having the aircraft at hand": the philosophy based on condition monitoring. In this case, aircraft components and systems are monitored to project when their failure is likely, under pre-established criteria of risk analysis. Therefore, ideally, the components are used for the entirety of their useful life, and without the need for premature replacement, reducing operating costs and keeping the preponderant advantage of always being replaced before the failures, potentially increasing the aircraft safety and reliability.

Furthermore, the HUMS gained prominence in the transition between the traditional preventive maintenance philosophy and the new condition-based philosophy. The HUMS had its first certified flight in 1991, aboard a transport helicopter in support of offshore activities in the United Kingdom (North Sea). Commissioned by the British Civil Aviation Authority (CAA), an investment was made in the development of systems that could provide the early detection of defects and, as far as possible, the ability to predict/manage a window of safe fleet operation. Later, the American civil aviation authority - FAA (Federal Aviation Administration) issued the airworthiness requirements for normal category helicopters AC-27-1B [15] and transport category helicopters AC-29-2C [16], as a guideline for the certification of HUMS installation.

To inhibit possible compromising distractions of the pilots from the flight situation awareness, there is a tendency, in the operations, in waiving the cockpit performance trend notification - essential data only to the evaluation at the monitoring center, on the ground.

The acceptance of the HUMS is growing, and the US Military continues to develop HUMS capabilities for more accurate diagnoses and prognoses. For example, it is worth mentioning the HUMS are already standard and fully operational on the helicopters Sikorsky S-92 and S-76 C+, and on the Airbus Helicopters H-135; also, the system is offered as an option on the AgustaWestland AW-139, among others. More details on HUMS Technology can be found in [17].

The HUMS is also operational on the Brazilian Armed Forces Airbus Helicopters H-225M aircraft, which are equipped also with CVR/FDR in the system. The Brazilian offshore market already has advanced systems technologies such as the HOMP (Helicopters Operation Monitoring Program), a system that monitors each flight in detail, standardizes operations, and identifies in advance any quality problem. These systems are associated with the HUMS, having been recently added to the S-92 and S-76 C++ aircraft, for example. In parallel, many other operators are adapting their helicopter fleets to this new equipment.

The list of major HUMS manufacturers includes Smiths Industries of the United Kingdom, which acquired SHL - responsible for the research that culminated in the pioneer flight; and the American Goodrich, a large and traditional supplier of this type of systems to the global civil and military market.

This market has new entrants from the area of structures, whose strategic planning focuses on expanding the number of customers through the development of low-cost similar systems. More information on HUMS for Light Commercial Helicopters can be found in [18].

For example, Smiths HUMS systems are installed in: Canadian Armed Forces (Bell 412); Airbus Helicopters H-225; Sikorsky S-61 and S-76; Safran Arriel engine; AgustaWestland EH-101; and Bell-Agusta 609 tiltrotor. Several units of this HUMS are in service and accumulating flight hours aboard the Boeing HC Mk II Royal British Air Force Chinooks, which continuously monitor the tracking and balancing of the rotors, thus dispensing extra flight tests and the use of specific balancing and tracking equipment on board.

Goodrich, in turn, is the supplier of the first HUMS incorporated on the Sikorsky S-92, and their mastery of diagnostics covers from failures in gears and bearings of gearboxes transmission to infiltration of water between the layers of composite blades. Their products are already in the 3rd and 4th generations. The company has demonstrated its ability to balance the Chinook's tandem main rotors without the use of a specific infrared detection device for tracking.

The algorithm built in their Integrated Mechanical Diagnostic HUMS (IMD-HUMS) can determine more accurate solutions to adjust rotating systems by making more detailed calculations related to the vibrations detected by the accelerometers in the helicopter cabin. In other words, a better use was made of the data usually collected by the HUMS. The trackerless concept by Goodrich presents faster results, eliminates repetitive and costly test flights, and has been proven on other IMD-HUMS equipped aircraft such as Sikorsky CH-53, H-60 BlackHawk, and MH-60R SeaHawk; and Bell AH-1 Cobra and UH-1.

A vibration monitoring equipment (HVM) is equipped in Bell 412 and 212 series, and Agusta A109 and A119 helicopters are supplied by IAC and Altair Avionics, which has been acquired by the Canadian engine manufacturer Pratt & Whitney aeronautics. The Altair SmartCycle+ system, with multiple channels, monitors the use of engines from the gas generator and turbine parameters such as torque, speed, and temperature; in addition to vibration levels and other HUMS parameters such as main rotor speed, outside airspeed, and temperature, and also altitude.

3.4 HUMS description and architecture

Briefly, the basic architecture of an HMS can be described as formed by sensors that transform the variables of interest of each aircraft into electrical signals, which are then processed and compared, using computational algorithms, with a historical database (reference) of the variable in question, and presented to an operator on board, or to a central monitoring system on the ground, to assess the current state of the component and its probability of failure, as shown in Figure 16.
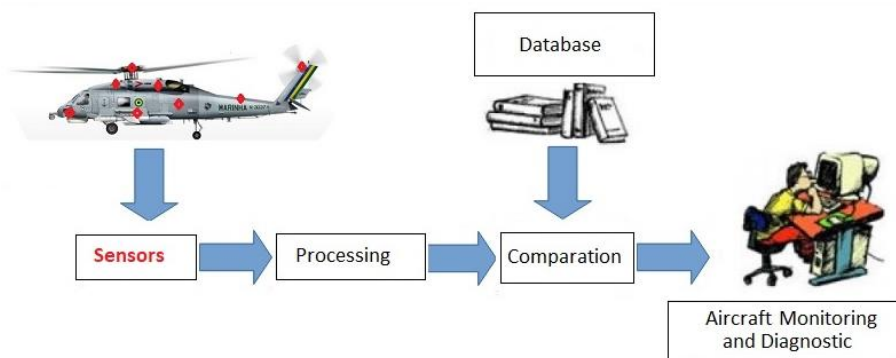
Figure 16: Simplified diagram of a Health Monitoring System (HMS) (adapted from [9])

Figure 17 shows a typical vibration spectrum, which is characteristic of each helicopter and acts as its fingerprint at a particular time or flight condition, to be added to the helicopter vibratory database. When analyzing this database, for each frequency band, any significant variations in the vibration at a particular frequency may be related to discrepancies of a corresponding dynamic component (rotating parts of engines, rotors, gearboxes, transmission shafts, etc.) or even a fixed element (such as fuselage stabilizers, etc.).
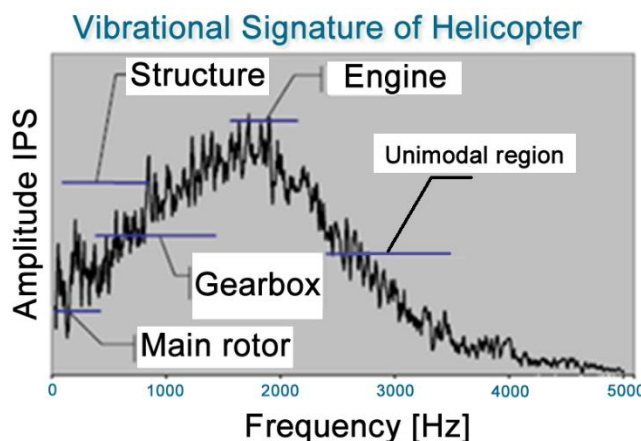
Figure 17: Vibration spectrum (signature) of a helicopter (Adapted from [9])

The sensors are essential to track aircraft conditions and can be primarily of magnetic, temperature, or inertial types. The inertial-type sensors include the accelerometers, which are responsible for collecting the oscillations of the fuselage in response to the external excitations, as seen in Figure 17. Some of these elements are built of quartz or ceramic, and HUMS use them under strict requirements of performance and reliability.

Most accelerometers need to be airtight to ensure efficient insulation in environments with high humidity and contaminants. Bandwidth, or frequency response, is the most important parameter in accelerometer selection. No accurate data is acquired if the bandwidth of the accelerometer does not include the frequency of the motion, vibration, or shock you are willing to measure. The sensitivity of an accelerometer defines at what rate the sensor converts mechanical energy into an electric signal (the output), and this will define the acceleration measurement range of the accelerometer. Sensitivity is usually expressed as mV/g (millivolts or per g) or pC/g (picocoulombs per g), where g is the acceleration due to gravity. The frequency response specification shows the maximum deviation of sensitivity over a frequency range. Great sensitivity and wide frequency response is a desirable feature for accelerometers, to ensure signal identification without significant sampling errors. As an example, high-quality accelerometers may present sensitivity in the order of 25 mV/g at 20,000 Hz (+15%).

Vibration-based damage detection techniques are associated with the combined condition and use monitoring (HUMS) or, more recently, condition management and prognosis (Prognostic and Health Management - PHM) systems. In a little more detail, in HUMS the monitoring of the mechanical or functional condition of a component or system aims, especially, to detect or possibly diagnose incipient degradations that could lead to a failure.

Condition management, on the other hand, describes the process of dealing with the information obtained from monitoring and prognosis to establish the real-time situation of the item and possibly, as desired, propose methods to extend the life of the item or limit its operation. The term "monitoring usage" means determining the lifetime consumption of critical components and systems according to operating records (cycles and hours) and loading history [12]. The generation of alerts is a differential of the HUMS and it boils down to establishing thresholds for each vibration condition and generating alerts as changes in the values in the trend reach them. In many cases, these thresholds need to be inferred from operational observation of HUMS in service, since there is no previous experience for helicopter manufacturers to issue their recommendations.

Threshold levels are not effective when applied to fleets due to the indication variations between components and aircraft. Therefore, these levels have been raised individually by automatic techniques that register those that were previously classified as statistically significant, through reasonableness tests and other processes [19]. Trends emerge from research suggesting that the performance of diagnostics can be improved by advances in the signal processing process and by advances in sensors [12]. To illustrate some performance statistics, information from the Civil Aviation Authority of the United Kingdom indicates that 69% of the increasing threats registered to continued airworthiness (mostly problems of balance and tracking in the rotor) were successful in detecting the failure, 17% had their evidence, but they did not carry out the alert, and only 14% of the cases the failures were not detected.

Provided that the results presented by the HUMS are properly interpreted under a risk analysis framework associated with the severity of the failure, the aim is to:

- guarantee the continued airworthiness of the aircraft - defined as the guarantee of the certified level of safety during the entire operational life cycle of the product [11];
- increase flight safety by increasing the situational awareness of the crew and supporting their operational decision-making; and
- reduce operating costs through Reliability Centered Maintenance (RCM) – which offers to track (anticipating/postponing) the best intervention opportunity (increasing availability); and to offer savings in the reduction of maintenance flights to adjust the main rotor, consumable material (sealants, sealing rings, lubricants, cleaning items, etc.), man-hours and the optimization of logistical support for spare parts.

HUMS must provide the precise status of the current use of critical components such that statistical models can be used to estimate the point in time when parts must be replaced, as well as indicate the presence of incipient damage that could lead to failure before the end of his cherished life in the safe-life philosophy. As for PHM systems, in general terms, it can be said that their prognosis is the prediction of the remaining life of this component or system. This requires propagation models of detected defects as a better approximation than monitoring usage [12].

The ultimate objective of HUMS and PHM is to allow predictive maintenance of the helicopter, that is, according to the philosophy that dictates that interventions should only occur associated with a predicted failure. However, for this, robust, reliable, and accurate HUMS or PHMs are necessary, which are not yet available in the current state of the art [12]. Meanwhile, manufacturers adopt it, at least, as a backup to primary conservative maintenance measures, according to safety factors and design redundancies, and frequently scheduled replacements in a safe-life context, complemented by damage tolerance techniques (fail-safe).

HUMS developers maintain a growing database of current vibration information inherent to the diagnostic function of HUMS associated with more than thirty faults detected and evidenced by vibration monitoring that can be related to maintenance actions. This information is used in the assistance service to different operators operating in different environments.

Brian D. Larder [19] categorizes the failures into classic and new in the diagnostic process, when he summarizes ten examples among more than twenty classes that make up this data in the HUMS library. The first ones refer to those that are the result of a known failure mechanism or that the associated indicators are a constant focus of attention, based on theoretical knowledge or bench tests. The failures of the so-called new category are those that do not allow for anticipation by the HUMS, nor are there any established indicators to recognize its effects. These can only be pointed out through lessons learned. The necessary experience can be maximized by combining information from the HUMS supplier, its operators, and the aircraft manufacturer [19].

3.5 HUMS advantages and benefits

Statistical information documented in the North Sea by the CAA indicates a high success rate in detecting failures, some of which could have turned into potentially catastrophic events, or could have even resulted in accidents. The benefits/return on investment in HUMS may include a reduction in inspections and maintenance test flights; and a decrease in unscheduled interventions. The advantages can be grouped into three main approaches: reliability, operational availability, and lower operating costs.

A- Increased reliability and flight safety level

Scheduled inspections (by calendar or lifecycle) in preventive maintenance are necessary for the reliability of components and systems, favoring flight safety. However, sometimes no damage (cracks, corrosion pits, deformations, etc.) is encountered, and also unforeseen failures may occur between two inspection deadlines, a situation that may culminate in accidents, as shown in Figure 18.

The employment of HMS-type tools, such as HUMS, offers constant monitoring which enables the identification of a future failure trend, according to some deviation from the known behavior pattern of the system. In this way, a predictive maintenance intervention could have been performed according to an established schedule, thus avoiding the occurrence of a failure, while still protecting against latent risks associated with manufacturing defects. Therefore, from the point of view of aviation safety, the main advantage is the fact that the components are always replaced before failures. Hence the potential of HUMS to improve safety and reliability, and reduce operating costs.
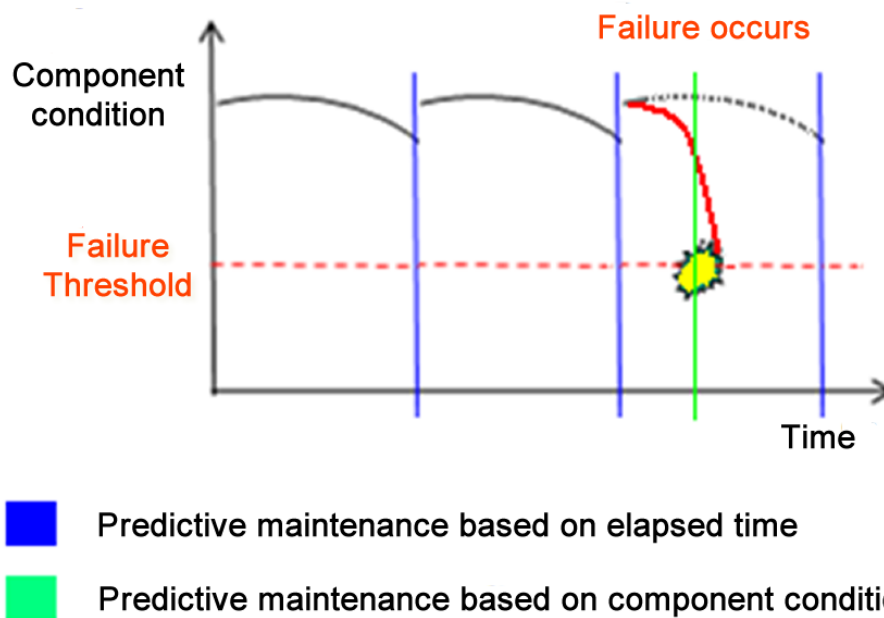
Figure 18: Condition (state) of the material over time using scheduled maintenance, based on time/cycles; and using predictive, condition-based maintenance (Adapted from [9])

B- Operational availability

The early identification of trends/variations in the amplitudes of aircraft vibration frequencies related to rotor assembly problems in helicopters often eliminates the need to carry out rotor flights for tuning the dynamic sets (balance and tracking adjustments). It should be noted that this feature allows the management of a Reliability Centered Maintenance (RCM) program to evaluate the possibility of defining the best opportunity to stop the aircraft, considerably increasing its availability in a company's operating schedule: operating units equipped with HUMS may fly more missions and may maintain a higher availability rate than units not equipped with these systems.

C- Reduction of operating costs

The maintenance cost reduction attributed to HUMS is a consequence of the reduction of dedicated or non-scheduled intervention actions themselves, due to scheduling optimization and the corresponding logistic support coordination, which allows the reduced use of consumable material (sealants, O-rings, lubricants, cleaning items, etc.), man-hours and spare parts storage.

This cost reduction is obtained through accurate and automated condition monitoring of equipment use; reduction of false failure events known as NFF (no-fault-found); reduction or consequential damages with the aid of early diagnosis; and improvement of the analysis of lessons learned from the trinomial event/incident/accident.

The use of HMS-type programs reduces maintenance delays and flight cancellations, avoids unnecessary maintenance, and reduces the price of insurance due to the reduction in the number of accidents and incidents and related expenses arising from claims.

Furthermore, when associated with systems such as HOMP via satellite (offshore activity), which monitors aircraft information (position, altitude, minimum altitude alert, take-off, and landing notifications), the system offers mission planning reports and reports of possible occurrences of non-conformities and condition alarms, which allow full control of the fleet, including computerized analysis of prevention reports.

The FAA estimates that aircraft employing state-of-the-art condition monitoring equipment may provide significant cost savings per year due to reduced fuel, maintenance, and direct costs related to accidents.

From the point of view of the manufacturer or the maintainer of an aircraft engine, who usually needs to provide warranties regarding the engine, it is desired to follow exactly the life condition and any possible abuse or misuse of the equipment.

3.6 HUMS disadvantages and limitations

There are records of incidents whose investigation pointed to the HUMS as contributing factors. In one of these cases, a sensor was inoperative. In another case, there was a serious incident due to the inability of the crew to confirm the correct diagnosis of the ongoing problem.

This latter case highlights the importance of considering and monitoring, also, the benefits of research on human factors and the cabin, crew, or corporate resources management (CRM), and/or the maintenance resources management (MRM), as both cases may affect predictions and the decision-making intrinsic to flight safety.

Therefore, the need for training and the challenges inherent in a change of organizational culture are decision-making factors whose costs should not be discarded.

Introducing fault detection information without the risk analysis associated with the severity of failure or their prognosis can be seen as a disadvantage due to the potential to increase unnecessary maintenance needs from the perspective of not compromising the continuity of airworthiness.

No operator wants to deal with the situation of an accident related to a known fault, no matter how well reasoned and structured the decision-making process, because will be charged for has been not having acted before.

The resulting civil liability would be unacceptable, with potentially dire ramifications for new insurance contracts, and the image and subsequent survival of the organization, in terms of continuity of its business.

Thus, forecasts with updated limits and continuous monitoring and diagnostics are essential resources to an HMS.

Another potential disadvantage of the HMS relates to the limits of prognosis. If, within the maximum level of uncertainty established for the continuous operating safety, they translate values consistently lower than half the range of traditional scheduled maintenance, the opportunity targeted for significant flexibility in maintenance management will be reduced and may limit the application of the HMS - unless the definitions of those intervals are based on statistical failure probabilities (based in the historical performance) and should be more conservative than the limits of prognosis adopted for HMS.

HUMS false alarms linked to NFF created by software or sensor errors also negatively affect operational availability, so that a rate of 10% of those in, for example, a fleet of 122 aircraft, would reduce operational availability by 4% (five units and 2,000 hours of flight/year).

With its current limitations, the maturity of the HMS philosophy still does not guarantee monitoring that covers the entire aircraft. For reasons of compromise between accuracy and cost viability, the HMS may never be able to provide the desired cost-effective follow-up of a component of a particular system or subsystem, and therefore it may always be necessary to require a combination with time-based maintenance. This limitation will vary depending on the nature of the system/subsystem and needs to be evaluated properly.

It is worth mentioning, considering the advantages mentioned in the previous section, that disadvantages and limitations will always be identified as new technology is adopted in the operational theater. The actors involved (manufacturers, maintainers, suppliers, users, and civil aviation authorities) should tirelessly discuss and refine these disadvantages and limitations to create viable alternatives to circumvent them or reduce them to acceptable risk levels, reaching a positive balance in favor of aviation safety.

3.7 HUMS certification challenges

Certification is understood to be proof that the project meets the requirements for its safe operation. The basic requirements for type certification (of an aeronautical product) are:

- qualification and installation of the system/equipment that collects, stores and presents the information;
- activities of validation/demonstrations of compliance with requirements (which involve the understanding of the physics involved in the failure mechanism) and of the methodology (means of each compliance by which it's analyzed how well HUMS can dictate maintenance actions based on the analysis of the condition and of use of data); and
- instructions for continued airworthiness, which implies, among others: instructions for operation life cycle and control for each item; procedures in case of inoperability; and training program and requirements for mitigation actions.

The criticality is defined here as the level of severity of the unintended consequences of using the HUMS in-flight safety. Through a Functional Hazard Assessment (FHA), this term is classified by the FAA into five categories (in decreasing sequence): catastrophic, potential danger, major, minor, and no effect), which determine the rigor of the certification process for the aeronautical product (equipment, software, or systems).

In this context, the unique challenge of certification lies in the creation and analysis of different scenarios in which safety must be provided, under the worst hypotheses, where there is a huge complexity associated with statistical & probabilistic models, and with the integration of multiple subsystems, both on-board and ground-based.

For these reasons, HUMS have been the focus of attention of civil aviation regulation agencies, such as the FAA, which issued certification requirements for the transport helicopter category through the circular advisory (AC 29-2C) [16]; and CAA, which issued AAD 001-05-99 CAP 693 Acceptable Means of Compliance Helicopter Health Monitoring.

That AC focuses on the aircraft maintenance process and describes a guide to requirements needed to certify the installation of an airworthy HUMS, with instructions for its continued airworthiness of a wide portfolio of applications, aiming at the approval of the aeronautical authority of certification. It is anticipated that developers may suggest other methods of proof of requirements beyond those recommended in this document; however, any methods must be previously approved by the FAA. The following key criticality elements must be met to guarantee safety:

1. Criticality assessment at application boundaries and effects on the helicopter. In the past, the data from the HUMS were already seen as valuable, but they were not critical for flight safety, as they were used in parallel to traditional maintenance regimes, or, for example, as instruments for after-sales support in monitoring equipment under warranty. From the moment the HUMS output information can be used to adjust established maintenance practices or whether it may be the only means of indication of the condition of the aircraft to the crew, the criticality of the system must be determined, and the rigor of certification adopted. It should be noted that the certification process of this system must be judicious at the level of possible dangerous consequences of inappropriate actions, which can be taken into consideration, as well as the impact of its installation;

2. Special considerations for ground equipment are relevant, given that the same criticalities of the on-board items must be considered; and as for the so-called off-the-shelf items (taken directly from the shelf), that is, without a certified system, considerations should be adopted to circumvent the rigors of a software certification;

3. Validation of monitoring techniques, algorithms, parameters, and rejection criteria;

4. Intervention actions associated with the monitoring data of the HUMS, which constitute extending the life of an item beyond preventive maintenance scheduling, saving costs, or reducing the life to avoid failure earlier than anticipated in the time-based maintenance; and

5. Certification actions for mitigation, that is, the establishment of criticality compensation factors to a low level, which would be autonomous, continuous, and independent of the HUMS. With this, the FAA does not certify any system as catastrophic.

Even after completing the initial certification process, the effort needs to be continually supplemented by information and evidence associated with the operational life cycle reality (Service Difficulties), which must be analyzed in the judgment of the effectiveness of the HUMS (for the guarantee of issuance of compulsory application service bulletins).

It is expected that the costs of certification will decline as more project models benefit from HUMS and more experience is gained in this process.

Goodrich HUMS has been certified to perform under the DO-178B Standard (titled *Software Considerations in Airborne Systems and Equipment Certification*), a criterion created by the RTCA (Radio Technical Commission for Aeronautics) for embedded software certification, and rated level B (potential to cause potentially hazardous/severe failures, identified and related to system security). This document determines verification, validation, documentation, and management of the software configuration, and disciplines the quality assurance to be used in microcomputer systems, as detailed in the advisory circular (AC 20-115C) [20]. As the HUMS is an open-architecture project, third parties can develop their systems to integrate with HUMS and still transmit real-time data to ground stations, which use common personal computers.

3.8 Application perspectives for HUMS

The aeronautical authorities continuously pay attention to the definition of the minimum certification requirements to ensure the airworthiness of future-equipped aircraft.

The new generations of HUMS are moving towards acting with greater reliability and integration of functions, increasingly changing the way maintenance is implemented. The growth in the use of these systems depends on the increase in the reliability of the sensors. Therefore, the critical point is the accuracy of the sensors, which yields much-related research, to develop sensors that are more reliable, cheaper, and resistant to a range of temperatures, environmental contaminants, and aircraft vibrations.

The expansion of the HUMS functions and capabilities is being made by improving the algorithms to make greater use of the collected data. New directions include transition changes, such as detection of the conditions of failure and diagnostics to anticipate the indication of potential problems and the diagnosis aimed at the reliable and detailed prognosis of the maintenance needs; and automatic usage tracking logbooks for each component for its full management, effectively updated by the data collected on the aircraft.

Composite structures, such as the carbon-fiber-reinforced type, have had their adoption expanded in recent projects such as citing in ascending order, the B777, B787, and A380 because they are lighter than metallic structures and considered equally durable because they suffer less fatigue. However, they are also susceptible to wear, often in the form of cracks or delamination, which often are not visible to the naked eye. The technology for monitoring the structural health condition, commonly known as Structural Health Monitoring (SHM), is in continuous development. The studied technology detects invisible deformations or cracks through optical fibers that are used as embedded sensors or bonded to the aircraft's composite structure. SHM technology uses Artificial Neural Network (ANN) systems to emulate the pain signals sent to the brain by the human nervous system, when fractures, fissures, or delamination occur, which destroy the fibers, interrupting this way the light signal. This interruption, in turn, allows the anomaly is identified and located. Challenges in this technology focus on the adoption on a large scale at non-prohibitive costs, in the addition of extra weight, and in the commitment to the strength of the composite material itself.

Other structural monitoring technologies are being envisioned, including the premise of using acoustic emission sensor devices attached to the surface of this type of structure to capture the energy released by crack propagation.

The near future of HUMS systems in the military arena also points to their integration with communication systems such as the Airborne Communications Addressing and Reporting System (ACARS), which consists of transmitting automatic in-flight data (thus eliminating the onboard storage of cards), to be analyzed in real-time by the monitoring stations on the ground. In this way, the operator maintains the immediate condition of its fleet, allowing the assessment of the safe length of time between revisions, or time between overhauls (TBO).

Shortly, the consolidation of the HUMS is a widely used item, even by the smallest operators (motivated by the most economical operation of their aircraft), is expected to contribute to the helicopter industry's goal of reducing the accident rate in the coming years.

HMS has arrived on the aviation market as something more than a new technology: it arrived as part of a philosophy that emerges in changing organizational cultures. Predictive maintenance, based on the life condition of the components and subsystems, in line with continuing technological advances, has met the incessant search for greater flight safety and availability of aircraft, and reduction of operating costs, all aspects essential to the improvement of the business aviation efficiency, both in the civil and military sectors.

The HUMS, besides the monitoring, also includes aircraft usage parameters and has earned more acceptance among aircraft operators, as their prognostic limits are expanded, and alternatives to current difficulties are discussed. In their various projects, the HUMS tend to become more accessible also with new possible low-cost options, culminating as a standard item in the helicopter industry. Under the unprecedented challenges required for the careful certification of the relevant authorities, even open-architecture projects can count on the guarantee of the required quality. HUMS/CVR/FDR integrations, automatic transmissions of data even via the Internet, and structural health (condition) monitoring (SHM) technologies in composites are just some of the perspectives that promise to guarantee the airworthiness of future equipped aircraft.

4 Vibration-based health and usage monitoring systems (HUMS) of dynamic components of helicopters: some numerical and experimental applications

This section is based on excerpts from Technical Reports [21] and [22], concerning the Offset Program of Transfer of Technology in Health and Usage Monitoring Systems (HUMS) of the aircraft EC-725, a program involving the companies AIRBUS HELICOPTERS (former EUROCOPTER), HELIBRAS, and also the Brazilian Universities UNIFEI and ITA.

4.1 Wavelet analysis

Transient events in time series data if well captured by algorithms provide a lot of information about the object that they refer to. The decomposing of a time series into time-frequency space enables the capture of both the dominant modes of variability and how those modes vary in time [23]. For example, an indication of an abrupt change in the data-generating mechanism makes it possible to detect and localize in time. Applications of this kind of analysis include faults in machinery and equipment, problems with sensors from acquired signals, financial bankruptcies in mass from economic time series, seismology, and many others.

In mathematics, the continuous wavelet transform (CWT) is a non-numerical tool that provides an overcomplete representation of a signal by letting the translation and scale parameters of the wavelets vary continuously [24]. In an overcomplete basis, the number of basis vectors is greater than the dimensionality of the input, and the representation of input is not a unique combination of basis vectors. Overcomplete representations have been useful because they present greater robustness in the presence of noise.

The MATLAB® command *cwt* (Continuous Wavelet Transform [24]) returns the continuous wavelet transform of a time signal [25]. The CWT is obtained by using the analytic Morse wavelet with the symmetry parameter, gamma (γ), equal to 3 and the time-bandwidth product equal to 60 [25]. The CWT is superior to the Short-time Fourier transform (STFT) for signals in which the instantaneous frequency experiences either a fast growth or decline [26].

Figure 19 shows an example of a reference signal that keeps its phase all along the timeframe shown in this figure. The signal designated as faulty is a departure from the reference signal by just a phase change beginning at time 13 s. Applying CWT to the faulty signal utilizing the analytic Morlet wavelet, the transient of the faulty signal is easily captured by the sudden rise in the magnitude of CWT coefficients (Figure 20).
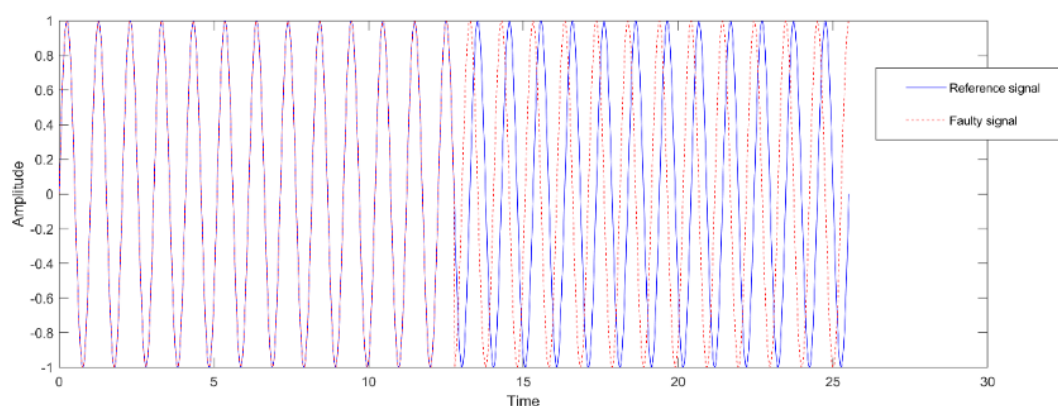
Figure 19: Example of a fault impacting a time signal
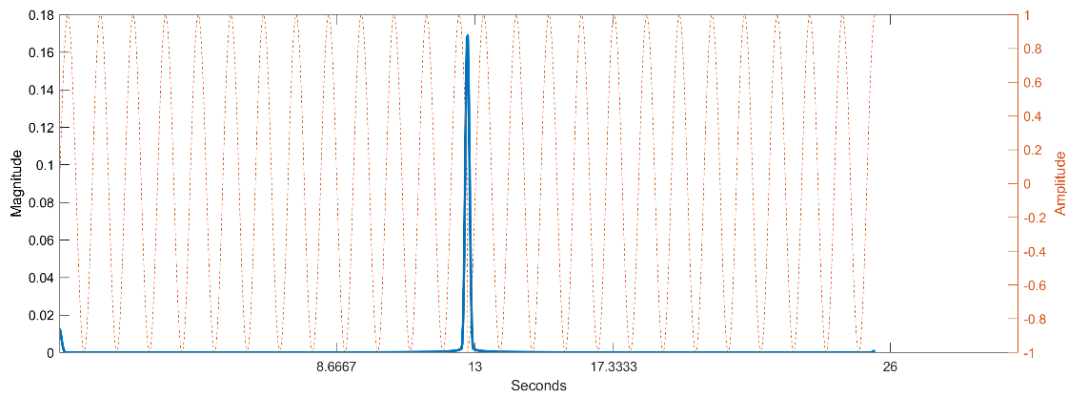
Figure 20: Finest-scale CWT coefficients

The CWT tiling of the plane is useful because many real-world signals have slowly oscillating content that occurs on long scales, while high-frequency events tend to be abrupt or transient. However, if it were natural for high-frequency events to be long in duration, the use of the CWT would then not be appropriate. The result is a poorer frequency resolution without gaining any time resolution. The human auditory system works this way because it provides much better frequency localization at lower frequencies and better time localization at high frequencies.

The MATLAB® command *wcoherence* returns the magnitude-squared wavelet coherence, which is a measure of the correlation between signals *x* and *y* in the time-frequency plane [27]. Wavelet coherence is useful for analyzing nonstationary signals. By using this command inputting the reference and faulty signals shown in Figure 19, the image in Figure 21 properly detects the phase change of the faulty signal relative to the reference one. The vectors change is a measure of the phase difference between the input signals (90º).
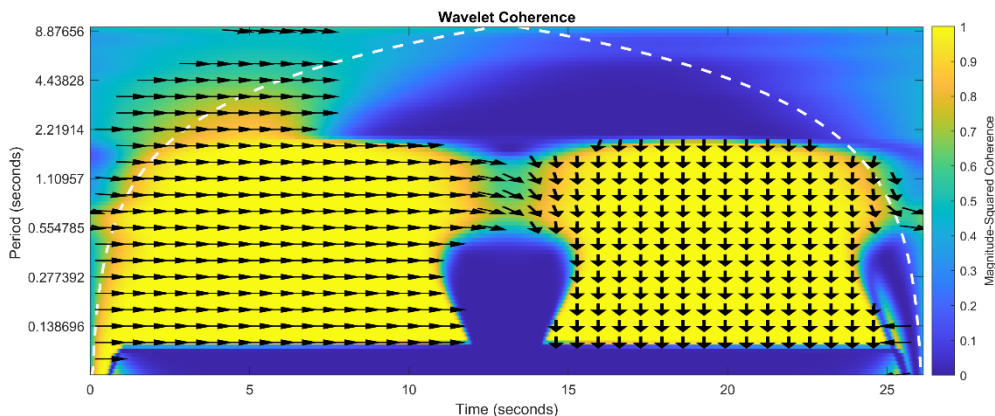
Figure 21: Wavelet coherence

Another example to demonstrate the capacity of wavelet analysis concerns the Earth's climate. Ice cores provide evidence for greenhouse gas concentration variations over the past 800,000 years. Both CO_2 and CH_4 vary between glacial and interglacial phases, and concentrations of these gases correlate strongly with temperature [28] [29] [30]. Figure 22 shows a data compilation of CO_2 concentration and temperature for the last 340 thousand years starting in the year 1870. The high correlation between the two variables is easy to observe. Higher temperatures due to higher CO_2 concentration lead to plant and algae proliferation, which, in turn, will absorb the carbon dioxide triggering a temperature drop in a second phase.
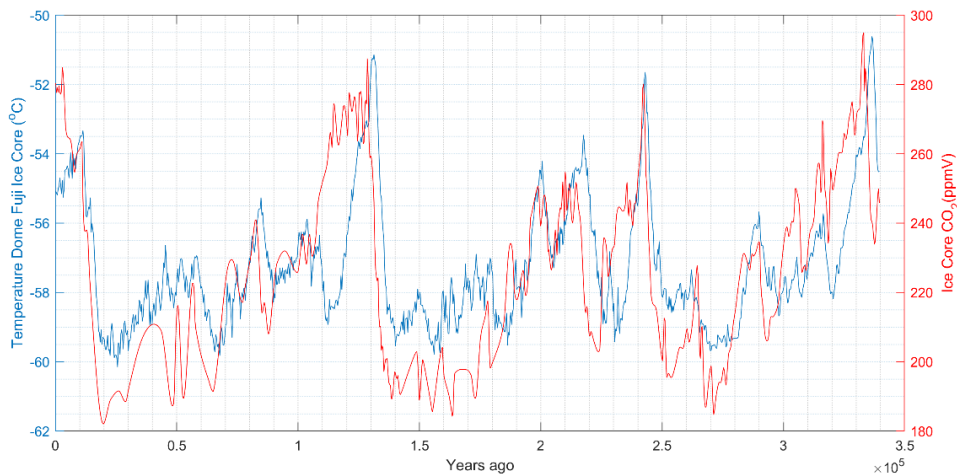
Figure 22: Ice core data indicate a strong correlation between temperature and CO_2 concentration [28] [29] [30]

The wavelet coherence and cross-spectrum showed in Figure 23 reveal a strong correlation along the time of the collected data for the periods ranging from 67 to 84 thousand years. This range encompasses three times the precession period of the rotation axis of the Earth. However, this correlation is not within the area delimited by the white circle and therefore it must be discharged. There is another high correlation coefficient revealed in Figure 23, for a period ranging from 16 to 33 thousand years with a time lag between the parameters. This fact should be taken into consideration, as it fits well with the precession period of the Earth's rotation axis of 26,000 years.
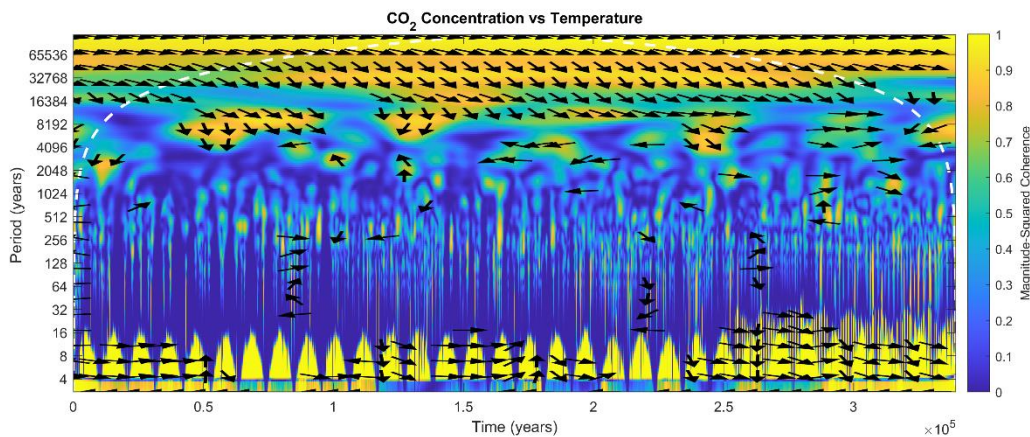
Figure 23: Wavelet coherence and cross-spectrum of CO_2 concentration and temperature data

Around the period of 10,000 years, some correlation is also tracked. This can be explained by a quick analysis of the graphs in Figure 22, as it reveals that the CO_2 concentration rise on some occasions is accompanied by the temperature surge with a delay of approximately 10,000 years.

Any time-frequency transform that uses filters, like wavelets in the case of the CWT, or modulated windows in the case of the short-time Fourier transform, necessarily smears the picture of the signal in time and frequency. The uncertainty in the localization of the signal's energy in time and frequency comes from the spread of the filters in time and frequency. Synchrosqueezing is a technique that attempts to compensate for this smearing by "squeezing" the transform along the frequency axis [31].

4.2 M'ARMS system

The Modular Aircraft Recording and Monitoring System (M'ARMS) is a sophisticated system that encompasses a HUMS subsystem.

The main objectives for the development of the M'ARMS were [32]:

1. Satisfy JAR OPS3's compliances relative to flight data parameters
2. Automation of flights and their analysis
3. Provide a maintenance report and optimize help for maintenance
4. Deliver a diagnostic for the main mechanical "critical parts".

The M'ARMS system is comprised basically of three subsystems:

1. HUMS
2. CVFDR (Cockpit Voice and Flight Data Recorder)
3. UMS

Functions of UMS and usage

- Monitoring Counters associated with helicopter components to inform maintenance about time reached and alarms displayed in flight
- Counting about Time in operation, counting flying time, counting landings, counting NR cycles, counting engines cycles N1(NG) et N2 (NF).

The main purpose is to monitor any exceedance of the usage threshold to:

1. Generate overshooting message in case of overshooting with the flight manual.
2. TQ1+TQ2 for Overtorque detection (damaging on MGB),
3. Engines exceedances (limitation on these 3 modes T4, NG, NF)
4. NR exceedance NR max (MRP damaging)

Engine Power checks basic functions on EC 225 will be done from VMS. M'ARMS system will record data for trend following. All these functions will be automatically linked with the operator after downloading data in the flight report. They will be saved inside GSC.

Reference [33] brings more details and information on fault diagnosis in helicopter HUMS, on some commercial solutions for HUMS, and specifically on the M'ARMS.

4.3 Description of the M'ARMS evolution: onboard MOD45 indicator.

A M'ARMS improvement enabled the HUMS systems on the EC225 and EC725 to indicate the cabin of a parameter during the flight. This is the first time that the HUMS system in a EUROCOPTER aircraft was used to control the condition of a specific component during flight. The certification of such usage was a technological step forward regarding the application of the HUMS [34]. Up to this milestone, the HUMS on helicopters has only been employed to provide maintenance crew with additional data to evaluate a possible degradation of the performance of different dynamic components, on the ground. Based on the scalar level of an indicator, the maintenance crew shall take actions to prevent an in-flight component failure. Thus way, the HUMS is considered a maintenance support tool, capable of monitoring and recording the usage and condition of different dynamic components. It mainly affects aircraft availability by providing a "no go." Thanks to this evolution, the M'ARMS system is now being used to improve the aircraft rate of dispatch.

The M'ARMS evolution described previously is presented in the Alert Service Bulletin No.EC725–45A008 and corresponds to mainly modifications 0726978 and 0726994. Its application is mandatory and is part of several improvements to the EC225/EC725 aircraft family following technical incidents that took place in 2012 [34].

Modification 0726994 installed two HUMS indicator lights on the instrument panel, which indicate the OM45 status for the pilot and copilot (Figure 24), while modification 0726978 consists of all the software and configuration updates to be performed. The application software version that was installed in the ACMS MFDAU++ at that time is version 1.6 and requires specific configuration files.
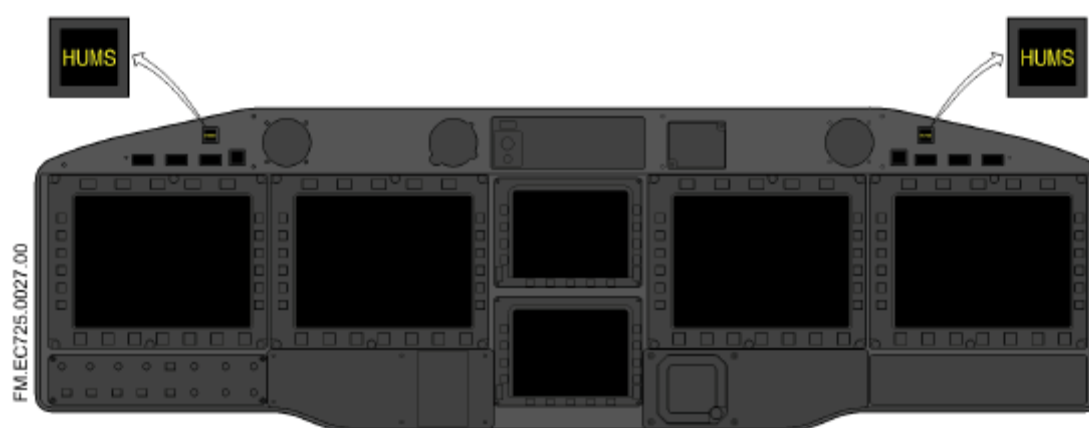
Figure 24: New "HUMS" indicator lights on the instrument panel, as presented in the
EC 725 AP Flight Manual SUP 7 [34]

It is important to notice that the ACMS MFDAU++ software version 1.6 is compatible with a limited combination of software and configuration files on the FDRS MFDAU++ card and the VPU (Vibration Processing Unit). The Information Notice 2100-I-45 provides all the information necessary to define the applicable combination for each aircraft configuration. The Alert Service Bulletin also presents additional maintenance aspects related to the M'ARMS modifications, as well as updated Technical Publication material.

The continuous monitoring of the OM45 is only executed in flight. During aircraft power-up, the system starts the power-on built-in test (Pbit), to assess its proper functioning. From the moment the aircraft is energized to the moment the Pbit has successfully been performed, the HUMS indicator lights on the instrument panel and in the M'ARMS control panel will be lighted (Figure 25). When the message "TEST MOD45 DONE" is presented in the M'ARMS control panel, all the HUMS indicator lights are shut off.
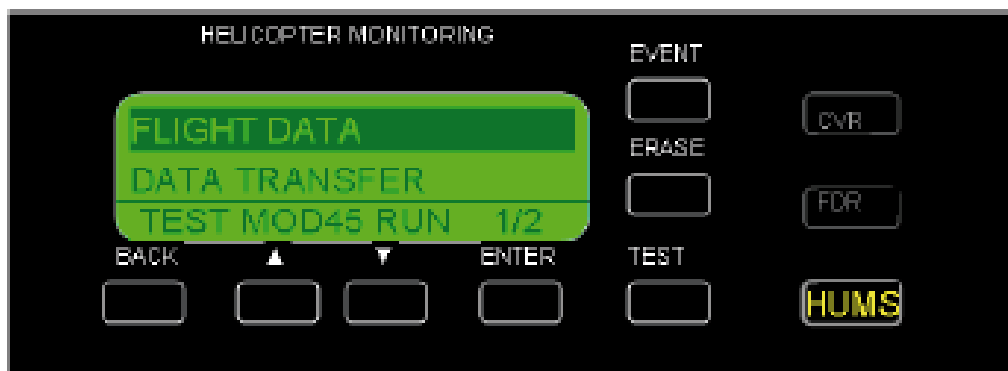
Figure 25: M'ARMS control panel, as presented in the EC 725 AP Flight Manual SUP 7 [34]

When airborne, the message "MOD45 RUNNING" is displayed when the indicator OM45 is being monitored. This happens approximately every five minutes when the aircraft is inside the monitoring flight envelope: indicated airspeed higher than 60 knots and torque over 60%.

In the event of OM45 acquisition exceeding the maximum threshold (0.5 grms), the message "MOD45 EXCEED" is displayed and the HUMS indicators lights light up. In this case, the maximum continuous torque is limited to 65% and in level flight must remain above 60 knots IAS. The maximum flight time in MOD45 exceed is limited to two hours.

Another possible situation is the failure of the in-flight OM45 monitoring. In that case, the airspeed must remain between 60 and 120 knots IAS (Indicated Airspeed), while torque is above 60% of maximum continuous torque.

4.4 System Errors (Signal/Electrical Errors): Case Study and Proposed Error Indicators

A- Introduction

In certain situations, the vibration signature obtained from a particular accelerometer may not represent a mechanical problem, but an error in the acquisition system itself, which may have appeared due to some type of signal failure such as an electrical problem in the acquisition system, problems in the sensors, problems in the signal processing, etc. In this Section, this type of problem is referred to as a "system error."

The objectives of the present Subsection are:

1. Extract lessons from a case study: to investigate different real cases in which a possible system error may have appeared, and to present the typical characteristics of this signal, in terms of values and plots of the different functions of interest that may be evaluated from the signal data

2. Error indicators: to propose possible error indicators and study these different error indicators regarding:

   o their ability to point out correctly the situations in which the system error is present; and

   o Their robustness to variations in the signal properties coming from other error sources, such as mechanical failures (i.e., their ability to present low false alarm rates).

Several sets of vibration data were made available for study, as shown on Table 2.

<p align="center">Table 2: sets of vibration data</p>

Helicopter model	Accelerometer name / position	Number of acquisitions	Total Flight Hours
Helicopter # 1	MGB LH first reduction pinion	208	291,5
Helicopter # 2	MGB Bevel Shaft and Wheels #6	5263	3514,9
Helicopter # 2	MGB Bevel Shaft and Wheels #6	4528	3555,2
Helicopter # 2	MGB Bevel Shaft and Wheels #6	12169	6499,8

The vibration data refers to the bevel wheel and shaft, a vertical shaft rotating at 2401 rpm, with an upper bevel wheel of 45 teeth and a lower oil pump wheel of 70 teeth, as shown in Figure 26, adapted from Reference [1]. The vibration data refers to accelerometer Nº 17 (11RK8), with synchronization at 2405 rpm, according to Reference [2].
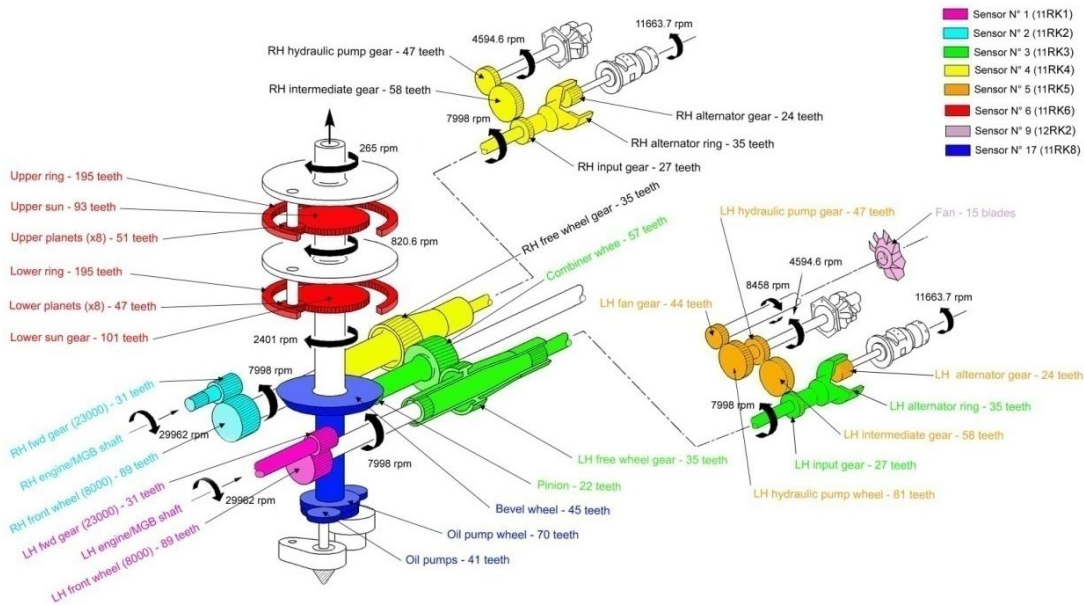
Figure 26: MGB Health monitoring and related sensors [33]

The vibration data available is processed data, obtained after a synchronous averaging procedure on the raw vibration data. This procedure is shown in Figure 27, adapted from Reference [35]. The objective of the synchronous averaging procedure is just to eliminate random vibration, keeping the periodic components which are multiples of the shaft rotation speed. For example, each revolution may be sampled generating 1024 points. After N samplings, an average of the N values is evaluated for each sampling point, generating a plot for the 1024 points of the signal average.
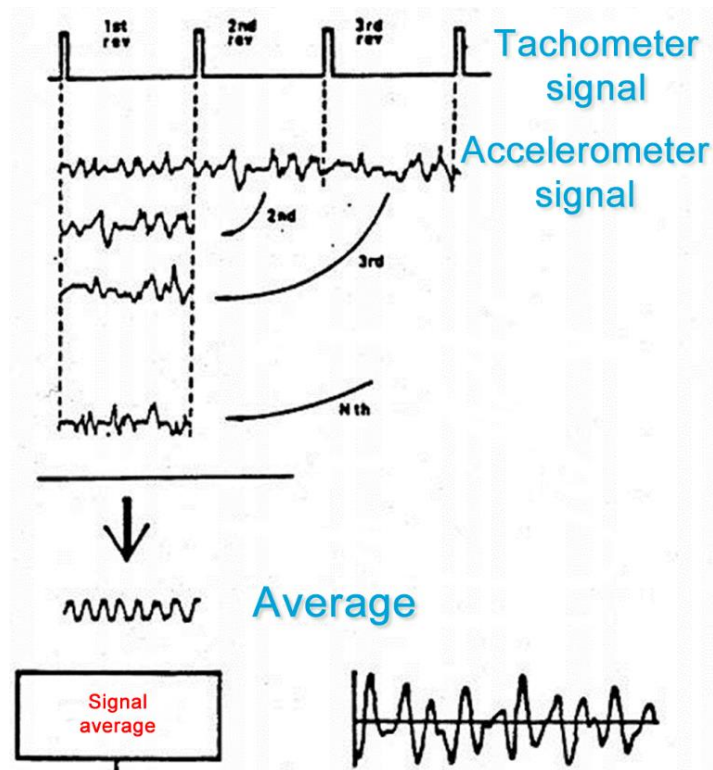
Figure 27: Signal treatment: synchronous averaging for eliminating random vibration [35]

For the averaged signal, a root-mean-square (RMS) indicator is evaluated. The value of RMS represents the total energy of the signal. Typically, most faults involving damage will increase the energy of the vibration signal. The RMS indicator can be evaluated as the area below the curve of the signal, either in the time domain or in the frequency domain. Figure 28 (adapted from Reference [1]) shows a plot of the signal in the frequency domain (obtained applying a Fast Fourier Transform (FFT) on the original signal in the time domain). The energy of the signal (the RMS value) is related to the area below the plotted curve.
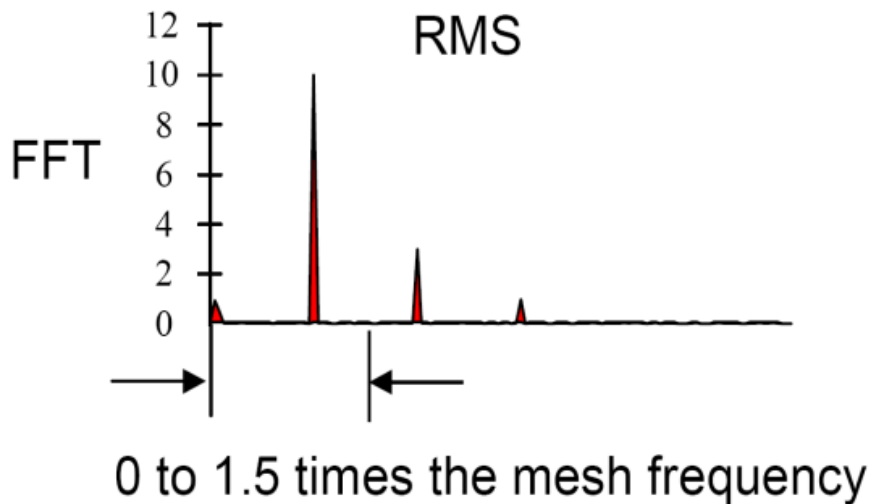
Figure 28: RMS value of the signal: area below the curve [35]

A plot of all the RMS values, for the 12169 cases available in the data described in Table 2, for the vibration of the bevel wheel and shaft, is shown in Figure 29.
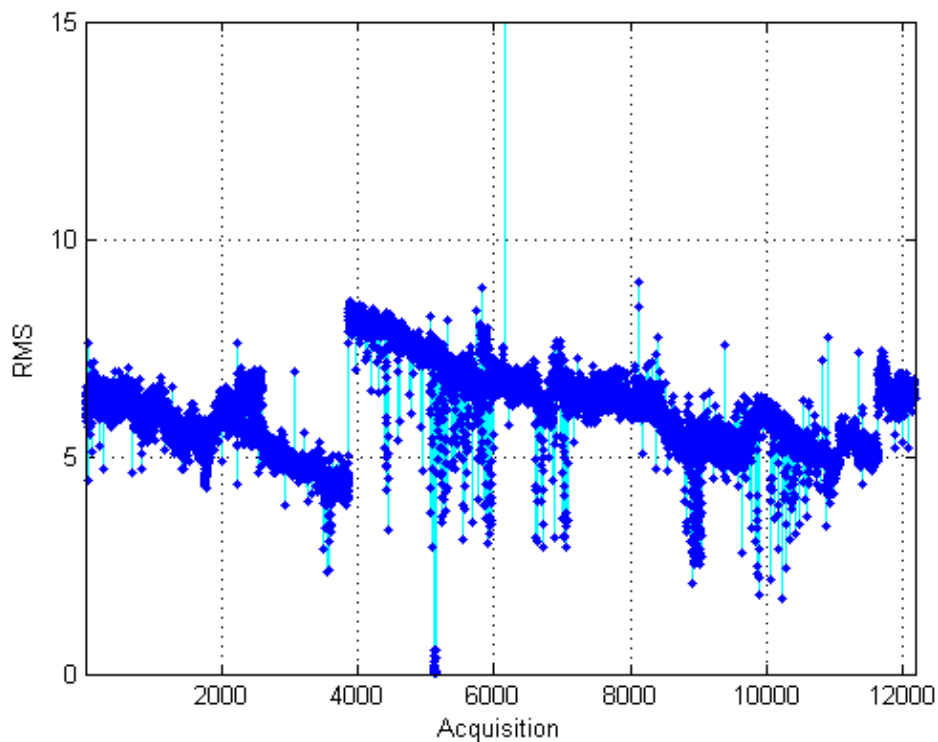
Figure 29: Bevel wheel & shaft RMS vibration (Helicopter # 2) [21]

From Figure 29, one can see two different cases:

1. The case in which the energy of the signal was high (thus, an alarm was triggered). In this case, with this RMS indicator only, if the energy of the signal is physically reasonable, no conclusion could be made whether the problem is of mechanical origin or system origin. Only when the energy of the signal is too high (which would be physically impossible) then one could infer that the defect was due to a system failure.

2. The case in which the energy of the system was too low (thus, no alarm was triggered). The system should be still vibrating, and it's not possible to have such a low level of energy, leading to the conclusion that there must be some type of system failure.

The RMS values for the vibration of the other aircraft described in Table 2 are plotted in Figure 30 to Figure 32.
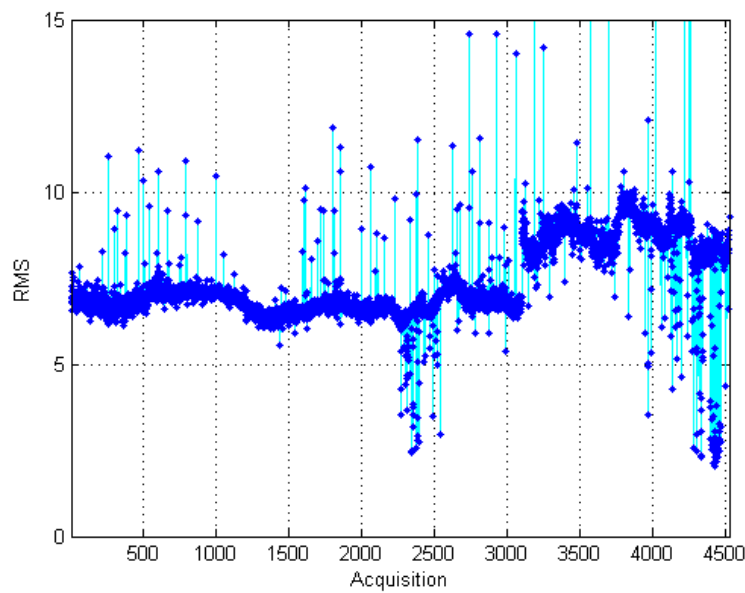
Figure 30: Bevel wheel & shaft RMS vibration (Helicopter # 2) [21]
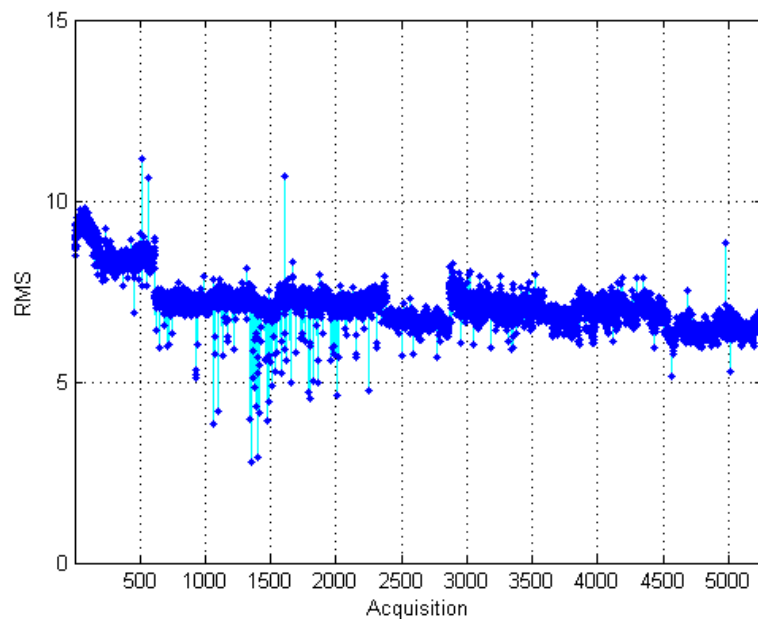
Figure 31: Bevel wheel & shaft RMS vibration (Helicopter # 2) [21]
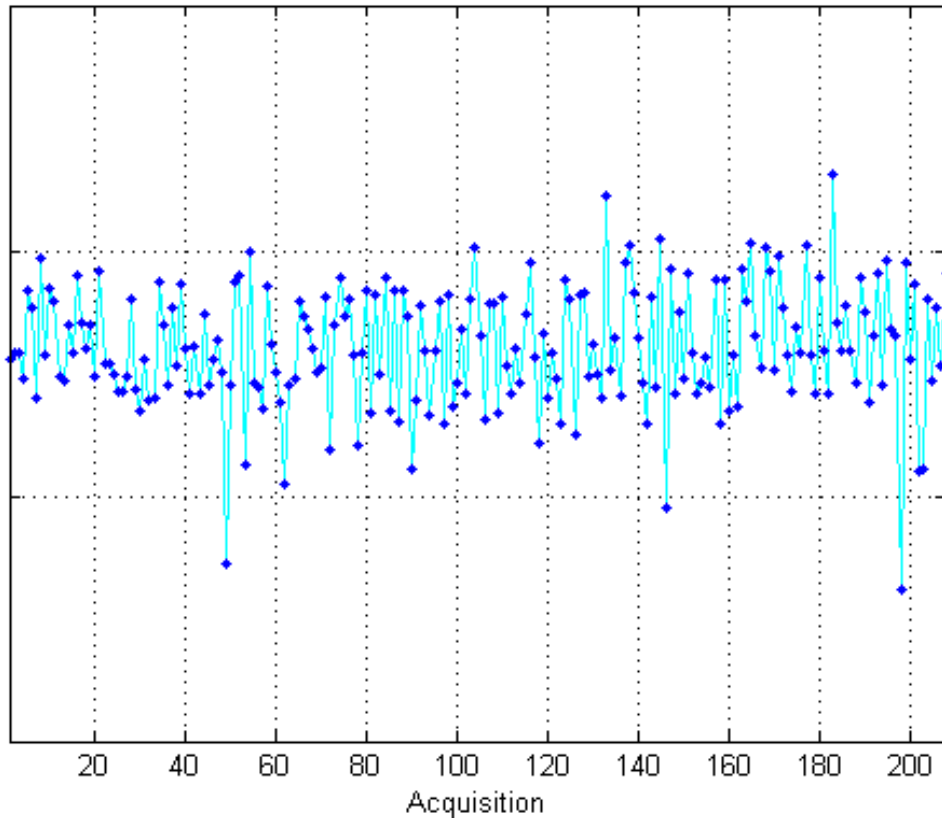
Figure 32: MGB LH first reduction pinion RMS vibration (Helicopter # 1) [21]

B- Signal analysis: parameters and characteristics of interest from the signal data

In this Subsection, a signal treatment is proposed, using correlation functions and phase diagrams, and error indicators are proposed, to capture the characteristics of a typical signal with system failure, trying to separate this case from the case of the signal that would come from mechanical failures.

Autocorrelation of signal x: $R_{xx}(t)$

Goal: To present a cleaner plot (of R_{xx} versus t), in which noise was filtered (comparing to the original signal), keeping the periodic characteristics of the original signal.

For a continuous case, the cross-correlation function is defined in Eq. (3) as

$$R_{xx}(\tau) = \lim_{T \to \infty} \frac{1}{T} \int_{-T/2}^{+T/2} x(t)x(t + \tau)dt \tag{3}$$

where τ is a parameter related to time.

For the cases being discussed, the available signals are presented in a discrete form, where N points are available, and the discrete cross-correlation function is given in Eq. (4) as

$$R_{xx}(k) = \frac{1}{N + 1 - k} \sum_{i=0}^{N-k} x_i x_{i+k} \tag{4}$$

where k is a time lag, and the sequence will have $(N+1-k)$ terms.

Cross-correlation between signal *x* and *y*: R_{xy} (t)

Goal: like Subsection A, to present a cleaner plot (of R_{xy} versus *t*), in which noise was filtered (comparing to the original signal), keeping the periodic characteristics of the original signal. In this case, the coherence between the periodic characteristics of the original signal x and the new signal *y* is enhanced. Thus, if signal y preserves the same periodic content as signal *x*, the correlation plots of R_{xx} and R_{xy} are expected to coincide. On the other hand, if signal y has different periodic content than *x*, the amplitude of the cross-correlation R_{xy} is expected to be small for all time t (the same behavior for R_{xy} is expected if y presents no periodic content at all, such as in the case of random signal). For a continuous case, the cross-correlation function is defined in Eq. (5) as

$$R_{xy}(\tau) = \lim_{T \to \infty} \frac{1}{T} \int_{-T/2}^{+T/2} x(t)y(t+\tau)dt \tag{5}$$

where τ is a time parameter.

For the cases being discussed, the available signals are presented in a discrete form, where *N* points are available, and the discrete cross-correlation function is given in Eq. (6) as

$$R_{xy}(k) = \frac{1}{N+1-k} \sum_{i=0}^{N-k} x_i y_{i+k} \tag{6}$$

where *k* is a time lag, and the sequence will have *(N+1-k)* terms.

Phase diagram for the correlation R: plot of *dR/dt* versus *R*

Goal: this diagram presents:

- a clearly defined plot of a smooth curve, for the case of the correlation function of a periodic signal;

- similar (almost identical) plots for the phase diagrams of the autocorrelation R_{xx} (of the reference signal) and the cross-correlation R_{xy} (between the current signal - at some time later - and the reference signal) if the periodic components of the signal have not changed between the two cases. In this case, the signal preserves the same amplitude and phase for all its spectral components; and

- a cloud of points for the cases of the autocorrelation function of a random signal x and the lack of coherence between two signals x and y (signals x and y having different periodic content).

Hypothesis for the typical response expected from system error

The signal *y* is expected to change its behavior concerning the original signal *x*, for a system without error. Thus, if this hypothesis holds:

- the amplitude of the cross-correlation R_{xy} is expected to be small, and

- the phase diagram of *dR_{xy}/dt* versus R_{xy} is expected to present a cloud of points without clearly defined curves.

Simulated example

An example of the expected typical response for signal error was simulated, in which a periodic signal (with noise) was simulated, and the signal was modified as a non-periodic signal, with erratic steps. The original signal x and the error signal y were generated and analyzed. The results of this simulation are presented in Figure 33 to Figure 35.
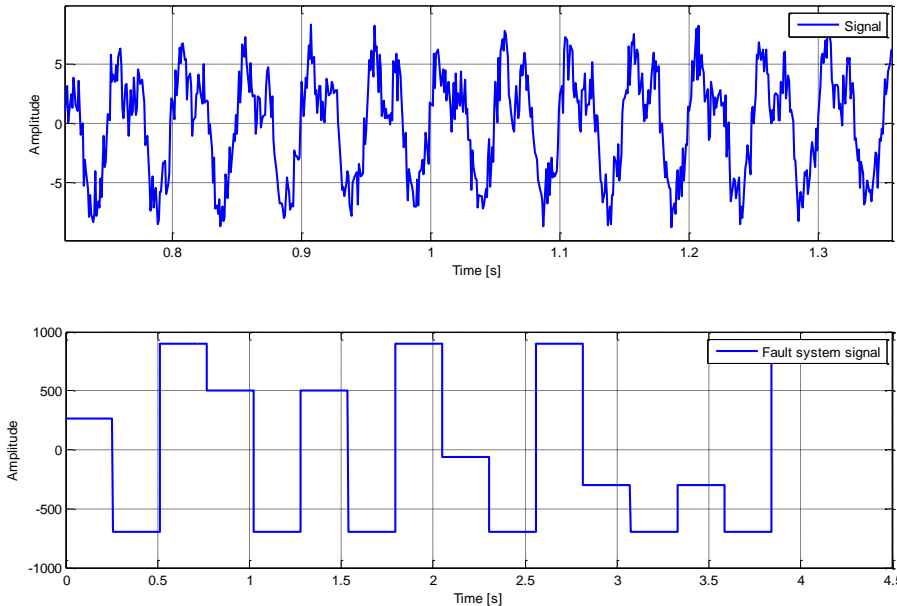
Figure 33: Plot of the original signals x and y [21]

From Figure 33, one can see that not much information can be obtained directly from the original signals, without processing.
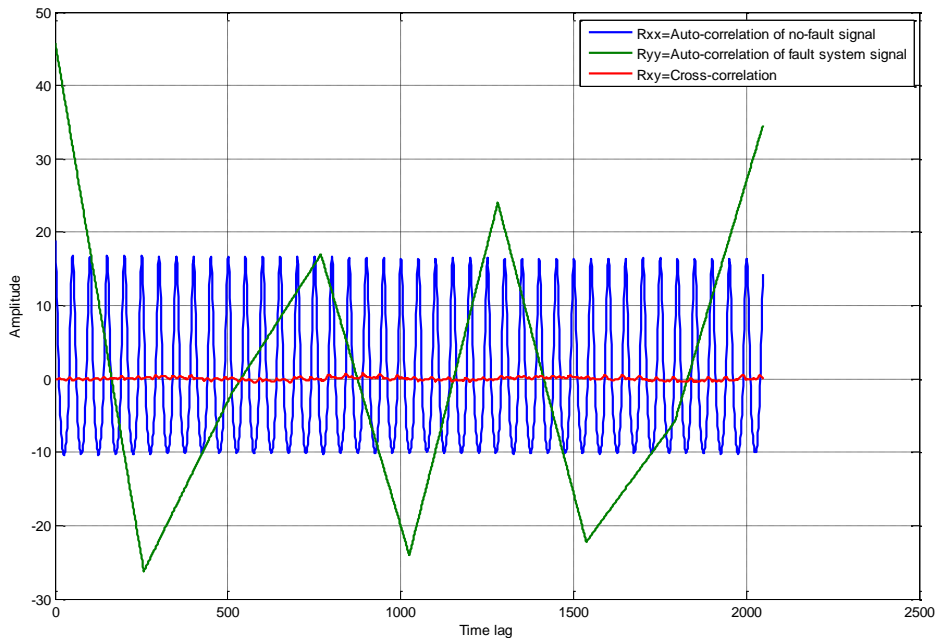
Figure 34: Plot of the correlations $R_{xx}(t)$ and $R_{xy}(t)$ [21]

From Figure 34, one can see the very low values of the cross-correlation coefficient, relative to the original autocorrelation, as expected.
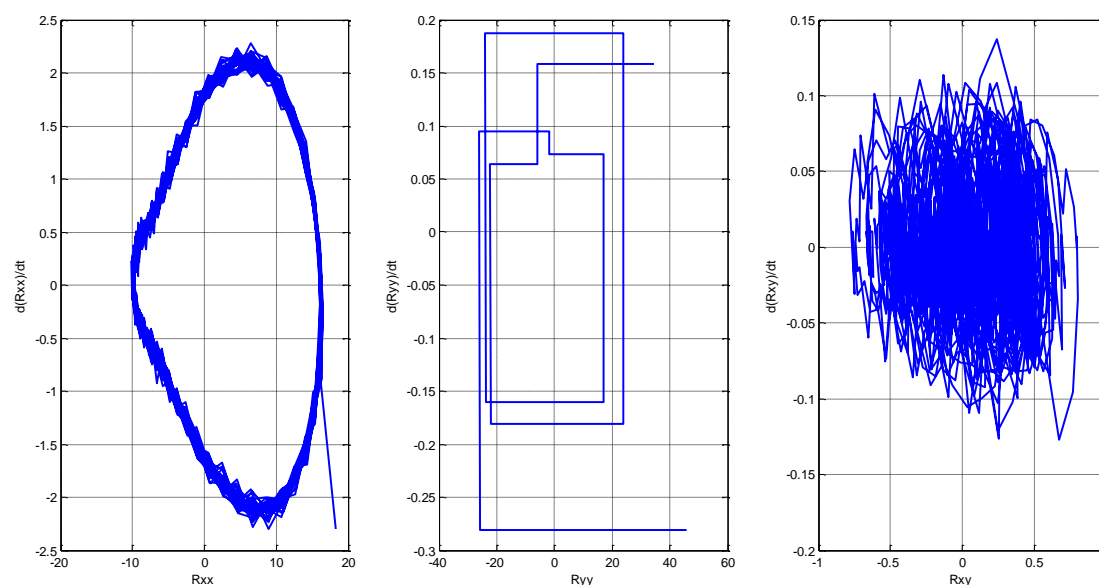
Figure 35: Plot of the phase diagrams of: a) dR_{xx}/dt **versus** R_{xx}**, b)** dR_{xy}/dt **versus** R_{xy}**, and c)** dR_{yy}/dt **versus** R_{yy} **[21]**

From Figure 35, one can see the neat curve plotted in the phase diagram of the original autocorrelation (case a), and the cloud characteristic present both in the cross-correlation plot (case b) and in the autocorrelation of the error signal (case c), as expected.

C- Cases studied

From the RMS data of aircraft Helicopter # 1 (Figure 32), one possible system failure was identified, described in Subsection C.1.

From the RMS data of aircraft Helicopter # 2 (Figure 29), several possible system failures were identified, described below in Subsections C.2 to C.5.

The available RMS data for aircraft Helicopter # 2 (Figure 30) and Helicopter # 2 (Figure 31) were not used in the discussion in Subsection C and will be used later for evaluation of the error indicators proposed in Section D.

C.1 Sampling errors: frequency sampling may be too low

This case refers to helicopter # 1, where the data (Figure 36), representing correlation functions of the signal, does not present clear periodic curves, which would be expected from the vibration of the helicopter mechanical component. The shape of the obtained curve suggests the presence of an error of conversion from the continuous signal to a discrete set of points (analog to digital conversion). This type of error typically is present when the sampling frequency is too low and does not follow Shannon's theorem, which states that the sampling frequency must be at least two times higher than the highest frequency component present in the analog signal (Reference [4]).

In this case, all signals analyzed contain this problem, including the reference signal *x*, used to obtain the cross-correlation functions plotted in Figure 36.
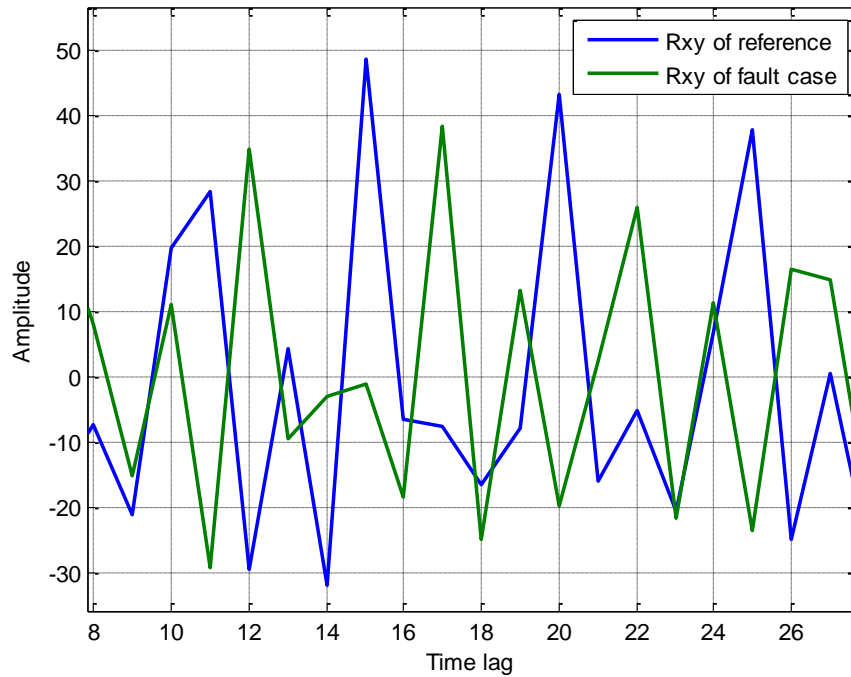
Figure 36: Correlation function for signals (Helicopter # 1) [21]

The phase diagram for this case (shown in Figure 37) indicates that the periodic components are not correctly represented, after the digitalization of the original signal. The hole in the plot shows that the lower frequencies are still well represented in the digital signal, but the cloud of points (around this hole) indicates that the high frequencies are not well represented in the digital signal. A good representation of the lowest frequencies combined with a poor representation of the highest frequencies corroborates the fact that there is a frequency sampling error in this data.
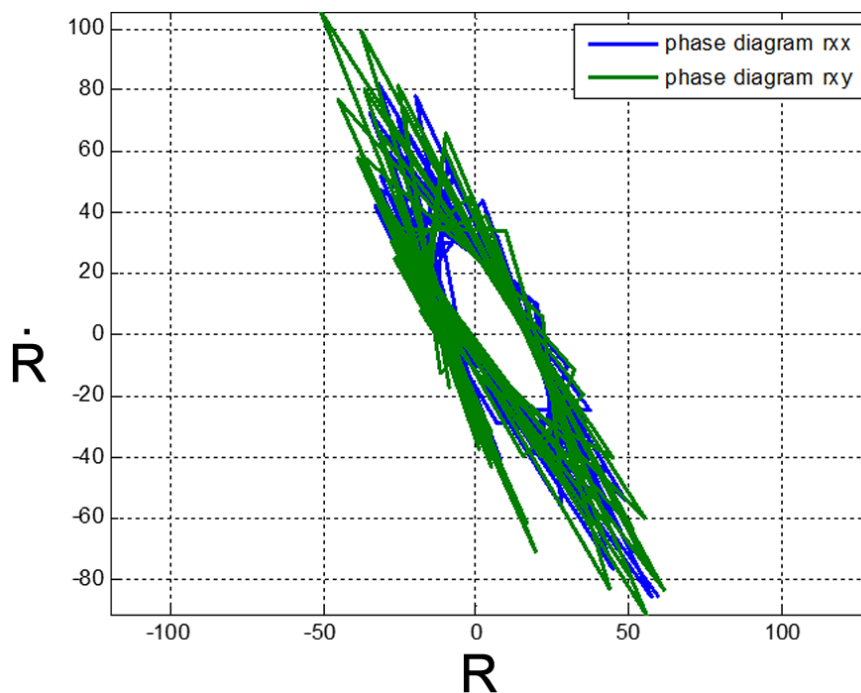
Figure 37: Phase diagram of correlations R_{xx} and R_{xy} (Helicopter # 1) [21]

C.2 – Signal with low gain errors: amplification gain may be close to zero

This case refers to Helicopter # 2. In Figure 29, some cases were identified as having a signal with a very low RMS value. Figure 38 and Figure 39 show a comparison between the reference case and one of these faulty cases. In Figure 38, the cross-correlation R_{xy} (between the faulty and the reference signal) is compared with the autocorrelation R_{xx} (of the reference signal).
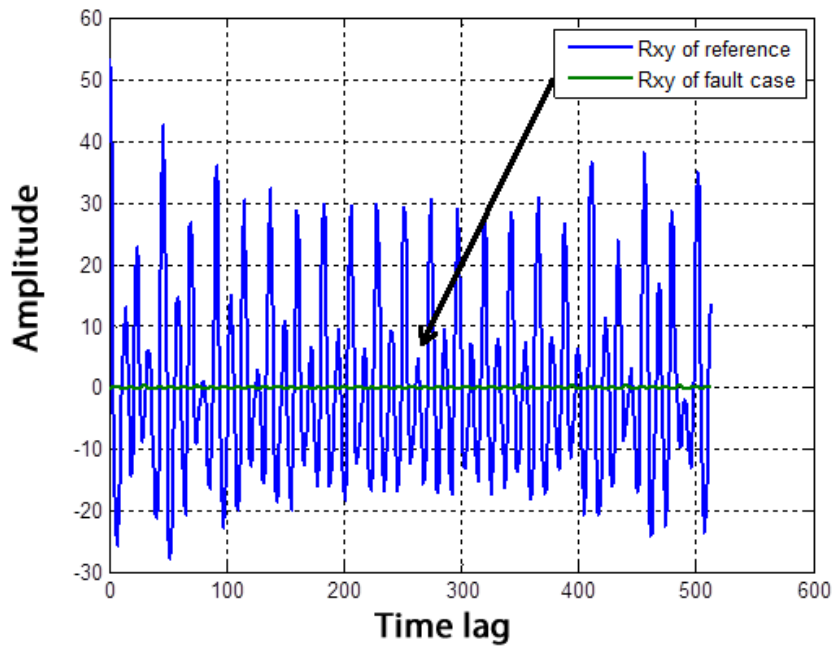
Figure 38: Correlation function for signals (Helicopter # 2) [21]

In Figure 39, the phase diagrams of R_{xy} (between the faulty and the reference signal) and R_{xx} (of the reference signal) are compared.
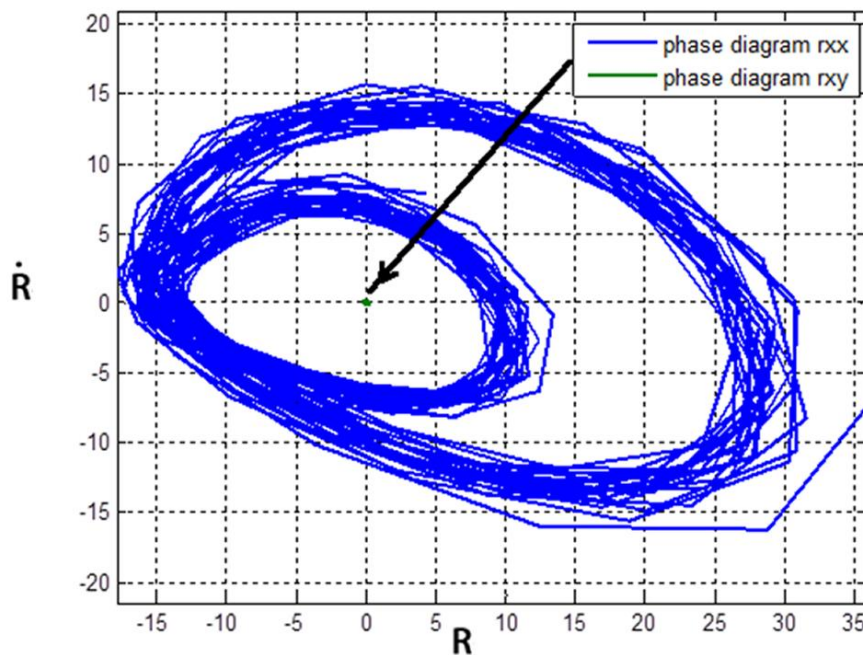
Figure 39: Phase diagram of correlations R_{xx} and R_{xy} (Helicopter # 2) [21]

The plot of the cross-correlation function presents a very small amplitude in Figure 38 and a very small size (almost like a point, as indicated by the arrow) in Figure 39. If the picture is enlarged, one can see that the format of the green plot, relative to the phase diagram of the cross-correlation function R_{xy}, is similar (almost identical in shape) to the phase diagram of the autocorrelation function of the reference signal, except for a scaling factor. A non-faulty signal should present a correlation function and phase diagram almost like their equivalent plots of the autocorrelation function R_{xx}, as mentioned before. Thus, Figure 38 and Figure 39 suggest that, in this case, there is no mechanical problem, but a system problem, probably due to a low amplification of the electric signal generated by the accelerometer. In this case, the signal $y(t)$ preserves the periodic components of the reference signal $x(t)$, only with a much smaller amplitude.

Investigating the available data recorded and other registers in the HUMS helped to clarify some issues. In this case, the data in Figure 29 presented several acquisitions with very low RMS amplitude. The data for the period reveals a fault described as "NO SIGNAL RECORDED," and a maintenance action related to ATA Chapter 45 was required (Central Maintenance System - CMS). After this acquisition point, the RMS results were back to normal values, indicating that the maintenance action solved the issue.

C.3 – Signal with time delay errors: may be due to poor synchronous averaging

This case refers to Helicopter # 2. Figure 40 shows that the two plots (of the autocorrelation function R_{xx} and the cross-correlation function R_{xy}) are quite similar, but one plot has a time delay concerning the other.
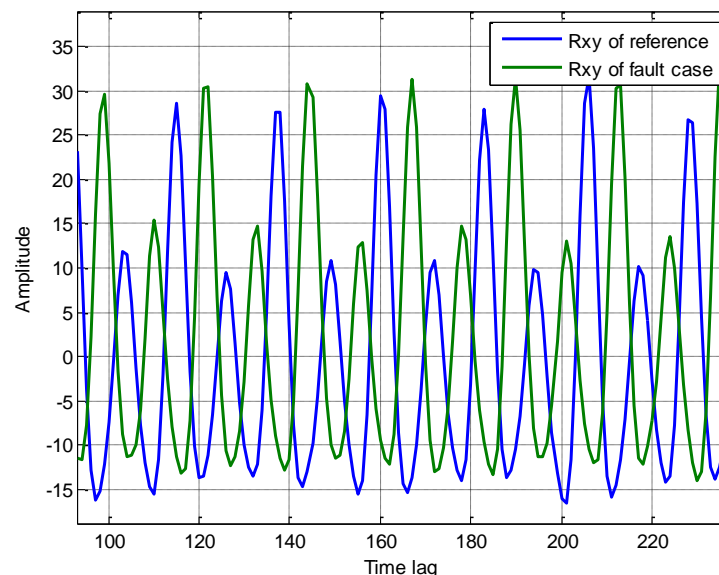
Figure 40: correlation function for signals (Helicopter # 2) [21]

This time difference in the correlation functions means that the starting time of the signal collection for the synchronous averaging process may be varying from one case to the other. If the starting points for the two cases were the same, the two plots should match, if there is no mechanical or system problem. By visual inspection, one can see that a shift of one curve on top to the other will give two curves very similar, which may indicate that there is no other problem with the aircraft component in the discussion, besides the difference in the starting point of the data collection for the two cases. Figure 41 shows the phase diagram of R_{xx} and R_{xy} for this case.
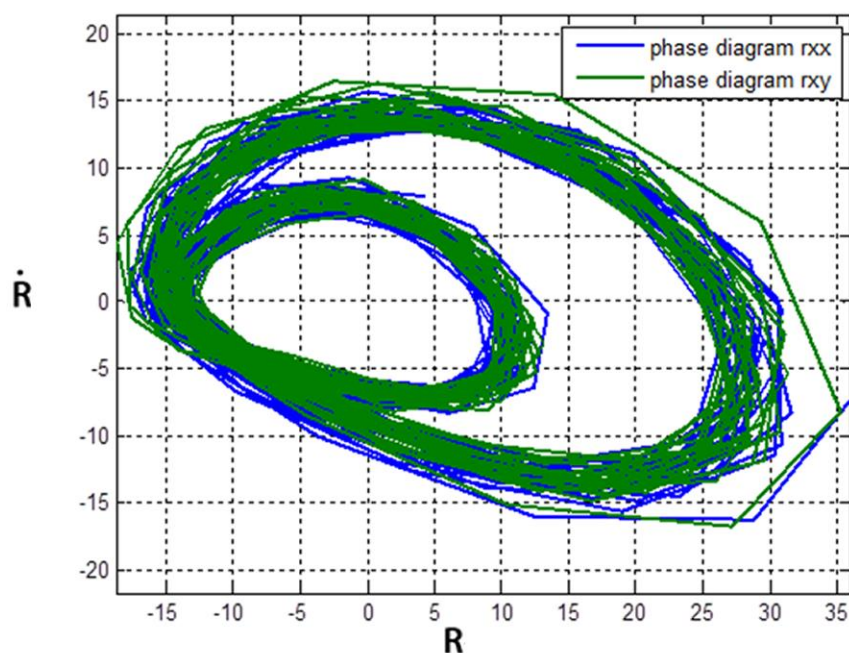
Figure 41: phase diagram of correlations R_{xx} and R_{xy} (Helicopter # 2) [21]

From Figure 41, one can note that the time difference, present in Figure 40, represents no significant difference in the phase diagrams of both correlation functions. This graph reveals that no physical difference exists between the two cases, except for the triggering time for the data collection, which can only be seen in Figure 41.

In this case, the acquisition is triggered by a magnetic captor located at the Phonic Wheel, giving a synchronization "top" to start and end the acquisition of the signal by the accelerometer.

According to maintenance staff, this problem does not represent a particularly critical problem, as it represents no mechanical or system failure. The only action that could be advised, in this case, would be to perform an inspection or maintenance procedure in the magnetic captor at the phonic wheel.

For this work, this type of problem might not be relevant to be captured or identified by the error indicators that would be proposed in Subsection D.

C. 4 – Signal high amplitude errors: signal amplitude may be too high, with peaks corresponding to a non-physical possibility (too much energy in the signal)

This case refers to Helicopter # 2. In Figure 29, some cases were identified as having a signal with a very high RMS value and having no physical significance. In this case, no physical system, when vibrating, will have such high energy, as compared to the energy of the reference case. Figure 42 and Figure 53 show a comparison between the reference case and one of these faulty cases. In Figure 42, the cross-correlation R_{xy} (between the faulty and the reference signal) is compared with the autocorrelation R_{xx} (of the reference signal).
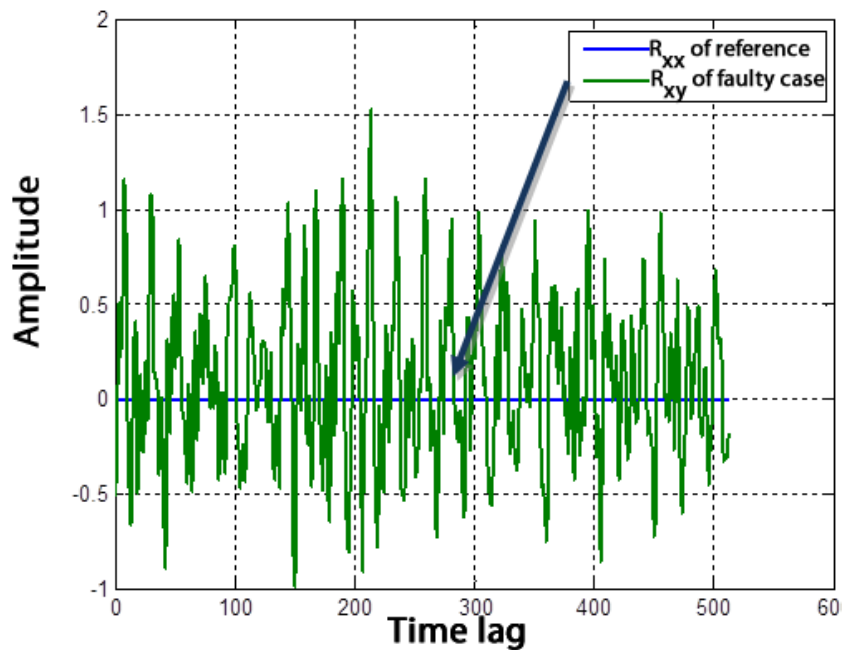
Figure 42: correlation functions for signals (Helicopter # 2) [21]

In Figure 43, the phase diagrams of R_{xy} (between the faulty and the reference signal) and R_{xx} (of the reference signal) are compared.
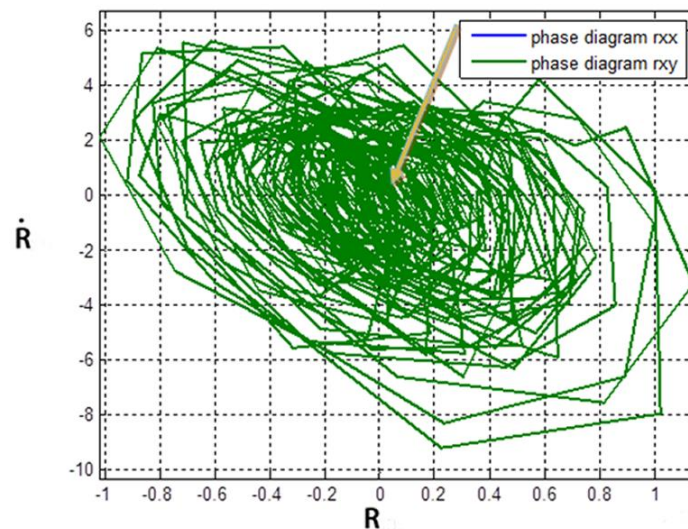
Figure 43: phase diagram of correlations R_{xx} and R_{xy} (Helicopter # 2) [21]

The plot of the autocorrelation function R_{xx} presents a very low amplitude (when compared to the cross-correlation function R_{xy}) in Figure 42 and a very small size (almost like a point, as indicated by the arrow) in Figure 43.

Differently from the low gain case seen in Subsection C.2, in this case, the signal y is random, as highlighted by the phase plot in the form of a cloud in Figure 43, for the cross-correlation function R_{xy}. The signal y does not preserve the periodic components of the reference signal x and has a very high amplitude.

Thus, Figure 42 and Figure 43 suggest that, in this case, there is no mechanical problem, but a system problem, probably due to the high amplification of a random signal generated by an error in the acquisition system.

C.5 – Signal with low amplitude and different periodic components

This case refers to Helicopter # 2 and concerns a case where a low RMS was noted, in Figure 29.

In Figure 44, one can see that the plot of the cross-correlation function R_{xy} presents lower amplitudes than the plot of the autocorrelation function R_{xx}. Also, different periodic components can be seen in the plot of the cross-correlation function R_{xy}, that were not present in the plot of the autocorrelation function R_{xx}.
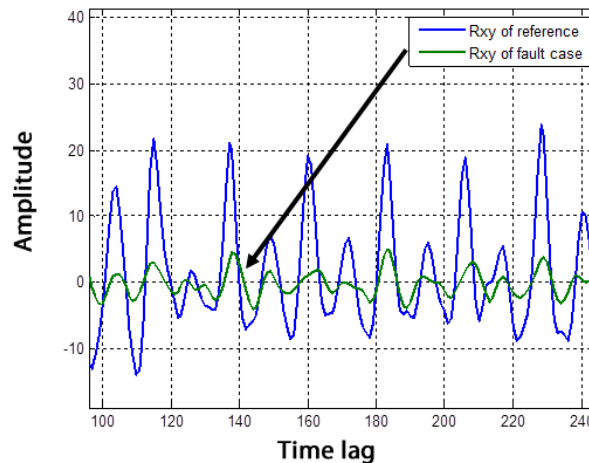
Figure 44: Correlation function for signals (Helicopter # 2) [21]

In Figure 45, the phase diagrams of R_{xy} (between the faulty and the reference signal) and R_{xx} (of the reference signal) are compared.
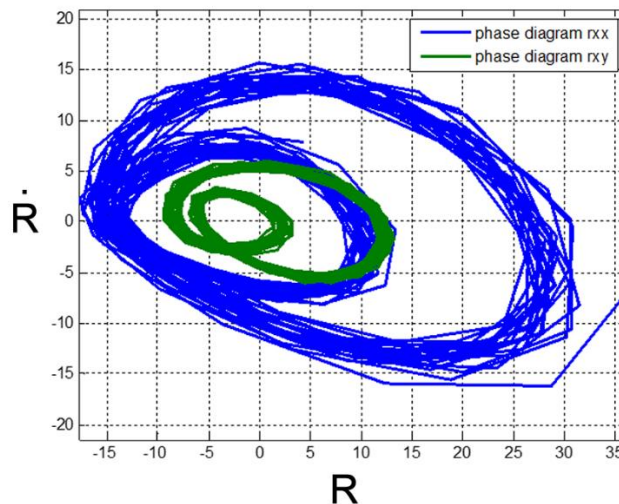
Figure 45: phase diagram of correlations R_{xx} and R_{xy} (Helicopter # 2) [21]

Figure 45 corroborates the fact that signal y has low energy (the size of the diagram is smaller, as both the amplitudes of R and dR/dt are lower for the cross-correlation R_{xy}, when compared to the autocorrelation R_{xx}). In addition, the change in the periodic components of the signal y is seen in Figure 45, as the shape of the phase diagram of R_{xy} has changed concerning the phase diagram of R_{xx}. The plot of the phase diagram of R_{xy} shows a clear change both in the correlation and phase and shows that y is not a random signal (as it has periodic components). Some of the periodic components of signal x are present in signal y, but signal y has additional periodic components, which were not seen in the reference signal x.

Figure 46 presents the correlation functions in the frequency domain, also indicating that the periodic components of signal x are still present in signal y (but with lower amplitude) and that a different component has appeared in signal y, at a high frequency (higher than the frequency components existing in signal x), which was not present in signal x.
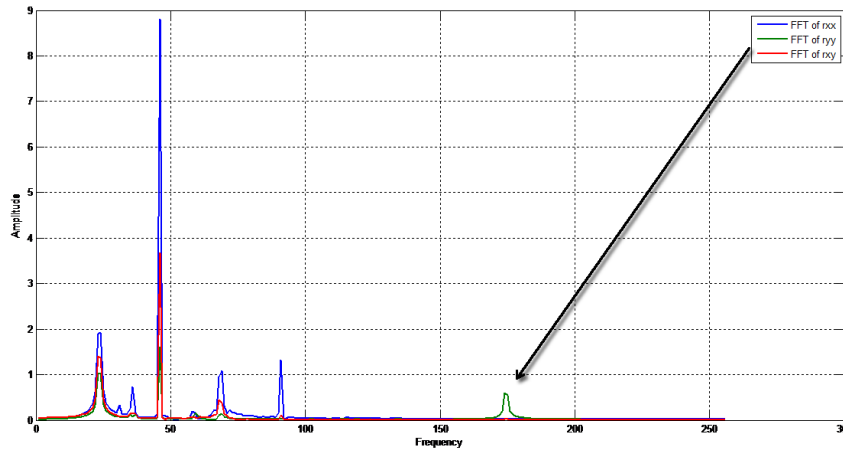
Figure 46: Correlation functions in the frequency domain (Helicopter # 2) [21]

The signal behavior seems to indicate both the possible presence of a system error (low amplitude of the cross-correlation R_{xy}, and different periodic components in signal y) and the possible presence of a mechanical problem (some periodic components of reference signal x are still present in signal y, although with a low amplitude). With the available information, no conclusion can be made regarding the origin of the defect being either a mechanical problem or a system error, or both.

According to maintenance staff, in this case, the RMS data in Figure 29 has not presented acquisitions with a clear problem. Instead, the problem for this case was only seen when analyzing the plots related to the data in the time domain, as seen in Figure 44 and Figure 45. No fault was detected in the period of interest, and no maintenance action was required to be performed, related to the component of interest or the acquisition system.

D – Proposed error indicator

D.1 – Indicator based on evaluating phase diagram plots of R_{xx} and R_{xy}

As described in Subsection C.3, the phase diagram for the correlation R is a plot of dR/dt versus R. A typical phase diagram for R_{xx} and R_{xy} is presented in Figure 47.
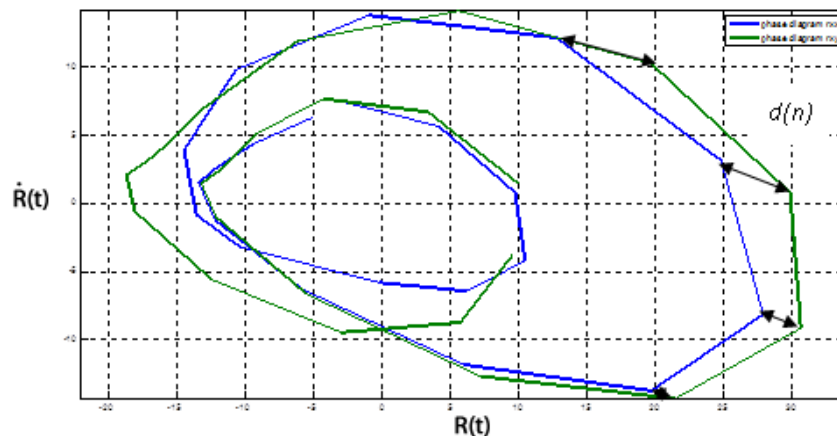
Figure 47: Phase diagram for R_{xx} and R_{xy} The arrows indicate the distances between points in the two plots for the same parameter n [21]

The proximity between the graphs is given by a point-by-point function *d(n),* which represents the distance between two points, one in the R_{xx} graph and the other in the R_{xy}, with the same parameter *n*. This distance is indicated by arrows in Figure 47. A residual case can be built as the summation of all distances *d(n)*, for all *n* points in the plot, as indicated in Equation (7).

$$D = \frac{1}{N}\sum_{n=1}^{N} d(n) \quad , d(n) = \sqrt{[Rxx(n) - Rxy(n)]^2 + \left[Rx\dot{x}(n) - Rx\dot{y}(n)\right]^2} \tag{7}$$

If the residual between the two curves is small, the autocorrelation R_{xx} and the cross-correlation R_{xy} are expected to represent a system with the same behavior, which means that both signal *x* and signal *y* would have practically the same periodic content, and thus signal *y* would not represent a system with errors (neither mechanical problem, nor system errors). On the contrary, if the residual is high, there are some causes:

> i) The phase diagram of R_{xy} is very small in shape (when compared to the phase diagram of R_{xx}). This case may represent a random signal y with lower amplitude (phase diagram is a cloud, but is almost a point in the plot), or a periodic signal *y* with lower amplitude (phase diagram is a well-defined curve, but is almost a point in the plot);
>
> ii) The phase diagram of R_{xy} has a shape of a cloud (with the same magnitude (general size) as the phase diagram of R_{xx}). This case may represent a random signal *y* with a certain amplitude (energy);
>
> iii) The phase diagram of R_{xy} is very big in shape (when compared to the phase diagram of R_{xx}). This case may represent a random signal y with higher amplitude (phase diagram is a big cloud, and the phase diagram of R_{xx} is almost a point in the plot), or a periodic signal *y* with higher amplitude (phase diagram is a big, well-defined curve, and phase diagram of R_{xx} is almost a point in the plot);

In the above-described cases, a correlation is expected, between a change in the signal (from *x* to *y*, as in cases i, ii, and iii) and a high value of the residual. Thus, an error indicator may be defined by high values of this residual, while small values in the residual would not represent an error in the signal.

E – Numerical results for cases identified from given data

E.1 – Sampling errors: frequency sampling may be too low

Figure 48 shows the plot of the residuals of the correlations (R_{xx} and R_{xy}) in the phase diagram, for 208 cases of vibration data for Helicopter # 1. The plot of the residuals is given by the sum of the geometric distances between the pairs of points in the phase diagram, one given for the reference case, and the other for the faulty case, both for the same value of the time parameter. As seen in Figure 48, sampling errors were identified in this case, as the time plot presented a non-physical shape.
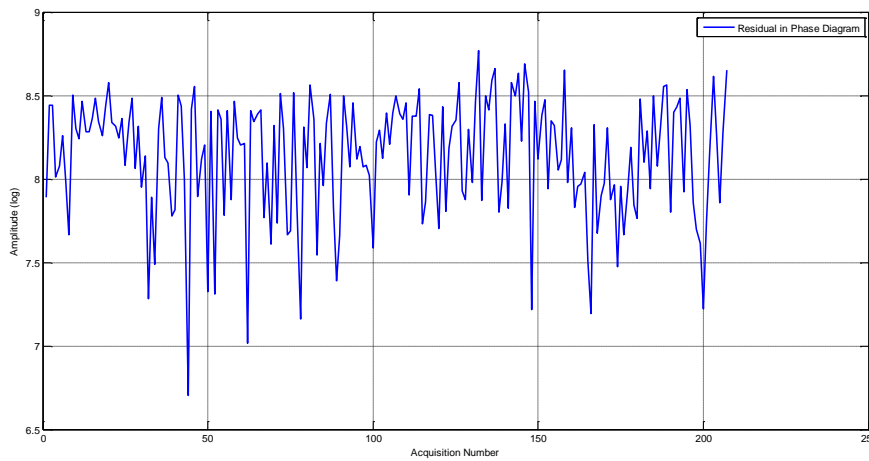
Figure 48: Residuals of distances in the phase diagram for vibration data with sampling errors [21]

In Figure 48, all acquisitions were poorly sampled (sampling frequency was not high enough, leading to errors in the analog-digital conversion), thus no clear information of possible system errors can be obtained from the residual in this case.

E.2 – Signal with low gain errors: amplification gain may be close to zero

Figure 49 shows the plot of the residuals of the phase diagram for the correlations (R_{xx} and R_{xy}), for 500 cases (out of the 12169 cases) of vibration data for Helicopter # 2, containing the case in which a signal with a very low amplitude was identified in Figure 3.4 (acquisition number 110, in Figure 49).
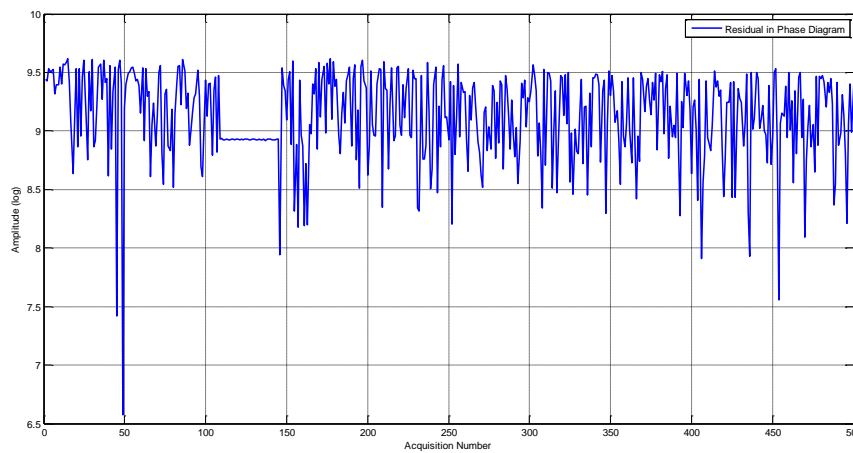
Figure 49: Residuals of in-phase diagram for vibration data with low amplitude errors [21]

In the discussion of cases 2 to 5, due to the high variation of the amplitudes of the residual, the vertical axis of the plot was set on a logarithmic scale, so all points (of high and low amplitudes) could fit in the plot.

The region where the signal has low amplification appears as a flat region in the plot (a "plateau", between acquisition numbers 110 to 145). One can see that the residual values in this region fit in the range of the residual values obtained in other regions, where no failure is envisaged. Thus, this indicator does not provide a clear indication of the failure region (in which signal amplification is low), as its value in this failure region remains inside the range of residual values typically obtained.

D.3 – Signal with time delay errors: may be due to poor synchronous averaging

Figure 50 shows the plot of the residuals of the phase diagram for the correlations (R_{xx} and R_{xy}), for 500 cases (out of the 12169 cases) of vibration data for Helicopter # 2, containing several cases in which a signal with a time delay (such as the one presented in Figure 5.3.1) was seen by inspection of the signals in the time domain. This case has appeared several times in the data analyzed.
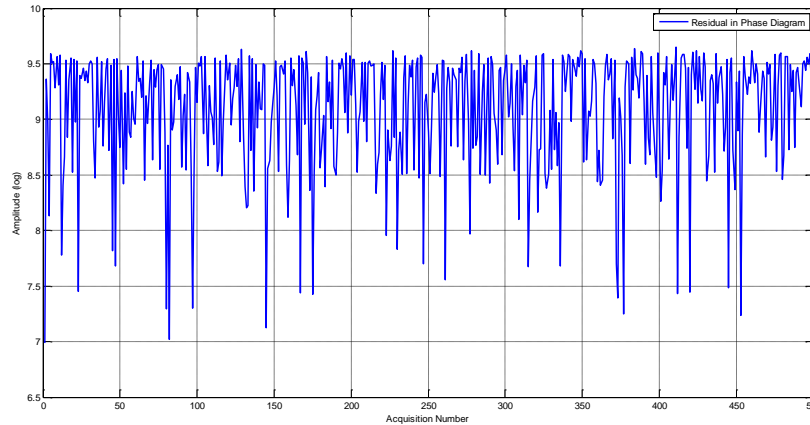
Figure 50: Residuals of in-phase diagram for vibration data with signal phase errors [21]

From expert information by the HUMS team, this problem does not represent a particularly critical problem, as it represents no mechanical or system failure, and typically no maintenance action is advised, in this case. For this case, the error indicator provided by this residual does not point to any region, and, thus, one can infer that this indicator is robust to this time delay error in the signal.

D. 4 – Signal high amplitude errors: signal amplitude may be too high, with peaks corresponding to a non-physical possibility (too much energy in the signal)

Figure 51 shows the plot of the residuals of the phase diagram for the correlations (R_{xx} and R_{xy}), for 500 cases (out of the 12169 cases) of vibration data for Helicopter # 2, containing the case in which a signal with a very high amplitude was identified in Figure 3.4. This case is represented in the plot of Figure 51 (acquisition case 155).
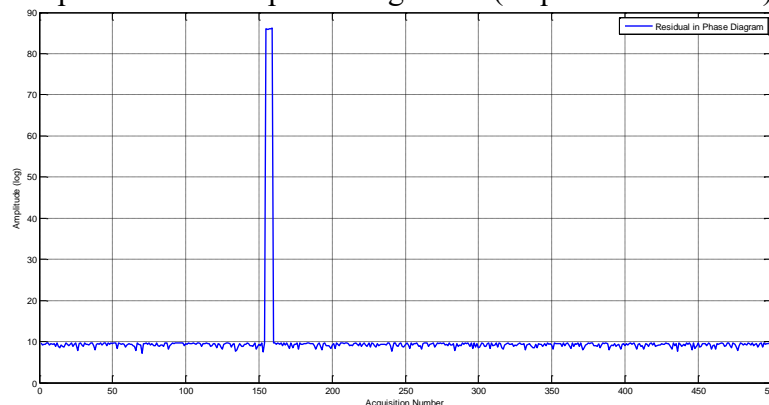
Figure 51: Residuals of in-phase diagram for vibration data with high amplitude errors [21]

The region where the signal has high amplification appears as a clear spike in the plot. Thus, the error indicator provided by this residual points out this type of system defect (in which signal amplification is high).

D.5 – Signal with low amplitude and different periodic components

Figure 52 shows the plot of the residuals of the phase diagram for the correlations (R_{xx} and R_{xy}), for 500 cases (out of the 12169 cases) of vibration data for the EC 225, containing one case in which a signal with low amplitude and different periodic components (such as the one presented in Figure 5.5.1) was seen by inspection of the signals in the time domain. This case is represented in the plot of Figure 51 as acquisition case 494.
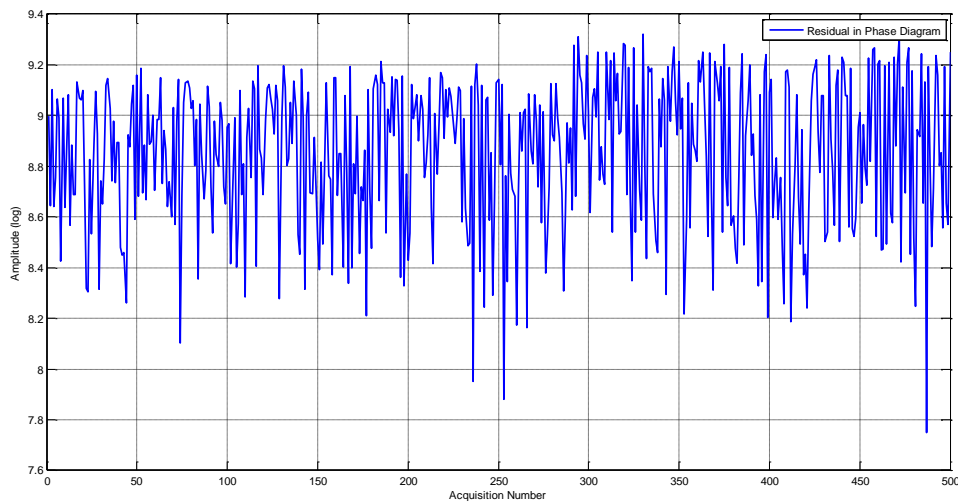
Figure 52: Residuals of in-phase diagram for vibration data with high signal noise errors [21]

From web HUMS information, no alarm was triggered at the time this acquisition was performed. For this case, the error indicator provided by this residual does not point to any region, and, thus, the indicator has not captured this type of system error.

5 Mechanical models for tail drive shaft

In this Section, the development of a mechanical model for helicopter tail drive shaft and Gaussian and Mixture Model algorithms are applied [36]. The phenomenon of the flexible coupling layer buckling is very complex, and it was analyzed using the software Abaqus®. The main objective was to check if the same opening between layers would be reproduced by the model. It is important to point out that this type of dynamic phenomenon may have an impact on the component life.

Statement of the problem

During a laboratory test, it was observed a buckling of the flexible coupling (Flectors) mounted on one side of the MGB shaft. A simplified diagram of the assembly is displayed in Figure 53.
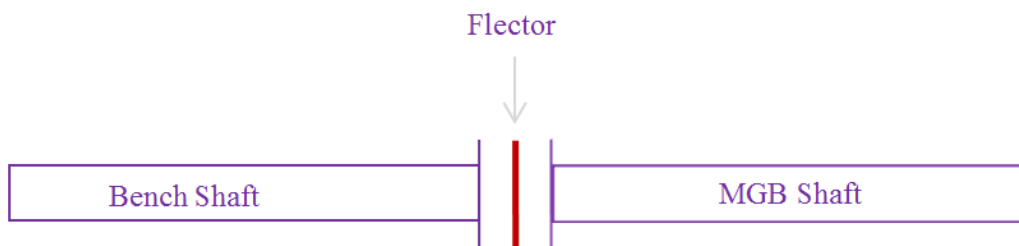
Figure 53: Schematic of assembly [36]

Since such a buckling would represent increased stress applied in the region, possibly anticipating fatigue damage, a study of the implication of misalignment and its relationship with the buckling phenomenon was performed.

It is assumed that the bench shaft bearing is rigid and the MGB shaft bearing is flexible. The main objective of the present analysis is to reproduce and explain buckling with radial and angular misalignment, as per Figure 54:
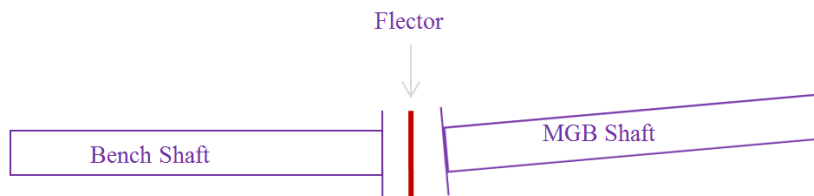
Figure 54: Misalignment modeling [36]

To properly verify the impact of such misalignment in the structure, a finite element model of the assembly was created on Abaqus®.

Finite element static model

A 3D finite element model was created to address the buckling issue [36]. The mesh was generated with Abaqus 6.12.1 [37]. The shafts are thin cylinders (4000 elements each shaft) and the Flector is modeled including layers (1900 elements each layer), bolds, and a washer (rigid link). Geometry and mesh are displayed in Figure 55.
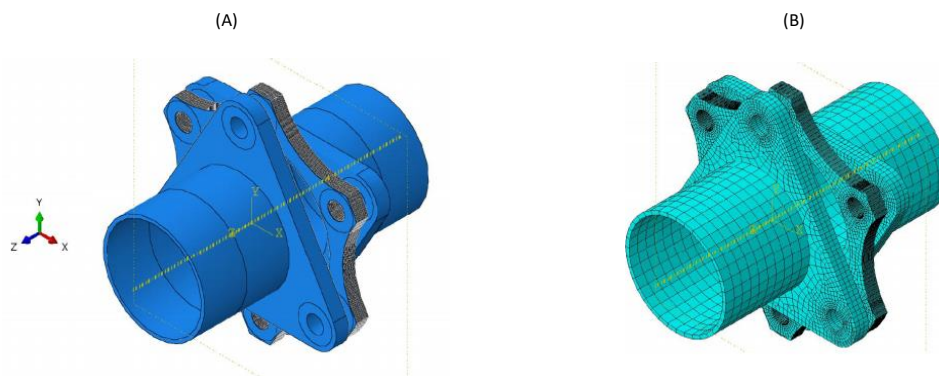
Figure 55: FEM model (A) Geometry (B) Mesh [36]

All degrees of freedom but the one related to axis rotation were set to zero on the left end of the shaft while a displacement was imposed on the other end as well as a torque equivalent to the one under which the structure is submitted when in operation, as displayed in Figure 56.
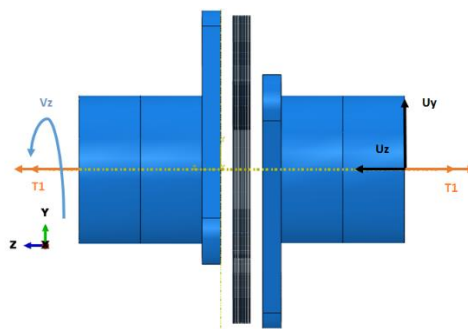
Figure 56: Boundary conditions and Loads applied [36]

The total displacement was set to obtain an angle of misalignment of 1°, for the shaft by determining U_y and U_z. And an analysis considering geometric nonlinearities and frictionless contact between each layer of the Flector was carried out. Due to the geometry of the problem, the zone expected to have the greater values for stress is right in the middle of the Flector, nevertheless, after 1^{9o} of misalignment is applied the response is as shown in Figure 57.
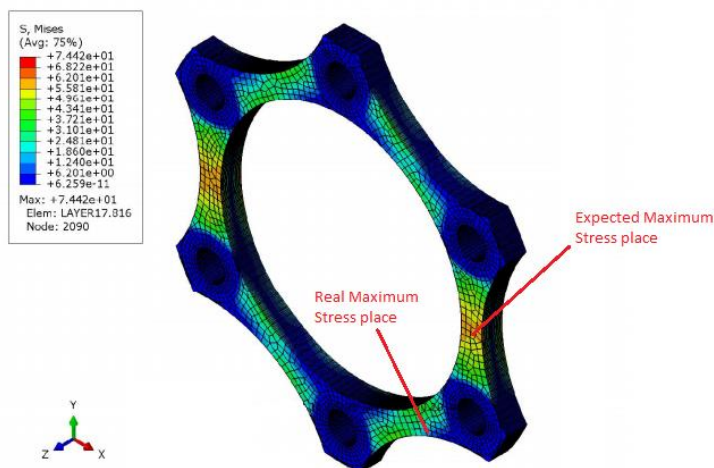
Figure 57: Difference on maximum stress spot – Expected vs. Calculated [36]

The unexpected stress concentration may be explained by a separation of the outer laminae of the coupling in what could be called a buckling phenomenon. One can check in Figure 59 that this buckling provides a stress concentration that increases the stress on that spot. The buckling observed by the model is coherent with the phenomenon observed in the laboratory.
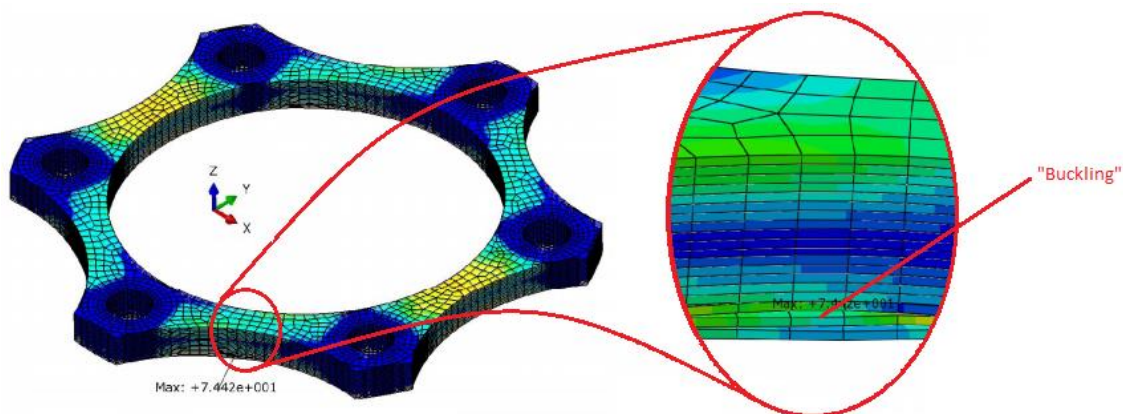
Figure 58: Maximum Stress spot after 1° of misalignment is applied [36]

By selecting the points right on the opening zone, a difference between their total displacements will be a good approximation for the value of the gap opening. This value is not exactly since one cannot guarantee that the maximum separation is not in the interior of the structure. The evolution of the separation while applying the displacement (Loads and boundary conditions as seen in Figure 56) is shown in Figure 59.
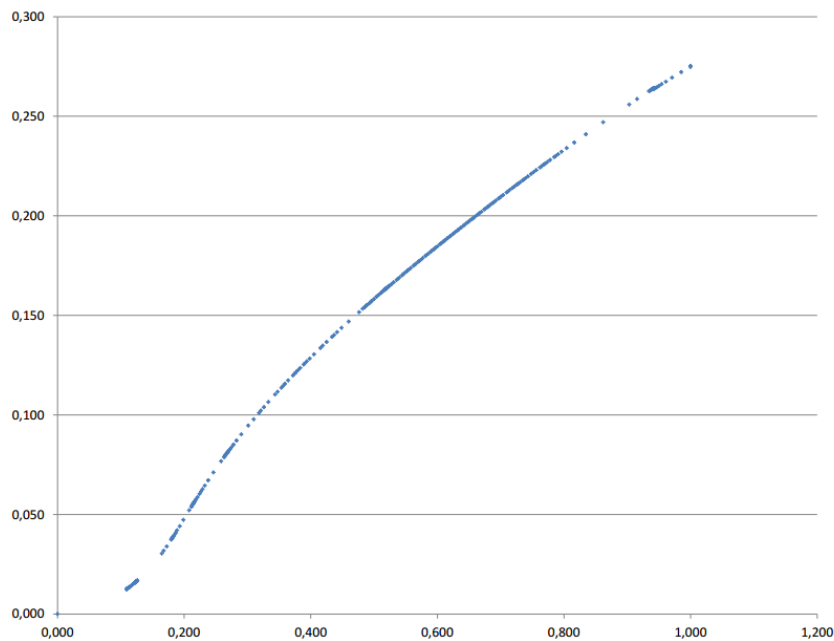
Figure 59: Evolution of the gap opening (mm) vs Degree of Shaft Misalignment [36]

One can notice, from Figure 59, a smooth, non-linear variation of the gap opening with the shaft misalignment. Along each revolution, the "breathing" of the gap between Flector layers will account for important phenomena which might require further dynamic analysis to determine the possible influence on the component vibration behavior and fatigue life.

Finite element dynamic model

The same model from Figure 55 was then submitted to dynamic analysis. Before the implicit dynamic step, a torque step and a misalignment step were carried out. A representation of the model may be seen in Figure 60.
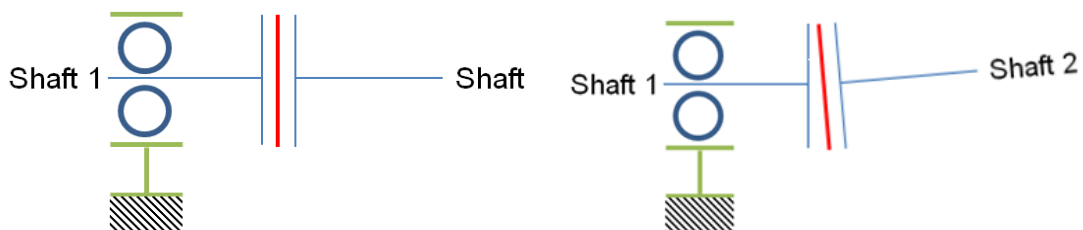
Figure 60 – Schematic modeling of the shaft for dynamic analysis [36]

In the model, the bearing and its support are considered rigid. Boundary conditions were applied similarly as displayed in Figure 56. According to the applied boundary condition, the reaction forces and moments are measured on the bearing region to simulate the response obtained in a real aircraft setup, which is presented in Figure 61.
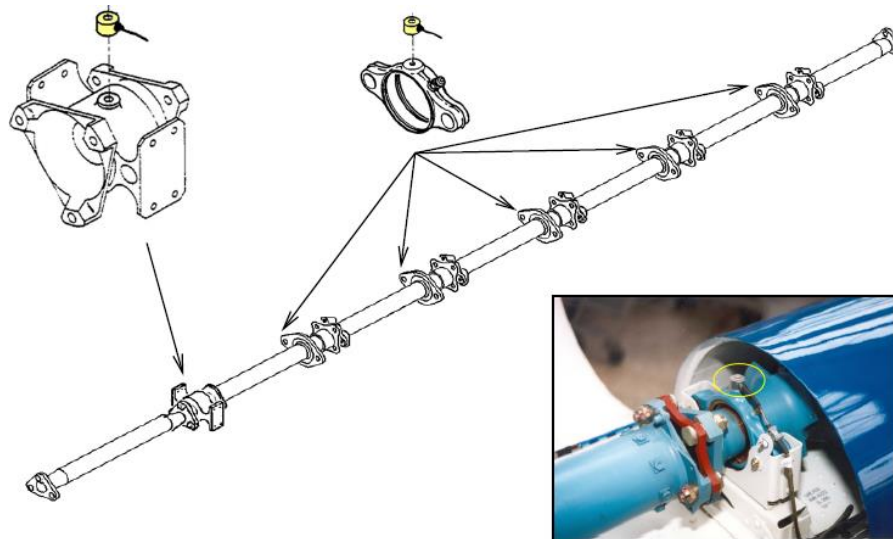
Figure 61: Aircraft simulated setup [36]

The procedure for analysis follows:

1. Static analysis is carried out in which displacements are imposed (black arrows) to simulate a 1° misalignment angle
2. Keeping the 1 degree of shaft misalignment, a torque equivalent to 28daNm is applied, simulating the torque transmitted through the tail drive shaft
3. A dynamic analysis is then started, with rotating speed increasing in a ramp, as displayed in Figure 62. The initial angular acceleration applied must be small, to avoid convergence issues to take place and to be physically consistent with the real operational conditions.
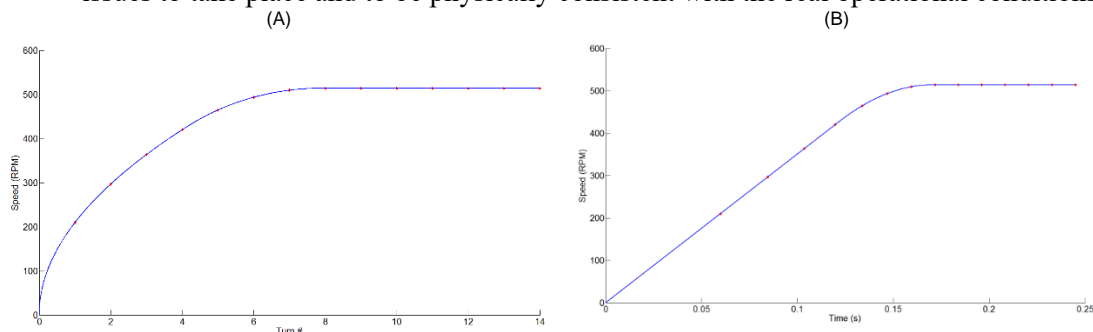
**Figure 62: Initialization of applied rotational speed from rest (A) per revolution (B)
vs. time (s)** [36]

The results were analyzed and the Fast Fourier Transform of the force and moment response on the bearing location was calculated for the portion of the analysis where the rotational speed was constant. An average was made between the 6 turns similarly presenting constant speed as the synchronous average is calculated on the embedded system. This arrangement simulates an accelerometer set on the bearing and monitors the 6-axis of freedom on the region. The FFT of reaction response is shown in Figure 63.
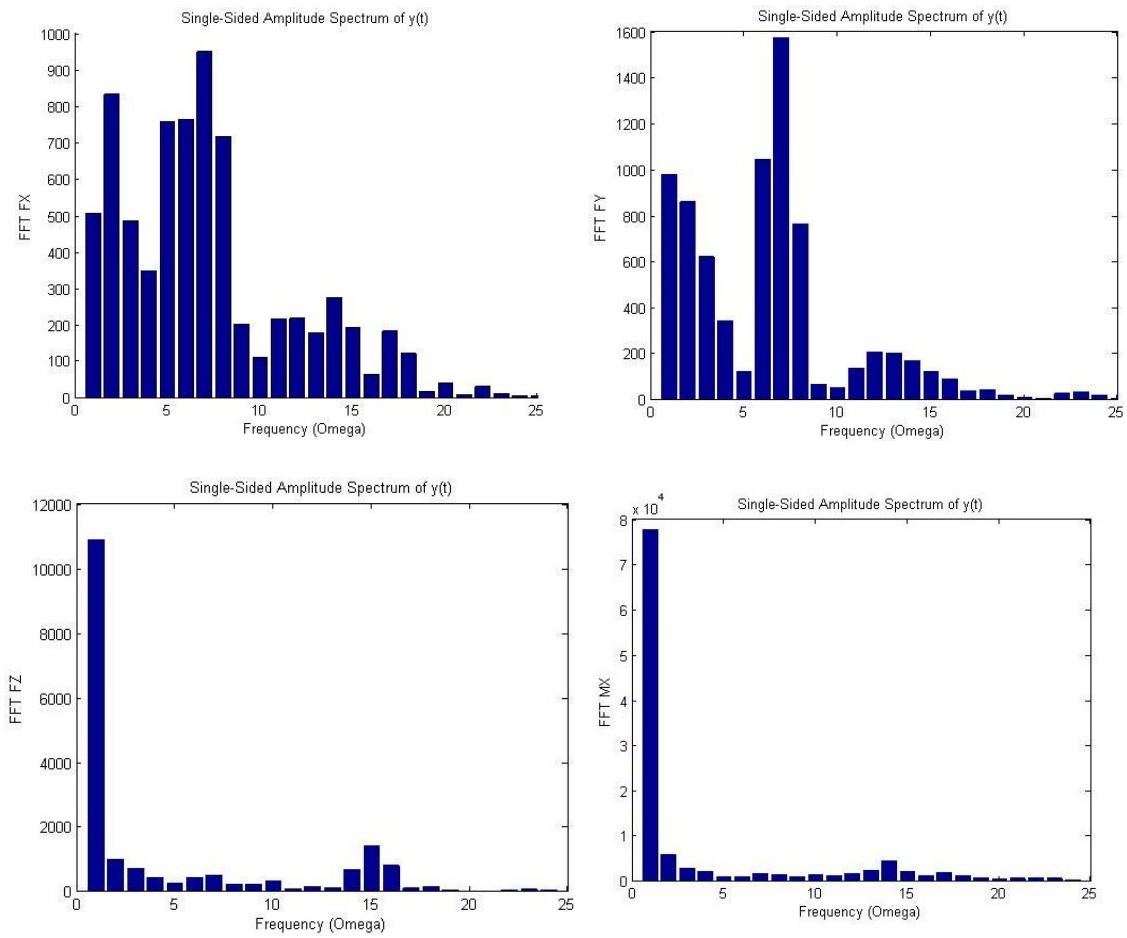
Figure 63: FFT of the reaction response for the 6 degrees of freedom [36]

From the figure, as expected and stated in the literature, a high peak at 1Ω and 2Ω are obtained. This is the typical response for a parallel-angular misalignment simulated by the conditions applied. The response is much clearer, and a special study must be carried out for *Mx* and *Mz*. These reaction moments presented high values that could be the root cause and explain the cracks that appeared on the coupling during the test. Another analysis, like the one here presented, is to be carried out with a crack on the outer layer of the coupling for the sake of comparison.

5 Concluding Remarks

This chapter presented a compilation of technical material and research work compiled or prepared by the authors and collaborators on the topics of vibration analysis and Health and Usage Monitoring Systems (HUMS) of dynamic components of helicopters.

The chapter concentrated on a discussion of vibration analysis techniques and the use of a framework of Health and Usage Monitoring Systems (HUMS) for helicopter dynamic components.

Some helicopter vibration reduction techniques focused on balancing and tracking the helicopter rotors are discussed in a separate chapter, concentrated on model-based parameter identification for balancing and tracking a helicopter's main rotor using once-per-revolution vibration data.

References

[1] R. V. Cruz, *Course Material on Foundations of Helicopter and Rotary Wing Engineering,* São José dos Campos: Instituto Tecnológico de Aeronáutica, 2021.

[2] V. A. Gomes e R. V. Cruz, *Flight Test Course,* São José dos Campos: PEV, DCTA, 2008.

[3] S. S. Rao, Mechanical Vibrations, Pearson, 2018.

[4] W. Johnson, Helicopter Theory, Dover, 1980.

[5] A. R. Bramwell, G. Done and D. Bamford, Helycopter Dynamics, Butterworth-Heinemann, 2001.

[6] Federal Aviation Administration, "Federal Aviation Administration Title 14 Part 27 - Airworthiness Standards: Normal Category Rotorcraft," Federal Aviation Administration, Washington, DC, 2020a.

[7] Federal AViation Administration, "Federal Aviation Administration Title 14 Part 29 - Airworthiness Standards: Transport Category Rotorcraft.," Federal Aviation Administration, Washington, DC, 2020b.

[8] A. B. Jorge e A. S. Torres Filho, "Vibration in Helicopters. Causes and Consequences on Equipment. How to live with the problem?," *BISAFO - Boletim Informativo - Segurança de Aviação em Foco, SIPAERM,* vol. 23, pp. 16-22, 1989.

[9] R. d. A. González e A. Donizeti, "Uma Análise Qualitativa da Filosofia HUMS na Manutenção Preditiva Focada no Nível Vibratório Devido a Condições Operacionais de Helicópteros," em *SIMPÓSIO DE APLICAÇÕES OPERACIONAIS EM ÁREAS DE DFESA*, São José dos Campos, 2009.

[10] R. d. A. González, "Helicopter Main Rotor Failure Analysis Using Vibration and HUMS Philosophy (In Portuguese: ANÁLISE PREDITIVA NA DETECÇÃO DE FALHAS NO ROTOR PRINCIPAL COM FOCO NA VIBRAÇÃO EM UM

HELICÓPTERO SEGUNDO A FILOSOFIA HUMS)," Instituto Tecnológico de Aeronáutica, Master Thesis, São José dos Campos, 2012.

[11] Agência Nacional de Aviação Civil, "Definições, Regras de Redação e Unidades de Medida Para Uso Nos Normativos Da ANAC," 2021. [Online]. Available: https://www.anac.gov.br/assuntos/legislacao/legislacao-1/rbha-e-rbac/rbac/rbac-21/@@display-file/arquivo_norma/RBAC21EMD08.pdf. [Accessed 2022].

[12] P. D. Samuel and D. J. Pines, "A Review of Vibration-based Techniques for Helicopter Transmission Diagnostics," *Jounal of Sound and Vibration,* pp. 475-508, 2005.

[13] R. Ganguli, I. Chopra and D. J. Haas, "Helicopter Rotor System Fault Detection Using Physics-based Model and Neural Networks," *AIAA Journal,* pp. 1078-1086, 1998.

[14] R. K. Mobley, Root Cause Failure Analysis, Butterworth-Heinemann, 1999.

[15] Federal Aviation Administration, "Federal Aviation Administration AC-27-1B. Certification of Normal Category Rotorcraft," Federal Aviation Administration, Washington, DC, 2014a.

[16] Federal Aviation Admistration, "Federal Aviation Administration AC-29-2C. Certification of Transport Category Rotorcraft," Federal Aviation Admistration, Washington, DC, 2014b.

[17] C. Adams, "HUMS technology," *Aviation Today,* 2012.

[18] F. Wolfe, "Light Commercial Helicopter Market Fertile for Health Usage Monitoring Systems," Aviation Today, October 2019. [Online]. Available: https://www.aviationtoday.com/2019/10/04/light-helicopter-market-fertile-field-hums/. [Accessed 2022].

[19] B. D. Larder, "An Analysis of HUMS Vibration Diagnostic Capabilities," *Journal of American helicopter Society,* pp. 28-33, 2000.

[20] Federal Aviation Administration, "Federal Aviation Administration AC-20-115C. Airborne Software Assurance," Federal Aviation Administration, Washington, DC, 2013.

[21] A. B. Jorge, B. S. Mattos, A. G. Chiarello, A. Nabarrete, M. V. Angelo and A. E. Montalverne, "Transfer of Technology - HUMS -AIRBUS HELICOPTERS - HELIBRAS - UNIFEI - ITA: Activities Reports -Months 1 to 12.," Eurocopter, Marignane, 2013.

[22] A. B. Jorge, A. G. Chiarello, L. C. Goes, A. Nabarrete, M. V. Angelo and A. E. Montalverne, "Transfer of Technology - HUMS -AIRBUS HELICOPTERS - HELIBRAS - UNIFEI - ITA: Activities Reports -Months 13 to 24.," Eurocopter, Marignane, 2014.

[23] C. Torrence and G. Compo, "A Practical Guide to Wavelet Analysis," *Bulletin of the American Meteorological Society,* vol. 79, no. 1, pp. 61-79, 1998.

[24] Wikipedia, The Free Encyclopedia, "Continuous wavelet transform," 2022. [Online]. Available: https://en.wikipedia.org/wiki/Continuous_wavelet_transform. [Accessed 2022].

[25] Mathworks, Inc, "Continous 1-D Wavelet Transform," 2022. [Online]. Available: https://www.mathworks.com/help/wavelet/ref/cwt.html. [Accessed 2022].

[26] Mathworks, Inc., "Choose a wavelet," Mathworks, Inc., 2022. [Online]. Available: https://www.mathworks.com/help/wavelet/gs/choose-a-wavelet.html. [Accessed 2022].

[27] Mathworks, Inc., "wcoherence," Mathworks, Inc., 2022. [Online]. Available: https://www.mathworks.com/help/wavelet/ref/wcoherence.html. [Accessed 2022].

[28] K. Kawamura, F. Parrenin, L. Lisiecki, R. Uemura, F. Vimeaux, J. P. Severinghaus, M. Hutterli, T. Nakazawa, S. Aoki, J. Jouzel, M. E. Raymo, K. Matsumoto, H. Nakata, H. Motoyama, S. Fujita, K. Goto-Azuma, Y. Fujii and O. Watanabe, "Northern Hemisphere forcing of climatic cycles in Antarctica over the past 360,000 years," *Nature,* vol. 448, pp. 912-916, 2007.

[29] E. e. a. Wolff, I. Basille, P. Jean-Robert and J. Schwander, "EPICA Dome C Core EDC96 Dielectric Profiling Data," *Annals of Glaciology,* vol. 29, no. 1, pp. 89-93, 2003.

[30] U. Siegenthaler, T. F. Stocker, E. Monnin, D. Lüthi, J. Schwander, B. Stauffer, D. Raynaud, J. Barnola, H. Fischer, V. Masson-Delmotte and J. Jouzel, "Stable Carbon Cycle-Climate Relationship During the Late Pleistocene," *Science,* vol. 310, pp. 1313-1317, 2005.

[31] Mathworks, Inc., "Wavelet Synchrosqueezing," Mathworks, Inc., 2022. [Online]. Available: https://www.mathworks.com/help/wavelet/gs/wavelet-synchrosqueezing.html. [Accessed 2022].

[32] Eurocopter, "M'ARMS EC 225/EC 725," Eurocopter, Marignane, 2012.

[33] J. Wiig, "Optimization ofFault Diagnosis in Helicopter Health and Usage Systems," École Nationale Supérieure d'Arts et Métiers, Docteur Thèse, Paris, 2006.

[34] A. B. Jorge, A. Chiarelli, B. S. Mattos, A. Nabarrete, A. Mont'Alverne and M. Angelo, "Activities Report No. 13," ITA/UNIFEI/EUROCOPTER, Marignane, 2013.

[35] Eurocopter, "M'ARMS Training Manual," Eurocopter, Marignane, 2012.

[36] A. Chiarello and A. B. Jorge, "Analysis of a Tail Drive Shaft," Eurocopter, Marignane, 2013.

[37] "Abaqus 6.10 User Manual," Dassault Systèmes, Providence, 2010.

Chapter 16

Model-Based Parameter Identification for Helicopter Main Rotor Balancing and Tracking Using Once-per-Revolution Vibration Data

Chapter details

Chapter DOI:

Chapter suggested citation / reference style:

P.S.: DOI may be included at the end of citation, for completeness.

Book details

Model–Based Parameter Identification for Helicopter Main Rotor Balancing and Tracking Using Once-per-Revolution Vibration Data

Ariosto B. Jorge[1*], Rafael de A. González[2],

Bento S. de Mattos[3], and Ronaldo V. Cruz[3]

[1]Post-Graduate Program - Integrity of Engineering Materials, University of Brasilia, Brazil. E-mail: ariosto.b.jorge@gmail.com
[2]Naval Studies Coordination Center in São Paulo, Brazilian Navy, Brazil. E-mail: rafaelgonzalez.eng@gmail.com
[3]Instituto Tecnológico de Aeronáutica, Brazil. E-mail: bmattos@ita.br; ronaldoc@ita.br

*Corresponding author

Abstract

This chapter presents a compilation of the research work accomplished by authors and collaborators on the topics of model-based balancing and tracking of the helicopter main rotor using once-per-revolution vibration data. Simplified analytical modeling is presented for the analysis of vibration signal in the monitored structure of any rotorcraft for the detection of defects, equivalent to a hub blade unbalancing and out-of-tracking blades. Those degradations are common in the main rotor and are the greatest source of periodic excitations transmitted to the fuselage. The vibratory responses under analysis are limited to the one-per-rev fundamental frequency of the main rotor and were numerically simulated both in FORTRAN and in MATLAB(R) environments. The direct problem is presented in two parts: The rotor-fuselage system is initially modeled as isotropic, and then anisotropies are introduced in the formulation, to simulate defects that generate vibration information (in amplitude and phase) at the selected points where accelerometers were located. The application of the model involves comparisons of the results from the obtained non-linear system of equations with either the information contained in the maintenance manual (for the case study of a four-blade main rotor helicopter) or with preliminary experimental data obtained by flight tests (for the case study of a three-blade main rotor helicopter. The comparison between the simulation results and either the maintenance manual information or the flight test measurements considered the accelerometers placed at the points of the fuselage as defined in the flight manual by the aircraft manufacturer.

Keywords: vibration of the helicopter rotor; vibration analysis; helicopter dynamic components

1 Helicopter vibration reduction techniques of balancing and tracking of the main rotor: introduction and chapter outline

This chapter discusses helicopter vibration reduction techniques focused on balancing and tracking the helicopter rotors and concentrated on a discussion of model-based parameter identification for balancing and tracking a helicopter's main rotor using once-per-revolution vibration data.

Signal-based vibration analysis techniques and the use of a framework of Health and Usage Monitoring Systems (HUMS) for helicopter dynamic components and aircraft engines are discussed in a separate chapter. Some HUMS systems include built-in features for the use of vibration data to help main-rotor and tail-rotor balancing and tracking.

1.1 Introduction

In the study of helicopter dynamics, rotor-induced vibration can be seen to arise from flapping and lead-lag blade motion, in different flight conditions. For detailed discussions on helicopter aerodynamics and dynamics, see references (Bramwell et al., 2001), (Bielawa, 2006), (Johnson, 2013a), (Venkatesan, 2015), (Padfield, 2018). Throughout the operational life cycle of a helicopter, routine corrective maintenance - reactive to the failure that has already occurred - is carried out to counter problems of maladjustment and misalignment of its rotating systems, including also problems due to other components secondarily degraded as a result of these defects in the rotor system. These maintenance procedures increase the helicopter operating costs, i. e., material, man-hours, and execution of test flights, including the loss of profit associated with the aircraft's unavailability. Mass unbalance and blade tip trajectory misalignment (out-of tracking) are the most common degradations foreseen in the main rotor, which are, for dynamic reasons, the source that contributes the most to the periodic excitations transmitted to the fuselage. For references on main rotor balancing and tracking models and procedures, see (Rosen & Ben-Ari, 1997), (Ben-Ari & Rosen, 1997), (Ventres & Hayden, 2000), (Wang & Danai, 2003), (Wang et al., 2005), (Miller & Kunz, 2008). For references on tail rotor balancing and tracking models and procedures, see (Kunz & Newkirk, 2009), (Damy, 2017).

1.1.1 Dynamics of structures: some concepts on vibration

In engineering, the term "structure" can be described as a system created to support loads, which are vector quantities, and, as such, it is a necessary and sufficient condition that they are defined by their magnitude, direction, and point of application. A load is said to be dynamic when any of these vector characteristics are functions of time, and thus the structure is also said to be dynamic. Deterministic dynamic loads can assume periodic forms, that is, they are repeated in time (harmonic or not), or non-periodic forms (transient or arbitrary). This study is restricted to deterministic periodic harmonic response loads. In the sense of state variation (position, velocity, etc.), the dynamic displacement associated with the second problem, in its most basic form, is represented by the harmonic function (sine or cosine trigonometric function). This function is the product of the amplitude of motion X_0 by a periodic function whose argument is the phase (composed of the initial phase at t=0) added to the product of time and the linear frequency f: $X = X_0 \sin(\Omega t)$. Figure 1(a) shows a representation in time and frequency, in which the displacement "X" of a point refers to a linear quantity of length.
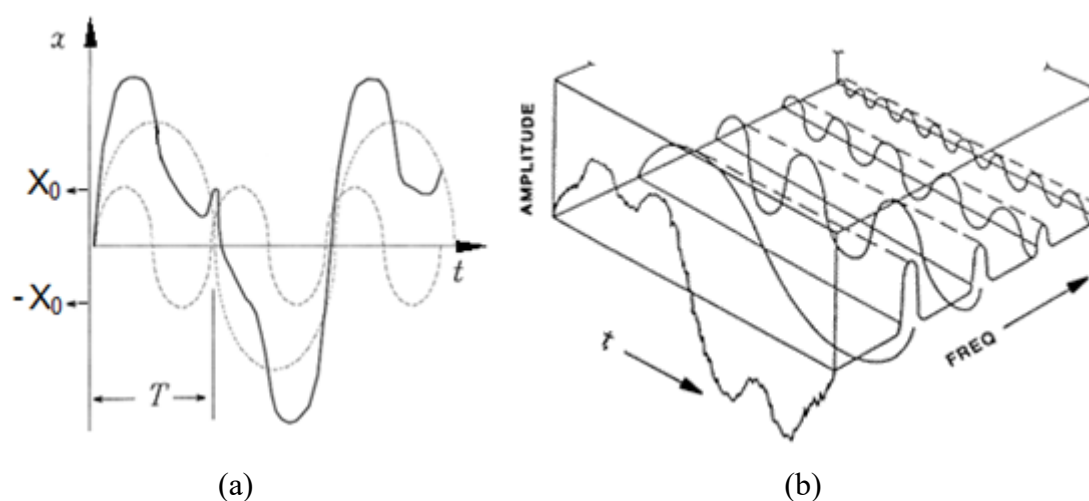
Figure 1: (a) Discrete (harmonics - dashed lines) and total (solid line) vibration curves in the time domain; (b) Representations in the time domain (on the left) and the frequency domain (on the right) - adapted from (Mobley, 1999)

These displacement profiles can be presented in the time domain (abscissa in s, for example) or frequency domain (abscissa in Hz, for example), as can be inferred from Figure 1(b). Their conversion takes place by techniques based on the application of the Fourier Transform.

When vibration information is plotted as amplitude or phase versus time, it is the time domain information profile, also called the global method for seeing the composition of all frequencies. However, these data are difficult to use in continuous systems modeled as multibody ones, as they represent the total displacement. This time-domain representation makes it difficult to verify the contribution of each oscillation source even after discretization as multiple degrees of freedom. And when the complex signal is composed of several sources and harmonics, one might have the effect of masking the defects. In obtaining graphical information, approximate methods of graphical analysis such as peak value, peak-to-peak, or peak RMS value can be used. Meanwhile, in the frequency domain, everything is clearer through the identification of amplitude and phase, which refer to the Theory of Complex Numbers associated with the solution of the governing differential equations of the oscillating systems.

1.1.2 Vibration: peculiarities of rotary-wing aircraft

Since helicopter engineering demands a dynamic set composed of a large number of rotating elements (in constant change of position in time), such as motors, transmission shafts, pumps, and fans, in addition to the rotors themselves, the helicopter is subject to a wide spectrum of vibration. In this chapter, the study is limited to working with vibrations associated only with the main rotor.

Helicopter rotor vibrations are evidence of the aeroelastic phenomena related to the dynamics of the rotating movement of the blades, submitted to the complex interaction of periodic inertial and aerodynamic forces of a non-linear nature with their flexible and damped structures. As they greatly influence the flight qualities, together with the structural loads, they delineate the boundaries of the operational flight envelope as shown in Figure 2.
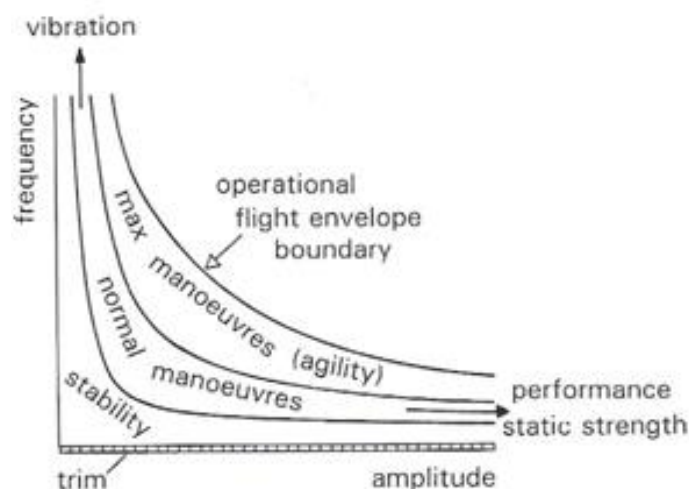
Figure 2: Vibrations (in terms of frequency and amplitude), delineating limits to flight envelopes in flight mechanics modeling - adapted from (Padfield, 2007)

The main rotor, due to its dimensions and vibration emission spectrum, is the main source of vibration, whose transmitted frequencies are multiples of the product of the number of blades "N" by the angular frequency of rotation "Ω". The amplitude of the periodic efforts decreases as their harmonic frequencies are increased, that is, multiples of the fundamental frequency. The blades' responses to the aerodynamic and inertia forces (forces and moments) that excite them interfere at the level of the rotor hub, where they are joined. Therefore, it acts as a filter during the transmission of forced vibrations (resulting from all blades) to the fuselage, adding and subtracting amplitudes. The fuselage, generally of a semi-monocoque design (which is a structure consisting of thin coverings fixed to frames and spars), reacts according to its flexible vibratory modes (in flexion and torsion). The vibration at a particular point in the helicopter depends on the fuselage's response to these forces transmitted by the rotor hub. To calculate the fuselage response it is necessary to know the frequencies and the modal shapes of the fuselage, which are difficult to obtain. Helicopter rotors are subject to high periodic forces due to the highly flexible blades and the severity of the non-stationarity of the aerodynamic environment, which leads to the wear of critical components to the airworthiness of these aircraft (Ganguli et al., 1998). The generation of oscillating aerodynamic loads at frequencies multiples of the rotational speed are fundamental to the rotor's operation in forwarding flight, and therefore these forced vibrations cannot be eliminated. Figure 3(i) illustrates the different velocity components that make up the linear velocity, as well as its variations throughout the blade rotation cycle, with the variation of lift on the blade. This behavior characterizes the lift asymmetry of the rotor when moving forward, which also brings the phenomena, shown in Figure 3(ii) that limit its performance under high displacement speeds (Müller et al., 1999). Among these are the disturbing interaction of vortices at the tip of the predecessor blade, detachments on the leading blade (due to shock wave rides linked to air compressibility) and reverse flow in the trailing blade (flow from the trailing edge to the leading edge), with temporal loss of sustain-dynamic stall (Padfield, 2007). Added to this is the Gyroscope Effect (manifestation of the Principle of Conservation of the Angular Momentum of the rotating system), of an inertial nature, which forces the design of the chain of command/cyclic platters to compensate for the displacement of the rotor response, in its majority, at 90º about the command input.

(i)   (ii)
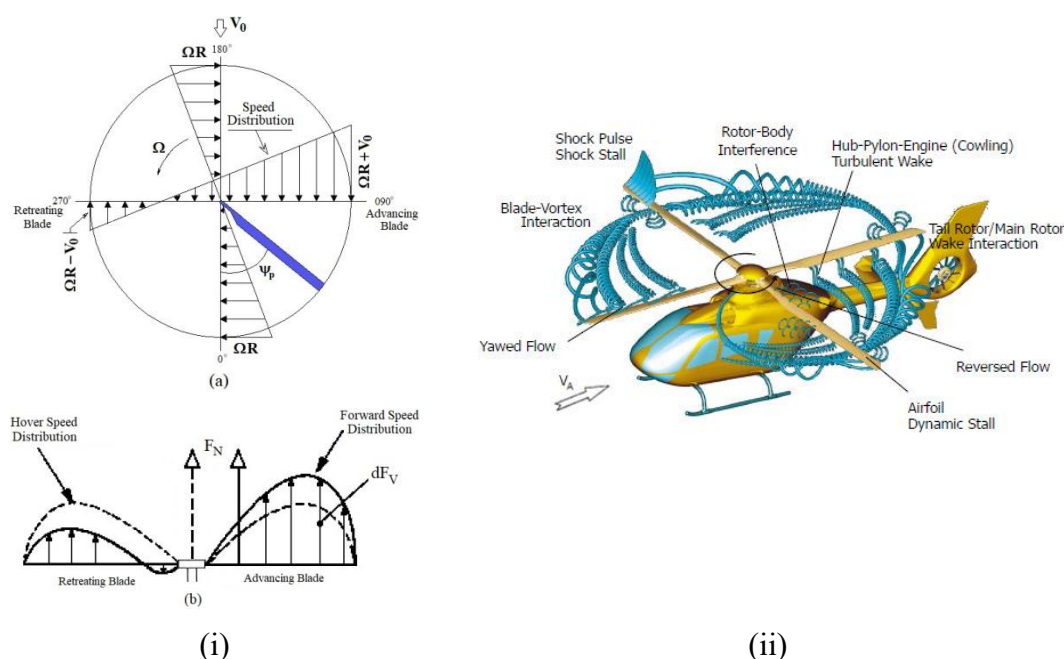
Figure 3: (i) For forwarding flight, distributions of (a) speed components in the rotor plane; (b) support on the blade at 90º and 270º of azimuthal angle - adapted from (Prouty, 1985); (ii) Limiting phenomena of rotor performance in high-speed flights - adapted from (EUROCOPTER, 2012)

Vibrations at the fundamental frequency of once-per-rev (1/rev), the focus of this research, are distributed in the vertical and lateral (rotational) planes. Another effect, the Coriolis effect, is related to the Coriolis force, acting on a rotating body and applied tangentially to its rotation. Thus, acting by flapping on the blade, creates the lead-lag motion. This effect is present by the tendency of the body to maintain its angular momentum (hence it's another inertial force) when simultaneously some of its mass elements are being moved radially in the plane of the disk, as a component in the blade flapping movement. For the detection of rotor defects, it is necessary to know the relationship between a defective blade and the response behavior of the aircraft. This knowledge can be numerically obtained by computer simulations of models based on the dynamics of these systems, where techniques based on artificial intelligence, until a properly trained artificial neural network, can be implemented permanently embedded in an aircraft to detect and identify damage (Ganguli et al., 1998). The literature reports several works regarding the detection of defects through vibration, as well as solutions to absorb or isolate unwanted permanent vibrations not associated with damage to systems. In (Ganguli et al., 1998) an aeroelastic analysis is presented based on finite elements in time and space to simulate a defective articulated rotor, both in hover and in flight in front of an SH-60 aircraft, validated through flight tests. In that work, it is stated that only localized structural damage such as cracks and delamination in the blades are not detectable by the global methodology. Several defect simulations indicate that global faults, such as lag damper defects, tab damage, pitch-link mismatches, or imbalances along the blade string, are detectable by remote measurements of global parameters such as fuselage vibration and deflection of the blades. Hence, those authors cite those special methods such as robust laser interferometer, photoelastic and ultrasonic techniques, and application of acoustic emission sensors complement these methods.

The combination of these approaches allows the design of devices for monitoring the condition of systems of this type. Simulated faults can be primary (only one type of rotor fault) or composite (a combination of more than one). The detection of the latter is important to highlight catastrophic failures such as cracks among the other fault types (Ganguli et al., 1998). However, for simplicity's sake, only primary faults are numerically simulated, such as rotor unbalance and maladjustment (out-of-tracking) of the blade tip trajectory, on one blade at a time.

1.1.3 Rotor unbalance and blade tracking problems

The oscillatory movement under consideration in this study presents itself as a vibration of lateral and vertical components (in 1Ω) and is associated with the imbalance and tracking misfits. However, for completeness, it is worth mentioning other less common causes, for example: in articulated rotor helicopters (such as in Sikorsky's Sea King helicopter), defective dampers can cause the blades to be out of phase, producing the same effect. The lateral and vertical vibrations acting on the rotor interact in a complex way, in such a way that the practice recommends correcting the trajectory of the blades first, followed by the balancing of the masses, according to the procedures described in the maintenance manual (MET, in the case of this study) and with the aid of specialized equipment that suggests corrections from the processing measures the vibration amplitude (the accelerometer), its phase angle (the "phasor") and the difference in the trajectory of the blades (the "strobex"). The correction of vibrations due to unbalance occurs in the phases of hovering inside the ground effect (IGE) and outside the ground (OGE), while the corresponding correction by trajectory difference (tracking) occurs in displacements in maximum continuous power (MCP) – straight and level flight, and also a curve at 45º. In the hover phases, the ground effect can occur, in which the presence of the ground changes the intensity and direction of the airflow around the rotor (IGE). With the rotor at a height of one rotor diameter, there is no more ground effect (OGE).

Main rotor imbalance issues

Unbalance is the most common cause of vibration. The main rotor is statically unbalanced when its center of gravity is outside the axis of rotation of this rotor. Among the two adjustment alternatives, there is the so-called single-plane balancing, which involves changing the axis of the bearing supports (impractical) or changing the rotor masses (Figure 4-A). The other case is the dynamic unbalance, established when its main axis of inertia (which contains its center of gravity) does not coincide with the structural axis of its tree due to the eccentric mass(es). In this situation, when the centrifugal forces and associated moments overcome the opposing forces of reaction in the bearings, the flexibility of the shaft allows oscillatory displacements in 1Ω in the plane of the main rotor (longitudinal and lateral). The corrective actions consecrated as a maintenance solution to carry out the balancing (said in two planes) consist of the redistribution of weights in the rotor (generally acting on the blade handle, according to the decomposition of the balancing mass, and according to the number of blades) in such a way that those two axes coincide (Figure 4-B). The second case can compromise the first, however, if the former is satisfied, then the latter is also resolved (which alone does not guarantee the latter).
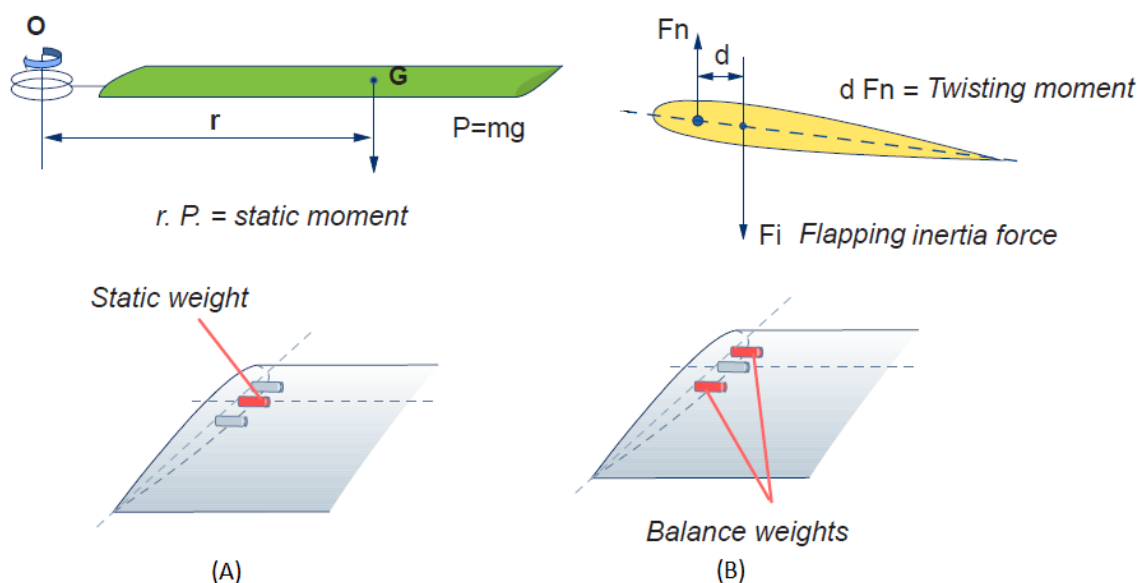
Figure 4: Blade adjustments for unbalance: (A) static moment and (B) dynamic moment - adapted from (EUROCOPTER, 2010)

Main rotor blade tracking issues

The maladjustment (out-of-tracking) in the trajectory of the tip of the blades referring to the plane of rotation is related to differences in lift between the blades. These differences result from changes in the blade's pitch angle and generate vertical vibrations at 1Ω. However, these height variations create the Coriolis Effect, arising from components of the instantaneous mass distribution, changed radially in that plane, thus also generating lateral vibrations. Due to this effect and the difference in drag of the blades, the trajectory of the blades is first corrected, to later conduct the balancing of the masses. Corrective actions aim to intervene in the blade height through the blade pitch angle by intervening in the length of the blade pitch control rod (pitch link), which promotes a uniform rotation throughout the blade around its pitch axis and/or by modifying the position of the compensators (or tab) available for this (changes the bowing of the blade profile, generally, in its outermost sections, promoting structural twists around the elastic axis of the blade by the action of aerodynamic forces resulting from the alteration of the blade lift distribution, therefore dependent on the azimuthal position, whose effect reverses that undesirable height of the blade. In the present work, for simplicity in the adopted modeling, there is no torsional degree of freedom for the blade. Hence, tab adjustment cannot be a corrective action in this case.

1.2 Chapter outline

Section 2 presents a discussion and details of vibration reduction techniques for helicopter rotors, from the point of view of the operational user and the technical maintenance of the helicopter. Section 3 presents a discussion and details of model-based helicopter main rotor balancing and tracking (case study: a 4-blade helicopter), including a subsection with perspectives on the inverse problem. Section 4 presents a discussion and details of model-based helicopter main rotor balancing and tracking (case study: a 3-blade helicopter), with modeling adapted from the previous 4-blade helicopter case. Section 5 presents some concluding remarks.

2 Vibration reduction techniques for helicopter rotors

This section is based on the article (Jorge & Torres Filho, 1989), presented at "XI Simpósio de Segurança de Aviação da MB", SIPAERM, 1989, Rio de Janeiro, RJ.

2.1 Vibration reduction for rotors

The vibration reduction techniques available for the helicopter users are concentrated in the correction of the trajectory traveled by the blade tips (adjustment of the blade "track") of the main and tail rotors, and/or in the correction of any imbalance present in these rotors. The statement of the problem, at the user level, is detailed below. In addition to vibration reduction techniques, some details of the equipment used for these purposes are described, as well as some prospects for the future.

2.2 Objectives of the Vibration Reduction

The reduction of vibrations has, among others, the objectives of:

a) Reduce the probability of failures in structural components before useful life expires. Components have an estimated life based on a certain magnitude of cyclic loads. In this way, considering that there is a direct relationship between the vibration level of the structure and the cyclic loads acting, a high level of vibration shows that the structural components of the helicopter are being subjected to unforeseen efforts consequently, present a high probability of in-service fatigue failures.

b) Minimize the effects of tiredness and fatigue on the crew. Prolonged and repeated exposure to vibrations of different frequencies, amplitudes, and directions can cause various types of aggressions that essentially consist of headaches, tinnitus, general malaise, feeling of drowsiness, general weakness, irritability, a reduction in the will and the ability to concentrate, a reduction in reflexes, a psychic depression as well as fatigue of the eyes and ears. These disturbances, depending on their intensity and persistence, can decisively contribute to pilot fatigue, as well as helicopter accidents.

Just for illustration, helicopter main rotors typically rotate between 3 and 7 Hz and the main vibrations perceived in the structure vary between 3 and 22 Hz; tail rotors and other accessories rotate at higher frequencies.

2.3 Causes of Vibration in helicopter rotors

The most common causes for the occurrence of vibration are categorized in 2 groups, according to operator procedures to mitigate the efforts that caused the vibration:

a) **Unavoidable causes:**

   I.   The variable aerodynamic forces resulting from the cyclic movement of the blades are necessary for translational flight. It is found that such forces predominantly induce vibrations at the multiple frequencies of the aircraft's main rotor rotation times the number of blades, that is, for a 4-blade helicopter with a main rotor rotation speed of 340 RPM (5.7 Hz), the cyclical variation of the pitch of this rotor blades will cause efforts that will induce vibrations in the frequencies of 22.8 Hz, 45.6 Hz, 91.2 Hz, etc., in the aircraft. These efforts increase with the aircraft's translational speed.

   II. Centrifugal forces resulting from CG variation from the flapping motion of the blades, are necessary to maintain translational flight. The resulting vibration occurs in the plane of the rotor, at the rotation frequency of the main rotor.

   III. Aerodynamic forces arise from the airflow over the rotors, acting on the helicopter fuselage, or from turbulence and gusts on the aircraft.

b) Avoidable causes

I. Unbalance of rotating parts and rotors: unbalance always exists, to a greater or lesser degree, in any set or rotating part and is characterized by vibration that occurs once per rotation as shown in Figure 5.
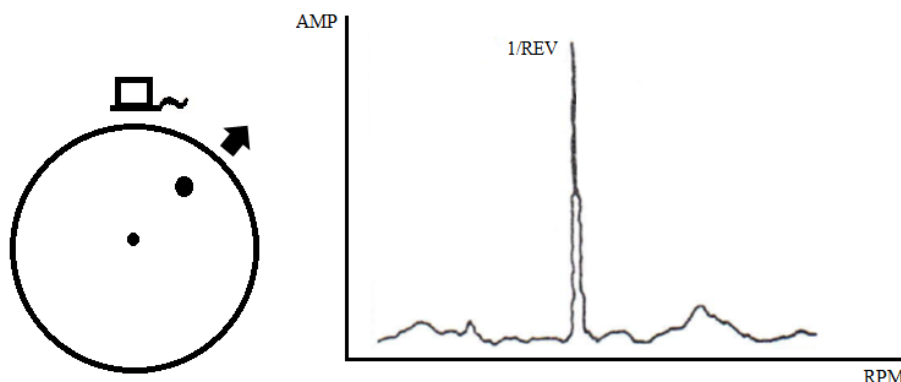
Figure 5: Unbalance (rotating parts / rotors) [Adapted from (Jorge & Torres Filho, 1989)]

Imbalance occurs when the center of mass of the rotating body is different from, or farther from, the center of rotation of that body. If the center of mass and the center of rotation are equal, the system is said to be balanced. As the center of rotation cannot be moved, the solution is to move the center of mass, adding weights in opposition to the inertia force produced by the imbalance, which is of form $F = M.r.\omega^2$, where: (i) F = Force produced by unbalancing; (ii) M = Mass of the set; (iii) r = Radius (radial position of the center of mass); and (iv) ω = Angular Velocity.

Vibration at the frequency of once per revolution is not always due to unbalance but could be indicative of another problem (such as mechanical backlash). The characteristics of unbalance are: (i) the vibration occurs at the frequency of once per revolution; (ii) the phase is stable. For example, if we are trying to balance a tail rotor that exceeds established vibration limits and the phase indication is not stable, this could be an indication of mechanical clearances rather than unbalance; and (iii) the amplitude of vibration increases with increasing rotational speed.

II. Helicopter rotor blades

1. Flying out-of-track causes elevated levels of vibration in the direction perpendicular to the rotor's plane of rotation at a frequency of once per revolution. The fact that all the blades are flying in the same plane does not always mean, however, that the aircraft will fly smoothly. Other aerodynamic forces may be involved and adjusting the blades to fly slightly out of the plane could as appropriate, counterbalance these dynamic forces to provide a smoother flight for the aircraft.

    The rotor blades of a helicopter must always travel the same path, which often does not occur, causing the aircraft to vibrate. If each blade on a rotor were identical in profile, torsion, weight distribution, stiffness distribution, and head installation, then, in steady flight, it would fly along the same path as the blade that preceded it in motion. In practice, however, not all blades are identical in these characteristics and the loss of track can always be related to effects classified as aerodynamic, dynamic, or a combination of the two, which is indeed aeroelasticity.

The major cause for out-of-track blades is when identical blades present unequal itch angles rotor and therefore generates different lifts. As this can easily occur, all helicopters have pitch control rods whose length can be adjusted in small increments between the rotating swashplate and the blades. Another common source of track loss is when the blades are attached to the head with the same collective pitch angle but produce different lifts because they are not identical. In this case, an adjustment to the pitch control rod may or may not bring the blade into the perfect track. If the differences between the blades are in the airfoil profile or the torsion distribution, adjustments are made to the trailing edge of the blade, slightly tilting an appropriate trim tab or the trailing edge itself, when possible. These changes have two effects: they change the zero-lift angle of the airfoil and produce a local pitching moment during flight, which tends to twist the blade to a different torsion distribution when in forward flight when compared to the existing torsion distribution of the blade when at rest.

The fact that the blades are out of track can also sometimes be related to a difference in balance along the chord between two otherwise identical blades. Centrifugal forces, operating on the mass elements close to the leading and trailing edges, produce a torque whose pitching moment tends to decrease the angle of attack of the blade profile, causing it to fly low. If this effect is greater on one blade than the other, due to the different weight distribution, that blade will twist downward more than the other and therefore have a lower lift in flight.

2. Unbalanced: cause vibration problems in the rotor plane at the frequency of once per revolution, as seen above (Avoidable Causes, item I). Thus, for the main rotor we will have vibrations in the lateral and longitudinal directions, and for the tail rotor, in the vertical and longitudinal directions.

3. With defects in the assembly, components, or installation: if the defect affects only one blade, we will have a vibration at the frequency of once per revolution. An indication of this type of defect appears in situations where, when trying to balance or track, the phase becomes unstable before we reach a specified threshold. If the defect occurs in items or installations that affect all rotor blades, we will have high levels of vibration at foot pass frequencies (2, 3, 4, etc. times per rotation, depending on the number of rotor blades).

2.4 Vibration Reduction Techniques for helicopter rotors

a) Balancing the main rotor

1) Amplitude and phase of vibration.

Helicopter vibrations are caused by external forces, due to unbalanced rotors. These efforts are periodic and generate a vibratory movement at all points on the aircraft. For this case of forced vibrations, the amplitudes of displacement (X), velocity (V), and acceleration (A), for a given excitation frequency, are related in the form $A = \omega V = \omega^2 X$, where ω is the vibration frequency.

In terms of phase, we have that acceleration is 90 degrees out of phase with velocity and 180 degrees out of phase with displacement. For a given frequency, the time delay between the forced response (vibration at a point of the structure, in a given direction) and the excitation (an external effort that caused this vibration) can be expressed in terms of the clockwise phase, whose angular value (measured in degrees or hours of a watch) can be measured directly on the rotor, by using vibration sensors (accelerometers) and synchronism signal generating devices at that frequency (magnetic pick-up, optical pickup, etc. .) or reference points (such as reflective tape).

2) Types of Balancing

Unbalance only occurs in the rotor plane (the plane perpendicular to the rotor's axis of rotation) and, therefore, it is sufficient to apply static balancing techniques. Normally, field balancing is chosen, with the rotor installed in the aircraft and its normal rotation regime, with the following advantages: (i) the removal of aircraft rotors is avoided; (ii) inaccuracies resulting from friction in the static balance benches are avoided; and (iii) the vibration measuring equipment is portable.

3) Field balancing methods

a) *Balance chart*. The amplitude and phase of vibration are measured and plotted on suitable balance charts, which provide the values of the necessary balance masses, as well as their installation position on the rotor. However, it may be necessary to make corrections to the balance chart to adapt it to the aircraft, because the vibration amplitude and phase vary as a function of the mass and stiffness of the structure. Thus, differences may occur between the "average" aircraft used by the manufacturer in determining the chart and the aircraft whose rotor is being balanced. The correction in the chart is made by direct comparison between the results obtained and those predicted.

b) *Method of the two measures*. The method consists of obtaining the vibration amplitude and phase values before and after the addition of a known balancing mass at a defined location on the rotor and, from these data, the position and value of the balancing mass to be placed are graphically or analytically determined.

c) *Three-mass method (four measures)*. This method is used when the measuring equipment of the vibration phase is not available. The method consists of placing a known balance mass in three angular positions: 0, 90, and 180 degrees and using the difference of the vibration phase and amplitude values about the initially measured value, to determine the position and value of the balance mass.

During the balancing procedure, any unexpected phase change after the addition of balancing masses may represent the existence of gaps in the set to be balanced (Avoidable Causes, item V, above). In this situation, the balancing process must be interrupted until the origin of the gap is found and the problem corrected since the existence of gaps prevents the use of Balance Charts and the 2- or 4- measurement methods.

b) Equalization of the lift force of the main rotor blades (adjustment of a track)

Equalization is performed by changing the length of the rotor pitch control rods, which modifies the angle of attack equally along the length of the blade and, consequently, the blade lift; or by changing the angle of the blade tab (sometimes known as trim tab), which changes the blade pitch incrementally along its length, due to the variation in its torsion. A rod length adjustment modifies the blade lift force in all flight conditions, while a tab adjustment only works when the aircraft is moving at higher forward speeds. While for the first case the angular variation of the blade pitch is of mechanical origin, for the second case this angular variation of the blade pitch is of aerodynamic origin. Thus, the variation in the blade torsion introduced by the tab is proportional to the air displacement over the blade section, the pitch angular variation becomes dependent on the forward flight speed. Figure 6 shows the variation in the position of the tip of the blades of a helicopter as the flight conditions change. For each blade, we have the position of the aircraft on the ground, in hover, and at 3 forward flight speeds. If the blade tends to fly high or low in all flight conditions, the typical adjustment will be at the control rod. If the blade tends to go out of track as forward flight speed increases, the typical adjustment will be in the tab.
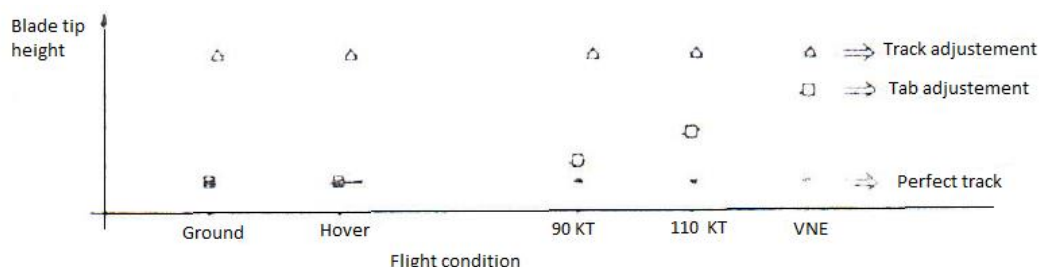
Figure 6: Blade tip path versus flight condition: a visualization of required adjustments – adapted from (Jorge & Torres Filho, 1989)

c) Main rotor blades: coupling between balancing and equalization of the lift force

If the main rotor blades do not produce the same lift force (L), they will be in equilibrium with different flap angles (θ), as shown in Figure 7. Thus, the loss of track is characterized by the blade tips rotating in different planes (different θ angles).
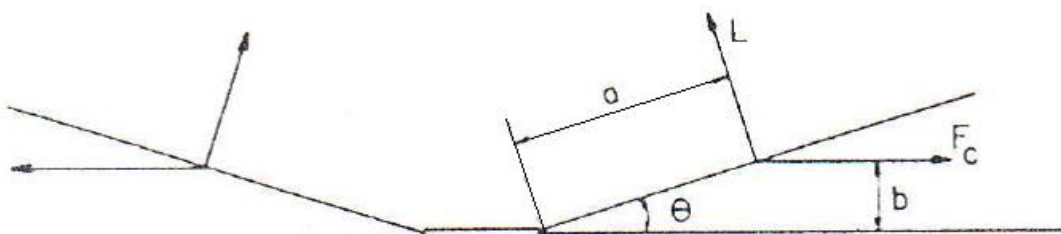
Figure 7: Blade equilibrium conditions – adapted from (Jorge & Torres Filho, 1989)

With $L.a = F_c.b$ and $\sin\theta = b/a = L/F_c$. Equal blades (same Lift L) lead to the same F_c, and thus to the same angle θ, which means that the blade's track is perfect. Blades with different L (that is, different blades) lead to different F_c, and thus the angle θ will be different for each blade, which means that the blades are out of track. The center of gravity of the blade which is flying higher (than the other blades) approaches the axis of rotation of the rotor. Thus, blades of the identical static moment (first moment of cross-sectional area) may have different centrifugal forces and therefore appear to be unbalanced, when they were producing different lift forces. Figure 6 also illustrates the case of blades with different static moments, but with the same lift. These blades will be out of track and may induce vertical vibration at the main rotor frequency of 1Ω, due to the difference in the vertical components of their lift forces. Therefore, the lift balancing and equalization operations must be carried out interspersed, until satisfactory results are obtained, for vertical and lateral vibration levels at 1Ω.

d) Balancing and equalization of the lift force of the tail rotor blades

The same theoretical considerations and techniques described for the case of the main rotor are applied in the case of the tail rotor. The existence of problems of lift difference is less common in the tail rotor case, due to the fixed-pitch adjustment of the blades and the lower susceptibility to aeroelastic effects. Normally, it is sufficient to statically balance the blades or field balance the rotor with the aircraft on the ground, or both, depending on the aircraft model.

By way of illustration, we describe the characteristics of two cases (Jorge & Torres Filho, 1989):

1. AS 332 SUPER PUMA: a tail rotor malfunction originates a vibration characterized by three times the rotation of the main rotor when in forward flight (frequency coupling).

2. AS 350 SQUIRREL: the tail rotor resonant frequency occurs when the main rotor rotation is around 310 RPM, and therefore, at start-up and final cut-off, the tail rotor passes through this frequency. If the vibration level measured near the tail rotor is greater than 1 IPS (inches per second) during this transient, the tail rotor must be statically balanced before field balancing is applied.

3 Model-based parameter identification for unbalanced and out-of-track helicopter rotor blades: a case study of a 4-blade main rotor

This section is based on the Master's Thesis (Jorge, 1992), for the Specialized Masters Program in Helicopter Techniques at ENSICA, Toulouse, France, 1992.

Case study of a 4-blade main rotor: model development and comparison with maintenance manual (Jorge, 1992)

Helicopter vibrations are one of the problems that require a lot of maintenance effort. Various practical procedures already exist relating the measured vibrations to the possible corrections to be introduced at the main rotor head. This work formulates a theoretical background that leads, from corrections, to the vibrations measured at the fuselage. The problem was split into two parts: the calculation of the isotropic rotor equilibrium and, then, the introduction of the defects from this equilibrium position.

The model here considered defects that generate vibrations in 1Ω (one-per-revolution), 2-D aerodynamics, rigid blades, articulated rotor, a rigid fuselage, and flight conditions without load factor. From the equations found, a software was created for different flight conditions and configurations of weight and balance. The results obtained were consistent with those from the aircraft's maintenance manual (MET) The algorithm obtained can be inserted into an on-board software, as part of a system of the HUMS type, providing information on rotor defects to reduce the maintenance time and cost.

3.1 Introduction

GENERAL

Vibration is, for a helicopter, one of the problems that require the most effort, either for the designers and manufacturers or for the users. In the design offices, during the conceptual design of the aircraft, a complete set of methods is used to tackle the problem, the origin of the vibratory forces, its transmission to the fuselage, and the response of the fuselage to this excitation.

When the helicopter is delivered to the user, it is already tuned and balanced. However, during its operational life, problems of maladjustment and unbalance appear on the various rotating systems, which requires a maintenance effort on the part of the user, with periodic adjustment procedures with, therefore, a very high maintenance cost, due to the maintenance flight hours required to perform the tasks of the various adjustments until an acceptable vibration level, measured at the fuselage, is reached. The necessary maintenance flight hours have an intrinsic or direct cost (fuel consumption, etc.) and a cost associated with the unavailability of the aircraft for its operational use, and therefore must be minimized.

The purpose of this study is the conceptual design of a system that can detect various defects at the rotor head, using fuselage vibration measurements, during normal or operational use of the helicopter, and that also can propose the adjustments or corrective procedures to be conducted at the next shutdown of the aircraft. Such a system leads to a reduction in maintenance time since it can replace maintenance flight hours for fault finding by flight hours in operational use.

This system also leads to an increase for in-flight safety, since it will detect faults when they appear, while in the current adjustment procedures (which are scheduled, with some periodicity), it will be necessary to reach a scheduled moment in the life of the device to be able to detect a fault. In this way, without such a system, a helicopter could fly for a certain time in a degraded configuration, with a defect in its rotor which could increase the risk of the appearance of various problems, such as the appearance of cracks in rotating parts subjected to alternating efforts and even, at the limit, a reduction in the operational performance of the crew due to human fatigue in a more degraded vibration environment. This study of vibration problems generated by faults in the main rotor can be generalized to vibration problems generated by faults in other rotating systems such as the tail rotor or the engines. Such a fault detection system can be installed onboard a helicopter in the context of HUMS (Health and Usage Monitoring Systems) type systems.

MODELING

Within the framework of sensitivity studies on the vibratory level of a helicopter, in all directions, due to the forces at the rotor head caused by defects of a geometric, kinematic, structural nature, etc... and of any origin (manufacture, maladjustment, wear, damage, etc.), a simulation will be performed of these defects on a helicopter rotor-structure model, to obtain the vibration level at different locations of the structure, to be able to carry out, in a next step, the inverse problem, i.e., from the vibrations measured at known points of the fuselage, being able to capture to the rotor defects.

The hypotheses

The model will study defects that generate vibrations in 1Ω (one-per-revolution), that is, once the rotation of the main rotor. This frequency, lower than 6 Hz (as is the case of some aircraft from Airbus Helicopters - former Eurocopter France), being lower than the first resonance frequency of the fuselage (around 12 Hz for the Super Puma, for example), allows us to have a model where we will retain: (i) the 6 degrees of freedom of the fuselage, seen as a rigid body; and (ii) the degrees of freedom in flapping, drag, and pitch of each blade, also seen as a rigid body linked to the main rotor through the joints.

The application case, for comparison between the model results and practical results, will be the Super Puma (AS 332 MKI long version and AS 332 MKII) helicopter. For the calculation of the aerodynamic forces, the approach will retain a two-dimensional steady-state aerodynamic model, with the hypotheses of small angles of incidence, flapping, drag, and pitch. In this model, two flight conditions with zero load factor will be considered: (i) hover; and (ii) stabilized level flight.

The settings

The parameters relating to the device, considered as "a priori" known data, necessary to initialize the system are: (i) the mass of the aircraft; (ii) the mass center; (iii) forward flight speed; and (iv) atmospheric density. These are the parameters necessary to establish a particular flight condition, where one can calculate the pitch, the flapping, and the drag of a rotor considered to be isotropic, without defects. From this flight condition, defects will be introduced on the different blades of the rotor.

Faults and possible corrections on a blade

Possible defects: (i) mass imbalance on one or more blades or even on the hub-rotor mast assembly; (ii) "detracking" (blade flying out of position) in flapping and/or drag; (iii) incorrect or inadequate twisting on a blade; (iv) the maladjustment of a pitch control rod and/or a slack/mechanical clearance of this rod; (v) the loss of stiffness and/or damping on a drag adapter of a blade; (vi) incorrect adjustment or locking of the tabs of a blade, etc... For all problems, whatever their origin, the Maintenance Manual offers the user only two options: (i) perform possible corrections and adjustments on a blade; or (ii) change the defective element, in the cases provided for, where it is no longer possible to adjust.

The modeling of the inverse problem must consider the maximum admissible values of the corrections to be introduced, to determine whether the calculated correction should be carried out or a replacement of a defective element (correction exceeding a threshold). The possible corrections and adjustments on a blade are: (i) the variation of the collective pitch of a blade from the variation in the length of the pitch control rod; (ii) the variation of the mass of a blade (and, consequently, of its static moment and of its inertia in flapping and in drag) by introducing or removing balancing weights (at the point of attachment between sleeve and blade, in our case study, i.e., the Super Puma); and (iii) The variation of the bracketing of the tab located most at the end of the blade.

The assumption in this model is that the various defects can be reduced to "equivalent defects" at the points where the corrections will be introduced. This "equivalence" means that a defect will generate a vibration in the fuselage equal to that which would be generated by the "equivalent defect(s)". The goal to be achieved is to introduce a correction (i.e., an "equivalent defect" of the same amplitude but opposite sign to the one just detected) to balance the rotor (if it is possible) and not to find the exact origin of the actual defect. Thus, the model is not going to simulate the real defect, but, instead, its "equivalent defect" at the points of introduction of the corrections.

PROJECT STAGES

Study of the equilibrium of the isotropic rotor

Initially, the model will take into account a so-called "isotropic" rotor, ie, without defects. All the blades being considered equal, we will have: (i) from the balance of moments around the joint, the equations of the movements of the blade, in flapping and in drag, which will be functions of 1 Ω; (ii) through the integration of the elementary forces on a current element of the blade, we will have the force of a blade on the rotor head; (iii) the summation of the forces of all the blades on the hub, including the moments introduced by the frequency adapters, gives us the wrench of the forces at the rotor head, which is constant concerning the azimuthal position of the blades (and, therefore, concerning in time) due to the hypothesis of an isotropic rotor that restricts in this study to the frequency 1 Ω; (iv) from the forces at the rotor head and other forces external to the helicopter, we will have the balance of the fuselage for this flight condition. We will retain, as external

forces: the thrust of the rear rotor, the own weight of the helicopter, the drag of the fuselage, and the downforce of the horizontal stabilizer. From the equations of the balance of the fuselage, we will obtain the longitudinal attitudes (in pitch), roll, and yaw. In addition to the assumption of stabilized flight (zero acceleration, that is to say, constant attitudes over time) we will assume that the flight is not skidded and that the yaw attitude is zero, retaining, instead, as unknown, the tail rotor thrust necessary to obtain this zero attitude.

Study of the effect of the introduction of defects

"Equivalent defects" will be introduced into the model, which is consistent with the reality, to study their effect: (i) on the rotor head forces; (ii) on the acceleration of the center of gravity of the fuselage; and (iii) on the acceleration of any point of the fuselage where it is planned to install accelerometers. The equations of the balance of the fuselage will no longer be equations in static equilibrium but dynamic equilibrium. The forces at the rotor head will no longer be constants, but functions of 1Ω, which brings us to inertial forces and, therefore, accelerations of the fuselage, also in 1Ω, neglecting the higher harmonics of the fuselage movement, which could be originated from the rotor head excitations in 1Ω.

Study of the inverse problem

The model

We have seen that, from the position of the equilibrium and the defects, one can obtain the forces at the rotor head and also the acceleration of the fuselage. For the inverse problem, we need to know the position of the equilibrium (as before) and the accelerations of the fuselage. The full motion of the fuselage, which was assumed to be rigid, is measured by accelerometers which record the fuselage's 6 degrees of freedom. The measurements of the accelerometers are then brought back to the movement of the center of gravity of the fuselage, through a formulation step which is the inverse of that which was previously made. This inversion is always possible. The movement of the fuselage is passed from the helicopter frame to the fixed rotor frame and then to the rotating rotor frame, so that: (i) the movement of the blade will therefore be its displacement plus the displacement of the fuselage; and (ii) the rotor head forces will be the sum of the constant forces, obtained from the balance of the isotropic rotor, plus the variable forces in the frequency 1Ω. As the model has more unknowns (defects) than information obtained from the accelerometers, certain restrictions must be imposed and the transformation can be called a "pseudo-inverse".

The optimization

The optimization will consist of seeking the optimal distribution of the accelerometers to minimize the calculations for obtaining the inverse of the "pseudo-inverse". For that, one must look for: (i) either defect decoupling or minimum coupling; (ii) harmonization of the orders of magnitude between the various "defect-acceleration" pairs; and (iii) the minimum number of calculation operations.

The application

The transition from simulation software to embedded software

Here, it is necessary to consider constraints and to operational limitations: (i) maximum collective pitch; (ii) maximum admissible movements in flapping and in drag; (iii) maximum admissible forces in connecting rods; (iv) maximum bracketing of tabs; (v) maximum balancing weight that can be inserted in the sleeve (in the rotor head); and (vi) accelerometer limitations: sensitivity, threshold, accuracy.

The expert system

This software can be inserted into a more complete embedded system, such as the HUMS, with: (i) setting of priorities and rules for the corrections to be introduced; (ii) the choice between the corrections or the replacement of the defective component; (iii) the use of this acceleration and force information for updating the calculation of the service life of vital parts; and (iv) the information on flight safety. For helicopters with a system for measuring the pitch of the blades, it is possible to consider, as an option, the pitch input as a parameter of the system, instead of the speed of forward flight. This system, in its first stage, i.e., the calculation of the balance of the isotropic rotor, could, therefore, provide us, in addition, the speed of flight, functioning as an anemometer, for example, for low speeds where conventional anemometry systems are inaccurate.

3.2 Balance study of the system: main rotor plus fuselage study of the articulated rotor in flapping and drag

Introduction

In this part, we will study a rotor composed of blades articulated in flapping and dragging. We are going to attack more particularly the establishment of the analytical expression of the wrench of the efforts in the rotor head. The assumption made was that the blade had a flapping angular movement (β) independent of the dragging angular movement (δ), followed by a small dragging movement $\delta = \delta_0 + \delta_{1C}\cos\psi_1 t + \delta_{1S}\sin\psi_1 t$, which is a function of the flapping angular movement.

Calculation of rotor head efforts

Each of the blades that constitute the rotor is subjected to inertia and aerodynamic forces. As a resultant effect, the fundamental principle of dynamics applied to the blade gives: the resultant of the efforts of connections at the level of the flapping joint is determined by the preceding relationship, which gives:

$\vec{R}_{\text{blade}\to\text{hub}} = \vec{R}_{\text{aerodynamic}} - \int_e^R \gamma\vec{M}.dm_i$. On the other hand, to calculate the moments at the rotor head, the Dynamic Moment Theorem is applied at the hub:

$\vec{\delta}^{\,\circ}_{\text{hub}/Rg} = \vec{M}_{\text{blade}\to\text{hub}} + \vec{M}_{\text{fuselage}\to\text{hub}}$. As the rotor hub is rotating at a constant speed, the dynamic moment $\delta^\circ{}_{\text{cube}/Rg}$ is zero and: $\vec{M}_{\text{hub}\to\text{fuselage}} = \vec{M}_{\text{blade}\to\text{hub}}$. We will note in the sequence the components of the wrench of efforts in the rotor head:

$\{T_{\text{eff}}\}_0 = \left\{ \begin{matrix} \vec{R}_{\text{blade}\to\text{hub}} \\ \vec{M}_{\text{blade}\to\text{hub}} \end{matrix} \right\}_0 = \left\{ \begin{matrix} F_x.\vec{X} + F_y.\vec{Y} + F_z.\vec{Z} \\ M_x.\vec{X} + M_y.\vec{Y} + M_z.\vec{Z} \end{matrix} \right\}_0$. Let's now calculate these components

for a blade. We will then make the sum according to the number of blades to obtain the wrench of the efforts of the complete rotor.

Calculation of the dynamic resultant

The blade is simply articulated in flapping and drag. Let *M* be a current point of the blade of radial coordinate r. The coordinates are represented in Figure 8.
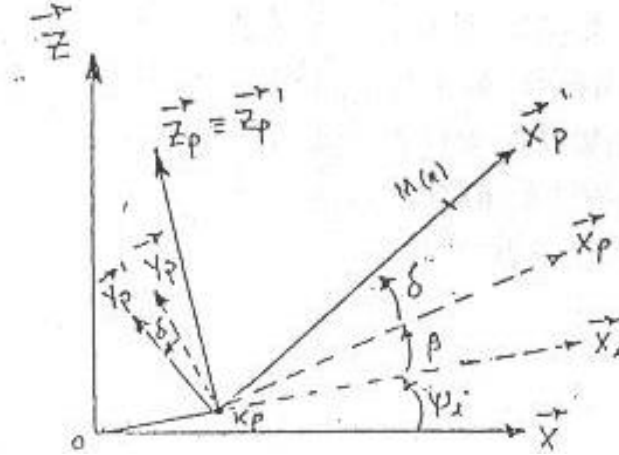
Figure 8: Representation of the coordinates – adapted from (Jorge, 1992)

We will calculate the acceleration of this point *M* in the fixed rotor frame and then integrate the obtained expressions along the blade. We have, in the fixed rotor frame:

$$\overline{OM} = \begin{bmatrix} e\cos\psi_i + (r-e)\cos\delta\,\cos\beta\,\cos\psi_i - (r-e)\sin\delta\,\sin\psi_i \\ e\sin\psi_i + (r-e)\cos\delta\,\cos\beta\,\sin\psi_i + (r-e)\sin\delta\,\cos\psi_i \\ (r-e)\cos\delta\,\sin\beta \end{bmatrix} \tag{1}$$

Notation: $\dfrac{d\beta}{dt} = \dot\beta_t$ e $\dfrac{d^2\beta}{dt^2} = \ddot\beta_{t.t}$; rotor constant speed $\dot\psi_i = \Omega$, what gives us:

$$\frac{d^2\overline{OM}}{dt^2} = \begin{bmatrix}
\begin{aligned}
&-e\Omega^2\cos\psi_i + 2(r-e)\Omega\dot\beta_t\cos\delta\sin\beta\sin\psi_i - (r-e)\ddot\beta_{t.t}\cos\delta\sin\beta\cos\psi_i \\
&-(r-e)\dot\beta_t^{\,2}\cos\delta\cos\beta\cos\psi_i - (r-e)\Omega^2\cos\delta\cos\beta\cos\psi_i + 2(r-e)\Omega\dot\delta_t\sin\delta\cos\beta\sin\psi_i \\
&+2(r-e)\dot\delta_t\dot\beta_t\sin\delta\sin\beta\cos\psi_i - (r-e)\dot\delta_t^{\,2}\cos\delta\cos\beta\cos\psi_i - (r-e)\ddot\delta_{t.t}\sin\delta\cos\beta\cos\psi_i \\
&+(r-e)\dot\delta_t^{\,2}\sin\delta\sin\psi_i - (r-e)\ddot\delta_{t.t}\cos\delta\sin\psi_i - 2(r-e)\dot\delta_t\Omega\cos\delta\cos\psi_i \\
&+(r-e)\Omega^2\sin\delta\sin\psi_i
\end{aligned} \\[2em]
\begin{aligned}
&-e\Omega^2\sin\psi_i - 2(r-e)\Omega\dot\beta_t\cos\delta\sin\beta\cos\psi_i - (r-e)\ddot\beta_{t.t}\cos\delta\sin\beta\sin\psi_i \\
&-(r-e)\dot\beta_t^{\,2}\cos\delta\cos\beta\sin\psi_i - (r-e)\Omega^2\cos\delta\cos\beta\sin\psi_i - 2(r-e)\Omega\dot\delta_t\sin\delta\cos\beta\cos\psi_i \\
&+2(r-e)\dot\delta_t\dot\beta_t\sin\delta\sin\beta\sin\psi_i - (r-e)\dot\delta_t^{\,2}\cos\delta\cos\beta\sin\psi_i - (r-e)\ddot\delta_{t.t}\sin\delta\cos\beta\sin\psi_i \\
&-(r-e)\dot\delta_t^{\,2}\sin\delta\cos\psi_i + (r-e)\ddot\delta_{t.t}\cos\delta\cos\psi_i - 2(r-e)\dot\delta_t\Omega\cos\delta\sin\psi_i \\
&-(r-e)\Omega^2\sin\delta\cos\psi_i
\end{aligned} \\[2em]
\begin{aligned}
&(r-e)\ddot\beta_{t.t}\cos\delta\cos\beta - (r-e)\dot\beta_t^{\,2}\cos\delta\sin\beta - 2(r-e)\dot\delta_t\dot\beta_t\sin\delta\cos\beta - (r-e)\dot\delta_t^{\,2}\cos\delta\sin\beta \\
&-(r-e)\ddot\delta_{t.t}\sin\delta\sin\beta
\end{aligned}
\end{bmatrix} \tag{2}$$

As β and δ are small angles, the following assumptions will be made: $\sin\beta \approx \beta$; $\sin\delta \approx \delta$; $\cos\beta \approx 1-(\beta^2/2)$; $\cos\delta \approx 1$; $\sin\beta\sin\delta \approx 0$; $\cos\beta\sin\delta \approx \delta$ (noting that, if taking $\cos\beta \approx 1$, then terms that are not negligible will not be taken into account), leading to:

$$\ddot{\gamma}_x = -e\Omega^2 \cos\psi_i + 2(r-e)\Omega\dot{\beta}_t \beta\sin\psi_i - (r-e)\ddot{\beta}_{t.t}\beta\cos\psi_i - (r-e)\dot{\beta}_t^2\left(1-\frac{\beta^2}{2}\right)\cos\psi_i$$

$$-(r-e)\Omega^2\left(1-\frac{\beta^2}{2}\right)\cos\psi_i + 2(r-e)\Omega\dot{\delta}_t\delta\sin\psi_i - (r-e)\dot{\delta}_t^2\cos\psi_i - (r-e)\ddot{\delta}_{t.t}\delta\cos\psi_i$$

$$+(r-e)\dot{\delta}_t^2\delta\sin\psi_i - (r-e)\ddot{\delta}_{t.t}\sin\psi_i - 2(r-e)\dot{\delta}_t\Omega\cos\psi_i + (r-e)\Omega^2\delta\sin\psi_i$$

$$\ddot{\gamma}_y = -e\Omega^2\sin\psi_i - 2(r-e)\Omega\dot{\beta}_t\beta\cos\psi_i - (r-e)\ddot{\beta}_{t.t}\beta\sin\psi_i - (r-e)\dot{\beta}_t^2\left(1-\frac{\beta^2}{2}\right)\sin\psi_i$$

$$-(r-e)\Omega^2\left(1-\frac{\beta^2}{2}\right)\sin\psi_i - 2(r-e)\Omega\dot{\delta}_t\delta\cos\psi_i - (r-e)\dot{\delta}_t^2\sin\psi_i - (r-e)\ddot{\delta}_{t.t}\delta\sin\psi_i$$

$$-(r-e)\dot{\delta}_t^2\delta\cos\psi_i + (r-e)\ddot{\delta}_{t.t}\cos\psi_i - 2(r-e)\dot{\delta}_t\Omega\sin\psi_i - (r-e)\Omega^2\delta\cos\psi_i$$

$$\ddot{\gamma}_z = (r-e)\ddot{\beta}_{t.t}\left(1-\frac{\beta^2}{2}\right) - (r-e)\dot{\beta}_t^2\beta - 2(r-e)\dot{\delta}_t\dot{\beta}_t\delta - (r-e)\dot{\delta}_t^2\beta$$

The final expression of the blade acceleration is obtained in the fixed rotor frame by integrating the acceleration of an element of mass dm_i:

$$m_i\gamma_i = \int_e^R \ddot{\gamma}_x \, dm_i$$

$$m_i\gamma_i = \int_e^R \ddot{\gamma}_x \, dm_i \quad \text{Avec} \int_e^R (r-e)\, dm_i = m_{si}$$

$$m_i\gamma_i = \int_e^R \ddot{\gamma}_x \, dm_i$$

What gives us:

$$m_{i\gamma x} = -m_i e\Omega^2\cos\psi_i + m_{si}\left[2\beta\dot{\beta}_t\Omega\sin\psi_i - \dot{\beta}_t^2\left(1-\frac{\beta^2}{2}\right)\cos\psi_i - \beta\ddot{\beta}_{t.t}\cos\psi_i - \Omega^2\left(1-\frac{\beta^2}{2}\right)\cos\psi_i\right]$$

$$+ m_{si}\left[2\Omega\dot{\delta}_t\delta\sin\psi_i - \dot{\delta}_t^2\cos\psi_i - \ddot{\delta}_{t.t}\delta\cos\psi_i + \dot{\delta}_t^2\delta\sin\psi_i - \ddot{\delta}_{t.t}\sin\psi_i - 2\dot{\delta}_t\Omega\cos\psi_i + \Omega^2\delta\sin\psi_i\right]$$

$$m_{i\gamma y} = -m_i e\Omega^2\sin\psi_i + m_{si}\left[2\beta\dot{\beta}_t\Omega\cos\psi_i - \dot{\beta}_t^2\left(1-\frac{\beta^2}{2}\right)\sin\psi_i - \beta\ddot{\beta}_{t.t}\sin\psi_i - \Omega^2\left(1-\frac{\beta^2}{2}\right)\sin\psi_i\right]$$

$$+ m_{si}\left[2\Omega\dot{\delta}_t\delta\cos\psi_i - \dot{\delta}_t^2\sin\psi_i - \ddot{\delta}_{t.t}\delta\sin\psi_i + \dot{\delta}_t^2\delta\cos\psi_i - \ddot{\delta}_{t.t}\cos\psi_i - 2\dot{\delta}_t\Omega\sin\psi_i\right.$$

$$\left. +\Omega^2\delta\cos\psi_i\right]$$

$$m_{i\gamma z} = m_{si}\left[\ddot{\beta}_{t.t}\left(1-\frac{\beta^2}{2}\right) - \beta\dot{\beta}_t^2\right] + m_{si}\left[-2\dot{\delta}_t\dot{\beta}_t\delta - \dot{\delta}_t^2\beta\right]$$

Aerodynamic loads

We are now interested in the aerodynamic forces generated in flight. Figure 9 shows the wind direction concerning the fixed rotor frame as well as the decomposition of the wind velocity into velocity tangential to the rotor plane (and perpendicular to the blade span) (U_T), and velocity perpendicular to the rotor plane (U_P).
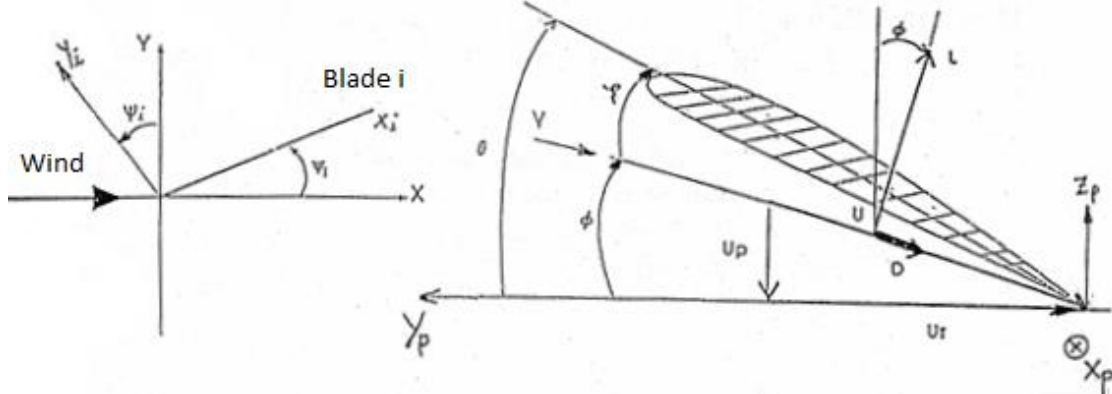
Figure 9: Representation of the forces acting on a blade – adapted from (Jorge, 1992)

The resulting speed is $U = \sqrt{U_T{}^2 + U_P{}^2}$ and $\tan \varphi \approx \varphi \approx U_P/U_T$. Additional notation adopted: $\dot{\beta}_t = \frac{d\beta}{dt} = \frac{d\beta}{d\psi}\frac{d\psi}{dt} = \Omega\dot{\beta}$, with $\dot{\beta} = \frac{d\beta}{d\psi}$.

Let us first calculate the velocity of a current point M (r) of the blade about the Galilean frame of reference (a reference frame where $\vec{V}_{ar/Rg} = \dot{\overrightarrow{VX}}_g$), leading to: $\vec{V}_{M\,blade/Rg} = \vec{V}_{M\,blade/fixed\,rotor} + \vec{V}_{M\,fixed\,rotor/air} + \vec{V}_{M\,air/Rg}$. The velocity of the current point of the blade can be obtained as the sum of the velocity due to blade rotation, flapping, and drag $\vec{V}_{blade}\,\Omega,\beta,\delta$ plus the velocity due to forward flight $\vec{V}_{blade\,V}$, plus the velocity component due to the induced velocity $\vec{V}_{blade\,V\,i}$, where

$$\left(\vec{V}_{blade\,\Omega\beta\delta}\right)_{R_f} = \left(\frac{d\overrightarrow{OM}}{dt}\right)_{R_f} = \left(\frac{d\overrightarrow{OM}}{dt}\right)_{R_f} + \vec{\Omega}(R_f/R_f) \wedge \overrightarrow{OM} \qquad (3)$$

with: R_f: fixed rotor reference frame
      R_t: rotating rotor reference frame
      R_p: blade reference frame
      $\overrightarrow{OM}$: in the R_f reference frame

What gives us:

$$\left(\frac{d\overrightarrow{OM}}{dt}\right)_{Rf} = \begin{bmatrix} (r-e)\left[-\sin\delta\,\dot{\delta}_t\cos\beta\cos\psi_i - \cos\delta\,\cos\beta\,\dot{\beta}_t\cos\psi_i - \cos\delta\,\dot{\delta}_t\sin\psi_i\right] \\ (r-e)\left[-\sin\delta\,\dot{\delta}_t\cos\beta\sin\psi_i - \cos\delta\sin\beta\,\dot{\beta}_t\sin\psi_i - \cos\delta\,\dot{\delta}_t\cos\psi_i\right] \\ (r-e)\left[-\sin\delta\,\dot{\delta}_t\sin\beta + \cos\delta\cos\beta\,\dot{\beta}_t\right] \end{bmatrix}$$
$$+ \begin{bmatrix} 0 \\ 0 \\ \Omega \end{bmatrix} \wedge \begin{bmatrix} e\cos\psi_i + (r-e)\cos\delta\cos\beta\cos\psi_i - (r-e)\sin\delta\sin\psi_i \\ e\sin\psi_i + (r-e)\cos\delta\cos\beta\sin\psi_i + (r-e)\sin\delta\cos\psi_i \\ (r-e)\cos\delta\sin\beta \end{bmatrix}$$

and, subsequently:

$$
\left(\overrightarrow{V_{blade\,\Omega\beta\delta}}\right)_{R_f} =
\begin{bmatrix}
-(r-e)\dot{\beta}_t\cos\delta\cos\beta\cos\psi_i - \Omega\sin\psi_i\left[(r-e)\cos\delta\cos\beta+e\right] \\[4pt]
\quad -(r-e)\left(\Omega\sin\delta\cos\psi_i + \dot{\delta}_t\sin\delta\cos\beta\cos\psi_i + \dot{\delta}_t\cos\delta\sin\psi_i\right) \\[12pt]
-(r-e)\dot{\beta}_t\cos\delta\sin\beta\sin\psi_i + \Omega\cos\psi_i\left[(r-e)\cos\delta\cos\beta+e\right] \\[4pt]
\quad +(r-e)\left(-\Omega\sin\delta\sin\psi_i - \dot{\delta}_t\sin\delta\cos\beta\sin\psi_i + \dot{\delta}_t\cos\delta\cos\psi_i\right) \\[12pt]
(r-e)\dot{\beta}_t\cos\delta\cos\beta - (r-e)\dot{\delta}_t\sin\delta\sin\beta
\end{bmatrix}
\tag{4}
$$

The same treatment can be done to the velocity due to forward flight: $\left(\overrightarrow{V_{blade_V}}\right)_{R_a} = \begin{vmatrix} -V \\ 0 \\ 0 \end{vmatrix}$

in the aerodynamic reference frame (Ra). A rotation (α_D) around $\overrightarrow{Ya} = \overrightarrow{Y}$ leads us to Rf

$$
\left(\dot{V}_{blade_V}\right)_{R_f} =
\begin{bmatrix} \cos\alpha_0 & 0 & \sin\alpha_0 \\ 0 & 1 & 0 \\ -\sin\alpha_0 & 0 & \cos\alpha_0 \end{bmatrix}
\begin{bmatrix} -V \\ 0 \\ 0 \end{bmatrix} =
\begin{bmatrix} -V\cos\alpha_0 \\ 0 \\ +V\sin\alpha_0 \end{bmatrix}
\tag{5}
$$

A rotation ($-\psi_i$) around $\overrightarrow{Z} \equiv \overrightarrow{Z_i}$ leads ($\overrightarrow{V_{pá\,\Omega,\beta,\delta}} + \overrightarrow{V_{pá\,V}}$) from Rf to Rt

$$
\left(\overrightarrow{V_{blade\,\Omega.\beta.\delta}}\right)_{R_t} + \left(\overrightarrow{V_{blade\,V}}\right)_{R_t} =
\begin{bmatrix}
-(r-e)\dot{\beta}_t\cos\delta\sin\beta - (r-e)\Omega\sin\delta - (r-e)\dot{\delta}_t\sin\delta\cos\beta - V\cos\alpha_0\cos\psi_i \\[8pt]
\Omega\left[(r-e)\cos\delta\cos\beta+e\right] + (r-e)\dot{\delta}_t\cos\delta + V\cos\alpha_0\sin\psi_i \\[8pt]
(r-e)\dot{\beta}_t\cos\delta\cos\beta - (r-e)\dot{\delta}_t\sin\delta\sin\beta + V\sin\alpha_0
\end{bmatrix}
$$

A rotation of (β) around $\overrightarrow{Y_i} = \overrightarrow{Y'_p}$ leads us to R'p, with flapping by:

$$
\left(\overrightarrow{V_{blade\,\Omega.\beta.\delta}}\right)_{R'_p} + \left(\overrightarrow{V_{blade\,V}}\right)_{R'_p} =
\begin{bmatrix}
-(r-e)\Omega\sin\delta\cos\beta - (r-e)\dot{\delta}_t\sin\delta - V\cos\alpha_D\cos\psi_i\cos\beta - V\sin\alpha_D\sin\beta \\[8pt]
\Omega\left[(r-e)\cos\delta\cos\beta+e\right] + (r-e)\dot{\delta}_t\cos\delta + V\cos\alpha_D\sin\psi_i \\[8pt]
(r-e)\dot{\beta}_t\cos\delta + (r-e)\Omega\sin\delta\sin\beta + V\cos\alpha_D\cos\psi_i\sin\beta + V\sin\alpha_D\cos\beta
\end{bmatrix}
$$

A rotation of (-δ) around $\vec{Z}'_p \equiv \vec{Z}_p$ leads us to R_p (flapping followed by drag motion)

$$\left(\overrightarrow{V_{blade\,\Omega.\beta.\delta}}\right)_{R_p} + \left(\overrightarrow{V_{blade\,V}}\right)_{R_p} = \begin{bmatrix} e\Omega\sin\delta - V\cos\alpha_D\cos\psi_i\cos\beta\cos\delta + V\sin\alpha_D\sin\beta\cos\delta + V\cos\alpha_D\sin\delta \\\\ e\Omega\cos\delta + (r-e)\Omega\cos\beta + (r-e)\dot{\delta}_t + V\cos\alpha_D\sin\psi_i\cos\delta \\ +V\cos\alpha_D\cos\psi_i\cos\beta\sin\delta - V\sin\alpha_D\sin\beta\cos\delta \\\\ (r-e)\dot{\beta}_t\cos\delta + (r-e)\Omega\sin\delta\sin\beta + V\cos\alpha_D\cos\psi_i\cos\beta + V\sin\alpha_D\sin\beta \end{bmatrix} \quad (6)$$

Finally, the relative motion of the blade due to the induced velocity is:

$$\left(\overrightarrow{V_{blade_{Vi}}}\right)_{R_p} = \begin{bmatrix} 0 \\ 0 \\ V_i \end{bmatrix} \quad (7)$$

The blade velocity is:

$$\left(\overrightarrow{V_{blade}}\right)_{R_p} = \left(\overrightarrow{V_{blade_{\Omega,\beta,\delta}}}\right)_{R_p} + \left(\overrightarrow{V_{blade_V}}\right)_{R_p} + \left(\overrightarrow{V_{blade_{Vi}}}\right)_{R_p} \quad (8)$$

The relative wind velocity is:

$$\left(\overrightarrow{U}\right)_{R_p} = \begin{bmatrix} U_{xp} \\ U_{yp} \\ U_{zp} \end{bmatrix} = -\left(\overrightarrow{V_{blade}}\right)_{R_p} \quad (9)$$

One can see that there is a third component of U along the blade span, that is, along with Xp, thus one can assume that its contribution to lift (L) and drag (D) is negligible. Assuming a two-dimensional aerodynamics problem for the profile of the current point of the blade, with the direction of U_P and U_T shown in the figure above. The wind velocity U will be taken as the composition of U_T and U_p. Therefore, we have tangential and vertical components of the velocity given as $U_T = -U_{yp}$; $U_p = -U_{zp}$ (Note: U_{xp} gives negligible aerodynamic efforts and is neglected). One has, finally:

$$U_T = V\cos\alpha_D\sin\psi_i\cos\delta + V\cos\alpha_D\cos\psi_i\cos\beta\sin\delta$$
$$+ V\sin\alpha_D\sin\beta\sin\delta + \Omega\,[(r-e)\cos\beta + e\cos\delta]$$
$$U_p = V\cos\alpha_D\cos\psi_i\sin\beta + V\sin\alpha_D\cos\beta + V_i$$
$$+ (r-e)\dot{\beta}_t\cos\delta + (R-e)\Omega\sin\delta\sin\beta$$

Let $\sin\beta \approx \beta$; $\sin\delta \approx \delta$; $\cos\beta \approx 1$; $\cos\delta \approx 1$; $\sin\beta\sin\delta \approx 0$; $(r-e)\cos\beta+e\cos\delta \approx r$, then:

$$\begin{cases} U_T = r\Omega + V\cos\alpha_D\sin\psi_i + V\cos\alpha_D\cos\psi_i\delta \\\\ U_p = (r-e)\dot{\beta}_t + V\cos\alpha_D\beta\cos\psi_i + V\sin\alpha_D + V_i \end{cases} \quad (10)$$

with $\dot{\beta}_t = \Omega\dot{\beta}$

The U_T speed is the sum of the speeds due to (i) the blade rotation (Ω r) and (ii) the translation of the helicopter The U_P speed is the sum of the speeds due to (i) the induced speed ($V . \sin\alpha_D + V_i$), (ii) the flapping speed $\left[\frac{d\beta}{dt}(r-e)\right]$, and (iii) the translation of the helicopter ($V . \cos\alpha_D . \cos\psi_i\,\beta$).

Also, as $\dfrac{d\beta}{dt} = \dot{\beta}_t = \Omega\dot{\beta}$, then:

$U_T = \Omega r + V\cos\alpha_D \sin\psi_i + V\cos\alpha_D \cos\psi_i \delta$

$U_p = V\sin\alpha_D + V_i + (r\text{-}e)\dot{\beta}\Omega + V.\cos\alpha_D \cos\psi_i \ \beta$. The lift (L) and drag (D) forces for

the element are, respectively, perpendicular and parallel to the plane of velocity U.

$$L = \frac{\rho}{2}U^2 \ ca \ (\theta \text{ - } \phi) \ dr \tag{11}$$

$$D = \frac{\rho}{2}U^2 \ c \ C_{d0} \ dr$$

Figure 9 shows us the lift and drag forces for the element. In the reference frame R_p, we have, for blade *i*:

$$\left[d\overline{F}_i^a\right]_{R_p} = \begin{bmatrix} 0 \\ L\sin\xi \text{ - } D\ \cos\xi \\ L\cos\xi \ + \ D\sin\xi \end{bmatrix} \tag{12}$$

A rotation of (δ) leads us to R'_p:

$$\left[dF_i^a\right]_{R'_p} = \begin{bmatrix} \cos\delta & \text{-}\sin\delta & 0 \\ \sin\delta & \cos\delta & 0 \\ 0 & 0 & 1 \end{bmatrix}\begin{bmatrix} 0 \\ L\ sen\xi \ \text{ - } \ D\ \cos\xi \\ L\ \cos\xi \ + \ D\ sen\xi \end{bmatrix}$$

$$= \begin{bmatrix} -\left(L\sin\xi \ \text{ - } \ D\cos\xi\right)\sin\delta \\ \left(L\sin\xi - D\cos\xi\right)\cos\delta \\ L\ \cos\xi \ + \ D\ sen\xi \end{bmatrix}$$

A rotation of ($-\beta$) leads us to R_t:

$$\left[dF_i^a\right]_{R_t} = \begin{bmatrix} \text{-}\left(L\ sen\xi \text{ - } D\ cos\xi\right)sen\delta\ cos\beta \text{ -}\left(L\ cos\xi \ + \ D\ sen\xi\right)sen\beta \\ \left(L\ sen\xi - D\cos\xi\right)\cos\delta \\ \text{-}\left(L\ sen\xi \text{ - } D\ cos\xi\right)sen\delta\ sen\beta + \left(L\ cos\xi \ + \ D\ sen\xi\right)cos\beta \end{bmatrix}$$

ξ, β and δ being small angles, we have: $\sin\xi \approx \xi = \theta\text{-}\phi \approx \theta\text{-}\tan\phi = \theta\text{-}U_p/U_T$; $\cos\xi \approx 1$; $\sin\beta \approx \beta$; $\sin\delta \approx \delta$; $\cos\beta \approx 1$; $\cos\delta \approx 1$; $\sin\xi \sin\delta \approx 0$; $\sin\delta \sin\beta \approx 0$; $\sin\xi \sin\beta \approx 0$. Assuming: $U^2 = U_T{}^2 + U_p{}^2 \approx U_T{}^2$, as $U_p \ll U_T$, and $a + C_{d0} \approx a$, as $C_{d0} \ll a$, leads to:

$$\{dF^a\}_{R_t} = \begin{bmatrix} -L\beta + D\delta \\ L\left(\theta - \phi\right) - D \\ L + D\left(\theta - \phi\right) \end{bmatrix} \tag{13}$$

What gives:

$$\begin{cases} dF_{xi}{}^a = \text{-}\dfrac{\rho\beta aC}{2} \ (U_T{}^2\theta \text{ - } U_p U_T) \ dr + \dfrac{\rho c C_{d0}}{2} \ U_T{}^2 \ \delta \ dr \\[2ex] dF_{yi}{}^a = \dfrac{\rho aC}{2} \ \left[U_T{}^2\theta - 2U_p U_T\theta + U_p{}^2\right] \ dr + \dfrac{\rho c C_{d0}}{2} \ U_T{}^2 \ dr \\[2ex] dF_{zi}{}^a = \dfrac{\rho aC}{2} \ \left[U_T{}^2\theta \text{ - } U_p U_T\right] \ dr \end{cases} \tag{14}$$

Introducing the following coefficients:

$\mu = \quad = \dfrac{V \cos \alpha_D}{\Omega R}$ is called the advance coefficient, which is the relationship between the component of velocity over the disc and the velocity at the tip of the blade; and

$\lambda = \quad = \dfrac{V sen \alpha_D + V_i}{\Omega R}$ is the axial flow parameter, which is the relationship between the component of velocity perpendicular to the disk and the velocity at the tip of the blade;

- $\chi = \dfrac{r}{R}$ e $\chi_e = \dfrac{e}{R}$; $\theta = \theta_{con} + \dfrac{r}{R}\theta_{tw}$ (θ_{tw}: twist); $\theta_{con} = \theta_0 + \theta_{1c} \cos\psi_i + \theta_{1s} sen\psi_i$. Thus:

$$dF_{xi}{}^a = \rho ac(\Omega R)^2 \Big\{ -\frac{\beta}{2}[\theta(\chi + \mu sen\psi_i + \mu\delta \cos\psi_i)^2 \\ - (\lambda + (\chi - \chi_e)\beta + \beta\mu \cos\psi_i) \\ (\chi + \mu sen\psi_i + \mu\delta \, sen\psi_i)] + \frac{C_{d0}}{2a}\delta(\chi + \mu sen\psi_i + \mu\delta \cos\psi_i)^2 \Big\}dr \tag{15}$$

$$dF_{yi}{}^a = \rho ac(\Omega R)^2 \Big\{ -\frac{1}{2}[2\theta(\chi + \mu sen\psi_i + \mu\delta \cos\psi_i)(\lambda + (\chi - \chi_e)\beta \\ + \beta\mu \cos\psi_i) \\ - (\chi + \mu sen\psi_i + \mu\delta \cos\psi_i)^2\theta^2 \\ - (\lambda + (\chi - \chi_e)\beta \\ + \beta\mu cos()^2)] - \frac{C_{d0}}{2a}(\chi + \mu sen\psi_i + \mu\delta \cos\psi_i)^2 \Big\} \Big]$$

$$dF_{zi}{}^a = \frac{\rho ac}{2}(\Omega R)^2 \Big\{ \theta\big(\chi + \mu sen\psi_i + \mu\delta\cos\psi_i\big)^2 \\ - \big(\chi + \mu sen\psi_i + \mu\delta\cos\psi_i\big)\big(\lambda + (\chi - \chi_e)\beta + \beta\mu\cos\psi_i\big)\Big\}dr$$

For the evaluation of the axial flux parameter λ, the Meijer-Drees modeling is used (Meijer Drees, 1949). This allows the consideration of a cyclic variation of the parameter λ. The Meijer-Drees formulation leads us to:

$$\lambda = \lambda_0 + \lambda_{1c}\chi \cos\psi_i + \lambda_{1s}\chi sen\psi_i$$
$$= \mu tg\alpha_D + \frac{C_T}{2\left(1 - \frac{3}{2}\mu^2\right)\sqrt{\mu^2 + \lambda^2}}\big(1 + K_x\chi \cos\psi_i + K_y\chi sen\psi_i\big) \tag{16}$$

Where

$$K_x = \frac{4}{3}\left[\big(1 - 1,8\mu^2\big)\sqrt{1 + \left[\frac{\lambda}{\mu}\right]^2} - \frac{\lambda}{\mu}\right] \tag{17}$$

$$K_y = -2\mu$$

Which gives the cyclic components:

$$\lambda_0 = \mu tg\alpha_D + \frac{C_T}{2\left(1 - \frac{3}{2}\mu^2\right)\sqrt{\lambda^2 + \mu^2}}$$

$$\lambda_{1c} = \frac{2\mu C_T}{3\left(1 - \frac{3}{2}\mu^2\right)}\left[\frac{1}{\sqrt{\lambda^2 + \mu^2}\big(\sqrt{\lambda^2 + \mu^2} + \lambda\big)} - 1,8\right] \tag{18}$$

$$\lambda_{1s} = -\frac{\mu C_T}{\left(1 - \frac{3}{2}\mu^2\right)\sqrt{\lambda^2 + \mu^2}}$$

λ_0 is calculated by an iterative method (Meijer Drees, 1949); get λ_{1c}, λ_{1s} by replacing λ with λ_0.

Let $S = \rho a c\,(\Omega R)^2$. Integrating $dF_{xi}{}^a$, $dF_{yi}{}^a$, $dF_{zi}{}^a$ along the blade leads to:

$$F_{xi}{}^a = S \int_e^R \left\{ -\frac{\beta}{2}\left[\left[\frac{r}{R} + \mu \operatorname{sen}\psi_i + \mu\delta\cos\psi_i\right]^2 \left[\theta_{con} + \frac{r}{R}\theta_{tw}\right] - \left[\frac{r}{R} + \mu \operatorname{sen}\psi_i + \mu\delta\cos\psi_i\right]\right.\right.$$

$$\left.\left[\lambda_0 + \lambda_{1c}\frac{r}{R}\cos\psi_i + \lambda_{1s}\frac{r}{R}\operatorname{sen}\psi_i + \frac{r\text{-}e}{R}\beta + \beta\mu\cos\psi_i\right]\right] + \frac{C_{d0}}{2a}\delta\left(\frac{r}{R} + \mu\operatorname{sen}\psi_i + \mu\delta\cos\psi_i\right)^2 \right\} dr$$

$$F_{yi}{}^a = S \int_e^R \left[-\frac{1}{2}\left[\frac{r}{R} + \mu\operatorname{sen}\psi_i + \mu\delta\cos\psi_i\right]\left[\theta_{con} + \frac{r}{R}\theta_{tw}\right]\chi 2 + \right.$$

$$\chi\left[\lambda_0 + \lambda_{1c}\frac{r}{R}\cos\psi_i + \lambda_{1s}\frac{r}{R}\operatorname{sen}\psi_i + \frac{r\text{-}e}{R}\beta + \beta\mu\cos\psi_i\right] + \frac{1}{2}\left[\lambda_0 + \lambda_{1c}\frac{r}{R}\cos\psi_i + \lambda_{1s}\frac{r}{R}\operatorname{sen}\psi_i + ...\right]^2 \tag{19}$$

$$\left.\left[...+\frac{r\text{-}e}{R}\beta + \beta\mu\cos\psi_i\right]^2\left[\theta_{con} + \frac{r}{R}\theta_{tw}\right]^2 - \frac{C_{d0}}{2a}\left[\frac{r}{R} + \mu\operatorname{sen}\psi_i + \mu\delta\cos\psi_i\right]^2\right] dr$$

$$F_{zi}{}^a = \frac{S}{2} \int_e^R \left[\left[\frac{r}{R} + \mu\operatorname{sen}\psi_i + \mu\delta\cos\psi_i\right]^2\left[\theta_{con} + \frac{r}{R}\theta_{tw}\right] - \left[\frac{r}{R} + \mu\operatorname{sen}\psi_i + \mu\delta\cos\psi_i\right]\right.$$

$$\left.\left[\lambda_0 + \lambda_{1c}\frac{r}{R}\cos\psi_i + \lambda_{1s}\frac{r}{R}\operatorname{sen}\psi_i + \frac{r\text{-}e}{R}\beta + \beta\mu\cos\psi_i\right]\right] dr$$

After integration leads to:

$$\frac{F_{xi}{}^a}{S} = \frac{1}{3}\left[\frac{R^3 - e^3}{R^2} + 3(R - e)\mu^2(\sin\psi_i + \delta\cos\psi_i)^2\right.$$

$$\left. + 3\frac{R^3 - e^3}{R}\mu(\sin\psi_i + \delta\cos\psi_i)\right]\left(-\theta_{con}\frac{\beta}{2} + \frac{C_{d0}}{2a}\delta\right)$$

$$-\frac{\beta}{2}\left[\frac{R^4 - e^4}{4R^3} + 2\mu\frac{R^3 - e^3}{3R^2}(\sin\psi_i + \delta\cos\psi_i)\right.$$

$$\left. + \mu^2\frac{R^2 - e^2}{R^2}(\sin\psi_i + \delta\cos\psi_i)^2\right]\theta_{tw}$$

$$+\frac{\beta}{2}\left[\frac{R^2 - e^2}{2R} + \mu(R - e)(\sin\psi_i + \delta\cos\psi_i)\right](\lambda_0 + \mu\delta\cos\psi_i)$$

$$+\frac{\beta}{2}\left[\frac{R^3 - e^3}{3R^2} + \mu\frac{R^2 - e^2}{2R}(\sin\psi_i + \delta\cos\psi_i)\right]\left(\lambda_{1c}\cos\psi_i + \lambda_{1s}\sin\psi_i + \dot{\beta}\right)$$

$$-e\dot{\beta}\frac{\beta}{2}\left[\frac{R^2 - e^2}{2R} + \frac{R - e}{R}\mu(\sin\psi_i + \delta\cos\psi_i)\right]$$

$$\frac{F_{yi}{}^a}{S} = -\left\{(R - e)\left(\lambda_0 - \frac{e}{R}\dot{\beta} + \mu\beta\cos\psi_i\right)\mu\,(\sin\psi_i + \delta\cos\psi_i)\theta_{con}\right.$$

$$\left. + \frac{R^2 - e^2}{2R}\left(\lambda_{1c}\cos\psi_i + \lambda_{1s}\sin\psi_i + \dot{\beta}\right)\mu(\sin\psi_i + \delta\cos\psi_i)\theta_{con}\right\}$$

$$+ \left[\frac{\theta_{con}^2}{2} - \frac{C_{d0}}{2a}\right]\left[\frac{R^3 - e^3}{3R^2} + \mu \frac{R^2 - e^2}{2R}(\sin\psi_i + \delta\cos\psi_i)\right.$$

$$\left. + \mu^2(R - e)\mu^2(\sin\psi_i + \delta\cos\psi_i)^2\right]$$

$$+ \frac{(R - e)}{2}\left(\lambda_0^2 + \beta^2\mu^2\cos^2\psi_i + 2\lambda_0\beta\mu\cos\psi_i - 2\frac{e}{R}\dot{\beta}(\lambda_0 + \beta\mu\cos\psi_i)\right.$$

$$\left. + \frac{e^2}{R^2}\dot{\beta}^2\right)$$

$$+ \frac{R^2 - e^2}{2R}\left[-\left(\lambda_0 - \frac{e}{R}\dot{\beta} + \mu\beta\cos\psi_i\right)(\mu(\sin\psi_i + \delta\cos\psi_i)\theta_{tw} + \theta_{con})\right.$$

$$\left. + \left(\lambda_{1c}\cos\psi_i + \lambda_{1s}\sin\psi_i + \dot{\beta}\right)\left(\lambda_0 + \beta\mu\cos\psi_i - \frac{e}{R}\dot{\beta}\right)\right]$$

$$+ \frac{R^3 - e^3}{3R^2}\left[-\left(\lambda_0 - \frac{e}{R}\dot{\beta} + \mu\beta\cos\psi_i\right)\theta_{tw} - \left(\lambda_{1c}\cos\psi_i + \lambda_{1s}\sin\psi_i + \dot{\beta}\right)\right.$$

$$(\mu(\sin\psi_i + \delta\cos\psi_i)\theta_{tw} + \theta_{con}) + \frac{\lambda_{1c}^2}{2}\cos^2\psi_i + \frac{\lambda_{1s}^2}{2}\sin^2\psi_i + \frac{\dot{\beta}^2}{2}$$

$$\left. + \lambda_{1c}\lambda_{1s}\cos\psi_i\sin\psi_i + \dot{\beta}(\lambda_{1c}\cos\psi_i + \lambda_{1s}\sin\psi_i)\right]$$

$$- \frac{R^4 - e^4}{4R^3}\theta_{tw}\left(\lambda_{1c}\cos\psi_i + \lambda_{1s}\sin\psi_i + \dot{\beta}\right)$$

$$+ \left[\frac{R^4 - e^4}{4R^3} + 2\mu\frac{R^3 - e^3}{3R^2}(\sin\psi_i + \delta\cos\psi_i)\right.$$

$$\left. + \mu^2\frac{R^2 - e^2}{2R}(\sin\psi_i + \delta\cos\psi_i)^2\right]\theta_{tw}\theta_{con}$$

$$+ \frac{\theta_{tw}^2}{2R^2}\left[\frac{R^5 - e^5}{5R^2} + \frac{\mu(\sin\psi_i + \delta\cos\psi_i)}{2R}(R^4 - e^4)\right.$$

$$\left. + \frac{\mu^2(\sin\psi_i + \delta\cos\psi_i)^2}{3}(R^3 - e^3)\right]$$

$$\frac{F_{zi}{}^a}{S} = \frac{1}{2}\left\{\left[\frac{R^3 - e^3}{3R^2} + (R - e)\mu^2(\sin\psi_i + \delta\cos\psi_i)^2\right.\right.$$

$$\left. + \frac{R^2 - e^2}{R}\mu(\sin\psi_i + \delta\cos\psi_i)\right]\theta_{con}$$

$$+ \left[\frac{R^4 - e^4}{4R^3} + 2\mu\frac{R^3 - e^3}{3R^2}(\sin\psi_i + \delta\cos\psi_i)\right.$$

$$\left. + \mu^2\frac{R^2 - e^2}{R^2}(\sin\psi_i + \delta\cos\psi_i)^2\right]\theta_{tw}$$

$$- \left[\frac{R^2 - e^2}{2R} + \mu(R - e)(\sin\psi_i + \delta\cos\psi_i)\right](\lambda_0 + \mu\delta\cos\psi_i)$$

$$- \left[\frac{R^3 - e^3}{3R^2} + \mu\frac{R^2 - e^2}{2R}(\sin\psi_i + \delta\cos\psi_i)\right]\left(\lambda_{1c}\cos\psi_i + \lambda_{1s}\sin\psi_i + \dot{\beta}\right)$$

$$+ e\dot{\beta}\frac{\beta}{2}\left[\frac{R^2 - e^2}{2R} + \frac{R - e}{R}\mu(\sin\psi_i + \delta\cos\psi_i)\right]\right\}$$

In general, the ratio e/R is very small. In the case of the Super Puma main rotor, one has R = 7.80 m and e = 0.27 m, which gives e/R = 0.035. Simplifying assumptions considered: $R^2 - e^2 \approx R^2$; $R^3 - e^3 \approx R^3$; $R^4 - e^4 \approx R^4$; $R^5 - e^5 \approx R^5$ (the only simplifying assumptions that will not be made is $R - e \approx R$), which will lead us to an error of 0.15% in the efforts calculations, which will be disregarded.

Thus, one obtains:

$$\frac{F_{xi}{}^a}{S} = \left[\frac{R}{3} + (R-e)\mu^2\left(\sin\psi_i + \delta\cos\psi_i\right)^2 + R\mu\left(\sin\psi_i + \delta\cos\psi_i\right)\right]\left[\theta_{con} - \frac{\beta}{2} + \frac{C_{d0}}{2a}\right]$$

$$-\frac{\beta}{2}\left[\frac{R}{4} + 2\mu\frac{R}{3}\left(\sin\psi_i + \delta\cos\psi_i\right) + \mu^2\frac{R}{2}\left(\sin\psi_i + \delta\cos\psi_i\right)^2\right]\theta_{tw}$$

$$+\frac{\beta}{2}\left[\frac{R}{2} + \mu(R-e)\left(\sin\psi_i + \delta\cos\psi_i\right)\right]\left(\lambda_0 + \mu\beta\cos\psi_i - \frac{e}{R}\dot\beta\right)$$

$$+\frac{\beta}{2}\left[\frac{R}{3} + \mu\frac{R}{2}\left(\sin\psi_i + \delta\cos\psi_i\right)\right]\left(\lambda_{1c}\cos\psi_i + \lambda_{1s}\sin\psi_i + \dot\beta\right)$$

$$\frac{F_{yi}{}^a}{S} = \left(\lambda_0 + \mu\beta\cos\psi_i - \frac{e}{R}\dot\beta\right)$$

$$-\left[(R-e)\mu\left(\sin\psi_i + \delta\cos\psi_i\right) + \frac{R}{2}\theta_{con} - \frac{R}{2}\mu\left(\sin\psi_i + \delta\cos\psi_i\right)\right.$$

$$\left. +\frac{R}{3}\theta_{tw} + \frac{R}{2}\left(\lambda_{1c}\cos\psi_i + \lambda_{1s}\sin\psi_i + \dot\beta\right)\right]$$

$$-\left(\lambda_{1c}\cos\psi_i + \lambda_{1s}\sin\psi_i + \dot\beta\right)$$

$$\left[\frac{R}{2}\mu\left(\sin\psi_i + \delta\cos\psi_i\right) + \frac{R}{3}\theta_{con} + \frac{R}{3}\mu\left(\sin\psi_i + \delta\cos\psi_i\right) + \frac{R}{4}\theta_{tw}\right]$$

$$+\left[\frac{\theta_{con}{}^2}{2} - \frac{C_{d0}}{2a}\right]\left[\frac{R}{3} + \mu R\left(\sin\psi_i + \delta\cos\psi_i\right) + \mu^2(R-e)\left(\sin\psi_i + \delta\cos\psi_i\right)^2\right]$$

$$+\theta_{tw}\theta_{con}\left[\frac{R}{4} + 2\mu\frac{R}{3}\left(\sin\psi_i + \delta\cos\psi_i\right) + \mu^2\left(\sin\psi_i + \delta\cos\psi_i\right)^2\frac{R}{2}\right]$$

$$+\frac{\theta_{tw}{}^2}{2}\left[\frac{R}{5} + \mu\left(\sin\psi_i + \delta\cos\psi_i\right)\frac{R}{2} + \mu^2\left(\sin\psi_i + \delta\cos\psi_i\right)^2\frac{R}{3}\right]$$

$$+\frac{(R-e)}{2}\left(\lambda_0 + \mu\beta\cos\psi_i - \frac{e}{R}\dot\beta\right)^2 + \frac{R}{6}\left(\lambda_{1c}\cos\psi_i + \lambda_{1s}\sin\psi_i + \dot\beta\right)^2$$

$$\frac{F_{zi}{}^a}{S} = \frac{1}{2}\left[\frac{R}{3} + (R-e)\mu^2\left(\sin\psi_i + \delta\cos\psi_i\right)^2 + R\mu\left(\sin\psi_i + \delta\cos\psi_i\right)\right]\theta_{con}$$

$$+\frac{1}{2}\left[\frac{R}{4} + 2\mu\frac{R}{3}\left(\sin\psi_i + \delta\cos\psi_i\right) + \mu^2\frac{R}{2}\left(\sin\psi_i + \delta\cos\psi_i\right)^2\right]\theta_{tw}$$

$$-\frac{1}{2}\left[\frac{R}{2} + \mu(R-e)\left(\sin\psi_i + \delta\cos\psi_i\right)\right]\left(\lambda_0 + \mu\beta\cos\psi_i - \frac{e}{R}\dot\beta\right)$$

$$+\frac{1}{2}\left[\frac{R}{3} + \mu\frac{R}{2}\left(\sin\psi_i + \delta\cos\psi_i\right)\right]\left(\lambda_{1c}\cos\psi_i + \lambda_{1s}\sin\psi_i + \dot\beta\right)$$

Calculation of the resultant effort in the rotor head

The resultant is obtained by applying the above relationship. The reference frame for the aerodynamic forces (calculated in the rotating rotor reference frame) is changed, as:

$$\begin{cases} F_x = F_{xi}{}^a \cos\psi_i - F_{yi}{}^a \sin\psi_i - m_{i\gamma x} \\ F_y = F_{xi}{}^a \sin\psi_i - F_{yi}{}^a \cos\psi_i - m_{i\gamma y} \\ F_z = F_{zi}{}^a - m_{i\gamma z} \end{cases} \qquad (20)$$

With $m_{i\gamma x}$, $m_{i\gamma y}$, $m_{i\gamma z}$, F_{xi}, F_{yi}, F_{zi}: components as previously calculated. What gives:

$$\frac{F_{xi}{}^a}{S} = \left[\frac{R}{3} + (R-e)\mu^2(\sin\psi_i + \delta\cos\psi_i)^2 + R\mu(\sin\psi_i + \delta\cos\psi_i)\right]$$
$$\left[\left(-\frac{\beta}{2}\theta_{con} + \frac{C_{d0}}{2a}\right)\cos\psi_i - \sin\psi_i\left(\frac{\theta_{con}{}^2}{2} - \frac{C_{d0}}{2a}\right)\right]$$
$$+ \left[\frac{R}{4} + 2\mu\frac{R}{3}(\sin\psi_i + \delta\cos\psi_i) + \mu^2\frac{R}{2}(\sin\psi_i + \delta\cos\psi_i)^2\right]$$
$$\left[-\frac{\beta}{2}\theta_{tw}\cos\psi_i - \sin\psi_i\,\theta_{tw}\theta_{con}\right]$$
$$+ \left(\lambda_0 + \mu\beta\cos\psi_i - \frac{e}{R}\dot{\beta}\right)$$
$$\left[\frac{\beta}{2}\cos\psi_i\left(\frac{R}{2} + \mu\frac{R}{2}(R-e)(\sin\psi_i + \delta\cos\psi_i)\right)\right.$$
$$+ \sin\psi_i\left[\left(\mu(R-e)(\sin\psi_i + \delta\cos\psi_i) + \frac{R}{2}\theta_{con}\right)\right.$$
$$+ \left.\left(\frac{R}{3} + \mu\frac{R}{2}(\sin\psi_i + \delta\cos\psi_i)\right)\theta_{tw}$$
$$\left.-\frac{R}{2}\left(\lambda_{1c}\cos\psi_i + \lambda_{1s}\sin\psi_i + \dot{\beta}\right)\right]\right]$$
$$+ \left(\lambda_{1c}\cos\psi_i + \lambda_{1s}\sin\psi_i + \dot{\beta}\right)$$
$$\left[\frac{\beta}{2}\cos\psi_i\left(\frac{R}{3} + \mu\frac{R}{2}(\sin\psi_i + \delta\cos\psi_i)\right)\right.$$
$$+ \sin\psi_i\left[\left(\frac{R}{2}\mu(\sin\psi_i + \delta\cos\psi_i) + \frac{R}{3}\right)\theta_{con}\right.$$
$$+ \left.\left.\left(\frac{R}{3} + \mu(\sin\psi_i + \delta\cos\psi_i) + \frac{R}{4}\right)\right]\right]$$
$$- \sin\psi_i\frac{\theta_{tw}{}^2}{2}\left[\frac{R}{5} + \mu\frac{R}{2}(\sin\psi_i + \delta\cos\psi_i) + \mu^2(\sin\psi_i + \delta\cos\psi_i)^2\frac{R}{3}\right]$$
$$- \sin\psi_i\frac{(R-e)}{2}\left(\lambda_0 + \mu\beta\cos\psi_i - \frac{e}{R}\dot{\beta}\right)^2$$
$$- \sin\psi_i\frac{R}{6}\left(\lambda_{1c}\cos\psi_i + \lambda_{1s}\sin\psi_i + \dot{\beta}\right)$$
$$+ \frac{m_i}{S}e\Omega^2\cos\psi_i$$
$$- \frac{m_{si}}{S}\left[2\beta\dot{\beta}_t\Omega\sin\psi_i - \dot{\beta}^2\left(1 - \frac{\beta^2}{2}\right)\cos\psi_i - \beta\ddot{\beta}_{t.t}\cos\psi_i\right.$$
$$\left.- \Omega^2\left(1 - \frac{\beta^2}{2}\right)\cos\psi_i\right]$$
$$- \frac{m_{si}}{S}\left[2\Omega\dot{\delta}_t\delta\sin\psi_i - \dot{\delta}_t{}^2\cos\psi_i - \ddot{\delta}_{t.t}\delta\cos\psi_i + \dot{\delta}_t{}^2\delta\sin\psi_i\right.$$
$$\left.-\ddot{\delta}_{t.t}\sin\psi_i - 2\dot{\delta}_t{}^2\Omega\cos\psi_i + \Omega^2\delta\sin\psi_i\right]$$

And:

$$
\frac{F_{yi}^{a}}{S} = \left[\frac{R}{3} + (R-e)\mu^2(\sin\psi_i + \delta\cos\psi_i)^2 + R\mu(\sin\psi_i + \delta\cos\psi_i)\right]
$$

$$
\left[-\frac{\beta}{2}\theta_{con} + \frac{C_{d0}\delta}{2a}\sin\psi_i + \cos\psi_i\left(\frac{\theta_{con}^2}{2} - \frac{C_{d0}}{2a}\right)\right]
$$

$$
+ \left[\frac{R}{4} + 2\mu\frac{R}{3}(\sin\psi_i + \delta\cos\psi_i) + \mu^2(\sin\psi_i + \delta\cos\psi_i)^2\frac{R}{2}\right]
$$

$$
\left[-\frac{\beta}{2}\theta_{tw}\sin\psi_i + \cos\psi_i\theta_{tw}\theta_{con}\right]
$$

$$
+ \left(\lambda_0 + \mu\beta\cos\psi_i - \frac{e}{R}\dot{\beta}\right)
$$

$$
\left[\frac{\beta}{2}\sin\psi_i\left(\frac{R}{2} + \mu(R-e)(\sin\psi_i + \delta\cos\psi_i)\right)\right.
$$

$$
- \cos\psi_i\left[\left(\mu(R-e)(\sin\psi_i + \delta\cos\psi_i) + \frac{R}{2}\right)\theta_{con}\right.
$$

$$
\left.\left. + \left(\frac{R}{2}(\sin\psi_i + \delta\cos\psi_i) + \frac{R}{3}\right)\theta_{tw} - \frac{R}{2}\left(\lambda_{1c}\cos\psi_i + \lambda_{1s}\sin\psi_i + \dot{\beta}\right)\right]\right]
$$

$$
+ \left(\lambda_{1c}\cos\psi_i + \lambda_{1s}\sin\psi_i + \dot{\beta}\right)\left[\frac{\beta}{2}\sin\psi_i\left(\frac{R}{3} + \mu\frac{R}{2}(\sin\psi_i + \delta\cos\psi_i)\right)\right.
$$

$$
\left. - \cos\psi_i\left[\left(\frac{R}{2}\mu(\sin\psi_i + \delta\cos\psi_i) + \frac{R}{3}\right)\theta_{con} + \left(\frac{R}{3}\mu(\sin\psi_i + \delta\cos\psi_i) + \frac{R}{4}\right)\theta_{tw}\right]\right]
$$

$$
+ \cos\psi_i\frac{\theta_{tw}^2}{2}\left[\frac{R}{5} + \mu(\sin\psi_i + \delta\cos\psi_i)\frac{R}{2} + \mu^2(\sin\psi_i + \delta\cos\psi_i)^2\frac{R}{3}\right]
$$

$$
+ \cos\psi_i\frac{(R-e)}{2}\left(\lambda_0 + \mu\beta\cos\psi_i - \frac{e}{R}\dot{\beta}\right)^2 + \cos\psi_i\frac{R}{6}\left(\lambda_{1c}\cos\psi_i + \lambda_{1s}\sin\psi_i + \dot{\beta}\right)^2
$$

$$
+ \frac{m_i}{S}e\Omega^2\sin\psi_i
$$

$$
+ \frac{m_{si}}{S}\left[-2\beta\dot{\beta}_t\Omega\cos\psi_i - \dot{\beta}_t^2\left(1-\frac{\beta^2}{2}\right)\sin\psi_i - \beta\dot{\beta}_{t.t}\sin\psi_i - \Omega^2\left(1-\frac{\beta^2}{2}\right)\sin\psi_i\right]
$$

$$
- \frac{m_{si}}{S}\left[-2\dot{\delta}_t^2\Omega\delta\cos\psi_i - \dot{\delta}_t^2\sin\psi_i - \ddot{\delta}_{t.t}^2\delta\sin\psi_i - \dot{\delta}_t^2\delta\cos\psi_i\right.
$$

$$
\left. - \ddot{\delta}_{t.t}\cos\psi_i - 2\dot{\delta}_t^2\Omega\sin\psi_i - \Omega^2\delta\cos\psi_i\right]
$$

$$
\frac{F_{zi}^{a}}{S} = \left[\frac{R}{3} + (R-e)\mu^2(\sin\psi_i + \delta\cos\psi_i)^2 + R\mu(\sin\psi_i + \delta\cos\psi_i)\right]\theta_{con}
$$

$$
+ \left[\frac{R}{4} + 2\mu\frac{R}{3}(\sin\psi_i + \delta\cos\psi_i) + \mu^2\frac{R}{2}(\sin\psi_i + \delta\cos\psi_i)^2\right]\theta_{tw}
$$

$$
- \left[\frac{R}{2} + (R-e)\mu(\sin\psi_i + \delta\cos\psi_i)\right]\left(\lambda_0 + \mu\beta\cos\psi_i - \frac{e}{R}\dot{\beta}\right)
$$

$$
- \left[\frac{R}{3} + \mu\frac{R}{2}(\sin\psi_i + \delta\cos\psi_i)\right]\left(\lambda_{1c}\cos\psi_i + \lambda_{1s}\sin\psi_i + \dot{\beta}\right)
$$

$$
- 2\frac{m_{si}}{S}\left[\ddot{\beta}_{t.t}\left(1-\frac{\beta^2}{2}\right) - \beta\dot{\beta}_t^2\right] - 2\frac{m_{si}}{S}\left[-2\dot{\delta}_t\dot{\beta}_t\delta - \dot{\delta}_t^2\beta\right]
$$

Calculation of the resultant moment in the rotor head

As seen above, by isolating the rotor hub we will be able to determine the rotor head moment M $_{\text{blade} \to \text{hub}}$., as indicated in Figure 10.
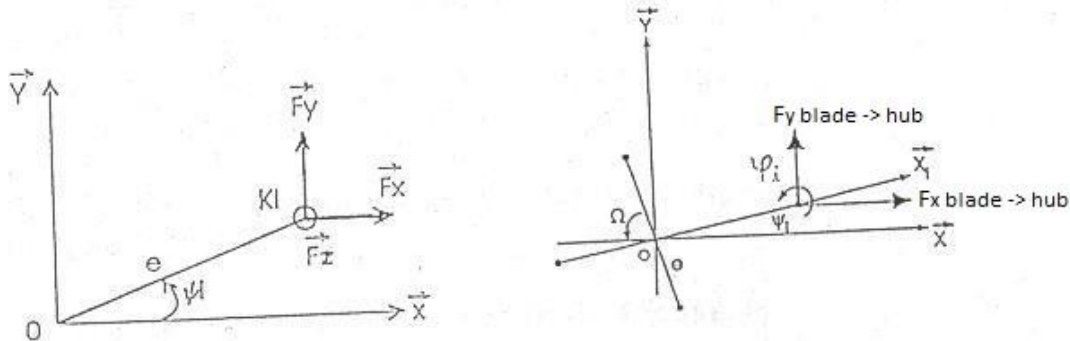
Figure 10: Resulting moment at the rotor head – adapted from (Jorge, 1992)

$$\phi_i = K_{i\delta}.\delta_i + C_{i\delta}\,\dot{\delta}_{it} \quad \text{(Torsional moment due to drag adapter)}$$

$$M_x = \left[\overrightarrow{OK_i} \Lambda \vec{F}_{\text{blade}\to\text{hub}} \right].\vec{X}$$

$$= e \sin\psi_i.F_z$$

$$M_y = \left[\overrightarrow{OK_i} \Lambda \vec{F}_{\text{blade}\to\text{hub}} \right].\vec{Y}$$

$$= e \cos\psi_i.F_z$$

$$M_z = \left[\overrightarrow{OK_i} \Lambda \vec{F}_{\text{blade}\to\text{hub}} \right].\vec{Z}$$

$$= e \cos\psi_i.F_y - e \sin\psi_i.F_x + K_{i\delta} + C_{i\delta}\,\dot{\delta}_t$$

It is obtained directly:

$$M_x = \frac{S}{2}e\left\{ \left[\frac{R}{3} + (R-e)\mu^2(\sin\psi_i + \delta\cos\psi_i)^2 + R\mu(\sin\psi_i + \delta\cos\psi_i) \right]\theta_{\text{con}}\sin\psi_i \right.$$

$$+ \left[\frac{R}{4} + \frac{2}{3}\mu R(\sin\psi_i + \delta\cos\psi_i) + \frac{R}{2}\mu^2(\sin\psi_i + \delta\cos\psi_i)^2 \right]\theta_{\text{tw}}\sin\psi_i$$

$$- \left[\frac{R}{2} + (R-e)\mu(\sin\psi_i + \delta\cos\psi_i) \right]\left(\lambda_0 + \mu\beta\cos\psi_i - \frac{e}{R}\dot{\beta} \right)\sin\psi_i$$

$$\left. - \left[\frac{R}{3} + \frac{R}{2}\mu(\sin\psi_i + \delta\cos\psi_i) \right]\left(\lambda_{1c}\cos\psi_i + \lambda_{1s}\sin\psi_i + \dot{\beta} \right)\sin\psi_i \right\}$$

$$- m_{si}e\sin\psi_i\left[\ddot{\beta}_{t.t}\left(1 - \frac{b^2}{2} \right) - \beta\dot{\beta}_t^2 - 2\dot{\delta}_t\dot{\beta}_t\delta - \dot{\delta}_t^2\beta \right]$$

$$M_y = \frac{S}{2}e\left\{ \left[\frac{R}{3} + (R-e)\mu^2(\sin\psi_i + \delta\cos\psi_i)^2 + R\mu(\sin\psi_i + \delta\cos\psi_i) \right]\theta_{\text{con}}\sin\psi_i \right.$$

$$+ \left[\frac{R}{4} + \frac{2}{3}\mu R(\sin\psi_i + \delta\cos\psi_i) + \frac{R}{2}\mu^2(\sin\psi_i + \delta\cos\psi_i)^2 \right]\theta_{\text{tw}}\sin\psi_i$$

$$- \left[\frac{R}{2} + (R-e)\mu(\sin\psi_i + \delta\cos\psi_i) \right]\left(\lambda_0 + \mu\beta\cos\psi_i - \frac{e}{R}\beta \right)\cos\psi_i$$

$$\left. - \left[\frac{R}{3} + \frac{R}{2}\mu(\sin\psi_i + \delta\cos\psi_i) \right]\left(\lambda_{1c}\cos\psi_i + \lambda_{1s}\sin\psi_i + \beta \right)\cos\psi_i \right\}$$

$$- m_{si}e\cos\psi_i\left[\ddot{\beta}_{t.t}\left(1 - \frac{b^2}{2} \right) - \beta\dot{\beta}_t^2 - 2\dot{\delta}_t\dot{\beta}_t\delta - \dot{\delta}_t^2\beta \right]$$

$$M_z = Se\left[\frac{R}{3} + (R-e)\mu^2(sin\,\psi_i + \delta\,cos\,\psi_i)^2 + R\mu(sin\,\psi_i + \delta\,cos\,\psi_i)\right]\left(\frac{\theta_{con}^2}{2}\right.$$

$$\left. -\frac{C_{d0}}{2a}\right)$$

$$+\left[\frac{R}{4} + 2\mu\frac{R}{3}(sin\,\psi_i + \delta\,cos\,\psi_i) + \frac{R}{2}\mu^2(sin\,\psi_i + \delta\,cos\,\psi_i)^2\right]\theta_{tw}\theta_{con}$$

$$-\left(\lambda_0 + \mu\beta\,cos\,\psi_i - \frac{e}{R}\dot{\beta}\right)\left[\left(\frac{R}{2} + (R-e)\mu(sin\,\psi_i + \delta\,cos\,\psi_i)\right)\right.$$

$$\left. + -\frac{R}{2}\left(\lambda_{1c}\,cos\,\psi_i + \lambda_{1s}\,sin\,\psi_i + \dot{\beta}\right)\right]$$

$$-\left(\lambda_{1c}\,cos\,\psi_i + \lambda_{1s}\,sin\,\psi_i + \dot{\beta}\right)\left[\left(\frac{R}{3} + \frac{R}{2}\mu(sin\,\psi_i + \delta\,cos\,\psi_i)\right)\theta_{con}\right.$$

$$\left. + \left(\frac{R}{3}\mu(sin\,\psi_i + \delta\,cos\,\psi_i) + \frac{R}{4}\right)\theta_{tw}\right]$$

$$+\left[\frac{R}{5} + \frac{R}{2}\mu(sin\,\psi_i + \delta\,cos\,\psi_i) + \frac{R}{3}\mu^2(sin\,\psi_i + \delta\,cos\,\psi_i)^2\right]\frac{\theta_{tw}^2}{2}$$

$$+\left(\lambda_0 + \mu\beta\,cos\,\psi_i - \frac{e}{R}\dot{\beta}\right)^2\frac{(R-e)}{2} + \frac{R}{6}\left(\lambda_{1c}\,cos\,\psi_i + \lambda_{1s}\,sin\,\psi_i + \dot{\beta}\right)^2$$

$$+ m_{si}e\left(2\beta\dot{\beta}_t\Omega + 2\dot{\delta}_t\Omega\delta + \dot{\delta}_t^2\delta - \ddot{\delta}_{t.t} + \Omega^2\delta\right) + K_{i\delta}.\delta + C_{i\delta}\dot{\delta}_t$$

Application to a rotor with N blades

The expressions we have just established are valid for each of the blades which compose the rotor. To get the overall effort wrench, it is needed to make a sum of the components for the total number of blades, as shown below.

$$\left[F_x\right]_{rotor} = \sum_{i=1}^{N}\left[F_x\right]_{blade\ i} \qquad\qquad \left[M_x\right]_{rotor} = \sum_{i=1}^{N}\left[M_x\right]_{blade\ i}$$

$$\left[F_y\right]_{rotor} = \sum_{i=1}^{N}\left[F_y\right]_{blade\ i} \qquad\qquad \left[M_y\right]_{rotor} = \sum_{i=1}^{N}\left[M_y\right]_{blade\ i} \qquad (21)$$

$$\left[F_z\right]_{rotor} = \sum_{i=1}^{N}\left[F_z\right]_{blade\ i} \qquad\qquad \left[M_z\right]_{rotor} = \sum_{i=1}^{N}\left[M_z\right]_{blade\ i}$$

Equilibrium equations

The blade is simply articulated in flapping and drag, one can apply the dynamic moment theorem, as indicated in Figure 11.
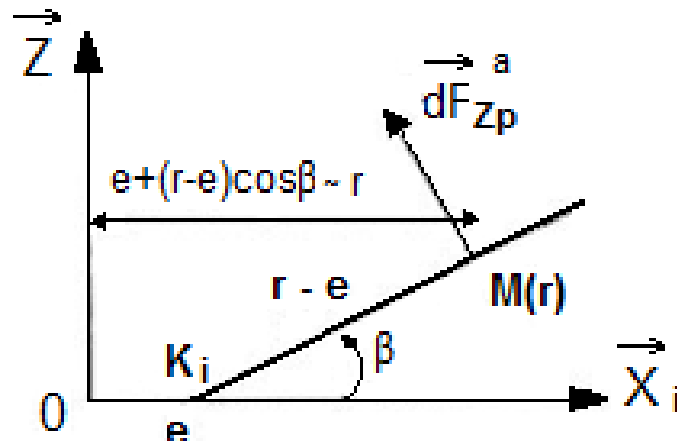
Figure 11: Application of the dynamic moment theorem – adapted from (Jorge, 1992)

$$\vec{\delta}^{K_i}_{blade/Rg} = \vec{M}^{K_i}_{Forces\ ext \to blade}$$

$$Or$$

$$\vec{\delta}^{K_i}_{blade/Rg} = \int_e^R \overrightarrow{K_\iota M}\ \Lambda \overrightarrow{\gamma_M} dm_i$$

with $\overrightarrow{\gamma M}$ t be calculated in what follows.

$$\left[\overrightarrow{K_\iota M}\Lambda\overrightarrow{\gamma_M}\right]_{R_f} = \begin{bmatrix} (r-e)\cos\delta\cos\beta\cos\psi_i - (r-e)\sin\delta\sin\psi_i \\ (r-e)\cos\delta\cos\beta\sin\psi_i - (r-e)\sin\delta\cos\psi_i\ \Lambda \\ (r-e)\cos\delta\sin\beta \end{bmatrix} \begin{bmatrix} \ddot{\gamma}_x \\ \ddot{\gamma}_y \\ \ddot{\gamma}_z \end{bmatrix} \qquad (22)$$

$$\left[\overrightarrow{K_\iota M}\Lambda\overrightarrow{\gamma_M}\right]_{R_f}$$

$$= \begin{bmatrix} [(r-e)\cos\delta\cos\beta\sin\psi_i + (r-e)\sin\delta\cos\psi_i]\ddot{\gamma}_z - (r-e)\cos\delta\sin\beta\ \ddot{\gamma}_y \\[2mm] -[(r-e)\cos\delta\cos\beta\cos\psi_i - (r-e)\sin\delta\sin\psi_i]\ddot{\gamma}_z + (r-e)\cos\delta\sin\beta\ \ddot{\gamma}_x \\[2mm] [(r-e)\cos\delta\cos\beta\cos\psi_i - (r-e)\sin\delta\sin\psi]\ddot{\gamma}_y \\ \quad - [(r-e)\cos\delta\cos\beta\sin\psi_i + (r-e)\sin\delta\cos\psi_i]\ddot{\gamma}_x \end{bmatrix}$$

One can pass to the rotating rotor reference frame through a rotation of (- ψᵢ)

$$\left[\overrightarrow{K_\iota M}\Lambda\overrightarrow{\gamma_M}\right]_{R_f} = \begin{bmatrix} \ddot{\gamma}_z(r-e)\sin\delta + (r-e)\cos\delta\sin\beta\left(\ddot{\gamma}_x\sin\psi_i - \ddot{\gamma}_y\cos\psi_i\right) \\[2mm] -\ddot{\gamma}_z(r-e)\cos\delta\cos\beta + (r-e)\cos\delta\sin\beta\left(\ddot{\gamma}\cos\psi_i - \ddot{\gamma}_y\sin\psi_i\right) \\[2mm] [(r-e)\cos\delta\cos\beta\cos\psi_i - (r-e)\sin\delta\sin\psi]\ddot{\gamma}_y \\ \quad - [(r-e)\cos\delta\cos\beta\sin\psi_i + (r-e)\sin\delta\cos\psi_i]\ddot{\gamma}_x \end{bmatrix}$$

This gives us, for small angles:

$$\left[\overrightarrow{K_\iota M}\Lambda\overrightarrow{\gamma_M}\right]_{R_f}$$

$$= \begin{bmatrix} (r-e)^2\left\{\delta\left[\ddot{\beta}_{t.t}\left(1-\dfrac{\beta^2}{2}\right) - \dot{\beta}_t^{\ 2}\beta - 2\dot{\delta}_t\dot{\beta}_t\delta - \dot{\delta}_t^{\ 2}\beta\right] \right. \\ \left. +\beta\left[2\Omega\dot{\beta}_t\beta + 2\Omega\dot{\delta}_t\delta + \dot{\delta}_t^{\ 2}\delta - \ddot{\delta}_{t.t} + \Omega^2\delta\right]\right\} \\[4mm] (r-e)^2\left\{\left(1-\dfrac{\beta^2}{2}\right)\left[-\ddot{\beta}_{t.t}\left(1-\dfrac{\beta^2}{2}\right) + \dot{\beta}_t^{\ 2}\beta + 2\dot{\delta}_t\dot{\beta}_t\delta + \dot{\delta}_t^{\ 2}\beta\right] + \beta\left[-\ddot{\beta}_{t.t}\beta - \right]\right\} \\ -(r-e)e\beta\Omega^2 \\[4mm] (r-e)^2\left[\left(1-\dfrac{\beta^2}{2}\right)\left(2\Omega\dot{\beta}_t\beta + 2\Omega\dot{\delta}_t\delta + \dot{\delta}_t^{\ 2}\delta - \ddot{\delta}_{t.t} + \Omega^2\delta\right)\right. \\ \left. +\delta\left(-\ddot{\beta}_{t.t}\beta - \dot{\beta}_t^{\ 2}\left(1-\dfrac{\beta^2}{2}\right) - \Omega^2\left(1-\dfrac{\beta^2}{2}\right) - \dot{\delta}_t^{\ 2} - \ddot{\delta}_{t.t}\delta - 2\dot{\delta}_t\Omega\right)\right] + (r-e)e\delta\Omega^2 \end{bmatrix}$$

$$[\overline{K_t \vec{M} \Lambda \overrightarrow{\gamma_M}}]_{R_f} = \begin{bmatrix} (r-e)^2 \left\{ \delta \left[\ddot{\beta}_{t.t} \left(1 - \frac{\beta^2}{2}\right) - \dot{\beta}_t^2 \beta - 2\dot{\delta}_t \dot{\beta}_t \delta \right] + \beta \left[2\Omega \dot{\beta}_t \beta + 2\Omega \dot{\delta}_t \delta - \ddot{\delta}_{t.t} + \Omega^2 \delta \right] \right\} \\[2em] (r-e)^2 \left[-\ddot{\beta}_{t.t} \left(1 - \frac{\beta^4}{4}\right) + 2 \left(1 - \frac{\beta^2}{2}\right) \dot{\delta}_t \dot{\beta}_t \delta + \dot{\delta}_t^2 \frac{\beta^3}{2} - \ddot{\delta}_{t.t} \delta \beta - 2\dot{\delta}_t \beta \Omega \right] \\ -(r-e)\beta\Omega^2 \left(e + (r-e)\left(1 - \frac{\beta^2}{2}\right) \right) \\[2em] (r-e)^2 \left[-2\Omega \dot{\beta}_t \beta \left(1 - \frac{\beta^2}{2}\right) + \Omega \dot{\delta}_t \delta \beta^2 + \dot{\delta}_t^2 \delta \frac{\beta^2}{2} + \ddot{\delta}_{t.t} \left(1 - \frac{\beta^2}{2} + \delta^2\right) \right. \\ \left. +\ddot{\beta}_{t.t} \beta \delta + \dot{\beta}_t^2 \delta \left(1 - \frac{\beta^2}{2}\right) \right] + (r-e)e\delta\Omega^2 \end{bmatrix}$$

Where one can assume: $1 + \beta^4/4 \approx 1$ and $e + (r-e)\cos\beta \approx e + (r-e)(1-\beta^2/2) \approx r$. We will also disregard the triple products of angles about the double products, since β, δ and δ are small angles, what finally gives:

$$[\overline{K_t \vec{M}} \Lambda \overrightarrow{\gamma_M}]_{R_t} = \begin{bmatrix} (r\text{-}e)^2 \left[\delta\ddot{\beta}_{t.t} + \beta\left(-\ddot{\delta}_{t.t} + \Omega^2\delta\right) \right] \\ (r\text{-}e)^2 \left[-\ddot{\beta}_{t.t} - 2\dot{\delta}_t\beta\Omega r \right] - (r\text{-}e)\beta\Omega^2 r \\ (r\text{-}e)^2 \left[-e\Omega\dot{\beta}_t\beta + \ddot{\delta}_{t.t} \right] - (r\text{-}e)\delta\Omega^2 e \end{bmatrix} \tag{23}$$

With $\ddot{\beta}_{t.t} = \Omega^2 \ddot{\beta}$; $\dot{\beta}_t = \Omega^2 \dot{\beta}$; $\ddot{\delta}_{t.t} = \Omega^2 \ddot{\delta}$; $\dot{\delta}_{t.t} = \Omega^2 \dot{\delta}$

Flapping motion equations

The dynamic momentum theorem gives us a projection on the y_i axis:

$$\int_e^R (r-e)^2 \, \Omega^2 \ddot{\beta} \, mdr + \int_e^R 2(r-e)^2 \, \Omega^2 \dot{\delta} \, \beta mdr + \int_e^R (r-e) r\Omega^2 \beta mdr$$

$$= \int_e^R (r-e) \, dF_{zp^a} \simeq \int_e^R (r-e) \, dF_{zi^a} \tag{24}$$

$$\text{with}: \ dm_i = mdr$$

The static moment of the blade is: $ms_i = \int_e^R (r-e) mdr$ .The flapping inertia of the blade

is: $I_\beta = \int_e^R (r-e)^2 mdr$.

Writing: $(r-e) r = r^2 - re = (r-e)^2 + e (r-e)$, we obtain

$$\dot{\beta} + \left[1 + 2\dot{\delta} + \frac{e.ms_i}{I_\beta} \right] \beta = \frac{1}{\Omega^2 I_\beta} \int_e^R (r-e) dF_{zi^a} \tag{25}$$

Introducing the previously obtained expression for $dF_{zi}{}^a$, we have

$$\ddot{\beta} + \left[1 + 2\dot{\delta} + \frac{e.ms_i}{I_\beta}\right]\beta = \frac{\rho ac R^2}{2I_\beta}\int_e^R (r-e)\left[\theta\left(\frac{r}{R} + \mu(sin\,\psi_i + \delta\,cos\,\psi_i)\right)\right.$$

$$\left. - \left(\frac{r}{R} + \mu(sin\,\psi_i + \delta\,cos\,\psi_i)\right)\left(\lambda + \frac{r\dot{\beta}}{R} - \frac{e}{R}\dot{\beta} + \beta\mu\,cos\,\psi_i\right)\right]dr$$

$$= \frac{\rho ac\,R^2}{2I_\beta}\int_e^R (r-e)\left[\left(\theta_{con} + \frac{r}{R}\theta_{tw}\right)\left(\frac{r}{R} + \mu(sin\,\psi_i + \delta\,cos\,\psi_i)\right)^2\right.$$

$$- \left(\frac{r}{R} + \mu(sin\,\psi_i + \delta\,cos\,\psi_i)\right)\left(\lambda_0 + \lambda_{1c}\frac{r}{R}cos\,\psi_i + \lambda_{1s}\frac{r}{R}sin\,\psi_i + \frac{r\dot{\beta}}{R} - \frac{e\dot{\beta}}{R}\right.$$

$$\left.\left. + \beta\mu\,cos\,\psi_i\right)\right]dr$$

And, after calculating the integral:

$$\ddot{\beta} + \left[1 + 2\dot{\delta} + \frac{e.ms_i}{I_\beta}\right]\beta = \frac{\rho ace}{2I_\beta}R^2\left\{\left[\frac{R^3 - e^3}{3R^2} + (R-e)\mu^2(sin\,\psi_i + \delta\,cos\,\psi_i)^2\right.\right.$$

$$\left. + \frac{R^2 - e^2}{R}\mu(sin\,\psi_i + \delta\,cos\,\psi_i)\right]\theta_{con}$$

$$+ \left[\frac{R^4 - e^4}{4R^3} + \frac{2}{3}\mu\frac{R^3 - e^3}{R^2}(sin\,\psi_i + \delta\,cos\,\psi_i)\right.$$

$$\left. + \frac{R^2 - e^2}{2R}\mu^2(sin\,\psi_i + \delta\,cos\,\psi_i)^2\right]\theta_{tw}$$

$$- \left[\frac{R^2 - e^2}{2R} + (R-e)\mu(sin\,\psi_i + \delta\,cos\,\psi_i)\right]$$

$$\left(\lambda_0 + \mu\beta\,cos\,\psi_i - \frac{e}{R}\dot{\beta}\right)$$

$$- \left[\frac{R^3 - e^3}{3R^2} + \frac{R^2 - e^2}{2R}\mu(sin\,\psi_i + \delta\,cos\,\psi_i)\right]$$

$$\left(\lambda_0 + \lambda_{1c}\,cos\,\psi_i + \lambda_{1s}\,sin\,\psi_i + \dot{\beta}\right)\right\}$$

$$+ \frac{\rho ac}{2I_\beta}R^2\left\{\left[\frac{R^4 - e^4}{4R^3} + \frac{R^2 - e^2}{2}\mu^2(sin\,\psi_i + \delta\,cos\,\psi_i)^2\right.\right.$$

$$\left. + \frac{2(R^3 - e^3)}{3R}\mu(sin\,\psi_i + \delta\,cos\,\psi_i)\right]\theta_{con}$$

$$+ \left[\frac{R^5 - e^5}{5R^3} + \frac{R^3 - e^3}{3R^2}\mu^2(sin\,\psi_i + \delta\,cos\,\psi_i)^2\right.$$

$$\left. + \frac{R^4 - e^4}{2R^2}\mu(sin\,\psi_i + \delta\,cos\,\psi_i)\right]\theta_{tw}$$

$$- \left[\frac{R^3 - e^3}{3R^2} + \frac{R^2 - e^2}{2}\mu(sin\,\psi_i + \delta\,cos\,\psi_i)\right]\left(\lambda_0 + \mu\beta\,cos\,\psi_i - \frac{e}{R}\beta\right)$$

$$- \left[\frac{R^4 - e^4}{4R^2} + \frac{R^3 - e^3}{3R^2}\mu(sin\,\psi_i + \delta\,cos\,\psi_i)\right]\left(\lambda_0 + \lambda_{1c}\,cos\,\psi_i + \lambda_{1s}\,sin\,\psi_i + \dot{\beta}\right)\right\}$$

Using the simplifications $R^2 - e^2 \approx R^2$; $R^3 - e^3 \approx R^3$; $R^4 - e^4 \approx R^4$; $R^5 - e^5 \approx R^5$ and the Coleman Transformation (Coleman & Feingold, 1957) ($\theta_{con} = \theta_0 + \theta_{1c}\cos\psi_i + \theta_{1s}\sin\psi_i$, $\beta = \beta_0 + \beta_{1c}\cos\psi_i + \beta_{1s}\sin\psi_i$, and $\delta = \delta_0 + \delta_{1c}\cos\psi_i + \delta_{1s}\sin\psi_i$), leads to:

$$\ddot{\beta} + \left[1 + 2\dot{\delta} + \frac{e.ms_i}{I_\beta}\right]\beta = \frac{\rho ace}{2I_\beta}R^2 \left\{\left[\frac{R}{3} + (R-e)\mu^2(\sin\psi_i + \delta\cos\psi_i)^2\right.\right.$$

$$\left. + R\mu(\sin\psi_i + \delta\cos\psi_i)\right](\theta_0 + \theta_{1c}\cos\psi_i + \theta_{1s}\sin\psi_i)$$

$$+ \left[\frac{R}{4} + 2\mu\frac{R}{3}(\sin\psi_i + \delta\cos\psi_i) + \frac{R}{2}\mu^2(\sin\psi_i + \delta\cos\psi_i)^2\right]\theta_{tw}$$

$$- \left[\frac{R}{2} + (R-e)\mu(\sin\psi_i + \delta\cos\psi_i)\right]\left(\lambda_0 + \mu\beta\cos\psi_i - \frac{e}{R}\dot{\beta}\right)$$

$$- \left[\frac{R}{3} + \frac{R}{2}\mu(\sin\psi_i + \delta\cos\psi_i)\right]\left(\lambda_0 + \lambda_{1c}\cos\psi_i + \lambda_{1s}\sin\psi_i + \dot{\beta}\right)\right\} \qquad (26)$$

$$+ \frac{\rho ac}{2I_\beta}R^2 \left\{\left[\frac{R^2}{4} + \frac{R^2}{2}\mu^2(\sin\psi_i + \delta\cos\psi_i)^2 + \frac{2}{3}R^2\mu(\sin\psi_i + \delta\cos\psi_i)\right](\theta_0 + \theta_{1c}\cos\psi_i + \theta_{1s}\sin\psi_i)\right.$$

$$+ \left[\frac{R^2}{5} + \frac{R^2}{3}\mu^2(\sin\psi_i + \delta\cos\psi_i)^2 + \frac{R^2}{2}\mu(\sin\psi_i + \delta\cos\psi_i)\right]\theta_{tw}$$

$$- \left[\frac{R^2}{3} + \frac{R^2}{2}\mu(\sin\psi_i + \delta\cos\psi_i)\right]\left(\lambda_0 + \mu\beta\cos\psi_i - \frac{e}{R}\dot{\beta}\right)$$

$$- \left[\frac{R^2}{4} + \frac{R^2}{3}\mu(\sin\psi_i + \delta\cos\psi_i)\right]\left(\lambda_0 + \lambda_{1c}\cos\psi_i + \lambda_{1s}\sin\psi_i + \dot{\beta}\right)\right\}$$

To decouple the different parameters involved in this equation, the following operators will be applied to the flapping equation: $\frac{1}{2\pi}\int_0^{2\pi}(...)d\psi$, $\frac{1}{2\pi}\int_0^{2\pi}(...)\cos\psi d\psi$ and $\frac{1}{2\pi}\int_0^{2\pi}(...)\sin\psi d\psi$. Disregarding the double products of angles concerning the angles themselves, the influence of the drag angle on the flapping motion will be disregarded. After some transformations and intermediate calculations, the following three equations are then obtained:

$$*\left[1 + \frac{e.m_{si}}{I_\beta}\right]\beta_0 = \frac{\rho ace}{2I_\beta}R^2\left[-e\left\{\frac{R-e}{2}\mu^2\theta_0 + \frac{R}{3}\theta_0 + \frac{R}{4}\theta_{tw} + \frac{R}{2}\left[\mu\theta_{1s} + \frac{\mu^2}{2}\theta_{tw} - \lambda_0 + \frac{\mu}{2}\beta_{1c} - \frac{\mu}{2}\lambda_{1s}\right]\right.\right.$$

$$\left. - \frac{\mu(r-e)^e}{2R}\beta_{1c}\right\} + \frac{R^2}{4}\theta_0 + \frac{R^2}{4}\mu^2\theta_0 + \frac{R^2}{3}\mu\theta_{1s} + \frac{R^2}{5}\theta_{tw} + \frac{R^2}{6}\mu^2\theta_{tw}$$

$$\left. - \frac{R^2}{3}\lambda_0 - \frac{R^2}{6}\mu\lambda_{1s}\right]$$

$$*\frac{e.m_{si}}{I_\beta}\beta_{1c} = \frac{\rho ac}{2I_\beta}R^2\left[-e\left\{\frac{R}{3}\theta_{1c} + \frac{R}{2}\mu\beta_0 + \frac{R-e}{4}\mu^2\beta_{1s} + \frac{R-e}{4}\mu^2\theta_{1c} - \frac{R}{3}\lambda_{1c} - \frac{R}{3}\beta_{1s} + \frac{e\beta_{1s}}{2}\right\}\right.$$

$$\left. - \frac{R^2}{3}\mu\beta_0 + \frac{R^2}{8}\mu^2\theta_{1c} - \frac{R^2}{4}\lambda_{1c} + \frac{Re}{3}\beta_{1s} + \frac{R^2}{4}\theta_{1c} - \frac{R^2}{4}\beta_{1s} - \frac{R^2}{8}\mu^2\beta_{1s}\right]$$

$$* \frac{e.m_{si}}{I_\beta} \beta_{si} = \frac{\rho ac}{2I_\beta} R^2 \left[-e \left\{ \frac{R}{3} \theta_{1s} + \frac{3(R-e)}{4} \mu^2 \theta_{1s} + R\mu\theta_0 + \frac{2R}{3}\mu\theta_{tw} - (R-e)\mu\lambda_0 \right. \right.$$

$$\left. - \frac{R-e}{4}\mu^2\beta_{1c} - \frac{e\beta_{1c}}{2} - \frac{R}{3}\lambda_{1s} + \frac{R}{3}\beta_{1c} \right\}$$

$$+ \frac{R^2}{4}\theta_{1s} + \frac{3R^2}{8}\mu^2\theta_{1s} + \frac{2R^2}{3}\mu\theta_0 + \frac{R^2}{2}\mu\theta_{tw} + \frac{R^2}{2}\mu\lambda_0 - \frac{R^2}{8}\mu^2\beta_{1c}$$

$$\left. - \frac{Re}{3}\beta_{1c} - \frac{R^2}{4}\lambda_{1s} + \frac{R^2}{4}\beta_{1c} \right]$$

Introducing the Lock Number: $\gamma = \rho ac \dfrac{R^4}{I_\beta}$, one obtains:

$$* \left[1 + \frac{e.m_{si}}{I_\beta} \right] \beta_0 = \frac{\gamma}{R^2} \left[\theta_{tw} \left[\frac{4R^2 - 5eR}{40} \right] - \left[\frac{R^2 - 2e(R-e)}{8R} e\mu \right] \beta_{1c} + \left(\mu^2\theta_{tw} + 2\mu\theta_{1s} - 2\lambda_0 - \mu\lambda_{1s} \right) \right.$$

$$\left. \left\{ \frac{2R^2 - 3eR}{24} \right\} + \theta_0 \left\{ \frac{R^2 - 2e(R-e)}{8}\mu^2 + \frac{3R^2 - 4eR}{24} \right\} \right]$$

$$* \frac{e.m_{si}}{I_\beta} \beta_{1c} = \frac{\gamma}{R^2} \left[\left(\theta_{1c} - \beta_{1s} \right) \left\{ \frac{R^2 - 2e(R-e)}{16}\mu^2 \right\} + \beta_{1s} \left(\frac{4eR - 6e^2}{24} \right) + \beta_0 \left\{ \frac{-2R^2 + 3eR}{12}\mu \right\} \right.$$

$$\left. + \left(\theta_{1c} - \beta_{1s} - \lambda_{1c} \right) \left\{ \frac{3R^2 - 4eR}{24} \right\} \right] \quad (27)$$

$$* \frac{e.m_{si}}{I_\beta} \beta_{si} = \frac{\gamma}{R^2} \left[\left(2\mu\theta_{tw} + \theta_{1s} + \beta_{1c} - \lambda_{1s} \right) \left\{ \frac{3R^2 - 4eR}{24} \right\} + \theta_0 \left\{ \frac{2R^2 - 3eR}{6}\mu \right\} + \beta_{1c} \left[\frac{6e^2 - 4eR}{24} \right] \right.$$

$$\left. + \left(3\mu\theta_{1s} - \mu\beta_{1c} - 4\lambda_0 \right) \left\{ \frac{R^2 - 4e(R-e)}{16}\mu \right\} \right]$$

Drag motion equations

The motion of interest is now around the drag axis, that is, $\vec{Z}_p \equiv \vec{Z}'_p$. But to have the reference frame, without changing it, one must apply the theorem in the reference frame R_t, for the component around Z_i (given that K_i is a joint, so it is articulate), assuming that the restitution moment due to the frequency adapter is also along the Z_i axis, as it was done previously for the calculation of M_z. The dynamic momentum theorem gives us, in projection onto the Z_i axis:

$$\int_e^R (r-e)^2 \left(-2\Omega\dot{\beta}_t \beta + \ddot{\delta}_{t.t} \right) m dr + \int_e^R (r-e)\delta\Omega^2 e \, m dr \quad (28)$$

$$= \int_e^R (r-e) dF_{yi^a} \cos\beta - K_\delta\delta - C_\delta \dot{\delta}_t \simeq \int_e^R (r-e) dF_{yi^a} - K_\delta\delta - C_\delta \dot{\delta}_t$$

And as $I_\beta = I_\delta = \int_e^R (r-e)^2 m dr$, we have, then:

$$\ddot{\delta} + \frac{C_\delta}{\Omega I_\beta}\dot{\delta} + \left(\frac{e.m_{si}}{I_\beta} + \frac{K_\delta}{\Omega^2 I_\beta} \right)\delta = 2\beta\dot{\beta} + \frac{1}{\Omega^2 I_\beta} \int_e^R (r-e) dF_{yi^a}$$

Introducing the previously obtained expression of dF_{yi}^a, we have:

$$\ddot{\delta}+\frac{C_{\delta}}{\Omega I_{\beta}}\dot{\delta}+\left(\frac{e.m_{si}}{I_{\beta}}+\frac{K_{\delta}}{\Omega^2 I_{\beta}}\right)\delta=2\beta\dot{\beta}+\frac{\rho ac(\Omega R)^2}{\Omega^2 I_{\beta}}\int_e^R(R-e)\left\{\frac{1}{2}\left[2\theta\left(x-\mu(\sin\psi_i+\delta)\right)\right.\right.$$

$$\left(\lambda+(x-xe)\dot{\beta}+\beta\mu\cos\psi_i\right)-\left(x-\mu(\sin\psi_i+\delta)\right)^2\theta^2 \tag{29}$$

$$\left.\left.-\left(\lambda+(x-xe)\dot{\beta}+\beta\mu\cos\psi_i\right)^2\right]-\frac{C_{d0}}{2a}\left(x-\mu(\sin\psi_i+\delta)\right)^2\right\}dr$$

After calculating the integral, we have:

$$\ddot{\delta}+\frac{C\delta}{\Omega I_{\beta}}\dot{\delta}+\left(\frac{e.m_{si}}{I_{\beta}}+\frac{K_{\delta}}{\Omega^2 I_{\beta}}\right)\delta$$

$$=2\beta\dot{\beta}+\frac{\rho acR^2}{I_{\beta}}\left[\left(\lambda_0+\mu\beta\cos\psi_i-\frac{e}{R}\dot{\beta}\right)\left[\mu(\sin\psi_i+\delta\cos\psi_i)\theta_{con}\left(-\frac{R^2-e^2}{2}+e(R-e)\right)\right.\right.$$

$$+\left(\mu(\sin\psi_i+\delta\cos\psi_i)\theta_{tw}+\theta_{con}\right)\left(-\frac{R^3-e^3}{3R}+e\frac{R^2-e^2}{2R}\right)+\left(\lambda_{1c}\cos\psi_i+\lambda_{1s}\sin\psi_i+\dot{\beta}\right)$$

$$\left.\left(-\frac{R^3-e^3}{3R}+e\frac{R^2-e^2}{2R}\right)-\theta_{tw}\left(\frac{R^4-e^4}{4R^2}+e\frac{R^3-e^3}{3R^2}\right)\right]\right]+\left(\lambda_{1c}\cos\psi_i+\lambda_{1s}\sin\psi_i+\dot{\beta}\right)$$

$$\left[\mu(\sin\psi_i+\delta\cos\psi_i)\theta_{con}\left(-\frac{R^3-e^3}{3R}+e\frac{R^2-e^2}{2R}\right)+\left(\mu(\sin\psi_i+\delta\cos\psi_i)\theta_{tw}+\theta_{con}\right)\right.$$

$$\left(\frac{R^4-e^4}{4R^2}+e\frac{R^3-e^3}{3R^2}\right)-\theta_{tw}\left(\frac{R^5-e^5}{5R^3}-e\frac{R^4-e^4}{4R^3}\right)\right]+\left[\frac{\theta_{con}^2}{2}-\frac{C_{d0}}{2a}\right]\left[\left(\frac{R^4-e^4}{4R^2}-e\frac{R^3-e^3}{3R^2}\right)\right.$$

$$\left.\left.+\mu(\sin\psi_i+\delta\cos\psi_i)\left(\frac{2(R^3-e^3)}{3R}-e\frac{R^2-e^2}{R}\right)+\mu^2(\sin\psi_i+\delta\cos\psi_i)^2\left(\frac{R^2-e^2}{2}-e(R-e)\right)\right]\right.$$

$$+\theta_{tw}\theta_{con}\left[\left(\frac{R^5-e^5}{5R^3}-e\frac{R^4-e^4}{4R^3}\right)+\mu(\sin\psi_i+\delta\cos\psi_i)\left(\frac{R^4-e^4}{2R^2}+e\frac{2(R^3-e^3)}{3R^2}\right)\right.$$

$$\left.+\mu^2(\sin\psi_i+\delta\cos\psi_i)^2\left(\frac{R^3-e^3}{3R}-e\frac{R^2-e^2}{2R}\right)\right]+\frac{\theta_{tw}^2}{2}\left[\left(\frac{R^6-e^6}{6R^4}-e\frac{R^5-e^5}{5R^4}\right)\right.$$

$$\left.+\mu(\sin\psi_i+\delta\cos\psi_i)\left(\frac{2(R^5-e^5)}{5R^3}-e\frac{R^4-e^4}{2R^3}\right)+\mu^2(\sin\psi_i+\delta\cos\psi_i)^2\left(\frac{R^4-e^4}{4R^2}-e\frac{R^3-e^3}{3R^2}\right)\right]$$

$$+\left(\lambda_0+\beta\mu\cos\psi_i-\frac{e}{R}\dot{\beta}\right)^2\left(\frac{R^2-e^2}{4}-e\frac{(R-e)}{2}\right)+\frac{1}{2}\left(\lambda_{1c}\cos\psi_i+\lambda_{1s}\sin\psi_i+\dot{\beta}\right)^2$$

$$\left.\left(\frac{R^4-e^4}{4R^2}-e\frac{R^3-e^3}{3R^2}\right)\right]$$

Making the assumptions: $R^2 - e^2 \approx R^2$; $R^3 - e^3 \approx R^3$; $R^4 - e^4 \approx R^4$; $R^5 - e^5 \approx R^5$; $R^6 - e^6 \approx R^6$; $R-2eR+2e^2 \approx R-2eR = R(1-2e)$, leads to:

$$\ddot{\delta} + \frac{C\delta}{\Omega I_\beta}\dot{\delta} + \left(\frac{e.m_{si}}{I_\beta} + \frac{K_\delta}{\Omega^2 I_\beta}\right)\delta$$

$$= 2\beta\dot{\beta} + \frac{\rho acR^2}{I_\beta}\left[\left(\lambda_0 + \mu\beta\cos\psi_i - \frac{e}{R}\dot{\beta}\right)\left[\mu(\sin\psi_i + \delta\cos\psi_i)\theta_{con}\frac{R}{2}(R-2e)\right.\right.$$

$$-(\mu(\sin\psi_i + \delta\cos\psi_i)\theta_{tw} + \theta_{con})\frac{R}{6}(2R-3e) + \left(\lambda_{1c}\cos\psi_i + \lambda_{1s}\sin\psi_i + \dot{\beta}\right)\frac{R}{6}(2R-3e)$$

$$-\theta_{tw}\frac{R}{12}(3R-4e)\Big] + \left(\lambda_{1c}\cos\psi_i + \lambda_{1s}\sin\psi_i + \dot{\beta}\right)\left[\mu(\sin\psi_i + \delta\cos\psi_i)\theta_{con}\frac{R}{6}(2R-3e)\right.$$

$$-(\mu(\sin\psi_i + \delta\cos\psi_i)\theta_{tw} + \theta_{con})\frac{R}{12}(3R-4e) - \theta_{tw}\frac{R}{20}(4R-5e)\Big]$$

$$+\left[\frac{\theta_{con}^2}{2} - \frac{C_{d0}}{2a}\right]\left[\frac{R}{12}(3R-4e) + \mu(\sin\psi_i + \delta\cos\psi_i)\frac{R}{3}(2R-3e)\right.$$

$$+\mu^2(\sin\psi_i + \delta\cos\psi_i)^2\frac{R}{2}(2R-3e)\Big] + \theta_{tw}\theta_{con}\left[\frac{R}{20}(4R-5e) + \mu(\sin\psi_i + \delta\cos\psi_i)\frac{R}{6}(3R-4e)\right.$$

$$+\mu^2(\sin\psi_i + \delta\cos\psi_i)^2\frac{R}{6}(2R-3e)\Big] + \frac{\theta_{tw}^2}{2}\left[\frac{R}{30}(5R-6e) + \mu(\sin\psi_i + \delta\cos\psi_i)\frac{R}{10}(4R-5e)\right.$$

$$+\mu^2(\sin\psi_i + \delta\cos\psi_i)^2\frac{R}{12}(3R-4e)\Big] + \left(\lambda_0 + \beta\mu\cos\psi_i - \frac{e}{R}\dot{\beta}\right)^2\frac{R}{2}(R-2e)$$

$$+\frac{1}{2}\left(\lambda_{1c}\cos\psi_i + \lambda_{1s}\sin\psi_i + \dot{\beta}\right)^2\frac{R}{12}(3R-4e)\Big]$$

with

$$\begin{aligned}
\theta_{con} &= \theta_0 + \theta_{1c}\cos\psi_i + \theta_{1s}\sin\psi_i \\
\beta &= \beta_0 + \beta_{1c}\cos\psi_i + \beta_{1s}\sin\psi_i \\
\dot{\beta} &= -\beta_{1c}\sin\psi_i + \beta_{1s}\cos\psi_i \\
\delta &= \delta_0 + \delta_{1c}\cos\psi_i + \delta_{1s}\sin\psi_i \\
\dot{\delta} &= -\delta_{1c}\sin\psi_i + \delta_{1s}\cos\psi_i \\
\ddot{\delta} &= -\delta_{1c}\cos\psi_i - \delta_{1s}\sin\psi_i
\end{aligned} \tag{30}$$

Next, we will disregard the terms, of triple products of angles (eg: $\theta_0\,\beta_{1c}\,\delta_{1s}= 0$, etc.) concerning the double products, since θ, β and δ are small angles.

Applying the operators: $\frac{1}{2\pi}\int_0^{2\pi}(\ldots)d\psi$, $\frac{1}{2\pi}\int_0^{2\pi}(\ldots)cos\psi d\psi$ and $\frac{1}{2\pi}\int_0^{2\pi}(\ldots)sin\psi d\psi$ leads to (after some intermediate calculations):

$$
\left(\frac{e.m_{si}}{I_\beta}+\frac{K\delta}{\Omega^2 I_\beta}\right)\delta_0
$$

$$
=\frac{\rho acR^2}{I_\beta}\left[\frac{R}{2}(R-2e)\left[\lambda_0^2-\frac{\mu\theta_0}{2}\frac{e}{R}\beta_{1c}\frac{\mu^2}{2}\left(\frac{\theta_0^2}{2}-\frac{C_{d0}}{2a}\right)+\frac{e^2}{2R^2}\left(\beta_{1c}^2+\beta_{1s}^2\right)+\frac{\mu\theta_{1s}}{2}\lambda_0+\lambda_0\beta_{1c}\mu\right.\right.
$$

$$
+\mu\frac{e}{R}\beta_0\beta_{1s}+\frac{\mu^2}{2}\beta_0^2+\frac{\theta_{1c}^2\mu^2}{16}+\frac{\mu^2\beta_{1s}^2}{8}+\frac{3\theta_{1s}^2\mu^2}{16}+\frac{3\mu^2\beta_{1c}^2}{8}-\frac{\mu^2}{8}\left(\beta_{1c}\theta_{1s}+\beta_{1s}\theta_{1c}\right)+\frac{R}{6}(2R-3e)
$$

$$
-\lambda_0\theta_0+\frac{e}{R}\frac{\beta_{1c}}{2}\left(-\mu\theta_{tw}-\theta_{1s}+\lambda_{1s}-\beta_{1c}\right)-\frac{\mu\theta_0}{2}\left(\lambda_{1s}-\beta_{1c}\right)+\mu\theta_0\theta_{1s}+\frac{\mu^2}{2}\theta_{tw}\theta_0
$$

$$
+\frac{\mu\beta_0-\frac{e}{R}\beta_{1s}}{2}\left(-\theta_{1c}+\lambda_{1c}+\beta_{1s}\right)-\frac{\mu}{2}\theta_0\beta_{1c}\left.\right]+\frac{R}{12}(3R-4e)\left[-\lambda_0\theta_{tw}+\left(\frac{\theta_0^2}{2}-\frac{C_{d0}}{2a}\right)\right.
$$

$$
+\frac{(\lambda_{1s}-\beta_{1c})}{2}\left(\mu\theta_{tw}+\theta_{1s}\right)+\frac{\theta_{1s}^2}{4}+\mu\theta_{tw}\theta_{1s}+\frac{\mu^2\theta_{tw}^2}{4}+\frac{\lambda_{1s}^2}{4}-\frac{\lambda_{1s}\beta_{1c}}{2}+\frac{\beta_{1c}^2}{4}-\frac{\theta_{1c}}{2}\left(\lambda_{1c}-\beta_{1c}\right)+\frac{\theta_{1c}^2}{4}
$$

$$
+\frac{\lambda_{1c}^2}{4}+\frac{\lambda_{1c}\beta_{1s}}{2}+\frac{\beta_{1s}^2}{4}-\mu\frac{\theta_{tw}}{2}\beta_{1c}\left.\right]+\frac{R}{20}(4R-5e)\theta_{tw}\theta_0+\frac{R}{30}(5R-6e)\frac{\theta_{tw}^2}{2}\left.\right]
$$

(31)

$$
\frac{1}{2}\left[-\delta_{1c}+\frac{C_\delta}{\Omega I_\beta}\delta_{1s}+\left(\frac{e.m_{si}}{I_\beta}+\frac{K_\delta}{\Omega^2 I_\beta}\right)\delta_{1c}-2\beta_0\beta_{1s}\right]
$$

$$
=\frac{\rho acR^2}{I_\beta}\left[\frac{R}{2}(R-2e)\left[\mu\lambda_0\beta_0-\frac{e}{R}\lambda_0\beta_{1s}-\frac{\mu\theta_{1c}}{8}\frac{e}{R}\beta_{1c}-\frac{\mu\theta_{1s}}{8}\left(\mu\beta_0-\frac{e}{R}\beta_{1s}\right)+\frac{\mu^2}{8}\theta_0\theta_{1c}\right.\right.
$$

$$
+\frac{\mu}{4}\frac{e}{R}\beta_{1s}\beta_{1c}-\frac{3}{4}\mu\frac{e}{R}\beta_{1c}\beta_{1s}+\frac{3}{4}\mu^2\beta_0\beta_{1c}-\frac{\mu^2}{8}\theta_0\beta_{1s}\left.\right]+\frac{R}{6}(2R-3e)\left[-\frac{\theta_0}{2}\left(\mu\beta_0-\frac{e}{R}\beta_{1s}\right)\right.
$$

$$
+\frac{\lambda_0}{2}\left(-\theta_{1c}+\lambda_{1c}+\beta_{1s}\right)-\frac{\mu\theta_{1c}}{8}\left(\lambda_{1s}-\beta_{1c}\right)-\frac{\mu\theta_{1s}}{8}\left(\lambda_{1c}+\beta_{1s}\right)+\frac{\mu}{4}\theta_{1c}\theta_{1s}+\frac{\mu^2}{8}\theta_{tw}\theta_{1c}
$$

$$
+\frac{3}{4}\mu\beta_{1c}\left(-\theta_{1c}+\lambda_{1c}+\beta_{1s}\right)+\mu\frac{\beta_{1s}}{8}\left(-\mu\theta_{tw}-\theta_{1s}+\lambda_{1s}+\beta_{1c}\right)\left.\right]+\frac{R}{12}(3R-4e)\left[-\frac{\theta_{tw}}{2}\left(\mu\beta_0-\frac{e}{R}\beta_{1s}\right)\right.
$$

$$
-\frac{\theta_0}{2}\left(\lambda_{1c}+\beta_{1s}\right)+\frac{\theta_0\theta_{1c}}{2}\left.\right]+\frac{R}{20}(4R-5e)\left[-\frac{\theta_{tw}}{2}\left(\lambda_{1s}+\beta_{1s}\right)+\frac{\theta_{tw}\theta_{1c}}{2}\right]\left.\right]\left.\right]
$$

(32)

$$
\frac{1}{2}\left[-\delta_{1s}+\frac{C_\delta}{\Omega I_\beta}\delta_{1c}+\left(\frac{e.m_{si}}{I_\beta}+\frac{K_\delta}{\Omega^2 I_\beta}\right)\delta_{1s}-2\beta_0\beta_{1c}\right]
$$

$$
=\frac{\rho acR^2}{I_\beta}\left[\frac{R}{2}(R-2e)\left[\frac{\mu\theta_0}{2}\lambda_0+\frac{e}{R}\lambda_0\beta_{1c}-\frac{3\mu\theta_{1s}}{8}\frac{e}{R}\beta_{1c}-\frac{3\mu^2}{8}\theta_0\theta_{1s}-\frac{\mu^2}{8}\theta_0\beta_{1c}\right.\right.
$$

$$
-\frac{\mu\theta_{1c}}{8}\left(\mu\beta_0-\frac{e}{R}\beta_{1s}\right)+\frac{\mu}{4}\frac{e}{R}\beta_{1c}^2-\frac{\mu}{4}\frac{e}{R}\beta_{1s}^2+\frac{\mu^2}{4}\beta_0\beta_{1s}\left.\right]+\frac{R}{6}(2R-3e)\left[-\frac{\theta_0}{2}\frac{e}{R}\beta_{1c}\right.
$$

$$
+\frac{\lambda_0}{2}\left(-\mu\theta_{tw}-\theta_{1s}+\lambda_{1s}+\beta_{1c}\right)+\mu\left(\frac{\theta_0^2}{2}-\frac{C_{d0}}{2a}\right)-\frac{3\mu\theta_{1s}}{8}\left(\lambda_{1s}-\beta_{1c}\right)+\frac{3\mu\theta_{1s}^2}{8}+\frac{3\mu^2\theta_{tw}}{8}\theta_{1s}
$$

$$
-\frac{\mu\theta_{1c}}{8}\left(\lambda_{1c}+\beta_{1s}\right)+\frac{\mu\theta_{1c}^2}{8}+\frac{\mu\beta_{1c}}{8}\left(-\mu\theta_{tw}-\theta_{1s}+\lambda_{1s}-\beta_{1c}\right)+\frac{\mu\beta_{1s}}{8}\left(-\theta_{1c}+\lambda_{1c}+\beta_{1s}\right)\left.\right]
$$

$$
+\frac{R}{12}(3R-4e)\left[-\frac{\theta_{tw}}{2}\frac{e}{R}\beta_{1c}-\frac{\theta_0}{2}\left(\lambda_{1s}+\beta_{1c}\right)+\frac{\theta_0\theta_{1s}}{2}+\mu\theta_{tw}\theta_0\right]
$$

$$
+\frac{R}{20}(4R-5e)\left[-\frac{\theta_{tw}}{2}\left(\lambda_{1s}-\beta_{1c}\right)+\frac{\theta_{tw}\theta_{1s}}{2}+\frac{\mu\theta_{tw}^2}{2}\right]\left.\right]\left.\right]
$$

(33)

There are, therefore, three equations that give us $\delta\left(\delta_0,\delta_{1c}\ e\ \delta_{1s}\right)$ a function of the setting of the pitch $\theta\left(\theta_0,\theta_{1c}\ e\ \theta_{1s}\right)$ and the flapping $\beta\left(\beta_0,\beta_{1c}\ e\ \beta_{1s}\right)$.

Calculation of Fuselage Balance and Pitch Setting for the Isotropic Rotor Case

We will return to the expressions of the wrench of the external forces calculated previously, and then apply them to the case of a rotor composed of N strictly identical blades. In this hypothesis, we can apply the Coleman Transformation to our expressions. Thus, we will obtain a linear formulation: in effect, each component will be written in the form of a linear combination of the flight parameters. Next, let's disregard: (i) the triple products of angles concerning the double products in the expressions of Fx, Fy, Mz; and (ii) the double products of angles about the angles themselves in the expressions of Fz, Mx, My.

Application of the Coleman Transformation

The set of coefficients necessary for the calculations is explained in the reference (Coleman & Feingold, 1957). After some intermediate calculations, the components of the wrench of efforts are then obtained as:

$$\frac{\{F_x\}_{rotor}}{NS} = \frac{R-e}{16}\left[-8\frac{e}{R}\lambda_0\beta_{1c} + \mu\left(\frac{e}{R}\left(-\beta_{1c}^2 - 2\beta_{1s}\theta_{1c} + 6\beta_{1c}\theta_{1s} + \beta_{1s}^2\right) + 8\lambda_0\theta_0\right)\right.$$

$$\left. + \mu^2\left(\beta_0\theta_{1c} - 6\theta_0\theta_{1s} + \beta_{1c}\theta_0 + \frac{C_{d0}}{a}\delta_{1c}\right)\right] + \frac{R}{8}\left[2\frac{e}{R}\beta_{1c}\theta_0 + \lambda_0\left(3\beta_{1c} - 2\lambda_{1s} + 2\theta_{1s}\right)\right.$$

$$\left. - \beta_0\beta_{1s}\frac{e}{R} + \theta_{tw}\left(-\theta_{1s} + \lambda_{1s} - \beta_{1c}\right) + \mu\left(2\frac{C_{d0}}{a} - 2\theta_0^2 + \beta_0^2 - \theta_{tw}^2 + 2\lambda_0\theta_{tw}\right)\right]$$

$$+ \frac{R}{12}\left[-\beta_0\theta_{1c} + \frac{C_{d0}}{a}\delta_{1c} + 2\frac{e}{R}\beta_{1c}\theta_{tw} + \theta_0\left(-3\beta_{1c} - 4\mu\theta_{tw} + 2\lambda_{1s} - 2\theta_{1s}\right) + \beta_0\left(\lambda_{1c} + \beta_{1s}\right)\right]$$

$$+ \frac{R}{32}\left[-2\beta_{1c}\theta_{tw} + \mu\left(-\beta_{1c}\lambda_{1s} - 2\theta_{1c}^2 + 4\beta_{1c}^2 - \beta_{1s}\lambda_{1c} + 6\theta_{1s}\left(\lambda_{1s} - \beta_{1c}\right) - 6\theta_{1s}^2 + 2\theta_{1c}\left(\lambda_{1c} - \beta_{1s}\right)\right)\right.$$

$$\left. + \mu^2\theta_{tw}\left(\beta_{1c} - 6\theta_{1s}\right)\right] + \frac{m_{si}\Omega^2}{S}\frac{\delta_{1s}\delta_0}{2}$$

$$\frac{\{F_y\}_{rotor}}{NS} = \frac{R-e}{16}\left[-8\frac{e}{R}\lambda_0\beta_{1s} + \mu\left(\frac{e}{R}\left(-2\beta_{1c}\beta_{1s} + 2\theta_{1s}\beta_{1s} - 2\theta_{1c}\beta_{1c}\right) + 12\lambda_0\beta_0\right)\right.$$

$$\left. + \mu^2\left(\beta_0\left(5\theta_{1s} + 8\beta_{1c}\right) + 3\frac{C_{d0}}{a}\delta_{1s} + \theta_0\left(-5\beta_{1s} + 2\theta_{1c}\right)\right)\right] + \frac{R}{8}\left[2\frac{e}{R}\beta_{1s}\theta_0 + \frac{e}{R}\beta_{1c}\beta_0\right.$$

$$+ \lambda_0\left(3\beta_{1s} - 2\theta_{1c} + 2\lambda_{1c}\right) + \theta_{tw}\left(\theta_{1c} - \lambda_{1c} - \beta_{1s}\right) + \mu\left(-4\beta_0\theta_0 + \theta_{1c}\theta_{1s} + 2\frac{C_{d0}}{a}\delta_0\right)\right]$$

$$+ \frac{R}{12}\left[\beta_0\left(-\theta_{1s} + \lambda_{1s} - \beta_{1c}\right) + \theta_0\left(2\theta_{1c} - 3\beta_{1s} - 2\lambda_{1c}\right) + \frac{C_{d0}}{a}\delta_{1s} + 2\frac{e}{R}\theta_{tw}\beta_{1s} - 4\mu\beta_0\theta_{tw}\right]$$

$$+ \frac{R}{32}\left[-2\beta_{1s}\theta_{tw} + \mu\left(-10\beta_{1s}\theta_{1s} + 4\beta_{1c}\beta_{1s} - 6\beta_{1c}\theta_{1s} + 7\beta_{1c}\lambda_{1c} + 5\beta_{1s}\lambda_{1s} - 2\theta_{1s}\lambda_{1c} - 2\theta_{1c}\lambda_{1s}\right)\right.$$

$$\left. + \mu^2\theta_{tw}\left(5\beta_{1s} + 2\theta_{1c}\right)\right] - \frac{m_{si}\Omega^2}{S}\frac{\delta_{1s}\delta_0}{2}$$

$$\frac{\{F_z\}_{rotor}}{NS} = \frac{1}{2}\left\{\frac{R-e}{2}\mu^2\theta_0 + \frac{R}{3}\theta_0 + \frac{R}{4}\theta_{tw} - \frac{R-e}{2}\mu\frac{e}{R}\beta_{1c} + \frac{R}{2}\left(\mu\theta_{1s} + \frac{\mu^2}{2}\theta_{tw} - \lambda_0 - \frac{\mu}{2}\lambda_{1s}\right)\right\}$$

$$\frac{\{M_x\}_{rotor}}{N.S.e} = \frac{R-e}{4}\left[\frac{\mu^2}{4}\left(3\theta_{1s} - \beta_{1c}\right) - \mu\lambda_0\right] + \frac{R}{4}\left[\mu\theta_0 - \frac{e}{R}\frac{\beta_{1c}}{2}\right] + \frac{R}{6}\left[\frac{\theta_{1s}}{2} + \mu\theta_{tw} - \frac{\lambda_{1s}}{2} + \frac{\beta_{1c}}{2}\right] + \frac{m_{si}}{2.S}\Omega^2\beta_{1s}$$

$$\frac{\{M_y\}_{rotor}}{N.S.e} = \frac{1}{2}\left[\frac{R-e}{8}\mu^2(\theta_{1c} - \beta_{1s}) + \frac{R}{4}\left[\mu\beta_0 - \frac{e}{R}\beta_{1s}\right] + \frac{R}{6}(\lambda_{1c} + \beta_{1s} - \theta_{1c})\right]$$
$$- \frac{m_{si}}{2.S}\Omega^2\beta_{1c}$$

$$\frac{\{M_z\}_{rotor}}{N.S.e} = \frac{R-e}{16}\left[8\lambda_0^2 + \frac{4e^2}{R^2}(\beta_{1s}^2 + \beta_{1c}^2)\right.$$
$$+ 8\mu\left(\lambda_0(\beta_{1c} - \theta_{1s}) - \frac{e}{R}(\beta_{1c}\theta_0 + \beta_{1s}\beta_0)\right)$$
$$+ \mu^2\left(4\theta_0^2 + \theta_{1c}^2 + 3\theta_{1s}^2 - \frac{4C_{d0}}{a} - 2\beta_{1c}\theta_{1s} - \beta_{1s}\theta_{1c} + 4\beta_0^2 + 3\beta_{1c}^2\right.$$
$$\left.\left. + \beta_{1s}^2\right)\right]$$
$$+ \frac{R}{8}\left[\theta_0(2\theta_{tw} - 4\lambda_0) + 2\frac{e}{R}\beta_{1s}(\theta_{1c} - \lambda_{1c} - \beta_{1s}) - \frac{2e}{R}\beta_{1c}(\theta_{1s} - \lambda_{1s} + \beta_{1c})\right.$$
$$\left. + \mu\left(2\theta_0(2\theta_{1s} - \lambda_{1s}) + 2\beta_0(\lambda_{1c} + \beta_{1s} - \theta_{1c}) - \frac{2e}{R}\beta_{1c}\theta_{tw}\right) + 2\mu^2\theta_{tw}\theta_0\right]$$
$$+ \frac{R}{10}\theta_{tw}^2$$
$$+ \frac{R}{12}\left[2\theta_0^2 + \theta_{1c}^2 + \theta_{1s}^2 - 2\frac{C_{d0}}{a} - 4\lambda_0\theta_{tw} - 2\theta_{1c}(\lambda_{1c} + \beta_{1s}) + 2\theta_{1s}(\beta_{1c}\right.$$
$$- \lambda_{1s})$$
$$+ \lambda_{1c}^2 + \lambda_{1s}^2 + \beta_{1s}^2 + \beta_{1c}^2 + \lambda_{1c}\beta_{1s} - 2\lambda_{1s}\beta_{1c}$$
$$\left. + 2\mu\theta_{tw}(2\theta_{1s} - \lambda_{1s}) + \mu^2\theta_{tw}^2\right]$$
$$+ \left[m_{si}\frac{\Omega^2}{.S} + \frac{K_{i\delta}}{Se}\right]\delta_0$$

Therefore, the rotor head forces are expressed as a function of the different flight parameters, where: (i) the induced velocity coefficients (λ_0, λ_{1c}, λ_{1s}) are determined by the Drees formulation (Meijer Drees, 1949); (ii) the twist θ_{tw} is given; (iii) the coefficients of the flapping motion (β_0, β_{1c}, β_{1s}) are calculated, using the previously obtained equilibrium equations, as a function of (θ_0, θ_{1c}, θ_{1s}) (and also of other parameters already known or calculated); and (iv) the drag coefficients (δ_0, δ_{1c}, δ_{1s}) are calculated, using previously obtained equilibrium equations, as functions of (θ_0, θ_{1c}, θ_{1s}) and (β_0, β_{1c}, β_{1s}). The six equations for the rotor head efforts are, therefore, functions of just three parameters: (θ_0, θ_{1c}, θ_{1s}).

Fuselage balance equations

The known parameters are the dimensions and the limits (of mass and mass center) of the helicopter (in this study, the AS 332L-Super Puma – elongated version):

- the total mass of the helicopter: M (minimum and maximum mass limits).
- the centering (position of the helicopter's CG, about the rotor head) (forward and rearward limits).

  $X_{CG} = X_{CG} - X_{Rp} = X_{CG} - 4.67m$ (> 0 for aft CG; < 0 for forward CG);

  Y_{CG} (> 0 to the right; < 0 to the left); $-Z_{CG} = 4p = 2.45m$
- The air density (ρ).
- The forward flight speed (V) is limited by the V_{ne} of the helicopter.

- The inclination of the main rotor mast of the helicopter ($\alpha_m = 5°$).
  The position of the helicopter tail rotor (relative to the rotor head): $X_{Ra} = 9.4$m; $Y_{Ra} = 0$;
  $-Z_{Ra} = 4p\ -4a = 2.45 - 2.1 = 0.35$m

- The position of the fuselage drag center (A), assumed to be independent of the longitudinal base (angle of attack relative to horizontal axis): (relative to the rotor head).
  $X_A = 0$; $Y_A = 0$; $-Z_A = 0.1$m

- The C_xS of the fuselage assumed independent of the base of the helicopter: $(C_xS)_f = 2,35$ m2

- The position of the center of the horizontal empennage (stabilizer), is assumed independent of the fuselage base: (relative to the rotor head).
  $X_{eh} = 9.4 - 0.1 = 9.3$m;
  $Y_{eh} = -2.113/3 \approx -0.7$m (assuming the empennage center at 1/3 of its wing span);
  $-Z_{eh} = 2.45 - 2.1 + 0.4 = 0.75$m (approx. value, taken directly from the figure)

- the negative lift effect of the horizontal tail, assumed equal to $T_{eh} = 1/2 \rho V^2 (C_zS)_{eh}$ where $(C_zS)_{eh}$ is assumed constant and equal to: $(C_zS)_{eh} = 0.135$ m^2 (independent of the helicopter base), which gives us, for $V = 280$ km/h, a negative lift of $T_{eh} = 500$ N. In the helicopter reference frame, we have:

$$\left(T_{eh}\right)_{Rh} = \begin{cases} 0 \\ 0 \\ -T_{eh} \end{cases}$$

- the anti-torque rotor thrust (T_{AR}) is what is needed to balance the main rotor reaction couple on the fuselage. The T_{AR} value is obtained to give a zero base rotation (ψ_f), that is, no skidding of the fuselage in forward flight. We have, in the helicopter reference frame:

$$\left(T_{Ra}\right)_{Rh} = \begin{cases} 0 \\ -T_{Ra} \\ 0 \end{cases}$$

One has, as unknowns: (i) the rotor head efforts, which are a function of only three parameters: (θ_0, θ_{1c}, θ_{1s}); (ii) The angular inclinations (tilts) of the fuselage: longitudinal (pitch) (α_f), lateral (roll) (γ_f); and (iii) The anti-couple rotor thrust (T_{Ra}) (obtained by assuming the rotation in yaw (ψ_f) is zero). The nose-tail balance (pitch) is illustrated in Figure 12.
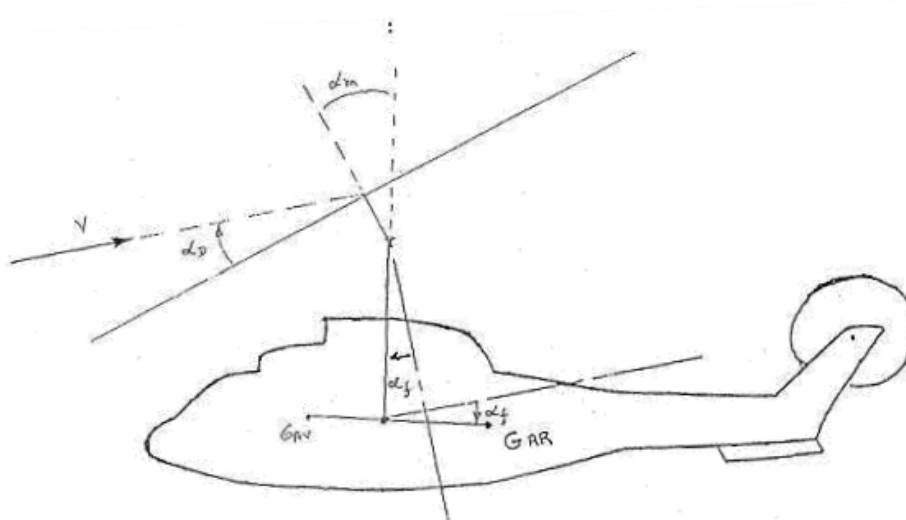
Figure 12: nose-tail balance (pitch) – adapted from (Jorge, 1992)

with: $\alpha_f = \alpha_D - \alpha_m$; rotor plane and CG limits (forward and aft) are indicated in Figure 13.
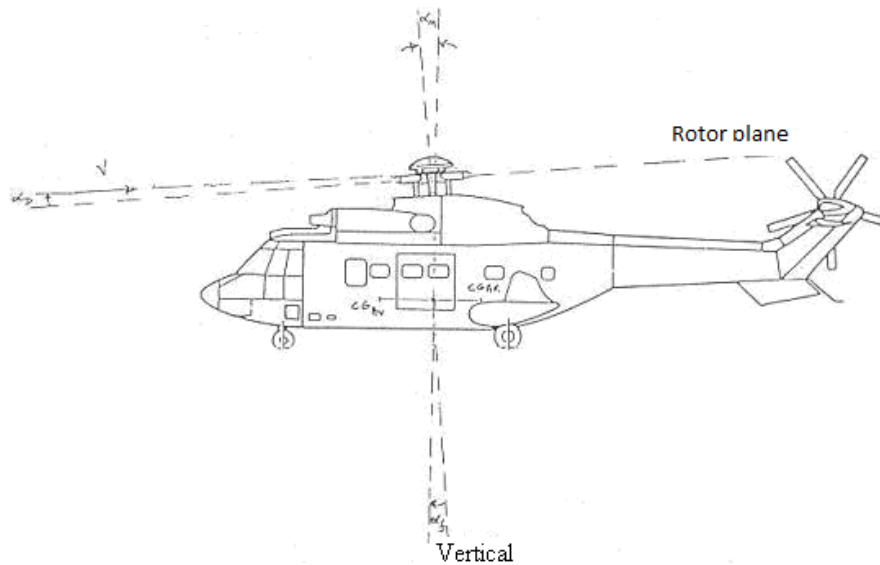
Figure 13: nose-tail balance (pitch): rotor plane; CG limits – adapted from (Jorge, 1992)

The rolling balance (roll) is illustrated in Figure 14, as seen from the front of the helicopter.
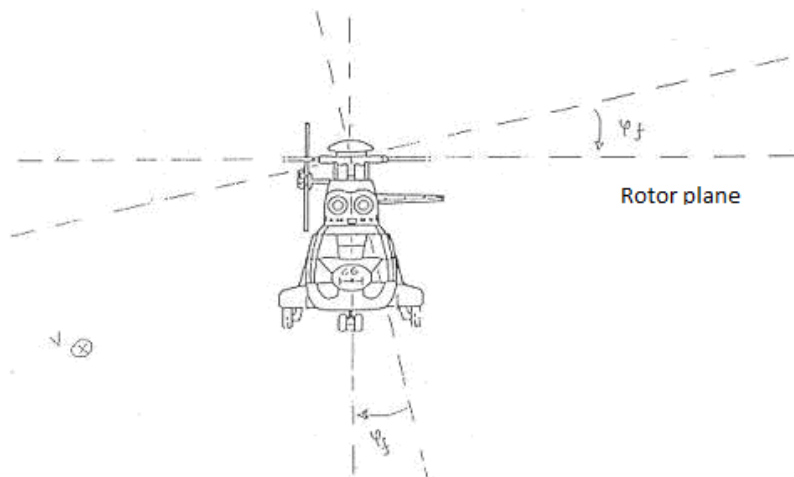
Figure 14: rolling balance (roll): rotor plane (front view) – adapted from (Jorge, 1992)

The rolling balance (roll) is illustrated in Figure 15, as seen from the rear of the helicopter.
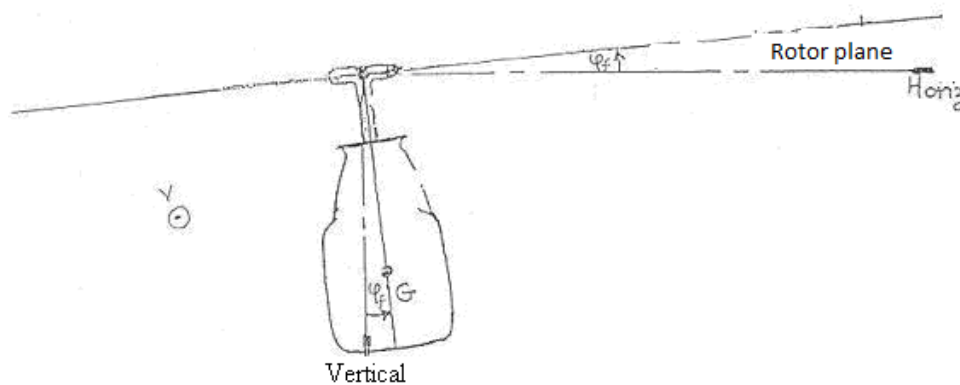
Figure 15: rolling balance (roll): rotor plane (rear view) – adapted from (Jorge, 1992)

The directional balance (yaw) is illustrated in Figure 16.
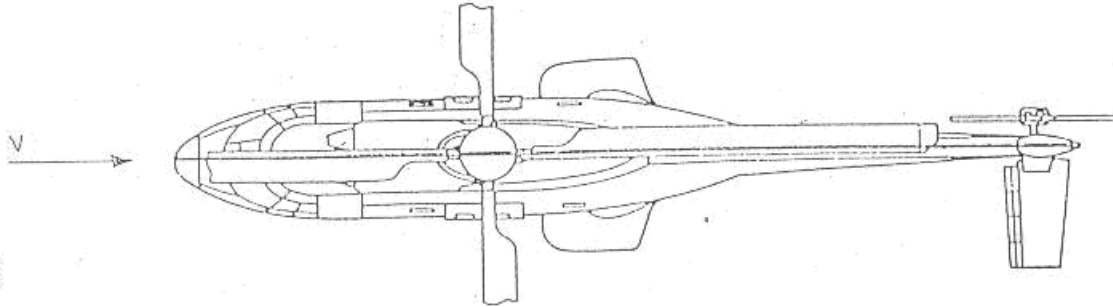
Figure 16: directional balance (yaw) – adapted from (Jorge, 1992)

A rotation of (- α_m) leads from the fixed rotor reference frame to the helicopter frame.

$$\begin{bmatrix} \{F_{x_h}\}_{rotor} \\ \{F_{y_h}\}_{rotor} \\ \{F_{z_h}\}_{rotor} \end{bmatrix}_{R_h} = \begin{bmatrix} \cos\alpha_m & 0 & -\sin\alpha_m \\ 0 & 1 & 0 \\ \sin\alpha_m & 0 & \cos\alpha_m \end{bmatrix} \begin{bmatrix} \{F_x\}_{rotor} \\ \{F_y\}_{rotor} \\ \{F_z\}_{rotor} \end{bmatrix}_{R_h} = \begin{bmatrix} \{F_x\}_{rotor}\cos\alpha_m - \{F_z\}_{rotor}\sin\alpha_m \\ \{F_y\}_{rotor} \\ \{F_x\}_{rotor}\sin\alpha_m + \{F_z\}_{rotor}\cos\alpha_m \end{bmatrix}$$

$$\begin{bmatrix} \{M_{x_h}\}_{rotor} \\ \{M_{y_h}\}_{rotor} \\ \{M_{z_h}\}_{rotor} \end{bmatrix}_{R_h} = \begin{bmatrix} \cos\alpha_m & 0 & -\sin\alpha_m \\ 0 & 1 & 0 \\ \sin\alpha_m & 0 & \cos\alpha_m \end{bmatrix} \begin{bmatrix} \{M_x\}_{rotor} \\ \{M_y\}_{rotor} \\ \{M_z\}_{rotor} \end{bmatrix}_{R_h} = \begin{bmatrix} \{M_x\}_{rotor}\cos\alpha_m - \{M_z\}_{rotor}\sin\alpha_m \\ \{M_y\}_{rotor} \\ \{M_x\}_{rotor}\sin\alpha_m + \{M_z\}_{rotor}\cos\alpha_m \end{bmatrix}$$

(34)

The forward speed (and therefore the relative wind (V)) was expressed in the aerodynamic reference frame. We pass from the aerodynamic reference frame to the helicopter frame by a rotation of $\alpha_f = \alpha_D - \alpha_m$:

$$\{\vec{V}\}_{Rh} = \begin{bmatrix} \cos\alpha_f & 0 & \sin\alpha_f \\ 0 & 1 & 0 \\ -\sin\alpha_f & 0 & \cos\alpha_f \end{bmatrix} \begin{bmatrix} V \\ 0 \\ 0 \end{bmatrix}_{Ra} = \begin{bmatrix} V\cos\alpha_f \\ 0 \\ -V\sin\alpha_f \end{bmatrix}$$

(35)

In the case considered here (horizontal forward flight, stabilized, with constant speed), the aerodynamic reference frame and the Galilean reference frame are confounded. The helicopter's net weight (Mg) is passed from this Galilean reference frame to the helicopter reference frame by a rotation of (-α_f) around $Y_g = Y_h$, and then a rotation of (-γ_f) around X_h.

$$\{M_{\bar{g}}\}_{Rh} = \begin{bmatrix} \cos\alpha_f & 0 & -\sin\alpha_f \\ 0 & 1 & 0 \\ \sin\alpha_f & 0 & \cos\alpha_f \end{bmatrix} \begin{bmatrix} 0 \\ 0 \\ -M_g \end{bmatrix}_{Rg} = \begin{bmatrix} M_g\sin\alpha_f \\ 0 \\ -M_g\cos\alpha_f \end{bmatrix}$$

(36)

$$\{M_{\bar{g}}\}_{Rh} = \begin{bmatrix} 1 & 0 & 0 \\ 0 & \cos\alpha_f & \sin\alpha_f \\ 0 & -\sin\alpha_f & \cos\alpha_f \end{bmatrix} \begin{bmatrix} M_g\sin\alpha_f \\ 0 \\ -M_g\cos\alpha_f \end{bmatrix}_{Rg} = \begin{bmatrix} M_g\sin\alpha_f \\ -M_g\sin\alpha_f\cos\alpha_f \\ -M_g\cos\alpha_f\cos\alpha_f \end{bmatrix}$$

(37)

The equilibrium, in the helicopter reference frame, gives us:

$$\sum F_{x_h} = 0$$

$$\left\{ F_{x_h} \right\}_{rotor} + M_g \sin\alpha_f + \frac{1}{2}\rho\left(C_x S\right)_f V^2 = 0$$

$$\sum F_{y_h} = 0 \tag{38}$$

$$\left\{ F_{y_h} \right\}_{rotor} + M_g \sin\gamma_f \cos\alpha_f - T_{Ra} = 0$$

$$\sum F_{z_h} = 0$$

$$\left\{ F_{z_h} \right\}_{rotor} + M_g \cos\gamma_f \cos\alpha_f + \frac{1}{2}\rho\left(C_z S\right)_{eh} V^2 = 0$$

Taking the balance of moments around the rotor hub: $\sum \vec{M}_0 = 0$

$$
\begin{bmatrix} M_{x_h} \\ M_{y_h} \\ M_{z_h} \end{bmatrix}_{rotor} + \begin{bmatrix} x_{CG} \\ y_{CG} \\ z_{CG} \end{bmatrix} \Lambda \begin{bmatrix} M_g \sin\alpha_f \\ -M_g \sin\gamma_f \cos\alpha_f \\ -M_g \cos\gamma_f \cos\alpha_f \end{bmatrix} + \begin{bmatrix} x_A \\ y_A \\ z_A \end{bmatrix} \Lambda \begin{bmatrix} \frac{1}{2}\rho\left(C_x S\right)_f V^2 \\ 0 \\ 0 \end{bmatrix}
$$

$$
+ \begin{bmatrix} x_{eh} \\ y_{eh} \\ z_{eh} \end{bmatrix} \Lambda \begin{bmatrix} 0 \\ 0 \\ \frac{1}{2}\rho\left(C_z S\right)_{eh} V^2 \end{bmatrix} + \begin{bmatrix} x_{Ra} \\ y_{Ra} \\ z_{Ra} \end{bmatrix} \Lambda \begin{bmatrix} 0 \\ -T_{Ra} \\ 0 \end{bmatrix} = \begin{bmatrix} 0 \\ 0 \\ 0 \end{bmatrix}
$$

$$\text{with : } y_{Ra} = x_A = y_A = 0$$

What gives us:

$$\left\{ M_{x_h} \right\}_{rotor} + \left[-y_{CG} M_g \cos\varphi_f \cos\alpha_f + z_{CG} M_g \sin\varphi_f \cos\alpha_f \right] - y_{eh}\frac{1}{2}\rho V^2 \left(C_z S\right)_{eh} + z_{Ra} T_{Ra} = 0$$

$$\left\{ M_{y_h} \right\}_{rotor} + \left[-x_{CG} M_g \cos\varphi_f \cos\alpha_f + z_{CG} M_g \sin\alpha_f \right] - z_A\frac{1}{2}\rho V^2 \left(C_x S\right)_f + x_{eh}\frac{1}{2}\rho V^2 \left(C_z S\right)_{eh} = 0 \tag{39}$$

$$\left\{ M_{z_h} \right\}_{rotor} + \left[-x_{CG} M_g \sin\varphi_f \cos\alpha_f + y_{CG} M_g \sin\alpha_f \right] - x_{Ra} T_{Ra} = 0$$

And we arrive at the six fuselage equilibrium equations:

$$\left\{ F_x \right\}_{rotor} \cos\alpha_m - \left\{ F_z \right\}_{rotor} \sin\alpha_m + M_g \sin\alpha_f + \frac{1}{2}\rho\left(C_x S\right)_f V^2 = 0$$

$$\left\{ F_y \right\}_{rotor} - M_g \sin\varphi_f \cos\alpha_f - T_{Ra} = 0$$

$$\left\{ F_x \right\}_{rotor} \sin\alpha_m + \left\{ F_z \right\}_{rotor} \cos\alpha_m - M_g \cos\varphi_f \cos\alpha_f - \frac{1}{2}\rho V^2 \left(C_z S\right)_{eh} = 0$$

$$\left\{ M_x \right\}_{rotor} \cos\alpha_m - \left\{ M_z \right\}_{rotor} \sin\alpha_m - y_{CG} M_g \cos\varphi_f \cos\alpha_f + z_{CG} M_g \sin\alpha_f \cos\alpha_f \tag{40}$$

$$- y_{eh}\frac{1}{2}\rho V^2 \left(C_z S\right)_{eh} + z_{Ra} T_{Ra} = 0$$

$$\left\{ M_y \right\}_{rotor} + x_{CG} M_g \cos\varphi_f \cos\alpha_f - z_{CG} M_g \sin\alpha_f + z_A \frac{1}{2}\rho\left(C_x S\right)_f V^2 + xeh \frac{1}{2}\rho V^2 \left(C_z S\right)_{eh} = 0$$

$$\left\{ M_x \right\}_{rotor} \sin\alpha_m + \left\{ M_z \right\}_{rotor} \cos\alpha_m - x_{CG} M_g \sin\varphi_f \cos\alpha_f - y_{CG} M_g \sin\alpha_f - x_{Ra} T_{Ra} = 0$$

The hypothesis of small angles: $\cos\alpha_m \approx \cos\alpha_f \approx \cos\varphi_f \approx 1$; $\sin\alpha_m \approx \alpha_m$; $\sin\alpha_f \approx \alpha_f$; $\sin\varphi_f \approx \varphi_f$ leads to:

$$\{F_x\}_{rotor} - \{F_z\}_{rotor}\,\alpha_m + M_g\alpha_f + \frac{1}{2}\rho(C_xS)_f\,V^2 = 0$$

$$\{F_y\}_{rotor} - M_g\varphi_f - T_{Ra} = 0$$

$$\{F_x\}_{rotor}\,\alpha_m + \{F_z\}_{rotor} - M_g - \frac{1}{2}\rho V^2(C_zS)_{eh} = 0$$

$$\{M_x\}_{rotor} - \{M_z\}_{rotor}\,\alpha_m - y_{CG}M_g + z_{CG}M_g\varphi_f - y_{eh}\frac{1}{2}\rho V^2(C_zS)_{eh} + z_{Ra}T_{Ra} = 0 \qquad (41)$$

$$\{M_y\}_{rotor} + x_{CG}M_g - z_{CG}M_g\alpha_f + z_A\frac{1}{2}\rho(C_xS)_f\,V^2 + xeh\frac{1}{2}\rho V^2(C_zS)_{eh} = 0$$

$$\{M_x\}_{rotor}\,\alpha_m + \{M_z\}_{rotor} - x_{CG}M_g\varphi_f - y_{CG}M_g\alpha_f - x_{Ra}T_{Ra} = 0$$

With the wrench of the rotor head efforts (in the fixed rotor reference frame) previously obtained, with the rotor incidence equal to $\alpha_0 = \alpha_f + \alpha_m$ and with:

$$C_T = \frac{\{F_z\}_{rotor}}{\rho A(\Omega R)^2} = \frac{\{F_z\}_{rotor}}{NS} \cdot \frac{\sigma a}{R} ,$$ where the rotor rigidity is defined as: $\sigma = \dfrac{Nc}{\pi R}$. With the

flapping and drag equations, therefore, we have a system of twelve nonlinear equations with twelve unknowns ($\theta_0, \theta_{1c}, \theta_{1s}, \alpha_f, \varphi_f, T_{Ra}, \beta_0, \beta_{1c}, \beta_{1s}, \delta_0, \delta_{1c}, \delta_{1s}$).

3.3 Study of the effect of the introduction of defects in the main rotor

Analysis of Influential Parameters

To calculate the wrench of the forces on the rotor head, in any azimuthal position (ψ_i) (corresponding to a certain time: $t = \psi_i/\Omega$, after passing the blades through the reference position, $\psi_i = 0$, which corresponds to the synchronism signal given by the magnetic sensor in the rotor head), it is necessary and sufficient to know $\lambda(\psi_i), \theta_i(\psi_i), \beta_i(\psi_i), \delta_i(\psi_i)$, the parameters of the blades (R, e, c), and their profile (C_{d0}, a), the advance rate μ, the air density (ρ), the mass of the blades (m_i), the static moment of the blades (m_{si}) and the inertia of the blades ($I_{\beta i}$). Analyzing each of the variables:

- A static moment of the blades (m_{si}): $m_{si} = \displaystyle\int_e^R r\,dm_i = \int_e^R rm\,dr$, where m is the mass per unit of the linear length of blade *i*. (m_{si} may be different for each blade, because of anisotropies).

- Blade masses (m_i): $m_i = \displaystyle\int_e^R dm_i = \int_e^R m\,dr$.

- The inertia of the blades ($I_{\beta i}$): $I\beta_i = \displaystyle\int_e^R r^2\,dm_i = \int_e^R r^2 m\,dr$ (m_i and $I_{\beta i}$ may also be different for each blade, due to anisotropies).

The three parameters: m_i, m_{si}, and $I_{\beta i}$ are interdependent. A change in m_i leads to a corresponding change in the values of m_{si} and $I_{\beta i}$. One can distinguish in the rotor:

- rotor hub, or rotor cube, is integral with the rotating mast, which supports the forces from the blades through four spherical joints made of laminated rubber (spherical abutments).

- the flapping part, consisting of a metal sleeve and a composite blade.

The rotor parts are illustrated in Figure 17, for the helicopter in the study
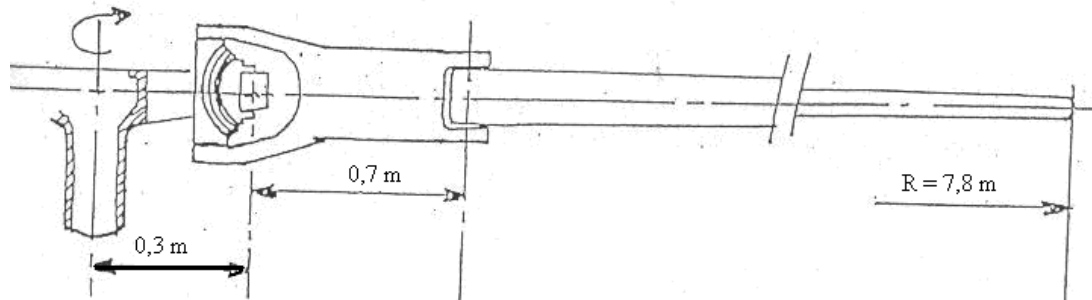
Figure 17: rotor parts: hub, sleeve, and blade – adapted from (Jorge, 1992)

- The balance masses (shot spheres), between 0 and 1 kg, can be inserted at the end of the sleeve, i.e., r = 1.0 m.
- The insertion of an equilibrium mass (Δm_i) leads us to changes in the parameters of blade *i*, from the isotropic values of m_{si} and of $I_{\beta i}$.:
  $m_{\rho i} = m_{\rho\ iso} + \Delta m_i$, where $m_{\rho\ iso} = 88.2$kg
  $m_{s\rho i} = m_{s\rho\ iso} + \Delta m_i (0.7)$, where $m_{s\rho\ iso} = 331.7$kg.m
  $I_{\beta i} = I_{\beta\ iso} + \Delta m_i (0.7)^2$, where $I_{\beta\ iso} = 1675$kg.m^2
- Air density (ρ): depends on pressure altitude and temperature. It is a parameter given, for example, from the standard atmosphere tables.
- Advance ratio (μ): depends on the speed of the helicopter relative to the air (V) and the pitch of the rotor disk (α_D). Note: The longitudinal attitude of the fuselage (α_f) depends on α_D and the tilt of the rotor mast (α_m) so that: $\alpha_f = \alpha_D - \alpha_m$ (α_f is smaller than α_D).
- The parameters of the blades (R, e, c) and their profile (Cd_0, a) can cause anisotropies but, within the scope of this study, they will be considered as constants, independent of the blades. All blade anisotropies will be considered to be "equivalent" anisotropies at the blade adjustment positions. In this way, an anisotropy in m_i (and, consequently, in m_{si} and $I_{\beta i}$) can be considered as an "equivalent" mass change in the radial position where the equilibrium mass can be added (in the Super Puma case, r = 1.0 m, i.e. at the end of the sleeve).
  In the same way, anisotropies to the lift of the profiles can be considered as "equivalent" variations of the blade pitch ($\theta_i(\psi_i)$) which can be changed by regulating the length of the blades' pitch rods, or pitch links (which changes the collective pitch θ_o of blade *i*) and the deflection of the tabs (which gives a moment around the axis $\overrightarrow{X}_i$, introducing efforts on the rods (which will be transmitted to the fuselage) and, at the same time, giving a variation of the blade lift, which is supposed to be proportional to the speed of forward flight (i.e., assuming that the bracketing of the tabs does not affect the taper (conicity) (β_0) of the rotor in stationary flight, that its effect increases with μ and that it is more important on the advancing blade side, and less important on the retreating blade side. Thus, we will be simulating the deflection of tabs as anisotropy in θ_{is}.
  In this way, if $\theta_{is} \neq 0$ (all the other parameters equal to zero) in the flapping motion equations, for stationary flight ($\mu = 0$), one obtains: $\beta_0 = 0$; $\beta_{1c} \approx -\theta_{1s}$; $\beta_{1s} \approx 0$. And for the forward flight, we will have: $\beta_0 = $ constant $\mu - \theta_{1s}$, which shows that there will be an increase in the taper (conicity) (β_0) that will be proportional to θ_{is} and μ, as we want to simulate.
- The induced velocity: depends on the advance rate (μ), the rotor disc inclination (α_D), the lift coefficient (C_T) (which expresses the lift (thrust) of the helicopter (F_z) and considers the air density (ρ)) and the azimuthal position (ψi). We will assume that there is no anisotropy on the induced velocity and, therefore, that λ does not depend on blade *i*.

- The blade pitch: θ_i (ψ_i): It depends on the azimuthal position (ψ_i) and the balance of the helicopter (that is, of the fuselage), exposed to external forces and considered in stationary flight or forward flight with a constant speed. For the balance of the fuselage, one has assumed, as external efforts: (i) rotor head efforts; (ii) the net weight of the helicopter (the mass and the balance, i.e. the position of the fuselage center of gravity); (iii) the drag of the fuselage (assumed as applied a fixed point (A) and as independent of the longitudinal base of the fuselage); (iv) the negative lift effect of the horizontal empennage (assumed to be applied at a fixed point, and independent of the longitudinal attitude (tilt) of the fuselage); (v) the thrust of the anti-torque rotor, necessary to balance the torque applied on the main rotor.

  The calculation of θ_i (ψ_i) is divided into two steps: 1°) assuming that there is no anisotropy on the rotor, we will have the blade pitch $(\theta_0, \theta_{1c}, \theta_{is})$ from the isotropic rotor equilibrium equations, as seen in the previous section; and 2°) the anisotropies are introduced on a blade $(\theta_{0i}, \theta_{1si})$ assuming that the fixation of the other blades will not change.

- The flapping movement β_i (ψ_i): As previously seen, β_i depends on the azimuthal position (ψ_i), the fixation of the pitch θ_i (ψ_i), the induced velocity λ (ψ_i), the air density (ρ), on the blade parameters $(R, e, c, a, m_{si}, I_{\beta i})$, on the advance rate (μ). We will divide the calculation of β_i (ψ_i) into two steps:

  1°) We will assume that there is no anisotropy on the rotor. All blades have the same: mass (m), static moment (m_s), the moment of inertia (I_β), the value of pitch (θ), and the pitch angle is calculated from the balance of the helicopter, as previously seen. We will have an expression of $\beta(\psi_i)$ which is valid for all blades;

  2°) The anisotropies to be studied on the blade (i) are introduced: (i) equilibrium mass on the sleeve (change of m_i, m_{si}, $I_{\beta i}$); (ii) adjustment of the blade control rod (change of θ_i); (iii) deflection of the tab (change of θ_{1si}).
  The flapping of this blade $(\beta_i (\psi_i))$ is calculated again, assuming that it will not influence the flapping movements of the other blades.

- The drag motion $\delta i(\psi i)$: We've seen above that δ_i depends on ψ_i, θ_i, λ_i, β_i, the air density (ρ), the advance rate (μ), and the blade parameters $(R, e, c, a, m_{si}, I_{\beta i})$. Like what was done for θ_i and β_i, we will split the calculation into two steps: 1°) assuming that there is no anisotropy on the rotor, the drag $(\delta_0, \delta_{1c}, \delta_{1s})$ will be obtained from the isotropic rotor equilibrium equations, as seen previously; and 2°) anisotropies are introduced on the blade (*i*) if this blade not influence the dragging motion of the other blades.

Apart from the change in δ due to the already mentioned variations in θ and β, one can also have a variation in the angle δ due to anisotropy in a frequency adapter (either in its stiffness $K_{\delta i}$, or in its damping $C_{\delta i}$). In the case of the isotropic rotor, the rotor head forces are constant (for a certain equilibrium position). These efforts are applied to a fuselage, assumed rigid, in equilibrium, either in stationary flight, or in forward flight at a constant speed, where, consequently, all the fuselage accelerations are null (the linear accelerations of the center of gravity of the fuselage and the angular accelerations around this center of gravity), and the balance, previously calculated as a static equilibrium, gave us the values of the attitudes of the fuselage, longitudinal (α_f), lateral (φ_f) and in rotation (ψ_f), which are all constant.

The introduction of anisotropies and the calculation of the new angles θ, β, and δ leads us to new rotor head forces, which will no longer be constant but will be functions of ψ_i, that is, they will be forces at the frequency 1Ω (one-per-revolution of the rotor). Assuming the fuselage attitudes are constant functions plus the functions in 1Ω. The constant part of these attitudes is the one previously calculated, which is assumed to be unchanged after

the introduction of anisotropies on the rotor. This means that the introduction of anisotropy will not change the stationary attitudes of the fuselage but will introduce variations of these attitudes around the equilibrium position and that these variations will be functions of 1Ω, which will lead us to accelerations of the fuselage which will also be functions of the 1Ω frequency.

Incorporation of defects into the formulation

Introduction

The wrench of the rotor head efforts, and the flight parameters (θ, β, δ, α_f, ψ_f, T_{Ra}) are calculated, for an isotropic rotor. With the application of the Coleman Transformation (Coleman & Feingold, 1957), the rotor head efforts, as well as the flight parameters, are constant concerning time.

When a defect is introduced, the rotor head efforts will be functions of ψ_i (and therefore functions of time, since $t = \psi_i/\Omega$), which will be introduced in the fuselage balance equations which, at this moment, will no longer be homogeneous (right-hand term equal to zero), as previously calculated, since there will be accelerations transmitted to the fuselage, due to the variable efforts in the rotor head. Whenever a defect is introduced on a blade, the flapping (β) and drag (δ) of the other blades are assumed to be unchanged, and we will recalculate, for a blade (i), the flapping (β_{0i}, β_{1ci}, β_{1si}) and the drag (δ_{0i}, δ_{1ci}, δ_{1si}) with the correspondent previously derived equations, since the defect to be introduced is known a priori: (i) Mass defects: change in m_i, m_{si} and $I_{\beta i}$; (ii) Rod defects: change in θ_{0i}; (iii) Tab defects: change in θ_{1si}.

We will assume that the introduction of defects does not lead to average attitude changes of the fuselage and, therefore, that the accelerations that we will have on the fuselage will not have constant terms, but only terms in 1Ω. In this way, for the center of gravity of the fuselage, we will have the accelerations:

$$\ddot{x}_{t.t} = \Omega^2 \ddot{x} = \Omega^2 \left(-x_{ic} \cos\psi - x_{is} \sin\psi \right)$$

$$\ddot{y}_{t.t} = \Omega^2 \ddot{y} = \Omega^2 \left(-y_{ic} \cos\psi - y_{is} \sin\psi \right)$$

$$\ddot{z}_{t.t} = \Omega^2 \ddot{z} = \Omega^2 \left(-z_{ic} \cos\psi - z_{is} \sin\psi \right)$$

$$\ddot{\alpha}_{f_{t.t}} = \Omega^2 \ddot{\alpha}_f = \Omega^2 \left(-\alpha_{f_{1c}} \cos\psi - \alpha_{f_{1s}} \sin\psi \right) \qquad (\text{pitch})$$

$$\ddot{\varphi}_{f_{t.t}} = \Omega^2 \ddot{\varphi}_f = \Omega^2 \left(-\varphi_{f_{1c}} \cos\psi - \varphi_{f_{1s}} \sin\psi \right) \qquad (\text{row})$$

$$\ddot{\psi}_{f_{t.t}} = \Omega^2 \ddot{\psi}_f = \Omega^2 \left(-\psi_{f_{1c}} \cos\psi - \psi_{f_{1s}} \sin\psi \right) \qquad (\text{yaw})$$

$$(42)$$

Efforts on the rotor head after the introduction of defects

The efforts on the rotor head will have, after the introduction of the defects, a constant component (the one previously calculated, with the isotropic rotor equilibrium) plus the cyclic components, that is, in 1Ω. Therefore, we will have:

$$\{F_x\}_{rotor} = \{F_{x_0}\}_{rotor} + \{F_{x_{1c}}\}_{rotor} \cos\psi + \{F_{x_{1s}}\}_{rotor} \sin\psi$$

$$\{F_y\}_{rotor} = \{F_{y_0}\}_{rotor} + \{F_{y_{1c}}\}_{rotor} \cos\psi + \{F_{y_{1s}}\}_{rotor} \sin\psi$$

$$\{F_z\}_{rotor} = \{F_{z_0}\}_{rotor} + \{F_{z_{1c}}\}_{rotor} \cos\psi + \{F_{z_{1s}}\}_{rotor} \sin\psi \qquad (43)$$

$$\{M_x\}_{rotor} = \{M_{x_0}\}_{rotor} + \{M_{x_{1c}}\}_{rotor} \cos\psi + \{M_{x_{1s}}\}_{rotor} \sin\psi$$

$$\{M_y\}_{rotor} = \{M_{y_0}\}_{rotor} + \{M_{y_{1c}}\}_{rotor} \cos\psi + \{M_{y_{1s}}\}_{rotor} \sin\psi$$

$$\{M_z\}_{rotor} = \{M_{z_0}\}_{rotor} + \{M_{z_{1c}}\}_{rotor} \cos\psi + \{M_{z_{1s}}\}_{rotor} \sin\psi$$

where the index "0" indicates the constant efforts, calculated assuming the isotropic rotor. These efforts are obtained from a sum, according to the number of blades, of the efforts due to each blade, as previously derived. For blade i, the new angles of pitch (θ_i), flapping (β_i), and drag (δ_i), were calculated as previously derived. The rotor head forces, for blade i, will be the ones due to these new angles, by using the previously derived expressions for forces and moments, knowing that these efforts and their resultant have cyclic components in $\sin\psi$ and $\cos\psi$, in addition to the constant component.

To make the components, in $\sin\psi$ and $\cos\psi$, for blade i, appear explicitly, we will apply to the expression of efforts the operators: $\dfrac{1}{2\pi}\displaystyle\int_0^{2\pi}(...)\sin\psi\,d\psi$ and $\dfrac{1}{2\pi}\displaystyle\int_0^{2\pi}(...)\cos\psi\,d\psi$, which leads to the twelve expressions below, where the index "i" of the angles (pitch, flapping, and drag) was suppressed for simplicity of the notation.

$$\frac{F_{x_{1si}}}{2S} = \frac{R-e}{32}\left[-8\lambda_0^2 - 2\frac{e^2}{R^2}\beta_{1s}^2 - 6\frac{e^2}{R^2}\beta_{1c}^2 + \mu\left(2\lambda_0\beta_{1c} + 12\lambda_0\theta_{1s} - 6\frac{e}{R}\beta_{1s}\beta_0 + 12\frac{e}{R}\beta_{1c}\theta_0 - 4\lambda_0\beta_{1c}\right)\right.$$

$$+\mu^2\left(\beta_{1c}\theta_{1s} + \beta_{1s}\theta_{1c} - 6\theta_0^2 + 6\frac{Cd_0}{a} - \theta_{1c}^2 - 5\theta_{1s}^2\right)\Bigg]$$

$$+\frac{R}{8}\left[-\theta_{tw}\theta_0 + 2\lambda_0\theta_0 + \lambda_{1s}\theta_{1s} - \beta_{1c}\theta_{1s} + \beta_{1c}\lambda_{1s} + \mu\left(-3\theta_0\theta_{1s} - 2\theta_{tw}\theta_{1s} + \theta_{tw}\lambda_{1s} - \theta_{tw}\beta_{1c}\right)\right]$$

$$+\frac{R}{48}\left[-\beta_{1c}\theta_{1s} + \beta_{1s}\theta_{1c} - 4\theta_0^2 - 4\frac{Cd_0}{a} - \theta_{1c}^2 + 8\lambda_0\theta_{tw} - \beta_{1s}\lambda_{1c} + 2\theta_{1c}\lambda_{1c} + \lambda_{1s}\beta_{1c} - \beta_{1c}^2 - \lambda_{1c}^2\right] \qquad (44)$$

$$+\frac{R}{32}-\left[2\theta_{1s}^2 - \frac{e}{R}\beta_{1s}\left(-\beta_{1s} + 2\theta_{1c} - 2\lambda_{1c}\right) + \frac{e}{R}\beta_{1c}\left(7\beta_{1c} + 6\theta_{1s} - 6\lambda_{1s}\right) - 2\lambda_{1s}^2 - 2\beta_{1c}^2\right.$$

$$+\mu\left(2\frac{Cd0}{a}\delta_{1c} - \lambda_{1c}\beta_0 + 6\frac{e}{R}\beta_{1c}\theta_{tw} + \beta_{1s}\beta_0 + 6\lambda_{1s}\theta_0 - 6\beta_{1c}\theta_0\right) + \mu^2\left(-6\theta_{tw}\theta_0 - 2\theta_{tw}^2\right)\Bigg]$$

$$+\frac{R}{20}\left(-\theta_{tw}^2\right) + \frac{m_{si}\Omega^2}{8S}\left[-\beta_{1c}\beta_{1s} - 4\delta_0\right]$$

$$\frac{F_{x_{1ci}}}{2S} = \frac{R-e}{32}\left[4\frac{e^2}{R^2}\beta_{1s}\beta_{1c} + \mu\left(-2\lambda_0\beta_{1s} + 4\lambda_0\theta_{1c} - 4\frac{e}{R}\beta_{1s}\theta_0 - 2\frac{e}{R}\beta_{1c}\beta_0\right)\right.$$

$$+ \mu^2\left(2\beta_0\theta_0 + \beta_{1c}\theta_{1c} + \beta_{1s}\theta_{1s} + 2\frac{Cd_0}{a}\delta_0 - 2\theta_{1c}\theta_{1s}\right)\Bigg]$$

$$+ \frac{R}{32}\Bigg[4\lambda_0\beta_0 - 2\beta_{1c}\theta_{1c} - 2\theta_{tw}\beta_0 - \frac{e}{R}\beta_{1s}\left(6\beta_{1c} + 2\theta_{1s} - 2\lambda_{1s}\right) + \frac{e}{R}\beta_{1c}\left(2\theta_{1c} - 2\lambda_{1c}\right) + 2\beta_{1c}\lambda_{1c}$$

$$+ 2\beta_{1c}\beta_{1s} + \mu\left(-2\frac{e}{R}\beta_{1s}\theta_{tw} + 2\frac{Cd_0}{a}\delta_{1s} - 4\theta_0\theta_{1c} + 7\beta_0\beta_{1c} - \beta_0\lambda_{1s} + 2\theta_0\lambda_{1c} + 2\theta_0\beta_{1s}\right) + \mu^2\theta_{tw}\beta_0\Bigg]$$

$$+ \frac{R}{48}\Bigg[-4\beta_0\theta_0 + \beta_{1s}\theta_{1s} + 4\frac{Cd_0}{a}\delta_0 - 2\theta_{1c}\theta_{1s} + 2\lambda_{1c}\theta_{1s} - \beta_{1s}\lambda_{1s} + \beta_{1c}\beta_{1s} + 2\theta_{1c}\lambda_{1s} - 2\theta_{1c}\beta_{1c} - 2\lambda_{1c}\lambda_{1s}$$

$$+ 2\lambda_{1c}\beta_{1c} + \mu\left(-4\theta_{tw}\theta_{1c} + 2\theta_{tw}\lambda_{1c} + 2\theta_{tw}\beta_{1s}\right)\Bigg] + \frac{m_i e\Omega^2}{2S} + \frac{m_{si}\Omega^2}{2S}\left[1 - \frac{\beta_0^2}{2} - \frac{3}{8}\beta_{1c}^2 - \frac{\beta_{1s}^2}{8}\right] \tag{45}$$

$$\frac{F_{y_{1si}}}{2S} = \frac{R-e}{32}\left[-4\frac{e^2}{R^2}\beta_{1s}\beta_{1c} + \mu\left(10\lambda_0\beta_{1s} - 4\lambda_0\theta_{1c} + 4\frac{e}{R}\beta_{1s}\theta_0 + 10\frac{e}{R}\beta_{1c}\beta_0\right)\right.$$

$$+ \mu^2\left(-10\beta_0\theta_0 - 3\beta_{1c}\theta_{1c} - 7\beta_{1s}\theta_{1s} + 6\frac{Cd_0}{a}\delta_0 + 2\theta_{1c}\theta_{1s} + 4\beta_{1c}\beta_{1s}\right)\Bigg]$$

$$+ \frac{R}{32}\Bigg[4\lambda_0\beta_0 - 2\beta_{1s}\theta_{1s} - 2\theta_{tw}\beta_0 - \frac{e}{R}\beta_{1s}\left(-6\beta_{1c} - 2\theta_{1s} + 2\lambda_{1s}\right) - \beta_{1s}\beta_{1c} + \frac{e}{R}\beta_{1c}\left(-2\theta_{1c} + 2\lambda_{1c}\right)$$

$$+ 2\beta_{1s}\lambda_{1s} + \mu\left(-2\beta_{1s}\theta_0 + 2\mu\frac{e}{R}\beta_{1s}\theta_{tw} - 8\beta_0\theta_{1s} - 8\beta_{1s}\theta_0 + 6\frac{Cd_0}{a}\delta_{1s} + 4\theta_0\theta_{1c} - 3\beta_0\beta_{1c} + 5\beta_0\lambda_{1s}\right.$$

$$\left.- 22\theta_0\lambda_{1c} - 4\theta_{tw}\beta_{1s}\right) - 5\mu^2\beta_0\theta_{tw}\Bigg]$$

$$+ \frac{R}{48}\Bigg[-4\beta_0\theta_0 + \beta_{1c}\theta_{1c} + 4\frac{Cd_0}{a}\delta_0 + 2\theta_{1c}\theta_{1s} - \beta_{1c}\lambda_{1c} - \beta_{1c}\beta_{1s} - 2\theta_{1s}\lambda_{1c} - 2\theta_{1s}\beta_{1s} - 2\theta_{1c}\lambda_{1s} + 2\lambda_{1c}\lambda_{1s}$$

$$+ 2\lambda_{1s}\beta_{1s} + \mu\left(4\theta_{tw}\theta_{1c} - 4\beta_{1s}\theta_{tw} - 2\lambda_{1c}\theta_{tw}\right)\Bigg] + \frac{m_i e\Omega^2}{2S} + \frac{m_{si}\Omega^2}{2S}\left[1 - \frac{\beta_0^2}{2} - \frac{\beta_{1c}^2}{8} - \frac{3}{8}\beta_{1s}^2\right] \tag{46}$$

$$\frac{F_{y_{1ci}}}{2S} = \frac{R-e}{32}\left[8\lambda_0^2 + 6\frac{e^2}{R^2}\beta_{1s}^2 + 2\frac{e^2}{R^2}\beta_{1c}^2 + \mu\left(2\lambda_0\beta_{1c} - 4\lambda_0\theta_{1s} - 14\frac{e}{R}\beta_{1s}\beta_0 - 4\frac{e}{R}\beta_{1c}\theta_0 + 12\lambda_0\beta_{1c}\right)\right.$$

$$+ \mu^2\left(-3\beta_{1c}\theta_{1s} - 3\beta_{1s}\theta_{1c} + 2\theta_0^2 - 2\frac{Cd_0}{a} + \theta_{1c}^2 + \theta_{1s}^2 + 8\beta_0^2 + 6\beta_{1c}^2 + 2\beta_{1s}^2\right)\Bigg]$$

$$+ \frac{R}{32}\Bigg[4\theta_{tw}\theta_0 - 8\lambda_0\theta_0 - 4\theta_{1c}\lambda_{1c} - 4\theta_{1c}\beta_{1s} + 2\theta_{1c}^2 - \frac{e}{R}\beta_{1s}\left(7\beta_{1s} - 6\theta_{1c} + 6\lambda_{1c}\right)$$

$$+ \frac{e}{R}\beta_{1c}\left(-\beta_{1c} - 2\theta_{1s} + 2\lambda_{1s}\right) + 2\lambda_{1c}^2 + 2\beta_{1s}^2 + 4\lambda_{1c}\beta_{1s} + \mu\left(-4\beta_{1c}\theta_{tw} - 8\beta_0\theta_{1c} - 6\beta_{1c}\theta_0\right.$$

$$\left.+ 2\frac{Cd_0}{a}\delta_{1c} + 4\theta_0\theta_{1s} + 9\beta_0\beta_{1s} + 7\beta_0\lambda_{1c} - 2\frac{e}{R}\beta_{1c}\theta_{tw} - 2\theta_0\lambda_{1s}\right) + 2\mu^2\theta_{tw}\theta_0\Bigg]$$

$$+ \frac{R}{48}\Bigg[\beta_{1c}\theta_{1s} - \beta_{1s}\theta_{1c} + 4\theta_0^2 - 4\frac{Cd_0}{a} + \theta_{1s}^2 - 8\lambda_0\theta_{tw} + \beta_{1s}\lambda_{1c} + \beta_{1s}^2 - \lambda_{1s}\beta_{1c} - 2\theta_{1s}\lambda_{1s} + \lambda_{1s}^2$$

$$+ \mu\left(4\theta_{tw}\theta_{1s} - 2\lambda_{1s}\theta_{tw}\right) + \mu^2\theta_{tw}^2\Bigg] + + \frac{R}{20}\theta_{tw}^2 + \frac{m_{si}\Omega^2}{8S}\left[-\beta_{1c}\beta_{1s} - 4\delta_0\right] \tag{47}$$

$$\frac{F_{z_{1si}}}{S} = \frac{R-e}{8}\left[3\mu^2\theta_{1s} - 4\mu\lambda_0 - \mu^2\beta_{1c}\right] + \frac{R}{6}\left[\theta_{1s} + 2\mu\theta_{tw} - \lambda_{1s} + \beta_{1c}\right]$$
$$+ \frac{R}{4}\left[2\mu\theta_0 - \frac{e}{R}\beta_{1c}\right] + \frac{m_{si}}{S}\Omega^2\beta_{1s} \tag{48}$$

$$\frac{F_{z_{1ci}}}{S} = \frac{R-e}{8}\left[\mu^2\theta_{1c} - \mu^2\beta_{1s}\right] + \frac{R}{6}\left[\theta_{1c} - \lambda_{1c} - \beta_{1s}\right] + \frac{R}{4}\left[-\mu\beta_0 + \frac{e}{R}\beta_{1s}\right] + \frac{m_{si}}{S}\Omega^2\beta_{1c} \tag{49}$$

$$M_{x_{1si}} = Se\left\{\frac{R-e}{8}\left[3\mu^2\theta_0 - 3\mu\frac{e}{R}\beta_{1c}\right] + \frac{R}{6}\theta_0 + \frac{R}{16}\left[6\mu\theta_{1s} + 2\theta_{tw} + 3\mu^2\theta_{tw} - 4\lambda_0 + 2\mu\beta_{1c} - 3\mu\lambda_{1s}\right]\right\} \tag{50}$$

$$M_{x_{1ci}} = Se\left\{\frac{R-e}{8}\left[-\mu^2\beta_0 + \mu\frac{e}{R}\beta_{1s}\right] + \frac{R}{16}\left[2\mu\theta_{1c} - 2\mu\beta_{1s} - 3\mu\lambda_{1c}\right]\right\} \tag{51}$$

$$M_{y_{1si}} = -Se\left\{\frac{R-e}{8}\left[-\mu^2\beta_0 - \mu\frac{e}{R}\beta_{1s}\right] + \frac{R}{16}\left[2\mu\theta_{1c} - 2\mu\beta_{1s} - \mu\lambda_{1c}\right]\right\} \tag{52}$$

$$M_{y_{1ci}} = -Se\left\{\frac{R-e}{8}\left[\mu^2\theta_0 - \mu\frac{e}{R}\beta_{1c}\right] + \frac{R}{6}\theta_0 + \frac{R}{16}\left[2\mu\theta_{1s} + 2\theta_{tw} + \mu^2\theta_{tw} - 4\lambda_0 + 2\mu\beta_{1c} - \mu\lambda_{1s}\right]\right\} \tag{53}$$

$$\frac{M_{z_{1si}}}{2} = Se\left\{\frac{R-e}{16}\left[8\frac{e}{R}\lambda_0\beta_{1c} + \mu\left(-8\lambda_0\theta_0 + 2\frac{e}{R}\theta_{1c}\beta_{1s} - 6\frac{e}{R}\beta_{1c}\theta_{1s} + 2\frac{e}{R}\beta_{1c}{}^2 - 2\frac{e}{R}\beta_{1s}{}^2\right)\right.\right.$$
$$+ \mu^2\left(6\theta_0\theta_{1s} - 2\theta_{1c}\beta_0 - 2\beta_{1c}\theta_0 + 2\beta_0\beta_{1s}\right)\lambda_{1s}\right] + \frac{R}{12}\left[2\theta_0\theta_{1s} - 2\frac{e}{R}\beta_{1c}\theta_{tw} - 2\theta_0\left(\lambda_{1s} - \beta_{1c}\right) + 4\mu\theta_{tw}\theta_0\right] \tag{54}$$
$$+ \frac{R}{16}\left[2\theta_{tw}\theta_{1s} - 4\lambda_0\left(\theta_{1s} - \lambda_{1s} + \beta_{1c}\right) - 4\frac{e}{R}\beta_{1c}\theta_0 - 2\theta_{tw}\left(\lambda_{1s} - \beta_{1c}\right) + \mu\left(4\theta_0{}^2 - 4\frac{Cd_0}{a} + \theta_{1c}{}^2 + 3\theta_{1s}{}^2\right.\right.$$
$$- 4\lambda_0\theta_{tw} - \beta_{1c}\left(-2\theta_{1s} - \lambda_{1s} + \beta_{1c}\right) - \beta_{1s}\left(2\theta_{1c} - \lambda_{1c} - \beta_{1s}\right) - \theta_{1c}\lambda_{1c} - 3\theta_{1s}\lambda_{1s} + 2\theta_{tw}{}^2\right)$$
$$\left.\left.+ \mu^2\left(3\theta_{tw}\theta_{1s} - \beta_{1c}\theta_{tw}\right)\right]\right\} + m_{si}e\Omega^2\left[-\beta_{1c}\beta_0 - \delta_{1c}\delta_0 + \delta_{1s}\right] + K_{i\delta}\frac{\delta_{1s}}{2} - C_{i\delta}\frac{\delta_{1c}}{2}\Omega$$

$$\frac{M_{z1ci}}{2} = Se\left\{\frac{R-e}{16}\left[-8\frac{e}{R}\lambda_0\beta_{1s} + \mu\left(2\frac{e}{R}\theta_{1s}\beta_{1s} - 2\frac{e}{R}\beta_{1c}\theta_{1c} + 8\lambda_0\beta_0 - 4\frac{e}{R}\beta_{1c}\beta_{1s}\right)\right.\right.$$
$$+ \mu^2\left(2\theta_0\theta_{1c} - 2\theta_{1s}\beta_0 - 2\beta_{1s}\theta_0 + 6\beta_0\beta_{1c}\right)\right]$$
$$+ \frac{R}{12}\left[2\theta_0\theta_{1c} + 2\frac{e}{R}\theta_{tw}\beta_{1s} - 2\theta_0\left(\lambda_{1c} + \beta_{1s}\right) - 2\mu\theta_{tw}\beta_0\right] \tag{55}$$
$$+ \frac{R}{16}\left[2\theta_{tw}\theta_{1c} - 4\lambda_0\left(\theta_{1c} - \lambda_{1c} - \beta_{1s}\right) + 4\frac{e}{R}\theta_0\beta_{1s} - 2\theta_{tw}\left(\lambda_{1c} + \beta_{1s}\right) + \mu\left(2\theta_{1c}\theta_{1s} - 4\theta_0\beta_0 + 3\beta_{1c}\lambda_{1c}\right.\right.$$
$$\left.\left.\left.+ 2\beta_{1c}\beta_{1s} - 2\beta_{1s}\theta_{1s} + \beta_{1s}\lambda_{1s} - \theta_{1s}\lambda_{1c} - \theta_{1c}\lambda_{1s} - 2\theta_{1c}\beta_{1c}\right) + \mu^2\left(\theta_{tw}\theta_{1c} - \beta_{1s}\theta_{tw}\right)\right]\right\}$$
$$+ m_{si}e\Omega^2\left[\beta_{1s}\beta_0 + \delta_{1s}\delta_0 + \delta_{1c}\right] + K_{i\delta}\frac{\delta_{1c}}{2} + C_{i\delta}\frac{\delta_{1s}}{2}\Omega$$

In order to apply the sum according to the number of blades, as previously derived, for the case of this study (rotor with N = 4 blades), we will have: $\varphi_1 = \varphi$ (yellow blade); $\varphi_2 = \varphi + \pi/2$ (blue blade); $\varphi_3 = \varphi + \pi$ (black blade); $\varphi_4 = \varphi + 3\pi/2$ (red blade), what gives:

$$Fx_1 = Fx_{01} + Fx_{1c1}\cos\varphi + Fx_{1s1}\sin\varphi$$

$$Fx_2 = Fx_{02} + Fx_{1c2}\cos(\varphi + \pi/2) + Fx_{1s2}\sin(\varphi + \pi/2)$$

$$= Fx_{02} + Fx_{1s2}\cos\varphi - Fx_{1c2}\sin\varphi$$

$$Fx_3 = Fx_{03} + Fx_{1c3}\cos(\varphi + \pi) + Fx_{1s3}\sin(\varphi + \pi)$$

$$= Fx_{03} - Fx_{1c3}\cos\varphi - Fx_{1s3}\sin\varphi$$

$$Fx_4 = Fx_{04} + Fx_{1c4}\cos(\varphi + 3\pi/2) + Fx_{1s4}\sin(\varphi + 3\pi/2)$$

$$= Fx_{04} - Fx_{1s4}\cos\varphi + Fx_{1c4}\sin\varphi$$

Finally, we will have:

$$\{Fx_{1c}\}_{rotor} = Fx_{1c1} + Fx_{1s2} - Fx_{1c3} - Fx_{1s4}$$

$$\{Fx_{1s}\}_{rotor} = Fx_{1s1} - Fx_{1c2} - Fx_{1s3} - Fx_{1c4}$$

Likewise, for the other components we will have:

$$\{Fy_{1c}\}_{rotor} = Fy_{1c1} + Fy_{1s2} - Fy_{1c3} - Fy_{1s4}$$

$$\{Fy_{1s}\}_{rotor} = Fy_{1s1} - Fy_{1c2} - Fy_{1s3} + Fy_{1c4}$$

$$\{Fz_{1c}\}_{rotor} = Fz_{1c1} + Fz_{1s2} - Fz_{1c3} - Fz_{1s4}$$

$$\{Fz_{1s}\}_{rotor} = Fz_{1s1} - Fz_{1c2} - Fz_{1s3} + Fz_{1c4}$$

$$\{Mx_{1c}\}_{rotor} = Mx_{1c1} + Mx_{1s2} - Mx_{1c3} - Mx_{1s4}$$

$$\{Mx_{1s}\}_{rotor} = Mx_{1s1} - Mx_{1c2} - Mx_{1s3} - Mx_{1c4}$$

$$\{My_{1c}\}_{rotor} = My_{1c1} + My_{1s2} - My_{1c3} - My_{1s4}$$

$$\{My_{1s}\}_{rotor} = My_{1s1} - My_{1c2} - My_{1s3} + My_{1c4}$$

$$\{Mz_{1c}\}_{rotor} = Mz_{1c1} + Mz_{1s2} - Mz_{1c3} - Mz_{1s4}$$

$$\{Mz_{1s}\}_{rotor} = FMz_{1s1} - Mz_{1c2} - Mz_{1s3} + Mz_{1c4}$$

Fuselage balance after the introduction of rotor defects

The fuselage balance equations are homogeneous. The balance of external forces gives:

$$\{Fx\}_{rotor} - \{Fz\}_{rotor}\alpha_m + Mg\alpha_f + 1/2\rho(Cx\,S)_f V^2 = M\,\ddot{x}_{t,t}$$

$$\{Fy\}_{rotor} - Mg\,\varphi_f - T_{Ra} = M\,\ddot{y}_{t,t} \qquad (56)$$

$$\alpha_m\{Fx\}_{rotor} + \{Fz\}_{rotor} - Mg - 1/2\rho V^2(Cz\,S)_{eh} = M\,\ddot{z}_{t,t}$$

The equations of moments were previously obtained for the equilibrium concerning the rotor head. As we are interested in the movement of the center of gravity of the aircraft, these equations must be rewritten to consider the wrench of the external forces, no longer at the rotor head, but at the center of gravity. In addition, we will need the fuselage moments of inertia about the center of gravity, whose position changes as a function of

mass centering: moments of inertia in roll (I_{xx}), pitch (I_{yy}), and yaw (I_{zz}), as well as the inertia product representing the yaw-roll coupling (I_{zx}). The other couplings are assumed to be null. From the moments and products of inertia $I=m\rho^2$, we have the radii of gyration. From the data of an aircraft with mass M and with moments and products of inertia, the radii of gyration will only be a function of the centering. For a helicopter with M = 9,500 kg (AS 332 MK II), the data is presented in Table 1.

Table 1: Data for the helicopter of the study case – adapted from (Jorge, 1992)

	AV centering X_{CG} = 4.48 m	Zero centering X_{CG} = 4.67 m	AR Center X_{CG} = 4.95 m
I_{xx} (m²kg)	16 104	14 707	12 650
I_{yy} (m²kg)	61 163	61 104	61 017
I_{zz} (m²kg)	54 101	52 684	50 596
I_{zx} (m²kg)	3 880	2 914	1 491
ρ_{xx} (m)	1.30	1.24	1.15
ρ_{yy} (m)	2.54	2.54	2.53
ρ_{zz} (m)	2.39	2.35	2.31
ρ_{xz} (m)	0.64	0.55	0.40

The inertias for zero centering were interpolated from the given inertias AV (forward) and AR (aft). The radii of gyration for any longitudinal centering can be interpolated from Table 1. The equilibrium of moments about the center of gravity is written as:

$$
\begin{bmatrix} Mx_h \\ My_h \\ Mz_h \end{bmatrix}_{rotor} + \begin{bmatrix} -x_{CG} \\ -y_{CG} \\ -z_{CG} \end{bmatrix} \Lambda \begin{bmatrix} Fx_h \\ Fy_h \\ Fz_h \end{bmatrix}_{rotor} + \begin{bmatrix} x_A - x_{CG} \\ y_A - y_{CG} \\ z_A - z_{CG} \end{bmatrix} \Lambda \begin{bmatrix} 1/2\,\rho(CxS)_f V^2 \\ 0 \\ 0 \end{bmatrix}
$$

$$
+ \begin{bmatrix} x_{eh} - x_{CG} \\ y_{eh} - y_{CG} \\ z_{eh} - z_{CG} \end{bmatrix} \Lambda \begin{bmatrix} 0 \\ 0 \\ -1/2\,\rho(CzS)_{eh}V^2 \end{bmatrix} + \begin{bmatrix} x_{Ra} - x_{CG} \\ y_{Ra} - y_{CG} \\ z_{Ra} - z_{CG} \end{bmatrix} \Lambda \begin{bmatrix} 0 \\ -T_{Ra} \\ 0 \end{bmatrix} =
$$

$$
= \begin{bmatrix} \rho_{xx}^2 & 0 & \rho_{xz}^2 \\ 0 & \rho_{yy}^2 & 0 \\ \rho_{xz}^2 & 0 & \rho_{zz}^2 \end{bmatrix} \begin{bmatrix} \ddot{\varphi}\,f_{t.t} \\ \ddot{\alpha}\,f_{t.t} \\ \ddot{\psi}\,f_{t.t} \end{bmatrix} = M \begin{bmatrix} \rho_{xx}^2\,\ddot{\varphi}\,f_{t.t} + \rho_{xz}^2\,\ddot{\psi}\,f_{t.t} \\ \rho_{yy}^2\,\ddot{\alpha}\,f_{t.t} \\ \rho_{xz}^2\,\ddot{\varphi}\,f_{t.t} + \rho_{zz}^2\,\ddot{\psi}\,f_{t.t} \end{bmatrix}
$$

with $y_{Ra} = x_A = y_A = 0$. Thus, Equation (57) is obtained as:

$$
\{Mx_h\}_{rotor} - y_{CG}\{Fz_h\}_{rotor} + z_{CG}\{Fy_h\}_{rotor} - (y_{eh} - y_{CG})\frac{1}{2}\rho V^2 (CzS)_{eh} + (z_{Ra} - z_{CG})T_{Ra}
$$

$$
= M\left(\rho_{xx}^2\,\ddot{\varphi}\,f_{t.t} + \rho_{xz}^2\,\ddot{\psi}\,f_{t.t}\right)
$$

$$
\{My_h\}_{rotor} - x_{CG}\{Fz_h\}_{rotor} - z_{CG}\{Fx_h\}_{rotor} + (z_A - z_{CG})\frac{1}{2}\rho V^2 (CxS)_f + (x_{eh} - x_{CG})\frac{1}{2}\rho V^2 (CzS)_{eh} \quad (57)
$$

$$
= M\rho_{yy}^2\,\ddot{\alpha}\,f_{t.t}
$$

$$\{Mz_h\}_{rotor} - x_{CG}\{Fy_h\}_{rotor} - y_{CG}\{Fx_h\}_{rotor} - y_{CG}\frac{1}{2}\rho V^2 (CxS)_f - (x_{Ra} - x_{CG})T_{Ra}$$

$$= M\left(\rho_{xz}^2 \ddot{\varphi} f_{t.t} + \rho_{zz}^2 \ddot{\psi} f_{t.t}\right)$$

And finally, Equation (58) is obtained as:

$$\{Mx_h\}_{rotor} - \{Mz_h\}_{rotor}\alpha_m - y_{CG}\left(\{Fx\}_{rotor}\alpha_m + \{Fz\}_{rotor}\right) + z_{CG}\{Fy_h\}_{rotor}$$

$$-(y_{eh} - y_{CG})\frac{1}{2}\rho V^2 (CzS)_{eh} + (z_{Ra} - z_{CG})T_{Ra} = M\left(\rho_{xx}^2 \ddot{\varphi} f_{t.t} + \rho_{xz}^2 \ddot{\psi} f_{t.t}\right)$$

$$\{My\}_{rotor} + x_{CG}\left(\{Fx\}_{rotor}\alpha_m + \{Fz\}_{rotor}\right) - z_{CG}\left(\{Fx\}_{rotor} - \{Fz\}_{rotor}\alpha_m\right) + (z_A - z_{CG})\frac{1}{2}\rho V^2 (CxS)_f$$

$$+(x_{eh} - x_{CG})\frac{1}{2}\rho V^2 (CzS)_{eh} = M\rho_{yy}^2 \ddot{\alpha} f_{t.t}$$

$$\{Mx\}_{rotor}\alpha_m + \{Mz\}_{rotor} - x_{CG}\{Fy\}_{rotor} + y_{CG}\left(\{Fx\}_{rotor} - \{Fz\}_{rotor}\alpha_m\right) - y_{CG}\frac{1}{2}\rho V^2 (CxS)_f$$

$$-(x_{Ra} - x_{CG})T_{Ra} = M\left(\rho_{xz}^2 \ddot{\varphi} f_{t.t} + \rho_{zz}^2 \ddot{\psi} f_{t.t}\right)$$

(58)

with :
ρ_{xx}: radius of gyration of the fuselage concerning the X_h axis (roll)
ρ_{yy}: radius of gyration of the fuselage about the Y_h axis (pitch)
ρ_{zz}: radius of gyration of the fuselage to the Z_h axis (yaw)

$$\alpha_f = \alpha_{f0} + \alpha f_{1c}\cos\psi + \alpha f_{1s}\sin\psi$$

And with: $\quad \varphi_f = \varphi_{f0} + \varphi f_{1c}\cos\psi + \varphi f_{1s}\sin\psi$

$$T_{Ra} = T_{Ra0} + T_{Ra1c}\cos\psi + T_{Ra1s}\sin\psi$$

where α_{f0}, φ_{f0}, and T_{Ra0} were previously obtained from the fuselage equilibrium with the isotropic rotor and T_{Ra1c}, T_{Ra1s} are the components of the tail rotor thrust needed to make the ψ_{f1c} and ψ_{f1s} components of the rotational motion null. Since ψ_{f1c} and ψ_{f1s} are assumed not to be zero in the calculation of $\ddot{\psi}_{ft,t}$, then $T_{Ra1c} = T_{Ra1s} = 0$ (therefore it is assumed that the tail rotor does not provide the cyclic thrust that could cancel the cyclic motion in yaw). To find the twelve unknowns of the fuselage accelerations: $-\Omega^2\left(x_{1c}, x_{1s}, y_{1c}, y_{1s}, z_{1c}, z_{1s}, \alpha f_{1c}, \alpha f_{1s}, \varphi f_{1c}, \varphi f_{1s}, \psi f_{1c}, \psi f_{1s}\right)$, we will apply, to the equilibrium equations, the operators: $\frac{1}{2\pi}\int_0^{2\pi}(...)\sin\psi d\psi$ and $\frac{1}{2\pi}\int_0^{2\pi}(...)\cos\psi d\psi$.

The rotor head efforts, after intermediate calculations, lead to Equations (59) to (70):

$$\frac{[Fx_{1s}]_{rotor}}{2} - \frac{[Fz_{1s}]_{rotor}}{2}.\alpha_m + Mg\frac{\alpha f_{1s}}{2} = -M\Omega^2\frac{x_{1s}}{2} \tag{59}$$

$$\frac{[Fx_{1c}]_{rotor}}{2} - \frac{[Fz_{1c}]_{rotor}}{2}.\alpha_m + Mg\frac{\alpha f_{1c}}{2} = -M\Omega^2\frac{x_{1c}}{2} \tag{60}$$

$$\frac{[Fy_{1s}]_{rotor}}{2} - Mg\frac{\varphi f_{1s}}{2} = -M\Omega^2\frac{y_{1s}}{2} \tag{61}$$

$$\frac{\left[Fy_{1c}\right]_{rotor}}{2} - Mg\,\frac{\varphi f_{1c}}{2} = -M\Omega^2\,\frac{y_{1c}}{2} \tag{62}$$

$$\frac{\left[Fx_{1s}\right]_{rotor}}{2}.\alpha_m - \frac{\left[Fz_{1s}\right]_{rotor}}{2} = -M\Omega^2\,\frac{z_{1s}}{2} \tag{63}$$

$$\frac{\left[Fx_{1c}\right]_{rotor}}{2}.\alpha_m - \frac{\left[Fz_{1c}\right]_{rotor}}{2} = -M\Omega^2\,\frac{z_{1c}}{2} \tag{64}$$

$$\frac{\left[Mx_{1s}\right]_{rotor}}{2} - \alpha_m\frac{\left[Mz_{1s}\right]_{rotor}}{2} - y_{cg}\alpha_m\frac{\left[Fx_{1s}\right]_{rotor}}{2} - y_{cg}\frac{\left[Fz_{1s}\right]_{rotor}}{2} + z_{cg}\frac{\left[Fy_{1s}\right]_{rotor}}{2} =$$
$$= -M\Omega^2\left(\rho_{xx}^{\ 2}\frac{\varphi f_{1s}}{2} + \rho_{xz}^{\ 2}\frac{\varphi f_{1c}}{2}\right) \tag{65}$$

$$\frac{\left[Mx_{1c}\right]_{rotor}}{2} - \alpha_m\frac{\left[Mz_{1c}\right]_{rotor}}{2} - y_{cg}\alpha_m\frac{\left[Fx_{1c}\right]_{rotor}}{2} - y_{cg}\frac{\left[Fz_{1c}\right]_{rotor}}{2} + z_{cg}\frac{\left[Fy_{1c}\right]_{rotor}}{2} =$$
$$= -M\Omega^2\left(\rho_{xx}^{\ 2}\frac{\varphi f_{1c}}{2} + \rho_{xz}^{\ 2}\frac{\varphi f_{1c}}{2}\right) \tag{66}$$

$$\frac{\left[My_{1s}\right]_{rotor}}{2} + \left(x_{cg}\alpha_m - z_{cg}\right)\frac{\left[Fx_{1s}\right]_{rotor}}{2} + \left(x_{cg} + z_{cg}\alpha_m\right)\frac{\left[Fz_{1s}\right]_{rotor}}{2} = -M\Omega^2\rho_{yy}^{\ 2}\frac{\varphi f_{1s}}{2} \tag{67}$$

$$\frac{\left[My_{1c}\right]_{rotor}}{2} + \left(x_{cg}\alpha_m - z_{cg}\right)\frac{\left[Fx_{1c}\right]_{rotor}}{2} + \left(x_{cg} + z_{cg}\alpha_m\right)\frac{\left[Fz_{1c}\right]_{rotor}}{2} = -M\Omega^2\rho_{yy}^{\ 2}\frac{\varphi f_{1c}}{2} \tag{68}$$

$$\alpha_m\frac{\left[Mx_{1s}\right]_{rotor}}{2} + \frac{\left[Mz_{1s}\right]_{rotor}}{2} - x_{cg}\frac{\left[Fy_{1s}\right]_{rotor}}{2} + y_{cg}\frac{\left[Fx_{1s}\right]_{rotor}}{2} - y_{cg}\alpha_m\frac{\left[Fz_{1s}\right]_{rotor}}{2}$$
$$= -M\Omega^2\left(\rho_{xz}^{\ 2}\frac{\varphi f_{1s}}{2} + \rho_{zz}^{\ 2}\frac{\varphi f_{1s}}{2}\right) \tag{69}$$

$$\alpha_m\frac{\left[Mx_{1c}\right]_{rotor}}{2} + \frac{\left[Mz_{1c}\right]_{rotor}}{2} - x_{cg}\frac{\left[Fy_{1c}\right]_{rotor}}{2} + y_{cg}\frac{\left[Fx_{1c}\right]_{rotor}}{2} - y_{cg}\alpha_m\frac{\left[Fz_{1c}\right]_{rotor}}{2}$$
$$= -M\Omega^2\left(\rho_{xz}^{\ 2}\frac{\varphi f_{1c}}{2} + \rho_{zz}^{\ 2}\frac{\varphi f_{1c}}{2}\right) \tag{70}$$

Passing the accelerations from the fuselage C.G. to the given measurement points
Fuselage helicopter vibration is measured through accelerometers, installed at given measurement points. The position vector of point (M) of the fuselage (assumed rigid) concerning its CG (G) is written in the Galilean reference frame, parallel to the aerodynamic frame, after rotation ($-\psi_f$, $-\alpha_f$, $-\varphi_f$) from the helicopter reference frame R_h.

$$\overline{GM} = \begin{bmatrix} \cos\psi_f & \sin\psi_f & 0 \\ -\sin\psi_f & \cos\psi_f & 0 \\ 0 & 0 & 1 \end{bmatrix}\begin{bmatrix} \cos\alpha_f & 0 & -\sin\alpha_f \\ 0 & 1 & 0 \\ \sin\alpha_f & 0 & \cos\alpha_f \end{bmatrix}\begin{bmatrix} 1 & 0 & 0 \\ 0 & \cos\varphi_f & \sin\alpha_f \\ 0 & -\sin\alpha_f & \cos\alpha_f \end{bmatrix}\begin{bmatrix} X_M - X_G \\ Y_M - Y_G \\ Z_M - Z_G \end{bmatrix} \tag{71}$$

with: X, Y, Z the coordinates of the points in the frame R_h.

The vector position is:

$$\overrightarrow{GM} = \begin{bmatrix} \begin{aligned} &(X_M - X_G)\cos\psi_f \cos\alpha_f + (Y_M - Y_G)\left(\cos\psi_f \sin\alpha_f \sin\phi_f + \sin\psi_f \cos\phi_f\right) \\ &+(Z_M - Z_G)\left(-\cos\psi_f \sin\alpha_f \cos\phi_f + \sin\psi_f \sin\phi_f\right) \end{aligned} \\ \begin{aligned} &(X_M - X_G)\left(-\sin\psi_f \cos\alpha_f\right) + (Y_M - Y_G)\left(-\sin\psi_f \sin\alpha_f \sin\phi_f + \cos\psi_f \cos\phi_f\right) \\ &+(Z_M - Z_G)\left(\sin\psi_f \sin\alpha_f \cos\phi_f + \cos\psi_f \sin\phi_f\right) \end{aligned} \\ \begin{aligned} &(X_M - X_G)\sin\alpha_f + (Y_M - Y_G)\left(-\cos\alpha_f \sin\phi_f\right) + (Z_M - Z_G)\left(\cos\alpha_f \cos\phi_f\right) \end{aligned} \end{bmatrix}$$

The first derivative of the vector position is written as:

$$\frac{d\overrightarrow{GM}}{dt} = \begin{bmatrix} \begin{aligned} &(X_M - X_G)\left(-\sin\psi_f \cos\alpha_f \dot{\psi}_{ft} - \cos\psi_f \sin\alpha_f \dot{\alpha}_{ft}\right) \\ &+(Y_M - Y_G)\left(-\sin\psi_f \sin\alpha_f \sin\phi_f \dot{\psi}_{ft} + \cos\psi_f \cos\alpha_f \sin\phi_f \dot{\alpha}_{ft} + \cos\psi_f \sin\alpha_f \cos\phi_f \dot{\phi}_{ft}\right. \\ &\left.+ \cos\psi_f \cos\phi_f \dot{\psi}_{ft} - \sin\psi_f \sin\phi_f \dot{\phi}_{ft}\right) \\ &+(Z_M - Z_G)\left(\sin\psi_f \sin\alpha_f \cos\phi_f \dot{\psi}_{ft} - \cos\psi_f \cos\alpha_f \cos\phi_f \dot{\alpha}_{ft} + \cos\psi_f \sin\alpha_f \sin\phi_f \dot{\phi}_{ft}\right. \\ &\left.+ \cos\psi_f \sin\phi_f \dot{\psi}_{ft} + \sin\psi_f \cos\phi_f \dot{\phi}_{ft}\right) \end{aligned} \\ \begin{aligned} &(X_M - X_G)\left(-\cos\psi_f \cos\alpha_f \dot{\psi}_{ft} + \sin\psi_f \sin\alpha_f \dot{\psi}_{ft}\dot{\alpha}_{ft}\right) \\ &+(Y_M - Y_G)\left(-\cos\psi_f \sin\alpha_f \sin\phi_f \dot{\psi}_{ft} - \sin\psi_f \cos\alpha_f \sin\phi_f \dot{\alpha}_{ft} - \sin\psi_f \sin\alpha_f \cos\phi_f \dot{\phi}_{ft}\right. \\ &\left.- \sin\psi_f \cos\phi_f \dot{\psi}_{ft} - \cos\psi_f \sin\phi_f \dot{\phi}_{ft}\right) \\ &+(Z_M - Z_G)\left(\cos\psi_f \sin\alpha_f \cos\phi_f \dot{\psi}_{ft} + \sin\psi_f \cos\alpha_f \cos\phi_f \dot{\alpha}_{ft} - \sin\psi_f \sin\alpha_f \sin\phi_f \dot{\phi}_{ft}\right. \\ &\left.- \sin\psi_f \sin\phi_f \dot{\psi}_{ft} + \cos\psi_f \cos\phi_f \dot{\phi}_{ft}\right) \end{aligned} \\ \begin{aligned} &(X_M - X_G)\cos\alpha_f \dot{\alpha}_{ft} + (Y_M - Y_G)\left(\sin\alpha_f \sin\phi_f \dot{\alpha}_{ft} - \cos\alpha_f \cos\phi_f \dot{\phi}_{ft}\right) \\ &+(Z_M - Z_G)\left(-\sin\alpha_f \cos\phi_f \dot{\alpha}_{ft} - \cos\alpha_f \sin\phi_f \dot{\phi}_{ft}\right) \end{aligned} \end{bmatrix}$$

The second derivative of the vector position is evaluated in R_g. The acceleration of M is:

$$\frac{d^2}{dt^2}\overrightarrow{GM} = \frac{d^2}{dt^2}\overrightarrow{G'G} + \frac{d^2}{dt^2}\overrightarrow{GM} \tag{72}$$

Point G' in Galileo's frame coincides with G at this instant. The acceleration of the CG is:

$$\left.\frac{d^2}{dt^2}\overrightarrow{G'G}\right]_{Rh} = \begin{bmatrix} \ddot{x}_{t.t} \\ \ddot{y}_{t.t} \\ \ddot{z}_{t.t} \end{bmatrix} \tag{73}$$

Thus, in the helicopter reference frame:

$$\left.\frac{d^2}{dt^2}\overrightarrow{GM}\right]_{Rh} = \begin{bmatrix} 1 & 0 & 0 \\ 0 & \cos\varphi_f & -\sin\varphi_f \\ 0 & \sin\varphi_f & \cos\varphi_f \end{bmatrix}\begin{bmatrix} \cos\varphi_f & 0 & \sin\varphi_f \\ 0 & 1 & 0 \\ \sin\varphi_f & 0 & \cos\varphi_f \end{bmatrix}\begin{bmatrix} \cos\varphi_f & -\sin\varphi_f & 0 \\ \sin\varphi_f & \cos\varphi_f & 0 \\ 0 & 0 & 1 \end{bmatrix}\left.\frac{d^2}{dt^2}\overrightarrow{GM}\right]_{Rg}$$

$$\frac{d^2}{dt^2}\overrightarrow{GM}\Bigg]_{Rh} = \begin{bmatrix} (X_M - X_G)\left(\dot{\alpha}_{ft}^2 - \cos\alpha_f \, \dot{\psi}_{ft}^2\right) \\[4pt] +(Y_M - Y_G)\left(2\cos\phi_f\,\dot{\alpha}_{ft}\dot{\phi}_{ft} + \sin\phi_f\,\ddot{\alpha}_{ft} + \cos^2\alpha_f\,\ddot{\psi}_{ft} - \cos\alpha_f\sin\alpha_f\sin\phi_f\,\dot{\phi}_{ft}^2\right. \\[4pt] \left. -2\cos\alpha_f\sin\alpha_f\,\dot{\psi}_{ft}\dot{\phi}_{ft}\right) \\[4pt] +(Z_M - Z_G)\left(2\sin\phi_f\,\dot{\alpha}_{ft}\dot{\phi}_{ft} - \cos\phi_f\,\ddot{\alpha}_{ft} + 2\cos^2\alpha_f\,\dot{\psi}_{ft}\dot{\phi}_{ft} + \cos\alpha_f\sin\alpha_f\,\ddot{\psi}_{ft}\right. \\[4pt] \left. + \cos\alpha_f\sin\alpha_f\cos\phi_f\,\dot{\phi}_{ft}^2\right) \\[14pt]

(X_M - X_G)\left(\;\left(2\cos\phi_f\sin\alpha_f\,\dot{\psi}_{ft}\dot{\alpha}_{ft} - \cos\phi_f\cos\alpha_f\,\ddot{\psi}_{ft} - \sin\phi_f\cos\alpha_f\sin\alpha_f\,\dot{\psi}^2_{ft}\right.\right. \\[4pt] \left. - \sin\phi_f\,\ddot{\alpha}_{ft}\right) + (Y_M - Y_G)\left(-\dot{\phi}_{ft}^2 - 2\cos^2\phi_f\sin\alpha_f\,\dot{\psi}_{ft}\dot{\phi}_{ft} - \cos^2\phi_f\,\dot{\psi}_{ft}^2 - sen^2\phi_f\dot{\alpha}_{ft}^2\right. \\[4pt] \left. - sen^2\alpha_f sen^2\phi_f\dot{\psi}_{ft}^2 - 2\sin\phi_f\, sen^2\alpha_f\dot{\psi}_{ft}\dot{\phi}_{ft} - 2\cos\alpha_f\cos\phi_f\sin\phi_f\,\dot{\psi}_{ft}\dot{\alpha}_{ft}\right) \\[4pt] +(Z_M - Z_G)\left(2\cos^2\phi_f\cos\alpha_{ff}\,\dot{\psi}_{ft}\dot{\alpha}_{ft} + \cos^2\phi_f\sin\alpha_f\,\ddot{\psi}_{ft} + \ddot{\phi}_{ft}\right. \\[4pt] \left. -2\cos\phi_f\sin\phi_f\sin\alpha_f\,\dot{\psi}_{ft}\dot{\phi}_{ft} - \cos\phi_f\sin\phi_f\,\dot{\alpha}_{ft}\dot{\psi}_{ft}^2 + 2\sin\phi_f\sin\alpha_f\cos\alpha_f\,\dot{\phi}_{ft}\dot{\psi}_{ft}\right. \\[4pt] \left. + \sin\phi_f\cos\phi_f\,\dot{\alpha}_{ft}^2 + \sin\phi_f\sin^2\alpha_f\,\ddot{\psi}_{ft} + \sin^2\alpha_f\sin\phi_f\cos\phi_f\,\dot{\psi}_{ft}^2\right) \\[14pt]

(X_M - X_G)\left(2\sin\phi_f\sin\alpha_f\,\dot{\psi}_{ft}\dot{\alpha}_{ft} - \sin\phi_f\cos\alpha_f\,\ddot{\psi}_{ft} + \cos\phi_f\cos\alpha_f\sin\alpha_f\,\dot{\psi}_{ft}^2\right. \\[4pt] \left. + \cos\phi_f\,\ddot{\alpha}_{ft}\right) + (Y_M - Y_G)\left(-2\sin\alpha_f\sin\phi_f\cos\phi_f\,\dot{\phi}_{ft}\dot{\psi}_{ft} - \sin\phi_f\cos\phi_f\,\dot{\psi}_{ft}^2\right. \\[4pt] \left. + \sin\phi_f\cos\phi_f\,\dot{\alpha}_{ft}^2 + \sin^2\alpha_f\cos\phi_f\sin\phi_f\,\dot{\psi}_{ft}^2 + 2\cos\phi_f\sin^2\alpha_f\,\dot{\psi}_{ft}\dot{\phi}_{ft}\right. \\[4pt] \left. - \sin\alpha_f\,\ddot{\psi}_{ft} + \ddot{\phi}_{ft} - 2\cos\alpha_f\sin^2\phi_f\,\dot{\psi}_{ft}\dot{\alpha}_{ft}\right) + (Z_M - Z_G)\left(2\cos\alpha_f\sin\phi_f\cos\phi_f\,\dot{\psi}_{ft}\dot{\alpha}_{ft}\right. \\[4pt] \left. + \sin\phi_f\cos\phi_f\sin\alpha_f\,\ddot{\psi}_{ft} - \dot{\phi}_{ft}^2 + 2\sin\alpha_f\sin^2\phi_f\,\dot{\psi}_{ft}\dot{\phi}_{ft} - \sin^2\phi_f\,\dot{\phi}_{ft}^2\right. \\[4pt] \left. -2\cos\phi_f\sin\alpha_f\cos\alpha_f\,\ddot{\psi}_{ft}\dot{\phi}_{ft} - \cos^2\phi_f\,\dot{\alpha}_{ft}^2 - \cos\phi_f\sin^2\alpha_f\,\ddot{\psi}_{ft} - \sin^2\alpha_f\cos^2\phi_f\,\dot{\psi}_{ft}^2\right) \end{bmatrix} \tag{74}$$

Assuming angles: $\sin\varphi_f \approx \varphi_f$; $\sin\alpha_f \approx \alpha_f$; $\sin\psi_f \approx \psi_f$; $\cos\varphi_f \approx 1$; $\cos\alpha_f \approx 1$; $\cos\psi_f \approx 1$, and disregarding triple products concerning the double products leads to:

$$\frac{d^2}{dt^2}\overrightarrow{GM}\Bigg]_{Rh} = \begin{bmatrix} \left(X_M - X_G\right)\left(-\dot{\alpha}_{ft}^2 - \dot{\psi}_{ft}^2\right) + \left(Y_M - Y_G\right)\left(2\dot{\alpha}_{ft}\dot{\varphi}_{ft} + \varphi_f\ddot{\alpha}_{ft} + \ddot{\psi}_{ft}\right) \\[4pt] +\left(Z_M - Z_G\right)\left(-\ddot{\alpha}_{ft} + 2\dot{\psi}_{ft}\dot{\varphi}_{ft} + \alpha_f\ddot{\psi}_{ft}\right) \\[14pt]

\left(X_M - X_G\right)\left(-\ddot{\psi}_{ft} - \varphi_f\ddot{\alpha}_{ft}\right) + \left(Y_M - Y_G\right)\left(-\dot{\varphi}_{ft}^2 - \dot{\psi}_{ft}^2\right) \\[4pt] +\left(Z_M - Z_G\right)\left(2\dot{\psi}_{ft}\dot{\alpha}_{ft} + \alpha_f\ddot{\psi}_{ft} + \ddot{\varphi}_{ft}\right) \\[14pt]

\left(X_M - X_G\right)\left(-\varphi_f\ddot{\psi}_{ft} + \ddot{\alpha}_{ft}\right) + \left(Y_M - Y_G\right)\left(-\alpha_f\ddot{\psi}_{ft} - \ddot{\varphi}_{ft}\right) \\[4pt] +\left(Z_M - Z_G\right)\left(-\dot{\varphi}_{ft}^2 - \dot{\alpha}_{ft}^2\right) \end{bmatrix} \tag{75}$$

The acceleration of point M is, therefore:
$$\frac{d^2}{dt^2}\overline{G'M}\Bigg]_{Rh} = \begin{bmatrix} \ddot{x}_{Mt.t} \\ \ddot{y}_{Mt.t} \\ \ddot{z}_{Mt.t} \end{bmatrix} = \begin{bmatrix} \ddot{x}_{Mt.t} \\ \ddot{y}_{Mt.t} \\ \ddot{z}_{Mt.t} \end{bmatrix} + \frac{d^2}{dt^2}\overline{GM}$$

With accelerations given by :
$$\ddot{x}_{Mt.t} = \Omega^2 \ddot{x}_M = \Omega^2\left(-x_{M1c}\cos\psi - x_{M1s}\sin\psi\right)$$
$$\ddot{y}_{Mt.t} = \Omega^2 \ddot{y}_M = \Omega^2\left(-y_{M1c}\cos\psi - y_{M1s}\sin\psi\right)$$
$$\ddot{z}_{Mt.t} = \Omega^2 \ddot{z}_M = \Omega^2\left(-z_{M1c}\cos\psi - z_{M1s}\sin\psi\right)$$

The six unknowns (accelerations of point M) can be found after applying the operators: $\frac{1}{2\pi}\int_0^{2\pi}(\ldots)sin\psi d\psi$ and $\frac{1}{2\pi}\int_0^{2\pi}(\ldots)cos\psi d\psi$, what gives, after intermediate calculations:

$$x_{M1s} = x_{1s} + \left(Y_M - Y_G\right)\left(\varphi_{f0}\alpha_{f1s} + \psi_{f1s}\right) + \left(Z_M - Z_G\right)\left(\alpha_{f0}\psi_{f1s} + \alpha_{f1s}\right)$$

$$x_{M1c} = x_{1c} + \left(Y_M - Y_G\right)\left(\varphi_{f0}\alpha_{f1c} + \psi_{f1c}\right) + \left(Z_M - Z_G\right)\left(\alpha_{f0}\psi_{f1c} + \alpha_{f1c}\right)$$

$$y_{M1s} = y_{1s} + \left(X_M - X_G\right)\left(-\varphi_{f0}\alpha_{f1s} - \psi_{f1s}\right) + \left(Z_M - Z_G\right)\left(\alpha_{f0}\psi_{f1s} + \varphi_{f1s}\right)$$

$$(76)$$

$$y_{M1c} = y_{1c} + \left(X_M - X_G\right)\left(-\varphi_{f0}\alpha_{f1c} - \psi_{f1c}\right) + \left(Z_M - Z_G\right)\left(\alpha_{f0}\psi_{f1c} + \varphi_{f1c}\right)$$

$$z_{M1s} = z_{1s} + \left(X_M - X_G\right)\left(-\varphi_{f0}\psi_{f1s} - \alpha_{f1s}\right) + \left(Y_M - Y_G\right)\left(-\alpha_{f0}\psi_{f1s} - \varphi_{f1s}\right)$$

$$z_{M1c} = z_{1c} + \left(X_M - X_G\right)\left(-\varphi_{f0}\psi_{f1c} - \alpha_{f1c}\right) + \left(Y_M - Y_G\right)\left(-\alpha_{f0}\psi_{f1c} - \varphi_{f1c}\right)$$

The amplitude and phase of the accelerations

The efforts on the rotor head were expressed as a function of the azimuthal coordinate of blade number 1: $\psi_1 = \psi = \Omega t$, where t represents the time that elapsed from the moment when this blade passed through the origin position ($\psi = 0$) and the magnetic sensor triggered the signal to synchronize the time. From this moment (t = 0) on, the vibration measured in the fuselage is expressed in terms of amplitude and phase, which can be calculated from the different components, as summarized in Tables 2 and 3.

Table 2: Acceleration at the fuselage CG – adapted from (Jorge, 1992)

Entry data	Vibration amplitude	Vibration phase
x_{1s}, x_{1c}	$AX = \Omega^2\sqrt{x_{1s}^2 + x_{1c}^2}$	$\phi X = \arctan\dfrac{x_{1c}}{x_{1s}}$
y_{1s}, y_{1c}	$AY = \Omega^2\sqrt{y_{1s}^2 + y_{1c}^2}$	$\phi Y = \arctan\dfrac{y_{1c}}{y_{1s}}$
z_{1s}, z_{1c}	$AZ = \Omega^2\sqrt{z_{1s}^2 + z_{1c}^2}$	$\phi Z = \arctan\dfrac{z_{1c}}{z_{1s}}$

Table 3: Acceleration of point M at the fuselage – adapted from (Jorge, 1992)

Entry data	Vibration amplitude	Vibration phase
x_{M1s}, x_{M1c}	$AX_M = \Omega^2 \sqrt{x_{M1s}^2 + x_{M1c}^2}$	$\phi X_M = \arctan \dfrac{x_{M1c}}{x_{M1s}}$
y_{M1s}, y_{M1c}	$AY_M = \Omega^2 \sqrt{y_{M1s}^2 + y_{M1c}^2}$	$\phi Y_M = \arctan \dfrac{y_{M1c}}{y_{M1s}}$
z_{M1s}, z_{M1c}	$AZ_M = \Omega^2 \sqrt{z_{M1s}^2 + z_{M1c}^2}$	$\phi Z_M = \arctan \dfrac{z_{M1c}}{z_{M1s}}$

3.4 Validation of the calculation code

The Possibilities

Several procedures for validating the calculation code can be envisaged, not only within the scope of the direct problem but also for the opposite inverse, which will be introduced in a later section.

The first possibility is to validate the codes with accelerometers installed as foreseen in the Maintenance Manual (MET) of the helicopter, to be able to compare the results obtained with the correction maps (which are experimental, obtained in-flight tests) that already exist in MET. We've simulated, in the scope of this work, some flight conditions, to validate the calculation code of the direct problem.

A second possibility is to validate the codes through flight tests, which can give us, the different flight conditions and known corrections introduced in the rotor, the efforts measured in the rotor head, as well as the accelerations at different points of the fuselage. This validation is adapted not only to the direct problem but also to the inverse problem, since it is possible to place the six accelerometers in the fuselage, necessary to find the CG accelerations of the fuselage and the efforts that result in the rotor head, as we will see in the discussion of the inverse problem, in a later section.

A third possibility is to validate the code with the help of a helicopter rotor numerical code, such as R85, HOST, etc. For references on numerical codes for helicopter rotor simulation see (Rabe & Wilke, 2018), (Wilke, 2017), (Johnson, 2013b), (Benoit et al., 2000). To be able to compare the codes, it is necessary to put the isotropy of the blades as a hypothesis, which leads us to the validation of the part of the code related to the isotropic rotor balance. This possibility can lead to a decrease in the workload required in the flight tests (second possibility, above), which will serve, therefore, to validate only the second part of the code (the introduction of defects in the rotor head).

Comparison with the MET

Several possibilities for installing accelerometers are provided in the MET: (i) Accelerometers (lateral and longitudinal) positioned on the electrical panel, to the left of the 3rd man's seat, at the top; (ii) Accelerometers (vertical, lateral, and longitudinal) positioned on the floor to the left, below the co-pilot seat; and (iii) Accelerometer (lateral) positioned below the main gearbox (BTP).

The calculation code, as previously derived, is composed of two parts: the first part corresponds to the calculation of the equilibrium, with the isotropic rotor, while the second part corresponds to the introduction of defects. The calculation of the isotropic rotor equilibrium is done by calculating the solution of a system of 12 nonlinear equations with 12 unknowns. These are the three flapping equations, the three drag equations, and the six fuselage balance equations, as seen before. As the equations are non-linear, a subroutine of the IMSL library was used in a FORTRAN software, which finds the solution of a system of non-linear equations with the Jacobian of this system provided a priori. For that, the Jacobian of the system of non-linear equations of isotropic rotor equilibrium is calculated as a matrix 12 x12, obtained from all the partial derivatives of the twelve equations concerning the twelve unknowns.

$$FJAC(1,1) = \frac{\partial F(1)}{\partial X(1)} = \frac{\partial F(1)}{\partial \theta_0} = \frac{\rho a c R^2}{2 I_\beta}\left[-e\left\{ \frac{R-e}{2}\mu^2 + \frac{R}{3} \right\} + \frac{R^2}{4} + \frac{R^2}{4}\mu^2 \right]$$

.... etc, up to   (77)

$$FJAC(12,12) = \frac{\partial F(12)}{\partial X(12)} = \frac{\partial F(12)}{\partial T_{Ra}} = -x_{Ra}$$

The unknowns are angles in radians and, therefore, very small, and a subroutine that works in double precision was used. Even with all the precautions from the numerical point of view, the system was always very sensitive to two parameters:

- The criterion to finish the calculation (a relative error criterion). A root is accepted if the relative error between two successive approximations of this root is less than the relative error criterion. The chosen value of the criterion is very important for the convergence of the subroutine; if the relative error criterion is too large, the subroutine fails to find a solution that can nullify the system of equations before the difference between two successive iterations, for root, be already reached. On the other hand, if the relative error criterion is too small, the subroutine may interrupt the iteration because it hasn't made good progress. The system of equations is extremely sensitive to the knowledge, with good precision, of the unknown parameter values.

- The approximate guess value of θ is used to initialize the subroutine. This value must be provided a priori and slight changes in this value may sometimes prevent the subroutine to find the system solution.

In this way, the simulation of all possibilities in terms of flight conditions, mass, and balance, with the subroutine, becomes a problem since, for each case, it is necessary to effectively evaluate the relative error criterion and the initial pitch θ values, to be supplied to the subroutine. For a more complete simulation, it will be necessary to find a system solution subroutine more adapted to this specific problem. The results of the isotropic rotor equilibrium can be found for different flight conditions (stationary flight, ground level, etc.), with different values for the helicopter mass and centering (mass center location). Limits of mass and centering are shown in Figure 18, for this case.
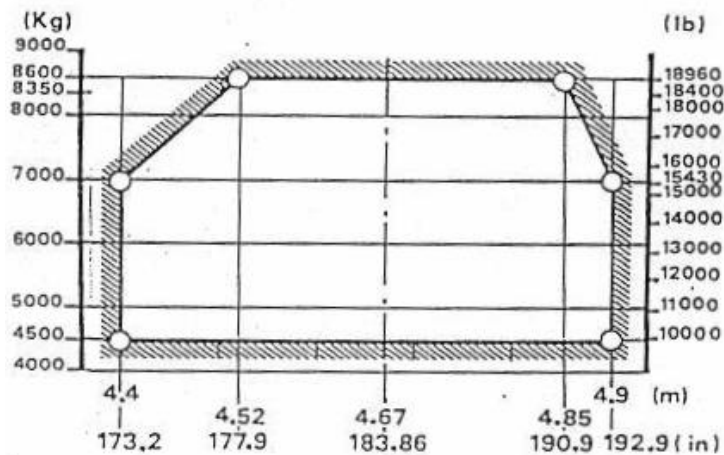
**Figure 18: limits of mass and centering: helicopter AS332L – adapted from
(Jorge, 1992)**

For the second part of the calculation code, there are no numerical problems in terms of convergence to the solution. Figure 19 shows a rotor balance chart, from the MET. Starting from the isotropic rotor, the introduction of an equilibrium mass $\Delta m = 500$ g on blade n° 2 leads us to a lateral vibration of 0.25 IPS amplitude, and 270° phase (point X on the chart). Entering the same mass in the software, for the obtained equilibrium, the deviation found (in amplitude and phase) is small (point O on the chart).
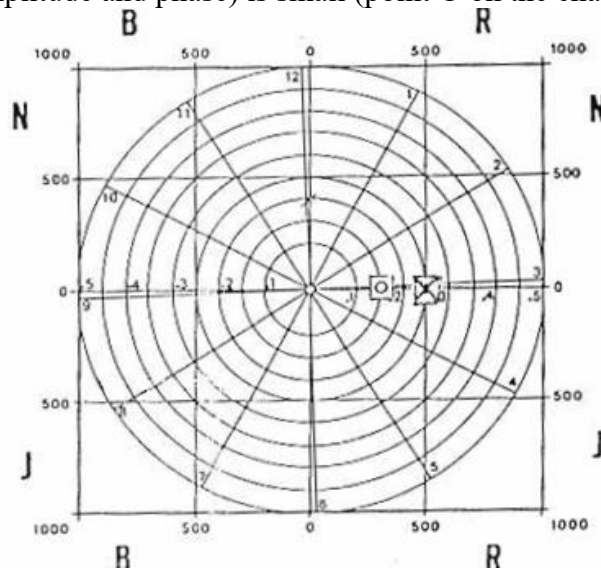
**Figure 19: Helicopter Maintenance Manual (MET) chart: simulation and predicted
vibration values – adapted from (Jorge, 1992)**

This small deviation can be explained by the fact that the balance chart is an average chart, obtained from the user experience of several aircraft whose characteristics were not identical. Furthermore, it is a map that is assumed to be valid throughout the helicopter flight domain, when one can see, in the previously obtained formulations, that the introduction of the same equilibrium mass under different flight conditions or with different configurations (in terms of weight and centering of the aircraft) can lead to different efforts on the rotor head and, consequently, to measured vibrations on the fuselage which are different, too. In this way, the comparison with the MET serves as an initial point of reference, knowing that the complete validation of the system must be done, in principle, by flight tests.

A comment on the results

The subroutine provided by the IMSL library for calculating the isotropic rotor balance is very sensitive to variations in the given parameters and the initial values considered for the unknown parameters (in particular, the initial pitch angle θ). A subroutine more adapted to this specific problem should be sought, to be more robust, that is, less affected by variations of parameters that have nothing to do with the flight condition as such, but with only numerical constraints (in this case, the need, for the subroutine, to know a priori what the maximum permissible error is, and to have initial values of the pitch angle θ, to initialize the subroutine.

It can also be seen that the simple comparison with the MET cannot be taken as a complete validation of the system but must be considered as an initial point of reference for more complete validation, with flight tests, for different flight conditions and aircraft settings.

3.5 The inverse problem for identification of unbalanced and out-of-track blades in a helicopter main rotor system and the optimization of the accelerometer positions– perspectives

Analysis of the Inverse Problem

As in the case of the study of the introduction of defects, the problem can be divided into two stages: (i) the study of the isotropic rotor; (ii) the study of the inverse problem as such from the vibrations measured on the fuselage.

For this second step, the equilibrium with the isotropic rotor (θ, β, δ, α_f, φ_f, T_{Ra}) is, therefore, known a priori. From the installation of accelerometers at different points of the fuselage, it is possible to have, as input data, the amplitude and phase of the accelerations at these locations. It was previously seen the passage of the six accelerations (three linear and three angular) to the three linear accelerations of any point M in the fuselage. To calculate the inverse, it is necessary and sufficient to have six linear accelerations at chosen points on the fuselage (example: the three accelerations in x, y, and z of two points: M_1 and M_2), to find the six accelerations of the CG, the fuselage seen as a rigid body.

From the twelve components (in sines and cosines) of the CG accelerations and the knowledge of the fuselage radii of gyration (which are a function of the centering of the aircraft, which is known from the isotropic rotor equilibrium), the twelve components (in sines and cosines) of the resulting efforts on the rotor head (Fx, Fy, Fz, Mx, My, Mz) are found.

From this point on, the inverse of the previously obtained expressions is no longer possible to be obtained without making additional assumptions, since each of the resulting efforts in the rotor head was obtained from the sum of the efforts generated by each of the four blades. One must note that, at this point, there are twelve equations and forty-eight unknowns. From the practical experience of balancing the rotors, it can be seen that in terms of the measured vibration: (i) the introduction of an equilibrium mass ($+\Delta m$) on a blade i is equivalent to the removal of the same mass ($-\Delta m$) on the blade that is diametrically opposite to it ($i + 180°$); (ii) the increase in rod (pitch link) length ($\Delta\theta_0$) on blade i is equivalent to the corresponding decrease ($-\Delta\theta_0$) on the opposite blade ($i + 180°$).

In addition, MET maintenance procedures generally prohibit the operator from making adjustments to one blade, called standard. For this blade, the rod length, as well as the

adjustment of the tabs and the balance mass at the sleeve will remain unchanged. Thanks to this equivalence between the balance corrections to be introduced either on blade *i*, or on blade *i + 180°*, we will consider only the introduction of corrections for two rotor blades (example: blades *i* and *i + 90°*), the other two will continue to be unchanged. In this way, we now have twelve equations and twenty-four unknowns (the forces generated in the rotor head by these two blades being considered), the forces generated for the two other blades are obtained with the isotropic rotor hypothesis. Maintenance procedures recommend not introducing two simultaneous corrections on two different blades. In this way, the process is iterative: corrections are introduced on a blade, the vibration measurement is re-done, new corrections are introduced on the same blade or another one, the measurements are re-done and so on, in sequence, until obtaining levels of vibrations below a certain value, defined a priori as acceptable, and predicted in the helicopter maintenance manual (MET).

We will solve the passage from the resulting efforts at the rotor head to the efforts in the rotor head due to a blade *i* in the same iterative way: (i) It is assumed that the other three blades are isotropic, and we will have a system of twelve equations with twelve unknowns (the efforts on the rotor head generated by blade *i*). Then, the corrections to be introduced on this blade are calculated (see below); (ii) Next, it is assumed an isotropic blade *i* to calculate the rotor head efforts generated by blade *i + 90°* (in our example) and, thus, the corrections to be introduced on this blade (see below); and (iii) The calculated correction is introduced, and then the accelerometer measurements and also all calculations to obtain new corrections are redone, until the vibration level is below an acceptable value.

For code validation regarding the inverse problem, it is sufficient to take the corrections calculated before for blade *i* and input them in the calculation code of the direct problem, to verify if the introduced corrections cause vibrations at the fuselage measurement points (M_1 and M_2), which are of similar amplitude but in phase opposition concerning the vibrations measured initially (which were the given parameters in the calculation of the inverse problem). Thus, the vibrations caused by the corrections will cancel out those from the beginning. It remains to analyze the corrections to be introduced on a blade *i*. It was obtained, above, the efforts in the head of the rotor generated by blade *i*. It was also seen that these efforts come from the introduction of defects in θ_0, θ_{1s}, and m_p, which generated the new flapping (β) and drag (δ) angles.

The mass effect is more important on "lateral" and "longitudinal" (in the rotor plane) vibrations, while the rod and tab effect is more important on "vertical" (orthogonal to the rotor plane) vibrations. In this way, we will separate the problem into two parts:

- For the efforts in the plane (Fx, Fy, and the moment generated by these two forces: Mz), we will assume that there is no variation due to the pitch (θ). In this way, θ, β and δ are the angles already obtained with the isotropic rotor hypothesis and the unknowns are now: m_p, m_{sp}, and I_β. Finally, these last three parameters have a relationship with the change in blade mass due to the introduction of the equilibrium mass (Δm), which will give us, in the end, the equilibrium mass to be introduced or withdrawn on this blade *i* (Δmi) to obtain the forces Fx, Fy and Mz.

- For the forces orthogonal to the rotor plane, we will assume that m_p, m_{sp}, and I_β are the parameters of the isotropic rotor. We will have six equations (Fz, Mx, My, in sines and cosines) in addition to the flapping and drag equations, to obtain the new pitch angles (θ), as well as the corresponding flapping (β) and drag (δ) angles. This problem can be treated in two parts, too. Current rotor balancing procedures are to perform, in the first step, a steady-state flight ($\mu = 0$) from which corrections are introduced on the pitch rod. Then, a stabilized level flight is carried out, where corrections tab adjustment are introduced since the tabs influences restricts to forward flight.

Thus, for simplicity of calculation, the inverse problem can be calculated:

- In the first step, for $\mu = 0$, with θ_{1c} and θ_{1s} calculated with the isotropic rotor and the only defect is the one in θ_0, with the corresponding changes in β and δ;
- In a second step, for $\mu \neq 0$, we will assume that θ_0 is the one calculated in the first step, and will have, as unknowns: θ_{1s} (equivalent to a change of tab, as seen in the analysis done previously) and the corresponding terms in β and δ.

Optimization of the accelerometer positions

To look for the optimal position of the accelerometers, it is necessary to use the second possibility of validating the calculation code, mentioned above, that is, the flight tests. The intention is to minimize the calculations to be made, and the possible couplings between the different parameters, during the calculation of the inverse problem, and, for that, the most adapted validation method is the flight tests. It is at this stage of the work that we will consider, also, the constraints or limitations of the problem, such as: (i) The maximum permissible balancing mass in the sleeve; (ii) The maximum permissible effort on the rod; (iii) The maximum adjustment of tabs, etc. Several possible positions of accelerometers should be studied. For example:

- Three accelerometers (vertical, lateral, and longitudinal) on the floor to the left, below the co-pilot seat;
- Two accelerometers (vertical and lateral) on the floor on the right, in the strong frame (Z = 6,815 mm) (the end of the floor and the beginning of the tail boom);
- One accelerometer (vertical) on the floor on the left (same frame: Z = 6,815 mm).

The 2nd step of the optimization process, the effect of the tab, as previously analyzed, can be considered as a change in θ_{1s} and, in addition, a change in blade twist, to account for the fact that the tab generates a torsion moment on the blade, which can lead to a twisting of this blade because the blade has a certain torsional flexibility, which can be considered. This can also lead us to calculate the efforts that will be passed to the fuselage through the rods and the chain of command. Non-linearities, such as, for example, the play of a connecting rod, can also be considered, as well as non-linearities in the operation of drag adapters.

4 Model-based parameter identification for unbalanced and out-of-track helicopter rotor blades: a case study of a 3-blade main rotor

This section is based on a Master's Thesis (González, 2012), Post Graduate Program in Mechanical & Aeronautical Engineering at ITA, São José dos Campos, Brazil, 2012.

4.1 Introduction

Case study: 3-blade main rotor: model development & comparison with flight tests

Following the steps of the above study for the 4-blade helicopter case, this Section focuses on the analytical modeling of the relationship between the simplified dynamics of a fuselage-main rotor system and the vibratory level of its response, measured at two points on the fuselage, for the case of a 3-blade helicopter. The mathematical model derived by (Jorge, 1992) was adapted for the peculiarities of a typical small helicopter with three blades. Most of the text from (González, 2012) was retained. Some equations at the beginning of these derivations, before adding the total number of blades, are similar to the ones obtained in the previous section, for the case of the 4-blade study, and thus their Equation numbers are only referenced in the following text, to avoid eventually repeating some previously obtained equations. As before, the response is limited to measurements of amplitude and phase of once-per-rev vibrations at the circular frequency of the main rotor (1-per-rev or 1Ω) on the x, y, and z axes. An additional limitation to this model comes from the approximations assumed for some design parameters, not available in the literature or manuals, thus adopted as representative of the 3-blade helicopter in the study, the AS355 F2 Squirrel model.

As in Section 3, this section presents mathematical modeling for the analytical expression of the wrench of the efforts in the rotor hub, modeled as a set of articulated blades under the degrees of freedom in pitch, flapping, and lead-lag. Three distinct phases make up any type of analysis: analytical modeling, mathematical modeling, and dynamic behavior. In line with good engineering practices to obtain adequate analytical modeling (among several always possible), a set of simplifying hypotheses is adopted to reduce a real dynamic system to another equivalent of the type represented by mass-spring-damper; and the same is represented by a free body diagram that reflects its properties also defined by the analyst, such as inertia (mass), rigidity (spring), energy dissipation (damper), and type of loading (forces). The model needs to be a compromise solution between the sophistication that brings it closer to the complex reality and the simplification that, moving away from it, analyzes the corresponding mathematical model viable, with the resources and deadlines available. Mathematical modeling includes small vibrations around an equilibrium position, and their associated accessory conditions (initial and/or boundary conditions). Among the basic and didactic approach techniques for deducing the differential equations governing the motion, one can group them into Lagrangian Mechanics (according to scalar energy concepts) and Newtonian Mechanics (based on vector quantities). Despite complex structures recommending the first (more systematic), the latter is chosen in this text, given the more intuitive nature of identifying the efforts and their visualization in the free body diagram (necessary in this option), conceived in a relatively simple way, given the simplifications to be discussed. The resolution of these equations, either in the time or frequency domain, then reveals the dynamic behavior resulting from the adopted analytical model, and in this text, it is performed numerically in the frequency domain with computational aid.

THE HYPOTHESES

The analytical modeling of the isotropic fuselage-rotor system begins by opting for the design of the free-body diagram only for the defect-free rotor system (from this point onwards, the term "isotropic" is adopted), or more precisely, of any of its three blades, since it concentrates, within the adopted hypotheses, all the dynamic efforts to be integrated by the rotor hub and then added up and transmitted to the fuselage (supposedly assumed as stationary concerning any other loads). Always looking for a compromise solution between the simplicity of the model and the accuracy of the results, for the necessary definition of the reference flight configuration, despite directly influencing the vibration index, for simplicity, this study adopts:

1. The fixed value of 1.225 kg/m³ of the air density, which flows through the profiles of the blades and empennages, and this is directly proportional to their lift and drag, also creates resistance to the fuselage advance. This value corresponds to the standard atmosphere ISA (International Standard Atmosphere - model established by the ICAO), without ΔT temperature adjustments (non-varied ISA), and at sea level (troposphere, under standardized conditions of temperature (15°C) and pressure (101325N/m2))

2. Zero load factor (acceleration of the body dimensionless by the acceleration of gravity g, a result of the ratio between the force applied to it and its weight), that is, stationary, straight, level, and stabilized flight (structure not subjected to any accelerations);

3. In the broad spectrum of frequencies, even when aware of the importance of other harmonics associated with other defects, for simplicity, only vibrations at the fundamental frequency of value 1Ω are considered here, equal to once the rotation of the main rotor, as it is still an important item associated with direct intervention actions in maintenance practice.

4. Articulated rotor according to the following degrees of freedom for each blade, under small-displacement angles to reduce non-linearities: (i) flapping (flexion out of the plane of rotation): as in forward flight it compensates for lift asymmetry; (ii) forward and backward movement or lead-lag (flexion in the plane of rotation): as it is due to the non-linear Coriolis force associated with the flapping motion (although independent of the lead-lag), according to a flap-lag coupling, for which relief is required bay means of a lead-lag joint normal to that plane; and (iii) variation of pitch or incidence in pitch or feathering or torsion (rotation around the elastic axis): as it is the end of the collective and/or cyclical chain of action, and its coupling with each of the above degrees of freedom.

For simplicity of the model to be calculated, the torsional freedom of the blade or twist associated with the tab adjustments (which here is associated with torsion) is disregarded, since it is assumed that it has sufficient stiffness to contain it. There is only the built-in, permanent and linear torsion, as a given intrinsic to the project. Furthermore, all nonlinearities linked to pitch-flap-lag couplings, represented by the triple products of their displacements or associated functions, are disregarded.

5. Rigid blades, for simplicity of calculations. Therefore, the degree of freedom in the flexible mode of torsion of the blade (twist) along its elastic line is disregarded. This positioning eliminates the adjustment through the tabs, which also corrects the tracking by variation of the lift in the respective section of the blade in which they are installed.

6. Blade submitted to aerodynamic loading resulting from two-dimensional flow according to the Blade Element Theory (Johnson, 2013b): adopts a high aspect ratio for the profile) in a steady-state, without gust-type disturbances being considered.

The actual blade is made of composite material and is reasonably flexible in bending and torsion, like most of them, so it is subject to aeroelastic effects related to flap-lag, pitch-flap, pitch-lag, and pitch-flap-lag couplings (only this one is disregarded here in the model). This study disregards the effects of flow on the retreating blade (flow detachments, dynamic stall and reverse flow), and on the forward blade tip (compressibility and associated advances implemented by modern blade tip designs, as well as the effects of tip loss), as well as at its root (offset loss), and large flap deformations of the blades (source of nonlinearities).

Aerodynamic forces are well determined by fundamental modes (rigid body movements), but excitation in elastic torsional and bending modes by high harmonics of these forces can produce large loads on the section, even under small deflections. Hence the natural frequency of the blade in these modes must be kept away from the harmonics of Ω (Johnson, 2013a).

7. It is assumed that the fuselage, assumed to be a semi-rigid body, can be dynamically equivalent to a rigid body with six degrees of freedom (three components of position and three orientation angles). Hence, the configuration of fuselage states can be described in terms of only six degrees of freedom, along with and around each of the three axes X, Y, and Z (the larger arrows shown in Figure 20) for their equilibrium under external forces, such as the aerodynamic forces, which, added to the blade motion equations (at small flapping and lead-lag angles) form twelve non-linear differential equations with twelve unknowns.
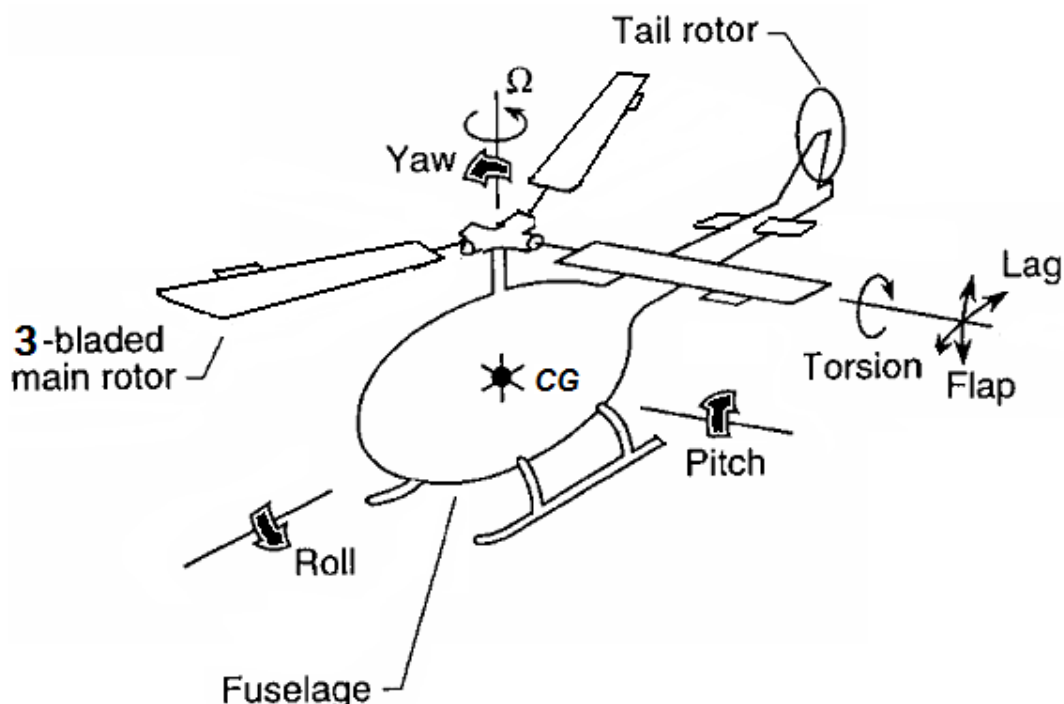
Figure 20: Degrees of Freedom (DoF) of the coupled system rotor-fuselage – adapted from (Friedmann & Hodges, 2003)

8. The loading on the rotor hub is determined from the sum of the three integrations (on each blade) of the efforts considered according to the Blade Element Theory.

In the modeling adopted in this study, despite all the simplifications that even disregard all the flap-torsion, lag-torsion, and flap-lag-torsion couplings, the nature of the system of equations of motion of the rotor-fuselage system, which takes the flap-lag, is still non-linear, and in its numerical resolution process, it is internally linearized by the computational algorithm selected in the MATLAB® software environment.

THE PARAMETERS

It is necessary to adopt some parameters to establish the aircraft object of the simulation and some flight condition(s), where the responses of the isotropic rotor-fuselage system will be investigated, and which later serve as a reference for the evaluations of the effects of the introduced anisotropies. These parameters are:

• system mass: fundamental proportionality factor in the evaluation of accelerations related to the submitted efforts. It is assumed constant, that is, the reduction due to fuel consumption is neglected, when compared to the original mass.

• aircraft centering: responsible for the positioning of its center of gravity (CG) and the definition of the relative moment arms (associated with the fuselage attitude states), as well as for the propagation of the vibration characteristics along the fuselage. Generally, the CG is presented by the manufacturer in the form of Figure 21, within which its "walk" is allowed (in the vicinity of the vertical of the mast and, therefore, of the main rotor traction), to guarantee longitudinal and lateral stability. directional, as well as the flight qualities desirable to the project. Figure 21 shows the relevant data used, such as the forward flight speed. In this study, the cases of null velocity and 222 knots (corresponding to the maximum not-to-exceed speed) were considered).
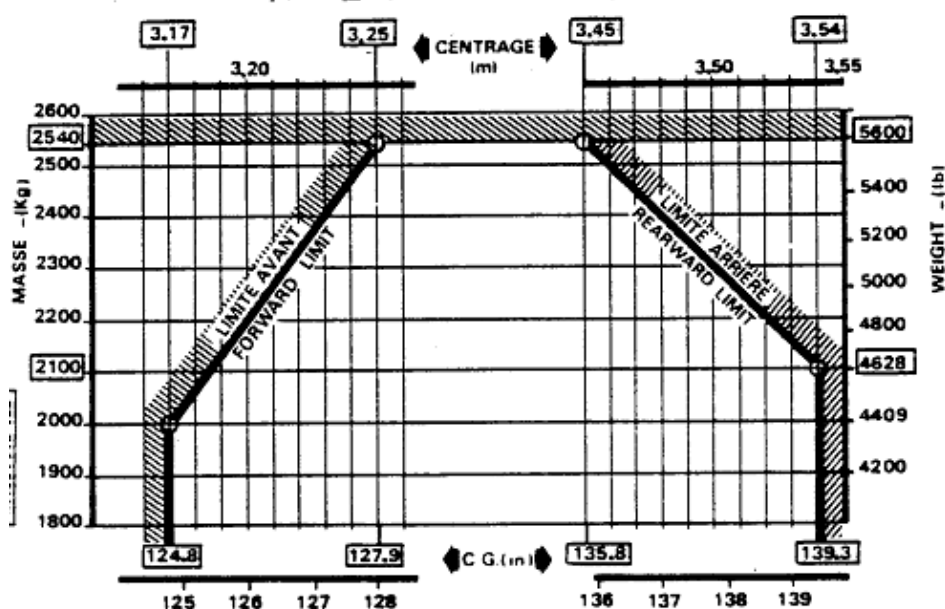
Figure 21: Longitudinal centering diagram for the adopted helicopter (AS355F2 Squirrel) (Note the 9cm maximum CG range) – adapted from (HELIBRAS, 1994)

It is worth mentioning that proprietary confidential information about helicopter design, in this work, some estimated values were assumed for the other parameters necessary for the application of the model. In the future, as the actual parameters are obtained and/or estimated by parameter identification, the model can easily be updated/refined to better represent the aircraft of interest. In the absence of better alternatives, the criterion for estimating these values which could not be obtained consisted of linearly associating, when feasible, the desired parameters with the analogs of the AS 332L Super Puma aircraft, shown in Section 3, and originally presented in (Jorge, 1992).

4.2 Balance study of the system: main rotor plus fuselage

BLADE MOTION EQUATION

In continuity, one evolves to mathematical modeling. A large part of the expressions was established in (Jorge, 1992), and conveniently adapted for this text.

Newton's 2nd Law of Classical Mechanics (Fundamental Principle of Dynamics) is used, chosen to obtain the equations of motion resulting from two phases: the determination of the free-body diagram of the system; followed by the application of this Law in its forms for translations and rotations. In this type of approach, care must be taken not to confuse the directions of efforts and their reactions, which is the most susceptible error when evaluating multibody systems with three-dimensional loads, which is the situation in this model.

BLADE DYNAMIC BALANCE

In the modeling shown in Figure 22, each of the blades that make up the rotor is subject to inertia ($\int_{e}^{R} (\frac{d^2\overrightarrow{OM}}{dt^2})dm_i$) and aerodynamic ($\vec{F}_{aerodynamic}$) efforts, respectively, constituting the parts of the equation that follows.
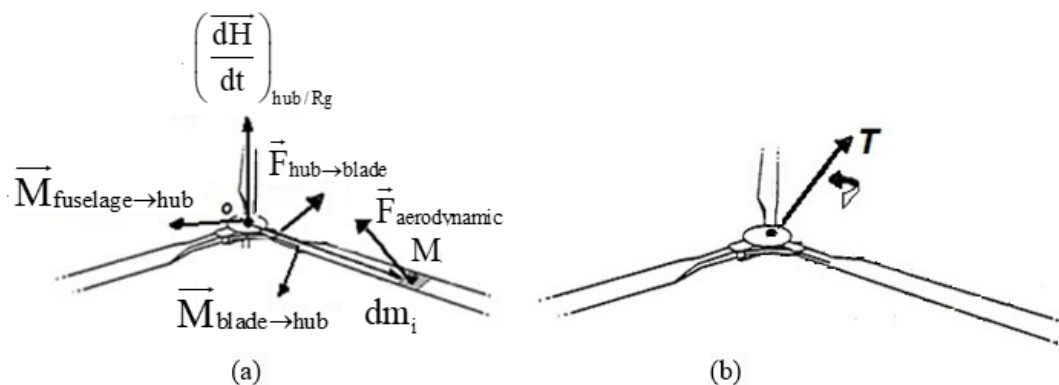
Figure 22: Rotor hub free-body diagram with efforts (forces F and moments M) applied to a blade (a) and their corresponding wrench T (b) – adapted from (González, 2012)

Applying Newton's 2nd Law to an element of mass dm_i of blade i, located by the position-vector $\overrightarrow{OM}$, about the Galilean Reference Frame - R_g (fixed to the center of the Earth, and considered non-inertial), one obtains vectorially that:

$$\int_e^R (\frac{d^2\overrightarrow{OM}}{dt^2})dm_i = \vec{F}_{hub\to blade} + \vec{F}_{aerodynamic} \text{, where:}$$

R_f: fixed rotor reference frame (O, X, Y, Z)
R_t: rotating reference frame of the rotor (O, X_i, Y_i, Z_i)
R_p: reference frame of the blade beating (O, $X_{p'}$, $Y_{p'}$, $Z_{p'}$)
R_p: blade reference frame in beating followed by lead-lag (O, X_p, Y_p, Z_p)
R_a: aerodynamic reference frame (O, X_a, Y_a, Z_a)
R_h: helicopter reference frame (O, X_h, Y_h, Z_h)

One has that, in R_g, the resultant of the vector of forces $\vec{F}$ of the blade on the hub, applied in the flapping joint, is $\vec{F}_{blade\to hub} = \vec{F}_{aerodynamic} - \int_e^R (\frac{d^2\overrightarrow{OM}}{dt^2})dm_i$. Now by applying Newton's 2nd Law again in terms of angular movements concerning R_g, around the rotor hub by the blade and fuselage, we obtain:

$$\left(\frac{\overrightarrow{dH}}{dt}\right)_{hub/Rg} = \overrightarrow{M}_{blade\to hub} + \overrightarrow{M}_{fuselage\to hub}$$

. As the cube is rotating at a constant speed (zero angular acceleration), the time derivative of angular momentum $\left(\frac{\overrightarrow{dH}}{dt}\right)_{hub/Rg}$

is zero. Hence $\overrightarrow{M}_{hub\to fuselage} = \overrightarrow{M}_{blade\to hub}$, that is, the moments applied by the hub to the fuselage, symmetrical to those received by the hub, are equivalent to the action of the moments applied by the blade to the hub. Given the above, it is clear that it is necessary to obtain $\int_e^R (\frac{d^2\overrightarrow{OM}}{dt^2})dm_i$, $\vec{F}_{aerodynamic}$ and $\overrightarrow{M}_{blade\to hub}$. The result of these three calculations gathers the components, in R_g, of the wrench of the efforts in the rotor hub $\{T\}_0$. A wrench, by definition, replaces all forces and moments acting on a rigid body by the representation of a force vector and a moment vector, applied at the same point (Beer et al., 2019). The zero index is justified since it is constant about the azimuth position of the blades (and therefore about time) due to the isotropic rotor hypothesis and that the study was limited to the 1Ω frequency.

$$\{T\}_0 = \left\{\begin{array}{c} \vec{F}_{blade\to hub} \\ \overrightarrow{M}_{blade\to hub} \end{array}\right\}_0 = \left\{\begin{array}{c} F_x\vec{X} + F_y\vec{Y} + F_z\vec{Z} \\ M_x\vec{X} + M_y\vec{Y} + M_z\vec{Z} \end{array}\right\}_0$$

After this calculation for a blade, the sum is performed according to the number of blades to obtain the wrench of the efforts of the complete rotor applied to its hub.

BLADE ACCELERATIONS

The dynamic resultant, applied to the body of blade *i* is obtained from the integral in space along the blade according to the distance *r* varying from the eccentricity *e* to the radius *R*. Thus, given the blade model as simply articulated in flapping and lead-lag, first, there is the following relationship between the rotor reference frames according to these adopted degrees of freedom. It can be observed that, except for the fixed reference (XYZ) to the hub and originating from it, all origins are established in the flapping joint, here modeled as the blade attachment point. For generality, any point M located on the blade surface at a radial coordinate r is considered, as previously shown in Figure 8. It is necessary to calculate the acceleration $\overrightarrow{\gamma_M}$ of this point M in the fixed rotor frame and then integrate the obtained expressions along the blade. As seen from the fixed rotor reference R_f (O, X, Y, Z), we have the position vector of the point M relative to the origin O as in the previously obtained Equation (1).

The rotor is assumed to rotate at a constant speed $\dot{\psi}_i = \Omega$. The position vector from Equation (1) is derived twice concerning time, and the acceleration vector of the point M concerning reference O is obtained, as previously seen, as Equation (2). As before, a simplifying notation is used for the derivatives of β, and similar simplifications are done, considering β and δ small angles, leading to the three components of the acceleration vector of point M in the fixed frame. Again, the integration $\int_e^R (\dfrac{d^2\overrightarrow{OM}}{dt^2})dm_i$ is required to calculate the inertial efforts on the blade in the fixed rotor frame R_f.

AERODYNAMIC FORCES ACTING ON A BLADE

At this point, attention is devoted to the portion of the dynamic resultant due to the aerodynamic efforts $\vec{F}_{aerodinâmico}$ applied to the blade, generated in flight, and in reaction to the airflow in which it is immersed.

The first step is to obtain the velocity of a current point M of the blade ($\overrightarrow{V_{M_{Pa/Rg}}}$) concerning Galileo's frame of reference R_g (O_g, X_g, Y_g, Z_g), because, if referring to the ground, one is stationary and immersed in an undisturbed atmospheric flow that blows on the blade. Considering the hypothesis of stabilized horizontal forward flight (with constant speed), for simplification purposes, the aerodynamic reference frame and the Galilean frame are made to coincide ($R_a \equiv R_g$) under the null wind assumption, that is, the velocity of the undisturbed flow that arrives at the blade is the $V_x = V$ itself (the displacement of the aircraft), and there are no lateral or vertical components. Hence it can be assumed that: $\overrightarrow{V_{M_{air/Rg}}} = \overrightarrow{V_{air/Rg}} = \overrightarrow{V_{X/Rg}} = \left(\overrightarrow{V_{blade_V}}\right)_{Ra}$. Considering $\overrightarrow{OM}$ the R_f frame of reference, the velocity of the blade point M, reasoning from R_f to R_g, can be decomposed into the sum of the velocity due to blade rotation, flapping, and lead-lag movements ($\overrightarrow{V_{M_{blade/fixed\,rotor}}} = \overrightarrow{V_{blade_{\Omega,\beta,\delta}}}$), added to the speed due to the forward flight ($\overrightarrow{V_{M_{fixed\,rotor/air}}} = \overrightarrow{V_{blade_V}}$), plus the induced velocity ($\overrightarrow{V_{M_{air/Rg}}} = \overrightarrow{V_{blade_{Vi}}}$), where the first term was previously obtained as Equation (3).

With the same notation as before, even with the given assumptions of stabilized flight (without accelerations), straight flight (contained in the XZ plane), and level flight (contained in the XY plane), one cannot consider $R_g \equiv R_f$ because constant pitch angles α_D are assumed in this model. Hence, from the derivative of the vector position, we have the velocity of the blade in terms of its degrees of freedom given as the previously obtained Equation (4). The same treatment can be done for the velocity due to the forward flight $\overrightarrow{V}_{pá_V}$ in the aerodynamic frame of reference R_a (O, X_a (positive against the movement of the aircraft, hence V negative), Y_a, Z_a (inclined pitch and $\alpha_D<0$ relative to the Z-axis)). A rotation ($\alpha_D>0$), i.e, a linear transformation via director cosines, around $\overrightarrow{Y_a} = \overrightarrow{Y}$ (as the element $W_{3,3}$ is unitary) leads this velocity from R_a to R_f, as previously shown in Equation (5). It is now necessary to consider the point M with its degrees of freedom (ie, to take from the current R_f to $R_{P'}$).

Similarly, a rotation (-ψi, counterclockwise, by the design of the AS355 F2 aircraft, represented in this work) around $\vec{z} \equiv \vec{Z_i}$ leads $\overrightarrow{V}_{pá_{\Omega,\beta,\delta}} + \overrightarrow{V}_{pá_V}$ from R_f to R_t. Subsequently, a rotation of β (descending blade) around $\overrightarrow{Y_i} = \overrightarrow{Y'_p}$ leads it from R_t to R_p, and a rotation of -δ (blade retreating in ψ) around $\vec{Z'_p} \equiv \vec{Z_p}$ leads it to $R_{P'}$ (flapping followed by lead-lag movement), leading to the previously obtained Equation (6). Finally, since V_i is a consequence of the blade motion, whatever the blade position is (ψ, β, and δ), the blade's relative motion (here in the frame $R_{P'}$) due to the induced velocity V_i is given, as before, by Equation (7), and the blade velocity is given, as before, by Equation (8). Figure 9 in Section 3 shows the wind direction concerning the fixed rotor reference frame R_f (O, X, Y, Z). $V=V_{ar/Rg}$ before reaching the blade. Figure 9 also shows the decomposition of the wind speed U in the rotating blade reference frame $R_{P'}$(O, $X_{P'}$, $Y_{P'}$, $Z_{P'}$) into a velocity component tangential to the rotor plane and perpendicular to the blade span (U_T), and another velocity component perpendicular to the first one (U_P).

The resultant speed is $U = \sqrt{U_T^2 + U_P^2}$, with $\tan\phi \approx \phi \approx U_P/U_T$, where ξ = blade angle of attack; Φ = induced angle; and θ = pitch angle. The wind velocity $\overrightarrow{V}$ in the blade reference frame $R_{P'}$ is given by the previously obtained Equation (9) (where $\psi = 0º$ is the phase reference for the blade). There is a third component of U (radial U_r or $U_{xP'}$) along the blade span, that is, along with X_P, whose value of contribution to the lift (L) and the drag (D) is assumed to be negligible.

Noting the assumption of a two-dimensional aerodynamics problem ($C_l=C_{l0\alpha}$) for the profile of the current point M of the blade (at position $\psi = 180º$), with the direction of U_P and U_T previously shown in Figure 9. The speed U of the impacting flow will be taken as the composition of U_T and U_P. Satisfying this hypothesis for C_l and C_{l0}, it is assumed a high aspect ratio for the profile, and the absence of stall and compressibility phenomena (Johnson, 1980). These assumptions, together with the tangential and vertical velocity components in $R_{P'}$ given as before, and with the previously adopted assumption of small angles for β and δ, lead to the previously obtained Equation (10).

Hence, it is noted that the velocity component U_T is the sum of the velocities due to the blade rotation ($\Omega.r$) and the translation (tangential component) of the helicopter $(V.\cos\alpha_D.\mathrm{sen}\psi_i + V\cos\alpha_D \cos\psi_i \delta)$. The velocity component U_P is the sum of the velocities due to the helicopter translation (vertical component), plus the induced velocity $(V . \mathrm{sen}\alpha_D + V_i)$, the flapping velocity (derivative in β), and the translation of the helicopter (tangential component) $(V . \cos\alpha_D . \cos\psi_i \beta)$.

The elementary lift (L) and drag (D) forces are, respectively, perpendicular and parallel to the plane of the resultant velocity U, $(\vec{U})_{R_p}$ (now known after transferring R_f to $R_{p'}$), and are given as previously obtained Equation (11).

The drag on the main rotor produces the torque associated with it. Figure 23 shows the elementary lift and drag forces on an infinitesimal element of the blade radius.
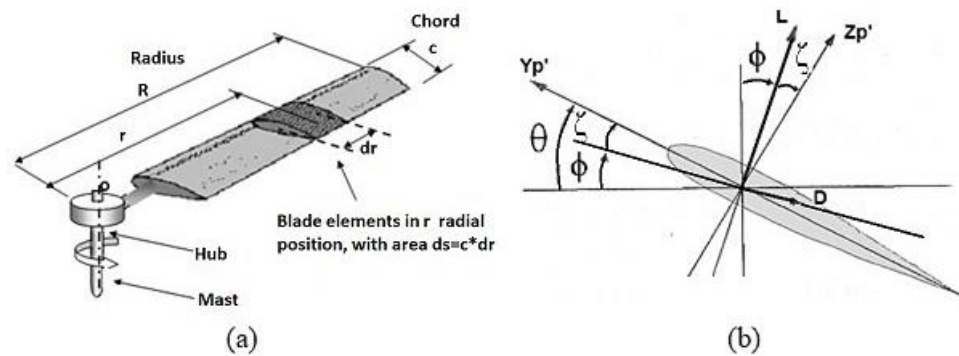
Figure 23: Elementary lift and drag in a blade section at ψ =90° immersed in flow: (a) blade view; (b) section view – adapted from (Gessow & Myers, 1952)

In the reference frame Rp', for blade *i*, the vector force in the element is given by the previously obtained equation (12). It is now necessary to go from $R_{p'}$ to R_f: a rotation of δ, blade advancing in ψ, around $Z_p \equiv Z_{p'}$ leads it to $R_{p'}$. A rotation of $-\beta$ (blade rising) takes it to R_t. With ξ, β and δ being small angles, we have: $\mathrm{sen}\xi \approx \xi = \theta-\phi \approx \theta-\tan\phi = \theta-U_p/U_T$; $\cos\xi \approx 1$; $\mathrm{sen}\beta \approx \beta$; $\mathrm{sen}\delta \approx \delta$; $\cos\beta \approx 1$; $\cos\delta \approx 1$; $\mathrm{sen}\xi \, \mathrm{sen}\delta \approx 0$; $\mathrm{sen}\delta \, \mathrm{sen}\beta \approx 0$; $\mathrm{sen}\xi \, \mathrm{sen}\beta \approx 0$. Assuming: $U^2 = U_T^2 + U_p^2 \approx U_T^2$, as $U_p \ll U_T$, and $a + C_{d0} \approx a$, as $C_{d0} \ll a$, leads to previously obtained Equations (13) and (14). For simplification, the following dimensionless coefficients are introduced:

- $\mu = \dfrac{V \cos\alpha_D}{\Omega R}$ is called lead ratio, and is defined as the relationship between the velocity component parallel to the disc and the speed of the blade tip;

- $\lambda = \dfrac{V\mathrm{sen}\alpha_D + V_i}{\Omega R}$ is a parameter of the axial flow, also called induced velocity, throughout this text, and is defined as the relationship between the velocity component perpendicular to the disk and the speed of the blade tip;

- $\chi = r / R$ and $\chi_e = e / R$.

$\theta(\psi)$ is expanded in components of a Fourier expansion: $\theta = \theta_{con} + \dfrac{r}{R}\theta_{tw}$, with θ_{tw} being the fixed torsion (by design) and $\theta_{con} = \theta_0 + \theta_{1c} \cos\psi_i + \theta_{1s} \mathrm{sen}\psi_i$. These last interventions lead to the previously obtained Equation (15), still in the reference frame R_t.

For the evaluation of the axial flux parameter $\lambda(\psi)$, the Meijer-Dress formulation (Meijer Drees, 1949) allows the consideration of a cyclic variation of the parameter λ in reference frame R_t, according to azimuth ψ. This formulation leads to the previously obtained Equations (16) and (17), which give the cyclic components as previously obtained in Equation (18). The value of λ_0 is calculated by an iterative method (Newton-Raphson), and the values of λ_{1c} and λ_{1s} are calculated by replacing λ with the value λ_0. The element forces dF_{xia}, dF_{yia}, dF_{zia} are spatially integrated along the blade (from 'e' to 'R'), still in reference frame R_t. The dynamic pressure is adopted as $S = \rho ac(\Omega R)^2$, leading to the previously obtained Equation (19).

In general, the ratio e/R is small. We have for the AS355 F2 aircraft: R = 5.34 m and e = 0.67 m, which leads to e/R = 0.12. The simplifying hypothesis $R^n - e^n \approx R^n$ is carried out (n being a natural number). In this way, except for $R - e \approx R$, the result leads to an error of less than 0.12% in the effort calculations, which is neglected.

RESULTANT FORCE APPLIED TO THE ROTOR HUB

The resultant is obtained from the previously established relationship:

$$\overrightarrow{\left(\frac{dH}{dt}\right)}_{hub/Rg} = \overrightarrow{M}_{blade \to hub} + \overrightarrow{M}_{fuselage \to hub} \, .$$

However, it is necessary to change the reference frame to the fixed R_f, for the aerodynamic efforts (since these were calculated in the rotating rotor frame R_t). The efforts of the blade on the hub were previously obtained as Equation (20). Substituting F_{xia}, F_{yia}, and F_{zia}, we obtain, in the reference frame R_f, the components of the resultant force on the rotor hub.

RESULTING MOMENTS IN THE ROTOR HUB

As previously presented, the moment in the rotor hub $\overrightarrow{M}_{blade \to hub}$ (concerning point O) due to the forces F acting on the blade, in the reference frame R_f, is determined with components given as

$$M_x = \left[\overrightarrow{OK_t} \Lambda \vec{F}_{blade \to hub}\right].\vec{X} = e \, \text{sen}\psi_i F_z$$
$$M_y = \left[\overrightarrow{OK_t} \Lambda \vec{F}_{blade \to hub}\right].\vec{Y} = e \cos\psi_i F_z$$
$$M_z = \left[\overrightarrow{OK_t} \Lambda \vec{F}_{blade \to hub}\right].\vec{Z} = e \cos\psi_i F_y - e \, \text{sen}\psi_i F_x + K_{i\delta} + C_{i\delta}\dot{\delta}_t$$

In the first vector of this dot product, the arm is OK and the inverted "V" denotes the cross product. Thus, the three components $\overrightarrow{M}_{blade \to hub}$ in the reference frame R_f are obtained directly.

RESULTING WRENCH IN THE HUB OF A N-BLADE ROTOR

The six expressions just established are equally valid for each of the blades that make up the rotor (so far they are periodic in ψ and therefore non-linear expressions). The global wrench of the efforts is obtained as the sum of these rigid body components, according to the number of blades, as previously obtained in Equation (21).

BLADE DISPLACEMENTS EQUATION - FLAPPING DEGREE OF FREEDOM

Applying Newton's 2nd Law in the reference frame R$_g$ to the simply articulated blade, now taking moments concerning K, as seen in Figure (11), in flapping, followed by lead-lag,

we obtain: $\left(\overrightarrow{\dfrac{dH}{dt}}\right)^{K_i}_{blade/Rg} = \overrightarrow{M}^{K_i}_{\substack{external\ forces\\on\ the\ blade}} = \int_e^R (\overrightarrow{K_iM} \wedge \overrightarrow{\gamma_M})dm_i$, where the moment of the

external forces is $\int_e^R (\overrightarrow{\gamma_M})dm_i$ and $dm_i=mdr$.

This time, the time derivative of the angular momentum (H=IΩ) is not zero, since it considers the product of the moment of inertia by the time derivative of the product of the radius and the linear velocity (in the X$_i$Z$_i$ plane) of the point M on the blade, which is equal to the angular velocity Ω. The value of 'I' is derived, internally, from the integral of the linear acceleration in *m*, and is assumed to be constant (rigid body). Then the calculation of the integrand follows the previously obtained Equation (22).

Through the linear transformation matrix corresponding to a rotation (- ψ) around Z, we move to the rotating rotor reference frame R$_t$. Considering small-displacement angles in β, δ, and θ (with the corresponding simplifications), and also neglecting the triple products between the angles β, δ and their derivatives, when compared to their double products, given that these are small angles, after some intermediate steps, we have, finally, in the reference frame R$_t$ the derivative concerning the time of the product of the radius times the linear velocity of point M over the blade, as previously obtained in Equation (23).

Flapping movement equations

With the above-calculated integrand in hand, we focus on the movement around the flapping axis in K, $\overrightarrow{Y}_p \equiv \overrightarrow{Y}_t$. Hence, for the projection on the Y$_i$ axis, the 2nd Law applied to the joint at K (in flapping), in the reference frame R$_t$, gives, with $dm_i=mdr$:

$$\left(\overrightarrow{\dfrac{dH}{dt}}\right)_{blade\ i/Rg} = \overrightarrow{M}_{\substack{forces\ on\ blade\ i\\flapping\ around\ K}} = \int_e^R (\overrightarrow{K_lM} \wedge \overrightarrow{\gamma_M})_Y dm_i.$$

The dynamic momentum theorem, in a projection on the *y$_i$* axis, after some intermediate calculations, leads to the previously obtained Equation (24). Considering the static moment and the flapping inertia for the blade as defined, the dynamic moment formulation leads to the Eq. (25). By using the aerodynamic forces on blade *i*, on axis Z$_t$, dFz$_i^a$ as previously obtained, calculating the integral on the blade, assuming the cyclic nature of ψ, as well as the truncation of the Fourier series expansion of each term

$$\theta_{con} = \theta_0 + \theta_{1c}\cos\psi_i + \theta_{1s}\sen\psi_i,$$

$$\beta = \beta_0 + \beta_{1c}\cos\psi_i + \beta_{1s}\sen\psi_i, \text{ and}$$

$$\delta = \delta_0 + \delta_{1c}\cos\psi_i + \delta_{1s}\sen\psi_i,$$

leads to the previously obtained Equation (26). Equation (26) identifies the consecrated form of the vibration equation, of a Mass-Spring-Damper System, by its resulting terms of stiffness and damping due to mass (inertia), where the latter is in the second coupled member with the forcing term (equally divided by the inertia term). To eliminate the periodic nature of these ODE obtained above, a change of their domain from *t* (in ψ) to

that of frequency (in cyclic θ) is made through the Coleman operators (Coleman & Feingold, 1957), as one of the so-called linear Fourier Transforms, through the Method of Operators. This method consists of the simultaneous application of each member of the flapping equation within the parentheses of each of the following operators: $\frac{1}{2\pi}\int_0^{2\pi}(...)d\psi$, $\frac{1}{2\pi}\int_0^{2\pi}(...)cos\psi d\psi$ and $\frac{1}{2\pi}\int_0^{2\pi}(...)sin\psi d\psi$. In practice, as mentioned before, the advantage achieved is shown in converting that ODE into several separable algebraic equations according to each of the constant components (β0, β1C, and β1S) independent of ψ. The double products of angles compared to the angles themselves are neglected. In this way, the influence of the lead-lag angle on the beating movement will be neglected, which means to neglect δcosψ or δsinψ in this equation. Following the same steps, with intermediate calculations as in Section 3, three algebraic equations are then obtained, independent of ψ, as coupled functions of the constant components β0, β1C, and

β1S. However, it is worth introducing, for simplification, the Lock Number $\gamma = \rho a c \dfrac{R^4}{I_\beta}$

(parameter of the blade that relates aerodynamic forces with inertia forces), leading to the previously obtained flapping Equation (27).

BLADE DISPLACEMENTS EQUATION: LEAD-LAG DEGREE OF FREEDOM

In this case, the aim is to move around the lead-lag axis at joint K, that is, we have that $\vec{Z}_p \equiv \vec{Z}'_p$. But in order not to change the referential of the previous results, the 2nd Law in rotational movements is applied again in the reference frame R_t, for the component around $Z_i(R_t)$, assuming that the restoring moment due to the frequency adapter (which avoids ground or air resonance by reducing the blade frequency in lead-lag, moving it away from the fuselage resonance frequency value) is also by the Z_i axis, as considered before for the calculation of M_z. This theorem gives, in projection onto the Z_i axis, the moment of the drag forces of the blade around point K as in the previously obtained Equation (28). This degree of freedom is maintained under mechanical artificial damping for reasons of dynamic stability (associated with ground and air resonances, which can destroy the aircraft in a few seconds). The restoring moment due to the frequency adapter in lead-lag

is: $K_{i\delta}\,\delta_i + C_{i\delta}\,\dot{\delta}_{it}$. Given that $I_\beta = I_\delta = \int_e^R (r-e)^2 m\,dr$ (since the blade is assumed to be modeled as a line independent of axes and there is no cross-section), introducing the obtained expression for dF_{yi}^a leads to the previously obtained Equation (29).

After calculating the integral on the blade, making the assumptions $R^n - e^n \approx R^n$, the truncation in the Fourier Series expansion previously described in Equation (30), and neglecting the triple angle terms (eg: $\theta_0 \cdot \beta_{1c} \cdot \delta_{1s} \approx 0$, etc.) against the double products, given that θ, β, and δ are small angles, one can resort once again to the application of the operators in the differential equation (29) (again representative of a Mass-Spring-Damper System), whose result is, finally, the algebraic equations of lead-lag motion previously obtained in Equations (31) (for δ0), (32) (for δ1c), and (33) (for δ1s), which describe the lead-lag angle $\delta(\delta_0, \delta_{1c}\ e\ \delta_{1s})$ as a function of the pitch angle $\theta(\theta_0, \theta_{1c}\ e\ \theta_{1s})$ and the flapping angle $\beta(\beta_0, \beta_{1c}\ e\ \beta_{1s})$.

ROTOR-FUSELAGE SYSTEM MODELING EQUATION (STATIONARY)

THE HYPOTHESES

We return to the six expressions of the wrench of the efforts on the rotor, as previously calculated, and apply them to the case of a rotor composed of N blades considered strictly identical. In this way, this wrench can be considered constant over time, and thus can be treated as stationary.

THE PARAMETERS

Added to the displacements θ, β, and δ (referring to the rotor state), α, ψ, and T_{RC} are considered to correspond to the fuselage attitude, with small angles which are used in the numerical simulation in radians. Thus, the parameters treated are the flight parameters $(\lambda_0, \lambda_{1c}, \lambda_{1s}, \beta_0, \beta_{1c}, \beta_{1s}, \theta_0, \theta_{1c}, \theta_{1s}, \delta_0, \delta_{1c}, \delta_{1s})$, which are added to the fuselage attitude ($\theta_0, \theta_{1c}, \theta_{1s}, \alpha_f, j_f, T_{Ra}, \beta_0, \beta_{1c}, \beta_{1s}, \delta_0, \delta_{1c}, \delta_{1s}$).

APPLICATION OF THE COLEMAN TRANSFORMATION

In this step, the same integral operators are applied to the six expressions of the previously calculated wrench of the efforts on the rotor, as they are then periodic functions, to obtain a linear formulation whose effect on each component F and M is its description in the form of a linear combination of the flight parameters $(\lambda_0, \lambda_{1c}, \lambda_{1s}, \beta_0, \beta_{1c}, \beta_{1s}, \theta_0, \theta_{1c}, \theta_{1s}, \delta_0, \delta_{1c}, \delta_{1s})$. Next, for simplification purposes, the triple products of angles are neglected against the double products in the expressions of F_x, F_y, and M_z, as well as the double products of angles, are neglected against the angles themselves in the expressions of F_z, M_x, M_y.

The efforts F and M of the rotor hub are expressed, therefore, as a function of the different flight parameters, post-Coleman Transformation (Coleman & Feingold, 1957) - now in the frequency domain and constant in time, where:

- the induced velocity coefficients $(\lambda_0, \lambda_{1c}, \lambda_{1s})$ (response or output) are determined by the Meijer-Dress formulation (Meijer Drees, 1949);

- the torsion θ_{tw} is an adopted design data (a built-in fixed-parameter);

- the coefficients of the flapping movement $(\beta_0, \beta_{1c}, \beta_{1s})$ (response or output) are calculated using the equilibrium equations as a function of $\theta_0, \theta_{1c}, \theta_{1s}$ (and other parameters already known or calculated);

- the coefficients of the lead-lag movement $(\delta_0, \delta_{1c}, \delta_{1s})$ (response or output) are calculated using the equilibrium equations as a function of $(\theta_0, \theta_{1c}, \theta_{1s})$ and $(\beta_0, \beta_{1c}, \beta_{1s})$.

The six equations of wrench (the efforts F and M) on the rotor hub are therefore functions of only three parameters: $\theta_0, \theta_{1c}, \theta_{1s}$ (excitation or input, as a pilot control action through collective and cyclic commands).

(STATIC) BALANCE OF THE ROTOR-FUSELAGE SYSTEM

Assumptions:

- known/adopted design parameters: dimensions and limits (in this case, for AS 355F2).

- the fuselage, moving immersed in the air, does not produce L but produces D (from pressure and friction).

- the negative lift effect of the horizontal empennage 'T$_{eh}$', assumed modeled as T$_{eh}$ = $1/2\rho V^2$(C$_z$S)$_{eh}$, where (C$_z$S)$_{eh}$ is the equivalent lift area factor, assumed independent of the empennage profile (C$_l$ and S).

- Tail rotor anti-torque thrust (T$_{RC}$), counterclockwise, is necessary to balance the rotor-fuselage system in reaction to the action of the main rotor on the fuselage. The value of T$_{RC}$ is obtained corresponding to a directional lateral attitude in yaw (γ_f) null, that is, without skidding of the fuselage in forward flight.

- the negative value: installation of the Squirrel's tail rotor being on the right side (a second puller).

The following variables are still unknown: the efforts F and M of the rotor hub are a function of the three parameters $\theta_0, \theta_{1c}, \theta_{1s}$ (excitation or input, as the pilot control action through collective and cyclic commands). The attitudes (responses or outputs) of the fuselage are: longitudinal in pitch (α_f), lateral in roll (ψ_f). The rotor anti-torque thrust (T$_{RC}$) (obtained by assuming zero yaw lateral (γ_f)). In the case to be studied (stationary stabilized horizontal forward flight with constant speed), the aerodynamic reference frame and the Galilean frame are confounded Ra≡Rg but, due to the pitch α_f, Rh≠Rg.

As the rotor hub efforts F and M were initially expressed in the fixed rotor frame R$_f$, a linear transformation is necessary according to a rotation (-α_m) around Y$_f$. With this, the wrench is transformed from the fixed rotor reference R$_f$ into the helicopter reference frame R$_h$, as previously shown in Equation (34).

Analogously:

- as the forward flight speed V was expressed in the aerodynamic reference R$_a$, a rotation (α_f) around Y$_f$ is applied. From there, V is leaded from the aerodynamic reference frame R$_a$ to the helicopter reference frame R$_h$, as previously shown in Equation (35), where:
$$\alpha_f = \alpha_D - \alpha_m .$$

- the helicopter's weight (descending) is passed from the Galilean frame R$_g$ to the helicopter frame R$_h$ by a rotation (- α_f) around Y$_g$ = Y$_h$. In continuation, another rotation (-φ_f) around X$_h$ follows, as previously shown in Equations (36) and (37).

The balance of F along the three axes, in the R$_h$ helicopter frame, leads to the previously shown Equation (38).

The equilibrium of moments M around the rotor hub, relative to which the fuselage rotation is zero, in the helicopter reference R$_h$, gives: $\sum \overrightarrow{\mathbf{M}}_0 = \mathbf{0}$, leading to the previously shown Equation (39).

And we finally arrive at the six homogeneous equations, previously shown in Equation (40), representing the balance of the fuselage in R$_h$. As this is an equilibrium equation, there are no accelerations (which arise with the introduction of defects in the discussion that follows).

The previous hypothesis of small angles is maintained to facilitate the mathematical treatment of the solution, and we have the wrench of the applied efforts on the rotor hub in the R_h reference frame, as previously shown in Equation (41).

Adding the three equations of flapping, the three equations of lead-lag, and the six equations of the rotor wrench, we have a system of twelve non-linear algebraic equations in the twelve unknowns ($\theta_0, \theta_{1c}, \theta_{1s}, \alpha_f, \varphi_f, T_{Ra}, \beta_0, \beta_{1c}, \beta_{1s}, \delta_0, \delta_{1c}, \delta_{1s}$).

4.3 Introduction of anisotropies in the main rotor (Direct Problem)

Here the model of the direct problem is addressed, meaning that here the defect is introduced, leading to changes in the vibration signature. The disturbance of equilibrium discussed above, by inserted anisotropies, from here on, also treated as defects. Therefore, as a system response, the vibrations are measured in the aircraft structure thanks to the associated accelerations. All anisotropies inserted in the blades are considered as if they were "equivalent" anisotropies to the different ones that are corrected by adjustments to the blade inertia (m_i) and/or the aerodynamic performance of its profile (θ_i).

From the previous equilibrium equations, it is known that, in the case of the conventional isotropic rotor, the Coleman Transformation (Coleman & Feingold, 1957) provides that the efforts F and M in the rotor hub, as well as the twelve flight parameters (response) θ, β, δ (these in their three cyclic components) and α_f, ψ_f, T_{Ra}, are constant concerning time for each equilibrium position (since it eliminates periodic terms sine(ψ_i) and cosine(ψ_i)). These efforts applied to a fuselage assumed to be rigid and in balance with external forces applied to the fuselage, in the conditions of the stationary flight, or forward flight at constant speed. Consequently, in both cases, all the predicted accelerations of the fuselage (the linear accelerations of its CG and the angular accelerations around it) are null. From this equilibrium position (as static equilibrium), the values of the resulting attitude of the fuselage are obtained: longitudinal pitch (α_f); lateral or roll (φ_f); and yaw (ψ_f).

The introduction of anisotropies for a blade i (while the other blades are assumed to be unchanged) and the calculation of their new angular displacements θ, β, and δ on the rotor leads to new forces in the hub, which are no longer constant (being functions of ψ_i), that is, they are time-varying efforts according to the frequency 1Ω. Hence, the fuselage equilibrium equations are no longer homogeneous (as previously calculated), as the 2nd part (the right-hand side of the equation) leads to fuselage accelerations of the same frequency. It is worth mentioning that the displacement of each blade is a result of the contribution of constant efforts in time (isotropic equilibrium) and of efforts in these variables under 1Ω frequency (small variations around that equilibrium position, with the defects generating accelerations). From this point of view, the movement of each blade can then be decomposed into the movement of the blade itself (translated by the three angular displacements in flapping and the three angular displacements in lead-lag) added to that of the fuselage with which the blade is linked (translated by the displacements of the rotor - angular displacements α_f, φ_f, T_{RC}, and the input θ_0, θ_{1C}, θ_{1S}). In this oscillation, it is assumed that a new attitude of the fuselage assumes another variable portion, added to the previous one (isotropic equilibrium), which is unique and assumed unchanged after the introduction of anisotropies. This means that the defects do not alter the fuselage equilibrium attitudes but introduce variations around 1Ω them. In this way, the accelerations do not have permanent terms in time and are constituted only by periodic parcels (since in the isotropic case they are null) in $\psi(t)=\Omega_t$, for the six degrees of freedom (DoF) about the fuselage CG, as previously shown in Equation (42).

INFLUENTIAL PARAMETERS

It is worth remembering that any azimuthal position (ψ_i) of a blade corresponds to the angular space (involving the angular frequency of the rotor) associated with time by the relation $t = \psi_i / \Omega$, counted from the moment of the passage of the blades through the reference position, $\psi_i = 0$.

This reference, in practice, corresponds to the synchronism signal given by the magnetic sensor installed on the fixed plateau of the main rotor mast. To calculate the torque of the forces acting on the rotor hub updated with defects, it is necessary and sufficient to know the corresponding new values of $\lambda(\psi_i), \theta_i(\psi_i), \beta_i(\psi_i), \delta_i(\psi_i)$, the mass of the blades (m_i), the static moment of the blades (m_{si}), and the inertia of the blades ($I_{\beta i}$). It is considered that there were no changes in the parameters of the blades (R, e, c) and their profile (C_{d0}, a), and neither in the advancing rate μ nor the air density ρ.

Regarding the before-mentioned parameters, one has that:

• mass of the blades: $m_i = \int_e^R dm_i = \int_e^R m \, dr$. An anisotropy in m_i (and consequently in m_{si} and $I_{\beta i}$) can be considered as an "equivalent" mass change in the radial position of the rotor, where the equilibrium mass (balance platelets, in this case) can be added.

• static moment of the blades: $m_{si} = \int_e^R r \, dm_i = \int_e^R r \, m \, dr$, where m is the blade mass;

• blade inertia: $I_{\beta_i} = \int_e^R r^2 dm_i = \int_e^R r^2 m \, dr$. The three parameters m_i, $m_{si,}$ and $I_{\beta i}$ can be different for each blade, due to the anisotropies. Furthermore, they are interdependent, that is, a variation of m_i implies a corresponding variation of the values of m_{si} and $I_{\beta i}$. The insertion of an equilibrium mass (Δm_i), associated with its RME (distance of the balance plate mounting to the rotor hub), leads us to changes in the parameters of blade i, based on the isotropic values of m_{si} and $I_{\beta i}$ ("iso" index, below):

$$m_{\rho_i} = m_{\rho_{iso}} + \Delta m_i$$
$$m_{s\rho_i} = m_{s\rho_{iso}} + \Delta m_i \times RME$$
$$I_{\beta_i} = I_{\beta_{iso}} + \Delta m_i \times RME^2$$

• air density (ρ): this parameter is provided, for example, from the standard atmosphere tables, and depends on pressure-altitude and temperature.

• advancing rate (μ): Dimensionless parameter of the helicopter's speed about the air (V) and of the rotor disk inclination (α_D) in pitch, which depends on the longitudinal position of the cyclic control. The fuselage pitch angle (α_f) depends on the inclinations of the disc, rotor (α_D), and mast (α_m) so that $\alpha_f = \alpha_D - \alpha_m$ (it is seen that α_f is smaller than α_D, justifying the compensation of α_m to meet maneuverability/flight quality requirements);

• the parameters of the blades (R, e, c) and their profile (C_{d0}, a): Although they also constitute possible anisotropies, within the scope of this study, they are considered constant and independent of the blades;

• The induced speed $\lambda_i(\psi_i)$: Proportional to the advancing rate (μ) - hence, to the rotor disk inclination (α_D); to the thrust coefficient (C_T) (which is due to the helicopter's thrust - Fz); the air density (ρ); and the azimuthal position (ψi). As it is assumed that there is no anisotropy on the induced velocity, λ does not depend on blade i;

• The blade pitch $\theta_i(\psi_i)$: As already introduced, anisotropies linked to the blade profiles can be considered as "equivalent" variations of the blade pitch $\theta_i(\psi_i)$, which varies according to the azimuthal position (ψi) of the blade and to the balance of the fuselage, in the cases considered of stationary flight or forward flight at a constant speed (μ = constant, non-zero).

For the case of fuselage equilibrium, it is assumed, as external forces acting:

- the rotor hub efforts;

- the weight of the helicopter applied at the CG position of the fuselage;

- the fuselage lead-lag, assumed to be applied at a fixed point (A) and acting independently of the fuselage pitch;

- the negative lift of the horizontal empennage assumed to be applied at a fixed point and acting independently of the fuselage pitch; and

- The anti-torque thrust of the rotor, is necessary to balance the torque applied by the main rotor. $\theta_i(\psi_i)$ can be changed through the length of the blades' control rods (which changes the collective pitch θ_0 of blade i); and/or

- the tab angle adjustment, whose profile bending creates an aerodynamic moment around the elastic axis of the blade (transmitting forces to the fuselage through the rods), is proportional to the forward flight speed. Hence, the tab angle adjustment does not affect the taper (β_0) of the rotor in stationary flight, however, it is proportional to μ, being more pronounced on the forward blade side than on the retreating blade. In this work, the tab angle adjustment is simulated as an anisotropy θ_{is}. Therefore, making $\theta_{is} \neq 0$ (and other parameters equal to zero) in the flapping motion equations, for stationary flight ($\mu = 0$), that is, hovering or vertical flight, one obtains: $\beta_0=0 \; ; \; \beta_{1c}» \text{-}\theta_{1s} \; ; \; \beta_{1s}=0$. Analogously, for the forward flight condition ($\mu \neq 0$), we have $\beta_0 = \mu - \theta_{1s}$, which points out to an increase in taper (β_0) proportional to θ_{is} (rotor pitch in forward flight) and μ, as wished. The calculation of $\theta_i(\psi_i)$ is divided into two steps:

1 - in the absence of anisotropies on the rotor, the blade pitch (θ_0, θ_{1c}, θ_{is}) comes from the isotropic rotor equilibrium equations, as previously seen;

2 - the anisotropies are introduced on a blade by adding the desired increment (according to only to θ_{0i}, θ_{1si}), under the assumption that the pitch of the other blades is not altered. Then, the resulting pitch of the blades (θ_0, θ_{1c}, θ_{is}) is calculated again, assuming that there is no influence on the pitch of the other blades.

• The flapping movement $\beta_i(\psi_i)$: As seen before, β_i depends on the azimuthal position (ψ_i), the pitch $\theta_i(\psi_i)$, the induced velocity $\lambda(\psi_i)$, the air density (ρ), the parameters of the blade (R, e, c, a, m_{si}, $I_{\beta i}$), and of the advancing rate (μ). Analogously to the previous parameter, the calculation of $\beta_i(\psi_i)$ is divided into two steps:

1 - in the condition of the absence of anisotropies on the rotor, all blades have the same mass (m), static moment (m_s), a moment of inertia (I_β), and pitch (θ) (obtained from the helicopter equilibrium, as seen before). Thus, we have an expression of $\beta(\psi_i)$ which is valid for all blades.

2 - the three types of anisotropies adopted as equivalent defects on a blade (i) are introduced, namely:

- balance mass on the blade handle (change of m_i, m_{si}, $I_{\beta i}$)
- adjustment of the blade control rod (full change of θ_i, as it acts on all ψ)
- the tab angle adjustment (change of θ_{1si}, as it acts according to the flow)

Then, the flapping of this blade ($\beta_i(\psi_i)$) is calculated again, assuming that there is no influence on the flapping movements of the other blades.

• The lead-lag movement $\delta_i(\psi_i)$: As seen before, δ_i depends on ψ_i, θ_i, λ_i, β_i, the air density (ρ), the advance rate (μ), and the blade parameters (R, e, c, a, m_{si}, $I_{\beta i}$).

The displacement δ can also be changed due to anisotropies in the frequency adapter (either in its stiffness $K_{\delta i}$, or in its damping, $C_{\delta i}$).

Like what was done for θ_i and β_i, this calculation is divided into two steps:
1 - in the condition of the absence of anisotropies on the rotor, the lead-lag (δ_0, δ_{1c}, δ_{1s}) comes from the isotropic rotor equilibrium equations, as seen before;
2 - the anisotropies considered on a blade *i* are introduced, assuming that there is no influence on the lead-lag movements of the other blades.

CORRECTIONS APPLICABLE TO THE MAIN ROTOR

This item addresses the nature of the defects inserted in the mathematical model in use, which is adopted according to the corrections available in this research. The defects to be introduced are among the following:

- Inertia or mass defects: change in m_i, $m_{si,}$ and $I_{\beta i}$;
- Defects in the aerodynamic performance of the profile;
- Length of the pitch link (pitch rod): change in θ_{0i}; and
- Adjustments in the angle of tab: change in θ_{1si} (not adopted in this work).

The above discussion referred to the Direct Problem, in which a change is made, leading to changes in the vibration signature. In the case of the Inverse Problem, changes in the signature lead to the possible rotor variables that may have caused that change, and to a suggestion of the possible corrections/adjustments to be performed, to correct the unbalance and/or out-of-track blade. It is important to mention that the correction values to be suggested (as a diagnosis of defects) according to the results of the Inverse Problem must be submitted to the limits recommended in the Manufacturer's Manual, beyond which the foreseen action is the replacement of the defective item indicated by the algorithm.

RESULTANT EFFORTS WRENCH IN THE ANISOTROPIC ROTOR HUB

Carrying out the same calculations as previously described, for blade *i*, now after introducing the defects (using the new values of m_i or θ), the new pitch angles (θ_i), flapping angles (β_i), and its associated lead-lag (δ_i). The efforts F and M on the rotor hub are due to these new angles. These efforts are updated according to the previously derived expressions for forces *F* and moments *M*, so the resultant output (associated accelerations) has components in $\sin\psi$ and $\cos\psi$ (cyclic terms, truncated in 1Ω) added to the 1st constant component (index zero - the same as in the case of the isotropic rotor equilibrium), leading to the previously derived Equation (43). As before, we will apply to the expression of efforts of the operators: $\frac{1}{2\pi}\int_0^{2\pi}(...)\sin\psi\,d\psi$ and $\frac{1}{2\pi}\int_0^{2\pi}(...)\cos\psi\,d\psi$ to the periodic components in $\sin\psi$ and $\cos\psi$ of the blade *i*, culminating in the constant terms 1C and 1S. These transformations lead to the twelve expressions previously obtained in Equations (44) to (55) (constant terms 1C and 1S), where the index "*i*" of the various angles (the pitch, flapping, and lead-lag) is suppressed for simplicity of notation. To apply the sum of the forces acting on each blade, at this time one proceeds differently from Section 3. In the case study (N = 3 blades), the azimuth of each of the three blades must

be considered, as they are now distinguished from each other, so it is not enough just to multiply by N. Adopting $\psi 1 = \psi$ (red blade), $\psi 2 = \psi + 2\pi/3$ (blue blade), and $\psi 3 = \psi + 4\pi/3$ (yellow blade), leads to:

$$Fx_1 = Fx_{01} + Fx_{1c1}\cos\psi + Fx_{1s1}\text{sen}\psi$$

$$Fx_2 = Fx_{02} + Fx_{1c2}\cos(\psi + 2\pi/3) + Fx_{1s2}\text{sen}(\psi + 2\pi/3) = Fx_{02} + Fx_{1s2}\cos\psi - Fx_{1c2}\text{sen}\psi$$

$$Fx_3 = Fx_{03} + Fx_{1c3}\cos(\psi + 4\pi/3) + Fx_{1s3}\text{sen}(\psi + 4\pi/3) = Fx_{03} - Fx_{1c3}\cos\psi - Fx_{1s3}\text{sen}\psi$$

Finally, by harmonic balance, we have:

$$\{Fx_{1c}\}_{rotor} = Fx_{1c1} + Fx_{1s2} - Fx_{1c3} \qquad \{Mx_{1c}\}_{rotor} = Mx_{1c1} + Mx_{1s2} - Mx_{1c3}$$

$$\{Fx_{1s}\}_{rotor} = Fx_{1s1} - Fx_{1c2} - Fx_{1s3} \qquad \{Mx_{1s}\}_{rotor} = Mx_{1s1} - Mx_{1c2} - Mx_{1s3}$$

$$\{Fy_{1c}\}_{rotor} = Fy_{1c1} + Fy_{1s2} - Fy_{1c3} \qquad \{My_{1c}\}_{rotor} = My_{1c1} + My_{1s2} - My_{1c3}$$

$$\{Fy_{1s}\}_{rotor} = Fy_{1s1} - Fy_{1c2} - Fy_{1s3} \qquad \{My_{1s}\}_{rotor} = My_{1s1} - My_{1c2} - My_{1s3}$$

$$\{Fz_{1c}\}_{rotor} = Fz_{1c1} + Fz_{1s2} - Fz_{1c3} \qquad \{Mz_{1c}\}_{rotor} = Mz_{1c1} + Mz_{1s2} - Mz_{1c3}$$

$$\{Fz_{1s}\}_{rotor} = Fz_{1s1} - Fz_{1c2} - Fz_{1s3} \qquad \{Mz_{1s}\}_{rotor} = Mz_{1s1} - Mz_{1c2} - Mz_{1s3}$$

(DYNAMIC) BALANCE OF THE ROTOR-FUSELAGE SYSTEM

The previously-derived balance equations of the rotor-fuselage system are no longer homogeneous after the introduction of rotor defects, hence the classification of the balance as dynamic. The balance of external forces is presented in the previously derived Equation (56). One can observe in Equation (56) that the 2nd term (the right-hand side) is the product of the total mass of the aircraft by the periodic acceleration of the CG along each axis.

The equations of moments were previously obtained with the equilibrium about the rotor hub. As the focus is on the motion of the CG of the aircraft, these equations must be rewritten to consider the wrench of the external efforts applied to the rotor hub (index zero) and this CG. Furthermore, there is a need to know the fuselage moments of inertia (due to its rotating movements) about the CG, which change as a function of the aircraft centering. Thus, the moments of inertia in roll (I_{xx}), pitch (I_{yy}), and yaw (I_{zz}) are considered, as well as the product of inertia representing the yaw-roll coupling (I_{zx}), while the other couplings are assumed to be null.

From the moments and products of inertia and the mass M, the radii of gyration ρ are obtained as a function only of the centering X_G and Y_G by the expression $I = M\rho^2$. The balance of moments about the CG is described by $\sum M = I\alpha$, where M comes from the global wrench of efforts on the hub, the linear measures are the moment arms, which leads to the previously derived Equations (57) and (58).

One must note in these Equations (57) and (58) that α_{f0}, φ_{f0}, and T_{RA0} were obtained from the fuselage equilibrium with the isotropic rotor, as derived before. Also, $T_{RC\ 1C}$ and $T_{RC\ 1S}$ are the periodic components of the tail rotor thrust required to nullify the ψ_{f1C} and ψ_{f1S} components of the yaw motion (assumed constant). Since ψ_{f1C} and ψ_{f1S} were assumed not

to be zero in the calculation of the second derivative of ψ_f, then it is required that $T_{RC\,1C}$ = $T_{RC\,1S}$ = 0 (therefore, it is assumed that the tail rotor does not provide cyclic thrust that can cancel the cyclic motion in yaw).

To find the 12 unknowns of the fuselage accelerations (6 linear and 6 angulars): Ω^2 (x_{1c}, x_{1s}, y_{1c}, y_{1s}, z_{1c}, z_{1s}, α_{f1c}, α_{f1s}, φ_{f1c}, φ_{f1s}, ψ_{f1c}, ψ_{f1s}), one must apply again, to the variable equilibrium equations (thanks to the expansion of the three angular accelerations), the operators: $\dfrac{1}{2\pi}\displaystyle\int_0^{2\pi}(...)\sin\psi\,d\psi$ and $\dfrac{1}{2\pi}\displaystyle\int_0^{2\pi}(...)\cos\psi\,d\psi$. The efforts on the rotor hub already obtained, leads to the previously derived Equations (59) to (70).

TRANSFER OF THE CG ACCELERATIONS TO FUSELAGE POINT 'M'

The accelerations of the rigid fuselage, excited by the rotor and by external forces applied to the fuselage, are known and they are applied to CG. Now, they need to be transported to the fuselage points indicated by manufacturers in which accelerometers are intended to be placed, and the vibration quantities are intended to be obtained. In this context, we have the position vector GM of a point (M) of the fuselage about its CG (origin as point G) of the helicopter reference frame R_h. From which, through linear transformations based on rotations of ($-\psi_f$), ($-\alpha_f$), and ($-\varphi_f$), as shown previously in Equation (71), the same vector position is written in the Galileo reference frame, parallel to the aerodynamic frame ($R_g \equiv R_a$), with X, Y, Z values of the coordinates of the points in the helicopter frame (R_h). Carrying out the necessary algebra, the vector is derived twice concerning time t to provide accelerations. Considering, in Galileo's frame of reference, a point G' coincident with point G, we have that the acceleration of the CG (point G) has only linear terms (because it is a point), and is given by previously obtained Equation (73). The acceleration of point M, in reference frame R_h is given by previously obtained Equation (72). From this frame, transforming to the helicopter frame, again, we have $(d^2GM/dt^2)_{Rh}$, as previously shown in Equation (74). Small angles ψ_f, α_f, and φ_f is again used and, for simplification, the triple products of angles are also neglected concerning the double products, leading to the previously obtained Equation (75). Considering in X that: $d^2X_M/dt^2 = \Omega^2 X_M = \Omega^2(-X_{M1c}\cos\psi - X_{M1s}\sin\psi)$, we will also have the analogue for Y and φ. To find the six unknowns of the three linear accelerations of the fuselage point M, we will apply, as before, the operators to these three equations. The six unknowns were previously detailed in Equation (76).

AMPLITUDE AND PHASE OF THE RESULTING ACCELERATIONS

The efforts on the rotor hub are expressed as a function of the azimuth coordinate of the red blade: $\psi_1 = \psi = \Omega_t$, where t represents the time after the red blade passes through the nose of the helicopter (home position $\psi = 0$) when the magnetic sensor triggers the timing signal. From this moment (then t = 0), the Theory of Complex Numbers, applied to the amplitudes of the sine and cosine vibration measured in the fuselage, allows the acceleration to be expressed in terms of amplitude and phase. Thus, from the measured information on x (x_{1s}, x_{1c}), y (y_{1s}, y_{1c}), and z (z_{1s}, z_{1c}), we have the amplitudes at the CG and point M, as previously detailed in Tables 2 and 3.

4.4 Validation of the calculation code

APPLICATION OF THE MODEL: COMPUTATIONAL SIMULATION

This computational resource constitutes a valuable tool for simulating the model's responses to the excitations associated with introduced anisotropies equivalent to typical defects, such as main rotor unbalance and out-of-tracking blades. Thus, the original computational code in FORTRAN for a 4-blade helicopter (Jorge, 1992) was written in MATLAB[(R)] for a 3-blade helicopter (González, 2012).

Within the so-called Direct Problem, the code is divided into two parts, as shown in Figure 24, by the structuring of the work: a first part for the calculation under the modeling of the fuselage-rotor system in equilibrium (this one called isotropic) in terms of the twelve parameters $\alpha(\psi)$, $\beta(\psi)$, $\delta(\psi)$, $\theta(\psi)$, $\varphi(\psi)$, T_{RC}, β_{0i}, β_{1ci}, β_{1si}, δ_{0i}, δ_{1ci}, δ_{1si}, θ_{0i}, θ_{1ci}, and θ_{1si}; and a second part to calculate the vibratory responses as variations (concerning the isotropic case), due to anisotropies, according to the amplitude and phase as obtained at a point M on the fuselage.
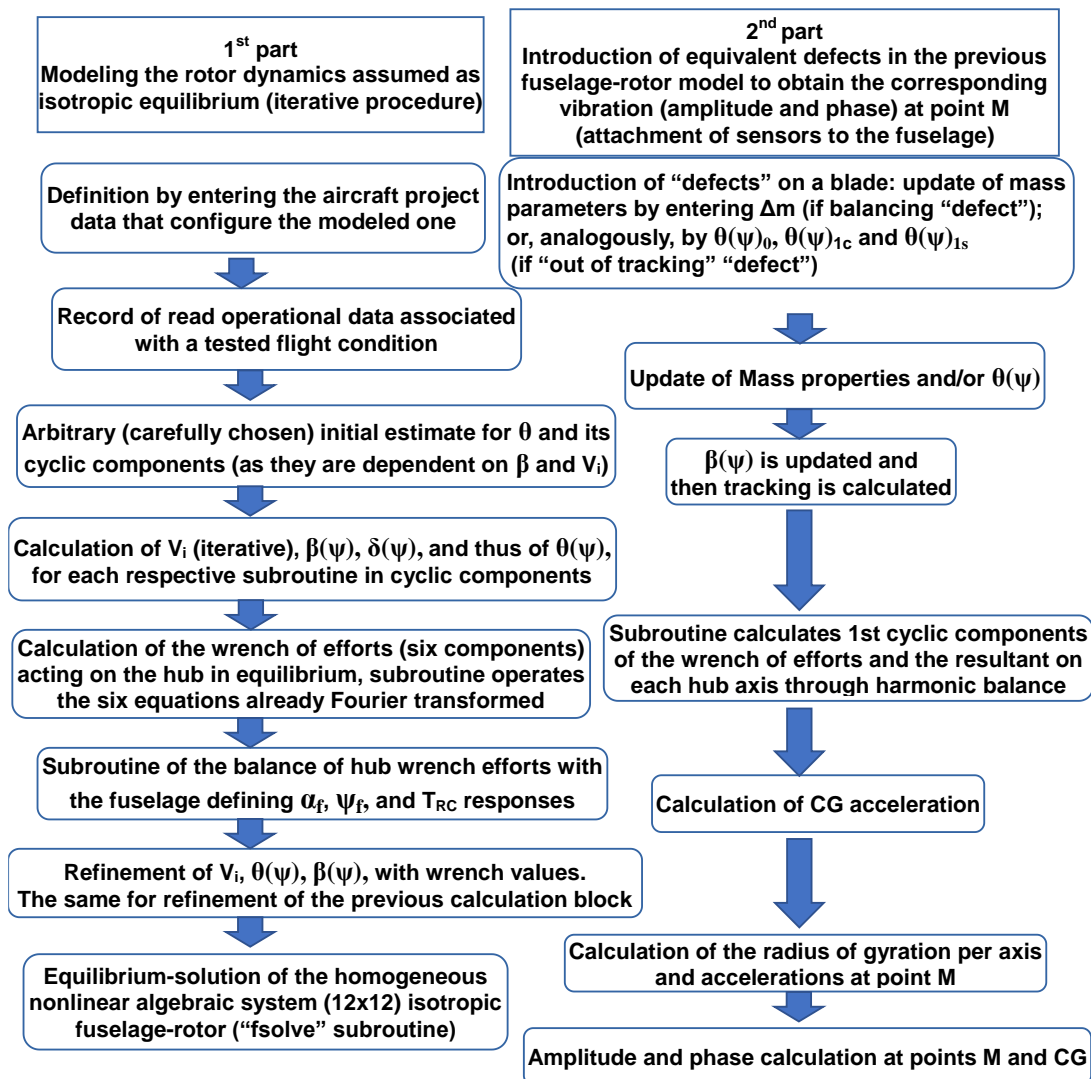
Figure 24: Flowchart of the subroutines of the computational code for the Direct Problem [Adapted from (González, 2012)]

The first part deals with the numerical resolution of a multidimensional system of twelve nonlinear algebraic equations (to twelve unknowns) governing the movement of the rotor-fuselage system, in the frequency domain (after applications of Fourier Integral Transform according to Coleman operators, as seen above). This first part requires a lot of iterations to define the proper input vector, as the components are linearly dependent and unknown. Internally, the solution process of this algebraic system includes its linearization by subroutines of the computational algorithm "fsolve", selected as the most adequate among the options available in the MATLAB$^{(R)}$ software environment.

Structured with aircraft design information, the resolution of these equations uses data from the executed flights as input and then reveals the dynamic behavior of the analytical model adopted according to small vibrations around the equilibrium. Briefly describing the code, Figure 24 presents a flowchart for the code. The code starts with the definition of the aircraft design data adopted, as previously presented, followed by the recording of obtained data associated with a flight condition. Once these data are gathered, a subroutine is activated that operates the previously discussed Meijer-Dress formulation, iteratively, according to the Newton-Raphson numerical method, to obtain the first estimate of the induced velocity Vi, as it is a requirement for the next task, which is to obtain, via the dedicated subroutines, the values of $\beta(\psi)$, $\delta(\psi)$ and $\theta(\psi)$, according to their cyclic components. These subroutines are initialized from a free but careful initial estimate for θ, whose value depends on β and Vi, which are not yet available, proving to be quite a sensitive part of the code. Numerical methods are expected to allow modeling with minimal simplifications while preserving the precision of the result. However, this approach requires a good initial estimation of the input vector to further find the solution to the system. In this case, although θ represents the command (from the pilot), around which the rotor needs to adapt, the convergence of the method of the 'fsolve' subroutine is sensitive to large variations, even though its internal algorithm predicts eventual problems of a distant estimate of the real root. These four variables are then used in the next subroutine that calculates the six components of the wrench acting on the hub in equilibrium, operating the post-Fourier Transform equations (six equations). In sequence, subroutines are called to provide the values of α_f, φ_f, and T_{RC}, based on the three equilibrium equations of the rotor-fuselage system. With these data, it is possible to recalculate, in a refinement step, the values of the first four variables before the next step: the calculation of the equilibrium of the fuselage-isotropic rotor nonlinear algebraic system. The best result of the 'fsolve' subroutine comes from the internal application of numerical optimization techniques that impose robustness to Newton's method in the calculation of each step, as offered by the MATLAB$^{(R)}$ software, and which makes use of its Jacobian matrix, previously evaluated as Equation (77), also provided by a specific subroutine. The result of this algorithm converges to the output vector composed of the twelve mentioned values. It is worth mentioning here the sensitivity of the functional parameters requested by this subroutine (according to the internal algorithm, the "fsolve" and the residual error), for each flight condition, to verify the convergence of the numerical method. Most optimization subroutines adopt a termination criterion, to end the calculation when the residual error (the difference between two successive iterations roots) and/or the difference between each iterative step are less than a value specified by the user. Hence, if this value is too large, the subroutine does not manage to find a solution that can effectively nullify the system of equations. Otherwise, if it is too small, the algorithm reaches the maximum number of iterations before the difference between two successive iterations, to obtain the root, has been reached. Having obtained the established

scenario for the equilibrium behavior of the system in context, we move on to the second part of the Direct Problem, which does not require iterations: the introduction of primary anisotropies, that is, one at a time. Firstly, this is done by updating the mass parameters (if the balance "defect" is adopted) or the three cyclic components of θ (such as in the case of an out-of-tracking type of "defect") of the selected blade, using the sum of increments associated with the last values obtained (these three ones, again, by initial estimates).

From this point on, it is possible to recalculate the first cyclical components of the forces and moments that are applied to each blade according to the three adopted Cartesian axes, which, as mentioned before, are no longer constant. The following steps are analogous calculations of the resulting wrench of efforts on the hub, according to similar terms in sine and cosine (harmonic balance); the CG acceleration; the radius of gyration of the fuselage, needed to obtain, in the subsequent step, the accelerations at the CG and point M; and, finally, the amplitude and phase calculation at these points (the CG and point M).

VALIDATING THE MODEL: FLIGHT TESTS

In the task of demonstrating the applicability of the proposed mathematical model, we choose to compare the simulated response with real experimental data. Among possible sources of the same, it was decided to start a flight test campaign on a platform with the same parameters of the considered model. The platform adopted is an Aerospatiale-AS 355 F2 Squirrel Twin Engine, a representative model of a series, and belonging to the then Special Group of Flight Tests - GEEV (currently called Flight Tests and Research Institute - IPEV), one of the military organizations of the Department of Aerospace Science and Technology - DCTA, located in São José dos Campos, SP, Brazil.

The tests performed were a valuable instrument to support the research in context, as they met the test requirements, and were performed in compliance with the established provisions of the test order, which presented the complete analysis of the main risks, with a description of the causes, consequences, and the mitigating actions to be taken, as well as the emergency procedures to be adopted. The flight test schedule established the following registration points, corresponding to the flight profiles provided in the MET 62.10.00.603 Maintenance Manual for the aircraft (HELIBRAS, 1994):

- ground turn with the throttle adjusted to flight setting;

- hovering IGE (in ground effect) at 2 m above the ground, heading with the wind;

- leveled forward flight in maximum power continuous (PMC); and

- forward flight at the PMC, underside turns, left and right, leaning 45°.

 Through these points, representative of the basic operating conditions, the aim is to collect vibration characteristics (amplitude and phase) of this aircraft, corresponding to balancing and tracking conditions at 1Ω frequency: first, in the condition within the tolerances recommended in the MET; and then outside them, as follows:
- yellow blade: two fewer balance platelets; all other blades balanced and inside tracking;
- analogous procedure with the red blade; and finally
- again with the rotor balanced, only the yellow blade is out of the ideal tracking.

The following references from the MET were adopted, for the case of rotor balanced, with adjusted tracking, for 1Ω: (with IPS being: " inches per second")
- ground turning and hovering at 2 m: in the Y direction < 0.2 IPS and tracking < 6 mm;
- level forward flight in PMC: in the Z direction < 0.2 IPS and tracking < 20 mm; and
- forward flight with lateral turns at ±45º incline in PMC: in Z < 0.35 IPS.

For the vibration data acquisition, a portable equipment ACES P2020 was used, coupled to two sets of accelerometers in positions defined in the maintenance manual: one accelerometer to capture the amplitudes of the accelerations in the Y-axis (located horizontally on the mast of the main rotor – it is a rigid point); another accelerometer to capture the accelerations on the Z-axis (vertically on the left front floor); and a magnetic sensor located on the fixed plateau to measure the phases, when it passes through the magnetic switch (emitter) permanently affixed to the mobile plateau. Figure 25 shows the equipment used (except the magnetic sensor) (images taken during the tests).
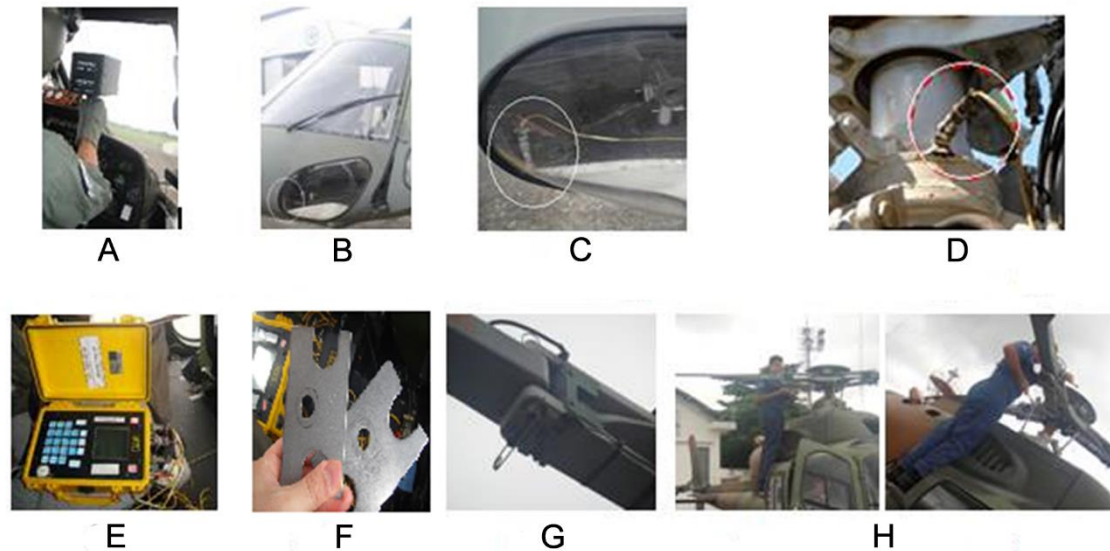
Figure 25: Flight test instrumentation: (A) strobex; (B), (C) Z-axis accelerometer; (D) Y-axis accelerometer; (E) ACES P2020 analyzer; (F) balance sheet; (G) platelets fixed to the blade handle; (H) change in platelet configuration [Adapted from (González, 2012)]

ASSESSMENT OF THE (PRELIMINARY) FLIGHT TEST RESULTS

As for the computational resource adopted to verify the model, the simulation would provide better results if the real design values (unavailable) were used. It is noteworthy that the consideration of flight conditions becomes a problem, given that, for each case of mass and balance, for example, it would be necessary to effectively evaluate the value of the initial θ fixation to be provided at the beginning of the code for the isotropic case. Therefore, for a more comprehensive simulation in terms of flight conditions/phases and the flight envelope of the aircraft, it would be necessary to build a numerical solution more adapted in robustness to this specific problem. Nevertheless, in the case limited to the range of this initial estimated of θ, as stated above, the code showed convergence after twelve iterations, consuming insignificant computational time, whose values were subjected to comparisons with the results of the flight tests. Tables 4 and 5 present a comparison between flight test and numerical simulation results, for 16 test points (cases in which flight tests were originally scheduled). For better use of the evaluation, and by the recommendations of the MET, the end signal of each installed accelerometer is considered. Therefore, in Tables 4 and 5, the data indicated is highlighted in the grids. In each cell corresponding to the reading at a test point, there are two lines for comparisons between test data (top line) and numerical simulation (bottom line). The grids guide the consideration of lateral vibrations Y (in the rotor plane) for test points 1 and 2, and vertical vibrations Z (orthogonal to the rotor plane) for the others, only.

Table 4: Comparison of flight test results and numerical simulation: test points 1 to 8
[Adapted from (González, 2012)]

Data	1	2	3	4	5	6	7	8
1Ω Z (IPS)	0,38 0,347	0,35 0,351	0,08 0,349	0,14 0,349	0,30 1,033	0,08 1,051	0,34 1,406	0,12 1,411
Phase Z (°)	326,50 -89,97	359,50 89,95	273 -89,953	309 -89,908	202,5 -55,581	185 -55,271	204,50 -49,200	189,50 -49,342
1Ω Y (IPS)	0,18 1,478	0,47 1,491	0,05 1,484	0,20 1,162	0,26 2,022	0,44 2,062	0,28 2,898	0,46 2,902
Phase Y (°)	358,50 -83,530	8,50 -83,601	358,50 -83,512	22,50 -83,475	16 -30,800	9,50 -30,181	6 -18,777	13 -18,942
Red Blade	-0,5 0.474	-1,3 0.473	No data 0.4763	0,7 0.478	No data 1.444	-5,8 1.462	No data 1.459	-6,6 1.899
Yellow blade	0,0 0.475	0,0 0.473	No data	0,0 0.478	No data 1.444	0,0 1.462	No data 1.459	0,0 1.899
Blue blade	0,0 0.475	2,0 0.474	No data	0,5 0.478	No data	-7,8 1.462	No data 1.459	-5,5 1.899

Table 4 additional details: Flight tests (1st day) Test point & description. Condition & description
1. Point 1: Ground turn. Condition 1: Rotor balanced and tracking adjusted - test/code.
2. Point 1: Ground turn. Condition 2: Yellow blade with two fewer platelets - test/code.
3. Point 3: Hover IGE. Condition 1: Rotor balanced and tracking adjusted - test/code.
4. Point 3: Hover IGE. Condition 2: Yellow blade with two fewer platelets - test/code.
5. Point 4: Level forward flight at PMC. Condition 1: balanced and tracking adjusted - test/code.
6. Point 4: Level forward flight at PMC. Condition 2: Yellow blade with two fewer platelets - test/code.
7. Point 5: Forward flight + Curves φ = 45º at PMC (Right Turn). Condition 1: balanced and tracking adjusted - test/code.
8. Point 5: Forward flight + Curves φ = 45º at PMC (Right Turn). Condition 2: Yellow blade with two fewer platelets - test/code.

Table 5: Comparison of flight test results and numerical simulation: test points 9 to 16
[adapted from (González, 2012)]

Data	9	10	11	12	13	14	15	16
1Ω Z (IPS)	0,16 0,343	0,04 0,339	0,06 0,349	0,03 0,340	0,37 1,345	0,33 1,356	0,40 1,356	No data
Phase Z (°)	333 -89,96	25,5 89,944	262 89,990	125 -89,96	172,5 -9,5583	114 -48,974	170,50 -49,537	No data
1Ω Y (IPS)	0,08 1,142	0,21 1,125	0,09 1,172	0,26 1,103	0,24 2,827	0,30 2,817	0,33 2,849	No data
Phase Y (°)	319 -83,531	116 -83,629	97 -83,541	122,50 -83,540	22 -18.845	55 -18.400	358 -18.807	No data
Red Blade	1,0 0.473	-0,7 0.467	0,0 0.476	1,0 0.471	-4,8 1.874	-0,2 1.890	-5,0 1.882	No data
Yellow blade	0,0 0.473	0,0 0.4677	0,0 0.476	0,0 0.471	0,0 1.874	0,0 1.890	0,0 1.882	No data
Blue blade	1,0 0.473	0,0 0.467	-1,7 0.476	-1,7 0.471	-5,6 1.874	-4,0 1.890	-4,6 1.882	No data

Table 5 additional details: Flight tests 2nd day. Test point & description. Condition & description
9. Point 1: Ground turn. Condition 1: Rotor balanced and tracking adjusted - test/code.
10. Point 1: Ground turn. Condition 2: Yellow blade with two fewer platelets - test/code.
11. Point 3: Hover IGE. Condition 1: Rotor balanced and tracking adjusted - test/code.
12. Point 3: Hover IGE. Condition 2: Yellow blade with two fewer platelets - test/code.
13. Point 4: Level forward flight at PMC. Condition 1: balanced and tracking adjusted - test/code.
14. Point 4: Level forward flight at PMC. Condition 2: Yellow blade with two fewer platelets - test/code.
15. Point 5: Forward flight + Curves φ = 45º at PMC (Right Turn). Condition 1: balanced and tracking adjusted - test/code.
16. Point 5: Forward flight + Curves φ = 45º at PMC (Right Turn). Condition 2: Yellow blade with two fewer platelets - test/code.

The flight test campaign could not complete the schedule in its entirety due to a failure related to the operation of the Main Gear Box (MGB) (presence of swarf/filings in the dedicated magnetic sensor), which also contributes to vibrations. This occurrence made the aircraft unavailable for a long period, in addition to what was compatible with this research work. Thus, there are no data tested from test point 16 (Table 5), nor the tracking variation per action in the pitch control rod length adjustments. It is worth mentioning the difficulties of the mechanics for the sensitive readjustments of the pitch rod to its original position, which is decisive for reference flights.

As for the flight tests, even though they are the best alternative in terms of the wealth of information, they also presented, in smaller numbers, some adverse results than expected (for example: in the evolution of trials 5 to 6; and 7 to 8; 13 to 14 - decrease instead of the expected increase in the amplitude of the oscillatory response. These inconsistencies are attributed to the complexity of the atmospheric environment in which the flight dynamics are immersed; to the instantaneous variation of aircraft parameters, including those sensitive to the recording instant (eg: speed and vibration reading, which are related to the test pilot's ability to identify and sustain the desired condition then reached); and to possible disturbances associated with the acting defect and only then detected. All these facts can be mitigated by considering an average of a large number of similar flights, which was not possible in this research.

As for the simulations, the same inconsistencies were manifested in the evolution of tests 3 to 4; 9 to 10; 11 to 12. It is attributed to the series of simplifying considerations that were necessary for this study as a determining influence on the small values of the variations and to the large ones in the module of the results of the amplitudes relative to the experimental data, as well as the large phase variations. Also noteworthy is the influence of the rigid blade hypothesis and the absence of relevant real project values, as these would be the only guarantee that the same tested aircraft is being simulated.

The results obtained are preliminary. A few results were encouraging, such as the evolution of flight tests 1 to 2; 3 to 5; and 7 to 8 – confirming the increasing trend in the amplitude of the oscillatory response. Especially in evolution 1 to 2 and 5 to 6 the phase change trend aligned with the experimental test data (taken as a reference for this reading).

A comment on the vibration absorbers in Z- and Y- directions

In the flight tests carried out, the accelerometer in the vertical Z-direction was located in the front section of the cabin, as shown in Figure 25, reasonably far away from the most rigid section of the fuselage (which would be near the station just below the main rotor).

This front section, at the nose of the aircraft, is a region that oscillates (and therefore has important natural modes of vibration) in this Z-direction (due to the elasticity of the structure). A suggestion for future work would be to choose a location to install the accelerometer and collect vibration data in the Z-direction as another point, in a more central region, perhaps near the vertical station below the main rotor.

Another important aspect is that under the floor of the Squirrel, more or less in the region below the pilot's seat, there is a vertical vibration absorber, tuned to the 3Ω frequency, as shown in Figure 26. This absorber is located in a station about halfway between the main rotor station and the region near the nose of the aircraft, where the accelerometer was placed in the flight tests that were carried out.

Typically, a linear absorber would not have an important effect on frequencies away from its design frequency (in this case, 3Ω), but, in the case of non-linearities in the vibration absorber behavior, there is a possibility (to be investigated) that this vibration absorber could have influenced the signal in 1Ω captured by the accelerometer.

The two reasons above (the location of the accelerometer at a forward station near the nose of the aircraft; and the presence of a nearby Z-direction vibration absorber) may have contributed to the discrepancy found between the flight test results (lower Z-vibration amplitudes) and the numerical model (higher Z-vibration amplitudes), in this cockpit accelerometer, installed in the vertical direction.

The vibration amplitude measured in the flight tests was about one order of magnitude lower than the vibration amplitude calculated by the numerical model, giving a hint that maybe some part of the vibration in 1Ω was also attenuated, maybe by some non-linear behavior of this vertical vibration absorber in 3Ω.

1 - Bottom structure beam
2 - Attachment backing plate
3 - Attachment plate
4 - Flexible steel blade
5 - Resonator weights

Chamfers
for movement of blade (4).
Comply
with installation direction.
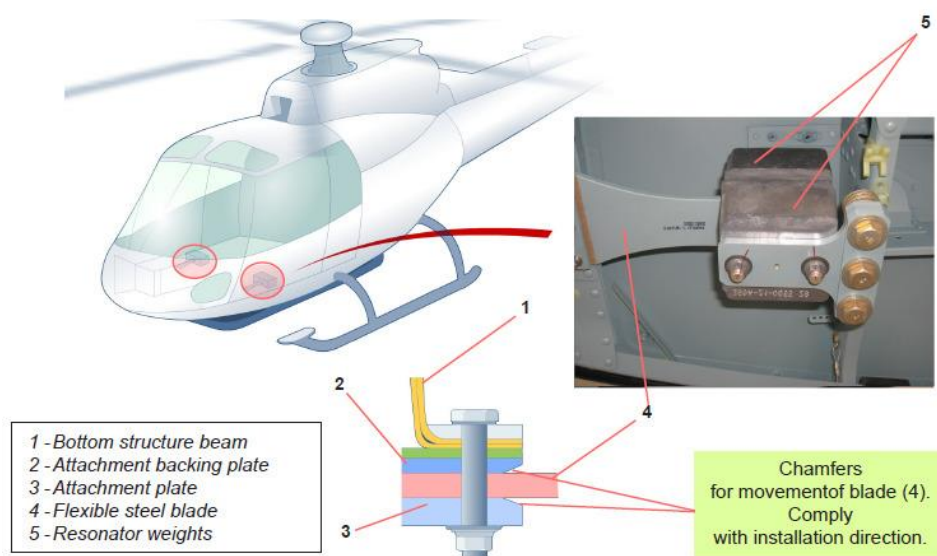
Figure 26: (AS 350B3 Squirrel) Z-direction vibration absorber (floor below pilot) – adapted from (EUROCOPTER, 2010)

As for the accelerometer in the Y-direction (therefore, practically in the rotor plane), it was correctly placed in a more central region, but because the location of this accelerometer was at a height very close to the rotor plane, the vibration measured in the Y-direction could have been influenced by the presence of the main rotor vibration absorber, with its resonator weights, as shown in Figure 27.

These resonator weights, inside the fairing, form a tuned set to absorb vibrations in the rotor plane at the 3Ω frequency. Thus, like the case of the absorber of vertical vibrations under the pilot's floor, this in-plane absorber may have influenced the Y-vibration measured results. Again, the Y-vibration amplitude measured in the flight tests was one order of magnitude lower than the Y-vibration amplitude calculated by the numerical model, giving a hint that maybe some part of the vibration in 1Ω was also attenuated, maybe by some non-linear behavior of this vibration absorber in 3Ω.

1 - Vibration absorber fairing
2 - Coil spring (3 springs)
3 - Vibrating weight
4 - Cylinder centering and retaining balljoint (5)
5 - Balljoint guiding weight (3) in the horizontal plane
6 - Protective boot keeping out external agents (e.g. dust, rain, etc.)
7 - Rotor hub star
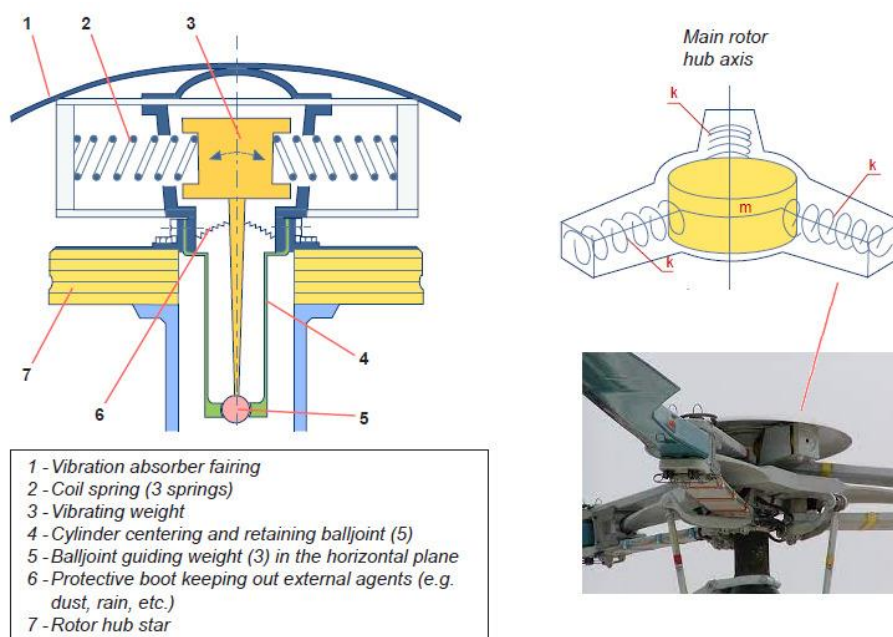
**Figure 27: (AS 350B3 Squirrel) Y-direction vibration absorber (rotor hub) –
adapted from (EUROCOPTER, 2010)**

The presence of these vibration absorbers in Z- and Y- directions near the location of the corresponding Z- and Y- accelerometers may have contributed to the lower amplitudes in the vibration signal obtained in the flight tests, when compared to the corresponding amplitudes calculated using the numerical model and may help to explain the differences in amplitudes that were found.

Thus, the presence of a Z- or Y- vibration absorber, in the vicinity of an accelerometer in the same Z- or Y- direction, requires further investigation and would demand a change in the location of the accelerometer in future test flights, and/or an improvement in the numerical model, to include the presence of such vibration absorbers.

4.5 Possibilities for future work

As suggestions for further work, one can consider:

- a thorough review of the model and its assumptions, to be able to refine and adapt the model to attain a higher level of fidelity of the model concerning the real aircraft, to properly represent the dynamics of the rotor-fuselage system, including the above-mentioned vibration absorbers in Z- and Y- directions (see Figures 26 and 27);

- real aircraft data is required to be used in the model, again to increase model fidelity concerning a real aircraft. Proper aircraft parameters must be given, and/or identified using data science/pattern recognition techniques (Artificial Neural Networks, for example), and must be validated before their use in the numerical model;

- the numerical model and the flight tests need to represent the same flight conditions, to validate the comparisons between numerical and experimental results. The observed trends for the code results as compared to the flight test results should present similar behavior, to provide evidence of the potential for this model to be used as a tool to help maintenance procedures of balancing and tracking of the helicopter main rotor, based on vibration measurements in the fuselage.

- after the model for the Direct Problem (given defects in the main rotor, leading to vibration changes (amplitude and phase) at particular fuselage points) is revised and validated, the research may concentrate on adequate approaches (optimization methods, identification approaches) for the Inverse Problem (vibration changes (in amplitude and phase) at particular fuselage points leading to detection/localization/classification/identification of defects in the main rotor, and, in consequence, leading to the suggestion of corrective maintenance procedures, such as the proper adding/subtracting of balance masses, or the increasing/decreasing of the pitch rod length).

5 Concluding Remarks

In this chapter helicopter, vibration reduction techniques were discussed, focused on balancing, and tracking the helicopter rotors, and concentrated on a discussion of model-based parameter identification for balancing and tracking a helicopter main rotor using once-per-revolution vibration data. Details of the models were presented for two study cases: a 4-blade main rotor, and a 3-blade main rotor. Simulation results were obtained in both cases from the models that were derived in this work. These results were compared, for the 4-blade rotor case, with the charts available in the maintenance manual, and for the 3-blade rotor case, with some preliminary flight tests that were performed under flight profiles recommended in the maintenance manual (MET), as an experimental phase of the work.

The results obtained for both cases showed that the models derived in this study, even with all the assumptions and simplifications in the derivation of the equations, are promising, and pointed out in the proper direction.

For the 4-blade case, the model has indicated a correction to be done in the proper blade and in the proper direction (for example, for correctly adding or subtracting balancing masses). Only the amount of mass to be added/subtracted differs slightly from the model to the experimental case.

For the 3-blade case, the computer code exhibited significant sensitivity to changes in flight conditions and, certainly, was influenced by the deficiency of real design data in the simulation, which could have limited the performance of the numerical results. Also, environmental factors during the experimental flight, as well as the instantaneous parameters in continuous variation, may have contributed to compromise the intentions of formal validation of the model.

The perspectives regarding the potential of the model derived in this work were deemed satisfactory, with a valuable experience arising from the investigation and analysis of the comparative results, with insights, such as the need to take into account the presence of the Z- and Y- vibration absorbers, in the vicinity of the accelerometers in the same Z- or Y- direction.

As suggestions for future work, the coefficients of the obtained equations could be seen as parameters to be identified in an inverse problem. With this approach, the values of the mass, centering, etc., will be identified for the actual helicopter, and used as the parameters in the derived equations, instead of using, in these equations, the average/typical values that were used in this work. Doing this model-based parameter identification for an already-derived equation should be more efficient and less time-consuming, when compared to the signal-based identification of the helicopter and rotor parameters from scratch, in which only input and output data would be available, without any prior knowledge of the mechanics of the system.

Acknowledgments

References

Beer, F., Johnston, E., Mazurek, D., Cornwell, P., & Self, B. (2019). *Vector Mechanics for Engineers: Statics and Dynamics* (12th ed.). Mc Graw Hill.

Ben-Ari, R., & Rosen, A. (1997). Mathematical Modelling of a Helicopter Rotor Track and Balance: Results. *Journal of Sound and Vibration*, *5*(200), 605–620.

Benoit, B., Dequin, A.-M., Kampa, K., Grunhagen, W. von, Basset, P.-M., & Gimonet, B. (2000). HOST, a General Helicopter Simulation Tool for Germany and France. *American Helicopter Society 56th Annual Forum,* 1–23. https://www.researchgate.net/publication/224792351_HOST_a_General_Helicopter_Simulation_Tool_for_Germany_and_France

Bielawa, R. L. (2006). *RotaryWing Structural Dynamics and Aeroelasticity*. AIAA.

Bramwell, A. R. S., Done, G., & Balmford, D. (2001). *Bramwell's Helicopter Dynamics* (2nd ed.). Butterworth-Heinemann.

Coleman, R. P., & Feingold, A. M. (1957). *Theory of self-excited mechanical oscillations of helicopter rotors*.

Damy, L. F. (2017). *Contribution to the development of helicopter tail rotor balancing techniques: proposition of an adaptive method and stochastic modeling (In Portuguese)* [Instituto Tecnológico de Aeronáutica]. http://www.bdita.bibl.ita.br/tesesdigitais/lista_resumo.php?num_tese=73533

EUROCOPTER. (2010). *THM AS 350B3 Squirrel: Mechanics Instruction Manual*.

EUROCOPTER. (2012). *Dynamics, Vibrations and Internal Noise: Module Presentation OFFSET BRASIL* (p. 127).

Friedmann, P. P., & Hodges, D. H. (2003). Rotary Wing Aeroelasticity—A Historical Perspective. *Journal of Aircraft*, *40*(6), 1019–1046.

Ganguli, R., Chopra, I., & Haas, D. J. (1998). Helicopter rotor system fault detection using physics-based model and neural networks. *AIAA Journal*, *36*(6), 1078–1086. https://doi.org/https://doi.org/10.2514/2.483

Gessow, A., & Myers, G. C. (1952). *Aerodynamics of the Helicopter*. McMillan.

González, R. de A. (2012). *Helicopter Main Rotor Failure Analysis using vibration and HUMS philosophy (In Portuguese: Análise Preditiva na Detecção de Falhas no Rotor Principal com Foco na Vibração em um Helicóptero Segundo a Filosofia HUMS)*. Instituto Tecnológico de Aeronáutica (ITA), Brazil.

HELIBRAS. (1994). *MET - Maintenance Manual 62.10.00.603 of AS355F2 helicopter*.

Johnson, W. (1980). *Helicopter Theory*. Dover Publications.

Johnson, W. (2013a). *Rotorcraft Aeromechanics*. Cambridge University Press.

Johnson, W. (2013b). A History of Rotorcraft Comprehensive Analyses. *AHS 69th Annual Forum*, 1–22. https://ntrs.nasa.gov/api/citations/20130014338/downloads/20130014338.pdf

Jorge, A. B. (1992). *Fault detection system of a helicopter rotor from the vibration level (In French: Systeme de detection de defauts d'un rotor d'helicoptere a partir du niveau vibratoire)*. Ecole Nationale Superieure D'ingenieurs de Constructions Aeronautiques (ENSICA), Toulouse, France.

Jorge, A. B., & Torres Filho, A. S. (1989). Vibration in Helicopters. Causes and Consequences on Equipment. How to live with the problem? (In Portuguese: Vibração em Helicópteros. Causas e Consequências nos Equipamentos. Como conviver com o problema?). *BISAFO - Boletim Informativo Segurança de Aviação Em Foco, SIPAERM, Brasil*, *23*, 16–22.

Kunz, D. L., & Newkirk, M. C. (2009). A generalized dynamic balancing procedure for the AH-64 tail rotor. *Journal of Sound and Vibrationnd Vibration*, *326*, 353–366. https://doi.org/10.1016/j.jsv.2009.04.043

Meijer Drees, J. (1949). A theory of airflow through rotors and its application to some helicopter problems. *Journal of the Helicopter Association of Great Britain*, *3*(2), 79–104.

Miller, N. A., & Kunz, D. L. (2008). A comparison of main rotor smoothing adjustments using linear and neural network algorithms. *Journal of Sound and Vibration*, *311*, 991–1003. https://doi.org/10.1016/j.jsv.2007.09.041

Mobley, R. K. M. (1999). *Root Cause Failure Analysis*. Butterworth-Heinemann.

Müller, M., Arnold, U. T. P., & Morbitzer, D. (1999). On the Importance and Effectiveness of 2/REV IBC for Noise, Vibration and Pitch Link Load Reduction. *25th European Rotorcraft Forum*.

Padfield, G. D. (2007). *Helicopter flight dynamics: the theory and application of flying qualities and simulation modeling* (AIAA (Ed.)).

Padfield, G. D. (2018). *Helicopter Flight Dynamics - Including a Treatment of Tiltrotor Aircraft* (3rd ed.). Wiley.

Prouty, R. W. (1985). *Helicopter Aerodynamics*. Phillips Pub.

Rabe, D., & Wilke, G. (2018). Parametric Design Studies of the Helicopter Rotor Noise using Variable-Fidelity Methods. *AHS International 74th Annual Forum & Technology Display*, 1–20. https://elib.dlr.de/125009/1/AHS-74-Paper.pdf

Rosen, A., & Ben-Ari, R. (1997). Mathematical Modelling of a Helicopter Rotor Track and Balance: Theory. *Journal of Sound and Vibration*, *5*(200), 589–603.

Venkatesan, C. (2015). *Fundamentals of Helicopter Dynamics*. CRC Press.

Ventres, S., & Hayden, R. E. (2000). Rotor Tuning Using Vibration Data Only. *VFS Annual Forum & Technology Display, Forum 56*.

Wang, S., & Danai, K. (2003). A probability-based approach to helicopter track and balance. *AHS 59th Annual Forum*, 1–10.

Wang, S., Danai, K., & Wilson, M. (2005). Adaptive Method of Helicopter Track and Balance. *Journal of Dynamic Systems, Measurement, and Control*, *127*, 275–282. https://doi.org/10.1115/1.1913683

Wilke, G. A. (2017). *Aerodynamic Optimization of Helicopter Rotor Blades using Variable Fidelity Methods* [TU Braunschweig]. https://core.ac.uk/download/pdf/158058408.pdf

Part II

Discrete Modeling:

Finite Element, Boundary Element, Meshfree Methods

Chapter 17

Finite Element Method for Structural Integrity Problems

Chapter details

Chapter DOI:

Chapter suggested citation / reference style:

P.S.: DOI may be included at the end of citation, for completeness.

Book details

Finite Element Method for Structural Problems

Thiago de P. Sales[1]*, Polliana C. O. Martins[2], Domingos A. Rade[3]

[1]Aeronautics Institute of Technology, Brazil, tpsales@ita.br
[2]University of Brasilia, Brazil, polliana.martins@unb.br
[3]Aeronautics Institute of Technology, Brazil, rade@ita.br

*Corresponding author

Abstract

The finite element method (FEM) has been applied to solve engineering problems in several areas during the last decades, fulfilling an important role, mainly in situations that present complex, or even non-existent, analytical solutions. As every numerical technique, this approach has limitations which are directly linked with digital computing capacity, since this method is widely and predominantly implemented using such tools. Thus, this chapter presents a contextualized and updated introduction to the FEM, including its fundamentals, such as important considerations about spatial discretization of the physical domain and formulation at element and global levels. Using the variational approach, the formulation of two different finite elements is presented in considerable depth, namely for a quadrilateral, two-dimensional elasticity FE, with four nodes; and for a Kirchhoff-Love plate, equivalent single layer composite/laminate FE, rectangular, with four nodes. In a second moment, two examples are discussed, the first of which is concerned with an H-shaped sheet, with one of its edges clamped, and being subject to a uniform pressure load. The second example studies a rectangular, four layer composite, clamped on one of its edges. By means of both of these, one highlights the importance of proper mesh generation and/or adequate selection of a FE for a given problem; as well as the various types of structural dynamics' analyzes one might be interested in performing. Additionally, most relevant information and discussion is provided concerning parameterization of FE models, particularly in association to model updating and damage identification. Particularly, a section is dedicated to model updating based on the sensitivity of eigenvalues and eigenvectors. Final remarks are also included, to point out most pertinent directions, in the view of the authors, for interested readers to follow. As a bonus, MATLAB® codes implemented by the authors, related to the two considered examples, are made available for download within the chapter material.

Keywords: Finite Element Method; quadrilateral two-dimensional finite element; rectangular Kirchhoff-Love plate; parameterization; model updating.

1   Introduction

From the Mathematics standpoint, the Finite Element Method (FEM) is a numerical technique intended to provided approximate solutions to differential equations. From the engineering perspective, the FEM has been conceived to obtain approximate solutions of a range of problems whose underlying physics are governed by differential equations. Despite the fact that the method has been originally developed for the analysis of structural systems, it has been widely used for the modeling of a variety of engineering problems, in the fields of Solid Mechanics, Fluid Mechanics, Heat Transfer, Electromagnetism, among others. Due to its accuracy, computational efficiency and modeling flexibility, besides its ease of implementation in digital computers, the FEM has achieved great diffusion, both in industry and academia, being considered as a high valued tool for the development of engineering projects and scientific investigations. One can surely say that the FEM is currently one of the most widely used numerical techniques in science and engineering. As a result, the method has been taught in most universities around the world, with the support of a variety of textbooks [Zimmerman, 2006, Lewis et al., 1996, Reddy, 2019, Jin, 2015, Bathe, 2014].

The main motivation for the use of the FEM lies in the fact that for highly complex Engineering problems, analytical solutions to the underlying differential equations are difficult – or even impossible – to obtain. In fact, mathematical models of those problems, represented by a single or a set of ordinary or partial differential equations, can be obtained from the application of well established physical principles governing the underlying phenomena. Very often, simplifications are adopted by neglecting effects considered to be less influential. However, the resolution of the governing equations by using classical mathematical techniques can be unfeasible due to existence of a number of complicating factors, such as complex geometry, combination of multiple materials, nonlinear behavior, variable material parameters (with time or environmental influences), etc. These complicating factors are very often present in actual industrial problems.

For illustration, let us consider the heat transfer problem on a thin plate, of arbitrary boundary shape and material composition, as illustrated in Fig. 1. As in many practical cases, simplification is made by assuming that, given that the plate is thin, temperature is constant across the thickness, which implies the absence of heat flux in that direction. Hence, the original three-dimensional problem is simplified to a two-dimensional counterpart.
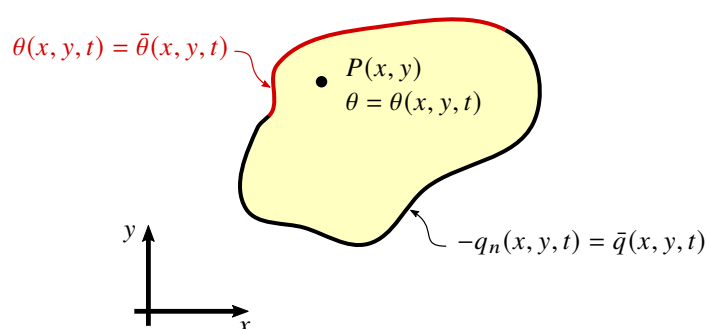
Figure 1: Illustration of a two-dimensional heat transfer problem on a plate of arbitrary shape.

Upon application of the law of energy conservation and Fourier's law of heat conduction to a differential element of the plate, the following partial differential equation, whose solution provides the transient temperature distribution over the plate, described by the so-called field variable, $\theta = \theta(x, y, t)$, is obtained:

$$\frac{\partial}{\partial x}\left(k_x(x, y, \theta)\frac{\partial \theta}{\partial x}\right) + \frac{\partial}{\partial y}\left(k_y(x, y, \theta)\frac{\partial \theta}{\partial y}\right) + Q(x, y, t) - \rho(x, y, \theta)c(x, y, \theta)\frac{\partial \theta}{\partial t} = 0, \quad (1)$$

where $Q(x, y, t)$ is the rate at which energy is generated per unit volume of the plate material, $\rho(x, y, \theta)$ and $c(x, y, \theta)$ are, respectively, the material mass density and specific heat, and $k_x(x, y, \theta)$ and $k_y(x, y, \theta)$ are the material heat transfer coefficients in directions x and y, respectively.

It should be recalled that the resolution of Eq. (1) must satisfy a set of initial and boundary conditions. Fig. 1 indicates that these later can be of two different categories, namely: enforcement of temperature values, $\theta(x, y, t) = \bar{\theta}(x, y, t)$ (a Dirichlet boundary condition), and enforcement of the heat flux in the direction normal to the contour line, $-q_n(x, y, t) = \bar{q}(x, y, t)$ (a Neumann boundary condition).

The complicating factors involved in Eq. (1) are material heterogeneity and anisotropy (i.e., material properties depend on direction and space coordinates) and non-linearity (material properties depend on the unknown temperature distribution). In addition, the arbitrary shape of the plate, which defines the domain to be covered by the solution.

Hence, a complicated problem such as this one can only be solved with recourse to numerical methods, among which, the FEM is a convenient one.

Currently, the Finite Element Method can be found implemented in a variety of commercial packages. Graphical interfaces are most often used, guiding the user across the different phases of modeling and numerical resolution. However, it is of utmost importance that the user fully understands the fundamentals of the method so as to be capable of making the appropriate modeling decisions and correctly interpreting results. In addition, there may be the need for the implementation of elements with particular characteristics, not available in the package's standard element library, and also the performance of the so-called *intrusive operations*. These later involve modifications of the FE model in its inner structure, as required in certain types of analyses, such as model adjustment to experimental data or system optimization. In such situations, mastering of physical, mathematical, numerical and computational aspects of the method is indispensable.

Therefore, in the subsection that follows, the basic steps involved in typical FE models are described aiming at, hopefully, providing the necessary understanding of how the method operates in commercial software and also helping the readers to implement their own code, should this be needed.

1.1   Fundamentals of the finite element method

Given the scope of the book to which this chapter belongs, an example focused on Solid Mechanics will be used for the description of the fundamental phases of FE modeling.
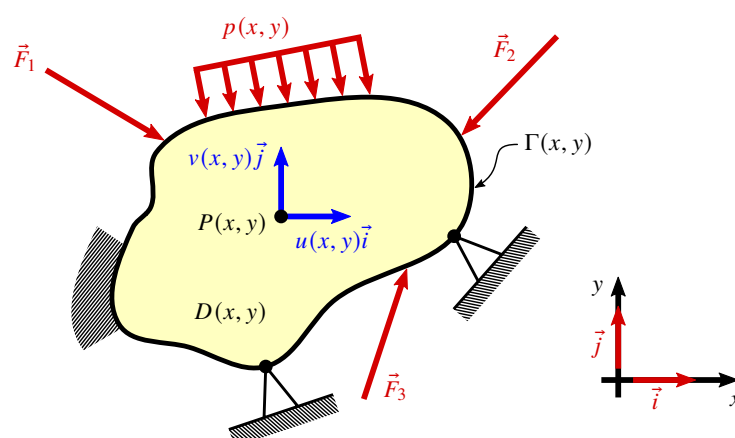
Figure 2: Illustration of a two-dimensional elasticity problem on a sheet of arbitrary shape.

Figure 2 illustrates a plane-stress elasticity problem, in which a thin sheet defining a domain $D(x, y)$ is subjected to in-plane loads, being constrained on a certain number of points on its boundary, which is indicated by $\Gamma(x, y)$. For simplicity, the assumptions of linear load-displacement material behavior and small displacements and rotations are adopted.

The classical problem to be solved consists in, given the loads and boundary conditions, determine the displacement Cartesian components $u(x, y)$ and $v(x, y)$ of each and every point $P(x, y)$ of the sheet, as well as the strain and stress distributions over the solid domain.

1.1.1 Spatial discretization of the domain

The first step of FE modeling is the division of the domain in which the problem is formulated (in the present example, the sheet and its boundary) in subdomains of predefined, user-selected, characteristics. These subdomains, called *elements*, are chosen to have simple geometry (triangles or quadrilaterals in two-dimensional problems; tetrahedrons or hexahedrons in three-dimensional problems), having given numbers of notable points, usually located on their edges, called *nodes*. Fig. 3 depicts the sheet of interest divided in a relatively large number of quadrilateral and triangular elements. Also shown is an amplified view of an element I, and its respective nodes, denoted by i, j, k, l. The entire set of elements and their nodes is named the model *mesh*.

Also indicated in Fig. 3 are the displacements of the four nodes of interest in directions x and y, denoted as $\vec{u}_i, \vec{v}_i, \vec{u}_j, \vec{v}_j, \vec{u}_k, \vec{v}_k, \vec{u}_l, \vec{v}_l$. In the finite element jargon, these displacements, or, more generally, the values of the unknown variables of the problem at the mesh nodes are called *degrees-of-freedom* (DOFs).
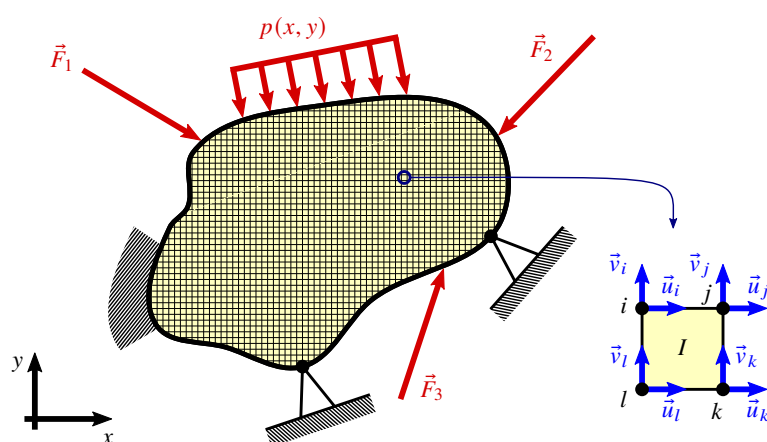
Figure 3: Illustration of a mesh defined for the discretization of a two-dimensional elasticity problem, and details of an element.

1.1.2 Interpolation of the field variables

Once defined the model mesh, the most distinguished idea underlying FE modeling is put forward, namely, the *interpolation* of the unknown variables, in the present case, the Cartesian components of the displacement field, *within each element of the mesh*. Accordingly, for a typical element I, these variables are mathematically expressed as follows:

$$u^{(I)}(x, y) = N_i(x, y)u_i + N_j(x, y)u_j + N_k(x, y)u_k + N_l(x, y)u_l, \tag{2a}$$

$$v^{(I)}(x, y) = N_i(x, y)v_i + N_j(x, y)v_j + N_k(x, y)v_k + N_l(x, y)v_l. \tag{2b}$$

It can be seen that, on each element, the displacement components at any point of coordinates (x, y) within the element, are expressed as linear combinations of the corresponding values evaluated at the four nodes. The coefficients of these linear combinations are the functions of the space coordinates $N_i(x, y), N_j(x, y), N_k(x, y), N_l(x, y)$. These functions, called *interpolation functions* or *shape functions*, are chosen for each particular type of element. In general, they are polynomial functions whose degrees are chosen according to the number of nodes (and DOFs, as a result) assigned to the elements.

It should be highlighted that, once the nodal values of the unknowns are determined, the values of the variables $u^{(I)}(x, y)$ and $v^{(I)}(x, y)$ are obtained as continuous functions of the nodal values, as given by Eqs. (2). Hence, the primary goal of finite element computations is the determination of the nodal values, the number of which is finite, as opposed to the number of variables in the original Solid Mechanics problem, governed by partial differential equations, whose solution over the entire domain $u(x, y), v(x, y)$ must be valid for the infinite number of points comprising the domain. It can, thus, be stated that the combination of the discretization and interpolation procedures enables to reduce the original infinite-dimensional problem to an associated finite-dimensional one, amenable to approximate numerical resolution. This entails transitions from one type of mathematical model (for the continuous problem) to another (for the discretized problem). For example, in the case of transient heat transfer problems, the transition leads from a partial differential equation to a set of (generally coupled) ordinary differential equations having the nodal temperature values as unknowns; in the case of equilibrium problems of elasticity, the transition is made from a set of partial differential equations to a set of coupled algebraic equations having the nodal displacement values as unknowns.

1.1.3   Formulation at element level

The formulation at the so-called *element level* is carried-out by considering the physics of the problem, starting either from basic governing principles or, more directly, the differential equations governing the underlying phenomena. For this purpose, three different formulation approaches can be followed, which are described next. Irrespective of the approach adopted, the goal is to establish differential or algebraic relations between inputs applied at the element nodes, and resulting outputs at the nodes. For example, in heat transfer problems, the inputs are heat fluxes and the outputs are temperatures; in static elasticity problems, the inputs are forces and the outputs are displacements. At this level, each element is considered individually, without any interaction with neighboring elements.

- **Direct approach:** in this approach, the equations describing the underlying principles are directly manipulated, in association with interpolation of the field variables to obtain the above-mentioned input-output relations. As examples, in heat transfer problems, energy balance and Fourier's law are jointly used with interpolated temperature field within the element to obtain relations between heat fluxes applied at the nodes and the corresponding nodal temperature values; in static elasticity problems, equilibrium equations and material constitutive laws, together with interpolated displacement fields lead to relations between forces applied at the nodes and the associated nodal displacement values. In spite of providing clear physical meaning of the operations performed during the derivation of the input-output relations at the element level, the direct approach is mostly used in the formulation of one-dimensional problems, since its extension to two- or three-dimensional problems tend to involve rather cumbersome manipulations.

- **Variational approach:** this approach is based on the exploration of the so-called *variational principles*, which establish stationarity conditions to be satisfied by certain functionals that,

in many cases, are integrals expressing the energy of the system. From the mathematical standpoint, methods for finding the extremals of such functionals are in the scope of a branch of Mathematics known as Variational Calculus [Weinstock, 1975, Lanczos, 1986]. In the case of mechanical systems of interest here, the most widely used variational principles are the *Principle of Minimal Potential Energy*, which, applied to elastic systems, states that, among all possible deformed configurations satisfying the prescribed boundary conditions, the actual configuration developed is the one that minimizes the total potential energy of the system; and the *Hamilton's Variational Principle*, which establishes that, for dynamic systems, the actual motion evolution, satisfying boundary and initial conditions, must extremize a functional expressing the net value of the difference between the kinetic and potential energies.

For the variational formulation at element level, the applicable variational principle is used in combination with the interpolation of field variables and, searching the conditions to be satisfied by the aproximate solution to ensure the stationarity of the associated functional. Eventually, the stationarity conditions are brought to the requirement that the derivatives of the algebraic form of functional with respect to each DOF of the element must vanish. This procedure leads to the input-output relations at element level that are searched for.

In spite of being very powerful and elegant, the use of the variational approach is confined to problems governed by variational principles, which is not always the case.

- **Weighted residuals approach**: this approach operates directly on the differential equations governing the problem into consideration. The main idea is to establish the conditions to be satisfied by the approximated solution in such a way to minimize the solution errors expressed as mean values of point-wise weighted residual functions, evaluated over an individual element. The number of errors considered is equal to the number of DOFs of the element, and each one is obtained from a different weighting function.

  The computation of the errors involve the integration of the corresponding weighted residual functions over the element. The use of Gauss' Theorem or Green's Theorem (according to the dimensionality of the problem) enables one to reduce the maximal order of the differential operators in the integrand, leading to the so-called *weak form* of the problem.

  Various weight residual methods have been devised, making use of different weighting functions. Among them, the most popular (at least in the scope of FE modeling) is the *Galerkin Method*, in which the shape functions are used as weighting functions.

  Similarly to the two previous formulation approaches, the weight residual approach eventually leads to the searched input-output relations at element level.

1.1.4   Formulation at global level

In the formulation at element level, each element of the mesh is considered individually, without any physical interaction among them. This means that, at that level, the formulation leads to a set of uncoupled equations expressing the input-output relations for each and every element of the mesh. However, as can be seen in Fig. 3, all the elements of the mesh will have at least one neighboring element with which it shares nodes and DOFs. This means, from the physics perspective, that at nodes shared by neighboring elements, the continuity of the field variables must be ensured, as well as other requirements depending of the specific nature of the problem, such as force equilibrium and null net heat flux. These conditions are enforced by appropriate modification and combination of the input-output relations previously established for each element at element level, which leads to relations between outputs and inputs at global level, represented, respectively by vectors containing

the whole set of nodal DOFs and nodal loads. These two vectors are related to each other by a square multiplicative matrix (known as *global stiffness matrix* in Solid Mechanics problems.

From the algorithmic standpoint, enforcement of the above-mentioned conditions is made by a sequence of well-defined matrix operations, known as *matrix/vector assembling* [Zienkiewicz et al., 2013, Reddy, 2019].

1.1.5   Enforcement of boundary conditions

Upon completion of matrix/vector assembling, the input-output relations for the whole FE model are available, nonetheless without any constraints imposed to the DOFs. Hence, the global matrices and vectors must be further modified to account for the boundary conditions. In Solid Mechanics problems, for example, very often those conditions represent specific values assigned to particular DOFs associated to nodes located on the boundary of the body.

1.1.6   Numerical resolution

The finite element equations at global level have to be solved by using appropriate numerical procedures. According to the nature of the problem, different types of equations must be solved: for equilibrium or steady-state problems, one has systems of algebraic equations, while for dynamic or transient problems, systems of ordinary differential equations are to be solved. Furthermore, within these broad categories of problems, some specific numerical problems may emerge. For example, static or dynamic stability problems require the resolution of *eigenvalue problems*, while the frequency response analysis in structural dynamics require the resolution of a series of sets of linear algebraic equations, each one corresponding to a discrete value of frequency.

In addition to the calculation of the primary unknowns of the FE model, by the resolution of the equations mentioned above, further computations are required to determine other quantities derived from those unknowns. As an example, in linear elasticity problems, most often the primary unknowns are the nodal displacements. In these cases, strain distributions must be determined by applying the appropriate differential operators to the displacement distributions at element level, according to the strain-displacement relations. Then, stress distributions are computed by making recourse to the stress-strain relations at element level, which involve the matrix of elastic parameters. These additional computations are most-often referred to as *post-processing* of the primary solution of the underlying problem.

At this point it is important to point-out that the efficiency of the FE method highly depends on the efficiency of the numerical algorithms used for the resolution of the different types of mathematical equations mentioned above. This is due to the fact that, to provide the necessary accuracy, complex finite element models must use highly refined discretization meshes, which leads to large numbers of DOFs and numbers of equations to be solved simultaneously (of the order of 10^5 to 10^7). In addition, in the majority of applications of practical interest (model updating based on experimental data, structural optimization, uncertainty propagation, etc.) the numerical resolution of the mathematical equations must be made multiple times. As a result, computational burden tend to be typically high and must be properly managed to render the computations feasible for the computer resources available. Besides the search for increasingly efficient numerical methods, the alleviation of computation cost can be achieved by employing techniques of model condensation and metamodeling [Zu-Qing, 2004, Gratiet et al., 2017, Sargsyan, 2017, Chen and Schwab, 2017].

2   Modeling of Problems in Solid Mechanics (Variational Approach)

The application and formulation of the FEM for problems in Solid Mechanics can be carried out using various strategies, as briefly explained in the previous section. Here, the variational approach is adopted, due to its versatility and relatively simple background requirements. While previous knowledge on Variational Calculus should not be required to follow the developments presented next, the reader can consult other material available on the matter if he/she has desire to do so [Weinstock, 1975, Lanczos, 1986].

Additionally, one assumes the reader to be reasonably familiar with Solid Mechanics. Various concepts invoked in the sequence can be found in more specific literature, e.g. [Fung et al., 2017].

Within the framework of the variational formulation of the FEM, one seeks to make a functional stationary. In the case of structural dynamics problems, such functional is directly related to the Lagrangian, $\mathcal{L}$, given by the difference between kinetic $\mathcal{K}$ and potential $\mathcal{U}$ energies:

$$\mathcal{L} = \mathcal{K} - \mathcal{U}. \tag{3}$$

Both contributions arise due to the motion of a solid body. Referring to Fig. 4, let us denote the velocities of an arbitrary point by $\dot{u}(x, y, z, t)$, $\dot{v}(x, y, z, t)$ and $\dot{w}(x, y, z, t)$ along the three Cartesian coordinate directions, where $(\dot{\ }) \equiv d(\ )/dt$. The kinetic energy of the solid body can therefore be obtained by:

$$\mathcal{K}(t) = \iiint_{\Omega_t} \frac{1}{2} \rho(x, y, z) \left[\dot{u}^2(x, y, z, t) + \dot{v}^2(x, y, z, t) + \dot{w}^2(x, y, z, t) \right] dx\, dy\, dz, \tag{4}$$

where ρ denotes the mass density, and Ω_t the volume occupied by the body at time t. In essence, the previous equation is the continuum counterpart of that one related to a collection of discrete particles; it can be interpreted as the (Riemann) sum of half the mass times the square of the velocity magnitude of each continuum (differential) particle.
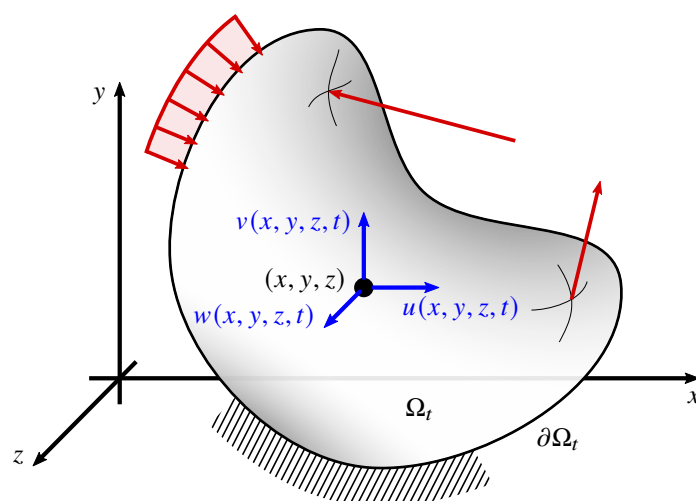
Figure 4: Snapshot of a solid body during its motion, at time t, with volume Ω_t and boundary $\partial\Omega_t$.

With regards to the potential energy, it can encompass various contributions (due to elasticity, gravity, ...), but all being related to conservative loads, i.e. those whose mechanical work do not depend on the load-path. Considering that the theory of elasticity holds (i.e. small/infinitesimal

displacements and strains are assumed), $\mathcal{U}$ can be obtained using:

$$\mathcal{U}(t) = \frac{1}{2} \iiint_{\Omega_t} \left[\sigma_x \epsilon_x + \sigma_y \epsilon_y + \sigma_z \epsilon_z + \tau_{xy} \gamma_{xy} + \tau_{xz} \gamma_{xz} + \tau_{yz} \gamma_{yz} \right] \mathrm{d}x\, \mathrm{d}y\, \mathrm{d}z - \mathcal{W}_{\text{ext}}, \quad (5)$$

where $\sigma_i = \sigma_i(x, y, z, t)$ and $\tau_{ij} = \tau_{ij}(x, y, z, t)$ $(i, j \in \{x, y, z\})$ stand for the Cartesian components of the engineering stress tensor; and $\epsilon_i = \epsilon_i(x, y, z, t)$ and $\gamma_{ij} = 2\epsilon_{ij} = \gamma_{ij}(x, y, z, t)$ $(i, j \in \{x, y, z\})$ represent the Cartesian components of the infinitesimal strain tensor and shear angles, respectively. Additionally, $\mathcal{W}_{\text{ext}}$ represents the work done by conservative external forces. It can be calculated, in general, according to:

$$
\begin{aligned}
\mathcal{W}_{\text{ext}}(t) = \iiint_{\Omega_t} &\left[u(x, y, z, t) f_b^x(x, y, z, t) + v(x, y, z, t) f_b^y(x, y, z, t) \right. \\
&\left. + w(x, y, z, t) f_b^z(x, y, z, t) \right] \mathrm{d}x\, \mathrm{d}y\, \mathrm{d}z \\
+ \iint_{\partial\Omega_t} &\left[u(x, y, z, t) f_s^x(x, y, z, t) + v(x, y, z, t) f_s^y(x, y, z, t) \right. \\
&\left. + w(x, y, z, t) f_s^z(x, y, z, t) \right] \mathrm{d}S, \quad (6)
\end{aligned}
$$

where f_b^x, f_b^y and f_b^z represent body forces (forces per unit volume, such as the one due to gravity) and f_s^x, f_s^y and f_s^s correspond to surface forces (forces per unit area, e.g. tractions, pressures, concentrated loads). The boundary of the body, on which surface forces can be applied, is denoted $\partial\Omega_t$, and $\mathrm{d}S$ represents a differential area/surface element.

Additional equations need to be taken into account to allow for specification of the solid's material behavior. These equations are known as constitutive equations. If the solid behavior is in accordance with linear elasticity, and its properties are the same in every direction (i.e. the material is isotropic), then its constitutive equations correspond to Hooke's law. In the case of three-dimensional elasticity, it reads:

$$\sigma_x = \tfrac{E}{(1+\nu)(1-2\nu)} \left[(1 - \nu)\epsilon_x - \nu\epsilon_y - \nu\epsilon_z \right]; \tag{7a}$$

$$\sigma_y = \tfrac{E}{(1+\nu)(1-2\nu)} \left[-\nu\epsilon_x + (1 - \nu)\epsilon_y - \nu\epsilon_z \right]; \tag{7b}$$

$$\sigma_z = \tfrac{E}{(1+\nu)(1-2\nu)} \left[-\nu\epsilon_x - \nu\epsilon_y + (1 - \nu)\epsilon_z \right]; \tag{7c}$$

$$\tau_{xy} = G\gamma_{xy}; \tag{7d}$$

$$\tau_{xz} = G\gamma_{xz}; \tag{7e}$$

$$\tau_{yz} = G\gamma_{yz}, \tag{7f}$$

with E, ν and $G = E/[2(1 + \nu)]$ corresponding to the material's Young's modulus, Poisson's ratio and shear modulus, respectively. Of course, more general constitutive relations can be considered, depending on the material one wants to model.

Other important equations which need to be recalled relate strains to the displacements experienced by the solid body during its motion. From the theory of linear elasticity, the following holds:

$$\epsilon_x = \frac{\partial u}{\partial x}; \quad \epsilon_y = \frac{\partial v}{\partial y}; \quad \epsilon_z = \frac{\partial w}{\partial z}; \quad \gamma_{xy} = \frac{\partial u}{\partial y} + \frac{\partial v}{\partial x}; \quad \gamma_{xz} = \frac{\partial u}{\partial z} + \frac{\partial w}{\partial x}; \quad \gamma_{yz} = \frac{\partial v}{\partial z} + \frac{\partial w}{\partial y}, \quad (8)$$

where dependencies have been omitted for conciseness.

As discussed in section 1 of this chapter, within the context of the FEM, the continuum solid body is replaced by a mesh, formed by finite elements and their respective nodes. In this process, the unknown displacement fields u, v and w have their spatial dependency become expressed in terms of nodal DOFs. In this sense, inside the domain of a given finite element, the displacement

fields are interpolated (approximated) based on the nodal DOFs. Mathematically, for a generic element e of the mesh, we have, akin to Eqs. (2), for example:

$$u^{(e)}(x, y, z, t) = \sum_{k=1}^{n^{(e)}} N_{uk}^{(e)}(x, y, z) q_k^{(e)}(t) = \mathbf{N}_u^{(e)}(x, y, z) \mathbf{q}^{(e)}(t); \tag{9a}$$

$$v^{(e)}(x, y, z, t) = \sum_{k=1}^{n^{(e)}} N_{vk}^{(e)}(x, y, z) q_k^{(e)}(t) = \mathbf{N}_v^{(e)}(x, y, z) \mathbf{q}^{(e)}(t); \tag{9b}$$

$$w^{(e)}(x, y, z, t) = \sum_{k=1}^{n^{(e)}} N_{wk}^{(e)}(x, y, z) q_k^{(e)}(t) = \mathbf{N}_w^{(e)}(x, y, z) \mathbf{q}^{(e)}(t), \tag{9c}$$

where the vector $\mathbf{q}^{(e)}(t) \in \mathbb{R}^{n^{(e)} \times 1}$ collects the element nodal DOFs, in a total of $n^{(e)}$. These could comprise, for instance, the displacements of the nodes. Matrices such as $\mathbf{N}_u^{(e)}(x, y, z)$, $\mathbf{N}_v^{(e)}(x, y, z)$ and $\mathbf{N}_v^{(e)}(x, y, z)$, of size $1 \times n^{(e)}$, contain the so-called *interpolation functions* or *shape functions* of the finite element. They enable us to compute the displacements of any point within the finite element domain in terms of its nodal DOFs, after these have been obtained.

An important note in this regard is that each type of finite element has its own particular set of interpolation functions. Hence, the choice of a finite element to be used in a particular analysis directly translates to which interpolation functions are used. This is important to be recognized because the interpolation functions can hinder its corresponding finite element from adequately representing certain behaviors. This is another reason for which it is of utmost significance for one to become aware of the formulation of the FEM, as well as of documentation and/or manuals of various commercial finite element packages.

Traditionally, in the formulation of finite elements, interpolation functions are chosen to be polynomials, although this is not the only option, nor necessarily the better. For instance, non-uniform rational B-splines (NURBS) can be used, as considered in the so-called isogeometric finite element analysis [Cottrell et al., 2009].

In the following, instead of presenting the mathematical formulation of a finite element method for three-dimensional elasticity, we favor the case of two-dimensional elasticity. A finite element for the more complicated case can be obtained following similar steps to those outlined next.

2.1 Quadrilateral finite element for two-dimensional elasticity problems

2.1.1 Element geometry and interpolation of field variables

The two-dimensional elasticity finite element we consider here has four nodes, and its geometry is quadrilateral, cf. Fig. 5.
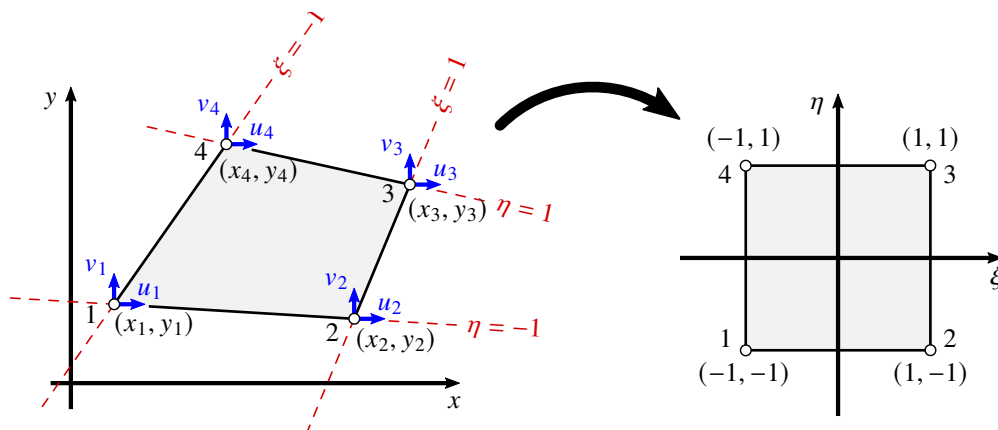
Figure 5: Geometry of a quadrilateral finite element with four nodes, and its corresponding representation in the natural coordinate space (ξ, η).

The degrees of freedom of the element are chosen to correspond to the displacements at the nodes. In this way, we have:

$$\mathbf{q}^{(e)}(t) = \{u_1(t) \quad v_1(t) \quad u_2(t) \quad v_2(t) \quad u_3(t) \quad v_3(t) \quad u_4(t) \quad v_4(t)\}^{\mathrm{T}}, \tag{10}$$

in which $u_i(t)$, $v_i(t)$ correspond to the displacements of node i along the x and y directions, respectively. At this stage, we drop the superscript $^{(e)}$ to avoid clutter – it will be used again later when needed to avoid possible confusion.

Having this at hand, we must select an interpolation scheme for evaluating the displacement fields inside the element domain. For this purpose, we choose the following polynomials:

$$u(x,y,t) = a_{00}(t) + a_{10}(t)x + a_{01}(t)y + a_{11}(t)xy = \begin{bmatrix} 1 & x & y & xy \end{bmatrix} \begin{Bmatrix} a_{00}(t) \\ a_{10}(t) \\ a_{01}(t) \\ a_{11}(t) \end{Bmatrix}; \tag{11a}$$

$$v(x,y,t) = b_{00}(t) + b_{10}(t)x + b_{01}(t)y + b_{11}(t)xy = \begin{bmatrix} 1 & x & y & xy \end{bmatrix} \begin{Bmatrix} b_{00}(t) \\ b_{10}(t) \\ b_{01}(t) \\ b_{11}(t) \end{Bmatrix}, \tag{11b}$$

for any $(x,y) \in \Omega_t^{(e)}$. The time-dependent weights a_{ij}, b_{ij} $(i, j \in \{0, 1\})$ can be determined by enforcing the value of the displacement fields at the element nodes, i.e.,

$$\begin{Bmatrix} u_1(t) \\ u_2(t) \\ u_3(t) \\ u_4(t) \end{Bmatrix} = \begin{Bmatrix} u(x_1, y_1, t) \\ u(x_2, y_2, t) \\ u(x_3, y_3, t) \\ u(x_4, y_4, t) \end{Bmatrix} = \begin{bmatrix} 1 & x_1 & y_1 & x_1 y_1 \\ 1 & x_2 & y_2 & x_2 y_2 \\ 1 & x_3 & y_3 & x_3 y_3 \\ 1 & x_4 & y_4 & x_4 y_4 \end{bmatrix} \begin{Bmatrix} a_{00}(t) \\ a_{10}(t) \\ a_{01}(t) \\ a_{11}(t) \end{Bmatrix} \Rightarrow$$

$$\Rightarrow \begin{Bmatrix} a_{00}(t) \\ a_{10}(t) \\ a_{01}(t) \\ a_{11}(t) \end{Bmatrix} = \begin{bmatrix} 1 & x_1 & y_1 & x_1 y_1 \\ 1 & x_2 & y_2 & x_2 y_2 \\ 1 & x_3 & y_3 & x_3 y_3 \\ 1 & x_4 & y_4 & x_4 y_4 \end{bmatrix}^{-1} \begin{Bmatrix} u_1(t) \\ u_2(t) \\ u_3(t) \\ u_4(t) \end{Bmatrix}; \tag{12a}$$

$$\begin{Bmatrix} v_1(t) \\ v_2(t) \\ v_3(t) \\ v_4(t) \end{Bmatrix} = \begin{Bmatrix} v(x_1, y_1, t) \\ v(x_2, y_2, t) \\ v(x_3, y_3, t) \\ v(x_4, y_4, t) \end{Bmatrix} = \begin{bmatrix} 1 & x_1 & y_1 & x_1 y_1 \\ 1 & x_2 & y_2 & x_2 y_2 \\ 1 & x_3 & y_3 & x_3 y_3 \\ 1 & x_4 & y_4 & x_4 y_4 \end{bmatrix} \begin{Bmatrix} b_{00}(t) \\ b_{10}(t) \\ b_{01}(t) \\ b_{11}(t) \end{Bmatrix} \Rightarrow$$

$$\Rightarrow \begin{Bmatrix} b_{00}(t) \\ b_{10}(t) \\ b_{01}(t) \\ b_{11}(t) \end{Bmatrix} = \begin{bmatrix} 1 & x_1 & y_1 & x_1 y_1 \\ 1 & x_2 & y_2 & x_2 y_2 \\ 1 & x_3 & y_3 & x_3 y_3 \\ 1 & x_4 & y_4 & x_4 y_4 \end{bmatrix}^{-1} \begin{Bmatrix} v_1(t) \\ v_2(t) \\ v_3(t) \\ v_4(t) \end{Bmatrix}. \tag{12b}$$

Combining these results with Eq. (11), we obtain:

$$u(x,y,t) = \begin{bmatrix} 1 & x & y & xy \end{bmatrix} \begin{Bmatrix} a_{00}(t) \\ a_{10}(t) \\ a_{01}(t) \\ a_{11}(t) \end{Bmatrix} = \begin{bmatrix} 1 & x & y & xy \end{bmatrix} \begin{bmatrix} 1 & x_1 & y_1 & x_1 y_1 \\ 1 & x_2 & y_2 & x_2 y_2 \\ 1 & x_3 & y_3 & x_3 y_3 \\ 1 & x_4 & y_4 & x_4 y_4 \end{bmatrix}^{-1} \begin{Bmatrix} u_1 \\ u_2 \\ u_3 \\ u_4 \end{Bmatrix}$$

$$= N_1(x,y)u_1(t) + N_2(x,y)u_2(t) + N_3(x,y)u_3(t) + N_4(x,y)u_4(t); \tag{13a}$$

$$v(x,y,t) = \begin{bmatrix} 1 & x & y & xy \end{bmatrix} \begin{Bmatrix} b_{00}(t) \\ b_{10}(t) \\ b_{01}(t) \\ b_{11}(t) \end{Bmatrix} = \begin{bmatrix} 1 & x & y & xy \end{bmatrix} \begin{bmatrix} 1 & x_1 & y_1 & x_1 y_1 \\ 1 & x_2 & y_2 & x_2 y_2 \\ 1 & x_3 & y_3 & x_3 y_3 \\ 1 & x_4 & y_4 & x_4 y_4 \end{bmatrix}^{-1} \begin{Bmatrix} v_1 \\ v_2 \\ v_3 \\ v_4 \end{Bmatrix}$$

$$= N_1(x, y)v_1(t) + N_2(x, y)v_2(t) + N_3(x, y)v_3(t) + N_4(x, y)v_4(t), \qquad (13b)$$

from which the expressions for $N_i(x, y)$ ($i \in \{1, 2, 3, 4\}$) can be identified. While the expressions for these shape functions can be established analytically (using symbolic algebra software, for example), they result relatively complicated and long, being for this reason omitted here.

It is sometimes more convenient in the formulation of finite elements to adopt a different strategy, which relies on the use of a natural coordinate system (ξ, η), instead of the Cartesian (x, y) one. In this setting, the positions of the nodes of a finite element assume normalized values, as can be seen in Fig. 5. Using the natural coordinate system, we can write:

$$u(\xi, \eta, t) = \begin{bmatrix} 1 & \xi & \eta & \xi\eta \end{bmatrix} \begin{bmatrix} 1 & \xi_1 & \eta_1 & \xi_1\eta_1 \\ 1 & \xi_2 & \eta_2 & \xi_2\eta_2 \\ 1 & \xi_3 & \eta_3 & \xi_3\eta_3 \\ 1 & \xi_4 & \eta_4 & \xi_4\eta_4 \end{bmatrix}^{-1} \begin{Bmatrix} u_1(t) \\ u_2(t) \\ u_3(t) \\ u_4(t) \end{Bmatrix}$$

$$= N_1(\xi, \eta)u_1(t) + N_2(\xi, \eta)u_2(t) + N_3(\xi, \eta)u_3(t) + N_4(\xi, \eta)u_4(t); \qquad (14a)$$

$$v(\xi, \eta, t) = \begin{bmatrix} 1 & \xi & \eta & \xi\eta \end{bmatrix} \begin{bmatrix} 1 & \xi_1 & \eta_1 & \xi_1\eta_1 \\ 1 & \xi_2 & \eta_2 & \xi_2\eta_2 \\ 1 & \xi_3 & \eta_3 & \xi_3\eta_3 \\ 1 & \xi_4 & \eta_4 & \xi_4\eta_4 \end{bmatrix}^{-1} \begin{Bmatrix} v_1(t) \\ v_2(t) \\ v_3(t) \\ v_4(t) \end{Bmatrix}$$

$$= N_1(\xi, \eta)v_1(t) + N_2(\xi, \eta)v_2(t) + N_3(\xi, \eta)v_3(t) + N_4(\xi, \eta)v_4(t), \qquad (14b)$$

where now it is easy to express $N_i(\xi, \eta)$ ($i \in \{1, 2, 3, 4\}$):

$$N_1(\xi, \eta) = \tfrac{1}{4}(1 - \xi)(1 - \eta); \qquad N_2(\xi, \eta) = \tfrac{1}{4}(1 + \xi)(1 - \eta);$$

$$N_3(\xi, \eta) = \tfrac{1}{4}(1 + \xi)(1 + \eta); \qquad N_4(\xi, \eta) = \tfrac{1}{4}(1 - \xi)(1 + \eta). \qquad (15)$$

We should note, at this stage, that the position of an arbitrary point on the domain of a given finite element (of the considered type) can be obtained using the same interpolation functions presented above, i.e.

$$x(\xi, \eta) = N_1(\xi, \eta)x_1 + N_2(\xi, \eta)x_2 + N_3(\xi, \eta)x_3 + N_4(\xi, \eta)x_4; \qquad (16a)$$

$$y(\xi, \eta) = N_1(\xi, \eta)y_1 + N_2(\xi, \eta)y_2 + N_3(\xi, \eta)y_3 + N_4(\xi, \eta)y_4. \qquad (16b)$$

Finite elements for which the same functions are used to interpolate the coordinates of a point on the element domain and unknown field variables (such as u and v in our presentation) are known as *isoparametric* finite elements [Bathe, 2014, Zienkiewicz et al., 2013].

As will be shown in developments which will follow soon, functions which depend on $N_i(x, y)$, as well as on their spatial derivatives, will need to be integrated on the domain of a finite element – so that relevant structural matrices can be obtained. Since one has favored the use of a natural coordinate system, we must be able to perform coordinate transformation between (x, y) and (ξ, η). By employing the chain-rule of differentiation:

$$\begin{cases} x = x(\xi, \eta) \\ y = y(\xi, \eta) \end{cases} \Rightarrow \begin{Bmatrix} \dfrac{\partial(\cdot)}{\partial\xi} \\ \dfrac{\partial(\cdot)}{\partial\eta} \end{Bmatrix} = \begin{bmatrix} \dfrac{\partial x}{\partial\xi} & \dfrac{\partial y}{\partial\xi} \\ \dfrac{\partial x}{\partial\eta} & \dfrac{\partial y}{\partial\eta} \end{bmatrix} \begin{Bmatrix} \dfrac{\partial(\cdot)}{\partial x} \\ \dfrac{\partial(\cdot)}{\partial y} \end{Bmatrix}$$

$$\text{and} \quad \begin{Bmatrix} \dfrac{\partial(\cdot)}{\partial x} \\ \dfrac{\partial(\cdot)}{\partial y} \end{Bmatrix} = \begin{bmatrix} \dfrac{\partial x}{\partial\xi} & \dfrac{\partial y}{\partial\xi} \\ \dfrac{\partial x}{\partial\eta} & \dfrac{\partial y}{\partial\eta} \end{bmatrix}^{-1} \begin{Bmatrix} \dfrac{\partial(\cdot)}{\partial\xi} \\ \dfrac{\partial(\cdot)}{\partial\eta} \end{Bmatrix}, \qquad (17)$$

based on which we define the Jacobian matrix related to an element:

$$\mathbf{J} = \begin{bmatrix} \dfrac{\partial x}{\partial \xi} & \dfrac{\partial y}{\partial \xi} \\[2mm] \dfrac{\partial x}{\partial \eta} & \dfrac{\partial y}{\partial \eta} \end{bmatrix}, \tag{18}$$

whose entries, from Eqs. (15) and (16), can be obtained as:

$$J_{11} = \frac{\partial x}{\partial \xi} = -\frac{1}{4}(1-\eta)x_1 + \frac{1}{4}(1-\eta)x_2 + \frac{1}{4}(1+\eta)x_3 - \frac{1}{4}(1+\eta)x_4; \tag{19a}$$

$$J_{12} = \frac{\partial y}{\partial \xi} = -\frac{1}{4}(1-\eta)y_1 + \frac{1}{4}(1-\eta)y_2 + \frac{1}{4}(1+\eta)y_3 - \frac{1}{4}(1+\eta)y_4; \tag{19b}$$

$$J_{21} = \frac{\partial x}{\partial \eta} = -\frac{1}{4}(1-\xi)x_1 - \frac{1}{4}(1+\xi)x_2 + \frac{1}{4}(1+\xi)x_3 + \frac{1}{4}(1-\xi)x_4; \tag{19c}$$

$$J_{22} = \frac{\partial y}{\partial \eta} = -\frac{1}{4}(1-\xi)y_1 - \frac{1}{4}(1+\xi)y_2 + \frac{1}{4}(1+\xi)y_3 + \frac{1}{4}(1-\xi)y_4. \tag{19d}$$

Having in mind the expression put forward for $\mathbf{q}^{(e)}(t)$, cf. Eq. (10), we can see that:

$$\begin{aligned} u^{(e)}(\xi, \eta, t) &= \mathbf{N}_u^{(e)}(\xi, \eta)\mathbf{q}^{(e)}(t) \\ &= \begin{bmatrix} N_1(\xi, \eta) & 0 & N_2(\xi, \eta) & 0 & N_3(\xi, \eta) & 0 & N_4(\xi, \eta) & 0 \end{bmatrix} \mathbf{q}^{(e)}(t); \end{aligned} \tag{20a}$$

$$\begin{aligned} v^{(e)}(\xi, \eta, t) &= \mathbf{N}_v^{(e)}(\xi, \eta)\mathbf{q}^{(e)}(t) \\ &= \begin{bmatrix} 0 & N_1(\xi, \eta) & 0 & N_2(\xi, \eta) & 0 & N_3(\xi, \eta) & 0 & N_4(\xi, \eta) \end{bmatrix} \mathbf{q}^{(e)}(t). \end{aligned} \tag{20b}$$

2.1.2 Formulation at element level

Having established the interpolation of the field variables of the problem at hand, now one aims toward obtaining expressions for the Lagrangian of an element, directly involving its nodal DOFs. After the Lagrangian is obtained, it can established the dynamic equilibrium equations which one seeks here, based on the stationarity of the relevant functional.

For this, firstly, interpolation relations for the relevant strains are derived. By combining Eqs. (8) and (20), it is possible to arrive at:

$$\epsilon_x^{(e)}(\xi, \eta, t) = \frac{\partial u^{(e)}}{\partial x} = \frac{\partial \mathbf{N}_u^{(e)}(\xi, \eta)}{\partial x}\mathbf{q}^{(e)}(t) = \mathbf{B}_x^{(e)}(\xi, \eta)\mathbf{q}^{(e)}(t); \tag{21a}$$

$$\epsilon_y^{(e)}(\xi, \eta, t) = \frac{\partial v^{(e)}}{\partial y} = \frac{\partial \mathbf{N}_v^{(e)}(\xi, \eta)}{\partial y}\mathbf{q}^{(e)}(t) = \mathbf{B}_y^{(e)}(\xi, \eta)\mathbf{q}^{(e)}(t); \tag{21b}$$

$$\gamma_{xy}^{(e)}(\xi, \eta, t) = \frac{\partial u^{(e)}}{\partial y} + \frac{\partial v^{(e)}}{\partial x} = \frac{\partial \mathbf{N}_u^{(e)}(\xi, \eta)}{\partial y}\mathbf{q}^{(e)}(t) + \frac{\partial \mathbf{N}_v^{(e)}(\xi, \eta)}{\partial x}\mathbf{q}^{(e)}(t) = \mathbf{B}_{xy}^{(e)}(\xi, \eta)\mathbf{q}^{(e)}(t). \tag{21c}$$

By invoking Eq. (17), explicit expressions can be established for the strain interpolation matrices,

if so desired:

$$
\mathbf{B}_x^{(e)} = \frac{1}{8 \det \mathbf{J}^{(e)}}
\begin{bmatrix}
(1-\eta)y_2 - (\xi-\eta)y_3 - (1-\xi)y_4 \\
0 \\
-(1-\eta)y_1 + (1+\xi)y_3 - (\xi+\eta)y_4 \\
0 \\
(\xi-\eta)y_1 - (1+\xi)y_2 + (1+\eta)y_4 \\
0 \\
(1-\xi)y_1 + (\xi+\eta)y_2 - (1+\eta)y_3 \\
0
\end{bmatrix}^{\mathrm{T}} ; \tag{22a}
$$

$$
\mathbf{B}_y^{(e)} = \frac{1}{8 \det \mathbf{J}^{(e)}}
\begin{bmatrix}
0 \\
-(1-\eta)x_2 + (\xi-\eta)x_3 + (1-\xi)x_4 \\
0 \\
(1-\eta)x_1 - (1+\xi)x_3 + (\xi+\eta)x_4 \\
0 \\
-(\xi-\eta)x_1 + (1+\xi)x_2 - (1+\eta)x_4 \\
0 \\
-(1-\xi)x_1 - (\xi+\eta)x_2 + (1+\eta)x_3
\end{bmatrix}^{\mathrm{T}} ; \tag{22b}
$$

$$
\mathbf{B}_{xy}^{(e)} = \frac{1}{8 \det \mathbf{J}^{(e)}}
\begin{bmatrix}
-(1-\eta)x_2 + (\xi-\eta)x_3 + (1-\xi)x_4 \\
(1-\eta)y_2 - (\xi-\eta)y_3 - (1-\xi)y_4 \\
(1-\eta)x_1 - (1+\xi)x_3 + (\xi+\eta)x_4 \\
-(1-\eta)y_1 + (1+\xi)y_3 - (\xi+\eta)y_4 \\
-(\xi-\eta)x_1 + (1+\xi)x_2 - (1+\eta)x_4 \\
(\xi-\eta)y_1 - (1+\xi)y_2 + (1+\eta)y_4 \\
-(1-\xi)x_1 - (\xi+\eta)x_2 + (1+\eta)x_3 \\
(1-\xi)y_1 + (\xi+\eta)y_2 - (1+\eta)y_3
\end{bmatrix}^{\mathrm{T}} , \tag{22c}
$$

where $\det \mathbf{J}^{(e)} = J_{11}^{(e)} J_{22}^{(e)} - J_{12}^{(e)} J_{21}^{(e)}$.

Now, to facilitate manipulations, it is more convenient to arrange the strains in a single vector, as follows:

$$
\boldsymbol{\epsilon}^{(e)}(\xi,\eta,t) =
\begin{Bmatrix}
\epsilon_x^{(e)}(\xi,\eta,t) \\
\epsilon_y^{(e)}(\xi,\eta,t) \\
\gamma_{xy}^{(e)}(\xi,\eta,t)
\end{Bmatrix}
=
\begin{bmatrix}
\mathbf{B}_x^{(e)}(\xi,\eta) \\
\mathbf{B}_y^{(e)}(\xi,\eta) \\
\mathbf{B}_{xy}^{(e)}(\xi,\eta)
\end{bmatrix}
\mathbf{q}^{(e)}(t) = \mathbf{B}^{(e)}(\xi,\eta)\mathbf{q}^{(e)}(t). \tag{23}
$$

Next, having a way to evaluate strains inside the finite element domain, one aims to establish how stresses can be interpolated as functions of the element nodal DOFs. For an isotropic material, one can recourse to Hooke's law, which has been given in Eq. (7) for three-dimensional problems. Since two-dimensional elasticity is being considered, Hooke's law can be simplified, in order to address the two available possibilities:

(i) Plane stress In this case, $\sigma_z^{(e)} = \tau_{xz}^{(e)} = \tau_{yz}^{(e)} \equiv 0$. The remaining stresses can be evaluated using:

$$
\boldsymbol{\sigma}^{(e)}(\xi,\eta,t) =
\begin{Bmatrix}
\sigma_x^{(e)}(\xi,\eta,t) \\
\sigma_y^{(e)}(\xi,\eta,t) \\
\tau_{xy}^{(e)}(\xi,\eta,t)
\end{Bmatrix}
= \frac{E}{1-\nu^2}
\begin{bmatrix}
1 & \nu & 0 \\
\nu & 1 & 0 \\
0 & 0 & \frac{1-\nu}{2}
\end{bmatrix}
\begin{Bmatrix}
\epsilon_x^{(e)}(\xi,\eta,t) \\
\epsilon_y^{(e)}(\xi,\eta,t) \\
\gamma_{xy}^{(e)}(\xi,\eta,t)
\end{Bmatrix}
$$
$$
= \mathbf{D}^{(e)} \boldsymbol{\epsilon}^{(e)}(\xi,\eta,t) = \mathbf{D}^{(e)}\mathbf{B}^{(e)}(\xi,\eta)\mathbf{q}^{(e)}(t). \tag{24a}
$$

Matrix $\mathbf{D}^{(e)}$ can be directly identified in the previous equation. While there is no stress on the plane whose normal is directed along z, a normal strain arises, due to the Poisson effect:

$$\epsilon_z^{(e)}(\xi, \eta, t) = -\frac{\nu}{E} \left[\sigma_x^{(e)}(\xi, \eta, t) + \sigma_y^{(e)}(\xi, \eta, t) \right]. \tag{24b}$$

The geometry of the solid is such that one of its characteristic dimensions (along z) is much smaller than the others, i.e. the solid is essentially a sheet, flat and thin. Applied loads are assumed to be distributed uniformly along the thickness.

(ii) Plane strain In this case, $\epsilon_z^{(e)} = \gamma_{xz}^{(e)} = \gamma_{yz}^{(e)} \equiv 0$. The stresses can be obtained from:

$$\boldsymbol{\sigma}^{(e)}(\xi, \eta, t) = \begin{Bmatrix} \sigma_x^{(e)}(\xi, \eta, t) \\ \sigma_y^{(e)}(\xi, \eta, t) \\ \tau_{xy}^{(e)}(\xi, \eta, t) \end{Bmatrix} = \frac{E}{(1+\nu)(1-2\nu)} \begin{bmatrix} 1-\nu & \nu & 0 \\ \nu & 1-\nu & 0 \\ 0 & 0 & \frac{1-2\nu}{2} \end{bmatrix} \begin{Bmatrix} \epsilon_x^{(e)}(\xi, \eta, t) \\ \epsilon_y^{(e)}(\xi, \eta, t) \\ \gamma_{xy}^{(e)}(\xi, \eta, t) \end{Bmatrix}$$

$$= \mathbf{D}^{(e)} \boldsymbol{\epsilon}^{(e)}(\xi, \eta, t) = \mathbf{D}^{(e)} \mathbf{B}^{(e)}(\xi, \eta) \mathbf{q}^{(e)}(t), \tag{25a}$$

and:

$$\sigma_z^{(e)}(\xi, \eta, t) = \frac{\nu E}{(1+\nu)(1-2\nu)} \left[\epsilon_x^{(e)}(\xi, \eta, t) + \epsilon_y^{(e)}(\xi, \eta, t) \right]. \tag{25b}$$

Matrix $\mathbf{D}^{(e)}$ can once again be determined for this case by inspecting the relations just presented. The case of plane strain is associated to solids which have one characteristic dimension (along z) much larger than the others, i.e. they correspond to right prisms. Applied loads are assumed to be distributed uniformly along the length (z-dimension) of the solid.

As can be seen, irrespective of the considered case, the relevant stresses can be obtained using a relationship of the type $\boldsymbol{\sigma}^{(e)}(\xi, \eta, t) = \mathbf{D}^{(e)} \boldsymbol{\epsilon}^{(e)}(\xi, \eta, t)$, with the constitutive matrix $\mathbf{D}^{(e)}$ taking distinct forms to accommodate for the possible scenarios.

We can now plug developed expressions in Eqs. (4) and (5) to evaluate the kinetic and potential energies related to the finite element under consideration. With regards to the first, we have:

$$\mathcal{K}^{(e)} = \iiint_{\Omega_t^{(e)}} \frac{1}{2} \rho^{(e)}(x, y, z) \left\{ \left[\dot{u}^{(e)}(x, y, z, t) \right]^2 + \left[\dot{v}^{(e)}(x, y, z, t) \right]^2 \right\} \mathrm{d}x \, \mathrm{d}y \, \mathrm{d}z$$

$$= \int_0^{L_z} \mathrm{d}z \int_{-1}^1 \int_{-1}^1 \frac{1}{2} \rho^{(e)}(\xi, \eta) \left\{ \left[\dot{u}^{(e)}(\xi, \eta, t) \right]^2 + \left[\dot{v}^{(e)}(\xi, \eta, t) \right]^2 \right\} \det \mathbf{J}^{(e)} \, \mathrm{d}\xi \, \mathrm{d}\eta$$

$$= L_z \int_{-1}^1 \int_{-1}^1 \frac{1}{2} \rho^{(e)} \left[\dot{\mathbf{q}}^{(e)\mathrm{T}} \mathbf{N}_u^{(e)\mathrm{T}} \mathbf{N}_u^{(e)} \dot{\mathbf{q}}^{(e)} + \dot{\mathbf{q}}^{(e)\mathrm{T}} \mathbf{N}_v^{(e)\mathrm{T}} \mathbf{N}_v^{(e)} \dot{\mathbf{q}}^{(e)} \right] \det \mathbf{J}^{(e)} \, \mathrm{d}\xi \, \mathrm{d}\eta$$

$$= \frac{1}{2} \dot{\mathbf{q}}^{(e)\mathrm{T}}(t) \left\{ L_z \int_{-1}^1 \int_{-1}^1 \rho^{(e)} \left[\mathbf{N}_u^{(e)\mathrm{T}} \mathbf{N}_u^{(e)} + \mathbf{N}_v^{(e)\mathrm{T}} \mathbf{N}_v^{(e)} \right] \det \mathbf{J}^{(e)} \, \mathrm{d}\xi \, \mathrm{d}\eta \right\} \dot{\mathbf{q}}^{(e)}(t)$$

$$= \frac{1}{2} \dot{\mathbf{q}}^{(e)\mathrm{T}}(t) \mathbf{M}^{(e)} \dot{\mathbf{q}}^{(e)}(t), \tag{26}$$

where we note, for instance, that $\dot{u}^{(e)} = \mathbf{N}_u^{(e)} \dot{\mathbf{q}}^{(e)} = \dot{\mathbf{q}}^{(e)\mathrm{T}} \mathbf{N}_u^{(e)\mathrm{T}}$, since $\dot{u}^{(e)}$ is a scalar quantity; and this implies that $\left(\dot{u}^{(e)} \right)^2$ can be evaluate through $\dot{\mathbf{q}}^{(e)\mathrm{T}} \mathbf{N}_u^{(e)\mathrm{T}} \mathbf{N}_u^{(e)} \dot{\mathbf{q}}^{(e)}$. Similar remarks hold for the other terms which contribute to the kinetic energy expression. One also should point out that L_z corresponds to the thickness of the finite element. From the last two lines of the previous equation,

$$\mathbf{M}^{(e)} = L_z \int_{-1}^1 \int_{-1}^1 \rho^{(e)} \left[\mathbf{N}_u^{(e)\mathrm{T}} \mathbf{N}_u^{(e)} + \mathbf{N}_v^{(e)\mathrm{T}} \mathbf{N}_v^{(e)} \right] \det \mathbf{J}^{(e)} \, \mathrm{d}\xi \, \mathrm{d}\eta, \tag{27}$$

which is recognized as the finite element mass matrix. It is symmetric, positive definite, and can be evaluated analytically, with the aid of symbolic algebra software; or using numerical integration

techniques, such as Gauss-Legendre quadrature (as is done in codes which are made available with this material). This latter option is interesting because the integration of polynomials can be performed exactly, while demanding a low computational cost. While not directly related to the formulation which is being considered here, numerical integration of finite element matrices or load vectors can also be resorted to: (i) for avoiding issues related to locking-phenomena (which depends on the finite element formulation), by performing reduced integration of relevant quantities; and/or (ii) for enabling nonlinear analyzes, in which system matrices and/or load vectors change with respect to the system configuration [Bathe, 2014, de Borst et al., 2012].

With regards to the potential energy contribution due to externally applied forces, we have:

$$
\begin{aligned}
\mathcal{W}_{\text{ext}}^{(e)} &= \iiint_{\Omega_t^{(e)}} \left[u^{(e)}(x,y,t) \quad v^{(e)}(x,y,t) \right] \begin{Bmatrix} f_b^x(x,y,t) \\ f_b^y(x,y,t) \end{Bmatrix} \mathrm{d}x\,\mathrm{d}y\,\mathrm{d}z \\
&\quad + \iint_{\partial\Omega_t^{(e)}} \left[u^{(e)}(x,y,t) \quad v^{(e)}(x,y,t) \right] \begin{Bmatrix} f_s^x(x,y,t) \\ f_s^y(x,y,t) \end{Bmatrix} \mathrm{d}S \\
&= L_z \int_{-1}^{1} \int_{-1}^{1} \left[u^{(e)}(\xi,\eta,t) \quad v^{(e)}(\xi,\eta,t) \right] \begin{Bmatrix} f_b^x(\xi,\eta,t) \\ f_b^y(\xi,\eta,t) \end{Bmatrix} \det \mathbf{J}^{(e)}\,\mathrm{d}\xi\,\mathrm{d}\eta \\
&\quad + L_z \int_{-1}^{1} \left[u^{(e)}(-1,\eta,t) \quad v^{(e)}(-1,\eta,t) \right] \begin{Bmatrix} f_s^x(-1,\eta,t) \\ f_s^y(-1,\eta,t) \end{Bmatrix} \sqrt{\left(\frac{\partial x}{\partial \eta}\right)^2 + \left(\frac{\partial y}{\partial \eta}\right)^2} \Bigg|_{\xi=-1} \mathrm{d}\eta \\
&\quad + L_z \int_{-1}^{1} \left[u^{(e)}(1,\eta,t) \quad v^{(e)}(1,\eta,t) \right] \begin{Bmatrix} f_s^x(1,\eta,t) \\ f_s^y(1,\eta,t) \end{Bmatrix} \sqrt{\left(\frac{\partial x}{\partial \eta}\right)^2 + \left(\frac{\partial y}{\partial \eta}\right)^2} \Bigg|_{\xi=1} \mathrm{d}\eta \\
&\quad + L_z \int_{-1}^{1} \left[u^{(e)}(\xi,-1,t) \quad v^{(e)}(\xi,-1,t) \right] \begin{Bmatrix} f_s^x(\xi,-1,t) \\ f_s^y(\xi,-1,t) \end{Bmatrix} \sqrt{\left(\frac{\partial x}{\partial \xi}\right)^2 + \left(\frac{\partial y}{\partial \xi}\right)^2} \Bigg|_{\eta=-1} \mathrm{d}\xi \\
&\quad + L_z \int_{-1}^{1} \left[u^{(e)}(\xi,1,t) \quad v^{(e)}(\xi,1,t) \right] \begin{Bmatrix} f_s^x(\xi,1,t) \\ f_s^y(\xi,1,t) \end{Bmatrix} \sqrt{\left(\frac{\partial x}{\partial \xi}\right)^2 + \left(\frac{\partial y}{\partial \xi}\right)^2} \Bigg|_{\eta=1} \mathrm{d}\xi \\
&= \mathbf{q}^{(e)\mathrm{T}} \left\{ L_z \int_{-1}^{1} \int_{-1}^{1} \left[\mathbf{N}_u^{(e)\mathrm{T}}(\xi,\eta) \quad \mathbf{N}_v^{(e)\mathrm{T}}(\xi,\eta) \right] \begin{Bmatrix} f_b^x(\xi,\eta,t) \\ f_b^y(\xi,\eta,t) \end{Bmatrix} \det \mathbf{J}^{(e)}\,\mathrm{d}\xi\,\mathrm{d}\eta \right\} \\
&\quad + \mathbf{q}^{(e)\mathrm{T}} \Bigg\{ L_z \int_{-1}^{1} \left[\mathbf{N}_u^{(e)\mathrm{T}}(-1,\eta) \quad \mathbf{N}_v^{(e)\mathrm{T}}(-1,\eta) \right] \begin{Bmatrix} f_s^x(-1,\eta,t) \\ f_s^y(-1,\eta,t) \end{Bmatrix} \sqrt{\left(\frac{\partial x}{\partial \eta}\right)^2 + \left(\frac{\partial y}{\partial \eta}\right)^2} \Bigg|_{\xi=-1} \mathrm{d}\eta \\
&\quad + L_z \int_{-1}^{1} \left[\mathbf{N}_u^{(e)\mathrm{T}}(1,\eta) \quad \mathbf{N}_v^{(e)\mathrm{T}}(1,\eta) \right] \begin{Bmatrix} f_s^x(1,\eta,t) \\ f_s^y(1,\eta,t) \end{Bmatrix} \sqrt{\left(\frac{\partial x}{\partial \eta}\right)^2 + \left(\frac{\partial y}{\partial \eta}\right)^2} \Bigg|_{\xi=1} \mathrm{d}\eta \\
&\quad + L_z \int_{-1}^{1} \left[\mathbf{N}_u^{(e)\mathrm{T}}(\xi,-1) \quad \mathbf{N}_v^{(e)\mathrm{T}}(\xi,-1) \right] \begin{Bmatrix} f_s^x(\xi,-1,t) \\ f_s^y(\xi,-1,t) \end{Bmatrix} \sqrt{\left(\frac{\partial x}{\partial \xi}\right)^2 + \left(\frac{\partial y}{\partial \xi}\right)^2} \Bigg|_{\eta=-1} \mathrm{d}\xi \\
&\quad + L_z \int_{-1}^{1} \left[\mathbf{N}_u^{(e)\mathrm{T}}(\xi,1) \quad \mathbf{N}_v^{(e)\mathrm{T}}(\xi,1) \right] \begin{Bmatrix} f_s^x(\xi,1,t) \\ f_s^y(\xi,1,t) \end{Bmatrix} \sqrt{\left(\frac{\partial x}{\partial \xi}\right)^2 + \left(\frac{\partial y}{\partial \xi}\right)^2} \Bigg|_{\eta=1} \mathrm{d}\xi \Bigg\} \\
&= \mathbf{q}^{(e)\mathrm{T}}(t)\mathbf{Q}_b^{(e)}(t) + \mathbf{q}^{(e)\mathrm{T}}(t)\mathbf{Q}_s^{(e)}(t),
\end{aligned}
\tag{28}
$$

where we considered $\mathrm{d}S = \mathrm{d}z\,\mathrm{d}l$, with $\mathrm{d}l$ corresponding to a differential length on the boundary of the finite element. The sides of the element (which in our case are straight lines) can be

described by the parametrizations $(x(\eta), y(\eta))$ for $\xi = \pm 1$ or $(x(\xi), y(\xi))$ for $\eta = \pm 1$, such that $dl = \sqrt{\left(\frac{\partial x}{\partial \eta}\right)^2 + \left(\frac{\partial y}{\partial \eta}\right)^2} d\eta$ or $dl = \sqrt{\left(\frac{\partial x}{\partial \xi}\right)^2 + \left(\frac{\partial y}{\partial \xi}\right)^2} d\xi$, respectively. The square-root terms in the previous expressions for dl are necessary to take into account the parametrization adopted for the boundary curves. It is also worth noticing that, for evaluating the load vector $\mathbf{Q}_s^{(e)}(t)$, the finite element boundary is split — contributions due to the each side of the finite element are treated separately, for convenience.

In order to evaluate both $\mathbf{Q}_b^{(e)}(t)$ and $\mathbf{Q}_s^{(e)}(t)$, it is useful to consider that:

$$\mathbf{f}_b^{(e)} = \left\{ \begin{matrix} f_b^x(\xi,\eta,t) \\ f_b^y(\xi,\eta,t) \end{matrix} \right\} = \left\{ \begin{matrix} \bar{f}_b^x(\xi,\eta)g_b^x(t) \\ \bar{f}_b^y(\xi,\eta)g_b^y(t) \end{matrix} \right\} = \begin{bmatrix} \bar{f}_b^x(\xi,\eta) & 0 \\ 0 & \bar{f}_b^y(\xi,\eta) \end{bmatrix} \left\{ \begin{matrix} g_b^x(t) \\ g_b^y(t) \end{matrix} \right\} = \bar{\mathbf{f}}_b^{(e)}(\xi,\eta)\mathbf{g}_b^{(e)}(t);$$
(29a)

$$\mathbf{f}_s^{(e)} = \left\{ \begin{matrix} f_s^x(\xi,\eta,t) \\ f_s^y(\xi,\eta,t) \end{matrix} \right\} = \left\{ \begin{matrix} \bar{f}_s^x(\xi,\eta)g_s^x(t) \\ \bar{f}_s^y(\xi,\eta)g_s^y(t) \end{matrix} \right\} = \begin{bmatrix} \bar{f}_s^x(\xi,\eta) & 0 \\ 0 & \bar{f}_s^y(\xi,\eta) \end{bmatrix} \left\{ \begin{matrix} g_s^x(t) \\ g_s^y(t) \end{matrix} \right\} = \bar{\mathbf{f}}_s^{(e)}(\xi,\eta)\mathbf{g}_s^{(e)}(t).$$
(29b)

Furthermore, we assume that the surface loads can vary linearly between the finite element's nodes:

$$\left\{ \begin{matrix} \bar{f}_s^x(\xi,-1) \\ \bar{f}_s^y(\xi,-1) \end{matrix} \right\} = \left\{ \begin{matrix} p_{12,1}^x \\ p_{12,1}^y \end{matrix} \right\} \frac{1}{2}(1-\xi) + \left\{ \begin{matrix} p_{12,2}^x \\ p_{12,2}^y \end{matrix} \right\} \frac{1}{2}(1+\xi);$$
(30a)

$$\left\{ \begin{matrix} \bar{f}_s^x(1,\eta) \\ \bar{f}_s^y(1,\eta) \end{matrix} \right\} = \left\{ \begin{matrix} p_{23,2}^x \\ p_{23,2}^y \end{matrix} \right\} \frac{1}{2}(1-\eta) + \left\{ \begin{matrix} p_{23,3}^x \\ p_{23,3}^y \end{matrix} \right\} \frac{1}{2}(1+\eta);$$
(30b)

$$\left\{ \begin{matrix} \bar{f}_s^x(\xi,1) \\ \bar{f}_s^y(\xi,1) \end{matrix} \right\} = \left\{ \begin{matrix} p_{34,3}^x \\ p_{34,3}^y \end{matrix} \right\} \frac{1}{2}(1+\xi) + \left\{ \begin{matrix} p_{34,4}^x \\ p_{34,4}^y \end{matrix} \right\} \frac{1}{2}(1-\xi);$$
(30c)

$$\left\{ \begin{matrix} \bar{f}_s^x(-1,\eta) \\ \bar{f}_s^y(-1,\eta) \end{matrix} \right\} = \left\{ \begin{matrix} p_{41,4}^x \\ p_{41,4}^y \end{matrix} \right\} \frac{1}{2}(1+\eta) + \left\{ \begin{matrix} p_{41,1}^x \\ p_{41,1}^y \end{matrix} \right\} \frac{1}{2}(1-\eta),$$
(30d)

in which $p_{ij,i}^x$, $p_{ij,i}^y$ represent loads per unit area applied on node i along the finite element side between nodes i and j.

Based on the previous developments, we can see that:

$$\mathbf{Q}_b^{(e)}(t) = L_z \left\{ \int_{-1}^{1} \int_{-1}^{1} \left[\mathbf{N}_u^{(e)\mathrm{T}}(\xi,\eta) \quad \mathbf{N}_v^{(e)\mathrm{T}}(\xi,\eta) \right] \bar{\mathbf{f}}_b^{(e)}(\xi,\eta) \det \mathbf{J}^{(e)} \, d\xi \, d\eta \right\} \mathbf{g}_b^{(e)}(t);$$
(31)

$$\mathbf{Q}_s^{(e)}(t) = L_z \left\{ \sum_{\bar{\xi} \in \{-1,1\}} \int_{-1}^{1} \left[\mathbf{N}_u^{(e)\mathrm{T}}(\bar{\xi},\eta) \quad \mathbf{N}_v^{(e)\mathrm{T}}(\bar{\xi},\eta) \right] \bar{\mathbf{f}}_s^{(e)}(\bar{\xi},\eta) \sqrt{\left(\frac{\partial x}{\partial \eta}\right)^2 + \left(\frac{\partial y}{\partial \eta}\right)^2} \Bigg|_{\xi=\bar{\xi}} d\eta \right.$$

$$\left. + \sum_{\bar{\eta} \in \{-1,1\}} \int_{-1}^{1} \left[\mathbf{N}_u^{(e)\mathrm{T}}(\xi,\bar{\eta}) \quad \mathbf{N}_v^{(e)\mathrm{T}}(\xi,\bar{\eta}) \right] \bar{\mathbf{f}}_s^{(e)}(\xi,\bar{\eta}) \sqrt{\left(\frac{\partial x}{\partial \xi}\right)^2 + \left(\frac{\partial y}{\partial \xi}\right)^2} \Bigg|_{\eta=\bar{\eta}} d\xi \right\} \mathbf{g}_s^{(e)}(t).$$
(32)

Having established Eq. (28), we consider Eq. (5) in order to obtain:

$$
\begin{aligned}
\mathcal{U}^{(e)} &= \frac{1}{2} \iiint_{\Omega_t^{(e)}} \left[\sigma_x^{(e)} \epsilon_x^{(e)} + \sigma_y^{(e)} \epsilon_y^{(e)} + \tau_{xy}^{(e)} \gamma_{xy}^{(e)} \right] \mathrm{d}x\,\mathrm{d}y\,\mathrm{d}z - \mathcal{W}_{\mathrm{ext}} \\
&= \frac{1}{2} L_z \int_{-1}^{1} \int_{-1}^{1} \boldsymbol{\sigma}^{(e)\mathrm{T}}(\xi, \eta, t) \boldsymbol{\epsilon}^{(e)}(\xi, \eta, t) \det \mathbf{J}^{(e)}\,\mathrm{d}\xi\,\mathrm{d}\eta - \mathbf{q}^{(e)\mathrm{T}} \left[\mathbf{Q}_b^{(e)}(t) + \mathbf{Q}_s^{(e)}(t) \right] \\
&= \frac{1}{2} \mathbf{q}^{(e)\mathrm{T}} \left\{ L_z \int_{-1}^{1} \int_{-1}^{1} \mathbf{B}^{(e)\mathrm{T}} \mathbf{D}^{(e)} \mathbf{B}^{(e)} \det \mathbf{J}^{(e)}\,\mathrm{d}\xi\,\mathrm{d}\eta \right\} \mathbf{q}^{(e)}(t) - \mathbf{q}^{(e)\mathrm{T}} \left[\mathbf{Q}_b^{(e)}(t) + \mathbf{Q}_s^{(e)}(t) \right] \\
&= \frac{1}{2} \mathbf{q}^{(e)\mathrm{T}}(t) \mathbf{K}^{(e)} \mathbf{q}^{(e)}(t) - \mathbf{q}^{(e)\mathrm{T}}(t) \left[\mathbf{Q}_b^{(e)}(t) + \mathbf{Q}_s^{(e)}(t) \right],
\end{aligned} \tag{33}
$$

where Eqs. (24a), (25a) were used, together with the fact that $\mathbf{D}^{(e)}$ is a symmetric matrix. We see that:

$$
\mathbf{K}^{(e)} = L_z \int_{-1}^{1} \int_{-1}^{1} \mathbf{B}^{(e)\mathrm{T}} \mathbf{D}^{(e)} \mathbf{B}^{(e)} \det \mathbf{J}^{(e)}\,\mathrm{d}\xi\,\mathrm{d}\eta, \tag{34}
$$

which is known as the finite element stiffness matrix – which is symmetric, and positive semi-definite.

By considering the earlier developments, the Lagrangian becomes:

$$
\mathcal{L}^{(e)} = \frac{1}{2} \dot{\mathbf{q}}^{(e)\mathrm{T}}(t) \mathbf{M}^{(e)} \dot{\mathbf{q}}^{(e)}(t) - \left\{ \frac{1}{2} \mathbf{q}^{(e)\mathrm{T}}(t) \mathbf{K}^{(e)} \mathbf{q}^{(e)}(t) - \mathbf{q}^{(e)\mathrm{T}}(t) \left[\mathbf{Q}_b^{(e)}(t) + \mathbf{Q}_s^{(e)}(t) \right] \right\}. \tag{35}
$$

Now, according to the Variational Principles of Mechanics, to make the relevant action functional stationary, the Lagrangian must be such that it complies with the Euler-Lagrange equations [Lanczos, 1986]:

$$
\frac{\mathrm{d}}{\mathrm{d}t} \left(\frac{\partial \mathcal{L}^{(e)}}{\partial \dot{\mathbf{q}}^{(e)}} \right) - \frac{\partial \mathcal{L}^{(e)}}{\partial \mathbf{q}^{(e)}} = \mathbf{Q}_{\mathrm{nc}}^{(e)}, \tag{36}
$$

where $\mathbf{Q}_{\mathrm{nc}}^{(e)}$ collects the non-conservative generalized loads. (These can be obtained by calculating the virtual work of the non-conservative actions.) The derivatives of the scalar function $\mathcal{L}^{(e)}$ with respect to the vectors $\mathbf{q}^{(e)}$ and $\dot{\mathbf{q}}^{(e)}$ produce vectors, whose components are given by the derivative of $\mathcal{L}^{(e)}$ with respect to the components of $\mathbf{q}^{(e)}$ and $\dot{\mathbf{q}}^{(e)}$, respectively. By substituting the Lagrangian expression given in Eq. (35), we are finally able to obtain the equations of motion for the finite element:

$$
\mathbf{M}^{(e)} \ddot{\mathbf{q}}^{(e)}(t) + \mathbf{K}^{(e)} \mathbf{q}^{(e)}(t) = \mathbf{Q}_{\mathrm{nc}}^{(e)}(t) + \mathbf{Q}_b^{(e)}(t) + \mathbf{Q}_s^{(e)}(t), \tag{37}
$$

which correspond to the input-output relationship one has sought during this subsection. This set of coupled, second-order, linear ordinary differential equations relate the nodal DOFs to loads that are ultimately applied at the element nodes. For instance, conservative distributed loads have been replaced by equivalent nodal contributions when one has put forward Eqs. (31) and (32).

2.1.3   Formulation at global level

The previous developments have addressed the mathematical formulation related to a single finite element of the considered type. In a practical application, various elements are combined in a mesh, to better represent the geometry of the continuum body or structure; and also to enable a good approximation of the exact response for the underlying model equations (being them differential or algebraic, cf. our discussion along section 1). In this sense, we have to remind ourselves that interpolation functions have been proposed to represent the field variables inside the element domain. Typically, the adopted interpolation schemes are not adequate to represent the response

of the structure or continuum body over its entire domain, i.e. the interpolation functions which are used are able to approximate responses only locally.

To assemble a finite element mesh, two basic conditions need to be fulfilled at every node of the mesh: (i) compatibility of field variables; and (ii) in the case of structural analyses, dynamic equilibrium of loads. It is important to realize that these conditions are fulfilled only at the nodes of the mesh. Hence, there is not guarantee that dynamic equilibrium is assured across boundaries of finite elements (unless at shared nodes).

For the purpose of abiding by these requirements, we initially attribute the required DOFs to each node of the complete finite element mesh, to make a global list of DOFs, which are collected in a vector $\mathbf{q}^{(g)}$. From this list, for a particular finite element e of the mesh, we can identify the relevant DOFs, which are those related to its nodes. Mathematically, this can be accomplished by constructing a Boolean "localization" matrix $\mathbf{L}^{(e)}$, such that:

$$\mathbf{q}^{(e)} = \mathbf{L}^{(e)}\mathbf{q}^{(g)}. \tag{38}$$

If our finite element mesh has $n^{(g)}$ DOFs, and each element of the mesh has four nodes with two DOFs per node, then $\mathbf{L}^{(e)}$ has size $8 \times n^{(g)}$.

For each finite element of the mesh, we can write Eq. (35). To obtain the Lagrangian of the complete structure, we can simply sum the contributions of all finite elements of the mesh:

$$
\begin{aligned}
\mathcal{L}^{(g)} = \sum_{e=1}^{n_{\text{ele}}} \mathcal{L}^{(e)} = {} & \sum_{e=1}^{n_{\text{ele}}} \frac{1}{2}\dot{\mathbf{q}}^{(e)\,\mathrm{T}}(t)\mathbf{M}^{(e)}\dot{\mathbf{q}}^{(e)}(t) - \sum_{e=1}^{n_{\text{ele}}} \frac{1}{2}\mathbf{q}^{(e)\,\mathrm{T}}(t)\mathbf{K}^{(e)}\mathbf{q}^{(e)}(t) \\
& + \sum_{e=1}^{n_{\text{ele}}} \mathbf{q}^{(e)\,\mathrm{T}}(t)\left[\mathbf{Q}_b^{(e)}(t) + \mathbf{Q}_s^{(e)}(t)\right] \\
= {} & \sum_{e=1}^{n_{\text{ele}}} \frac{1}{2}\dot{\mathbf{q}}^{(g)\,\mathrm{T}}(t)\mathbf{L}^{(e)\,\mathrm{T}}\mathbf{M}^{(e)}\mathbf{L}^{(e)}\dot{\mathbf{q}}^{(g)}(t) - \sum_{e=1}^{n_{\text{ele}}} \frac{1}{2}\mathbf{q}^{(g)\,\mathrm{T}}(t)\mathbf{L}^{(e)\,\mathrm{T}}\mathbf{K}^{(e)}\mathbf{L}^{(e)}\mathbf{q}^{(g)}(t) \\
& + \sum_{e=1}^{n_{\text{ele}}} \mathbf{q}^{(g)\,\mathrm{T}}(t)\left[\mathbf{L}^{(e)\,\mathrm{T}}\mathbf{Q}_b^{(e)}(t) + \mathbf{L}^{(e)\,\mathrm{T}}\mathbf{Q}_s^{(e)}(t)\right] \\
= {} & \frac{1}{2}\dot{\mathbf{q}}^{(g)\,\mathrm{T}}(t)\left[\sum_{e=1}^{n_{\text{ele}}} \mathbf{L}^{(e)\,\mathrm{T}}\mathbf{M}^{(e)}\mathbf{L}^{(e)}\right]\dot{\mathbf{q}}^{(g)}(t) - \frac{1}{2}\mathbf{q}^{(g)\,\mathrm{T}}(t)\left[\sum_{e=1}^{n_{\text{ele}}} \mathbf{L}^{(e)\,\mathrm{T}}\mathbf{K}^{(e)}\mathbf{L}^{(e)}\right]\mathbf{q}^{(g)}(t) \\
& + \mathbf{q}^{(g)\,\mathrm{T}}(t)\sum_{e=1}^{n_{\text{ele}}}\left[\mathbf{L}^{(e)\,\mathrm{T}}\mathbf{Q}_b^{(e)}(t) + \mathbf{L}^{(e)\,\mathrm{T}}\mathbf{Q}_s^{(e)}(t)\right] \\
= {} & \frac{1}{2}\dot{\mathbf{q}}^{(g)\,\mathrm{T}}(t)\mathbf{M}^{(g)}\dot{\mathbf{q}}^{(g)}(t) - \frac{1}{2}\mathbf{q}^{(g)\,\mathrm{T}}(t)\mathbf{K}^{(g)}\mathbf{q}^{(g)}(t) + \mathbf{q}^{(g)\,\mathrm{T}}(t)\left[\mathbf{Q}_b^{(g)}(t) + \mathbf{Q}_s^{(g)}(t)\right], \tag{39}
\end{aligned}
$$

in which:

$$\mathbf{M}^{(g)} = \sum_{e=1}^{n_{\text{ele}}} \mathbf{L}^{(e)\,\mathrm{T}}\mathbf{M}^{(e)}\mathbf{L}^{(e)} \qquad \text{and} \qquad \mathbf{K}^{(g)} = \sum_{e=1}^{n_{\text{ele}}} \mathbf{L}^{(e)\,\mathrm{T}}\mathbf{K}^{(e)}\mathbf{L}^{(e)} \tag{40}$$

are the global mass and stiffness matrices, respectively. For the considered case, these are symmetric. Also, due to how the global matrices are assembled, they are frequently sparse and banded, specially when the complete finite element model possess a large number of nodes/DOFs. These facts can be exploited by solution algorithms to speed up computations and/or alleviate computer memory availability requirements. Regarding conservative body and surface loads, we see from the previous developments that their global form can be obtained from:

$$\mathbf{Q}_b^{(g)}(t) = \sum_{e=1}^{n_{\text{ele}}} \mathbf{L}^{(e)\,\mathrm{T}}\mathbf{Q}_b^{(e)}(t) \qquad \text{and} \qquad \mathbf{Q}_s^{(g)}(t) = \sum_{e=1}^{n_{\text{ele}}} \mathbf{L}^{(e)\,\mathrm{T}}\mathbf{Q}_s^{(e)}(t). \tag{41}$$

Having established Eq. (39), the Euler-Lagrange equations, applied to the global Lagrangian, then lead to the global equations of motion:

$$\mathbf{M}^{(g)}\ddot{\mathbf{q}}^{(g)}(t) + \mathbf{K}^{(g)}\mathbf{q}^{(g)}(t) = \mathbf{Q}_{\text{nc}}^{(g)}(t) + \mathbf{Q}_b^{(g)}(t) + \mathbf{Q}_s^{(g)}(t). \tag{42}$$

Since we are considering linear structural behavior, we have obtained a set of linear, second-order, ordinary differential equations to model the motion of a continuum solid body under plane-stress or plane-strain conditions. In essence, the finite element method was used to spatially discretize the partial differential equations (of infinite dimension in space and time) which apply under the same underlying assumptions. The resulting system of ordinary differential equations can be analyzed in various forms, as discussed in section 3 with examples.

2.2 Rectangular Kirchhoff-Love plate, equivalent single layer laminate finite element

2.2.1 Kinematics

To provide another example of the formulation of a finite element, we now address the case of a plate which is subjected to bending motion, whose kinematic behavior can be described by the Kirchhoff-Love plate theory. In this setting, some assumptions should hold: (i) straight lines normal to the mid-surface remain straight and normal to the mid-surface after deformation; and (ii) the thickness of the plate does not change during its motion. This theory is more adequate for plates of small thickness. Referring to Fig. 6, due to the previous hypotheses, and also taking into account that displacements are small (infinitesimal), we can see that the rotation and the displacement fields can be expressed according to:

$$w(x, y, z, t) = w_0(x, y, t); \qquad \theta_x(x, y, t) = \frac{\partial w_0(x, y, t)}{\partial y}; \qquad \theta_y(x, y, t) = -\frac{\partial w_0(x, y, t)}{\partial x};$$

$$u(x, y, z, t) = u_0(x, y, t) + z\theta_y(x, y, t); \qquad v(x, y, z, t) = v_0(x, y, t) - z\theta_x(x, y, t), \quad (43)$$

where the transversal displacement w is assumed to be independent of z.

The strains can then be evaluated with the help of Eq. (8) as:

$$\epsilon_x = \frac{\partial u_0(x, y, t)}{\partial x} - z\frac{\partial^2 w_0(x, y, t)}{\partial x^2}, \qquad \epsilon_y = \frac{\partial v_0(x, y, t)}{\partial y} - z\frac{\partial^2 w_0(x, y, t)}{\partial y^2},$$

$$\gamma_{xy} = \frac{\partial u_0(x, y, t)}{\partial y} + \frac{\partial v_0(x, y, t)}{\partial x} - 2z\frac{\partial^2 w_0(x, y, t)}{\partial x \partial y}, \qquad \epsilon_z = \gamma_{xz} = \gamma_{xz} \equiv 0. \quad (44)$$
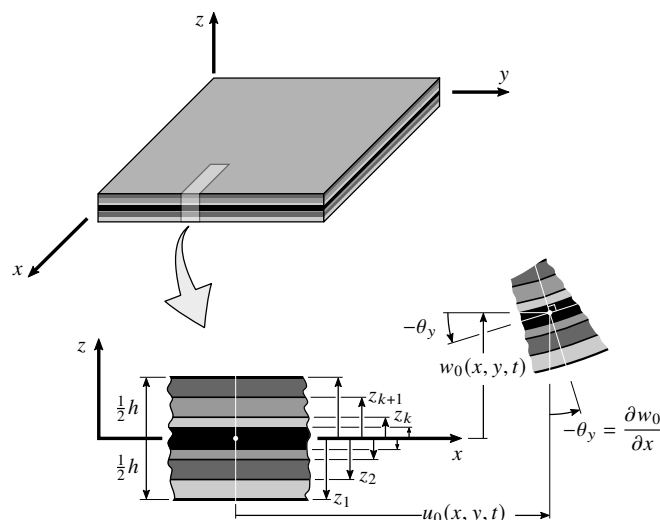
Figure 6: Plate (laminate) kinematic behavior along x-z plane according to Kirchhoff-Love theory.

2.2.2   Element geometry and interpolation of field variables

The finite element we consider here to model plate bending is but one of several which are available for this problem. If more detailed literature is consulted, the reader should see that conforming and non-conforming plate elements exist [Bathe, 2014, Reddy, 2019]. The one presented by us here is of the latter type, which means it does not guarantee continuity of the normal slope across the boundaries of finite elements which are neighbors. This issue results due to the formulation of the finite element itself (i.e. it is related to the interpolation functions which are adopted and the number of nodes of the element). Being it a non-conforming finite element, convergence of results can become problematic, especially if coarse meshes are employed.

Fig. 7 shows the geometry of the plate element. It is rectangular (not an arbitrary quadrilateral), with only four nodes. The nodal DOFs directly related to bending are $w_{0,i}^{(e)}(t) = w_0^{(e)}(x_i, y_i, t)$, $\theta_{x,i}^{(e)}(t) = \theta_x^{(e)}(x_i, y_i, t)$ and $\theta_{y,i}^{(e)}(t) = \theta_y^{(e)}(x_i, y_i, t)$, for $i \in \{1, 2, 3, 4\}$. The other DOFs, related to in-plane motions, are $u_{0,i}^{(e)}(t) = u_0^{(e)}(x_i, y_i, t)$ and $v_{0,i}^{(e)}(t) = v_0^{(e)}(x_i, y_i, t)$. Interpolation of the latter two can be performed according to Eqs. (13)–(15). For the remaining fields, we adopt [Junior et al., 2009]:

$$w_0^{(e)} = \begin{bmatrix} 1 & x & y & x^2 & xy & y^2 & x^3 & x^2y & xy^2 & y^3 & x^3y & xy^3 \end{bmatrix} \times$$
$$\times \left\{ a_{00} \quad a_{10} \quad a_{01} \quad a_{20} \quad a_{11} \quad a_{02} \quad a_{30} \quad a_{21} \quad a_{12} \quad a_{03} \quad a_{31} \quad a_{13} \right\}^{\mathrm{T}} = \mathbf{P}(x, y)\, \mathbf{a}(t);$$
$$(45a)$$

$$\theta_x^{(e)} = \frac{\partial w_0^{(e)}(x, y, t)}{\partial x} = \begin{bmatrix} 0 & 1 & 0 & 2x & y & 0 & 3x^2 & 2xy & y^2 & 0 & 3x^2y & y^3 \end{bmatrix} \times$$
$$\times \left\{ a_{00} \quad a_{10} \quad a_{01} \quad a_{20} \quad a_{11} \quad a_{02} \quad a_{30} \quad a_{21} \quad a_{12} \quad a_{03} \quad a_{31} \quad a_{13} \right\}^{\mathrm{T}} = \frac{\partial \mathbf{P}}{\partial y}(x, y)\, \mathbf{a}(t);$$
$$(45b)$$

$$\theta_y^{(e)} = \frac{\partial w_0^{(e)}(x, y, t)}{\partial y} = \begin{bmatrix} 0 & 0 & 1 & 0 & x & 2y & 0 & x^2 & 2xy & 3y^2 & x^3 & 3xy^2 \end{bmatrix} \times$$
$$\times \left\{ a_{00} \quad a_{10} \quad a_{01} \quad a_{20} \quad a_{11} \quad a_{02} \quad a_{30} \quad a_{21} \quad a_{12} \quad a_{03} \quad a_{31} \quad a_{13} \right\}^{\mathrm{T}} = -\frac{\partial \mathbf{P}}{\partial x}(x, y)\, \mathbf{a}(t),$$
$$(45c)$$

where $\mathbf{P}$ is a row-matrix containing polynomials, and the column vector $\mathbf{a}$ comprises time-dependent
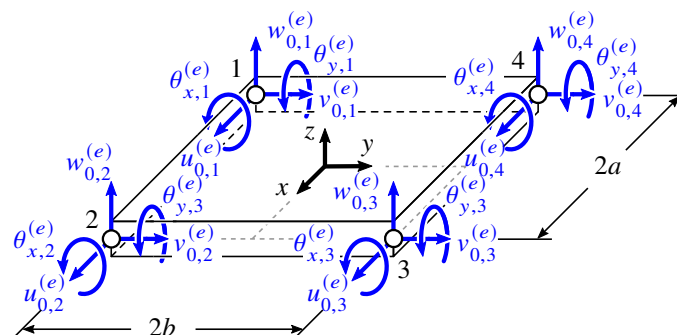
Figure 7: Non-conforming, rectangular plate (laminate) finite element with four nodes.

weights. The latter can be expressed in terms of the element nodal DOFs by enforcing:

$$
\bar{\mathbf{q}}^{(e)}(t) =
\begin{Bmatrix}
w_{0,1}^{(e)}(t) \\
\theta_{x,1}^{(e)}(t) \\
\theta_{y,1}^{(e)}(t) \\
w_{0,2}^{(e)}(t) \\
\theta_{x,2}^{(e)}(t) \\
\theta_{y,2}^{(e)}(t) \\
w_{0,3}^{(e)}(t) \\
\theta_{x,3}^{(e)}(t) \\
\theta_{y,3}^{(e)}(t) \\
w_{0,4}^{(e)}(t) \\
\theta_{x,4}^{(e)}(t) \\
\theta_{y,4}^{(e)}(t)
\end{Bmatrix}
=
\begin{bmatrix}
\mathbf{P}(x_1, y_1) \\
\frac{\partial \mathbf{P}}{\partial y}(x_1, y_1) \\
-\frac{\partial \mathbf{P}}{\partial x}(x_1, y_1) \\
\mathbf{P}(x_2, y_2) \\
\frac{\partial \mathbf{P}}{\partial y}(x_2, y_2) \\
-\frac{\partial \mathbf{P}}{\partial x}(x_2, y_2) \\
\mathbf{P}(x_3, y_3) \\
\frac{\partial \mathbf{P}}{\partial y}(x_3, y_3) \\
-\frac{\partial \mathbf{P}}{\partial x}(x_3, y_3) \\
\mathbf{P}(x_4, y_4) \\
\frac{\partial \mathbf{P}}{\partial y}(x_4, y_4) \\
-\frac{\partial \mathbf{P}}{\partial x}(x_4, y_4)
\end{bmatrix}
\mathbf{a}(t) = \mathbf{A}\mathbf{a}(t) \qquad \Rightarrow \qquad \mathbf{a}(t) = \mathbf{A}^{-1}\bar{\mathbf{q}}^{(e)}(t). \qquad (46)
$$

Combining this last result with Eqs. (45), we are able to obtain the FE interpolation function matrices for the relevant displacement fields:

$$
w_0^{(e)}(x, y, t) = \bar{\mathbf{N}}_w^{(e)}(x, y)\bar{\mathbf{q}}^{(e)}(t) = \left(\mathbf{P}(x, y)\mathbf{A}^{-1}\right)\bar{\mathbf{q}}^{(e)}(t); \qquad (47a)
$$

$$
\theta_x^{(e)}(x, y, t) = \bar{\mathbf{N}}_{\theta_x}^{(e)}(x, y)\bar{\mathbf{q}}^{(e)}(t) = \left(\frac{\partial \mathbf{P}}{\partial y}(x, y)\mathbf{A}^{-1}\right)\bar{\mathbf{q}}^{(e)}(t); \qquad (47b)
$$

$$
\theta_y^{(e)}(x, y, t) = \bar{\mathbf{N}}_{\theta_y}^{(e)}(x, y)\bar{\mathbf{q}}^{(e)}(t) = \left(-\frac{\partial \mathbf{P}}{\partial x}(x, y)\mathbf{A}^{-1}\right)\bar{\mathbf{q}}^{(e)}(t). \qquad (47c)
$$

The previous interpolations can be combined with those presented earlier in Eq. (13), permitting us to write:

$$
\begin{Bmatrix}
u_0^{(e)}(x, y, t) \\
v_0^{(e)}(x, y, t) \\
w_0^{(e)}(x, y, t) \\
\theta_x^{(e)}(x, y, t) \\
\theta_y^{(e)}(x, y, t)
\end{Bmatrix}
=
\begin{bmatrix}
N_1\mathbf{I}_2 & \mathbf{0}_{2\times3} & N_2\mathbf{I}_2 & \mathbf{0}_{2\times3} & N_3\mathbf{I}_2 & \mathbf{0}_{2\times3} & N_4\mathbf{I}_2 & \mathbf{0}_{2\times3} \\
\mathbf{0}_{1\times2} & \bar{\mathbf{N}}_{w,1}^{(e)} & \mathbf{0}_{1\times2} & \bar{\mathbf{N}}_{w,2}^{(e)} & \mathbf{0}_{1\times2} & \bar{\mathbf{N}}_{w,3}^{(e)} & \mathbf{0}_{1\times2} & \bar{\mathbf{N}}_{w,4}^{(e)} \\
\mathbf{0}_{1\times2} & \bar{\mathbf{N}}_{\theta_x,1}^{(e)} & \mathbf{0}_{1\times2} & \bar{\mathbf{N}}_{\theta_x,2}^{(e)} & \mathbf{0}_{1\times2} & \bar{\mathbf{N}}_{\theta_x,3}^{(e)} & \mathbf{0}_{1\times2} & \bar{\mathbf{N}}_{\theta_x,4}^{(e)} \\
\mathbf{0}_{3\times2} & \bar{\mathbf{N}}_{\theta_x,1}^{(e)} & \mathbf{0}_{1\times2} & \bar{\mathbf{N}}_{\theta_x,2}^{(e)} & \mathbf{0}_{1\times2} & \bar{\mathbf{N}}_{\theta_x,3}^{(e)} & \mathbf{0}_{1\times2} & \bar{\mathbf{N}}_{\theta_x,4}^{(e)}
\end{bmatrix}
\begin{Bmatrix}
\mathbf{q}_1^{(e)}(t) \\
\mathbf{q}_2^{(e)}(t) \\
\mathbf{q}_3^{(e)}(t) \\
\mathbf{q}_4^{(e)}(t)
\end{Bmatrix}, \qquad (48)
$$

where $\mathbf{q}_i^{(e)}(t) = \left\{u_{0,i}^{(e)}(t) \quad v_{0,i}^{(e)}(t) \quad w_{0,i}^{(e)}(t) \quad \theta_{x,i}^{(e)}(t) \quad \theta_{y,i}^{(e)}(t)\right\}^{\mathrm{T}}$ collects the DOFs related to node i, for $i \in \{1, 2, 3, 4\}$; $N_i = N_i(x, y)$ correspond to the interpolation functions introduced in Eq. (13); and $\mathbf{N}_{w,i}^{(e)}$, $\mathbf{N}_{\theta_x,i}^{(e)}$, $\mathbf{N}_{\theta_y,i}^{(e)}$ stand for 1×3 sub-matrices of $\mathbf{N}_w^{(e)}$, $\mathbf{N}_{\theta_x}^{(e)}$, $\mathbf{N}_{\theta_y}^{(e)}$, respectively, related to degrees of freedom of node i. For example, $\mathbf{N}_w^{(e)} = \begin{bmatrix} \mathbf{N}_{w,1}^{(e)} & \mathbf{N}_{w,2}^{(e)} & \mathbf{N}_{w,3}^{(e)} & \mathbf{N}_{w,4}^{(e)} \end{bmatrix}$. Equation (48) can be rewritten as:

$$
\begin{Bmatrix}
u_0^{(e)}(x, y, t) \\
v_0^{(e)}(x, y, t) \\
w_0^{(e)}(x, y, t) \\
\theta_x^{(e)}(x, y, t) \\
\theta_y^{(e)}(x, y, t)
\end{Bmatrix}
=
\begin{bmatrix}
\mathbf{N}_u^{(e)}(x, y) \\
\mathbf{N}_v^{(e)}(x, y) \\
\mathbf{N}_w^{(e)}(x, y) \\
\mathbf{N}_{\theta_x}^{(e)}(x, y) \\
\mathbf{N}_{\theta_y}^{(e)}(x, y)
\end{bmatrix}
\mathbf{q}^{(e)}(t), \qquad \text{with} \qquad \mathbf{q}^{(e)}(t) =
\begin{Bmatrix}
\mathbf{q}_1^{(e)}(t) \\
\mathbf{q}_2^{(e)}(t) \\
\mathbf{q}_3^{(e)}(t) \\
\mathbf{q}_4^{(e)}(t)
\end{Bmatrix}
\qquad (49)
$$

and $\mathbf{N}_u^{(e)}$, $\mathbf{N}_v^{(e)}$, $\mathbf{N}_w^{(e)}$, $\mathbf{N}_{\theta_x}^{(e)}$, $\mathbf{N}_{\theta_y}^{(e)}$ corresponding to the rows of the interpolation matrix seen in Eq. (48).

2.2.3   Formulation at element level

The strains which are not identically equal to zero can be interpolated inside the domain of the FE now considered according to the relations:

$$\epsilon_x^{(e)}(x,y,z,t) = \left[\mathbf{B}_{x,0}^{(e)}(x,y) + z\mathbf{B}_{x,1}^{(e)}(x,y) \right] \mathbf{q}^{(e)}(t) = \left[\frac{\partial \mathbf{N}_u^{(e)}}{\partial x} - z\frac{\partial^2 \mathbf{N}_w^{(e)}}{\partial x^2} \right] \mathbf{q}^{(e)}(t); \qquad (50a)$$

$$\epsilon_y^{(e)}(x,y,z,t) = \left[\mathbf{B}_{y,0}^{(e)}(x,y) + z\mathbf{B}_{y,1}^{(e)}(x,y) \right] \mathbf{q}^{(e)}(t) = \left[\frac{\partial \mathbf{N}_v^{(e)}}{\partial y} - z\frac{\partial^2 \mathbf{N}_w^{(e)}}{\partial y^2} \right] \mathbf{q}^{(e)}(t); \qquad (50b)$$

$$\gamma_{xy}^{(e)}(x,y,z,t) = \left[\mathbf{B}_{xy,0}^{(e)}(x,y) + z\mathbf{B}_{xy,1}^{(e)}(x,y) \right] \mathbf{q}^{(e)}(t) = \left[\frac{\partial \mathbf{N}_u^{(e)}}{\partial y} + \frac{\partial \mathbf{N}_v^{(e)}}{\partial x} - 2z\frac{\partial^2 \mathbf{N}_w^{(e)}}{\partial x \partial y} \right] \mathbf{q}^{(e)}(t), \quad (50c)$$

which can be derived by combining Eqs. (49) and (44).

To showcase a situation in which the material of the plate does not exhibit linear isotropic behavior, here we consider the plate corresponds to a laminate, i.e. a collection of plies made of fibers, which are laid-up on top of one another, bonded with the aid of some resin, to produce a composite material. At this point, an important warning must be made by us, the authors: the adopted formulation, known as classical laminated plate theory, which copes with the Kirchhoff-Love plate theory, is the simplest available for performing analyzes of such structures. Hence, various results which might be derived (such as stresses and strains on individual plies) do not necessarily model reality with high fidelity. Other more advanced models do exist, such as equivalent single-layer theories that take into account shear deformations, and three-dimensional elasticity theories that model the laminate layers independently of one-another, while taking into account displacement compatibility between them (known as layerwise theories) [Reddy, 2003].

Having said this, the classical laminate theory can be used for simpler assessments. For the k-th lamina, stresses can be obtained using [Reddy, 2003]:

$$\begin{Bmatrix} \sigma_x^{(e)} \\ \sigma_y^{(e)} \\ \tau_{xy}^{(e)} \end{Bmatrix}^{(k)} = \begin{bmatrix} \bar{Q}_{11} & \bar{Q}_{12} & \bar{Q}_{16} \\ \bar{Q}_{12} & \bar{Q}_{22} & \bar{Q}_{26} \\ \bar{Q}_{16} & \bar{Q}_{26} & \bar{Q}_{66} \end{bmatrix}^{(k)} \begin{Bmatrix} \epsilon_x^{(e)} \\ \epsilon_y^{(e)} \\ \gamma_{xy}^{(e)} \end{Bmatrix}^{(k)} \quad \Leftrightarrow \quad \boldsymbol{\sigma}^{(e)} = \bar{\mathbf{Q}}^{(k)} \boldsymbol{\epsilon}^{(e)}, \quad \text{for } z_k \leq z \leq z_{k+1}, \quad (51)$$

where the superscript $^{(k)}$ appended to the vectors and matrix is used to indicate their entries are related to the k-th lamina of the laminate. The $\bar{Q}_{ij}^{(k)}$ components ($i,j \in \{1,2,6\}$) correspond to plane-stress reduced stiffnesses related to the material of the lamina, expressed in the global coordinate frame. They can be retrieved after performing a coordinate transformation of the material properties of the lamina, that is:

$$\bar{Q}_{11}^{(k)} = Q_{11}^{(k)} c_\alpha^4 + 2\left(Q_{12}^{(k)} + 2Q_{66}^{(k)} \right) s_\alpha^2 c_\alpha^2 + Q_{22}^{(k)} s_\alpha^4; \qquad (52a)$$

$$\bar{Q}_{12}^{(k)} = \left(Q_{11}^{(k)} + Q_{22}^{(k)} - 4Q_{66}^{(k)} \right) s_\alpha^2 c_\alpha^2 + Q_{12}^{(k)} \left(s_\alpha^4 + c_\alpha^4 \right); \qquad (52b)$$

$$\bar{Q}_{22}^{(k)} = Q_{11}^{(k)} s_\alpha^4 + 2\left(Q_{12}^{(k)} + 2Q_{66}^{(k)} \right) s_\alpha^2 c_\alpha^2 + Q_{22}^{(k)} c_\alpha^4; \qquad (52c)$$

$$\bar{Q}_{16}^{(k)} = \left(Q_{11}^{(k)} - Q_{12}^{(k)} - 2Q_{66}^{(k)} \right) s_\alpha c_\alpha^3 + \left(Q_{12}^{(k)} - Q_{22}^{(k)} + 2Q_{66}^{(k)} \right) s_\alpha^3 c_\alpha; \qquad (52d)$$

$$\bar{Q}_{26}^{(k)} = \left(Q_{11}^{(k)} - Q_{12}^{(k)} - 2Q_{66}^{(k)} \right) s_\alpha^3 c_\alpha + \left(Q_{12}^{(k)} - Q_{22}^{(k)} + 2Q_{66}^{(k)} \right) s_\alpha c_\alpha^3; \qquad (52e)$$

$$\bar{Q}_{66}^{(k)} = \left(Q_{11}^{(k)} + Q_{22}^{(k)} - 2Q_{12}^{(k)} - 2Q_{66}^{(k)} \right) s_\alpha^2 c_\alpha^2 + Q_{66}^{(k)} \left(s_\alpha^4 + c_\alpha^4 \right). \qquad (52f)$$

In these, $s_\alpha := \sin \alpha^{(k)}$ and $c_\alpha := \cos \alpha^{(k)}$, with $\alpha^{(k)}$ denoting the angle between the x principal direction of the k-th lamina with respect to the global x axis, cf. Fig. 8. The stiffnesses $Q_{ij}^{(k)}$ can be obtained from the engineering constants of the lamina, whose elastic behavior is assumed to be orthotropic:

$$Q_{11}^{(k)} = \frac{E_1^{(k)}}{1-\nu_{12}^{(k)}\nu_{21}^{(k)}}, \quad Q_{12}^{(k)} = \frac{\nu_{12}^{(k)} E_2^{(k)}}{1-\nu_{12}^{(k)}\nu_{21}^{(k)}} = \frac{\nu_{21}^{(k)} E_1^{(k)}}{1-\nu_{12}^{(k)}\nu_{21}^{(k)}}, \quad Q_{22}^{(k)} = \frac{E_2^{(k)}}{1-\nu_{12}^{(k)}\nu_{21}^{(k)}}, \quad Q_{66}^{(k)} = G_{12}^{(k)}. \quad (53)$$
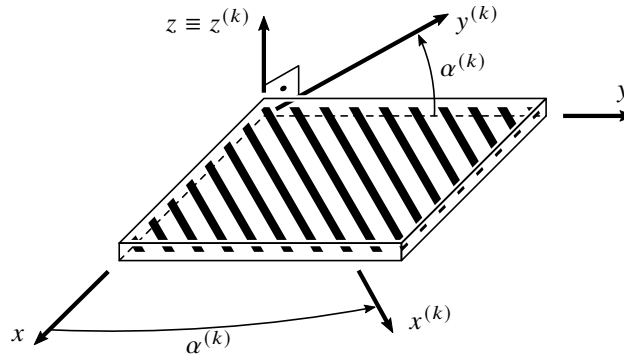
Figure 8: Principal coordinate system $x^{(k)}y^{(k)}z^{(k)}$ related to an uni-directional ply of a laminate, whose orientation with respect to the global reference frame xyz is given by $\alpha^{(k)}$.

With the previous expressions at hand, we can obtain the kinetic and potential energies necessary for establishing the finite element matrices, when the variational formulation approach is used. For the kinetic energy, we have:

$$\mathcal{K}^{(e)} = \iiint_{\Omega_t^{(e)}} \frac{1}{2}\rho^{(e)} \left\{ \left[\dot{u}^{(e)}(x,y,z,t)\right]^2 + \left[\dot{v}^{(e)}(x,y,z,t)\right]^2 + \left[\dot{w}^{(e)}(x,y,z,t)\right]^2 \right\} \mathrm{d}x\,\mathrm{d}y\,\mathrm{d}z$$

$$= \sum_{k=1}^{N_{\text{layers}}} \int_{z_k}^{z_{z+1}} \int_{-b}^{b} \int_{-a}^{a} \frac{1}{2}\rho^{(e)} \left\{ \left[\dot{u}^{(e)}(x,y,z,t)\right]^2 \right.$$

$$\left. + \left[\dot{v}^{(e)}(x,y,z,t)\right]^2 + \left[\dot{w}^{(e)}(x,y,z,t)\right]^2 \right\} \mathrm{d}x\,\mathrm{d}y\,\mathrm{d}z$$

$$= \sum_{k=1}^{N_{\text{layers}}} \int_{z_k}^{z_{z+1}} \int_{-b}^{b} \int_{-a}^{a} \frac{1}{2}\rho^{(e)} \left\{ \dot{\mathbf{q}}^{(e)\mathrm{T}} \left(\mathbf{N}_u^{(e)} + z\mathbf{N}_{\theta_y}^{(e)}\right)^{\mathrm{T}} \left(\mathbf{N}_u^{(e)} + z\mathbf{N}_{\theta_y}^{(e)}\right) \dot{\mathbf{q}}^{(e)} \right.$$

$$\left. + \dot{\mathbf{q}}^{(e)\mathrm{T}} \left(\mathbf{N}_v^{(e)} - z\mathbf{N}_{\theta_x}^{(e)}\right)^{\mathrm{T}} \left(\mathbf{N}_v^{(e)} - z\mathbf{N}_{\theta_x}^{(e)}\right) \dot{\mathbf{q}}^{(e)} + \dot{\mathbf{q}}^{(e)\mathrm{T}} \mathbf{N}_w^{(e)\mathrm{T}} \mathbf{N}_w^{(e)} \dot{\mathbf{q}}^{(e)} \right\} \mathrm{d}x\,\mathrm{d}y\,\mathrm{d}z$$

$$= \frac{1}{2}\dot{\mathbf{q}}^{(e)\mathrm{T}} \left[\sum_{k=1}^{N_{\text{layers}}} \int_{z_k}^{z_{z+1}} \int_{-b}^{b} \int_{-a}^{a} \rho^{(e)} \left\{ \left(\mathbf{N}_u^{(e)} + z\mathbf{N}_{\theta_y}^{(e)}\right)^{\mathrm{T}} \left(\mathbf{N}_u^{(e)} + z\mathbf{N}_{\theta_y}^{(e)}\right) \right. \right.$$

$$\left. \left. + \left(\mathbf{N}_v^{(e)} - z\mathbf{N}_{\theta_x}^{(e)}\right)^{\mathrm{T}} \left(\mathbf{N}_v^{(e)} - z\mathbf{N}_{\theta_x}^{(e)}\right) + \mathbf{N}_w^{(e)\mathrm{T}} \mathbf{N}_w^{(e)} \right\} \mathrm{d}x\,\mathrm{d}y\,\mathrm{d}z \right] \dot{\mathbf{q}}^{(e)}$$

$$= \frac{1}{2}\dot{\mathbf{q}}^{(e)\mathrm{T}} \left[\sum_{k=1}^{N_{\text{layers}}} \int_{z_k}^{z_{z+1}} \int_{-b}^{b} \int_{-a}^{a} \rho^{(e)} \left\{ \mathbf{N}_u^{(e)\mathrm{T}} \mathbf{N}_u^{(e)} + z\left(\mathbf{N}_{\theta_y}^{(e)\mathrm{T}} \mathbf{N}_u^{(e)} + \mathbf{N}_u^{(e)\mathrm{T}} \mathbf{N}_{\theta_y}^{(e)}\right) \right. \right.$$

$$\left. + z^2 \mathbf{N}_{\theta_y}^{(e)\mathrm{T}} \mathbf{N}_{\theta_y}^{(e)} + \mathbf{N}_v^{(e)\mathrm{T}} \mathbf{N}_v^{(e)} - z\left(\mathbf{N}_{\theta_x}^{(e)\mathrm{T}} \mathbf{N}_v^{(e)} + \mathbf{N}_v^{(e)\mathrm{T}} \mathbf{N}_{\theta_x}^{(e)}\right) \right.$$

$$\left. \left. + z^2 \mathbf{N}_{\theta_x}^{(e)\mathrm{T}} \mathbf{N}_{\theta_x}^{(e)} + \mathbf{N}_w^{(e)\mathrm{T}} \mathbf{N}_w^{(e)} \right\} \mathrm{d}x\,\mathrm{d}y\,\mathrm{d}z \right] \dot{\mathbf{q}}^{(e)}$$

$$= \frac{1}{2}\dot{\mathbf{q}}^{(e)\mathrm{T}}(t) \left[\sum_{k=1}^{N_{\text{layers}}} \mathbf{M}^{(e)\,(k)} \right] \dot{\mathbf{q}}^{(e)}(t) = \frac{1}{2}\dot{\mathbf{q}}^{(e)\mathrm{T}}(t) \mathbf{M}^{(e)} \dot{\mathbf{q}}^{(e)}(t), \quad (54)$$

where:

$$\mathbf{M}^{(e)\,(k)} = (z_{k+1} - z_k) \int_{-b}^{b} \int_{-a}^{a} \rho^{(e)\,(k)} \left(\mathbf{N}_u^{(e)\,\mathrm{T}} \mathbf{N}_u^{(e)} + \mathbf{N}_v^{(e)\,\mathrm{T}} \mathbf{N}_v^{(e)} + \mathbf{N}_w^{(e)\,\mathrm{T}} \mathbf{N}_w^{(e)} \right) \mathrm{d}x\,\mathrm{d}y$$

$$+ \frac{1}{2} \left(z_{k+1}^2 - z_k^2 \right) \int_{-b}^{b} \int_{-a}^{a} \rho^{(e)\,(k)} \left(\mathbf{N}_{\theta_y}^{(e)\,\mathrm{T}} \mathbf{N}_u^{(e)} + \mathbf{N}_u^{(e)\,\mathrm{T}} \mathbf{N}_{\theta_y}^{(e)} - \mathbf{N}_{\theta_x}^{(e)\,\mathrm{T}} \mathbf{N}_v^{(e)} - \mathbf{N}_v^{(e)\,\mathrm{T}} \mathbf{N}_{\theta_x}^{(e)} \right) \mathrm{d}x\,\mathrm{d}y$$

$$+ \frac{1}{3} \left(z_{k+1}^3 - z_k^3 \right) \int_{-b}^{b} \int_{-a}^{a} \rho^{(e)\,(k)} \left(\mathbf{N}_{\theta_y}^{(e)\,\mathrm{T}} \mathbf{N}_{\theta_y}^{(e)} + \mathbf{N}_{\theta_x}^{(e)\,\mathrm{T}} \mathbf{N}_{\theta_x}^{(e)} \right) \mathrm{d}x\,\mathrm{d}y \quad (55)$$

corresponds to the mass matrix contribution owed to the k-th layer of the laminate. The total mass matrix of the plate/laminate finite element is obtained by summing the contributions of all its laminas:

$$\mathbf{M}^{(e)} = \sum_{k=1}^{N_{\mathrm{layers}}} \mathbf{M}^{(e)\,(k)}. \quad (56)$$

With regards to the contribution due to elastic deformation of the structure towards the finite element potential energy, it can be obtained from:

$$\mathcal{U}_{\mathrm{elast}}^{(e)} = \frac{1}{2} \iiint_{\Omega_t^{(e)}} \left[\sigma_x^{(e)} \epsilon_x^{(e)} + \sigma_y^{(e)} \epsilon_y^{(e)} + \tau_{xy}^{(e)} \gamma_{xy}^{(e)} \right] \mathrm{d}x\,\mathrm{d}y\,\mathrm{d}z$$

$$= \frac{1}{2} \sum_{k=1}^{N_{\mathrm{layers}}} \int_{z_k}^{z_{z+1}} \int_{-b}^{b} \int_{-a}^{a} \boldsymbol{\sigma}^{(e)\,\mathrm{T}}(x, y, z, t)\, \boldsymbol{\epsilon}^{(e)}(x, y, z, t)\, \mathrm{d}x\,\mathrm{d}y\,\mathrm{d}z$$

$$= \frac{1}{2} \mathbf{q}^{(e)\,\mathrm{T}}(t) \left[\sum_{k=1}^{N_{\mathrm{layers}}} \int_{z_k}^{z_{z+1}} \int_{-b}^{b} \int_{-a}^{a} \left(\mathbf{B}_0^{(e)} + z \mathbf{B}_1^{(e)} \right)^{\mathrm{T}} \bar{\mathbf{Q}}^{(k)} \left(\mathbf{B}_0^{(e)} + z \mathbf{B}_1^{(e)} \right) \mathrm{d}x\,\mathrm{d}y\,\mathrm{d}z \right] \mathbf{q}^{(e)}(t)$$

$$= \frac{1}{2} \mathbf{q}^{(e)\,\mathrm{T}}(t) \left[\sum_{k=1}^{N_{\mathrm{layers}}} \mathbf{K}^{(e)\,(k)} \right] \mathbf{q}^{(e)}(t) = \frac{1}{2} \mathbf{q}^{(e)\,\mathrm{T}}(t) \mathbf{K}^{(e)} \mathbf{q}^{(e)}(t), \quad (57)$$

where $\mathbf{K}^{(e)\,(k)}$ is the stiffness matrix contribution due to the k-th layer of the laminate, whose expression is given by:

$$\mathbf{K}^{(e)\,(k)} = (z_{k+1} - z_k) \int_{-b}^{b} \int_{-a}^{a} \mathbf{B}_0^{(e)\,\mathrm{T}} \bar{\mathbf{Q}}^{(k)} \mathbf{B}_0^{(e)} \mathrm{d}x\,\mathrm{d}y$$

$$+ \frac{1}{2} \left(z_{k+1}^2 - z_k^2 \right) \int_{-b}^{b} \int_{-a}^{a} \left(\mathbf{B}_1^{(e)\,\mathrm{T}} \bar{\mathbf{Q}}^{(k)} \mathbf{B}_0^{(e)} + \mathbf{B}_0^{(e)\,\mathrm{T}} \bar{\mathbf{Q}}^{(k)} \mathbf{B}_1^{(e)} \right) \mathrm{d}x\,\mathrm{d}y$$

$$+ \frac{1}{3} \left(z_{k+1}^3 - z_k^3 \right) \int_{-b}^{b} \int_{-a}^{a} \mathbf{B}_1^{(e)\,\mathrm{T}} \bar{\mathbf{Q}}^{(k)} \mathbf{B}_1^{(e)} \mathrm{d}x\,\mathrm{d}y. \quad (58)$$

In the previous developments, we have made use of matrices $\mathbf{B}_0^{(e)}$ and $\mathbf{B}_1^{(e)}$, which are employed for interpolating the strain vector $\boldsymbol{\epsilon}^{(e)}$ inside the finite element domain. They can be evaluated using:

$$\mathbf{B}_0^{(e)} = \begin{bmatrix} \mathbf{B}_{x,0}^{(e)} \\ \mathbf{B}_{y,0}^{(e)} \\ \mathbf{B}_{xy,0}^{(e)} \end{bmatrix} \quad \text{and} \quad \mathbf{B}_1^{(e)} = \begin{bmatrix} \mathbf{B}_{x,1}^{(e)} \\ \mathbf{B}_{y,1}^{(e)} \\ \mathbf{B}_{xy,1}^{(e)} \end{bmatrix}, \quad (59)$$

with entries being implicitly defined in Eq. (50). The complete finite element stiffness matrix can then be obtained via:

$$\mathbf{K}^{(e)} = \sum_{k=1}^{N_{\mathrm{layers}}} \mathbf{K}^{(e)\,(k)}. \quad (60)$$

As for conservative external loads which can be applied to the finite element, their contribution can be obtained following similar steps to those which have led to Eq. (28) in the previous section. Here, we simply consider that:

$$\mathcal{W}_{\mathrm{ext}}^{(e)} = \mathbf{q}^{(e)\,\mathrm{T}}(t) \mathbf{Q}_b^{(e)}(t) + \mathbf{q}^{(e)\,\mathrm{T}}(t) \mathbf{Q}_s^{(e)}(t), \quad (61)$$

without going into details, or providing expressions that result for the element body and surface forces, $\mathbf{Q}_b^{(e)}(t)$ and $\mathbf{Q}_s^{(e)}(t)$, respectively.

At this point, we are able to evaluate the finite element Lagrangian, which takes the same form seen in Eq. (35), albeit expressions for the element mass and stiffness matrices, as well as conservative load vectors resulted different. The equations of motion for the plate/laminate finite element can also be established, and look exactly like what has been presented in Eq. (37) — but with $\mathbf{M}^{(e)}$ and $\mathbf{K}^{(e)}$ given by Eqs. (56) and (60), for example.

Finally, the procedure outlined in the previous section for obtaining global matrices for a finite element mesh can be easily generalized to account for finite elements with any number of DOFs. Henceforth, it can be readily used to establish global matrices related to a mesh assembled using plate/laminate elements, such as the one just presented.

3   Examples

In order to showcase the use of the finite elements whose mathematical formulation has been discussed previously in section 2, in this section we consider two relatively simple examples. The first one makes use of the quadrilateral two-dimensional elasticity finite element presented in section 2.1, whilst the second example concerns itself with the rectangular laminate finite element introduced in section 2.2. Numerical codes used to perform computations have been implemented in MATLAB ® by the authors, and are made publicly available through this link.

3.1   Static analysis of an H-shaped material sheet

Problem: Consider a H-shaped sheet, clamped at its left edge and subjected to a distributed load $q(x)$ at its top-right portion, as illustrated in Fig. 9. The structure is made up of an isotropic metallic material and its physical and geometric properties are listed in Tab. 1. By employing quadrilateral two-dimensional elasticity finite elements, let us estimate the stress and strain fields distribution in the sheet domain.
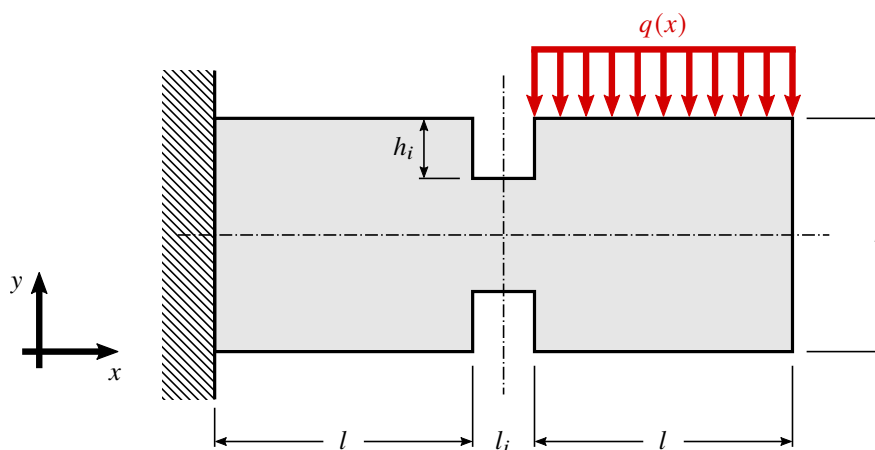
Figure 9: H-shaped sheet clamped at its left edge and subjected to a vertical distributed load on part of its boundary.

Table 1: H-shaped sheet dimensions and material properties.

Variable	Description	Value	Units
l_t	Total length	1	m
l	Length of first and third sections	0.4	m
l_i	Length of intermediate section	0.2	m
h	Total height	0.4	m
h_i	Height of the intermediate cutout	60	mm
L_z	Thickness along z	5	mm
E	Young's modulus	69	GPa
ν	Poisson's ratio	0.3	
ρ	Mass density	2.7	$\mathrm{g\,m^{-3}}$

Solution: Considering that the thickness of the solid medium is negligible in comparison to its other dimensions, and that stresses are confined to the sheet plane, only, the Solid Mechanics problem at hand consists of a plane stress one.

As previously mentioned in section 2.1.2, for plane stress problems, the nonzero stresses are σ_x, σ_y and τ_{xy}, if the solid sheet is located on the x-y plane. For this scenario, considering linear, isotropic elasticity, Hooke's law, stated in Eqs. (7), can be duly modified, to provide a reduced set of constitutive relations, cf. Eqs. (24).

The first step which must be made to obtain the desired stress distributions using the FEM is to define the mesh for the domain of the considered sheet. For this purpose, we make use of the quadrilateral two-dimensional continuum elasticity finite element presented in section 2.1. One recalls that, for this element, the nodal DOFs comprise displacements, only, and that its interpolation functions are linear for displacements.

In order to better organize the mesh, the domain of the H-shaped sheet is divided in seven rectangular sub-regions, as illustrated in Fig. 10. This makes it more straightforward to establish the number of finite elements and the location of nodes, in such a way that rectangular elements are used to make a mapped mesh for the whole domain.
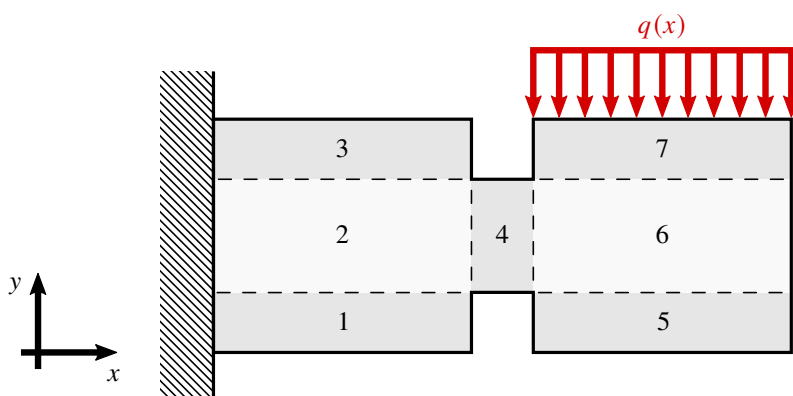
Figure 10: Division of the H-shaped sheet into seven rectangular sub-domains.

One then has to ensure that edges shared by neighbour rectangular sub-domains have the same amount of nodes. Besides simplifying the generation of a mapped mesh, this reasoning facilitates

adequately coupling the motion of sub-domains which are neighbors, for which meshes are initially generated independently of one another. This coupling can be made by enforcing the same nodal DOFs for distinct nodes, which is essentially the same as merging the coincident nodes, at this setting. More complicated coupling of sub-domains is also possible, taking into account *constraint equations*, which can be enforced via Lagrange multipliers or penalty methods [Bathe, 2014]. For the example at hand, for the correct link between nodes of the rectangular sub-domains, one must abide by the following pattern for the number of elements for the edges of the rectangular partitions:

- Edges parallel to the *x* direction of rectangles 1, 2 and 3 must have the same number of elements;

- Edges parallel to the *y* direction of rectangles 2, 4 and 6 must have the same number of elements;

- Edges parallel to the *x* direction of rectangles 5, 6 and 7 must have the same number of elements.

Given the above, one must now choose the number of finite elements (and consequently, nodes) that will compose the mesh. In general terms, the accuracy of the result tends to improve as the mesh gets refined, because the interpolation of field variables inside the domain of a finite element becomes more and more representative of the actual solution. On the other hand, as consequence of reducing the size of elements, the cost of computational simulations, in terms of resources and time, increases as well. In these terms, sometimes it becomes necessary to adopt a compromise solution, since the computational cost to perform various simulations with a mesh comprising a large number of elements can be prohibitive. Several authors, e.g. [Zienkiewicz et al., 2013], propose performing *convergence analysis* of the mesh, based on the results which are sought, in order to find a reasonable cost-benefit ratio for the mesh employed for numerical simulations; or to assure that results are independent of the mesh, i.e. that they have converged to the actual solution of the problem at hand.

In order to highlight the importance of a suitable specification for a finite element mesh, the example one is considering has been resolved for two different meshes, made of elements with distinct sizes:

- **Case 1:** the element size (length and height) is 5% of the largest dimension (50 mm, for this problem).

- **Case 2:** the element size (length and height) is 1% of the largest dimension (10 mm, for this problem).

Accordingly, the number of divisions used for the edges of each rectangular sub-domain, along the *x* and *y* directions, n_{elex} and n_{eley}, respectively, is presented in Tab. 2. Additionally, Tab. 3 shows some statistics of the resulting meshes, such as the total number of elements, nodes and DOFs. The meshes associated with Cases 1 and 2 are presented in Figs. 11(a) and 11(b), respectively, by means of the location occupied by nodes. By comparing both figures, it is clear that reducing the finite element size by 5 times (Case 1 to Case 2) implies in a much denser mesh.

As explained in section 2.1.1, the quadrilateral finite element used for this problem has four nodes, and two DOFs per node (displacements *u* and *v* along the *x* and *y* directions, respectively). Accordingly, the total number of DOFs related to the mesh associated with Case 2 increases significantly in comparison to the one observed for Case 1. Furthermore, the time spent to perform computations increases substantially, as well, as can be seen from the last row presented in Tab. 3. One should clarify that the reported times have been measured for a laptop computer, running Microsoft Windows 10 operating system, equipped with an Intel® Core™ i7-6500U central processing unit, and 8 GB of RAM memory.

Table 2: Number of elements along x and y directions adopted for each of the rectangular sub-domains identified in Fig. 10.

Rectangle number	Case 1		Case 2	
	n_{ele_x}	n_{ele_y}	n_{ele_x}	n_{ele_y}
1	8	2	40	7
2	8	6	40	28
3	8	2	40	7
4	4	6	20	28
5	8	5	40	7
6	8	6	40	28
7	8	7	40	7

Table 3: Statistics related to the meshes obtained for the H-shaped sheet considered in this example.

Statistic	Case 1	Case 2
Total number of elements	184	3920
Total number of nodes	269 (219)[†]	4299 (4077)[†]
Total number of DOFs	538 (438)[†]	8598 (8154)[†]
Elapsed time [s]	9.1	433.1

[†] Values reported between parentheses are related to the number of nodes and DOFs after coincident entities were merged.

It is important to note that, after the initial mesh has been generated individually for each rectangular sub-domain, some overlapping nodes could be found. "Duplicated" and "triplicated" nodes were then eliminated, to ensure the continuity of the finite element mesh. Underlying data of the finite element mesh model also need to be taken care of during this process. For example, various information are encoded in matrices used in finite element codes, related to properties of elements and nodes, and are therefore affected when nodes and DOFs get merged together. In this regard, in our code, some prominent matrices are:

- the "node matrix", which stores information about which nodes are related to each element;

- the "node position matrix", which caches the location initially occupied by nodes;

- the "connectivity matrix", which stores which DOFs are related to each element.

Hence, after coincident nodes are dealt with, these matrices are properly adjusted. One should remark that, to facilitate further operations, such as assembling global matrices, nodes and DOFs can be renumbered, if desired.

After nodes and DOFs have been updated, one has to input what are the boundary conditions. For this purpose, the nodes which are located on the boundary of the H-shaped sheet are identified. The DOFs related to those nodes at the left must be enforced to be zero. (A mathematical procedure which can be used for this purpose is presented in our next example, in section 3.2.) With regards to those elements at the top of rectangle 7, one has to impose a distributed pressure load, $q(x) = 500\,\text{kPa}$, to their appropriate boundary/edge, cf. Eq. (32). All other segments that compose the boundary of the structure are free. In Figs. 12(a) and 12(b), it is possible to visualize

(a) Case 1

(b) Case 2
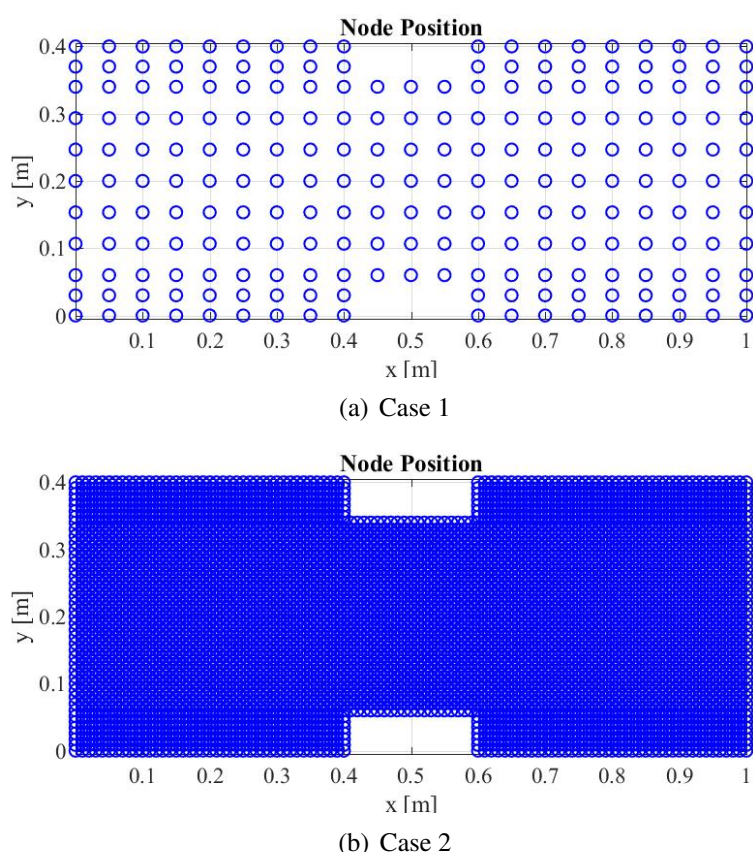
Figure 11: Location of nodes that compose the meshes of the H-shaped sheet of this example.

which nodes are related to each type of boundary condition just described, i.e. those which are totally blocked/restrained, related to the distributed pressure load, and/or free to move, without externally applied loads.

With boundary conditions defined, element level matrices can be computed (cf. Eqs. (27) and (34)) and global level matrices assembled (cf. Eq. (40)). The external distributed, surface load contribution can be evaluated by resorting to Eqs. (32) and (41). Having calculated global matrices and vectors, one can resolve a linear system of equations to determine the nodal DOFs of the mesh. This corresponds to a static analysis of the considered structure. The equations which needs to be solved come directly from Eq. (42) — one only needs to disregard the inertia/mass contribution term on its left-hand side to arrive at the appropriate global level input-output relationship for the analyzed system.

Figures 13(a) and 13(b) show how nodes get displaced when the H-shaped sheet is solicited by the external pressure load, for the two different meshes which we are considering. For Case 1, the largest displacement value occurs for the node at the top-right vertex of the sheet (with coordinates $x = 1$ m, $y = 0.4$ m), being its value equal to $0.199\,27$ mm. For Case 2, the maximum displacement is $0.205\,449$ mm, occurring at the same location observed for the previous case. To make for a better visualization of the displacement results, in Figs. 13(a) and 13(b) one has used amplification factors, whose values have been automatically computed, based on a characteristic dimension of the sheet and the maximum node displacement.

(a) Case 1

(b) Case 2
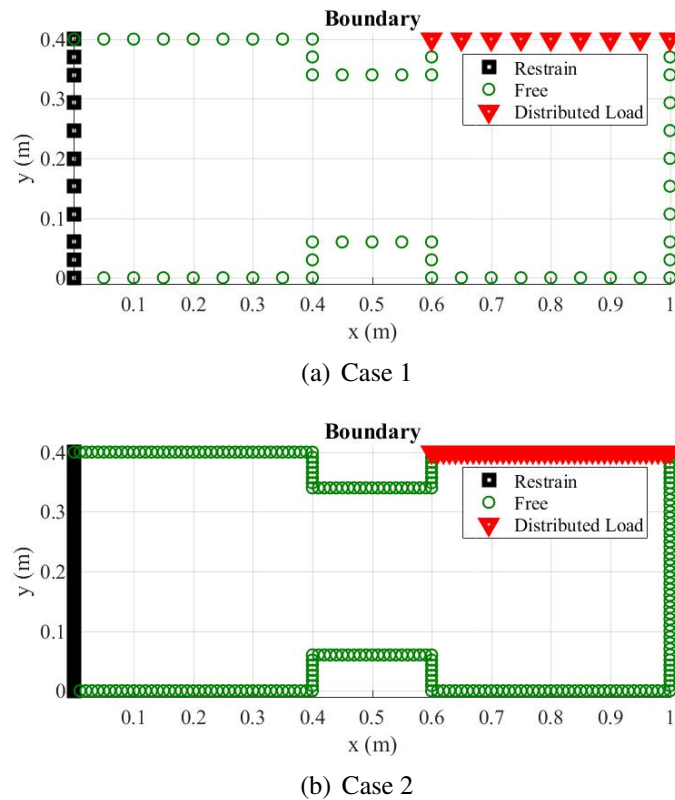
Figure 12: Boundary conditions implemented for analyzing the H-shaped sheet considered in this example.

(a) Case 1

(b) Case 2
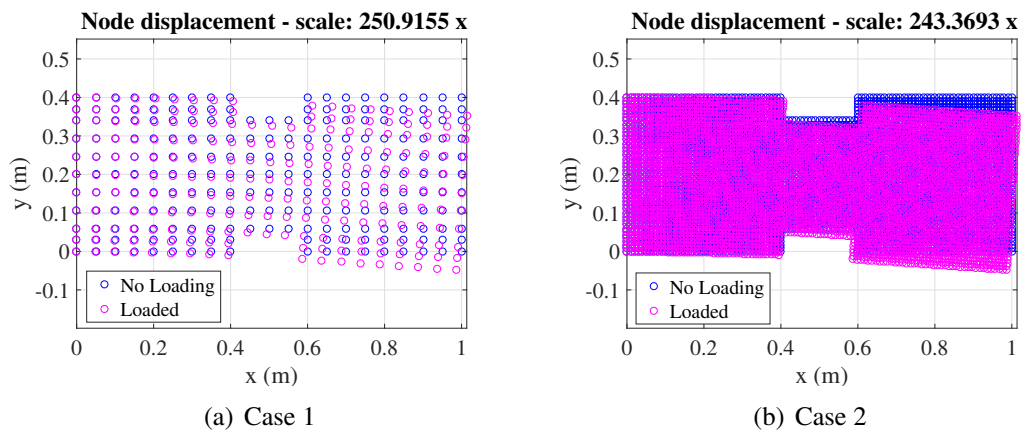
Figure 13: Node displacements resulting for the H-shaped sheet considered in this example.

With the complete nodal DOFs' vector being calculated, stress and strain results can be established via post-processing, for each element of the mesh. The displacements related to the nodes of an element can be initially obtained by considering the element DOFs' localization matrix, cf. (38). The strains can then be evaluated with the help of the element strain-displacement matrix $\mathbf{B}^{(e)}$, cf. Eq. (23). Stresses can then be retrieved by recalling the material constitutive relations, cf. Eq. (24) in the present case. Taking into account that strains and stresses vary linearly inside

the domain of each finite element of the mesh, due to the element formulation, one can establish the plots shown in Figs. 14 and 15 for Cases 1 and 2, respectively.
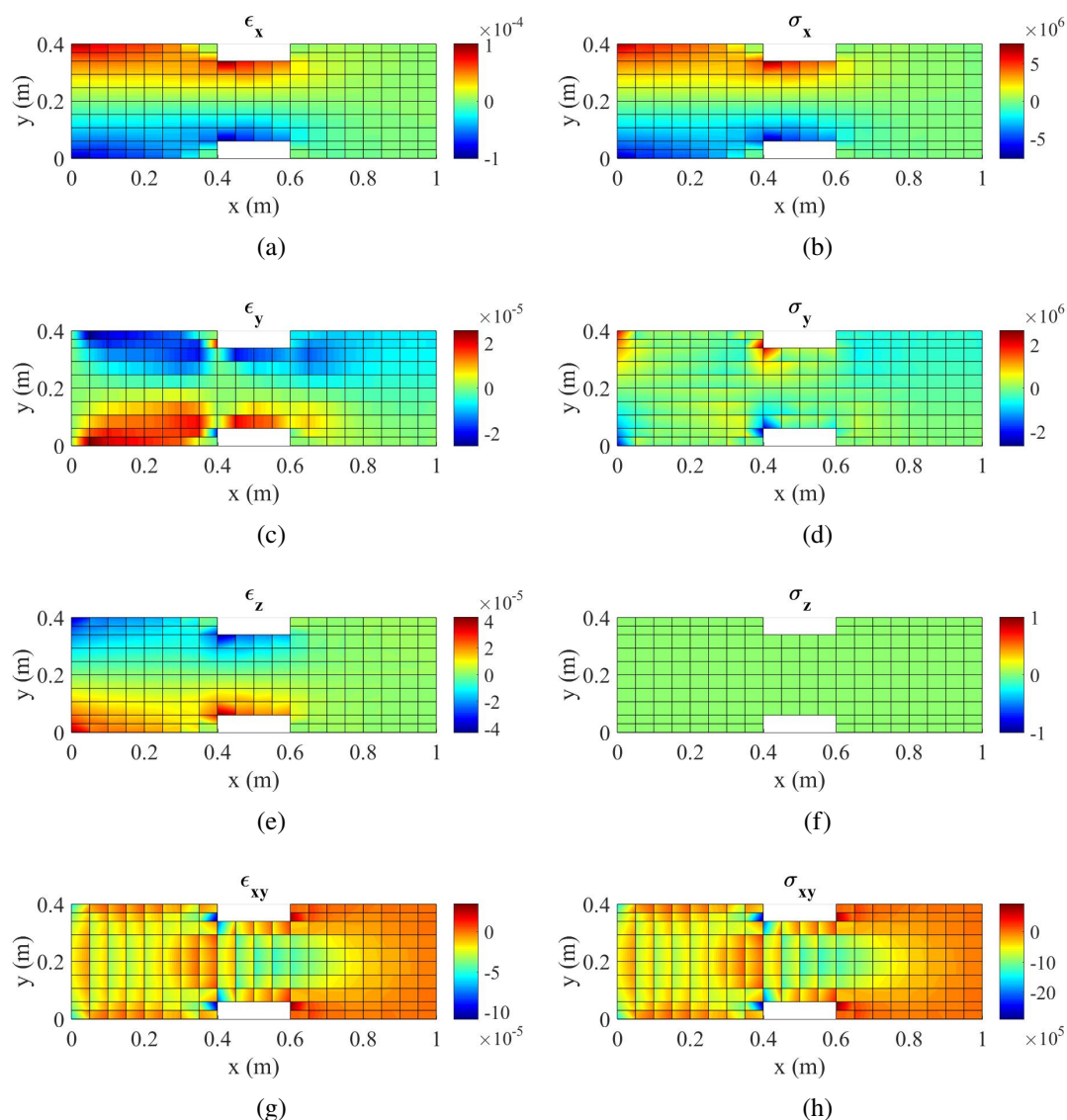
Figure 14: Distributions of strains and stresses in the H-shaped sheet considered in this example, using the coarser mesh of Case 1.

Regarding the maximum and minimum values observed for stresses and strains, σ_x reaches its maximum at the left internal corner of the top cutout, precisely at coordinates $x = 0.4\,\text{m}$, $y = 0.34\,\text{m}$. The minimum value of σ_x occurs at the equivalent place of the bottom cutout, at $x = 0.4\,\text{m}$, $y = 0.06\,\text{m}$, as expected for this configuration. The behavior of the normal strain ϵ_x is very similar, which is in accordance with the constitutive relation (24). For the normal stress and strain along the y direction (σ_y, ϵ_y), maximum and minimum values are seen at the same locations. With regards to the out-of-plane strain ϵ_z, it takes extrema values in the same cutouts, but in this case the maximum is seen to happen in the bottom location, whilst the minimum ϵ_z strain happens at the left internal corner of the top cutout. The stress σ_z is always zero, in accordance with the hypothesis if plane stress behavior.
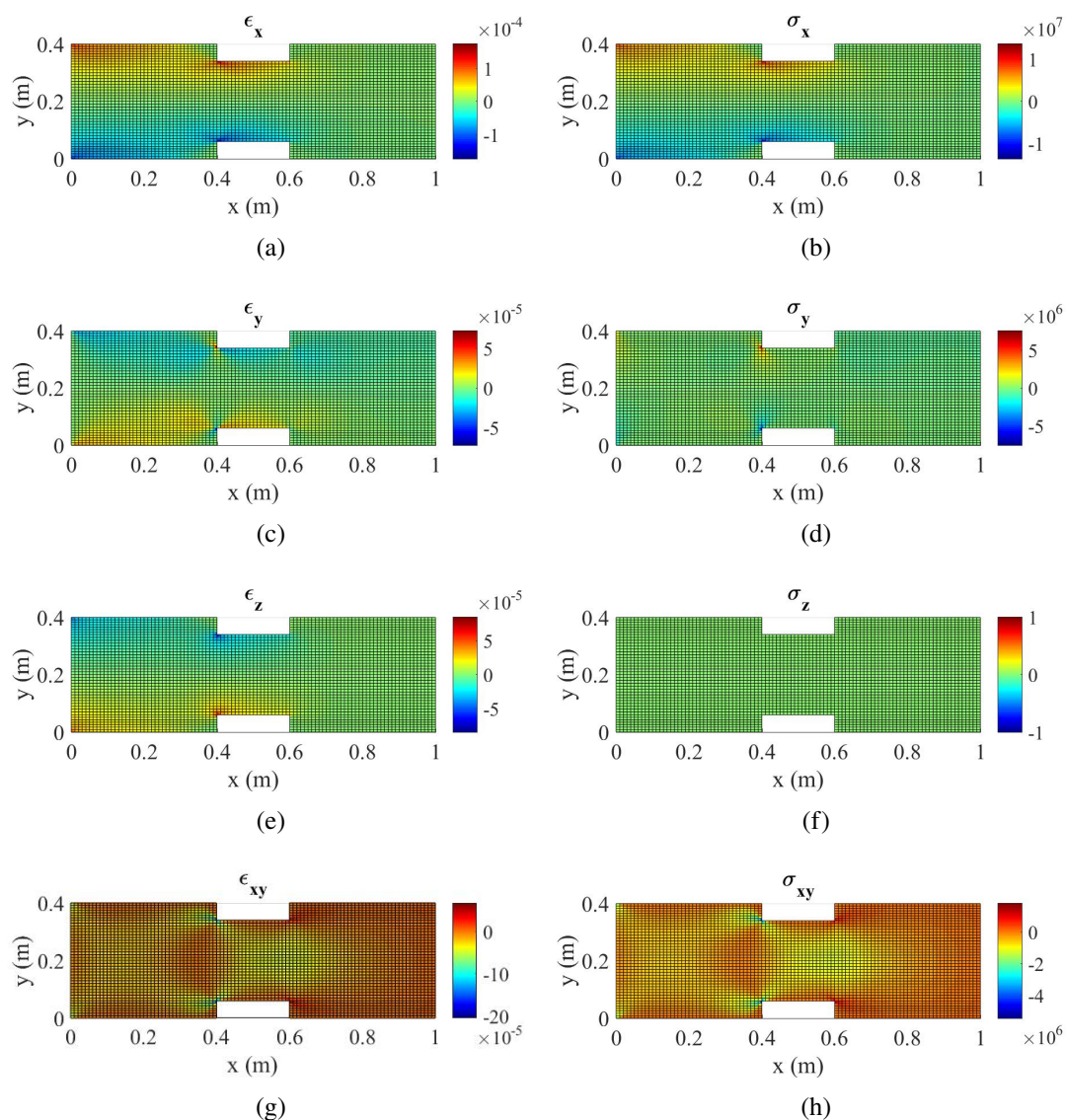
Figure 15: Distributions of strains and stresses in the H-shaped sheet considered in this example, using the finer mesh of Case 2.

Table 4: Comparison of the results obtained for the H-shaped sheet using the two generated meshes, in terms of the calculated maximum stresses.

	Case 1		Case 2	
	$\sigma_{\max}$ [MPa]	(x, y) [m]	$\sigma_{\max}$ [MPa]	(x, y) [m]
σ_x	7.6902	(0.40, 0.34)	13.7456	(0.40, 0.34)
σ_y	2.6720	(0.40, 0.34)	7.5453	(0.40, 0.34)
τ_{xy}	0.9190	(0.60, 0.06)	1.7960	(0.60, 0.06)

Table 5: Comparison of the results obtained for the H-shaped sheet using the two generated meshes, in terms of the calculated minimum stresses.

	Case 1		Case 2	
	$\sigma_{\min}$ [MPa]	(x, y) [m]	$\sigma_{\min}$ [MPa]	(x, y) [m]
σ_x	-7.6465	$(0.40, 0.06)$	-13.7084	$(0.40, 0.06)$
σ_y	-2.6692	$(0.40, 0.06)$	-7.5453	$(0.40, 0.06)$
τ_{xy}	-2.8987	$(0.40, 0.34)$	-5.4430	$(0.40, 0.34)$

From the results obtained for the maximum and minimum stresses, which are reported in Tabs. 4 and 5, respectively, it becomes clear that the values for the stresses obtained with the coarser (Case 1) and finer (Case 2) meshes are quite different between themselves. This is specially true because the analyzed structure has cutouts with right angle corners, which act as stress risers. For this, if one wants to obtain a better convergence of stress results using the four-nodes, quadrilateral, two-dimensional elasticity finite elements, it is necessary to develop a more complex mesh, using finer discretization, specially at the locations where stress concentration is expected to occur.
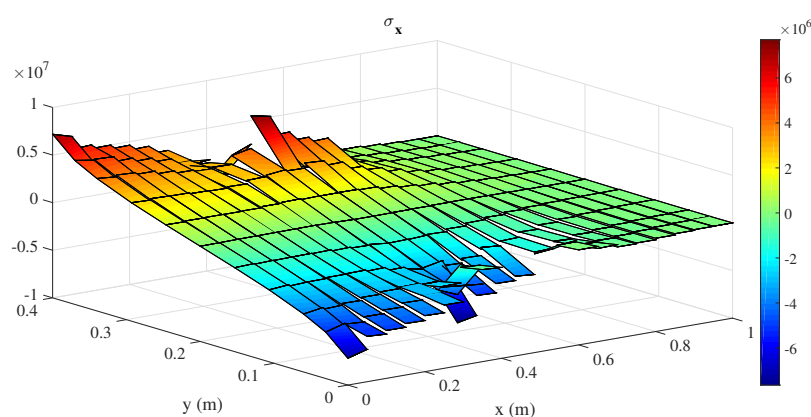
(a) Case 1
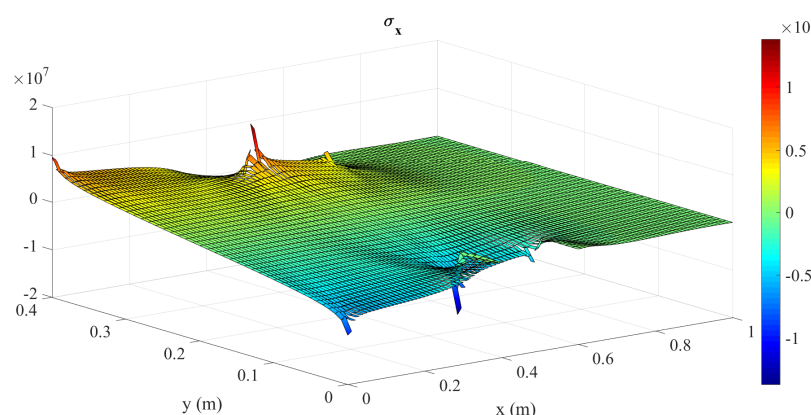
(b) Case 2

Figure 16: Three-dimensional visualization of the σ_x stress field for Cases 1 and 2 related to the H-shaped sheet considered in this example.

To help enlighten this remark, three-dimensional views are presented in Fig. 16 for the σ_x normal stress field, for both considered meshes. In Fig. 16(a), it is possible to see that the shown stress result has various discontinuities between adjacent finite elements, even at shared nodes. This is a clear indication that the considered stress result has not converged to the true solution of the problem, indicating that further mesh refinement should be considered; or that another type of finite element should be used, to provide better interpolation capability. When the three-dimensional visualization shown in Fig. 16(b) is considered, then fewer discontinuities are seen, and those which are related to significant jumps in value are confined exclusively to right angle corners at the cutouts and at the clamped region. If Saint-Venant's principle is invoked [Fung et al., 2017], then the computed results are reasonably representative of the actual solution of the Solid Mechanics problem at hand, except at the stress concentration regions just identified. Similar observations can be made if one analyzes the three-dimensional plots depicted in Fig. 17 for ϵ_y.
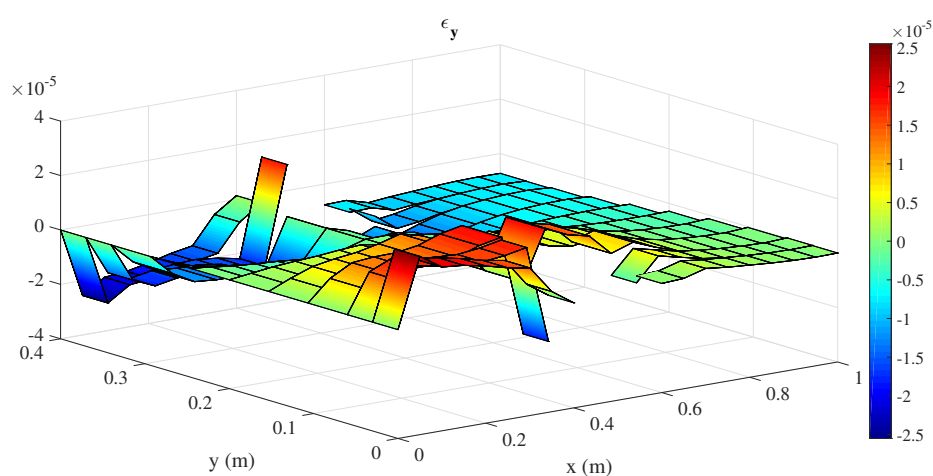
(a) Case 1
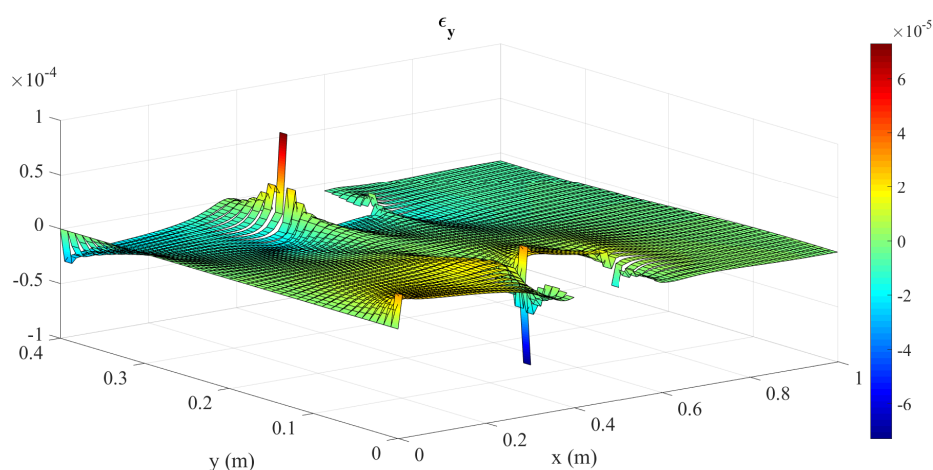
(b) Case 2

Figure 17: Three-dimensional visualization of the ϵ_y strain field for Cases 1 and 2 related to the H-shaped sheet considered in this example.

3.2 Dynamic analysis of a rectangular laminate

As a second example, now we consider a rectangular laminate, as illustrated in Fig. 18. It has dimensions $a = 287$ mm and $b = 287$ mm, being composed of four layers with individual thickness $h^{(k)} = 0.184$ mm, for $k \in \{1, 2, 3, 4\}$. The orientation of the layers is such that $\alpha^{(k)} = (-1)^k 45°$. Additionally, each layer is made of HexPly® M21/IM7, for which $E_1 = 160$ GPa, $E_2 = 8.6$ GPa, $\nu_{12} = 0.31$, $G_{12} = 4.7$ GPa, $\rho = 1580$ kg m^{-3} [Pereira et al., 2020]. The laminate is clamped on one of its sides, located at $x = 0$, as shown.

Based on the global level equations of motion for the considered system, which read:

$$\mathbf{M}^{(g)} \ddot{\mathbf{q}}^{(g)}(t) + \mathbf{K}^{(g)} \mathbf{q}^{(g)}(t) = \mathbf{Q}^{(g)}(t), \tag{62}$$

different types of dynamic analyzes can be made. Here, $\mathbf{Q}^{(g)}$ corresponds to a vector of arbitrary external forces. Furthermore, depending on the dynamic analysis which is of interest, initial conditions must be provided, in the form of initial displacements $\mathbf{q}_0^{(g)}$ and initial velocities $\dot{\mathbf{q}}_0^{(g)}$.

To take into account the clamp boundary condition, or other ones, which can be explicitly written in terms of the global nodal DOFs vector $\mathbf{q}^{(g)}(t)$, we partition it in unconstrained (free) and constrained subsets, such that:

$$\mathbf{q}^{(g)}(t) = \begin{Bmatrix} \mathbf{q}_u^{(g)}(t) \\ \mathbf{q}_c^{(g)}(t) \end{Bmatrix}. \tag{63}$$

For the considered case, all DOFs related to nodes located on the clamped edge are included in $\mathbf{q}_c^{(g)}(t)$, for which $\mathbf{q}_c^{(g)}(t) \equiv \mathbf{0}$. The remaining DOFs pertain to $\mathbf{q}_u^{(g)}(t)$. Then, to ensure constraints are enforced, we can write the global equations of motion in partitioned form:

$$\begin{bmatrix} \mathbf{M}_{uu}^{(g)} & \mathbf{M}_{uc}^{(g)} \\ \mathbf{M}_{cu}^{(g)} & \mathbf{M}_{cc}^{(g)} \end{bmatrix} \begin{Bmatrix} \ddot{\mathbf{q}}_u^{(g)}(t) \\ \ddot{\mathbf{q}}_c^{(g)}(t) \end{Bmatrix} + \begin{bmatrix} \mathbf{K}_{uu}^{(g)} & \mathbf{K}_{uc}^{(g)} \\ \mathbf{K}_{cu}^{(g)} & \mathbf{K}_{cc}^{(g)} \end{bmatrix} \begin{Bmatrix} \mathbf{q}_u^{(g)}(t) \\ \mathbf{q}_c^{(g)}(t) \end{Bmatrix} = \begin{Bmatrix} \mathbf{Q}_u^{(g)}(t) \\ \mathbf{Q}_c^{(g)}(t) \end{Bmatrix}. \tag{64}$$

From the first block of equations, we see that:

$$\mathbf{M}_{uu}^{(g)} \ddot{\mathbf{q}}_u^{(g)}(t) + \mathbf{K}_{uu}^{(g)} \mathbf{q}_u^{(g)}(t) = \mathbf{Q}_u^{(g)}(t) - \mathbf{M}_{uc}^{(g)} \ddot{\mathbf{q}}_c^{(g)}(t) - \mathbf{K}_{uc}^{(g)} \mathbf{q}_c^{(g)}(t), \tag{65}$$

which is a set of linear, second-order, ordinary differential equations for $\mathbf{q}_u^{(g)}(t)$. If $\mathbf{q}_c^{(g)}(t)$ is prescribed, then $\ddot{\mathbf{q}}_c^{(g)}(t)$ is also known. The loads applied on the unconstrained DOFs, collected in $\mathbf{Q}_u^{(g)}(t)$, are also provided as an input, if one is dealing with a direct dynamic problem (i.e. if one wants to find the motion which results due to applied loads).
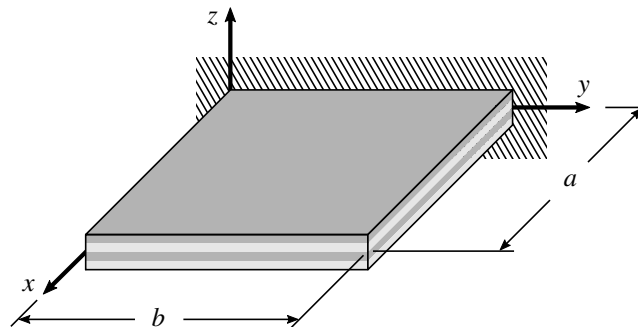
Figure 18: Laminate with four layers, clamped on one of its edges, considered in this section.

Once $\mathbf{q}_u^{(g)}(t)$ is known, then the second block of equations in (64) can be used to assess the reaction loads, which are required to constrain the DOFs in $\mathbf{q}_c^{(g)}(t)$ accordingly:

$$\mathbf{Q}_c^{(g)}(t) = \mathbf{M}_{cu}^{(g)}\ddot{\mathbf{q}}_u^{(g)}(t) + \mathbf{M}_{cc}^{(g)}\ddot{\mathbf{q}}_c^{(g)}(t) + \mathbf{K}_{cu}^{(g)}\mathbf{q}_u^{(g)}(t) + \mathbf{K}_{cc}^{(g)}\mathbf{q}_c^{(g)}(t). \tag{66}$$

For the clamp boundary condition, the previous equations simplify considerably, to provide:

$$\mathbf{M}_{uu}^{(g)}\ddot{\mathbf{q}}_u^{(g)}(t) + \mathbf{K}_{uu}^{(g)}\mathbf{q}_u^{(g)}(t) = \mathbf{Q}_u^{(g)}(t); \tag{67}$$

$$\mathbf{Q}_c^{(g)}(t) = \mathbf{M}_{cu}^{(g)}\ddot{\mathbf{q}}_u^{(g)}(t) + \mathbf{K}_{cu}^{(g)}\mathbf{q}_u^{(g)}(t). \tag{68}$$

Modal analysis The first type of dynamic analysis one might be interested in relates to the determination of natural frequencies and corresponding vibration mode shapes. These dynamic properties of a structural system fully characterize its behavior in the absence of externally applied loads. For obtaining them, one admits $\mathbf{Q}_u^{(g)}(t) = \mathbf{0}$, and that $\mathbf{q}_u^{(g)}(t) = \hat{\mathbf{q}}_u^{(g)}\mathrm{e}^{st}$, with s an undetermined scalar, and $\hat{\mathbf{q}}^{(g)}$ a vector of amplitudes. Substituting this ansatz on the equations of motion, we obtain:

$$\left[s^2\mathbf{M}_{uu}^{(g)} + \mathbf{K}_{uu}^{(g)} \right] \hat{\mathbf{q}}_u^{(g)} = \mathbf{0}, \tag{69}$$

which admits a non-trivial solution (i.e. for which $\hat{\mathbf{q}}_u^{(g)} \neq \mathbf{0}$) only if $\det\left[s^2\mathbf{M}_{uu}^{(g)} + \mathbf{K}_{uu}^{(g)} \right] = 0$. The previous equation, in fact, corresponds to an eigenvalue problem, with eigenvalues $s = j\omega$ and eigenvectors $\hat{\mathbf{q}}_u^{(g)}$, with $j = \sqrt{-1}$ the imaginary unit. The natural frequencies are given by ω, whereas vibration mode shapes are proportional to $\hat{\mathbf{q}}_u^{(g)}$. Depending on future analyzes which might be performed, and that rely on the so-called modal superposition technique, eigenmodes can be normalized, if desired.

Harmonic analysis In this case, one is interested in the steady-state response of the structure when it is subjected to harmonically-varying loads. We then consider $\mathbf{Q}_u^{(g)}(t) = \tilde{\mathbf{Q}}_u^{(g)}\mathrm{e}^{j\Omega t}$, with $\tilde{\mathbf{Q}}_u^{(g)}$ representing amplitudes and Ω the forcing frequency. If the system is linear, as considered here, then steady-state responses must occur with the same frequency as the one of the excitation, such that $\mathbf{q}_u^{(g)}(t) = \tilde{\mathbf{q}}_u^{(g)}\mathrm{e}^{j\Omega t}$, with $\tilde{\mathbf{q}}_u^{(g)}$ potentially being complex, to account for phase differences between responses and excitation (if damping is considered, for example). One then obtains:

$$\left(-\Omega^2\mathbf{M}_{uu}^{(g)} + \mathbf{K}_{uu}^{(g)}\right)\tilde{\mathbf{q}}_u^{(g)} = \tilde{\mathbf{Q}}_u^{(g)} \qquad \Rightarrow \qquad \tilde{\mathbf{q}}_u^{(g)} = \left(-\Omega^2\mathbf{M}_{uu}^{(g)} + \mathbf{K}_{uu}^{(g)}\right)^{-1}\tilde{\mathbf{Q}}_u^{(g)}. \tag{70}$$

Transient analysis When arbitrary external loads are applied to the structure, or initial conditions are given and the resulting motion is sought, then the ordinary differential equations of motion need to be integrated in time. This corresponds to a transient analysis, which can usually be performed by resorting to numerical integration algorithms, such as the Newmark method, the Runge-Kutta methods, the Hilber-Hughes-Taylor (HHT) method, etc. If the integration method is of first order, then the equations of motion (65) can be recast in the form:

$$\mathbf{A}\dot{\mathbf{z}}(t) + \mathbf{B}\mathbf{z}(t) = \mathbf{u}(t), \tag{71}$$

with:

$$\mathbf{A} = \begin{bmatrix} \mathbf{C}_{uu}^{(g)} & \mathbf{M}_{uu}^{(g)} \\ \mathbf{M}_{uu}^{(g)} & \mathbf{0} \end{bmatrix}; \qquad \mathbf{B} = \begin{bmatrix} \mathbf{K}_{uu}^{(g)} & \mathbf{0} \\ \mathbf{0} & -\mathbf{M}_{uu}^{(g)} \end{bmatrix}; \qquad \mathbf{z}(t) = \begin{Bmatrix} \mathbf{q}_u^{(g)}(t) \\ \dot{\mathbf{q}}_u^{(g)}(t) \end{Bmatrix};$$

$$\mathbf{u}(t) = \begin{Bmatrix} \mathbf{Q}_u^{(g)}(t) - \mathbf{M}_{uc}^{(g)}\ddot{\mathbf{q}}_c^{(g)}(t) - \mathbf{C}_{uc}^{(g)}\dot{\mathbf{q}}_c^{(g)}(t) - \mathbf{K}_{uc}^{(g)}\mathbf{q}_c^{(g)}(t) \\ \mathbf{0} \end{Bmatrix}, \tag{72}$$

which take into account contributions related to viscous damping, through partitions of the global damping matrix $\mathbf{C}^{(g)}$, seen in the expressions put forward for $\mathbf{A}$ and $\mathbf{u}$.

Besides, as discussed in the introduction of this chapter, various strategies can be considered to reduce computation time and/or alleviate memory allocation demanded by a transient analysis. One of such strategies, which is known as modal superposition, consists in representing the unknown solution as a weighted sum of the structure mode shapes. Typically, the number of wave modes adopted in this setting is much smaller than the original, complete number of global DOFs of the finite element mesh. Because the number of unknowns gets reduced, the equations of motion are also projected onto the vector space spanned by the wave modes used to represent the response, aiming to reduce the error of the approximation. If the wave modes used to represent the responses are grouped in a matrix $\mathbf{T}$, then one can write $\boldsymbol{\eta}(t) = \mathbf{T}\mathbf{q}_u^{(g)}(t)$, with the size of $\boldsymbol{\eta}(t)$ much smaller than the size of $\mathbf{q}_u^{(g)}(t)$. Variables grouped in $\boldsymbol{\eta}$ are commonly named *modal coordinates*. In the modal superposition setting, Eq. (71) remains valid, as long as quantities given in Eq. (72) are redefined according to:

$$
\mathbf{A} = \begin{bmatrix} \mathbf{T}^{\mathrm{T}}\mathbf{C}_{uu}^{(g)}\mathbf{T} & \mathbf{T}^{\mathrm{T}}\mathbf{M}_{uu}^{(g)}\mathbf{T} \\ \mathbf{T}^{\mathrm{T}}\mathbf{M}_{uu}^{(g)}\mathbf{T} & \mathbf{0} \end{bmatrix}; \qquad \mathbf{B} = \begin{bmatrix} \mathbf{T}^{\mathrm{T}}\mathbf{K}_{uu}^{(g)}\mathbf{T} & \mathbf{0} \\ \mathbf{0} & -\mathbf{T}^{\mathrm{T}}\mathbf{M}_{uu}^{(g)}\mathbf{T} \end{bmatrix}; \qquad \mathbf{z}(t) = \begin{Bmatrix} \boldsymbol{\eta}(t) \\ \dot{\boldsymbol{\eta}}(t) \end{Bmatrix};
$$

$$
\mathbf{u}(t) = \begin{Bmatrix} \mathbf{T}^{\mathrm{T}}\left[\mathbf{Q}_u^{(g)}(t) - \mathbf{M}_{uc}^{(g)}\ddot{\mathbf{q}}_c^{(g)}(t) - \mathbf{C}_{uc}^{(g)}\dot{\mathbf{q}}_c^{(g)}(t) - \mathbf{K}_{uc}^{(g)}\mathbf{q}_c^{(g)}(t) \right] \\ \mathbf{0} \end{Bmatrix}. \quad (73)
$$

At this point, one note that the laminate considered in this example has been discretized using a mesh with 15×15 elements. This mesh therefore comprises 256 nodes and 1280 DOFs (with five DOFs per node, cf. the finite element formulation discussed in section 2.2), prior to enforcing the clamp constraint. The number of unconstrained DOFs equals 1200.

By performing a modal analysis, one obtained the first 10 natural frequencies of the considered laminate, which are reported in Tab. 6. The corresponding vibration mode shapes can be visualized in Fig. 19. Notice that, for all modes, the edge of the laminate at $x = 0$ does not move, in accordance with the specified boundary condition.

Table 6: Natural frequencies of the laminate considered in this section.

n	1	2	3	4	5	6	7	8	9	10
$\frac{1}{2\pi}\omega_n$ [Hz]	6.85	24.9	39.7	65.6	81.6	123.8	137.3	154.3	170.1	241.0

A harmonic analysis is also carried out. The external load is a force acting along z, with unit magnitude, $\vec{F} = 1\vec{k}$ [N], on the node located at $x = a$, $y = b$. It is duly incorporated into the adequate row of $\tilde{\mathbf{Q}}_u^{(g)}$. The response is obtained at the same node, corresponding to its transverse displacement DOF. The forcing frequency is varied from 0 to 200 Hz, in 800 increments. The harmonic response is shown in Fig. 20, in the form of a Bode plot.
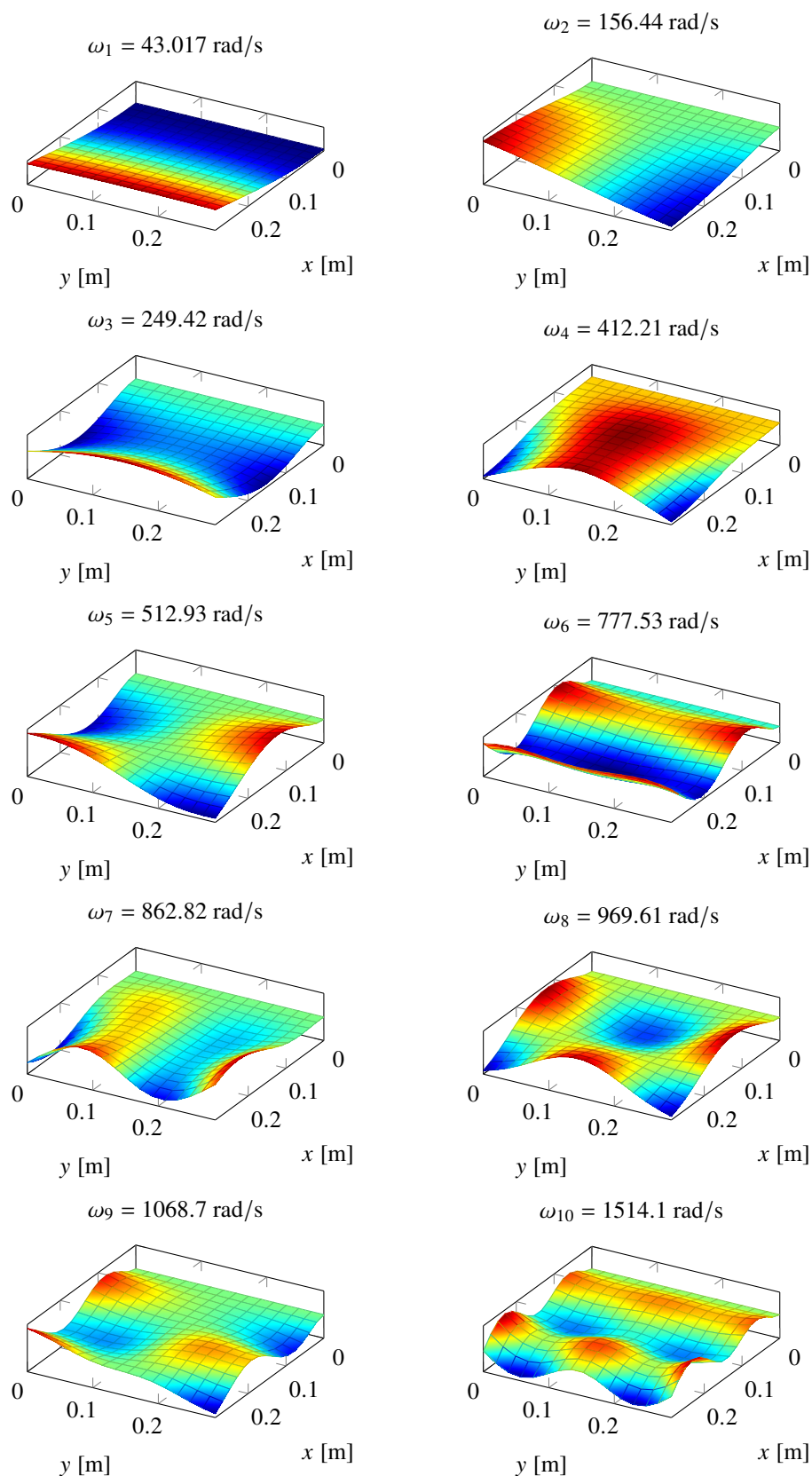
Figure 19: Vibration mode shapes (eigenvectors) of the laminate considered in this section.

Finally, a result related to a transient analysis is also reported. For this investigation, it has been assumed that a force $\vec{F} = \bar{F}(t)\vec{k}$ was applied at the node located at $x = a$, $y = 0$, with the magnitude $\bar{F}(t)$ corresponding to a triangular pulse with amplitude 1 N and duration of 20 ms, as shown in Fig. 21. The initial conditions were assumed to be null. Also, the mode superposition approach was considered for integrating the equations of motion. The first 30 mode shapes were used to approximate the unknowns. The largest natural frequency of the former is roughly equal to 746.4 Hz. It is usually recommended for one to include all modes bellow at least twice the maximum frequency of interest in the transformation matrix $\mathbf{T}$ used in the modal superposition approach [Craig and Kurdila, 2006]. Based on this premise, obtained responses should be relatively accurate for as long as the frequency content of the excitation load remains below, say, 373 Hz. The spectrum of $\bar{F}(t)$ illustrated in Fig. 21 indicates that this is not entirely true – so obtained results may not be completely correct.

For computing the transient response, a discrete viscous damper was also included in the model. It was placed between the node at $x = 8a/15 \cong 153.07$ mm, $y = 8b/15 \cong 153.07$ mm (close to the center of the laminate) and the ground. Also, the damper was assumed to dissipate energy based on the transverse motion of the corresponding node of the mesh, based on a viscous damping coefficient equal to $0.5\,\mathrm{N\,s\,m^{-1}}$. The damping matrix $\mathbf{C}^{(g)}$ therefore is almost entirely zero, except for the diagonal entry related to the transverse displacement w DOF of the node to which the damper is attached.

A single response of the laminate due to the transient excitation load is depicted here, in Fig. 22. It corresponds to the transverse displacement of the node located at $x = a$, $y = b$. As one can see, some vibration induced by the external load gets mitigated by the damper. The laminate continues
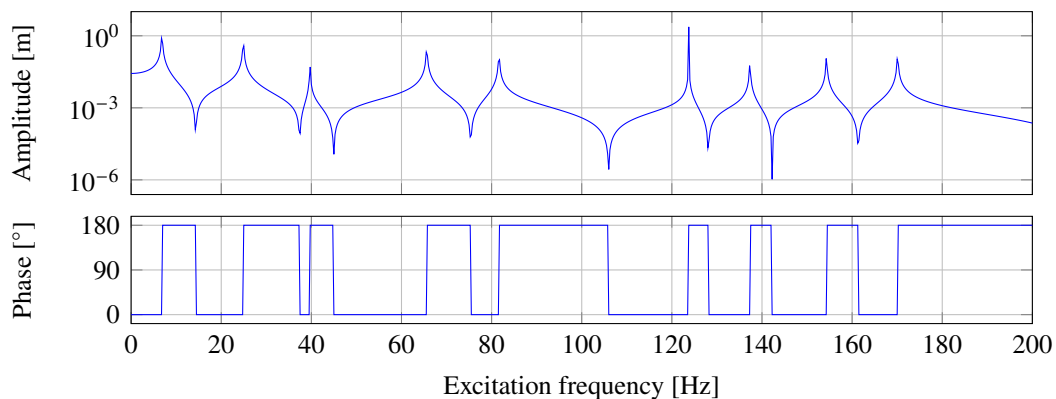
Figure 20: Harmonic response (transverse displacement DOF) at the driving point $x = a$, $y = b$ of the laminate considered in this section.
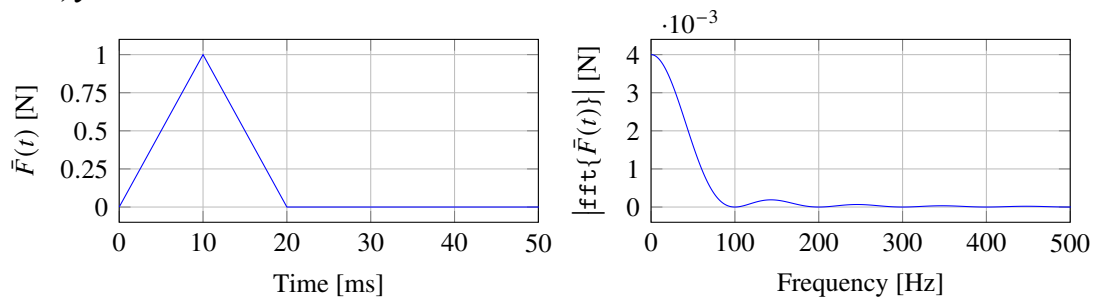
Figure 21: Time history (left) and spectrum (right) of the force amplitude $\bar{F}$ adopted for the transient analysis of the laminate considered in this section.

to vibrate somewhat, however, due to the damper not being able to adequately attenuate motion related to particular wave modes of the structure. A low decay rate can still be seen, even for such condition. We remark that the time integration algorithm used to obtain the result shown in Fig. 22 should not be responsible for the observed damping.
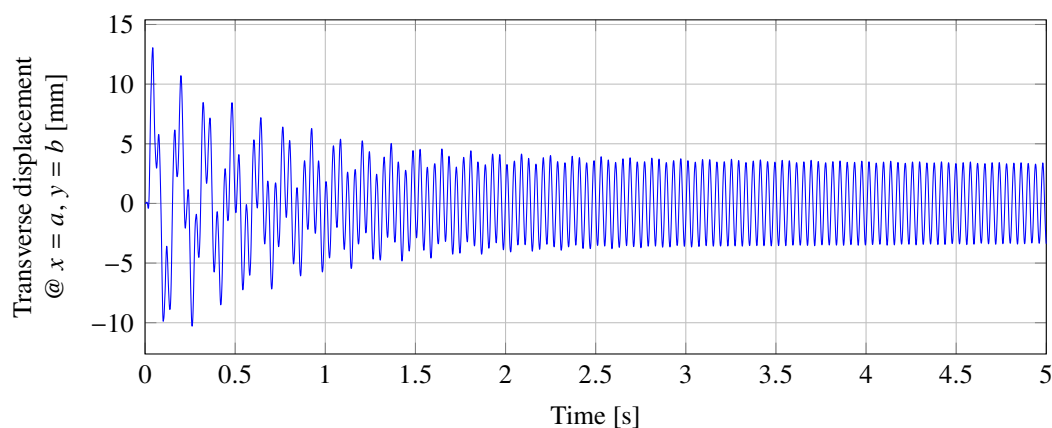
Figure 22: Transverse displacement of the point at $x = a$, $y = b$ of the laminate considered in this section, when it is subjected to the transverse force given in Fig. 21 at $x = a$, $y = 0$.

4   Parameterization of FE models for model updating and damage identification

Most often, the finite element modeling of complex engineering systems involves uncertainties affecting some physical or geometrical parameters (material parameters, geometrical dimensions, etc.). Other sources of uncertainties are boundary conditions and internal joints, the properties of which, due to the presence of contact, are difficult to characterize.

Hence, to reduce the errors involved in FE modeling, and obtain models sufficiently accurate to ensure reliable predictions, one strategy consists in performing the so-called *model updating* of an initial FE model. This can be achieved by performing experimental tests on the real structure (when it is available) and then introducing corrections in the FE model in such a way to minimize, as much as possible, the differences between a set of experimental responses and the corresponding model predictions. For this goal, since it is not reasonable to adjust the properties of each element of the mesh individually, it is convenient to assume the structure divided in a certain number of regions (macro-elements), and assign correction factors to the stiffness and/or inertia of each of these regions. Such an approach enables to consider modeling errors in terms of a reduced number of parameters, associated to the regions assumed to concentrate the dominant modeling errors. The model updating problem can thus be formulated as an optimization problem in which the objective function represents the difference between experimental responses and model predictions, and the design variables are the correction factors to be applied to the macro-elements of the model.

Considering problems in the field of structural dynamics, we recall the global equations of motion in the form:

$$\mathbf{M}^{(g)}\ddot{\mathbf{q}}^{(g)}(t) + \mathbf{K}^{(g)}\mathbf{q}^{(g)}(t) = \mathbf{Q}_{\mathrm{nc}}^{(g)}(t) + \mathbf{Q}_{b}^{(g)}(t) + \mathbf{Q}_{s}^{(g)}(t). \tag{74}$$

Assuming the structure divided in p regions, the mass and stiffness correction matrices to be

introduced in the updated FE model can be represented as follows:

$$\Delta \mathbf{M}^{(g)} = \bigcup_{r=1}^{R_m} m_r \mathbf{M}^{(r)}, \tag{75a}$$

$$\Delta \mathbf{K}^{(g)} = \bigcup_{r=1}^{R_k} k_r \mathbf{K}^{(r)}, \tag{75b}$$

where $\mathbf{M}^{(r)}$ and $\mathbf{K}^{(r)}$ are, respectively, the mass and stiffness contributions of region r to the corresponding global matrices, m_r and k_r are the associated correction parameters, and symbol $\bigcup$ indicates the operation of matrix assembling. Also, R_m and R_k stand for the number of different regions which are considered for correcting the mass and stiffness matrices, respectively.

A similar approach can be used for model-based damage identification, in which damage is assumed to be represented by error indicators, assigned to the probable damaged regions of the structure. The damage identification problem then consists in determining the set of damage indicators which makes the FE model to reproduce the experimentally measured responses of the damaged structure.

Different strategies for FE model updating and damage identification based on structural dynamic responses have been developed [Friswell and Mottershead, 1995]. In the next section, a classical approach, based on the sensitivity of eigenvalues and eigenvectors, is described.

5   Model updating based on the sensitivity of eigenvalues and eigenvectors

Neglecting damping, and assuming that S pairs of experimental eigensolutions – natural frequencies and natural vibration modes, $(\omega_s^{(\text{exp})} \in \mathbb{R}, \mathbf{X}_s^{(\text{exp})} \in \mathbb{R}^c, s = 1, \ldots, S)$ – are available, the approach starts by expressing the eigensolutions as linearized Taylor series expansions about the corresponding ones obtained from the FE model $(\lambda_s^{(m)} = \omega_s^{(m)^2}, \mathbf{X}_s^{(m)}, s = 1, \ldots, S)$:

$$\lambda_s^{(\text{exp})} = \lambda_s^{(m)} + \sum_{r=1}^{R_m} \frac{\partial \lambda_r^{(m)}}{\partial m_r} \Delta m_r + \sum_{r=1}^{R_k} \frac{\partial \lambda_r^{(m)}}{\partial k_r} \Delta k_r, \qquad s = 1, 2, \ldots, S, \tag{76a}$$

$$\mathbf{X}_s^{(\text{exp})} = \mathbf{X}_s^{(m)} + \sum_{r=1}^{R_m} \frac{\partial \mathbf{X}_r^{(m)}}{\partial m_r} \Delta m_r + \sum_{r=1}^{R_k} \frac{\partial \mathbf{X}_r^{(m)}}{\partial k_r} \Delta k_r, \qquad s = 1, 2, \ldots, S. \tag{76b}$$

It should be explained that, in the equations above, $\mathbf{X}_s^{(\text{exp})} \in \mathbb{R}^c$, for $s = 1, 2, \ldots, S$, are sub-eigenvectors formed only by the c components identified during experimental tests (e.g. from experimental modal analysis), while $\mathbf{X}_s^{(m)} \in \mathbb{R}^c$, for $s = 1, 2, \ldots, S$ are the counterparts provided by the FE model.

Since the parameters m_r and k_r intervene nonlinearly in the eigensolutions, their determination has to be done iteratively by solving Eqs. (76) for the increments Δm_r and Δk_r, starting from initial guessed values. In each iteration, the following linear system of equations has to be solved:

$$
\begin{Bmatrix} \Delta \lambda_1 \\ \vdots \\ \Delta \lambda_S \\ \Delta \mathbf{X}_1 \\ \vdots \\ \Delta \mathbf{X}_S \end{Bmatrix}
=
\begin{bmatrix}
\frac{\partial \lambda_1^{(m)}}{\partial m_1} & \cdots & \frac{\partial \lambda_1^{(m)}}{\partial m_{R_m}} & \frac{\partial \lambda_1^{(m)}}{\partial k_1} & \cdots & \frac{\partial \lambda_1^{(m)}}{\partial k_{R_k}} \\
\vdots & \ddots & \vdots & \vdots & \ddots & \vdots \\
\frac{\partial \lambda_S^{(m)}}{\partial m_1} & \cdots & \frac{\partial \lambda_S^{(m)}}{\partial m_{R_m}} & \frac{\partial \lambda_S^{(m)}}{\partial k_1} & \cdots & \frac{\partial \lambda_S^{(m)}}{\partial k_{R_k}} \\
\frac{\partial \mathbf{X}_1^{(m)}}{\partial m_1} & \cdots & \frac{\partial \mathbf{X}_1^{(m)}}{\partial m_{R_m}} & \frac{\partial \mathbf{X}_1^{(m)}}{\partial k_1} & \cdots & \frac{\partial \mathbf{X}_1^{(m)}}{\partial k_{R_k}} \\
\vdots & \ddots & \vdots & \ddots & \vdots & \vdots \\
\frac{\partial \mathbf{X}_S^{(m)}}{\partial m_1} & \cdots & \frac{\partial \mathbf{X}_S^{(m)}}{\partial m_R} & \frac{\partial \mathbf{X}_S^{(m)}}{\partial k_1} & \cdots & \frac{\partial \mathbf{X}_S^{(m)}}{\partial k_{R_k}}
\end{bmatrix}
\begin{Bmatrix} \Delta m_1 \\ \vdots \\ \Delta m_{R_m} \\ \Delta k_1 \\ \vdots \\ \Delta k_{R_k} \end{Bmatrix}
\tag{77}
$$

or

$$\Delta \mathbf{L} = \mathbf{S} \, \Delta \mathbf{P}. \tag{78}$$

As long as the number of equations $(S(1+c))$ is larger than the number of unknowns $(R_m + R_k)$ and matrix $\mathbf{S}$ is full-rank, the system of equations has a unique least-square solution:

$$\Delta \mathbf{P} = \left(\mathbf{S}^{\mathrm{T}} \mathbf{S} \right)^{-1} \mathbf{S}^{\mathrm{T}} \Delta \mathbf{L}. \tag{79}$$

Matrix $\mathbf{S}$ is formed by the sensitivities of the eigensolutions with respect to the correction parameters. As stated in [Friswell and Mottershead, 1995], different methods have been devised to compute those sensitivities.

Given the undamped eigenvalue problem associated to Eq. (74),

$$\left[\mathbf{K}^{(g)} - \lambda_s \mathbf{M}^{(g)} \right] \mathbf{X}_s = \mathbf{0}, \tag{80}$$

the derivation with respect to a given mass m_r or stiffness correction parameter k_r leads, respectively, to

$$\left[\mathbf{K}^{(g)} - \lambda_s \mathbf{M}^{(g)} \right] \frac{\partial \mathbf{X}_s}{\partial m_r} = - \left[\lambda_s \frac{\partial \mathbf{M}^{(g)}}{\partial m_r} + \frac{\partial \lambda_s}{\partial m_r} \mathbf{M}^{(g)} \right] \mathbf{X}_s, \qquad s = 1, 2, \ldots, S, \tag{81a}$$

$$\left[\mathbf{K}^{(g)} - \lambda_s \mathbf{M}^{(g)} \right] \frac{\partial \mathbf{X}_s}{\partial k_r} = \left[\frac{\partial \mathbf{K}^{(g)}}{\partial k_r} - \frac{\partial \lambda_s}{\partial k_r} \mathbf{M}^{(g)} \right] \mathbf{X}_s, \qquad s = 1, 2, \ldots, S. \tag{81b}$$

Assuming that the derivative of the s-th eigenvector can be projected on the basis formed by a set of Q eigenvectors, one writes:

$$\frac{\partial \mathbf{X}_s}{\partial m_r} = \sum_{q=1}^{Q} \mathbf{X}_q c_{sq}^r, \tag{82a}$$

$$\frac{\partial \mathbf{X}_s}{\partial k_r} = \sum_{q=1}^{Q} \mathbf{X}_q d_{sq}^r. \tag{82b}$$

Associating Eqs. (81) and (82), pre-multiplying both sides of the resulting equations by the eigenvector $\mathbf{X}_s$, which is assumed to be normalized to unit modal mass, one obtains the following expressions for the sensitivity of the r-th eigenvalue with respect to the mass and stiffness correction parameters, respectively:

$$\frac{\partial \lambda_s}{\partial m_r} = -\lambda_s \mathbf{X}_s^{\mathrm{T}} \frac{\partial \mathbf{M}^{(g)}}{\partial m_r} \mathbf{X}_s = -\lambda_s \mathbf{X}_s^{\mathrm{T}} \mathbf{M}^{(r)} \mathbf{X}_s, \tag{83a}$$

$$\frac{\partial \lambda_s}{\partial k_r} = \mathbf{X}_s^{\mathrm{T}} \frac{\partial \mathbf{K}^{(g)}}{\partial k_r} \mathbf{X}_s = \mathbf{X}_s^{\mathrm{T}} \mathbf{K}^{(r)} \mathbf{X}_s. \tag{83b}$$

Regarding Eqs. (83), it is worth pointing-out that the computation of the sensitivity of the s-th eigenvalue is straightforward and depends on the s-th eigenvector, only.

The computation of the sensitivities of the eigenvectors is somewhat more involved. The fundamental idea is to determine the expressions for the coefficients c_{sq}^r and d_{sq}^r in Eqs. (82). This is done by first deriving the normalization equations for the eigenvectors with respect to the correction parameters, as indicated next:

$$\mathbf{X}_s^{\mathrm{T}} \mathbf{M}^{(g)} \mathbf{X}_s = 1 \qquad \Rightarrow \qquad \mathbf{X}_s^{\mathrm{T}} \frac{\partial \mathbf{M}^{(g)}}{\partial m_r} \mathbf{X}_s + 2 \mathbf{X}_s^{\mathrm{T}} \mathbf{M}^{(g)} \frac{\partial \mathbf{X}_s}{\partial m_r} = 0, \tag{84a}$$

$$\mathbf{X}_s^{\mathrm{T}} \mathbf{K}^{(g)} \mathbf{X}_s = \lambda_s \qquad \Rightarrow \qquad \mathbf{X}_s^{\mathrm{T}} \frac{\partial \mathbf{K}^{(g)}}{\partial k_r} \mathbf{X}_s + 2 \mathbf{X}_s^{\mathrm{T}} \mathbf{K}^{(g)} \frac{\partial \mathbf{X}_s}{\partial k_r} = \frac{\partial \lambda_s}{\partial k_r}. \tag{84b}$$

Making use of Eqs. (82) and (83) and the orthogonality relations of the eigenvectors, one gets:

$$c_{ss}^r = -\frac{1}{2}\mathbf{X}_s^T\mathbf{M}^{(r)}\mathbf{X}_s, \tag{85a}$$

$$d_{ss}^r = 0. \tag{85b}$$

The determination of the remaining coefficients c_{qs}^r and d_{qs}^r with $r \neq s$ requires the use of Eqs. (81) in combination with Eqs. (82) and, again, the orthogonality relations of the eigenvectors. This procedure leads to the following expressions:

$$c_{sq}^r = \lambda_s \frac{\mathbf{X}_q^T\mathbf{M}^{(r)}\mathbf{X}_s}{\lambda_q - \lambda_s}, \qquad r \neq s, \tag{86a}$$

$$d_{sq}^r = -\frac{\mathbf{X}_q^T\mathbf{K}^{(r)}\mathbf{X}_s}{\lambda_q - \lambda_s}, \qquad r \neq s. \tag{86b}$$

Regarding the method presented above, it is worth highlighting its following features:

a) it requires one-to-one pairing between the natural frequencies and natural vibration modes obtained experimentally with those computed from the FE model. This can be a difficult task, especially when the modeling errors are large enough so as to render direct comparison ineffective for pairing. Hence, a number of numerical techniques have been devised to assist the comparison between the two sets of eigensolutions, such as the Modal Assurance Criterion (MAC) and the Coordinate Modal Assurance Criterion (COMAC) [e Silva and Maia, 2012];

b) as the components of the experimental and FE eigenvectors are directly paired, the method does not require the condensation of the FE model to ensure dimensional compatibility of both sets of eigenvectors.

c) it follows a fully deterministic approach, which means that random noise affecting the measured quantities or modeling errors are not considered. However, it is possible to formulate the model updating in a stochastic framework, where various estimators, can be used to deal with random uncertainties [Fonseca et al., 2005, Mares et al., 2006, Simoen et al., 2013].

6   Final remarks

The finite element method is, undoubtedly, a very powerful method, which has been playing a significant role in scientific and technological developments lately. However, in the authors' opinion, users must be fully aware, not only of its capabilities, but also of its limitations. In fact, it is widely recognized that modeling of complex systems is a combination of science and art, meaning that it is never a fully automated procedure, requiring, from the user: a) knowledge of the physics underlying the problem at hand, necessary to make adequate modeling choices and correct interpretation of the results; b) knowledge of the various resources available in commercial packages (in case these are used), necessary for the construction of representative, accurate and cost-effective models for the problem at hand; c) expert judgement, obtained from previous experience gathered in the modeling of similar problems.

It should be mentioned that, in many cases of scientific or industrial interest, FE models are constructed for use in combination with other numerical analyses, in broader frameworks. As relevant examples, one can cite:

- **Structural optimization:** a finite element model of a given structure is coupled to numerical optimization routines aiming at improving one or a set of desired responses or structural characteristics. In this case, the degree to which the improvement is obtained is quantified by one or various *cost functions* or *objective functions*, and the structural features to be modified form a set of *design variables*. Most often, the optimization problem is subject to the so-called *constraints*, which limit the range of possible solutions (design space). Generally, optimization problems must be solved iteratively, the FE model being used to compute the value of the objective and other necessary quantities at each iteration;

- **Uncertainty quantification:** a single FE model of a given structure is inherently, a deterministic model. As the modeling of complex systems most frequently involve uncertainties affecting external loads and physical and geometrical characteristics of the structure, it is of utmost importance, in many situations, to assess how those uncertainties can influence the responses predicted by the FE model. In a probabilistic scope, the immediate assessment can be made by the Monte Carlo method, which consists in generating a typically large number of samples of the assumed random variables and, for each sample, compute a corresponding response sample. These later can then be used to compute statistics of the structural responses, which, to have ensured statistical confidence, require a large number of samples and, as a result, of FE response evaluations. Other relevant problems related to uncertainty quantification are the assessment of structural reliability [Ditlevsen and Madsen, 1996] and robust optimization [Ben-Tal et al., 2009].

- **Damage identification:** this problem can be included in the more general scope of model-based parameter identification problems. More specifically, it can be regarded as a dual problem of model updating, described in section 5, as long as the correction coefficients are interpreted as damage indicators [Friswell, 2007, Fan and Qiao, 2011].

- **Sensitivity analysis:** this type of numerical analysis aims at assessing the degrees to which the structural responses of interest are influenced by variations of certain physical and/or geometrical structural characteristics [Saltelli et al., 2008]. This analysis is highly useful in structural design and also in other applications, such as structural optimization and uncertainty propagation.

References

K.-J. Bathe. *Finite Element Procedures*. Klaus-Jürgen Bathe, Watertown, MA, Jan. 2014. ISBN 978-0-9790049-5-7.

A. Ben-Tal, L. El Ghaoui, and A. Nemirovski. *Robust optimization*, volume 28. Princeton university press, 2009.

P. Chen and C. Schwab. Model order reduction methods in computational uncertainty quantification. In *Handbook of Uncertainty Quantification*, pages 937–990. Springer International Publishing, 2017. doi: 10.1007/978-3-319-12385-1_70. URL https://doi.org/10.1007/978-3-319-12385-1_70.

J. A. Cottrell, T. J. R. Hughes, and Y. Bazilevs. *Isogeometric analysis*. Wiley-Blackwell, Hoboken, NJ, Aug. 2009.

R. R. Craig and A. J. Kurdila. *Fundamentals of structural dynamics*. John Wiley & Sons, Nashville, TN, 2 edition, June 2006.

R. de Borst, M. A. Crisfield, J. J. C. Remmers, and C. V. Verhoosel. *Nonlinear finite element analysis of solids and structures*. Wiley Series in Computational Mechanics. Wiley-Blackwell, Hoboken, NJ, 2 edition, Aug. 2012.

O. Ditlevsen and H. O. Madsen. *Structural reliability methods*, volume 178. Wiley New York, 1996.

J. M. M. e Silva and N. M. Maia. *Modal analysis and testing*, volume 363. Springer Science & Business Media, 2012.

W. Fan and P. Qiao. Vibration-based damage identification methods: a review and comparative study. *Structural health monitoring*, 10(1):83–111, 2011.

J. R. Fonseca, M. I. Friswell, J. E. Mottershead, and A. W. Lees. Uncertainty identification by the maximum likelihood method. *Journal of Sound and Vibration*, 288(3):587–599, 2005.

M. Friswell and J. E. Mottershead. *Finite element model updating in structural dynamics*, volume 38. Springer Science & Business Media, 1995.

M. I. Friswell. Damage identification using inverse methods. *Philosophical Transactions of the Royal Society A: Mathematical, Physical and Engineering Sciences*, 365(1851):393–410, 2007.

Y. C. Fung, P. Tong, and X. Chen. *Classical and Computational Solid Mechanics*. WORLD SCIENTIFIC, July 2017. doi: 10.1142/9744. URL https://doi.org/10.1142/9744.

L. L. Gratiet, S. Marelli, and B. Sudret. Metamodel-based sensitivity analysis: Polynomial chaos expansions and gaussian processes. In *Handbook of Uncertainty Quantification*, pages 1289–1325. Springer International Publishing, 2017. doi: 10.1007/978-3-319-12385-1_38. URL https://doi.org/10.1007/978-3-319-12385-1_38.

J.-M. Jin. *The finite element method in electromagnetics*. John Wiley & Sons, 2015.

C. D. M. Junior, A. Erturk, and D. J. Inman. An electromechanical finite element model for piezoelectric energy harvester plates. *Journal of Sound and Vibration*, 327(1-2):9–25, Oct. 2009. doi: 10.1016/j.jsv.2009.05.015. URL https://doi.org/10.1016/j.jsv.2009.05.015.

C. Lanczos. *The variational principles of mechanics*. Dover Books on Physics. Dover Publications, Mineola, NY, Mar. 1986.

R. W. Lewis, K. Morgan, H. Thomas, and K. N. Seetharamu. *The finite element method in heat transfer analysis*. John Wiley & Sons, 1996.

C. Mares, J. Mottershead, and M. Friswell. Stochastic model updating: part 1—theory and simulated example. *Mechanical systems and signal processing*, 20(7):1674–1695, 2006.

D. Pereira, T. Guimarães, H. Resende, and D. Rade. Numerical and experimental analyses of modal frequency and damping in tow-steered CFRP laminates. *Composite Structures*, 244: 112190, July 2020. doi: 10.1016/j.compstruct.2020.112190. URL https://doi.org/10.1016/j.compstruct.2020.112190.

J. N. Reddy. *Mechanics of laminated composite plates and shells*. CRC Press, Boca Raton, FL, 2 edition, Nov. 2003.

J. N. Reddy. *Introduction to the finite element method*. McGraw-Hill Education, 2019.

A. Saltelli, M. Ratto, T. Andres, F. Campolongo, J. Cariboni, D. Gatelli, M. Saisana, and S. Tarantola. Introduction to sensitivity analysis. *Global sensitivity analysis. The primer*, pages 1–51, 2008.

K. Sargsyan. Surrogate models for uncertainty propagation and sensitivity analysis. In *Handbook of Uncertainty Quantification*, pages 673–698. Springer International Publishing, 2017. doi: 10.1007/978-3-319-12385-1_22. URL https://doi.org/10.1007/978-3-319-12385-1_22.

E. Simoen, C. Papadimitriou, and G. Lombaert. On prediction error correlation in bayesian model updating. *Journal of Sound and Vibration*, 332(18):4136–4152, 2013.

R. Weinstock. *Calculus of Variations*. Dover Books on Mathematics. Dover Publications, Mineola, NY, July 1975.

O. C. Zienkiewicz, R. L. Taylor, and J. Z. Zhu. *The finite element method: Its basis and fundamentals*. The Finite Element Method. Butterworth-Heinemann, Oxford, England, 7 edition, Oct. 2013.

W. B. Zimmerman. *Multiphysics modeling with finite element methods*, volume 18. World Scientific Publishing Company, 2006.

Q. Zu-Qing. *Model order reduction techniques with applications in finite element analysis*. Springer, London, England, 2004 edition, Aug. 2004.

Chapter 18

An Application of Finite Element Method and Sensitivity Analysis in Structural Dynamics

An Application of Finite Element Method and Sensitivity Analysis in Structural Dynamics

Suzana Moreira Avila[1][*] and Zenon J. Guzman del Prado[2],

[1]Post-Graduate Program - Integrity of Engineering Materials, University of Brasilia, Brazil. E-mail: avilas@unb.br
[2]Graduate Program in Geotechnics, Structures and Civil Construction, Federal University of Goiás, Brazil. E-mail: zenon@ufg.br

*Corresponding author

Abstract

In this chapter a short description of finite element method applied to linear structural dynamics is initially described. Modal analysis, modal superposition method, and numerical methods for the eigenvalue and eigenvector problem are described. Finally, a sensitivity analysis of free vibration problem applied to plane frames is performed to study the sensitivity of loss of stiffness on the natural frequencies and corresponding vibration modes.

Keywords: Structural dynamics, finite element method, sensitivity analysis, eigenvalue problem

1 Introduction

Structural dynamics is a research area focused on the analysis of the behavior of structural members subjected to dynamic loads, responsible for generating a response that includes the emergence of accelerations and velocities, in addition to displacements, all varying in time. Dynamic loads originating from several factors (people, wind, sea waves, vehicle traffic, earthquakes and explosions, among others) are characterized by having their magnitude, direction and application point varying in time. Applications of structural dynamics can be widely found in several engineering areas, such as: aerospace, automotive, mechanical and civil engineering. It is worth mentioning that the principles and solution techniques are the same, despite the variety of applications (Figure 1).
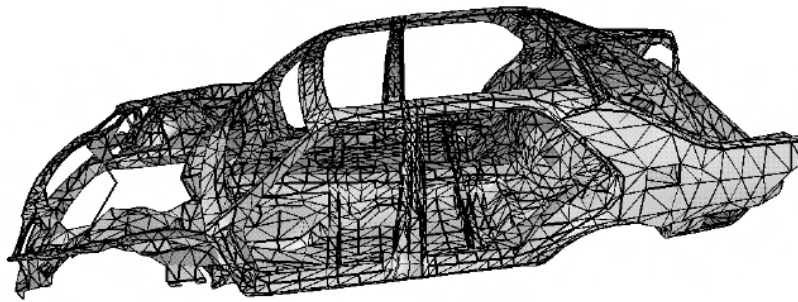
Figure 1 – Finite Element Model of the Car Structure (Hemez & Pagnacco [2000])

The importance of this kind of analysis is supported by the occurrence of structural failures caused by excessive dynamic response, which can result not only in impairing the functioning of machines and equipment, in economic damage due to the structural collapse, but also in the inestimable loss of human lives.

Structural dynamics has a vast literature available and several good textbooks. (Paz & Kim [2019], Cook et al [1989]; Clough & Penzien [1993], Chopra [1995], Craig & Kurdila [2006], Tedesco et al [1998], Rao [2011]). The problems studied in this area include, among others, two broad categories: obtaining frequencies and associated vibration modes and analyzing the response in the time domain.

The Finite Element Method (FEM) was originally conceived by Clough in the 60s (Clough [1960]), currently it is a computational tool consecrated not only in structural analysis, but also in solving problems in the areas of fluid dynamics and thermodynamics, among others. It is a numerical procedure to solve engineering boundary value problems that are very complex to solve via classical analytical methods. This complexity is present for example on non trivial geometrical configurations, material properties or loading conditions. The philosophy of the method is based on discretizing the continuum into a finite number of elements interconnected at certain points called nodes or joints, building a system mesh. Formulating the boundary value problem results in a system of algebraic equations. The idea is that the solution of the various appropriately selected elements falls into a solution that converges to the exact solution of the global system as the size of the elements is reduced.

The application of FEM to the structural dynamic analysis is made by establishing the equations of motion for a finite element given, then setting up the global equations of motion of the system from the chosen discretized mesh. The problem lies in the solution of the resulting system of ordinary differential equations for the case of undamped free vibrations that provide natural frequencies and associated modes of vibration. Additionally, the solution of the forced vibration problem will result in the response of the structure in the time domain.

In this chapter, a short description of finite element modelling will be described, then modal analysis and orthogonality of modes will be considered. Description of different methods to solve the eigenvalue and eigenvector problem is considered, as well as modal superposition

method. Finally, sensitivity analysis is performed to study the effect of loss of stiffness in the system natural frequencies and associated mode vibrations.

2 Modelling in Finite Element

To perform a dynamic analysis using the finite element method, the system of dynamic equilibrium equations should be assembled. For this, the element time dependent field displacements vector $\hat{\mathbf{u}}(t, x_1, x_2, x_3)_{(e)}$, in x_1, x_2, and x_3 directions, is composed by displacements $u_1(t,x_1,x_2,x_3)$, $u_2(t,x_1,x_2,x_3)$ and $u_3(t,x_1,x_2,x_3)$, respectively. This displacements vector can be described as a linear combination of time dependent nodal displacements $\mathbf{u}(t)$ and shape functions $\mathbf{N}(x_1,x_2,x_3)$ given by (Busby and Staab [2018], Bathe [1996] and Rao [2004]):

$$\hat{\mathbf{u}}(t, x_1, x_2, x_3)_{(e)} = \begin{Bmatrix} u_1(t, x_1, x_2, x_3) \\ u_2(t, x_1, x_2, x_3) \\ u_3(t, x_1, x_2, x_3) \end{Bmatrix}_{(e)} = \mathbf{N}(x_1, x_2, x_3)\mathbf{u}(t) \qquad (1)$$

Considering both small displacements and small rotations and linear elastic material, the strain-displacements, and stress-strain relations, in index notation, are given by:

$$\varepsilon_{ij} = \frac{1}{2}\left(\frac{\partial u_i}{\partial x_j} + \frac{\partial u_j}{\partial x_i}\right) = \frac{1}{2}\left(u_{i,j} + u_{j,i}\right) \quad i,j = 1,2,3 \qquad (2)$$

$$\sigma_{ij} = C_{ijkl}\varepsilon_{kl} \quad i,j,k,l = 1,2,3 \qquad (3)$$

where ε_{ij} are the linear strain components, σ_{ij} are the stress components and C_{ijkl} is the fourth order constitutive tensor.

Substituting Eq (1) into Eq. (2), the finite element strain-stress relations can be given as:

$$\boldsymbol{\varepsilon} = \mathbf{D}\mathbf{N}(x_1, x_2, x_3)\mathbf{u}(t)_e = \mathbf{B}\mathbf{u}(t)_e \qquad (4)$$

where $\mathbf{D}$ is the derivatives matrix and $\mathbf{B}$ is the deformation matrix.

Substituting Eq. (4) in Eq. (3) the stress-strain relations result as:

$$\boldsymbol{\sigma} = \mathbf{C}\boldsymbol{\varepsilon} = \mathbf{C}\mathbf{B}\mathbf{u}(t)_e \qquad (5)$$

where $\mathbf{C}$ is the constitutive matrix.

The elastic strain energy of a finite element can be written as:

$$\mathrm{U}^{(e)} = \frac{1}{2}\iiint_{V^{(e)}} \boldsymbol{\varepsilon}^T \boldsymbol{\sigma}\, dV \qquad (6)$$

The total work of external forces is given by:

$$\mathrm{W}^{(e)} = \iiint_{V^{(e)}} \hat{\mathbf{u}}_{(e)}^T \mathbf{b}\, dV + \iint_{S_t^{(e)}} \hat{\mathbf{u}}_{(e)}^T \mathbf{t}\, dS + \sum_{i=1}^{N} \hat{\mathbf{u}}_{(e)}^T \mathbf{F}_i \qquad (7)$$

Where vector **b** represents the body forces of the finite element, vector **t** represents the surface forces acting on finite element and $\mathbf{F}_i$ represents the concentrated nodal forces acting on the finite element.

Then, the potential energy of a finite element can be written as:

$$\Pi^{(e)} = U - W$$

$$\Pi^{(e)} = \frac{1}{2} \iiint_{V^{(e)}} \boldsymbol{\varepsilon}^T \boldsymbol{\sigma} dV - \iiint_{V^{(e)}} \hat{\mathbf{u}}_{(e)}^T \mathbf{b} \ dV - \iint_{S_t^{(e)}} \hat{\mathbf{u}}_{(e)}^T \mathbf{t} \ dS - \sum_{i=1}^{N} \hat{\mathbf{u}}_{(e)}^T \mathbf{F}_i \tag{8}$$

Substituting Eq. (4) and Eq. (5) in Eq. (8), the potential energy can be written as:

$$\Pi^{(e)} = \frac{1}{2} \mathbf{u}^T \iiint_{V^{(e)}} \mathbf{B}^T \mathbf{CB} \ dV \ \mathbf{u}$$
$$- \mathbf{u}^T \left(\iiint_{V^{(e)}} \mathbf{N}^T \mathbf{b} \ dV - \iint_{S_t^{(e)}} \mathbf{N}^T \mathbf{t} dS - \sum_{i=1}^{N} \mathbf{N}^T \mathbf{F}_i \right) \tag{9}$$

and simplifying:

$$\Pi^{(e)} = \frac{1}{2} \mathbf{u}^T \mathbf{k} \mathbf{u} - \mathbf{u}^T \mathbf{f} \tag{10}$$

Where the finite element stiffness matrix is given by:

$$\mathbf{k} = \iiint_{V^{(e)}} \mathbf{B}^T \mathbf{CB} \ dV \tag{11}$$

And the finite element load vector is given by:

$$\mathbf{f} = \iiint_{V^{(e)}} \mathbf{N}^T \mathbf{b} \ dV + \iint_{S_t^{(e)}} \mathbf{N}^T \mathbf{t} dS + \sum_{i=1}^{N} \mathbf{N}^T \mathbf{F}_i \tag{12}$$

For a finite element, the kinetic energy can be written as:

$$T^{(e)} = \frac{1}{2} \iiint_{V^{(e)}} \rho \dot{\hat{\mathbf{u}}}_{(e)}^T \dot{\hat{\mathbf{u}}}_{(e)} \ dV \tag{13}$$

Substituting Eq. (1) in Eq. (13), the kinetic energy of a finite element results in:

$$T^{(e)} = \frac{1}{2} \iiint_{V^{(e)}} \rho \dot{\mathbf{u}}^T \mathbf{N}^T \mathbf{N} \dot{\mathbf{u}} \ dV = \frac{1}{2} \dot{\mathbf{u}}^T \left[\iiint_{V^{(e)}} \rho \mathbf{N}^T \mathbf{N} \ dV \right] \dot{\mathbf{u}} = \frac{1}{2} \dot{\mathbf{u}}^T \mathbf{m} \dot{\mathbf{u}} \tag{14}$$

Where m is the mass matrix of the finite element given by

$$\mathbf{m} = \iiint_{V^{(e)}} \rho \mathbf{N}^T \mathbf{N} \ dV \tag{15}$$

Matrix **m** is known as consistent matrix because it is a full matrix containing the coupling of inertial contribution of all nodal displacements. However, it is possible to consider a

lumped mass matrix where there is not coupling between inertial contribution of nodal displacements, and it is a diagonal mass matrix and every term in diagonal is associated to a concentrated mass in the direction of each nodal displacement.

Energy dissipation is a non-conservative force and can be considered in several ways, one of the most common is to consider that damping is proportional to velocity of displacements, known as viscous damping.

The energy dissipation of a finite element can be written as:

$$R^{(e)} = \frac{1}{2} \iiint_{V^{(e)}} \xi \dot{\hat{\mathbf{u}}}_{(e)}^T \dot{\hat{\mathbf{u}}}_{(e)} \, dV \tag{16}$$

Where ξ is the distributed damping coefficient.

Substituting Eq. (1) in Eq. (17), the damping of a finite element is given by:

$$R^{(e)} = \frac{1}{2} \iiint_{V^{(e)}} \xi \dot{\mathbf{u}}^T \mathbf{N}^T \mathbf{N} \dot{\mathbf{u}} \, dV = \frac{1}{2} \dot{\mathbf{u}}^T \iiint_{V^{(e)}} \xi \mathbf{N}^T \mathbf{N} \, dV \, \dot{\mathbf{u}} = \frac{1}{2} \dot{\mathbf{u}}^T \mathbf{c} \dot{\mathbf{u}} \tag{17}$$

Where the damping matrix of a finite element is:

$$\mathbf{c} = \iiint_{V^{(e)}} \xi \mathbf{N}^T \mathbf{N} \, dV \tag{18}$$

The global mass (**M**), stiffness (**K**) and damping (**C**) matrix, as well as the global vector loads are assembled by adding or combining the contribution of all elements that are connected to a specific node. This matrix can be written as:

$$\mathbf{M} = \sum_{e=1}^{N_e} \mathbf{m} \tag{19}$$

$$\mathbf{K} = \sum_{e=1}^{N_e} \mathbf{k} \tag{20}$$

$$\mathbf{C} = \sum_{e=1}^{N_e} \mathbf{c} \tag{21}$$

$$\mathbf{F} = \sum_{e=1}^{N_e} \mathbf{f} \tag{22}$$

Finally, the system of coupled ordinary differential dynamic equilibrium equations is given by:

$$\mathbf{M}\ddot{\mathbf{u}} + \mathbf{C}\dot{\mathbf{u}} + \mathbf{K}\mathbf{u} = \mathbf{F} \tag{23}$$

Before solving it, the boundary conditions and initial conditions should be applied. Equations (23) can be solved directly or by using the modal superposition method to uncouple the system of equations and some direct numerical integration method can be considered (Newmark, Central difference, Runge Kutta methods) (Bathe and Wilson [1976]).

3 Modal Analysis

A modal analysis of a system of multiple degrees of freedom (MDOF) provides the system characteristic features which are its natural vibration frequencies and associated modes of vibration. These properties are intrinsic to the system and are related to its material and geometry.

The modal analysis can be performed experimentally through tests where the system is monitored through sensors, such as accelerometers, and undergoes an external disturbance as a source of excitation.

Natural frequencies and associated vibration modes can still be determined numerically. The solution of the free vibration problem provides these characteristics of the system. There is no action by outside forces and the movement is governed only by the initial conditions.

An undamped MDOF system subjected to free vibration is governed by the following equations of motion:

$$\mathbf{M\ddot{u} + Ku = 0} \tag{24}$$

The system is subjected to the following set of initial conditions:

$$\mathbf{u = u}(0); \quad \mathbf{\dot{u} = \dot{u}}(0) \tag{25}$$

This system has a solution in the form:

$$\mathbf{u = \phi}\sin{(\omega t + \phi)} \tag{26}$$

Substituting Eq. (26) into Eq. (24), we obtain:

$$(\mathbf{K} - \omega^2\mathbf{M})\mathbf{\phi = 0} \tag{27}$$

This problem has a trivial solution $\mathbf{\tilde{u} = 0}$ and only has non-trivial solutions if:

$$(\mathbf{K} - \omega^2\mathbf{M}) = \mathbf{0} \tag{28}$$

Eq. (28) is known as the characteristic equation and the roots of the characteristic equation determine the n natural frequencies ω_n (eigenvalues). For each ω_n there is a corresponding $\mathbf{\phi}$ vector (eigenvector). The eigenvectors determine the natural modes of vibration ϕ_n.

The modal matrix $\mathbf{\Phi}$ is constructed with n columns, where each column corresponds to a mode of vibration of the system. The fundamental mode is associated with the lowest frequency, meanwhile the other modes are called harmonics and the movement of the system is given by the superposition of the harmonics.

3.1 Modal orthogonality

The vibration modes of a MDOF system have a very important property called orthogonality. The orthogonality of the eigenvector system is with respect to the mass matrix $\mathbf{M}$ and the stiffness matrix $\mathbf{K}$. This property constitutes the basis for one of the most important methods of solving dynamical systems: the Modal Superposition Method.

Rewriting Eq. (27) in the form

$$K\boldsymbol{\phi} = \omega^2 M\boldsymbol{\phi} \tag{29}$$

Considering two pairs of different solutions $(\omega_r^2, \boldsymbol{\phi}_r$ e $\omega_s^2, \boldsymbol{\phi}_s)$, eq. (29) can be rewritten as:

$$K\boldsymbol{\phi}_r = \omega_r^2 M\boldsymbol{\phi}_r \tag{30}$$

$$K\boldsymbol{\phi}_s = \omega_s^2 M\boldsymbol{\phi}_s \tag{31}$$

Pre-multiplying both sides of eq. (30) by $\boldsymbol{\phi}_s^T$ then:

$$\boldsymbol{\phi}_s^T K\boldsymbol{\phi}_r = \omega_r^2 \boldsymbol{\phi}_s^T M\boldsymbol{\phi}_r \tag{32}$$

Similarly for equation (31) multiplying both sides by $\boldsymbol{\phi}_r^T$ comes to

$$\boldsymbol{\phi}_r^T K\boldsymbol{\phi}_s = \omega_s^2 \boldsymbol{\phi}_r^T M\boldsymbol{\phi}_s \tag{33}$$

As the matrices M and K are symmetric, then $K = K^T$ and $M = M^T$. Therefore equation (33) can be transposed and rewritten as

$$\boldsymbol{\phi}_s^T K\boldsymbol{\phi}_r = \omega_s^2 \boldsymbol{\phi}_s^T M\boldsymbol{\phi}_r \tag{34}$$

Equation (32) can be subtracted from eq. (33) provides

$$(\omega_r^2 - \omega_s^2)\boldsymbol{\phi}_s^T M\boldsymbol{\phi}_r = 0 \tag{35}$$

For modes with different frequencies $\omega_r \neq \omega_s$ it is necessary that

$$\boldsymbol{\phi}_s^T M\boldsymbol{\phi}_r = 0 \tag{36}$$

The r-th and s-th modes are said to be orthogonal to the mass matrix. Equation (36) can be substituted into Equation (32) to show that the r-th mode and the s-th mode are also orthogonal with respect to the stiffness matrix:

$$\boldsymbol{\phi}_s^T K\boldsymbol{\phi}_r = 0 \tag{37}$$

These mode orthogonality conditions are the essence of the Modal Superposition Method.

3.2 Mode normalization

The vibration amplitudes in a mode are just relative values that can be scaled or normalized to some extent, as a matter of choice. A convenient form of normalization for a general system is:

$$\boldsymbol{\phi}'_{ij} = \frac{\boldsymbol{\phi}_{ij}}{\sqrt{\boldsymbol{\phi}_i^T M\boldsymbol{\phi}_j}} \tag{38}$$

i= i-th element of the eigenvector

j= jth vibration mode

For a system with a diagonal mass matrix

$$\boldsymbol{\phi}'_{ij} = \frac{\boldsymbol{\phi}_{ij}}{\sqrt{\sum_{k=1}^n m_k \boldsymbol{\phi}_{kj}^2}} \tag{39}$$

$$\phi'_{ij} = \frac{\phi_{ij}}{\sqrt{\phi_j^\mathsf{T} M \phi_j}} \tag{40}$$

For normalized eigenvectors the orthogonality condition is given by:

$$\begin{aligned} \phi'^T_i M \phi_j &= 0 \text{ with } i \neq j \\ &= 1 \text{ with } i = j \end{aligned} \tag{41}$$

Another orthogonality condition is obtained by writing Equation (29) for the normalized mode *j* as:

$$K\phi'_j = \omega_j^2 M \phi'_j \tag{42}$$

Pre-multiplying eq. (42) by ϕ_i^T we obtain the following orthogonality condition between the eigenvectors

$$\begin{aligned} \phi'^T_i K \phi_j &= 0 \quad \text{with } i \neq j \\ &= \omega_j^2 \text{ with } i = j \end{aligned} \tag{43}$$

4 Numerical Solution for Natural Frequencies and Vibration Modes

A critical step in the dynamic analysis of a MDOF system is the solution or determination of the corresponding natural frequencies and associated vibration modes. Especially in the case of an analysis by Modal Superposition.

For minor problems the solution to this problem lies in the determination of a characteristic polynomial. For high-order MDOF systems, extracting these roots manually becomes prohibitive.

Over the years, several numerical techniques have been developed to solve this type of problem. They are essentially iterative techniques and can mean a considerable computational effort. The present mathematical problem is given by:

$$K\Phi = \lambda M \phi \tag{44}$$

where the eigenvalues are $\lambda_r = \omega^2$ and the eigenvectors are ϕ_r.

The response of a MDOF system with a large number of degrees of freedom is generally restricted to a relatively small subset of the system's lowest vibration modes. Thus, it is only necessary to solve for a number p of eigenvalue / eigenvector sets.

Most solution techniques for this type of problem can be classified into 3 basic categories:
- Vector iteration methods
- Transformation methods
- Polynomial iteration methods.

The most common eigenproblems that are encountered in general scientific analysis are standard eigenproblems, and most other eigenproblems can be reduced to a standard form.

For this reason, the solution of standard eigenproblems has attracted much attention in numerical analysis, and many solution algorithms are available.

When the mode superposition method is performed, the computational effort relays on obtaining natural frequencies and associated vibration modes. Effective numerical algorithms for this calculation have been widely studied since the exact solution of this type of problem is prohibitive when the system order is large.

In the literature it can be found several eigenvalue/eigenvector solution algorithms. They are generally formulated for ordinary matrices. When working on a finite element method perspective the matrices involved have peculiarities, such as being banded, positive definite among others. It is recommendable that the solution techniques benefit from these properties searching a more economic solution.

The approximate solution techniques have primarily been developed to calculate the lowest eigenvalues and corresponding eigenvectors in the Eq. (44), when the order of the system is large. Most programs use exact solution techniques in the analysis of small-order systems. However, the problem of calculating the few lowest eigenpairs of relatively large-order systems is very important and is encountered in all branches of structural engineering. In the following sections we present three major techniques, all of which, in fact, can be considered to be a Ritz analysis.

Consider that we have mass and stiffness matrices, K and M, definite positives. The consistent or lumped mass matrix has all the elements outside of the diagonal different from zero. The eigenvalue calculated by Ritz analysis is an upper limit of the system exact eigenvalue. The associated error is not taken into account. This error will depend on the Ritz vector base considered, since the eigenvector ϕ is a linear combination of this vector base.

The Ritz procedure is a very general one, various analysis methods known by different names can be classified as Ritz analysis. One of the most important aspects in the analysis is the base vector choice.

All the methods are iterative by nature since they try to solve the eigenvalue problem that is equivalent to calculate the roots of the characteristic polynomial $P(\lambda)$ that has the same order of the mass and stiffness matrices. There is no exact solution to polynomials with order higher than four, so it is necessary to perform iterative techniques.

What can be done before the iterative method is to transform K and M in a way to allow a more economic computational effort, one example is the static condensation technique.

There is no such as an unique algorithm that gives an efficient solution. The method accuracy depends considerably on two factors: reliability and computational effort.

4.1 Vector iteration methods

The philosophy of this family method is to satisfy the equation (44) by operating directly on it. It is assumed a vector $\mathbf{x}_1$ for ϕ, and assume the associated eigenvalue λ equal to $\mathbf{1}$. Equation (44) can be rewritten as

$$\mathbf{R}_1 = \mathbf{1}M\mathbf{x}_1 \tag{45}$$

$\mathbf{R}_1$ is not yet determined since not necessarily an eigenvector. There is an equilibrium equation given by

$$\mathbf{Kx}_2 = \mathbf{R}_1, \mathbf{x}_2 \neq \mathbf{x}_1 \tag{46}$$

$\mathbf{x}_2$ is the displacement solution to the applied forces $\mathbf{R}_1$. It means to be a better approximation to the eigenvector than $\mathbf{x}_2$, repeating the procedure several times it can be obtained a superior approximation to $\boldsymbol{\phi}$.

This methodology is the way of work basically of inverse iteration. This procedure has a good performance on obtaining an eigenvector and also the eigenvalue associated.

Assume that $\mathbf{K}$ is positive definite and $\mathbf{M}$ is a diagonal matrix without zero diagonal elements. Assume an initial iteration vector $\mathbf{x}_1$ and then evaluate in each iteration step $k = 1,2,...$

$$\mathbf{K}\bar{\mathbf{x}}_{k+1} = \mathbf{Mx}_k \tag{47}$$

and

$$\mathbf{x}_{k+1} = \frac{\bar{\mathbf{x}}_{k+1}}{\left(\bar{\mathbf{x}}_{k+1}^T \mathbf{M}\bar{\mathbf{x}}_{k+1}\right)^{1/2}} \tag{48}$$

It has to be assured that $\mathbf{x}_1^T \mathbf{M}\boldsymbol{\phi}_1 \neq 0$, in other words $\mathbf{x}_1$ is not orthonormal to $\boldsymbol{\phi}_1$, so we can assume that

$$\mathbf{x}_{k+1} \longrightarrow \boldsymbol{\phi}_1 \text{ as } k \longrightarrow \infty \tag{49}$$

Equation (47) has to be solved evaluating a vector $\bar{\mathbf{x}}_{k+1}$ getting closer to an eigenvector compared to the preceding iteration $\mathbf{x}_k$. According to (48) it is needed that the orthonormality relation above is complied

$$\mathbf{x}_{k+1}^T \mathbf{Mx}_{k+1} = 1 \tag{50}$$

The equations (47) and (48) depict the basic inverse iteration algorithm. for computational implementation we can consolidate in the form

$$\mathbf{K}\bar{\mathbf{x}}_{k+1} = \mathbf{y}_k \tag{51}$$

$$\bar{\mathbf{y}}_{k+1} = \mathbf{M}\bar{\mathbf{x}}_{k+1} \tag{52}$$

$$\rho\left(\bar{\mathbf{x}}_{k+1}\right) = \frac{\bar{\mathbf{x}}_{k+1}^T \mathbf{y}_k}{\bar{\mathbf{x}}_{k+1}^T \bar{\mathbf{y}}_{k+1}} \tag{53}$$

$$\mathbf{y}_{k+1} = \frac{\bar{\mathbf{y}}_{k+1}}{\left(\bar{\mathbf{x}}_{k+1}^T \bar{\mathbf{y}}_{k+1}\right)^{1/2}} \tag{54}$$

Consider that $\mathbf{y}_1^T \boldsymbol{\phi}_1 \neq 0$, is guaranteed,

$$\mathbf{y}_{k+1} \longrightarrow \mathbf{M}\boldsymbol{\phi}_1 \tag{55}$$

$$\rho\left(\bar{\mathbf{x}}_{k+1}\right) \longrightarrow \lambda_1 \text{ as } k \longrightarrow \infty \tag{56}$$

The Raylegh quotient $\rho\left(\bar{\mathbf{x}}_{k+1}\right)$ gives an approximation to the eigenvalue λ_1 that is considered to set up the convergence criterion

$$\frac{\left|\lambda_1^{(k+1)} - \lambda_1^{(k)}\right|}{\lambda_1^{(k+1)}} \leq \text{tol} \tag{57}$$

For the last iteration we have

$$\lambda_1 \doteq \rho\left(\bar{\mathbf{x}}_{l+1}\right) \tag{58}$$

and

$$\phi_1 \doteq \frac{\bar{\mathbf{x}}_{l+1}}{\left(\bar{\mathbf{x}}_{l+1}^T \bar{\mathbf{y}}_{l+1}\right)^{1/2}} \tag{59}$$

Transformation methods

This set of techniques called Transformation Methods include procedures that take into account basic properties of the eigenvectors in matrix $\mathbf{\Phi}$,

$$\mathbf{\Phi}^T \mathbf{K} \, \mathbf{\Phi} = \mathbf{\Lambda} \tag{60}$$

$$\mathbf{\Phi}^T \mathbf{M} \mathbf{\Phi} = \mathbf{I} \tag{61}$$

The matrix $\mathbf{\Phi}$ that diagonalize $\mathbf{K}$ and $\mathbf{M}$ is unique, it can be found iteratively.

We have to reduce $\mathbf{K}$ and $\mathbf{M}$ to their diagonal way pre and post multiplying them by the matrices $\mathbf{P}_k^T$ and $\mathbf{P}_k$, respectively where $k = 1,2,\dots$ It starts with $\mathbf{K}_1 = \mathbf{K}$ and $\mathbf{M}_1 = \mathbf{M}$, and it follows:

$$\begin{aligned}
\mathbf{K}_2 &= \mathbf{P}_1^T \mathbf{K}_1 \mathbf{P}_1 \\
\mathbf{K}_3 &= \mathbf{P}_2^T \mathbf{K}_2 \mathbf{P}_2 \\
&\quad . \\
&\quad . \\
\mathbf{K}_{k+1} &= \mathbf{P}_k^T \mathbf{K}_k \mathbf{P}_k
\end{aligned} \tag{62}$$

In the same way

$$\begin{aligned}
\mathbf{M}_2 &= \mathbf{P}_1^T \mathbf{M}_1 \mathbf{P}_1 \\
\mathbf{M}_3 &= \mathbf{P}_2^T \mathbf{M}_2 \mathbf{P}_2 \\
&\quad . \\
&\quad . \\
\mathbf{M}_{k+1} &= \mathbf{P}_k^T \mathbf{M}_k \mathbf{P}_k
\end{aligned} \tag{63}$$

To converge the process, it is necessary that

$$\mathbf{K}_{k+1} \longrightarrow \mathbf{\Lambda}$$
$$\mathbf{M}_{k+1} \longrightarrow \mathbf{I} \tag{64}$$
$$k \longrightarrow \infty$$

The last iteration is given by:

$$\mathbf{\Phi} = \mathbf{P}_1 \mathbf{P}_2 \dots \mathbf{P}_l \tag{65}$$

It is not really necessary that $\mathbf{M}_{k+1} \longrightarrow \mathbf{I}$ and $\mathbf{K}_{k+1} \longrightarrow \mathbf{\Lambda}$ but yes that they converge to a diagonal form. Based on the methodology described above several iteractive methods have been proposed such as Jacobi and the Householder-QR methods, very effective in finite element analysis.

Polynomial iteration techniques

The eigenvalue and eigenvector problem lies in the solution of calculating the zeros of a polynomial of degree n, known as a characteristic polynomial, given by

$$P(\lambda) = \det(\mathbf{K} - \lambda \mathbf{M}) \tag{66}$$

The characteristic polynomial roots represent the eigenvalues of the eigenproblem

$$\mathbf{K}\boldsymbol{\phi} = \lambda \mathbf{M}\boldsymbol{\phi} \tag{67}$$

Solving this problem relay in two different strategies: explicit and implicit evaluation procedures, which can use the same basic iteration schemes. It directly uses the K and M matrices from finite element modeling without transforming the problem to a different form. Only the eigenvalues are obtained and the eigenvectors can be obtained by inverse iteration with substitution.

Explicit polynomial iteration

The characteristic polynomial is written as

$$P(\lambda) = a_0 + a_1\lambda + a_2\lambda^2 + \cdots + a_n\lambda^n \tag{68}$$

and the polynomial coefficients $a_0, a_1, \ldots, a_n$ are evaluated. Then the polynomial roots are calculated. Small errors in the coefficients cause considerable errors in the roots of the polynomial. For this reason this method fell into disuse for the eigenproblem solution.

Implicit polynomial iteration

In this method the value of the characteristic polynomial is evaluated directly without the need to calculate the coefficients. The value of $P(\lambda)$ can be obtained effectively by decomposing $\mathbf{K} - \lambda \mathbf{M}$ into a lower triangular matrix L and an upper triangular matrix S:

$$\mathbf{K} - \lambda \mathbf{M} = \mathbf{LS} \tag{69}$$

$$\det(\mathbf{K} - \lambda \mathbf{M}) = \prod_{i=1}^{n} s_{ii} \tag{70}$$

5 Modal Superposition Method

If the main vibration modes of a MDOF system are used as a generalized coordinate system to define the motion response, the *n* motion equations become decoupled. In these independent coordinates, each uncoupled equation can be solved independently, as if each equation belonged to an independent single degree of freedom system.

Therefore, the individual responses of the *n* MDOF system decoupled equations (one for each vibration mode) for any form of excitation can be determined by applying analysis techniques to onde degree of freedom (1DOF) system. The modal superposition MDOF system response is then defined by the sum of the individual mode responses.

The Modal Superposition Method is a very popular vibration analysis technique, but it has some important limitations. The method is valid only for linear and proportional damping systems. This is most useful when the response can be accurately evaluated considering only a relatively small subset of system modes.

It should be noted, however, that for most dynamic loadings on structural and mechanical systems, the contributions of the various modes to the dynamic response are generally more considerable at lower frequencies and tend to decay at higher frequencies.

Consequently, it is not necessary to include the higher modes in the superposition process.

The motion equation for a structural system subjected to dynamic excitations is given by

$$\mathbf{M\ddot{x} + C\dot{x} + Kx = P}(t) \tag{71}$$

Where **M**, **C** and **K** are the mass, damping and stiffness matrices of the structure and P(t) is the dynamic loading vector. $\ddot{x}$, $\dot{x}$ e x are the vectors of acceleration, velocities and displacements, respectively.

The natural frequencies ω_i and the vibration modes $\boldsymbol{\phi}_i$ corresponding to each i-th degree of freedom of the structure (i = 1,2,...,N) can be obtained by solving the eigenvalue problem

$$\mathbf{K}\boldsymbol{\phi}_i = \omega_i^2 \mathbf{M}\boldsymbol{\phi}_i \tag{72}$$

The matrix whose columns are the modal forms $\boldsymbol{\phi}_i$ is called $\boldsymbol{\Phi}$, which presents orthogonality properties in relation to the structure's mass and stiffness matrices.

The modes can then be normalized such that the generalized mass and stiffness matrices are:

$$\overline{\mathbf{M}} = \Phi^\mathrm{T}\mathbf{M}\Phi = \mathbf{I} \tag{73}$$

$$\overline{\mathbf{K}} = \Phi^\mathrm{T}\mathbf{K}\Phi \tag{74}$$

$\overline{K}$ is a diagonal matrix whose diagonal elements are the squared natural frequencies.

Through the modal matrix the physical coordinates **x** can be transformed into generalized coordinates **y** through the equation

$$\mathbf{x = \Phi y} \tag{75}$$

The equation of motion in modal coordinates is expressed by

$$\overline{\mathbf{M}}\ddot{\mathbf{y}} + \overline{\mathbf{C}}\dot{\mathbf{y}} + \overline{\mathbf{K}}\mathbf{y} = \overline{\mathbf{P}} \tag{76}$$

In Equation (76) the generalized damping matrix and the generalized loading vector are given, respectively by

$$\bar{\mathbf{C}} = \mathbf{\Phi}^{\mathrm{T}}\mathbf{C}\mathbf{\Phi} \tag{77}$$

$$\bar{\mathbf{P}} = \mathbf{\Phi}^{\mathrm{T}}\mathbf{P} \tag{78}$$

The generalized mass and stiffness matrices are diagonal matrices due to the orthogonality of the vibration modes. For the generalized damping matrix this is not necessarily true, only for the case of the proportional damping matrix

$$\mathbf{C} = a_0\mathbf{M} + a_1\mathbf{K} \tag{79}$$

In the case of proportional damping, the modal matrix $\overline{\boldsymbol{C}}$ is also diagonal and the modal equations of motion become decoupled

$$\boldsymbol{\phi}_i^T\mathbf{C}\boldsymbol{\phi}_i = \begin{cases} 2\omega_i\xi_i\bar{m}_i & i = j \\ 0 & i \neq j \end{cases} \tag{80}$$

The equation of motion of the n vibration mode is given by

$$\bar{m}_n\ddot{y}_n + 2\xi_n\omega_n\bar{m}_n\dot{y}_n + \bar{k}_ny_n = \bar{p}_n(t) \tag{81}$$

or

$$\ddot{y}_n + 2\xi_n\omega_n\dot{y}_n + \omega_n^2y_n = \frac{\bar{p}_n}{\bar{m}_n}(t) \tag{82}$$

with

$$\begin{aligned} \bar{m}_n &= \boldsymbol{\phi}_n^{\mathrm{T}}\mathbf{M}\boldsymbol{\phi}_n \\ \bar{k}_n &= \boldsymbol{\phi}_n^{\mathrm{T}}\mathbf{K}\boldsymbol{\phi}_n \\ \bar{p}_n(t) &= \boldsymbol{\phi}_n^{\mathrm{T}}\mathbf{p}(t) \\ \bar{c}_n &= \boldsymbol{\phi}_n^{T}\mathbf{C}\boldsymbol{\phi}_n = 2\xi_n\omega_n\bar{m}_n \end{aligned} \tag{83}$$

The superposition of the effects corresponding to each modal equation provides the structure response

$$\boldsymbol{x}(t) = \boldsymbol{\phi}_1y_1(t) + \boldsymbol{\phi}_2y_2(t) + \cdots + \boldsymbol{\phi}_ny_n(t) \tag{84}$$

It is not necessary to include all higher modes as for most loads the displacement contributions are greater for lower modes and reduced for higher modes.

6 Sensitivity Analysis in Plane Frames

Consider a beam element of length L, cross section A, inertia I, Young's modulus E, distributed mass m and rotated an angle θ in relation to global coordinates x-y, as seen in Fig. 2. Figure 2(a) shows the six degrees of freedom ($u_1^L, u_2^L, u_3^L, u_4^L, u_5^L$ and u_6^L) in local coordinates and Figure 2(b) shows the six degrees of freedom (u_1, u_2, u_3, u_4, u_5 and u_6) in global coordinates.

(a)   (b)
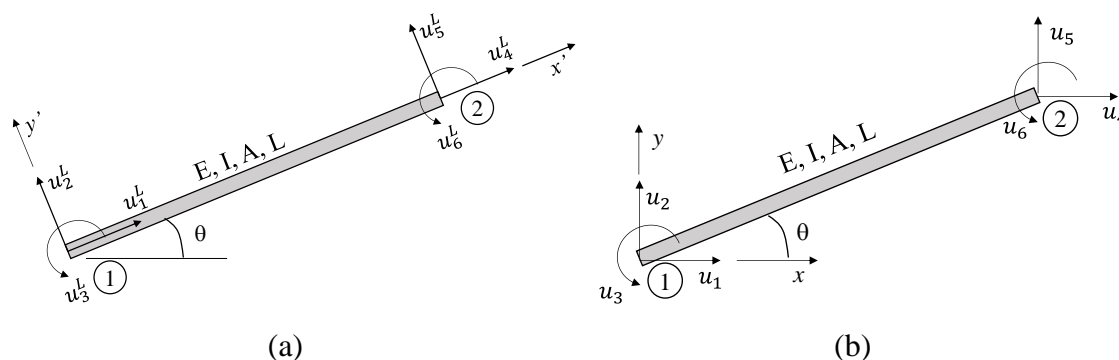
Figure 2 – Beam element. (a) Local coordinates and b) Global coordinates

In order to simulate loss of stiffness at beam joints, it is possible to consider rotational springs of stiffness K_1 and K_2 located at both ends of the beam, which represent semi-rigid joints, as seen in Figure 3 (McGuire, Gallagher and Ziemian, 2000 and Paz and Kim, 2019).

Figure 3 – Beam element with rotational springs at both ends.

Each rotational spring has the following stiffness:

$$K_1 = \alpha_1 \frac{EI}{L} \tag{85}$$

$$K_2 = \alpha_2 \frac{EI}{L} \tag{86}$$

By applying shape functions and compatibility equations, the local beam stiffness matrix can be written as (Paz and Kim, 2019 and McGuire, Gallagher and Ziemian, 2000):

$$\mathbf{k} = \begin{bmatrix} a & 0 & 0 & a & 0 & 0 \\ 0 & b & c & 0 & -b & d \\ 0 & c & e & 0 & -c & f \\ a & 0 & 0 & a & 0 & 0 \\ 0 & -b & -c & 0 & b & -d \\ 0 & d & f & 0 & -d & g \end{bmatrix} \tag{87}$$

Where:

$$a = \frac{EA}{L} \qquad\qquad e = 4\frac{EI}{L}\alpha\left(1 + \frac{3}{\alpha_2}\right) \tag{88}$$

$$b = 12\frac{EI}{L^3}\alpha\left(1 + \frac{\alpha_1 + \alpha_2}{\alpha_1\alpha_2}\right) \qquad\qquad f = 2\frac{EI}{L}\alpha$$

$$c = 6\frac{EI}{L^2}\alpha\left(1 + \frac{2}{\alpha_2}\right) \qquad\qquad g = 4\frac{EI}{L}\alpha\left(1 + \frac{3}{\alpha_1}\right)$$

$$d = 6\frac{EI}{L^2}\alpha\left(1 + \frac{2}{\alpha_1}\right) \qquad\qquad \alpha = \frac{\alpha_1\alpha_2}{\alpha_1\alpha_2 + 4\alpha_1 + 4\alpha_2 + 12}$$

The local beam consistent mass matrix, can be written as:

$$\mathbf{m} = \rho\frac{AL}{420}\begin{bmatrix} 140 & 0 & 0 & 70 & 0 & 0 \\ 0 & 156 & 22L & 0 & 54 & -13L \\ 0 & 22L & 4L^2 & 0 & 13L & -3L^2 \\ 70 & 0 & 0 & 140 & 0 & 0 \\ 0 & 54 & 13L & 0 & 156 & -22L \\ 0 & -13L & -3L^2 & 0 & -22L & 4L^2 \end{bmatrix} \tag{89}$$

The global stiffness and mass matrix can be obtained by applying the rotation matrix as:

$$\mathbf{K} = \mathbf{\Phi}^T\mathbf{k}\mathbf{\Phi} \tag{90}$$

$$\mathbf{M} = \mathbf{\Phi}^T\mathbf{m}\mathbf{\Phi} \tag{91}$$

Where the rotation matrix can be written as:

$$\mathbf{\Phi} = \begin{bmatrix} \cos(\theta) & \sin(\theta) & 0 & 0 & 0 & 0 \\ \sin(\theta) & \cos(\theta) & 0 & 0 & 0 & 0 \\ 0 & 0 & 1 & 0 & 0 & 0 \\ 0 & 0 & 0 & \cos(\theta) & \sin(\theta) & 0 \\ 0 & 0 & 0 & \sin(\theta) & \cos(\theta) & 0 \\ 0 & 0 & 0 & 0 & 0 & 1 \end{bmatrix} \tag{92}$$

To study the effect of loss of stiffness in some joint on the natural frequencies of a system, consider a plane frame as seen in Figure 4.
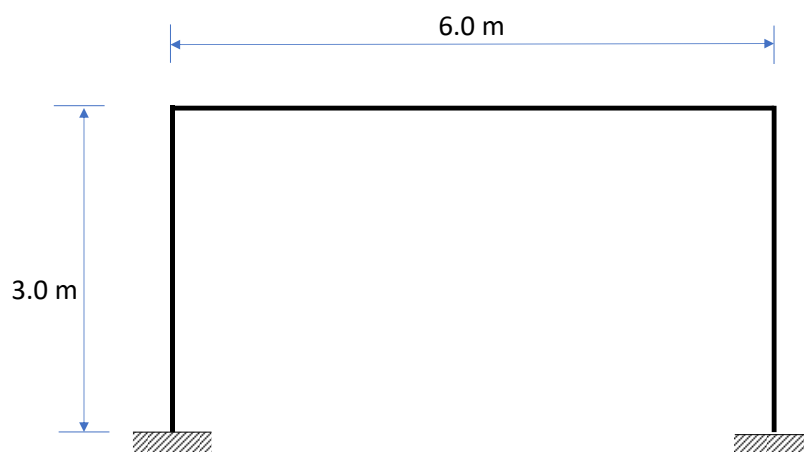
Figure 4 – Plane frame.

The frame has the following geometric and physical properties:

Young´s modulus (E) = 250e5 N/m^2, mass density (ρ) = 3000 kg/m^3.

Beam: Cross section (A) = 0.08 m^2, Moment of inertia (I) = 1.0667e-3 m^4.

Columns: Cross section (A) = 0.048 m^2, Moment of inertia (I) = 6.4e-4 m^4.

The frame was modeled with six beam elements and six nodes as seen in Fig. 5(a) and, at the left joint of element three, a rotational spring was considered to model the loss of stiffness due to reduction of stiffness on the cross section as displayed in Fig. 5(b).

(a)
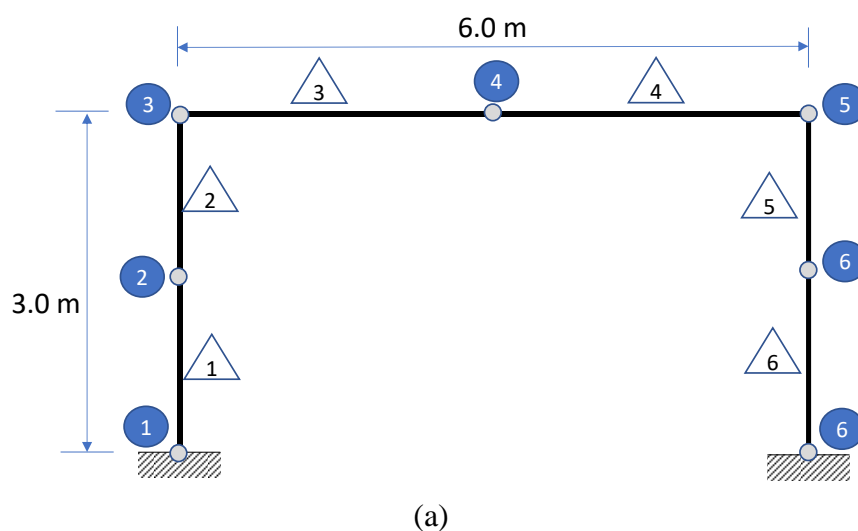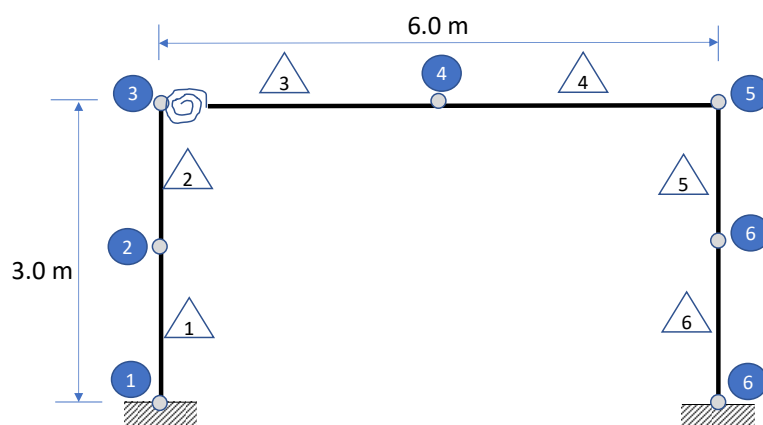
(b)

Figure 5 – Discretized plane frame

To study the influence of loss of stiffness on the natural frequencies and vibration modes of the plane frame, the stiffness of rotational spring was varied. Figure 6 displays the first three natural frequencies and associated vibration modes s the value of α_1 is reduced. As can be seen, there reduction of α_1 generates a reduction the natural frequencies as well as changes on the shape of vibration modes.

Figure 7 displays the variation of the normalized first three natural frequencies for variation of α_1, and as can be observed, the variation of α_1 parameter, does not affect linearly the natural frequencies but, it affects in a non-linear relation. For high values of α_1, the frame is considered with rigid joints and as this parameter is reduced, there is also a reduction of the natural frequencies. All natural frequencies are affected by reduction of α_1 parameter and, it is possible to see, that the first natural frequency is more than second and third natural frequencies.

(a)

(b)

(c)

(d)
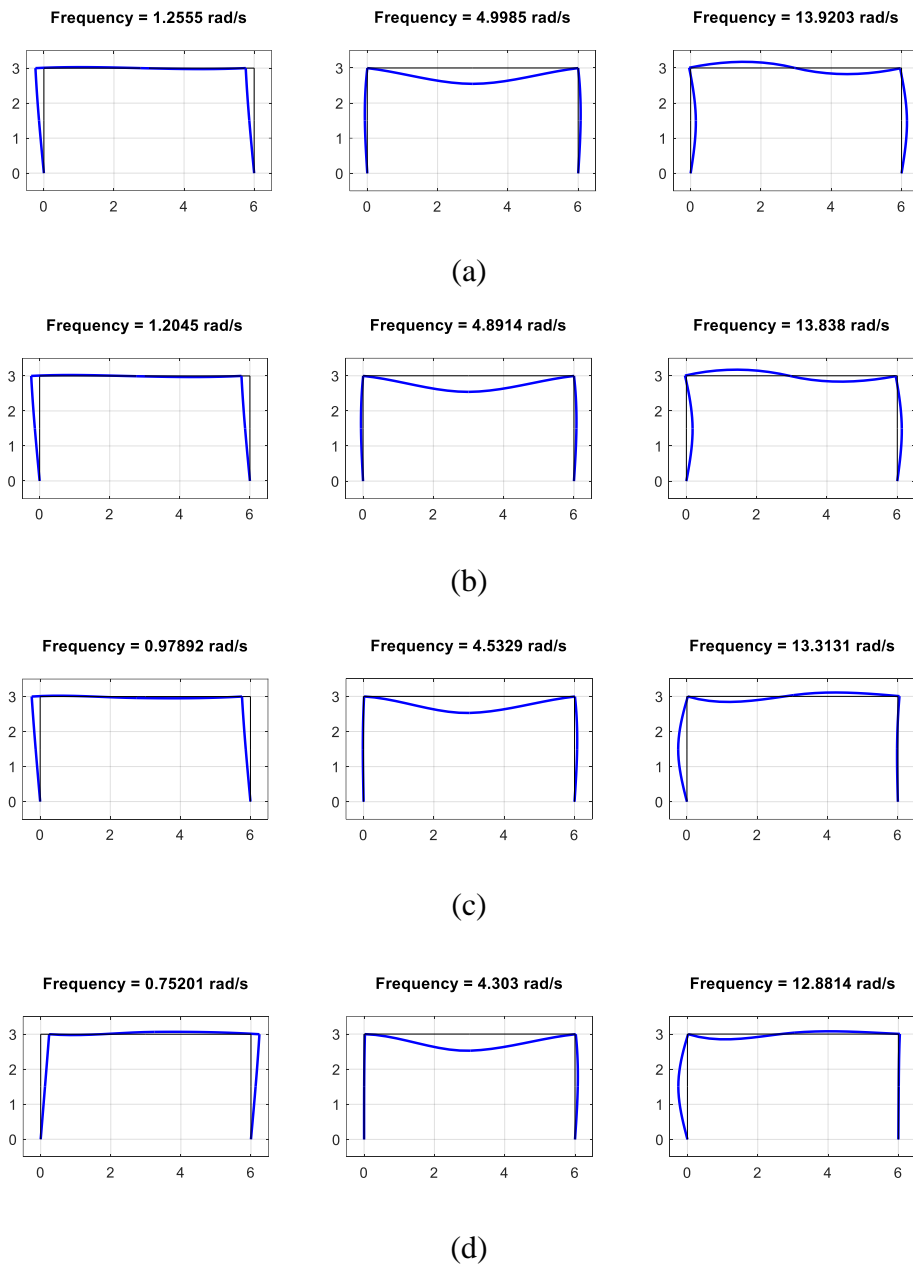
Figure 6: First natural frequencies and associated vibration modes for variation of α_1.
a) $\alpha_1 = 1000.0$, b) $\alpha_1 = 10.0$, c) $\alpha_1 = 1.0$ and d) $\alpha_1 = 0.01$.
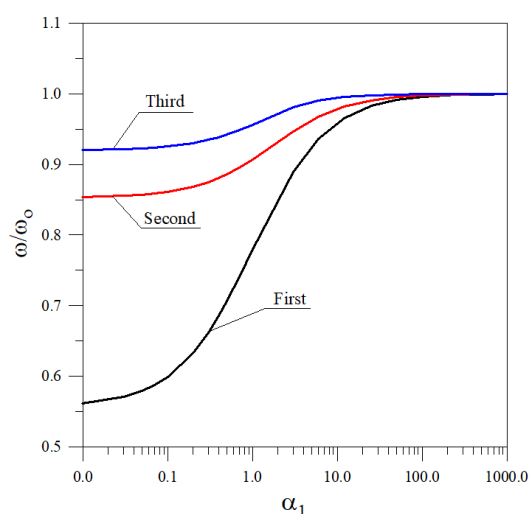
Figure 7: Variation of first natural frequencies for variation of α_1.

7 Concluding Remarks

In this chapter the application of the Finite Element Method to structural dynamics problems was addressed and topics such as modal analysis, modal superposition method were presented. Also, numerical methods for solving eigenvalue and eigenvector problems were briefly discussed. At the end, results of the computational simulation of a structure are presented, considering the effects generated on the natural frequencies of vibration and vibration modes when there is a loss of stiffness in the connections: a sensitivity analysis.

This subject is a wide field for future studies and research, among them we can mention the application of inverse problems and uncertainty modeling techniques in the variables of the problem.

References

K. Bathe and E.L. Wilson, Numerical Methods in Finite Element Analysis, Prentice-Hall, New Jersey, 1976

K.J. Bathe. Finite Element Procedures. Prentice Hall. 1996.

R. Boulic and O. Renault. 3d hierarchies for animation. Technical report, John Wiley and Sons, 1991.

H. Busby and G. Staab. Structural Dynamics – Concepts and Applications. CRC Press. 2018.

A. H. Cheng and D. T. Cheng. Heritage and early history of the boundary element method. Eng. Anal. Bound. Elem., 2005. ISSN 09557997. doi: 10.1016/j.enganabound.2004.12.001.

A.K. Chopra Dynamics of Structures: Theory and Applications to Earthquake Engineering, Prentice Hall, New Jersey, 1st edition,1995

R.W. Clough The Finite Element Method in Plane Stress Analysis, Publisher, American Society of Civil Engineers, 1960.

R.W. Clough and J. Penzien, Dynamics of Structures, McGraw-Hill, New York, 2nd edition, 1993.

R.R. Craig Jr. and A.J. Kurdila, Fundamentals of Structural Dynamics, John Wiley and Sons, New York, 2nd edition, 2006.

R.D. Cook, D.S. Malkus and M.E. Plesha, Concepts and Applications of Finite Element Analysis, John Wiley and Sons, New York, 3rd edition, 1989.

S. Dyer, J. Martin, and J. Zulauf. Motion capture white paper. 1995.

F. M. Hemez and Emmanuel Pagnacco, Statics and inverse dynamics solvers based on strain-mode disassembly, Revue Européenne des Éléments Finis, 2000. DOI: 10.1080/12506559.2000.10511468

M. Holton and S. Alexander. Soft cellular modelling: A technique que for the simulation of non-rigid materials. In Computer graphics, pages 449460. Elsevier, 1995.

D. E. Knuth and D. Bibby. The texbook, volume 15. Addison-Wesley Reading, 1984.

W. McGuire, R.H. Gallagher and R.D. Ziemian. Matrix Structural Analysis. John Wiley & Sons. 2000.

P. W. Partridge, C. A. Brebbia, and L. C. Wrobel. The Dual Reciprocity Boundary Element Method. 1992.

M. Paz and Y.H. Kim. Structural Dynamics – Theory and Computation. Springer. 2019.

S.S. Rao. The Finite Element method in Engineering. Elsevier Science & Technology Books. 2004

S.S. Rao, Mechanical Vibrations, Prentice Hall, Boston, 5th edition, 2011

J. Tedesco, W. McDougal and C. Ross, Structural Dynamics: Theory and Applications, Pearson, 1st edition, 1998.

Chapter 19

The Boundary Element Method for Potential Problems

The Boundary Element Method for Potential Problems

Éder Lima de Albuquerque[1*], Ariosto Bretanha Jorge[2], and
Carla Tatiana Mota Anflor[3]

[1*]Department of Mechanical Engineering, University of Brasilia, Brazil. E-mail: eder@unb.br
[2] Post-Graduate Program - Integrity of Engineering Materials, University of Brasilia, Brazil.
E-mail: ariosto.b.jorge@gmail.com

[3]Faculty UnB Gama, University of Brasilia, Brazil. E-mail: anflor@unb.br

[*]Corresponding author

Abstract

This chapter presents the boundary element method applied to potential problems. The integral equation is obtained for the Laplace equation and discretized into boundary elements. Constant, linear, and quadratic boundary elements are considered. The method is applied to some numerical examples and results are compared to analytical solutions. A convergence study is carried out in order to access the behaviour of the method with mesh refinement.

1 Introduction

Several physical problems in nature can be modeled as a boundary value problem (BVP), in which a partial differential equation is valid in the domain being considered, some boundary conditions are prescribed in the domain boundary, and also some initial conditions may be given, for transient, non-stationary, problems.

The Finite Element Method (FEM) is a numerical method to solve a BVP by replacing the original problem by an approximate domain integral representation, obtained from a weighted residuals approach.

In the FEM equations, an auxiliary problem is introduced, from which weight functions were used in the integral representation of the problem. Also, the geometric discretization of the problem domain is followed by the representation of the unknown functions over the defined sub-domains (or, finite elements) satisfying certain continuity requirements at the boundaries of each sub-domain. An appropriate choice of the weight functions leads to the formation of a system equations comprising of symmetric matrices, assembled from the contribution of each finite element. The element equations are said to have local support, as all information required to solve these equations is limited to the geometry and quantities of interest inside the element and in its boundaries, and no information is needed from the other elements elsewhere in the domain.

The boundary element method (BEM) is another numerical method to solve a BVP, in which the original problem is replaced by an exact boundary integral representation,

obtained from the application of the proper integral identities for the particular problem being studied. The resulting boundary integral representation of the original BVP relates domain integrals to boundary integrals. Unlike the finite element method, where the whole problem domain is discretized, the numerical solution scheme in this method requires discretization of the boundary of the problem, reducing the number of unknowns. For instance, in the case of a 3D domain, it is necessary to discretize the surface.

2   Boundary integral equations

In this section, the boundary integral equation for the Laplace problem will be developed. This equation will then be discretized into boundary elements, thus obtaining the boundary element formulation.

Given Laplace's equation

$$\nabla^2 T = 0, \tag{1}$$

multiplying the equation (1) by a weight function $\omega(x, y)$ and integrating over the domain A, it is assumed that the result of the integral is zero (weighted residual method). Thus, one has:

$$
\begin{aligned}
\iint_A (\nabla^2 T)\omega \, dA &= 0, \\
\iint_A \left(\frac{\partial^2 T}{\partial x^2} + \frac{\partial^2 T}{\partial y^2} \right) \omega \, dA &= 0, \\
\iint_A \frac{\partial^2 T}{\partial x^2} \omega \, dA + \iint_A \frac{\partial^2 T}{\partial y^2} \omega \, dA &= 0
\end{aligned}
\tag{2}
$$

By the Gauss-Green theorem, we have:

$$\int_s f(x, y) n_x \, ds = \int_A \frac{\partial f}{\partial x} \, dA$$

where f is a function, n_x is the component in the x direction of the vector $\vec{n}$ normal to the boundary s of the area A. Applying the theorem given in the first part of Eq.(2), we have:

$$\int_s \frac{\partial T}{\partial x} \omega n_x \, ds = \int_A \frac{\partial}{\partial x} \left(\frac{\partial T}{\partial x} \omega \right) dA.$$

Applying the product of functions derivative rule, we have:

$$\int_s \frac{\partial T}{\partial x} \omega n_x \, ds = \int_A \frac{\partial^2 T}{\partial x^2} \omega \, dA + \int_A \frac{\partial T}{\partial x} \frac{\partial \omega}{\partial x} \, dA.$$

Rewriting the terms of the previous equation, follows:

$$\int_A \frac{\partial^2 T}{\partial x^2} \omega \, dA = \int_s \frac{\partial T}{\partial x} \omega n_x \, ds - \int_A \frac{\partial T}{\partial x} \frac{\partial \omega}{\partial x} \, dA. \tag{3}$$

Similarly, we obtain:

$$\int_A \frac{\partial^2 T}{\partial y^2} \omega \, dA = \int_s \frac{\partial T}{\partial y} \omega n_y \, ds - \int_A \frac{\partial T}{\partial y} \frac{\partial \omega}{\partial y} \, dA. \tag{4}$$

Replacing Eqs.(3) and (4) in Eq.(2), we have:

$$\int_s \left(\frac{\partial T}{\partial x}\omega n_x + \frac{\partial T}{\partial y}\omega n_y \right) ds - \int_A \left(\frac{\partial T}{\partial x}\frac{\partial \omega}{\partial x} + \frac{\partial T}{\partial y}\frac{\partial \omega}{\partial y} \right) dA = 0.$$

Simply put

$$\int_s \frac{\partial T}{\partial n}\omega ds - \int_A \left(\frac{\partial T}{\partial x}\frac{\partial \omega}{\partial x} + \frac{\partial T}{\partial y}\frac{\partial \omega}{\partial y} \right) dA = 0. \tag{5}$$

Considering the equalities:

$$\int_A \frac{\partial T}{\partial x}\frac{\partial \omega}{\partial x} dA = \int_s T\frac{\partial \omega}{\partial x}n_x ds - \int_A T\frac{\partial^2 \omega}{\partial x^2} dA \tag{6}$$

and

$$\int_A \frac{\partial T}{\partial y}\frac{\partial \omega}{\partial y} dA = \int_s T\frac{\partial \omega}{\partial y}n_y ds - \int_A T\frac{\partial^2 \omega}{\partial y^2}n_y dA. \tag{7}$$

Replacing equations (6) and (7) in the equation (5), we have:

$$\int_s \frac{\partial T}{\partial n}\omega ds - \int_s \left(T\frac{\partial \omega}{\partial x}n_x + T\frac{\partial \omega}{\partial y}n_y \right) ds + \int_A T\left(\frac{\partial^2 \omega}{\partial x^2} + \frac{\partial^2 \omega}{\partial y^2} \right) dA = 0.$$

$$\int_s \frac{\partial T}{\partial n}\omega ds - \int_s T\frac{\partial \omega}{\partial n} ds + \int_A T\Delta\omega dA = 0. \tag{8}$$

In order to obtain an integral equation that does not have domain integrals (area integrals) the function ω must be chosen so that the domain integral of Eq.(2.19) disappears. Any harmonic function, that is, a function that Laplacian is equal to zero, satisfies this requirement. However, for numerical reasons, the most suitable choice is the function whose Laplacian is the Dirac delta.

$$\Delta\omega = -\frac{\delta(x - x_d)}{k},$$

which implies that $\omega = T^*$. So you have:

$$\int_s \frac{\partial T}{\partial n}T^* ds - \int_s T\frac{\partial T^*}{\partial n} ds + \int_A T\frac{[-\delta(x - x_d)]}{k} dA, \tag{9}$$

where x_d is the coordinate of the source point.

Taking the source point within the A domain, by the property of the Dirac delta, we have:

$$\int_s \frac{\partial T}{\partial n}T^* ds - \int_s T\frac{\partial T^*}{\partial n} ds - \frac{T(x_d, y_d)}{k} = 0.$$

Multiplying the terms by $-k$, you get:

$$\int -k\frac{\partial T}{\partial n}T^* ds + \int_s T\left(\frac{k\partial T^*}{\partial n} \right) ds + T(x_d, y_d) = 0.$$

$$T(x_d, y_d) = \int_s Tq^* ds - \int_s qT^* ds. \tag{10}$$
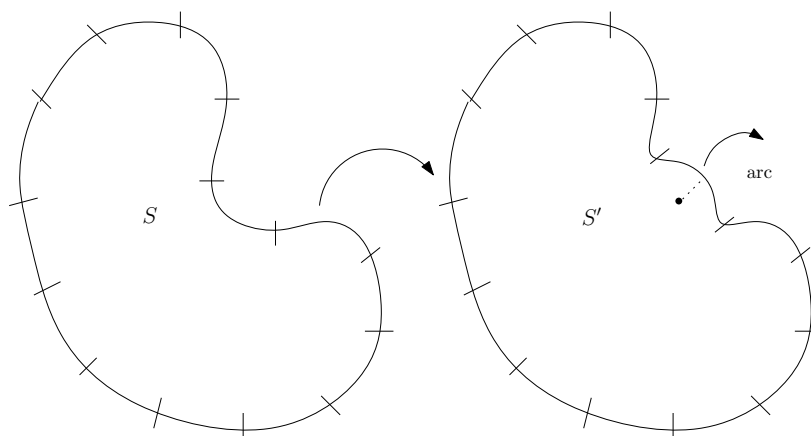
Figure 1: Original and modified outlines.

Eq.(10) is the *integral boundary equation* when the source point is inside the domain.

In order to consider the point (x_d, y_d) on the boundary, a small modification is made to it, as shown in Fig. 1:

Thus, one has:

$$T(x_d, y_d) = \int_{s-s'} Tq^* ds - \int_{s-s'} T^* q ds + \int_{s^*} Tq^* ds - \int_{s^*} T^* q ds. \qquad (11)$$

The flux fundamental solution is given by:

$$q^* = \frac{1}{2\pi r^2}[(x - x_d)n_x + (y - y_d)n_y],$$

with $r = \sqrt{(x - x_d)^2 + (y - y_d)^2}$,. Thus,

$$\int_{s^*} Tq^* ds = \int_{\theta_1}^{\theta_2} T \frac{1}{2\pi r^2}[(x - x_d)n_x + (y - y_d)n_y]\varepsilon d\theta.$$

In s^*, you have:

$$\vec{r} = (x - x_d)\vec{i} + (y - y_d)\vec{j},$$

$$|\vec{r}| = r = \sqrt{(x - x_d)^2 + (y - y_d)^2},$$

$$\vec{n} = \frac{(x - x_d)\vec{i} + (y - y_d)\vec{j}}{r},$$

where $\vec{n}$ is a unit vector. As $r_x = (x - x_d)$ and $r_y = (y - y_d)$, we have:

$$\vec{n} = \frac{r_x\vec{i} + r_y\vec{j}}{r}$$

with

$$n_x = \frac{r_x}{r} \quad \text{e} \quad n_y = \frac{r_y}{r}.$$

So

$$\int_{s^*}^{s} Tq^* ds = \int_{\theta_1}^{\theta_2} \frac{T}{2\pi r^2} \left(r_x \frac{r_x}{r} + r_y \frac{r_y}{r} \right) \varepsilon d\theta.$$

Noting that $r = \varepsilon$ for any θ, we have;

$$\int_{s*} Tq^* ds = \int_{\theta_1}^{\theta_2} \frac{T}{2\pi\varepsilon^2} \left(\frac{r_x^2 + r_y^2}{\varepsilon} \right) \varepsilon d\theta = \int_{\theta_1}^{\theta_2} \frac{T}{2\pi} d\theta.$$

By making $\varepsilon \longrightarrow 0$, T takes the value of $T(d)$. Finally, there is

$$\int_{s*} Tq^* ds = \frac{T(d)(\theta_2 - \theta_1)}{2\pi}.$$

The same analysis must be done for:

$$\int_{s*} T^* q ds = \int_{\theta_1}^{\theta_2} \frac{-1}{2\pi k} \ln r q r d\theta.$$

As $r = \varepsilon = $ constant, we have:

$$\int_{s*} T^* q ds = \frac{-1}{2\pi k} \varepsilon \ln \varepsilon \int_{\theta_1}^{\theta_2} q d\theta.$$

Making $\varepsilon \longrightarrow 0$, you get:

$$\int_{s*} T^* q ds = \frac{-1}{2\pi k} \lim_{\varepsilon \to 0} \varepsilon \ln \varepsilon (\theta_2 - theta_1),$$

$$\int_{s*} T^* q ds = 0.$$

Returning to the original equation, follows:

$$T(x_d, y_d) = \int_s Tq^* ds - \int_s T^* q ds + \frac{T(x_d, y_d)(\theta_2 - \theta_1)}{2\pi} - 0,$$

$$T(x_d, y_d) \left[1 - \frac{(\theta_2 - \theta_1)}{2\pi} \right] = \int_s Tq^* ds - \int_s T^* q ds,$$

$$T(x_d, y_d) \left[\frac{2\pi - (\theta_2 - \theta_1)}{2\pi} \right] = \int_s Tq^* ds - \int_s T^* q ds.$$

As shown in Fig. 2, θ_{int} is the inner angle of the boundary.

$$\frac{\theta_{int}}{2\pi} T(x_d, y_d) = \int_s Tq^* ds - \int_s T^* q ds,$$

which is the boundary integral when the source point belongs to the boundary.

When the source point does not belong to the boundary or the domain, due to the property of the Dirac delta, we have:

$$\int_s Tq^* ds - \int_s T^* q ds = 0. \tag{12}$$

Generally speaking, the integral boundary equation can be written as
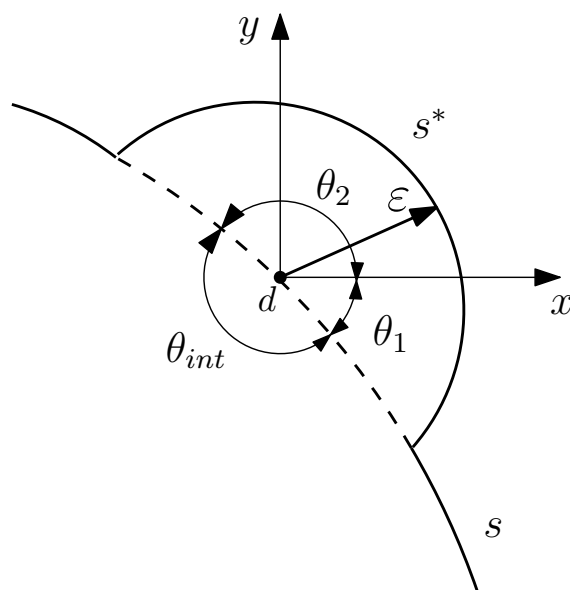
Figure 2: Internal boundary angle.

$$cT(x_d, y_d) = \int_s Tq^* ds - \int_s T^* q ds, \tag{13}$$

Where

$$c = \begin{cases} 1, & \text{if} \quad (x_d, y_d) \in \text{domain} \\ \frac{\theta_{int}}{2\pi}, & \text{if} \quad (x_d, y_d) \in \text{boundary} \\ 0, & \text{if} \quad (x_d, y_d) \notin \text{domain or boundary} \end{cases}$$

When the source point is at a smooth point of the boundary, that is, it is not a corner, you have:

$$c = \frac{\theta_{int}}{2\pi} = \frac{\pi}{2\pi} = \frac{1}{2}. \tag{14}$$

3   Integral equation for heat flux

To obtain an integral equation for the heat flux, it is necessary to derive the equation (10) in relation to the coordinates of the source point, that is:

$$\frac{\partial T(x_d, y_d)}{\partial x_d} = \frac{\partial}{\partial x_d} \left[\int_s Tq^* ds - \int_s qT^* ds \right]. \tag{15}$$

$$\frac{\partial T(x_d, y_d)}{\partial x_d} = \int_s T \frac{\partial q^*}{\partial x_d} ds - \int_s q \frac{\partial T^*}{\partial x_d} ds. \tag{16}$$

where:

$$\frac{\partial T^*}{\partial x_d} = \frac{r_x}{2\pi k r^2}, \tag{17}$$

$$\frac{\partial T^*}{\partial y_d} = \frac{r_y}{2\pi k r^2},$$

(18)

$$\frac{\partial q^*}{\partial x_d} = \frac{\left[n_x\left(r_x^2 - r_y^2\right) + 2n_y r_x r_y\right]}{2\pi r^4}$$

(19)

and

$$\frac{\partial q^*}{\partial y_d} = \frac{\left[n_y\left(-r_x^2 + r_y^2\right) + 2n_x r_x r_y\right]}{2\pi r^4}.$$

(20)

4   Discretization of integral boundary equations

Basically, the MEC formulation transforms differential equations into integral boundary equations, thus eliminating domain discretization. These integrals can be solved numerically and analytically with the integration made along the boundary, which is discretized by dividing it into elements called *boundary elements* in which boundary conditions are prescribed.

Once the boundary integral is obtained, the next step is to discretize this equation so that the integrals along the boundary are written as the sum of integrals along parts of the boundary.
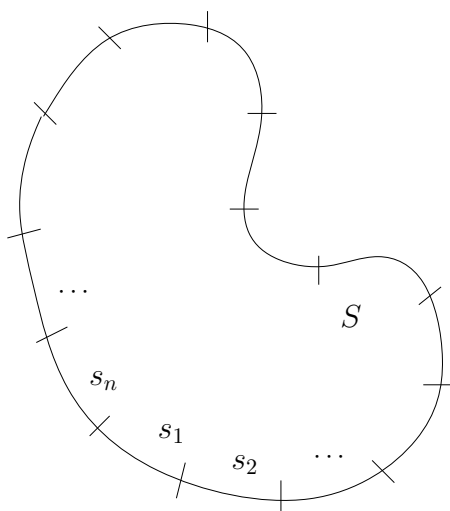
Figure 3: Discretization of boundary in n parts.

In this way, the integral boundary equation (13) is written as:

$$cT(x_d, y_d) = \sum_{j=1}^{n} \int_{s_j} Tq^* ds - \sum_{j=1}^{n} \int_{s_j} T^* q ds.$$

(21)

where

$$S = s_1 + s_2 + \ldots + s_n.$$

5   Constant boundary elements

In discretization using constant elements, the geometry is approximated by straight line segments with a node in the middle of each element. Thus, consider that the parts of the boundary $s_1, s_2, ..., s_n$ are approximated by straight segments and that along these segments, both temperature and flux are assumed as constants.
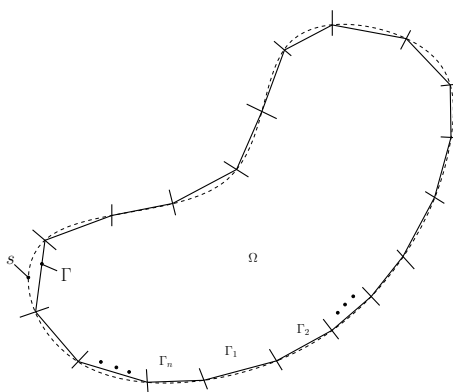
Figure 4: boundary approximation by line segments.

The j node will always be at the center position of the j element (it will always be in a smooth region of the boundary, so $c = \frac{1}{2}$). The integral equation is approximated by:

$$\frac{1}{2}T^{(i)}(x_d, y_d) = \sum_{j=1}^{n}\left[T_j \int_{\Gamma_j} q^* d\Gamma\right] - \sum_{j=1}^{n}\left[q_j \int_{\Gamma_j} T^* d\Gamma\right], \tag{22}$$

where i corresponds to the node of the i-th element. Hence, we have:

$$-\frac{1}{2}T^{(i)}(x_d, y_d) + \sum_{j=1}^{n}\left[T_j \int_{\Gamma_j} q^* d\Gamma\right] = \sum_{j=1}^{n}\left[q_j \int_{\Gamma_j} T^* d\Gamma\right]. \tag{23}$$

Calling

$$H_{ij} = \begin{cases} \int_{\Gamma_j} q^* d\Gamma, & \text{se} \quad i \neq j \\ -\frac{1}{2} + \int_{\Gamma_j} q^* d\Gamma, & \text{se} \quad i = j \end{cases}$$

and

$$G_{ij} = \int_{\Gamma_j} T^* d\Gamma \tag{24}$$

you can write the matrix equation as follows:

$$\sum_{j=1}^{n}[H_{ij}T_j] = \sum_{j=1}^{n}[G_{ij}q_j]. \tag{25}$$

Example 5.1 *In order to illustrate how to apply the boundary conditions and calculate the unknown variables, a unidirectional heat conduction problem with a discretization of one element per side will be analyzed (see Figure 5).*
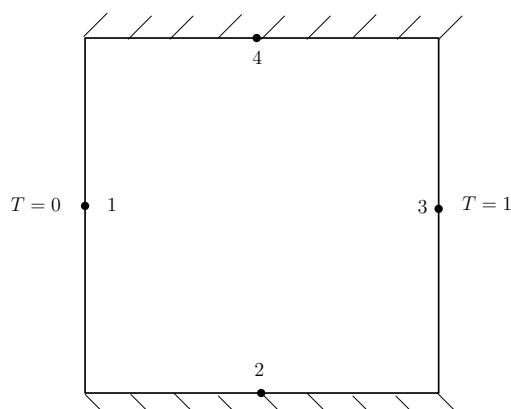
Figure 5: Temperature and flux on plate.

Table 1: Qualification of variables in each node.

node	known variables	unknown variables
1	T_1	q_1
2	q_2	T_2
3	T_3	q_3
4	q_4	T_4

In this case, the known and unknown variables in the problem outline are given by Table (2.1).

Considering that the source point is at node 1 and subscribing the known variables with a slash, we have:

$$H_{11}\bar{T}_1 + H_{12}T_2 + H_{13}\bar{T}_3 + H_{14}T_4 = G_{11}q_1 + G_{12}\bar{q}_2 + G_{13}q_3 + G_{14}\bar{q}_4,$$

where $\bar{T}$ and $\bar{q}$ are known terms. Since there is only 1 equation and 4 unknown variables, three more equations must be generated. To do this, just place the source point on each of the nodes. For this reason the choice of the weight function ω must be that Lapaltian is equal to Dirac's delta and not Laplacian equal to zero. Thus, one has:

For the source point at node 2, we have:

$$H_{21}\bar{T}_1 + H_{22}T_2 + H_{23}\bar{T}_3 + H_{24}\bar{T}_4 = G_{21}q_1 + G_{22}\bar{q}_2 + G_{23}q_3 + G_{24}\bar{q}_4.$$

Likewise, the source point is made at nodes 3 and 4. The equations obtained can be written in matrix form, as:

$$\begin{pmatrix} H_{11} & H_{12} & H_{13} & H_{14} \\ H_{21} & H_{22} & H_{23} & H_{24} \\ H_{31} & H_{32} & H_{33} & H_{34} \\ H_{41} & H_{42} & H_{43} & H_{44} \end{pmatrix} \begin{pmatrix} \bar{T}_1 \\ T_2 \\ \bar{T}_3 \\ T_4 \end{pmatrix} = \begin{pmatrix} G_{11} & G_{12} & G_{13} & G_{14} \\ G_{21} & G_{22} & G_{23} & G_{24} \\ G_{31} & G_{32} & G_{33} & G_{34} \\ G_{41} & G_{42} & G_{43} & G_{44} \end{pmatrix} \begin{pmatrix} q_1 \\ \bar{q}_2 \\ q_3 \\ \bar{q}_4 \end{pmatrix}$$

which can be briefly written as:

$$[H]\{T\} = [G]\{q\}. \tag{26}$$

Separating the known terms from the unknown, it follows:

$$
\begin{pmatrix} -G_{11} & H_{12} & -G_{13} & H_{14} \\ -G_{21} & H_{22} & -G_{23} & H_{24} \\ -G_{31} & H_{32} & -G_{33} & H_{34} \\ -G_{41} & H_{42} & -G_{43} & H_{44} \end{pmatrix} \begin{pmatrix} q_1 \\ T_2 \\ q_3 \\ T_4 \end{pmatrix} = \begin{pmatrix} -H_{11} & G_{12} & -H_{13} & G_{14} \\ -H_{21} & G_{22} & -H_{23} & G_{24} \\ -H_{31} & G_{32} & -H_{33} & G_{34} \\ -H_{41} & G_{42} & -H_{43} & G_{44} \end{pmatrix} \begin{pmatrix} \bar{T}_1 \\ \bar{q}_2 \\ \bar{T}_3 \\ \bar{q}_4 \end{pmatrix}
$$

So you can write

$$[A]\{x\} = \{b\}, \tag{27}$$

or yet

$$\{x\} = [A]^{-1}\{b\}. \tag{28}$$

Then, solve the linear system above and calculate the values of the unknown variables.

5.1   Integration of matrices $[H]$ and $[G]$ when source point belongs to element

In this case, in the case of constant elements, the integration is done analytically, that is:

- Matrix H

$$
H_{ij} = -\frac{1}{2} + \frac{1}{2\pi} \int_{\Gamma_j} \frac{r_x n_x + r_y n_y}{r} d\Gamma
$$

Like

$$
r_x n_x + r_y n_y = \vec{r}.\vec{n} = 0
$$

$$
\therefore H_{ij} = -\frac{1}{2} \tag{29}
$$

- Matrix G

For constant boundary element, matrix G is given by:

$$
G = -\frac{1}{2\pi k} \int_{\Gamma_j} \ln r \, d\Gamma \tag{30}
$$

Thus, one has:

$$
\begin{aligned}
G_{ij} &= -\frac{1}{2\pi k} \times 2 \int_0^{\frac{L}{2}} \ln r \, dr \\
&= -\frac{1}{\pi k} (-r + r \ln r) \Big|_0^{\frac{L}{2}} \\
&= -\frac{1}{\pi k} \left(-\frac{L}{2} + \frac{L}{2} \ln \frac{L}{2} + 0 - \lim_{r \to 0} r \ln r \right). \\
&= \frac{L}{2\pi k} \left(1 - \ln \frac{L}{2} \right)
\end{aligned}
$$
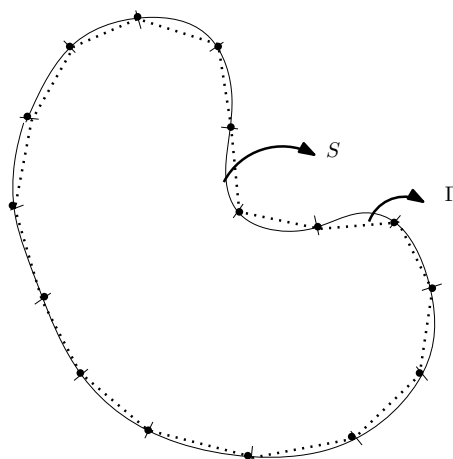
Figure 6: Continuous linear elements.

6   Continuous linear boundary elements

In linear element discretization, the geometry is approximated by a 1st degree polynomial, requiring two nodes in each element, one at each end of the element. Temperature and flux are also approximated by a 1st degree polynomial. The formulation is isoparametric, that is, the same shape functions used to interpolate the geometry are also used to interpolate the physical variables (temperature and flux).

In this case, the integral equation is given by:

$$cT(x_d, y_d) = \int_s Tq^* dS - \int_s T^* q dS.$$

Discretizing in continuous linear boundary elements, it follows:

$$cT(x_d, y_d) = \sum_{j=1}^{n_{elem}} \left[\int_{\Gamma_j} Tq^* d\Gamma \right] - \sum_{j=1}^{n_{elem}} \left[\int_{\Gamma_j} T^* q d\Gamma \right]$$

Observing that T and q are assumed with linear variation along the element, that is,

$$T = N_1 T_1 + N_2 T_2$$

and

$$q = N_1 q_1 + N_2 q_2.$$

where T_1 is the temperature at local node 1, T_2 the temperature at local node 2, q_1 is the flux at local node 1 and q_2 is the flux at local node 2, N_1 is the form function 1 and N_2 is the form function 2.

Likewise, it follows:

$$\begin{cases} x = N_1 x_1 + N_2 x_2 \\ y = N_1 y_1 + N_2 y_2 \end{cases}$$

Writing in matrix form, follows:

$$T = \begin{bmatrix} N_1 & N_2 \end{bmatrix} \begin{bmatrix} T_1 \\ T_2 \end{bmatrix}$$

and

$$q = \begin{bmatrix} N_1 & N_2 \end{bmatrix} \begin{bmatrix} q_1 \\ q_2 \end{bmatrix}.$$

The discretized integral equation is then written as:

$$cT(x_d, y_d) = \sum_{j=1}^{n_{elem}} \left\{ \int_{\Gamma_j} \begin{bmatrix} N_1 & N_2 \end{bmatrix} \begin{bmatrix} T_1 \\ T_2 \end{bmatrix}_j q^* d\Gamma \right\} - \sum_{j=1}^{n_{elem}} \left\{ \int_{\Gamma_j} T^* \begin{bmatrix} N_1 & N_2 \end{bmatrix} \begin{bmatrix} q_1 \\ q_2 \end{bmatrix}_j d\Gamma \right\}.$$

Since T_1, T_2, q_1 and q_2 are nodal values, it follows:

$$cT(x_d, y_d) = \sum_{j=1}^{n_{elem}} \left\{ \int_{\Gamma_j} \begin{bmatrix} N_1 & N_2 \end{bmatrix} q^* d\Gamma \begin{bmatrix} T_1 \\ T_2 \end{bmatrix}_j \right\} - \sum_{j=1}^{n_{elem}} \left\{ \int_{\Gamma_j} \begin{bmatrix} N_1 & N_2 \end{bmatrix} T^* d\Gamma \begin{bmatrix} q_1 \\ q_2 \end{bmatrix}_j \right\}.$$

which can be written as follows:

$$cT(x_d, y_d) = \sum_{j=1}^{n_{elem}} \left\{ \begin{bmatrix} h_1 & h_2 \end{bmatrix}_j \begin{bmatrix} T_1 \\ T_2 \end{bmatrix}_j - \begin{bmatrix} g_1 & g_2 \end{bmatrix}_j \begin{bmatrix} q_1 \\ q_2 \end{bmatrix}_j \right\},$$

Where

$$h_1 = \int_{\Gamma_j} N_1 q^* d\Gamma,$$

$$h_2 = \int_{\Gamma_j} N_2 q^* d\Gamma,$$

$$g_1 = \int_{\Gamma_j} N_1 T^* d\Gamma$$

and

$$g_2 = \int_{\Gamma_j} N_2 T^* d\Gamma.$$

Example 6.1 *Applying the formulation developed in the heat conduction problem discussed above (Figure 7), the boundary conditions and unknown variables are given as shown in table 2. Note in Table 2 that the temperature is continuous at node j. In turn, the flux q_j can be discontinuous, that is, the flux q_j^a, before the node j can be different from the flux q_j^d, after the node j. However, given the order of the Laplace differential equation (second order), only one variable can be unknown per node.*

Table 2: Qualification of the variables in each node for the given problem.

node	known variables	unknown variables
1	T_1 and q_1^a	q_1^d
2	T_2 and q_2^d	q_2^a
3	T_3 and q_3^a	q_3^d
4	T_4 and q_4^d	q_4^a
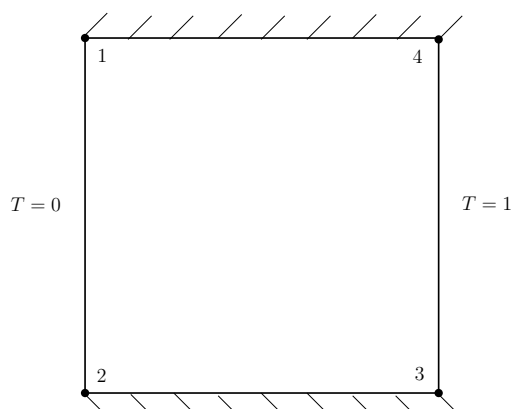
Figure 7: Temperature and flux on plate.

Considering the source point at node 1, the integral equation is described as:

$$cT_1 \;=\; \begin{bmatrix} h_1 & h_2 \end{bmatrix}_1 \begin{bmatrix} T_1 \\ T_2 \end{bmatrix}_1 + \begin{bmatrix} h_1 & h_2 \end{bmatrix}_2 \begin{bmatrix} T_1 \\ T_2 \end{bmatrix}_2 + \cdots - \begin{bmatrix} g_1 & g_2 \end{bmatrix}_1 \begin{bmatrix} q_1 \\ q_2 \end{bmatrix}_1 -$$

$$- \begin{bmatrix} g_1 & g_2 \end{bmatrix}_2 \begin{bmatrix} q_1 \\ q_2 \end{bmatrix}_2 \cdots .$$

Using the global node number, it follows:

$$cT_1 \;=\; \begin{bmatrix} h_1 & h_2 \end{bmatrix}_1 \begin{bmatrix} \bar{T}_1 \\ \bar{T}_2 \end{bmatrix} + \begin{bmatrix} h_1 & h_2 \end{bmatrix}_2 \begin{bmatrix} \bar{T}_2 \\ \bar{T}_3 \end{bmatrix} + \begin{bmatrix} h_1 & h_2 \end{bmatrix}_3 \begin{bmatrix} \bar{T}_3 \\ \bar{T}_4 \end{bmatrix} +$$

$$+ \begin{bmatrix} h_1 & h_2 \end{bmatrix}_4 \begin{bmatrix} \bar{T}_4 \\ \bar{T}_1 \end{bmatrix} - \begin{bmatrix} g_1 & g_2 \end{bmatrix}_1 \begin{bmatrix} q_1^d \\ q_2^a \end{bmatrix} - \begin{bmatrix} g_1 & g_2 \end{bmatrix}_2 \begin{bmatrix} \bar{q}_2^d \\ \bar{q}_3^a \end{bmatrix} -$$

$$- \begin{bmatrix} g_1 & g_2 \end{bmatrix}_3 \begin{bmatrix} q_3^d \\ q_4^a \end{bmatrix} - \begin{bmatrix} g_1 & g_4 \end{bmatrix}_1 \begin{bmatrix} \bar{q}_4^d \\ \bar{q}_1^a \end{bmatrix},$$

Writing the global G and H matrices, follows:

$$H_{11}T_1 + H_{12}T_2 + H_{13}T_3 + H_{14}T_4 = G_{11}^d q_1^d + G_{12}^a q_2^a$$
$$+ G_{12}^d \bar{q}_2^d + G_{13}^a \bar{q}_3^a + G_{13}^d q_3^d + G_{14}^a q_4^a + G_{14}^d \bar{q}_4^d + G_{11}^a \bar{q}_1^a. \tag{31}$$

Note that there is 1 equation and 4 unknown variables. In order to generate 3 more equations, just place the source point at the other 3 nodes. Hence, the following matrix equation is obtained:

$$
\begin{bmatrix}
H_{11} & H_{12} & H_{13} & H_{14} \\
H_{21} & H_{22} & H_{23} & H_{24} \\
H_{31} & H_{32} & H_{33} & H_{34} \\
H_{41} & H_{42} & H_{43} & H_{44}
\end{bmatrix}
\begin{bmatrix}
\bar{T}_1 \\ \bar{T}_2 \\ \bar{T}_3 \\ \bar{T}_4
\end{bmatrix} =
$$

$$
\begin{bmatrix}
G_{11}^d & G_{12}^a & G_{12}^d & G_{13}^a & G_{13}^d & G_{14}^a & G_{14}^d & G_{11}^a \\
G_{21}^d & G_{22}^a & G_{22}^d & G_{23}^a & G_{23}^d & G_{24}^a & G_{24}^d & G_{21}^a \\
G_{31}^d & G_{32}^a & G_{32}^d & G_{33}^a & G_{33}^d & G_{34}^a & G_{34}^d & G_{31}^a \\
G_{41}^d & G_{42}^a & G_{42}^d & G_{43}^a & G_{43}^d & G_{44}^a & G_{44}^d & G_{41}^a
\end{bmatrix}
\begin{bmatrix}
q_1^d \\ q_2^a \\ \bar{q}_2^d \\ \bar{q}_3^a \\ q_3^d \\ \bar{q}_4^a \\ q_4^d \\ \bar{q}_1^a
\end{bmatrix} .
$$

(32)

Manipulating the matrix equation so that the unknown terms are all on the left side and the other terms on the right side, follows:

$$
\begin{bmatrix}
-G_{11}^d & -G_{12}^a & -G_{13}^d & -G_{14}^a \\
-G_{21}^d & -G_{22}^a & -G_{23}^d & -G_{24}^a \\
-G_{31}^d & -G_{32}^a & -G_{33}^d & -G_{34}^a \\
-G_{41}^d & -G_{42}^a & -G_{43}^d & -G_{44}^a
\end{bmatrix}
\begin{bmatrix}
q_1^d \\ q_2^a \\ q_3^d \\ \bar{q}_4^a
\end{bmatrix}
$$

$$
=
\begin{bmatrix}
-H_{11} & -H_{12} & G_{12}^d & G_{13}^a & -H_{13} & -H_{14} & G_{14}^d & G_{11}^a \\
-H_{21} & -H_{22} & G_{22}^d & G_{23}^a & -H_{23} & -H_{24} & G_{24}^d & G_{21}^a \\
-H_{11} & -H_{32} & G_{32}^d & G_{33}^a & -H_{33} & -H_{34} & G_{34}^d & G_{31}^a \\
-H_{11} & -H_{42} & G_{42}^d & G_{43}^a & -H_{43} & -H_{44} & G_{44}^d & G_{41}^a
\end{bmatrix}
\begin{bmatrix}
\bar{T}_1 \\ \bar{T}_2 \\ q_2^d \\ q_3^a \\ \bar{T}_3 \\ \bar{T}_4 \\ \bar{q}_4^d \\ \bar{q}_1^a
\end{bmatrix} ,
$$

(33)

that can be written in linear form as:

$$
[A]\{x\} = \{b\}
$$
(34)

Example 6.2 *Applying the formulation developed in the heat conduction problem represented in Figure 8, the boundary conditions and unknown variables are given as shown in table 3. Note in Table 2 that the temperature is continuous at node j. In turn, the flux q_j can be discontinuous, that is, the flux q_j^a, before the node j can be different from the flux q_j^d, after the node j. However, given the order of the Laplace differential equation (second order), only one variable can be unknown per node.*

Table 3: Qualification of the variables in each node for the given problem.

node	known variables	unknown variables
1	q_1^a and q_1^d	T_1
2	T_2 and q_2^a	q_2^d
3	T_3	$q_3^a = q_3^d = q_3$
4	T_4 and q_4^d	q_4^a
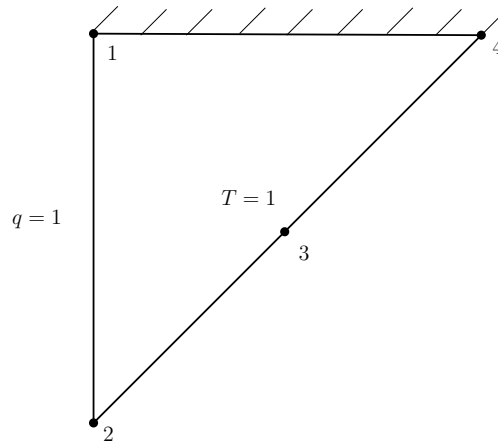
Figure 8: Temperature and flux on plate.

$$
\begin{bmatrix} H_{11} & H_{12} & H_{13} & H_{14} \\ H_{21} & H_{22} & H_{23} & H_{24} \\ H_{31} & H_{32} & H_{33} & H_{34} \\ H_{41} & H_{42} & H_{43} & H_{44} \end{bmatrix} \begin{bmatrix} T_1 \\ \bar{T}_2 \\ \bar{T}_3 \\ \bar{T}_4 \end{bmatrix}
$$

$$
= \begin{bmatrix} G_{11}^d & G_{12}^a & G_{12}^d & G_{13}^a & G_{13}^d & G_{14}^a & G_{14}^d & G_{11}^a \\ G_{21}^d & G_{22}^a & G_{22}^d & G_{23}^a & G_{23}^d & G_{24}^a & G_{24}^d & G_{21}^a \\ G_{31}^d & G_{32}^a & G_{32}^d & G_{33}^a & G_{33}^d & G_{34}^a & G_{34}^d & G_{31}^a \\ G_{41}^d & G_{42}^a & G_{42}^d & G_{43}^a & G_{43}^d & G_{44}^a & G_{44}^d & G_{41}^a \end{bmatrix} \begin{bmatrix} \bar{q}_1^d \\ \bar{q}_2^a \\ q_2^d \\ q_3^a = q_3 \\ q_3^d = q_3 \\ q_4^a \\ \bar{q}_4^d \\ \bar{q}_1^a \end{bmatrix}.
$$

$$(35)$$

Manipulating the matrix equation so that the unknown terms are all on the left side and the other terms on the right side, follows:

$$
\begin{bmatrix}
H_{11} & -G_{12}^d & (-G_{13}^a - G_{13}^d) & -G_{14} \\
H_{21} & -G_{22}^d & (-G_{23}^a - G_{23}^d) & -G_{24} \\
H_{31} & -G_{32}^d & (-G_{33}^a - G_{33}^d) & -G_{34} \\
H_{41} & -G_{42}^d & (-G_{43}^a - G_{43}^d) & -G_{44}
\end{bmatrix}
\begin{bmatrix}
T_1 \\
q_2^d \\
q_3 \\
q_4^a
\end{bmatrix}
$$

$$
=
\begin{bmatrix}
G_{11}^d & G_{12}^a & -H_{12} & -H_{13} & 0 & -H_{14} & G_{14}^d & G_{11}^a \\
G_{21}^d & G_{22}^a & -H_{22} & -H_{23} & 0 & -H_{24} & G_{24}^d & G_{21}^a \\
G_{31}^d & G_{32}^a & -H_{32} & -H_{33} & 0 & -H_{34} & G_{34}^d & G_{31}^a \\
G_{41}^d & G_{42}^a & -H_{42} & -H_{43} & 0 & -H_{44} & G_{44}^d & G_{41}^a
\end{bmatrix}
\begin{bmatrix}
\bar{q}_1^d \\
\bar{q}_2^a \\
\bar{T}_2 \\
\bar{T}_3 \\
0 \\
\bar{T}_4 \\
\bar{q}_4^d \\
\bar{q}_1^a
\end{bmatrix}, \qquad (36)
$$

that can be written in linear form as:

$$
[A]\{x\} = \{b\} \tag{37}
$$

6.1 Algorithm to apply boundary conditions

As seen in the examples 6.1 and 6.2, the procedures to apply the boundary conditions when you have continuous elements (where a node is shared by 2 elements) are more complex than for discontinuous elements. This section presents a simple algorithm that does this task well. Although the case shown is restricted to continuous linear elements, this algorithm can be easily extended to other types of continuous elements, both in the formulations of 2D boundary elements and 3D boundary elements.

Initially, assume that an array $[T_{pr}]$ will be created that contains information about the nodes at which the temperature is prescribed (known). This matrix has 5 columns and the number of rows is equal to the number of nodes for which the temperature is known. For ease of understanding, consider that the matrix columns are represented by five vectors $\{a_1\}$, $\{a_2\}$, $\{a_3\}$, $\{a_4\}$ and $\{a_5\}$. Thus, the line i of the matrix $[T_{pr}]$ is given by:

$$
T_{pr_i} = \begin{bmatrix} a_{1i} & a_{2i} & a_{3i} & a_{4i} & a_{5i} \end{bmatrix} \tag{38}
$$

where each element i of the vectors $\{a_1\}$, $\{a_2\}$, $\{a_3\}$, $\{a_4\}$ and $\{a_5\}$ contains:

a_{1i}: number of the $i-$th node with known temperature.
a_{2i}: number of the first element **with prescribed temperature** to which this node belongs.
a_{3i}: local node number in this element.
a_{4i}: if the temperature is also prescribed in the second element to which this node belongs, then a_{4i} will contain the number of this element, otherwise it will contain zero.
a_{5i}: if a_{4i} is non-zero, a_{5i} will contain the local number of the node in the second element, otherwise it will contain zero.

In the definition of a_{2i}, the term "with prescribed temperature" is in bold to draw attention to the fact that, if the temperature is prescribed in only one of the elements to

which the node i belongs , the element that does not have a prescribed temperature should not be considered in the matrix $[T_{pr}]$.

The matrices $[T_{pr}]$ for the examples 6.1 and 6.2 are given, respectively, by:

$$[T_{pr}] = \begin{bmatrix} 1 & 1 & 1 & 0 & 0 \\ 2 & 1 & 2 & 0 & 0 \\ 3 & 3 & 1 & 0 & 0 \\ 4 & 3 & 2 & 0 & 0 \end{bmatrix} \tag{39}$$

and

$$[T_{pr}] = \begin{bmatrix} 2 & 2 & 1 & 0 & 0 \\ 3 & 2 & 2 & 3 & 1 \\ 4 & 3 & 2 & 0 & 0 \end{bmatrix} \tag{40}$$

Once the matrix $[T_{pr}]$ has been constructed, the exchange of the columns of the matrices $[H]$ and $[G]$ follows the following algorithm:

For i = 1 up to the number of nodes with known temperature:

- $i_{no} = T_{pr\,i1}$; (number of the $i-$th node with known temperature);
- $i_{el} = T_{pr\,i2}$; (first element with prescribed temperature that contains this node);
- $i_{noloc} = T_{pr\,i3}$; (local node number in this element);
- $ind_H = i_{no}$; (index of the $[H]$ matrix column that will be swapped);
- $ind_G = 2 \times i_{el} + i_{noloc} - 2$; (index of the $[G]$ matrix column that will be swapped);
- the vector $\{exchange\}$ receives the column ind_G of the matrix $[G]$;
- column ind_G of matrix $[G]$ receives column ind_H of matrix $[H]$ with inverted sign;
- column ind_H of matrix $[H]$ receives vector $\{exchange\}$ with inverted sign;
- If $T_{pr\,i4}$ is non-zero $\Rightarrow$ the temperature is also known in the second element to which the node i_{no} belongs:
  - $i_{el} = T_{pr\,i4}$; (number of the second element to which the node belongs);
  - $i_{noloc} = T_{pr\,i5}$; (local number of this node in the second element);
  - $ind_G = 2 \times i_{el} + i_{noloc} - 2$; (index of the column of the matrix $[G]$ which will be assigned zero);
  - Subtracts from the elements of the column ind_H of the matrix $[H]$ the value of the elements of the column ind_G of the matrix $[G]$;
  - Assign zeros in column ind_G of matrix $[G]$;
- End of If;

End of For.

6.2 Integration of matrices $[H]$ and $[G]$ when source point does not belong to element

The integration of the terms of the arrays $[H]$ and $[G]$ when the source point does not belong to the element is regular and does not present great differences in relation to the integration of the constant element. To avoid unnecessary repetition, the integration for the linear element will not be detailed.

6.3 Matrix integration $[G]$ when source point belongs to element

The integration of the matrix $[G]$ when the source point belongs to the element is done analytically, in the same way as the constant element.

As already seen, the element's geometry is approximated by:

$$x = N_1 x_1 + N_2 x_2 = \frac{1}{2}(1 - \xi)x_1 + \frac{1}{2}(1 + \xi)x_2$$
$$= \frac{x_1 - \xi x_1 + x_2 + \xi x_2}{2} = \frac{1}{2}\left[(x_2 - x_1)\,\xi + x_2 + x_1\right] \tag{41}$$

and

$$y = \frac{1}{2}\left[(y_2 - y_1)\,\xi + y_2 + y_1\right]. \tag{42}$$

The coordinate x of the source point is given by $x_d = x(\xi = \xi_d)$ and $y_d = y(\xi = \xi_d)$, where $\xi_d = -1$ for the source point at node 1 and $\xi_d = +1$ for the source point at node 2. Hence:

$$x_d = \frac{1}{2}\left[(x_2 - x_1)\,\xi_d + x_2 + x_1\right], \tag{43}$$

$$y_d = \frac{1}{2}\left[(y_2 - y_1)\,\xi_d + y_2 + y_1\right] \tag{44}$$

and

$$r = \sqrt{(x - x_d)^2 + (y - y_d)^2} = \sqrt{r_x^2 + r_y^2}, \tag{45}$$

where

$$r_x = x - x_d = \frac{1}{2}\left[(x_2 - x_1)\xi + x_2 + x_1\right] - \left\{\frac{1}{2}\left[(x_2 - x_1)\xi_d + x_2 + x_1\right]\right\} \tag{46}$$

$$r_x = \frac{1}{2}(x_2 - x_1)(\xi - \xi_d) \tag{47}$$

Likewise, you have:

$$r_y = \frac{1}{2}(y_2 - y_1)(\xi - \xi_d) \tag{48}$$

and

$$r = \sqrt{\left[\frac{1}{2}(x_2 - x_1)(\xi - \xi_d)\right]^2 + \left[\frac{1}{2}(y_2 - y_1)(\xi - \xi_d)\right]^2}$$

$$= \frac{1}{2}(\xi - \xi_d)\sqrt{(x_2 - x_1)^2 + (y_2 - y_1)^2} = \frac{1}{2}(\xi - \xi_d)L \tag{49}$$

The terms of the matrix $[G]$ are given by:

$$g_1 = \int_{\Gamma_j} T^* N_1 d\Gamma \tag{50}$$

and

$$g_2 = \int_{\Gamma_j} T^* N_2 d\Gamma. \tag{51}$$

In this way, you have:

$$g_1 = \int_{\Gamma_j} T^* N_1 d\Gamma = \int_{-1}^{1} T^* N_1 \frac{d\Gamma}{d\xi} d\xi$$

$$= \int_{-1}^{1} \frac{-1}{2\pi k} \log(r) \frac{L}{2} \frac{1}{2}(1 - \xi) d\xi$$

$$= \frac{-L}{8\pi k} \int_{-1}^{1} \log\left[L\left(\frac{\xi - \xi_d}{2}\right)\right](1 - \xi) d\xi \tag{52}$$

- Source point at node 1: $\xi_d = -1$.

$$g_1 = \frac{-L}{8\pi k}\left[\int_{-1}^{1} \log\left(\frac{\xi + 1}{2}\right)(1 - \xi) d\xi + \int_{-1}^{1} \log(L)(1 - \xi) d\xi\right] \tag{53}$$

Making

$$\eta = \frac{\xi + 1}{2} \Rightarrow \frac{d\eta}{d\xi} = \frac{1}{2} \tag{54}$$

one has:

$$\eta(\xi = -1) = \frac{-1 + 1}{2} = 0 \tag{55}$$

$$\eta(\xi = 1) = \frac{1 + 1}{2} = 1 \tag{56}$$

$$\xi = 2\eta - 1 \Rightarrow 1 - \xi = 1 - 2\eta + 1 = 2(1 - \eta) \tag{57}$$

Hence, we have:

$$g_1 = -\frac{L}{8\pi k}\left[\int_0^1 \log(\eta)2(1-\eta)\frac{d\xi}{d\eta}d\eta + \ log(L)\left(\xi - \frac{\xi^2}{2}\right)\Big|_{-1}^{1}\right]$$

$$= -\frac{L}{8\pi k}\left\{\int_0^1 2(1-\eta)2\log(\eta)d\eta\right.$$

$$+ \log(L)\left[1 - \left(\frac{1}{2}\right)^2 - (-1) + \left(\frac{-1}{2}\right)^2\right]\right\}$$

$$= -\frac{L}{8\pi k}\left[4\left(\int_0^1 \log(\eta)d\eta - \int_0^1 \eta\log(\eta)d\eta\right) + 2\log(L)\right] \tag{58}$$

$$g_1 = \frac{L}{4\pi k}\left[\frac{3}{2} - \log(L)\right]; \tag{59}$$

The integral g_2 is not singular when the source point is node 1 because $N_2 = 0$ at node 1, where $T^* \to \infty$.

- Source point at node 2: $\xi_d = 1$.

The integral g_1 is not singular when the source point is node 2 because $N_1 = 0$ at node 2, where $T^* \to \infty$.

$$\int_{-1}^1 N_1 T^*\frac{d\Gamma}{d\xi}d\xi\Big|_{\xi_d=-1} = \int_{-1}^1 N_2 T^*\frac{d\Gamma}{d\xi}d\xi\Big|_{\xi_d=1} \tag{60}$$

This way you have:

$$g_2 = \frac{L}{4\pi k}\left[\frac{3}{2} - \log(L)\right]. \tag{61}$$

6.4   Indirect method for calculating the diagonal of the matrix $[H]$

The singular terms of the matrix $[H]$ can also be calculated analytically, just as it was done for constant elements. However, since the nodes are now at the ends of the element rather than at the center, the source point may not belong to a smooth boundary if it is a corner node. Then, you must calculate the internal angle θ_{int} because the term c of the equation (13) is no longer equal to 1/2. Although this calculation does not present great difficulties, there is an alternative implementation that is usually preferred when dealing with continuous elements. This implementation does not make the integration explicitly but uses a property of the matrix $[H]$ resulting from the modeling of a body under constant temperature. Without losing the generality, consider that all nodes of a body meet the temperature $T = 1$. In this case, the flux will be null on all nodes, that is, $q = 0$ on all nodes. In this way, the matrix equation is rewritten as:

$$[H]\{1\} = [G]\{0\} \tag{62}$$

where $\{1\}$ is a vector with all elements equal to 1 and $\{0\}$ is a vector with all elements equal to zero. In this case, it is easy to see that:

$$\sum_{j=1}^{N} H_{ij} = 0, \ \text{for } i = 1, 2, ..., N. \tag{63}$$

where N is the number of nodes.

Hence, the diagonal terms of the matrix $[H]$ can be calculated as follows:

$$H_{ii} = \sum_{j=1}^{N} H_{ij}, \ \text{with } i \ \neq j, \ \text{for } i = 1, 2 \ , ..., N, \tag{64}$$

since all terms outside the diagonal are regular integrals and have been previously computed.

7   Continuous quadratic boundary elements

In discretization using quadratic elements, the geometry is approximated by a quadratic function along each element, requiring three nodal points per element as shown in Fig. 9.
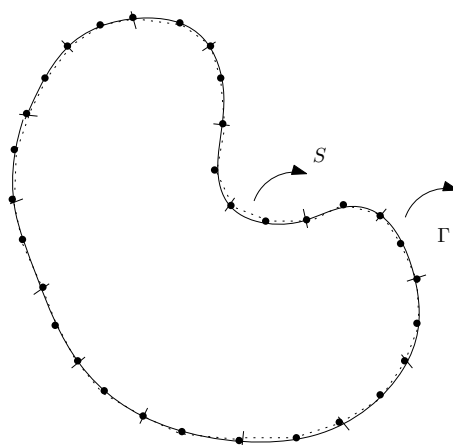
Figure 9: Continuous quadratic elements.

Thus temperature and flux are approximated as follows:

$$
\begin{aligned}
T &= N_1 T_1 + N_2 T_2 + N_3 T_3 \\
q &= N_1 q_1 + N_2 q_2 + N_3 q_3
\end{aligned}
$$

where T_1 is the temperature at local node 1, T_2 the temperature at local node 2, T_3 the temperature at local node 3, q_1 is the flux at local node 1, q_2 is the flux at local node 2, q_3 is flux at local node 3, N_1 is form function 1, N_2 is form function 2, and N_3 is form function 3.

The continuous quadratic form functions N_1, N_2 and N_3 are given by:

$$N_1 = \frac{\xi}{2}(\xi - 1) \tag{65}$$

$$N_2 = (1 - \xi)(1 + \xi) = 1 - \xi^2 \tag{66}$$

$$N_3 = \frac{\xi}{2}(\xi + 1) \tag{67}$$

In this case, the integral equation is given by:

$$cT(d) = \int_s Tq^* dS - \int_s T^* q dS.$$

Discretizing in continuous quadratic boundary elements, it follows:

$$cT(d) = \sum_{j=1}^{n_{elem}} \left[\int_{\Gamma_j} Tq^* d\Gamma \right] - \sum_{j=1}^{n_{elem}} \left[\int_{\Gamma_j} T^* q d\Gamma \right]$$

Likewise, it follows:

$$\begin{cases} x = N_1 x_1 + N_2 x_2 + N_3 x_3 \\ y = N_1 y_1 + N_2 y_2 + N_3 y_3 \end{cases}$$

Writing in matrix form, follows:

$$T = \begin{bmatrix} N_1 & N_2 & N_3 \end{bmatrix} \begin{bmatrix} T_1 \\ T_2 \\ T_3 \end{bmatrix}$$

and

$$q = \begin{bmatrix} N_1 & N_2 & N_3 \end{bmatrix} \begin{bmatrix} q_1 \\ q_2 \\ q_3 \end{bmatrix}.$$

The discretized integral equation is then written as:

$$cT(d) = \sum_{j=1}^{n_{elem}} \left\{ \int_{\Gamma_j} \begin{bmatrix} N_1 & N_2 & N_3 \end{bmatrix} \begin{bmatrix} T_1 \\ T_2 \\ T_3 \end{bmatrix}_j q^* d\Gamma \right\}$$
$$- \sum_{j=1}^{n_{elem}} \left\{ \int_{\Gamma_j} T^* \begin{bmatrix} N_1 & N_2 & T_3 \end{bmatrix} \begin{bmatrix} q_1 \\ q_2 \\ q_3 \end{bmatrix}_j d\Gamma \right\}. \tag{68}$$

Since T_1, T_2, T_3, q_1, q_2 and q_3 are nodal values, it follows:

$$cT(d) = \sum_{j=1}^{n_{elem}} \left\{ \int_{\Gamma_j} \begin{bmatrix} N_1 & N_2 & N_3 \end{bmatrix} q^* d\Gamma \begin{bmatrix} T_1 \\ T_2 \\ T_3 \end{bmatrix}_j \right\}$$
$$- sum_{j=1}^{n_{elem}} \left\{ \int_{\Gamma_j} \begin{bmatrix} N_1 & N_2 & N_3 \end{bmatrix} T^* d\Gamma \begin{bmatrix} q_1 \\ q_2 \\ q_3 \end{bmatrix}_j \right\}, \tag{69}$$

which can be written as follows:

$$cT(d) = \sum_{j=1}^{n_{elem}} \left\{ \begin{bmatrix} h_1 & h_2 & h_3 \end{bmatrix}_j \begin{bmatrix} T_1 \\ T_2 \\ T_3 \end{bmatrix}_j - \begin{bmatrix} g_1 & g_2 & g_3 \end{bmatrix}_j \begin{bmatrix} q_1 \\ q_2 \\ q_3 \end{bmatrix}_j \right\},$$

where

$$h_1 = \int_{\Gamma_j} N_1 q^* d\Gamma,$$

$$h_2 = \int_{\Gamma_j} N_2 q^* d\Gamma,$$

$$h_3 = \int_{\Gamma_j} N_3 q^* d\Gamma,$$

$$g_1 = \int_{\Gamma_j} N_1 T^* d\Gamma,$$

$$g_2 = \int_{\Gamma_j} N_2 T^* d\Gamma$$

and

$$g_3 = \int_{\Gamma_j} N_3 T^* d\Gamma.$$

7.1   Integration of matrices $[H]$ and $[G]$ when source point does not belong to element

The integration of the terms of the arrays $[H]$ and $[G]$ when the source point does not belong to the element is regular and does not present great differences in relation to the integration of the constant element. To avoid unnecessary repetition, the integration for the quadratic element will not be detailed.

7.2   Matrix integration $[H]$ and $[G]$ when source point belongs to element

As already shown, the MEC presents some integrals of singular functions (functions that tend to infinity). In the case of the developed formulation, singular integrals are of two types:

1. In the matrix $[G]$ it is of the form $\log r$ which is called a weak singularity (improper integral);

2. In the matrix $[H]$ it is of the form $\frac{1}{r}$ which is called strong singularity (integral in the sense of Cauchy's principal value);

Therefore, the treatment of strong singularity can be done indirectly due to the properties of the matrix $[H]$, as shown in section 6.4. In the case of the matrix $[G]$, there are two possibilities, either numerically or analytically, the latter being only recommended for constant or linear elements. In the case of higher order form functions (quadratic, for

example), the Jacobian of the transformation from Γ to ξ is no longer constant along the element, making the analytical treatment unfeasible. Therefore, numerical treatment is recommended.

Singular integrals of the order $(\log r)$ can be efficiently evaluated by the Gauss quadrature with a cubic variable transformation, as proposed by Telles Telles [1987], which exactly cancels the logarithmic singularity. Another possibility is the use of the logarithmic Gauss quadrature Brebbia and Dominguez [1992] which is among the most used numerical methods for the treatment of integrals with weak singularity in two-dimensional problems $(\log r)$.

The integration of the terms of the matrix $[H]$ for continuous quadratic elements is done indirectly, as already described in the section 6.4 for continuous linear elements.

The integration of the terms of the matrix $[G]$ for continuous quadratic elements is done using the logarithmic quadrature of Gauss, as will be detailed in the following paragraphs.

The coordinate x of a point belonging to a quadratic element is approximated by:

$$
\begin{aligned}
x = N_1 x_1 + N_2 x_2 + N_3 x_3 &= \frac{\xi}{2}(\xi - 1)x_1 + (1 - \xi^2)x_2 + \frac{\xi}{2}(\xi + 1)x_3 \\
&= \frac{1}{2}\xi^2 (x_1 - 2x_2 + x_3) + \frac{1}{2}\xi (x_3 - x_1)) + x_2
\end{aligned}
\tag{70}
$$

Likewise, you have:

$$
y = \frac{1}{2}\xi^2 (y_1 - 2y_2 + y_3) + \frac{1}{2}\xi (y_3 - y_1) + y_2
\tag{71}
$$

The source point has coordinate (x_d, y_d), where $x_d = x(\xi = \xi_d)$ and $y_d = y(\xi = \xi_d)$. Thus, we have $\xi_d = -1$ for the source point at node 1, $\xi_d = 0$ for the source point at node 2 and $\xi_d = +1$ for the source point at node 3. Hence, we have:

$$
x_d = \frac{1}{2}\xi_d^2 (x_1 - 2x_2 + x_3) + \frac{1}{2}\xi_d (x_3 - x_1) + x_2
\tag{72}
$$

$$
y_d = \frac{1}{2}\xi_d^2 (y_1 - 2y_2 + y_3) + \frac{1}{2}\xi_d (y_3 - y_1) + y_2
\tag{73}
$$

$$
r = \sqrt{(x - x_d)^2 + (y - y_d)^2} = \sqrt{r_x^2 + r_y^2}
\tag{74}
$$

where

$$
r_x = x - x_d = \frac{1}{2}\left(\xi^2 - \xi_d^2\right)(x_1 - 2x_2 + x_3) + \frac{1}{2}(\xi - \xi_d)(x_3 - x_1)
\tag{75}
$$

$$
r_x = \frac{1}{2}(\xi - \xi_d)\left[(x_1 - 2x_2 + x_3)(\xi + \xi_d) + x_3 - x_1\right]
\tag{76}
$$

Likewise, you have:

$$
r_y = \frac{1}{2}(\xi - \xi_d)\left[(y_1 - 2y_2 + y_3)(\xi + \xi_d) + y_3 - y_1\right]
\tag{77}
$$

and

$$r = \frac{1}{2} (\xi - \xi_d) \left\{ [(x_1 - 2x_2 + x_3)(\xi + \xi_d) + x_3 - x_1]^2 \right.$$
$$\left. + [(y_1 - 2y_2 + y_3)(\xi + \xi_d) + y_3 - y_1]^2 \right\}^{\frac{1}{2}} \tag{78}$$

Calling

$$r_A = \frac{1}{2} (\xi - \xi_d) \tag{79}$$

and

$$r_B = \left\{ [(x_1 - 2x_2 + x_3)(\xi + \xi_d) + x_3 - x_1]^2 \right.$$
$$\left. + [(y_1 - 2y_2 + y_3)(\xi + \xi_d) + y_3 - y_1]^2 \right\}^{\frac{1}{2}} \tag{80}$$

one has to

$$r = r_A r_B \tag{81}$$

where $r_B > 0$.

$$[g] = \int T^* [N_1 \quad N_2 \quad N_3] d\Gamma = [g_1 \quad g_2 \quad g_3] \tag{82}$$

where

$$g_1 = \int_{\Gamma_j} T^* N_1 d\Gamma, \tag{83}$$

$$g_2 = \int_{\Gamma_j} T^* N_2 d\Gamma \tag{84}$$

and

$$g_3 = \int_{\Gamma_j} T^* N_3 d\Gamma. \tag{85}$$

The integral g_1 is given by:

$$g_1 = \int_{\Gamma_j} T^* N_1 d\Gamma = \int_{-1}^{1} T^* N_1 \frac{d\Gamma}{d\xi} d\xi$$
$$= \int_{-1}^{1} \frac{-1}{2\pi k} \log(r_A r_B) N_1 \frac{d\Gamma}{d\,xi} d\xi$$
$$= \frac{-1}{2\pi k} \int_{-1}^{1} [\log(r_A) + \log(r_B)] N_1 \frac{d\Gamma}{d\,xi} d\xi = g_{1s} + g_{1ns} \tag{86}$$

where

$$g_{1s} = \frac{-1}{2\pi k} \int_{-1}^{1} \log(r_A) N_1 \frac{d\Gamma}{d\xi} d\xi \tag{87}$$

is a weak singularity integral that will be integrated using logarithmic Gauss quadrature and

$$g_{1ns} = \frac{-1}{2\pi k} \int_{-1}^{1} \log(r_B) N_1 \frac{d\Gamma}{d\xi} d\xi \tag{88}$$

is a regular (non-singular) integral that will be integrated using standard Gaussian quadrature.

- Source point at node 1: $\xi_d = -1$.

$$g_{1s} = \frac{-1}{2\pi k} \int_{-1}^{1} \log(r_A) \frac{\xi}{2}(\xi - 1) \frac{d\Gamma}{d\xi} d\xi \tag{89}$$

Making

$$\eta = \frac{\xi + 1}{2} \Rightarrow \frac{d\eta}{d\xi} = \frac{1}{2} \tag{90}$$

one has:

$$\eta(\xi = -1) = \frac{-1 + 1}{2} = 0 \tag{91}$$

$$\eta(\xi = 1) = \frac{1 + 1}{2} = 1 \tag{92}$$

$$\xi = 2\eta - 1 \Rightarrow 1 - \xi = 1 - 2\eta + 1 = 2(1 - \eta) \tag{93}$$

$$r_A = \frac{\xi - \xi_d}{2} = \eta \tag{94}$$

Hence, we have:

$$g_{1s} = \frac{-1}{2\pi k} \int_{0}^{1} \log(\eta) N_1(\xi(\eta)) \frac{d\,Gamma}{d\xi} \frac{d\xi}{d\eta} d\eta = \frac{-1}{\pi k} \int_{0}^{1} \log(\eta) N_1(\xi(\eta)) \frac{d\Gamma}{d\xi} d\eta \tag{95}$$

The integrals g_2 and g_3 are not singular when the source point is node 1 because $N_2 = N_3 = 0$ at node 1, where $T^* \to \infty$.

- Source point at node 2: $\xi_d = 0$.

$$r_A = \frac{\xi - \xi_d}{2} = \frac{\xi - 0}{2} = \frac{\xi}{2} \tag{96}$$

$$g_{2s} = \frac{-1}{2\pi k} \int_{-1}^{1} \log(\frac{\xi}{2}) N_2 \frac{d\Gamma}{d\xi} d\xi = \frac{-1}{2\pi k} \int_{-1}^{1} \log(\xi) N_2 \frac{d\Gamma}{d\xi} d\,xi$$

$$- \frac{-1}{2\pi k} \int_{-1}^{1} \log(2) N_2 \frac{d\Gamma}{d\,xi} d\xi = g_{2s1} + g_{2s2} \qquad (97)$$

where

$$g_{2s2} = \frac{-1}{2\pi k} \int_{-1}^{1} \log(2) N_2 \frac{d\Gamma}{d\xi} d\xi \qquad (98)$$

is a regular integral and can be integrated using standard Gaussian quadrature.

$$g_{2s1} = \frac{-1}{2\pi k} \int_{-1}^{1} \log(\xi) N_2 \frac{d\Gamma}{d\xi} d\xi \qquad (99)$$

is an integral with weak singularity and must be calculated using logarithmic Gauss quadrature through the following transformation:

$$\eta = \xi \Rightarrow \frac{d\eta}{d\xi} = 1 \qquad (100)$$

one has:

$$\eta(\xi = 0) = 0 \qquad (101)$$

$$\eta(\xi = 1) = 1 \qquad (102)$$

$$r_A = \frac{\xi - \xi_d}{2} = \frac{\xi}{2} = \frac{\eta}{2} \qquad (103)$$

Hence, we have:

$$g_{2s1} = 2 \times \frac{-1}{2\pi k} \int_{0}^{1} \log\left(\frac{\eta}{2}\right) N_2(\xi(\eta)) \frac{d\Gamma}{d\xi} \frac{d\xi}{d\eta} d\eta = \frac{-1}{\pi k} \int_{0}^{1} \log(\eta) N_2(\xi(\eta)) \frac{d\Gamma}{d\xi} d\eta \quad (104)$$

The integrals g_1 and g_3 are not singular when the source point is node 2 because $N_1 = N_3 = 0$ at node 2, where $T^* \to \infty$.

- Source point at node 3: $\xi_d = 1$.

The integrals g_1 and g_2 are not singular when the source point is node 3 because $N_1 = N_2 = 0$ at node 3, where $T^* \to \infty$.

$$\int_{-1}^{1} N_1 T^* \frac{d\Gamma}{d\xi} d\xi \bigg|_{\xi_d=-1} = \int_{-1}^{1} N_3 T^* \frac{d\Gamma}{d\xi} d\xi \bigg|_{\xi_d=1} \qquad (105)$$

In this way, the integral g_3 does not need to be calculated when the source point is node 3 because it uses the calculated value of the integral g_1 when the source point is node 1.

8   Heat sources

Given Laplace's equation for a heat conduction problem, as seen:

$$\frac{\partial^2 T}{\partial x^2} + \frac{\partial^2 T}{\partial y^2} = 0$$

with its respective integral boundary equation

$$cT(x_d, y_d) = \int_\Gamma q^* T d\Gamma - \int_\Gamma T^* q d\Gamma.$$

If there is heat generation, the Poisson formulation given by:

$$\frac{\partial^2 T}{\partial x^2} + \frac{\partial^2 T}{\partial y^2} = f(x, y), \tag{106}$$

where $f(x, y)$ is the heat generation function (heat source).

Multiplying Eq.(106) by a weight function and integrating along the boundary we obtain a residual function. Assuming that this residue is equal to zero, we have:

$$\int_A \left[\frac{\partial^2 T}{\partial x^2} + \frac{\partial^2 T}{\partial y^2} - f(x, y) \right] \omega dA = 0.$$

In order to obtain the integral boundary equation, it follows:

$$\int_A \left[\frac{\partial^2 T}{\partial x^2} + \frac{\partial^2 T}{\partial y^2} \right] \omega dA - \int_A f(x, y) \omega dA = 0 \tag{107}$$

that works

$$cT(x_d, y_d) = \int_s q^* T ds - \int_s T^* q ds + \int_A T^* f(x, y) dA. \tag{108}$$

Observing that there is a domain integral in the formulation of Eq.(108) that has to be transformed into a boundary integral, otherwise, the problem domain will have to be discretized.

8.1   Concentrated heat sources

If the heat source is concentrated, it will be represented by a Dirac delta function, ie:

$$f(x, y) = C\delta(x - x_c, y - y_c) \tag{109}$$

where (x_c, y_c) are the coordinates of the point where the applied heat source and C is the value of the heat source. If C is negative, $f(x, y)$ is a concentrated heat sink. Substituting the equation (109) into the equation (108) we have:

$$cT(x_d, y_d) = \int_s q^* T ds - \int_s T^* q ds + \int_A T^* C\delta(x - x_c, y - y_c) dA. \tag{110}$$

By the properties of the Dirac delta, the domain integral becomes the value of the function at the point, that is:

$$cT(x_d, y_d) = \int_s q^* T ds - \int_s T^* q ds + CT^*(x_c - x_d, y_c - y_d). \tag{111}$$

8.2   Domain distributed heat sources

If the heat source $f(x, y)$ is distributed in the domain, the radial integration method can be used to transform the domain integral into a boundary integral, as follows:

$$\int_A T^* f(x, y) dA = \int_{\theta_1}^{\theta_2} \underbrace{\int_0^r T^* f[x(rho, \theta), y(\rho, \theta)] \rho d\rho}_{F} \, d\theta.$$

Making

$$F = \int_0^r T^* f[x(\rho, \theta), y(\rho, \theta)] \rho d\rho, \tag{112}$$

results

$$\int_A T^* f(x, y) dA = \int_{\theta_1}^{\theta_2} F d\theta. \tag{113}$$
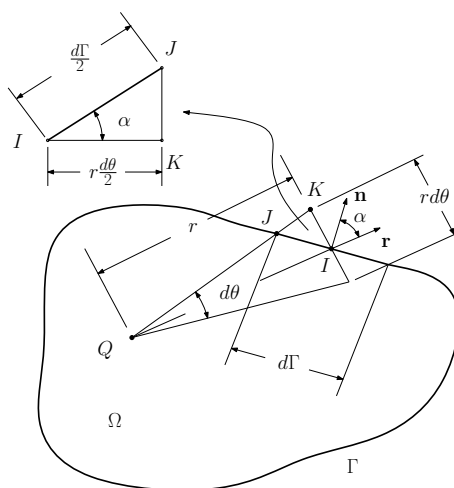
Figure 10: Transformation from domain to boundary.

From the triangle in the figure 10, it follows:

$$\cos\alpha = \frac{r\frac{d\theta}{2}}{\frac{d\Gamma}{2}}$$

$$d\theta = \frac{\cos\alpha}{r} ds. \tag{114}$$

Since $\vec{n}$ and $\vec{r}$ are unit vectors, we have:

$$\cos\alpha = \vec{n}.\vec{r}. \tag{115}$$

Replacing Eq.(115) in Eq.(114) and then in Eq.(113), we have

$$\int_A T^* f(x, y) dA = \int_s F \frac{\vec{n}.\vec{r}}{r} ds. \tag{116}$$

Replacing Eq.(116) in Eq.(107), follows

$$cT(x_d, y_d) = \int_s q^* T ds - \int_s T^* q ds + \int_s F \frac{\vec{n}.\vec{r}}{r} ds,$$

which is the integral boundary equation when heat is generated.

9   Numerical examples

To evaluate the boundary element formulations using constant, linear and quadratic elements, the temperature distribution in a cylinder and a rectangular plate was analyzed. In the cylinder, the boundary conditions are constant in the outer and inner diameters, while in the plate, the boundary conditions vary at each point of the boundary.

Example 9.1 Conduction of heat in a cylinder *Consider a cylinder with dimensions shown in figure 11. The problem was discretized with different meshes, from the coarsest to the most refined. It was considered* $r_i = 1$, $r_o=2$, $T(r_i)= 100$ and $q(r_o)= -200$, k = 1.
  The analytical solution for temperature is given by:

$$T(r) = T(r_i) - q(r_o)\, r_o \log(r/r_i) \tag{117}$$

and to the stream by:

$$q(r) = -q(r_o)\frac{r_o}{r}. \tag{118}$$
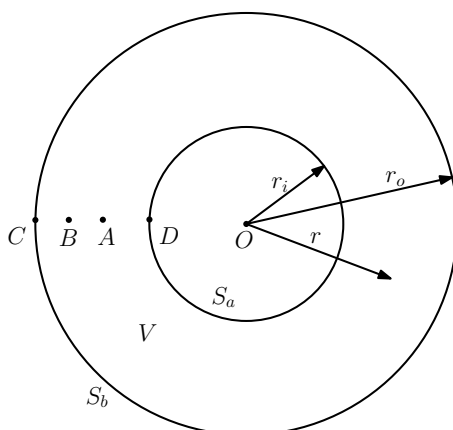
Figure 11: Cylinder dimensions

The figures 12, 13 and 14 show, respectively, a 16-node mesh with constant boundary elements, a 112-node mesh with constant boundary elements, and a 16-node mesh with quadratic boundary elements. Note that, for a coarse discretization, with 16 nodes, the approximation of a circle with quadratic elements, which can be curved, is better satisfied than with straight elements (constant or linear elements).
  Results were rated at 4 points. The first two points are the internal points A and B, where $r_A = (r_i + r_o)/2 = 1.50$ and $r_B = (r_i + 3r_o)/4 = 1.75$. The two others are the boundary points C and D. The value of temperature T and flux q at these points were calculated with different meshes and different types of elements and the results were compared with analytical solutions of the problem for temperature and flux, given by the equations (117) and (118), respectively. The figures 16, 17, 18, 19, 20 and 21 show these comparisons.
  Care was taken that the number of nodes was the same in each comparison. For this, the number of quadratic elements was half the number of linear and constant elements. Furthermore, so that the accuracy of the integration did not influence the analysis, a
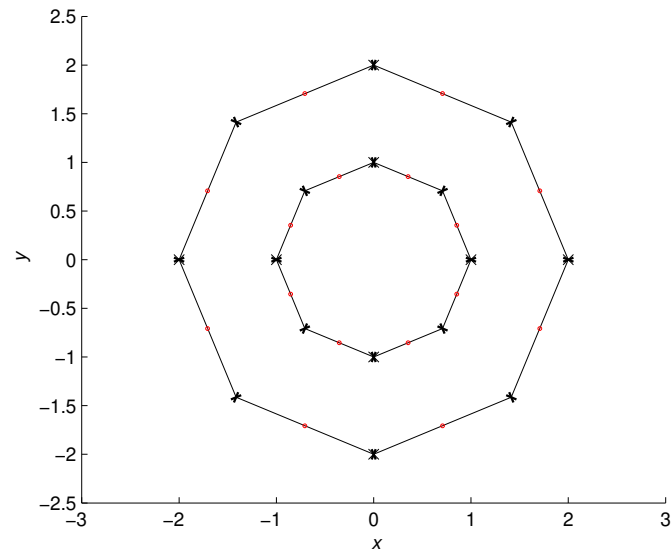
Figure 12: 16-node boundary element mesh with constant elements (8 on the outer boundary and 8 on the inner boundary)
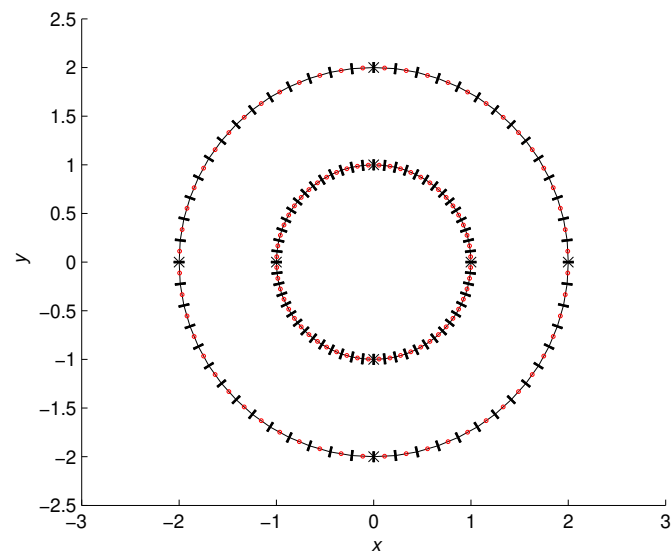
Figure 13: Boundary element mesh with 112 nodes with constant elements (56 on the outer boundary and 56 on the inner boundary)
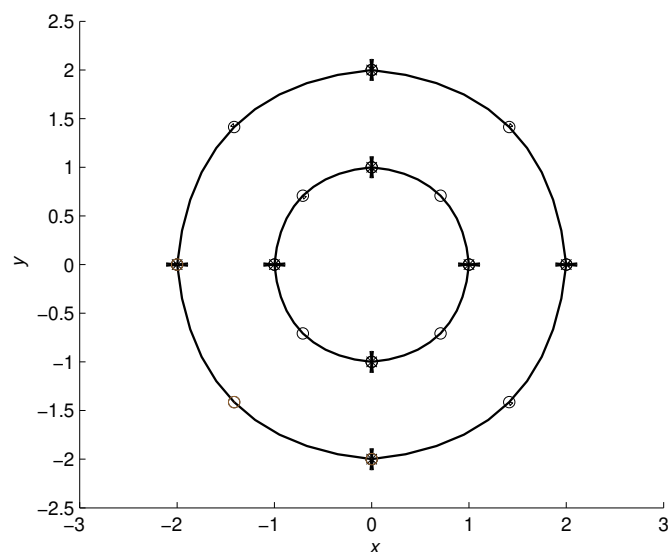
Figure 14: Boundary element mesh with 16 nodes with quadratic elements (8 on the outer boundary and 8 on the inner boundary)

large number of integration points were used in all the integrals of the boundary elements method. All integrals were calculated with 16 Gauss points, which represents a number more than enough for an integration with good precision.

Analyzing the figures 16, 17, 18, 19, 20 and 21, it is noted that all formulations converge to the solution analytical as the mesh is refined. However, it was not possible to observe any element that showed faster convergence in all cases. For the temperature at the inner points A and B, the quadratic elements showed the fastest convergence and the constant elements the slower convergence. For the flux at the inner points A and B, the linear elements showed the slowest convergence while the constant elements converged faster at the point A and the quadratic ones converge faster at the point B. At the points C and D, belonging to the inner and outer boundaries, respectively, the results for quadratic elements were analyzed both at the element's endpoints and at the element's middle nodes. In the case of point C, where temperature was the unknown variable, the fastest convergence was presented by the constant elements while the slower one was presented by the linear elements. In the case of point D, where the flux was calculated, the fastest convergence was that of the constant elements, while the slowest was presented by the linear elements. In the last two cases the convergence to the grid of quadratic elements was faster at the middle nodes than at the endpoints of the elements.
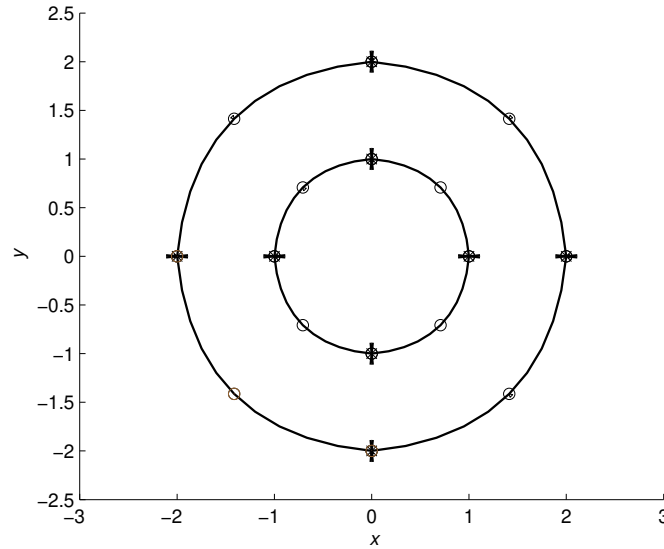
Figure 15: 16-node boundary element mesh with quadratic elements (8 on the outer boundary and 8 on the inner boundary)
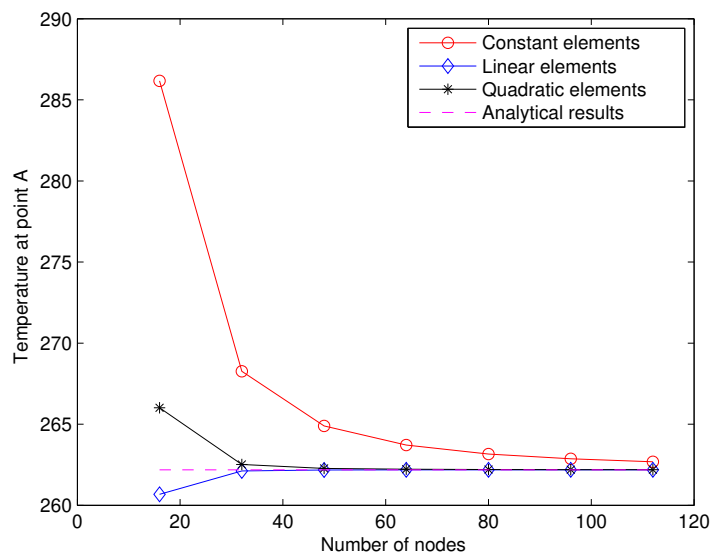
Figure 16: Temperature at point A.
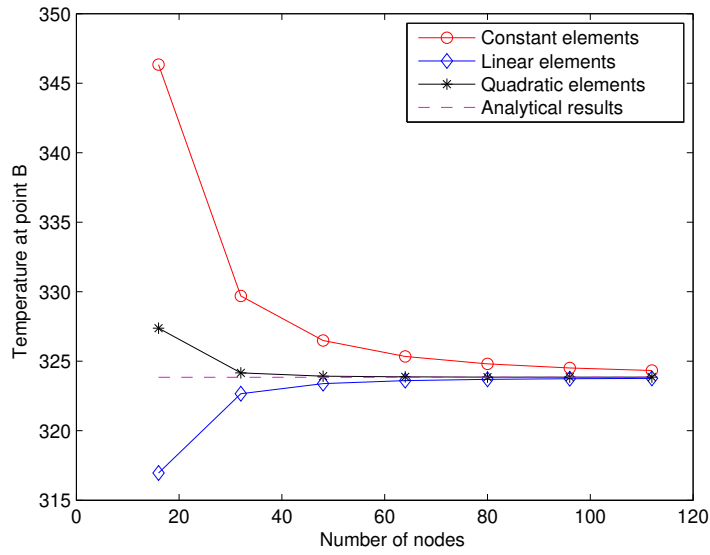
Figure 17: Temperature at point B.
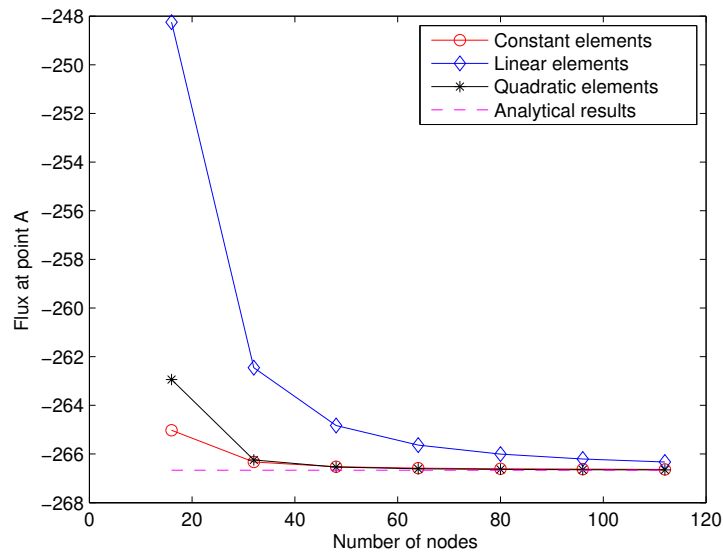
Figure 18: flux at point A.
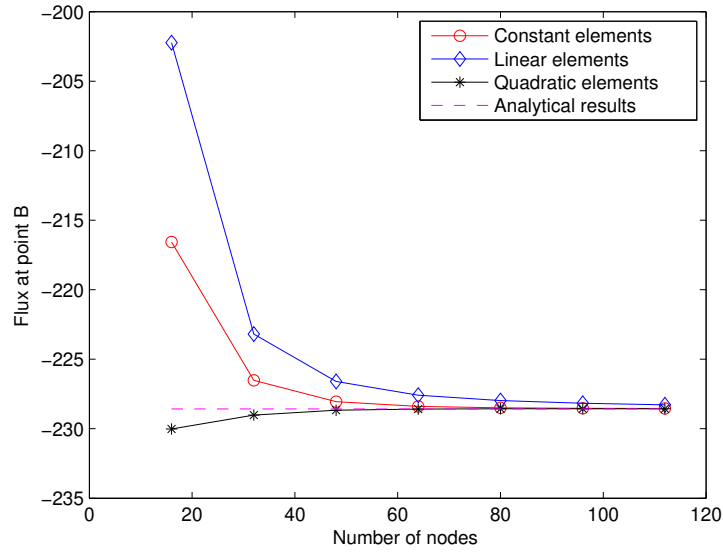
Figure 19: flux at point B.
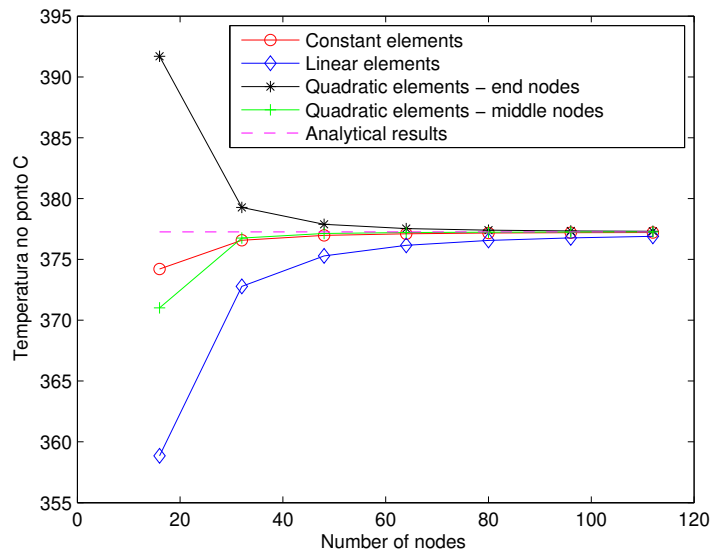
Figure 20: Temperature at point C.
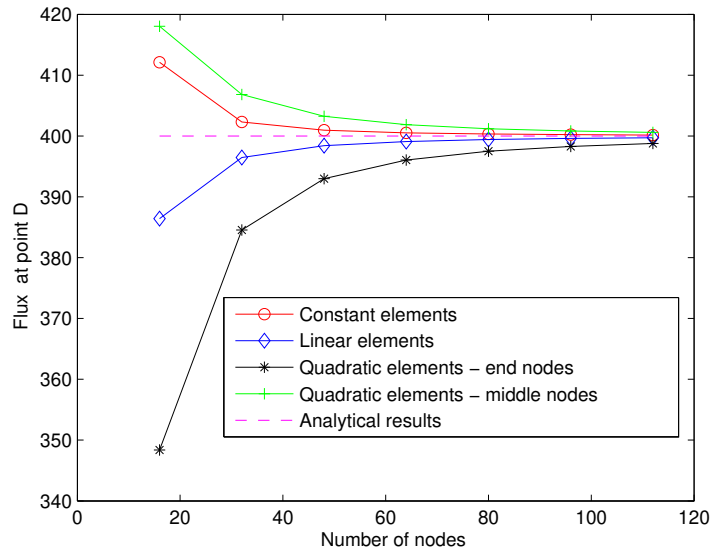
Figure 21: flux at point D.
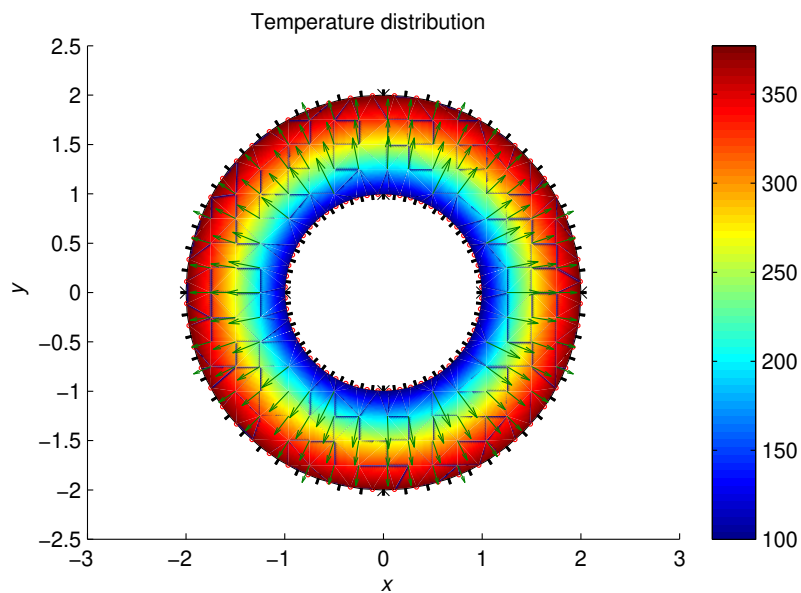
Figure 22: Distribution of temperature and heat flux across the cylinder.

Example 9.2 Conduction of heat on a plate

Consider a rectangular plate $ABCD$ as shown in figure 23. It was considered $k = 1$. The boundary conditions on the plate are as follows:
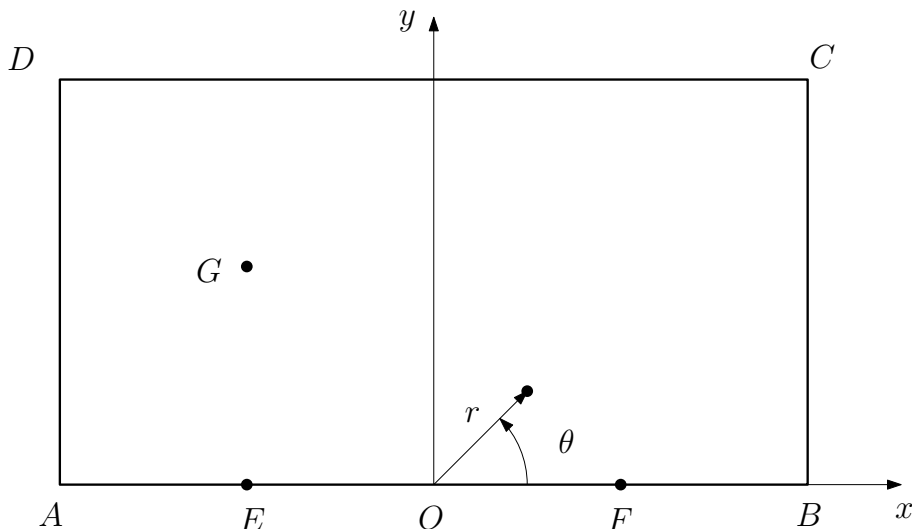
Figure 23: Rectangular plate.

$$q = -\frac{1}{2\sqrt{r}} \left(\cos \frac{\theta}{2} \cos \theta + \sin \frac{\theta}{2} \sin \theta \right) \quad \text{in} \quad BC, \tag{119}$$

$$q = -\frac{1}{2\sqrt{r}} \left(\cos \frac{\theta}{2} \sin \theta - \sin \frac{\theta}{2} \cos \theta \right) \quad \text{in} \quad CD, \tag{120}$$

$$q = \frac{1}{2\sqrt{r}} \left(\cos \frac{\theta}{2} \cos \theta + \sin \frac{\theta}{2} \sin \theta \right) \quad \text{in} \quad DA, \tag{121}$$

$$T = 0 \quad \text{in} \quad AO \tag{122}$$

and

$$q = 0 \quad \text{in} \quad OB. \tag{123}$$

The analytical solution to this problem is given by:

$$u = \sqrt{r} \cos \frac{\theta}{2}, \tag{124}$$

$$q_x = \frac{\cos \frac{\theta}{2}}{2\sqrt{r}} \tag{125}$$

and

$$q_y = \frac{\sin \frac{\theta}{2}}{2\sqrt{r}}. \tag{126}$$

The coordinates of the points A and C are, respectively (-1.0; 0.0) and (1.0; 1.0). The E point is the midpoint of the AO segment and the F point is the midpoint of the OB segment. The point G has coordinate (-0.5; 0.5).

As in the previous example, the rectangular plate was also discretized with different meshes, from the coarsest (24 knots) to the most refined (120 knots). In all cases, the elements used were close in size but not equal in size. The temperature value T was calculated at points F and G, the flux normal to the boundary q was calculated at point E and fluxs q_x and q_y, in the directions x and y, respectively, were calculated at point G. The figures 24, 25, 26, 27, 28 show the values of temperatures and fluxs at these points.
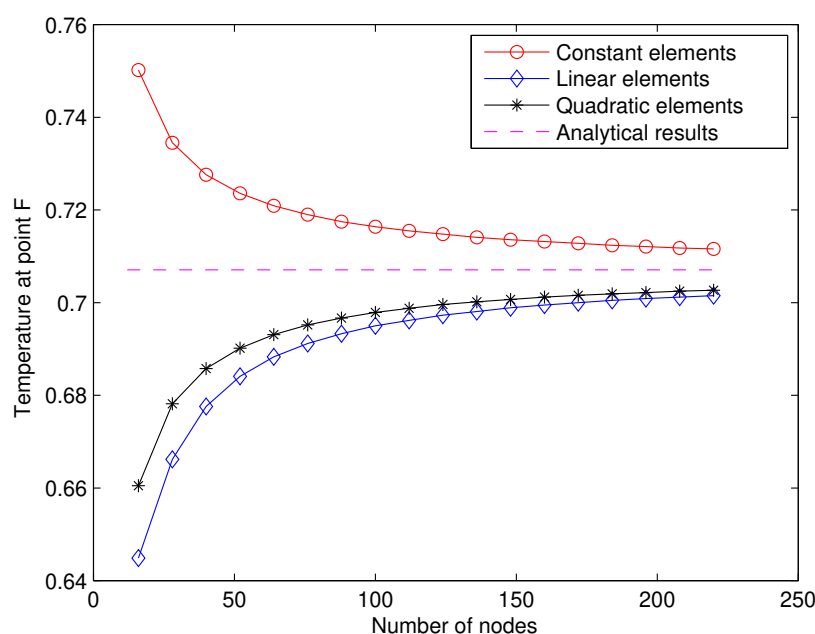
Figure 24: Temperature at point F.

Figure 29 shows the temperature distribution and heat flux in the rectangular plate.

The behavior of the results obtained in this example are, in most cases, very similar to the behavior obtained in the previous example. All formulations converge into the analytical solution at all points for both temperature and flux. The linear elements showed a slightly slower convergence than the quadratic and constant elements, the latter two having very similar convergence, although they approach the analytical solution from opposite sides (one above and one below the analytical solution). In the case of Figure 25, the quadratic and linear elements presented expressive oscillations for the coarser meshes, which stabilized with the refinement of the mesh. These oscillations also occurred in a less expressive way in Figure 28.
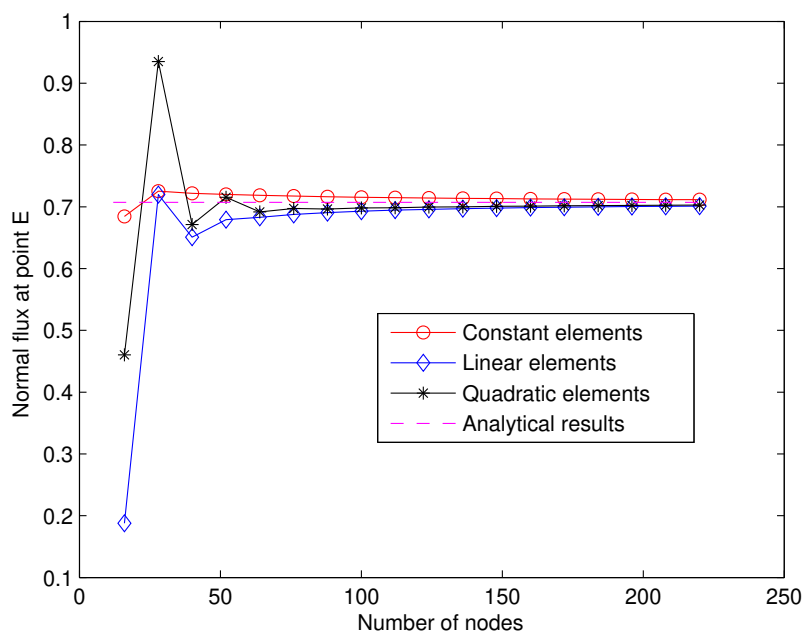
Figure 25: Heat flux normal to the boundary at point E.
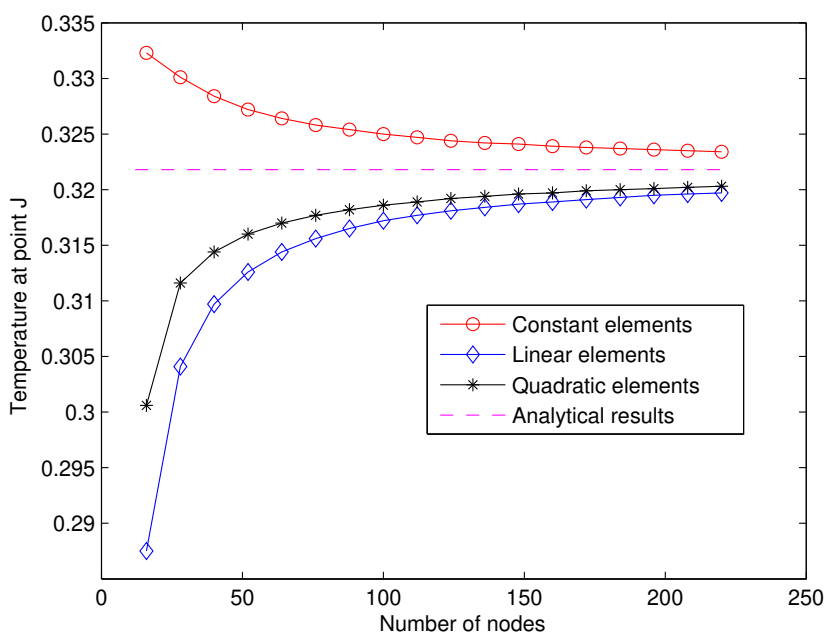
Figure 26: Temperature at point G.
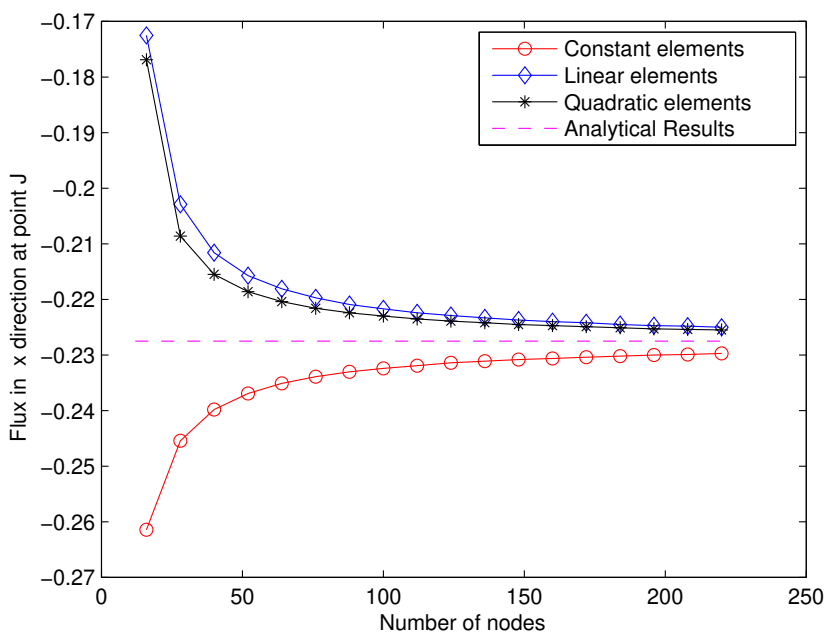
Figure 27: Heat flux in the direction x at point G.
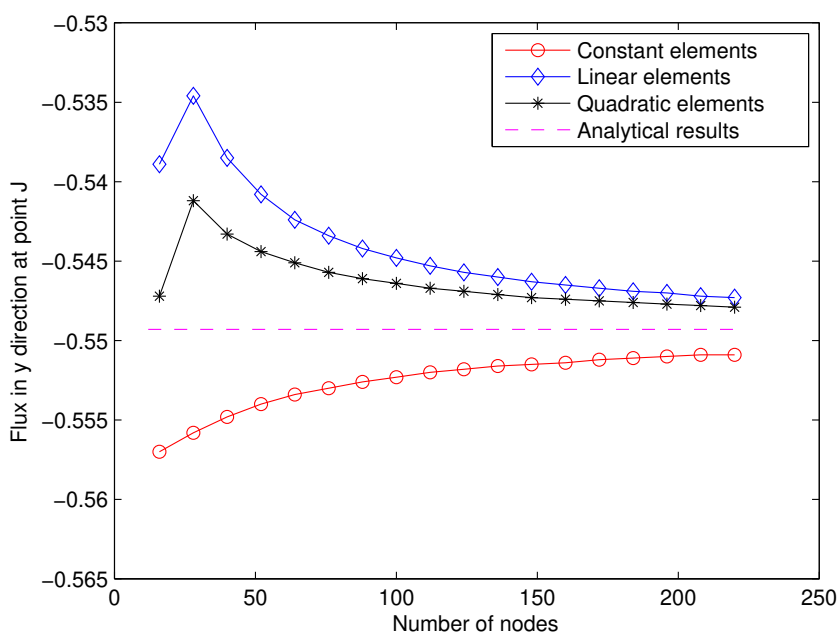
Figure 28: Heat flux in the y direction at the point G.
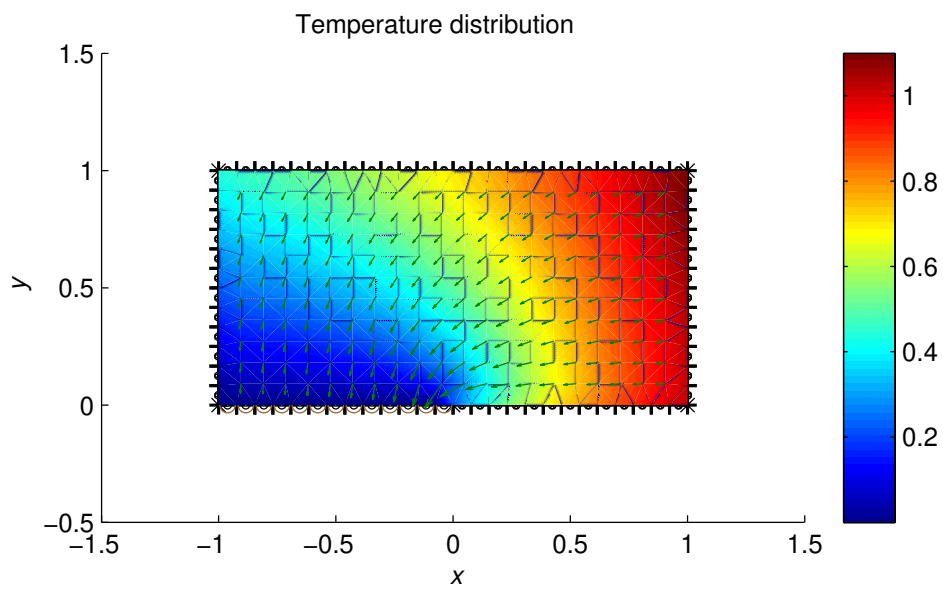
Figure 29: Distribution of temperature and heat flux on the plate.

10   Concluding remarks

For certain problems, if an appropriate auxiliary field, known as the fundamental solution for the problem, is used in the integral formulation, the domain integrals may be resolved and rewritten as non-integral terms, thus leading to an integral representation wherein only boundary integrals remain. The equation obtained from the use of integral identities and fundamental solutions is called the boundary integral equation (BIE). The fundamental solution is an auxiliary field that satisfies the partial differential equation for the problem being modeled, and is valid for an extended, infinite domain that surrounds and encompasses the domain of the BVP being studied. For a particular problem, the fundamental solution is a function of the distance between two different points in the extended domain, among other possible variables. The usual way to understand the fundamental solution is to let an observer sit in one of these points, called the collocation point, while the other point, called the field point, is allowed to vary throughout the extended domain. When the distance between these two points becomes zero, the fundamental solution is singular. As the fundamental solution is part of the integrand of the BIE, the solution of this boundary integral representation requires the understanding of singular integrals, which arise when the collocation and field points coincide. One must note that although a mathematical singularity will appear due to the use of fundamental solutions, the original variable of interest represents a field that usually is not physically singular, and thus, although the integrand may be singular, the integral exists and has a non singular value, in this case. A numerical solution for a particular BIE, containing boundary integrals only, can be performed through the discretization of the domain boundary into boundary elements. To perform this discretization, interpolation functions need to be used for each boundary element, both for the geometry and for the unknown variables of the problem. A usual approach is to use polynomial interpolation functions similar to the ones adopted for the finite element method (FEM). Again, the interpolation functions can be expressed in terms of shape functions (isoparametric elements). After the discretization of the boundary, the integrals can be numerically solved by some quadrature scheme, to obtain an algebraic equation in terms of the boundary variables at the nodes. The numerical integration for non-singular integrals may follow standard Gauss quadrature procedures, for example, but the integration of the singular integrals may require some special techniques.

When collocation is performed for one particular point at the boundary, only one integral equation is obtained. The discretization of this integral equation leads to only one algebraic equation written in terms of the quantities of interest at the boundary nodes. Collocating at a different boundary point leads to another boundary integral equation, which is independent from the equation obtained from the collocation at the first boundary point. But, for the discretized problem, for a given number of boundary unknowns at the nodes (for example, n nodes with one unknown per node, leading to a total of n boundary unknowns) only the first set of discretized algebraic equations (in this example, the first n algebraic equations), obtained by changing the collocation point from one boundary location to another, will consist of independent equations. Thus, to 99 be able to obtain a system of linearly independent equations to be solved, one must collocate at a number of different boundary points, so that the matrix of the system of equations is a square, invertible matrix. Although collocation could have been performed at any boundary point, an usual procedure is to collocate at the boundary nodes, so that all the boundary

information necessary to solve the problem is represented in terms of the boundary nodal variables. Usually, there are more boundary unknowns than available independent algebraic equations obtained from this approach. Only by imposing the boundary conditions, for the prescribed boundary quantities, the system of equations could be determined, for the remaining boundary unknowns.

After obtaining the unknown boundary quantities of interest as the solution of the system of equations, a post-processing approach can be used, performing further collocation at any other points, either in the domain (interior points) our outside the domain (exterior points), to obtain the quantities of interest at these points. The above-outlined method was originally known as the Boundary Integral Equation (BIE) method, and later has become to known as the Boundary Element Method (BEM). Some important points must be made:

- When the boundary integral equation is written for collocation points outside the boundary (interior or exterior points), as the field point remains a boundary point, no singular integrals are obtained for collocation at these interior or exterior points.

- One must note that, differently from the FEM, although element interpolating functions are being used for each boundary element, this numerical approach does not lead to local support, as the auxiliary function being used is a fundamental solution, which is eminently non-local. The fundamental solution requires information from a field point, which belongs to the element being integrated, and from a collocation point, which may be in the element being integrated, or may be at some other location elsewhere in the boundary, thus outside this element. Thus, the matrix of the system of equations, obtained after the discretization of the boundary and after imposing the boundary conditions, is non-symmetric and fully-populated.

- Every boundary integral equation obtained from collocation at a particular point is an exact equation, as both the proper integral identity and the fundamental solution used are, in fact, exact representations for the problem being modeled. In the BEM, the only approximation occurs when the boundary is discretized into boundary elements. Therefore, in the BEM, exact integral equations are written for the approximate boundary, while in the FEM, an approximate integral representation in the domain was used, and another approximation was also used in every finite element, as the geometry and the quantities of interest were described in terms of the interpolating functions.

For further reading on the Boundary Element Method for potential, fluids, acoustics, elasticity, plates, and shells, some books ate indicated on references Paris et al. [1997], Beer et al. [2008], Gaul et al. [2003], Wrobel [2002], Aliabadi [2002], Katsikadelis [2002], Bonnet [1999], Beer and Watson [1992], Jaswon [1977].

References

Aliabadi. *Boundary Element Method V 2*. John Wiley & Sons, Apr. 2002. ISBN 0470842989.

G. Beer and J. Watson. *Introduction to Finite and Boundary Element Methods for Engineers*. Wiley, 1992. ISBN 0 471 92813 5.

G. Beer, I. Smith, and C. Duenser. *The Boundary Element Method with Programming*. Springer Vienna, Apr. 2008. ISBN 3211715746.

M. B. Bonnet. *Boundary Integral Equation Methods*. John Wiley & Sons, June 1999. ISBN 0471971847.

C. Brebbia and J. Dominguez. *Boundary Element an Introductory Course*. Computation Mechanics Publications, Southampton, Boston, second edition, 1992.

L. Gaul, M. KÃ¶gl, and M. Wagner. *Boundary Element Methods for Engineers and Scientists*. Springer Berlin Heidelberg, Feb. 2003. ISBN 3540004637.

M. A. Jaswon. *Integral equation methods in potential theory and elastostatics (Computational mathematics and applications)*. Academic Press, 1977. ISBN 9780123810502.

J. T. Katsikadelis. *Boundary Elements: Theory and Applications*. Elsevier Science & Techn., May 2002. ISBN 9780080528243.

F. Paris, J. Canas, and J. Cañas. *Boundary element method: fundamentals and applications*. Oxford University Press, USA, 1997.

J. C. F. Telles. A self adptive co-ordinate transformation for efficient numerical evaluation of general boundary element integrals. *International Journal for Numerical Methods in Engineering*, 24:959–973, 1987.

L. C. Wrobel. *Boundary Element Method V 1*. John Wiley & Sons, Apr. 2002. ISBN 0471720399.

Chapter 20

The Boundary Element Method for Structural Problems

Chapter details

Chapter DOI:

Chapter suggested citation / reference style:

P.S.: DOI may be included at the end of citation, for completeness.

Book details

The Boundary Element Method for Structural Problems

E. L. Albuquerque[1*], P. Sollero[2], M. H. Aliabadi[3]

[1*]Department of Mechanical Engineering, University of Brasilia, Brazil. E-mail: eder@unb.br
[2]Faculty of Mechanical Engineering, University of Campinas, Brazil. E-mail: sollero@fem.unicamp.br
[3]Department of Aeronautics, Imperial College London, London, UK. E-mail: m.h.aliabadi@imperial.ac.uk

[*]Corresponding author

Abstract

In this chapter, some boundary element formulations applied to anisotropic materials are reviewed. Firstly, the plane elasticity is presented, with special attention to dynamic problems. Then, the thin plate formulation is shown, with application to transient dynamic problems, modal analysis, and buckling. Finally, thin shallow shell formulation is presented. Body forces are treated by the dual reciprocity boundary element method or by the radial integration method. Some numerical examples are presented in order to access the accuracy of the formulations.

1   Introduction

The extensive use of composite material structures in engineering design has demanded reliable and accurate numerical procedures for the treatment of anisotropic material structural problems. As anisotropy increases the number of material elastic constants, difficulties in the modelling arise in the analysis of laminate composite structures. Particularly, in boundary element formulation, larger number of variables means far more difficulties in deriving fundamental solutions. This aspect is evident in literature. It can be noted that the number of references in which boundary element method is applied for anisotropic structures is significantly smaller than those treating isotropic ones. However, in the last ten years, important advances on boundary element techniques applied to anisotropic materials were published in the literature. For example, plane elasticity problems were analysed by Sollero and Aliabadi [1993, 1995], Deb [1996], and Albuquerque et al. [2002, 2003a,b, 2004], out of plane elasticity problems by Zhang [2000], tri-dimensional problems by Kogl and Gaul [2000a,b, 2003], Kirchhoff plates by Shi and Bezine [1988], Rajamohan and Raamachandran [1999], Albuquerque et al. [2006], and shear deformable plates by Wang and Schweizerhof [1995, 1996, 1997].

Many alternative procedures have been presented to treat domain integrals in the BEM as shown in books like Nowak Nowak and Neves [1994] and Partridge *et al.* Partridge

et al. [1992]. Among them, the most established is the dual reciprocity boundary element method (DRM), proposed by Nardini and Brebbia Nardini and Brebbia [1982] for the analysis of dynamic problems in plane elasticity and extended by many other authors for different applications (see the book of Partridge *et al.* Partridge et al. [1992]).

Boundary element formulations have been applied to plate bending anisotropic problems considering Kirchhoff as well as shear deformable plate theories. Shi and Bezine [1988] presented a boundary element analysis of plate bending problems using fundamental solutions proposed by Wu and Altiero [1981] based on Kirchhoff plate bending assumptions. Rajamohan and Raamachandran [1999] proposed a formulation that the singularities were avoided by placing source points outside the domain. Paiva et al. [2003] presented an analytical treatment for singular and hypersingular integrals of the formulation proposed by Shi and Bezine [1988]. Shear deformable plates have been analysed using boundary element method by Wang and Schweizerhof [1996, 1997] with the fundamental solution proposed by Wang and Schweizerhof [1995].

In general plate bending boundary element method, domain integrals arise in the formulation due to the distributed load in the domain. In order to evaluate these integrals, cell integration scheme can give accurate results, as carried out by Shi and Bezine [1988] for anisotropic plate bending problems. However, the discretization of the domain into cells reduces one of the main advantages of boundary element method that is the boundary only discretization. An alternative for this procedure was presented by Rajamohan and Raamachandran [1999] which proposes the use of particular solutions to avoid domain discretization. Nevertheless, the use of particular solutions demands to find a suitable function which satisfy the governing equation. Depending on how complicated the governing equation is, this function is quite difficult to be found.

Although the large majority of papers about the numerical analysis of composite shells are related to the finite element method, there are few works in literature that present boundary element formulations applied to orthotropic or even anisotropic shells Wang [1992], Lu and Mahrenholtz [1994], Wang and Schweizerhof [1995]. However, all these works involve complicated fundamental solutions that need to be computed numerically. An alternative approach to the these previous formulations is the coupling of plate bending and plane elasticity formulations, as proposed by Zhang and Atluri Zhang and Atluri [1986] who derived a formulation for static and dynamic analysis of isotropic classical shallow shells. Domain integrals were computed by the domain discretization into cells. Dirgantara and Aliabadi Dirgantara and Aliabadi [1999] extended this approach to the analysis of shear deformable isotropic shallow shells. Later, Wen, Aliabadi, and Young Wen et al. [2000] used the formulation proposed by Dirgantara and Aliabadi Dirgantara and Aliabadi [1999] and transformed the domain integrals into boundary integrals using the dual reciprocity method (DRM). Baiz and Aliabadi Baiz and Aliabadi [2006] presented a boundary element formulation for the analysis of linear buckling of shear deformable shallow shells.

In this report, boundary element formulations are presented for anisotropic problems. In all problems, the static fundamental solution is used and domain integrals which come from domain distributed loads are transformed into boundary integrals by exact transformation using the radial integration method or by the dual reciprocity boundary element method. The radial integration method was initially presented by Venturini [1988] in 1988 for isotropic plate bending problems. Recently, Gao [2002] extended it for three

dimensional isotropic elastic problems. Two cases of loading are considered: uniformly distributed and linearly distributed loads. As stated by Gao [2002], this method can be applied to transform any of domain integral to the boundary. The most attractive feature of the method is its simplicity since only the radial variable is integrated. For domain integrals which include unknown variables, the proposed procedure can be performed using radial basis function as in the dual reciprocity method as suggested by Gao [2002]. The formulations are presented for plane elasticity, plate bending, and shallow shell problems.

2 Boundary element method applied to the dynamic analysis of anisotropic plane elasticity

2.1 Introduction

Nowadays, the structural dynamic analysis of anistropic plates by the boundary element method (BEM) has been treated by two different approaches. In the first, the fundamental solution is obtained considering all terms of the equation of motion. As a consequence, this approach has no domain integrals but uses complicated fundamental solutions (Wang and Schweizerhof Wang and Schweizerhof [1997]). In the second, the static fundamental solution is used and the inertia term of the equation of motion is considered as a body force. This body force generates domain integrals that can be computed by the discretization of the domain into cells. However, this procedure eliminates, to a certain extent, one of the most interesting advantage of the BEM that is the absence of domain discretization. The DRM has been successfully used in the dynamic analysis of anisotropic structures as presented by Albuquerque *et al.* Albuquerque et al. [2002, 2003a,b, 2004] for bidimensional problems, and by Kögl and Gaul Kogl and Gaul [2000a,b, 2003] for three-dimensional problems. Due to the complexity of governing equations of anisotropic materials, the analytical computation of particular solutions used in the DRM is restricted to some approximation functions, all of them are functions of material properties.

In this chapter, a boundary element formulation applied to transient dynamic anisotropic problems is presented. The fundamental solutions for elastostatics presented by Cruse and Swedlow Cruse and Swedlow [1971] are used and the inertia terms are treated as body forces. The dual reciprocity boundary element is used to transform the domain integral into a boundary integral. The particular solutions and the approximation function used here are both simple. The results are stable and strongly dependent on the material anisotropy. When they are compared with results obtained by other formulations, there is a good agreement in all the cases.

2.2 Anisotropic Elasticity

The equilibrium and compatibility equation are independent of the type material. However, the stress-strain relationship depends on the specific type of material behaviour. The constitutive equations for linear elastic anisotropic materials, leading to the governing differential equations of the stress function, will be reviewed in this section.

2.3   Constitutive equations

A linear relationship between stress and strain is assured only when the strain energy W is a quadratic function of strain. If W is the quadratic function

$$W = \frac{1}{2}C_{ijkl}\epsilon_{ij}\epsilon_{kl} \tag{1}$$

the equation (1) yields the generalized Hooke's law, or constitutive equation for fully anisotropic three-dimensional body, given by

$$\sigma_{ij} = C_{ijkl}\epsilon_{kl} \ . \tag{2}$$

The components of the fourth-order tensor C_{ijkl} are known as elastic constants of the material. Symmetry of the stress and strain tensors requires the $C_{ijkl} = C_{jikl}$ and $C_{ijkl} = C_{ijlk}$, respectively. The condition for the existence of a strain energy function also requires that $C_{ijkl} = C_{klij}$. These latter conditions reduce the number of elastic constants from 81 to 21.

For two-dimensional elasticity a fully anisotropic material can be described using only six independent elastic constants, rewriting equation (2) as

$$\epsilon_i = \sum_j a_{ij}\sigma_j \qquad\qquad i,j = 1,2,6 \tag{3}$$

where a_{ij} are compliance coefficients with $a_{ij} = a_{ji}$. The simplified notation for the strains in equation (3) is defined as

$$\epsilon_i = \left\{ \begin{array}{c} \epsilon_1 \\ \epsilon_2 \\ \epsilon_6 \end{array} \right\} = \left\{ \begin{array}{c} \epsilon_{11} \\ \epsilon_{22} \\ \epsilon_{12} \end{array} \right\} , \tag{4}$$

and for stresses

$$\sigma_j = \left\{ \begin{array}{c} \sigma_1 \\ \sigma_2 \\ \sigma_6 \end{array} \right\} = \left\{ \begin{array}{c} \sigma_{11} \\ \sigma_{22} \\ \sigma_{12} \end{array} \right\} . \tag{5}$$

The compliance coefficients can be expressed in terms of engineering constants as:

$$
\begin{array}{ll}
a_{11} = 1/E_1 & a_{12} = -\nu_{12}/E_1 = -\nu_{21}/E_2 \\
a_{16} = \eta_{12,1}/E_1 = \eta_{1,12}/G_{12} & a_{22} = 1/E_2 \\
a_{26} = \eta_{12,2}/E_2 = \eta_{2,12}/G_{12} & a_{66} = 1/G_{12}
\end{array} \tag{6}
$$

where E_k are the Young's moduli referring to the axes x_k , G_{12} is the shear modulus for the plane, ν_{ij} are the Poisson's ratios and $\eta_{jk,l}$ and $\eta_{l,jk}$ are the mutual coefficients of first and second kind respectively. For orthotropic materials $a_{16} = a_{26} = 0$.

2.3.1   Governing Differential Equation

The Airy stress function can be used to compute the stresses and displacements in a loaded anisotropic body by the method described in References Lekhnitskii [1968].

$$a_{11}\frac{\partial^4 F}{\partial x_2^4} - 2a_{16}\frac{\partial^4 F}{\partial x_1\partial x_2^3} + (2a_{12} + a_{66})\frac{\partial^4 F}{\partial x_1^2\partial x_2^2} - 2a_{26}\frac{\partial^4 F}{\partial x_1^3\partial x_2} + a_{22}\frac{\partial^4 F}{\partial x_1^4} = 0 \tag{7}$$

Equation (7) can be integrated in the characteristic complex planes

$$z = x_1 + \mu x_2 \ , \qquad \mu = r + is \ , \tag{8}$$

where r and s are the real and imaginary parts of μ, respectively.

Using equation (8), equation (7) can be rewritten as

$$\frac{d^4 F}{dz^4} \left[a_{11}\mu^4 - 2a_{16}\mu^3 + (2a_{12} + a_{66})\,\mu^2 - 2a_{26}\mu + a_{22} \right] = 0 \ . \tag{9}$$

The existence of non trivial solutions of equation (9) requires the fulfillment of its characteristic equation

$$a_{11}\mu^4 - 2a_{16}\mu^3 + (2a_{12} + a_{66})\,\mu^2 - 2a_{26}\mu + a_{22} = 0 \ . \tag{10}$$

The roots of equation (10) are always complex or pure imaginary, occur in conjugate pairs (μ_k and $\overline{\mu}_k$) and s is always positive, as shown by Lekhnitskii Lekhnitskii [1968]. Thus, the characteristic directions become

$$z_k = x_1 + \mu_k x_2 \ , \qquad k = 1,2 \tag{11}$$

and their conjugates.

The general form of the stress function is then given by

$$F(x_1, x_2) = 2Re[F_1(z_1) + F_2(z_2)] \ . \tag{12}$$

Introducing the notation

$$\frac{\mathrm{d}F_k(z_k)}{\mathrm{d}z_k} = \Phi_k(z_k) \ , \tag{13}$$

where no summation is implied on k. From equation (12), we obtain the stress components

$$\sigma_{11} = 2\mathrm{Re}[\mu_1^2 \Phi_1^{(1)}(z_1) + \mu_2^2 \Phi_2^{(1)}(z_2)] \ ,$$

$$\sigma_{22} = 2\mathrm{Re}[\Phi_1^{(1)}(z_1) + \Phi_2^{(1)}(z_2)] \ , \tag{14}$$

$$\sigma_{12} = -2\mathrm{Re}[\mu_1 \Phi_1^{(1)}(z_1) + \mu_2 \Phi_2^{(1)}(z_2)] \ ,$$

where $\Phi_k^{(1)}$ denotes the first derivative of Φ_k.

Substituting equation (14) into equation (3), neglecting rigid body motion and integrating, we obtain the displacements

$$u_1 = 2\mathrm{Re}[p_{11}\Phi_1(z_1) + p_{12}\Phi_2(z_2)] \ ,$$
$$u_2 = 2\mathrm{Re}[p_{21}\Phi_1(z_1) + p_{22}\Phi_2(z_2)] \ , \tag{15}$$

where

$$[p_{ik}] = \left[\begin{array}{c} a_{11}\mu_k^2 + a_{12} - a_{16}\mu_k \\ a_{12}\mu_k + a_{22}/\mu_k - a_{26} \end{array} \right] \tag{16}$$

is a matrix of complex parameters.

Equations (14) and (15) together with traction boundary conditions

$$t_j = \sigma_{ij}n_i = g_j \tag{17}$$

or displacements boundary conditions

$$u_j = h_j \tag{18}$$

constitute the mathematical problem to be solved.

2.4 Anisotropic Elastostatics Fundamental Solutions

The solution of a point force in the infinite anisotropic plane is called fundamental solution and is the basic relation for the development of integral equations for the solution of the anisotropic elasticity problem. The fundamental solutions U_{ij} and T_{ij} are the displacements and tractions in the j-direction at $\mathbf{z}$ due to a unit point force acting in the i-direction at $\mathbf{z}^{'}$. The points $\mathbf{z}$ and $\mathbf{z}^{'}$ are the source (or load) and field points and are defined by

$$\mathbf{z}^{'} = \left\{ \begin{array}{c} z_1^{'} \\ z_2^{'} \end{array} \right\} = \left\{ \begin{array}{c} x_1^{'} + \mu_1 x_2^{'} \\ x_1^{'} + \mu_2 x_2^{'} \end{array} \right\} \tag{19}$$

and

$$\mathbf{z} = \left\{ \begin{array}{c} z_1 \\ z_2 \end{array} \right\} = \left\{ \begin{array}{c} x_1 + \mu_1 x_2 \\ x_1 + \mu_2 x_2 \end{array} \right\} \tag{20}$$

where μ_k are the complex roots of equation (10).

If we consider a closed contour Γ surrounding the source point and use the tractions computed by equation (17) and the stresses defined by equation (14), it can be shown that

$$\int_\Gamma t_1 \mathrm{d}\Gamma = 2\mathrm{Re}\left[\!\left[\mu_1 \Phi_1 + \mu_2 \Phi_2 \right]\!\right] \ ,$$

$$\int_\Gamma t_2 \mathrm{d}\Gamma = 2\mathrm{Re}\left[\!\left[\Phi_1 + \Phi_2 \right]\!\right] \ , \tag{21}$$

where the double brackets denote the jump in the function for a closed contour surrounding the source point. If the contour Γ encloses $\mathbf{z}^{'}$, the point of load application, then the results of equations (21) will be non-zero.

The fundamental solutions in an infinite anisotropic plane can be obtained by finding the Airy stress function resulting from the fundamental tractions. The Airy stress function for a point load in the x_i direction can be represented by Φ_{ik}. As the contour integrals of equation (21) are of opposite signs to the applied loads it can be expressed for the point load solution as

$$2\mathrm{Re}\left[\!\left[\mu_1 \Phi_{i1} + \mu_2 \Phi_{i2} \right]\!\right] = -\delta_{i1} \ ,$$

$$2\mathrm{Re}\left[\!\left[\Phi_{i1} + \Phi_{i2} \right]\!\right] = \delta_{i2} \ . \tag{22}$$

Equation (22) may be satisfied for any closed contour enclosing $\mathbf{z}^{'}$ by taking

$$\Phi_{ik} = A_{ik} \ln\left(\mathbf{z} - \mathbf{z}^{'} \right) \tag{23}$$

where A_{ik} are complex constants. It can be shown that for any contour enclosing the point $\mathbf{z}^{'}$

$$\ln\left(\mathbf{z} - \mathbf{z}^{'} \right) = 2\pi i \ . \tag{24}$$

Using equations (22), (23), and (24) it can be obtained two equations for the unknown constants A_{ik}, or

$$A_{i1} - \overline{A}_{i1} + A_{i2} - \overline{A}_{i2} = \delta_{i2}/(2\pi i)$$

$$\mu_1 A_{i1} - \overline{\mu_1}\overline{A}_{i1} + \mu_2 A_{i2} - \overline{\mu_2}\overline{A}_{i2} = -\delta_{i1}/(2\pi i) \ . \tag{25}$$

The remaining two equations result from the requirement that the displacements be single valued, or

$$[\![u_i]\!] = 0 \ . \tag{26}$$

Using the displacements equation (15) and equation (23) and (24), equation (26) can be rewritten as

$$p_{11}A_{i1} - \overline{p_{11}}\,\overline{A_{i1}} + p_{12}A_{i2} - \overline{p_{12}}\,\overline{A_{i2}} = 0 \ ,$$
$$p_{21}A_{i1} - \overline{p_{21}}\,\overline{A_{i1}} + p_{22}A_{i2} - \overline{p_{22}}\,\overline{A_{i2}} = 0 \ , \tag{27}$$

where p_{ik} is given by equation (16) and the overbar denotes the conjugate of the complex constant. Equations (25) and (27) can be rearranged in the usual matricial form as

$$
\begin{bmatrix}
1 & -1 & 1 & -1 \\
\mu_1 & -\overline{\mu}_1 & \mu_2 & -\overline{\mu}_2 \\
p_{11} & -\overline{p}_{11} & p_{12} & -\overline{p}_{12} \\
p_{21} & -\overline{p}_{21} & p_{22} & -\overline{p}_{22}
\end{bmatrix}
\left\{
\begin{array}{c}
A_{i1} \\
\overline{A}_{i1} \\
A_{i2} \\
\overline{A}_{i2}
\end{array}
\right\}
=
\left\{
\begin{array}{c}
\delta_{i2}/(2\pi i) \\
-\delta_{i1}/(2\pi i) \\
0 \\
0
\end{array}
\right\} ,
\tag{28}
$$

which is sufficient to find the complex constants A_{ik}.

The fundamental solution for displacements can be obtained by inserting the stress function given by equation (23) into the displacements equation (15) to give

$$U_{ij}(\mathbf{z}', \mathbf{z}) = 2\mathrm{Re}\left[p_{j1}A_{i1}\ln(z_1 - z_1') + p_{j2}A_{i2}\ln(z_2 - z_2')\right] \ . \tag{29}$$

Similarly, the fundamental solution for tractions is obtained by substituting equation (23) into the stress equations (14) and using equation (17) to give

$$T_{ij}(\mathbf{z}', \mathbf{z}) = 2\mathrm{Re}\left[\frac{1}{(z_1 - z_1')}q_{j1}(\mu_1 n_1 - n_2)A_{i1} + \frac{1}{(z_2 - z_2')}q_{j2}(\mu_2 n_1 - n_2)A_{i2}\right] \ . \tag{30}$$

where

$$[q_{jk}] = \begin{bmatrix} \mu_1 & \mu_2 \\ -1 & -1 \end{bmatrix} \tag{31}$$

and n_k are the components of the normal outward vector.

2.5 Boundary Integral Equation

Since the governing partial differential equation (7) of the anisotropic elasticity problem admits no real characteristic surface, the problem is elliptic and the continuity of the stresses and displacement fields is assured. Consequently, it can be verified that Betti's reciprocal work theorem for two self-equilibrated states $(\mathbf{u}, \mathbf{t}, \mathbf{b})$ and $(\mathbf{u}^*, \mathbf{t}^*, \mathbf{b}^*)$ must be valid and expressed as

$$\int_\Omega b_i^* u_i \mathrm{d}\Omega + \int_\Gamma t_i^* u_i \mathrm{d}\Gamma = \int_\Omega b_i u_i^* \mathrm{d}\Omega + \int_\Gamma t_i u_i^* \mathrm{d}\Gamma \ . \tag{32}$$

The self-equilibrated states are described by the displacements $\mathbf{u}$ and $\mathbf{u}^*$, the tractions $\mathbf{t}$ and $\mathbf{t}^*$ and the body forces $\mathbf{b}$ and $\mathbf{b}^*$. It is assumed that the domain Ω with boundary

Γ and the domain Ω^* with boundary Γ^* encompass the states $(\mathbf{u}, \mathbf{t}, \mathbf{b})$ and $(\mathbf{u}^*, \mathbf{t}^*, \mathbf{b}^*)$, respectively. The problem under consideration in domain Ω is contained within a general region Ω^*, having the same anisotropic properties.

For the present purposes it is convenient to let the state $(\mathbf{u}, \mathbf{t}, \mathbf{b})$ be the required solution, and the state $(\mathbf{u}^*, \mathbf{t}^*, \mathbf{b}^*)$ be the fundamental solution. The displacement and traction field corresponding to the solution of the governing equation can be written as

$$u_i^* = u_j^* \delta_{ij} = U_{ij}(\mathbf{z}', \mathbf{z}) \delta_{ij} e_i \ ,$$

$$t_i^* = t_j^* \delta_{ij} = T_{ij}(\mathbf{z}', \mathbf{z}) \delta_{ij} e_i \ , \tag{33}$$

where δ_{ij} is the Kronecker's delta, U_{ij} and T_{ij} are the anisotropic fundamental solution for elastostatics given by equations (29) and (30), respectively, and e_i are the components of the unit vector corresponding to a unit force in the i direction applied at $\mathbf{z}'$. The body force component b_i^* corresponds to a point force and is given by

$$b_i^* = \delta(\mathbf{z} - \mathbf{z}') e_i \ , \tag{34}$$

where $\delta(\mathbf{z} - \mathbf{z}')$ is the Dirac delta function, that has the property

$$\int_\Omega g(x) \delta(\mathbf{z} - \mathbf{z}') \mathrm{d}\Omega(\mathbf{z}) = g(\mathbf{z}') \ . \tag{35}$$

From this property of the Dirac delta function, the first integral in equation (32) can be written as

$$\int_\Omega b_i^* u_i \mathrm{d}\Omega = u_i(\mathbf{z}') e_i \ . \tag{36}$$

Using equations (33) and (36), equation (32) can be rewritten as

$$u_i(\mathbf{z}') + \int_\Gamma T_{ij}(\mathbf{z}', \mathbf{z}) u_j(\mathbf{z}) \mathrm{d}\Gamma(\mathbf{z}) = \int_\Gamma U_{ij}(\mathbf{z}', \mathbf{z}) t_j(\mathbf{z}) \mathrm{d}\Gamma(\mathbf{z}) + \int_\Omega U_{ij}(\mathbf{z}', \mathbf{z}) b_j(\mathbf{z}) \mathrm{d}\Omega(\mathbf{z}) \tag{37}$$

which is known as Somigliana's identity that in absence of body forces is expressed as

$$u_i(\mathbf{z}') + \int_\Gamma T_{ij}(\mathbf{z}', \mathbf{z}) \, u_j(\mathbf{z}) \, \mathrm{d}\Gamma(\mathbf{z}) = \int_\Gamma U_{ij}(\mathbf{z}', \mathbf{z}) \, t_j(\mathbf{z}) \, \mathrm{d}\Gamma(\mathbf{z}) \ . \tag{38}$$

Equation (38) does not constitute a solution to a well-posed boundary value problem because the boundary tractions and boundary displacements are not simultaneously known for all boundary points. A relation between boundary tractions and displacements is obtained when the source point is taken to the boundary, which represents the solution for the elastic problem.

When there is body forces in the formulation, the integral equation is given by:

$$c_{ij}(\mathbf{z}') u_j(\mathbf{z}') + \fint_\Gamma T_{ij}(\mathbf{z}', \mathbf{z}) \, u_j(\mathbf{z}) \, d\Gamma(\mathbf{z}) = \int_\Gamma U_{ij}(\mathbf{z}', \mathbf{z}) \, t_j(\mathbf{z}) \, d\Gamma(\mathbf{z}) + \int_\Omega U_{ij}(\mathbf{z}', \mathbf{z}) \, b_j(\mathbf{z}) \, d\Gamma(\mathbf{z}). \tag{39}$$

where $b_j(\mathbf{z})$ is a load distributed along the domain Ω.

2.6   The dual reciprocity boundary element method for dynamic problems

The reciprocal relation between the fundamental solution and another elastostatic state defined over a domain Ω is given by the following integral equation

$$c_{ik}u_i + \int_\Gamma T_{ik}u_i d\Gamma = \int_\Gamma U_{ik}t_i d\Gamma - \int_\Omega U_{ik}\rho\ddot{u}_i d\Omega \tag{40}$$

where c_{ik} is equal to $\delta_{ik}/2$ to smooth boundary.

In order to transform the domain integral of equation (40) into a boundary one, the dual reciprocity boundary element method will be used. In this method, the acceleration is approximated as a sum of M function $f^m(x)$ multiplied by unknown time dependent coefficients $\ddot{\alpha}_k(\tau)$

$$\ddot{u}_i(x, \tau) = \sum_{m=1}^{M} \ddot{\alpha}_k(\tau)f^m(x) \tag{41}$$

The domain integral in equation (40) can be written as

$$\int_\Omega U_{li}\rho\ddot{u}_i = \rho\sum_{m=1}^{M}\ddot{\alpha}_i^m \int_\Omega U_{li}f^m d\Omega \tag{42}$$

The solutions of the equilibrium equation

$$C_{mnrs}\hat{u}_{rk,ns}^j = f_{mk}^j \tag{43}$$

are required in order to transform the domain integral into an equivalent boundary integral. The solutions $\hat{u}_{rk}$ are known as particular solutions.

The reciprocal relation between the fundamental solution and the particular solution is given by

$$c_{li}\hat{u}_{in}^m + \int_\Gamma T_{li}\hat{u}_{in}^m d\Gamma = -\int_\Omega f^m U_{ln} d\Omega + \int_\Gamma U_{li}\hat{t}_{in}^m d\Gamma \tag{44}$$

Substituting equation (44) into equation (42), and then into equation (40), the following equation is obtained

$$c_{li}u_i + \int_\Omega T_{li}u_i d\Gamma = \int_\Gamma U_{li}t_i d\Gamma +$$

$$\rho\sum_{m=1}^{M}\ddot{\alpha}_n^m\left\{c_{li}\hat{u}_{in}^m - \int_\Gamma \hat{t}_{in}^m U_{li} d\Gamma + \int_\Gamma T_{li}\hat{u}_{in}^m d\Gamma\right\} \tag{45}$$

The equation (45) is the basis of dual reciprocity boundary element method. In it can be noted the absence of domain integral.

The traditional procedure to solve the differential equation (43) when the problem is isotropic is to assume the approximation function and compute the corresponding particular solutions. This procedure is quite difficult for anisotropic materials because the anisotropy increases the number of constants in the equilibrium equation. An alternative is to assume a particular solution and find the correspondent approximation function.

This procedure was used by Schclar Schclar [1994] to steady state anisotropic problems and by Albuquerque and Sollero Albuquerque and Sollero [1998] to transient anisotropic problems.

In this work it is used for the displacement particular solution

$$\hat{u}_{mk} = r^3 \delta_{km} \tag{46}$$

where r is the radial vector from the source to the field point and δ_{km} is the Dirac delta.

The corresponding approximation function, obtained by the substitution of equation (46) into equation (43) is given by

$$f_{im} = C_{ijkl} \left\{ 3r \left(r_{,l} r_{,j} \delta_{km} + \delta_{jl} \delta_{km} \right) \right\}. \tag{47}$$

The traction particular solution is given by

$$\hat{t}_{mr} = \hat{\sigma}_{mrs} n_s \tag{48}$$

where the particular stress $\hat{\sigma}_{mrs}$, which is obtained by differentiating the equation (46) and using Hooke's law, is given by

$$\hat{\sigma}_{mrs} = C_{rsjk} \frac{3r^2}{2} (r_{,j} \delta_{km} + r_{,k} \delta_{jm}) \tag{49}$$

In order to solve the elastodynamics problem, the boundary is divided into boundary elements and the displacements and tractions are interpolated in these elements using quadratic shape functions. Then the integral equation (45) can be written in a matrix form as

$$\mathbf{Hu} - \mathbf{Gt} = \rho(\mathbf{H\hat{u}} - \mathbf{G\hat{t}})\ddot{\boldsymbol{\alpha}} \tag{50}$$

The coefficient $\ddot{\boldsymbol{\alpha}}$ are computed using the relationship

$$\ddot{\mathbf{u}} = \mathbf{F}\ddot{\boldsymbol{\alpha}} \tag{51}$$

where $\mathbf{F}$ is a matrix whose elements are formed computing the approximation function to every node.

Equation (50) can be written as

$$\mathbf{Hu} - \mathbf{Gt} = \rho(\mathbf{H\hat{u}} - \mathbf{G\hat{t}})\mathbf{E\ddot{u}} \tag{52}$$

where $\mathbf{E} = \mathbf{F}^{-1}$.

Equation (52) can be written as

$$\mathbf{M\ddot{u}} + \mathbf{Hu} = \mathbf{Gt} \tag{53}$$

where

$$\mathbf{M} = \rho[\mathbf{G\hat{t}} - \mathbf{H\hat{u}}]\mathbf{E} \tag{54}$$

Several time integration schemes have been proposed to compute the acceleration $\ddot{\mathbf{u}}$ as it was reported by Bathe and Wilson Bath and Wilson [1976]. However, it has been

found by Loffler and Mansur Loeffler and Mansur [1987] that Houbolt method (Houbolt Houbolt [1950]) is the most appropriated to be used with dual reciprocity boundary element method. Because this, the Houbolt method was chosen to proceed the time integration of equation (52). Following Houbolt expression, the acceleration in the instant $\tau + \Delta\tau$ is approximated by

$$\ddot{\mathbf{u}}_{\tau+\Delta\tau} = \frac{1}{\Delta\tau^2}(2\mathbf{u}_{\tau+\Delta\tau} - 5\mathbf{u}_\tau + 4\mathbf{u}_{\tau-\Delta\tau} - \mathbf{u}_{t-2\Delta t}) \tag{55}$$

which can be used to write equation (52) as

$$\mathbf{B}\mathbf{u} = \mathbf{G}\mathbf{t} + \frac{1}{\Delta\tau^2}\mathbf{M}\mathbf{u}_b \tag{56}$$

where $\mathbf{u} = \mathbf{u}_{\tau+\Delta\tau}$, $\mathbf{t} = \mathbf{t}_{\tau+\Delta\tau}$,

$$\mathbf{B} = \left[\frac{2}{\Delta\tau^2}\mathbf{M} + \mathbf{H}\right], \tag{57}$$

and $\mathbf{u}_b = 5\mathbf{u}_\tau - 4\mathbf{u}_{\tau-\Delta\tau} + \mathbf{u}_{\tau-2\Delta\tau}$.

The time step $\Delta\tau$ should be chosen taking into account the material properties and the mesh used. In this work, considering the non-dimensional number

$$\beta = \sqrt{\frac{E_{\max}}{\rho}}\frac{\Delta\tau}{l_{\min}}, \tag{58}$$

where $E_{\max}$ is the value of the biggest Young modulus, and $l_{\min}$ is the length of the smallest boundary element, the time step is chosen so that

$$\beta \geq 0.4716 \tag{59}$$

.

2.7   Numerical Results

2.7.1   Infinity long strip

The first problem to be treated is an infinite long strip (Figure 1) subjected to a step load function applied at time $\tau_o = 0$ (Figure 2). A state of plane stress is assumed with load $\sigma_o = 1$ N. The material is considered quasi-isotropic with the following properties: Young's Moduli $E_1 = 10.6667\ 10^4$ Pa and $E_2 = 10.68\ 10^4$ Pa, Poisson's ratio $\nu_{12} = 0.3333$, shear stress modulus $G_{12} = 4\ 10^4$ Pa, and density $\rho = 1$ Kg/m^3.

The mesh used has 12 equal quadratic boundary elements (Figure 3). The results are computed without any internal point and with 3 internal points (Figure 3). The time step used was $\Delta\tau = 7.22\ 10^{-4}$s ($\beta = 0.4716$ for the quasi-isotropic case).

The vertical displacement at the mid point of the free edge are plotted in Figure 4 and the normal tractions at the base mid point are plotted in Figure 5, when using 0 and 3 internal points. The results show good agreement with the exact solution. Although in this problem the use of internal points causes slightly differences in the solution, in many cases the use of internal points are necessary to improve the results and it will be adopted in all other problems treated in this work.
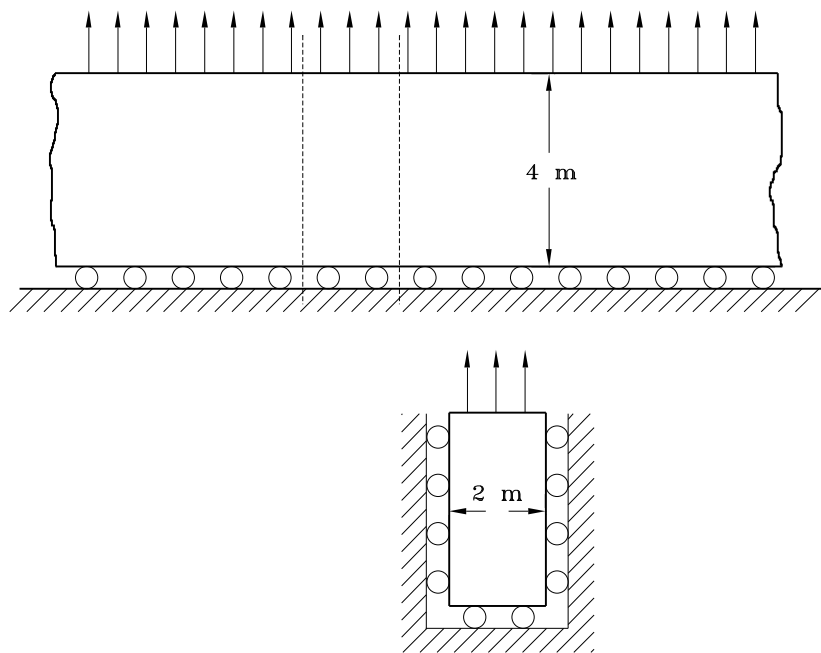
Figure 1: Infinity long strip under an uniform step load.

The same problem is treated now varying the ratio between the Young's Moduli E_1 and E_2 ($R = E_2/E_1$, where E_1 and all other material constants are maintained with a constant value).

Figures 6 and 7 show the results to three different values of R to the vertical displacement to a node in the top and the normal traction to a node in the bottom of the strip, respectively. In these orthotropic cases, analytical solutions were not found in the literature. However the results are the expected ones: the bigger the value of R, the more rigid is the strip, the smaller are the displacements and the higher are the frequencies. In all the cases the results are stable even after many cycles.
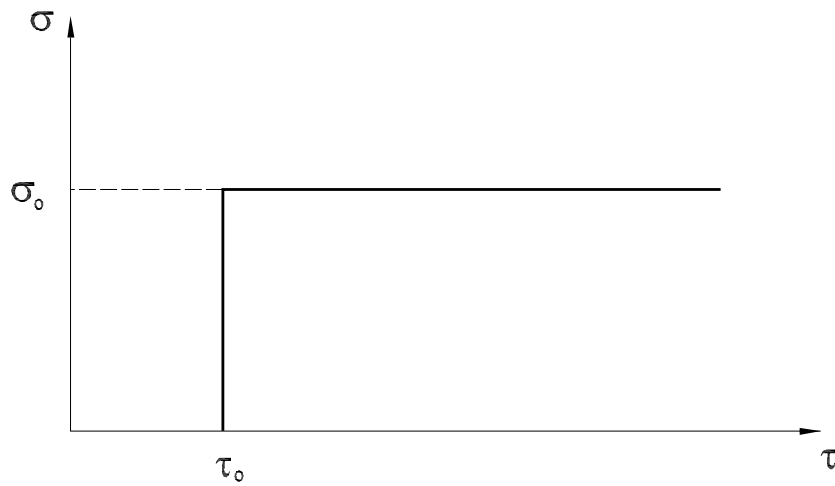
Figure 2: Step load function.
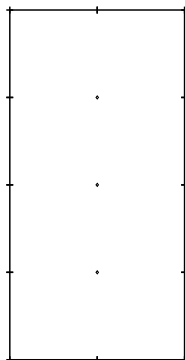
Figure 3: Boundary element mesh and internal points to a part of the infinity strip.
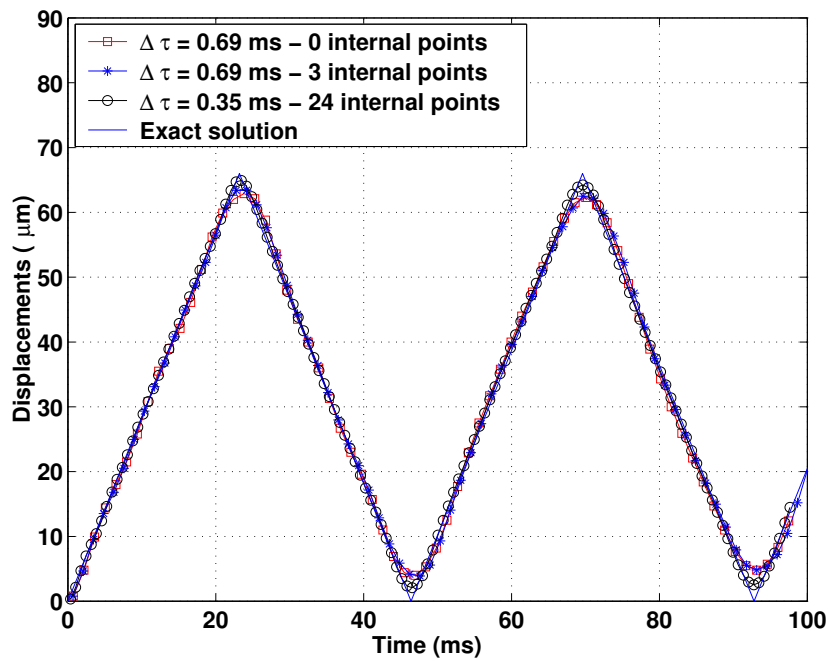
Figure 4: Vertical displacements for a node at mid point of the quasi-isotropic infinity long strip free edge.
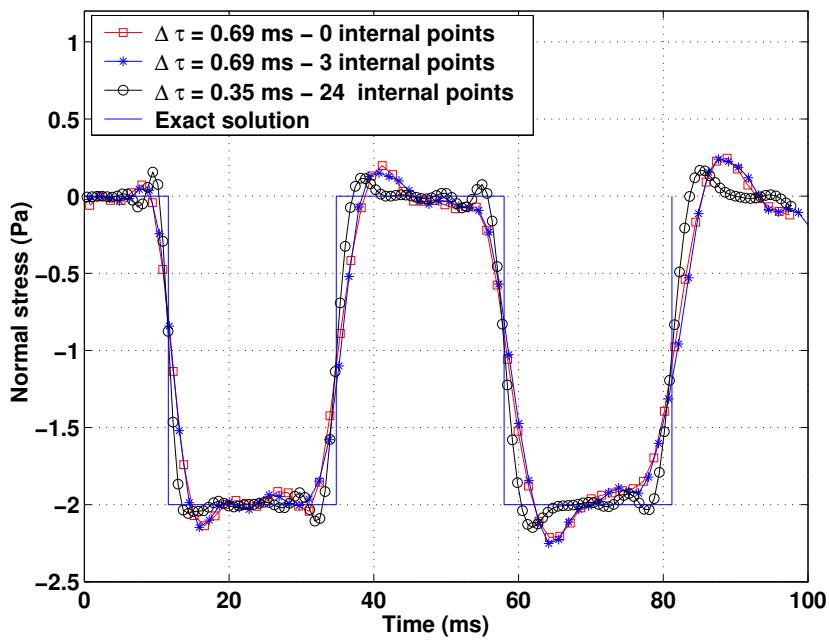
Figure 5: Normal tractions for a node at mid point of the quasi-isotropic infinity long strip base edge.
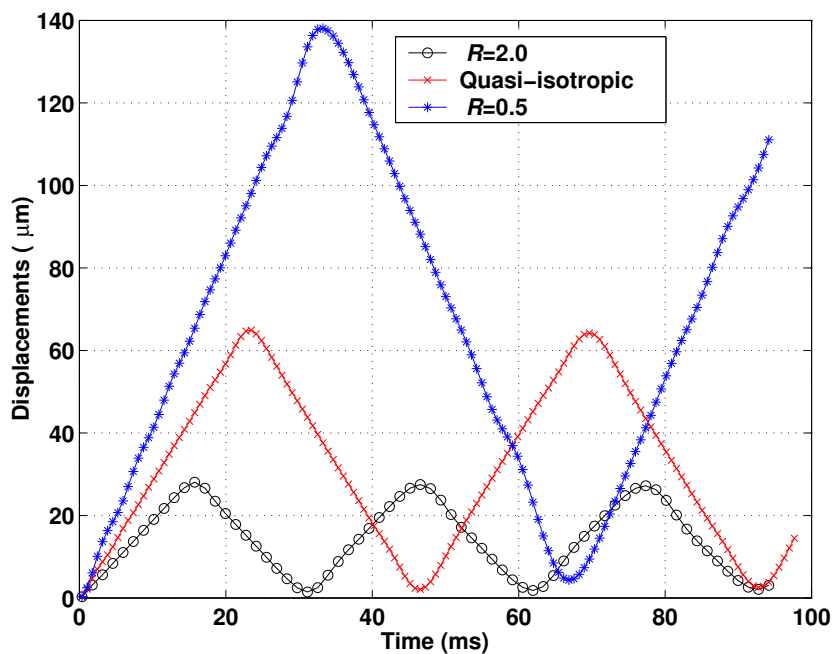
Figure 6: Vertical displacements for a node at mid point of the infinity long strip free edge considering three different Young's Modulus ratios.
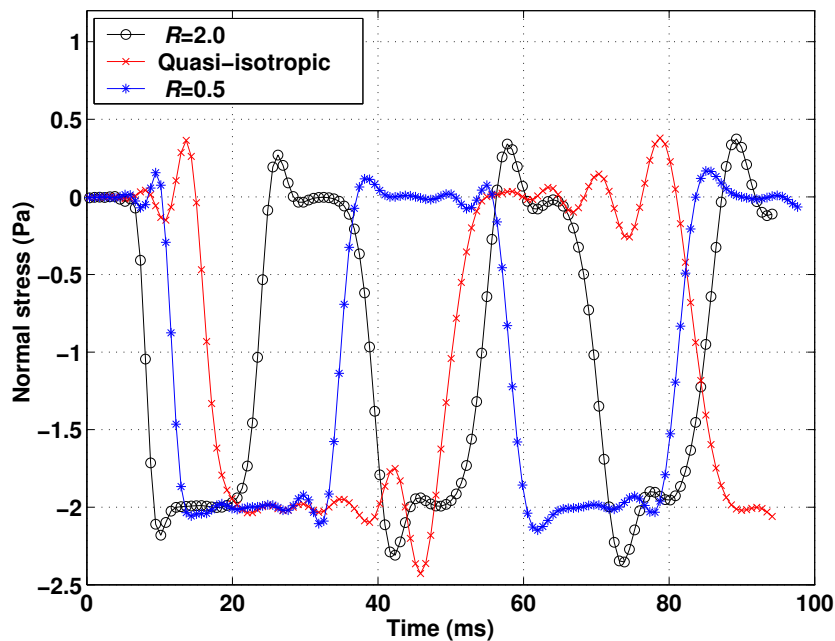
Figure 7: Normal tractions for a node at mid point of the infinity long strip base edge considering three different Young's Modulus ratios.

3   Theory of bending of anisotropic thin plate

A plate is a structural element defined by two flat parallel surfaces (Figure 8) where loads
are transversely applied. The distance between these two surfaces defines the thickness
of the plate, which is small when compared to other plate dimensions.

Considering its material properties, a plate can be either anisotropic, with different
properties in different directions, or isotropic, with equal properties in all directions. De-
pending on its thickness, a plate can be considered either a thin or a thick plate. In this
work, formulations will be developed for anisotropic thin plates.
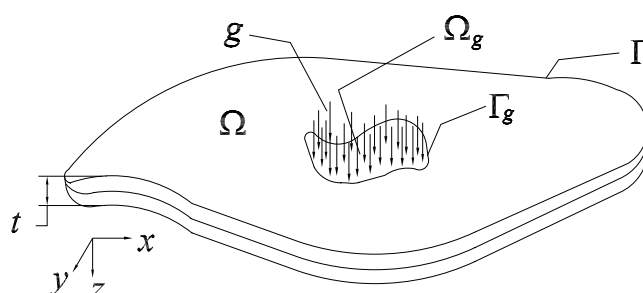
Figure 8: Thin plate.

The theory of anisotropic thin plates bending is based on the following assumptions
Lekhnitskii [1968]:

1. Straight sections, which in the undeformed state are normal to its middle surface,
   remain straight and normal to the deformed middle surface after loading;

2. Normal stress σ_z in cross sections parallel to the middle plane is small if compared
   with stresses in the transverse cross section, i.e., σ_x, σ_y, τ_{xy}.

3.1   Basic relations for anisotropic plates

Consider a plate element following the assumptions previously defined. Figure 9 shows
this element with a stress state acting on it and a distributed load applied on its area.
Integrating stress components along the plate thickness, we can define moments and loads
(Figure 10):

$$m_x = \int_{-t/2}^{t/2} \sigma_x z dz, \tag{60}$$

$$m_y = \int_{-t/2}^{t/2} \sigma_y z dz, \tag{61}$$

$$m_{xy} = \int_{-t/2}^{t/2} \tau_{xy} z dz, \tag{62}$$

$$m_{yx} = \int_{-t/2}^{t/2} \tau_{yx} z dz, \tag{63}$$
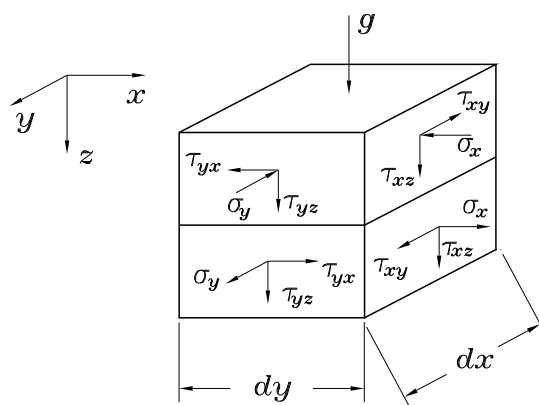
Figure 9: Stresses in a plate element

$$q_x = \int_{-t/2}^{t/2} \tau_{xz} dz, \tag{64}$$

and

$$q_y = \int_{-t/2}^{t/2} \tau_{yz} dz. \tag{65}$$
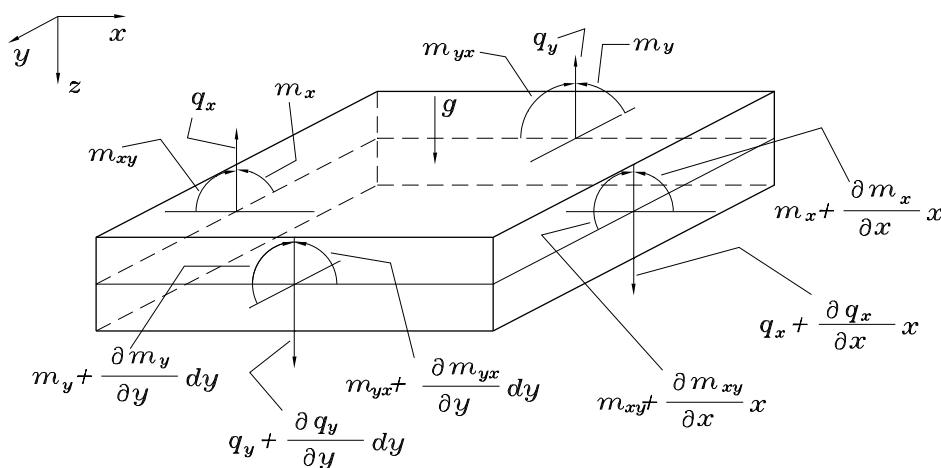
Figure 10: Loads and moments in a plate element

From equilibrium of forces and moments, we can write:

$$\frac{\partial q_x}{\partial x} + \frac{\partial q_y}{\partial y} + g = 0, \tag{66}$$

$$\frac{\partial m_x}{\partial x} + \frac{\partial m_{yx}}{\partial y} - q_x = 0, \tag{67}$$

$$\frac{\partial m_y}{\partial y} + \frac{\partial m_{xy}}{\partial x} - q_y = 0. \tag{68}$$

Solving equations (67) and (68) for q_x and q_y, respectively, substituting in equation (66), and considering symmetry of moments ($m_{xy} = m_{yx}$), we have:

$$\frac{\partial^2 m_x}{\partial x^2} + 2\frac{\partial^2 m_{xy}}{\partial x \partial y} + \frac{\partial^2 m_y}{\partial y^2} = -g. \tag{69}$$

Consider the initial and final position of a plate element given by $abcd$ parallel to the middle plane with sides ab and ad parallel to x and y axes, respectively, at a distance z from the middle plane (Figure 11).
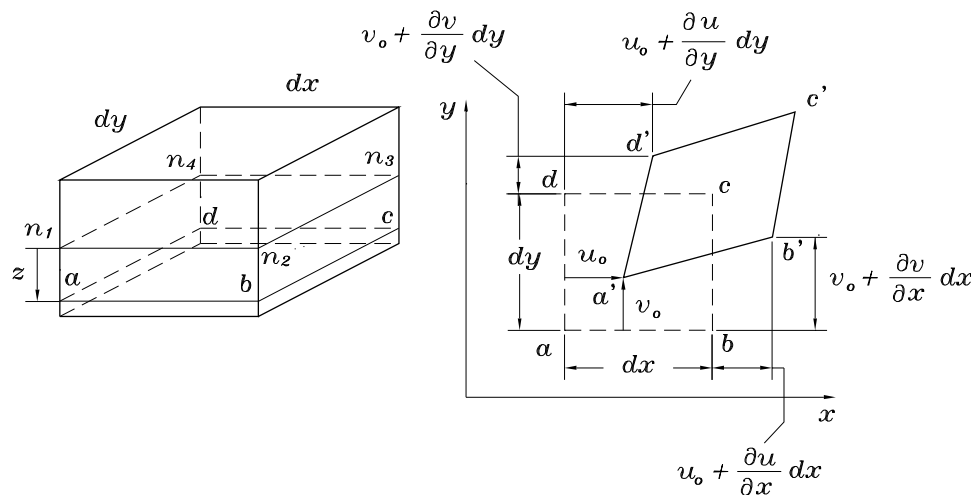
Figure 11: Deformation in a plate element.

Assuming that, during plate bending, points a, b, c, and d, move to a', b', c', and d', calling u_o and v_o displacement components of point a in x and y direction (Figure 11), respectively, the displacement of a point b in the x direction is given by:

$$b'_x - b_x = u_o + \frac{\partial u}{\partial x} dx. \tag{70}$$

So, the increment in the length dx in x direction is given by:

$$\Delta dx = \frac{\partial u}{\partial x} dx, \tag{71}$$

and strain in x direction is given by:

$$\varepsilon_x = \frac{\Delta dx}{dx} = \frac{\partial u}{\partial x}. \tag{72}$$

In a similar way, we can write:

$$\varepsilon_y = \frac{\partial v}{\partial y}, \tag{73}$$

$$\gamma_{xy} = \frac{\partial u}{\partial y} + \frac{\partial v}{\partial x}. \tag{74}$$

Figure 12 shows initial and final positions of a plate section, parallel to xz plane, which contains points a, b, n_1, and n_2. The rotation of element an_1, initially placed in

vertical position, is equal to $\frac{\partial w}{\partial x}$ (Figure 12). So, the displacement of a point in x direction, at a distance z from middle surface can be written as:

$$u = -z\frac{\partial w}{\partial x}. \tag{75}$$
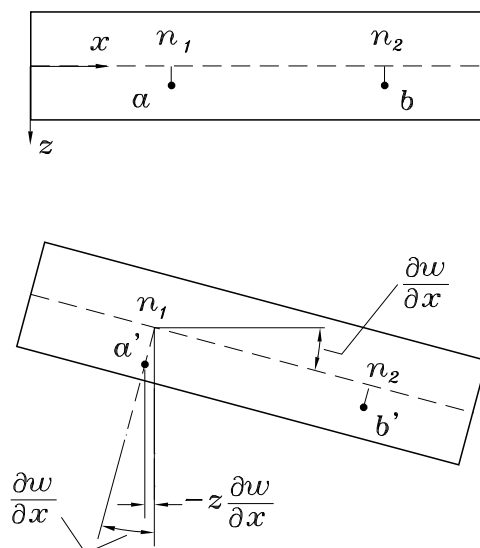
Figure 12: Initial and final position of an element plate abn_1n_2.

Following similar procedure, the displacement of a point in y direction is given by:

$$v = -z\frac{\partial w}{\partial y}. \tag{76}$$

Substituting equations (75) and (76) into equations (72), (73), and (74), we can write:

$$
\begin{aligned}
\varepsilon_x &= -z\frac{\partial^2 w}{\partial x^2}, \\
\varepsilon_y &= -z\frac{\partial^2 w}{\partial x^2}, \\
\gamma_{xy} &= -2z\frac{\partial^2 w}{\partial x\partial y}.
\end{aligned} \tag{77}
$$

The constitutive equations for anisotropic material is given by (Lekhnitskii Lekhnitskii [1968]):

$$
\begin{aligned}
\varepsilon_x &= a_{11}\sigma_x + a_{12}\sigma_y + a_{16}\tau_{xy}, \\
\varepsilon_y &= a_{12}\sigma_x + a_{22}\sigma_y + a_{26}\tau_{xy}, \\
\gamma_{xy} &= a_{16}\sigma_x + a_{26}\sigma_y + a_{66}\tau_{xy}.
\end{aligned} \tag{78}
$$

Substituting equations (77) into equations (78), we obtain:

$$\sigma_x = -z \left(B_{11} \frac{\partial^2 w}{\partial x^2} + B_{12} \frac{\partial^2 w}{\partial y^2} + 2B_{16} \frac{\partial^2 w}{\partial x \partial y} \right),$$

$$\sigma_y = -z \left(B_{12} \frac{\partial^2 w}{\partial x^2} + B_{22} \frac{\partial^2 w}{\partial y^2} + 2B_{26} \frac{\partial^2 w}{\partial x \partial y} \right),$$

$$\tau_{xy} = -z \left(B_{16} \frac{\partial^2 w}{\partial x^2} + B_{26} \frac{\partial^2 w}{\partial y^2} + 2B_{66} \frac{\partial^2 w}{\partial x \partial y} \right), \tag{79}$$

where B_{ij} are constants given by:

$$B_{11} = \frac{1}{\Delta} \left(a_{22}a_{66} - a_{26}^2 \right), \qquad B_{22} = \frac{1}{\Delta} \left(a_{11}a_{66} - a_{16}^2 \right),$$

$$B_{12} = \frac{1}{\Delta} \left(a_{16}a_{26} - a_{12}a_{66} \right), \qquad B_{66} = \frac{1}{\Delta} \left(a_{11}a_{22} - a_{12}^2 \right), \tag{80}$$

$$B_{16} = \frac{1}{\Delta} \left(a_{12}a_{26} - a_{22}a_{16} \right), \qquad B_{26} = \frac{1}{\Delta} \left(a_{12}a_{16} - a_{11}a_{26} \right),$$

and

$$\Delta = \begin{vmatrix} a_{11} & a_{12} & a_{16} \\ a_{12} & a_{22} & a_{26} \\ a_{16} & a_{26} & a_{66} \end{vmatrix}. \tag{81}$$

Substituting equation (79) into equation (77) and integrating, we have:

$$m_x = -\left(D_{11} \frac{\partial^2 w}{\partial x^2} + D_{12} \frac{\partial^2 w}{\partial y^2} + 2D_{16} \frac{\partial^2 w}{\partial x \partial y} \right),$$

$$m_y = -\left(D_{12} \frac{\partial^2 w}{\partial x^2} + D_{22} \frac{\partial^2 w}{\partial y^2} + 2D_{26} \frac{\partial^2 w}{\partial x \partial y} \right), \tag{82}$$

$$m_{xy} = -\left(D_{16} \frac{\partial^2 w}{\partial x^2} + D_{26} \frac{\partial^2 w}{\partial y^2} + 2D_{66} \frac{\partial^2 w}{\partial x \partial y} \right),$$

where

$$D_{ij} = B_{ij} \frac{t^3}{12}. \tag{83}$$

Substituting equation (82) into equations (67) and (68), we can write:

$$q_x = \left[D_{11} \frac{\partial^3 w}{\partial x^3} + 3D_{16} \frac{\partial^3 w}{\partial x^2 \partial y} + (D_{12} + 2D_{66}) \frac{\partial^3 w}{\partial x \partial y^2} + D_{26} \frac{\partial^3 w}{\partial y^3} \right],$$

$$q_y = \left[D_{16} \frac{\partial^3 w}{\partial x^3} + (D_{12} + 2D_{66}) \frac{\partial^3 w}{\partial x^2 \partial y} + 3D_{26} \frac{\partial^3 w}{\partial x \partial y^2} + D_{22} \frac{\partial^3 w}{\partial y^3} \right].$$

$$\tag{84}$$

Equation (69) can be rewritten using equations (82) as:

$$D_{11}\frac{\partial^4 w}{\partial x^4} + 4D_{16}\frac{\partial^4 w}{\partial x^3 \partial y} + 2(D_{12} + D_{66})\frac{\partial^4 w}{\partial x^2 \partial y^2} + 4D_{26}\frac{\partial^4 w}{\partial x \partial y^3} + D_{22}\frac{\partial^4 w}{\partial y^4} = g. \quad (85)$$

General solution to w in equation (85) depends on μ_1, μ_2, $\bar{\mu}_1$, and $\bar{\mu}_2$ roots of characteristic equation given by:

$$D_{22}\mu^4 + 4D_{26}\mu^3 + 2(D_{12} + 2D_{66})\mu^2 + 4D_{16}\mu + D_{11} = 0. \quad (86)$$

Roots of this equation, as shown by Lekhnitskii Lekhnitskii [1968], are always complex for homogeneous material. The complex roots $\mu_1 = d_1 + e_1 i$ and $\mu_2 = d_2 + e_2 i$ are known as deflexion complex parameters. In general, these roots are different complex numbers.

A general expression for the deflexion has the form:

1. in case of different complex parameters ($\mu_1 \neq \mu_2$):

$$w = w_o + 2\text{Re}[w_1(z_1) + w_2(z_2)]. \quad (87)$$

2. in case of equal complex parameters ($\mu_1 = \mu_2$):

$$w = w_o + 2\text{Re}[w_1(z_1) + \bar{z}_1 w_2(z_1)]. \quad (88)$$

where w_o is a particular solution of equation (85) that depends on the distributed load q in the plate surface, $w_1(z_1)$ and $w_2(z_2)$ are arbitrary analytic functions of complex variable $z_1 = x + \mu_1 y$ and $z_2 = x + \mu_2 y$.

Based on equations (82) and (84), general expressions for forces and moments can be obtained as (for the case $\mu_1 \neq \mu_2$):

$$m_x = m_x^o - 2\text{Re}[p_1 w''(z_1) + p_2 w''(z_2)],$$

$$m_y = m_y^o - 2\text{Re}[q_1 w''(z_1) + q_2 w''(z_2)],$$

$$m_{xy} = m_{xy}^o - 2\text{Re}[r_1 w''(z_1) + r_2 w''(z_2)],$$

$$q_x = q_x^o - 2\text{Re}[\mu_1 s_1 w'''(z_1) + \mu_2 s_2 w'''(z_2)],$$

$$q_y = q_y^o - 2\text{Re}[s_1 w'''(z_1) + s_2 w'''(z_2)]. \quad (89)$$

where m_x^o, m_y^o, m_{xy}^o, q_x^o, and q_y^o are moments and shear forces corresponding to function w_o computed from equations (82) and (84). The other constants are given by:

$$p_1 = D_{11} + D_{12}\mu_1^2 + 2D_{16}\mu_1, \qquad\qquad p_2 = D_{11} + D_{12}\mu_2^2 + 2D_{16}\mu_2,$$

$$q_1 = D_{12} + D_{22}\mu_1^2 + 2D_{26}\mu_1, \qquad\qquad q_2 = D_{12} + D_{22}\mu_2^2 + 2D_{26}\mu_2,$$

$$r_1 = D_{16} + D_{26}\mu_1^2 + 2D_{66}\mu_1, \qquad\qquad p_2 = D_{16} + D_{26}\mu_2^2 + 2D_{66}\mu_2,$$

$$s_1 = \frac{D_{11}}{\mu_1} + 3D_{16} + D_{12} + D_{66}\mu_1 + D_{26}\mu_1^2, \tag{90}$$

$$s_2 = \frac{D_{11}}{\mu_2} + 3D_{16} + D_{12} + D_{66}\mu_2 + D_{26}\mu_2^2,$$

$$s_1 - r_1 = \frac{p_1}{\mu_1}, \qquad\qquad s_2 - r_2 = \frac{p_2}{\mu_2},$$

$$s_1 + r_1 = -q_1\mu_1, \qquad\qquad s_2 + r_2 = -q_2\mu_2.$$

Similar expressions can be obtained for the case where $\mu_1 = \mu_2$. However, this case will not be shown in this work as in general anisotropic problems μ_1 is different from μ_2.

3.2   Computation of bending stiffness in an arbitrary direction

Considering that stiffness bending constants of a plate in a x, y, z coordinate system are given by D_{ij} $(i, j = 1, 2, 6)$ and in a x', y', z' coordinate system, rotated α with respect to the first coordinate system, are given by D'_{ij} $(i, j = 1, 2, 6)$, the equation relating these constants, as shown by Lekhnitskii Lekhnitskii [1968], are given by:

$$D'_{11} = D_{11}\cos^4\phi + 2(D_{12} + 2D_{66})\sin^2\phi\cos^2\phi + D_{22}\sin^4\phi +$$

$$2(D_{16}\cos^2\phi + D_{26}\sin^2\phi)\sin 2\phi, \tag{91}$$

$$D'_{22} = D_{11}\sin^4\phi + 2(D_{12} + 2D_{66})\sin^2\phi\cos^2\phi + D_{22}\cos^4\phi +$$

$$2(D_{16}\sin^2\phi + D_{26}\cos^2\phi)\sin 2\phi, \tag{92}$$

$$D'_{12} = D_{12} + [D_{11} + D_{22} - 2(D_{12} + 2D_{66})]\sin^2\phi\cos^2\phi +$$

$$(D_{26} - D_{16})\cos 2\phi\sin 2\phi, \tag{93}$$

$$D'_{66} = D_{66} + [D_{11} + D_{22} - 2(D_{12} + 2D_{66})] \sin^2 \phi \cos^2 \phi +$$

$$(D_{26} - D_{16}) \cos 2\phi \sin 2\phi, \tag{94}$$

$$D'_{16} = \frac{1}{2}[D_{22} \sin^2 \phi - D_{11} \cos^2 \phi + (D_{12} + 2D_{66}) \cos 2\phi] \sin 2\phi +$$

$$D_{16} \cos^2 \phi(\cos^2 \phi - 3\sin^2 \phi) + D_{26} \sin^2 \phi(3\cos^2 \phi - \sin^2 \phi), \tag{95}$$

$$D'_{26} = \frac{1}{2}[D_{22} \cos^2 \phi - D_{11} \sin^2 \phi + (D_{12} + 2D_{66}) \cos 2\phi] \sin 2\phi +$$

$$D_{16} \sin^2 \phi(\cos^2 \phi - 3\sin^2 \phi) + D_{26} \cos^2 \phi(3\cos^2 \phi - \sin^2 \phi). \tag{96}$$

The stress components σ_n and τ_{ns}, normal and shear stress, respectively, are related with stress σ_x, σ_y, and τ_{xy} by:

$$\sigma_n = \sigma_x \cos^2 \alpha + \sigma_y \sin^2 \alpha + 2\tau_{xy} \sin \alpha \cos \alpha, \tag{97}$$

$$\tau_{ns} = (\sigma_y - \sigma_x) \sin \alpha \cos \alpha + \tau_{xy}(\cos^2 \alpha - \sin^2 \alpha). \tag{98}$$

The components of moment, initially written considering axis x and y, can now be rewritten in a generic coordinate system n, s (Paiva Paiva [1987]). The bending moments referring to directions n and s are given by:

$$m_n = m_x \cos^2 \alpha + m_y \sin^2 \alpha + 2m_{xy} \sin \alpha \cos \alpha, \tag{99}$$

$$m_{ns} = (m_y - m_x) \sin \alpha \cos \alpha + m_{xy}(\cos^2 \alpha - \sin^2 \alpha). \tag{100}$$

Similarly, q_n, the shear force in the n axis, can be written as:

$$q_n ds = q_x ds \cos \alpha + q_y ds \sin \alpha, \tag{101}$$

or

$$q_n = q_x \cos \alpha + q_y \sin \alpha. \tag{102}$$

In order to solve the plate differential equation (85), it is necessary to impose boundary conditions to displacement w and its derivative $\partial w / \partial n$. Kirchhoff Kirchhoff [1950] has shown that the boundary conditions of shear force q_n and twisting moment m_{ns} can be written as one single boundary condition given by:

$$V_n = q_n + \frac{\partial m_{ns}}{\partial s}. \tag{103}$$

The other loading boundary condition is the moment m_n.

3.3   Boundary element method for bending problems of anisotropic plates

3.3.1   Boundary integral equations

Using Betti theorem, we can relate two states of stress-deformation of a linear material as:

$$\int_\Omega \sigma_{ij}^* \varepsilon_{ij} d\Omega = \int_\Omega \sigma_{ij} \varepsilon_{ij}^* d\Omega. \tag{104}$$

Writing the right hand side of equation (104) in von Karman's notation, we have:

$$\int_\Omega \sigma_{ij} \varepsilon_{ij}^* d\Omega = \int_\Omega \left(\sigma_x \varepsilon_x^* + \sigma_y \varepsilon_y^* + \sigma_z \varepsilon_z^* + \tau_{xy} \gamma_{xy}^* + \tau_{xz} \gamma_{xz}^* + \tau_{yz} \gamma_{yz}^* \right) d\Omega. \tag{105}$$

Neglecting stresses normal to the plate, equation (105) is given by:

$$\int_\Omega \sigma_{ij} \varepsilon_{ij}^* d\Omega = \int_\Omega \left(\sigma_x \varepsilon_x^* + \sigma_y \varepsilon_y^* + \tau_{xy} \gamma_{xy}^* \right) d\Omega. \tag{106}$$

Substituting equations (77) and (78) into equation (106), we can write the first term of the integral in the right hand side of equation (106) as:

$$\int_\Omega \sigma_x \varepsilon_x^* d\Omega = \int_\Omega \left[\int_z \left(B_{11} \frac{\partial^2 w}{\partial x^2} + B_{12} \frac{\partial^2 w}{\partial y^2} + 2B_{16} \frac{\partial^2 w}{\partial x \partial y} \right) \left(z \frac{\partial^2 w}{\partial x^2} \right) dz \right] d\Omega. \tag{107}$$

Integrating (107) throughout the thickness of the plate, we have:

$$\int_\Omega \sigma_x \varepsilon_x^* d\Omega = \int_\Omega \left(D_{11} \frac{\partial^2 w}{\partial x^2} + D_{12} \frac{\partial^2 w}{\partial y^2} + 2D_{16} \frac{\partial^2 w}{\partial x \partial y} \right) \frac{\partial^2 w}{\partial x^2} d\Omega = - \int_\Omega m_x \frac{\partial^2 w}{\partial x^2} d\Omega. \tag{108}$$

In order to obtain equations of the boundary element method, it is necessary to transform domain integrals into boundary integrals.

Consider two functions $f(x)$ and $g(x)$. The derivative of their product can be written as:

$$\frac{\partial}{\partial x}[f(x)g(x)] = \frac{\partial f(x)}{\partial x} g(x) + \frac{\partial g(x)}{\partial x} f(x). \tag{109}$$

Using the derivative property (109) in equation (108), we can write:

$$\int_\Omega \sigma_x \varepsilon_x^* d\Omega = - \int_\Omega \left[\frac{\partial}{\partial x} \left(m_x \frac{\partial w^*}{\partial x} \right) - \frac{\partial w^*}{\partial x} \frac{\partial m_x}{\partial x} \right] d\Omega. \tag{110}$$

Using Green theorem, equation (110) can be written as:

$$\int_\Omega \sigma_x \varepsilon_x^* d\Omega = - \int_\Gamma m_x \frac{\partial w^*}{\partial x} \cos \alpha d\Gamma + \int_\Omega \frac{\partial w^*}{\partial x} \frac{\partial m_x}{\partial x} d\Omega. \tag{111}$$

Applying the derivative property (109) in the second right hand side term of equation (111), we have:

$$\int_\Omega \sigma_x \varepsilon_x^* d\Omega = - \int_\Gamma m_x \frac{\partial w^*}{\partial x} \cos\alpha \, d\Gamma + \int_\Omega \left[\frac{\partial}{\partial x}\left(w^* \frac{\partial m_x}{\partial x} \right) - w^* \frac{\partial^2 m_x}{\partial x^2} \right] d\Omega. \quad (112)$$

After using Green theorem, we can write:

$$\int_\Omega \sigma_x \varepsilon_x^* d\Omega = \int_\Gamma \left(-m_x \frac{\partial w^*}{\partial x} \cos\alpha + w^* \frac{\partial m_x}{\partial x} \cos\alpha \right) d\Gamma - \int_\Omega w^* \frac{\partial^2 m_x}{\partial x^2} d\Omega. \quad (113)$$

Following similar procedure, we can show that:

$$\int_\Omega \sigma_y \varepsilon_y^* d\Omega = \int_\Gamma \left(-m_y \frac{\partial w^*}{\partial y} \sin\alpha + w^* \frac{\partial m_y}{\partial y} \sin\alpha \right) d\Gamma - \int_\Omega w^* \frac{\partial^2 m_y}{\partial y^2} d\Omega, \quad (114)$$

and

$$\int_\Omega \tau_{xy} \gamma_{xy}^* d\Omega = \int_\Gamma \left(-m_{xy} \frac{\partial w^*}{\partial y} \cos\alpha - m_{xy} \frac{\partial w^*}{\partial x} \sin\alpha + w^* \frac{\partial m_{xy}}{\partial x} \sin\alpha + \right.$$
$$\left. w^* \frac{\partial m_{xy}}{\partial y} \cos\alpha \right) d\Gamma - \int_\Omega 2w^* \frac{\partial^2 m_{xy}}{\partial x \partial y} d\Omega. \quad (115)$$

Thus, equation (106) is written as:

$$\int_\Omega \sigma_{ij} \varepsilon_{ij}^* d\Omega = - \int_\Gamma \left(m_x \frac{\partial w^*}{\partial x} \cos\alpha + m_y \frac{\partial w^*}{\partial y} \sin\alpha + m_{xy} \frac{\partial w^*}{\partial y} \cos\alpha + \right.$$
$$\left. m_{xy} \frac{\partial w^*}{\partial x} \sin\alpha \right) d\Gamma + \int_\Gamma w^* \left[\cos\alpha \left(\frac{\partial m_x}{\partial x} + \frac{\partial m_{xy}}{\partial y} \right) \sin\alpha \left(\frac{\partial m_y}{\partial y} + \frac{\partial m_{xy}}{\partial x} \right) \right] d\Gamma -$$
$$\int_\Omega w^* \left(\frac{\partial^2 m_x}{\partial x^2} + 2\frac{\partial^2 m_{xy}}{\partial x \partial y} + \frac{\partial^2 m_y}{\partial y^2} \right) d\Omega. \quad (116)$$

Substituting equations (67) and (68) and using equation (102), equation (116) can be written as:

$$\int_\Omega \sigma_{ij} \varepsilon_{ij}^* d\Omega = - \int_\Gamma \left(m_x \frac{\partial w^*}{\partial x} \cos\alpha + m_y \frac{\partial w^*}{\partial y} \sin\alpha + m_{xy} \frac{\partial w^*}{\partial y} \cos\alpha + \right.$$
$$\left. m_{xy} \frac{\partial w^*}{\partial x} \sin\alpha \right) d\Gamma + \int_\Gamma w^* q_n \, d\Gamma + \int_\Omega g w^* d\Omega. \quad (117)$$

From the relation between two coordinate systems (x, y) and (n, s), we have:

$$\frac{\partial w^*}{\partial x} = \frac{\partial w^*}{\partial n} \cos\alpha - \frac{\partial w^*}{\partial s} \sin\alpha,$$

$$\frac{\partial w^*}{\partial y} = \frac{\partial w^*}{\partial n} \sin\alpha + \frac{\partial w^*}{\partial s} \cos\alpha. \quad (118)$$

Substituting equations (118) into equation (117), we have:

$$
\int_{\Omega} \sigma_{ij}\varepsilon_{ij}^{*}d\Omega = -\int_{\Gamma}\left[m_x\cos\alpha\left(\frac{\partial w^*}{\partial n}\cos\alpha - \frac{\partial w^*}{\partial s}\sin\alpha\right) + \right.
$$

$$
m_y\sin\alpha\left(\frac{\partial w^*}{\partial n}\sin\alpha + \frac{\partial w^*}{\partial s}\cos\alpha\right) + m_{xy}\cos\alpha\left(\frac{\partial w^*}{\partial n}\sin\alpha + \frac{\partial w^*}{\partial s}\cos\alpha\right) +
$$

$$
\left. m_{xy}\sin\alpha\left(\frac{\partial w^*}{\partial n}\cos\alpha - \frac{\partial w^*}{\partial s}\sin\alpha\right)\right]d\Gamma + \int_{\Gamma}w^*q_n d\Gamma + \int_{\Omega}gw^*d\Omega. \qquad (119)
$$

After some algebraic manipulations, equation (119) can be rewritten as:

$$
\int_{\Omega}\sigma_{ij}\varepsilon_{ij}^{*}d\Omega = -\int_{\Gamma}\left\{\frac{\partial w^*}{\partial n}\left(m_x\cos^2\alpha + m_y\sin^2\alpha + 2m_{xy}\sin\alpha\cos\alpha\right) + \right.
$$

$$
\left. \frac{\partial w^*}{\partial s}\left[m_{xy}\left(\cos^2\alpha - \sin^2\alpha\right) + (m_y - m_x)\sin\alpha\cos\alpha\right]\right\}d\Gamma +
$$

$$
\int_{\Gamma}w^*q_n d\Gamma + \int_{\Omega}gw^*d\Omega. \qquad (120)
$$

Substituting equations (99) and (100) into equation (120), we have:

$$
\int_{\Omega}\sigma_{ij}\varepsilon_{ij}^{*}d\Omega = -\int_{\Gamma}\left(m_n\frac{\partial w^*}{\partial n} + m_{ns}\frac{\partial w^*}{\partial s} - q_n w^*\right)d\Gamma + \int_{\Omega}gw^*d\Omega. \qquad (121)
$$

Computing the second term of the first integral in the right hand side of equation (121), we have:

$$
\int_{\Gamma}m_{ns}\frac{\partial w^*}{\partial s}d\Gamma = m_{ns}w^*\Big|_{\Gamma_1}^{\Gamma_2} - \int_{\Gamma}\frac{\partial m_{ns}}{\partial s}w^*d\Gamma, \qquad (122)
$$

where Γ_1 and Γ_2 are coordinates of ends of the boundary where the integration is being carried out.

In the case of a closed boundary without corner, i.e., the function that describes the boundary curve and its derivative are continuous, the first term in the right hand side of equation (122) vanishes. In the case where there are corners, equation (122) can be written as:

$$
\int_{\Gamma}m_{ns}\frac{\partial w^*}{\partial s}d\Gamma = -\sum_{i=1}^{N_c}R_{c_i}w_{c_i}^* - \int_{\Gamma}\frac{\partial m_{ns}}{\partial s}w^*d\Gamma, \qquad (123)
$$

where

$$
R_{c_i} = m_{ns_i}^+ - m_{ns_i}^-, \qquad (124)
$$

and the terms w_{c_i}, $m_{ns_i}^+$, $m_{ns_i}^-$ are values of displacements and twisting moments after and before the i corner of the plate, N_c are the total number of boundary corners (Paiva Paiva [1987]).

From equation (121) and (123), we can write:

$$\int_\Omega \sigma_{ij}\varepsilon_{ij}^* d\Omega = \int_\Gamma \left(q_n w^* - m_n \frac{\partial w^*}{\partial n} + \frac{\partial m_{ns}}{\partial s} w^* \right) d\Gamma + \sum_{i=1}^{N_c} R_{c_i} w_{c_i}^* + \int_\Omega g w^* d\Omega. \quad (125)$$

From equations (125) and (103), we have:

$$\int_\Omega \sigma_{ij}\varepsilon_{ij}^* d\Omega = \int_\Gamma \left(V_n w^* - m_n \frac{\partial w^*}{\partial n} \right) d\Gamma + \sum_{i=1}^{N_c} R_{c_i} w_{c_i}^* + \int_\Omega g w^* d\Omega. \quad (126)$$

Following a similar procedure to that used to obtain equation (126), the left hand side of equation (104) can be written as:

$$\int_\Omega \sigma_{ij}^*\varepsilon_{ij} d\Omega = \int_\Gamma \left(V_n^* w - m_n \frac{\partial w^*}{\partial n} \right) d\Gamma + \sum_{i=1}^{N_c} R_{c_i}^* w_{c_i} + \int_\Omega g^* w d\Omega. \quad (127)$$

Substituting equations (126) and (127) into equation (104), we can write:

$$\int_\Gamma \left(V_n w^* - m_n \frac{\partial w^*}{\partial n} \right) d\Gamma + \sum_{i=1}^{N_c} R_{c_i} w_{c_i}^* + \int_\Omega g w^* d\Omega =$$

$$\int_\Gamma \left(V_n^* w - m_n^* \frac{\partial w}{\partial n} \right) d\Gamma + \sum_{i=1}^{N_c} R_{c_i}^* w_{c_i} + \int_\Omega g^* w d\Omega. \quad (128)$$

Equation (128) relates two states of an elastic material. In order to apply this equation to solve bending problems, we need to consider one of states as known and other as the state which stands for the problem which we want to analyse. To obtain a boundary integral equation, the known state is chosen so that the domain integral given by

$$\int_\Omega g^* w d\Omega \quad (129)$$

vanishes. Using the properties of Dirac delta function $\delta(P, Q)$, so that integral $g^* = \delta(P, q)$, integral (129) is written as:

$$\int_\Omega \delta(P, Q) w(P) d\Omega(P) = w(Q), \quad (130)$$

where Q is the point where the load is applied, known as source point, and P is the point where the deflexion is observed, known as field point.

The state corresponding to a linear material under loading of a Dirac delta function is known as fundamental state and the variables of equation (128) related to this state (w^*, V_n^* and m_n^*) are known as fundamental solutions which are computed analytically from the differential equation (85).

Considering the state "*" as the fundamental state, equation (128) can be written as:

$$Kw(Q) + \int_\Gamma \left[V_n^*(Q,P)w(P) - m_n^*(Q,P)\frac{\partial w(P)}{\partial n} \right] d\Gamma(P) + \sum_{i=1}^{N_c} R_{c_i}^*(Q,P)w_{c_i}(P) -$$

$$\int_\Gamma \left[V_n(P)w^*(Q,P) - m_n(P)\frac{\partial w^*}{\partial n}(Q,P) \right] d\Gamma(P) + \sum_{i=1}^{N_c} R_{c_i}(P)w_{c_i}^*(Q,P) +$$

$$\int_\Omega g(P)w^*(Q,P)d\Omega. \tag{131}$$

The constant K is introduced in order to consider that the Dirac delta function can be applied in the domain, in the boundary, or outside the domain. If the Dirac delta function is applied in a point where the boundary is smooth, than $K = 1/2$.

Variables of equation (131) are displacements $w(P)$, rotations $\partial w(P)/\partial n$, moments $m_n(P)$, and loads $V_n(P)$. For a given boundary condition, some of these variables are known. In order to have an equal number of equations and unknown variables, it is necessary to write an integral equation corresponding to the derivative of displacement $w(q)$ in relation to a cartesian coordinate system fixed in the source point, i.e., the point where the Dirac delta of the fundamental state is applied. The axis directions of this coordinate system are coincident with normal and tangent to the boundary directions in the source point.

For a particular case where the source point is placed in a point where the boundary is smooth, the boundary equation is given by (Paiva Paiva [1987]):

$$\frac{1}{2}\frac{\partial w(Q)}{\partial n_1} + \int_\Gamma \left[\frac{\partial V^*}{\partial n_1}(Q,P)w(P) - \frac{\partial m_n^*}{\partial n_1}(Q,P)\frac{\partial w}{\partial n}(P) \right] d\Gamma(P) +$$

$$\sum_{i=1}^{N_c} \frac{\partial R_{c_i}^*}{\partial n_1}(Q,P)w_{c_i}(P) = \int_\Gamma \left\{ V_n(P)\frac{\partial w^*}{\partial n_1}(Q,P) - m_n(P)\frac{\partial}{\partial n_1}\left[\frac{\partial w^*}{\partial n}(Q,P) \right] \right\} d\Gamma(P) +$$

$$\sum_{i=1}^{N_c} R_{c_i}(P)\frac{\partial w_{c_i}^*}{\partial n_1}(Q,P) + \int_\Omega g(P)\frac{\partial w^*}{\partial n_1}(Q,P)d\Omega. \tag{132}$$

It is important to say that it is possible to use only equation (131) in a boundary element formulation by using as source points the boundary nodes and an equal number of points external to the domain of the problem.

3.4 Fundamental solutions for bending problems in anisotropic materials

The fundamental solution is an essential part of the boundary element method. Fundamental solutions for anisotropic plates utilize complex variable theory following groundwork laid by Lekhnitskii Lekhnitskii [1968]. Mossakowski Mossakowski [1955] presented a solution for a point force on an infinite plate using complex parameters of the firs kind, and Suchar Suchar [1964] presented the solutions for a point force and point moment in terms of complex parameters of second kind. Lamattina Lamattina [1997] derived a more general solution for the point force using the same mapping functions as

Mossakowski Mossakowski [1955]. Lamatina *et al.* Lamattina et al. [1998] presented a comparison between three fundamental solutions and discussed the differences between these solutions.

The transversal displacement plate bending fundamental solution is computed by placing the non-homogeneous term of the differential equation (85) equal to a concentrated force given by a Dirac delta function $\delta(Q, P)$, i.e.,

$$\Delta\Delta w^*(Q, P) = \delta(Q, P), \tag{133}$$

where $\Delta\Delta(.)$ is the differential operator:

$$\Delta\Delta(.) = \frac{D_{11}}{D_{22}}\frac{\partial^4(.)}{\partial x^4} + 4\frac{D_{16}}{D_{22}}\frac{\partial^4(.)}{\partial^3\partial y} + \frac{2(D_{12} + 2D_{66})}{D_{22}}\frac{\partial^4(.)}{\partial x^2\partial y^2} + $$
$$4\frac{D_{26}}{D_{22}}\frac{\partial^4(.)}{\partial x\partial y^3} + \frac{\partial^4(.)}{\partial y^4}. \tag{134}$$

As shown by Shi and Bezine [1988], the transversal displacement fundamental solution is given by:

$$w^*(\rho, \theta) = \frac{1}{8\pi}\left\{C_1 R_1(\rho, \theta) + C_2 R_2(\rho, \theta) + C_3\left[S_1(\rho, \theta) - S_2(\rho, \theta)\right]\right\}, \tag{135}$$

where

$$\rho = [(x - x_o)^2 + (y - y_o)^2]^{1/2}, \tag{136}$$

x and y are the coordinates of the field point P, x_o and y_o are coordinates of the source point Q,

$$\theta = \arctan\frac{y - y_o}{x - x_o}, \tag{137}$$

$$C_1 = \frac{(d_1 - d_2)^2 - (e_1^2 - e_2^2)}{GHe_1}, \tag{138}$$

$$C_2 = \frac{(d_1 - d_2)^2 + (e_1^2 - e_2^2)}{GHe_2}, \tag{139}$$

$$C_3 = \frac{4(d_1 - d_2)}{GH}, \tag{140}$$

$$G = (d_1 - d_2)^2 + (e_1 + e_2)^2, \tag{141}$$

$$H = (d_1 - d_2)^2 + (e_1 - e_2)^2, \tag{142}$$

$$R_i = \rho^2 \left[(\cos\theta + d_i \sin\theta)^2 - e_i^2 \sin^2\theta \right] \times$$

$$\left\{ \log\left[\frac{\rho^2}{a^2} \left((\cos\theta + d_i \sin\theta)^2 + e_i^2 \sin^2\theta \right) \right] - 3 \right\} -$$

$$4\rho^2 e_i \sin\theta \, (\cos\theta + d_i \sin\theta) \arctan \frac{e_i \sin\theta}{\cos\theta + d_i \sin\theta}, \qquad (143)$$

and

$$S_i = \rho^2 e_i \sin\theta \, (\cos\theta + d_i \sin\theta) \times$$

$$\left\{ \log\left[\frac{\rho^2}{a^2} \left((\cos\theta + d_i \sin\theta)^2 + e_i^2 \sin^2\theta \right) \right] - 3 \right\} +$$

$$\rho^2 \left[(\cos\theta + d_i \sin\theta)^2 - e_i^2 \sin^2\theta \right] \arctan \frac{e_i \sin\theta}{\cos\theta + d_i \sin\theta}. \qquad (144)$$

The repeated index i in the terms of R_i and S_i does not imply summation. The coefficient a is an arbitrary constant taken as $a = 1$.

Other fundamental solutions are given by:

$$m_n^* = -\left(f_1 \frac{\partial^2 w^*}{\partial x^2} + f_2 \frac{\partial^2 w^*}{\partial x \partial y} + f_3 \frac{\partial^2 w^*}{\partial y^2} \right), \qquad (145)$$

$$R_{c_i}^* = -\left(g_1 \frac{\partial^2 w^*}{\partial x^2} + g_2 \frac{\partial^2 w^*}{\partial x \partial y} + g_3 \frac{\partial^2 w^*}{\partial y^2} \right), \qquad (146)$$

$$V_n^* = -\left(h_1 \frac{\partial^3 w^*}{\partial x^3} + h_2 \frac{\partial^3 w^*}{\partial x^2 \partial y} + h_3 \frac{\partial^3 w^*}{\partial x \partial y^2} + h_4 \frac{\partial^3 w^*}{\partial y^3} \right) -$$

$$\frac{1}{\bar{R}} \left(h_5 \frac{\partial^2 w^*}{\partial x^2} + h_6 \frac{\partial^2 w^*}{\partial x \partial y} + h_7 \frac{\partial^2 w^*}{\partial y^2} \right). \qquad (147)$$

where $\bar{R}$ is the curvature radius at a smooth point of the boundary Γ. Other constants are defined as:

$$f_1 = D_{11}n_x^2 + 2D_{16}n_xn_y + D_{12}n_y^2, \tag{148}$$

$$f_2 = 2(D_{16}n_x^2 + 2D_{66}n_xn_y + D_{26}n_y^2), \tag{149}$$

$$f_3 = D_{12}n_x^2 + 2D_{26}n_xn_y + D_{22}n_y^2, \tag{150}$$

$$g_1 = (D_{12} - D_{11})\cos\beta\sin\beta + D_{16}(\cos^2\beta - \sin^2\beta), \tag{151}$$

$$g_2 = 2(D_{26} - D_{16})\cos\beta\sin\beta + 2D_{66}(\cos^2\beta - \sin^2\beta), \tag{152}$$

$$g_3 = (D_{22} - D_{12})\cos\beta\sin\beta + D_{26}(\cos^2\beta - \sin^2\beta), \tag{153}$$

$$h_1 = D_{11}n_x(1 + n_y^2) + 2D_{16}n_y^3 - D_{12}n_xn_y^2, \tag{154}$$

$$h_2 = 4D_{16}n_x + D_{12}n_y(1 + n_x^2) + 4D_{66}n_y^3 - D_{11}n_x^2n_y - 2D_{26}n_xn_y^2, \tag{155}$$

$$h_3 = 4D_{26}n_y + D_{12}n_x(1 + n_y^2) + 4D_{66}n_x^3 - D_{22}n_xn_y^2 - 2D_{16}n_x^2n_y, \tag{156}$$

$$h_4 = D_{22}n_y(1 + n_x^2) + 2D_{26}n_x^3 - D_{12}n_x^2n_y, \tag{157}$$

$$h_5 = (D_{12} - D_{11})\cos 2\beta - 4D_{16}\sin 2\beta, \tag{158}$$

$$h_6 = 2(D_{26} - D_{16})\cos 2\beta - 4D_{66}\sin 2\beta, \tag{159}$$

$$h_7 = (D_{22} - D_{12})\cos 2\beta - 4D_{26}\sin 2\beta, \tag{160}$$

and β is the angle between the global coordinate system xy and a coordinate system ns in which their axis directions are parallels to vectors $\mathbf{n}$ and $\mathbf{s}$, normal and tangent, respectively, to the boundary in the field point Q. The derivatives of the transversal displacement fundamental solution can be expressed by linear combination of derivatives of functions R_i and S_i. For example:

$$\frac{\partial^2 w^*}{\partial y^2} = \frac{1}{8\pi}\left[C_1\frac{\partial^2 R_1}{\partial y^2} + C_2\frac{\partial^2 R_2}{\partial y^2} + C_3\left(\frac{\partial^2 S_1}{\partial y^2} - \frac{\partial^2 S_2}{\partial y^2}\right)\right]. \tag{161}$$

The derivatives of R_i and S_i are given by:

$$\frac{\partial R_i}{\partial x} = 2r\left(\cos\theta + d_i\sin\theta\right)\left\{\log\left[\frac{r^2}{a^2}\left(\left(\cos\theta + d_i\sin\theta\right)^2 + e_i^2\sin^2\theta\right)\right] - 2\right\} -$$

$$4re_i\sin\theta\arctan\frac{e_i\sin\theta}{\cos\theta + d_i\sin\theta}, \tag{162}$$

$$\frac{\partial R_i}{\partial y} = 2r\left[d_i\left(\cos\theta + d_i\sin\theta\right) - e_i^2\sin\theta\right] \times$$

$$\left\{\log\left[\frac{r^2}{a^2}\left(\left(\cos\theta + d_i\sin\theta\right)^2 + e_i^2\sin^2\theta\right)\right] - 2\right\} -$$

$$4re_i\left(\cos\theta + 2d_i\sin\theta\right)\arctan\frac{e_i\sin\theta}{\cos\theta + d_i\sin\theta}, \tag{163}$$

$$\frac{\partial^2 R_i}{\partial x^2} = 2\log\left\{\frac{r^2}{a^2}\left[\left(\cos\theta + d_i\sin\theta\right)^2 + e_i^2\sin^2\theta\right]\right\} \tag{164}$$

$$\frac{\partial^2 R_i}{\partial x\partial y} = 2d_i\log\left\{\frac{r^2}{a^2}\left[\left(\cos\theta + d_i\sin\theta\right)^2 + e_i^2\sin^2\theta\right]\right\} -$$

$$4e_i\arctan\frac{e_i\sin\theta}{\cos\theta + d_i\sin\theta}, \tag{165}$$

$$\tag{166}$$

$$\frac{\partial^2 R_i}{\partial y^2} = 2\left(d_i^2 - e_i^2\right)\log\left\{\frac{r^2}{a^2}\left[\left(\cos\theta + d_i\sin\theta\right)^2 + e_i^2\sin^2\theta\right]\right\} -$$

$$8d_ie_i\arctan\frac{e_i\sin\theta}{\cos\theta + d_i\sin\theta}, \tag{167}$$

$$\frac{\partial^3 R_i}{\partial x^3} = \frac{4\left(\cos\theta + d_i\sin\theta\right)}{r\left[\left(\cos\theta + d_i\sin\theta\right)^2 + e_i^2\sin^2\theta\right]}, \tag{168}$$

$$\frac{\partial^3 R_i}{\partial x^2\partial y} = \frac{4\left[d_i\left(\cos\theta + d_i\sin\theta\right) + e_i^2\sin\theta\right]}{r\left[\left(\cos\theta + d_i\sin\theta\right)^2 + e_i^2\sin^2\theta\right]}, \tag{169}$$

$$\frac{\partial^3 R_i}{\partial x\partial y^2} = \frac{4\left[\left(d_i^2 - e_i^2\right)\cos\theta + \left(d_i^2 + e_i^2\right)d_i\sin\theta\right]}{r\left[\left(\cos\theta + d_i\sin\theta\right)^2 + e_i^2\sin^2\theta\right]}, \tag{170}$$

$$\tag{171}$$

$$\frac{\partial^3 R_i}{\partial y^3} = \frac{4\left[d_i\left(d_i^2 - 3e_i^2\right)\cos\theta + \left(d_i^4 - e_i^4\right)\sin\theta\right]}{r\left[\left(\cos\theta + d_i\sin\theta\right)^2 + e_i^2\sin^2\theta\right]}, \tag{172}$$

$$\frac{\partial^4 R_i}{\partial x^4} = -\frac{4\left[\left(\cos\theta + d_i\sin\theta\right)^2 - e_i^2\sin^2\theta\right]}{r^2\left[\left(\cos\theta + d_i\sin\theta\right)^2 + e_i^2\sin^2\theta\right]^2}, \tag{173}$$

$$\frac{\partial^4 R_i}{\partial x^3 \partial y} = -\frac{4}{r^2}\left\{\frac{d_i}{\left(\cos\theta + d_i\sin\theta\right)^2 + e_i^2\sin^2\theta} + \frac{2e_i^2\sin\theta\cos\theta}{\left[\left(\cos\theta + d_i\sin\theta\right)^2 + e_i^2\sin^2\theta\right]^2}\right\}, \tag{174}$$

$$\frac{\partial^4 R_i}{\partial x^2 \partial y^2} = -\frac{4}{r^2}\left\{\frac{\left(d_i^2 + e_i^2\right)}{\left(\left(\cos\theta + d_i\sin\theta\right)^2 + e_i^2\sin^2\theta\right)} - \frac{2e_i^2\cos^2\theta}{\left[\left(\cos\theta + d_i\sin\theta\right)^2 + e_i^2\sin^2\theta\right]^2}\right\}, \tag{175}$$

$$\tag{176}$$

$$\frac{\partial^4 R_i}{\partial x \partial y^3} = -\frac{4}{r^2}\left\{\frac{d_i\left(d_i^2 + e_i^2\right)}{\left(\left(\cos\theta + d_i\sin\theta\right)^2 + e_i^2\sin^2\theta\right)} - \frac{2e_i^2\cos\theta\left(2d_i\cos\theta + \left(d_i^2 + e_i^2\right)\sin\theta\right)}{\left[\left(\cos\theta + d_i\sin\theta\right)^2 + e_i^2\sin^2\theta\right]^2}\right\}, \tag{177}$$

$$\frac{\partial^4 R_i}{\partial y^4} = -\frac{4}{r^2}\left\{\frac{\left(d_i^4 - e_i^4\right)}{\left(\cos\theta + d_i\sin\theta\right)^2 + e_i^2\sin^2\theta} - \frac{2e_i^2\cos\theta\left[\left(3d_i^2 - e_i^2\right)\cos\theta + 2d_i\left(d_i^2 + e_i^2\right)\sin\theta\right]}{\left[\left(\cos\theta + d_i\sin\theta\right)^2 + e_i^2\sin^2\theta\right]^2}\right\}, \tag{178}$$

$$\tag{179}$$

$$\frac{\partial S_i}{\partial x} = re_i \sin\theta \left\{ \log\left[\frac{r^2}{a^2}\left((\cos\theta + d_i\sin\theta)^2 + e_i^2\sin^2\theta\right)\right] - 2 \right\} +$$

$$2r(\cos\theta + d_i\sin\theta)\arctan\frac{e_i\sin\theta}{\cos\theta + d_i\sin\theta}, \tag{180}$$

$$\frac{\partial S_i}{\partial y} = re_i(\cos\theta + 2d_i\sin\theta)\left\{ \log\left[\frac{r^2}{a^2}\left((\cos\theta + d_i\sin\theta)^2 + e_i^2\sin^2\theta\right)\right] - 2 \right\} +$$

$$2r\left[d_i(\cos\theta + d_i\sin\theta) - e_i^2\sin\theta\right]\arctan\frac{e_i\sin\theta}{\cos\theta + d_i\sin\theta}, \tag{181}$$

$$\frac{\partial^2 S_i}{\partial x^2} = 2\arctan\frac{e_i\sin\theta}{\cos\theta + d_i\sin\theta}, \tag{182}$$

$$\frac{\partial^2 S_i}{\partial x\partial y} = e_i\log\left\{ \frac{r^2}{a^2}\left[(\cos\theta + d_i\sin\theta)^2 + e_i^2\sin^2\theta\right] \right\} +$$

$$2d_i\arctan\frac{e_i\sin\theta}{\cos\theta + d_i\sin\theta}, \tag{183}$$

$$\tag{184}$$

$$\frac{\partial^2 S_i}{\partial y^2} = 2d_ie_i\log\left\{ \frac{r^2}{a^2}\left[(\cos\theta + d_i\sin\theta)^2 + e_i^2\sin^2\theta\right] \right\} +$$

$$2\left(d_i^2 - e_i^2\right)\arctan\frac{e_i\sin\theta}{\cos\theta + d_i\sin\theta}, \tag{185}$$

$$\frac{\partial^3 S_i}{\partial x^3} = -\frac{2e_i\sin\theta}{r\left[(\cos\theta + d_i\sin\theta)^2 + e_i^2\sin^2\theta\right]}, \tag{186}$$

$$\frac{\partial^3 S_i}{\partial x^2\partial y} = \frac{2e_i\cos\theta}{r\left[(\cos\theta + d_i\sin\theta)^2 + e_i^2\sin^2\theta\right]}, \tag{187}$$

$$\frac{\partial^3 S_i}{\partial x\partial y^2} = \frac{2e_i\left[2d_i(\cos\theta + d_i\sin\theta) - (d_i^2 - e_i^2)\sin\theta\right]}{r\left[(\cos\theta + d_i\sin\theta)^2 + e_i^2\sin^2\theta\right]}, \tag{188}$$

$$\frac{\partial^3 S_i}{\partial y^3} = \frac{2e_i\left[(3d_i^2 - e_i^2)\cos\theta + 2d_i(d_i^2 + e_i^2)\sin\theta\right]}{r\left((\cos\theta + d_i\sin\theta)^2 + e_i^2\sin^2\theta\right)}, \tag{189}$$

$$\tag{190}$$

$$\frac{\partial^4 S_i}{\partial x^4} = \frac{4e_i \sin\theta \left(\cos\theta + d_i \sin\theta\right)}{r^2 \left[\left(\cos\theta + d_i \sin\theta\right)^2 + e_i^2 \sin^2\theta\right]^2}, \tag{191}$$

$$\frac{\partial^4 S_i}{\partial x^3 \partial y} = \frac{2e_i}{r^2} \left\{ \frac{1}{\left(\cos\theta + d_i \sin\theta\right)^2 + e_i^2 \sin^2\theta} - \right.$$

$$\left. \frac{2\cos\theta \left(\cos\theta + d_i \sin\theta\right)}{\left[\left(\cos\theta + d_i \sin\theta\right)^2 + e_i^2 \sin^2\theta\right]^2} \right\}, \tag{192}$$

$$\frac{\partial^4 S_i}{\partial x^2 \partial y^2} = -\frac{4e_i \cos\theta \left[d_i \left(\cos\theta + d_i \sin\theta\right) + e_i^2 \sin\theta\right]}{r^2 \left[\left(\cos\theta + d_i \sin\theta\right)^2 + e_i^2 \sin^2\theta\right]^2}, \tag{193}$$

$$\frac{\partial^4 S_i}{\partial x \partial y^3} = -\frac{2e_i}{r^2} \left\{ \frac{\left(d_i^2 + e_i^2\right)}{\left(\cos\theta + d_i \sin\theta\right)^2 + e_i^2 \sin^2\theta} + \right.$$

$$\left. \frac{2\left(d_i^2 + e_i^2\right)\cos\theta \left(\cos\theta + d_i \sin\theta\right) - 4e_i^2 \cos^2\theta}{\left[\left(\cos\theta + d_i \sin\theta\right)^2 + e_i^2 \sin^2\theta\right]^2} \right\}, \tag{194}$$

$$\tag{195}$$

$$\frac{\partial^4 S_i}{\partial y^4} = -\frac{4e_i}{r^2} \left\{ \frac{d_i \left(d_i^2 + e_i^2\right)}{\left(\cos\theta + d_i \sin\theta\right)^2 + e_i^2 \sin^2\theta} + \right.$$

$$\left. \frac{\cos\theta \left[d_i \left(d_i^2 - 3e_i^2\right)\cos\theta + \left(d_i^4 - e_i^4\right)\sin\theta\right]}{\left[\left(\cos\theta + d_i \sin\theta\right)^2 + e_i^2 \sin^2\theta\right]^2} \right\}. \tag{196}$$

As it can be seen, derivatives of R_i and S_i present weak ($\log r$), strong ($1/r$), and hyper ($1/r^2$) singularities that will need special attention during their integration in boundary element kernels.

3.5   Transformation of domain integrals into boundary integrals in anisotropic plate bending problems

As it can be seen in equations (131) and (132), there are domain integrals in the formulation due to the distributed load in the domain. These integrals can be computed in the domain by direct integration in the area Ω_g (see Figure 8). However, the boundary element formulation loses its main feature that is the boundary only discretization. In this work, domain integrals which come from distributed loads are transformed into boundary integrals by an exact transformation.

Consider the plate of Figure 8, under loading g, applied in an area Ω_g. Assuming that loading g has a linear distribution $(Ax + By + C)$ in the area Ω_g, the domain integral can be written as:

$$\int_{\Omega_g} g w^* d\Omega = \int_{\Omega_g} (Ax + By + C) w^* \rho d\rho d\theta \tag{197}$$

or

$$\int_{\Omega_g} gw^* d\Omega = \int_\theta \int_0^r (Ax + By + C)w^* \rho d\rho d\theta, \tag{198}$$

where r is the value of ρ in a point of boundary Γ_g.

Defining F^* as the following integral:

$$F^* = \int_0^r (Ax + By + C)w^* \rho d\rho, \tag{199}$$

we can write:

$$\int_{\Omega_g} gw^* d\Omega = \int_\theta F^* d\theta. \tag{200}$$

Considering an infinitesimal angle $d\theta$ (Figure 13), the relation between the arch length $r d\theta$ and the infinitesimal boundary length $d\Gamma$, can be written as:
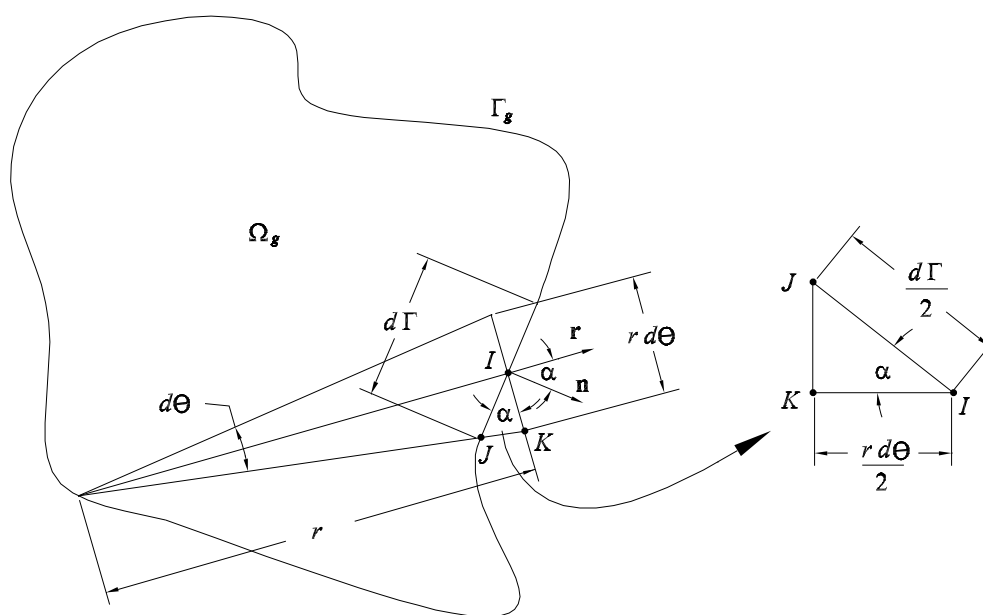
Figure 13: Transformation of domain integral into boundary integral.

$$\cos \alpha = \frac{r\frac{d\theta}{2}}{\frac{d\Gamma}{2}}, \tag{201}$$

or

$$d\theta = \frac{\cos \alpha}{r} d\Gamma. \tag{202}$$

Using the properties of internal product of unity vectors $\mathbf{n}$ and $\mathbf{r}$, indicated in Figure 13, we can write:

$$d\theta = \frac{\mathbf{n.r}}{r} d\Gamma. \tag{203}$$

Finally, substituting equation (203) into equation (200), the domain integral of equation (131) can be written as a boundary integral given by:

$$\int_{\Omega_g} g w^* d\Omega = \int_{\Gamma_g} \frac{F^*}{r} \mathbf{n}.\mathbf{r} d\Gamma.$$

(204)

Provided that

$$x = \rho \cos \theta$$

(205)

and

$$y = \rho \sin \theta,$$

(206)

the integral F^* can be written as:

$$F^* = \int_0^r \frac{1}{8\pi} (A\rho \cos \theta + B\rho \sin \theta + C) [C_1 R_1 + C_2 R_2 + C_3 (S_1 - S_2)] \rho d\rho,$$

(207)

where C_1, C_2, and C_3 are given by equations (138), (139), (140), respectively. Equation (207) can be rewritten as:

$$F^* = \frac{1}{8\pi} \left\{ (A\cos \theta + B\sin \theta) \int_0^r \rho^2 [C_1 R_1 + C_2 R_2 + C_3 (S_1 - S_2)] d\rho + \right.$$

$$\left. C \int_0^r \rho [C_1 R_1 + C_2 R_2 + C_3 (S_1 - S_2)] d\rho \right\}.$$

(208)

Following similar procedure to obtain equation (204), the domain term of equation (132) can be written as:

$$\int_{\Omega_g} g \frac{\partial w^*}{\partial n_1} d\Omega = \int_\theta \frac{G^*}{r} \mathbf{n}.\mathbf{r} d\Gamma,$$

(209)

where

$$G^* = \int_0^r (Ax + By + C) \frac{\partial w^*}{\partial n_1} \rho d\rho$$

(210)

or

$$G^* = \frac{1}{8\pi} \left\{ (A\cos \theta + B\sin \theta) \int_0^r \rho^2 \left[C_1 \frac{\partial R_1}{\partial n_1} + C_2 \frac{\partial R_2}{\partial n_1} + \right. \right.$$

$$\left. \left. C_3 \left(\frac{\partial S_1}{\partial n_1} - \frac{\partial S_2}{\partial n_1} \right) \right] d\rho + C \int_0^r \rho \left[C_1 \frac{\partial R_1}{\partial n_1} + C_2 \frac{\partial R_2}{\partial n_1} + C_3 \left(\frac{\partial S_1}{\partial n_1} - \frac{\partial S_2}{\partial n_1} \right) \right] d\rho \right\}.$$

(211)

As it can be seen, equations (208) and (211) are not θ dependent. By analytical integration, we can obtain:

$$\int_0^r R_i \rho \, d\rho \;=\; \frac{r^4}{16}\left\{ -16 e_i \arctan \frac{e_i \sin\theta}{\cos\theta + d_i \sin\theta} \, \sin\theta \left(\cos\theta + d_i \sin\theta\right) - \right.$$

$$\left[-7 + 2\log \frac{r^2\left(e_i^2 \sin^2\theta + \left(\cos\theta + d_i \sin\theta\right)^2\right)}{a^2}\right] \times$$

$$\left. \left[-1 - d_i^2 + e_i^2 + \left(-1 + d_i^2 - e_i^2\right)\cos 2\theta - 2 d_i \sin 2\theta\right] \right\}, \qquad (212)$$

$$\int_0^r S_i \rho \, d\rho \;=\; \frac{r^4}{16}\left\{ 2 e_i \left[-7 + 2\log \frac{r^2\left(e_i^2 \sin^2\theta + \left(\cos\theta + d_i \sin\theta\right)^2\right)}{a^2}\right] \times\right.$$

$$\sin\theta \left(\cos\theta + d_i \sin\theta\right) + 2\arctan \frac{e_i \sin\theta}{\cos\theta + d_i \sin\theta} \times$$

$$\left. \left[1 + d_i^2 - e_i^2 + \left(1 - d_i^2 + e_i^2\right)\cos 2\theta + 2 d_i \sin 2\theta\right] \right\}, \qquad (213)$$

$$(214)$$

$$\int_0^r R_i \rho^2 d\rho = \frac{r^5}{50} \left\{ -40 e_i \arctan \frac{e_i \sin\theta}{\cos\theta + d_i \sin\theta} \sin\theta \left(\cos\theta + d_i \sin\theta\right) - \right.$$
$$\left[-17 + 5 \log \frac{r^2 \left(e_i^2 \sin^2\theta + \left(\cos\theta + d_i \sin\theta\right)^2\right)}{a^2} \right] \times$$
$$\left. \left[-1 - d_i^2 + e_i^2 + \left(-1 + d_i^2 - e_i^2\right) \cos 2\theta - 2 d_i \sin 2\theta \right] \right\}, \quad (215)$$

$$\int_0^r S_i \rho^2 d\rho = \frac{r^5}{50} \left\{ 2 e_i \left[-17 + 5 \log \frac{r^2 \left(e_i^2 \sin^2\theta + \left(\cos\theta + d_i \sin\theta\right)^2\right)}{a^2} \right] \times \right.$$
$$\sin\theta \left(\cos\theta + d_i \sin\theta\right) + 5 \arctan \frac{e_i \sin\theta}{\cos\theta + d_i \sin\theta} \times$$
$$\left. \left[1 + d_i^2 - e_i^2 + \left(1 - d_i^2 + e_i^2\right) \cos 2\theta + 2 d_i \sin 2\theta \right] \right\}, \quad (216)$$

$$\int_0^r \frac{\partial R_i}{\partial x} \rho \, d\rho = \frac{2 r^3}{9} \left\{ -6 e_i \arctan \frac{e_i \sin\theta}{\cos\theta + d_i \sin\theta} \sin\theta + \right.$$
$$\left. \left[-8 + 3 \log \frac{r^2 \left(e_i^2 \sin^2\theta + \left(\cos\theta + d_i \sin\theta\right)^2\right)}{a^2} \right] \left(\cos\theta + d_i \sin\theta\right) \right\}, \quad (217)$$
$$(218)$$

$$\int_0^r \frac{\partial R_i}{\partial y} \rho \, d\rho = \frac{2 r^3}{9} \left\{ -6 e_i \arctan \frac{e_i \sin\theta}{\cos\theta + d_i \sin\theta} \left(\cos\theta + 2 d_i \sin\theta\right) + \right.$$
$$\left. \left[-8 + 3 \log \frac{r^2 \left(e_i^2 \sin^2\theta + \left(\cos\theta + d_i \sin\theta\right)^2\right)}{a^2} \right] \left[d_i \cos\theta + \left(d_i^2 - e_i^2\right) \sin\theta \right] \right\}, \quad$$
$$(219)$$

$$\int_0^r \frac{\partial S_i}{\partial x} \rho \, d\rho = \frac{r^3}{9} \left\{ e_i \left[-8 + 3 \log \frac{r^2 \left(e_i^2 \sin^2\theta + \left(\cos\theta + d_i \sin\theta\right)^2\right)}{a^2} \right] \sin\theta + \right.$$
$$\left. 6 \arctan \frac{e_i \sin\theta}{\cos\theta + d_i \sin\theta} \left(\cos\theta + d_i \sin\theta\right) \right\}, \quad (220)$$
$$(221)$$

$$\int_0^r \frac{\partial S_i}{\partial y} \rho \, d\rho \;=\; \frac{r^3}{9} \left\{ e_i \left[-8 + 3 \log \frac{r^2 \left(e_i^2 \sin^2 \theta + (\cos \theta + d_i \sin \theta)^2 \right)}{a^2} \right] \times \right.$$

$$\left. (\cos \theta + 2d_i \sin \theta) - 6 \arctan \frac{e_i \sin \theta}{\cos \theta + d_i \sin \theta} \left[d_i \cos \theta + \left(d_i^2 - e_i^2 \right) \sin \theta \right] \right\},$$

$$(222)$$

$$\int_0^r \frac{\partial R_i}{\partial x} \rho^2 \, d\rho \;=\; \frac{r^4}{4} \left\{ -4e_i \arctan \frac{e_i \sin \theta}{\cos \theta + d_i \sin \theta} \sin \theta + \right.$$

$$\left. \left[-5 + 2 \log \frac{r^2 \left(e_i^2 \sin^2 \theta + (\cos \theta + d_i \sin \theta)^2 \right)}{a^2} \right] (\cos \theta + d_i \sin \theta) \right\},$$

$$(223)$$

$$\int_0^r \frac{\partial R_i}{\partial y} \rho^2 \, d\rho \;=\; \frac{r^4}{4} \left\{ -4e_i \arctan \frac{e_i \sin \theta}{\cos \theta + d_i \sin \theta} (\cos \theta + 2d_i \sin \theta) + \right.$$

$$\left. \left[-5 + 2 \log \frac{r^2 \left(e_i^2 \sin^2 \theta + (\cos \theta + d_i \sin \theta)^2 \right)}{a^2} \right] \left[d_i \cos \theta + \left(d_i^2 - e_i^2 \right) \sin \theta \right] \right\},$$

$$(224)$$

$$\int_0^r \frac{\partial S_i}{\partial x} \rho^2 \, d\rho \;=\; \frac{r^4}{8} \left\{ e_i \left[-5 + 2 \log \frac{r^2 \left(e_i^2 \sin^2 \theta + (\cos \theta + d_i \sin \theta)^2 \right)}{a^2} \right] \sin \theta + \right.$$

$$\left. 4 \arctan \frac{e_i \sin \theta}{\cos \theta + d_i \sin \theta} (\cos \theta + d_i \sin \theta) \right\},$$

$$(225)$$

$$(226)$$

$$\int_0^r \frac{\partial S_i}{\partial y} \rho^2 \, d\rho \;=\; \frac{r^4}{8} \left\{ e_i \left[-5 + 2 \log \frac{r^2 \left(e_i^2 \sin^2 \theta + (\cos \theta + d_i \sin \theta)^2 \right)}{a^2} \right] \right.$$

$$\left. (\cos \theta + 2d_i \sin \theta) + 4 \arctan \frac{e_i \sin \theta}{\cos \theta + d_i \sin \theta} \left[d_i \cos \theta + \left(d_i^2 - e_i^2 \right) \sin \theta \right] \right\}.$$

$$(227)$$

Although in this work the domain loads are considered as uniformly distributed or linearly distributed, the procedure presented in this section can be extended to other higher order loads.

3.6 Matrix equation

In order to compute unknown boundary variables, the boundary Γ is discretized in N_e straight elements and the boundary variables w, $\partial w/\partial n$, m_n, and V_n are assumed constant along each element. Taking a node d as the source point, equations (131) and (132) can be written in a matrix form as:

$$\frac{1}{2}\left\{\begin{array}{c} w^{(d)} \\ \frac{\partial w^{(d)}}{\partial n_1} \end{array}\right\} + \sum_{i=1}^{N_e}\left(\left[\begin{array}{cc} h_{11}^{(i,d)} & h_{12}^{(i,d)} \\ h_{21}^{(i,d)} & h_{22}^{(i,d)} \end{array}\right]\left\{\begin{array}{c} w^{(i)} \\ \frac{\partial w^{(i)}}{\partial n} \end{array}\right\}\right) =$$

$$\sum_{i=1}^{N_e}\left(\left[\begin{array}{cc} g_{11}^{(i,d)} & g_{12}^{(i,d)} \\ g_{21}^{(i,d)} & g_{22}^{(i,d)} \end{array}\right]\left\{\begin{array}{c} V_n^{(i)} \\ m_n^{(i)} \end{array}\right\}\right) + \sum_{i=1}^{N_c}\left(\left\{\begin{array}{c} R_1^{(i,d)} \\ R_2^{(i,d)} \end{array}\right\} w_c^{(i)}\right) +$$

$$\sum_{i=1}^{N_c}\left(\left\{\begin{array}{c} c_1^{(i,d)} \\ c_2^{(i,d)} \end{array}\right\} R_c^{(i)}\right) + \left\{\begin{array}{c} P_1^{(d)} \\ P_2^{(d)} \end{array}\right\} \tag{228}$$

Terms of equation (228) are integrals given by:

$$h_{11}^{(i,d)} = \int_{\Gamma_i} V_n^* d\Gamma, \qquad h_{12}^{(i,d)} = -\int_{\Gamma_i} m_n^* d\Gamma, \tag{229}$$

$$h_{21}^{(i,d)} = \int_{\Gamma_i} \frac{\partial V_n^*}{\partial n_1} d\Gamma, \qquad h_{22}^{(i,d)} = -\int_{\Gamma_i} \frac{\partial m_n^*}{\partial n_1} d\Gamma, \tag{230}$$

$$g_{11}^{(i,d)} = \int_{\Gamma_i} w^* d\Gamma, \qquad g_{12}^{(i,d)} = -\int_{\Gamma_i} \frac{\partial w^*}{\partial n} d\Gamma, \tag{231}$$

$$g_{21}^{(i,d)} = \int_{\Gamma_i} \frac{\partial w^*}{\partial n_1} d\Gamma, \qquad g_{22}^{(i,d)} = -\int_{\Gamma_i} \frac{\partial}{\partial n_1}\frac{\partial m_n^*}{\partial n} d\Gamma, \tag{232}$$

$$c_1^{(i,d)} = w_{ci}^*, \qquad c_2^{(i,d)} = \frac{\partial w_{ci}^*}{\partial n_1}, \tag{233}$$

$$R_1^{(i,d)} = R_{ci}^*, \qquad R_2^{(i,d)} = \frac{\partial R_{ci}^*}{\partial n_1}, \tag{234}$$

$$P_1^{(d)} = \int_\Omega g w^* d\Omega, \qquad P_2^{(d)} = \int_\Omega g \frac{\partial w}{\partial n_1} d\Omega. \tag{235}$$

Matrix equation (228) has two equations and $2N_e + N_c$ unknown variables. In order to obtain a solvable linear system, the source point is placed successively in each boundary node ($d = 1, ..., N_e$) as well as in each corner node ($d = N_e + 1, ..., N_e + N_c$). It is worth noting that while both equations, (131) and (132), are used for each boundary node (providing the first $2N_e$ equations), only the equation (131) is used for each corner (providing other N_c equations). So, the following matrix equation is obtained:

$$\left[\begin{array}{cc} \mathbf{H}' & \mathbf{R}' \\ \mathbf{H}'' & \mathbf{R}'' \end{array}\right]\left\{\begin{array}{c} \mathbf{w}_{bn} \\ \mathbf{w}_c \end{array}\right\} = \left[\begin{array}{cc} \mathbf{G}' & \mathbf{C}' \\ \mathbf{G}'' & \mathbf{C}'' \end{array}\right]\left\{\begin{array}{c} \mathbf{V}_{bn} \\ \mathbf{V}_c \end{array}\right\} + \left\{\begin{array}{c} \mathbf{P}_{bn} \\ \mathbf{P}_c \end{array}\right\} \tag{236}$$

where $\mathbf{w}_{bn}$ contains the transversal displacement and the rotation of each boundary node, $\mathbf{V}_{bn}$ contains the shear force and the twisting moment of each boundary node, $\mathbf{P}_{bn}$ contains the domain integral for each boundary node, $\mathbf{w}_c$ contains the transversal displacement of each corner, and $\mathbf{V}_c$ contains the corner reaction of each corner, $\mathbf{P}_c$ contains the domain integral for each corner. Terms $\mathbf{H}'$, $\mathbf{C}'$, $\mathbf{R}'$, and $\mathbf{G}'$ are matrices which contain the respective terms of equation (228) written to the N_e boundary nodes; $\boldsymbol{\gamma}$ is the vector that contains coefficients γ^m. Terms $\mathbf{H}''$, $\mathbf{C}''$, $\mathbf{R}''$, and $\mathbf{G}''$ are matrices which contain the respective first line terms of equation (228) written to N_c corners.

Equation (236) can be rewritten as:

$$\mathbf{Hw} = \mathbf{GV} + \mathbf{P} \tag{237}$$

where

$$\mathbf{H} = \begin{bmatrix} \mathbf{H}' & \mathbf{R}' \\ \mathbf{H}'' & \mathbf{R}'' \end{bmatrix} \tag{238}$$

$$\mathbf{w} = \left\{ \begin{array}{c} \mathbf{w}_{bn} \\ \mathbf{w}_c \end{array} \right\} \tag{239}$$

$$\mathbf{G} = \begin{bmatrix} \mathbf{G}' & \mathbf{C}' \\ \mathbf{G}'' & \mathbf{C}'' \end{bmatrix} \tag{240}$$

$$\mathbf{V} = \left\{ \begin{array}{c} \mathbf{V}_{bn} \\ \mathbf{V}_c \end{array} \right\} \tag{241}$$

$$\mathbf{P} = \left\{ \begin{array}{c} \mathbf{P}_{bn} \\ \mathbf{P}_c \end{array} \right\} \tag{242}$$

Applying boundary conditions, equation (236) can be rearranged as

$$\mathbf{Ax} = \mathbf{b} \tag{243}$$

which can be solved by standard procedure for linear systems.

3.7   Quadratic Elements

In order to increase the convergency of results to the formulation presented here, quadratic elements were implemented. As the formulation has integrals with singular integrands, these integrals need to be computed in the Cauchy sense, in the case of strong singularities, or Hadamard sense, in the case of hyper singularities. Integration in the Hadamard sense demands Holder's continuity in the nodes. Because this, discontinuous elements are strongly recommended. In this work, discontinuous quadratic elements with nodes placed at $\xi = -2/3$, $\xi = 0$, and $\xi = +2/3$ (Figure 14) were implemented. The shape functions for these elements are given by:

$$N_1 = \xi \left(\frac{9}{8}\xi - \frac{3}{4} \right); \tag{244}$$

$$N_2 = \left(1 - \frac{3}{2}\xi \right) \left(1 + \frac{3}{2}\xi \right); \tag{245}$$

$$N_3 = \xi \left(\frac{9}{8}\xi + \frac{3}{4} \right). \tag{246}$$

-1   -2/3   0   2/3   1 $\longrightarrow \xi$

Figure 14: Discontinuous quadratic boundary element.

3.8 Transformation of domain integrals into boundary integrals for unknown body forces

3.8.1 Dual reciprocity method

The procedure presented in section 3.5 to transform domain integrals into boundary integral is suitable when body forces are constants or functions of coordinates x and y coordinates along the domain. When these body forces are functions of deflexion w, as in dynamic problems for example, the exact transformation is no longer useful. In this case, approaches as the dual reciprocity method is very suitable. The dual reciprocity formulation for anisotropic plate bending problems is presented in this section.

Consider that the term b of equation (131) is approximated over the domain as a sum of the M products between radial basis functions f^m and unknown coefficients γ^m, that is:

$$b(P) = \sum_{m=1}^{M} \gamma^m f^m. \tag{247}$$

for approximation functions based on pure radial basis function, or

$$b(P) = \sum_{m=1}^{M} \gamma_m f_m + ax + by + c \tag{248}$$

with

$$\sum_{m=1}^{M} \gamma_m x_m = \sum_{m=1}^{M} \gamma_m y_m = \sum_{m=1}^{M} \gamma_m = 0 \tag{249}$$

for approximation functions based on radial basis function combined with augmentation functions.

Thus, the domain integral of equation (131) can be written as:

$$P_1(Q) = \int_{\Omega_g} b(P)w^*(Q,P)d\Omega = \sum_{m=1}^{M} \gamma^m \int_{\Omega_g} f^m w^*(Q)d\Omega. \tag{250}$$

Particular solutions $\hat{w}$ can be obtained by solving the following differential equation:

$$D_{11}\frac{\partial^4 \hat{w}}{\partial x^4} + 4D_{16}\frac{\partial^4 \hat{w}}{\partial x^3 \partial y} + 2(D_{12}+D_{66})\frac{\partial^4 \hat{w}}{\partial x^2 \partial y^2} + 4D_{26}\frac{\partial^4 \hat{w}}{\partial x \partial y^3} + D_{22}\frac{\partial^4 \hat{w}}{\partial y^4} = f. \tag{251}$$

The reciprocal relation between the fundamental solution and the particular solution can be written as:

$$K\hat{w}(Q) + \int_{\Gamma} \left[V_n^*(Q,P)\hat{w}(P) - m_n^*(Q,P)\frac{\partial \hat{w}(P)}{\partial n} \right] d\Gamma(P) + \sum_{i=1}^{N_c} R_{c_i}^*(Q,P)\hat{w}_{c_i}(P) =$$

$$\int_{\Gamma} \left[\hat{V}_n(P)w^*(Q,P) - \hat{m}_n(P)\frac{\partial w^*}{\partial n}(Q,P) \right] d\Gamma(P) + \sum_{i=1}^{N_c} \hat{R}_{c_i}(P)w_{c_i}^*(Q,P) +$$

$$\int_{\Omega} f(P)w^*(Q,P)d\Omega. \tag{252}$$

Substituting equation (252) into equation (250), we have:

$$P_1(Q) = \int_{\Omega} gw^* d\Omega = \sum_{m=1}^{M} \gamma_n^m \left\{ K\hat{w}(Q) + \int_{\Gamma} \left[V_n^*(Q,P)\hat{w}(P) - m_n^*(Q,P)\frac{\partial \hat{w}(P)}{\partial n} \right] d\Gamma(P) + \right.$$

$$\sum_{i=1}^{N_c} R_{c_i}^*(Q,P)\hat{w}_{c_i}(P) - \int_{\Gamma} \left[V_n(P)w^*(Q,P) - \hat{m}_n(P)\frac{\partial w^*}{\partial n}(Q,P) \right] d\Gamma(P) +$$

$$\left. \sum_{i=1}^{N_c} \hat{R}_{c_i}(P)w_{c_i}^*(Q,P) \right\}. \tag{253}$$

Following the same procedure, the domain integral of equation (132) can be approximated as:

$$P_2(Q) = \int_{\Omega_g} b\frac{\partial w^*(Q,P)}{\partial n_1}d\Omega = \sum_{m=1}^{M} \gamma^m \int_{\Omega_g} f^m \frac{\partial w^*(Q)}{\partial n_1}d\Omega, \tag{254}$$

Using the dual reciprocity boundary element method, the integral P_2, given by the sum of domain integrals (254), is transformed into a sum of boundary integrals.

Following the same procedure to obtain equation (253), equation (254) can be written as:

$$P_2(Q) = \int_{\Omega_g} b(P) \frac{\partial w^*(Q,P)}{\partial n_1} d\Omega = \sum_{m=1}^{M} \gamma_n^m \left\{ \frac{1}{2} \frac{\partial \hat{w}(Q)}{\partial n_1} + \int_{\Gamma} \left[\frac{\partial V^*}{\partial n_1}(Q,P) \hat{w}(P) - \right. \right.$$

$$\left. \frac{\partial m_n^*}{\partial n_1}(Q,P) \frac{\partial \hat{w}}{\partial n}(P) \right] d\Gamma(P) + \sum_{i=1}^{N_c} \frac{\partial R^*_{c_i}}{\partial n_1}(Q,P) \hat{w}_{c_i}(P) -$$

$$\int_{\Gamma} \left\{ \hat{V}_n(P) \frac{\partial w^*}{\partial n_1}(Q,P) - \hat{m}_n(P) \frac{\partial}{\partial n_1} \left[\frac{\partial w^*}{\partial n_1}(Q,P) \right] \right\} d\Gamma(P) -$$

$$\left. \sum_{i=1}^{N_c} R_{c_i}(P) \frac{\partial w^*_{c_i}}{\partial n_1}(Q,P) \right\}.$$

$$\tag{255}$$

Equations (253) and (255) are the basis of the dual reciprocity boundary element method for bending problems. As it can be seen, the domain integral where transformed in a sum of boundary integrals.

Particular solutions need to satisfy the equilibrium equation (251). The traditional solution procedure to solve the differential equation (251), when the problem is isotropic, is to assume an approximation function, $f = 1 + r$ for example, and compute the correspondent particular solutions. This procedure is quite difficult to apply to anisotropic materials, as the anisotropy increases the number of constants in the equilibrium equation. An alternative approach is to assume a particular solution $\hat{w}$ and evaluate the corresponding approximation function f. This approach was proposed by Schclar Schclar [1994] for anisotropic three dimensional problems and later it was used by different researchers in different anisotropic problems Albuquerque et al. [2002, 2003a,b, 2004], Kogl and Gaul [2000a,b, 2003].

Here it is used for the particular solution:

$$\hat{w} = c \ r^5, \tag{256}$$

where c is an arbitrary constant. The approximation function f is computed by equation (251) using the derivatives of particular solution (256). Other particular solutions are given by:

$$\hat{m}_n = -\left(f_1 \frac{\partial^2 \hat{w}}{\partial x^2} + f_2 \frac{\partial^2 \hat{w}}{\partial x \partial y} + f_3 \frac{\partial^2 \hat{w}}{\partial y^2} \right), \tag{257}$$

$$\hat{R}_{c_i} = -\left(g_1 \frac{\partial^2 \hat{w}}{\partial x^2} + g_2 \frac{\partial^2 \hat{w}}{\partial x \partial y} + g_3 \frac{\partial^2 \hat{w}}{\partial y^2} \right), \tag{258}$$

$$\hat{V}_n = -\left(h_1 \frac{\partial^3 \hat{w}}{\partial x^3} + h_2 \frac{\partial^3 \hat{w}}{\partial x^2 \partial y} + h_3 \frac{\partial^3 \hat{w}}{\partial x \partial y^2} + h_4 \frac{\partial^3 \hat{w}}{\partial y^3} \right) -$$

$$\frac{1}{R} \left(h_5 \frac{\partial^2 \hat{w}}{\partial x^2} + h_6 \frac{\partial^2 \hat{w}}{\partial x \partial y} + h_7 \frac{\partial^2 \hat{w}}{\partial y^2} \right). \tag{259}$$

Although the particular solutions are given by known expressions, they are approximated in the boundary by the same shape functions used in the approximation of the

unknown variables. So, discretizing the boundary in boundary elements, equations (253) and (255) can be written in a matrix form as:

$$\mathbf{P} = \left[\mathbf{H}\hat{\mathbf{w}} - \mathbf{G}\hat{\mathbf{V}} \right] \boldsymbol{\gamma} \tag{260}$$

where

$$\hat{\mathbf{w}} = \left\{ \begin{array}{c} \hat{\mathbf{w}}_{bn} \\ \hat{\mathbf{w}}_c \end{array} \right\}, \tag{261}$$

$$\hat{\mathbf{V}} = \left\{ \begin{array}{c} \hat{\mathbf{V}}_{bn} \\ \hat{\mathbf{V}}_c \end{array} \right\}, \tag{262}$$

$\hat{\mathbf{w}}_{bn}$ contains the displacement and rotation particular solutions to each boundary node, $\hat{\mathbf{V}}_{bn}$ contains the shear force and the twisting moment particular solutions for each boundary node, $\hat{\mathbf{V}}_{bn}$ contains the displacement particular solution for each corner, and $\hat{\mathbf{V}}_c$ contains the corner reaction particular solution for each corner.

Defining

$$\mathbf{S} = \left[\mathbf{H}\hat{\mathbf{w}} - \mathbf{G}\hat{\mathbf{V}} \right] \tag{263}$$

Equation (260) can be rewritten as:

$$\mathbf{P} = \mathbf{S}\boldsymbol{\gamma} \tag{264}$$

Equation (247) can be written in a matrix form, considering all source points, as:

$$\mathbf{b} = \mathbf{F}\boldsymbol{\gamma} \tag{265}$$

Thus, $\boldsymbol{\gamma}$ can be computed as:

$$\boldsymbol{\gamma} = \mathbf{F}^{-1}\mathbf{b} \tag{266}$$

Terms P_1 of equation (250) and P_2 of equation (254) can be written in a matrix form, considering all source points, as:

$$\mathbf{P} = \mathbf{S}\mathbf{F}^{-1}\mathbf{b} \tag{267}$$

For free vibration dynamic problems, the body force vector is given by:

$$\mathbf{b} = \varrho h \omega^2 \mathbf{w} \tag{268}$$

where ϱ is the material density, h is the plate thickness, and ω is the circular frequency of vibration.

So, equation (267) can be written as:

$$\mathbf{P} = \omega^2 \varrho h \mathbf{S}\mathbf{F}^{-1}\mathbf{w} \tag{269}$$

or

$$\mathbf{P} = \omega^2 \mathbf{M}\mathbf{w} \tag{270}$$

where $\mathbf{M}$ is the mass matrix given by:

$$\mathbf{M} = \varrho h \mathbf{S} \mathbf{F}^{-1} \tag{271}$$

Finally, equation (237) for dynamic problems can be written as:

$$\mathbf{H}\mathbf{w} = \mathbf{G}\mathbf{V} + \omega^2 \mathbf{M}\mathbf{w} \tag{272}$$

3.9   The radial integration method

The domain integral of equation (250) can be written as:

$$P_1(Q) = \sum_{m=1}^{M} \gamma^m \int_{\Omega_g} f^m w^*(Q, P) \rho \, d\rho \, d\theta \tag{273}$$

or

$$P_1(Q) = \sum_{m=1}^{M} \gamma^m \int_{\theta} \int_0^r f^m w^*(Q, P) \rho \, d\rho \, d\theta, \tag{274}$$

where r is the value of ρ in a point of the boundary Γ_g (see Figure 13).

Defining $F^m(Q)$ as the following integral:

$$F^m(Q) = \int_0^r f^m w^*(Q, P) \rho \, d\rho, \tag{275}$$

we can write:

$$P_1(Q) = \sum_{m=1}^{M} \gamma^m \int_{\theta} F^m(Q) \, d\theta. \tag{276}$$

Considering an infinitesimal angle $d\theta$ (Figure 13), the relation between the arch length $r d\theta$ and the infinitesimal boundary length $d\Gamma$, can be written as:

$$\cos \alpha = \frac{r \frac{d\theta}{2}}{\frac{d\Gamma}{2}}, \tag{277}$$

or

$$d\theta = \frac{\cos \alpha}{r} d\Gamma. \tag{278}$$

where α is the angle between unity vectors $\mathbf{r}$ and $\mathbf{n}$.

Using the inner product properties of the unity vectors $\mathbf{n}$ and $\mathbf{r}$, showed in Figure 13, we can write:

$$d\theta = \frac{\mathbf{n}.\mathbf{r}}{r} d\Gamma. \tag{279}$$

Finally, substituting equation (279) into equation (276), the domain integral of equation (131) can be written as a boundary integral given by:

$$P_1(Q) = \sum_{m=1}^{M} \gamma^m \int_{\Gamma_g} \frac{F^m(Q)}{r} \mathbf{n}.\mathbf{r}d\Gamma. \tag{280}$$

Following similar procedure to obtain equation (280), the domain term of equation (254) can be written as:

$$P_2(Q) = \int_{\Omega_g} b\frac{\partial w^*(Q,P)}{\partial n_1} d\Omega = \sum_{m=1}^{M} \gamma^m \int_{\Gamma_g} \frac{G^m(Q)}{r} \mathbf{n}.\mathbf{r}d\Gamma, \tag{281}$$

where

$$G^m(Q) = \int_0^r f^m \frac{\partial w^*(Q,P)}{\partial n_1} \rho d\rho. \tag{282}$$

So, the domain integrals of matrix equation (228) can be written as

$$\left\{ \begin{array}{c} P_1^{(d)} \\ P_2^{(d)} \end{array} \right\} = \sum_{m=1}^{M} \gamma^m \sum_{i=1}^{N_e} \left\{ \begin{array}{c} p_1^{(d,m)} \\ p_2^{(d,m)} \end{array} \right\} \tag{283}$$

where

$$p_1^{(d,m)} = \int_{\Gamma_i} \frac{F^{(d,m)}}{r} \mathbf{n}.\mathbf{r}d\Gamma, \qquad p_2^{(d,m)} = \int_{\Gamma_i} \frac{G^{(d,m)}}{r} \mathbf{n}.\mathbf{r}d\Gamma. \tag{284}$$

In this work, the approximation functions f^m are radial basis function written in terms of R, where R is the distance between the centre S of the radial basis function and the integration point P (Figure 15). From Figure 15, we can write:

$$R = \sqrt{\rho^2 + l^2 - 2\rho l \cos\beta}, \tag{285}$$

where l is the vector from S to Q, and β is the angle between ρ and l.

As already mentioned, the RIM is more time-consuming than the DRM since integrals given by equations (275) and (282) cannot be computed analytically for the majority of the approximation fuctions. For example, if $f^m = R$, equation (275) is written as:

$$F^m(Q) = \int_0^r c_1 \sqrt{\rho^2 + l^2 - 2\rho l \cos\beta} \, \ln(c_2\rho)\rho^3 d\rho, \tag{286}$$

where c_1 and c_2 are coefficients that don't depend on ρ. The integral of equation (286) cannot be computed analytically. The numerical integration of these integrals needs to be performed accurately, what demands an expressive number of integration points. In this work the numerical integration is carried out using Gauss quadrature with 10 integration points.

The most interesting advantage of the RIM over the DRM is that the approximation function can be freely chosen. As shown by Paiva et al. [2004], the choice of the approximation function in the DRM is restricted to the analytical computation of the particular solution $\hat{w}$ of the equation (251).

In this work, in order to compare the RIM and the DRM, the same approximation function is used in both methods. This approximation function is given by equation (251) when the particular solution is given by equation (256).
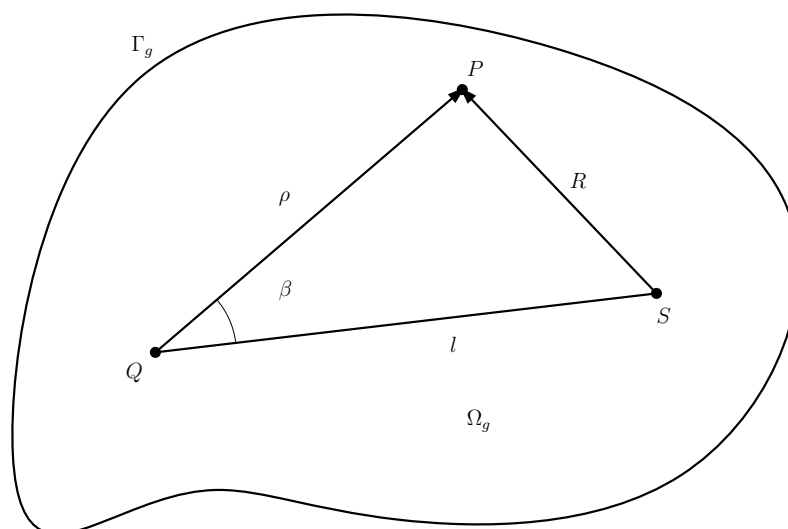
Figure 15: Positions of points in the domain.

3.9.1   Numerical results

A plate under a uniformely distributed load

In order to compare the accuracy of the RIM and the DRM, these methods were first applied to a problem with a known domain load. In this case, domain integrals given by equations (250) and (254) can be exactly computed, as shown by equations (204) and (209)

We considered a square plate of side length $a = 1$ m and thickness $h = 0.01$ m. The material is orthotropic and its material properties are: $E_x = 2.068 \times 10^{11}$ Pa, $E_y = E_x/15$, $\nu_{xy} = 0.3$, $G_{xy} = 6.055 \times 10^8$ Pa. The plate is under a uniformly distributed load $q = 1 \times 10^4$ Pa applied along its domain (Figure 16) and simply supported along its four edges. The plate was discretized with a mesh of 40 constant boundary elements and 64 internal points as shown in Figure 17.

Tables 1 and 2 show the values of domain integrals P_1 and P_2, respectively, computed by the exact transformation, the DRM, and the RIM.

As can be seen, the DRM and the RIM have good agreement with the exact integration for the term P_1 in all nodes. For the term P_2, at some nodes near corners errors for the DRM are greater than 10%. Errors in these nodes remain around 10% even for more refined mesh. The reason for large errors to compute P_2 at some nodes by the DRM might be owing to the use of constant elements to approximate particular solutions at the boundary. Although the particular solutions are given by analytical expressions, in the DRM they are approximated at the boundary by the same shape functions used to approximate physical variables w, $\partial w/\partial n$, V_n, and m_n. Instead of this, in the RIM, domain integrals that contain approximation functions are exact transformed into boundary integrals. However, in the most part of time, these boundary integrals need to be computed numerically, making the RIM more time-consuming than the DRM.

Table 1: Domain integral P_1 computed by the exact transformation, the DRM, and the RIM.

Node	Exact transformation	DRM		RIM	
	P_1 ($10^{-5} \times$ m)	P_1 ($10^{-5} \times$ m)	Error (%)	P_1 ($10^{-5} \times$ m)	Error (%)
1	0.4212	0.4190	0.53	0.4205	0.18
2	0.3824	0.3814	0.25	0.3817	0.18
3	0.3524	0.3516	0.21	0.3518	0.16
4	0.3320	0.3313	0.19	0.3314	0.18
5	0.3216	0.3210	0.18	0.3210	0.18
11	0.4570	0.4559	0.24	0.4561	0.18
12	0.4700	0.4691	0.19	0.4692	0.18
13	0.4722	0.4714	0.18	0.4714	0.18
14	0.4701	0.4693	0.18	0.4693	0.18
15	0.4680	0.4672	0.18	0.4672	0.18

Table 2: Domain integral P_2 computed by the exact transformation, the DRM, and the RIM.

Node	Exact transformation	DRM		RIM	
	P_2 ($10^{-5} \times$ rad)	P_2 ($10^{-5} \times$ rad)	Error (%)	P_2 ($10^{-5} \times$ rad)	Error (%)
1	-0.2832	-0.2549	10.0151	-0.2827	0.18
2	-0.2120	-0.2130	0.48	-0.2116	0.18
3	-0.1568	-0.1555	0.82	-0.1565	0.21
4	-0.1192	-0.1184	0.69	-0.1189	0.21
5	-0.1002	-0.0995	0.66	-0.0999	0.25
11	0.5086	0.5119	0.64	0.5078	0.16
12	0.5816	0.5815	0.03	0.5807	0.16
13	0.6381	0.6376	0.09	0.6372	0.16
14	0.6763	0.6756	0.118	0.6752	0.15
15	0.6954	0.6946	0.11	0.6944	0.15
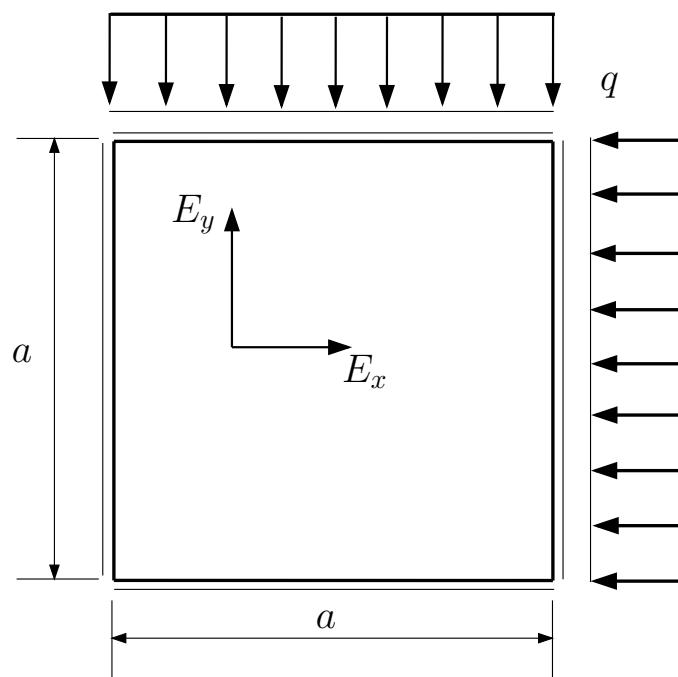
Figure 16: Orthotropic square plate with simply-supported edges under uniformly distributed load.

3.10   Modal analysis

In order to transform equation (272) in an eigenproblem, the boundary is divided into Γ_1 and Γ_2 (Figure 18), where Γ_1 stands for constrained degrees of freedom and Γ_2 stands for free degrees of freedom. Thus, equation (272) can be written as:

$$\begin{bmatrix} \mathbf{H_{11}} & \mathbf{H_{12}} \\ \mathbf{H_{21}} & \mathbf{H_{22}} \end{bmatrix} \begin{Bmatrix} \mathbf{w_1} \\ \mathbf{w_2} \end{Bmatrix} - \begin{bmatrix} \mathbf{G_{11}} & \mathbf{G_{12}} \\ \mathbf{G_{21}} & \mathbf{G_{22}} \end{bmatrix} \begin{Bmatrix} \mathbf{V_1} \\ \mathbf{V_2} \end{Bmatrix} = \omega^2 \begin{bmatrix} \mathbf{M_{11}} & \mathbf{M_{12}} \\ \mathbf{M_{21}} & \mathbf{M_{22}} \end{bmatrix} \begin{Bmatrix} \mathbf{w_1} \\ \mathbf{w_2} \end{Bmatrix},$$
(287)

where indices 1 and 2 stand for boundaries Γ_1 and Γ_2, respectively.

As $\mathbf{w_1} = \mathbf{0}$ and $\mathbf{V_2} = \mathbf{0}$, equation (287) can be written as:

$$\begin{aligned} \mathbf{H_{12}w_2} - \mathbf{G_{11}V_1} &= \omega^2 \mathbf{M_{12}w_2}, \\ \mathbf{H_{22}w_2} - \mathbf{G_{21}V_1} &= \omega^2 \mathbf{M_{22}w_2} \end{aligned}$$
(288)

or

$$\hat{\mathbf{H}}\mathbf{w_2} = \omega^2 \hat{\mathbf{M}}\mathbf{w_2},$$
(289)

where $\hat{\mathbf{H}}$ and $\hat{\mathbf{M}}$ are given by:

$$\begin{aligned} \hat{\mathbf{H}} &= \mathbf{H_{22}} - \mathbf{G_{21}G_{11}^{-1}H_{12}}, \\ \hat{\mathbf{M}} &= \mathbf{M_{22}} - \mathbf{G_{21}G_{11}^{-1}M_{12}}. \end{aligned}$$
(290)
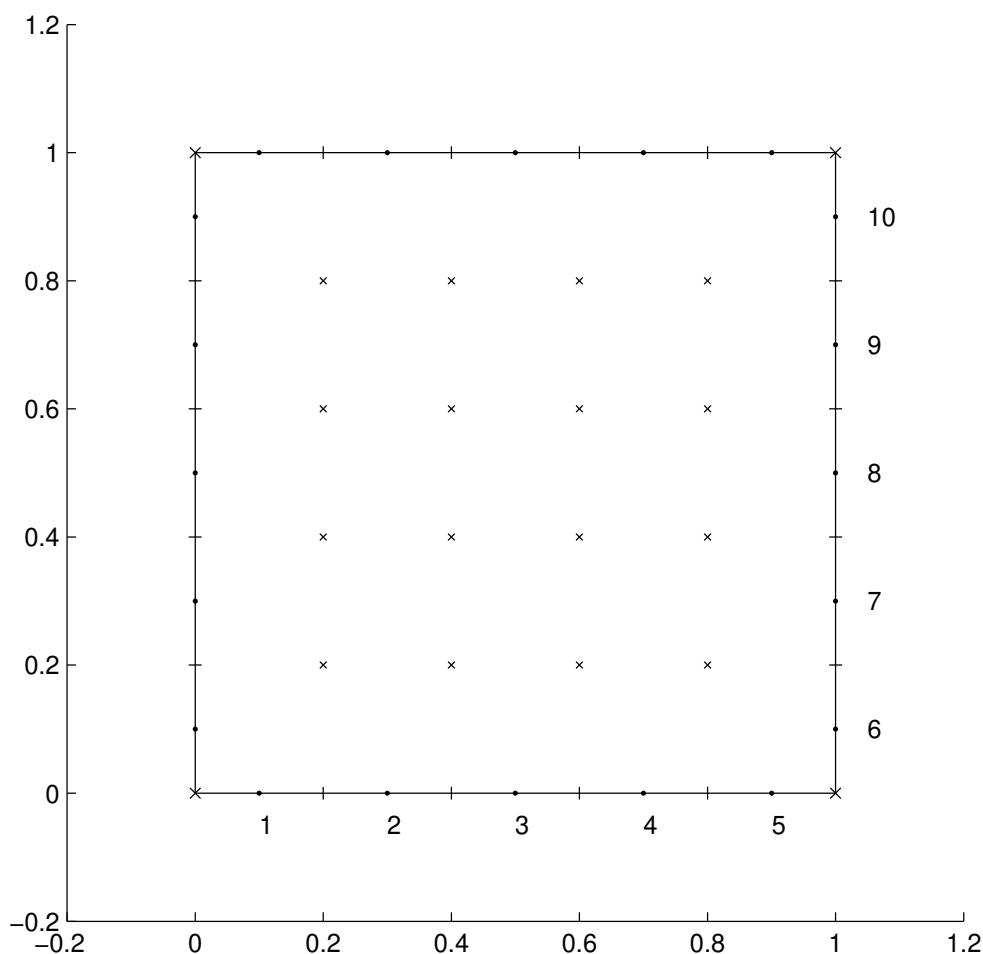
Figure 17: Boundary elements and internal points for the square plate.

The matrix equation (289) can be rewritten as an eigenproblem

$$\mathbf{A}\mathbf{w_2} = \lambda \mathbf{w_2}, \tag{291}$$

where

$$\mathbf{A} = \hat{\mathbf{H}}^{-1}\hat{\mathbf{M}}, \tag{292}$$

λ is the eigenvalue that can be written as:

$$\lambda = \frac{1}{\omega^2}, \tag{293}$$

and $\mathbf{w_2}$ is the eigenvector that is equivalent to the vibration mode shape of the plate.

Provided that $\mathbf{A}$ is nosymmetric, eigenvalues and eigenvectors of equation (291) can be found using standard numerical procedures for nonsymmetric matrices.

3.10.1 Numerical results

Square plate with clampled edges

The problem to be analysed in this section is a square plate of side length $a = 1$ m and thickness $h = 0.01$ m. The material is orthotropic and its material properties are:
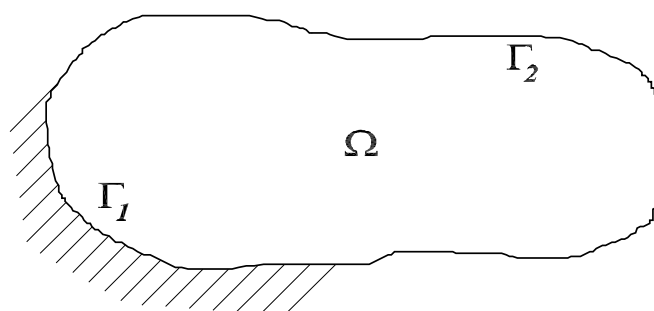
Figure 18: Domain with constrained and free degrees of freedom.

$E_1 = 118.3 \times 10^9$ Pa, $E_2 = 236.6 \times 10^9$ Pa, $G_{12} = 236.6 \times 10^9$ Pa, $\nu_{12} = 0.415$, and $\rho = 1900$ kg/m^3.

The plate has its four edges clamped. The problem was discretized by 44 constant boundary elements of equal lengths and 121 internal points (Figure 19).
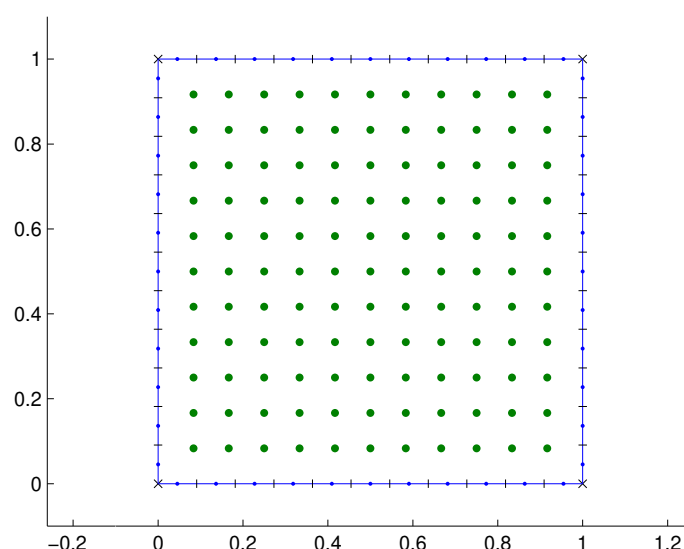
Figure 19: Boundary element mesh and internal points (44 constant boundary elements and 121 internal points).

Table 3 shows the first five natural frequencies computed by the dual reciprocity boundary element method compared to the first five frequencies computed by the finite element method using a commercial code with a very fine mesh (6400 rectangular eight node elements). As it can be seen, all results are in good agreement.

Rectangular plate with free and simply supported edges

Consider a rectangular plate with width $b = 350$ mm, length $a = 450$ mm, and thickness $h = 2.1$ mm (Figure 20). The plate is orthotropic with the following material properties: $E_x = 120$ GPa, $E_y = 10$ GPa, $G_{xy} = 4.8$ GPa, $\nu_{12} = 0.3$ and $\varrho = 1510$ kg/m^3.

Two meshes were used: a) 28 constant boundary elements and 77 internal points (Figure 21); and b) 72 constant boundary elements and 391 internal points (Figure 22).

Table 3: Natural frequencies for the orthotropic plate with clamped edges computed by the dual reciprocity boundary element method (DRM) and by the finite element method (FEM).

Mode number	Natural frequency (Hz)		Difference (%)
	DRM	FEM	
1	165.82	165.72	0.061
2	303.74	302.95	0.260
3	367.14	367.15	0.003
4	510.94	507.33	0.712
5	524.88	515.75	1.771
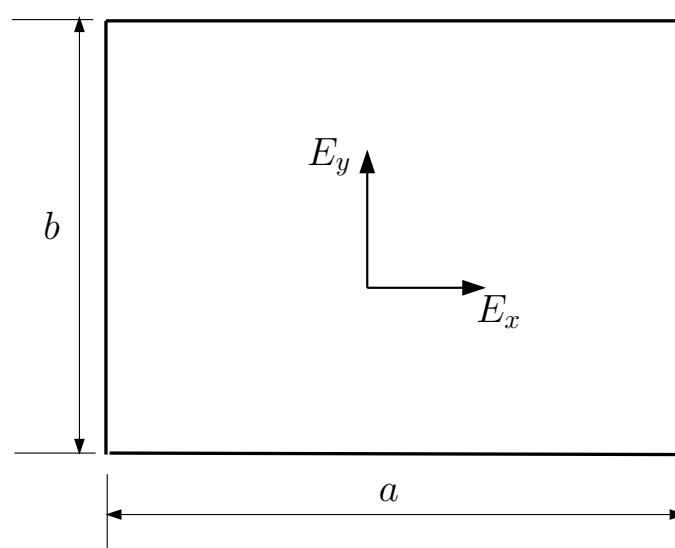
Figure 20: Orthotropic rectangular plate.

Results for the simply supported edges were compared to the exact solution presented by Gibson [1994] while for free edges where compared to the finite element method using a commercial code with a very fine mesh (6400 rectangular eight node elements).

Table 4 and 5 show the first five natural frequencies of plate with free edges computed by the dual reciprocity boundary element method with the mesh given by Figures 21 and 22, respectively, compared to the first five frequencies computed by the finite element method. As can be seen, all results are in good agreement. It also can be seen that there is a convergency to the finite element results as the discretization and number of internal node increses.

Tables 6 and 7 show the first five natural frequencies of plate with simply supported edges computed by the dual reciprocity boundary element method with meshes shown in Figures 21 and 22, respectively, compared to the exact solution presented by Gibson [1994]. As can be seen, all results are in good agreement, excepeted for the second mode. Results converges to the exact solution as the discretization and number of internal points increases.

Dual reciprocity boundary element method $\times$ radial integration method for modal analysis
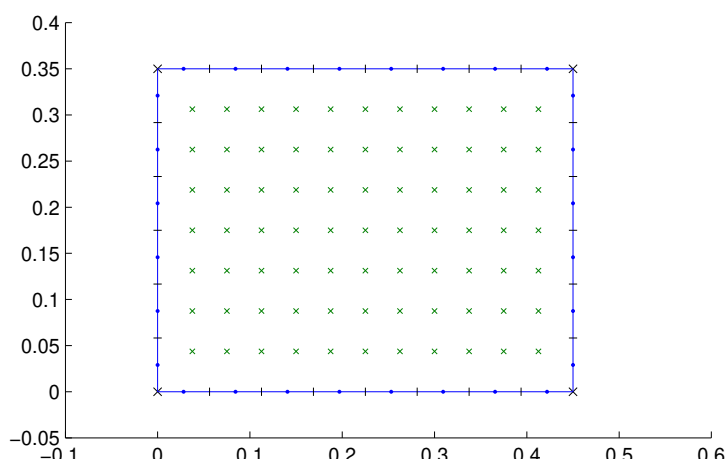
Figure 21: Boundary element mesh and internal points (28 constant boundary elements and 77 internal points).

Table 4: Natural frequencies for the orthotropic plate with free edges computed by the dual reciprocity boundary element method (DRM) and by the finite element method (FEM). 28 boundary elements and 77 internal points.

Mode number	Natural frequency (Hz)		Difference (%)
	DRM	FEM	
1	24.6222	25.4970	3.4310
2	45.9983	45.3480	1.4340
3	66.2378	68.7790	3.6947
4	90.3550	95.2470	5.1361
5	101.2286	107.6100	5.9301

Now the dual reciprocity boundary element method and the radial integration method are applied in the analysis of a problem in that body forces are unknown. Consider a rectangular plate with free edges and width $b = 350$ mm, length $a = 450$ mm, and thickness $h = 2.1$ mm (Figure 20). The plate is orthotropic with the following material properties: $E_x = 120$ GPa, $E_y = 10$ GPa, $G_{xy} = 4.8$ GPa, $\nu_{12} = 0.3$ and $\varrho = 1510$ kg/m^3.

This plate was analysed using a mesh of 66 constant boundary elements and 63 internal points as shown in Figure 23.

Table 8 shows the first five natural frequencies computed by the finite element method (FEM), the dual reciprocity boundary element method (DRM), and the radial integration method (RIM), and the respective relative differences between the last two methods and the FEM. The finite element mesh has 150 (15×10) quadrilateral finite elements (8 nodes per element). As it can be seen, the agreement of the RIM and the DRM with the FEM is similar when the same approximation function is used. The numerical integration used in the RIM is the Gauss quadrature with 10 points. There is the possibility of improve
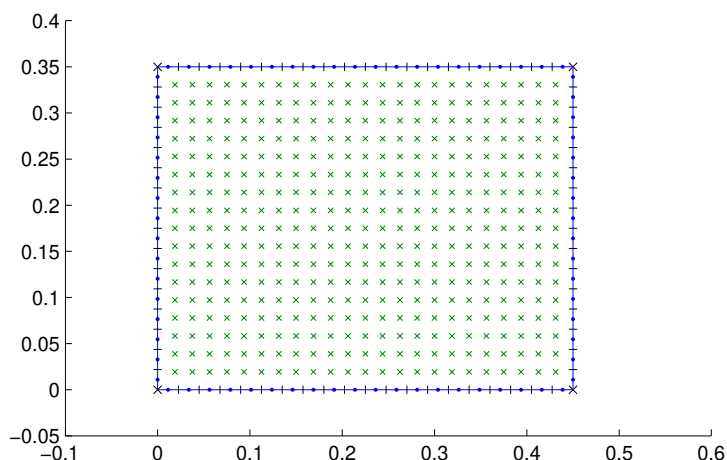
Figure 22: Boundary element mesh and internal points (72 constant boundary elements and 391 internal points).

Table 5: Natural frequencies for the orthotropic plate with free edges computed by the dual reciprocity boundary element method (DRM) and by the finite element method (FEM). 72 boundary elements and 391 internal points.

Mode number	Natural frequency (Hz)		Difference (%)
	DRM	FEM	
1	24.7545	25.4970	2.9122
2	44.9061	45.3480	0.9744
3	69.2577	68.7790	0.6960
4	96.8308	95.2470	1.6628
5	101.4698	107.6100	5.7060

accuracy of the numerical integration by using more integration points. The price of the gain in the accuracy is a larger computation time. However, this analysis is out of the scope of this article and will be treated in future works.

3.11   Buckling analysis

Demand by an accurate stability analysis of anisotropic materials has increase with the increasing use of composite materials in engineering projects. In general, composites panels are very light structures that present high stiffness and strength. However, due to their slenderness, buckling is one of the main concern during their design.

The boundary element method (BEM) has provided a powerful solution to the field of plate buckling. Syngellakis and Elzein Syngellakis and Elzein [1994] presented a boundary element solution of the plate buckling based on Kirchhoff theory under any combination of loadings and support conditions. Nerantzaki and Katsidelakis Nerantzaki

Table 6: Natural frequencies for the orthotropic plate with supported edges computed by the dual reciprocity boundary element method (DRM) compared to the exact solution. 28 boundary elements and 77 internal points.

| Mode number	Natural frequency (Hz)		Error (%)
	DRM	Exact solution	
1	50.8502	52.7700	3.6381
2	118.6346	103.2800	14.8669
3	169.5112	176.5700	3.9978
4	216.9047	199.8300	8.5446
5	228.1276	211.0900	8.0713

Table 7: Natural frequencies for the orthotropic plate with supported edges computed by the dual reciprocity boundary element method (DRM) compared to exact solution. 72 boundary elements and 391 internal points.

Mode number	Natural frequency (Hz)		Error (%)
	DRM	Exact solution	
1	51.5836	52.7700	2.2482
2	110.6339	103.2800	7.1204
3	171.3100	176.5700	2.9790
4	205.2756	199.8300	2.7251
5	212.4413	211.0900	0.6402

and Katsikadelis [1996] developed a boundary element method for buckling analysis of plates with variable thickness. Elastic buckling analysis of plates using boundary elements can also be found in Lin et al. [1999]. Buckling analysis of shear deformable isotropic plates was presented in Purbolaksono and Aliabadi [2005]. To the best of author's knowledge, the only work that presents a boundary element formulation applied to non-isotropic plates is due to Shi [1990] who presented an orthotropic formulation with a domain discretization.

In this paper, a boundary element formulation for the stability analysis of general anisotropic plates with no domain discretization is presented. Classical plate bending and plane elasticity formulations are used and the domain integrals due to body forces

Table 8: Natural frequencies computed by the FEM, the DRM and the RIM.

Mode shape	FEM	DRM		RIM	
	$\omega/(2\pi)$ (Hz)	$\omega/(2\pi)$ (Hz)	Difference (%)	$\omega/(2\pi)$ (Hz)	Difference (%)
1	25.50	24.64	3.38	24.3932	4.34
2	45.35	45.03	0.71	45.5682	0.48
3	68.78	68.69	0.13	67.3678	2.05
4	95.25	98.06	2.95	94.6026	0.68
5	107.61	100.93	6.21	106.3381	1.18
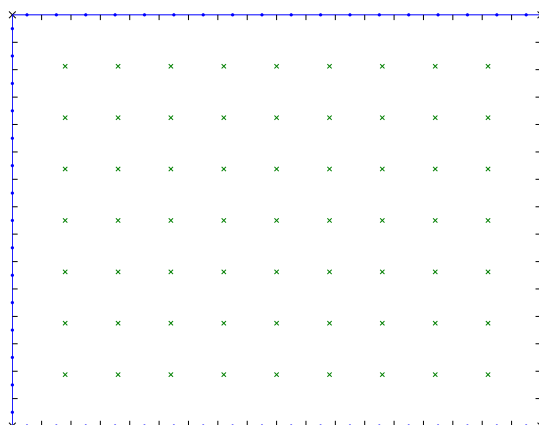
Figure 23: Boundary elements and internal points for the rectangular plate.

are transformed into boundary integrals using the radial integration method. Numerical results are presented to assess the accuracy of the method. Buckling coefficients computed using the proposed formulation are in good agreement with results available in literature.

3.11.1   Boundary integral equations

In the absence of body forces, the governing equation of the anisotropic thin plate buckling is given by:

$$N_{ij,j} = 0, \tag{294}$$

$$D_{11}u_{3,1111} + 4D_{16}u_{3,1112} + 2(D_{12} + D_{66})u_{3,1122} + 4D_{26}u_{3,1222} + D_{22}u_{3,2222} = N_{ij}u_{3,ij}, \tag{295}$$

where $i, j, k = 1, 2$; u_k is the displacement in directions x_1 and x_2, u_3 stands for the displacement in the normal direction of the plate surface; N_{ij} are the in-plane stress components, D_{11}, D_{22}, D_{66}, D_{12}, D_{16}, and D_{26} are the anisotropic thin plate stiffness constants.

The boundary integral equation for in-plane displacements, obtained by applying reciprocity and Green theorems at equation (294), is given by Aliabadi [2002]:

$$c_{ij}u_j(Q) + \int_\Gamma t_{ik}^*(Q, P)u_k(P)d\Gamma(P) = \int_\Gamma u_{ik}^*(Q, P)t_k(P)d\Gamma(P) \tag{296}$$

where $t_i = N_{ij}n_j$ is the traction in the boundary of the plate in the plane $x_1 - x_2$, and n_j is the normal at the boundary point; P is the field point; Q is the source point; and asterisks denote fundamental solutions. The anisotropic plane elasticity fundamental solutions can be found, for example, in Sollero and Aliabadi [1993]. The constant c_{ij} is introduced in order to take into account the possibility that the point Q can be placed in the domain, on the boundary, or outside the domain.

The in-plane stress resultants at a point $Q \in \Omega$ are written as:

$$c_{ik}N_{kj}(Q) + \int_\Gamma S^*_{ikj}(Q,P)u_k(P)d\Gamma(P) = \int_\Gamma D^*_{ijk}(Q,P)t_k(P)d\Gamma(P) \qquad (297)$$

where D_{ikj} and S_{ikj} are linear combinations of the plane-elasticity fundamental solutions.

The integral equation for the plate buckling formulation, obtained by applying reciprocity and Green theorems at equation (295), is given by:

$$Ku_3(Q) + \int_\Gamma \left[V^*_n(Q,P)w(P) - m^*_n(Q,P)\frac{\partial w(P)}{\partial n} \right] d\Gamma(P) + \sum_{i=1}^{N_c} R^*_{c_i}(Q,P)u_{3_{ci}}(P)$$

$$= \sum_{i=1}^{N_c} R_{c_i}(P)u^*_{3_{ci}}(Q,P) + \int_\Gamma \left[V_n(P)u^*_3(Q,P) - m_n(P)\frac{\partial u^*_3}{\partial n}(Q,P) \right] d\Gamma(P)$$

$$+\lambda \left[\int_\Omega u_3 N_{ij} u^*_{3,ij}\, d\Omega + \int_\Gamma \left(t_i u^*_3 u_{3,i} - t_i u_3 u^*_{3,i} \right)\, d\Gamma \right], \qquad (298)$$

where $\frac{\partial()}{\partial n}$ is the derivative in the direction of the outward vector $\mathbf{n}$ that is normal to the boundary Γ; m_n and V_n are, respectively, the normal bending moment and the Kirchhoff equivalent shear force on the boundary Γ; R_c is the thin-plate reaction of corners; $u^*_{3_{ci}}$ is the transverse displacement of corners; λ is the critical load factor; the constant K is introduced in order to take into account the possibility that the point Q can be placed in the domain, on the boundary, or outside the domain. As in the previous equation, an asterisk denotes a fundamental solution. Fundamental solutions for anisotropic thin plates can be found, for example, in Albuquerque et al. [2006].

A second integral equation is necessary in order to obtain the thin plate buckling boundary element formulation. This equation is given by:

$$K\frac{\partial u_3}{\partial m}(Q) + \int_\Gamma \left[\frac{\partial V^*_n}{\partial m}(Q,P)w(P) - \frac{\partial M^*_n}{\partial m}(Q,P)\frac{\partial w(P)}{\partial n} \right] d\Gamma(P) + \sum_{i=1}^{N_c} \frac{\partial R^*_{c_i}}{\partial m}(Q,P)u_{3_{ci}}(P)$$

$$= \sum_{i=1}^{N_c} R_{c_i}(P)\frac{\partial u^*_{3_{ci}}}{\partial m}(Q,P) + \int_\Gamma \left[V_n(P)\frac{\partial u^*_3(Q,P)}{\partial m} - m_n(P)\frac{\partial^2 u^*_3}{\partial n \partial m}(Q,P) \right] d\Gamma(P)$$

$$+\lambda \left[\int_\Omega u_3 N_{ij} \frac{\partial u^*_{3,ij}}{\partial m}\, d\Omega + \int_\Gamma \left(t_i u^*_3 \frac{\partial u_{3,i}}{\partial m} - t_i u_3 \frac{\partial u^*_{3,i}}{\partial m} \right)\, d\Gamma \right], \qquad (299)$$

where $\frac{\partial()}{\partial m}$ is the derivative in the direction of the outward vector $\mathbf{m}$ that is normal to the boundary Γ at the source point Q.

As can be seen in equations (298) and (299), domain integrals arise in the formulation owing to the contribution of in-plane stresses to the out of plane direction. In order to transform these integrals into boundary integrals, consider that a body force b is approximated over the domain Ω as a sum of M products between approximation functions f_m and unknown coefficients γ_m, as given by equation (247).

Body forces of integral equations (298) and (299) depend on displacements. So, following the procedure presented by Albuquerque *et al.* Albuquerque et al. [2007], domain integrals that come from these body forces can be transformed into boundary integrals.

3.11.2 Matrix Equations

After the discretization of equations (298) and (299) into boundary elements and collocation of the source points in all boundary nodes, a linear system is generated. It is worth notice that the only loads considered in the linear buckling equations are that related to the in-plane stress N_{ij} and tractions t_i that are multiplied by the critical load factor λ. This means that all the known values of u_3, $\partial u_3/\partial n$, M_n, V_n, w_{ci}, R_{ci} (boundary conditions) are set to zero.

Dividing the boundary into Γ_1 and Γ_2 (Figure 18), this linear system can be written in the same way of equation (287).

3.11.3 Numerical results

The numerical results are presented in terms of the dimensionless parameter K_{cr} which is given by:

$$K_{cr} = \frac{N_{cr}a^2}{D_{22}} \tag{300}$$

where N_{cr} is the critical load ($N_{cr} = \lambda \times$ the applied load) and a is the edge length of the square plate.

Consider a square graphite/epoxy plate under different boundary conditions. The thickness of the plate is $h = 0.01$ m. The material properties are: elastic moduli $E_1 = 181$ GPa and $E_2 = 10.3$ GPa, Poisson ratio $\nu_{12} = 0.28$, and shear modulus $G_{12} = 7.17$ GPa.

The mesh used has 28 quadratic discontinuous boundary elements of the same length (7 per edge) and 49 (7×7) uniformly distributed internal points.

The plate is under uniformly uniaxial compression and the critical load parameter K_{cr} is computed considering all edges simply-supported (SSSS), all edges clamped (CCCC), and two edges clamped and two edges simply supported (CSCS). In the last case, the two edges where the load is applied are simply supported and the two remaining edges are clamped. The results are shown in Table 9 together with results obtained by Shi [1990] using a boundary element formulation with domain discretization and the analytical solution presented by Lekhnitskii [1968].

As it can be seen, there is a good agreement between the results obtained in this work and those presented in literature.

4 Shallow Shells

4.1 Introduction

The demand for construction of advanced aerospace, automotive, and marine structures has increased the interest in composite laminated shells. Some requirements, as for example high strength-to-weight ratio, good resistance to corrosion, as well as long fatigue

Table 9: Critical load parameter K_{cr} for a graphite/epoxy plate with different boundary conditions.

Case	B. Conditions	Loads	This work	Shi [1990]	Lekhnitskii [1968]
1	SSSS	$N_1 \neq 0$	130.82	–	129.78
2	SSSS	$N_2 \neq 0$	71.53	71.36	69.46
3	CCCC	$N_1 \neq 0$	493.70	481.21	–
4	CCCC	$N_2 \neq 0$	168.27	168.16	–
5	CSCS	$N_1 \neq 0$	161.47	163.24	162.03
6	CSCS	$N_2 \neq 0$	146.47	143.89	141.33
7	SSSS	$N_{12} \neq 0$	417.44		

life, cannot be obtained with the use of metallic or any other engineering materials except composites. Other requirements, as aerodynamic profile and good stealth characteristics demand curved structures or shell like structures.

The DRM has been shown as a powerful technique to transform domain integrals into boundary integrals and it has been extensively applied in many different formulation for this purpose. In this technique, the domain terms are approximated using a finite series expansion involving proposed approximation functions and coefficients to be determined. In order to accomplish the transformation, it is necessary to compute particular solutions for the governing differential equation, considering the approximation function as the non-homogeneous term. It is quite suitable for potential problems as well as for isotropic structures. However, when it is applied to anisotropic structures, the complexity of the differential equation become quite difficult, or even impossible, to compute the particular solutions for many chosen approximation functions.

An alternative approach to overcome the main drawback of the DRM, that is the lack of free choice of the approximation function, is the radial integration method (RIM). This method was proposed by Gao Gao [2002] and its use has been extended for the anisotropic thin plate formulation by Albuquerque *et al.* Albuquerque et al. [2006, 2007]. As in the DRM, the RIM also approximate the domain terms by a sum of approximation functions and coefficients to be determined. However, the RIM doesn't demand the computation of any particular solution, what become this technique specially suitable for anisotropic formulations.

In this chapter, a boundary element formulation for anisotropic shallow shells with no domain discretization is presented. Classical plate bending and plane elasticity formulations are coupled and effects of curvature are treated as body forces. The domain integrals due to body forces are transformed into boundary integrals using the radial integration method. Numerical results are presented to assess the accuracy of the method. Displacements computed using the proposed formulation are in good agreement with results available in literature. For the best of authors knowledge, there is no paper in the literature for anisotropic shells using the coupling of plate bending and plane elasticity formulations.

4.2   Boundary integral equations

Consider a shallow shell of an anisotropic elastic material with the mid-surface being described by $z = z(x_1, x_2)$ as shown in Figure 24. The base-plane of the shell is defined by a domain Ω in the plane x_1, x_2 whose boundary is given by Γ.
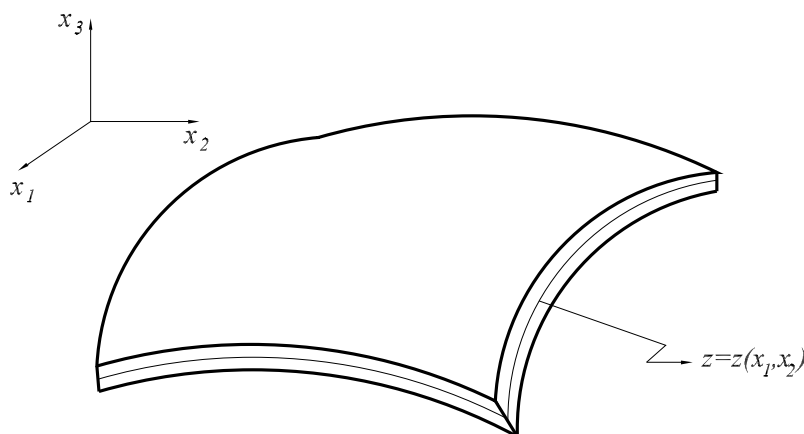
Figure 24: Shallow shell.

As shown by Reissner, the equilibrium equation for this structure can be written as:

$$N_{ij,j} + q_i = 0, \tag{301}$$

$$D_{11}w_{,1111} + 4D_{16}w_{,1112} + 2(D_{12} + D_{66})w_{,1122} + 4D_{26}w_{,1222} + D_{22}w_{,2222} + \frac{N_{ij}}{R_{ij}} \tag{302}$$

where $i, j, k = 1, 2$; N_{ij} are membrane forces applied in the shell; D_{11}, D_{22}, D_{66}, D_{12}, D_{16}, and D_{26} are the flexural rigidities of the anisotropic plate w stands for the displacement in the normal direction of the shell surface; q_i are domain loads applied in directions of axis x_1 and x_2, q_3 is the domain load applied in direction of axis x_3; and

$$R_{ij} = \frac{-1}{z_{,ij}} \tag{303}$$

are the radii of curvature of the undeformed shell.

Using equilibrium equations of isotropic shallow shells, the reciprocity relation, and the Green theorem, Zhang and Atluri Zhang and Atluri [1986] derived integral equations that can be divided in terms of plane elasticity and plate bending formulations. These formulations are coupled by the domain integrals that arise in equations. Plane elasticity integral equations (membrane equations) are given by:

$$c_{ij}u_j + \int_\Gamma t_{ik}^*(Q,P)u_k(P)d\Gamma(P)$$

$$= \int_\Gamma u_{ik}^*(Q,P)t_k(P)d\Gamma(P)$$

$$+ \int_\Omega C\kappa_{kj}wu_{ik,j}^*(Q,P)d\Omega$$

$$+ \int_\Omega u_{ik}^*(Q,P)q_k(P)d\Omega(P), \tag{304}$$

where u_k is the displacement in directions x_1 and x_2, $t_i = N_{ij}n_j$, P is the field point; Q is the source point. The constant c_{ij} is introduced in order to take into account the possibility that the point Q can be placed in the domain, on the boundary, or outside the domain. The symbol * stands for fundamental solutions (see Aliabadi, Aliabadi [2002]). Constant κ_{kj} depends on the curvature radii R_{kj} of the shallow shell.

The plate bending integral equation is given by:

$$Kw(Q)$$

$$+ \int_\Gamma \left[V_n^*(Q,P)w(P) - m_n^*(Q,P)\frac{\partial w(P)}{\partial n} \right] d\Gamma(P)$$

$$+ \sum_{i=1}^{N_c} R_{c_i}^*(Q,P)w_{ci}(P) = \sum_{i=1}^{N_c} R_{c_i}^*(P)w_{ci}(Q,P)$$

$$+ \int_\Omega q_3(P)w^*(Q,P)\,d\Omega$$

$$+ \int_\Gamma \left[V_n(P)w^*(Q,P) - m_n(P)\frac{\partial w^*}{\partial n}(Q,P) \right] d\Gamma(P)$$

$$+ \int_\Gamma C\kappa_{ij}n_j u_i(P)w^*(Q,P)\,d\Gamma(P)$$

$$+ \int_\Omega C\frac{\kappa_{ij}}{\rho_{ij}}w^*(Q,P)w(P)\,d\Omega$$

$$+ \int_\Omega \left[C\kappa_{ij}(P)w^*(Q,P) \right]_{,j} u_i(P)\,d\Omega, \tag{305}$$

where $\frac{\partial()}{\partial n}$ is the derivative in the direction of the outward vector $\mathbf{n}$ that is normal to the boundary Γ; m_n and V_n are, respectively, the normal bending moment and the Kirchhoff equivalent shear force on the boundary Γ; R_c is the thin-plate reaction of corners; w_{ci} is the transverse displacement of corners; q_3 is the domain force in the transversal direction; K is a constant equivalent to c_{ij} of equation (304).

In order to have an equal number of equations and unknowns, it is necessary to write an integral equation corresponding to the derivative of the displacement $w(Q)$ in relation to the unity vector $\mathbf{m}$ that is normal to the boundary in the source point Q. This equation is given by:

$$
\begin{aligned}
&K\frac{\partial w}{\partial m}(Q)\\
&+\int_\Gamma \left[\frac{\partial V_n^*(Q,P)}{\partial m}w(P) - \frac{\partial m_n^*(Q,P)}{\partial m}\frac{\partial w(P)}{\partial n}\right]d\Gamma(P)\\
&+\sum_{i=1}^{N_c}\frac{\partial R_{c_i}^*(Q,P)}{\partial m}w_{ci}(P) = \sum_{i=1}^{N_c}\frac{\partial R_{c_i}(P)^*}{\partial m}w_{ci}(Q,P)\\
&+\int_\Omega q_3(P)\frac{\partial w^*(Q,P)}{\partial m}d\Omega\\
&+\int_\Gamma \left[V_n(P)\frac{\partial w^*(Q,P)}{\partial m} - m_n(P)\frac{\partial^2 w^*}{\partial n\partial m}(Q,P)\right]d\Gamma(P)\\
&+\int_\Gamma C\kappa_{ij}n_j u_i(P)\frac{\partial w^*(Q,P)}{\partial m}d\Gamma(P)\\
&+\int_\Omega C\frac{\kappa_{ij}}{\rho_{ij}}\frac{\partial w^*(Q,P)}{\partial m}w(P)\,d\Omega\\
&+\int_\Omega \left[C\kappa_{ij}(P)\frac{\partial w^*(Q,P)}{\partial m}\right]_{,j}u_i(P)\,d\Omega.
\end{aligned}
\tag{306}
$$

As can be seen in equations (304), (305), and (306), domain integrals arise in the formulation owing to the curvature of the shell. These domain integrals are:

$$
P_1(Q) = \int_\Omega C\kappa_{kj}w u_{ik,j}^*(Q,P)d\Omega,
\tag{307}
$$

$$
P_2(Q) = \int_\Omega C\frac{\kappa_{ij}}{\rho_{ij}}w^*(Q,P)w(P)\,d\Omega,
\tag{308}
$$

$$
P_3(Q) = \int_\Omega [C\kappa_{ij}(P)w^*(Q,P)]_{,j}\,u_i(P)\,d\Omega,
\tag{309}
$$

$$
P_4(Q) = \int_\Omega C\frac{\kappa_{ij}}{\rho_{ij}}\frac{\partial w^*(Q,P)}{\partial m}w(P)\,d\Omega,
\tag{310}
$$

and

$$
P_5(Q) = \int_\Omega \left[C\kappa_{ij}(P)\frac{\partial w^*(Q,P)}{\partial m}\right]_{,j}u_i(P)\,d\Omega.
\tag{311}
$$

In order to transform these integrals into boundary integrals, the RIM is used. Details of this method can be found in Albuquerque, Sollero, and Paiva (Albuquerque et al. [2007]). However, for sake of completeness, some steps of the method are repeated here, in the next section.

4.3 The radial integration method

Consider, in a general case, the following domain integration:

$$P(Q) = \int_\Omega b(P)v^*(Q,P)d\Omega, \tag{312}$$

where b and v^* are generic body force and fundamental solution, respectively.

The body force is approximated over the domain Ω as a sum of M products between approximation functions f_m and unknown coefficients γ_m, as given by equation (247).

Now, considering that the body force is approximated, for simplicity, by equation (247), the domain integral (312) can be written as:

$$P(Q) = \int_\Omega b(P)v^*(Q,P)d\Omega = \sum_{m=1}^{M} \gamma_m \int_\Omega f_m v^*(Q,P)d\Omega, \tag{313}$$

that can be transformed into a sum o boundary integrals by using the RIM as already presented in section 3.9.

In a matrix form, we can write:

$$P(Q) = \left[\begin{array}{cc} \int_\Gamma \frac{F_1(Q)}{r}\mathbf{n.r}d\Gamma & \int_\Gamma \frac{F_2(Q)}{r}\mathbf{n.r}d\Gamma \end{array} \right.$$
$$\left. \begin{array}{cc} \cdots & \int_\Gamma \frac{F_M(Q)}{r}\mathbf{n.r}d\Gamma \end{array} \right] \left\{ \begin{array}{c} \gamma_1 \\ \gamma_2 \\ \vdots \\ \gamma_M \end{array} \right\}. \tag{314}$$

To compute γ_m, it is necessary to consider the body force in M points of the domain and of the boundary. In the case of this work, these points are the boundary nodes and some internal points. Thus, equation (247) can be written as:

$$\mathbf{b} = \mathbf{F}\boldsymbol{\gamma}, \tag{315}$$

and $\boldsymbol{\gamma}$ can be computed as:

$$\boldsymbol{\gamma} = \mathbf{F}^{-1}\mathbf{b}. \tag{316}$$

Substituting (316) into equation (314), we have:

$$P(Q) = \left[\begin{array}{cc} \int_\Gamma \frac{F_1(Q)}{r}\mathbf{n.r}d\Gamma & \int_\Gamma \frac{F_2(Q)}{r}\mathbf{n.r}d\Gamma \end{array} \right.$$
$$\left. \begin{array}{cc} \cdots & \int_\Gamma \frac{F_M(Q)}{r}\mathbf{n.r}d\Gamma \end{array} \right] \mathbf{F}^{-1}\mathbf{b}. \tag{317}$$

Writing equation (317) for all source points, i.e., all boundary nodes and internal points, we have the following matrix equation:

$$\mathbf{P} = \mathbf{R}\mathbf{F}^{-1}\mathbf{b} = \mathbf{S}\mathbf{b}, \tag{318}$$

where $\mathbf{S} = \mathbf{R}\mathbf{F}^{-1}$, $\mathbf{P}$ is a vector that contains the value of $P(Q)$ in all source points Q, and $\mathbf{R}$ is a matrix that contains the value of integrals of equation (317) when this equation is written for all source points Q.

4.4   Matrix equation

Considering all body forces that appears in equations (296), (298), and (306), the vector $\mathbf{P}$ for these equations are given by:

$$\mathbf{P} = \begin{bmatrix} \mathbf{0} & \mathbf{0} & \mathbf{S}_{bb}^{mc} & \mathbf{S}_{bi}^{mc} & \mathbf{S}_{bc}^{mc} \\ \mathbf{0} & \mathbf{0} & \mathbf{S}_{ib}^{mc} & \mathbf{S}_{ii}^{mc} & \mathbf{S}_{ic}^{mc} \\ \mathbf{S}_{bb}^{p1c} & \mathbf{S}_{bi}^{p1c} & \mathbf{S}_{bb}^{p1} & \mathbf{S}_{bi}^{p1} & \mathbf{S}_{bc}^{p1} \\ \mathbf{S}_{bb}^{p2c} & \mathbf{S}_{bi}^{p2c} & \mathbf{S}_{bb}^{p2} & \mathbf{S}_{bi}^{p2} & \mathbf{S}_{bc}^{p2} \\ \mathbf{S}_{ib}^{p1c} & \mathbf{S}_{ii}^{p1c} & \mathbf{S}_{ib}^{p1} & \mathbf{S}_{ii}^{p2} & \mathbf{S}_{ic}^{p1} \\ \mathbf{S}_{cb}^{p1c} & \mathbf{S}_{ci}^{p1c} & \mathbf{S}_{cb}^{p1} & \mathbf{S}_{ci}^{p1} & \mathbf{S}_{cc}^{p1} \end{bmatrix} \begin{Bmatrix} \mathbf{u}_b \\ \mathbf{u}_i \\ \mathbf{w}_b \\ \mathbf{w}_i \\ \mathbf{w}_c \end{Bmatrix} \tag{319}$$

where the superscript index of matrix $\mathbf{S}$ stands for the type of equation that is being used, i.e., m stands for the membrane equation given by equation (296), $p1$ stands for the first plate equation, given by equation (298), and $p2$ stands for the second plate equation, given by equation (306). The letter c in the superscript index means that these are coupling terms. In matrix $\mathbf{S}$, the first subscript index stands for the location of the source points (b if source points are at a smooth part of the boundary, i if they are in the domain and c if they are at corners). The second subscript index shows where are the body forces that are multiplied by terms of the matrix $\mathbf{S}$. For the second index, the same letters of the first subscript index are used with the same meaning. The right hand side vector has nodal values of the body forces that in this case are given by displacements (all the remaining terms of domain integrals are considered as part of the fundamental solution v^*). The letter $\mathbf{u}$ stands for displacements in the x_1 and x_2 directions and $\mathbf{w}$ stands for displacement in the transversal direction. Subscript indices in the right hand side vector indicate the location of nodes where displacements are computed.

Finally, if the boundary Γ is discretized in boundary elements and equations (296), (298), and (306) is written for all source points, the following matrix equation can be obtained:

$$
\begin{bmatrix}
\mathbf{H}_{bb}^{m} & \mathbf{0} & \mathbf{0} & \mathbf{0} & \mathbf{0} \\
\mathbf{H}_{ib}^{m} & \mathbf{I} & \mathbf{0} & \mathbf{0} & \mathbf{0} \\
\mathbf{H}_{bb}^{p1c} & \mathbf{0} & \mathbf{H}_{bb}^{p1} & \mathbf{0} & \mathbf{H}_{bc}^{p1} \\
\mathbf{H}_{bb}^{p2c} & \mathbf{0} & \mathbf{H}_{bb}^{p2} & \mathbf{0} & \mathbf{H}_{bc}^{p2} \\
\mathbf{H}_{ib}^{p1c} & \mathbf{0} & \mathbf{H}_{ib}^{p1} & \mathbf{I} & \mathbf{H}_{ic}^{p1} \\
\mathbf{H}_{cb}^{p1c} & \mathbf{0} & \mathbf{H}_{cb}^{p1} & \mathbf{0} & \mathbf{H}_{cc}^{p1}
\end{bmatrix}
\begin{Bmatrix}
\mathbf{u}_b \\ \mathbf{u}_i \\ \mathbf{v}_b \\ \mathbf{w}_i \\ \mathbf{w}_c
\end{Bmatrix}
$$

$$
=
\begin{bmatrix}
\mathbf{G}_{bb}^{m} & \mathbf{0} & \mathbf{0} \\
\mathbf{G}_{ib}^{m} & \mathbf{0} & \mathbf{0} \\
\mathbf{0} & \mathbf{G}_{bb}^{p1} & \mathbf{G}_{bc}^{p1} \\
\mathbf{0} & \mathbf{G}_{bb}^{p2} & \mathbf{G}_{bc}^{p2} \\
\mathbf{0} & \mathbf{G}_{ib}^{p1} & \mathbf{G}_{ic}^{p1} \\
\mathbf{0} & \mathbf{G}_{cb}^{p1} & \mathbf{G}_{cc}^{p1}
\end{bmatrix}
\begin{Bmatrix}
\mathbf{t}_b \\ \mathbf{p}_b \\ \mathbf{p}_c
\end{Bmatrix}
$$

$$
+
\begin{bmatrix}
\mathbf{0} & \mathbf{0} & \mathbf{S}_{bb}^{mc} & \mathbf{S}_{bi}^{mc} & \mathbf{S}_{bc}^{mc} \\
\mathbf{0} & \mathbf{0} & \mathbf{S}_{ib}^{mc} & \mathbf{S}_{ii}^{mc} & \mathbf{S}_{ic}^{mc} \\
\mathbf{S}_{bb}^{p1c} & \mathbf{S}_{bi}^{p1c} & \mathbf{S}_{bb}^{p1} & \mathbf{S}_{bi}^{p1} & \mathbf{S}_{bc}^{p1} \\
\mathbf{S}_{bb}^{p2c} & \mathbf{S}_{bi}^{p2c} & \mathbf{S}_{bb}^{p2} & \mathbf{S}_{bi}^{p2} & \mathbf{S}_{bc}^{p2} \\
\mathbf{S}_{ib}^{p1c} & \mathbf{S}_{ii}^{p1c} & \mathbf{S}_{ib}^{p1} & \mathbf{S}_{ii}^{p2} & \mathbf{S}_{ic}^{p1} \\
\mathbf{S}_{cb}^{p1c} & \mathbf{S}_{ci}^{p1c} & \mathbf{S}_{cb}^{p1} & \mathbf{S}_{ci}^{p1} & \mathbf{S}_{cc}^{p1}
\end{bmatrix}
\begin{Bmatrix}
\mathbf{u}_b \\ \mathbf{u}_i \\ \mathbf{w}_b \\ \mathbf{w}_i \\ \mathbf{w}_c
\end{Bmatrix}
+ \mathbf{q}
$$

$$(320)$$

where $\mathbf{H}$ and $\mathbf{G}$ are influence matrices of the BEM; the vector $\mathbf{v}$ contains transversal displacements and rotations of the nodes (not only transversal displacement as vector $\mathbf{w}$). Vectors $\mathbf{t}$ and $\mathbf{p}$ contain boundary node reactions for membrane and plate equations, respectively. The vector $\mathbf{q}$ is due to the domain load q_i. Domain integrals due to q_i's are transformed exactly into boundary integrals using the procedure presented in Albuquerque, Sollero, Venturini, and Aliabadi (Albuquerque et al. [2007]).

Equation (320) can be written in a more concise form as:

$$\mathbf{H}\mathbf{v} = \mathbf{G}\mathbf{t} + \mathbf{S}\mathbf{u} + \mathbf{q} \qquad (321)$$

Finally, columns of matrices of equation (321) can be reordered in accordance with boundary conditions and a linear equation system can be obtained where the unknown displacements and reactions can be computed.

4.5 Approximation functions

Two approximation functions are used in this work. The first is a radial basis function that has been used extensively in the DRM and is given by:

$$f_{m_1} = 1 + R. \qquad (322)$$

The second is the well known thin plate spline:

$$f_{m_3} = R^2 \log(R), \qquad (323)$$

used with the augmentation function given by equations (248) and (249).

4.6   Numerical results

4.6.1   Square spherical shallow shell

In order to assess the accuracy of the proposed formulation, consider a square spherical shallow shell, as shown in Figure 25. The geometry and material properties of the shell are as follow: length of the base edge of the shell a =0.254 m, thickness $h = 0.0127$ m, curvature radii $R_1 = R_2 = R = 2.54$ m ($R_{12} = R_{21} = 0$), elastic moduli $E_2 = 6.895$ GPa and $E_1 = 2E_1$, Poisson ratio $\nu_{12} = 0.3$, and shear modulus $G_{12} = E_2/[2(1 - \nu_{12})]$. The shell is under a uniformly distributed load in the transversal direction (internal pressure) $q_3 = 2.07$ MPa ($q_1 = q_2 = 0$).
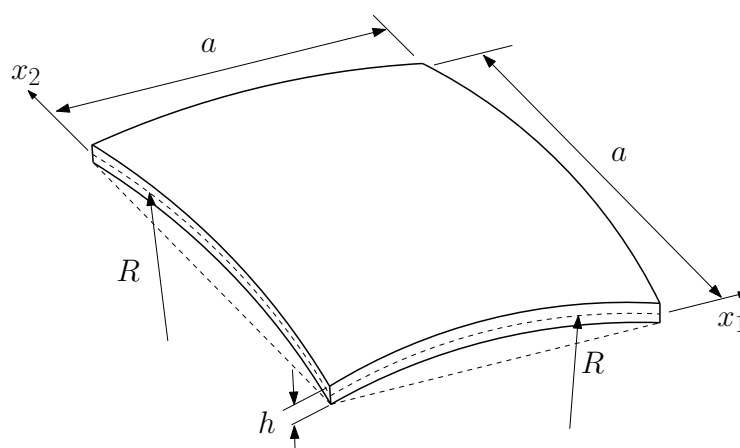
Figure 25: Square spherical shallow shell.

This problem was analysed considering two types of boundary conditions, i.e., clamped and simply-supported. Three meshes were used. Mesh 1 has 12 constant boundary elements and 9 internal points, mesh 2 has 20 boundary elements and 25 internal points, and mesh 3 has 28 boundary elements and 49 internal points. Mesh 3 is shown in Figure 26. All meshes have elements of equal length and uniformly distributed internal points.

Figures 27 and 28 show results for the clamped and simply-supported boundary conditions, respectively, together with meshless results obtained by Sladek et al. Sladek et al. [2007] for the same problems but considering the shell as shear deformable.

As it can be seen, the results for the clamped boundary conditions are in good agreement with the meshless results while for the simply-supported boundary conditions they are slightly lower.
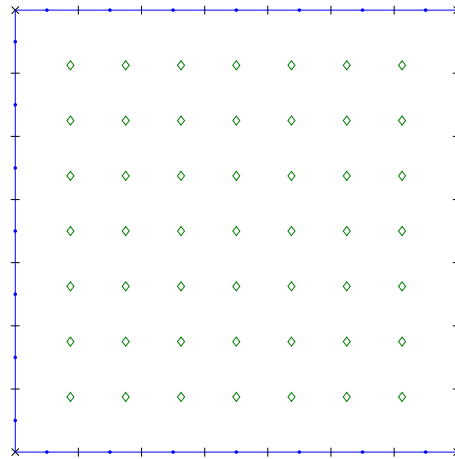
Figure 26: Boundary elements and internal points for the square spherical shallow shell (mesh 3, 28 boundary elements and 49 internal points).
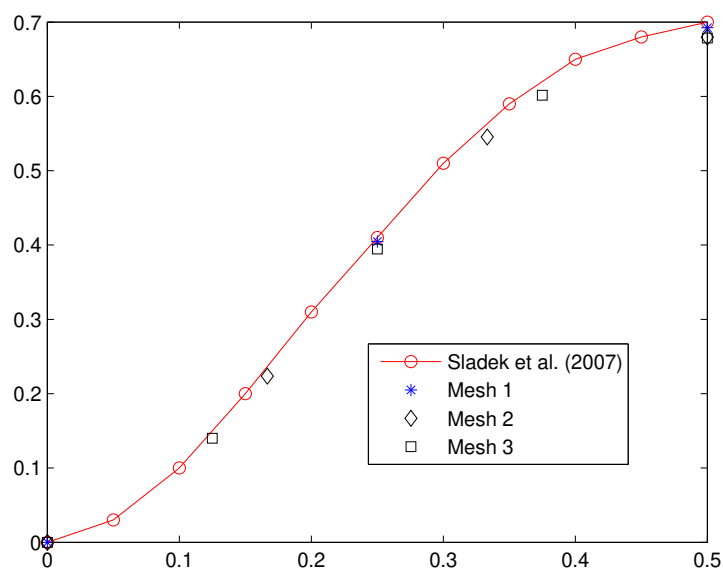
Figure 27: Transversal displacement for the spherical shell with clamped edge.
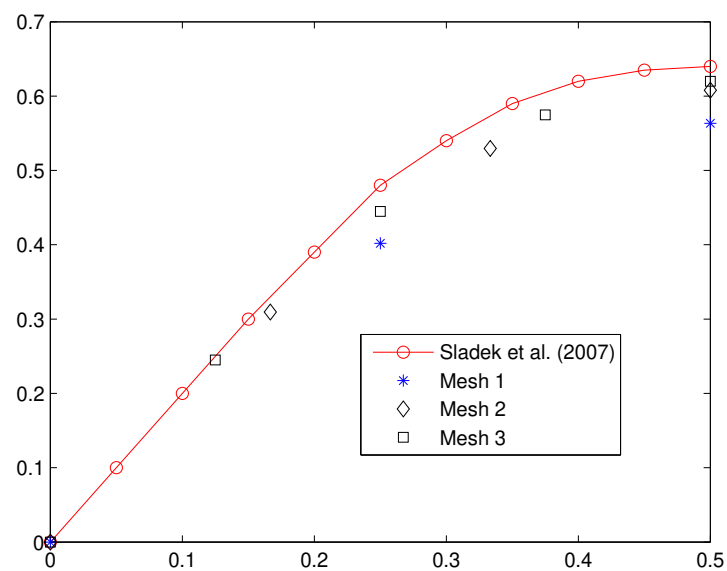
Figure 28: Transversal displacement for the spherical shell with simply-supported edge.

5   Conclusions

5.1   Conclusions

This chapter presented a boundary element formulation for the numerical analysis of static and dynamic problems in laminated composite plates and shallow shells. Two boundary integral equations, for transverse displacement and rotation, were used, and these integral equations were discretized into constant and quadratic boundary elements. For elastostatics, the domain integrals which arise from linearly and uniformly distributed loads were transformed into boundary integrals by an exact radial transformation. Several numerical examples were shown for quasi-isotropic, orthotropic, and general anisotropic materials. The numerical results obtained with the present boundary element technique were compared with results obtained analytically in the form of a series solution and results obtained by the finite element method, and show good agreement.

The use of the dual reciprocity boundary element method (DRM) and the radial integration method (RIM) for problems in which the body forces are unknowns was explored. In both methods body forces are approximated as a sum of the product between radial basis function and unknown coefficients. The main advantage of the RIM over the DRM is that there is no need to compute analytical particular solutions in the former, which allows a free choice of the approximation function for problems of anisotropic materials. As some of the integrals that arises in the formulation cannot be computed analytically, the use of numerical integration becomes the RIM more time-consuming than the DRM. Results have shown that similar accuracy is obtained with the RIM and the DRM when the same approximation function is used for problems of unknown body forces. This is a first work and both methods still demands a lot of research. An important analysis that should be carried out in order to improve the accuracy of the RIM is the use of other approximation functions, such as radial basis functions augmented by polynomials or thin plate splines. However, this analysis was not in the scope of this work.

In the analysis of thin shallow shells, domain integrals are transformed into boundary integrals by the radial integration method. As the radial integration method doesn't demand particular solutions, it is easier to implement than the dual reciprocity boundary element method. Besides, strong singularities in domain integrals are cancelled by the radial integration. Two different approximation functions are used in the radial integration method. Results obtained with both approximation functions are in good agreement with results presented in literature. As in the dual reciprocity method, the accuracy of the method is improved by increasing the number of boundary nodes and internal points. However, different from dual reciprocity and even from other applications of the radial integration method, the use of radial basis function augmented by polynomials hasn't produced significantly changes in results.

References

E. L. Albuquerque and P. Sollero. The boundary element method applied to transient dynamic anisotropic problems. In A. J. Kassab, C. A. Brebbia, and M. Chopra, editors, *Proc. Boundary Element Method XX*, pages 617–624, Orlando - USA, jul 1998.

E. L. Albuquerque, P. Sollero, and M. H. Aliabadi. The boundary element method applied

to time dependent problems in anisotropic materials. *International Journal of Solids and Structures*, 39:1405–1422, 2002.

E. L. Albuquerque, P. Sollero, and P. Fedelinski. Dual reciprocity boundary element method in laplace domain applied to anisotropic dynamic crack problems. *Computers and Structures*, 81:1703–1713, 2003a.

E. L. Albuquerque, P. Sollero, and P. Fedelinski. Free vibration analysis of anisotropic material structures using the boundary element method. *Engineering Analysis with Boundary Elements*, 27:977–985, 2003b.

E. L. Albuquerque, P. Sollero, and M. H. Aliabadi. Dual boundary element method for anisotropic dynamic fracture mechanics. *International Journal for Numerical Methods in Engineering*, 59:1187–1205, 2004.

E. L. Albuquerque, P. Sollero, W. Venturini, and M. H. Aliabadi. Boundary element analysis of anisotropic kirchhoff plates. *International Journal of Solids and Structures*, 43:4029–4046, 2006.

E. L. Albuquerque, P. Sollero, and W. P. Paiva. The radial integration method applied to dynamic problems of anisotropic plates. *Communications in Numerical Methods in Engineering*, 23:805–818, 2007.

M. H. Aliabadi. *Boundary element method, the application in solids and structures*. John Wiley and Sons Ltd, New York, 2002.

P. M. Baiz and M. H. Aliabadi. Linear buckling of shear deformable shallow shells by the boundary domain element method. *CMES - Computer Modeling in Engineering and Sciences*, 13:19–34, 2006.

K. Bath and E. L. Wilson. *Numerical methods in finite element analysis*. Prentice-Hall Inc., Englewood Cliffs, New Jersey, 1976.

T. A. Cruse and J. L. Swedlow. Interactive program for analysis and design problems in advanced composites. Technical report, Carnegie-Mellon University, Report AFLM-TR-71-268, 1971.

A. Deb. Boundary elements analysis of anisotropic bodies under thermo mechanical body force loadings. *Computers and Structures*, 58:715–726, 1996.

T. Dirgantara and M. H. Aliabadi. A new boundary element formulation for shear deformable shells analysis. *Int. J. for Numerical Methods in Engn.*, 45:1257–1275, 1999.

X. Gao. The radial integration method for evaluation of domain integrals with boundary only discretization. *Engn. Analysis with Boundary Elements*, 26:905–916, 2002.

R. F. Gibson. *Principles of composite material mechanics*. McGraw Hill, New York, 1994.

J. C. Houbolt. A reccurrence matrix solution for the dynamic response of elastic aircraft. *J. of Aeronautical and Science*, 17:540–550, 1950.

G. Kirchhoff. On the equilibrium and motion of an elastic plate. *J. Math.*, 40:51–58, 1950. In German.

M. Kogl and L. Gaul. A boundary element method for transient piezoelectric analysis. *Engineering Analysis with Boundary Elements*, 24:591–598, 2000a.

M. Kogl and L. Gaul. A 3-d boundary element method for dynamic analysis of anisotropic elastic solids. *CMES - Computational Modelling in Engineering and Science*, 1:27–43, 2000b.

M. Kogl and L. Gaul. Free vibration analysis of anisotropic solids with the boundary element method. *Engineering Analysis with Boundary Elements*, 27:107–114, 2003.

B. Lamattina. *Anisotropic plate bendign analysis using complex variable methods*. PhD thesis, North Carolina State University, Raleigh - USA, 1997.

B. Lamattina, E. C. Klang, and J. W. Eischen. A study of solutions for the anisotropic plate subjected to a concentrated force. *Journal of Applied Mechanics*, 65:273–276, 1998.

S. G. Lekhnitskii. *Anisotropic plates*. Gordon and Breach, New York, 1968.

J. Lin, R. C. Duffield, and H. Shih. Buckling analysis of elastic plates by boundary element method. *Engineering Analysis with Boundary Element*, 23:131–137, 1999.

C. Loeffler and W. J. Mansur. Analysis of time integration schemes for boundary element applications to transient wave propagation problems. In C. A. Brebbia and W. S. Venturini, editors, *Boundary Element techniques: Applications in stress analysis and heat transfer*, pages 105–122, Computational Mechanics Publications, Southhampton, 1987.

P. Lu and O. Mahrenholtz. The fundamental solution for the theory of orthotropic shallow shells involving shear deformation. *Int. J. of Solids and Structures*, 31:913–923, 1994.

J. Mossakowski. Singular solutions of anisotropic plates. *Arch. Mech. Stos.*, 7:97–110, 1955. In Polish.

D. Nardini and C. A. Brebbia. A new approach to free vibration analysis using boundary elements. In *Boundary Element Method in Engineering - IV International Seminar*, 1982.

M. S. Nerantzaki and J. T. Katsikadelis. Buckling of plates with variable thickness, an analog equation solution. *Engineering Analysis with Boundary Element*, 18:149–154, 1996.

A. J. Nowak and A. C. Neves. *The multiple reciprocity boundary element method*. Computational Mechanics Publication, Southampton, 1994.

J. B. Paiva. *Boundary element formulation for plate bending and its aplication in engineering*. PhD thesis, University of São Paulo, São Carlos School of Engineering, 1987. In Portuguese.

W. P. Paiva, P. Sollero, and E. L. Albuquerque. Treatment of hypersingularities in boundary element anisotropic plate bending problems. *Latin American Journal of Solids and Structures*, 1:49–73, 2003.

W. P. Paiva, P. Sollero, E. L. Albuquerque, R. Pavanello, and M. H. Aliabadi. Dynamics of thin anisotropic plates. In *Advances in Boundary Element Techniques V*, 2004.

P. W. Partridge, C. A. Brebbia, and L. C. Wrobel. *The dual reciprocity boundary element method*. Computational Mechanics Publications, Southampton, Boston, 1992.

J. Purbolaksono and M. H. Aliabadi. Buckling analysis of shear deformable plates by boundary element method. *International Journal for Numerical Methods in Engineering*, 62:537–563, 2005.

C. Rajamohan and J. Raamachandran. Bending of anisotropic plates by charge simulation method. *Advances in Engn. Software*, 30:369–373, 1999.

N. A. Schclar. *Anisotropic analysis using boundary elements*. Computational Mechanics Publications, Southampton, Boston, 1994.

G. Shi. Flexural vibration and buckling analysis of orthotropic plates by the boundary element method. *J. of Solids and Structures*, 26:1351–1370, 1990.

G. Shi and G. Bezine. A general boundary integral formulation for the anisotropic plate bending problems. *J. Composite Materials*, 22:694–716, 1988.

J. Sladek, V. Sladek, J. Krivacek, and M. H. Aliabadi. Local boundary integral equations for orthotropic shallow shells. *International Journal of Solids and Structures*, 44:2285–2303, 2007.

P. Sollero and M. H. Aliabadi. Fracture mechanics analysis of anisotropic plates by the boundary element method. *Int. J. of Fracture*, 64:269–284, 1993.

P. Sollero and M. H. Aliabadi. Anisotropic analysis of composite laminates using the dual boundary element methods. *Composite Structures*, 31:229–234, 1995.

M. Suchar. On singular solutions in the theory of anisotropic plates. *Bulletin de l'Academie Polonaise des Sciences: Series Science Techniques*, 12:29–38, 1964.

S. Syngellakis and E. Elzein. Plate buckling loads by the boundary element method. *International Journal for Numerical Methods in Engineering*, 37:1763–1778, 1994.

W. S. Venturini. *A study of boundary element method and its application on engineering problems*. PhD thesis, University of São Paulo, São Carlos School of Engineering, 1988. In Portuguese.

J. Wang. The fundamental solutions of orthotropic shallow shells. *Acta Mechanica*, 94:113–121, 1992.

J. Wang and K. Schweizerhof. The fundamental solution of moderately thick laminated anisotropic shallow shells. *Int. J. Engng. Sci.*, 33:995–1004, 1995.

J. Wang and K. Schweizerhof. Study on free vibration of moderately thick orthotropic laminated shallow shells by boundary-domain elements. *Applied Mathematical Modelling*, 20:579–584, 1996.

J. Wang and K. Schweizerhof. Free vibration of laminated anisotropic shallow shells including transverse shear deformation by the boundary-domain element method. *Computers and Structures*, 62:151–156, 1997.

P. H. Wen, M. H. Aliabadi, and A. Young. Application of dual reciprocity method to plates and shells. *Engn. Anal. with Boundary Elements*, 24:583–590, 2000.

B. C. Wu and N. J. Altiero. A new numerical method for the analysis of anisotropic thin plate bending problems. *Computer Meth. in Appl. Mechanics and Engineering*, 25: 343–353, 1981.

C. Zhang. Transient elastodynamic antiplane crack analysis of anisotropic solids. *Int. J. of Solids and Structures*, 37:6107–6130, 2000.

J. D. Zhang and S. N. Atluri. A boundary/interior element method for quasi-static and transient response analysis of shallow shells. *Computers and Structures*, 24:213–223, 1986.

Chapter 21

The Boundary Element Method for Damage Modeling

The Boundary Element Method for Damage Modeling

Rodrigo G. Peixoto[1*] and Alisson P. Chaves[2]

[1]Department of Structural Engineering, Federal University of Minas Gerais, Brazil.
E-mail: rgpeixoto@ufmg.br
[2]Department of Computation and Civil Construction, Federal Center of Technological
Education of Minas Gerais, Timóteo-MG, Brazil. E-mail: alisson.chaves@cefetmg.br

*Corresponding author

Abstract

*Materials physically non linear behaviour that arises when energy dissipation
mechanisms occur, can be described by elastoplastic or elastic-degrading constitu-
tive models. Such approaches can be summarized in a unified theoretical framework.
The appearance of discontinuities in the strain field during inelastic loading with
softening, and its transition until the emergence of jumps in the displacement fields
can be analyzed with the Continuum Strong Discontinuity Approach (CSDA). These
techniques, associated to the Implicit form of the Boundary Element Method (BEM)
are discussed in this chapter, from the basic formulation concepts, to the numerical
features and algorithms. The efficiency and versatility of the methodology can be
observed through numerical simulation of typical plane state and three-dimensional
analyzes.*

Keywords: Boundary Element Method; damage modeling; strong discontinuity approach

1 Introduction

Analyses with the Boundary Element Method (BEM) are general and efficient when it makes
use of algorithms capable to deal with independent constitutive modeling frameworks, which can
be easily modified or expanded to encompass different material representations and particular
behaviours, and also, to be evaluated with appropriated solution strategy.

The first developments of boundary integral equations for the treatment of elastoplastic mate-
rials may be attributed to Swedlow and Cruse [1971], Mendelson [1973] and Riccardella [1973].
Considering the incompressibility of the plastic strain tensor, Mukherjee [1977] verified some er-
rors in the kernels involving inelastic fields for plane strain case and, later, Bui [1978] presented a
corrected way to evaluate derivatives of the singular integrals involving such inelastic fields, intro-
ducing new free terms. Those results were then applied to the BEM by Telles and Brebbia [1979].
They used an explicit formulation, where the increment of the initial fields (plastic strains or its cor-
responding fictitious plastic stresses) explicitly appears in the non linear discretized equations and
the equilibrium is achieved by a recursive procedure. Considering the proportional relationship

between stresses and elastic strains, Telles and Carrer [1991] proposed an implicit formulation, where the initial field increments are written in terms of total strains (actually, in the original work they used the fictitious elastic stresses related to total strains by the linear elastic Hooke's constitutive tensor), resulting in an accumulated equilibrium matrix equation, which is incrementally solved.

Some material behaviours, e.g., the quasi-brittle ones, requires the introduction of strain softening laws for a correct representation. A direct way to do this is to consider a plasticity model with yield limit degradation, as done by Lin et al. [2002] and Sládek et al. [2003]. The presence of strain softening results in a loss of objectiveness with respect to mesh refinements, as the solution tends to an infinitely small localization bandwidth with zero energy dissipation during failure. For that reason, in both works, a non-local procedure, based on the spatial averaging of the plastic multiplier, was also introduced. Another non-local plasticity model, based on a re-definition of the yield surface, including a dependency on the Laplacian of the plastic multiplier, was applied to the implicit formulation of the BEM by Benallal et al. [2002]. In that work, a complementary integral representation of the plastic multiplier was discretized and solved together (in a coupled way) to the incremental implicit equation.

Other constitutive models, such as continuum damage mechanics (CDM) based ones, have also been used with the BEM. CDM has been established to close the gap between classical continuum and fracture mechanics. In the BEM context, some works can be cited, such as Rajgelj et al. [1992], Herding and Kuhn [1996], García et al. [1999] and Botta et al. [2005]. Specifically, in the last work, the damage model presented by Comi and Perego [2001] was employed. As expected, they also reported mesh dependence when this model is locally applied and an averaging procedure of some strain invariants was introduced, regularizing the model.

Summarizing a large number of works devoted to damage modeling of material media, Carol et al. [1994] proposed a theoretical unification of elastic-degrading models based on a single loading function. In that reference, the authors developed a unified framework including a large range of damage models in analogy to the concepts and notations of classical plasticity. With this formalism, the two parameters required by the solution strategy mentioned above can be organized and numerically implemented in a completely independent way.

In the work of Simo et al. [1993], a new idea was introduced, based on the application of standard continuum constitutive models to unbounded strain fields, related to discontinuous displacements over a given surface (strong discontinuity surface). This methodology was latter called as continuum strong discontinuity approach (CSDA). Basically, a set of kinematic equations (in a regularized formulation) is used to describe displacements and strains at a discontinuity surface. Thus, applying this regularized kinematic on ordinary continuous constitutive models, the consistent discrete model obtained can relate traction with displacement jumps where the discontinuity is established.

The use of CSDA in the context of the BEM was firstly proposed in Manzoli and Venturini [2004] and Manzoli and Venturini [2007], who used the implicit BEM formulation for non linear analysis, and introduced discontinuity interfaces inside cells that dicretized the whole domain. This idea was extended in Manzoli et al. [2009] using an isotropic damage model and a tracking algorithm to generate cells automatically, in the direction of the crack path determined during the analyses. A further improvement was presented by Peixoto et al. [2017] and Peixoto et al. [2018], who sophisticated the non linear analysis, involving inelastic dissipation with softening in continuous media, bifurcation analysis and transition between weak and strong discontinuities.

The material failure process can also be modeled by a geometrical point of view using the fracture mechanics concepts, in which the singular character of the stress state at a crack tip is substituted by stress intensity factors, obtained from energetic considerations. This idea was notably well adapted for the BEM, in its dual formulation used by Portela et al. [1992], where distinct

integral equations are applied in each side of a discontinuous surface.

The Einstein's index notation is adopted for tensors algebra throughout the chapter. This chapter is divided in eleven sections. In the next section some fundamental equations for physically linear and non linear solid mechanics are reviewed. In Section 3, the integral equations considering initial strain fields, appropriate to deal with standard physically non linear problems, are presented. Following, in Section 4 presents a numerical counterpart of such equations, and a solution strategy with the required rearrangement for the implicit BEM formulation, and the control methods for non linear analyses. Some numerical examples of continuum non linear analysis of simple problems are presented in Section 5. Strain localization and material bifurcation analysis are discussed in Section 6, while in Section 7 the CSDA is presented, including the weak and strong discontinuity kinematics, the strong discontinuity analysis and variable bandwidth model. In Section 8 the boundary integral equations are reformulated for the consideration of discontinuous surface effects. Numerical features of the BEM formulation, regarding cell with embedded discontinuity and displacement jump evaluation are described in Section 9. Some the numerical examples of non linear problems with discontinuities are treated in Section 10, and Section 11 have some final remarks. Additionally, in Appendix A, elastoplastic and isotropic damage models are presented.

2   Basic Equations for Physically Non Linear Solid Mechanics

2.1   Linear Elasticity

Before presenting the physically non linear constitutive models, in which some energy dissipation phenomena take place, basic equations associated to conservative (elastic) deformation are firstly presented. Only small displacements are considered, such that a strain tensor can be defined from the gradient of the displacement field, configuring which is called as linear elasticity.

2.1.1   Cauchy stress tensor

Figure 1 represents a solid body Ω, delimited by a surface Γ.

(a)   (b)
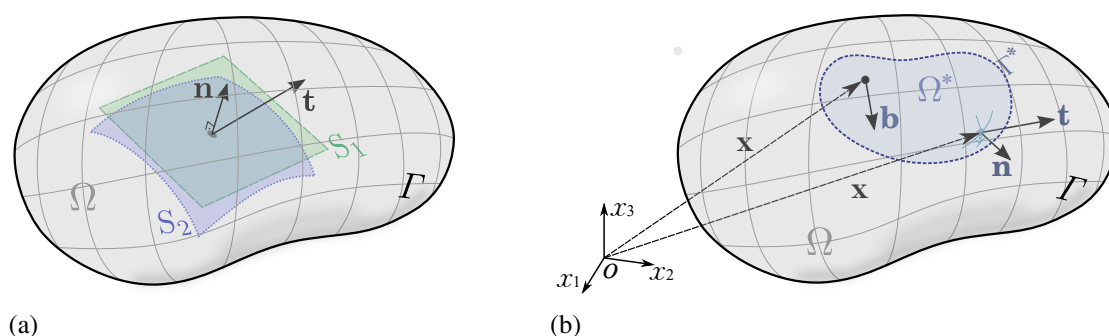
Figure 1: A solid body Ω with boundary Γ – (a) Traction vector, (b) Arbitrary subdomain Ω^*

If the body is loaded, at any point of a given internal surface, say S_1 or S_2 (figure 1-a), a traction vector, $\mathbf{t}$ (units of force per area), can be defined as a function of the the unit normal vector, $\mathbf{n}$, to the surface at this point. The second order tensor that relate these vectors is called as Cauchy Stress Tensor, i.e.,

$$t_i = \sigma_{ij} n_j \tag{1}$$

Considering an arbitrary closed sub-domain, Ω^*, inside the body, as illustrated in Figure 1-b, and calling as $\mathbf{b}(\mathbf{x})$ the external forces (per volume unit) that act along the solid domain, the equilibrium condition can be expressed by

$$\oint_{\Gamma^*} t_i d\Gamma + \int_{\Omega^*} b_i d\Omega = \oint_{\Gamma^*} (\sigma_{ij} n_j) d\Gamma + \int_{\Omega^*} b_i d\Omega = \int_{\Omega^*} (\sigma_{ij,j} + b_i) d\Omega = 0$$

in which the surface integral was transformed to a volumetric one by applying the Divergence Theorem. Thus, from the arbitrariness of Ω^*, it is possible to conclude that, for any material point $\mathbf{x}$, the following equilibrium equation can be written

$$\sigma_{ij,j} + b_i = 0 \tag{2}$$

The Cauchy Stress Tensor is symmetric, i.e., $\sigma_{ij} = \sigma_{ji}$, which means that only six components are sufficient to describe the stress state at a given point. This property can be demonstrated by taking the angular momentum resultant of an arbitrary sub-domain, Ω^*, as developed below, making reference again to Figure 1-b.

$$\oint_\Gamma (\mathbf{x} \times \mathbf{t}) d\Gamma + \int_\Omega (\mathbf{x} \times \mathbf{b}) d\Omega = \oint_\Gamma (\varepsilon_{ijk} x_j \sigma_{kl} n_l) d\Gamma + \int_\Omega (\varepsilon_{ijk} x_j b_k) d\Omega = 0$$

$$= \int_\Omega (\varepsilon_{ijk} x_j \sigma_{kl})_{,l}\, d\Omega + \int_\Omega (\varepsilon_{ijk} x_j b_k) d\Omega = 0$$

$$= \int_\Omega (\varepsilon_{ijk} \underbrace{x_{j,l}}_{\delta_{jl}} \sigma_{kl}) d\Omega + \int_\Omega \big[\varepsilon_{ijk} x_j \underbrace{(\sigma_{kl,l} + b_k)}_{=0} \big] d\Omega = 0$$

$$= \int_\Omega (\varepsilon_{ijk} \sigma_{kj}) d\Omega = 0 \;\Rightarrow\; \varepsilon_{ijk} \sigma_{kj} = 0 \;\Rightarrow\; \sigma_{jk} = \sigma_{kj}$$

where δ_{ij} is the Kronecker delta and ε_{ijk} is the permutation operator, respectively defined by

$$\delta_{ij} = \begin{cases} 0 & \text{if} \;\; i \neq j \\ 1 & \text{if} \;\; i = j \end{cases} \tag{3}$$

and

$$\varepsilon_{ijk} = \begin{cases} 0 & \text{if there is repetition of, at least, two indexes} \\ -1 & \text{if} \;\; (i,j,k) = (3,2,1) \text{ or } (1,3,2) \text{ or } (2,1,3) \\ +1 & \text{if} \;\; (i,j,k) = (1,2,3) \text{ or } (3,1,2) \text{ or } (2,3,1) \end{cases} \tag{4}$$

Independently of the stress state in a given point, it is always possible to choose a coordinates system in which the stress tensor becomes diagonal, i.e., $\sigma_{ij} = 0$ if $i \neq j$. The directions of each axis of this system are called as principal directions and the normal stresses, action on perpendicular planes to these axis, are called as principal stresses. Evaluating such principal stress components is a typical eigenvalue problem, since the traction vector parallel a principal direction can be written as

$$t_i = \sigma_{ij} n_j = \lambda \delta_{ij} n_j \quad \Rightarrow \quad (\sigma_{ij} - \lambda \delta_{ij}) n_j = 0$$

where λ represents a scalar constant. For non-trivial solutions of this last equation,

$$\det(\sigma_{ij} - \lambda \delta_{ij}) = 0 \quad \Rightarrow \quad \lambda^3 - I_1 \lambda^2 - I_2 \lambda - I_3 = 0 \tag{5}$$

in which I_k are the stress tensor invariants, given by

$$I_1 = \sigma_{ii}, \quad I_2 = \frac{1}{2}(\sigma_{ij}\sigma_{ij} - I_1^2), \quad I_3 = \frac{1}{6}\varepsilon_{ijk}\varepsilon_{pqr}\sigma_{ip}\sigma_{jq}\sigma_{kr} \tag{6}$$

Equation (5) is the characteristic polynomial and its roots are the principal stress components.

2.1.2 Linear strain tensor

A displacement field, $\mathbf{u}(\mathbf{x})$, in a loaded solid body is represented in Figure 2.

$x_i \rightarrow$ position of a given point in the initial (undeformed) configuration

$x_i + u_i \rightarrow$ position of the same point in a deformed configuration

$u_i \rightarrow$ displacement components, $u_i \equiv u_i(\mathbf{x})$
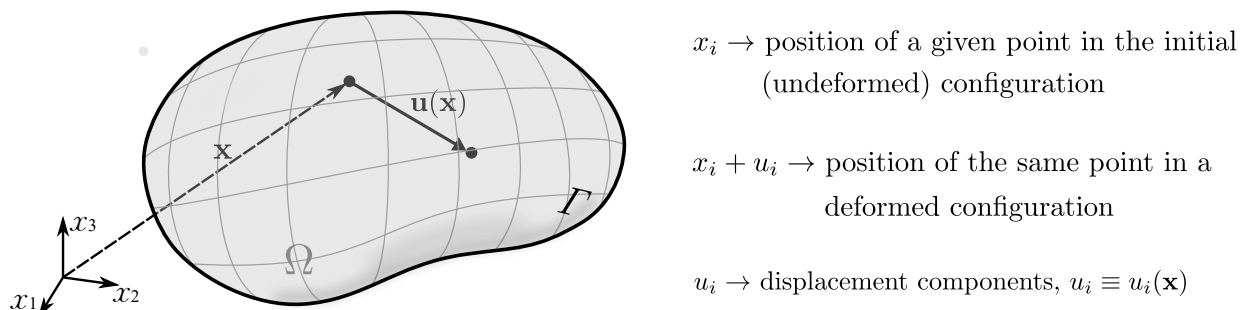
Figure 2: Displacements in a solid body

If the displacement field is such that its first order derivatives are sufficiently small, in order that the product of partial derivatives of $\mathbf{u}(\mathbf{x})$ become negligible, the strain field in the solid body can be described by linear strains, i.e., by the symmetric part of the displacement gradient tensor:

$$\epsilon_{ij} = \frac{1}{2}(u_{i,j} + u_{j,i}) \tag{7}$$

Although the displacements uniquely define the components of the strain tensor, the inverse problem, i.e., obtaining the displacements from a strain field, is not so straightforward. Since equation (7) is equivalent to six differential equations, the three components of u_i are not uniquely defined, unless additional conditions are imposed on the deformation components. Such conditions are defined by compatibility equations, which can be generically written in the form:

$$\epsilon_{ij,kl} + \epsilon_{kl,ij} - \epsilon_{ik,jl} - \epsilon_{jl,ik} = 0 \tag{8}$$

2.1.3 Hooke's Law

The strain field caused by a distributed stress state in a solid body depends on the material properties. In a conservative regime, the relation between strain and stress is known as Hooke's Law or linear elastic constitutive equation. Mathematically,

$$\sigma_{ij} = C_{ijkl}\epsilon_{kl} \tag{9}$$

where the fourth order tensor C_{ijkl} is the so-called constitutive tensor.

Considering an isotropic and homogeneous material, the expression of the constitutive tensor is

$$C_{ijkl} = \bar{\lambda}\delta_{ij}\delta_{kl} + \mu(\delta_{ik}\delta_{jl} + \delta_{il}\delta_{jk}) \tag{10}$$

where

$$\mu = \frac{E}{2(1+\nu)}, \quad \bar{\lambda} = \frac{2\mu\bar{\nu}}{1 - 2\bar{\nu}}, \quad \bar{\nu} = \begin{cases} \nu & \text{(3D or Plane Strain)} \\ \dfrac{\nu}{1+\nu} & \text{(Plane Stress)} \end{cases} \tag{11}$$

in which E represents the material Young's modulus and ν is the Poisson ratio.

An inverse of equation (9) can be written as

$$\epsilon_{ij} = C_{ijkl}^{-1}\sigma_{kl} \tag{12}$$

where

$$C_{ijkl}^{-1} = \frac{1}{2\mu}\left[\frac{1}{2}(\delta_{ik}\delta_{jl} + \delta_{il}\delta_{jk}) - \tilde{\nu}\delta_{ij}\delta_{kl}\right] \tag{13}$$

and

$$\tilde{\nu} = \begin{cases} \nu & \text{(Plane Strain)} \\ \dfrac{\nu}{1+\nu} & \text{(3D or Plane Stress)} \end{cases} \tag{14}$$

2.1.4   Navier Equation

Navier Equation represents the equilibrium condition rewritten in terms of the displacement field. It is obtained from the application of equation (7) into (9), followed by introducing the this result into equation (2), i.e.,

$$\sigma_{ij,j} + b_i = \frac{1}{2}C_{ijkl}(u_{k,lj} + u_{l,kj}) + b_i = 0$$

Then, applying equation (10) and considering the definition of the Kronecker delta (equation 3), the next result is achieved:

$$\frac{1}{2}\left[\bar{\lambda}(u_{k,ki} + u_{k,ki}) + \mu(u_{i,jj} + u_{j,ij}) + \mu(u_{j,ij} + u_{i,jj})\right] + b_i = 0$$

Finally, reorganizing,

$$\mu u_{i,jj} + (\bar{\lambda} + \mu)u_{j,ji} + b_i = 0 \tag{15}$$

which is the Navier Equation.

2.2   Kelvin Fundamental Solution

Lets consider now an infinite homogeneous and isotropic solid domain, loaded by punctual unit forces, namely $P_i = 1$, acting on a given point, $\boldsymbol{\xi}$, and directed at each cartesian direction, as illustrated in Figure 3. This problem is called as Kelvin fundamental problem of elasticity.
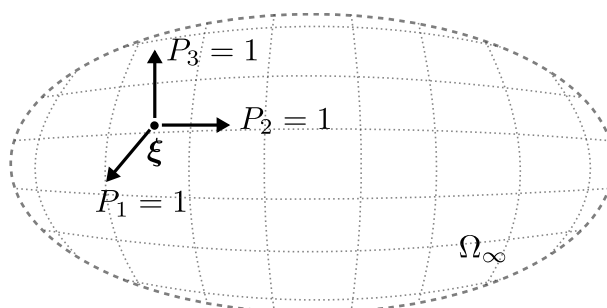
Figure 3: Infinite solid domain with punctual concentrated unit forces

To give a distributional character to concentrated loads, the Dirac delta function, $\delta(\mathbf{x}_0, \mathbf{x})$, might be used. Such function presents the following property:

$$\int_{\Omega} f(\mathbf{x})\delta(\mathbf{x}_0, \mathbf{x})d\Omega = f(\mathbf{x}_0) \tag{16}$$

Thus, in the case of the Kelvin fundamental problem, the body forces, previously defined, can be written as

$$b_i(\mathbf{x}) = \delta(\boldsymbol{\xi}, \mathbf{x})P_i \tag{17}$$

Substituting equation (17) into (15), and calling as $\mathbf{u}^*(\mathbf{x})$ the displacement field resulting from the Kelvin fundamental problem, one obtains

$$\mu u_{j,kk}^*(\mathbf{x}) + (\bar{\lambda} + \mu)u_{k,kj}^*(\mathbf{x}) + \delta(\boldsymbol{\xi}, \mathbf{x})P_j = 0 \tag{18}$$

Among the different existing solution techniques for this problem, probably the most popular is the Galerkin vector formulation. This vector, G_i, is defined by the next expression:

$$u_j^* = G_{j,ii} - \left(\frac{\bar{\lambda} + \mu}{\bar{\lambda} + 2\mu}\right)G_{i,ji} \tag{19}$$

Applying equation (19) to (18),

$$\mu G_{j,iikk} - \underbrace{\left[\mu\left(\frac{\bar{\lambda} + \mu}{\bar{\lambda} + 2\mu}\right) - (\bar{\lambda} + \mu) + (\bar{\lambda} + \mu)\left(\frac{\bar{\lambda} + \mu}{\bar{\lambda} + 2\mu}\right)\right]}_{=0}G_{i,jikk} + \delta(\boldsymbol{\xi}, \mathbf{x})P_j = 0$$

Thus,

$$\mu G_{j,iikk} + \delta(\boldsymbol{\xi}, \mathbf{x})P_j = 0 \tag{20}$$

Equations (20) can be transformed into a set of typical equations for scalar potential problems, by defining a vector F_i as the Laplacian of the Galerkin vector, i.e.,

$$F_j = G_{j,ii} \tag{21}$$

Substituting equation (21) into (20) gives

$$F_{j,kk} + \frac{1}{\mu}\delta(\boldsymbol{\xi}, \mathbf{x})P_j = 0 \tag{22}$$

Consider now a sub-domain Ω', delimited by Γ', that encloses the source point of load application, $\boldsymbol{\xi}$, whereas $\boldsymbol{\xi} \notin \Gamma'$, as shown in Figure 4.
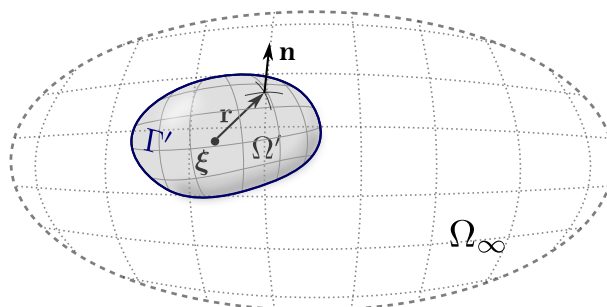
Figure 4: Sub-domain Ω' enclosing the source point in the Kelvin fundamental problem

Integrating equation (22) in this sob-domain,

$$\int_{\Omega'} F_{j,kk}d\Omega = -\frac{P_j}{\mu}\int_{\Omega'}\delta(\boldsymbol{\xi}, \mathbf{x})d\Omega = -\frac{P_j}{\mu} \quad \Rightarrow \quad \oint_{\Gamma'} F_{j,k}n_k d\Gamma = -\frac{P_j}{\mu} \tag{23}$$

where equation (16) was applied and the integral at the left-hand side was transformed from Ω' to Γ' using the Divergence Theorem. In equation (23), n_k refer to the components of the unit normal vector on Γ', pointing outside to Ω'.

Note that equations (18) to (23) are valid for three dimensional and plane state problems, considering the appropriate definition of $\bar{\lambda}$ from equation (11) and that indexes vary only from 1 to 2. For convenience, in the next two subsections, each case is separately treated.

2.2.1   Three dimensional domains

For three dimensional domains, it is convenient to particularize Ω' by a sphere centred on the source point. Thus, defining an spherical coordinate system, $\{\hat{\mathbf{e}}_r, \hat{\mathbf{e}}_\theta, \hat{\mathbf{e}}_\phi\}$, with its origin at $\boldsymbol{\xi}$, the gradient of F_i can be written as

$$F_{j,k} \equiv F_{j,r}\hat{\mathbf{e}}_r + \frac{1}{r}F_{j,\theta}\hat{\mathbf{e}}_\theta + \frac{1}{r(\sin\theta)}F_{j,\phi}\hat{\mathbf{e}}_\phi \tag{24}$$

Noting that $\hat{\mathbf{e}}_r \equiv \mathbf{n}$, in such a way that $\hat{\mathbf{e}}_\theta \cdot \mathbf{n} = \hat{\mathbf{e}}_\phi \cdot \mathbf{n} = 0$, it is straightforward to conclude that the last two parcels of equation (24) result in null values when applied to equation (23). Thus,

$$\oint_{\Gamma'} F_{j,k}n_k d\Gamma = \int_0^{2\pi}\int_0^\pi F_{j,r}r^2(\sin\theta)d\phi d\theta = -\frac{P_j}{\mu} \quad \Rightarrow \quad F_{j,r} = -\frac{P_j}{4\pi\mu r^2}$$

Integrating this last result,

$$F_j = \frac{P_j}{4\pi\mu r} \tag{25}$$

It should be noted now that the sphere Ω' has been defined with an arbitrary size. Therefore, the radius r in the equation (25) can be interpreted as the distance between the source point, $\boldsymbol{\xi}$, and any field point, $\mathbf{x}$. Thus, one might write

$$r \equiv r(\boldsymbol{\xi}, \mathbf{x}) \tag{26}$$

for which the following properties are valid:

$$r_i = x_i - \xi_i \tag{27a}$$

$$r = (r_i r_i)^{1/2} \tag{27b}$$

$$r_{,i} \equiv r_{,i}\big|_{\mathbf{x}} = \frac{\partial r}{\partial x_i} = \frac{\partial r}{\partial r_j}\frac{\partial r_j}{\partial x_i} = \frac{r_j}{r}\delta_{ij} = \frac{r_i}{r} \tag{27c}$$

$$r_{,ij} \equiv r_{,ij}\big|_{\mathbf{x}} = \left(\frac{r_i}{r}\right)_{,j} = \frac{r_{i,j}}{r} - \frac{r_i}{r^2}r_{,j} = \frac{\delta_{ij}}{r} - \frac{r_{,i}\,r_{,j}}{r} \tag{27d}$$

Applying now equation (25) to (21),

$$G_{j,ii} = \frac{P_j}{4\pi\mu r} \tag{28}$$

and considering the radial symmetry of the Kelvin fundamental problem around $\boldsymbol{\xi}$, i.e., $G_i \equiv G_i(r)$ for the spherical coordinate system, it is possible to write

$$G_{j,ii} = \left(\frac{\partial G_j}{\partial r}r_{,i}\right)_{,i} = r_{,ii}\frac{\partial G_j}{\partial r} + \frac{\partial^2 G_j}{\partial r^2}\underbrace{(r_{,i}\,r_{,i})}_{=1} = r_{,ii}\frac{\partial G_j}{\partial r} + \frac{\partial^2 G_j}{\partial r^2} \tag{29}$$

Thus, from equations (27d), (28) and (29), the following set of non-homogeneous second order ordinary differential equations for the Galerkin vector components are obtained:

$$\frac{\partial^2 G_j}{\partial r^2} + \frac{2}{r}\frac{\partial G_j}{\partial r} = \frac{P_j}{4\pi\mu r} \tag{30}$$

Particular solutions for these equations are

$$G_j = \frac{P_j}{8\pi\mu}r \tag{31}$$

Finally, replacing equation (31) into (19) and taking into account the equations (11) and (27d), a displacement field is obtained, which is the solution of the problem represented by equation (18), i.e.,

$$u_j^*(\boldsymbol{\xi}, \mathbf{x}) = \frac{1}{16\pi\mu(1-\nu)r}[(3-4\nu)\delta_{ij} + r_{,i}\, r_{,j}\,]P_i \tag{32}$$

Equation (32) is the Kelvin fundamental solution to three dimensional problems. It should be noted that this equation gives the displacement component in direction j, at a field point, $\mathbf{x}$, caused by a concentrated force, given by unit components in each direction (once summation is implicit by repetition of i index and $P_i = 1$; $i = 1, 2, 3$) and applied at the source point, $\boldsymbol{\xi}$. Taking each component of P_i separately, we can write:

$$u_{ij}^*(\boldsymbol{\xi}, \mathbf{x}) = \frac{1}{16\pi\mu(1-\nu)r}[(3-4\nu)\delta_{ij} + r_{,i}\, r_{,j}\,] \tag{33}$$

Thus, tensor $u_{ij}^*(\boldsymbol{\xi}, \mathbf{x})$ represents the displacement in the direction j, at a field point, $\mathbf{x}$, caused by a unit concentrated force at a source point, $\boldsymbol{\xi}$, applied in the direction i.

2.2.2   Plane state problems

A similar idea might be adopted for two dimensional elastic domains, noting that now the indexes vary between 1 and 2 and that Γ' is particularized by a circumference centred on $\boldsymbol{\xi}$. Considering also a polar system of coordinates with origin at the source point, it is possible to write the gradient of F_i as

$$F_{j,k} \equiv F_{j,r}\hat{\mathbf{e}}_r + \frac{1}{r}F_{j,\theta}\hat{\mathbf{e}}_\theta \tag{34}$$

Thus, applying equation (34) to (23),

$$\oint_{\Gamma'} F_{j,k}n_k d\Gamma = \int_0^{2\pi} F_{j,r}rd\theta = -\frac{P_j}{\mu} \quad \Rightarrow \quad F_{j,r} = -\frac{P_j}{2\pi\mu r}$$

which leads to

$$F_j = -\frac{P_j}{2\pi\mu}\ln(r) \tag{35}$$

As in the three dimensional case, $r \equiv r(\boldsymbol{\xi}, \mathbf{x})$ is the distance of any field point, $\mathbf{x}$, from $\boldsymbol{\xi}$, in order that equations (26) and (27) remain valid for plane problems.

From equations (21) and (35),

$$G_{j,ii} = -\frac{P_j}{2\pi\mu}\ln(r) \tag{36}$$

Considering again the radial symmetry of the fundamental problem, equation (29) is also valid for two dimensional domains and, together with equations (27d) and (36), the following set of equations is obtained:

$$\frac{\partial^2 G_j}{\partial r^2} + \frac{1}{r}\frac{\partial G_j}{\partial r} = -\frac{P_j}{2\pi\mu}\ln(r) \tag{37}$$

which have as particular solutions,

$$G_j = \frac{P_j}{8\pi\mu}r^2 - \frac{P_j}{8\pi\mu}r^2\ln(r) \tag{38}$$

Applying equation (38) to (19) – note that the first parcel of equation (38) leads to rigid body motion, i.e., vanishes in this process – and taking into account equations (11) and (27d), the fundamental displacements can be written as

$$u_j^*(\boldsymbol{\xi}, \mathbf{x}) = \frac{-1}{8\pi\mu(1-\bar{\nu})}[(3-4\bar{\nu})\ln(r)\delta_{ij} - r_{,i}\, r_{,j}\,]P_i \tag{39}$$

Taking again each component separately,

$$u_{ij}^*(\boldsymbol{\xi}, \mathbf{x}) = \frac{-1}{8\pi\mu(1 - \bar{\nu})}[(3 - 4\bar{\nu})\ln(r)\delta_{ij} - r_{,i}\,r_{,j}] \tag{40}$$

The same physical interpretation of this second order tensor, given for the three dimensional case, remains valid here.

2.3   Non Linear Constitutive Modeling

Equations presented in section 2.1 are restricted to conservative behaviour of elastic bodies. If any energy dissipation mechanism takes place, such relations needs to be reviewed. For example, the constitutive relation depicted in equation (9) needs to be rewritten by its rate form (since, when energy is dissipated, stress-strain relation becomes dependent from the load history) and the strain field is commonly decomposed into two parts, one elastic and other associated to the dissipative mechanism.

In this section, two classical approaches to represent the physically non linear behaviour of materials under non conservative loading are described, namely elastoplastic (EP) and elastic-degrading (ED) constitutive models, are described. Despite its differences, such approaches can be presented in a unified theoretical framework as shown in Peixoto et al. [2016]. This idea is used here.

Figure 5 shows the difference between ED and EP constitutive models. In the first case, if the body is unloaded after some energy dissipation, the stress-strain relation follows a secant trajectory returning to the initial unstrained configuration. Elastoplastic materials, however, presents a loading-unloading curve which is a straight segment with the same initial elastic slope, keeping a residual strain even after the total unload. It is clear that both are simplifications of the actual behaviour observed in experiments as shown in Figure 5-c, where both stiffness degradation and irreversible plastic strain take place.
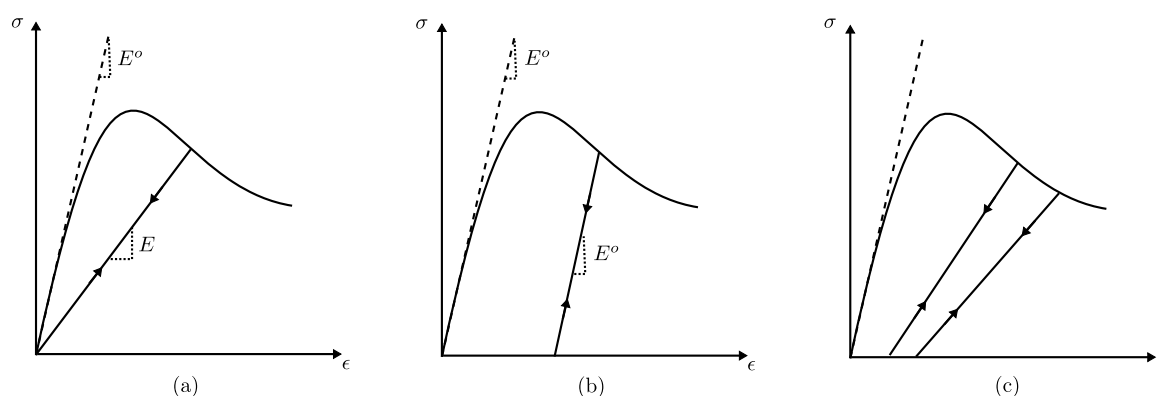
Figure 5: Non linear constitutive models: (a) Elastic-degrading material, (b) Elasto-plastic material, (c) Realistic behaviour

As will be seen in the next sections, the non linear solution algorithm only requires, during each iteration, the local evaluation of two parameters: the stresses, σ_{ij}, and the tangential stiffness operator, C_{ijkl}^t, relating incremental stresses and strains. How they are obtained is briefly described next. It is shown that the incremental governing equations have the same form in both constitutive models classes, regarding as the only difference the meaning of the inelastic strains and the presence of the secant stiffness tensor, C_{ijkl}^s, in ED equations, in place of the initial elastic stiffness tensor, C_{ijkl}, in EP equations.

2.3.1   Elastoplastic models

As a secant relationship is not defined a priori for EP models (see figure 5-b), a trial-return algorithm is required for numerical evaluation of the stress tensor as described, for example, in Simo and Hughes [1998].

Assuming a loading function that can be expressed as $F(\sigma_{ij}, \mathbf{q})$, where $\mathbf{q}$ is a vector of internal variables – which can be tensors of different orders – determining the current configuration of the elastic domain, the following rate equations can be defined:

$$\dot{\sigma}_{ij} = C_{ijkl}(\dot{\epsilon}_{kl} - \dot{\epsilon}_{kl}^{p}) \tag{41}$$

$$\dot{\epsilon}_{kl}^{p} = \dot{\lambda} m_{kl} \tag{42}$$

$$\dot{\mathbf{q}} = -\dot{\lambda}\mathbf{h} \tag{43}$$

$$\dot{F} = \left.\frac{\partial F}{\partial \sigma_{ij}}\right|_{\mathbf{q}} \dot{\sigma}_{ij} + \left.\frac{\partial F}{\partial \mathbf{q}}\right|_{\boldsymbol{\sigma}} : \dot{\mathbf{q}} = 0 \tag{44}$$

where equation (41) is the rate form of stress-strain relationship for elastoplastic materials, in which ϵ_{kl}^{p} is the plastic strain tensor, whose rate magnitude is defined by the plastic multiplier, $\dot{\lambda}$, and m_{kl} specifies its rate direction. The symbol (:) in the second term of equation (44) means tensors contraction and were used in function of the unspecified orders of internal variables in $\mathbf{q}$.

Equation (42) is called as plastic flow rule, while equation (43) is called as hardening-softening law and represents the evolution of the hardening-softening internal variables. Equation (44) is the linearised form of the consistency condition, meaning that during plastic loading the current stress state always remains on the current loading surface, commonly called as yield surface in elastoplastic theory.

Considering the set of internal variables, $\mathbf{q}$, as functions of the plastic strain, such as $\dot{\mathbf{q}} = (\partial \mathbf{q}/\partial \epsilon_{kl}^{p})\dot{\epsilon}_{kl}^{p}$, and using equation (42), one can rewrite equation (44) as

$$n_{ij}\dot{\sigma}_{ij} - H\dot{\lambda} = 0 \tag{45}$$

where,

$$\begin{cases} n_{ij} = \left.\dfrac{\partial F}{\partial \sigma_{ij}}\right|_{\lambda} \\[4mm] H = -\left.\dfrac{\partial F}{\partial \lambda}\right|_{\boldsymbol{\sigma}} = -\left.\dfrac{\partial F}{\partial \mathbf{q}}\right|_{\boldsymbol{\sigma}} : \dfrac{\partial \mathbf{q}}{\partial \epsilon_{kl}^{p}} m_{kl} \end{cases} \tag{46}$$

The second-order tensor n_{ij}, involving derivatives of F for constant plastic strain ($\dot{\lambda} = \dot{\epsilon}_{kl}^{p} = 0$), has the geometrical meaning of the direction normal to the current loading surface, $F = 0$, in stress space, while the derivatives for constant stress, give the hardening-softening modulus H. For positive values of H (hardening), the loading surface expands in the stress space and, for negative values (softening), the loading surface contracts during plastic loading. If $H = 0$ (perfect plasticity), the loading surface is static. No kinematic effects, i.e., translation of loading surface, are considered here. The model is called associative if n_{ij} and m_{ij} are fully proportional. Loading/unloading conditions are determined by $\dot{\lambda} \geq 0$; $F \leq 0$; $\dot{\lambda}F = 0$ and $\dot{\lambda}\dot{F} = 0$.

Now, applying equations (41) and (42) to equation (45), the following expression for the plastic multiplier is obtained:

$$\dot{\lambda} = \frac{n_{ij}C_{ijkl}\dot{\epsilon}_{kl}}{H + n_{pq}C_{pqrs}m_{rs}} \tag{47}$$

Finally, the tangential stiffness operator is obtained by introducing equations (47) and (42) into equation (41), i.e.,

$$\dot{\sigma}_{ij} = C^t_{ijkl}\dot{\epsilon}_{kl}, \qquad C^t_{ijkl} = C_{ijkl} - \frac{C_{ijab}m_{ab}n_{cd}C_{cdkl}}{H + n_{pq}C_{pqrs}m_{rs}} \tag{48}$$

Equations (41) to 48 were defined in a stress-based formulation. Alternatively, a strain-based formulation can be developed beginning with a loading function defined in strain space, such as $\bar{F}(\epsilon_{ij}, \boldsymbol{\alpha})$, as detailed in Carol et al. [1994], and where $\boldsymbol{\alpha}$ represents the strain-like internal variables, thermodynamically conjugated to $\mathbf{q}$. Here, we are only interested in the result for the tangential stiffness operator, equivalent to equation (48), i.e.,

$$C^t_{ijkl} = C_{ijkl} + \frac{1}{\bar{H}}\bar{m}_{ij}\bar{n}_{kl} \tag{49}$$

where,

$$\begin{cases} \bar{m}_{ij} = -C_{ijkl}m_{kl} \\\\ \bar{n}_{ij} = C_{ijkl}n_{kl} \\\\ \bar{H} = H + n_{ij}C_{ijkl}m_{kl} \end{cases} \tag{50}$$

The equations presented in this subsection are particularized for the elastoplastic von Mises associative isotropic model in Appendix A.

2.3.2   Elastic-degrading models

In ED models, full unloading always leads to the original unstrained configuration, i.e., zero stresses with no permanent strains (see figure 5a), in opposition to classical EP models. For that reason, the next total stress-strain relationship can be formulated for ED models:

$$\sigma_{ij} = C^s_{ijkl}\epsilon_{kl} \tag{51}$$

where C^s_{ijkl} is the current secant stiffness tensor.

Taking the time derivative of equation (51), an expression for incremental stress can be obtained, i.e.,

$$\dot{\sigma}_{ij} = C^s_{ijkl}\dot{\epsilon}_{kl} + \dot{C}^s_{ijkl}\epsilon_{kl} \tag{52}$$

Each parcel of equation (52) is represented in the simplified uni-axial diagram of Figure 6, from which, one can conclude that

$$\dot{C}^s_{ijkl}\epsilon_{kl} = -C^s_{ijkl}\dot{\epsilon}^d_{kl} \tag{53}$$

where ϵ^d_{kl} is called as degrading strain, representing the inelastic part of total strain. It is important to note here that degrading strain of an ED model is intrinsically associated with the degradation of the secant stiffness.

Applying equation (53) to (52), the following result is obtained

$$\dot{\sigma}_{ij} = C^s_{ijkl}(\dot{\epsilon}_{kl} - \dot{\epsilon}^d_{kl}) \tag{54}$$

Now, it is convenient to define a degradation rule for the secant stiffness or, considering the stress-based formulation, for the secant compliance, i.e.,

$$\dot{C}^{s,-1}_{ijkl} = \dot{\lambda}M_{ijkl} \tag{55}$$
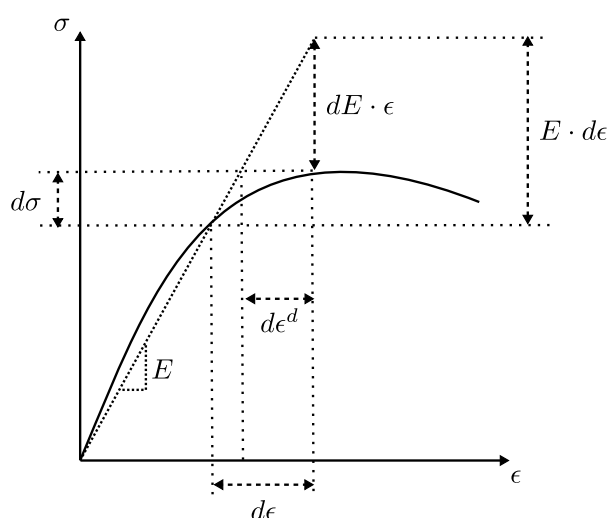
Figure 6: Representation of incremental stress and strain for elastic degrading models

where, in this new context, the multiplier, $\dot{\lambda}$, defines the magnitude and M_{ijkl}, the direction, of the rate of change of the secant compliance tensor.

For the unified framework proposed, it is necessary to write an evolution law for the degrading strains, in a similar way to the plastic flow rule of equation (42). This can be done by first taking the time derivative of the inverse of equation (51), substituting the incremental stresses by the right side of equation (54), to obtain

$$\dot{\epsilon}^d_{kl} = \dot{C}^{s,-1}_{klrs} \sigma_{rs} \tag{56}$$

and then introducing equation (55) to result in

$$\dot{\epsilon}^d_{kl} = \dot{\lambda} m_{kl}, \qquad m_{kl} = M_{klrs} \sigma_{rs} \tag{57}$$

Concepts of loading function and loading surface can be applied for ED models in a very similar manner as EP models, in such a way that the following expression for linearised consistency condition can be defined:

$$\dot{F}(\sigma_{ij}, \mathbf{q}) = n_{ij} \dot{\sigma}_{ij} - H\dot{\lambda} = 0 \quad \text{with} \quad n_{ij} = \left.\frac{\partial F}{\partial \sigma_{ij}}\right|_\lambda \quad \text{and} \quad H = -\left.\frac{\partial F}{\partial \lambda}\right|_\sigma = -\left.\frac{\partial F}{\partial \mathbf{q}}\right|_\sigma : \frac{\partial \mathbf{q}}{\partial \epsilon^d_{kl}} m_{kl} \tag{58}$$

where, in the ED context, the internal variables defines the current value of the compliance tensor, i.e., $C^{s,-1}_{ijkl} \equiv C^{s,-1}_{ijkl}(C^{-1}_{ijkl}, \mathbf{q})$, and a hardening-softening law, similar to equation (43), is postulated to describe the evolution of $\mathbf{q}$. Thus,

$$\dot{C}^{s,-1}_{ijkl} = \frac{\partial C^{s,-1}_{ijkl}}{\partial \mathbf{q}} : \dot{\mathbf{q}} = -\dot{\lambda}\left[\frac{\partial C^{s,-1}_{ijkl}}{\partial \mathbf{q}} : \mathbf{h}\right] \tag{59}$$

Comparing equations (55) and (59), one can conclude that

$$M_{ijkl} = -\frac{\partial C^{s,-1}_{ijkl}}{\partial \mathbf{q}} : \mathbf{h} \tag{60}$$

Now, noting the similarities between equations (41) to (46) and equations (54), (57) and (58), the same algebraic manipulations described in the last subsection can be repeated here, generating

expressions for the degrading multiplier and tangent stiffness, analogous to equations (47) and (48), i.e.,

$$\dot{\lambda} = \frac{n_{ij} C^s_{ijkl} \dot{\epsilon}_{kl}}{H + n_{pq} C^s_{pqrs} m_{rs}} \tag{61}$$

$$\dot{\sigma}_{ij} = C^t_{ijkl} \dot{\epsilon}_{kl}, \qquad C^t_{ijkl} = C^s_{ijkl} - \frac{C^s_{ijab} m_{ab} n_{cd} C^s_{cdkl}}{H + n_{pq} C^s_{pqrs} m_{rs}} \tag{62}$$

In the same way as mentioned for EP models, equations (51) to (62) were developed in a stress-based formulation. If this procedure is repeated beginning with a loading function defined in the strain space, $\bar{F}(\epsilon_{ij}, \boldsymbol{\alpha})$, the tangential stiffness operator takes the form:

$$C^t_{ijkl} = C^s_{ijkl} + \frac{1}{\bar{H}} \bar{m}_{ij} \bar{n}_{kl} \tag{63}$$

where,

$$\begin{cases} \bar{m}_{ij} = \bar{M}_{ijkl} \epsilon_{kl} = -C^s_{ijkl} m_{kl} \\[2mm] \bar{M}_{ijkl} = \dfrac{\partial C^s_{ijkl}}{\partial \boldsymbol{\alpha}} : \dfrac{\partial \boldsymbol{\alpha}}{\partial \lambda} = -\dfrac{\partial C^s_{ijkl}}{\partial \boldsymbol{\alpha}} : \bar{\mathbf{h}} \\[2mm] \bar{n}_{ij} = \dfrac{\partial \bar{F}}{\partial \epsilon_{ij}} \bigg|_{\lambda} = C^s_{ijkl} n_{kl} \\[2mm] \bar{H} = -\dfrac{\partial \bar{F}}{\partial \lambda} \bigg|_{\epsilon} = H + n_{ij} C^s_{ijkl} m_{kl} \end{cases} \tag{64}$$

The equations presented in this subsection are particularized for isotropic damage constitutive models in Appendix A.

Comparing equations (41), (48), (49) and (50) with equations (54), (62), (63) and (64), it is clear that the only differences are related to the definition of the inelastic part of total strains, ϵ^p_{ij} to EP models and ϵ^d_{ij} to ED models, and the presence of the secant stiffness tensor, C^s_{ijkl}, in ED equations, in place of the initial linear elastic constitutive tensor, C_{ijkl}, present in EP equations. For that reason, in a computational point of view, a large range of different constitutive models can be implemented in a completely independent way from the solution strategy described next. It is only necessary to appropriate define expressions for $\bar{n}_{ij}$, $\bar{m}_{ij}$ and $\bar{H}$, beyond a correct evaluation of stresses from a known strain state.

3   Boundary Integral Equations with Initial Fields

To develop the integral equations which constitute the basis of the BEM for inelastic solid mechanics, it is important to note that any point in a non linear equilibrium path can be defined, independently of the constitutive model, as a combination of two linear parts.

Consider, for example, the uni-axial equilibrium paths presented in Figure 7. In both cases, for an arbitrary strain state ϵ, the actual stress state which is given by a non linear constitutive model is represented by $\sigma(\epsilon)$. Additionally, a stress state evaluated using a purely linear elastic relationship for the same arbitrary strain state is given by $E^o \epsilon$, where E^o represents the initial elasticity modulus. Also, in both cases, the residual quantities ϵ^o and σ^o are defined as the difference between the actual and the purely elastic states. As is possible to note in Figure 7, and generalizing to a multi-axial solid domain, the total strain ϵ_{ij} and the actual stress $\sigma_{ij}(\epsilon_{ij})$ can be given by

$$\epsilon_{ij} = \epsilon^e_{ij} + \epsilon^o_{ij} \tag{65}$$
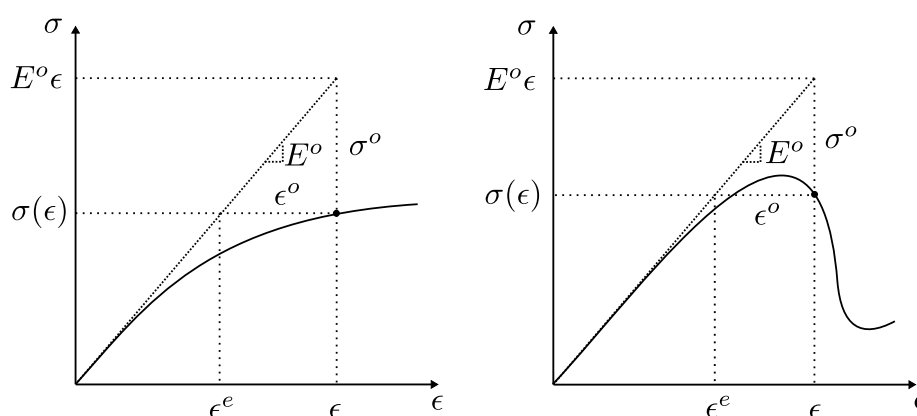
Figure 7: Relations between stress and strain for two distinct equilibrium paths

$$\sigma_{ij}(\epsilon_{ij}) = C_{ijkl}(\epsilon_{kl} - \epsilon_{kl}^o) = C_{ijkl}\epsilon_{kl} - \sigma_{ij}^o \tag{66}$$

Thus, the non linear integral equations in the BEM context are deduced considering the existence of an initial strain field ϵ_{ij}^o, or a corresponding initial stress field $\sigma_{ij}^o = C_{ijkl}\epsilon_{kl}^o$. For constitutive models based on plasticity theory, the initial strain hold the same value as the irreversible plastic strain ϵ_{ij}^p (see equation 41). However, these terms should not be the same when aiming for a more comprehensive non linear application of the method. For example, in the class of isotropic damage models described in Appendix A, where the secant tensor is given by $C_{ijkl}^s = (1-D)C_{ijkl}$ (see equation 244), the correspondence $\epsilon_{ij}^o = D\epsilon_{ij}$ can be verified from equation (51).

Such mentioned integral equations, that are relevant for physically non linear formulations of the BEM, can be obtained from a physical approach based on the Betti's Reciprocity Theorem or by an entirely numerical approach based on a generalization of the Method of Weighted Residuals. In the first case, the Kelvin's fundamental problem, described in Section 2.2, is used as auxiliary field, while in the second case, its solution is adopted as weighting function. A detailed derivation of these equations are easily found in many BEM textbooks, among which can be cited Telles [1983], Brebbia et al. [1984], Aliabadi [2002], Gao and Davies [2002]. Thus, such derivations are omitted here and only the final results (completely enough to implementation purposes) are presented.

Consider a solid domain Ω, delimited by boundary Γ, as previously illustrated in Figure 1, with an initial strain field distribution, ϵ_{ij}^o. The first relevant integral equation is the Somigliana's Identity, which gives the displacement vector at an internal point, $\boldsymbol{\xi}$ ($\boldsymbol{\xi} \in \Omega$ but $\boldsymbol{\xi} \notin \Gamma$), i.e.,

$$u_i(\boldsymbol{\xi}) = \int_\Gamma u_{ij}^*(\boldsymbol{\xi},\mathbf{x})t_j(\mathbf{x})\,d\Gamma - \int_\Gamma t_{ij}^*(\boldsymbol{\xi},\mathbf{x})u_j(\mathbf{x})\,d\Gamma + \int_\Omega u_{ij}^*(\boldsymbol{\xi},\mathbf{x})b_j(\mathbf{x})\,d\Omega + \int_\Omega \sigma_{ijk}^*(\boldsymbol{\xi},\mathbf{x})\epsilon_{jk}^o(\mathbf{x})\,d\Omega \tag{67}$$

where $u_{ij}^*(\boldsymbol{\xi},\mathbf{x})$ refer to Kelvin's fundamental displacements, given in equations (33) and (40), respectively for three and two dimensional cases. In the same way, $t_{ij}^*(\boldsymbol{\xi},\mathbf{x})$ represents the traction field on Γ and $\sigma_{ijk}^*(\boldsymbol{\xi},\mathbf{x})$ is the Cauchy stress at any point of Ω, both associated to the Kelvin's fundamental solution. Remember that the first index of these tensors (i) refer to the direction of the concentrated force that act on the source point $\boldsymbol{\xi}$, while the other indexes (j or jk) designate the field components (displacement, traction or stress) that emerge at a field point $\mathbf{x}$. Expressions for t_{ij}^* and σ_{ijk}^* are presented further in section 3.1.

If the collocation point is taken as a boundary point, i.e., $\boldsymbol{\xi} \in \Gamma$, the fundamental solution second-order tensors introduce a weakly and a strongly singular character, respectively for the first and second integrals in equation (67). Similarly, the kernel of the domain integral involving the initial strain field becomes weakly singular. Thus, a correct deduction of the boundary dis-

placement integral equation requires, in this case, a limit process considering a radius of exclusion around the singular point, leading to the following expression:

$$c_{ij}(\boldsymbol{\xi})u_j(\boldsymbol{\xi}) = \int_\Gamma u_{ij}^*(\boldsymbol{\xi},\mathbf{x})t_j(\mathbf{x})\,d\Gamma - \fint_\Gamma t_{ij}^*(\boldsymbol{\xi},\mathbf{x})u_j(\mathbf{x})\,d\Gamma + \int_\Omega u_{ij}^*(\boldsymbol{\xi},\mathbf{x})b_j(\mathbf{x})\,d\Omega + \int_\Omega \sigma_{ijk}^*(\boldsymbol{\xi},\mathbf{x})\epsilon_{jk}^o(\mathbf{x})\,d\Omega$$

(68)

where $c_{ij}(\boldsymbol{\xi})$ is a function of the boundary's geometry around the collocation point and the elastic properties of the material. Explicit forms for this free term is also presented further in this section.

The weakly singular integrals can be evaluated as improper integrals, since they are convergent in the conventional Riemann interpretation. Numerical solutions of these integrals, however, require special methods (other than standard Gauss-Legedre quadrature) to guarantee its accuracy. On the other hand, strongly singular integrals are bounded only in Cauchy Principal Value sense, as indicated by the crossed integral symbol, requiring more rigorous numerical methods in its evaluation. Such methods are always based in some kind of singularity elimination strategy.

Furthermore, internal strains can be obtained by taking the symmetric part of the gradient of equation (67), related to the source point (see equation 7, which is also valid for the total strain from equation 65), resulting in

$$\epsilon_{ij}(\boldsymbol{\xi}) = \int_\Gamma u_{ijk}^*(\boldsymbol{\xi},\mathbf{x})t_k(\mathbf{x})\,d\Gamma - \int_\Gamma t_{ijk}^*(\boldsymbol{\xi},\mathbf{x})u_k(\mathbf{x})\,d\Gamma + \int_\Omega u_{ijk}^*(\boldsymbol{\xi},\mathbf{x})b_k(\mathbf{x})\,d\Gamma$$
$$+ \fint_\Omega \sigma_{ijkl}^*(\boldsymbol{\xi},\mathbf{x})\epsilon_{kl}^o(\mathbf{x})\,d\Omega + F_{ijkl}^{\epsilon\epsilon}\epsilon_{kl}^o(\boldsymbol{\xi})$$

(69)

where the last domain integral have a strongly singular kernel when the collocation and field points coincide and, again, its evaluation exists only in the CPV sense. Tensors u_{ijk}^*, t_{ijk}^* and σ_{ijkl}^* are respectively obtained by taking the gradients of fundamental solutions u_{ij}^*, t_{ij}^* and σ_{ijk}^*, while $F_{ijkl}^{\epsilon\epsilon}$ is a free term, which existence was firstly verified by Bui [1978]. Explicit expressions for these parameters are also shown next.

3.1 Fields derived from Kelvin Fundamental Solution

From equations (33) and (40) – the Kelvin fundamental displacements, respectively, for three-dimensional and plane cases –, it is possible to obtain the associated strain and stress fields, at a given point $\mathbf{x}$, using equations (7) and (9). Moreover, the traction field on a surface oriented by a normal vector $\mathbf{n}$ at $\mathbf{x}$ can be obtained from equation (1). Explicitly, the following results are achieved.

Three-dimensional problems:

$$\epsilon_{ijk}^*(\boldsymbol{\xi},\mathbf{x}) \equiv \frac{1}{2}\left[u_{ij,k}^*\big|_{\mathbf{x}} + u_{ik,j}^*\big|_{\mathbf{x}}\right] = \frac{-1}{16\pi\mu(1-\nu)r^2}[(1-2\nu)(\delta_{ik}r_{,j} + \delta_{ij}r_{,k}) - \delta_{jk}r_{,i} + 3r_{,i}\,r_{,j}\,r_{,k}]$$

(70)

$$\sigma_{ijk}^*(\boldsymbol{\xi},\mathbf{x}) \equiv C_{jklm}\epsilon_{ilm}^*(\boldsymbol{\xi},\mathbf{x}) = \frac{-1}{8\pi(1-\nu)r^2}[(1-2\nu)(-\delta_{jk}r_{,i} + \delta_{ik}r_{,j} + \delta_{ij}r_{,k}) + 3r_{,i}\,r_{,j}\,r_{,k}]$$

(71)

$$t_{ij}^*(\boldsymbol{\xi},\mathbf{x}) \equiv \sigma_{ijk}^*(\boldsymbol{\xi},\mathbf{x})n_k(\mathbf{x}) = \frac{-1}{8\pi(1-\nu)r^2}\left\{\frac{\partial r}{\partial n}[(1-2\nu)\delta_{ij} + 3r_{,i}\,r_{,j}] - (1-2\nu)(n_jr_{,i} - n_ir_{,j})\right\}$$

(72)

Plane state problems:

$$\epsilon_{ijk}^*(\boldsymbol{\xi},\mathbf{x}) \equiv \frac{1}{2}\left[u_{ij,k}^*\big|_{\mathbf{x}} + u_{ik,j}^*\big|_{\mathbf{x}}\right] = \frac{-1}{8\pi\mu(1-\bar{\nu})r}[(1-2\bar{\nu})(\delta_{ik}r_{,j} + \delta_{ij}r_{,k}) - \delta_{jk}r_{,i} + 2r_{,i}\,r_{,j}\,r_{,k}]$$

(73)

$$\sigma^*_{ijk}(\boldsymbol{\xi}, \mathbf{x}) \equiv C_{jklm}\epsilon^*_{ilm}(\boldsymbol{\xi}, \mathbf{x}) = \frac{-1}{4\pi(1-\bar{\nu})r}[(1-2\bar{\nu})(-\delta_{jk}r_{,i}+\delta_{ik}r_{,j}+\delta_{ij}r_{,k})+2r_{,i}\,r_{,j}\,r_{,k}]$$

(74)

$$t^*_{ij}(\boldsymbol{\xi}, \mathbf{x}) \equiv \sigma^*_{ijk}(\boldsymbol{\xi}, \mathbf{x})n_k(\mathbf{x}) = \frac{-1}{4\pi(1-\bar{\nu})r}\left\{\frac{\partial r}{\partial n}[(1-2\bar{\nu})\delta_{ij}+2r_{,i}\,r_{,j}]-(1-2\bar{\nu})(n_j r_{,i}-n_i r_{,j})\right\}$$

(75)

In equations (72) and (75), the following result is valid:

$$\frac{\partial r}{\partial n} = \frac{r_i}{r}n_i = r_{,i}\,n_i$$

(76)

Note that results from equations (71) and (72) – or (74) and (75) – must be used in integral equations (67) and (68). Particularly for this second equation, the free term, $c_{ij}(\boldsymbol{\xi})$, still needs to be presented. Its deduction is intrinsically associated to the mentioned process of taking an augmented region around the source point (which is located at boundary Γ in this case), in order that only the final results are presented here, using Figure 8.

$$c_{ij}(\boldsymbol{\xi}) = \delta_{ij} + \lim_{\varepsilon \to 0}\int_{\bar{\Gamma}_\varepsilon} t^*_{ij}(\boldsymbol{\xi}, \mathbf{x})d\Gamma$$
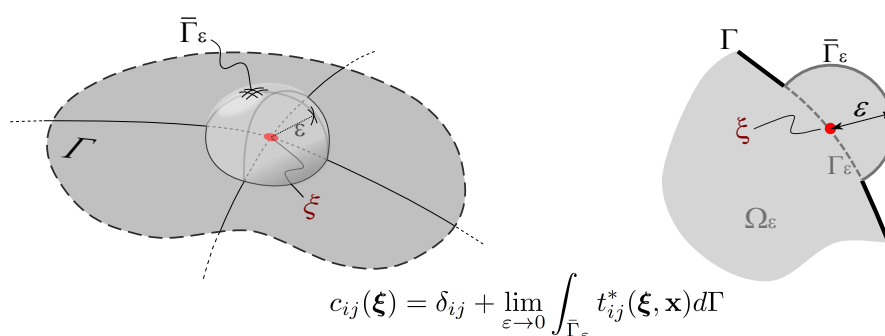
Figure 8: Expression for $c_{ij}(\boldsymbol{\xi})$ and the augmented region

Equation (69), on the other hand, is obtained by taking derivatives of equation (67), associated to the source point, $\boldsymbol{\xi}$. Thus, the parameters that appear in its integrals kernels are given by the next expressions.

Three-dimensional problems:

$$u^*_{ijk}(\boldsymbol{\xi}, \mathbf{x}) \equiv \frac{1}{2}\left[u^*_{ik,j}\big|_{\boldsymbol{\xi}}+u^*_{jk,i}\big|_{\boldsymbol{\xi}}\right] = \frac{1}{16\pi\mu(1-\nu)r^2}[(1-2\nu)(\delta_{ik}r_{,j}+\delta_{jk}r_{,i})-\delta_{ij}r_{,k}+3r_{,i}\,r_{,j}\,r_{,k}]$$

(77)

$$t^*_{ijk}(\boldsymbol{\xi}, \mathbf{x}) \equiv \frac{1}{2}\left[t^*_{ik,j}\big|_{\boldsymbol{\xi}}+t^*_{jk,i}\big|_{\boldsymbol{\xi}}\right] = \frac{1}{8\pi(1-\nu)r^3}\Big\{(1-2\nu)[n_i\delta_{jk}+n_j\delta_{ik}-n_k\delta_{ij}+3r_{,i}\,r_{,j}\,n_k]$$
$$+3\frac{\partial r}{\partial n}[\nu(r_{,j}\,\delta_{ik}+r_{,i}\,\delta_{jk})+r_{,k}\,\delta_{ij}-5r_{,i}\,r_{,j}\,r_{,k}]$$
$$+3\nu(n_j r_{,i}\,r_{,k}+n_i r_{,j}\,r_{,k})\Big\}$$

(78)

$$\sigma^*_{ijkl}(\boldsymbol{\xi}, \mathbf{x}) \equiv \frac{1}{2}\left[\sigma^*_{ikl,j}\big|_{\boldsymbol{\xi}}+\sigma^*_{jkl,i}\big|_{\boldsymbol{\xi}}\right] = \frac{1}{8\pi(1-\nu)r^3}\Big\{(1-2\nu)(\delta_{ik}\delta_{jl}+\delta_{jk}\delta_{il}-\delta_{ij}\delta_{kl})$$
$$+3\nu(\delta_{il}r_{,j}\,r_{,k}+\delta_{ik}r_{,j}\,r_{,l}+\delta_{jk}r_{,i}\,r_{,l}+\delta_{jl}r_{,i}\,r_{,k})$$
$$+3[(1-2\nu)\delta_{kl}r_{,i}\,r_{,j}+\delta_{ij}r_{,k}\,r_{,l}]-15r_{,i}\,r_{,j}\,r_{,k}\,r_{,l}\Big\}$$

(79)

Plane state problems:

$$u^*_{ijk}(\boldsymbol{\xi}, \mathbf{x}) \equiv \frac{1}{2}\left[u^*_{ik,j}\big|_{\boldsymbol{\xi}} + u^*_{jk,i}\big|_{\boldsymbol{\xi}}\right] = \frac{1}{8\pi\mu(1-\bar{\nu})r}[(1-2\bar{\nu})(\delta_{ik}r,_j + \delta_{jk}r,_i) - \delta_{ij}r,_k + 2r,_i\, r,_j\, r,_k]$$

(80)

$$t^*_{ijk}(\boldsymbol{\xi}, \mathbf{x}) \equiv \frac{1}{2}\left[t^*_{ik,j}\big|_{\boldsymbol{\xi}} + t^*_{jk,i}\big|_{\boldsymbol{\xi}}\right] = \frac{1}{4\pi(1-\bar{\nu})r^2}\Big\{(1-2\bar{\nu})[n_i\delta_{jk} + n_j\delta_{ik} - n_k\delta_{ij}$$

$$+ 2r,_i\, r,_j\, n_k] + 2\frac{\partial r}{\partial n}[\bar{\nu}(r,_j\,\delta_{ik} + r,_i\,\delta_{jk}) + r,_k\,\delta_{ij}$$

(81)

$$- 4r,_i\, r,_j\, r,_k] + 2\bar{\nu}(n_j r,_i\, r,_k + n_i r,_j\, r,_k)\Big\}$$

$$\sigma^*_{ijkl}(\boldsymbol{\xi}, \mathbf{x}) \equiv \frac{1}{2}\left[\sigma^*_{ikl,j}\big|_{\boldsymbol{\xi}} + \sigma^*_{jkl,i}\big|_{\boldsymbol{\xi}}\right] = \frac{1}{4\pi(1-\bar{\nu})r^2}\Big\{(1-2\bar{\nu})(\delta_{ik}\delta_{jl} + \delta_{jk}\delta_{il} - \delta_{ij}\delta_{kl})$$

$$+ 2\bar{\nu}(\delta_{il}r,_j\, r,_k + \delta_{ik}r,_j\, r,_l + \delta_{jk}r,_i\, r,_l + \delta_{jl}r,_i\, r,_k)$$

(82)

$$+ 2[(1-2\bar{\nu})\delta_{kl}r,_i\, r,_j + \delta_{ij}r,_k\, r,_l] - 8r,_i\, r,_j\, r,_k\, r,_l\Big\}$$

In equations (77) to (82), the following results were considered:

$$r,_i\big|_{\boldsymbol{\xi}} = \frac{\partial r}{\partial \xi_i} = \frac{\partial r}{\partial r_j}\frac{\partial r_j}{\partial \xi_i} = \frac{r_j}{r}(-\delta_{ij}) = -\frac{r_i}{r} = -r,_i$$

(83a)

$$\left(r,_i\big|_{\mathbf{x}}\right),_j\big|_{\boldsymbol{\xi}} \equiv (r,_i),_j\big|_{\boldsymbol{\xi}} = \left(\frac{r_i}{r}\right),_j\Big|_{\boldsymbol{\xi}} = -\frac{\delta_{ij}}{r} + \frac{r,_i\, r,_j}{r} = -r,_{ij}$$

(83b)

Finally, the free terms $F^{\epsilon\epsilon}_{ijkl}$ are given by

$$F^{\epsilon\epsilon}_{ijkl} = \begin{cases} \dfrac{1}{15(1-\nu)}[(4-5\nu)(\delta_{ik}\delta_{jl} + \delta_{il}\delta_{jk}) - (1-5\nu)\delta_{ij}\delta_{kl}] & \text{(for 3D problems)} \\[4mm] \dfrac{1}{8(1-\bar{\nu})}[(3-4\bar{\nu})(\delta_{ik}\delta_{jl} + \delta_{il}\delta_{jk}) - (1-4\bar{\nu})\delta_{ij}\delta_{kl}] & \text{(for plane state problems)} \end{cases}$$

(84)

4 The Implicit BEM Formulation for Physically Non Linear Problems

Discrete versions of equations (67), (68) and (69), that are related to the BEM are presented in this section, followed by a re-organization of the matrices, according to the implicit formulation of the method. Moreover, the non linear solution strategy is described in detail.

The body forces, $b_i(\mathbf{x})$, are disregarded here, since it is negligible, when compared to boundary loads, or even, can be substituted by boundary tractions, for many types of problems.

4.1 Discrete equations

Obtaining the typical matrix equations of the BEM starts with the definition of a discrete set of source points (or collocation points), with a total of N points located on the boundary and M points internal to the domain, Ω. Next, the boundary, Γ, is divided into N_e boundary elements, while the region of the domain where inelastic dissipative effects occur is divided into N_c cells, as illustrated in Figure 9.
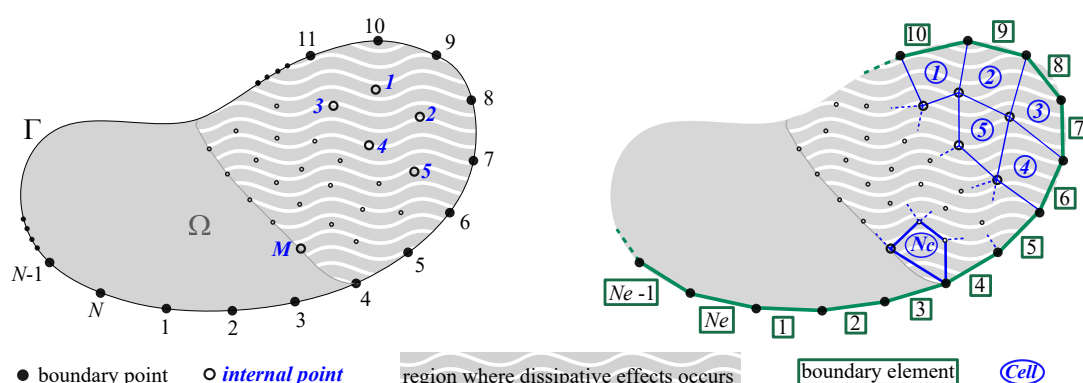
Figure 9: Plane solid with discrete division: points, elements and cells

In this way, equations (67), (68) and (69) can be rewritten in the following forms:

$$\dot{u}_i(\boldsymbol{\xi}^J) = \sum_{e=1}^{N_e} \int_{\Gamma_e} u_{ij}^*(\boldsymbol{\xi}^J, \mathbf{x})\dot{t}_j(\mathbf{x})d\Gamma - \sum_{e=1}^{N_e} \int_{\Gamma_e} t_{ij}^*(\boldsymbol{\xi}^J, \mathbf{x})\dot{u}_j(\mathbf{x})d\Gamma + \sum_{c=1}^{N_c} \int_{\Omega_c} \sigma_{ijk}^*(\boldsymbol{\xi}^J, \mathbf{x})\dot{\epsilon}_{jk}^o(\mathbf{x})d\Omega$$

(85)

$$c_{ij}(\boldsymbol{\xi}^I)\dot{u}_j(\boldsymbol{\xi}^I) = \sum_{e=1}^{N_e} \int_{\Gamma_e} u_{ij}^*(\boldsymbol{\xi}^I, \mathbf{x})\dot{t}_j(\mathbf{x})d\Gamma - \sum_{e=1}^{N_e} \int_{\Gamma_e} t_{ij}^*(\boldsymbol{\xi}^I, \mathbf{x})\dot{u}_j(\mathbf{x})d\Gamma +$$

$$\sum_{c=1}^{N_c} \int_{\Omega_c} \sigma_{ijk}^*(\boldsymbol{\xi}^I, \mathbf{x})\dot{\epsilon}_{jk}^o(\mathbf{x})d\Omega$$

(86)

$$\dot{\epsilon}_{ij}(\boldsymbol{\xi}^J) = \sum_{e=1}^{N_e} \int_{\Gamma_e} u_{ijk}^*(\boldsymbol{\xi}^J, \mathbf{x})\dot{t}_k(\mathbf{x})d\Gamma - \sum_{e=1}^{N_e} \int_{\Gamma_e} t_{ijk}^*(\boldsymbol{\xi}^J, \mathbf{x})\dot{u}_k(\mathbf{x})d\Gamma$$

$$+ \sum_{c=1}^{N_c} \int_{\Omega_c} \sigma_{ijkl}^*(\boldsymbol{\xi}^J, \mathbf{x})\dot{\epsilon}_{kl}^o(\mathbf{x})d\Omega + F_{ijkl}^{\epsilon\epsilon}\dot{\epsilon}_{kl}^o(\boldsymbol{\xi}^J)$$

(87)

where $I = 1, \ldots, N$ e $J = 1, \ldots, M$. The domains of each boundary element and each cell are referenced, respectively, by Γ_e and Ω_c.

For the boundary elements, subparametric or isoparametric formulations are commonly used. Here, only the case of isoparametric elements is considered. In this kind of boundary elements, displacements, tractions and the geometry are approximated by the same interpolation functions over the collocation points. Thus, inside an element, it is possible to write:

$$x_j(\eta_k) \approx \sum_{\gamma=1}^{n_e} N_\gamma(\eta_k) x_j^\gamma$$

(88a)

$$\dot{u}_j(\mathbf{x}(\eta_k)) \approx \sum_{\gamma=1}^{n_e} N_\gamma(\eta_k) \dot{u}_j^\gamma$$

(88b)

$$\dot{t}_j(\mathbf{x}(\eta_k)) \approx \sum_{\gamma=1}^{n_e} N_\gamma(\eta_k) \dot{t}_j^\gamma$$

(88c)

where η_k ($\in [-1, +1]$) are parametric coordinates (k varies from 1 to 2 for 3D problems, while a single coordinate is necessary for boundary elements in plane problems – see Figure 10). Index γ is associated to the collocation points inside the element, $N^\gamma(\eta)$ are the interpolation functions and n_e represents the total number of collocation points in the element. In this way, x_j^γ, $\dot{u}_j^\gamma$ and

$\dot{t}_j^\gamma$ represent, respectively, the x_j coordinate, the u_j displacement component and the t_j traction component at the collocation point referenced by γ.
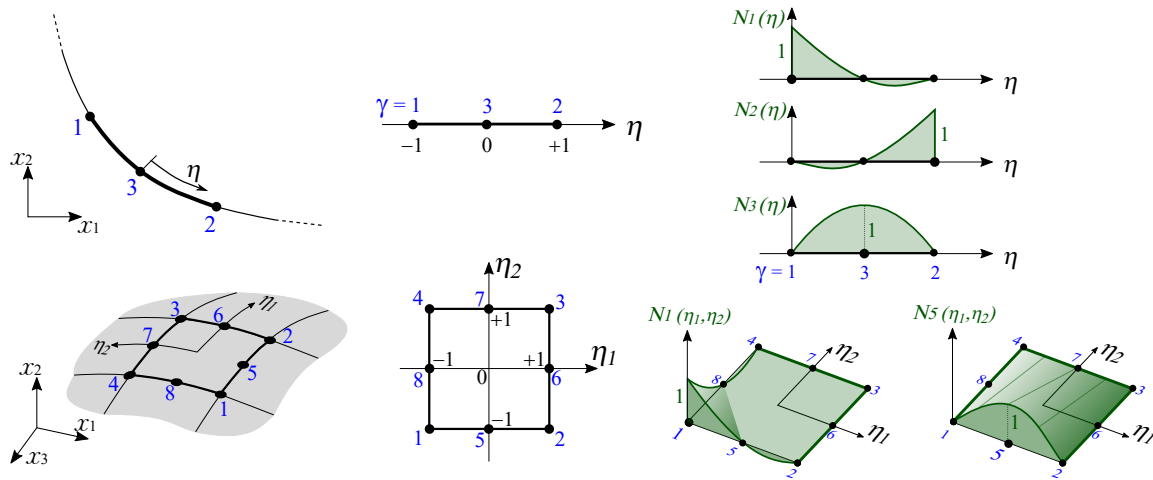
Figure 10: Linear and quadrilateral boundary elements, parametric coordinates, and quadratic interpolation functions

Equations (88b) and (88c) can be conveniently rewritten in the following matrix forms:

$$\{\dot{u}\} = [N(\eta_k)]\{\dot{u}^e\} \qquad \text{and} \qquad \{\dot{t}\} = [N(\eta_k)]\{\dot{t}^e\} \tag{89}$$

where, for three-dimensional problems,

$$\{\dot{u}\} = \begin{Bmatrix} \dot{u}_1(\mathbf{x}(\eta_1, \eta_2)) \\ \dot{u}_2(\mathbf{x}(\eta_1, \eta_2)) \\ \dot{u}_3(\mathbf{x}(\eta_1, \eta_2)) \end{Bmatrix}, \quad \{\dot{t}\} = \begin{Bmatrix} \dot{t}_1(\mathbf{x}(\eta_1, \eta_2)) \\ \dot{t}_2(\mathbf{x}(\eta_1, \eta_2)) \\ \dot{t}_3(\mathbf{x}(\eta_1, \eta_2)) \end{Bmatrix}$$

$$\{\dot{u}^e\} = \{\dot{u}_1^1 \quad \dot{u}_2^1 \quad \dot{u}_3^1 \quad \cdots \quad \dot{u}_1^{n_e} \quad \dot{u}_2^{n_e} \quad \dot{u}_3^{n_e}\}^T, \quad \{\dot{t}^e\} = \{\dot{t}_1^1 \quad \dot{t}_2^1 \quad \dot{t}_3^1 \quad \cdots \quad \dot{t}_1^{n_e} \quad \dot{t}_2^{n_e} \quad \dot{t}_3^{n_e}\}^T$$

$$[N(\eta_k)] = \begin{bmatrix} N_1(\eta_1, \eta_2) & 0 & 0 & \cdots & N_{n_e}(\eta_1, \eta_2) & 0 & 0 \\ 0 & N_1(\eta_1, \eta_2) & 0 & \cdots & 0 & N_{n_e}(\eta_1, \eta_2) & 0 \\ 0 & 0 & N_1(\eta_1, \eta_2) & \cdots & 0 & 0 & N_{n_e}(\eta_1, \eta_2) \end{bmatrix}$$

and, for plane problems,

$$\{\dot{u}\} = \begin{Bmatrix} \dot{u}_1(\mathbf{x}(\eta)) \\ \dot{u}_2(\mathbf{x}(\eta)) \end{Bmatrix}, \quad \{\dot{t}\} = \begin{Bmatrix} \dot{t}_1(\mathbf{x}(\eta)) \\ \dot{t}_2(\mathbf{x}(\eta)) \end{Bmatrix}$$

$$\{\dot{u}^e\} = \{\dot{u}_1^1 \quad \dot{u}_2^1 \quad \cdots \quad \dot{u}_1^{n_e} \quad \dot{u}_2^{n_e}\}^T, \quad \{\dot{t}^e\} = \{\dot{t}_1^1 \quad \dot{t}_2^1 \quad \cdots \quad \dot{t}_1^{n_e} \quad \dot{t}_2^{n_e}\}^T$$

$$[N(\eta_k)] = \begin{bmatrix} N_1(\eta) & 0 & \cdots & N_{n_e}(\eta) & 0 \\ 0 & N_1(\eta) & \cdots & 0 & N_{n_e}(\eta) \end{bmatrix}$$

Moreover, a boundary infinitesimal surface, $d\Gamma$, relates itself with the parametric coordinates by the next expression:

$$d\Gamma(\mathbf{x}(\eta_k)) = \mathcal{J}(\eta_k)\, d\eta_k \tag{90}$$

where, for three-dimensional problems, $d\eta_k \equiv d\eta_1\, d\eta_2$ and

$$\mathcal{J}(\eta_k) \equiv \mathcal{J}(\eta_1, \eta_2) = \sqrt{J_1^2 + J_2^2 + J_3^2}$$

with

$$
J_1 = \frac{\partial x_2}{\partial \eta_1}\frac{\partial x_3}{\partial \eta_2} - \frac{\partial x_2}{\partial \eta_2}\frac{\partial x_3}{\partial \eta_1}, \quad J_2 = \frac{\partial x_3}{\partial \eta_1}\frac{\partial x_1}{\partial \eta_2} - \frac{\partial x_3}{\partial \eta_2}\frac{\partial x_1}{\partial \eta_1}, \quad J_3 = \frac{\partial x_1}{\partial \eta_1}\frac{\partial x_2}{\partial \eta_2} - \frac{\partial x_2}{\partial \eta_2}\frac{\partial x_1}{\partial \eta_1},
$$

while, for plane state problems,

$$
\mathcal{J}(\eta_k) \equiv \mathcal{J}(\eta) = \sqrt{J_1^2 + J_2^2}
$$

with

$$
J_1 = \frac{dx_1}{d\eta}, \quad J_1 = \frac{dx_2}{d\eta}.
$$

In an analogous way, the initial strain field is interpolated inside each cell, i.e.,

$$
\dot{\epsilon}_{ij}^o(\mathbf{x}(\eta_k)) \approx \sum_{\gamma=1}^{n_c} M_\gamma(\eta_k)\dot{\epsilon}_{ij}^{o,\gamma} \tag{91}
$$

where, again, η_k ($\in [-1, +1]$), but now k varies between 1 and 3 for 3D problems and between 1 and 2 for 2D problems, as depicted in Figure 11. The interpolation functions, $M_\gamma(\eta)$, follow the same idea from the boundary elements, regarding the appropriate dimensions for each case. For example, considering also isoparametric cells, $M_\gamma(\eta)$ for a two-dimensional problem are exactly the same as $N_\gamma(\eta)$ for a three-dimensional one. Index n_c is associated to the number of collocation points in the cell.
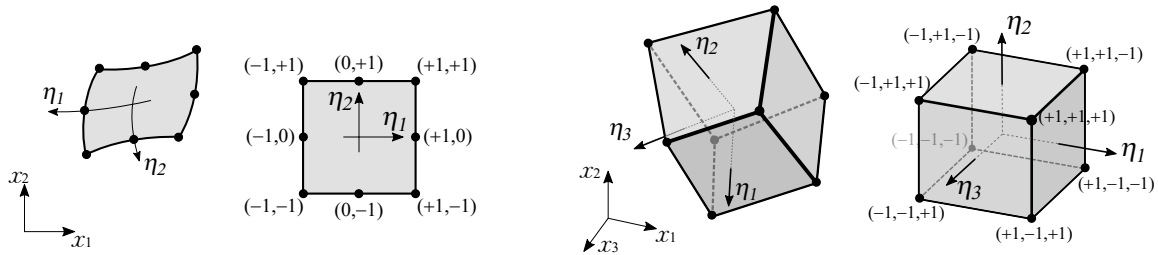
Figure 11: Quadrilateral and hexahedral cells, and parametric coordinates

In a matrix form, equation (91) is written as

$$
\{\dot{\epsilon}^o\} = [M(\eta_k)]\{\dot{\epsilon}^{o,c}\} \tag{92}
$$

where,

$$
\{\dot{\epsilon}^o\} = \begin{Bmatrix} \dot{\epsilon}_{11}^o(\mathbf{x}(\eta_1,\eta_2,\eta_3)) \\ \dot{\epsilon}_{22}^o(\mathbf{x}(\eta_1,\eta_2,\eta_3)) \\ \dot{\epsilon}_{33}^o(\mathbf{x}(\eta_1,\eta_2,\eta_3)) \\ \dot{\epsilon}_{12}^o(\mathbf{x}(\eta_1,\eta_2,\eta_3)) \\ \dot{\epsilon}_{13}^o(\mathbf{x}(\eta_1,\eta_2,\eta_3)) \\ \dot{\epsilon}_{23}^o(\mathbf{x}(\eta_1,\eta_2,\eta_3)) \end{Bmatrix} \quad \text{(for 3D)}, \qquad \{\dot{\epsilon}^o\} = \begin{Bmatrix} \dot{\epsilon}_{11}^o(\mathbf{x}(\eta_1,\eta_2)) \\ \dot{\epsilon}_{22}^o(\mathbf{x}(\eta_1,\eta_2)) \\ \dot{\epsilon}_{12}^o(\mathbf{x}(\eta_1,\eta_2)) \end{Bmatrix} \quad \text{(for 2D)}
$$

$$
\{\dot{\epsilon}^{o,c}\} = \begin{Bmatrix} \{\dot{\epsilon}^{o,1}\} \\ \vdots \\ \{\dot{\epsilon}^{o,n_c}\} \end{Bmatrix}, \qquad \text{with} \qquad \{\dot{\epsilon}^{o,k}\} = \begin{Bmatrix} \dot{\epsilon}_{11}^{o,k} \\ \dot{\epsilon}_{22}^{o,k} \\ \dot{\epsilon}_{33}^{o,k} \\ \dot{\epsilon}_{12}^{o,k} \\ \dot{\epsilon}_{13}^{o,k} \\ \dot{\epsilon}_{23}^{o,k} \end{Bmatrix} \quad \text{(for 3D)}, \qquad \begin{Bmatrix} \dot{\epsilon}_{11}^{o,k} \\ \dot{\epsilon}_{22}^{o,k} \\ \dot{\epsilon}_{12}^{o,k} \end{Bmatrix} \quad \text{(for 2D)}
$$

$$[M(\eta_k)] = \begin{bmatrix} M_1(\eta_1, \eta_2, \eta_3)[I] & \cdots & M_{n_c}(\eta_1, \eta_2, \eta_3)[I] \end{bmatrix}, \quad [I] \rightarrow \begin{cases} \text{6x6 indentity matrix (for 3D)} \\ \text{3x3 indentity matrix (for 2D)} \end{cases}$$

As a matter of completeness, the geometry of a cell can be parametrized as

$$x_j(\mathbf{x}(\eta_k)) \approx \sum_{\gamma=1}^{n_c} M_\gamma(\eta_k) x_j^\gamma \tag{93}$$

from which is possible to obtain

$$d\Omega(\mathbf{x}(\eta_k)) = \bar{\mathcal{J}}(\eta_k)\, d\eta_k \tag{94}$$

4.1.1   Discrete form of Somigliana Identity

Considering an internal source point, integrals in equation (85) assume the following forms, after using equations (89), (90), (92) and (94):

$$\int_{\Gamma_e} u_{ij}^*(\boldsymbol{\xi}^J, \mathbf{x}) \dot{t}_j(\mathbf{x}) d\Gamma \approx \left(\int_{-1}^{+1} [u^*(\boldsymbol{\xi}^J, \eta_k)][N(\eta_k)]\mathcal{J}(\eta_k)\, d\eta_k \right) \{\dot{t}^e\} = [G_e^J]\{\dot{t}^e\} \tag{95}$$

$$\int_{\Gamma_e} t_{ij}^*(\boldsymbol{\xi}^J, \mathbf{x}) \dot{u}_j(\mathbf{x}) d\Gamma \approx \left(\int_{-1}^{+1} [t^*(\boldsymbol{\xi}^J, \eta_k)][N(\eta_k)]\mathcal{J}(\eta_k)\, d\eta_k \right) \{\dot{u}^e\} = [H_e^J]\{\dot{u}^e\} \tag{96}$$

$$\int_{\Omega_c} \sigma_{ijk}^*(\boldsymbol{\xi}^J, \mathbf{x}) \dot{\epsilon}_{jk}^o(\mathbf{x}) d\Omega \approx \left(\int_{-1}^{+1} [\sigma^*(\boldsymbol{\xi}^J, \eta_k)][M(\eta_k)]\bar{\mathcal{J}}(\eta_k)\, d\eta_k \right) \{\dot{\epsilon}^{o,c}\} = [Q_c^J]\{\dot{\epsilon}^{o,c}\} \tag{97}$$

where, for three-dimensional problems,

$$[u^*(\boldsymbol{\xi}, \mathbf{x})] = \begin{bmatrix} u_{11}^*(\boldsymbol{\xi}, \mathbf{x}) & u_{12}^*(\boldsymbol{\xi}, \mathbf{x}) & u_{13}^*(\boldsymbol{\xi}, \mathbf{x}) \\ u_{21}^*(\boldsymbol{\xi}, \mathbf{x}) & u_{22}^*(\boldsymbol{\xi}, \mathbf{x}) & u_{23}^*(\boldsymbol{\xi}, \mathbf{x}) \\ u_{31}^*(\boldsymbol{\xi}, \mathbf{x}) & u_{32}^*(\boldsymbol{\xi}, \mathbf{x}) & u_{33}^*(\boldsymbol{\xi}, \mathbf{x}) \end{bmatrix}, \qquad [t^*(\boldsymbol{\xi}, \mathbf{x})] = \begin{bmatrix} t_{11}^*(\boldsymbol{\xi}, \mathbf{x}) & t_{12}^*(\boldsymbol{\xi}, \mathbf{x}) & t_{13}^*(\boldsymbol{\xi}, \mathbf{x}) \\ t_{21}^*(\boldsymbol{\xi}, \mathbf{x}) & t_{22}^*(\boldsymbol{\xi}, \mathbf{x}) & t_{23}^*(\boldsymbol{\xi}, \mathbf{x}) \\ t_{31}^*(\boldsymbol{\xi}, \mathbf{x}) & t_{32}^*(\boldsymbol{\xi}, \mathbf{x}) & t_{33}^*(\boldsymbol{\xi}, \mathbf{x}) \end{bmatrix} \tag{98}$$

$$[\sigma^*(\boldsymbol{\xi}, \mathbf{x})] = \begin{bmatrix} \sigma_{111}^*(\boldsymbol{\xi}, \mathbf{x}) & \sigma_{122}^*(\boldsymbol{\xi}, \mathbf{x}) & \sigma_{133}^*(\boldsymbol{\xi}, \mathbf{x}) & 2\sigma_{112}^*(\boldsymbol{\xi}, \mathbf{x}) & 2\sigma_{113}^*(\boldsymbol{\xi}, \mathbf{x}) & 2\sigma_{123}^*(\boldsymbol{\xi}, \mathbf{x}) \\ \sigma_{211}^*(\boldsymbol{\xi}, \mathbf{x}) & \sigma_{222}^*(\boldsymbol{\xi}, \mathbf{x}) & \sigma_{233}^*(\boldsymbol{\xi}, \mathbf{x}) & 2\sigma_{212}^*(\boldsymbol{\xi}, \mathbf{x}) & 2\sigma_{213}^*(\boldsymbol{\xi}, \mathbf{x}) & 2\sigma_{223}^*(\boldsymbol{\xi}, \mathbf{x}) \\ \sigma_{311}^*(\boldsymbol{\xi}, \mathbf{x}) & \sigma_{322}^*(\boldsymbol{\xi}, \mathbf{x}) & \sigma_{333}^*(\boldsymbol{\xi}, \mathbf{x}) & 2\sigma_{312}^*(\boldsymbol{\xi}, \mathbf{x}) & 2\sigma_{313}^*(\boldsymbol{\xi}, \mathbf{x}) & 2\sigma_{323}^*(\boldsymbol{\xi}, \mathbf{x}) \end{bmatrix} \tag{99}$$

and, for two-dimensional problems,

$$[u^*(\boldsymbol{\xi}, \mathbf{x})] = \begin{bmatrix} u_{11}^*(\boldsymbol{\xi}, \mathbf{x}) & u_{12}^*(\boldsymbol{\xi}, \mathbf{x}) \\ u_{21}^*(\boldsymbol{\xi}, \mathbf{x}) & u_{22}^*(\boldsymbol{\xi}, \mathbf{x}) \end{bmatrix}, \qquad [t^*(\boldsymbol{\xi}, \mathbf{x})] = \begin{bmatrix} t_{11}^*(\boldsymbol{\xi}, \mathbf{x}) & t_{12}^*(\boldsymbol{\xi}, \mathbf{x}) \\ t_{21}^*(\boldsymbol{\xi}, \mathbf{x}) & t_{22}^*(\boldsymbol{\xi}, \mathbf{x}) \end{bmatrix} \tag{100}$$

$$[\sigma^*(\boldsymbol{\xi}, \mathbf{x})] = \begin{bmatrix} \sigma_{111}^*(\boldsymbol{\xi}, \mathbf{x}) & \sigma_{122}^*(\boldsymbol{\xi}, \mathbf{x}) & 2\sigma_{112}^*(\boldsymbol{\xi}, \mathbf{x}) \\ \sigma_{211}^*(\boldsymbol{\xi}, \mathbf{x}) & \sigma_{222}^*(\boldsymbol{\xi}, \mathbf{x}) & 2\sigma_{212}^*(\boldsymbol{\xi}, \mathbf{x}) \end{bmatrix} \tag{101}$$

In equations (99) and (101), the symmetry $\sigma_{ijk}^* = \sigma_{ikj}^*$ was used. Moreover, in equation (101), for the plane strain case, a fourth column might be added to contemplate terms σ_{i33}^*.

Also, note that, despite of the single integration symbol, integrals in equations (95) and (96) are in fact double integrals over the element domain, $(\eta_1, \eta_2) \rightarrow [-1, +1] \times [-1, +1]$, while integrals in equation (97) are triple integrals over the cell domain, for three-dimensional problems. On the other hand, for two-dimensional case, equations (95) and (96) refer to single integrals, while in equation (97) we have double integrals.

The left-hand-side term in equation (85), in turn, can be written as

$$\dot{u}_i(\boldsymbol{\xi}^J) \to \{\dot{u}^J\}, \quad \text{where} \quad \{\dot{u}^J\} = \begin{Bmatrix} \dot{u}_1(\boldsymbol{\xi}^J) \\ \dot{u}_2(\boldsymbol{\xi}^J) \\ \dot{u}_3(\boldsymbol{\xi}^J) \end{Bmatrix} \text{ (for 3D)}, \quad \begin{Bmatrix} \dot{u}_1(\boldsymbol{\xi}^J) \\ \dot{u}_2(\boldsymbol{\xi}^J) \end{Bmatrix} \text{ (for 2D)} \qquad (102)$$

Thus, applying equation (85) to the complete set of internal points results in the following matrix expression, after introducing equations (95), (96), (97) and (102),

$$\bigcup_{J=1}^{M} (\{\dot{u}^J\}) = \bigcup_{J=1}^{M} \biguplus_{e=1}^{N_e} ([G_e^J]) \biguplus_{e=1}^{N_e} (\{\dot{t}^e\}) - \bigcup_{J=1}^{M} \bigcup_{e=1}^{N_e} ([H_e^J]) \bigcup_{e=1}^{N_e} (\{\dot{u}^e\}) + \bigcup_{J=1}^{M} \bigcup_{c=1}^{N_c} ([Q_c^J]) \bigcup_{c=1}^{N_c} (\{\dot{\epsilon}^{o,c}\}),$$

i.e.,

$$\{\dot{u}^\Omega\} = [G^u]\{\dot{t}\} - [H^u]\{\dot{u}\} + [Q^u]\{\dot{\epsilon}^o\} \qquad (103)$$

where the superscript Ω in $\{\dot{u}^\Omega\}$ was adopted to indicate that the vector in question is formed by components referring to internal points. Symbols $\bigcup$ and $\biguplus$ are associated with the arrays' assembly forms. The first of them indicates that coefficients relative to the same geometric point are allocated in the same row or column of the matrix. The second indicates that coefficients referring to the interpolation points of two distinct elements, even if such points are geometrically coincident, are allocated in different lines or columns. The presence of only one symbol indicates the assembly of the lines of a vector. If two symbols are used, the first (or left) refers to the assembly of the rows and the second to the columns.

4.1.2   Discrete form of displacement boundary equation

Integrals in equation (86) differ from those of the equation (85) only by the location of the source point: in the former it is on the boundary, Γ. Therefore, equations (95) to (101) remain valid here, as long as the index J is replaced by I (questions concerning the degrees of singularity of the integral kernels are addressed further in this text). In this way, you can write, for a fixed source point on the boundary:

$$\int_{\Gamma_e} u_{ij}^*(\boldsymbol{\xi}^I, \mathbf{x})\dot{t}_j(\mathbf{x})d\Gamma \approx \left(\int_{-1}^{+1} [u^*(\boldsymbol{\xi}^I, \eta_k)][N(\eta_k)]\mathcal{J}(\eta_k)\, d\eta_k \right)\{\dot{t}^e\} = [G_e^I]\{\dot{t}^e\} \qquad (104)$$

$$\int_{\Gamma_e} t_{ij}^*(\boldsymbol{\xi}^I, \mathbf{x})\dot{u}_j(\mathbf{x})d\Gamma \approx \left(\int_{-1}^{+1} [t^*(\boldsymbol{\xi}^I, \eta_k)][N(\eta_k)]\mathcal{J}(\eta_k)\, d\eta_k \right)\{\dot{u}^e\} = [H_e^I]\{\dot{u}^e\} \qquad (105)$$

$$\int_{\Omega_c} \sigma_{ijk}^*(\boldsymbol{\xi}^I, \mathbf{x})\dot{\epsilon}_{jk}^o(\mathbf{x})d\Omega \approx \left(\int_{-1}^{+1} [\sigma^*(\boldsymbol{\xi}^I, \eta_k)][M(\eta_k)]\bar{\mathcal{J}}(\eta_k)\, d\eta_k \right)\{\dot{\epsilon}^{o,c}\} = [Q_c^I]\{\dot{\epsilon}^{o,c}\} \qquad (106)$$

The free term at the left-hand-side in equation (86), on the other hand, assumes the following forms:

$$c_{ij}(\boldsymbol{\xi}^I) \to [C^I], \quad \text{where}$$

$$[C^I] = \begin{bmatrix} c_{11}(\boldsymbol{\xi}^I) & c_{12}(\boldsymbol{\xi}^I) & c_{13}(\boldsymbol{\xi}^I) \\ c_{21}(\boldsymbol{\xi}^I) & c_{22}(\boldsymbol{\xi}^I) & c_{23}(\boldsymbol{\xi}^I) \\ c_{31}(\boldsymbol{\xi}^I) & c_{32}(\boldsymbol{\xi}^I) & c_{33}(\boldsymbol{\xi}^I) \end{bmatrix} \text{ (3D)}, \quad [C^I] = \begin{bmatrix} c_{11}(\boldsymbol{\xi}^I) & c_{12}(\boldsymbol{\xi}^I) \\ c_{21}(\boldsymbol{\xi}^I) & c_{22}(\boldsymbol{\xi}^I) \end{bmatrix} \text{ (2D)} \qquad (107)$$

Taking into account equations (104) to (107), the application of equation (86) to the set of collocation points localized on the boundary, $\boldsymbol{\xi}^I$, leads to

$$\bigcup_{I=1}^{N} \bigcup_{e=1}^{N_e} ([C^I] + [H_e^I]) \bigcup_{e=1}^{N_e} (\{\dot{u}^e\}) = \bigcup_{I=1}^{N} \biguplus_{e=1}^{N_e} ([G_e^I]) \biguplus_{e=1}^{N_e} (\{\dot{t}^e\}) + \bigcup_{I=1}^{N} \bigcup_{c=1}^{N_c} ([Q_c^I]) \bigcup_{c=1}^{N_c} (\{\dot{\epsilon}^{o,c}\}),$$

i.e.,

$$[H]\{\dot{u}\} = [G]\{\dot{t}\} + [Q]\{\dot{\epsilon}^o\} \qquad (108)$$

4.1.3   Discrete form of internal strain boundary equation

Considering again a fixed internal collocation point, integrals in equation (87) take the following forms, after introduction of equations (89), (90), (92) and (94):

$$\int_{\Gamma_e} u^*_{ijk}(\boldsymbol{\xi}^J, \mathbf{x})\dot{t}_k(\mathbf{x})d\Gamma \approx \left(\int_{-1}^{1} [\nabla_{\boldsymbol{\xi}} u^*(\boldsymbol{\xi}^J, \eta_k)][N(\eta_k)]\mathcal{J}(\eta_k)d\eta_k \right)\{\dot{t}^e\} = [\bar{G}_e^J]\{\dot{t}^e\} \quad (109)$$

$$\int_{\Gamma_e} t^*_{ijk}(\boldsymbol{\xi}^J, \mathbf{x})\dot{u}_k(\mathbf{x})d\Gamma \approx \left(\int_{-1}^{1} [\nabla_{\boldsymbol{\xi}} t^*(\boldsymbol{\xi}^J, \eta_k)][N(\eta_k)]\mathcal{J}(\eta_k)d\eta_k \right)\{\dot{u}^e\} = [\bar{H}_e^J]\{\dot{u}^e\} \quad (110)$$

$$\int_{\Omega_c} \sigma^*_{ijkl}(\boldsymbol{\xi}^J, \mathbf{x})\dot{\epsilon}^o_{kl}(\mathbf{x})d\Omega \approx \left(\int_{-1}^{1}\int_{-1}^{1} [\nabla_{\boldsymbol{\xi}} \sigma^*(\boldsymbol{\xi}^J, \eta_k)][M(\eta_k)]\bar{\mathcal{J}}(\eta_k)d\eta_k \right)\{\dot{\epsilon}^{o,c}\} = [\bar{Q}_c^J]\{\dot{\epsilon}^{o,c}\}$$
$$(111)$$

where, for plane problems,

$$[\nabla_{\boldsymbol{\xi}} u^*(\boldsymbol{\xi}, \mathbf{x})] = \begin{bmatrix} u^*_{111}(\boldsymbol{\xi}, \mathbf{x}) & u^*_{112}(\boldsymbol{\xi}, \mathbf{x}) \\ u^*_{221}(\boldsymbol{\xi}, \mathbf{x}) & u^*_{222}(\boldsymbol{\xi}, \mathbf{x}) \\ u^*_{121}(\boldsymbol{\xi}, \mathbf{x}) & u^*_{122}(\boldsymbol{\xi}, \mathbf{x}) \end{bmatrix}, \quad [\nabla_{\boldsymbol{\xi}} t^*(\boldsymbol{\xi}, \mathbf{x})] = \begin{bmatrix} t^*_{111}(\boldsymbol{\xi}, \mathbf{x}) & t^*_{112}(\boldsymbol{\xi}, \mathbf{x}) \\ t^*_{221}(\boldsymbol{\xi}, \mathbf{x}) & t^*_{222}(\boldsymbol{\xi}, \mathbf{x}) \\ t^*_{121}(\boldsymbol{\xi}, \mathbf{x}) & t^*_{122}(\boldsymbol{\xi}, \mathbf{x}) \end{bmatrix} \quad (112)$$

$$[\nabla_{\boldsymbol{\xi}} \sigma^*(\boldsymbol{\xi}, \mathbf{x})] = \begin{bmatrix} \sigma^*_{1111}(\boldsymbol{\xi}, \mathbf{x}) & \sigma^*_{1122}(\boldsymbol{\xi}, \mathbf{x}) & 2\sigma^*_{1112}(\boldsymbol{\xi}, \mathbf{x}) \\ \sigma^*_{2211}(\boldsymbol{\xi}, \mathbf{x}) & \sigma^*_{2222}(\boldsymbol{\xi}, \mathbf{x}) & 2\sigma^*_{2212}(\boldsymbol{\xi}, \mathbf{x}) \\ \sigma^*_{1211}(\boldsymbol{\xi}, \mathbf{x}) & \sigma^*_{1222}(\boldsymbol{\xi}, \mathbf{x}) & 2\sigma^*_{1212}(\boldsymbol{\xi}, \mathbf{x}) \end{bmatrix} \quad (113)$$

Such matrices can be easily extended to three-dimensional problems.

In equation (113), the symmetry $\sigma^*_{ij12} = \sigma^*_{ij21}$ was considered and, again, a fourth column needs to be added for plane strain problems, to take into account terms σ^*_{ij33}.

Matrix forms for the left-hand side vector and for the last term in equation (87) are given, respectively, by

$$\dot{\epsilon}_{ij}(\boldsymbol{\xi}^J) \to \{\dot{\epsilon}^J\} \quad \text{where} \quad \{\dot{\epsilon}^J\} = \begin{Bmatrix} \dot{\epsilon}_{11}(\boldsymbol{\xi}^J) \\ \dot{\epsilon}_{22}(\boldsymbol{\xi}^J) \\ \dot{\epsilon}_{33}(\boldsymbol{\xi}^J) \\ \dot{\epsilon}_{12}(\boldsymbol{\xi}^J) \\ \dot{\epsilon}_{13}(\boldsymbol{\xi}^J) \\ \dot{\epsilon}_{23}(\boldsymbol{\xi}^J) \end{Bmatrix} \text{ (for 3D)}, \quad \{\dot{\epsilon}^J\} = \begin{Bmatrix} \dot{\epsilon}_{11}(\boldsymbol{\xi}^J) \\ \dot{\epsilon}_{22}(\boldsymbol{\xi}^J) \\ \dot{\epsilon}_{12}(\boldsymbol{\xi}^J) \end{Bmatrix} \text{ (for 2D)}$$
$$(114)$$

and

$$F^{\epsilon\epsilon}_{ijkl}\dot{\epsilon}^o_{kl}(\boldsymbol{\xi}^J) = \begin{bmatrix} F^{\epsilon\epsilon}_{1111} & F^{\epsilon\epsilon}_{1122} & 2F^{\epsilon\epsilon}_{1112} \\ F^{\epsilon\epsilon}_{2211} & F^{\epsilon\epsilon}_{2222} & 2F^{\epsilon\epsilon}_{2212} \\ F^{\epsilon\epsilon}_{1211} & F^{\epsilon\epsilon}_{1222} & 2F^{\epsilon\epsilon}_{1212} \end{bmatrix} \begin{Bmatrix} \dot{\epsilon}^o_{11}(\boldsymbol{\xi}^J) \\ \dot{\epsilon}^o_{22}(\boldsymbol{\xi}^J) \\ \dot{\epsilon}^o_{12}(\boldsymbol{\xi}^J) \end{Bmatrix} = [F^{\epsilon\epsilon,J}]\{\dot{\epsilon}^{o,J}\} \quad \text{(for 2D)} \quad (115)$$

where this last relation also can be easily extended to the 3D case.

Finally, considering the above equations and applying equation (87) to all internal collocation points, we obtain:

$$\bigcup_{J=1}^{M} (\{\dot{\epsilon}^J\}) = \bigcup_{J=1}^{M}\biguplus_{e=1}^{N_e} ([\bar{G}_e^J]) \biguplus_{e=1}^{N_e} (\{\dot{t}^e\}) - \bigcup_{J=1}^{M}\bigcup_{e=1}^{N_e} ([\bar{H}_e^J]) \bigcup_{e=1}^{N_e} (\{\dot{u}^e\})$$

$$+ \bigcup_{J=1}^{M}\bigcup_{c=1}^{N_c} ([\bar{Q}_c^J] + [F^{\epsilon\epsilon,J}]) \bigcup_{c=1}^{N_c} (\{\dot{\epsilon}^{o,c}\}),$$

i.e.,

$$\{\dot{\epsilon}\} = [G^\epsilon]\{\dot{t}\} - [H^\epsilon]\{\dot{u}\} + [Q^\epsilon]\{\dot{\epsilon}^o\} \quad (116)$$

4.1.4   Integrals numerical treatment

The integrals of the discrete equations (85), (86) and (87) are usually performed numerically, through the boundary elements and cells. For plane problems the integrals are line integrals on the boundary and area integrals at the domain, while for three-dimensional problems the integrals are area integrals on the boundary and volume integrals at the domain. The nature of the kernel, and the relative position of the collocation point with respect to the element on which the integration is being performed, defines if the type of the integral, that can be classified as regular or singular. The technique to solve those integrals are chosen accordingly.

Regular Integrals and Nearly Singular Integrals

Integrals are considered regular when the collocation point do not coincides with an element point. The regular integrals are performed through standard Gauss quadrature. For computational efficiency it is possible to choose the number of integration points according to a fixed tolerance error (e.g. 10^{-3}), therefore, it varies according to the distance from the collocation point to the element where integration is being carried out. Criterium proposed by Eberwien et al. [2005] present the number of integration points according to the line integral kernel singularity. This criterion can be extended for area and volume integrals.

When the collocation point is close to the element under consideration, the integral is said to be nearly singular, and special treatment is required as the integrand varies sharply. The element subdivision technique is an efficient approach for dealing with these integrals. A simple way is to subdivide the element into equal subintervals, as presented in Beer et al. [2008], where the number of subdivision is determined in order to preserve the integration accuracy. This technique can be extended for area and volume integrals aswell.

Singular Integrals

Singular integral occurs when the collocation point lies within the element being integrated. They are classified as weakly singular integrals when the singularity of the kernel is of order $O(ln(1/r))$ for two-dimensional problems or $O(1/r)$ for three-dimensional problems. The integrals in equations (95) and (104) are possibly in this case. On the other hand, if the singularity of the integral kernel is of order $O(1/r)$ for two-dimensional problems or $O(1/r^2)$ for three-dimensional problems, they are classified as strongly singular integrals, and are considered in the Cauchy principal value sense. This might be the case for the integrals in equations (96), (105), (106) and (109). Finally, integrals with kernel of high singularity order, i.e., $O(1/r^2)$ for two-dimensional or $O(1/r^3)$ for three-dimensional problems, respectively, are said to be hypersingular integrals, considered as Hadamard principal value sense. Equations (110) and (111) may carry this type of integrals.

For two-dimensional problems boundary elements (one dimension) the weakly singular integrals can be evaluated using a logarithmic Gauss quadrature, as presented by Huang [1993], while for the the strongly singular integrals the technique proposed by Guiggiani and Casalini [1987] is usual.

The treatment of integrals for cells in two-dimensional problems and the boundary elements in three-dimensional problems are similar (area integrals). Weakly singular integrals can be performed through a variable transformation by an element subdivision technique proposed by Lachat and Watson [1976], while for the strongly singular integrals Guiggiani and Gigante [1990] presented an efficient technique.

The volume weakly singular integrals in three-dimensional cells can also be performed using the cell subdivision technique proposed by Lachat and Watson [1976]. Strongly singular integrals cam be evaluated using the technique proposed by Gao and Davies [2000], where the integral can

be divided in two parts, in such way that the first part is weakly singular and can be integrated by the technique previously mentioned, whilst the second part, with the strong singularity, is evaluated semi-analytically.

Direct evaluation of CPV integrals in the free-therm c_{ij}, present in equation (86) (see figure 8), can be avoided by using the rigid body motion concept. Similarly, the use of the so called stress recovery technique may dispense the direct evaluation of hypersingular integrals, for the assessment of strains and stresses on the boundary. These well known approaches are detailed in Beer et al. [2008] and Gao and Davies [2002].

4.2 Solution strategy

The matrix equations obtained in section 4.1 can be algebraically manipulated in order to generate a single non linear equation, typical of the implicit BEM formulation, developed by Telles and Carrer [1991]. Such equation is first obtained in the present section, followed by its the solution strategy, presented in Peixoto et al. [2016], which has the advantage of encapsulate different control methods in a single computational framework.

Considering the essential and natural boundary conditions, equations (103), (108) and (116) can be respectively reorganized in the next forms:

$$\{\dot{u}^{\Omega}\} = [A^u]\{\dot{x}\} + [B^u]\{\dot{y}\} + [Q^u]\{\dot{\epsilon}^o\} \tag{117}$$

$$[A]\{\dot{x}\} = [B]\{\dot{y}\} + [Q]\{\dot{\epsilon}^o\} \tag{118}$$

$$\{\dot{\epsilon}\} = [A^\epsilon]\{\dot{x}\} + [B^\epsilon]\{\dot{y}\} + [Q^\epsilon]\{\dot{\epsilon}^o\} \tag{119}$$

where, in $\{\dot{y}\}$ the prescribed values on the boundary are grouped, coming from $\{\dot{u}\}$ or $\{\dot{t}\}$, while the vector $\{\dot{x}\}$ contains the unknown components of these fields. Matrices referenced by $[A]$ and $[B]$, on the other hand, are composed by coefficients from those referenced by $[H]$ and $[G]$. In reality, computationally speaking, the matrix equations are already assembled directly in these last forms, without the need to go through a rearrangement step.

Solving for $\{\dot{x}\}$ in equation (118), we obtain

$$\{\dot{x}\} = [N]\{\dot{y}\} + [M]\{\dot{\epsilon}^o\} \tag{120}$$

where

$$[N] = [A]^{-1}[B]; \quad [M] = [A]^{-1}[Q] \tag{121}$$

Thus, applying equation (120) into (117) and (119), the following results are respectively ontained:

$$\{\dot{u}^{\Omega}\} = [N^u]\{\dot{y}\} + [M^u]\{\dot{\epsilon}^o\} \tag{122}$$

$$\{\dot{\epsilon}\} = [N^\epsilon]\{\dot{y}\} + [M^\epsilon]\{\dot{\epsilon}^o\} \tag{123}$$

where

$$[N^u] = [A^u][A]^{-1}[B] + [B^u]; \quad [M^u] = [A^u][A]^{-1}[Q] + [Q^u] \tag{124}$$

$$[N^\epsilon] = [A^\epsilon][A]^{-1}[B] + [B^\epsilon]; \quad [M^\epsilon] = [A^\epsilon][A]^{-1}[Q] + [Q^\epsilon] \tag{125}$$

For rate independent constitutive models (as the ones presented in Appendix A), the time derivatives can be substituted by finite increments, i.e., $(\dot{\cdot}) = \Delta(\cdot) \equiv (\cdot)_i - (\cdot)_{i-1}$, where i is an incremental index. In this way, for the i-th increment of the the prescribed loads, $\{y\}$, equations (120), (122) and (123) can be rewritten as

$$\{x\}^i = \lambda^i[N]\{y\} + [M]\{\epsilon^o\}^i \tag{126}$$

$$\{u^\Omega\}^i = \lambda^i[N^u]\{y\} + [M^u]\{\epsilon^o\}^i \tag{127}$$

$$\{\epsilon\}^i = \lambda^i[N^\epsilon]\{y\} + [M^\epsilon]\{\epsilon^o\}^i \tag{128}$$

where the parameter λ^i, known as load factor, is a cumulative scalar quantity that defines the amount of external load is necessary, at each increment, to guarantee the mechanical equilibrium.

From equation (128), it is possible to define an equilibrium vector in function of strain and the load factor, $\{Q\}^i \equiv \{Q(\epsilon^i, \lambda^i)\}$, introducing also equation (66), i.e.,

$$\{Q\}^i = \lambda^i[N^\epsilon]\{y\} + [M^\epsilon]\big(\{\epsilon\}^i - [C]^{-1}\{\sigma(\epsilon)\}^i\big) - \{\epsilon\}^i = \{0\} \tag{129}$$

where $[C]$ represents the quasi-diagonal linear elastic constitutive matrix, referring to the set of internal collocation points.

Vector $\{\sigma(\epsilon)\}$ refers to the stress field obtained from a given strain state, according with the constitutive model adopted.

The fact that the initial fields, ϵ^o_{ij}, do not appear explicitly in the equation (129) justifies the naming of implicit formulation originally adopted by Telles and Carrer [1991]. Normally, this equation is solved by Newton's method, based on its linearization in relation to the total strain vector, together with a specific equation that adequately establishes the increase in external loads. On the other hand, in the solution strategy presented in Peixoto et al. [2016], which is based on the ideas of Batoz and Dhatt [1979] and Yang and Shieh [1990], the load factor is treated as an additional variable of $\{Q\}^i$ and the linearization procedure must be performed taking this into account. In this way, the algorithm becomes generic enough to adopt different control methods for non linear analysis. The description of this strategy begins, rewriting equation 129 as follows:

$$\{Q\}^i = \lambda^i\{P\} - \{F\}^i = \{0\} \tag{130}$$

where

$$\{P\} = [N^\epsilon]\{y\} \tag{131}$$

$$\{F\}^i = \{\epsilon\}^i - [M^\epsilon]\big(\{\epsilon\}^i - [C]^{-1}\{\sigma(\epsilon)\}^i\big) \tag{132}$$

Thus, linearizing equation (130), i.e.,

$$\{Q\}^i_{j-1} + \left[\frac{\partial\{Q\}}{\partial\{\epsilon\}}\right]^i_{j-1}\{\delta\epsilon\}^i_j + \left[\frac{\partial\{Q\}}{\partial\lambda}\right]^i_{j-1}\delta\lambda^i_j \approx \{0\} \tag{133}$$

where j is an iterative index and $\delta(\cdot)^i_j = (\cdot)^i_j - (\cdot)^i_{j-1}$, the following result is obtained:

$$[D]^i_{j-1}\{\delta\epsilon\}^i_j = \delta\lambda^i_j\{P\} + \{Q\}^i_{j-1} \tag{134}$$

in which

$$[D]^i_{j-1} = \left[[I] - [M^\epsilon][C]^{-1}\left([C] - \left[\frac{\partial\sigma}{\partial\epsilon}\right]^i_{j-1}\right)\right] \tag{135}$$

where $[I]$ is an identity matrix and $\left[\frac{\partial\sigma}{\partial\epsilon}\right]$ is assembled from the tangent operator of the constitutive model, C^t_{ijkl}, particularized by equations (49) or (63), respectively, for elastoplastic or elastic-degrading constitutive models.

The iterative strain vector in equation (134), $\{\delta\epsilon\}^i_j$, can be dismembered in the following parcels:

$$\{\delta\epsilon\}^i_j = \delta\lambda^i_j\{\epsilon^P\}^i_j + \{\delta\epsilon^Q\}^i_j \tag{136}$$

where vector $\{\epsilon^P\}^i_j$ corresponds to the solution associated to the external load $\{P\}$, while $\{\delta\epsilon^Q\}^i_j$ is associated to the residual, $\{Q\}^i_{j-1}$, i.e.,

$$[D]^i_{j-1}\{\epsilon^P\}^i_j = \{P\} \tag{137}$$

$$[D]^i_{j-1}\{\delta\epsilon^Q\}^i_j = \{Q\}^i_{j-1} \tag{138}$$

Thus, in a given iteration, equations (137) and (138) can be solved independently and the correction of strains is obtained by equation (136), after evaluation of $\delta\lambda^i_j$, through a chosen control method. This sequence of activities is further systematized in section 4.2.1. Before that, expressions for the iterative corrections of vectors containing the boundary unknowns and the internal displacements, i.e., $\{\delta x\}^i_j$ and $\{\delta u^\Omega\}^i_j$, are shown. The same idea of breaking up equation (134) is followed and such expressions are important for application to the different control methods, listed in section 4.2.2.

Considering equations (126) and (128), it is possible to write

$$\{\delta x\}^i_j = \{x\}^i_j - \{x\}^i_{j-1} = \delta\lambda^i_j[N]\{y\} + [M]\{\delta\epsilon^o\}^i_j \tag{139}$$

$$\{\delta\epsilon\}^i_j = \{\epsilon\}^i_j - \{\epsilon\}^i_{j-1} = \delta\lambda^i_j[N^\epsilon]\{y\} + [M^\epsilon]\{\delta\epsilon^o\}^i_j \tag{140}$$

Isolating vector $\{\delta\epsilon^\varphi\}^i_j$ in equation (140) and substituting the result into the last term of equation (139), after application of equations (131), (136) and (137), the next result is obtained:

$$\{\delta x\}^i_j = \delta\lambda^i_j\{x^P\}^i_j + \{\delta x^Q\}^i_j \tag{141}$$

where

$$\{x^P\}^i_j = [N]\{y\} + [M][M^\epsilon]^{-1}\big([I] - [D]^i_{j-1}\big)\{\epsilon^P\}^i_j \tag{142}$$

$$\{\delta x^Q\}^i_j = [M][M^\epsilon]^{-1}\{\delta\epsilon^Q\}^i_j \tag{143}$$

Similarly, starting from equation (127), one can show that

$$\{\delta u^\Omega\}^i_j = \delta\lambda^i_j\{u^{\Omega,P}\}^i_j + \{\delta u^{\Omega,Q}\}^i_j \tag{144}$$

where

$$\{u^{\Omega,P}\}^i_j = [N^u]\{y\} + [M^u][M^\epsilon]^{-1}\big([I] - [D]^i_{j-1}\big)\{\epsilon^P\}^i_j \tag{145}$$

$$\{\delta u^{\Omega,Q}\}^i_j = [M^u][M^\epsilon]^{-1}\{\delta\epsilon^Q\}^i_j \tag{146}$$

4.2.1   Non linear algorithm

The above equations, can be organized in a systematic procedure as described below.

   i. Evaluate $\{P\}$, using equation (131), and initialize $i = 0$;

   ii. $i = i + 1$, $j = 0$;

   iii. Se $i >$ maximum number of increments $\Rightarrow$ STOP;

   iv. $\{Q\}^i_j = \{0\}$, $\{F\}^i_j = \{0\}$;

   v. $j = j + 1$;

   vi. Se $j >$ maximum number of iterations $\Rightarrow$ STOP;

   vii. Mount matrix $[D]^i_{j-1}$, from equation (135);

   viii. Solve equations (137) and (138) for $\{\epsilon^P\}^i_j$ e $\{\delta\epsilon^Q\}^i_j$;

   ix. Evaluate $\{x^P\}^i_j$, $\{\delta x^Q\}^i_j$, $\{u^{\Omega,P}\}^i_j$ e $\{\delta u^{\Omega,Q}\}^i_j$, using equations (142), (143), (145) and (146);

   x. Evaluate $\delta\lambda_j^i$, from a chosen control method (see section 4.2.2);

   xi. Mount $\{\delta\epsilon\}_j^i$, $\{\delta x\}_j^i$ e $\{\delta u^\Omega\}_j^i$, using equations (136), (141) and (144);

  xii. Actualize λ_j^i, $\{\hat\epsilon\}_j^i$, $\{x\}_j^i$ and $\{\hat u^\Omega\}_j^i$, using $(\cdot)_j^i = (\cdot)_{j-1}^i + \delta(\cdot)_j^i$;

 xiii. Mount $\{F\}_j^i$, from equation (132);

 xiv. Evaluate $\{Q\}_j^i = \lambda_j^i\{P\} - \{F\}_j^i$ (equation 130);

  xv. Verify convergence:

If $\dfrac{\|\{Q\}_j^i\|}{\|\lambda_j^i\{P\}\|} <$ Tolerance, return to step (ii) for the next load increment, else, return to step (v) for a new iteration.

4.2.2 Control methods

The most prominent advantage of the approach described above is its generality, especially for being able to work with different control methods.

Control methods are equations which determine the load factor increment, $\delta\lambda_j^i$, at each iteration. Depending mainly on the material behaviour, a specific control method has its advantages and its limitations or disadvantages. For this reason, a great number of them were developed and some are summarized in table 1.

Table 1: Types of control methods.

Control method	$\delta\lambda_j$ for $j = 1$	$\delta\lambda_j$ for $j > 1$
Load control	constant	$\delta\lambda_j = 0$
Direct displacement	$\dfrac{\delta U_1^k}{U_1^{P,k}}$	$-\dfrac{\delta U_j^{Q,k}}{U_j^{P,k}}$
Arc length	$\pm\dfrac{\Delta S}{\sqrt{\{U^P\}_1^T\{U^P\}_1}}$	$-\dfrac{\{\Delta U\}_1^T\{\delta U^Q\}_j}{\{\Delta U\}_1^T\{U^P\}_j}$
Generalized displacement	$\delta\lambda_1^1\sqrt{\dfrac{\{U^P\}_1^{1,T}\{U^P\}_1^1}{\{U^P\}_1^{i-1,T}\{U^P\}_1^{i-1}}}$	$-\dfrac{\{U^P\}_1^{i-1,T}\{U^Q\}_j^i}{\{U^P\}_1^{i-1,T}\{U^P\}_j^{i-1}}$
Strain control	$\dfrac{\Delta e}{\{C^\Omega\}^T\{\epsilon^P\}_1}$	$-\dfrac{\{C^\Omega\}^T\{\delta\epsilon^Q\}_j}{\{C^\Omega\}^T\{\epsilon^P\}_j}$

Herein the vector $\{U\}$ stands for a simple collection of all displacements values at boundary and domain collocation points which, when not prescribed, are evaluated at each iteration, and has the following increment decomposition:

$$\{\delta U\}_j = \delta\lambda_j\{U^P\}_j + \{\delta U^Q\}_j \tag{147}$$

where index j stands for an iteration in an increment i, which has been omitted for clearer presentation.

In the standard load control method, the load factor is pre-defined at the beginning of the increment and no variations are made during the iterative procedure. As is well known, this method inevitably results in non-convergence when the material exhibits softening behaviour. In the direct

displacement control method, as developed by Batoz and Dhatt [1979], a specific displacement component (of a specific point), identified by the superscript k in table 1, is selected to be controlled. If this component is correctly chosen, the divergence problem in softening behaviour can be solved, however, instabilities may occur if a snap-back trajectory is present in the equilibrium path. For that reason, arc-length methods, where a combination of displacement components and load factor increments is controlled, were developed. In expressions for this method, ΔS is the constant which limits the increment advance and $\{\Delta U\}_j$ means the cumulative displacements in the current increment, until iteration j. Usually, two different variations of arc-length control can be adopted. In the first, as used by Riks [1972] and Riks [1979], the iterative correction trajectory is always orthogonal to the first tangent of the increment, as represented in column for $j > 1$ in table 1. In the second variation, proposed by Crisfield [1981] and Crisfield [1983], a cylindrical trajectory is taken from the solution of a quadratic equation. With the intention to automatize the size of the incremental step, Yang and Shieh [1990], introduced the generalized displacement method, which relates two successive incremental steps, designated by i and $i - 1$ in the expressions presented in table 1.

For some problems, it seems to be more efficient to control a linear combination of some strain components of a limited region of the domain. Thus, the strain control method, developed by Chen and Schreyer [1990], can be used as an alternative. In the equations of table 1, Δe is a scalar value which limits the mentioned linear combination and $\{C^\Omega\}$ is the weight vector which determines the influence of each strain component.

5   Examples of Continuum Non Linear Problems

In this section the numerical analyses of three-dimensional and plane problems, involving elastoplastic and continuum damage models, performed with the presented formulation and algorithm, are presented. The results are compared to those obtained experimentally or analytically. For all examples, the control method adopted to drive the incremental-iterative procedure in the non linear analyses, considered a convergence tolerance of 10^{-4}.

In the first and second examples, the von Mises elastoplastic model is applied to a perforated strip with linear hardening and a pressurized thick cylinder, respectively. For the third example, the isotropic constitutive models of Simo and Ju [1987] and Oliver et al. [1990] were applied with an exponential damage evolution law for the analysis of a three-point bending beam. Three-dimensional and plane analysis were performed in all examples.

5.1   Example 1: perforated strip

In this example the case of a perforated strip under uniaxial tension is analyzed. Reference results where obtained experimentally by Theocaris and Marketos [1964] using the aluminum alloy $57S$, who assume the Mises yield criterion to be the most suitable and accepted as governing the mode of nucleation and evolution of plastic enclaves for such material. The geometry of this thin plate is presented in Figure 12, were the geometric parameters are $h = 18$ mm, $r = 5$ mm and thickness 1 mm.

The elastoplastic von Mises associative constitutive model, as detailed in Appendix A.1, is used with the Young's modulus $E = 70$ GPa, the Poisson's ratio $\nu = 0.2$, the initial yield limit $\sigma_Y = 243$ MPa and a linear hardening law with $H = 0.032E$. The tensile load is taken to be $\sigma = 0.47\sigma_Y$.

Due to the symmetry, only a quarter of the plane problem is discretized, following the analysis presented in Aliabadi [2002]. Only part of the domain, where dissipative effects are probable to occur, need to be discretized.
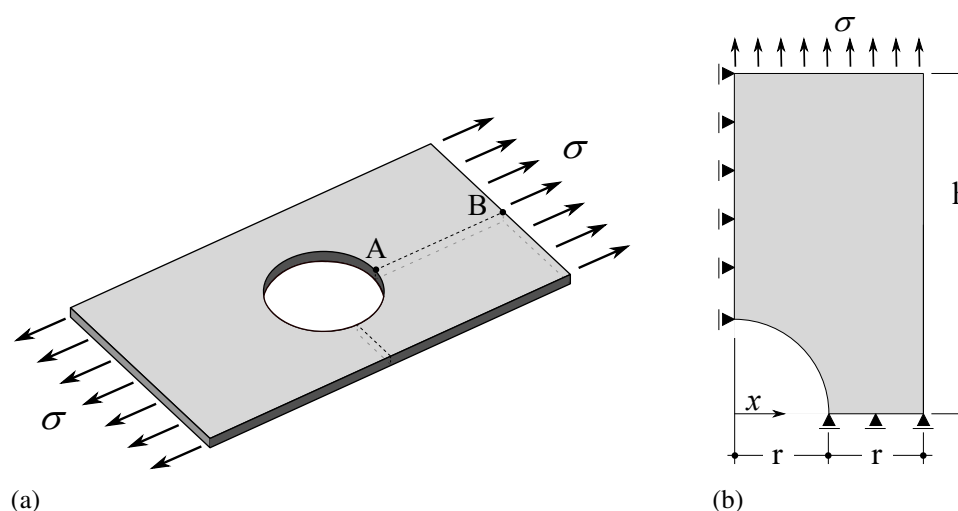
Figure 12: Example 1 – Perforated strip; (a) Geometry and load, (b) Plane model dimensions

Plane stress was considered in bidimensional analysis, where the analysis were performed with two different meshes: a coarse one (Mesh 1) with 32 quadratic boundary elements and 16 quadratic quadrilateral cells, and a fine one (Mesh 2) with 64 linear boundary elements and 64 linear quadrilateral cells. Also, the analysis where performed with three-dimensional model. In this case, due to the symmetry, only one eight of the problem was discretized in other two meshes: a coarse one (Mesh 3) with 448 linear quadrilateral boundary elements and 64 constant hexahedral cells, and a fine one (Mesh 4) with 1664 boundary elements and 256 cells. The used meshes can be seen in Figure 13.

In both analysis, the usual load control was adopt, with a total of 50 load steps. Experimental and numerical results are plotted in Figure 14. Additionally, in Figure 15 stress-displacement plots obtained for the refined meshes (Mesh 2 and Mesh4) are shown for some key positions on the strip, together with FEM results presented by Aliabadi [2002].

5.2   Example 2: pressurized thick cylinder

This example presents a steel thick cylinder subjected to internal pressure. The internal and external radius were taken as 100 mm and 200 mm, respectively. Due to the symmetry of the problem, only one quarter of a section is modelled. The problem is considered under plain strain conditions. For three-dimensional analysis, the transversal section planes have displacements restricted in the longitudinal direction, in order to make the analysis under a plane strain condition. The solid modelled also consider one quarter of a section, with width 5.0 mm. Figure 16 illustrates the geometry, load and support conditions.

Again, the elastoplastic von Mises associative constitutive model was adopted, with the Young's modulus $E = 210$ GPa, the Poisson's ratio $\nu = 0.3$ and the yield limit $\sigma_Y = 240$ MPa. Perfect plasticity were considered, with hardening parameter $H = 0$. The internal pressure was taken to be $\sigma = 180$ MPa. An analytical solution for this problem, performed by Hill [1950], is presented in de Souza Neto et al. [2006].

Two different meshes were analysed under plane strain conditions. The coarse mesh (Mesh 1) has 24 quadratic boundary elements and 32 quadratic internal cells, while the (Mesh 2) has 48 quadratic boundary elements and 128 quadratic cells. The mesh used in the three-dimensional analysis (Mesh 3) has 648 linear quadrilateral boundary elements and 288 hexahedral constant

(a)   (b)   (c)

(d)
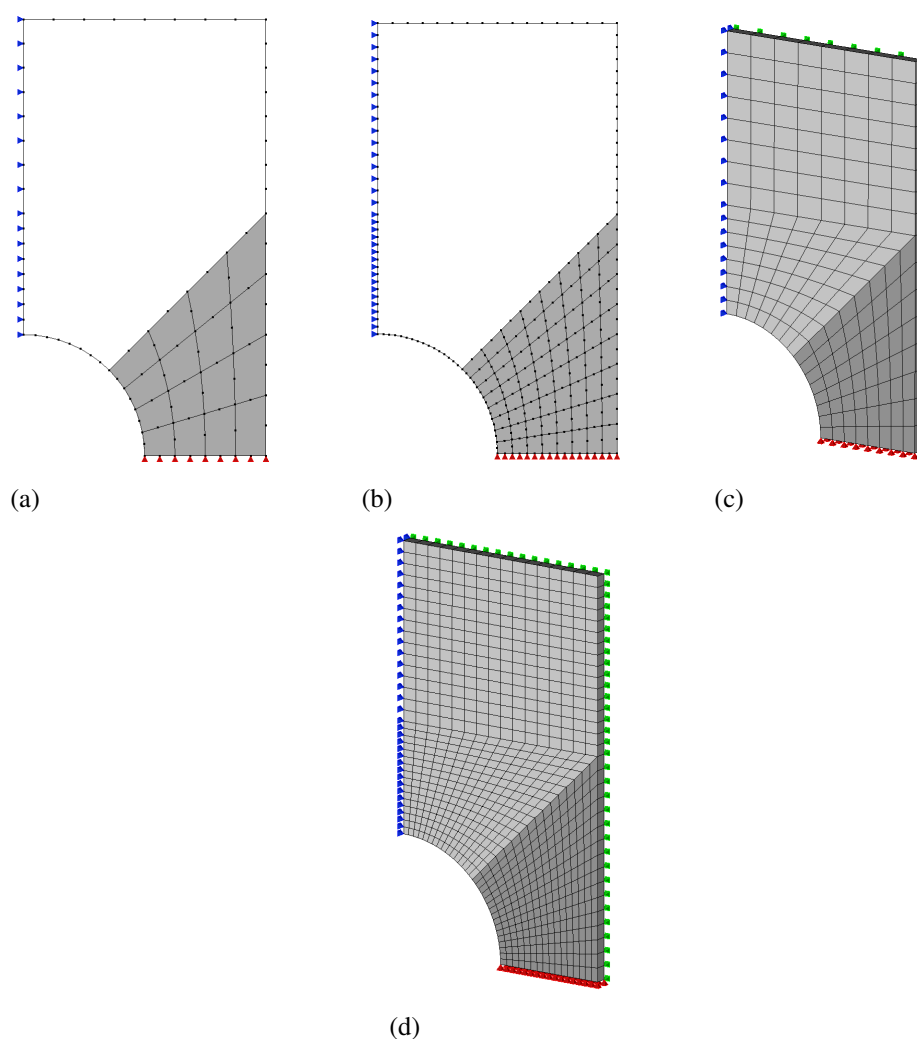
Figure 13: Example 1 – Meshes considered in the analyses; (a) Mesh 1, (b) Mesh 2, (c) Mesh 3, (d) Mesh 4

cells. A total of 30 steps, with load control, were used in the whole cases. Figure17 illustrates the the refereed meshes.

The results achieved for hoop and radial stresses components, together with the analytical solution are plotted in Figures 18 and 19 respectively.

## 5.3   Example 3: three point bending

The three point bending of a notched concrete beam, experimentally treated by Petersson [1981], is addressed in this example. The problem geometry, load and supports are depicted in Figure 20. The geometrical parameters were taken as $l = 1000$ mm, $h = 200$ mm, $a = 100$ mm and $w = 20$ mm. A width $t = 50$ mm was considered for the beam.

To represent the concrete softening behaviour, the isotropic constitutive models of Simo and Ju [1987] and Oliver et al. [1990] were applied with an exponential damage evolution law of the form

$$D(\phi) = 1 - \left[\frac{\kappa_o}{\phi}\right] e^{-b(\phi - \kappa_o)}, \quad \text{with} \quad \kappa_o = \frac{f_t}{\sqrt{E}} \quad \text{and} \quad b = \frac{h f_t}{G_f \sqrt{E}} \tag{148}$$
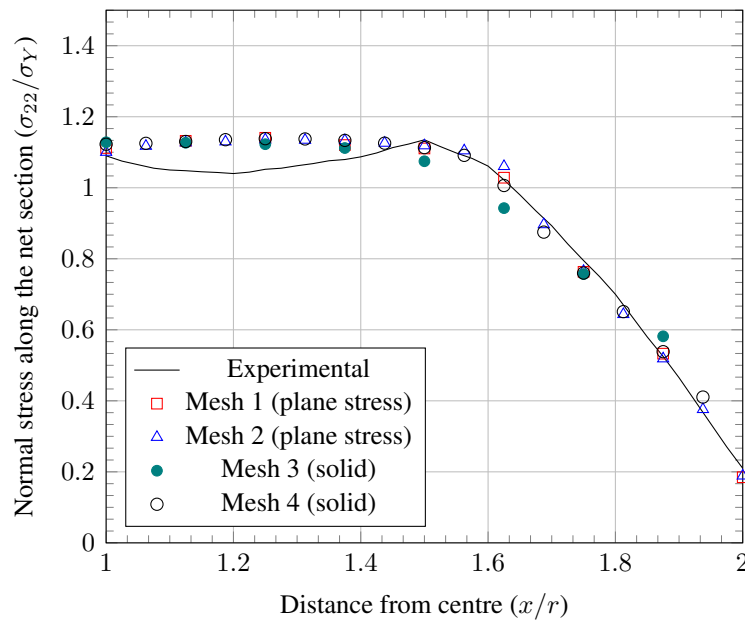
Figure 14: Example 1 – Computed stresses on net section of the plate for a load of $0.47\sigma_Y$, and the experimental reference [Theocaris and Marketos, 1964].
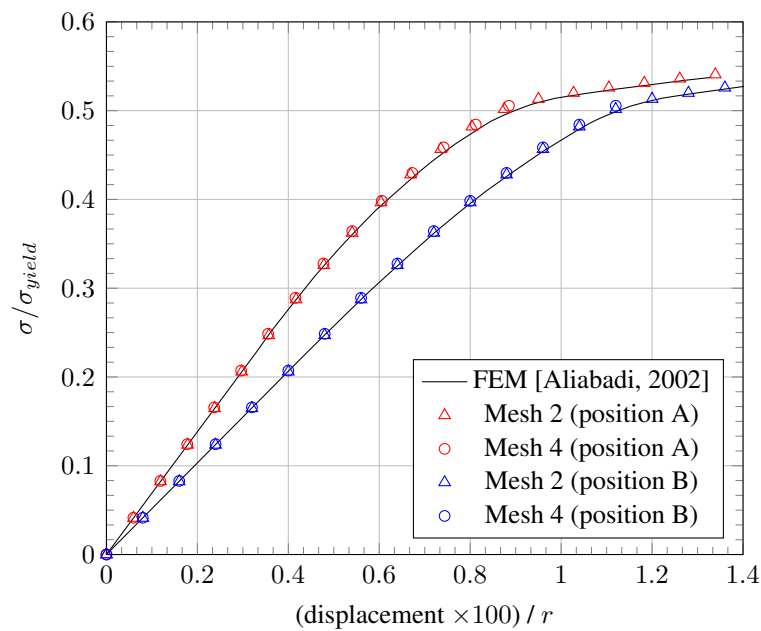

**Figure 15: Example 1 – Displacements at positions A and B (from Figure 12)**

where f_t is the uni-axial tensile strength, G_f is the fracture energy, h is a material's characteristic length and E is the Young's modulus. For concrete mechanical properties, the following values were adopted: $f_t = 3.33$ MPa, $G_f = 0.124$ N/mm, $h = 30$ mm and $E = 30$ GPa and Poisson's ratio $\nu = 0.20$.

Only the domain's region around the expected area to be damaged was discretized by cells. For the plane stress analysis a total of 100 constant internal cells were employed, while the boundary was divided in 392 linear elements. For the three-dimensional analysis, the mesh has 952 quadri-

(a)   (b)
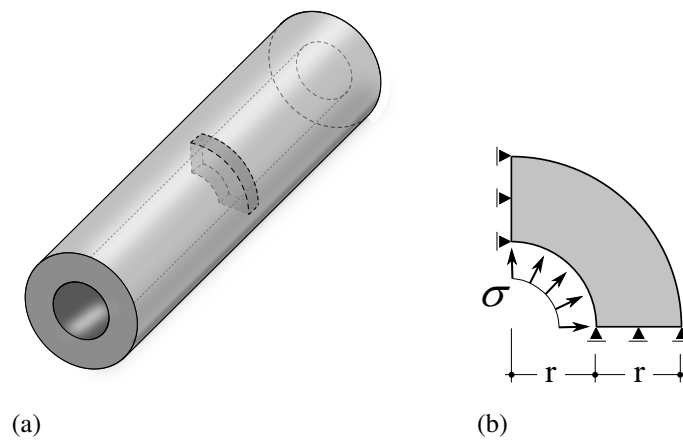
Figure 16: Example 2 – Pressurized thick cilinder; (a) Geometry, (b) Plane model dimensions and supports

(a)
Mesh1

(b)
Mesh2

(c)
Mesh3
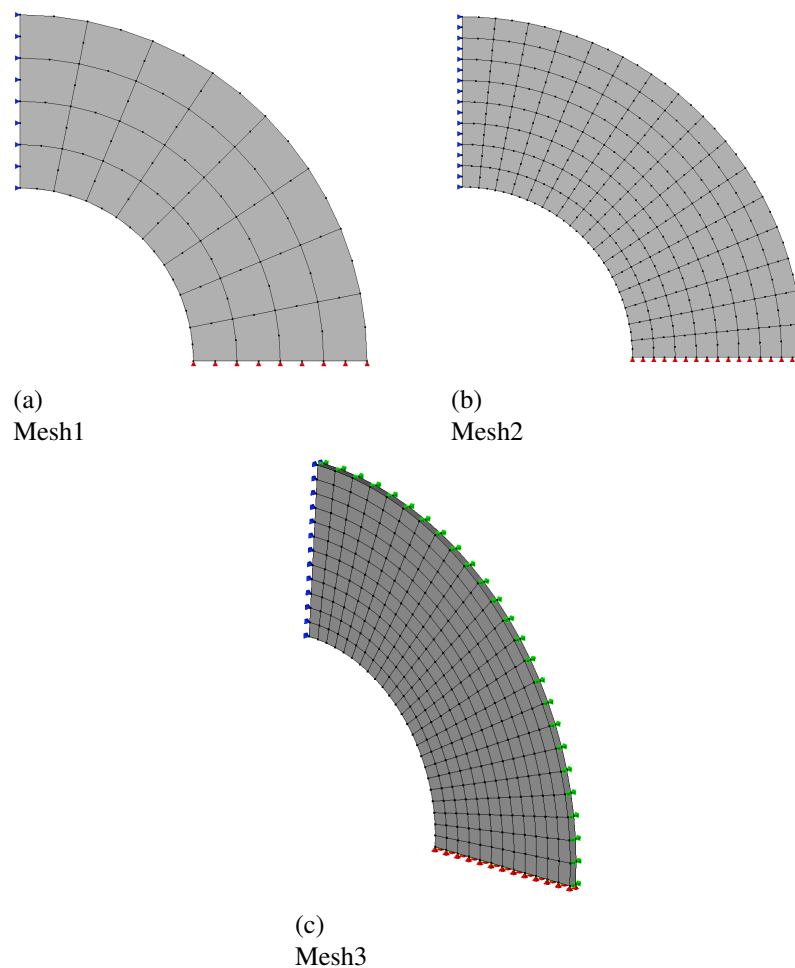
Figure 17: Example 2 – Meshes considered in the analyses

lateral quadratic elements and 36 hexahedral constant cells. Figure 21 illustrates these meshes. The analyses were performed by controlling the vertical displacement of a loaded element node.

A comparison between the models results and Petersson's experimental envelopment is pre-
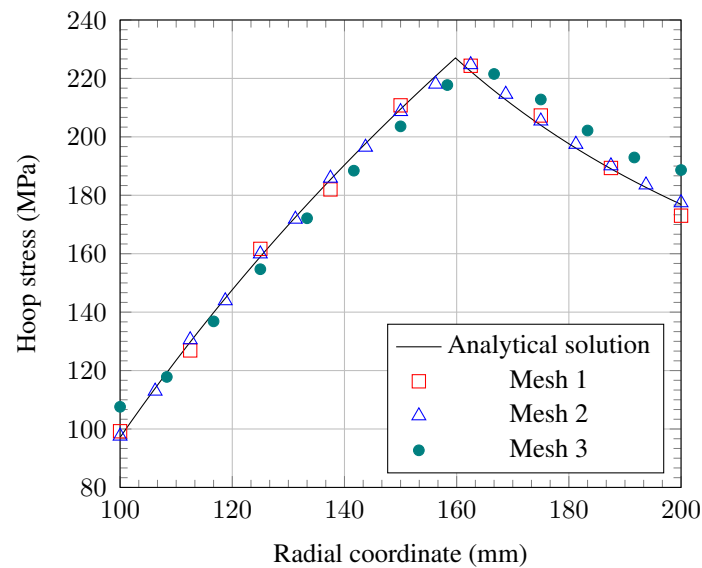
Figure 18: Example 2 – Computed circumferential stress distribution in the pressurized cylinder along the radial coordinate, and the analytical solution [de Souza Neto et al., 2006].
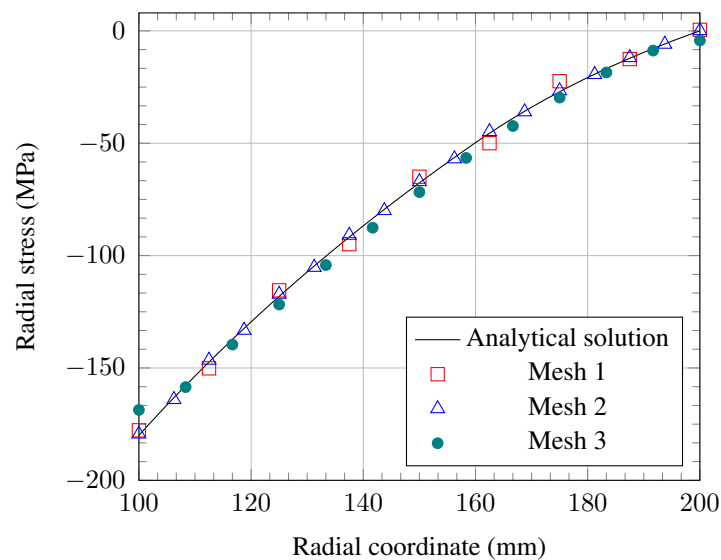

Figure 19: Example 2 – Computed radial stress distribution in the pressurized cylinder along the radial coordinate, and the analytical solution [de Souza Neto et al., 2006].

sented in Figure 22.

Since the region close to the applied load is subjected to compressive stress states, spurious damage evolution is verified for Simo and Ju [1987] model, leading to a premature loss of structural strength. However, for the Oliver et al. [1990] model, where the equivalent strain norm involves only positive strain components, as detailed in Appendix A.2, such problem is overcome and a good agreement between the numerical and experimental results is obtained.
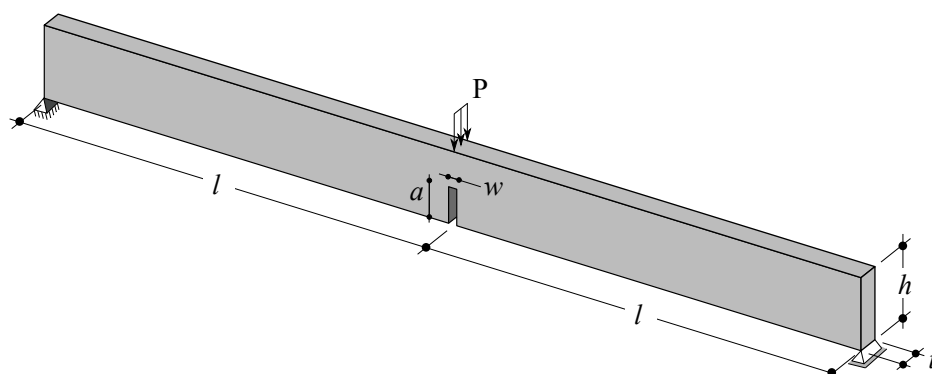
Figure 20: Example 3 – Three point bending of a concrete notched beam: geometry, load and supports.


(a)

(b)
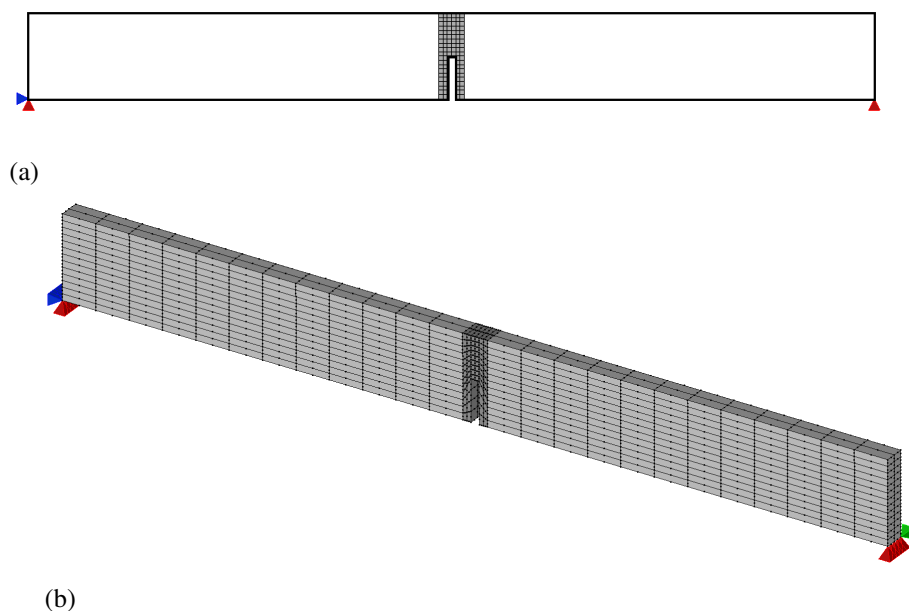
Figure 21: Example 3 – Meshes considered in the analyses (a) plane stress and (b) three-dimensional

6   Strain Localization and Material Bifurcation Analysis

This section addresses the necessary conditions for the occurrence of discontinuous bifurcation in material media that present softening laws in their continuous (or macroscopic) constitutive formulation. By bifurcation, we mean the instant of inelastic loading at which the strain field is no longer continuous, which does not necessarily correspond to the appearance of discontinuities in the displacement field. In this case, there is the emergence of the so-called weak discontinuity surfaces. From there, strain localization bands (regions of high strain values) can be formed, delimited by such surfaces.

Strain localization in homogeneous media with softening is associated with the loss of the elliptical character of the set of differential equations and, consequently, the boundary value problem becomes ill-defined. As a result, the solution is no longer unique and, in numerical analyses, a lack of objectivity in relation to mesh refining is verified, since the most stable solution corresponds to
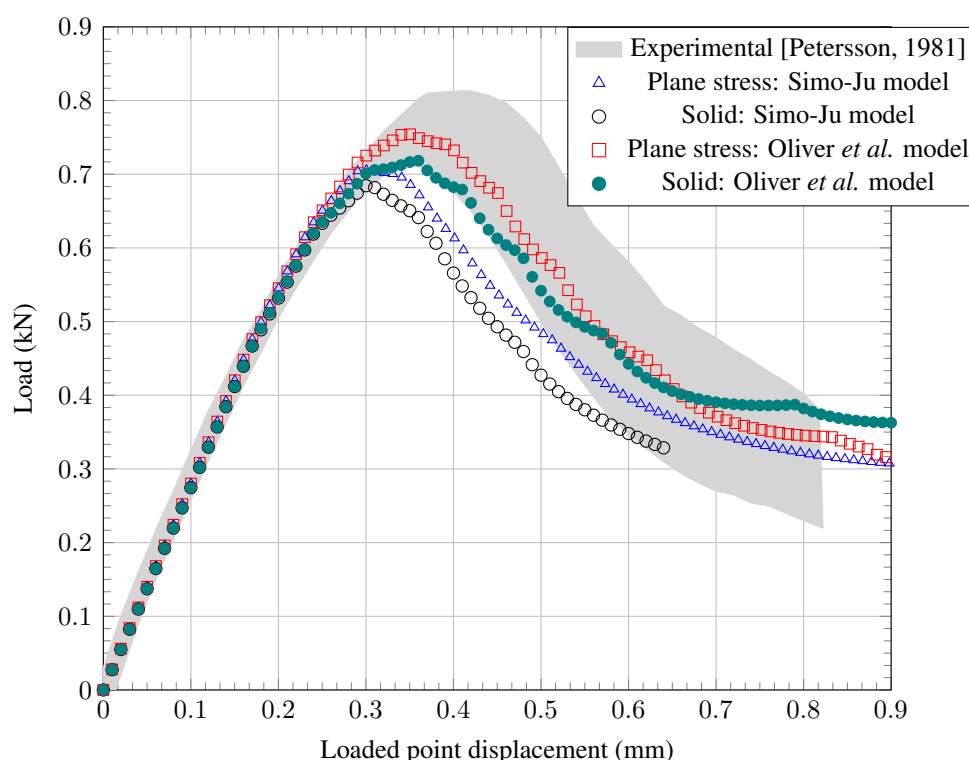
Figure 22: Example 3 – Results for vertical displacement of the loaded point: numerical BEM analyses and experimental.

a zero-thickness localization band without energy dissipation during failure.

In general, bifurcation does not coincide with the beginning of the inelastic regime. Normally, from a macroscopic point of view, it is preceded by a dissipation phase in a continuous medium. Thus, based on a valid mathematical formalism for time-independent constitutive models, the necessary conditions for the appearance of strain localization are established in the following.

It starts by assuming a homogeneous three-dimensional solid domain Ω, subject to a uniform state of small deformations ϵ_{ij}. We then look for the necessary conditions so that the rate of the strain field, $\dot{\epsilon}_{ij}$, can become discontinuous on two surfaces that delimit a band $\Omega_b \subset \Omega$, as indicated in Figure 23. It is also assumed that the two surfaces have parallel tangent planes at the point under analysis, so that a single orthonormal basis $\{\mathbf{n}, \mathbf{p}, \mathbf{q}\}$ can be established, where $\mathbf{n}$ is the unit vector normal to these planes.
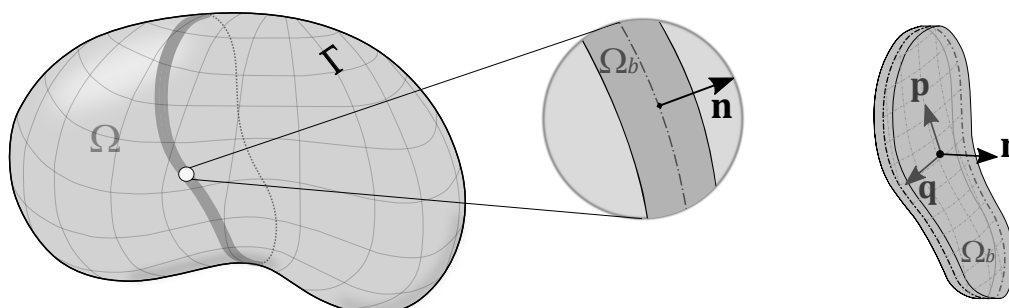
Figure 23: Solid domain with strain localization band

Considering now that the displacement rate, $\dot{u}_i$, remains continuous on the two surfaces, we

have:

$$[\![\partial_{\mathbf{q}} \dot{u}_i]\!] = [\![\dot{u}_{i,j}]\!] q_j = 0 \tag{149a}$$

$$[\![\partial_{\mathbf{p}} \dot{u}_i]\!] = [\![\dot{u}_{i,j}]\!] p_j = 0 \tag{149b}$$

where $[\![\cdot]\!]$ represents the difference between the values of field $(\cdot)$, in and out of the localization band, while $\partial_{\mathbf{q}}(\cdot)$ and $\partial_{\mathbf{p}}(\cdot)$ are the directional derivatives of $(\cdot)$, respectively in the directions of $\mathbf{q}$ and $\mathbf{p}$.

From equations (149), to occur discontinuity in the strain rate, one must have:

$$[\![\dot{u}_{i,j}]\!] n_j = \dot{\alpha} m_i \neq 0 \quad \Rightarrow \quad [\![\dot{u}_{i,j}]\!] = \dot{\alpha} m_i n_j \tag{150}$$

where $\dot{\alpha}$ is a scalar corresponding to the magnitude of the jump in the velocity field and m_i is a unit vector referring to the direction of this jump. It can also be noted that the angle between the vectors n_i and m_i determines the failure mode, which can vary from simple opening, when they are parallel (mode I), to pure shear, when they are perpendicular to each other (mode II). For intermediate angles, there are so-called mixed modes.

As a consequence of equation (150), the strain rate must satisfy the following compatibility equation:

$$[\![\dot{\epsilon}_{ij}]\!] = \frac{1}{2}([\![\dot{u}_{i,j}]\!] + [\![\dot{u}_{j,i}]\!]) = \frac{1}{2}(m_i n_j + m_j n_i)\dot{\alpha} \tag{151}$$

On the other hand, the equilibrium condition states that tractions, as well as their rates, must be continuous on surfaces of weak discontinuity, i.e.,

$$[\![\dot{\sigma}_{ij} n_j]\!] = [\![\dot{\sigma}_{ij}]\!] n_j = 0 \tag{152}$$

Thus, remembering that stress and strain rates are related to each other by a tangential operator – see equations (48) and (62) –, introduction of equation (151) into (152) gives

$$(n_i C_{ijkl}^{t,\Omega_b} n_l)\dot{\alpha} m_k = n_i (C_{ijkl}^{t,\Omega\backslash\Omega_b} - C_{ijkl}^{t,\Omega_b})\dot{\epsilon}_{kl}^{\Omega\backslash\Omega_b} \tag{153}$$

where $C_{ijkl}^{t,\Omega\backslash\Omega_b}$ and $\epsilon_{kl}^{\Omega\backslash\Omega_b}$ represent, respectively, the tangent stiffness operator and strain field outside the strain localization band, while C_{ijkl}^{t,Ω_b} is the tangent operator inside it.

At this point, one can differentiate between discontinuous bifurcation, when, in fact, $C_{ijkl}^{t,\Omega_b} \neq C_{ijkl}^{t,\Omega\backslash\Omega_b}$, and continuous bifurcation, when the constitutive tangent tensors inside and outside the localization band are the same. In the latter case, equation (153) takes the form:

$$(n_i C_{ijkl}^{t} n_l)m_k = Q_{jk} m_k = 0 \tag{154}$$

where Q_{jk} is called the localization tensor or acoustic tensor. This second term is adopted for historical reasons, since in elastic problems, the eigenvalues of this tensor, divided by the specific mass of the material, are associated with the propagation speeds of waves in the solid medium [van der Giessen and de Borst, 1998].

Rice and Rudnicki [1980] showed that the continuous bifurcation condition corresponds to a limiting case of the discontinuous one, with a tendency to occur firstly during inelastic loading. Thus, equation (154) can be understood as the most unfavourable case for the occurrence of discontinuous bifurcation and can be adopted as a necessary condition for the beginning of strain localization.

It should also be noted that the trivial solution of the equation (154), $m_k = 0$, corresponds to $[\![\dot{\epsilon}_{ij}]\!] = 0$ and therefore the localization will start only when Q_{jk} is singular, i.e., the bifurcation condition becomes:

$$\det(Q_{jk}) = \det(n_i C_{ijkl}^{t} n_l) = 0 \tag{155}$$

In a general way, solution of equation (155) is associated to a optimization problem of find, between all possible directions that satisfy the singularity condition (if exists at least one), the n_i that gives the maximum softening modulus, H. However, for some cases, a closed set of equations can be analytically obtained. For example, considering an isotropic damage model with particular parameters defined in Oliver et al. [2006], detailed in Appendix A, a critical softening modulus and the associated band orientation can be obtained for plane problems, as described by Peixoto et al. [2018]. On the other hand, for associative elastoplastic models, closed solutions can be found in Oliver et al. [1999].

7   The Continuum Strong Discontinuity Approach

In the previous section, the necessary conditions for bifurcation, i.e., the appearance of discontinuities in the strain field during inelastic loading with softening, were established. It is now a subsequent step, referring to the transition between these discontinuities, called weak, and the emergence of jumps in the displacement field, known as strong discontinuities. Such a transition can be interpreted as a model with a localization band of variable thickness. When standard continuous constitutive models are employed together with these discontinuous kinematics, in order to represent dissipative effects, we have the so-called Continuum Strong Discontinuity Approach (CSDA), which is the scope of the present section.

Firstly, a kinematic formulation, valid for weak and strong discontinuities, is presented. Next, the Strong Discontinuity Analysis where, from the imposition of equilibrium conditions on the discontinuous surface, cohesive constitutive model is obtained – which relates tractions to displacement jumps – associated with the original continuous constitutive model, is addressed. As a consequence of this analysis, the necessary conditions for the establishment of the strong discontinuity are obtained, in addition to a reinterpretation of the softening modulus of the continuous constitutive model to make it compatible with the discrete model. Finally, the numerical aspects that define the variable bandwidth model are presented.

7.1   Weak and Strong Discontinuity Kinematics

Kinematic equations involving weak and strong discontinuities are presented in this section, followed by the establishment of a regularized formulation capable of treating the two cases in a single set of equations, as developed by Oliver et al. [1998, 1999].
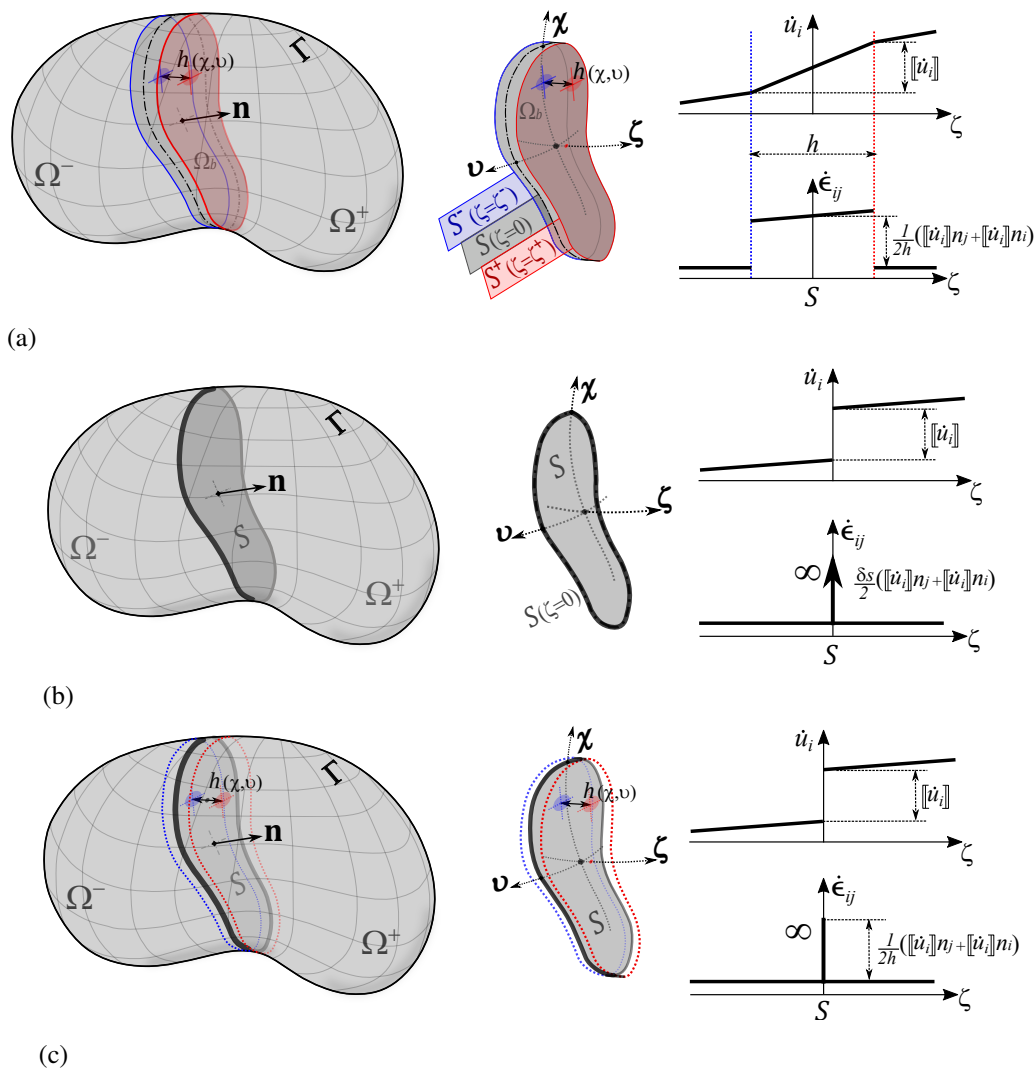
7.1.1   Weak discontinuity kinematics

Referring to Figure 24a, a two-dimensional domain Ω is assumed, where the material points are designated by $\mathbf{x}$. We also consider a curvilinear coordinate system, $\{\chi, \upsilon, \zeta\}$, so that $\zeta = 0$ defines a surface $\mathcal{S}$, entirely contained into a localization band, Ω_b. The boundaries of this band are also formed by surfaces of a fixed coordinate ζ, i.e., $\mathcal{S}^-(\zeta = \zeta^-)$ and $\mathcal{S}^+(\zeta = \zeta^+)$, which allows to define its thickness as a function of only $(\chi, \upsilon) : h(\chi, \upsilon)$. The surface $\mathcal{S}$ divides the domain into two parts, Ω^- and Ω^+, and defines a unit vector n_i, normal to $\mathcal{S}$ and directed to Ω^+.

Being $\{\hat{\mathbf{e}}_\chi, \hat{\mathbf{e}}_\upsilon, \hat{\mathbf{e}}_\zeta\}$ the orthonormal basis associated with the curvilinear coordinates and defining by $r_\chi(\chi, \upsilon, \zeta)$, $r_\upsilon(\chi, \upsilon, \zeta)$ and $r_\zeta(\chi, \upsilon, \zeta)$ their corresponding scale factors, such that $ds_\chi = r_\chi d\chi$, $ds_\upsilon = r_\upsilon d\upsilon$ and $ds_\zeta = r_\zeta d\zeta$ are the arc lengths, respectively along χ, υ and ζ, one can write $h(\chi, \upsilon) = r_\zeta(\chi, \upsilon, 0)(\zeta^+ - \zeta^-)$. It should also be noted that, for points located on $\mathcal{S}$, the unit vector $\hat{\mathbf{e}}_\zeta$ coincides with the normal n_i.

Assuming now the following velocity field in Ω:

$$\dot{u}_i(\mathbf{x}, t) = \dot{\bar{u}}_i(\mathbf{x}, t) + \mathcal{H}_{\Omega_b}(\mathbf{x}, t)[\![\dot{u}_i]\!](\mathbf{x}, t) \tag{156}$$

Figure 24: Kinematics with discontinuities: (a) weak discontinuity, (b) strong discontinuity, (c) regularized formulation

where t represents time, $\bar{u}(\mathbf{x}, t)$ and $[\![u_i]\!](\mathbf{x}, t)$ are displacement fields $\mathcal{C}^0$-continuous and $\mathcal{H}_{\Omega_b}(\mathbf{x}, t) = \mathcal{H}_{\Omega_b}(\zeta, t)$ is a ramp function, given by:

$$
\mathcal{H}_{\Omega_b} = \begin{cases} 0, & \text{para } \mathbf{x} \in \Omega^- \backslash \Omega_b \\ 1, & \text{para } \mathbf{x} \in \Omega^+ \backslash \Omega_b \\ \dfrac{\zeta - \zeta^-}{\zeta^+ - \zeta^-}, & \text{para } \mathbf{x} \in \Omega_b \end{cases} \tag{157}
$$

where $a \backslash b$ means the part of a excluding b, i.e., $a \backslash b = a - (a \cap b)$.

It can be seen that $\mathcal{H}_{\Omega_b}$ represents a unit jump between the surfaces $\mathcal{S}^-$ and $\mathcal{S}^+$, since, for the same coordinate χ, $\{[\![\mathcal{H}_{\Omega_b}]\!] = \mathcal{H}_{\Omega_b}(\zeta^+, t) - \mathcal{H}_{\Omega_b}(\zeta^-, t) = 1 \ \forall (\chi, \upsilon)\}$. Its gradient, in curvilinear coordinates and written in an extended form, is given by:

$$
\begin{aligned}
\mathcal{H}_{\Omega_b,i} &= \frac{1}{r_\zeta} \frac{\partial H_{\Omega_b}}{\partial \zeta} \hat{\mathbf{e}}_\zeta + \frac{1}{r_\chi} \frac{\partial H_{\Omega_b}}{\partial \chi} \hat{\mathbf{e}}_\chi + \frac{1}{r_\upsilon} \frac{\partial H_{\Omega_b}}{\partial \upsilon} \hat{\mathbf{e}}_\upsilon = \mu_{\Omega_b} \frac{1}{h_\zeta} \hat{\mathbf{e}}_\zeta \\
h_\zeta(\chi, \upsilon, \zeta) &= r_\zeta(\chi, \upsilon, \zeta)(\zeta^+ - \zeta^-) \\
h_\zeta(\chi, \upsilon, 0) &= r_\zeta(\chi, \upsilon, 0)(\zeta^+ - \zeta^-) = h(\chi, \upsilon)
\end{aligned} \tag{158}
$$

where μ_{Ω_b} is a collocation function in Ω_b, i.e., $\{\mu_{\Omega_b}(\mathbf{x}) = 1 \text{ if } \mathbf{x} \in \Omega_b \text{ and } \mu_{\Omega_b}(\mathbf{x}) = 0 \text{ if } \mathbf{x} \notin \Omega_b\}$.

Thus, taking the symmetrical part of the gradient of equation (156) and making use of equation (158), the following field of infinitesimal strain rates is obtained:

$$\dot{\epsilon}_{ij}(\mathbf{x}, t) = \frac{1}{2}(\dot{\bar{u}}_{i,j} + \dot{\bar{u}}_{j,i}) + \frac{\mathcal{H}_{\Omega_b}}{2}(\llbracket \dot{u}_{i,j} \rrbracket + \llbracket \dot{u}_{j,i} \rrbracket) + \frac{\mu_{\Omega_b}}{2h_\zeta}(\llbracket \dot{u}_i \rrbracket \hat{e}_j^\zeta + \llbracket \dot{u}_j \rrbracket \hat{e}_i^\zeta) \qquad (159)$$

where $\hat{e}_i^\zeta$ refer to the projections of $\hat{\mathbf{e}}_\zeta$ in the original cartesian coordinate system.

Note that the first two terms on the right hand side in equation (159) represent a continuous portion of the strain field, while the last one, as indicated in Figure 24a, has non-zero values only in the (localization) band Ω_b, characterizing strain discontinuities on the surfaces $\mathcal{S}^-$ and $\mathcal{S}^+$.

7.1.2   Strong discontinuity kinematics

Strong discontinuity kinematics can be defined as a limiting case of weak discontinuity kinematics when the strain localization band tends towards the surface $\mathcal{S}$, i.e., towards a band of zero thickness, as represented in the Figure 24b. Thus, as $\zeta^- \to 0$ and $\zeta^+ \to 0$ simultaneously, the ramp function of equation (157) collapses into the Heaviside (step) function, given by:

$$\mathcal{H}_\mathcal{S}(\mathbf{x}) = \begin{cases} 0, & \text{to } \mathbf{x} \in \Omega^- \\ 1, & \text{to } \mathbf{x} \in \Omega^+ \end{cases} \qquad (160)$$

Thus, the displacement rate field takes the form:

$$\dot{u}_i(\mathbf{x}, t) = \dot{\bar{u}}_i(\mathbf{x}, t) + \mathcal{H}_\mathcal{S}(\mathbf{x})\llbracket \dot{u}_i \rrbracket(\mathbf{x}, t) \qquad (161)$$

i.e., becoming discontinuous on $\mathcal{S}$. In this case, function $\llbracket u_i \rrbracket(\mathbf{x}, t)$ represents the magnitude of the jump components in the displacement field over the strong discontinuity surface.

The infinitesimal strain rate field, compatible with the equation 161, is, in turn, written as:

$$\dot{\epsilon}_{ij}(\mathbf{x}, t) = \frac{1}{2}(\dot{\bar{u}}_{i,j} + \dot{\bar{u}}_{j,i}) + \frac{\mathcal{H}_\mathcal{S}}{2}(\llbracket \dot{u}_{i,j} \rrbracket + \llbracket \dot{u}_{j,i} \rrbracket) + \frac{\delta_\mathcal{S}}{2}(\llbracket \dot{u}_i \rrbracket n_j + \llbracket \dot{u}_j \rrbracket n_i) \qquad (162)$$

where $\delta_\mathcal{S}$ is the Dirac delta function over the surface $\mathcal{S}$.

It can be seen that the first two terms on the right in the equation (162) correspond to a parcel containing, at most, finite discontinuities, while the last term becomes infinite over $\mathcal{S}$.

7.1.3   Regularized kinematics

Now, a regularized formulation of kinematics with discontinuities, capable of representing both cases (weak and strong discontinuities) through a single set of equations, is presented. Such formulation will prove useful, later, in the development of a numerical model with variable localization bandwidth.

From the Figure 24c, the displacement and strain fields are written in the following forms:

$$\dot{u}_i(\mathbf{x}, t) = \dot{\bar{u}}_i(\mathbf{x}, t) + \mathcal{H}_\mathcal{S}(\mathbf{x})\llbracket \dot{u}_i \rrbracket(\mathbf{x}, t) \qquad (163)$$

$$\dot{\epsilon}_{ij}(\mathbf{x}, t) = \underbrace{\frac{1}{2}(\dot{\bar{u}}_{i,j} + \dot{\bar{u}}_{j,i}) + \frac{\mathcal{H}_\mathcal{S}}{2}(\llbracket \dot{u}_{i,j} \rrbracket + \llbracket \dot{u}_{j,i} \rrbracket)}_{\dot{\bar{\epsilon}}_{ij} \text{ (finite)}} + \underbrace{\frac{\mu_\mathcal{S}}{2h(\zeta)}(\llbracket \dot{u}_i \rrbracket n_j + \llbracket \dot{u}_j \rrbracket n_i)}_{\text{infinity when } h(\zeta) \to 0} \qquad (164)$$

where $\mu_\mathcal{S}$ is a collocation function over $\mathcal{S}$, i.e., $\{\mu_\mathcal{S}(\mathbf{x}) = 1 \text{ if } \mathbf{x} \in \mathcal{S} \text{ and } \mu_\mathcal{S}(\mathbf{x}) = 0 \text{ if } \mathbf{x} \notin \mathcal{S}\}$.

When the bandwidth, $h(\zeta)$, approaches zero, $\left(\frac{\mu_{\mathcal{S}}}{2h(\zeta)}\right) \to \delta_{\mathcal{S}}$, and equations (163) and (164) become equivalent to equations (161) and (162). In this way, the kinematics of strong discontinuities is completely recovered.

On the other hand, since $h(\zeta) = h_\zeta(\chi, \upsilon, 0)$ and n_i corresponds to $\hat{\mathbf{e}}_\zeta$ in $\mathcal{S}$, the strain rate of equation (164) represents its correspondent in the presence of weak discontinuities (equation 159), provided that the localization band thickness is sufficiently small. It should be noted, however, that in this case, $h(\zeta) \neq 0$, and the fields of equations (163) and (164) are not compatible, in the sense that $\dot{\epsilon}_{ij} \neq \frac{1}{2}(\dot{u}_{i,j} + \dot{u}_{j,i})$. Compatibility is achieved only when $h(\zeta) \to 0$.

As will be discussed later, a variable bandwidth model can be adopted, characterized by the evolution of the strain localization band, from a finite thickness h, defined at the bifurcation instant, t_B, to a null thickness , numerically characterized by a small constant k, representing the regime with strong discontinuity, that begins at time t_{SD}. In this way, the state of total strains for an instant of time after the start of the strong discontinuity regime, i.e., $t \geqslant t_{SD}$, can be obtained from time integration of equation (164), i.e.,

$$\epsilon_{ij}(\mathbf{x},t)|_{t \geqslant t_{SD}} = \underbrace{\int_0^t \dot{\bar{\epsilon}}_{ij}dt + \frac{\mu_{\mathcal{S}}}{2}\int_{t_B}^{t_{SD}}\frac{1}{h}(\llbracket\dot{u}_i\rrbracket n_j + \llbracket\dot{u}_j\rrbracket n_i)dt + \frac{\mu_{\mathcal{S}}}{2}\int_{t_{SD}}^t\frac{1}{h}(\llbracket\dot{u}_i\rrbracket n_j + \llbracket\dot{u}_j\rrbracket n_i)dt}_{\bar{\epsilon}_{ij}}$$

$$= \underbrace{\bar{\epsilon}_{ij}}_{\text{finite for } h \equiv k \to 0} + \underbrace{\mu_{\mathcal{S}}\frac{1}{2h}(\Delta\llbracket u_i\rrbracket n_j + \Delta\llbracket u_j\rrbracket n_i)}_{\text{infinity for } h \equiv k \to 0}$$

(165)

where $\Delta\llbracket u_i\rrbracket = \llbracket u_i\rrbracket(\mathbf{x},t) - \llbracket u_i\rrbracket(\mathbf{x},t_{SD})$ is the increment in the displacement jump during the strong discontinuity regime and the material character of the discontinuous surface, i.e., $\dot{n}_i = 0$, was adopted.

7.2   The Strong Discontinuity Analysis

The objective of Strong Discontinuity Analysis (SDA) is to identify the necessary conditions for continuous constitutive models to be compatible with the kinematics represented by the equation (165). As a starting point, it should be noted that the continuity of traction (and its rate), through the interface $\mathcal{S}$, is a necessary condition for meeting the equilibrium equations, i.e.,

$$t_i(\mathbf{x},t) = \sigma_{ij}^{\Omega\backslash\mathcal{S}}(\mathbf{x},t)n_j(\mathbf{x}) = \sigma_{ij}^{\mathcal{S}}(\mathbf{x},t)n_j(\mathbf{x}) \tag{166a}$$

$$\dot{t}_i(\mathbf{x},t) = \dot{\sigma}_{ij}^{\Omega\backslash\mathcal{S}}(\mathbf{x},t)n_j(\mathbf{x}) = \dot{\sigma}_{ij}^{\mathcal{S}}(\mathbf{x},t)n_j(\mathbf{x}) \tag{166b}$$

where $\sigma_{ij}^{\mathcal{S}}$ are the stress components at a point on $\mathcal{S}$, while $\sigma_{ij}^{\Omega\backslash\mathcal{S}}$ are the stress components of an infinitesimally close point localized, however, at $\Omega\backslash\mathcal{S}$.

Thus, it is verified that, as the strains are finite in $\Omega\backslash\mathcal{S}$ ($\epsilon_{ij} = \bar{\epsilon}_{ij}$), the components $\sigma_{ij}^{\Omega\backslash\mathcal{S}}$ will also be, as will t_i ($t_i = \sigma_{ij}^{\Omega\backslash\mathcal{S}}n_j$). The same arguments are valid for equation (166b). On the other hand, it should be noted that $\sigma_{ij}^{\mathcal{S}}$ and $\dot{\sigma}_{ij}^{\mathcal{S}}$ must also be finite , although $\epsilon_{ij}^{\mathcal{S}}$ and $\dot{\epsilon}_{ij}^{\mathcal{S}}$ are not, so that the physical sense of the stress field is preserved.

As previously mentioned, the SDA establishes a discrete constitutive model, which relates traction to jumps in displacements on $\mathcal{S}$, associated with the continuum one. It also leads to a reinterpretation of the original model's softening modulus, causing it to be rewritten as a function of its counterpart in the discrete model (called discrete or intrinsic softening modulus). Therefore, such an analysis must be carried out in the light of a specific continuous model. Thus, for now on, the discussion is particularized for the isotropic damage model (see Appendix A.2), with the

particular parameters defined by Oliver et al. [2006]. Such a model can be summarized by the following set of equations:

Free energy: $\quad \psi(\epsilon_{ij}, r) = [1 - D(r)]\psi_o(\epsilon_{ij}), \quad \psi_o(\epsilon_{ij}) = \frac{1}{2}\epsilon_{ij}C_{ijkl}\epsilon_{kl}$ $\qquad$ (167a)

Constitutive equation: $\quad \sigma_{ij} = \frac{\partial \psi(\epsilon_{ij}, r)}{\partial \epsilon_{ij}} = (1 - D)C_{ijkl}\epsilon_{kl} = C^s_{ijkl}\epsilon_{kl}$ $\qquad$ (167b)

Damage variable: $\quad D \equiv D(r) = 1 - \frac{q(r)}{r}, \quad D \in [0, 1]$ $\qquad$ (167c)

Internal variable evolution law: $\quad \dot{r} = \dot{\lambda}, \quad \begin{cases} r \in [r_o, \infty), \\ r_o = r|_{t=0} = \frac{f_t}{\sqrt{E}} \end{cases}$ $\qquad$ (167d)

Damage criterion: $\quad \bar{F}(\epsilon_{ij}, r) \equiv \phi - r = \sqrt{\epsilon^+_{ij}C_{ijkl}\epsilon_{kl}} - r$ $\qquad$ (167e)

Loading–unloading conditions: $\quad \bar{F} \leqslant 0, \quad \dot{\lambda} \geqslant 0, \quad \dot{\lambda}\bar{F} = 0, \quad \dot{\lambda}\dot{\bar{F}} = 0$ $\qquad$ (167f)

Softening law: $\quad \dot{q} = H(r)\dot{r}, \quad (H = q'(r) \leqslant 0), \quad \begin{cases} q \in [0, r_o], \\ q|_{t=0} = r_o \end{cases}$ $\qquad$ (167g)

In equation (167d), f_t refer to the material's tensile strength.

A detailed application of SDA to this model, which is shown by Oliver [2000], leads to the following correspondent discrete model:

Free energy: $\quad \hat{\psi}(\Delta[\![u_i]\!], \omega) = [1 - \omega(\Delta\alpha)]\hat{\psi}_o(\Delta[\![u_i]\!]), \quad \hat{\psi}_o(\Delta[\![u_i]\!]) = \frac{1}{2}\Delta[\![u_i]\!]Q^e_{ij}\Delta[\![u_j]\!]$

$\qquad$ (168a)

Constitutive equation: $\quad t_i = \frac{\partial \hat{\psi}(\Delta[\![u_i]\!], \omega)}{\partial(\Delta[\![u_i]\!])} = (1 - \omega)Q^e_{ij}\Delta[\![u_j]\!] = Q^s_{ij}\Delta[\![u_j]\!]$ $\qquad$ (168b)

Damage variable: $\quad \omega \equiv \omega(\Delta\alpha) = 1 - \frac{q^*(\Delta\alpha)}{\Delta\alpha}, \quad \omega \in (-\infty, 1]$ $\qquad$ (168c)

Internal variable evolution law: $\quad \omega \equiv \omega(\Delta\alpha) = 1 - \frac{q^*(\Delta\alpha)}{\Delta\alpha}, \quad \omega \in (-\infty, 1]$ $\qquad$ (168d)

Damage criterion: $\quad \bar{G}(\Delta[\![u_i]\!], \Delta\alpha) \equiv \tau_{\Delta[\![u]\!]} - \Delta\alpha = \sqrt{\Delta[\![u_i]\!]Q^e_{ij}\Delta[\![u_j]\!]} - \Delta\alpha$ $\qquad$ (168e)

Loading–unloading conditions: $\quad \bar{G} \leqslant 0, \quad \dot{\lambda}^* \geqslant 0, \quad \dot{\lambda}^*\bar{G} = 0, \quad \dot{\lambda}^*\dot{\bar{G}} = 0$ $\qquad$ (168f)

Softening law: $\quad \dot{q}^* = H^*\dot{\alpha}, \quad (H^* = (1/h)H < 0), \quad \begin{cases} q^* \in [0, q_{SD}], \\ q^*|_{t=t_{SD}} = q_{SD} \end{cases}$ $\qquad$ (168g)

In the above equations, ω is the discrete damage variable, analogous to the continuum variable D; t_i is the traction vector over the discontinuity surface; Q^e_{ij} is the elastic localization tensor, given by $Q^e_{ij} = n_k C_{kijl}n_l$; q^* and α are the discrete internal variables, analogous respectively to q and r ($\Delta\alpha$ meaning the cumulative variation in α since the beginning of the strong discontinuity regime); and H^* is the discrete softening modulus, which value is obtained from the analysis of the power expended in the strong discontinuity regime as described later.

Particularly, deduction of equations (168b) and (168f) are detailed here, since they lead to the mentioned reinterpretation of the softening modulus, which is a key point in the compatibility between discontinuous kinematics and the continuous constitutive model.

From equations (167b), (167c) and (165), the stress tensor for a point on $\mathcal{S}$ is given by:

$$\sigma^{\mathcal{S}}_{ij} = \frac{q_{\mathcal{S}}}{r_{\mathcal{S}}}C_{ijkl}\left[\bar{\epsilon}_{kl} + \frac{1}{2h}(\Delta[\![u_k]\!]n_l + \Delta[\![u_l]\!]n_k)\right] \qquad (169)$$

Assuming that this point is in the strong discontinuity regime, that is, $t > t_{SD} \Rightarrow h \equiv k \to 0$, we have from equation (166a) that

$$
\begin{aligned}
t_j = n_i \sigma_{ij}^{\mathcal{S}} &= \lim_{h \to 0} \left\{ \frac{q_{\mathcal{S}}}{r_{\mathcal{S}}} n_i C_{ijkl} \left[\bar{\epsilon}_{kl} + \frac{1}{2h} (\Delta \llbracket u_k \rrbracket n_l + \Delta \llbracket u_l \rrbracket n_k) \right] \right\} \\
&= \lim_{h \to 0} \left(\frac{1}{h r_{\mathcal{S}}} \right) q_{\mathcal{S}} (\underbrace{n_i C_{ijkl} n_l}_{Q_{jk}^e}) \Delta \llbracket u_k \rrbracket \\
&= \lim_{h \to 0} \left(\frac{1}{h r_{\mathcal{S}}} \right) q_{\mathcal{S}} Q_{jk}^e \Delta \llbracket u_k \rrbracket
\end{aligned}
\tag{170}
$$

Since Q_{jk}^e is a positive definite tensor, for $\Delta \llbracket u_i \rrbracket \neq 0$, the term $q_{\mathcal{S}} Q_{jk}^e \Delta \llbracket u_k \rrbracket$ must be finite and non-zero. Thus, for the traction vector to also remain finite, as argued earlier, one must have:

$$
\lim_{h \to 0} (h r_{\mathcal{S}}) \neq 0 \quad \text{if} \quad \Delta \llbracket u_k \rrbracket \neq 0
\tag{171}
$$

In order for this condition to be fully satisfied, the following structure is assumed for the evolution of the internal variable of strain-type at points on the discontinuous surface:

$$
\dot{r}_{\mathcal{S}} = \frac{1}{h} \dot{\alpha} \quad \forall t \geqslant t_B; \quad \alpha|_{t=t_B} = 0
\tag{172}
$$

where α is the discrete internal variable that appears in equations (168), considered finite (as well as $\dot{\alpha}$).

Equation (172) can be integrated up to an instant $t \geqslant t_{SD}$, resulting in

$$
\begin{aligned}
r_{\mathcal{S}} = \int_0^t \dot{r}_{\mathcal{S}} dt &= \underbrace{r_B + \int_{t_B}^{t_{SD}} \frac{1}{h(\tau)} \dot{\alpha}(\tau) d\tau}_{:=r_{SD}} + \int_{t_{SD}}^t \underbrace{\frac{1}{h(\tau)}}_{h \equiv k} \dot{\alpha}(\tau) d\tau \\
&= r_{SD} + \frac{1}{k} \int_{t_{SD}}^t \dot{\alpha}(\tau) d\tau = r_{SD} + \frac{1}{k} \Delta \alpha
\end{aligned}
\tag{173}
$$

where $\Delta \alpha = \alpha|_t - \alpha|_{t_{SD}}$ and $r_B = r_{\mathcal{S}}|_{t=t_B}$.

Note now that the term r_{SD}, defined in the equation (173), for $t \geqslant t_{SD}$ satisfies the condition:

$$
\lim_{h \to 0} (h r_{SD}) = \lim_{k \to 0} (k r_{SD}) = \lim_{k \to 0} \left[k r_B + \int_{t_B}^{t_{SD}} \frac{k}{h(\tau)} \dot{\alpha}(\tau) d\tau \right] = 0
\tag{174}
$$

Thus, applying equation (173) to (171) and taking into account the result of the equation (174), we obtain:

$$
\lim_{h \to 0} (h r_{\mathcal{S}}) = \lim_{h \to 0} (h r_{SD} + \Delta \alpha) = \Delta \alpha \neq 0
\tag{175}
$$

which demonstrates that the evolution law proposed in equation (172) is consistent with the condition pointed out in equation (171) and makes equation (170) compatible with $\Delta \llbracket u_i \rrbracket \neq 0$.

Finally, replacing the equation (175) in equation (170), results in

$$
t_i = \frac{q_{\mathcal{S}}}{\Delta \alpha} Q_{ij}^e \Delta \llbracket u_j \rrbracket; \quad \forall t \geqslant t_{SD}
$$

which corresponds to equation (168b), i.e., the discrete constitutive equation, relating surface forces in $\mathcal{S}$ to increments in the jump of displacements.

Moreover, applying the equation(172) to (167g), the following expression is obtained for the evolution of stress-type internal variable, in points over $\mathcal{S}$:

$$\dot{q}_\mathcal{S} = H\dot{r}_\mathcal{S} = H\frac{1}{h}\dot{\alpha} \tag{176}$$

Since $\dot{q}_\mathcal{S}$ and $\dot{\alpha}$ are, by definition, finite quantities, we have that the term $\lim_{h\to 0}(H/h)$ must also assume finite values. Thus, the following relation is expected:

$$H = hH^*; \quad \forall t > t_B \tag{177}$$

where $H^* < 0$ is defined as finite and is called, as already said, as discrete or intrinsic softening modulus.

Equation (177) refers to the mentioned reinterpretation of the softening modulus of the continuous constitutive model. When $h \to 0$, the law of softening assumes the distributive character highlighted in the original work of Simo et al. [1993], since $H^* \to \delta_\mathcal{S} H$. On the other hand, in the structure considered here, where h assumes finite values during the regime with weak discontinuities, equation (177) can be considered an appropriate extension to the variable band model.

Now, substituting the equation (177) into (176), we obtain:

$$\dot{q}_\mathcal{S} = H^*\dot{\alpha}$$

which corresponds to equation (168g).

7.2.1   Strong discontinuity conditions

Applying equation (165) to (167b) leads to the following result for points over $\mathcal{S}$ in the strong discontinuity regime:

$$\begin{aligned}
\sigma_{ij}^\mathcal{S} = \frac{q_\mathcal{S}}{r_\mathcal{S}}C_{ijkl}\epsilon_{kl}^\mathcal{S} &= \lim_{h\to 0}\left\{\frac{q_\mathcal{S}}{r_{SD} + \frac{1}{h}\Delta\alpha}C_{ijkl}\left[\bar{\epsilon}_{kl} + \frac{1}{2h}(\Delta[\![u_k]\!]n_l + \Delta[\![u_l]\!]n_k)\right]\right\} \\
&= \lim_{h\to 0}\left\{\frac{q_\mathcal{S}}{hr_{SD} + \Delta\alpha}C_{ijkl}\left[h\bar{\epsilon}_{kl} + \frac{1}{2}(\Delta[\![u_k]\!]n_l + \Delta[\![u_l]\!]n_k)\right]\right\} \tag{178} \\
&= \frac{q_\mathcal{S}}{\Delta\alpha}C_{ijkl}\left[\frac{1}{2}(\Delta[\![u_k]\!]n_l + \Delta[\![u_l]\!]n_k)\right]
\end{aligned}$$

where equations (167c) and (173) were also used. In this way, one can write:

$$\frac{1}{2}(\Delta[\![u_i]\!]n_j + \Delta[\![u_j]\!]n_i) = \frac{\Delta\alpha}{q_\mathcal{S}}C_{ijkl}^{-1}\sigma_{kl}^\mathcal{S} = \frac{\Delta\alpha}{q_\mathcal{S}}\epsilon_{ij}^{\mathcal{S},ef} \tag{179}$$

where $\epsilon_{ij}^{ef} := C_{ijkl}^{-1}\sigma_{kl} = (1-D)\epsilon_{ij}$ is the so-called effective strain. The finite character of $\sigma_{ij}^\mathcal{S}$ makes $\epsilon_{ij}^{\mathcal{S},ef}$ also to be limited.

Equation (179) is called the strong discontinuity equation and can be seen as a set of six algebraic equations (due to symmetry), relating the stress components, $\sigma_{ij}^\mathcal{S}$, (or of effective deformation, $\epsilon_{ij}^{\mathcal{S},ef}$) to the components of the jumps in the displacements, $\Delta[\![u_i]\!]$. Three of them are, in fact, the discrete constitutive equations (168b), which can be retrieved by pre-multiplying both sides of equation (179) by n_i. The other three, involving only stress components in $\mathcal{S}$, correspond to the so-called strong discontinuity conditions, which must be satisfied throughout $t \geqslant t_{SD}$. To obtain them in a more direct way, we rewrite the equation (179) in its matrix form, considering the orthonormal basis $\{\mathbf{n}, \mathbf{p}, \mathbf{q}\}$, with $\mathbf{p}$ and $\mathbf{q}$ tangent to $\mathcal{S}$, i.e.,

$$\begin{bmatrix} \Delta[\![u_n]\!] & \frac{1}{2}\Delta[\![u_p]\!] & \frac{1}{2}\Delta[\![u_q]\!] \\ \frac{1}{2}\Delta[\![u_p]\!] & 0 & 0 \\ \frac{1}{2}\Delta[\![u_q]\!] & 0 & 0 \end{bmatrix} = \frac{\Delta\alpha}{q^\mathcal{S}}\begin{bmatrix} \epsilon_{nn}^{\mathcal{S},ef} & \epsilon_{np}^{\mathcal{S},ef} & \epsilon_{nq}^{\mathcal{S},ef} \\ \epsilon_{pn}^{\mathcal{S},ef} & \epsilon_{pp}^{\mathcal{S},ef} & \epsilon_{pq}^{\mathcal{S},ef} \\ \epsilon_{qn}^{\mathcal{S},ef} & \epsilon_{qp}^{\mathcal{S},ef} & \epsilon_{qq}^{\mathcal{S},ef} \end{bmatrix} \tag{180}$$

from which it follows that, for $\mathcal{S}$ to actually correspond to a strong discontinuity line, one must have:

$$\epsilon_{pp}^{ef} = \epsilon_{pq}^{ef} = \epsilon_{qq}^{ef} = 0 \tag{181}$$

In other words, the strong discontinuity regime is immediately initiated after bifurcation only if these conditions are satisfied. As in general it is not the case, a bandwidth variable model, in which a transient step with weak discontinuities is adopted, is often necessary for the correct simulation of material failures. This model will be detailed in section 7.4. Before that, explicit expressions for the discrete softening modulus, H^*, are deduced in the next section, from the analysis of the energy consumed during the strong discontinuity regime.

7.3   Energy expended in the strong discontinuity regime

The power consumed, $\mathcal{P}$, during a quasi-static loading process in a solid domain Ω is given by:

$$\mathcal{P} = \int_{\Omega} \sigma_{ij} \dot{\epsilon}_{ij} d\Omega \tag{182}$$

Restricting the analysis to the period after the start of the strong discontinuity regime, i.e., $t \geqslant t_{SD}$, we can substitute equation (162) into equation (182), getting

$$\int_{\Omega} \sigma_{ij} \dot{\epsilon}_{ij} d\Omega = \int_{\Omega} \sigma_{ij} \left[\dot{\bar{\epsilon}}_{ij} + \frac{\delta_{\mathcal{S}}}{2} ([\![\dot{u}_i]\!] n_j + [\![\dot{u}_j]\!] n_i) \right] d\Omega$$
$$= \int_{\Omega \backslash \mathcal{S}} \sigma_{ij}^{\Omega \backslash \mathcal{S}} \dot{\bar{\epsilon}}_{ij} d\Omega + \underbrace{\int_{\mathcal{S}} \sigma_{ij}^{\mathcal{S}} \left[\frac{1}{2} ([\![\dot{u}_i]\!] n_j + [\![\dot{u}_j]\!] n_i) \right] d\mathcal{S}}_{\mathcal{P}_{\mathcal{S}}} \tag{183}$$

where definition of $\dot{\bar{\epsilon}}_{ij}$ was given in equation (164) and $\mathcal{P}_{\mathcal{S}}$ is the power consumed in the development of the jump in the displacement field.

Considering equation (166a) and the symmetry of stress tensor, one can rewrite:

$$\mathcal{P}_{\mathcal{S}} = \int_{\mathcal{S}} t_i [\![\dot{u}_i]\!] d\mathcal{S} \tag{184}$$

In this way, the total energy consumed, from the beginning of the strong discontinuity regime until the total stress relief, is given by:

$$\mathcal{W}_{\mathcal{S}} = \int_{t_{SD}}^{t_\infty} \mathcal{P}_{\mathcal{S}} dt = \int_{t_{SD}}^{t_\infty} \int_{\mathcal{S}} t_i [\![\dot{u}_i]\!] d\mathcal{S} dt = \int_{\mathcal{S}} \left[\underbrace{\int_{t_{SD}}^{t_\infty} t_i [\![\dot{u}_i]\!] dt}_{G_{SD}} \right] d\mathcal{S} \tag{185}$$

where G_{SD} is the energy released in $\mathcal{S}$, per unit area, during the strong discontinuity regime. Assuming that the energy released during the transition in a weak discontinuity regime is small when compared to G_{SD}, this term can be understood as the fracture energy, G_f, usually adopted as a property of the material and whose value can be determined by standardized tests.

We now seek to rewrite the kernel of the integral in equation (184) in a more convenient form, taking into account the discrete damage model of the equations (168). Firstly, from equation (168e), we have:

$$\dot{\tau}_{\Delta[\![u]\!]} = \frac{1}{\tau_{\Delta[\![u]\!]}} (\Delta[\![u_i]\!] Q_{ij}^e [\![\dot{u}_j]\!]) \tag{186}$$

i.e.,

$$\Delta[\![u_i]\!] Q_{ij}^e [\![\dot{u}_j]\!] = \dot{\tau}_{\Delta[\![u]\!]} \tau_{\Delta[\![u]\!]} \tag{187}$$

Thus, post-multiplying $[\![\dot{u}_i]\!]$ in the constitutive equation (168b) – after applying equation (168c) – and considering the symmetry of Q_{ij}^e, in addition to the equivalence $q_{\mathcal{S}} = q^*(\Delta\alpha)$, one arrives to the following result:

$$t_i[\![\dot{u}_i]\!] = \left[\underbrace{\frac{q_{\mathcal{S}}}{\Delta\alpha}\Delta[\![u_j]\!]Q_{ji}^e}_{t_i}\right][\![\dot{u}_i]\!] = \frac{q_{\mathcal{S}}}{\Delta\alpha}(\dot{\tau}_{\Delta[\![u]\!]}\tau_{\Delta[\![u]\!]}) \tag{188}$$

Moreover, from equations (168e) and (168f), it is verified that dissipation occurs only if $\tau_{\Delta[\![u]\!]} = \Delta\alpha$ and $\dot{\tau}_{\Delta[\![u]\!]} = \dot{\alpha}$. Therefore, equation (188) is equivalent to

$$t_i[\![\dot{u}_i]\!] = q_{\mathcal{S}}\dot{\alpha} \tag{189}$$

Now, replacing equation (189) into the expression of G_{SD}, defined in equation (185), we obtain

$$G_{SD} = \int_{t_{SD}}^{t_\infty} q_{\mathcal{S}}\dot{\alpha}\,dt = \int_{t_{SD}}^{t_\infty} q_{\mathcal{S}}\frac{\dot{q}_{\mathcal{S}}}{H^*}\,dt = \int_{q_{SD}}^{0} q\frac{1}{H^*}\,dq \tag{190}$$

where the softening law discriminated in the equation (168g) was used. In the case $G_{SD} \approx G_f$, we have $q_{SD} \approx q_o = r_o = \dfrac{f_t}{\sqrt{E}}$, so that:

$$G_f = \int_{\frac{f_t}{\sqrt{E}}}^{0} q\frac{1}{H^*}\,dq \tag{191}$$

Finally, it is highlighted that different softening laws can be defined according to the structure of the discrete softening module. For example, linear softening is obtained from a constant H^*, while exponential softening requires an expression like $H^*(q) = A^*q$, where A^* is a constant . Thus, for each of these two cases, the solution of equation (191) results in:

i. Linear softening:

$$G_f = \frac{1}{H^*}\frac{q^2}{2}\bigg|_{\frac{f_t}{\sqrt{E}}}^{0} = -\frac{1}{H^*}\left[\frac{f_t^2}{2E}\right] \Rightarrow H^* = -\frac{f_t^2}{2EG_f} \tag{192}$$

ii. Exponential softening:

$$G_f = \frac{1}{A^*}q\bigg|_{\frac{f_t}{\sqrt{E}}}^{0} \Rightarrow A^* = -\frac{f_t}{G_f\,sqrtE}; \quad \therefore H^* = -\frac{f_t}{G_f\sqrt{E}}q \tag{193}$$

7.4   Variable bandwidth model

With the theoretical background presented until here, it is possible to distinguish between four steps that compose the fracture process in a solid body (in particular, the ones composed by quasi-brittle materials), as shown in Figure 25.

Each step is briefly described below:

I. **Elastic phase**: proportional stress-strain relation until the limit point **Y**;

II. **Inelastic phase**: non linear behaviour with continuous strain and displacement fields. In this phase, the isotropic damage constitutive model summarized in equations (167) is directly applied and for each new strain state the bifurcation analysis, presented in section 6, is performed;
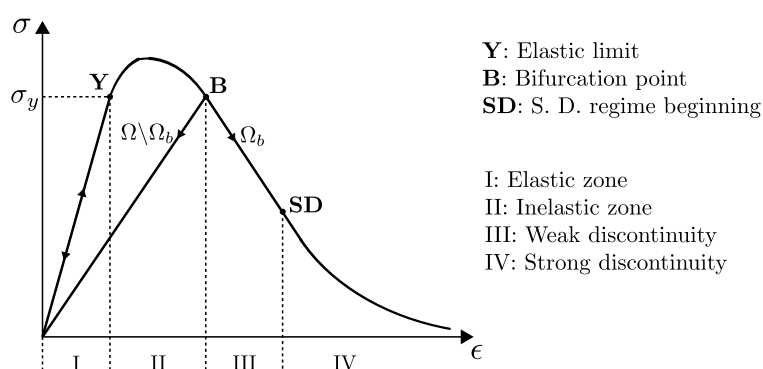
Figure 25: Fracture evolution process

III. **Weak discontinuity regime**: characterized by the presence of discontinuities in the strain field. The regularized kinematic equations presented in section 7.1.3 are adopted, with finite values for h, which can be interpreted as the localization bandwidth. As the loading process advances, its value reduces from h_B, on the bifurcation instant, **B**, until a null value (numerically speaking, a small parameter, k) on the point **SD**, which defines the beginning of the strong discontinuity regime;

IV. **Strong discontinuity regime**: characterized by discontinuities in the displacement field. the regularized kinematics is also used, with $h = k \approx 0$.

If on the bifurcation time (point **B**) the strong discontinuity condition of equation (181) is also achieved, we have $\mathbf{B} \equiv \mathbf{SD}$ and step III above is suppressed. This is a typical case of brittle fracture.

The bandwidth evolution is governed by a pre-defined law. One can define, for example, a linear variation with the stress-like internal variable of the continuous constitutive model was considered, as illustrated in Figure 26, where $\bar{\beta}$ is an scalar value between 0 and 1.
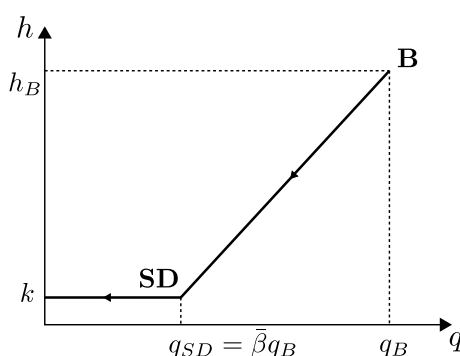
Figure 26: Bandwidth evolution law

Particularly, the initial width of the localization band, can be obtained from Eq. (177), i.e.,

$$h_B = \left| \frac{H(q_B)}{H^*(q_B)} \right| \tag{194}$$

From equations (167c), (167g) and (177), besides the specification of a bandwidth evolution law, the three steps of the inelastic loading differ basically by the expression of $q(r)$ and, consequently, of $D(r)$. Such expressions considering an exponential softening law are:

i. Continuum inelastic regime:

$$D(r) = 1 - \frac{q(r)}{r} = \begin{cases} 0 & \text{if } r \leqslant r_o \\ 1 - \dfrac{r_o}{r} e^{A(1 - \frac{r}{r_o})} & \text{if } r > r_o \end{cases} \tag{195}$$

where A is a positive scalar constant. For example, the next expression presented in Oliver et al. [1990] can be adopted:

$$A = \left[\frac{G_f}{r_o^2 l^*} - \frac{1}{2} \right]^{-1} \tag{196}$$

in which l^* represents a length parameter associated to the numerical discretization size (the average of cells edges sizes in the BEM formulation used here).

ii. Weak discontinuity regime:

$$D(r) = 1 - \frac{b}{r} \left[-a + \left(\frac{b + aq_B}{q_B} \right) e^{b(r_B - r)} \right]^{-1} \quad \text{(for } r_B < r < r_{SD}) \tag{197}$$

where

$$a = -\frac{f_t R}{G_f \sqrt{E}}; \quad b = -\frac{f_t}{G_f \sqrt{E}} (k - Rq_{SD}) \tag{198}$$

and r_B and r_{SD} are, respectively, the values of r on the bifurcation time and on the beginning of the strong discontinuity regime, this last one given by

$$r_{SD} = r_B - \frac{1}{b} \ln \left[\frac{q_B}{q_{SD}} \left(\frac{b + aq_{SD}}{b + aq_B} \right) \right] \tag{199}$$

iii. Strong discontinuity regime:

$$D(r) = 1 - \frac{q_{SD}}{r} e^{\frac{f_t k}{G_f \sqrt{E}} (r_{SD} - r)} \quad \text{(for } \; r > r_{SD}) \tag{200}$$

More details about the deduction of above equations are presented in Peixoto et al. [2018].

8   Boundary integral equations with presence of discontinuities

To obtain the BIE when discontinuities – whether weak or strong – are present, the regularized kinematics presented in the section 7.1.3 can be used. However, for numerical reasons, it is important to reformulate it again, allowing the distribution of discontinuous surface effects over a finite (and arbitrary) region of the domain. Such a reformulation is presented initially. Then, starting from the differential formulation of the problem, the integral equations are obtained. Finally, the imposition of the equilibrium equation on the discontinuous interface, in its strong form, is highlighted as a necessary condition to complement the integral formulations.
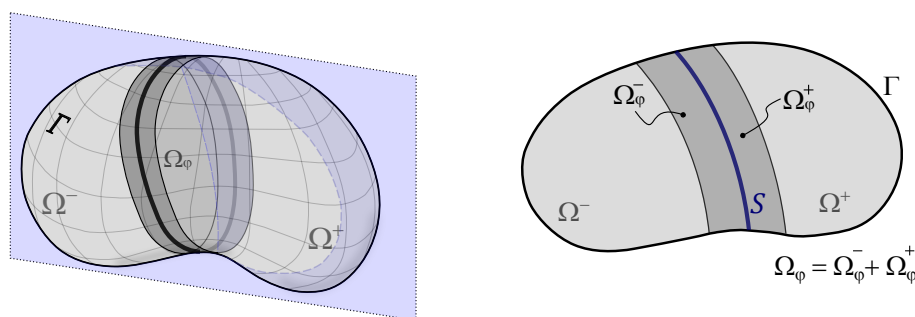
8.1   Kinematic equations reformulation

Taking as a starting point Figure 24c, the reformulation of the kinematics with discontinuities starts with the definition of an arbitrary subdomain Ω_φ ($\subset \Omega$), around $\mathcal{S}$, as shown in Figure 27.

We also define a continuous function $\varphi(\mathbf{x})$, also arbitrary in Ω_φ, but satisfying the following conditions:

$$\varphi(\mathbf{x}) = \begin{cases} 0, & \text{for } \mathbf{x} \in \Omega^- \backslash \Omega_\varphi^- \\ 1, & \text{for } \mathbf{x} \in \Omega^+ \backslash \Omega_\varphi^+ \end{cases} \tag{201}$$

Figure 27: Arbitrary subdomain Ω_φ around the discontinuous surface.

Thus, equation (163) can be rewritten in the form:

$$\dot{u}_i(\mathbf{x}, t) = \underbrace{\dot{\bar{u}}_i(\mathbf{x}, t) + \varphi(\mathbf{x}) [\![\dot{u}_i]\!](\mathbf{x}, t)}_{\dot{\hat{u}}_i(\mathbf{x},t)} + \underbrace{[\mathcal{H}_\mathcal{S}(\mathbf{x}) - \varphi(\mathbf{x})]}_{\mathcal{M}_\mathcal{S}^\varphi(\mathbf{x})} [\![\dot{u}_i]\!](\mathbf{x}, t)$$

$$= \dot{\hat{u}}_i(\mathbf{x}, t) + \mathcal{M}_\mathcal{S}^\varphi(\mathbf{x}) [\![\dot{u}_i]\!](\mathbf{x}, t) \tag{202}$$

where $\dot{\hat{u}}_i(\mathbf{x}, t)$ are continuous functions and $\mathcal{M}_\mathcal{S}^\varphi(\mathbf{x})$ has null value for all $\mathbf{x}$ in Ω, except in subdomain Ω_φ. Note, therefore, that the displacement field (or velocity field) is composed of a regular portion, $\hat{u}_i(\mathbf{x}, t)$, and another that contains the jump components, $\mathcal{M}_\mathcal{S}^\varphi(\mathbf{x}) [\![u_i]\!](\mathbf{x}, t)$, whose region of influence is Ω_φ.

It should also be noted, as described by Oliver [1996], that essential boundary conditions could not be imposed directly on the $\bar{u}_i$ or $[\![u_i]\!]$ parcels of the displacement field. However, with the reformulation defined in the equation (202), such conditions can be applied exclusively to the term $\hat{u}_i$, provided that $\Gamma_u \cap \Omega_\varphi = 0$.

Equation (164), in turn, takes the form:

$$\dot{\epsilon}_{ij}(\mathbf{x}, t) = \underbrace{\frac{1}{2}(\dot{\hat{u}}_{i,j} + \dot{\hat{u}}_{j,i})}_{\dot{\hat{\epsilon}}_{ij}} + \underbrace{\frac{\mathcal{M}_\mathcal{S}^\varphi}{2}([\![\dot{u}_{i,j}]\!] + [\![\dot{u}_{j,i}]\!]) - \frac{1}{2}(\varphi_{,i} [\![\dot{u}_j]\!] + \varphi_{,j} [\![\dot{u}_i]\!])}_{-\dot{\epsilon}_{ij}^\varphi} + \frac{\mu_\mathcal{S}}{2h}([\![\dot{u}_i]\!]n_j + [\![\dot{u}_j]\!]n_i)$$

$$= \dot{\hat{\epsilon}}_{ij} - \dot{\epsilon}_{ij}^\varphi + \frac{\mu_\mathcal{S}}{2h}([\![\dot{u}_i]\!]n_j + [\![\dot{u}_j]\!]n_i)$$

(203)

where $\hat{\epsilon}_{ij}$ is a regular portion of the strain field, ϵ_{ij}^φ has non-null values only in the subdomain Ω_φ and the last term is restricted to points on $\mathcal{S}$.

As in the case of equations (163) and (164), equations (202) and (203) are kinematically compatible only under strong discontinuity regime, i.e., when $\lim_{h \to 0} \left[\frac{\mu_\mathcal{S}(\mathbf{x})}{h} \right] = \delta_\mathcal{S}(\mathbf{x})$.

8.2   Boundary Value Problem formulations

The boundary value problem, considering the presence of a discontinuity surface $\mathcal{S}$, is fully defined through the following set of differential equations:

$$\dot{\sigma}_{ij,j} + \dot{b}_i = 0 \quad \text{in} \quad \Omega\backslash\mathcal{S} \quad \text{(internal equilibrium)} \tag{204a}$$

$$\dot{\sigma}_{ij}^+ n_j - \dot{\sigma}_{ij}^- n_j = 0 \quad \text{on} \quad \mathcal{S} \quad \text{(external traction continuity)} \tag{204b}$$

$$\dot{\sigma}_{ij}^+ n_j - \dot{\sigma}_{ij}^{\mathcal{S}} n_j = \dot{\sigma}_{ij}^- n_j - \dot{\sigma}_{ij}^{\mathcal{S}} n_j = 0 \quad \text{on} \quad \mathcal{S} \quad \text{(internal traction continuity)} \tag{204c}$$

$$\dot{\epsilon}_{ij} - \frac{1}{2}(\dot{u}_{i,j} + \dot{u}_{j,i}) = 0 \quad \text{in} \quad \Omega \quad \text{(kinematic compatibility)} \tag{204d}$$

$$\dot{\sigma}_{ij} = \dot{\sigma}_{ij}^{\mathcal{S}}(\dot{\epsilon}_{ij}) \quad \text{on} \quad \mathcal{S} \quad \text{(constitutive compatibility)} \tag{204e}$$

$$\dot{\sigma}_{ij} = \dot{\sigma}_{ij}^{\Omega\backslash\mathcal{S}}(\dot{\epsilon}_{ij}) = C_{ijkl}\dot{\epsilon}_{kl} \quad \text{in} \quad \Omega\backslash\mathcal{S} \quad \text{(constitutive compatibility)} \tag{204f}$$

$$\dot{\hat{u}}_i = \dot{\tilde{u}}_i \quad \text{in} \quad \Gamma_u \quad \text{(essential boundary conditions)} \tag{204g}$$

$$\dot{\sigma}_{ij} n_j = \dot{\tilde{t}}_i \quad \text{in} \quad \Gamma_\sigma \quad \text{(natural boundary conditions)} \tag{204h}$$

where $\sigma_{ij}^{\mathcal{S}}(\epsilon_{ij})$ represents an appropriate continuous constitutive relation, e.g., equations (167), and a linear elastic regime is considered for $\Omega\backslash\mathcal{S}$. Terms σ_{ij}^+ and σ_{ij}^- refer, respectively, to the stress at Ω^+ and Ω^-. The complementary equilibrium equations (204b) and (204c) are associated with the external and internal (to $\mathcal{S}$) traction continuity. Equation (204d) corresponds to (203).

Considering the arbitrariness of $\varphi(\mathbf{x})$ and a fixed orientation of the discontinuity surface after its establishment (material character of $\mathcal{S}$), the constitutive relations in equations (204e) and (204f), after applying equation (203), can be rewritten in the following forms:

$$\dot{\sigma}_{ij}^{\mathcal{S}}(\dot{\epsilon}_{ij}) = \dot{\sigma}_{ij}^{\mathcal{S}}(\dot{\hat{\epsilon}}_{ij}, [\![\dot{u}_i]\!], [\![\dot{u}_{i,j}]\!]) \tag{205}$$

$$\dot{\sigma}_{ij}^{\Omega\backslash\mathcal{S}}(\dot{\epsilon}_{ij}) = C_{ijkl}\dot{\epsilon}_{kl} = C_{ijkl}\left[\dot{\hat{\epsilon}}_{kl} - \dot{\epsilon}_{kl}^{\varphi}([\![\dot{u}_i]\!], [\![\dot{u}_{i,j}]\!])\right] \tag{206}$$

A first integral formulation of this problem can be obtained from the following weighted residual equation:

$$\int_{\Omega\backslash\mathcal{S}} (\dot{\sigma}_{ij,j}^{\Omega\backslash\mathcal{S}} + \dot{b}_i)u_i^* d\Omega + \int_{\mathcal{S}} n_j(\dot{\sigma}_{ij}^+ - \dot{\sigma}_{ij}^-)u_i^* d\Gamma + \int_{\Gamma_\sigma} (\dot{\tilde{t}}_i - \dot{t}_i)u_i^* d\Gamma + \int_{\Gamma_u} (\dot{\hat{u}}_i - \dot{\tilde{u}}_i)t_i^* d\Gamma = 0 \tag{207}$$

where u_i^* and t_i^* represent arbitrary weighting fields.

Integrating the first term of equation (207) by parts, we obtain:

$$\int_{\Omega\backslash\mathcal{S}} \dot{\sigma}_{ij,j}^{\Omega\backslash\mathcal{S}} u_i^* d\Omega = \int_{\Gamma} \dot{t}_i u_i^* d\Gamma + \int_{\mathcal{S}} (\dot{\sigma}_{ij}^- - \dot{\sigma}_{ij}^+)n_j u_i^* d\Gamma - \int_{\Omega\backslash\mathcal{S}} \dot{\sigma}_{ij}^{\Omega\backslash\mathcal{S}} u_{i,j}^* d\Omega \tag{208}$$

and, substituting equation (208) into equation (207),

$$\int_{\Omega\backslash\mathcal{S}} \dot{\sigma}_{ij}^{\Omega\backslash\mathcal{S}} u_{i,j}^* d\Omega = \int_{\Omega\backslash\mathcal{S}} \dot{b}_i u_i^* d\Omega + \int_{\Gamma_\sigma} \dot{\tilde{t}}_i u_i^* d\Gamma + \int_{\Gamma_u} [(\dot{\hat{u}}_i - \dot{\tilde{u}}_i)t_i^* + \dot{t}_i u_i^*]d\Gamma \tag{209}$$

From equations (203) and (206) and considering the symmetries associated with the regime of small displacements in isotropic media, one can write:

$$\dot{\sigma}_{ij}^{\Omega\backslash\mathcal{S}} = C_{ijkl}\dot{\hat{u}}_{k,l} - C_{ijkl}\dot{\epsilon}_{kl}^{\varphi} \tag{210}$$

In this way, applying equation (210) to the kernel of the integral on the left side in equation (209), we obtain:

$$\int_{\Omega\backslash\mathcal{S}} \dot{\sigma}_{ij}^{\Omega\backslash\mathcal{S}} u_{i,j}^* d\Omega = \int_{\Gamma} \dot{\hat{u}}_i t_i^* d\Gamma - \int_{\Omega} \sigma_{ij,j}^* \dot{\hat{u}}_i d\Omega - \int_{\Omega} \sigma_{ij}^* \dot{\epsilon}_{ij}^{\varphi} d\Omega \tag{211}$$

and, finally, substituting equation (211) in equation (209), we arrive in the following result:

$$-\int_{\Omega} \sigma^*_{ij,j}\dot{\hat{u}}_i d\Omega = \int_{\Omega} \dot{b}_i u^*_i d\Omega + \int_{\Gamma} \dot{t}_i u^*_i d\Gamma - \int_{\Gamma} \dot{\hat{u}}_i t^*_i d\Gamma + \int_{\Omega} \sigma^*_{ij}\dot{\epsilon}^{\varphi}_{ij} d\Omega \qquad (212)$$

The integral equations of interest are obtained next, through the particularization of the weighting fields.

8.3   Integral equations with discontinuities

If the solutions from the Kelvin's fundamental problem are adopted as the weighting fields in equation (212), similar equations as those presented in section 3 are obtained, regarding only the substitution of terms depicted in table 2.

Table 2: Terms correspondence for integral equations.

Continuum media	Presence of discontinuities
u_i	$\hat{u}_i$
ϵ_{ij}	$\hat{\epsilon}_{ij}$
ϵ^o_{ij}	ϵ^{φ}_{ij}

Thus, equations (67), (68) and (69) take the following forms:

$$\dot{\hat{u}}_i(\boldsymbol{\xi}) = \int_{\Gamma} u^*_{ij}(\boldsymbol{\xi},\mathbf{x})\dot{t}_j(\mathbf{x})\,d\Gamma - \int_{\Gamma} t^*_{ij}(\boldsymbol{\xi},\mathbf{x})\dot{\hat{u}}_j(\mathbf{x})\,d\Gamma + \int_{\Omega} u^*_{ij}(\boldsymbol{\xi},\mathbf{x})\dot{b}_j(\mathbf{x})\,d\Omega$$
$$+ \int_{\Omega} \sigma^*_{ijk}(\boldsymbol{\xi},\mathbf{x})\dot{\epsilon}^{\varphi}_{jk}(\mathbf{x})\,d\Omega \qquad (213)$$

$$c_{ij}(\boldsymbol{\xi})\dot{\hat{u}}_j(\boldsymbol{\xi}) = \int_{\Gamma} u^*_{ij}(\boldsymbol{\xi},\mathbf{x})\dot{t}_j(\mathbf{x})\,d\Gamma - \fint_{\Gamma} t^*_{ij}(\boldsymbol{\xi},\mathbf{x})\dot{\hat{u}}_j(\mathbf{x})\,d\Gamma$$
$$+ \int_{\Omega} u^*_{ij}(\boldsymbol{\xi},\mathbf{x})\dot{b}_j(\mathbf{x})\,d\Omega + \int_{\Omega} \sigma^*_{ijk}(\boldsymbol{\xi},\mathbf{x})\dot{\epsilon}^{\varphi}_{jk}(\mathbf{x})\,d\Omega \qquad (214)$$

$$\dot{\hat{\epsilon}}_{ij}(\boldsymbol{\xi}) = \int_{\Gamma} u^*_{ijk}(\boldsymbol{\xi},\mathbf{x})\dot{t}_k(\mathbf{x})\,d\Gamma - \int_{\Gamma} t^*_{ijk}(\boldsymbol{\xi},\mathbf{x})\dot{\hat{u}}_k(\mathbf{x})\,d\Gamma + \int_{\Omega} u^*_{ijk}(\boldsymbol{\xi},\mathbf{x})\dot{b}_k(\mathbf{x})\,d\Gamma$$
$$+ \fint_{\Omega} \sigma^*_{ijkl}(\boldsymbol{\xi},\mathbf{x})\dot{\epsilon}^{\varphi}_{kl}(\mathbf{x})\,d\Omega + F^{\epsilon\epsilon}_{ijkl}\dot{\epsilon}^{\varphi}_{kl}(\boldsymbol{\xi}) \qquad (215)$$

8.4   Equilibrium equation on the discontinuity surface

Differently from what happens with conventional continuous solids, the integral formulations considering the presence of discontinuities do not completely define the boundary value problem represented by the equations (204). In fact, a simple inspection of equation (207) indicates that the condition of traction external continuity – equation (204b) – is implicitly satisfied, however, the same does not occur with equation (204c). Therefore, the condition of internal continuity must be imposed separately. As in Oliver et al. [2003], this is done by taking the strong form of the equation.

Noting that equation (204c) corresponds to (166b), one can work with its corresponding instantaneous version: equation (166a). Thus, considering equations (205) and (206), we obtain:

$$f_i = \left\{ C_{ijkl} \left[\hat{\epsilon}_{kl} - \epsilon_{kl}^{\varphi} (\llbracket u_i \rrbracket, \llbracket u_{i,j} \rrbracket) \right] - \sigma_{ij}^{\mathcal{S}}(\epsilon_{ij}) \right\} n_j = 0 \tag{216}$$

where ϵ_{ij} is given by the instantaneous version of equation (203) which, for points on $\mathcal{S}$, corresponds to

$$\epsilon_{ij} = \hat{\epsilon}_{ij} - \epsilon_{ij}^{\varphi} + \frac{1}{2h} (\llbracket u_i \rrbracket n_j + \llbracket u_j \rrbracket n_i) \tag{217}$$

Equation (216) is called the interface equilibrium equation and, in the context of the BEM, discussed in the next section, its numerical solution is obtained by adopting cells with embedded discontinuities, providing the components of the displacement jumps, $\llbracket u_i \rrbracket$, needed to calculate ϵ_{ij}^{φ}. As will become clear, these components are assumed to be constants within a cell, resulting in null gradient tensors, i.e., $\llbracket u_{i,j} \rrbracket = 0$. Thus, for a given regular strain, $\hat{\epsilon}_{ij}$, and considering equation (217), equation (216) has as unknowns only the components $\llbracket u_i \rrbracket$, i.e., one can write $f_i \equiv f_i(\llbracket u_i \rrbracket) = 0$. In this format, its solution can be obtained by Newton's method after its linearisation.

Thus, a regularized constitutive equation, relating stresses to regular strains, $\hat{\epsilon}_{ij}$, can be defined using equation (206):

$$\tilde{\sigma}_{ij}(\hat{\epsilon}_{ij}) = \sigma_{ij}^{\Omega \backslash \mathcal{S}} \left(\hat{\epsilon}_{ij} - \epsilon_{ij}^{\varphi} (\llbracket u_i \rrbracket (\hat{\epsilon}_{ij})) \right) = C_{ijkl}(\hat{\epsilon}_{kl} - \epsilon_{kl}^{\varphi}) \tag{218}$$

where $\llbracket u_i \rrbracket (\hat{\epsilon}_{ij})$ represents the solution of equation (216).

9   A BEM Formulation for Problems with discontinuities

Discretization of the boundary equations (213) to (215), follows the same procedures already discussed in section 4. The same can be said about the solution strategy presented there. In this way, only the main special aspects, regarding the analysis involving discontinuities, are described here. Such main aspects are: cells with embedded discontinuity, displacement jump evaluation and the numerical counterpart of the regularized constitutive equation (218).

9.1   Cells with embedded discontinuity

Subdomain Ω_{φ}, illustrated in Figure 27, needs to be discretized by new concept of internal cells, called as cells with embedded discontinuity, which are now described. Furthermore, regions under inelastic behaviour, but still in the pre-bifurcation phase, must also be divided into standard cells, as illustrated in Figure 28a.

In cells with embedded discontinuity, only one collocation point is commonly adopted, so that the initial strains are considered constant in its interior. Thus, for such cells, typically represented in Figure 28b, one can write, for $\mathbf{x} \in \Omega_c$,

$$\begin{Bmatrix} \dot{\epsilon}_{11}^{\varphi}(\mathbf{x}) \\ \dot{\epsilon}_{22}^{\varphi}(\mathbf{x}) \\ \dot{\epsilon}_{12}^{\varphi}(\mathbf{x}) \end{Bmatrix} \approx \begin{Bmatrix} \dot{\epsilon}_{11}^{\varphi,c} \\ \dot{\epsilon}_{22}^{\varphi,c} \\ \dot{\epsilon}_{12}^{\varphi,c} \end{Bmatrix} = \left\{ \dot{\epsilon}^{\varphi,c} \right\} \text{ (for 2D)}, \quad \begin{Bmatrix} \dot{\epsilon}_{11}^{\varphi}(\mathbf{x}) \\ \dot{\epsilon}_{22}^{\varphi}(\mathbf{x}) \\ \dot{\epsilon}_{33}^{\varphi}(\mathbf{x}) \\ \dot{\epsilon}_{12}^{\varphi}(\mathbf{x}) \\ \dot{\epsilon}_{13}^{\varphi}(\mathbf{x}) \\ \dot{\epsilon}_{23}^{\varphi}(\mathbf{x}) \end{Bmatrix} \approx \begin{Bmatrix} \dot{\epsilon}_{11}^{\varphi,c} \\ \dot{\epsilon}_{22}^{\varphi,c} \\ \dot{\epsilon}_{33}^{\varphi,c} \\ \dot{\epsilon}_{12}^{\varphi,c} \\ \dot{\epsilon}_{13}^{\varphi,c} \\ \dot{\epsilon}_{23}^{\varphi,c} \end{Bmatrix} = \left\{ \dot{\epsilon}^{\varphi,c} \right\} \text{ (for 3D)}, \tag{219}$$

[○] and [●] are geometry interpolation points (α)
[○] are α^+, and [●] are α^-, $\Omega_c = \Omega_c^- \cup \Omega_c^+$

(a)   (b)
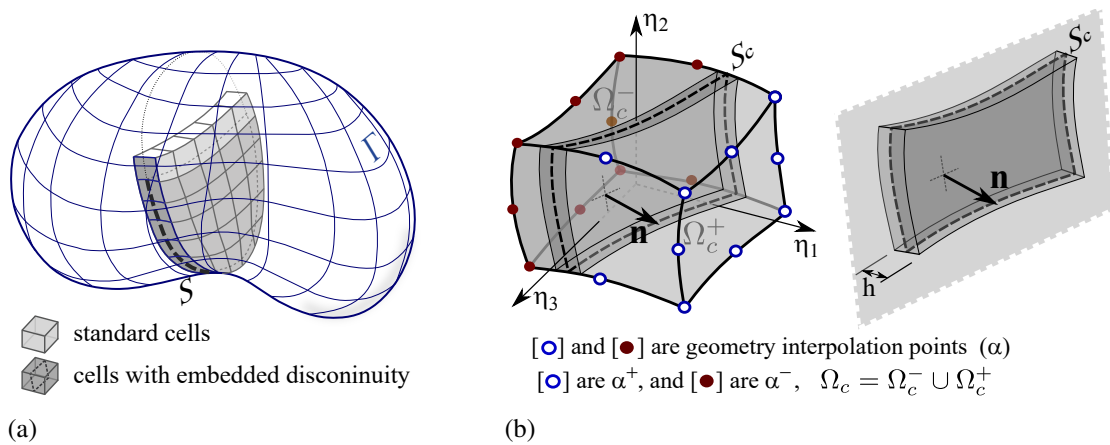
Figure 28: (a) Solid with region divided into cells, (b) Cell with embedded strong discontinuity

whereas, in the pre-bifurcation phase (in which ϵ_{ij}^{φ} is replaced by ϵ_{ij}^{o}) and in the case of plane strain state, a fourth term must be added to this vector: $\dot{\epsilon}_{33}^{o}(\mathbf{x}) = \dot{\epsilon}_{33}^{o,c}$, since the out-of-plane component σ_{i33}^{*} is not necessarily null. In the post-bifurcation steps, this fourth term is naturally null.

On the other hand, the cell geometry is parameterized through conventional linear or quadratic shape functions:

$$X_j(\eta_1, \eta_2) \approx M^{\alpha}(\eta_1, \eta_2)X_j^{\alpha} \text{ (for 2D)}, \quad X_j(\eta_1, \eta_2, \eta_3) \approx M^{\alpha}(\eta_1, \eta_2, \eta_3)X_j^{\alpha} \text{ (for 3D)}, \quad (220)$$

where the index α refers to the cell's geometry interpolation points (indicated in Figure 28b – in which quadratic shape functions are considered) and η_i are natural coordinates, such that $\eta_i \in [-1, +1]$.

The geometry interpolation functions can also be used to define the function $\varphi(\mathbf{x})$ inside a cell with embedded discontinuity, since the conditions of equation (201) are fully satisfied from the choice:

$$\varphi(\mathbf{x}(\eta_1, \eta_2)) = \sum_{\alpha^+} M^{\alpha^+}(\eta_1, \eta_2) \text{ (for 2D)}, \quad \varphi(\mathbf{x}(\eta_1, \eta_2, \eta_3)) = \sum_{\alpha^+} M^{\alpha^+}(\eta_1, \eta_2, \eta_3) \text{ (for 3D)},$$

$$(221)$$

where the summation is performed over the interpolation functions associated with the cell's points located on the Ω_c^+ side of the cell. For example, in Figure 28b, the points associated to α^- or α^+ are indicated.

Within a cell with embedded discontinuity, it is further assumed that the jump components in the displacements are constant, so that, for plane problems

$$\begin{cases} [\![u_i]\!](\mathbf{x}) \approx [\![u_i^c]\!] = \begin{Bmatrix} [\![u_1^c]\!] \\ [\![u_2^c]\!] \end{Bmatrix} = \{[\![u^c]\!]\}, & \text{para } \mathbf{x} \in \Omega_c \\ [\![u_{i,j}]\!] = 0, & \text{para } \mathbf{x} \in \Omega_c \end{cases} \quad (222)$$

analogously for three-dimensional problems.

In the next subsection, the way to obtain these components is detailed, based on the numerical solution of the equation (216).

9.2   Displacement jump evaluation

The components of the displacement jump inside a cell with embedded discontinuity are obtained through the numerical solution of the interface equilibrium equation. For this, it is necessary to

determine the gradient of the regularizing function, $\varphi(\mathbf{x})$, which can be done from equation (221), i.e.,

$$\varphi_{,i} = \frac{\partial \varphi}{\partial \eta_k} \frac{\partial \eta_k}{\partial x_i} = \left(\frac{\partial M^\alpha}{\partial \eta_k} x_i^\alpha \right)^{-1} \frac{\partial \varphi}{\partial \eta_k} = \left(\frac{\partial M^\alpha}{\partial \eta_k} X_i^\alpha \right)^{-1} \left[\frac{\partial}{\partial \eta_k} \left(\sum_{\alpha^+} M^{\alpha^+} \right) \right] \tag{223}$$

Rewriting in a matrix form and applying to the collocation point:

$$\{\nabla \varphi(\boldsymbol{\xi}^c)\} = [J(\eta_1^{\xi_c}, \eta_2^{\xi_c})]^{-1} \{\nabla_\eta \varphi(\eta_1^{\xi_c}, \eta_2^{\xi_c})\} \text{ (for 2D), and,}$$
$$\{\nabla \varphi(\boldsymbol{\xi}^c)\} = [J(\eta_1^{\xi_c}, \eta_2^{\xi_c}, \eta_3^{\xi_c})]^{-1} \{\nabla_\eta \varphi(\eta_1^{\xi_c}, \eta_2^{\xi_c}, \eta_3^{\xi_c})\} \text{ (for 3D),} \tag{224}$$

where $\eta_i^{\xi_c}$ refer to the natural coordinates of the cell's collocation point, $\{\nabla_\eta \varphi(\eta_1^{\xi_c}, \eta_2^{\xi_c})\}$ (or $\{\nabla_\eta \varphi(\eta_1^{\xi_c}, \eta_2^{\xi_c})\}$) correspond to the vector defined by the term in square brackets in equation (223) and matrix $[J(\eta_1^{\xi_c}, \eta_2^{\xi_c}, \eta_3^{\xi_c})]$ for plane problems is given by

$$[J(\eta_1, \eta_2)] = \begin{bmatrix} \dfrac{\partial M^1(\eta_1, \eta_2)}{\partial \eta_1} & \cdots & \dfrac{\partial M^{n_c}(\eta_1, \eta_2)}{\partial \eta_1} \\ \dfrac{\partial M^1(\eta_1, \eta_2)}{\partial \eta_2} & \cdots & \dfrac{\partial M^{n_c}(\eta_1, \eta_2)}{\partial \eta_2} \end{bmatrix} \begin{bmatrix} X_1^1 & X_2^1 \\ \vdots & \vdots \\ X_1^{n_c} & X_2^{n_c} \end{bmatrix} \tag{225}$$

in which n_c represents the number of geometry interpolation points for the cell. Similar expression can be easily extended to three-dimensional problems.

Returning now to equation (203) and taking into account equation (222), it can be noted that, for three-dimensional problems,

$$\{\epsilon^{\varphi,c}\} = \begin{bmatrix} \varphi_{,1}(\boldsymbol{\xi}^c) & 0 & 0 \\ 0 & \varphi_{,2}(\boldsymbol{\xi}^c) & 0 \\ 0 & 0 & \varphi_{,3}(\boldsymbol{\xi}^c) \\ \frac{1}{2}\varphi_{,2}(\boldsymbol{\xi}^c) & \frac{1}{2}\varphi_{,1}(\boldsymbol{\xi}^c) & 0 \\ \frac{1}{2}\varphi_{,3}(\boldsymbol{\xi}^c) & 0 & \frac{1}{2}\varphi_{,1}(\boldsymbol{\xi}^c) \\ 0 & \frac{1}{2}\varphi_{,3}(\boldsymbol{\xi}^c) & \frac{1}{2}\varphi_{,2}(\boldsymbol{\xi}^c) \end{bmatrix} \begin{Bmatrix} [\![u_1^c]\!] \\ [\![u_2^c]\!] \\ [\![u_3^c]\!] \end{Bmatrix} = [\nabla^s \varphi]\{[\![u^c]\!]\} \tag{226}$$

and, for two-dimensional problems,

$$\{\epsilon^{\varphi,c}\} = \begin{bmatrix} \varphi_{,1}(\boldsymbol{\xi}^c) & 0 \\ 0 & \varphi_{,2}(\boldsymbol{\xi}^c) \\ \frac{1}{2}\varphi_{,2}(\boldsymbol{\xi}^c) & \frac{1}{2}\varphi_{,1}(\boldsymbol{\xi}^c) \end{bmatrix} \begin{Bmatrix} [\![u_1^c]\!] \\ [\![u_2^c]\!] \end{Bmatrix} = [\nabla^s \varphi]\{[\![u^c]\!]\} \tag{227}$$

Thus, using equations (217), (222) and (227) (or(226)), the following matrix form is obtained for equation (216):

$$\{f\} = [\bar{N}^c]^T \left([C]\{\hat{\epsilon}^c\} - [C][\nabla^s \varphi]\{[\![u^c]\!]\} - \{\sigma^{\mathcal{S}}(\{\hat{\epsilon}^c\} - [\nabla^s \varphi]\{[\![u^c]\!]\} + \frac{1}{h}[N^c]\{[\![u^c]\!]\})\} \right) = \{0\} \tag{228}$$

where $[C]$ is the elastic linear constitutive matrix, corresponding to the tensor C_{ijkl}, and

$$[\bar{N}^c] = \begin{bmatrix} n_1 & 0 & 0 \\ 0 & n_2 & 0 \\ 0 & 0 & n_3 \\ n_2 & n_1 & 0 \\ n_3 & 0 & n_1 \\ 0 & n_3 & n_2 \end{bmatrix} ; \quad [N^c] = \begin{bmatrix} n_1 & 0 & 0 \\ 0 & n_2 & 0 \\ 0 & 0 & n_3 \\ \frac{1}{2}n_2 & \frac{1}{2}n_1 & 0 \\ \frac{1}{2}n_3 & 0 & \frac{1}{2}n_1 \\ 0 & \frac{1}{2}n_3 & \frac{1}{2}n_2 \end{bmatrix} \tag{229}$$

for three-dimensional problems, while for two-dimensional problems

$$[\bar{N}^c] = \begin{bmatrix} n_1 & 0 \\ 0 & n_2 \\ n_2 & n_1 \end{bmatrix} \; ; \quad [N^c] = \begin{bmatrix} n_1 & 0 \\ 0 & n_2 \\ \frac{1}{2}n_2 & \frac{1}{2}n_1 \end{bmatrix} \tag{230}$$

For a given state of regular strains, $\{\hat{\epsilon}^c\}$, equation (228) can then be solved from its linearisation, i.e.,

$$\{f\}_{j-1} + \left[\frac{\partial\{f\}}{\partial\{\llbracket u^c \rrbracket\}} \right]_{j-1} \{\delta\llbracket u^c \rrbracket\}_j \approx 0 \tag{231}$$

where j is an iterative index, $\{\delta\llbracket u^c \rrbracket\}_j = \{\llbracket u^c \rrbracket\}_j - \{\llbracket u^c \rrbracket\}_{j-1}$ and

$$\left[\frac{\partial\{f\}}{\partial\{\llbracket u^c \rrbracket\}} \right]_{j-1} = [\bar{N}^c]^T \left[- [C][\nabla^s\varphi] - \left[\frac{\partial\sigma^{\mathcal{S}}}{\partial\epsilon} \right]_{j-1} \left[\frac{1}{h}[N^c] - [\nabla^s\varphi] \right] \right] \tag{232}$$

It is emphasized here that vector $\{\sigma^{\mathcal{S}}(\cdot)\}$, present in equation (228), corresponds to the stress provided by the constitutive model adopted to represent the effects of the discontinuity. For example, such stresses can be given by equation (167b), with the damage variable being provided by one of the equations: (197) or (200), depending on the discontinuity regime (weak or strong). Term $\left[\frac{\partial\sigma^{\mathcal{S}}}{\partial\epsilon} \right]$, present in the equation (232), is the matrix form of the tangent operator defined, for example, in equation (62).

The complete algorithm to evaluate the displacement jump inside a cell is:

   i. Set $j = 0$ and $\{\llbracket u^c \rrbracket\}_0$ with the final values of the last displacement jump components evaluation;

   ii. $j = j + 1$;

   iii. If $j >$ maximum number of iterations specified, the process is interrupted;

   iv. Calculate $\{f\}_{j-1}$ and $\left[\frac{\partial\{f\}}{\partial\{\llbracket u^c \rrbracket\}} \right]_{j-1}$, respectively from equations (228) and (232);

   v. Solve equation (231), $\left[\frac{\partial\{f\}}{\partial\{\llbracket u^c \rrbracket\}} \right]_{j-1} \{\delta\llbracket u^c \rrbracket\}_j = -\{f\}_{j-1}$, for $\{\delta\llbracket u^c \rrbracket\}_j$;

   vi. Actualize $\{\llbracket u^c \rrbracket\}_j = \{\llbracket u^c \rrbracket\}_{j-1} + \{\delta\llbracket u^c \rrbracket\}_j$;

   vii. If $\frac{\| \{\delta\llbracket u^c \rrbracket\}_j \|}{\| \{\llbracket u^c \rrbracket\}_j \|} >$ TOL, where TOL is a pre-defined scalar tolerance, return to step (ii). Else:

   viii. Return with the result $\{\llbracket u^c \rrbracket\} = \{\llbracket u^c \rrbracket\}_j$.

9.3   Regularized constitutive equation

Through equation (226) or (227), one can also write the matrix form of the regularized constitutive equation (218) for a cell with discontinuity, i.e.,

$$\{\tilde{\sigma}(\hat{\epsilon}^c)\} = [C](\{\hat{\epsilon}^c\} - \{\epsilon^{\varphi,c}\}) = [C](\{\hat{\epsilon}^c\} - [\nabla^s\varphi]\{\llbracket u^c \rrbracket\}) \tag{233}$$

The stresses provided by this equation are necessary for the non linear solution strategy, for the post-bifurcation steps. In addition to them, one must define a tangent operator for the regularized constitutive equation, which can be done by taking its derivative:

$$\left[\frac{\partial\tilde{\sigma}}{\partial\hat{\epsilon}^c} \right] = [C] \left([I] - [\nabla^s\varphi] \left[\frac{\partial\{f\}}{\partial\{\llbracket u^c \rrbracket\}} \right]^{-1} [\bar{N}^c]^T \left([C] - \left[\frac{\partial\sigma^{\mathcal{S}}}{\partial\epsilon} \right] \right) \right) \tag{234}$$

9.4   Solution strategy

The algorithm for a complete analysis involving discontinuities, follows exactly the same steps as listed in section 4.2.1. The only exceptions are in steps (vii) and (xiii) for post-bifurcation phases, as described below:

vii. The tangent matrix $[\partial\sigma/\partial\epsilon]$ present in equation (135) is substituted by equation (234) during evaluation of $[D]^i_{j-1}$;

xiii. To evaluate the stress inside a cell with discontinuity, firstly the displacement jumps are calculated, as described in the algorithm at the end of section 9.2. Then, such result is applied to equation (233).

10   Examples of Non Linear Problems with discontinuities

This section presents numerical analyses of problems where occur the presence of discontinuity – like analysis of crack propagation in quasi-brittle materials – to illustrate the application of the formulation and algorithms discussed in the last sections. The first two examples are concrete fracture experiments available in the literature, that consider mixed-mode crack propagation: the first presented by Arrea and Ingraffea [1982], and the second by Gálvez et al. [1998]. They were modeled under plane stress assumption, with the CSDA. The third example consider a prismatic bar under simple tension, with a circular corner notch, where a three-dimensional model containing cells with embedded strong discontinuity was used. For all examples, the control method adopted to drive the incremental-iterative procedure in the non linear analyses, considered a convergence tolerance of 10^{-4}.

10.1   Example 1: Arrea and Ingraffea four point bending of a notched beam

The four point bending of a concrete notched beam, experimentally studied by Arrea and Ingraffea [1982], was analyzed in this example to present the capability of the formulation for the treatment of mixed-mode fracture problems. Geometry, loads, boundary conditions and material properties are presented in Figure 29, together with the approximate crack path observed in the experiments. As non linear analysis control method, the vertical displacement of the right point in the notch mouth (point A in fig. 29), was considered.

$l_1 = 203\text{mm}, l_2 = 397\text{mm}, l_3 = 61\text{mm}, h = 224\text{mm}, a = 82\text{mm}, w = 5\text{mm}$
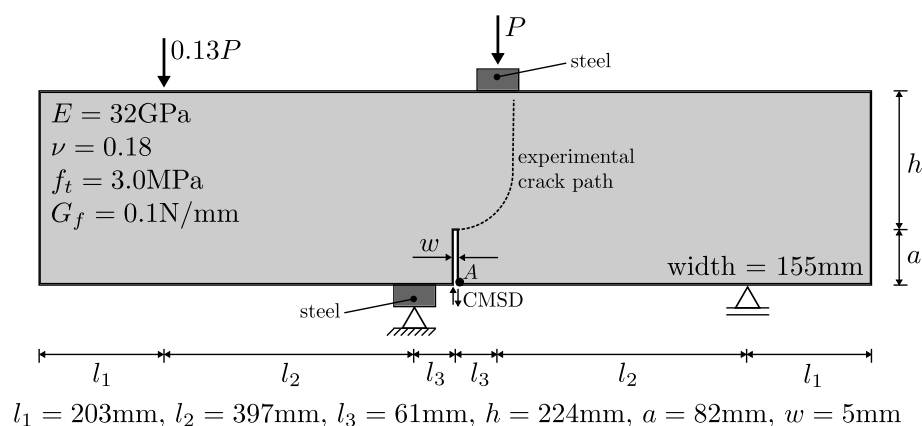
Figure 29: Example 1 – Arrea and Ingraffea experiment: four point bending of a notched concrete beam.

The boundary was divided by 642 linear elements and a initial square cell with diagonal of 1.6 mm was introduced at the tip of the initial notch, such that, the origin of the discontinuity line is imposed in the midpoint of that cell edge on the notch.

Initially, this cell works in elastic regime. Once the bifurcation condition is reached, the discontinuity activation occurs, and a new cell is generated in elastic regime, and this process is repeated through the analysis. The discontinuity tracking algorithm used, starts with a cell of 0.7 mm side length, and with a growth factor of cell size $\beta = 1.001$, until a maximum crack segment size of 8 mm.

This example consider analysis with strong discontinuity regime is imposed directly after the end of the elastic regime, and also, analysis with variable bandwidth model. The final mesh achieved with the variable bandwidth model is presented in Figure 30, in which 72 new cells were generated. The final mesh for the analysis with direct strong discontinuity is quite similar. The curve of load P in function of the Crack Mouth Sliding Displacement (CMSD) of the original notch is presented in Figure 31. The numerical results are plotted over the empirical envelopment taken from the reference, showing a good accuracy.

(a)   (b)
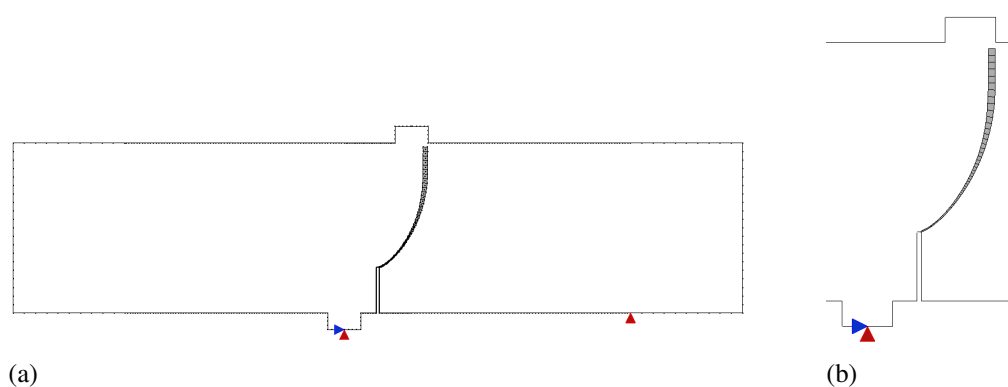
Figure 30: Example 1 - Final mesh: (a) Total mesh, (b) Detail
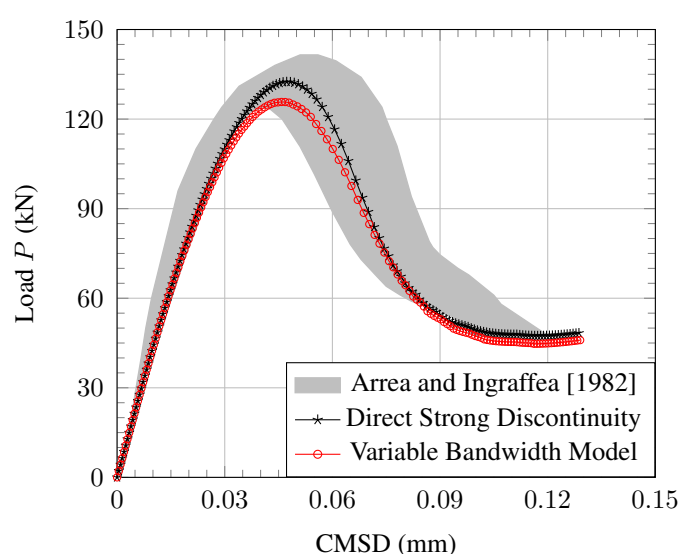
Figure 31: Example 1 - Crack mouth sliding displacement equilibrium path

10.2   Example 2: Gálvez et al. three and four point bending

Other shear tests, resulting in mixed-mode fracture patterns of a pre-notched concrete beam, reported by Gálvez et al. [1998], were also analysed with the numerical formulation with CSDA. The problem description is represented in Figure 32.
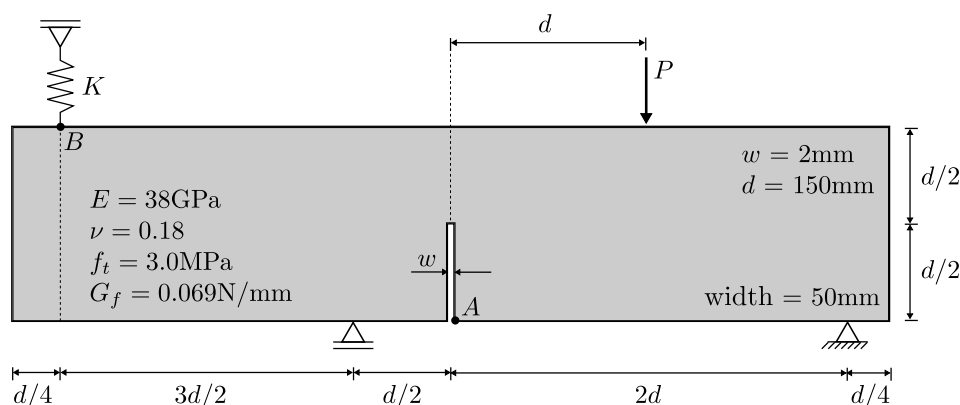
Figure 32: Example 2 – Gálvez et al. experiment data

Two cases were considered: three and four point bending. In the first one, point B in Figure 32 is free (K = 0), while in the second, the vertical displacement of such point was constrained (K = ∞). Each analysis is individually described next.

10.2.1   Three point bending

The non linear procedure was controlled by fixed increments of the vertical displacement of point B.

Problem boundary was divided by 607 linear elements and a initial square cell, with diagonal of 1.2 mm, was placed at the notch tip. The tracking algorithm was used, however with no variation of cells sizes ($\beta = 1.0$). The final mesh, where 92 new cells were generated, is shown in Figure 33.

(a)   (b)
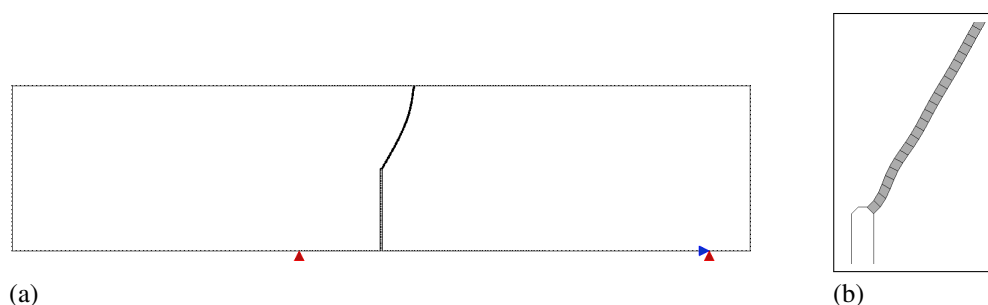
Figure 33: Example 2 - Final mesh: (a) Complete mesh, (b) Detail

Results for the external load P in function of point B vertical displacement and of the crack mouth opening displacement (CMOD) are presented in Figure 34, for the analysis with variable bandwidth model. Moreover, the numerical crack path is plotted in Figure 35. All these results are compared, in the mentioned figures, with experimental data.
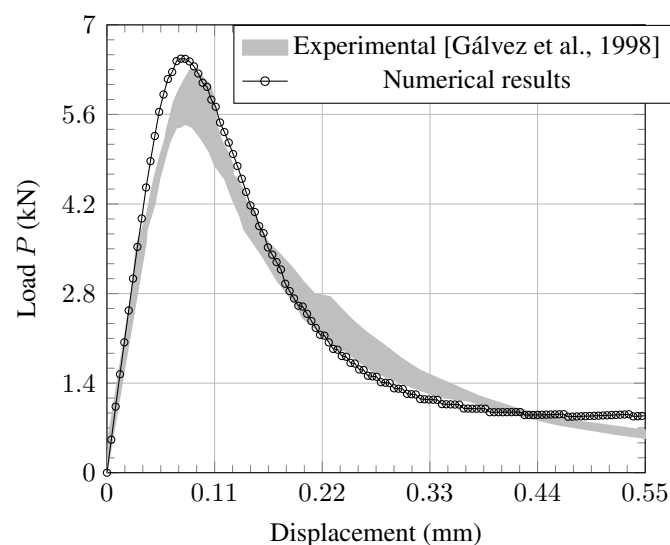
(a)
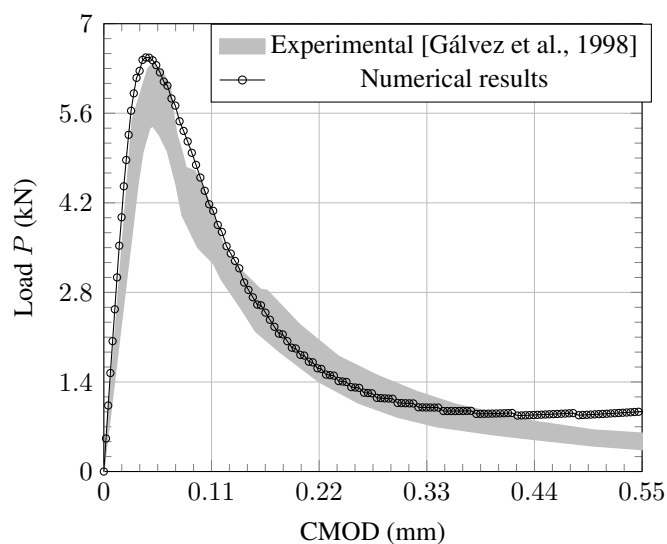
(b)

Figure 34: Example 2 - Results for three point bending: (a) Point B vertical displacement, (b) Crack mouth opening displacement

10.2.2 Four point bending

In the four point bending case of Gálvez et al. [1998] experiment, the vertical displacement component of point A (see Fig. 32) was used to control the non linear increments.

The boundary discretization was the same of the three point bending case, i.e., 607 linear elements. The initial cell was again squared, however with a diagonal of 0.6 mm. The generated cells had their sizes incremented by the adoption of $\beta = 1.001$ in the tracking algorithm. Such increment was suspended when a new discontinuity segment exceeded 0.75 mm length. The final mesh is shown in Figure 36, in which 188 additional cells were generated.

To compare the numerical and experimental results, a curve of the applied load P versus the loaded point vertical displacement is presented in Figure 37, while the crack path is plotted in Figure 38.
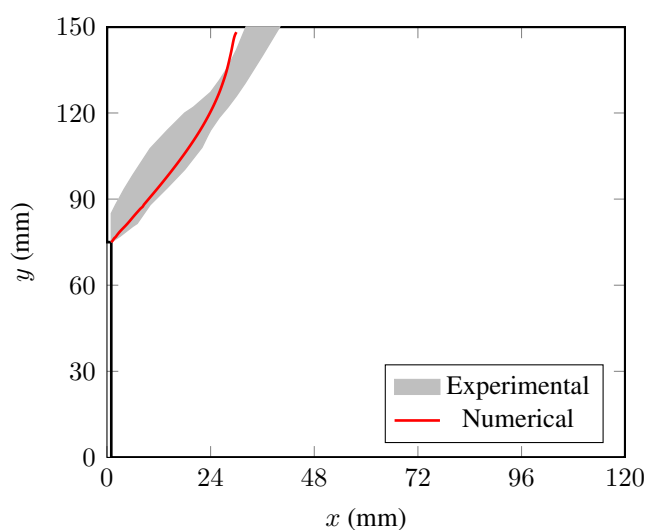
Figure 35: Example 2 - Results for three point bending crack path [Gálvez et al., 1998]

(a)

(b)   (c)
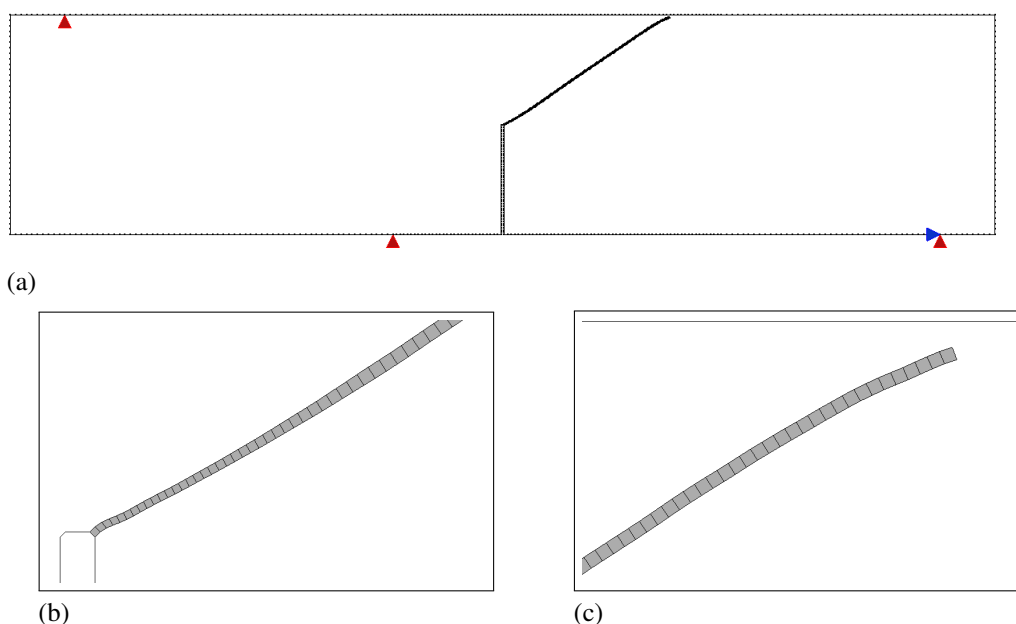
Figure 36: Example 2 - Final mesh for simulation of four point bending [Gálvez et al., 1998]: (a) Complete mesh, (b) First cell detail, (c) Final cells detail.

10.3   Example 3: Prismatic bar with a circular corner notch

A prismatic bar under simple tension, with a circular corner notch is considered in this example. Dimensions and material properties are presented in Figure 39. The failure surface is supposed to occur at the horizontal notch plane highlighted, with the discontinuity fracture surface spreading from the interior notch border. Quadrilateral boundary elements were used, and hexahedral cells with embedded uniform strong discontinuity were applied for the discretization of specific regions of the solids, where cracks were expected to propagate. Strong discontinuity regime is imposed directly after the end of the elastic regime. Direct displacement control method was adopted to
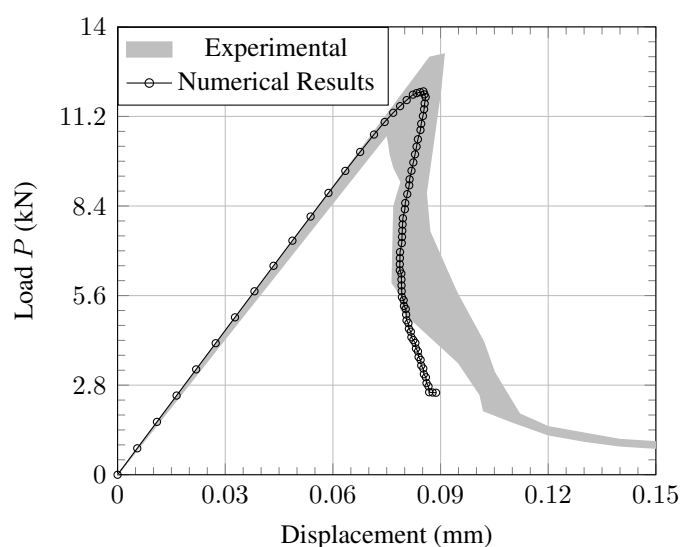
Figure 37: Exemplo 2 - Results for four point bending: Loaded point vertical displacement
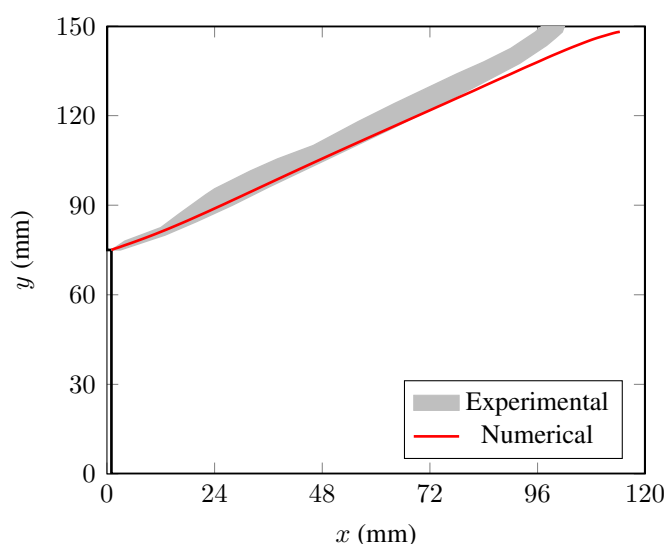
Figure 38: Exemplo 2 - Results for four point bending: Crack path

drive the incremental-iterative procedure of the non linear analyses.

Two meshes, with different refinements, were considered as shown in Figure 40. Displacement control of the corner point A (figure 39) was adopted for the non linear analysis progress. Results for the displacement equilibrium path of point A and an intermediate point B are plotted in Figure 41. The reference critical fracture stress σ_{fcrit}, shown in Figure 41, was achieved as a particular case of the stress-intensity solution for a quarter-elliptical corner crack, given by Anderson [2005].

The equilibrium path present a peak stress a little under the reference critical fracture stress. The increase in mesh refinement provides an accurate representation of the unload behaviour. Also, from the results for point B (not a control node) it is possible to note a typical snap-back of the equilibrium path. At this point neighbourhood, the discontinuity is activated only when the unload stress is around 0.136 MPa. The unloading branches of all equilibrium paths present a non
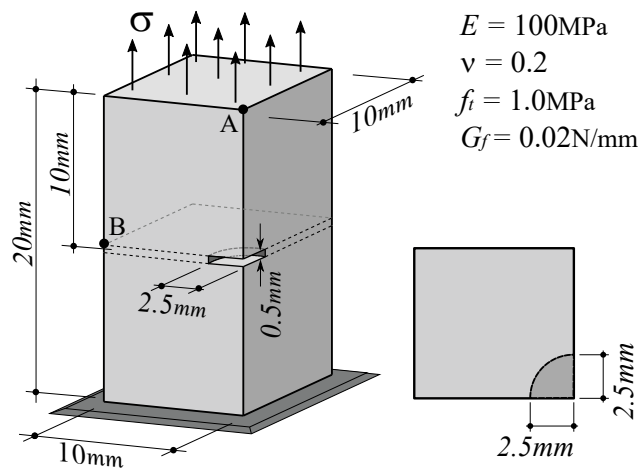
Figure 39: Example 3 - Prismatic bar under simple tension, with a circular corner notch - dimensions and material properties
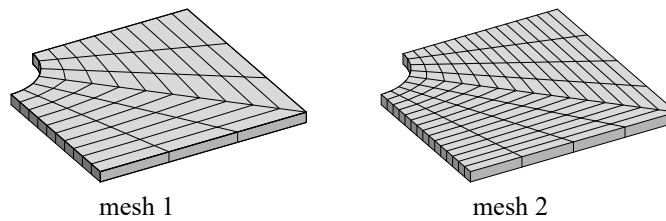

Figure 40: Example 3 - Cells distribution for mesh 1 and mesh 2
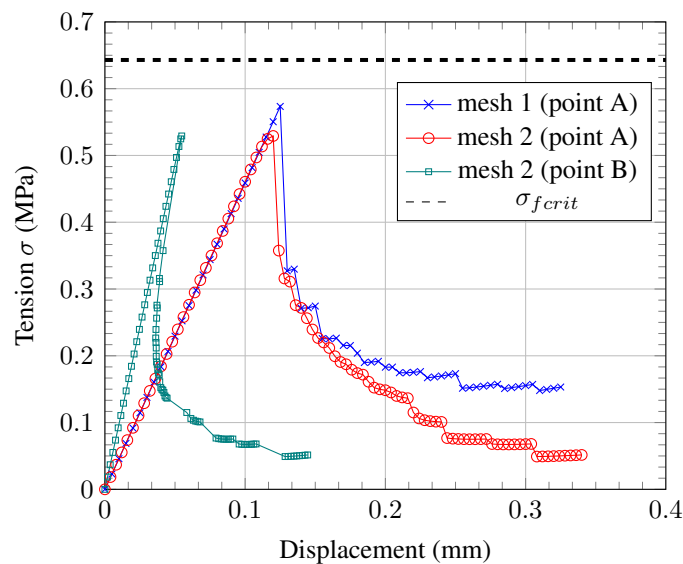
Figure 41: Example 3 - Displacement equilibrium path for control point A, for point B, and the reference critical fracture stress σ_{fcrit}.

smooth curve. This can be explained by the gradual activation of discontinuity at the cells on the fracture plane, in different load steps, schematically presented in Figure 42.
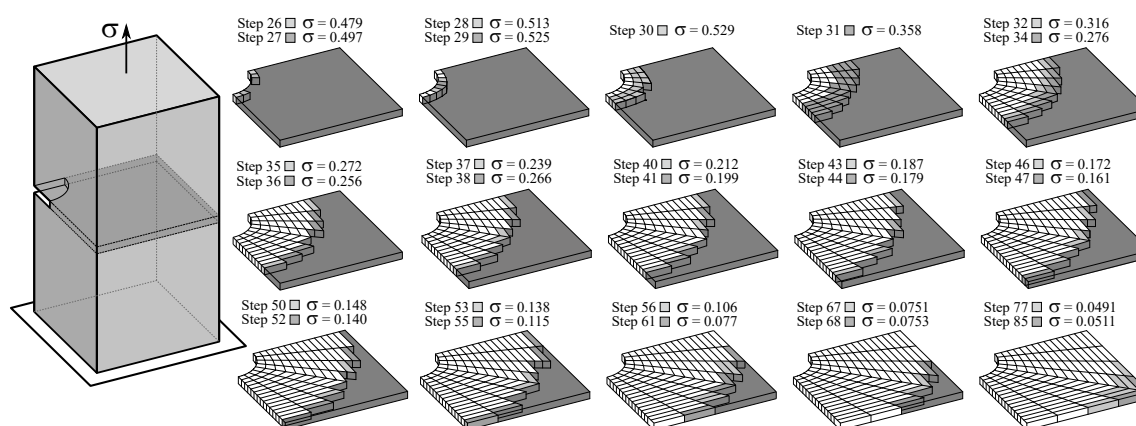
Figure 42: Example 3 - Gradual activation of discontinuity at the crack plane

11   Final Remarks

This chapter has presented the Boundary Element Method as a versatile technique for dealing with damage modeling analysis, both for continuum medium and in the presence of discontinuity.

The non linear constitutive modelling, with elastoplastic or elasto-degrading models were associated with the implicit BEM formulation for physically non linear problems. The solution strategy was detailed in a general algorithm applicable to different control methods.

For dealing with problems with discontinuity in the strain or displacement fields, the CSDA was introduced with a variable bandwidth model, together with a review in the boundary element equations. The integral equations with discontinuity and the equilibrium equation on the discontinuity surface allowed the evaluation of displacement jumps that occur in the non linear analysis. Algorithms for the evaluation of displacement jumps and strategy solution were presented.

The techniques presented in this chapter requires the discretization of the region of the domain where dissipation effects occur, using cells. Conventional cells were used for the continuum non linear analysis, while, in the possible presence of discontinuities there were needed the use of cells with embedded discontinuity, presented in a section, with its particularities.

The results for some problems presented, showed the potential of the application of BEM in the analysis of physically non linear problems, using a minimum of domain discretization.

Acknowledgements

Acknowledgements are optional, at the discretion of the chapter co-authors.

12   References

M. H. Aliabadi. *The boundary element method – Aplications in solids and structures.* John Wiley and Sons, Chichester, West Sussex, UK, 2002.

T. L. Anderson. *Fracture Mechanics – Fundamentals and applications.* Taylor & Francis Group, third edition, 2005.

M. Arrea and A. R. Ingraffea. Mixed-mode crack propagation in mortar and concrete. Technical report, 81-13, Department of Structural Engineering, Cornell University, Ithaca, USA, 1982.

J. L. Batoz and G. Dhatt. Incremental displacement algorithms for nonlinear problems. *International Journal for Numerical Methods in Engineering*, 14:1262–1267, 1979.

G. Beer, I. Smith, and C. Duenser. *The Boundary Element Method with Programming: For Engineers and Scientists*. SpringerWienNewYork, 2008.

A. Benallal, C. A. Fudoli, and W. S. Venturini. An implicit BEM formulation for gradient plasticity and localization phenomena. *International Journal for Numerical Methods in Engineering*, 53: 1853–1869, 2002.

A. S. Botta, W. S. Venturini, and A. Benallal. BEM applied to damage models emphasizing localization and associated regularization techniques. *Engineering Analysis with Boundary Elements*, 29(8):814–827, 2005.

C. A. Brebbia, J. C. F. Telles, and L. C. Wrobel. *Boundary element techniques – Theory and applications in engineering*. Springer-Verlag, Berlin, 1984.

H. D. Bui. Some remarks about the formulation of three-dimensional thermoelastoplastic problems by integral equations. *International Journal of Solids and Structures*, 14:935–939, 1978.

I. Carol, E. Rizzi, and K. Willam. A unified theory of elastic degradation and damage based on a loading surface. *International Journal of Solids and Structures*, 31(20):2835–2865, 1994.

Z. Chen and H. L. Schreyer. A numerical solution scheme for softening problems involving total strain control. *Computers & Structures*, 37(6):1043–1050, 1990.

C. Comi and U. Perego. Fracture energy based bi-dissipative damage model for concrete. *International Journal of Solids and Structures*, 38(36):6427–6454, 2001.

M. A. Crisfield. A fast incremental-iterative solution procedure that handles snap-through. *Computers & Structures*, 13:55–62, 1981.

M. A. Crisfield. An arc length method including line searches and acelerations. *International Journal for Numerical Methods in Engineering*, 19:1269–1289, 1983.

E. A. de Souza Neto, D. Peric, and D. R. J. Owen. *Computational Methods For Plasticity: Theory and Application*. Wiley, Chichester, West Sussex, UK, 2006.

U. Eberwien, C. Duenser, and W. Moser. Efficient calculation of internal results in 2d elasticity BEM. *Engineering Analysis with Boundary Elements*, 29:447–453, 2005.

J. C. Gálvez, M. Elices, G. V. Guinea, and J. Planas. Mixed mode fracture of concrete under proportional and nonproportional loading. *International Journal of Fracture*, 94:267–284, 1998.

X.-W. Gao and T. G. Davies. An effective boundary element algorithm for 2D and 3D elastoplastic problems. *International Journal of Solids and Structures*, 37:4987–5008, 2000.

X. W. Gao and T. G. Davies. *Boundary element programming in mechanics*. Cambridge University Press, Cambridge, 2002.

R. García, J. Flórez-López, and M. Cerrolaza. A boundary element formulation for a class of non-local damage models. *International Journal of Solids and Structures*, 36(24):3617–3638, 1999.

M. Guiggiani and P. Casalini. Direct computation of Cauchy principal value integrals in advanced boundary elements. *International Journal for Numerical Methods in Engineering*, 24:1711–1720, 1987.

M. Guiggiani and A. Gigante. A general algorithm for multidimensional cauchy principal value integrals in the boundary element method. *The American Society of Mechanical Engineers*, 57:906–915, 1990.

U. Herding and G. Kuhn. A field boundary element formulation for damage mechanics. *Engineering Analysis with Boundary Elements*, 18(2):137–147, 1996.

R. Hill. *The mathematical theory of plasticity*. Oxford University Press, 1950.

Q. Huang. Boundary element method: an introduction. Technical report, Department of Mechanical Engineering – Vanderbilt University, USA, 1993.

L. M. Kachanov. Time rupture process under creep conditions (in russian). *Izr. ARad. Nauk SSSR otd Tekh. Nauk.*, 8:26–31, 1958. Cited by Carol et al. [1994].

J. C. Lachat and J. O. Watson. Effective numerical treatment of boundary integral equations – A formulation for three dimensional elastostatics. *International Journal for Numerical Methods in Engineering*, 10:991–1005, 1976.

J. Lemaitre and J. L. Chaboche. *Mechanics of Solid Materials*. Cambridge University Press, Cambridge, UK, 1990.

F.-B. Lin, G. Yan, Z. P. Bažant, and F. Ding. Non-local strain softening model of quasi-brittle materials using boundary element method. *Engineering Analysis with Boundary Elements*, 26:417– 424, 2002.

O. L. Manzoli and W. S. Venturini. Uma formulação do MEC para simulação numérica de descontinuidades fortes. *Revista Internacional de Métodos Numéricos para Cálculo y Diseño en Ingeniería*, 20(3):215–234, 2004.

O. L. Manzoli and W. S. Venturini. An implicit BEM formulation to model strong discontinuities. *Computational Mechanics*, 40:901–909, 2007.

O. L. Manzoli, R. A. Pedrini, and W. S. Venturini. Strong discontinuity analysis in solid mechanics using boundary element method. In E. J. Spountzakis and M. H. Aliabadi, editors, *Avances in Boundary Element Techniques X*, pages 323–329, Athens, Greece, 2009.

J. Mazars and J. Lemaitre. Application of continuous damage mechanics to strain and fracture behavior of concrete. *Application of Fracture Mechanics to Cementitious Composites. NATO Advanced Research Workshop*, 47:375–378, September 1984.

A. Mendelson. Boundary-integral methods in elasticity and plasticity. Technical report, TN-D-7418, National Aeronautics and Space Administration, NASA, USA, 1973.

S. Mukherjee. Corrected boundary-integral equations in planar thermoelastoplasticity. *International Journal of Solids and Structures*, 13:331–335, 1977.

J. Oliver. Modelling strong discontinuities in solid mechanics via strain softening constitutive equations. Part 1: Fundamentals. *International Journal for Numerical Methods in Engineering*, 39:3575–3600, 1996.

J. Oliver. On the discrete constitutive models induced by strong discontinuity kinematics and continuum constitutive equations. *International Journal of Solids and Structures*, 37:7207–7229, 2000.

J. Oliver, M. Cervera, S. Oller, and J. Lubliner. Isotropic damage models and smeared crack analysis of concrete. In *SCI-C Computer Aided Analysis and Design of Concrete Structures*, pages 945–957, 1990.

J. Oliver, M. Cervera, and O. Manzoli. On the use of strain-softening models for the simulation of strong discontinuities in solids. In R. de Borst and E. van der Giessen, editors, *Material instabilities in solids*, chapter 8, pages 107–123. John Wiley & Sons, Chichester, 1998.

J. Oliver, M. Cervera, and O. Manzoli. Strong discontinuities and continuum plasticity models: the strong discontinuity approach. *International Journal of Plasticity*, 15:319–351, 1999.

J. Oliver, A. E. Huespe, and E. Samaniego. A study on finite elements for capturing strong discontinuities. *International Journal for Numerical Methods in Engineering*, 56:2135–2161, 2003.

J. Oliver, A. E. Huespe, S. Blanco, and D. L. Linero. Stability and robustness issues in numerical modeling of material failure with the strong discontinuity approach. *Computer Methods in Applied Mechanics and Engineering*, 195:7093–7114, 2006.

R. G. Peixoto, F. E. S. Anacleto, G. O. Ribeiro, R. L. S. Pitangueira, and S. S. Penna. A solution strategy for non-linear implicit BEM formulation using a unified constitutive framework. *Engineering Analysis with Boundary Elements*, 64:295–310, 2016.

R. G. Peixoto, G. O. Ribeiro, R. L. S. Pitangueira, and S. S. Penna. The strong discontinuity approach as a limit case of strain localization in the implicit BEM formulation. *Engineering Analysis with Boundary Elements*, 80:127–141, 2017.

R. G. Peixoto, G. O. Ribeiro, and R. L. S. Pitangueira. A boundary element method formulation for quasi-brittle material fracture analysis using the continuum strong discontinuity approach. *Engineering Fracture Mechanics*, 202:47–74, 2018.

P. E. Petersson. Crack growth and development of fracture zones in plain concrete and similar materials. TVBM-1006. Technical report, Division of Building Materials, Lund Institute of Technology, Lund, Sweden, 1981.

A. Portela, M. H. Aliabadi, and D. P. Rooke. The dual boundary element method: effective implementation for cracked problems. *International Journal for Numerical Methods in Engineering*, 33:1269–1287, 1992.

S. Rajgelj, C. Amadio, and A. Nappi. Application of damage mechanics concepts to the boundary element method. In C. A. Brebbia and M. S. Ingber, editors, *Proceedings of the Seventh International Conference on Boundary Element Technology (BETECH 92)*, pages 617–634, Springer, Dordrecht., 1992.

P. C. Riccardella. An implementation of the boundary-integral technique for planar problems in elasticity and elasto-plasticity. Technical report, SM-73-10, Department of Mechanical Engineering, Carnegie Institute of Technology, Carnegie-Mellon University, Pittsburgh, USA, 1973.

J. R. Rice and J. W. Rudnicki. A note on some features of the theory of localization of deformation. *International Journal of Solids and Structures*, 16:597–605, 1980.

E. Riks. The application of Newton's method to the problem of elastic stability. *Journal of Applied Mechanics*, 39:1060–1066, 1972.

E. Riks. An incremental approach to the solution of snapping and buckling problems. *International Journal of Solids and Structures*, 15:529–551, 1979.

J. C. Simo and T. J. R. Hughes. *Computational Ineslaticity*. Springer-Verlag, Nova York, USA, 1998.

J. C. Simo and J. W. Ju. Strain- and stress-based continuum damage models - i. formulation. *International Journal of Solids and Structures*, 23(7):821–840, 1987.

J. C. Simo, J. Oliver, and F. Armero. An analysis of strong discontinuities induced by strain-softening in rate-independent inelastic solids. *Computational Mechanics*, 12:277–296, 1993.

J. Sládek, V. Sládek, and Z. P. Bažant. Non-local boundary integral formulation for softening damage. *International Journal for Numerical Methods in Engineering*, 57:103–116, 2003.

J. Swedlow and T. Cruse. Formulation of boundary integral equations for three-dimensional elasto-plastic flow. *International Journal of Solids and Structures*, 7(12):1673–1683, 1971.

J. C. F. Telles. *The boundary element method applied to inelastic problems*. Springer-Verlag, Berlin, 1983.

J. C. F. Telles and C. A. Brebbia. On the application of the boundary element method to plasticity. *Applied Mathematical Modelling*, 3:466–470, 1979.

J. C. F. Telles and J. A. M. Carrer. Implicit procedures for the solution of elastoplastic problems by the boundary element method. *Mathematical and Computer Modelling*, 15:303–311, 1991.

P. S. Theocaris and E. Marketos. Elastic-plastic analysis of perforated thin strips of a strain-hardening material. *Journal of Mechanics and Physics of Solids*, 12:377–390, 1964.

E. van der Giessen and R. de Borst. Introduction to material instabilities in solids. In R. de Borst and E. van der Giessen, editors, *Material instabilities in solids*, chapter 1. John Wiley & Sons, Chichester, 1998.

Y.-B. Yang and M.-S. Shieh. Solution method for nonlinear problems with multiple critical points. *AIAA Journal*, 28:2110–2116, 1990.

A   Particular non linear constitutive models

Particular constitutive models, associated with the general equations presented in section 2.3, are presented here. As an example of the elastic-plastic class, the von Mises associative isotropic model is detailed, while for the elastic-degrading class, several isotropic damage models are presented.

A.1   Elastoplastic von Mises associative isotropic model

The elastoplastic von Mises yield criterion defines a loading function of the type

$$F(\sigma_{ij}, q) = \sqrt{3J_2(s_{ij})} + q(r) - \sigma_Y \tag{235}$$

where,

$$s_{ij} = \sigma_{ij} - \frac{1}{3}\sigma_{kk}\delta_{ij} \quad \text{and} \quad J_2(s_{ij}) = \frac{1}{2}s_{ij}s_{ij}, \tag{236}$$

σ_Y is the original material's yield stress and q is a scalar stress-like internal variable, thermodynamically conjugated to the scalar strain-like variable, r, by the hardening-softening modulus:

$$\dot{q} = -H(r)\dot{r} \tag{237}$$

Particularly, the strain-like hardening-softening internal variable is the so called equivalent plastic strain, defined by

$$r(t) = \int_0^t \| \dot{\epsilon}_{ij}^p(\tau) \| \, d\tau \tag{238}$$

in which the variable t is associated to time.

The first term in the right side of equation (235) is known as von Mises equivalent stress, while the second and third terms, represent the current yield limit.

Equation (237) makes the role of the hardening-softening law of equation (43), since, from equations (46-b) and (235),

$$H = -\frac{\partial q}{\partial \epsilon_{ij}^p} m_{ij} \tag{239}$$

and thus, using equation (42),

$$\dot{q} = -\dot{\lambda}h = \frac{\partial q}{\partial \epsilon_{ij}^p}\dot{\epsilon}_{ij}^p = \frac{\partial q}{\partial \epsilon_{ij}^p}m_{ij}\dot{\lambda} = -H\dot{\lambda} \quad \Rightarrow \quad h = H, \quad \dot{r} = \dot{\lambda} \tag{240}$$

Such law is a material property. For example, a linear hardening is defined by taking $H(r)$ as a constant (positive for hardening and negative for softening).

Moreover, as the model is associative,

$$m_{ij} = n_{ij} = \frac{\partial F}{\partial \sigma_{ij}} = \sqrt{\frac{3}{2}}\frac{s_{ij}}{\sqrt{s_{kl}s_{kl}}} = \sqrt{\frac{3}{2}}\frac{s_{ij}}{\| s_{ij} \|} \tag{241}$$

Now, to rewrite the loading function gradients and the hardening-softening modulus in a strain-based formulation, equations (50) may be used to give

$$\bar{m}_{ij} = -\bar{n}_{ij} = -\sqrt{6}\mu\frac{s_{ij}}{\| s_{ij} \|} \tag{242}$$

$$\bar{H} = -q'(r) + 3\mu \tag{243}$$

where, μ is the shear modulus, defined in equation (11).

Thus, applying equations (242) and (243) to equation (49), the appropriate tangential stiffness operator is directly obtained.

It is worthy to mention that the development made in this subsection is valid for three-dimensional and plane strain problems, but not for plane stress case, for which an operator is commonly applied to account for the constraint of zero out-of-plane stress (see, for example, references Simo and Hughes [1998] or de Souza Neto et al. [2006]).

A.2   Isotropic damage models

A simple isotropic damage model can be characterized by a single scalar damage variable, D, which defines the relation between initial and current secant stiffness, in the spirit of the original damage interpretation by Kachanov [1958], i.e.,

$$C^s_{ijkl} = (1 - D)C_{ijkl}, \qquad D \in [0, 1] \tag{244}$$

The loading function, in the strain space, can be written in the following generalized form

$$\bar{F}(\epsilon_{ij}, r) \equiv \bar{F}(\epsilon_{ij}, D) = \phi(\epsilon_{ij}) - r(D) \tag{245}$$

where $\phi(\epsilon_{ij})$ is called as equivalent strain and $r(D)$ is the (scalar) strain-like variable and represents the current limit value of this equivalent strain for elastic behaviour.

For the hardening-softening law, the following generic assumptions are made

$$\dot{r} = -\dot{\lambda}\bar{h}, \quad \bar{h} = -\frac{\partial r}{\partial D} \quad \Rightarrow \quad \dot{D} = \dot{\lambda} \tag{246}$$

Thus, using equations (244) and (246), equations (64-b) and (64-a) assume the respective forms

$$\bar{M}_{ijkl} = \frac{\partial C^s_{ijkl}}{\partial D} = -C_{ijkl} \tag{247}$$

$$\bar{m}_{ij} = \bar{M}_{ijkl}\epsilon_{kl} = -C_{ijkl}\epsilon_{kl} \tag{248}$$

Moreover, from equations (64-c) and (245),

$$\bar{n}_{ij} = \frac{\partial \phi}{\partial \epsilon_{ij}} \tag{249}$$

Different constitutive models can be defined here simply by changing the definition of the equivalent strain. Some examples are presented in table 3.

Table 3: Particular parameters for isotropic damage models.

Model	$\phi(\epsilon_{ij})$	$\bar{n}_{kl}$
Mazars and Lemaitre [1984]	$\sqrt{\epsilon_{ij}\epsilon_{ij}}$	$\dfrac{\epsilon_{kl}}{\phi(\epsilon_{ij})}$
Simo and Ju [1987]	$\sqrt{\epsilon_{ij}C_{ijkl}\epsilon_{kl}}$	$\dfrac{\epsilon_{ij}C_{ijkl}}{\phi(\epsilon_{ij})}$
Oliver et al. [1990]	$\sqrt{\epsilon^+_{ij}C_{ijkl}\epsilon^+_{kl}}$	$\dfrac{\epsilon^+_{ij}C_{ijkl}}{\phi(\epsilon_{ij})}$
Oliver et al. [2006]	$\sqrt{\epsilon^+_{ij}C_{ijkl}\epsilon_{kl}}$	$\dfrac{\epsilon^+_{ij}C_{ijkl}}{\phi(\epsilon_{ij})}$
Lemaitre and Chaboche [1990]	$\sqrt{\dfrac{1}{E}\epsilon_{ij}C_{ijkl}\epsilon_{kl}}$	$\dfrac{1}{E}\dfrac{\epsilon_{ij}C_{ijkl}}{\phi(\epsilon_{ij})}$

Particularly, for Oliver et al. [1990] constitutive model,

$$\epsilon^+_{ij} = \langle \epsilon_{ij} \rangle = \sum_{k=1}^{n_{dim}} \langle \epsilon_k \rangle \hat{p}_k \otimes \hat{p}_k \tag{250}$$

where n_{dim} is the problem's dimension, ϵ_k represents the k-th principal strain, $\hat{p}_k$ is the unit vector in the corresponding principal direction and $\langle \epsilon_k \rangle = (|\epsilon_k| + \epsilon_k)/2$.

Finally, the hardening-softening modulus is given from equation (64-d), using equations (245) and (246), i.e.,

$$\bar{H} = \frac{\partial r}{\partial D} \tag{251}$$

or, as during damage loading, $r = \phi$,

$$\bar{H}^{-1} = \left[\frac{\partial r}{\partial D} \right]^{-1} = \frac{\partial D}{\partial \phi} \tag{252}$$

and an expression for evaluation of D is usually postulated as a function of the equivalent strain.

The tangent operator is then obtained by substitution of equations (244), (248), (249) and (252) into equation (63).

Chapter 22

Application of Roving Mass Technique Associated with Wavelet Transform to Structural Damage Detection and Localization

Application of Roving Mass Technique Associated with Wavelet Transform to Structural Damage Detection and Localization

Erwin Ulises Lopez Palechor[1], Juliana C. Santos[2], Ramon Saleno, Yure Costa Silva[3], Marcela R. Machado[2,3], Marcus V. Girão de Morais[2,3*], Luciano Mendes Bezerra[4] and Ariosto Bretanha Jorge[2]

[1] Science and Technology Center, Federal University of Cariri, Brazil. e-mail: erwin.lopez@ufca.edu.br

[2] Post-Graduate Program in Integrity of Engineering Materials, University of Brasilia, Brazil. e-mail: ariosto.b.jorge@gmail.com

[3] Faculty of Technology, University of Brasilia, Brazil. e-mail: ggomes@unb.br; ramon.silva@unb.br; mvmorais@unb.br

[4] Post-Graduate Program in Structures and Civil Construction, University of Brasilia, Brazil. e-mail: lmbz@unb.br

*Corresponding author

Abstract

This chapter presents applications of the roving mass technique associated to Wavelet transforms in damage identification and localization, in beam-like structures, using numerical and experimental data, the research works developed at the Graduate Programs of Integrity of Engineering Materials and Structures and Civil Construction of University of Brasília.

Keywords: Wavelet application, Structural Health Monitoring, Wavelet Transform, Continuous Wavelet, Discrete Wavelet, Wavelet Family Function.

1   Introduction

Structural pathologies or even structural collapse are often initiated by cracks in structural members. Structural damages must be identified in its initial state before compromising the integrity and service life of the structure. However, in its initial state, a crack is relatively small making it difficult to detect changes in the dynamic properties. Moreover, there are situations where damages may be hidden due to external cover façade, finishing, or skinning of buildings, bridges, etc. turning the detection of damages a difficult process. Therefore, auxiliary tools to indicate possible existence of damages are always welcome.

Aktan et all (1997) introduced the firsts concepts of structural identification. However, methods for identifying cracks, based on the changes of dynamic properties of bridges and buildings, are not very well effective and practical. Moreover, depending on the size of the surface crack, a crack can be detected using traditional technique like

the visual inspection. However, it is not possible to visually identify cracks when the structure surface is covered, insulated or located in unreachable locations. To overcome these difficulties, numerical/computational techniques have been under development (Breysse *et al.*, 2008; Schabowicz, 2010) thus enabling quick decision-making process concerning the minimization or elimination of damages.

From the point of view of safety and economy, the detection of damages especially in bridges is an important issue. It is essential to perform periodic inspection to detect changes in the structural stability (Radzieński, Krawczuk and Palacz, 2011). Recent research on the technical literature shows that many damage identification algorithms were developed using dynamic characteristics, especially in the frequency domain (Doebling *et al.*, 1996). In general, these techniques use comparisons between the intact and damaged response of the structure. Techniques based on Wavelet Transforms can overcome this limitation. Such techniques have been applied over the years and have been presented satisfactory results (Wang and Deng, 1999; Law *et al.*, 2005; Ren and Sun, 2008; Liu, Li and Zhang, 2009; Mikami, Beskhyroun and Oshima, 2009; Palechor *et al.*, 2014).

The purpose of this report is presents applications of the roving mass technique associated to Wavelet transforms in damage identification and localization, in beam-like structures, using numerical and experimental data. The research works was developed at the Graduate Programs of Integrity of Engineering Materials and Structures and Civil Construction of University of Brasilia. The numerical analysis models damage beams by Timoshenko FE model with additional mass. And the experimental essay applies non-stationary forces signal to excite commercial profiles of steel beams simply supported (close to real situations).

Firstly, Section 2 presents a description of the roving mass technique and a dimensional analysis of principal parameters. Section 3 carries out a numerical analysis using Timoshenko FE model combined with wavelet transform. Finally, section 4 presents experimental results of a steel beam obtained in Vibration Laboratory of Dynamical Systems Group developed by Graduate Programs of Structures and Civil Construction and Integrity of Engineering Materials of University of Brasília.

2   Roving Masses Technique

Damage identification may be seen as an inverse problem of identification of a system whose input signals and output signals are known, but the geometry of the damage location and shape are unknown (Ticona Melo *et al.*, 2016). This means that the purpose of damage detection is to describe a damage in an existing structural model, based on output data obtained experimentally (dynamic response) from specific input signals. It is often desirable to detect irregularities or changes in structure response, considering properties that have been altered by the presence of the damage in the structure.

Studies of identification of damage in structures using an auxiliary mass have been done (Mermetas and Erol, 2001; Zhong and Oyadiji, 2008; Zhong, Oyadiji and Ding, 2008; Erwin Ulises Lopez Palechor *et al.*, 2018; Palechor, Bezerra, Morais, *et al.*, 2019; Santos *et al.*, 2019). This technique consists of the application of an additional mass along the length of structure to magnify the effect of the discontinuities.

In free vibration case, the Euler-Bernoulli beam's motion equation beams is described by follow expression,

$$EI\frac{\partial^4 u}{\partial x^4} + [\rho A + m_a \delta(x - L_d)]\frac{\partial^2 u}{\partial t^2} = 0, \tag{1}$$

where E and ρ are Young modulus and density, respectively, cross-sectional area A, beam length L, u is the transverse displacements (and acceleration $\ddot{u}$), and m_d is the damage mass.

To obtain the dimensionless of Euler-Bernoulli beam equation, we assume $u = \delta_u \bar{u}$, (beam static deflection δ_u), $x = L\bar{x}$ and $t = T\bar{t} = \bar{t}/f_n$ ($f_n = 1/T$ is the fundamental frequency) in which $\bar{u}$, $\bar{x}$, and $\bar{t}$ are dimensionless parameters.

$$\frac{4\pi^2}{\beta^4}\bar{u}^{IV} + \ddot{\bar{u}} + \frac{m_d}{\rho AL}\ddot{\bar{u}}\delta\left(\bar{x} - \frac{L_d}{L}\right) = 0, \tag{2}$$

where, the dynamic characteristic of beam is described by the parameters β (done by expression $2\pi f_n = (\beta^2/L^2)\sqrt{EI/\rho A}$) and function of boundary conditions), mass discontinuity m_d and its position L_d. For the present analysis, the damage beam is characterized by the presence of mass discontinuity to simulate an open crack, i.e., a rigidity discontinuity. Santos (2019; 2020) shows the correspondence between mass and rigidity discontinuity for small values.

Frequency-shift curve is the modal frequency of damage beam (with mass discontinuity for this analysis) as function of a roving mass along essayed beam. Zhong Oyadiji (2008) and Zhong Oyadiji and Ding (2008) shows the possibility to determine damage location in beam-like structures by discontinuity in curvature of frequency-shift for first frequencies. Palechor et al. (2014; 2018; 2019) use Discrete Wavelet Transform (DWT) to evidence discontinuity in frequency-shift curves with good results.

## 3 Numerical Damage Identification in Beam-like Structures with Roving Masses Technique

This work section presented a numerical study of additional mass spatial probing identification technique using DWT of frequency shift curves of damaged Timoshenko FE 2-nodes beam (Santos *et al.*, 2019; Santos, 2020). Simply supported and free-free beams was analyzed for two damage mass, ¼ and ½ of beam span. WDR index is proposed to analyze the magnitude of the damage.

Numerical analyses of an aluminum beam with geometric and material properties are presented in Table 1.

Table 1: Geometric and material properties of the aluminum beam.

Characteristics of the beam	
Mass [g]	385,33
Length [m]	395,00
Base of the cross-section [m]	19,00
Height of the cross-section [m]	19,00
Cross section area [mm²]	361,00
Moment of inertia [mm⁴]	$1,09.10^{-4}$
Modulus of elasticity [GPa]	66,66
Shear modulus [GPa]	24,18
Density [kg/m³]	2702,27
Poisson's ratio	0,33

Free-Free (F-F) and Supported-Supported (S-S) boundary conditions are studied. The damage was simulated as discontinuity mass positioned at half and a quarter span from left support, respectively, L/2 and L/4 (Figure 1).
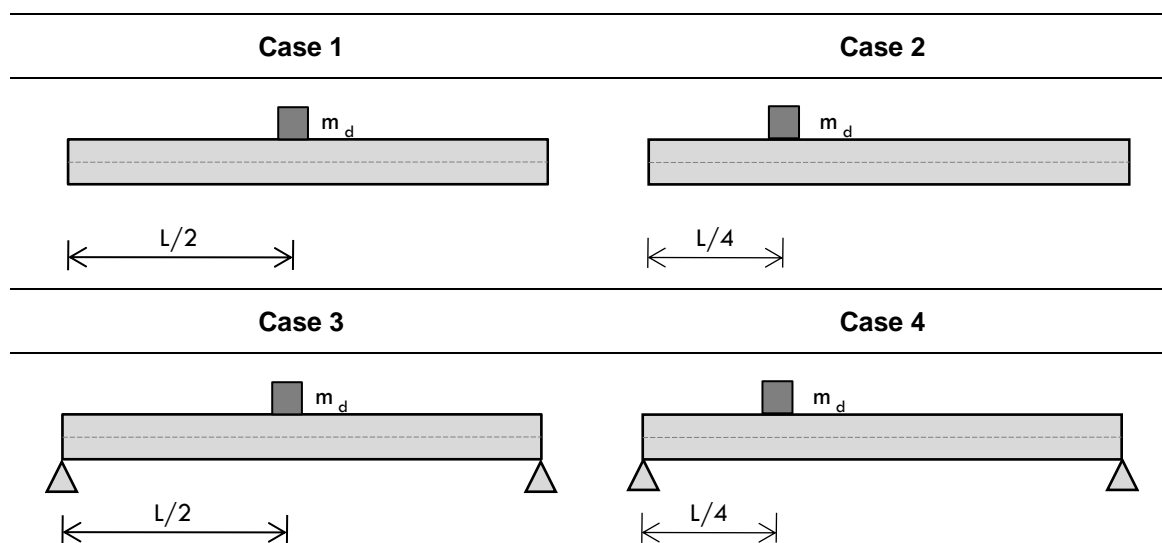
Figure 1: Beam cases with different boundary conditions and damage positions.

3.1   Frequency-Shift Curve

The frequency-shift technique was applied for three first modal frequencies for each case. Using a roving mass m_a of 2% of total beam mass m_t, the frequency-shift curve was used to determine a discontinuity mass m_d varied from 1% to 10% of m_t. Figure 2 and Figure 3 shows the frequency-shift curves for F-F and S-S beams, respectively, as function of discontinuity mass m_d. It was observed the influence of the structure's mode shape. But, also, it was observed minor variations in frequency-shift

curve when discontinuity mass is located at a nodal point (Figure 2b1, Figure 2a2 nd Figure 3b1).
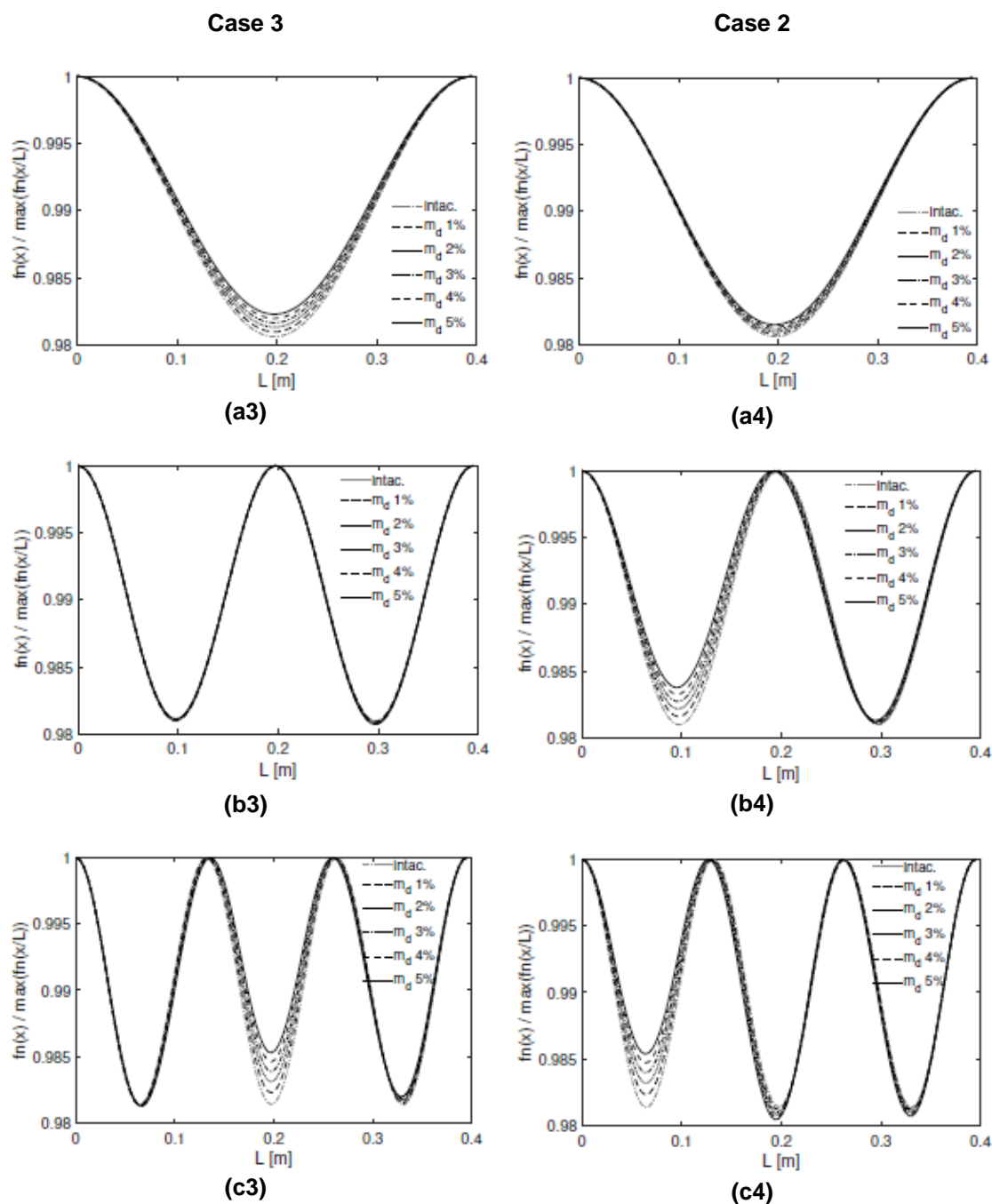
Case 1

Case 2

(a1)   **(a2)**

(b1)   **(b2)**

(c1)   **(c2)**
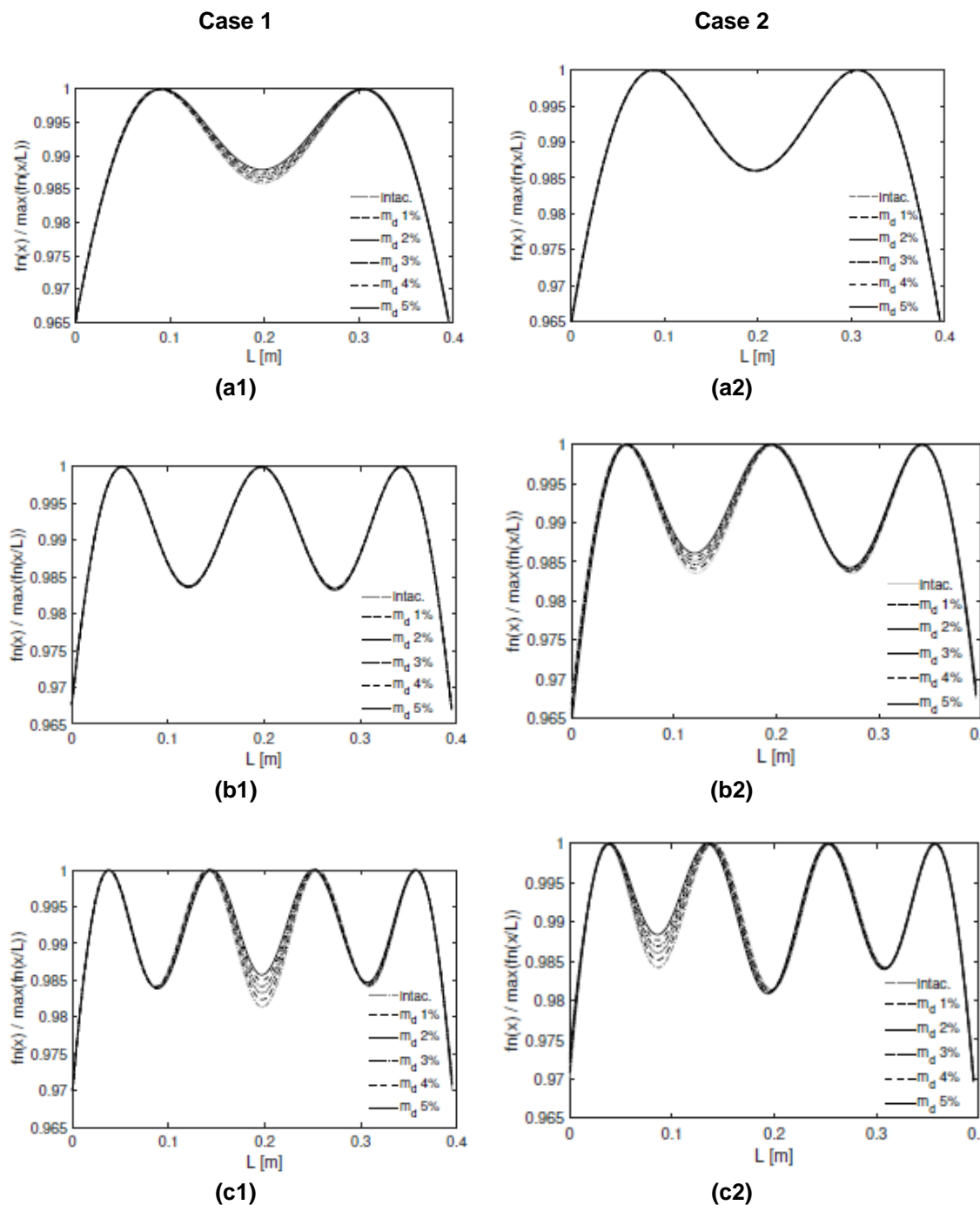
Figure 2: Frequency-shift $f_n(x/L)/$max ($f_n(x/L)$) function of m_a position in F-F beams (cases C1 and C)2: (a) first frequency, (b) second frequency and (c) third frequency.

Case 3   **Case 2**

(a3)   (a4)

(b3)   (b4)

(c3)   (c4)

Figure 3: Frequency-shift $f_n(x/L)$/max $(f_n(x/L))$ function of m_a position in S-S beams (cases C1 and C)2: (a) first frequency, (b) second frequency and (c) third frequency.

3.2   DWT of roving mass (m_a) and damage mass (m_d) relationship

For a discontinuity mass located at middle span of F-F (C1) and S-S (C3) beams, using the bior6.8 mother wavelet, the influence of the additional mass m_a on the frequency shift curve is studied. To define a useful metric, it is proposed wavelet damage ratio (WDR) that relate damage level by the ratio between damage signal S_d and base signal S_b (Figure 4).
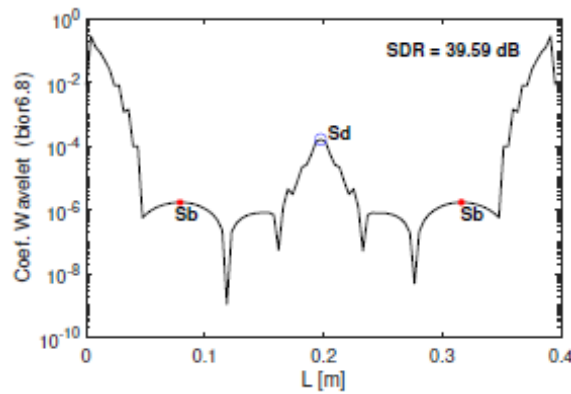
Figure 4: WDR index determination using the wavelet functions bior6.8.

The WDR index is expressed by equation,

$$WDR[dB] = 20log_{10}\left(\frac{Sd}{Sb}\right), \tag{3}$$

in which S_d and S_b corresponds, respectively, to the maximum absolute value of DWT coefficient at damage position and without singularities positions, as shown in Figure 4. Figure   and Figure 6 present frequency-shift curve for 1 and 10% damage relative to roving masses of 1, 2 and 5% additional mass.
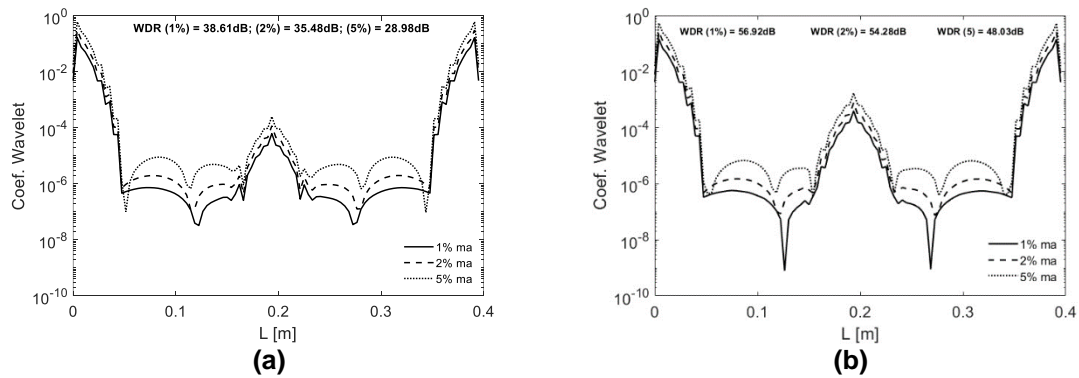

Figure 5: Frequency-shift curve of C1 beam as function of roving mass m_a for damage mass m_d of 1% (a) and 10% (b).
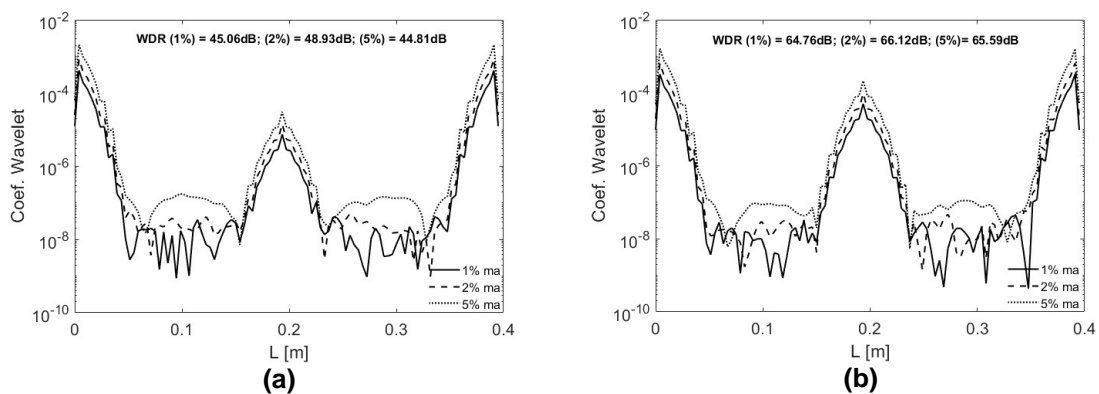
Figure 6: Frequency-shift curve of C1 beam as function of roving mass m_a for damage mass m_d of 1% (a) and 10% (b).

Figure show WDR index for additional mass of 5% with a slight tendency to saturation. Figure 6 present the same tendency in this regard. Increasing of roving mass does not improve the damage perception, i.e., an increase in WDR.

3.3   Final Comments on the Numerical Example

The frequency-shift curve makes possible detect and locate a damage using only damaged response, eliminating comparison to an intact response. The proposition of WDR index as a metric to reduce frequency-shift curve to a value need more analysis. The damage perception was not increased with more roving mass. Palechor (2013) have the same impression in his experimental study. But it is necessary more numerical and experimental observation about this question.

4   Experimental Damage Identification in Beam-like Structures with Roving Masses Technique

This work presents the application of an identification methodology based on the analysis of the dynamic properties of simply supported steel beams. Beams here are submitted to the action of additional masses that can generate progressive changes of the natural frequencies (Mermetas and Erol, 2001; E. U.L. Palechor *et al.*, 2018). The change in the structural stiffness due to the existence of damage in the beam may not be so evident. Therefore, in this research, the Wavelet Transform is used to help in the process of locating possible stiffness changes due to damages (Rizos, Aspragathos and Dimarogonas, 1990; Mermetas and Erol, 2001; Kotambkar, 2014; Khoa and Quang, 2016). This research also presents experimental tests results on steel beams with simulated damages. The experimental tests were carried out in the Laboratory of Vibrations of the Department of Mechanical Engineering in the University of Brasília. Even though the experiments were conducted within the laboratory, the size of the beams tested corresponds to small commercialized steel beams available in the market.

The additional mass placed on the beams were small steel plates fixed with braces and bolts. The assembly of the added masses is schematically shown in Figure 7.
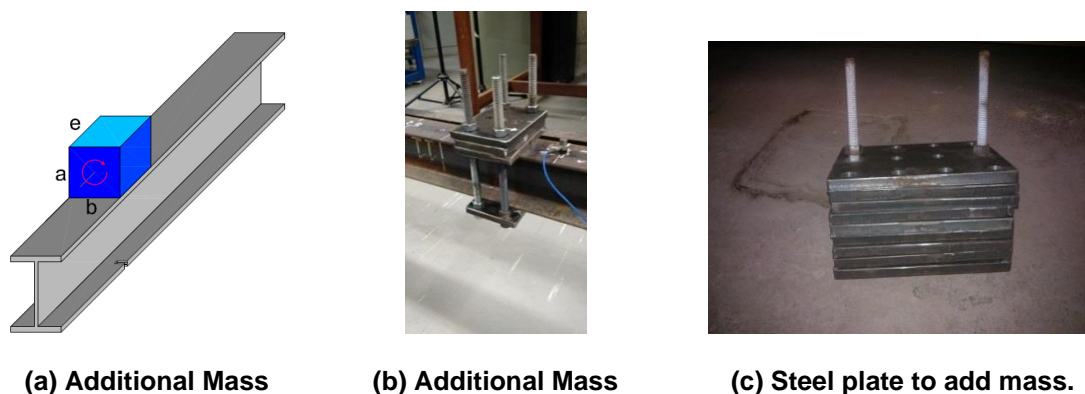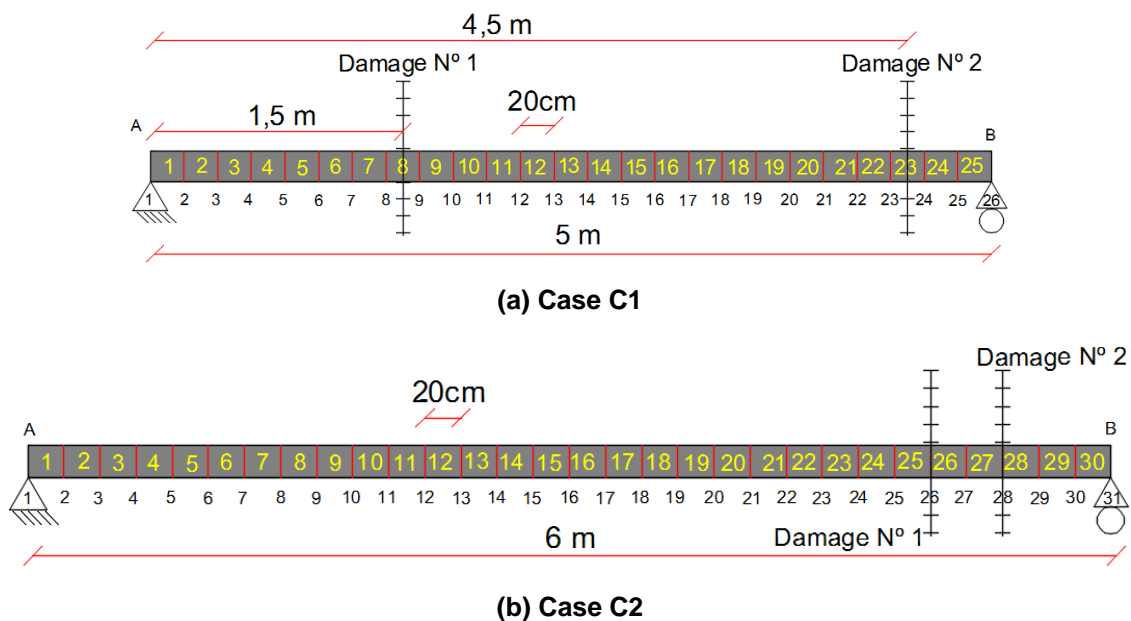

(a) Additional Mass   (b) Additional Mass   (c) Steel plate to add mass.

Figure 7: Additional mass on the beam.

Figure 8 show schematic representation for location and characteristics of induced damage on essayed beams. The additional masses (M) add together 3.366 kg for Case C1 and 24.718 kg for Case C2.

(a) Case C1

(b) Case C2

Figure 8: Schematic representation of Damage Position for Cases 1 (a) and 2 (b)

Figure 9 shows details of the test scheme assemblage the steel beams in the Laboratory of Vibration and Dynamics of Systems of the University of Brasília.
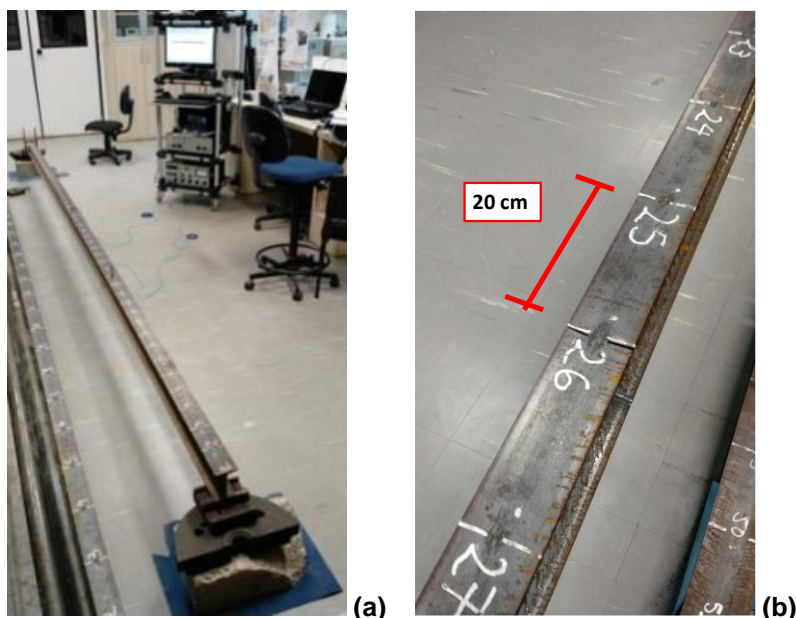

Figure 9: Experimental setup of simply support beam: (a) general view of essayed beam, and (b) detail of measurement points (discretization of 20cm).

To ensure simple support (Figure 10a), two plane plates and a roller were used to allow displacement only in the x direction. For the hinged support (Figure 10b), two

grooved plates with a roller were designed to restrict the translation in all direction, permitting only rotation.


(a) Left Support.   (b) Right support.
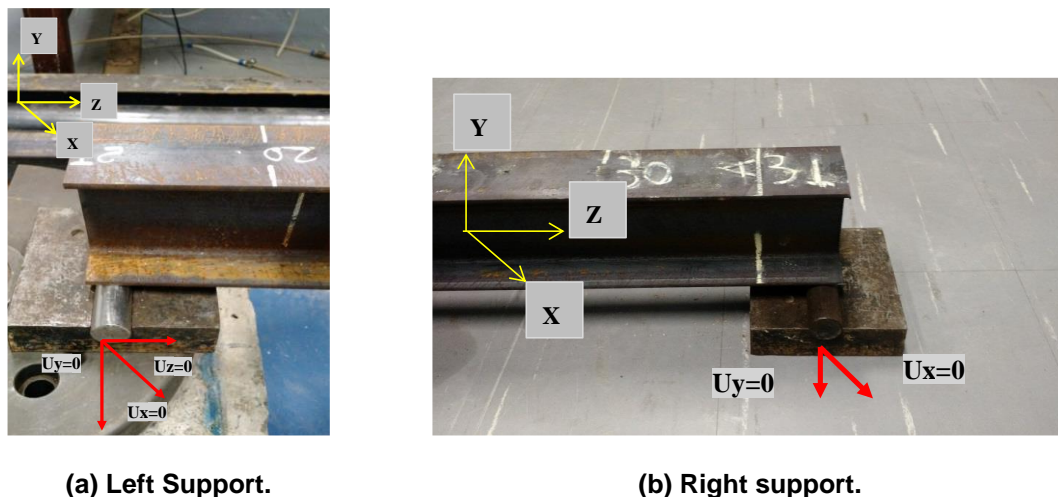
Figure 10: Detail for simple support at steel beam ends.

In order to carry out the dynamic tests the following tools are used accelerometers PCB 352C34 and PCB352C33, modal hammer PCB 086C0 (with steel tip) and NI cDAQ + NI 9187 + LabView software as data acquisition.

The experimental procedure follows the steps below for each roving mass position:

- **Step 1**: the experimental specimens were subjected to impact load (modal hammer) applied in middle span (Figure 11).
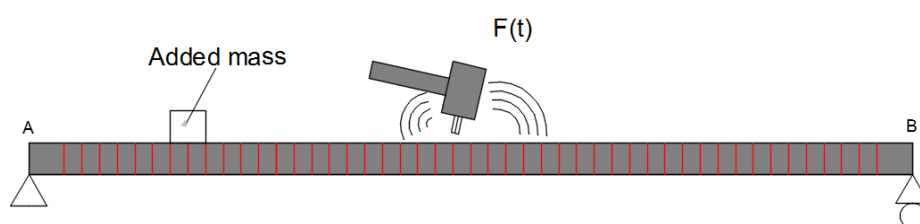
Figure 11: Impact modal analysis for beam essayed with roving mass.

- **Step 2**: Force and acceleration dynamic signals was acquired by NI+Labview signal conditioner (Figure 12). This modal impact test was carried out four times. Exponential ad force windows were applied to acceleration and force signal, respectively, to reduce leakage effect. Force and acceleration temporal signals were saved for posterior treatment.
- **Step 3**: Estimation of inertance response of force and acceleration dynamic signals by a Matlab script. First modal frequencies were accurately identified performing a weighted average of values around a peak detected in spectrum response.
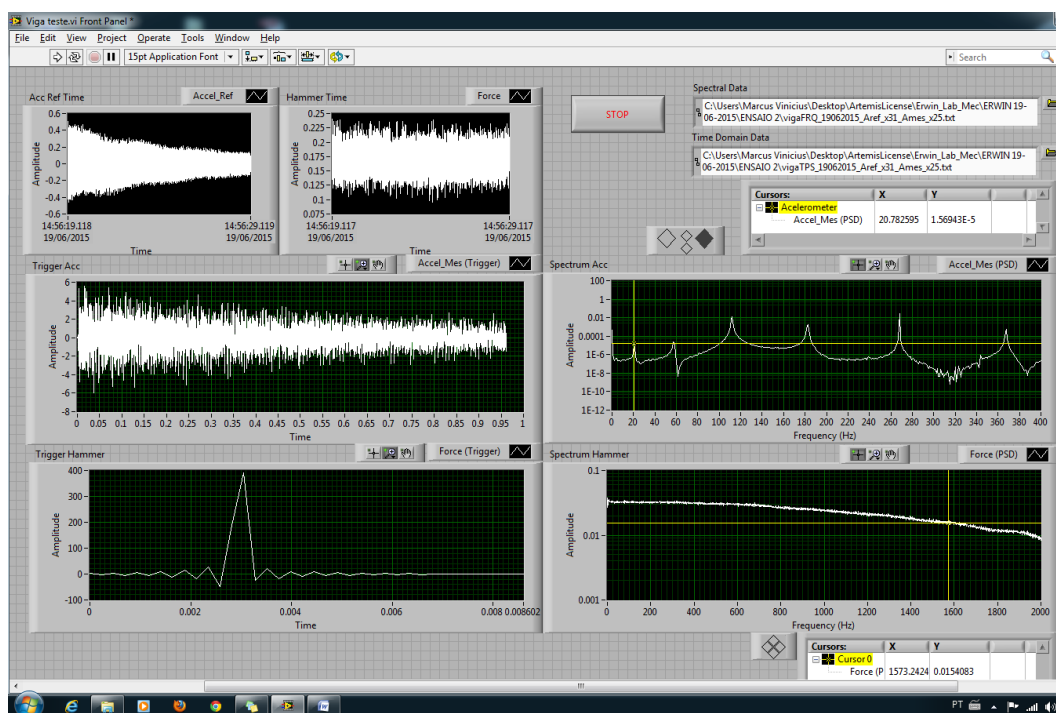
Figure 12: LabView control panel.

The frequency resolution is very important to determine frequency variations due to additional mass location along essayed beam. Thus, several parameters are necessary configure to be able the analysis of dynamic signals: analyzed data size (N), acquisition rate (Δt) and sampling frequency (Fs). The best results were obtained with the following parameters: (a) $Fs = 1653\ Hz$, (b) $\Delta t = 0.000605\ s$, and (c) $N = 16384\ (2^{14})$.

Once inertance FRF estimated (Figure 13), the peaks correspond to firsts modal frequencies are identified for each roving mass position. After the peak identification, the estimated modal frequency $f_{n,est}$ is performed a weighted average of frequencies around the lobe of spectrum frequency (National Instruments, 2009).

$$f_{n,est} = \frac{\sum_{i=j-m}^{j+m} Power(i)\ i\ \Delta f}{\sum_{i=j-m}^{j+m} Power(i)} \tag{4}$$

where, j is array position of frequency peak and $Power\ (i)$ represents the amplitude value of FRF spectral line.

Once the corrected frequencies are obtained, these values are plotted to compound the frequency-shift curve. The discretization of essayed beam for roving mass position was done by 20 cm. For C1 and C2 beams (5m and 6m long), respectively, there are 26 and 31 positions for the roving mass. The frequency-shift curve are interpolated to obtain a vector with a larger number of data and thus calculate the wavelet coefficients as described in Palechor *et al.* (Palechor, 2013; Palechor, Bezerra, Morais, *et al.*, 2019; Palechor *et al.*, 2022).
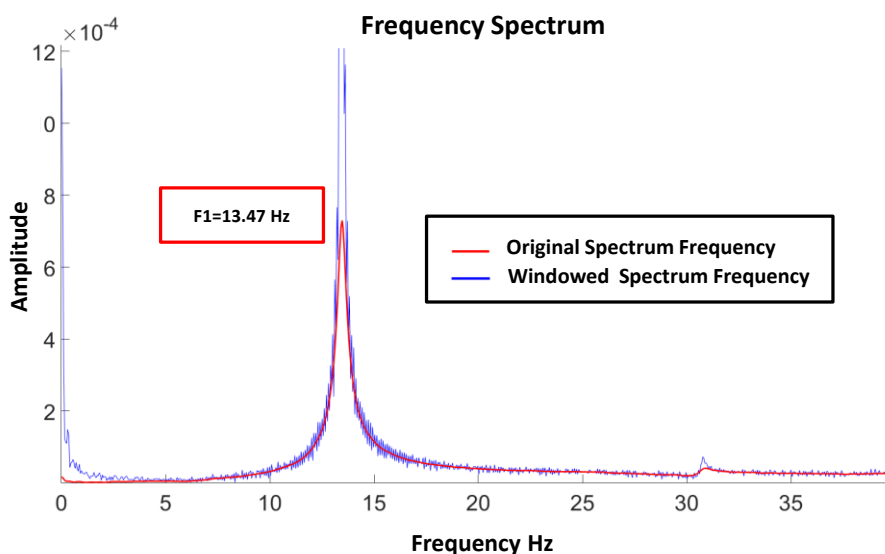
Figure 13: Example of inertance FRF spectrum for essayed beam with a roving mass.

In the frequency domain, the peaks corresponding to the first natural frequency of the structure are identified. Figure 13 shows an example inertance FRF spectrum with/without application of the exponential window. Noise reduction and signal stabilization are clearly visible due to the use of the exponential window.

4.1   Experimental Results of Case C1

Figure 14 represents the frequency-shift curve for first frequency of case C1 beam. This graph corresponds to first frequency of C1 beam as function of roving mass position along its 26 measured nodes. The added mass used was 3.266 kg, positioned on each node.
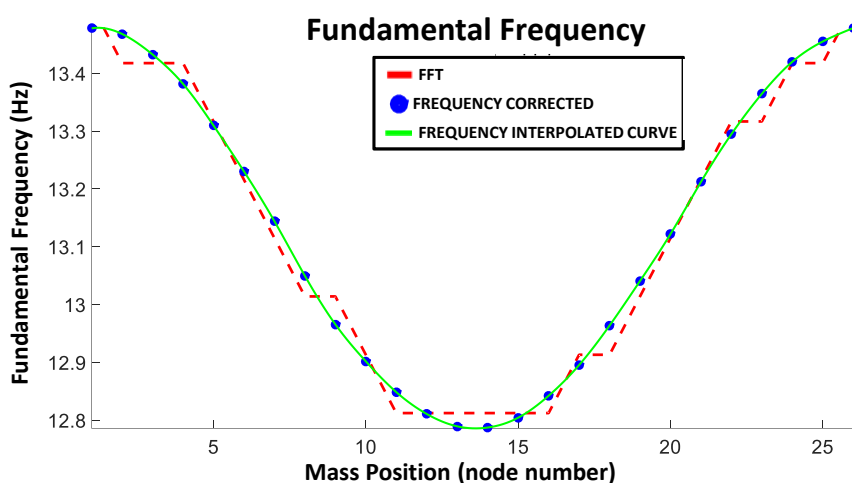

Figure 14: Frequency-shift curve for first frequency of beam C1.

In Figure 14, the dashed line represents the FRF peak frequencies. The dotted line is estimated frequency using Equation (4). And the solid line is the cubic spline

interpolation of estimated frequency (Erwin Ulises Lopez Palechor *et al.*, 2018; Palechor, Bezerra, Morais, *et al.*, 2019; Palechor *et al.*, 2022). This numerical interpolation obtains best fits signals to damage location.

Figure 15 are the DWT of frequency-shift curve using four mother wavelet functions (sym6, rbio2.6, db5 and bior6.8). It can be observed a group of spikes between nodes 8 and 9 and between nodes 23 and 24 which matches to damage located at 1.5m and 4.5m, respectively. This last one shows less prominent, but still noticeable. Such peaks are big enough to be seen compared with the other peaks exists.
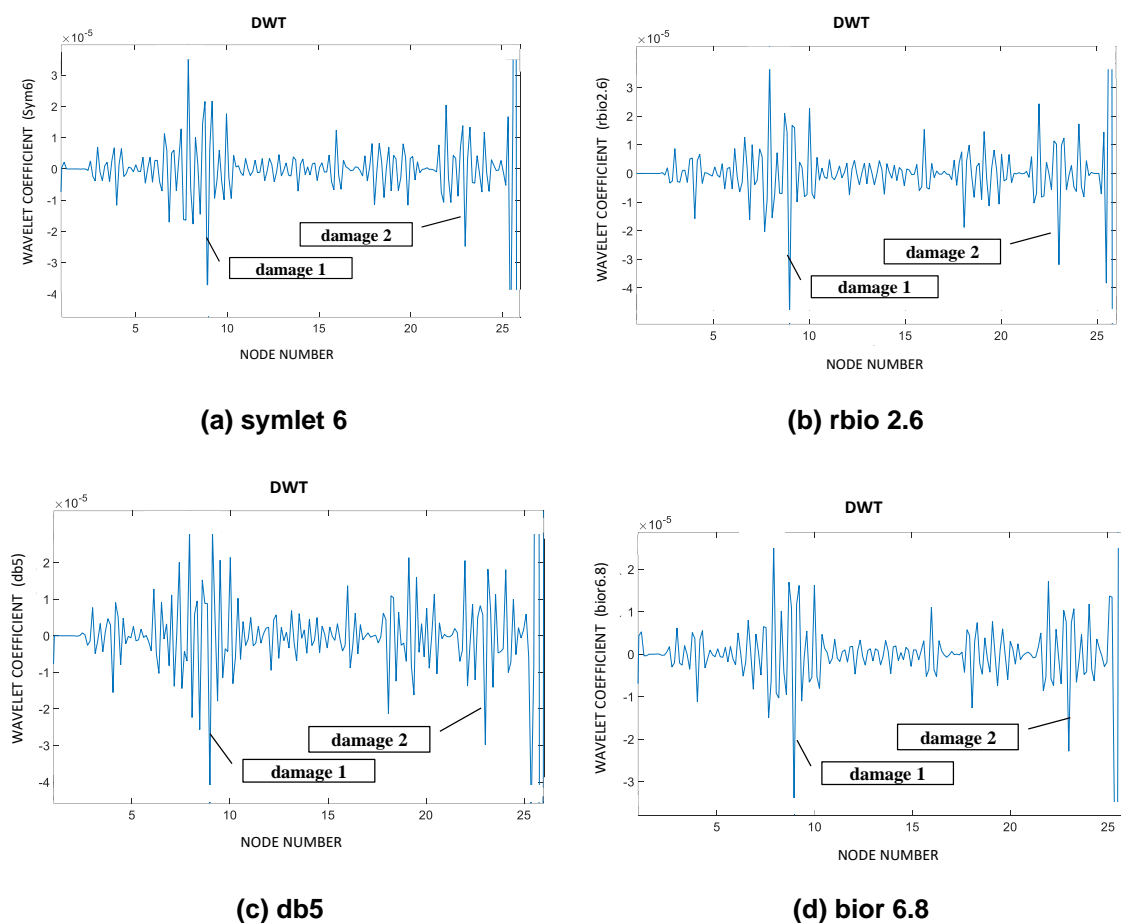

(a) symlet 6

(b) rbio 2.6

(c) db5

(d) bior 6.8

Figure 15: DWT first frequency using (a) symlet 6, (b) rbio2.6, (c) db5 and (d) bior 6.8 mother wavelets.

4.2   Experimental Results of Case C2

Figure 16 represents frequency-shift curve for first frequency of case C2 beam. This graph corresponds to first frequency of C2 beam as function of roving mass position along its 31 measured nodes. The roving mass used was 24.718 kg, positioned on each node.
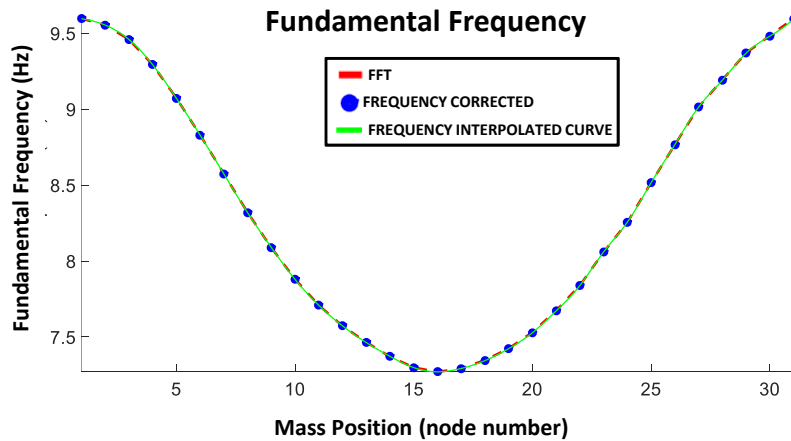
Figure 16: Frequency-shift curve for first frequency of beam C2.

Figure 17 presents the DWT of frequency-shift curve using four mother wavelet functions (sym6, rbio2.6, db5 and bior6.8). It can be observed a group of spikes between nodes 25 and 27 and between nodes 28 and 29 which matches to damages induced. The techniques of signal interpolation with the cubic spline in the frequency domain and the method of main lobe correction showed good results.
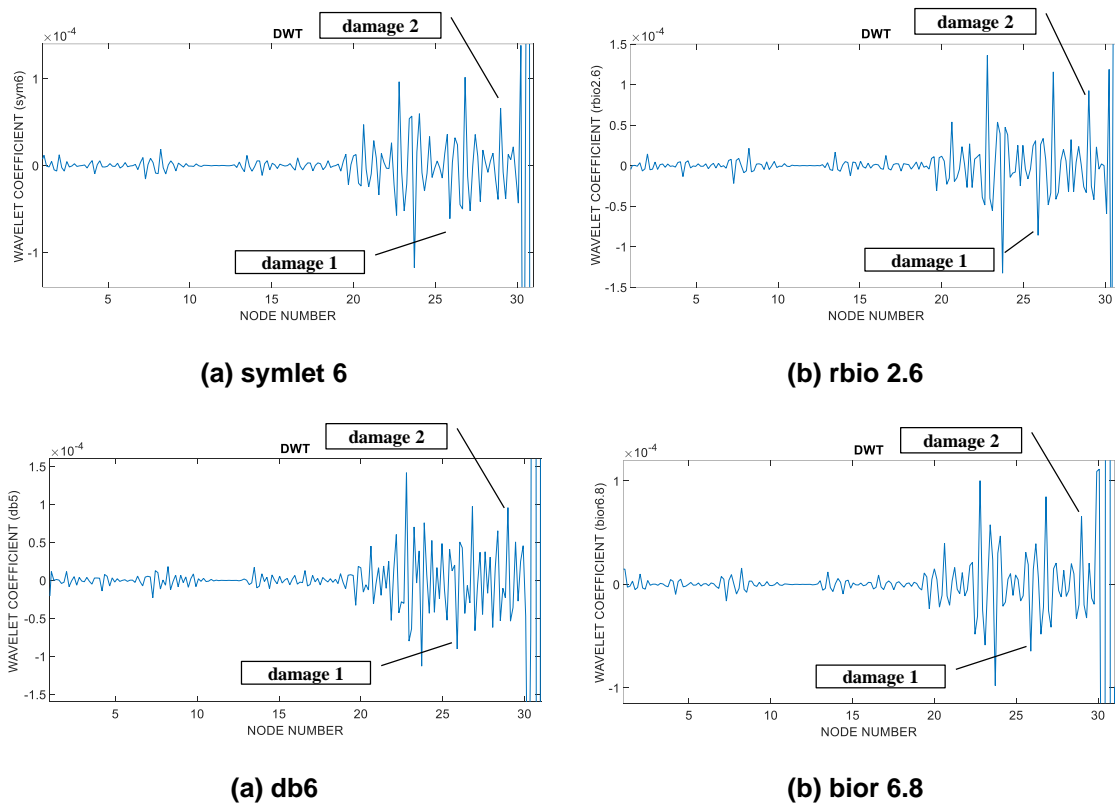

(a) symlet 6

(b) rbio 2.6

(a) db6

(b) bior 6.8

Figure 17: DWT first frequency using (a) symlet 6, (b) rbio2.6,
(c) db5 and (d) bior 6.8 mother wavelets.

4.3   Final Comments on the Experimental Example

This section presented experimental results using roving mass technique to locate damages in essayed beams with simulated open cracks. Measuring of fundamental frequency of essayed beams with an added mass positioned along it. Two cases were analyzed: case C1 and C2, respectively, with 5m and 6m. Both beams are commercial steel I-section. The damage is responsible for pronounced peaks clusters on DWT coefficients of frequency-shift curve.

The experimental results illustrate the roving mass methodology for damage identification based only on structure damaged response. According to Rytter classification (Palechor, Bezerra, de Morais, *et al.*, 2019; Silva *et al.*, 2019), this method has level II, i.e., determine damage location but not damage quantification. The amplitudes of the wavelet coefficients can vary even if the same beam and damage are used in the same test since the signal processing is affected by the noise signal present, but the coefficients wavelets do not stop generating larger amplitudes in the regions proximate to the damage location.

5   Conclusions

This chapter presents applications of a non-destructive method called roving mass technique. This technique based on the frequencies shift using an additional roving mass presented coherent results for the two cases that were investigated (free-free and simply supported beam). This response-only technique, associated to Wavelet transforms, carry out damage localization in beam-like structures using numerical and experimental data. It was possible to locate the damage presence due to a discontinuity in modal frequency curve along beam. Also, it is possible to observe that the bigger the damage, the bigger this variation. The research works is developed at the Graduate Programs of Integrity of Engineering Materials and Structures and Civil Construction of University of Brasília.

Different mother wavelet functions (db5, coif3, sym6, and bior6.8) were analyzed with a better signal to noise ratio.

Finally, the proposed methodology has shown promise as it only needs to analyze the dynamic data of the damaged structure to successfully localize the damage, unlike other techniques that require the intact and damaged response.

References

Aktan, A. E. *et al.* (1997) 'Structural Identification for Condition Assessment: Experimental Arts', *Journal of Structural Engineering*, 123(12), pp. 1674–1684. doi: 10.1061/(ASCE)0733-9445(1997)123:12(1674).

Breysse, D. *et al.* (2008) 'How to combine several non-destructive techniques for a better assessment of concrete structures', 38, pp. 783–793. doi: 10.1016/j.cemconres.2008.01.016.

Doebling, S. W. *et al.* (1996) *Damage identification and health monitoring of structural and mechanical systems from changes in their vibration characteristics.* California: Los Alamos National Laboratory.

Khoa, N. V. and Quang, N. Van (2016) 'Free vibration of a cracked double-beam

carrying a concentrated mass', *Vietnam Journal of Mechanics*. Publishing House for Science and Technology, Vietnam Academy of Science and Technology (Publications), 38(4), pp. 279–293. doi: 10.15625/0866-7136/7118.

Kotambkar, M. S. (2014) 'Mass Loading Effect on Natural Frequency of Cracked Beam in Free-Free Condition', *International Journal of Engineering Research & Technology*. IJERT-International Journal of Engineering Research & Technology, 3(9). doi: 10.17577/IJERTV3IS090113.

Law, S. S. *et al.* (2005) 'Structural damage detection from wavelet packet sensitivity', *Engineering Structures*. Elsevier, 27(9), pp. 1339–1348. doi: 10.1016/J.ENGSTRUCT.2005.03.014.

Liu, Y., Li, Z. and Zhang, W. (2009) 'Crack detection of fibre reinforced composite beams based on continuous wavelet transform', *https://doi.org/10.1080/10589750902744992*. Taylor & Francis Group , 25(1), pp. 25–44. doi: 10.1080/10589750902744992.

Mermetas, V. and Erol, H. (2001) 'Effect of Mass Attachment on the Free Vibration', in *Proceedings of 8th International Congress on Sound and Vibration (ICSV 2001)*, pp. 2803–2810.

Mikami, S., Beskhyroun, S. and Oshima, T. (2009) 'Wavelet packet based damage detection in beam-like structures without baseline modal parameters', *http://dx.doi.org/10.1080/15732470802334795*. Taylor & Francis , 7(3), pp. 211–227. doi: 10.1080/15732470802334795.

National Instruments (2009) *The Fundamentals of FFT-Based Signal Analysis and Measurement in LabVIEW and LabWindows/CVI - National Instruments*.

Palechor, E. U. L. (2013) *Damage Identification in Steel Beams by Wavelets and Numerical/Experimental Signal (por. Identificação de Danos em Vigas Metálicas Utilizando Wavelets e Dados Numéricos e Experimentais)*. Universidade de Brasília. Available at: https://repositorio.unb.br/handle/10482/14814.

Palechor, E. U. L. *et al.* (2014) 'Damage Identification in Beams Using Experimental Data', *Key Engineering Materials*, 607, pp. 21–29. doi: 10.4028/www.scientific.net/KEM.607.21.

Palechor, E. U.L. *et al.* (2018) 'Dynamic Analysis of a Beam with Additional Auxiliary Mass Spatial Via Spectral Element Method', *Springer Proceedings in Mathematics and Statistics*. Springer New York LLC, 249, pp. 279–289. doi: 10.1007/978-3-319-96601-4_25/COVER/.

Palechor, Erwin Ulises Lopez *et al.* (2018) 'Identificação De Danos Em Vigas Metálicas Utilizando Massas Itinerantes Adicionais, Análise Experimental.', *Revista Sul-americana de Engenharia Estrutural*, 15(3). doi: 10.5335/rsaee.v15i3.7886.

Palechor, E. U. L., Bezerra, L. M., Morais, M. V. G. de, *et al.* (2019) 'Damage identification in beams using additional rove mass and wavelet transform', *Frattura ed Integrità Strutturale*, 13(49), pp. 614–629. doi: 10.3221/IGF-ESIS.49.56.

Palechor, E. U. L., Bezerra, L. M., de Morais, M. V., *et al.* (2019) 'Damage identification in beams using additional rove mass and wavelet transform', *Frattura ed Integrità Strutturale*, 13(49), pp. 614–629. doi: 10.3221/IGF-ESIS.49.56.

Palechor, E. U. L. *et al.* (2022) 'Fundamental Concepts on Wavelet Transforms', in.

Radzieński, M., Krawczuk, M. and Palacz, M. (2011) 'Improvement of damage detection methods based on experimental modal parameters', *Mechanical Systems and Signal Processing*, 25(6), pp. 2169–2190. doi: 10.1016/j.ymssp.2011.01.007.

Ren, W. X. and Sun, Z. S. (2008) 'Structural damage identification by using wavelet entropy', *Engineering Structures*. Elsevier, 30(10), pp. 2840–2849. doi: 10.1016/J.ENGSTRUCT.2008.03.013.

Rizos, P. F., Aspragathos, N. and Dimarogonas, A. D. (1990) 'Identification of crack location and magnitude in a cantilever beam from the vibration modes', *Journal of Sound and Vibration*. Academic Press, 138(3), pp. 381–388. doi: 10.1016/0022-460X(90)90593-O.

Santos, J. C. *et al.* (2019) 'FREQUENCY-BASED DAMAGE DETECTION IN BEAMS USING AN ADDITIONAL ROVING MASS', in UFU (ed.) *Proceedings of the 25th International Congress of Mechanical Engineering*. Uberlândia: ABCM. doi: 10.26678/ABCM.COBEM2019.COB2019-1103.

Santos, J. C. (2020) *Detecção de danos em vigas Timoshenko utilizando técnicas de variação de frequência por wavelet*. University of Brasilia. Available at: https://repositorio.unb.br/handle/10482/39090.

Schabowicz, K. (2010) 'State-of-the-art non-destructive methods for diagnostic testing of building structures – anticipated development trends', X(3), pp. 8–9. doi: 10.1016/S1644-9665(12)60133-2.

Silva, R. S. Y. R. C. *et al.* (2019) 'Damage detection in a reinforced concrete bridge applying wavelet transform in experimental and numerical data', *Frattura ed Integrità Strutturale*, 13(48), pp. 693–705. doi: 10.3221/IGF-ESIS.48.65.

Ticona Melo, L. R. *et al.* (2016) 'Identification of Modal Parameters in a Scale Model for a Railway Bridge', *http://dx.doi.org/10.1142/S0219455415500595*. World Scientific Publishing Company , 16(9). doi: 10.1142/S0219455415500595.

Wang, Q. and Deng, X. (1999) 'Damage detection with spatial wavelets', *International Journal of Solids and Structures*. Pergamon, 36(23), pp. 3443–3468. doi: 10.1016/S0020-7683(98)00152-8.

Zhong, S. and Oyadiji, S. O. (2008) 'Identification of cracks in beams with auxiliary mass spatial probing by stationary wavelet transform', *Journal of Vibration and Acoustics, Transactions of the ASME*. doi: 10.1115/1.2891242.

Zhong, S., Oyadiji, S. O. and Ding, K. (2008) 'Response-only method for damage detection of beam-like structures using high accuracy frequencies with auxiliary mass spatial probing', *Journal of Sound and Vibration*, 311(3–5), pp. 1075–1099. doi: 10.1016/j.jsv.2007.10.004.

Chapter 23

Local Mesh Free Methods in Linear Elasticity and Fracture Mechanics

Local Mesh Free Methods in Linear Elasticity and Fracture Mechanics

Tiago Oliveira[1], Wilber Vélez[1] and Artur Portela[2*]

[1]Post-Graduate Program - Structural Engineering and Construction, University of Brasilia, Brazil. E-mail: tiago.antuney@gmail.com and wilbervelez@hotmail.com
[2]Post-Graduate Program - Structural Engineering and Construction, University of Brasilia, Brazil. E-mail: a3portela@gmail.com
[*]Corresponding author

Abstract

This chapter presents the most recent developments on mesh free numerical methods at the Department of Civil Engineering and Environment of the University of Brasília. Therefore, the concern of this chapter is a local mesh free method for solving linear elastic and fracture mechanics two-dimensional problems. For a nodal discretization of the problem domain, based in the work theorem from the theory of structures, the global system of equilibrium equations is constructed using a node-by-node process, performed in the local domain of each node. The reduced numerical integration is implemented to improves the model accuracy. Both regular and irregular nodal distributions can be considered, which makes it a reliable model. Local mesh free numerical methods depends on two arbitrary parameters for the analysis: the size of the compact support, which control the accuracy; and the local domain of integration, which control the efficiency. Both parameters are automatically defined by means of a multi-objective optimization process, based on genetic algorithms and symbiotic organism search algorithm, which makes it a robust model. Linear elastic fracture mechanics applications of local mesh free are performed through the singularity subtraction technique (SST), which regularizes the elastic field, before the numerical solution, thus introducing the stress intensity factors (SIF) as additional primary unknowns of the problem. Hence, the numerical model performs a direct computation of the SIF and does not require a refined discretization to obtain accurate results which, therefore, is an efficient model strategy. On all this cases, benchmark problems were solved for an assessment of the accuracy and efficiency of these techniques.

Keywords: Meshfree; Work theorem; Multi-objective optimization; Singularity Subtraction Technique.

1 Introduction

This section provides a brief overview on mesh free numerical methods over the recent years. Several widely used numerical methods are outlined in a concise manner and should be a good way to introduce the reader to those methods.

Mesh free, or meshless, have some advantages when compared to mesh-based methods, such as the Finite Element Method (FEM) and the Boundary Element Method (BEM), see Basu et al. [2003]. The essential feature of these methods is that they perform the discretization of the problem domain and boundaries with a set of scattered field nodes that do not require any mesh for the approximation of the field variables. In general, their formulation is based in the weighted-residual method, see Finalyson [1972].

Some of these meshless methods are based on a weighted-residual weak-form formulation. After discretization, the weak form is used to derive a system of algebraic equations through a process of numerical integration using sets of background cells, globally or locally constructed in the domain of the problem. Research on meshfree methods, based on a weighted-residual weak-form formulation, significantly increased after the publication of the Diffuse Element Method (DEM), introduced by Nayroles et al. [1992]. The Reproducing Kernel Particle Method (RKPM), presented by Liu et al. [1995], and the Element-free Galerkin (EFG) method, presented by Belytschko et al. [1994b], were the first weak-form meshless methods applied in solid mechanics.

All these weak-form meshless methods rely on background cells for the integration of the weighted-residual weak form over the global domain, in the process of the generation of the system of algebraic equations and therefore, they are not truly meshless methods.

In order to overcome the use of a global integration background mesh, a class of mesh-free methods based on local weighted-residual weak forms, such as the Meshless Local Petrov–Galerkin (MLPG) method, presented by Atluri and Zhu [1998] and also by Atluri and Shen [2002]; the Meshless Local Boundary Integral Equation (MLBIE) method, presented by Zhu et al. [1998]; the Local Point Interpolation Method (LPIM), presented by Liu and Gu [2001], and the Local Radial Point Interpolation Method (LRPIM) presented by Liu et al. [2002], have been developed. Among them, the most popular of these methods is the MLPG, based on a moving least-squares (MLS) approximation. Later, the MLPG was implemented with the Finite Volume Method (FVM), as presented by Atluri et al. [2004], which improved the efficiency of the previous method.

The main difference of the MLPG method to other global meshless methods, such as EFG or RKPM, is that local weak forms are used for integration on overlapping regular-shaped local subdomains, instead of global weak forms and consequently the method does not require the use of a background global mesh, but only a background local grid which usually has a simple shape.

One of the issues faced by many numerical methods is solution instability when reduced integration is considered. In FEM, elements with a reduced integration are commonly employed because they are computationally efficient and avoid locking of fully integrated elements. But the main drawback is that these elements are susceptible to spurious singular modes, named as hourglass modes, which are zero-energy modes in which the element can deform without an associated increase of the internal energy. Stabilization techniques are usually employed to prevent these undesired effects, as presented by Zienkiewicz and Taylor [1983] and Bathe [2014].

This is also an issue faced by many mesh free methods, resulting in well known unstable hourglass deformation and zero-energy modes, such as the EFG, as reported by Beissel and Belytschko [1996], and the RKPM, as reported by Belytschko et al. [2000]. For local mesh free methods, the nodal integration was considered to improve computational efficiency, leading to unstable performance during the integration and formation of the stiffness matrix. Since each domain of integration is associated with just one integration point, which is the node, the integration of higher order functions inevitably causes fatal instabilities. In order to overcome these instabilities that are present in direct nodal integration, Taylor series expansions have been used, to serve as stabilization terms, as presented by Liu et al. [1985] for FEM, and by Liu et al. [1996] and Liu et al. [2007] for mesh free methods. While stable, the main problem of this stabilization technique is that it requires the computation of high order derivatives, nevertheless.

The mesh free discretization parameters, the compact support size and the local domain size,

are paramount and greatly affect the efficiency of a mesh free analysis. Most mesh free methods and author define both parameters arbitrarily depending on the nodal distribution, later studied by Moussaoui and Bouziane [2013] for the MLPG. Heuristically defined discretization parameters are not optimal and in most cases, inefficient.

Later, optimization attempts were carried out by Baradaran and Mahmoodabadi [2009] for two dimensional heat conduction problems, by Bagheri et al. [2011] for three dimensional elastostatic problems, and by Ebrahimnejad et al. [2015] for MLPG-FVM with adaptive refinement technique; all of them with Genectic Algorithm (GA). Even though successful, their attempts were time consuming and bounded to the analytical solution, which limits their usefulness.

In linear elastic fracture mechanics, the stress field becomes infinite at the crack tip, as presented by Brahtz [1933] and Williams [1952], becoming a source of singularity in numerical modeling. In order to overcome this difficulty, different ways have been used to model crack discontinuities.

In early attempts, Carpinteri et al. [2003] used the EFG considering a virtual extension of the crack in the tangent direction at the crack tip, meanwhile Wen and Aliabadi [2007] and Fleming et al. [1997] consider enriched basis/weight functions to mathematically capture jumps across crack displacement fields. More recently, Nguyen et al. [2020] used the mesh free particle method for thermal-mechanical crack growth analysis and Qingbo et al. [2021] used LRPIM to model shear crack propagation, both with enriched functions. The main drawback of this modeling strategy is that a limitation of the enrichment area must be considered in the presence of a densely distribution of cracks or crack tips too close to the boundaries. Different approaches were attempted to overcome this drawback. Rabczuk and Belytschko [2007] presented a method without the representation of the crack topology, Bordas et al. [2008] performed the analysis without near-tip enrichment, with extrinsic discontinuous enrichment; and Liu et al. [2004] presented a method with crack-tip specific enrichment functions used to simulate failure.

To avoid representing the singularity entirely, Symm [1963] subtracted the singularity from the numerical model, introducing the Singularity Subtraction Technique (SST). The method was used by Xanthis et al. [1981] to solve anti-plane problems and by Aliabadi et al. [1987] to solve crack problems with the Boundary Element Method (BEM).

2   Moving Least Square (MLS) Approximation

MLS approximation, schematically represented in Figure 1 for one-dimensional approximation,
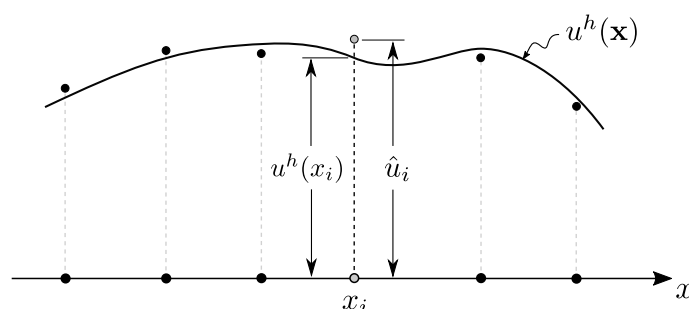
Figure 1: Schematic representation of the MLS approximation in one dimension.

is based on three components: a weight function of compact support associated with each node, a complete set of polynomial basis functions and a set of coefficients that are function of the space coordinates, as presented by Atluri and Zhu [1998]. In the following, the local mesh free method uses the basic MLS mesh-free terminology presented by Atluri and Zhu [2000].

Consider the domain of a body Ω with boundary Γ and let $N = \{\mathbf{x}_1, \mathbf{x}_2, ..., \mathbf{x}_N\} \in \Omega$ be a set of scattered nodal points that represents a mesh free discretization. It can be seen that some of them are located on the boundary Γ, as represented in Figure 2. The distribution of nodes in Ω and Γ is represented by $\mathbf{x}_i$, while Ω_s, represented as Ω_P, Ω_Q and Ω_R, is the local compact support of a node $\mathbf{x}_i$, represented as $\mathbf{x}_P$, $\mathbf{x}_Q$ and $\mathbf{x}_R$. $\Omega_{\mathbf{x}}$ is the domain of definition of a sampling point $\mathbf{x}$ and Ω_q is the local weak-form domain or quadrature domain of a node $\mathbf{x}_i$.
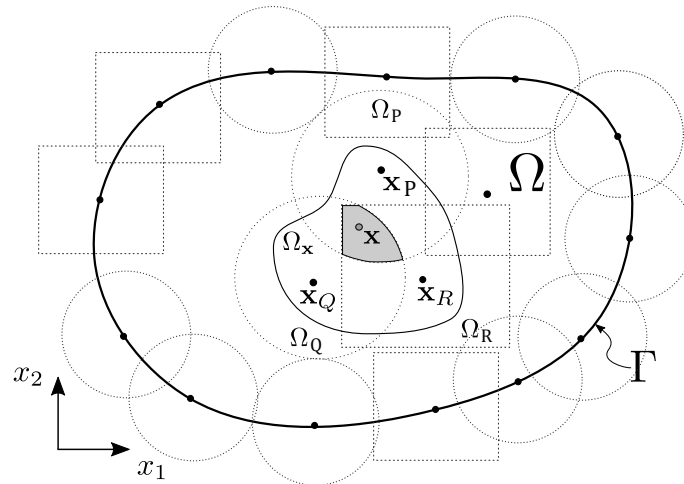
Figure 2: Representation of a meshless discretization of the domain.

Circular or rectangular local supports, centered at each nodal point, can be used. In a neighborhood of a sampling point $\mathbf{x}$, the domain of definition of MLS approximation is the subdomain $\Omega_{\mathbf{x}}$.

2.1 Shape Functions

Now, let $\Omega_{\mathbf{x}}$ be the MLS approximation domain of definition, in a neighborhood of a sampling point $\mathbf{x}$. To approximate the displacement $u(\mathbf{x}) \in \Omega_{\mathbf{x}}$, over a number of scattered nodes $\mathbf{x}_i \in \Omega$, $i = 1, 2, \ldots, n$, where the nodal parameters $\hat{u}_i$ are defined, the MLS approximation is given by

$$u^h(\mathbf{x}) = \mathbf{p}^T(\mathbf{x})\mathbf{a}(\mathbf{x}), \tag{1}$$

for $\mathbf{x} \in \Omega_{\mathbf{x}}$, in which

$$\mathbf{p}^T(\mathbf{x}) = [p_1(\mathbf{x}), p_2(\mathbf{x}), \ldots, p_m(\mathbf{x})], \tag{2}$$

is a vector of the complete monomial basis of order m and $\mathbf{a}(\mathbf{x})$ is the vector of unknown coefficients $a_j(\mathbf{x})$, $j = 1, 2, \ldots, m$ that are functions of the space coordinates $\mathbf{x} = [x_1, x_2]^T$, for two-dimensional problems.

The coefficient vector $\mathbf{a}(\mathbf{x})$ is determined by minimizing the weighted discrete L_2 norm

$$J(\mathbf{x}) = \frac{1}{2}\sum_{i=1}^{n} w_i(\mathbf{x})\left[u^h(\mathbf{x_i}) - \hat{u}_i\right]^2 = \frac{1}{2}\sum_{i=1}^{n} w_i(\mathbf{x})\left[\mathbf{p}^T(\mathbf{x}_i)\mathbf{a}(\mathbf{x}) - \hat{u}_i\right]^2, \tag{3}$$

with respect to each term of $\mathbf{a}(\mathbf{x})$, where $w_i(\mathbf{x})$ is the weight function associated with the node $\mathbf{x}_i$, with compact support that is $w_i(\mathbf{x}) > 0$, for all $\mathbf{x}$ in the support of $w_i(\mathbf{x})$. Figure 2 represents schematically the compact support of the MLS weight functions associated with a few scattered nodes. Finding the extremum of $J(\mathbf{x})$ with respect to each term of $\mathbf{a}(\mathbf{x})$, leads to

$$\mathbf{A}(\mathbf{x})\mathbf{a}(\mathbf{x}) = \mathbf{B}(\mathbf{x})\hat{\mathbf{u}}, \tag{4}$$

in which

$$\mathbf{A}(\mathbf{x}) = \sum_{i=1}^{n} w_i(\mathbf{x}) \mathbf{p}(\mathbf{x}_i) \mathbf{p}^T(\mathbf{x}_i), \tag{5}$$

$$\mathbf{B}(\mathbf{x}) = [w_1(\mathbf{x})\mathbf{p}(\mathbf{x}_1), w_2(\mathbf{x})\mathbf{p}(\mathbf{x}_2), \ldots, w_n(\mathbf{x})\mathbf{p}(\mathbf{x}_n)] \tag{6}$$

and

$$\hat{\mathbf{u}} = [\hat{u}_1, \hat{u}_2, \ldots, \hat{u}_n]. \tag{7}$$

Solving equation (4) for $\mathbf{a}(\mathbf{x})$ yields

$$\mathbf{a}(\mathbf{x}) = \mathbf{A}^{-1}(\mathbf{x})\mathbf{B}(\mathbf{x})\hat{\mathbf{u}}, \tag{8}$$

provided $n \geq m$, for each sampling point $\mathbf{x}$, as a necessary condition for a well-defined MLS approximation. Finally, substituting for $\mathbf{a}(\mathbf{x})$ into equation (1) leads to the MLS approximation

$$u^h(\mathbf{x}) = \sum_{i=1}^{n} \phi_i(\mathbf{x}) \hat{u}_i, \tag{9}$$

in which

$$\phi_i(\mathbf{x}) = \sum_{j=1}^{m} p_j(\mathbf{x}) \left[\mathbf{A}^{-1}(\mathbf{x})\mathbf{B}(\mathbf{x}) \right]_{ji} \tag{10}$$

is the shape function of the MLS approximation corresponding to the node $\mathbf{x}_i$, schematically represented in Figure 3.

(a) Weight function　　　　　　　　　(b) Shape function
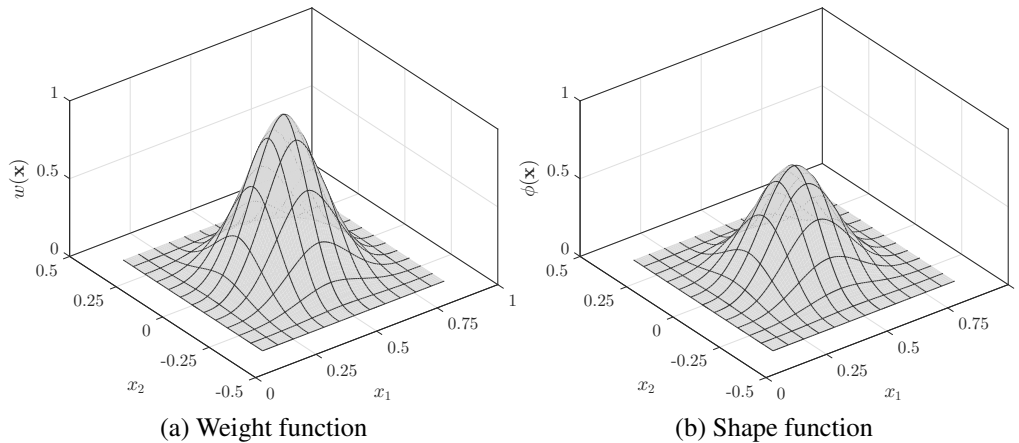
Figure 3: Typical weight function and shape function of the MLS approximation for a node at $\mathbf{x} = \begin{bmatrix} 1/2 & 0 \end{bmatrix}^{\mathbf{T}}$.

The MLS shape functions are not nodal interpolants that is $\phi_i(\mathbf{x}_j) \neq \delta_{ij}$. Since $\phi_i(\mathbf{x})$ vanishes for $\mathbf{x}$ not in the local domain of the node $\mathbf{x}_i$, the local character of the MLS approximation is preserved. The nodal shape function is complete up to the order of the basis. The smoothness of the nodal shape function is determined by the smoothness of the basis and of the weight function. The spatial derivatives of the shape function $\phi_i(\mathbf{x})$ are given by

$$\phi_{i,k} = \sum_{j=1}^{m} \left[p_{j,k}(\mathbf{A}^{-1}\mathbf{B})_{ji} + p_j(\mathbf{A}^{-1}\mathbf{B}_{,k} - \mathbf{A}^{-1}\mathbf{A}_{,k}\,\mathbf{A}^{-1}\mathbf{B})_{ji} \right], \tag{11}$$

in which $()_{,k} = \partial()/\partial x_k$.

2.2 Weight Functions

Weight functions $w_i(\mathbf{x})$, schematically represented in Figure 3, introduced in equation (3) for each node $\mathbf{x}_i$, have a compact support which defines the subdomain where $w_i(\mathbf{x}) > 0$, for all $\mathbf{x}$. For the sake of simplicity, this chapter considers rectangular compact supports with weight functions defined as

$$w_i(\mathbf{x}) = w_{i_x}(\mathbf{x})\, w_{i_y}(\mathbf{x}) \tag{12}$$

with the weight function given by the quartic spline function

$$w_{i_x}(\mathbf{x}) = \begin{cases} 1 - 6\left(\dfrac{d_{i_x}}{r_{i_x}}\right)^2 + 8\left(\dfrac{d_{i_x}}{r_{i_x}}\right)^3 - 3\left(\dfrac{d_{i_x}}{r_{i_x}}\right)^4 & \text{for } 0 \le d_{i_x} \le r_{i_x} \\ 0 & \text{for } d_{i_x} > r_{i_x} \end{cases} \tag{13}$$

and

$$w_{i_y}(\mathbf{x}) = \begin{cases} 1 - 6\left(\dfrac{d_{i_y}}{r_{i_y}}\right)^2 + 8\left(\dfrac{d_{i_y}}{r_{i_y}}\right)^3 - 3\left(\dfrac{d_{i_y}}{r_{i_y}}\right)^4 & \text{for } 0 \le d_{i_y} \le r_{i_y} \\ 0 & \text{for } d_{i_y} > r_{i_y}, \end{cases} \tag{14}$$

in which $d_{i_x} = \|x - x_i\|$ and $d_{i_y} = \|y - y_i\|$. The parameters r_{i_x} and r_{i_y} represent the size of the support for the node i, respectively in the x and y directions.

3 Structural Modeling

Consider the domain Ω of a body with boundary Γ, further divided in Γ_u and Γ_t, with $\Gamma = \Gamma_u \cup \Gamma_t$, as Figure 4 represents. The work theorem is defined in an arbitrary domain $\Omega_Q \in \Omega \cup \Gamma$, assigned to a reference point $Q \in \Omega_Q$, with boundary $\Gamma_Q = \Gamma_{Qi} \cup \Gamma_{Qt} \cup \Gamma_{Qu}$, in which Γ_{Qi} is the interior local boundary, and Γ_{Qt} and Γ_{Qu} are local boundaries that share the global boundaries, respectively the static boundary Γ_t and the kinematic boundary Γ_u; points P and R, have arbitrary local domains, respectively Ω_P and Ω_R.
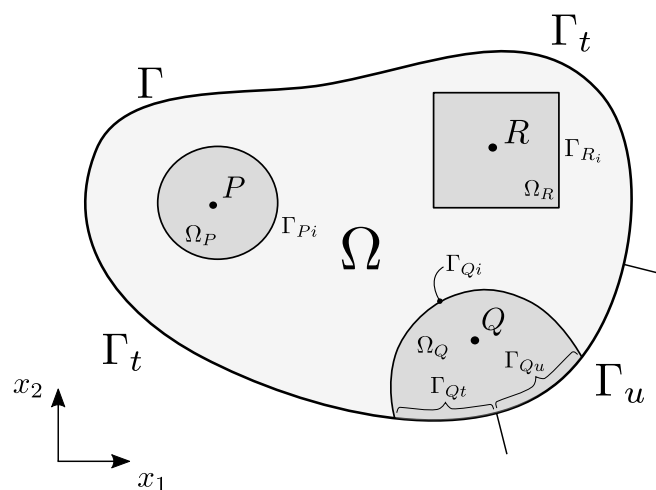
Figure 4: Representation of the body's domain Ω, with boundary Γ.

The mixed fundamental boundary value problem of linear elastostatics aims to find, in Ω, the distribution of stresses $\boldsymbol{\sigma}$, strains $\boldsymbol{\varepsilon}$ and displacements $\mathbf{u}$, when it has displacements $\bar{\mathbf{u}}$, constrained

on Γ_u, and is under the action of an external system of distributed surface and body forces with densities represented, respectively by $\bar{\mathbf{t}}$, on Γ_t and $\mathbf{b}$, in Ω.

The solution of the posed problem is a totally admissible elastic field that simultaneously satisfies the kinematic admissibility and the static admissibility. If this solution exists, see Fichera [2006], it can be shown that it is unique, provided linearity and stability of the material are admitted. Such is the uniqueness theorem of Kirchhoff [1859] which, in the framework of the variational calculus, leads to the theorem of virtual displacements and the theorem of virtual stresses. Since these theorems consider the totally admissible elastic field that is the actual solution of the posed problem, they are only particular cases of the general work theorem. Therefore, the general work theorem will be used to solve the posed problem.

Now consider the domain Ω of a body, loaded by a system of external forces under the conditions already mentioned, and a statically admissible stress field $\boldsymbol{\sigma}$, which therefore satisfies

$$\mathbf{L}^T\boldsymbol{\sigma} + \mathbf{b} = \mathbf{0}, \tag{15}$$

in Ω, with boundary conditions

$$\mathbf{t} = \mathbf{n}\,\boldsymbol{\sigma} = \bar{\mathbf{t}}, \tag{16}$$

specified on Γ_t; where $\mathbf{L}$ is a matrix differential operator; $\mathbf{t}$ denotes traction components; $\bar{\mathbf{t}}$ denotes prescribed tractions and $\mathbf{n}$ is the matrix of the components of the unit normal to the boundary outwardly directed.

In the body, consider an arbitrary local domain $\Omega_Q \in \Omega \cup \Gamma$, assigned to a reference point $Q \in \Omega_Q$, with boundary $\Gamma_Q = \Gamma_{Qi} \cup \Gamma_{Qt} \cup \Gamma_{Qu}$, in which Γ_{Qi} is the interior local boundary, with local boundaries Γ_{Qt} and Γ_{Qu} sharing the global boundaries, respectively the static boundary Γ_t and the kinematic boundary Γ_u, as Figure 4 clearly represents. The work theorem will be derived for this arbitrary local domain Ω_Q. This local domain $\Omega_Q \cup \Gamma_Q \in \Omega \cup \Gamma$ can be overlapping with other similar sub-domains that can be defined in the body, due to its arbitrariness.

3.1   The Work Theorem

The work theorem establishes an energy relationship, in an arbitrary local domain $\Omega_Q \in \Omega$, between two independent elastic fields that can be defined in the body. These elastic fields are, respectively, a statically admissible stress field $\boldsymbol{\sigma}$ that satisfies equilibrium with a system of external forces, and a kinematically admissible strain field $\boldsymbol{\varepsilon}^*$ that satisfies compatibility with a set of constrained displacements. Expressed as an integral form, defined in the domain $\Omega_Q \cup \Gamma_Q$, the work theorem can be written in a compact way, simply as

$$\int\limits_{\Gamma_Q} \mathbf{t}^T\mathbf{u}^*\,\mathrm{d}\Gamma + \int\limits_{\Omega_Q} \mathbf{b}^T\mathbf{u}^*\,\mathrm{d}\Omega = \int\limits_{\Omega_Q} \boldsymbol{\sigma}^T\boldsymbol{\varepsilon}^*\,\mathrm{d}\Omega, \tag{17}$$

in which no constitutive relation links the stress $\boldsymbol{\sigma}$ and the strain $\boldsymbol{\varepsilon}^*$. Therefore, they do not depend on each other, as Figure 5 schematically represents, where Dbc and Tbc stands for Displacement boundary condition and Traction boundary condition, respectively.

The statically admissible stress field $\boldsymbol{\sigma}$, can be any field that guarantee the equilibrium with the system of external forces, therefore satisfying equations (15) and (16). This elastic field is not necessarily the stress that the system of external forces actually introduces in the body.

The kinematically admissible strain field $\boldsymbol{\varepsilon}^*$, can be any field, assuming continuous displacements $\mathbf{u}^*$ with small derivatives, compatible with an arbitrary set of constraints specified on the kinematic boundary. This elastic field is not necessarily the strain that actually settled in the body.

Lastly, the local domain $\Omega_Q \cup \Gamma_Q$ is an arbitrary sub-domain of the body, associated with the reference point Q, as represented in Figure 4, where the independent fields $\boldsymbol{\sigma}$ and $\boldsymbol{\varepsilon}^*$ are established.
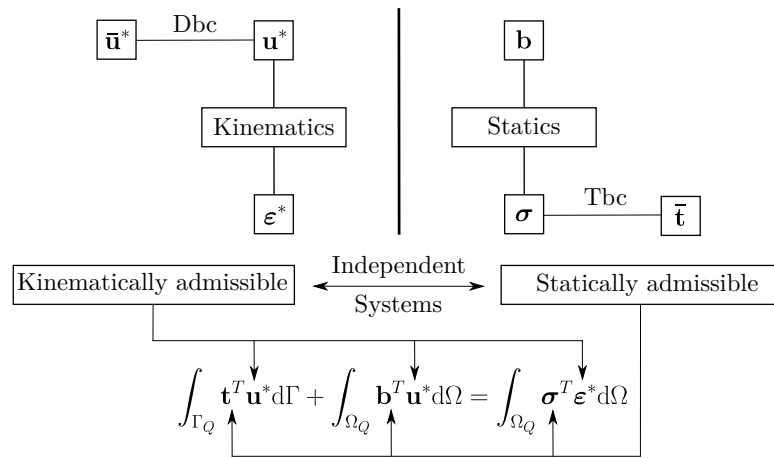
Figure 5: Schematic representation of the work theorem, an energy relationship, valid in an arbitrary local domain $\Omega_{\mathbf{Q}} \cup \Gamma_{\mathbf{Q}} \in \Omega$, between two independent fields.

3.2   Kinematic Formulation

Different formulations of local mesh free methods can be derived when one of the two independent fields are locally defined in the body, usually in accordance with some particular convenience of the numerical method formulation.

Kinematic formulations consider a particular specification of the strain field ε^*, leading thus to a mechanical equilibrium equation, which is used in numerical model to generate the respective stiffness matrix. A simple case of a kinematic formulation, based on a strain field generated by a rigid-body displacement, is therefore presented.

3.3   Rigid-Body Displacement Formulation

One of the key feature of the work theorem, the complete independence of the admissible fields σ and ε^*, allow the formulation to be simplified by defining kinematically admissible strain fields. Hence, the simplest and obvious choice is to use a strain field generated by a rigid-body displacement that can be defined as

$$\mathbf{u}^*(\mathbf{x}) = \mathbf{c}, \tag{18}$$

in which $\mathbf{c}$ is a constant vector that conveniently generates null strains

$$\varepsilon^*(\mathbf{x}) = \mathbf{0}. \tag{19}$$

The great virtue of this formulation is the simplicity used in the generation of the strain field. Additionally, this formulation leads to a simple form of equilibrium equations that, in the absence of body forces, involves only non-singular boundary integrals with no domain terms.

When the rigid-body displacement formulation is considered, the work theorem, equation (17), simply leads to the equation

$$\int_{\Gamma_Q - \Gamma_{Qt}} \mathbf{t} \, \mathrm{d}\Gamma + \int_{\Gamma_{Qt}} \bar{\mathbf{t}} \, \mathrm{d}\Gamma + \int_{\Omega_Q} \mathbf{b} \, \mathrm{d}\Omega = \mathbf{0} \tag{20}$$

which is nothing else other than the local version of Euler-Cauchy stress principle that is sometimes referred to as the defining principle of continuum mechanics. Equation (20) presents the mechanical equilibrium of tractions and body forces, in the domain Ω_Q, in an integral form. Therefore, it is used to generate the stiffness matrix associated to the local node.

4　Numerical Modeling Strategy

Based on the work theorem and choosing a proper and convenient kinematic formulation, the numerical model can derive the equilibrium equations that are used to generate the stiffness matrix. This numerical modeling strategy is adopted to solve the actual elastic problem set up in Section 3.

First of all, locally defined in the work theorem, an appropriate strain field ε^* is specified in the kinematic formulation. The mesh free numerical model considers the arbitrary rigid-body displacement, presented in Section 3.2, thus leading to the equilibrium equation (20).

On the other hand, the statically-admissible local field σ, will be always assumed as the elastic field that actually settles in the body, required to satisfy equilibrium with a system of external forces and loaded by the actual system of distributed surface and body forces, with the actual displacement constraints.

Besides satisfying static admissibility, through equations (15) and (16), , or through equation (20), this elastic field also satisfies kinematic admissibility defined as

$$\varepsilon = \mathbf{L}\,\mathbf{u}, \tag{21}$$

in Ω, with boundary conditions

$$\mathbf{u} = \overline{\mathbf{u}}, \tag{22}$$

on Γ_u, in which continuous displacements are assumed with small derivatives, leading to geometrical linearity of the strain field, in order to satisfy compatibility. Therefore, equations (22), which specifies the constraints of the actual displacements, must be enforced in the numerical model, in order to provide a unique solution of the posed problem.
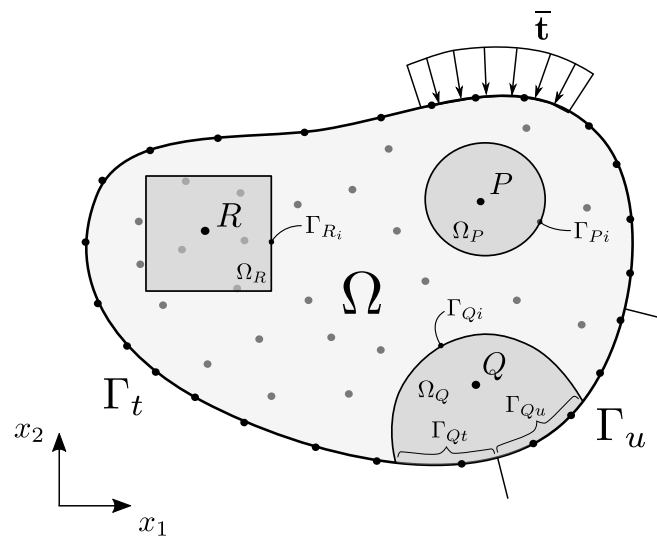
5　Local Mesh free Method

The discretization of the domain is performed considering a set of scattered nodes in the domain Ω and boundary $\Gamma = \Gamma_u \cup \Gamma_t$. Each node of the mesh free discretization is associated with its local domain, as schematically represented in Figure 6, where the reference nodes P, Q and R can be seen. These nodes have associated local domains Ω_P, Ω_Q and Ω_R; the local domain Ω_Q, assigned to the node Q, where the work theorem is defined, has boundary $\Gamma_Q = \Gamma_{Qi} \cup \Gamma_{Qt} \cup \Gamma_{Qu}$, in which Γ_{Qi} is the interior local boundary and $\Gamma_{Qt} \in \Gamma_t$ and $\Gamma_{Qu} \in \Gamma_u$.

In general, this local domain is a circular or rectangular region and centered at the respective node, for the sake o simplicity, where the rigid-body displacement formulation of the work theorem is defined as a local form of mechanical equilibrium. This local domain can assume any geometry and is highly susceptible to optimization and topology studies.

The MLS approximation uphold the local aspect of the formulation,throughout the compact support of each node, where the respective MLS shape functions are defined. As presented in Section 2, local compact supports can also have circular or rectangular shapes, centered at each node. The size of the compact support determines, in a neighborhood of a sampling point, the respective MLS domain of definition of this reference point, as schematically represented in Figure 2.

The domain of definition contains all the nodes that do not vanish, within a compact support at a sampling point, when constructing the MLS shape functions. Therefore, the union of the MLS domains of definition of all points in the local domain of each node, defines the domain of influence

Figure 6: Mesh free discretization of the domain Ω and boundary $\Gamma = \Gamma_{\mathbf{u}} \cup \Gamma_{\mathbf{t}}$.

of the node. Based on this domain of influence of each node, the local mesh free method perform a node-by-node stiffness computation to generate the respective rows of the global stiffness matrix of the node.

The rigid-body displacement mesh free formulation of the local work theorem, equation (20), can be written, in the absence of body forces, simply as

$$\int_{\Gamma_Q - \Gamma_{Qt}} \mathbf{t} \, \mathrm{d}\Gamma = -\int_{\Gamma_{Qt}} \bar{\mathbf{t}} \, \mathrm{d}\Gamma \tag{23}$$

which is nothing else than the mechanical equilibrium of the boundary tractions in the local domain Ω_Q.

Local mesh free numerical methods can be effectively formulated through a reduced integration of the equilibrium equation (23). For simplicity sake, linear variation of tractions is assumed on each boundary of the local domain, leading to a point-wise discrete form.

The reduced integration presented readily overcomes the well-known difficulties posed by the reduced integration on mesh-based methods, regarding accuracy and stability of the solution, which makes the local mesh free formulation a reliable and robust method.

Therefore, for a linear variation of tractions, along each boundary segment of the local domain, the local form of equilibrium (23), can be accurately evaluated with only one quadrature point, centered on each segment, thus leading to

$$\frac{L_i}{n_i} \sum_{j=1}^{n_i} \mathbf{t}_{\mathbf{x}_j} = -\frac{L_t}{n_t} \sum_{k=1}^{n_t} \bar{\mathbf{t}}_{\mathbf{x}_k}, \tag{24}$$

in which n_i and n_t denote the total number of integration/quadrature points, or linear segments, defined on, respectively the interior local boundary $\Gamma_{Qi} = \Gamma_Q - \Gamma_{Qt} - \Gamma_{Qu}$, with length L_i, and the local boundary Γ_{Qt}, with length L_t. This equation effectively represents a point-wise discrete form of mechanical equilibrium of boundary tractions, evaluated at a set of points of the local domain Ω_Q.

For any given nodal distribution of scattered nodes, the local mesh free method with linear reduced integration, symbolically referred from now on as ILMF, an simple acronym that stands

for Integrated Local Mesh Free method, is used to compute the stiffness matrix. ILMF uses a node-by-node process to construct the stiffness matrix, throughout traction evaluation at each central point of boundary segments, by using equation (24) assigned to each node.

These local domains can assume rectangular or circular geometries, as schematically represented in Figure 7 for interior nodes, Figure 8 for corner nodes and Figure 9 for boundary nodes.

(a) Rectangular   (b) Circular
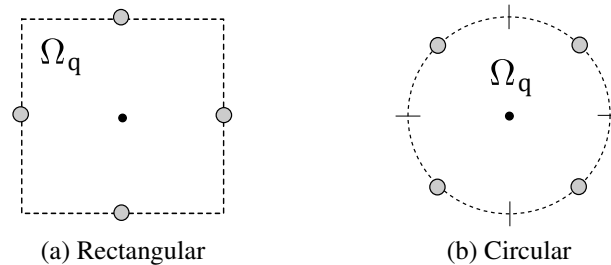
Figure 7: Schematic representation of rectangular and circular local domains, with 1 integration point per side, or quadrant, of the local domain, for the computation of the local form (24) of ILMF.

(a) Rectangular   (b) Circular
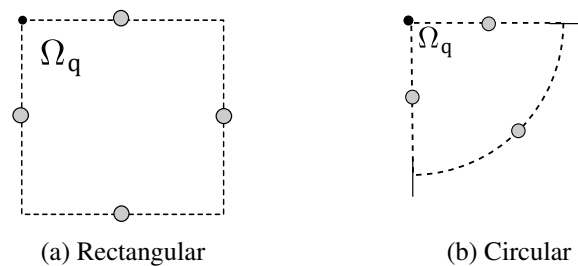
Figure 8: Schematic representation of rectangular and circular local domains on corner nodes, with 1 integration point per side, or quadrant, of the local domain.

(a) Rectangular   (b) Circular
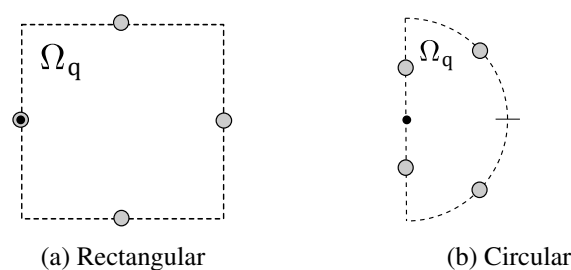
Figure 9: Schematic representation of rectangular and circular local domains on boundary nodes, with 1 integration point per side, or quadrant, of the local domain. The integration point and the node share the same coordinates on one of the boundaries.

As ti can be seen, any special treatment for traction evaluation is considered in the linear reduced integration process.

The MLS approximation of a displacement component $u^h(\mathbf{x})$, is performed in terms of the unknown nodal parameters $\hat{u}_i$. Consequently, the approximation of the elastic field is also performed

in terms of the unknown nodal parameters $\hat{\mathbf{u}}$, as

$$\mathbf{u} = \begin{bmatrix} u^h(\mathbf{x}) \\ v^h(\mathbf{x}) \end{bmatrix} = \begin{bmatrix} \phi_1(\mathbf{x}) & 0 & \dots & \phi_n(\mathbf{x}) & 0 \\ 0 & \phi_1(\mathbf{x}) & \dots & 0 & \phi_n(\mathbf{x}) \end{bmatrix} \begin{bmatrix} \hat{u}_1 \\ \hat{v}_1 \\ \vdots \\ \hat{u}_n \\ \hat{v}_n \end{bmatrix} = \mathbf{\Phi}\,\hat{\mathbf{u}} \tag{25}$$

and

$$\boldsymbol{\varepsilon} = \mathbf{L}\,\mathbf{u} = \mathbf{L}\,\mathbf{\Phi}\,\hat{\mathbf{u}} = \mathbf{B}\,\hat{\mathbf{u}}, \tag{26}$$

in which geometrical linearity is assumed in the differential operator $\mathbf{L}$ and thus,

$$\mathbf{B} = \begin{bmatrix} \phi_{1,1} & 0 & \dots & \phi_{n,1} & 0 \\ 0 & \phi_{1,2} & \dots & 0 & \phi_{n,2} \\ \phi_{1,2} & \phi_{1,1} & \dots & \phi_{n,2} & \phi_{n,1} \end{bmatrix}. \tag{27}$$

Stress and traction components are respectively approximated as

$$\boldsymbol{\sigma} = \mathbf{D}\,\boldsymbol{\varepsilon} = \mathbf{D}\,\mathbf{B}\,\hat{\mathbf{u}} \tag{28}$$

and

$$\mathbf{t} = \mathbf{n}\,\boldsymbol{\sigma} = \mathbf{n}\,\mathbf{D}\,\mathbf{B}\,\hat{\mathbf{u}}, \tag{29}$$

in which $\mathbf{D}$ is the matrix of the elastic constants and $\mathbf{n}$ is the matrix of the components of the unit outward normal, defined as

$$\mathbf{n} = \begin{bmatrix} n_1 & 0 & n_2 \\ 0 & n_2 & n_1 \end{bmatrix}. \tag{30}$$

Accordingly, the MLS approximation of the integrated local form (24) is carried out in terms of the unknown nodal parameters $\hat{\mathbf{u}}$. Hence, this process leads to the system of two algebraic equations

$$\frac{L_i}{n_i} \sum_{j=1}^{n_i} \mathbf{n}_{\mathbf{x}_j} \mathbf{DB}_{\mathbf{x}_j} \hat{\mathbf{u}} = -\frac{L_t}{n_t} \sum_{k=1}^{n_t} \bar{\mathbf{t}}_{\mathbf{x}_k} \tag{31}$$

that can be written as

$$\mathbf{K}_Q\,\hat{\mathbf{u}} = \mathbf{F}_Q, \tag{32}$$

in which $\mathbf{K}_Q$, denotes the stiffness matrix of the node Q, which is of the order $2 \times 2n$, where n represents the number of nodes of the influence domain of Q, given by

$$\mathbf{K}_Q = \frac{L_i}{n_i} \sum_{j=1}^{n_i} \mathbf{n}_{\mathbf{x}_j} \mathbf{DB}_{\mathbf{x}_j} \tag{33}$$

and $\mathbf{F}_Q$ denotes the vector of forces

$$\mathbf{F}_Q = -\frac{L_t}{n_t} \sum_{k=1}^{n_t} \bar{\mathbf{t}}_{\mathbf{x}_k}. \tag{34}$$

For a numerical model with N nodes in total, in which M is the number of interior and static-boundary nodes, the assembly of equations (32) for all M nodes leads to the $2M \times 2N$ system of equations

$$\mathbf{K}\,\hat{\mathbf{u}} = \mathbf{F}. \tag{35}$$

Finally, the $N - M$ kinematic-boundary nodes, are used to generate the remaining equations of the problem. For each of these nodes, the kinematic boundary condition is imposed through a direct interpolation method as

$$\mathbf{u}_k = \mathbf{\Phi}_k \, \hat{\mathbf{u}} = \overline{\mathbf{u}}_k, \tag{36}$$

with $k = 1, 2$, where $\overline{\mathbf{u}}_k$ denotes the specified displacement component. These equations are assembled into the global system (35).

ILMF naturally compute a symmetric and banded global system of equations, even though it generates the global system of equations in a node-by-node process, through equations (32) to (35). This generation process is systematically different from the one used in the traditional FEM that considers an element-by-element process to generate the global stiffness matrix.

A very short processing time to run the analysis is expected from ILMF, since the nodal stiffness matrix is computed, in equations (33), with only 4 integration points, one point for each segment of the local domain.

Another advantage is that the reduced integration leads to very accurate results. ILMF integration process plays an important role in the behavior of the numerical model, since it results in a reduction of the stiffness of the body, corresponding to an increase of the strain energy, which has the desirable effect of increasing the solution accuracy and, most important, presents no instabilities. It is important to highlight that this improved accuracy, generated by the reduced integration, has been already used in the standard FEM and other mesh free methods to prevent locking of fully integrated elements.

5.1 Convergence Analysis

The convergence analysis of ILMF can be done in a similar way of the convergence analysis of the standard displacement-assumed FEM, see Oliveira and Portela [2016].

A virtual displacement $\delta\mathbf{u}$, which is a continuous virtual variation of the displacement field $\mathbf{u}$ that actually settles in the body's domain Ω, is such a way that

$$\delta\mathbf{u} = \mathbf{0} \tag{37}$$

on Γ_u is where the prescribed kinematic boundary conditions cannot be varied.

In the local domain Ω_Q, with $\Gamma_Q = \Gamma_{Qi} \cup \Gamma_{Qt}$, consider the stress field $\boldsymbol{\sigma}$, that settles in the body's domain Ω. Now consider the work theorem, equation (17), with displacements defined as $\mathbf{u}^* = \delta\mathbf{u}$, leading to the theorem of virtual displacements that is

$$\int_{\Gamma_Q - \Gamma_{Qt}} \mathbf{t}^T \delta\mathbf{u}\, \mathrm{d}\Gamma + \int_{\Gamma_{Qt}} \overline{\mathbf{t}}^T \delta\mathbf{u}\, \mathrm{d}\Gamma = \int_{\Omega_Q} \boldsymbol{\sigma}^T \delta\boldsymbol{\varepsilon}\, \mathrm{d}\Omega, \tag{38}$$

or simply

$$\int_{\Gamma_Q} \mathbf{t}^T \delta\mathbf{u}\, \mathrm{d}\Gamma = \int_{\Omega_Q} \boldsymbol{\sigma}^T \delta\boldsymbol{\varepsilon}\, \mathrm{d}\Omega, \tag{39}$$

in which $\delta\boldsymbol{\varepsilon}$ denotes the strain variation corresponding to the virtual displacement $\delta\mathbf{u}$.

The total potential energy functional in the local domain Ω_Q, is defined as

$$T = U + P, \tag{40}$$

in which the strain energy U is defined in terms of the respective density w as

$$U = \int_{\Omega_Q} w\, \mathrm{d}\Omega = \int_{\Omega_Q} \frac{1}{2} \boldsymbol{\sigma}^T \delta\boldsymbol{\varepsilon}\, \mathrm{d}\Omega \tag{41}$$

and the potential energy P of the external forces is defined as

$$P = -\int_{\Gamma_Q} \mathbf{t}^T \delta\mathbf{u}\,\mathrm{d}\Gamma. \tag{42}$$

The theorem of the total potential energy states that the elastic field that satisfies static admissibility, with the applied tractions, makes the total potential energy stationary, in the set of all elastic fields that satisfy kinematic admissibility, with the displacement constraints of the body. As a matter of fact, the first variation of the total energy T generates virtual variations of displacements $\delta\mathbf{u}$ and strains $\delta\boldsymbol{\varepsilon}$ and thus, equation (39) of the theorem of virtual displacements leads to a stationary condition

$$\delta T = \delta U + \delta P = \int_{\Omega_Q} \boldsymbol{\sigma}^T \delta\boldsymbol{\varepsilon}\,\mathrm{d}\Omega - \int_{\Gamma_Q} \mathbf{t}^T \delta\mathbf{u}\,\mathrm{d}\Gamma = 0, \tag{43}$$

that is a minimum, when the material stability of the body is assumed. Under these circumstances, the total potential energy theorem limits to a minimum value the total potential energy of the exact solution settled in the body. For now, consider that the work theorem (17), applied for the case of the elastic field that settles in the body, leads to $P = -2U$ and consequently $T = -U$. It can be seen that the minimum value of the total potential energy corresponds to a maximum value of the strain energy, which is, therefore, equivalent to a minimum value of the stiffness of the elastic field that settles in the body.

Discretization of the local form (24) is performed with the MLS approximation, generating a system of two algebraic equations. When more refined nodal distributions are considered, the approximated solution converge monotonically to the exact solution, likewise the standard FEM, provided the MLS approximation satisfies completeness and continuity, as FEM does.

As a final remark on the matter, it is important to point out that the presented reduced integration of the ILMF model does not lead to any sort of spurious instability. This behavior is a direct consequence of the use of 4 integration points to calculate the stiffness associated to each local node, on each boundary of the local domain. Therefore, this integration prevents the generation of spurious zero-energy modes, unlike nodal integration methods without stabilization.

5.2   Discretization Parameters

Local mesh free methods posses two key parameters that can greatly effect the analysis. The first is the size r_{Ω_s} of the compact support Ω_s, where shape functions are defined; and the second is the size r_{Ω_q} of the local integration domain Ω_q, where the work theorem is defined. Usually these parameters are heuristically determined by most authors employing mesh free methods.

For a node i, in a mesh free nodal distribution, these parameters can be defined, respectively as

$$r_{\Omega_s} = \alpha_s\, c_i \tag{44}$$

and

$$r_{\Omega_q} = \alpha_q\, c_i, \tag{45}$$

in which c_i denotes the distance of the reference node i, to the nearest node and α_s and α_q are arbitrary constant parameters that must be defined in any application.

Equations (44) and (45) show that the accuracy of a mesh free numerical application can be controlled an even improved through a proper specification of these discretization parameters α_s and α_q. In general, the discretization parameters are considered as $\alpha_s > 1.0$ and $\alpha_q < 1.0$, for regular node distributions on linear elastic problems.

The discretization parameter α_s, which is the size of the influence domain of each node, is directly determined by the compact supports, as seen in Section 2. The parameter is primarily linked to the accuracy of the mesh free formulation since it defines the total number of nodes required to build the respective nodal shape functions, in order to perform the MLS approximation of variables.

Meanwhile, The discretization parameter α_q, which is the local domain of integration of each node, where the stiffness matrix of each node is build, is primarily linked to the efficiency of the formulation. This domain must be within the solution domain, without intersecting the boundary of the body.

In order to further the efficiency of ILMF, proper values for these discretization parameters, α_s and α_q, are obtained automatically through a multi-objective optimization scheme.

6   Optimization Scheme for Discretization Parameters

The required background and terminology of multi-objective optimization, evolutionary algorithms and Pareto optimality are defined in optimization literature, formally introduced here by Hwang and Masud [1979], Sawaragi et al. [1985], Steuer [1986] and Ringuest [1992]. Some basic concepts and premises, important for comprehension of the optimization scheme formulated are presented here, for the sake of completeness.

6.1   Genetic Algorithms (GA)

GA belong to a broad category of evolutionary algorithms, which are optimization techniques that perform a search motivated by the principles of natural genetics and natural selection, proposed by Holland [1975]. They are known for performing a non-derivative global heuristic search and solve a wide rage of optimization problems, as presented by Kelner and Leonard [2004], McCall [2005] and Ebrahimnejad et al. [2015], for mesh free methods.

Basically, GA keep a population of individuals, in this case $\mathbf{P}(\mathbf{t})$, for generation $\mathbf{t}$. Each individual contains a possible solution to the posed problem. Each individual is programmed to give some measure of its fitness that will be evaluated later. Some of these individuals undergo stochastic transformations by means of genetic operations to form new individuals. This transformation can be a mutation, which creates new individuals by making changes in a single individual, or can be a crossover, which creates new individuals by combining parts from two others. The offspring $\mathbf{C}(\mathbf{t})$, the new individuals created, are then evaluated. A brand new population is formed by selecting the more fit individuals from the parent population and the offspring population. After several generations, or function evaluations, the algorithm converges to the best and most fit individual, which hopefully represents an optimal or sub-optimal solution to the problem, see Gen and Cheng [2000].

6.2   Symbiotic Organisms Search (SOS)

SOS is a powerful meta-heuristic optimization algorithm, also member of the broad category of evolutionary algorithms, originally introduced by Cheng and Prayogo [2014]. The method is described by a relationship between any two distinct species, from the Greek word for "living together".

The relationship between species can be either obligate, meaning the two organisms depend on each other for survival, or facultative, meaning the two organisms choose to cohabitate in a mutually beneficial but nonessential relationship. Mutualism, commensalism, and parasitism are

the most common symbiotic relationships found in nature. Mutualism denotes a symbiotic relationship between two different species in which both benefit, while commensalism is a symbiotic relationship between two different species in which one benefits and the other is unaffected or neutral. Parasitism is a symbiotic relationship between two different species in which one benefits and the other is actively harmed. Naturally, organisms develop symbiotic relationships as a strategy to adapt to changes in their environment. Symbiotic relationships may also help organisms increase fitness and survival advantage over the long-term.

Similar to other meta-heuristic algorithms, SOS is population-based and also uses a candidate solution to search for the optimal solution in the search space. Both GA and SOS provide a directed random search in complex landscapes. Genetic operations and symbiotic relationships perform essentially a blindfold search, while selection operators hopefully direct the search toward the desirable area of the solution space. The key feature of evolutionary algorithms is that they make a good balance between exploration and exploitation of the search space.

6.3   Objective Functions

The objective function provide the output required for the algorithm to evaluate a function. The optimization performance is highly dependable on well defined functions.

The first objective function results from the features of the parameter α_s. Consider any state of the elastic field that actually settles in the body, the strain energy U is given by

$$U = \int\limits_{\Omega} \frac{1}{2} \boldsymbol{\sigma}^T \boldsymbol{\varepsilon} \, \mathrm{d}\Omega \tag{46}$$

and the potential energy P, of the external loads, given by

$$P = -\int\limits_{\Gamma_t} \bar{\mathbf{t}}^T \mathbf{u} \, \mathrm{d}\Gamma, \tag{47}$$

can be used to handle the total potential energy T. The work theorem for the global domain of the body, results in $P = -2U$ and therefore $T = -U$, as well as $T = P/2$; for the actual elastic field of the body. It is clear that the minimum value of the total potential energy of the body corresponds to a minimum value of the potential energy P or a maximum value of the strain energy U.

There are two ways to handle the evaluation of the energy. The first is to evaluate the strain energy U of the body, which is computationally inefficient, since it requires the computation of the stress field for all nodal values and the evaluation of derivatives of shape functions that can degrade the numerical accuracy. The second is to evaluate the potential energy P, which is computationally more efficient, since only nodes with no-null applied external forces, albeit the ones at the static boundary, need to be evaluated. As it can be seen, this process is performed only at a few nodes and does not require the computation of derivatives of shape functions. Therefore, the objective function can be defined with the structural compliance C, as

$$C = \frac{1}{2} \int\limits_{\Gamma_t} \bar{\mathbf{t}}^T \mathbf{u} \, \mathrm{d}\Gamma = -\frac{1}{2}P. \tag{48}$$

In the end, the minimum value of the potential energy P is equivalent to a minimum value of C that corresponds to a maximum value of $-C$.

The second objective function results from the features of the parameter α_q. The total area of integration of the body, the combined area of all local integration domains for each node, in

a nodal discretization, must be as close as possible to the geometrical area of the domain of the body. The objective function is defined by the resulting local domain area

$$A_q = \sum_{l=1}^{n} \frac{A_{\Omega_q}}{\Omega_q} \, , \tag{49}$$

in which A_{Ω_q} considers equation (45) to compute the total area of integration of each node and Ω_q is the total area of the domain of the body. Since the local domain can be defined with an arbitrary geometrical shape, usually a rectangular or a circular domain, that can intersect each other if necessary; the efficiency of the approximation is dependent on the geometry of the domain of the problem, which is adaptable through optimization.

6.4   Mathematical Formulation and Algorithm Implementation

The numerical problem optimization obtain optimal values for mesh free parameters α_s and/or α_q by minimizing the objective function through mesh free models, in this case ILMF, such that the geometrical constraints of the problem are satisfied. Three optimization schemes based on relative error, compliance and local domain are presented in the following.

The first multi-objective optimization scheme mathematical formulation is presented as

$$
\begin{aligned}
&\text{minimize} && r_{\varepsilon}(\boldsymbol{\alpha_s}, \boldsymbol{\alpha_q}) \\
&&& r_{u}(\boldsymbol{\alpha_s}, \boldsymbol{\alpha_q}) \\
&\text{subject to} && \mathbf{e}(\boldsymbol{\alpha_s}) = \alpha_s{}^{min} \leq \alpha_s \leq \alpha_s{}^{max} \\
&&& \mathbf{e}(\boldsymbol{\alpha_q}) = \alpha_q{}^{min} \leq \alpha_q \leq \alpha_q{}^{max} \\
&\text{where} && \boldsymbol{\alpha_s} = (\alpha_{s1}, \alpha_{s2}, ..., \alpha_{sn}) \in \boldsymbol{\alpha} \\
&&& \boldsymbol{\alpha_q} = (\alpha_{q_1}, \alpha_{q_2}, ..., \alpha_{q_n}) \in \boldsymbol{\alpha} \, ,
\end{aligned}
\tag{50}
$$

in which r_{ε} and r_u are, respectively the energy and displacement relative error, to be presented in section 8 and commonly used to measure numerical methods accuracy; $\alpha_s{}^{min}/\alpha_q{}^{min}$ and $\alpha_s{}^{max}/\alpha_q{}^{max}$ denote the minimum and the maximum allowable limits for the mesh free discretization parameters α_s and α_q, respectively.

The second multi-objective optimization scheme mathematical formulation is presented as

$$
\begin{aligned}
&\text{minimize} && C(\boldsymbol{\alpha_s}) \\
&&& \text{CPU time}(\boldsymbol{\alpha_s}) \\
&\text{subject to} && \mathbf{e}(\boldsymbol{\alpha_s}) = \alpha_s{}^{min} \leq \alpha_s \leq \alpha_s{}^{max} \\
&\text{where} && \boldsymbol{\alpha_s} = (\alpha_{s1}, \alpha_{s2}, ..., \alpha_{sn}) \in \boldsymbol{\alpha} \, ,
\end{aligned}
\tag{51}
$$

for GA and for SOS is defined in a mono-objective form as

$$
\begin{aligned}
&\text{minimize} && C(\boldsymbol{\alpha_s}) \\
&\text{subject to} && \mathbf{e}(\boldsymbol{\alpha_s}) = \alpha_s{}^{min} \leq \alpha_s \leq \alpha_s{}^{max} \\
&\text{where} && \boldsymbol{\alpha_s} = (\alpha_{s1}, \alpha_{s2}, ..., \alpha_{sn}) \in \boldsymbol{\alpha} \, ,
\end{aligned}
\tag{52}
$$

in which C is the structural compliance, presented in equation (48), and CPU time is the processing time required to generate and solve the global system of algebraic equations.

Finally, the third multi-objective optimization scheme mathematical formulation is presented as

$$
\begin{aligned}
&\text{minimize} && A_q(\boldsymbol{\alpha_q}) \\
&\text{subject to} && \mathbf{e}(\boldsymbol{\alpha_q}) = \alpha_q{}^{min} \leq \alpha_q \leq \alpha_q{}^{max} \\
&\text{where} && \boldsymbol{\alpha_q} = (\alpha_{q_1}, \alpha_{q_2}, ..., \alpha_{q_n}) \in \boldsymbol{\alpha} \, ,
\end{aligned}
\tag{53}
$$

in which A_q is the resulting local domain area, as presented in equation (49).

When mono-objective optimization is considered, the fitness function containing the mesh free formulation should accept a vector, whose length is the number of independent variables α_q, one for each node of the problem domain, and return a scalar value (A_q), the objective function. For multi-objective optimization, the same mesh free formulation should return a row vector of objective function values C, CPU time, r_ε and r_u. This process can be easily be extended to any local mesh free method from other authors.

Global variable is a function that can be used to perform multiple optimization processes and carry over the output of one optimization iteration phase, usually to optimize α_q first, to a second phase, where α_s can be optimized.

For GA, the proper values for population size, selection function, scaling function and etc, are different in each optimization scheme and will be properly addressed later. SOS requires only the population size and the maximum number of function evaluations, which is a key advantage of this method and will be addressed later.

Lastly, the automatic optimization of the discretization parameters is a combination of the features presented in section 6.3 into a single and unique routine, to automatically compute mesh free discretization parameters, α_s and α_q, in a robust and efficient way.

The optimization is divided in two distinct procedures, as presented in Figure 10.

In the first step, a single-objective optimization is performed, considering the mesh free model to evaluate A_q as an objective function. By the end of this process, the parameter α_q is optimized for n nodes of the model, as a vector $n \times 1$, which will be eventually introduced in the next iteration phase. In the second step, the parameter α_s is optimized as a scalar value, in a multi-objective optimization using the mesh free model to evaluate the compliance and the CPU time as objective functions.

The process is separated in two steps so that the parameter α_q is completely independent from α_s. As consequence, both can be calculated considering only the boundary conditions of the posed problem and the local domain of integration geometry. When combined, the routine guarantee that the integration will be effectively computed in the first phase and later that parameter α_s is effectively calculated considering the compliance and the CPU time, just to ensure that this optimization will result in fast computations, with no detriment for the solution accuracy.

As it can be seen from the optimization scheme, the fully automated routine can perform the optimization without the need of any analytical solution and for any bi-dimensional domain. Parallel environment can be included in the routine to improve the processing time of the optimization, which makes a robust tool to solve complex mesh free problems, although only ILMF and linear elastic problems are presented.

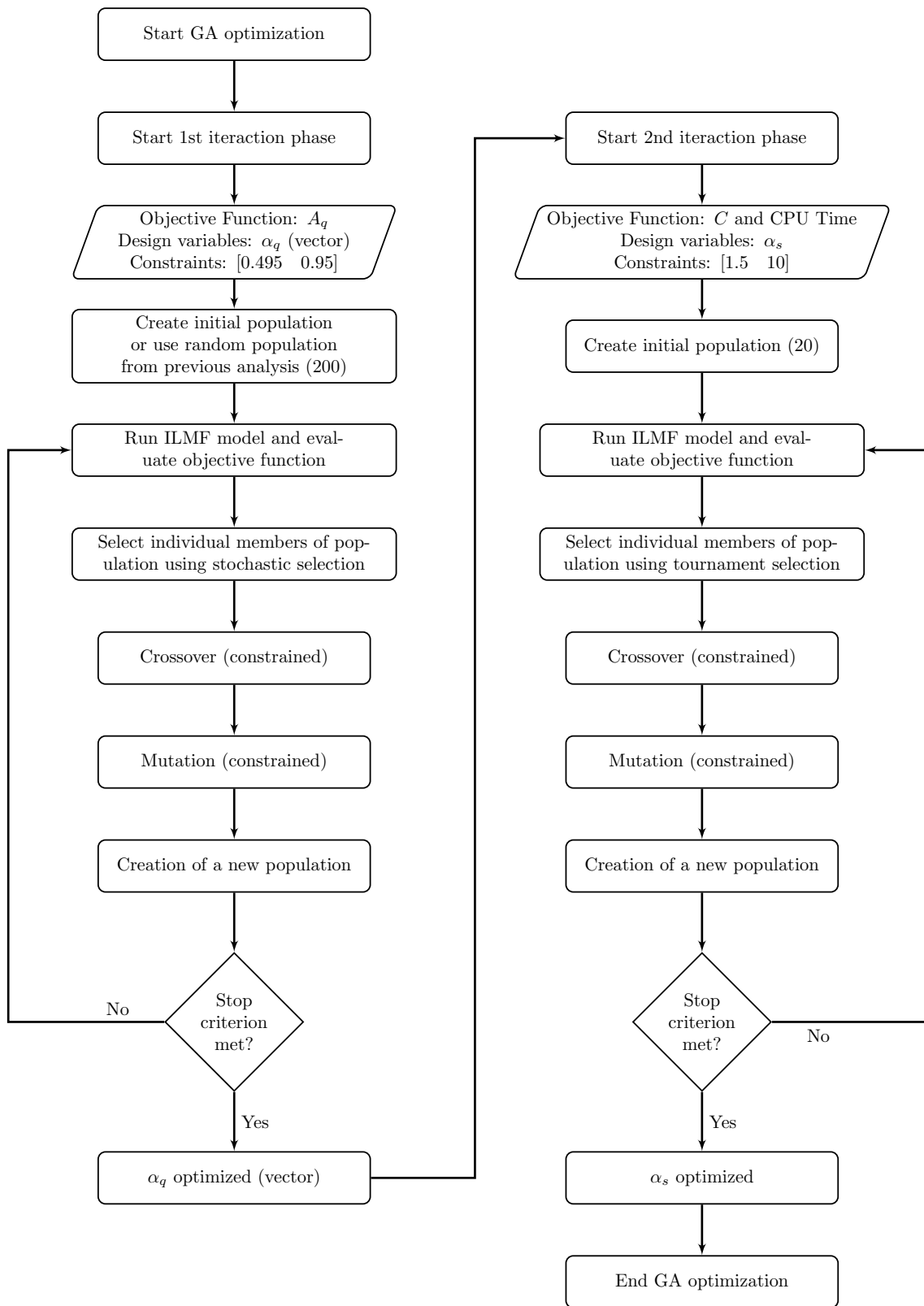## 7   Linear Elastic Fracture Mechanics

Mixed-mode deformation of cracked plates can be effectively analyzed through the direct computation of the Stress Intensity Factor (SIF), carried out with the Singularity Subtraction Technique (SST). After implemented in a mesh free model, SST introduces the SIF as primary unknowns of the numerical model, by subtracting the crack tip singularity before the numerical solution.

Consider a two-dimensional cracked plate, with domain Ω and boundary $\Gamma = \Gamma_u \cup \Gamma_t$, in the absence of body forces, satisfies the equations

$$\mathbf{L}^T \boldsymbol{\sigma} = \mathbf{0} \tag{54}$$

$$\boldsymbol{\varepsilon} = \mathbf{L}\,\mathbf{u} \tag{55}$$

$$\boldsymbol{\sigma} = \mathbf{D}\,\boldsymbol{\varepsilon} \tag{56}$$

Figure 10: Optimization flowchart showing the required steps for the fully automated routine; the 1st step is presented on the left and the 2nd step is presented on the right.

in the domain Ω, with boundary conditions

$$\mathbf{u} = \bar{\mathbf{u}} \quad \text{on} \quad \Gamma_u \tag{57}$$

and

$$\mathbf{t} = \mathbf{n}\,\boldsymbol{\sigma} = \bar{\mathbf{t}} \quad \text{on} \quad \Gamma_t, \tag{58}$$

in which matrix $\mathbf{L}$ represents a differential operator; vectors $\boldsymbol{\sigma}$ represent the stresses and $\boldsymbol{\varepsilon}$ represent the strains; matrix $\mathbf{D}$ represents the elastic constants; vectors $\mathbf{u}$, $\mathbf{t}$ $\bar{\mathbf{u}}$ and $\bar{\mathbf{t}}$ represent, respectively displacements, tractions, prescribed values of displacements and tractions; and $\mathbf{n}$ denotes the components of the unit normal to the boundary, outwardly directed.

The singularity subtraction can be used to avoid inaccuracies due to unbounded stress at one point but with displacements bounded everywhere, in the numerical method. In linear elastic fracture mechanics, the stress field is singular at the crack tip and can be conveniently modified even before the solution is carried out with mesh free analysis. Based non the principle of superposition that allows linear behavior, the elastic field can be decomposed into a regular (R) and a singular (S) component as

$$\sigma_{ij} = (\sigma_{ij} - \sigma_{ij}^S) + \sigma_{ij}^S = \sigma_{ij}^R + \sigma_{ij}^S \tag{59}$$

and

$$u_i = (u_i - u_i^S) + u_i^S = u_i^R + u_i^S, \tag{60}$$

where $\sigma_{ij}^R = \sigma_{ij} - \sigma_{ij}^S$ and $u_i^R = u_i - u_i^S$ denotes the regular parts of the stress and displacement of the initial problem, respectively; σ_{ij}^S and u_i^S represents, respectively the stress and displacement of a particular solution of the initial problem that is the singular field in this case. The particular singular field, equations (59) and (60), regularize the initial elastic field when proper functions are used, since the stress σ_{ij}^R become non-singular.

The regularization strategy employed allow the analysis of the initial problem to be performed with the only regular elastic field, given by components σ_{ij}^R and u_i^R. Therefore, these components automatically satisfy the field equations, because they represent a particular solution of the initial problem. Hence, elasticity equations (54) to (56) are now written as

$$\mathbf{L}^T \boldsymbol{\sigma}^R = \mathbf{0} \tag{61}$$

$$\boldsymbol{\varepsilon}^R = \mathbf{L}\,\mathbf{u}^R \tag{62}$$

$$\boldsymbol{\sigma}^R = \mathbf{D}\,\boldsymbol{\varepsilon}^R \tag{63}$$

in domain Ω, with boundary conditions

$$\mathbf{u}^R = \bar{\mathbf{u}} - \mathbf{u}^S \quad \text{on} \quad \Gamma_u \tag{64}$$

and

$$\mathbf{t}^R = \bar{\mathbf{t}} - \mathbf{t}^S \quad \text{on} \quad \Gamma_t. \tag{65}$$

Note that, except for boundary conditions from equations (64) and (65), this regularized problem is governed by the same equations of the initial problem, where the additional terms, components $\mathbf{u}^S$ and $\mathbf{t}^S$ of a singular particular solution of the initial problem, are included.

The singular field around the crack tip, represented by components of the particular solution σ_{ij}^S and u_i^S in equations (59) and (60), can be defined through the first term of the Williams [1952] eigenexpansion, derived for a semi-infinite edge crack. The stress components are

$$\sigma_{11}^S = \frac{K_I}{\sqrt{2\pi r}} \cos\frac{\theta}{2} \left(1 - \sin\frac{\theta}{2}\sin\frac{3\theta}{2}\right) + \frac{K_{II}}{\sqrt{2\pi r}} \sin\frac{\theta}{2} \left(2 + \cos\frac{\theta}{2}\cos\frac{3\theta}{2}\right), \tag{66}$$

$$\sigma_{22}^S = \frac{K_I}{\sqrt{2\pi r}} \cos\frac{\theta}{2} \left(1 + \sin\frac{\theta}{2} \sin\frac{3\theta}{2}\right) - \frac{K_{II}}{\sqrt{2\pi r}} \sin\frac{\theta}{2} \cos\frac{\theta}{2} \cos\frac{3\theta}{2} \tag{67}$$

and

$$\sigma_{12}^S = \frac{K_I}{\sqrt{2\pi r}} \cos\frac{\theta}{2} \sin\frac{\theta}{2} \cos\frac{3\theta}{2} + \frac{K_{II}}{\sqrt{2\pi r}} \cos\frac{\theta}{2} \left(1 - \sin\frac{\theta}{2} \sin\frac{3\theta}{2}\right) \tag{68}$$

and the displacement components are

$$u_1^S = \frac{K_I}{4\mu} \sqrt{\frac{r}{2\pi}} \left[(2\kappa - 1)\cos\frac{\theta}{2} - \cos\frac{3\theta}{2}\right] +$$
$$+ \frac{K_{II}}{4\mu} \sqrt{\frac{r}{2\pi}} \left[(2\kappa + 3)\sin\frac{\theta}{2} + \sin\frac{3\theta}{2}\right] \tag{69}$$

and

$$u_2^S = \frac{K_I}{4\mu} \sqrt{\frac{r}{2\pi}} \left[(2\kappa + 1)\sin\frac{\theta}{2} - \sin\frac{3\theta}{2}\right] +$$
$$+ \frac{K_{II}}{4\mu} \sqrt{\frac{r}{2\pi}} \left[(2\kappa - 3)\cos\frac{\theta}{2} + \cos\frac{3\theta}{2}\right], \tag{70}$$

where K_I and K_{II} represent the SIF, respectively of the opening and sliding modes; the constant $\kappa = 3 - 4\nu$ is established for plain strain and $\kappa = (3 - \nu)/(1 + \nu)$ for plain stress, in which ν is Poisson's ratio; and constant μ is the shear modulus. A polar coordinate reference system (r, θ), centered at the crack tip, is defined such that $\theta = 0$ is the crack axis, ahead of the crack tip, as Figure 11 represents.
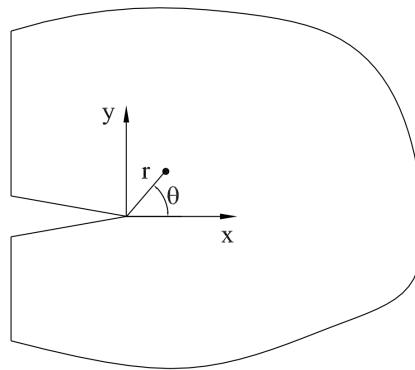
Figure 11: Polar coordinate reference system for William's singular particular solution.

It is noticeable that the order $r^{-1/2}$ of the stress field becomes singular when r tends to zero. Note also that rigid-body terms are not included in the displacement field, which leads to null components at the crack tip. As demonstrated by Caicedo and Portela [2015], the first term of the William's eigenexpansion, derived for an edge crack, can also be used to represent the elastic field around the crack-tip, where the singular behavior of the stress field is dominant, for the case of internal piecewise-flat multi-cracked finite plates, under mixed-mode deformation.

Traction components are defined, at a boundary point, through the singular stress of equations (66) to (68), as follow

$$\mathbf{t}^S = \begin{bmatrix} t_1^S \\ t_2^S \end{bmatrix} = \begin{bmatrix} \sigma_{11}^S & \sigma_{21}^S \\ \sigma_{12}^S & \sigma_{22}^S \end{bmatrix} \begin{bmatrix} n_1 \\ n_2 \end{bmatrix} = \begin{bmatrix} g_{11} & g_{12} \\ g_{21} & g_{22} \end{bmatrix} \begin{bmatrix} K_I \\ K_{II} \end{bmatrix} = \mathbf{g}\,\mathbf{k}, \tag{71}$$

where n_i refers to the i-th component of the unit normal to the boundary, outwardly directed; functions $g_{ij} = g_{ij}(r^{-1/2}, \theta)$ were introduced for a convenient notation of equations (66) to (68) and the vector $\mathbf{k}$ contains the SIF.

The displacement field, presented in equations (69) and (70), similar to the stress field, can be defined in a vector form as

$$\mathbf{u}^S = \begin{bmatrix} u_1^S \\ u_2^S \end{bmatrix} = \begin{bmatrix} f_{11} & f_{12} \\ f_{21} & f_{22} \end{bmatrix} \begin{bmatrix} K_I \\ K_{II} \end{bmatrix} = \mathbf{f}\ \mathbf{k}, \tag{72}$$

where functions $f_{ij} = f_{ij}(r^{1/2}, \theta)$ are a convenient notation of equations (69) and (70).

7.1   Mesh free Formulation for Fracture Mechanics

Generally, an analytical solution of the regularized problem, equations (61) to (63), with boundary conditions (64) and (65), are not available for practical problems. Therefore, numerical methods, in this case ILMF, are employed and considered to obtain the approximate solution.

Consider the domain Ω_Q associated with the node $Q \in \Omega_Q \cup \Gamma_Q$, the equilibrium equations (23) are now rewritten as

$$\int_{\Gamma_Q - \Gamma_{Qt}} \mathbf{t}^R \, d\Gamma = -\int_{\Gamma_{Qt}} \left(\bar{\mathbf{t}} - \mathbf{t}^S \right) d\Gamma, \tag{73}$$

in which the static boundary conditions (65), of the regularized problem, are considered.

Therefore, for a linear reduced integration, along each boundary segment of the local domain, equation (73) simply leads to

$$\frac{L_i}{n_i} \sum_{j=1}^{n_i} \mathbf{t}_{\mathbf{x}_j}^R = -\frac{L_t}{n_t} \sum_{k=1}^{n_t} \bar{\mathbf{t}}_{\mathbf{x}_k} + \int_{\Gamma_{Qt}} \mathbf{t}^S \, d\Gamma, \tag{74}$$

in which n_i and n_t denote the total number of integration points, or boundary segments, defined on, respectively the interior local boundary $\Gamma_{Qi} = \Gamma_Q - \Gamma_{Qt} - \Gamma_{Qu}$, with length L_i, and the local static boundary Γ_{Qt}, with length L_t.

Now, consider a mesh free discretization of the domain Ω, with circular or rectangular local domains, as Figure 7 schematically represents. The MLS approximation is used to perform the discretization of the local form, equation (74), in terms of the unknown nodal parameters $\hat{\mathbf{u}}^R$, which leads to the system of two linear algebraic equations

$$\frac{L_i}{n_i} \sum_{j=1}^{n_i} \mathbf{n}_{\mathbf{x}_j} \mathbf{D} \mathbf{B}_{\mathbf{x}_j} \hat{\mathbf{u}}^R = -\frac{L_t}{n_t} \sum_{k=1}^{n_t} \bar{\mathbf{t}}_{\mathbf{x}_k} + \int_{\Gamma_{Qt}} \mathbf{g} \, d\Gamma\ \mathbf{k} \tag{75}$$

that can be written as

$$\mathbf{K}_Q\, \hat{\mathbf{u}}^R + \mathbf{G}_Q\, \mathbf{k} = \mathbf{F}_Q, \tag{76}$$

in which the stiffness matrix $\mathbf{K}_Q$ is given by

$$\mathbf{K}_Q = \frac{L_i}{n_i} \sum_{j=1}^{n_i} \mathbf{n}_{\mathbf{x}_j} \mathbf{D} \mathbf{B}_{\mathbf{x}_j}, \tag{77}$$

of the order $2 \times 2n$, where n is the number of nodes inside the influence domain of the node Q. Matrix $\mathbf{G}_Q$, of the order 2×2, computed from equations (71), is presented as

$$\mathbf{G}_Q = -\int_{\Gamma_{Qt}} \mathbf{g} \, d\Gamma \tag{78}$$

and $\mathbf{F}_Q$ is the force vector given by

$$\mathbf{F}_Q = -\frac{L_t}{n_t} \sum_{k=1}^{n_t} \overline{\mathbf{t}}_{\mathbf{x}_k}. \tag{79}$$

In the case of an interior node, it can be seen that matrix $\mathbf{G}_Q$ and vector $\mathbf{F}_Q$ are null. For a problem with a total of N nodes, the assembly of equations (76) for all M interior and static-boundary nodes generates the global system of $2M \times (2N + 2)$ equations

$$\mathbf{K}\, \hat{\mathbf{u}}^R + \mathbf{G}\, \mathbf{k} = \mathbf{F}. \tag{80}$$

On the kinematic boundary, the $N - M$ nodes are used to generate the remaining equations of the model, adding the kinematic boundary conditions of the regularized problem, equations (64). Thus, for a kinematic-boundary node, the boundary conditions of the regularized problem are enforced by a direct interpolation method as

$$\mathbf{u}_k^R = \mathbf{\Phi}_k\, \hat{\mathbf{u}}^R = \overline{\mathbf{u}}_k - \mathbf{u}_k^S = \overline{\mathbf{u}}_k - \mathbf{f}_k\, \mathbf{k}, \tag{81}$$

with $k = 1, 2$, where $\overline{\mathbf{u}}_k$ denotes the specified displacement component and $\mathbf{u}_k^S = \mathbf{f}_k\, \mathbf{k}$ is the displacement component of the particular singular solution, derived from equations (72). Equations (81) are written in the same form of equations (76), for a point Q, as

$$\mathbf{K}_{Q_k}\, \hat{\mathbf{u}}^R + \mathbf{G}_{Q_k}\, \mathbf{k} = \mathbf{F}_{Q_k}, \tag{82}$$

in which $\mathbf{K}_{Q_k}$ is now given by

$$\mathbf{K}_{Q_k} = \mathbf{\Phi}_k, \tag{83}$$

while $\mathbf{G}_{Q_k}$ is given by

$$\mathbf{G}_{Q_k} = \mathbf{f}_k \tag{84}$$

and $\mathbf{F}_{Q_k}$ is given by

$$\mathbf{F}_{Q_k} = \overline{\mathbf{u}}_k. \tag{85}$$

Local equations (82) are assembled into the global system of equations (80) which results in

$$\begin{bmatrix} \mathbf{K} & \mathbf{G} \end{bmatrix} \begin{bmatrix} \hat{\mathbf{u}}^R \\ \mathbf{k} \end{bmatrix} = \begin{bmatrix} \mathbf{F} \end{bmatrix}, \tag{86}$$

in which $\mathbf{K}$ is a matrix of the order $2N \times 2N$, $\mathbf{G}$ is a matrix of the order $2N \times 2$ and $\mathbf{F}$ is a vector of the order $2N$; the unknowns are the vector $\hat{\mathbf{u}}^R$, of the order $2N$, and the vector $\mathbf{k}$ of the order 2. Is important to highlight that this global system of equations introduce the SIF K_I and K_{II}, in the vector $\mathbf{k}$, as additional unknowns of the numerical problem. Hence, to end with a well-posed problem, additional constraint equations are necessary, , one for each mode considered in the analysis, in order to obtain a unique solution. These additional constraint are defined as two rows that goes into to the bottom of the system of equations (86).

Considering the regularized problem, the required additional constraints enforce the singularity cancellation. The regular displacement components or the regular stress components can be canceled out at the crack tip, that is

$$u_i^R = 0 \;\Rightarrow\; u_i = u_i^S, \tag{87}$$

or

$$\sigma_{ij}^R = 0 \;\Rightarrow\; \sigma_{ij} = \sigma_{ij}^S \tag{88}$$

which ensure that, at the crack tip, the initial problem is singular.

In order to be more effective, the additional constraints must be defined in terms of the unknown regularized MLS nodal parameters of $\hat{\mathbf{u}}^R$. Null displacement components are obtained from the use of conditions (87) at the crack tip, which can over-constrain the initial problem, because the singular displacement components, equations (69) and (70), do not include rigid-body terms. Thus, can not be used as the required additional constraints.

Conditions (88) can be redefined, in terms of the respective traction components at the crack tip, as

$$t_j^R = \sigma_{ij}^R n_i = 0 \;\Rightarrow\; t_j = t_j^S, \tag{89}$$

where n_i denotes the unit normal components of the crack faces, as represented schematically in Figure 12. After the MLS approximation, conditions (89), defined at the crack tip $\mathbf{x}_{tip}$, can be
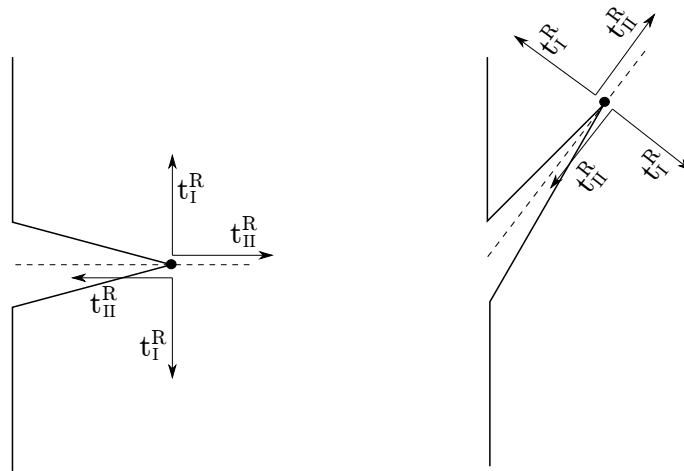
Figure 12: Crack tip tractions of the regularized elastic field.

defined as

$$\mathbf{t}_{\mathbf{x}_{tip}}^R = \mathbf{n}_{\mathbf{x}_{tip}} \mathbf{D}\, \mathbf{B}_{\mathbf{x}_{tip}}\; \hat{\mathbf{u}}^R = \mathbf{0}, \tag{90}$$

or

$$\mathbf{C}\, \hat{\mathbf{u}}^R = \mathbf{0}, \tag{91}$$

in which matrix $\mathbf{C}$ is written as

$$\mathbf{C} = \mathbf{n}_{\mathbf{x}_{tip}} \mathbf{D}\, \mathbf{B}_{\mathbf{x}_{tip}}. \tag{92}$$

Moreover, the additional constraints (92) can now be added into the global system of equations (86), leading to the final system of equations of the order $(2N + 2) \times (2N + 2)$

$$\begin{bmatrix} \mathbf{K} & \mathbf{G} \\ \mathbf{C} & \mathbf{0} \end{bmatrix} \begin{bmatrix} \hat{\mathbf{u}}^R \\ \mathbf{k} \end{bmatrix} = \begin{bmatrix} \mathbf{F} \\ \mathbf{0} \end{bmatrix}, \tag{93}$$

which can be solved without any inconsistency.

8   Numerical Results

Some numerical results are presented in this section to illustrate the accuracy and efficiency of the ILMF numerical formulation, under linear elastic problems and linear elastic fracture mechanics problems, on two-dimensional spaces. The results are compared with the analytical solution and the MLPG-5, presented by Atluri and Shen [2002], from now on refereed as MLPG; and for some

applications with the MLPG-FVM, introduced by Atluri et al. [2004] and the EFG, presented by Belytschko et al. [1994b].

For error estimation, important to measure the accuracy of numerical methods, displacement and energy L_2 norms can be used, respectively as

$$\|\mathbf{u}\| = \left[\int_\Omega \mathbf{u}^T \mathbf{u} \, \mathrm{d}\Omega\right]^{1/2} \tag{94}$$

and

$$\|\varepsilon\| = \left[\frac{1}{2}\int_\Omega \varepsilon^T \mathbf{D}\, \varepsilon \, \mathrm{d}\Omega\right]^{1/2}. \tag{95}$$

Moreover, the relative errors, respectively for $\|\mathbf{u}\|$ and $\|\varepsilon\|$ are given by

$$r_u = \frac{\|\mathbf{u}_{num} - \mathbf{u}_{exact}\|}{\|\mathbf{u}_{exact}\|} \tag{96}$$

and

$$r_\varepsilon = \frac{\|\varepsilon_{num} - \varepsilon_{exact}\|}{\|\varepsilon_{exact}\|}. \tag{97}$$

All the routines and numerical applications were compared when using MATLAB 2015a on an Intel Core I7-4700MQ computer with CPU of 2.4GHz and 16 GB of RAM.

8.1   Benchmark Problem 1 – Cantilever-Beam

First, consider a beam of dimensions $L \times D$ and of unit depth, subjected to a parabolic traction at the free end as shown in Figure 13.
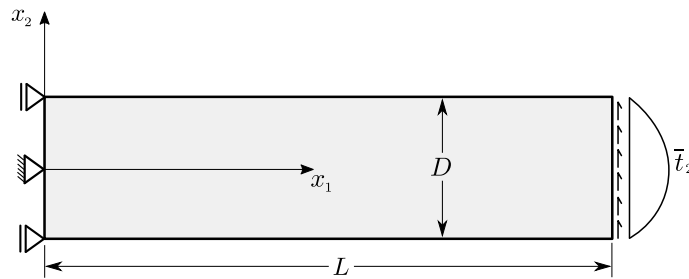
Figure 13: Timoshenko cantilever beam.

The beam is assumed in a plane stress state and the parabolic traction is given by

$$\bar{t}_2(x_2) = -\frac{P}{2I}\left(\frac{D^2}{4} - x_2^2\right), \tag{98}$$

where $I = D^3/12$ is the moment of inertia. The exact displacement components for this problem are given by

$$u_1(x_1, x_2) = -\frac{Px_2}{6EI}\left[(6L - 3x_1)x_1 + (2+\nu)\left(x_2^2 - \frac{D^2}{4}\right)\right] \tag{99}$$

and

$$u_2(x_1, x_2) = \frac{P}{6EI}\left[3\nu x_2^2(L - x_1) + (4 + 5\nu)\frac{D^2 x_1}{4} + (3L - x_1)x_1^2\right] \tag{100}$$

and the exact stress components are given by

$$\sigma_{11}(x_1, x_2) = -\frac{P(L - x_1)x_2}{I}, \quad \sigma_{12}(x_1, x_2) = -\frac{P}{2I}\left(\frac{D^2}{4} - x_2^2\right) \quad \text{and} \quad \sigma_{22}(x_1, x_2) = 0.$$
(101)

Material properties are taken as Young's modulus $E = 3.0 \times 10^7$ and the Poisson's ratio $\nu = 0.3$ and the beam dimensions are $D = 12$ and $L = 48$. The shear force applied is $P = 1000$. To solve this problem, a regular nodal distribution, represented in Figure 14, was considered with
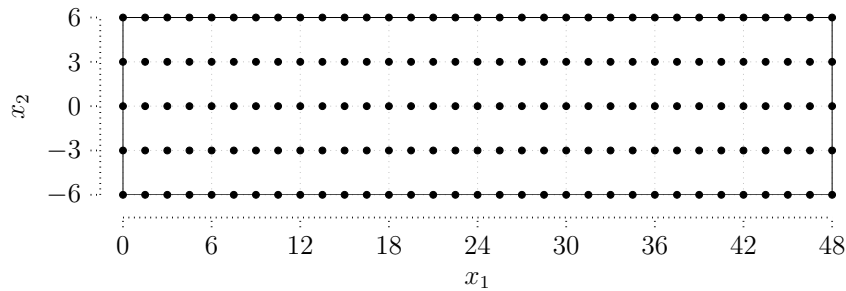
Figure 14: The regular nodal distribution of the cantilever-beam discretization with $33 \times 5 = 165$ nodes.

a nodal distribution of $33 \times 5 = 165$ nodes. The discretization parameters, α_s and α_q, need to be properly defined, through equations (44) and (45), in order to obtain a stable and accurate solution. for the applications presented in this first example, these parameters are heuristically defined as $\alpha_s = 3.0 \sim 4.5$ and $\alpha_q = 0.5 \sim 0.6$.

A first-order polynomial basis was considered in MLS approximation. Rectangular local domains Ω_q of each node were considered, with 1 point for ILMF integration and 10 Gauss-quadrature points to integrate the MLPG, placed along the sides of the local domain, as schematically represented in Figure 15.


(a) ILMF   (b) MLPG
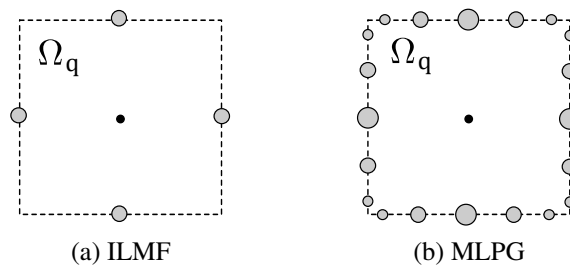
Figure 15: Integration points placed on each side of the local domain Ω_q, to compute the equilibrium equations of ILMF and MLPG.

8.1.1   Displacement and Stress

The displacements resulting from this analysis, represented in Figure 16, show very good agreement with the results of the analytical solution. Albeit this relatively coarse nodal configuration, relative errors of $r_u = 6.33 \times 10^{-4}$ and $r_\epsilon = 7.51 \times 10^{-5}$ were obtained with ILMF. Stresses, computed at the center of the beam that is $x_1 = L/2$ and $x_2 \in [-D/2, D/2]$, also present excellent agreement with the results of the exact solution, as shown in Figure 17.

(a) for $x_2 = 0$
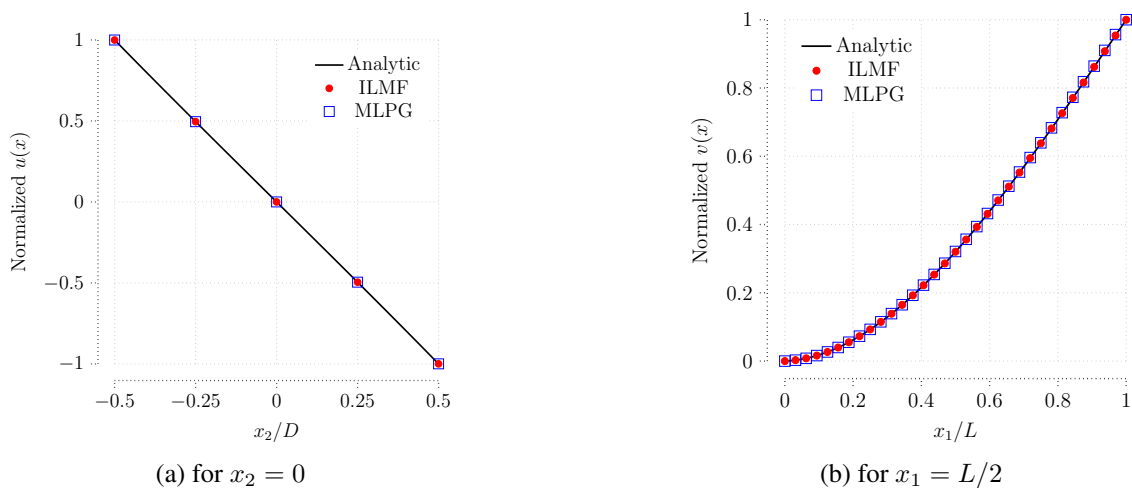
(b) for $x_1 = L/2$

Figure 16: Normalized displacements of the beam with nodal distribution of $33 \times 5 = 165$ nodes.
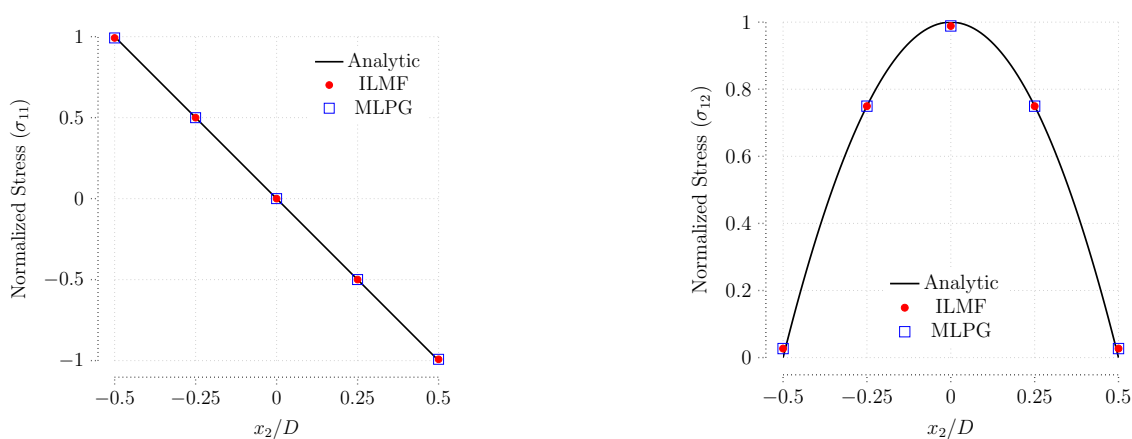
Figure 17: Stress distribution for $x_1 = L/2$ and $x_2 \in [-D/2, D/2]$ of the beam with nodal distribution of $33 \times 5 = 165$ nodes.
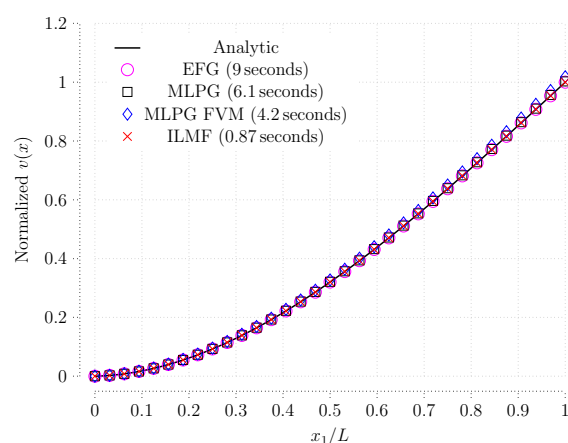
Figure 18: Normalized displacements of different mesh free methods, along with CPU time in seconds, for nodal distribution of $33 \times 5 = 165$ nodes.

When compared to other local mesh free methods, ILMF obtained a good accuracy and efficiency, as shown in Figure 18, where the processing time is also present. The EFG considered 10 Gauss-quadrature points on each background cell and the MLPG FVM considered 10 Gauss-quadrature points distributed on the local domain, for this application. In this initial performance analysis, the fastest computation is obtained with the ILMF, which is 21% faster than the MLPG FVM, the second best result.

8.1.2   Reduced Integration performance

One of the key advantages of ILMF is the reduced integration that differentiates it from other mesh free numerical methods. The linear reduced integration employed by ILMF consider only 1 point per segment of the local boundary. If necessary, additional integration points can be placed by subdividing a boundary segment in identical segments, which leads to equally-spaced integration points. for the general case, it is necessary to assess the performance of ILMF, driven by the location of integration points on each boundary of the local domain. Figure 19 shows the behavior
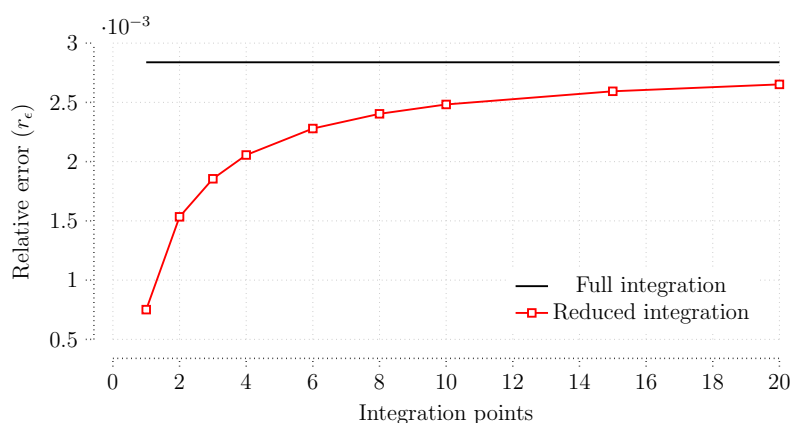

Figure 19: ILMF and MLPG relative error r_ϵ, as a function of the number of equally-spaced integration points, on each boundary of the respective local domain, for a regular distribution of $33 \times 5 = 165$ nodes.

of the relative error r_ϵ of ILMF, as a function of the number of integration points, for the nodal

distribution of $33 \times 5 = 165$ nodes; for comparison, the relative error of MLPG, computed with 10 Gauss points, is also plotted. It can be seen that the relative error of ILMF always monotonically converge for the relative error of MLPG with full integration. Physically, this means that the MLPG approximation always leads to stiffer models than the ones of the ILMF approximation. The minimum value of the error is always obtained for 1 collocation point. This is a very important result that evidences that ILMF linear reduced integration leads to better results than those obtained with the MLPG full integration.

Another test was required to assess the influence of the discretization on the accuracy of ILMF, regarding the number of integration points along the boundaries of the local domain. Therefore, four regular distributions of $13 \times 4 = 52, 65 \times 9 = 585, 97 \times 13 = 1261$ and $129 \times 17 = 2193$ nodes were considered. he results obtained for the ILMF relative error r_ϵ, as a function of the integration points are presented in Figure 20, where it can be seen that the accuracy of ILMF increases with
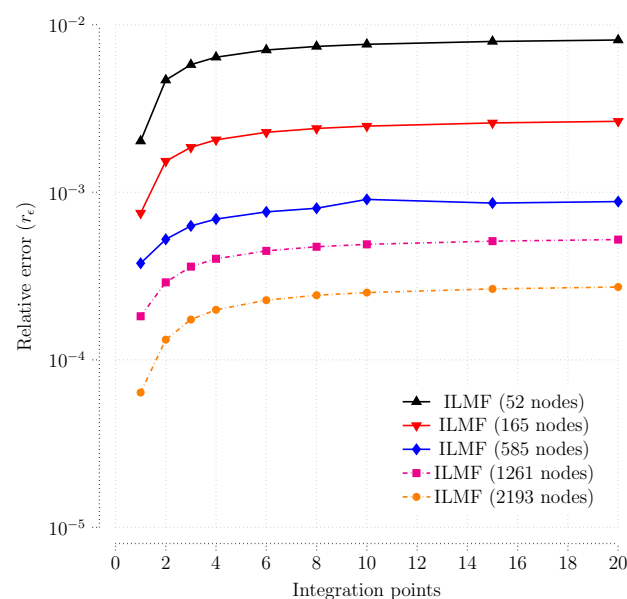

Figure 20: ILMF relative error r_ϵ, for beam discretizations with $13 \times 4 = 52$, $65 \times 9 = 585$, $97 \times 13 = 1261$ and $129 \times 17 = 2193$ nodes, as a function of the equally-spaced integration points, on the boundaries of the respective local domain.

the total number of nodes of the discretization, as expected. Effectively, the overall relative error of ILMF decreases with finer nodal distributions, requiring only one integration point along each boundary to obtain the most accurate results. This is a very important result that evidences that ILMF is a very efficient method.

The accuracy of the proposed method when considering higher order polynomial basis need to be addressed, hence another test was carried out. For this case, three regular distributions of $13 \times 4 = 52, 33 \times 5 = 165$ and $65 \times 9 = 585$ nodes were considered. The results, presented in Figure 21 clearly evidence the accuracy of the reduced integration even for high-order polynomial basis, providing a stable convergence rate regardless of the polynomial basis.

8.1.3   Irregular Nodal Distributions

Irregularity on a nodal distribution can be introduced into a regular distribution by randomly changing nodal coordinates, within a local domain of integration. This procedure, referred to as level-1 of irregularity, can be addressed through an arbitrary variable c_n that varies in the range from 0.0 to 0.4, where $c_n = 0.4$ corresponds to a maximum irregularity, as seen in Liu [2003].
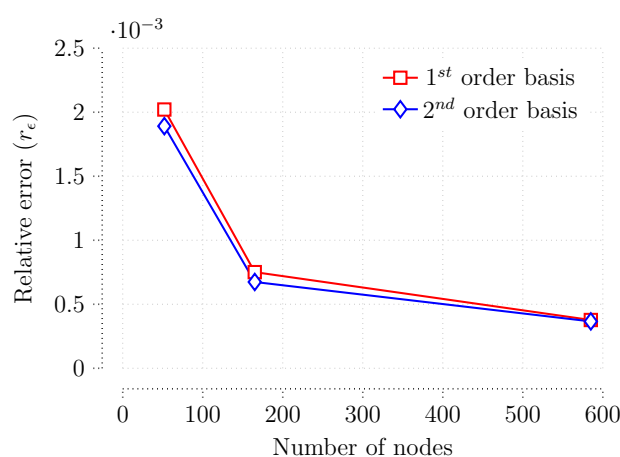
Figure 21: ILMF relative error r_ϵ for the beam modal distribution of $13 \times 4 = 52$, $33 \times 5 = 165$ and $65 \times 9 = 585$ nodes, as a function of the number of nodes, considering a complete set of first and second order polynomial basis for the MLS approximation.

Irregularity of a nodal distribution can greatly affect the solution accuracy, since it has a direct influence in the size of the compact support α_s and the size of the local integration domain α_q. If the distance between nodes is too large, the support regions around each node do not intersect with each other, thus providing no output. In the other extreme, if the distance between nodes is too small, too many nodes are crammed, thus losing the local character of the approximation. For this specific example, these parameters are heuristically defined as $\alpha_s = 2.11$ and $\alpha_q = 0.5$.

Three nodal distributions of the beam discretization, with 189 nodes and level-1 of irregularity, with two different irregularity configurations, regarding the boundary nodes, are presented in Figure 22. In configuration A, only interior nodes have an irregular distribution, as presented by Liu [2003], while in configuration B, all nodes are irregularly distributed. Results for this level-1 irregularity are presented in Figure 23, where it can be seen that ILMF obtained stable results with a high accuracy, even for mild irregular nodal distributions.
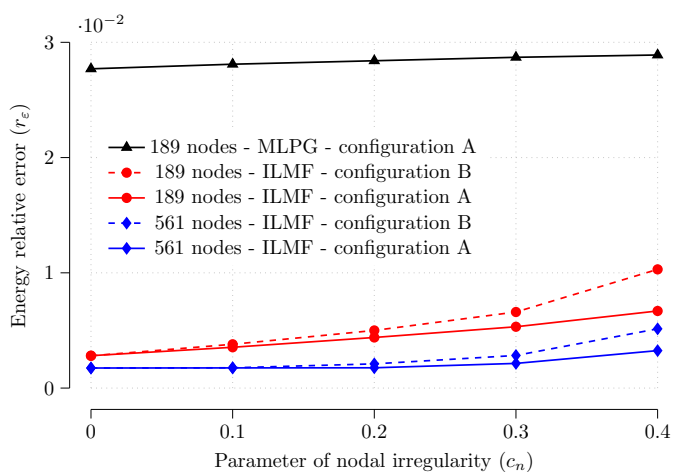
The generation of nodal distributions with severe irregularity are divide in two major steps. First, the coordinates of a nodal regular distribution are randomly changed, allowing each node to move outside the respective local domain of integration. Second, each local domain is regenerated, in order to include the new location of the respective node, by considering the middle of the distance between the node and its neighboring nodes. This procedure, referred to as level-2 of irregularity, can be addressed through an arbitrary variable c_n that now varies in the range from 0.0 to 0.9, where $c_n = 0.9$ corresponds to a maximum irregularity, as seen in Liu [2003].Figure 24 represent three nodal distributions of the beam discretization, with 55 and 189 nodes with irregularity of level-2 for interior nodes. Due to the high irregularity, $\alpha_s = 12.00$ was considered for this case.

Figure 25 show the results obtained for irregular nodal distributions of level-2, preserving the high accuracy level obtained by ILMF. These results demonstrate that high irregularities require higher values for parameter α_s, in order to keep the accuracy of results. The results show that ILMF is a reliable mesh free numerical model, since even with nodal distributions with severe irregularities, the solution is still accurate.
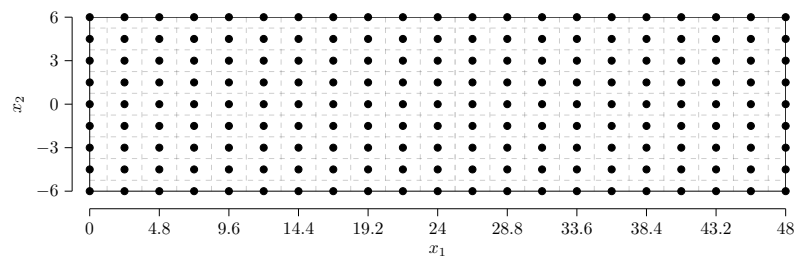
(a) $c_n = 0.0$
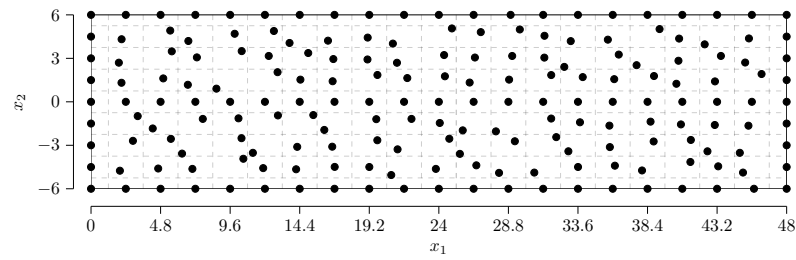
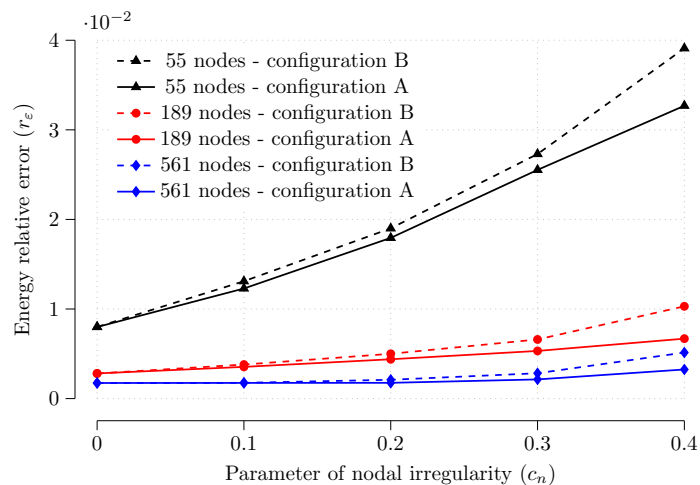
(b) $c_n = 0.4$, configuration A
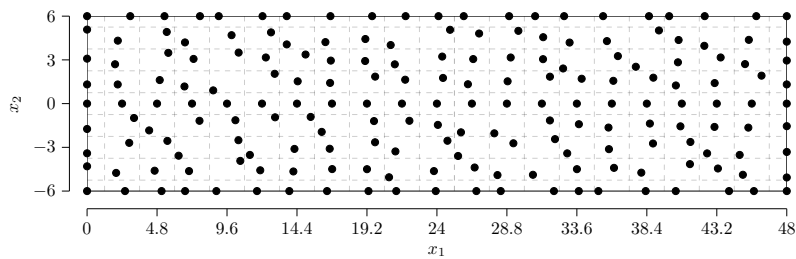
(c) $c_n = 0.4$, configuration B

Figure 22: Nodal distributions of the beam discretization with 189 nodes and level-1 of irregularity.

(a) ILMF and MLPG

(b) ILMF

Figure 23: ILMF and MLPG energy error, as a function of the irregularity parameter c_n, obtained with irregular nodal distributions with 189 and 561 nodes of the beam discretization.
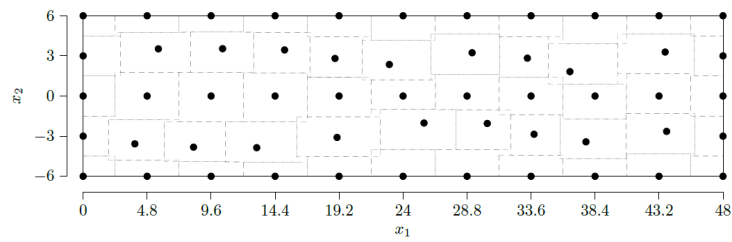
(a) 55 nodes with $c_n = 0.4$
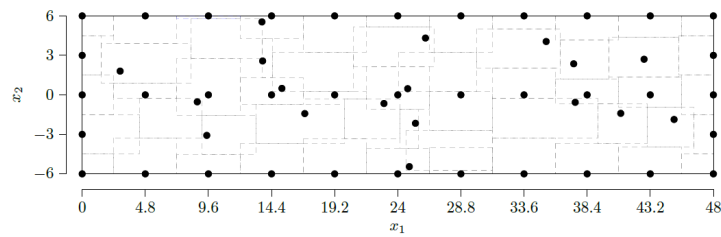
(b) 55 nodes with $c_n = 0.8$
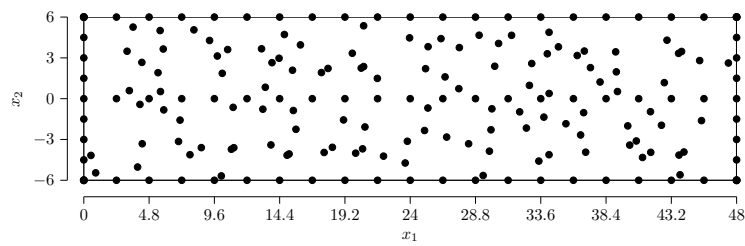
(c) 189 nodes with $c_n = 0.8$

Figure 24: Nodal distributions of the beam discretization, with 55 and 189 nodes with level-2 irregularity.

(a) Level-1 and level-2 irregularities

(b) ILMF with level-2 irregularities

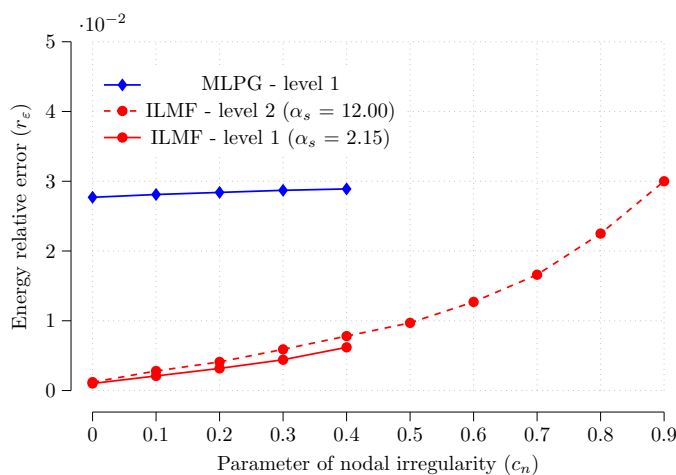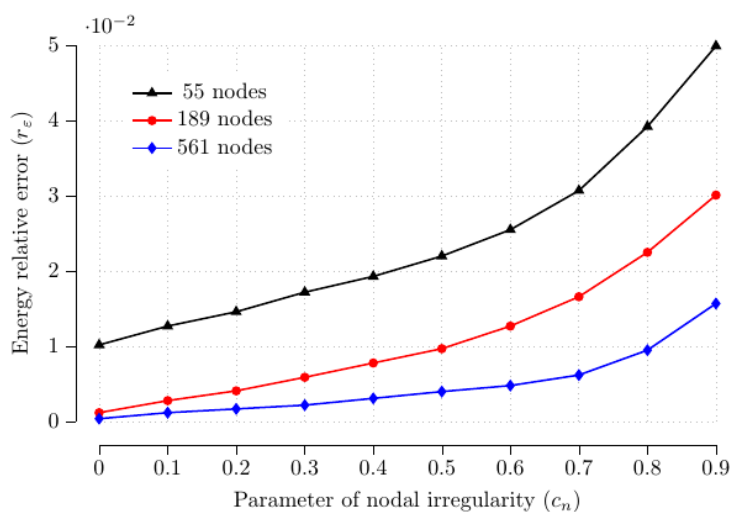**Figure 25: Energy relative error of ILMF and MLPG, as a function of the irregularity parameter c_n, obtained with irregular nodal distributions of the beam discretization.**

8.1.4   Automatic Parameter Optimization

Several optimization schemes are presented with different objective functions. In the end, the ultimate optimization approach computes automatically the ILMF discretization parameters, α_s and α_q, in a very efficient way.

In the first scheme, GA is implemented in order to minimize the CPU time and the relative error r_ε and r_u, defined as objective functions for this approach. Tha main goal is to asses the performance of the optimization process related to the accuracy and the computational effort. Only the major computational cost that is the cost of generating and solving the global system of algebraic equations, was measured. The decision variables, α_s and α_q, are defined as continuous in the intervals, respectively

$$\alpha_s = [1.1 \ 10] \quad and \quad \alpha_q = [0.1 \ 0.9]. \tag{102}$$

There is a strong relationship between the objective functions and the decision variables. This means that by choosing different values for the design variables, α_s and α_q, we can change the output in the objective functions CPU time, r_ε and r_u, during a msh free numerical analysis.

The initial population is 20 individuals, randomly generated. Then, the fitness function is evaluated for each individual and scaled using a rank process, to be later used in the selection process. The reproduction operator is implemented based on a tournament selection, with constraint dependent mutation and crossover. The optimization process is terminated if the number of generations exceeds 100, or if the average change in fitness function is less than 1×10^{-6}.

The results obtained for this first multi-objective optimization process are presented in Figure 26, for the first two objective functions, and Tables 1 to 3;

Table 1: The multi-objective Pareto front results for the regular nodal distribution of 52 nodes.

Index	CPU Time(s)	r_ε	r_u	α_s	α_q
1	0.2513	0.06615	0.06682	1.3628	0.4930
2	0.6347	1.413E-5	4.772E-4	3.9200	0.506
3	0.6437	7.194E-4	4.211E-4	3.7666	0.5109
4	0.2507	0.2327	0.2531	1.3818	0.5067

Table 2: The multi-objective Pareto front results for the regular nodal distribution of 165 nodes.

Index	CPU Time (s)	r_ε	r_u	α_s	α_q
1	3.7081	6.557E-5	2.009E-7	5.2789	0.5138
2	3.6090	1.336E-7	7.075E-5	5.2775	0.5137
3	3.6585	5.171E-5	1.552E-5	5.2788	0.5139

all the presented points are considered optimum from a computational point of view and non-dominated to each other, see Eberhart and Shi [2007]. For each point of the Pareto front, a couple of optimized parameters α_s and α_q are presented. As it can be seen, the optimization can lead to very accurate and convergent results. Moreover, the results show that α_s is constantly changing when different nodal distributions are considered, usually steadily increasing when more nodes are added to the model discretization, even though for α_q the best results are always obtained for values close to 0.5, regardless of the nodal distribution used.

This approach has one major drawback that is extremely high computational effort required, which could take hour, or days, depending on the number of nodes, even when running in parallel.
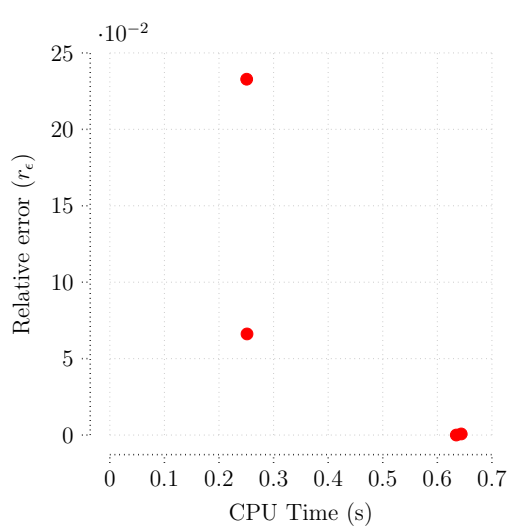
(a) Regular nodal distribution of 52 nodes.
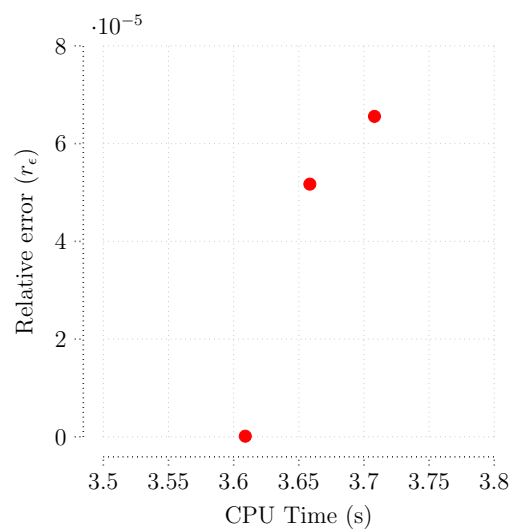
(b) Regular nodal distribution of 165 nodes.
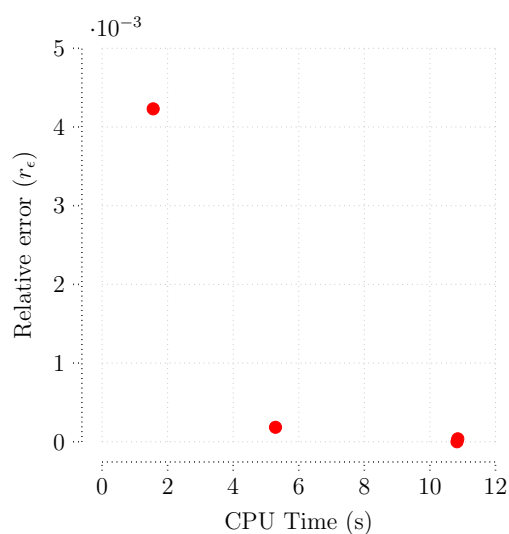
(c) Regular nodal distribution of 585 nodes.

Figure 26: The multi-objective Pareto front for regular nodal distributions of the beam discretization, considering CPU time, r_ε and r_u as objective functions; only the first two are graphically presented.

Table 3: The multi-objective Pareto front results for the regular nodal distribution of 585 nodes.

Index	CPU Time (s)	r_ε	r_u	α_s	α_q
1	10.8267	6.190E-10	0.0001	7.2685	0.4971
2	5.2903	0.0002	1.314E-07	4.2103	0.4971
3	10.8503	3.733E-05	6.978E-05	7.2686	0.4973
4	1.5595	0.0042	0.0046	1.7677	0.4995

Another major drawback is analytical solution requirement, which is necessary to compute the relative error and is not available for more complex problems. Both drawbacks are unacceptable and require a more efficient approach, such as the one presented by the end of this section.

In the second optimization scheme, the compliance indicator, also known as flexibility indicator, derived from the local work theorem and computed only on the static boundary Γ_t, is chosen as objective function. CPU time is added as a objective function to control the analysis efficiency. Figures 27 to 29 demonstrate the behavior of the compliance indicator C and the relative energy
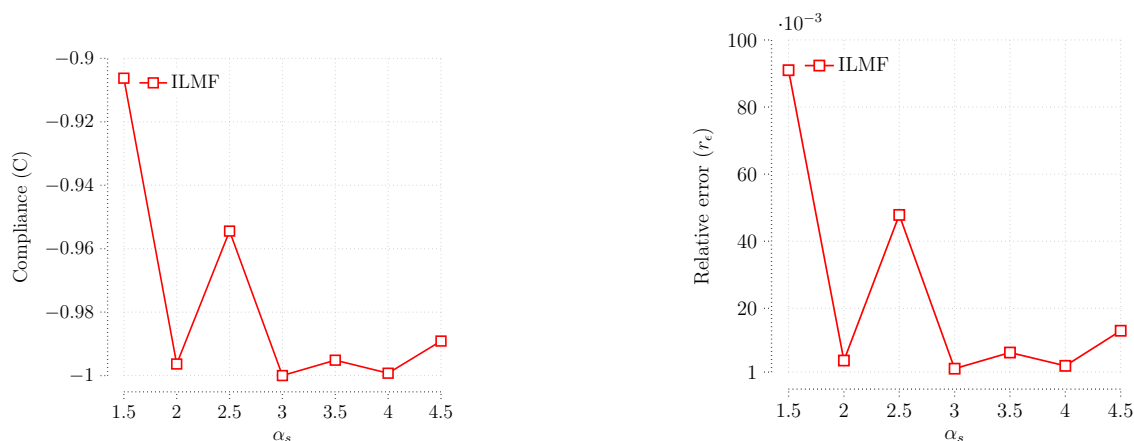
Figure 27: Compliance and relative error r_ε of the beam discretization with $13 \times 4 = 52$ nodes, as function of α_s and for a fixed $\alpha_q = 0.5$.

error r_ε, function of α_s and a fixed $\alpha_q = 0.5$. Both parameters showed to have a similar behavior, thus proving that C can be effectively used instead of r_ε. Furthermore, the computational effort required to perform the analysis is about 15 times faster for the compliance.

Consequently, for this second optimization approach, the GA is implemented in order to minimize the objective functions CPU time and the compliance indicator C. The decision variable α_s is defined as continuous in the interval

$$\alpha_s = [1.5 \ 10]. \tag{103}$$

The initial population is 20 individuals, randomly generated. Then, the fitness function is evaluated for each individual and scaled using a rank process, to be later used in the selection process. The reproduction operator is implemented based on a tournament selection, with constraint dependent mutation and crossover. The optimization process is terminated if the number of generations exceeds 100, or if the average change in fitness function is less than 1×10^{-6}.

The results obtained with the multi-objective optimization process are presented in Figure 26 and Tables 4 to 6, for a fixed $\alpha_q = 0.5$. From the results, it can be seen that all points in the Pareto front obtained a good accuracy, regardless of the nodal distribution. Once more, the convergence

Figure 28: Compliance and relative error r_ε of the beam discretization with $33 \times 5 = 165$ nodes, as function of α_s and for a fixed $\alpha_q = 0.5$.
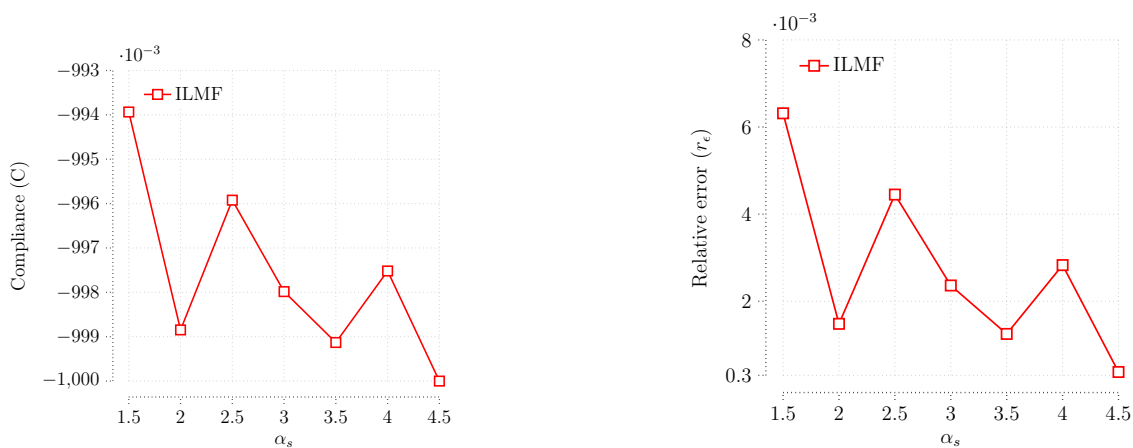
Figure 29: Compliance and relative error r_ε of the beam discretization with $65 \times 9 = 585$ nodes, as function of α_s and for a fixed $\alpha_q = 0.5$.
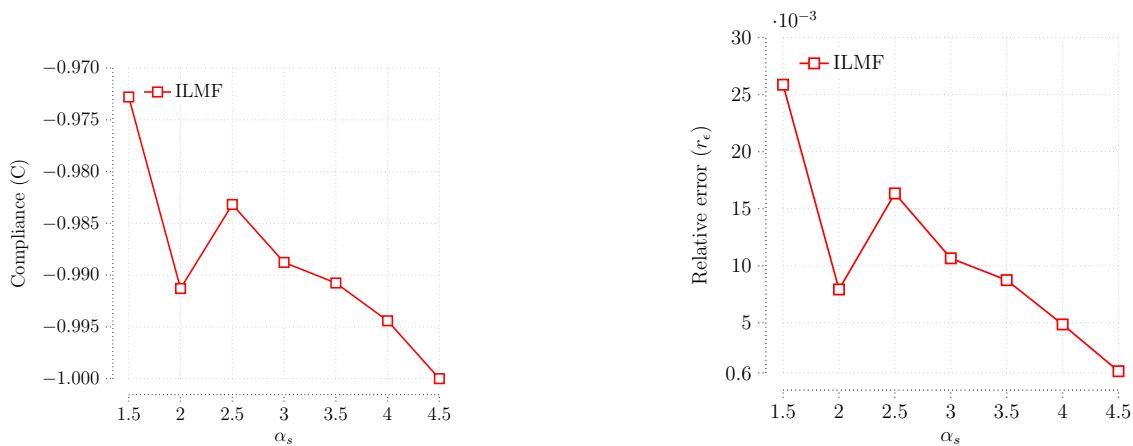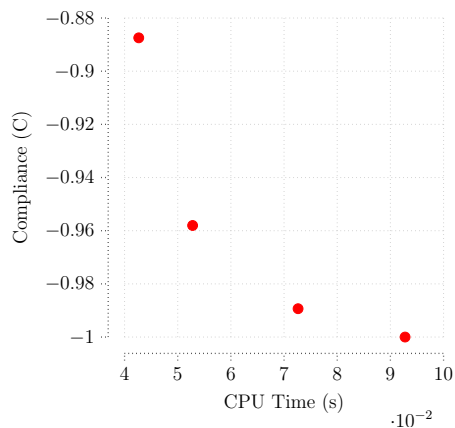
(a) Regular nodal distribution of 52 nodes.
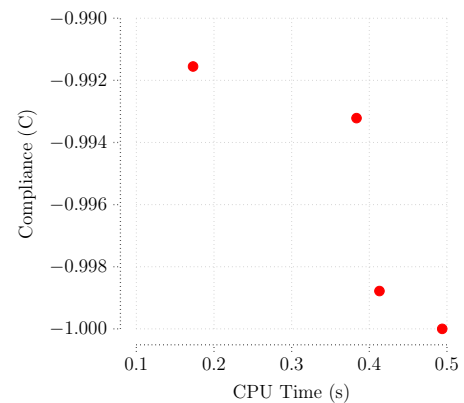
(b) Regular nodal distribution of 165 nodes.
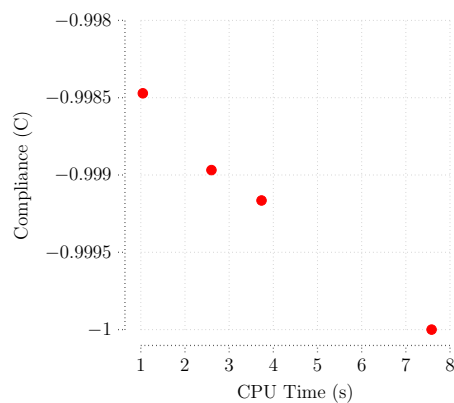
(c) Regular nodal distribution of 585 nodes.

Figure 30: The multi-objective Pareto front for regular nodal distributions of the beam discretization with $13 \times 4 = 52$, $33 \times 5 = 165$ and $65 \times 9 = 585$ nodes, considering CPU time and compliance indicator as objective functions; for a fixed $\alpha_{\mathbf{q}} = 0.5.$

Table 4: The multi-objective Pareto front results for the regular nodal distribution of 52 nodes and a fixed $\alpha_{\mathbf{q}} = 0.5$

Index	CPU Time (s)	Compliance	$\mathbf{r}_\varepsilon$	$\mathbf{r_u}$	$\alpha_{\mathbf{s}}$
1	0.0427	-0.887	0.0993	0.1069	1.3585
2	0.0923	-1	0.0051	0.0042	3.1515
3	0.0726	-0.989	0.0044	0.0067	2.0053
4	0.0528	-0.958	0.0346	0.0373	1.7414

Table 5: The multi-objective Pareto front results for the regular nodal distribution of 165 nodes and a fixed $\alpha_{\mathbf{q}} = 0.5$

Index	CPU Time (s)	Compliance	$\mathbf{r}_\varepsilon$	$\mathbf{r_u}$	$\alpha_{\mathbf{s}}$
1	0.4131	-0.9987	6.660E-04	5.510E-04	4.4932
2	0.4940	-1	0.0019	0.0017	4.7085
3	0.1730	-0.9915	0.0064	0.0066	1.8935
4	0.3835	-0.9932	0.0049	0.0050	3.9966

Table 6: The multi-objective Pareto front results for the regular nodal distribution of 585 nodes and a fixed $\alpha_{\mathbf{q}} = 0.5$

Index	CPU Time (s)	Compliance	$\mathbf{r}_\varepsilon$	$\mathbf{r_u}$	$\alpha_{\mathbf{s}}$
1	2.5991	-0.9989	4.022E-04	3.821E-04	4.4965
2	3.7328	-0.9991	2.040E-04	1.883E-04	4.5330
3	1.0455	-0.9984	8.209E-04	8.768E-04	1.8733
4	7.5833	-1	6.614E-04	6.352E-04	9.6232

is guaranteed, meaning that an increase in the overall number of nodes of the nodal distribution also increases the overall accuracy. Although the lowest relative error is not always obtained with the lowest compliance indicator, this is barely a problem since the local Pareto-optimal is always close to the global Pareto-optimal, leading to very good results for all points. The aforementioned reduced computational effort is also present in this analysis, as expected, performing computations in minutes instead of hours.

For a complete optimization of mesh free parameters, α_q also need to be addressed. The shortest and most convenient approach is to guarantee that the total area of the local weak form domain is as similar as possible to the overall area of the whole body domain. Hence, the output area of the local domain, equation (49), is chosen as an objective function for this optimization. For the sake of simplicity, a single-objective optimization is performed. If a problem has N nodes in total, the design variable α_q is a vector containing N components defined as continuous in the interval

$$\alpha_q = [0.495 \ 0.95], \tag{104}$$

to ensure the locality of the MLS approximation and that the local sub-domains of the internal nodes are entirely within the solution domain, without being intersected by the global boundary.

The initial population is 200 individuals, randomly generated. Also, random populations from previous analysis within the optimization process are introduced randomly to increase the computational efficiency. Then, the fitness function is evaluated for each individual and scaled using a rank process, to be later used in the selection process. The reproduction operator is implemented based on a stochastic uniform selection, with constraint dependent mutation and crossover. The optimization process is terminated if the number of generations exceeds predefined values, or if the average change in fitness function is less than 1×10^{-6}.

Figure 31 presented the results of the single-objective optimization, as function of different
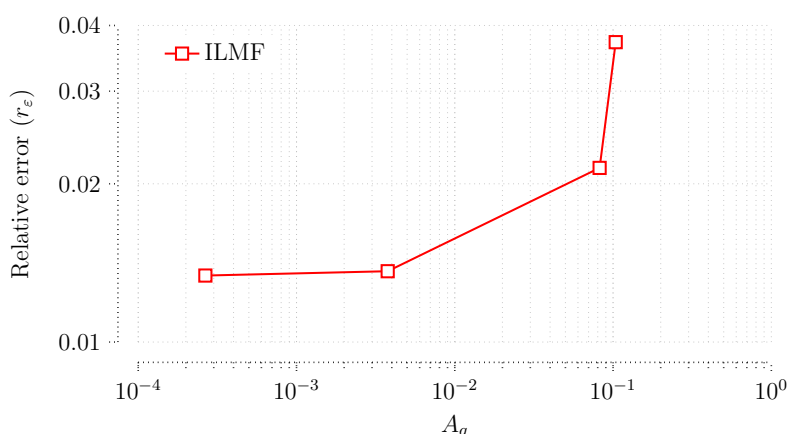
Figure 31: Relative energy error of ILMF as function of the local sub-domain of integration area A_q, for the regular nodal distribution of 165 nodes.

predefined maximum number of generations in the algorithm stopping criteria, considering 100, 200, 400 and 800 generations, for a fixed $\alpha_s = 4.5$. The accuracy gradually improves as A_q converge to the area of the posed problem.

Note that the computational effort of this analysis is also very low, thus leading to fast results. This is mostly due to the introduction of random populations from previous analysis. The first analysis, preferably from a smaller nodal distribution, can be performed really fast and the population used saved in MATLAB internal memory. Later, now for a greater nodal distributions, the optimization will run faster since it will use random feasible results from the previous analysis, accelerating the whole process.

Lastly, this final optimization approach combines the features of the previous optimization schemes into a single fully automated routine to compute ILMF discretization parameters α_s and α_q, preserving the presented effectiveness.

This last optimization is divided in two steps. First, α_q is optimized using A_q as objective function. The output of this process is a vector containing one value of α_q for each node in the nodal distribution. Second, α_s is optimized using compliance C and CPU time as objective functions, considering the results obtained in the previous optimization.

The results obtained from the automated multi-objective optimization are presented in Figure 32 and Tables 7 to 9, in which all of the presented points in the Pareto front are feasible,

Table 7: Pareto front of the multi-objective optimization for the regular nodal distribution of 52 nodes using the automatic parameters optimization routine.

Index	CPU Time (s)	Compliance	r_ε	r_u	α_s
1	0.0495	-0.942	0.0495	0.0522	1.6919
2	0.0773	-0.990	0.0046	0.0051	2.9747
3	0.0821	-1	0.0052	0.0043	3.1443
4	0.0649	-0.984	0.0091	0.0117	1.9415
5	0.0507	-0.959	0.0091	0.0117	1.7464

non-dominated and optimum, from a computational perspective. The results are a clear evidence of the accuracy and efficiency of the automated routine, effectively combining the aforementioned features into a single process.

In order to present the efficiency of the optimization process, regardless of the optimization technique, GA and SOS algorithms are compared. Thus, similar settings and stopping criteria
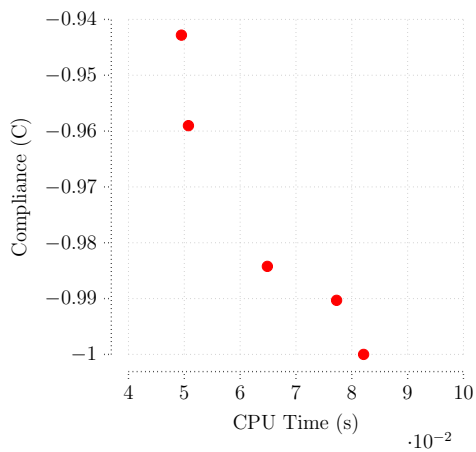
(a) Regular nodal distribution of 52 nodes.
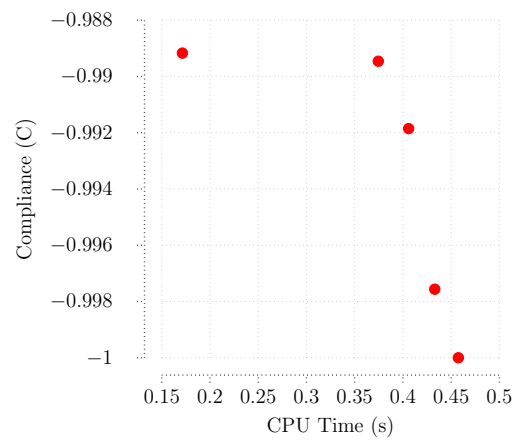
(b) Regular nodal distribution of 165 nodes.
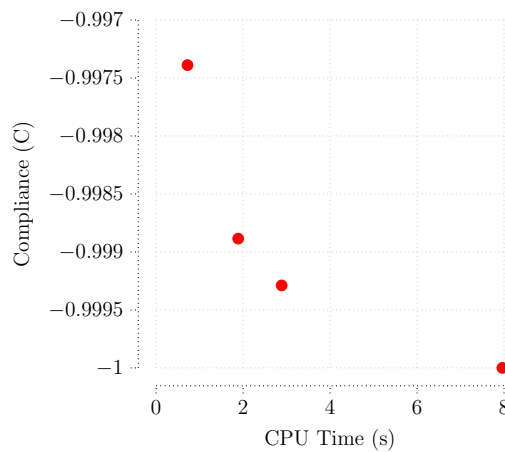
(c) Regular nodal distribution of 585 nodes.

Figure 32: The multi-objective Pareto front for regular nodal distributions of the beam discretization with the automatic parameters optimization routine.

Table 8: Pareto front of the multi-objective optimization for the regular nodal distribution of 165 nodes using the automatic parameters optimization routine.

Index	CPU Time (s)	Compliance	r_ε	r_u	α_s
1	0.3744	-0.9894	0.0083	0.0083	3.8145
2	0.4575	-1	0.0023	0.0022	4.6639
3	0.1713	-0.9891	0.0084	0.0087	1.9470
4	0.4330	-0.9975	1.281E-04	1.980E-04	4.3474
5	0.4059	-0.9918	0.0059	0.0059	3.9606

Table 9: Pareto front of the multi-objective optimization for the regular nodal distribution of 585 nodes using the automatic parameters optimization routine.

Index	CPU Time (s)	Compliance	r_ε	r_u	α_s
1	0.7201	-0.997	0.0016	9.535E-04	1.5
2	2.8858	-0.999	1.660E-04	2.557E-04	4.5010
3	1.8870	-0.998	2.463E-04	6.637E-05	3.4838
4	7.9617	-1	9.110E-04	9.074E-04	9.5744

were defined for both of them. Because SOS is a parameter-free optimization method, only the population size and the maximum number of function evaluations were defined, for this case as 20 and 100, respectively. Both algorithms stop if the average change in fitness function is less than 1×10^{-6} or the maximum number of function evaluations or generations is reached.

The compliance C is chosen as the objective function, for a fixed scalar $\alpha_q = 0.5$. The decision variable α_s is defined as continuous in the interval

$$\alpha_s = [1.5 \ 10]. \tag{105}$$

The comparison is presented in Figure 33, based on the number of generations or function it-
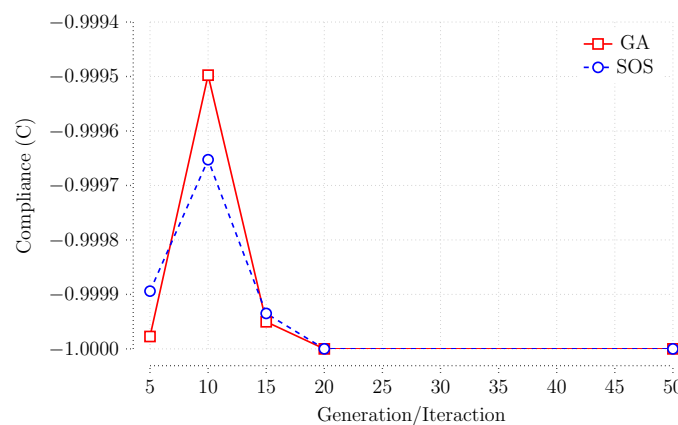
Figure 33: Comparison between GA and SOS relative to the maximum number of generations/iterations.

erations, and Table 10, where the optimization efficiency of both techniques can be seen. Note that GA is slightly less efficient than SOS. Nevertheless, the values of α_s obtained on both approaches are very similar, close to the ones previously obtained and therefore leading to very accurate results. SOS as a computational cost higher than GA due to the efficiency of the genetic operators that are refined for this type of problem.

Table 10: The comparative analysis of GA and SOS, for a single-objective optimization of the cantilever beam. C and OCE stands for structural compliance and optimization computational effort, respectively.

Nodes	SOS			GA		
	C	OCE (s)	$\alpha_{\mathbf{s}}$	C	OCE (s)	$\alpha_{\mathbf{s}}$
52	-0.999993	7.05	3.156	-1	5.94	3.151
165	-0.981476	52.28	4.705	-0.981477	26.48	4.708
585	-0.962864	144.40	9.631	-0.962865	127.70	9.623

The simplicity is a key advantage provided by the SOS optimization, which requires only 2 parameters to be set, in contrast to the GA optimization that requires a lot more parameters. Even though SOS is a very promising optimization algorithm, there is a set of libraries and optimization option on MATLAB environment for GA that are not yet available for SOS.

8.2   Benchmark Problem 2 – Plate with a Circular Hole

On this example, an infinite plate with a centered circular hole under unidirectional unit tension along the x_1 direction is analyzed, as portrait in Figure 34. The symmetry of the problem about
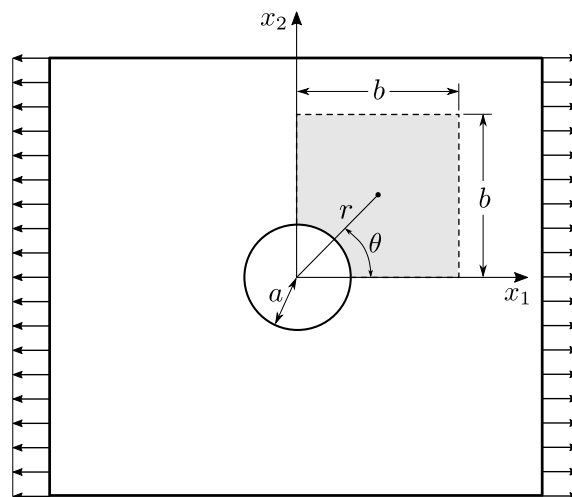
Figure 34: Plate with a hole.

the horizontal and the vertical axes allow the use of only a portion of the upper right quadrant of the plate. The section has dimensions $b \times b$ and the center circle has a radius $a = 1$, with $b = 5a$.

The analytical stress distribution in the plate is

$$\sigma_{11}(r, \theta) = 1 - \frac{a^2}{r^2} \left(\frac{3}{2} \cos 2\theta + \cos 4\theta \right) + \frac{3}{2} \frac{a^4}{r^4} \cos 4\theta$$

$$\sigma_{22}(r, \theta) = -\frac{a^2}{r^2} \left(\frac{1}{2} \cos 2\theta - \cos 4\theta \right) - \frac{3}{2} \frac{a^4}{r^4} \cos 4\theta \qquad (106)$$

$$\sigma_{12}(r, \theta) = -\frac{a^2}{r^2} \left(\frac{1}{2} \sin 2\theta + \sin 4\theta \right) + \frac{3}{2} \frac{a^4}{r^4} \sin 4\theta,$$

where r and θ are the usual polar coordinates, centered at the center of the hole. A plane-stress

state is considered, which leads to displacements

$$
\begin{aligned}
u_1(r,\theta) &= -\frac{\cos\theta}{2r^3 E}\left[4a^4\cos^2\theta\,(1+\nu)\left(1-r^2\right)-3a^4(1+\nu)+(ar)^2(1-3\nu)-2r^4\right] \\
u_2(r,\theta) &= -\frac{\sin\theta}{2r^3 E}\left[4a^4\cos^2\theta\,(1+\nu)\left(1-r^2\right)-a^4(1+\nu)+(ar)^2(\nu-3)+2r^4\nu\right].
\end{aligned}
\tag{107}
$$

In the bottom and left edges of the plate are defined as kinematic boundaries, with displacements $u_2(x_1, x_2 = 0)$ specified on the bottom and $(u_1(x_1 = 0, x_1 = L, x_2) = 0)$ specified on the left edges. For the right and top edges, static boundaries are assumed, with tractions computed from the stresses of the analytical solution (106) applied as $t_j = \sigma_{ij}n_i$, in which n_i represents the components of the unit outward normal to the edge of the plate. Young's modulus $E = 1.0 \times 10^5$ and the Poisson's ratio $\nu = 0.25$ are considered.

In order to solve this plate, discretization with 9 nodes in the tangential direction and 15 nodes in the radial direction, distributed as shown in Figure 35, with circular local domains and second
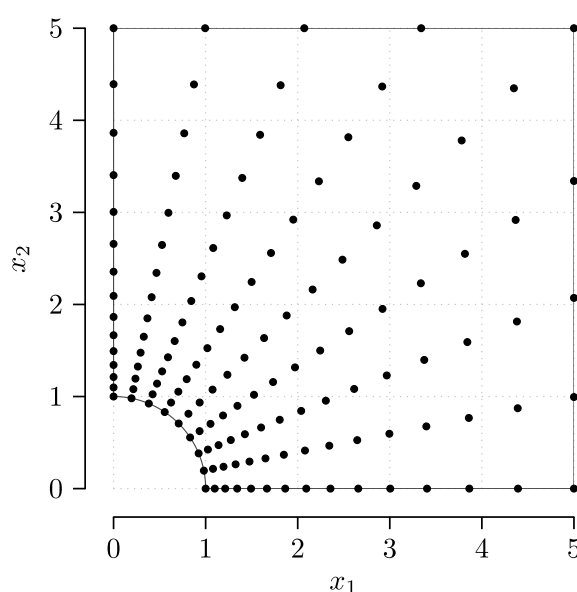
Figure 35: Discretization of the plate with a hole.

order polynomial basis for the MLS approximation. ILMF integration was performed with 1 point at the boundary of each quadrant of the circular integration domain, as schematically represented in Figure 7.

The computed displacements are shown in Figure 36, where it can be seen a very good agreement with the results of the analytical solution. The stresses at nodes also provided very good outputs when compared to the exact solution, as shown in Figure 37.

Relative errors of $r_u = 9.2 \times 10^{-3}$ and $r_\epsilon = 4.1 \times 10^{-3}$ were obtained for this simple discretization, which highlight the versatility of ILMF.

8.3   Benchmark Problem 3 – Edge-Cracked Plate

This benchmark problem presents the direct evaluation of SIF, through the SST implemented in the ILMF model, an efficient and accurate tool for the analysis of cracked plates. For this analysis, two problems of edge-cracked square plates, respectively under mode-I and mode-II loadings are presented; and a third case of a square plate with an edge slant crack, under mixed-mode deformation, is also presented.
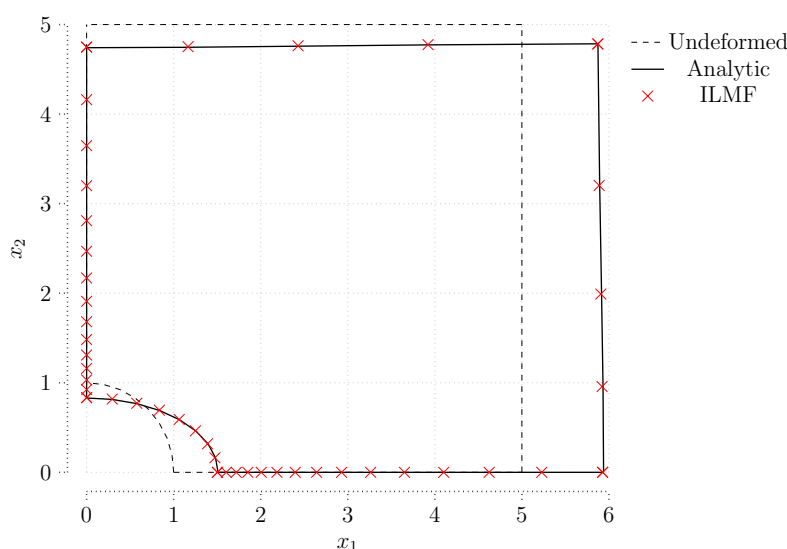
Figure 36: Boundary displacements of the plate with a hole.

The presence of the crack in a mesh free model requires a special treatment of the non-convex domain resulting from the crack discontinuity. Crack faces are modeled with two sets of overlapping nodes, in a way that the nodes of each line have influence only in the respective side, shared by a single crack tip with influence in both sides of the crack. For each node within the crack, the visibility criterion is used to define the compact support, as represented in Figure 38. Therefore, for nodes within the crack faces, the compact support and the local integration domain are defined as in the case of a traction-free boundary node. However, for the crack tip node, the compact support is defined as in the case of an interior node, while for the local integration domain the size as half of the case of the interior nodes.

Matrices g and f, containing the William's singular solution at each crack tip, equations (71) and (72) respectively, are computed with 3 Gauss quadrature points.

The DBEM with the J-integral (J-DBEM), presented by Portela and Aliabadi [1993], is used to compare the results obtained with ILMF formulation. The DBEM modeling strategy considers piecewise-straight cracks that are discretized with straight discontinuous quadratic boundary elements. Continuous quadratic boundary elements are used along the remaining boundaries of the problem, except at the intersection between a crack and an edge, where semi-discontinuous boundary elements are used on the edge. Self-point discontinuous boundary elements are integrated analytically, while Gaussian quadrature, with sub-element integration, is carried out for the remaining integrations.

In the ILMF numerical model, rectangular local domains of integration, with discretization parameters $\alpha_s = 1.5 \sim 3$ and $\alpha_q = 0.5$ are considered. The MLS approximation with first-order polynomial basis and quartic spline weighting function are also considered.

8.3.1 Mode-I Loading

First, a square edge-cracked plate, represented in Figure 39, is considered for the analysis, in which a denote the length of the crack, w the width of the plate and the height by $h = w/2$. The uniform traction $\bar{t} = \sigma$ is applied at the plate, symmetrically at the ends. In order to compare the ILMF accuracy with the highly accurate values reported by Civelek and Erdogan [1982], $h/w = 0.5$ is considered on this problem. Five cases are presented, for $a/w = 0.2, 0.3, 0.4, 0.5$ and 0.6. The nodal distribution used in the analysis is represented in Figure 40, with a regular nodal distribution
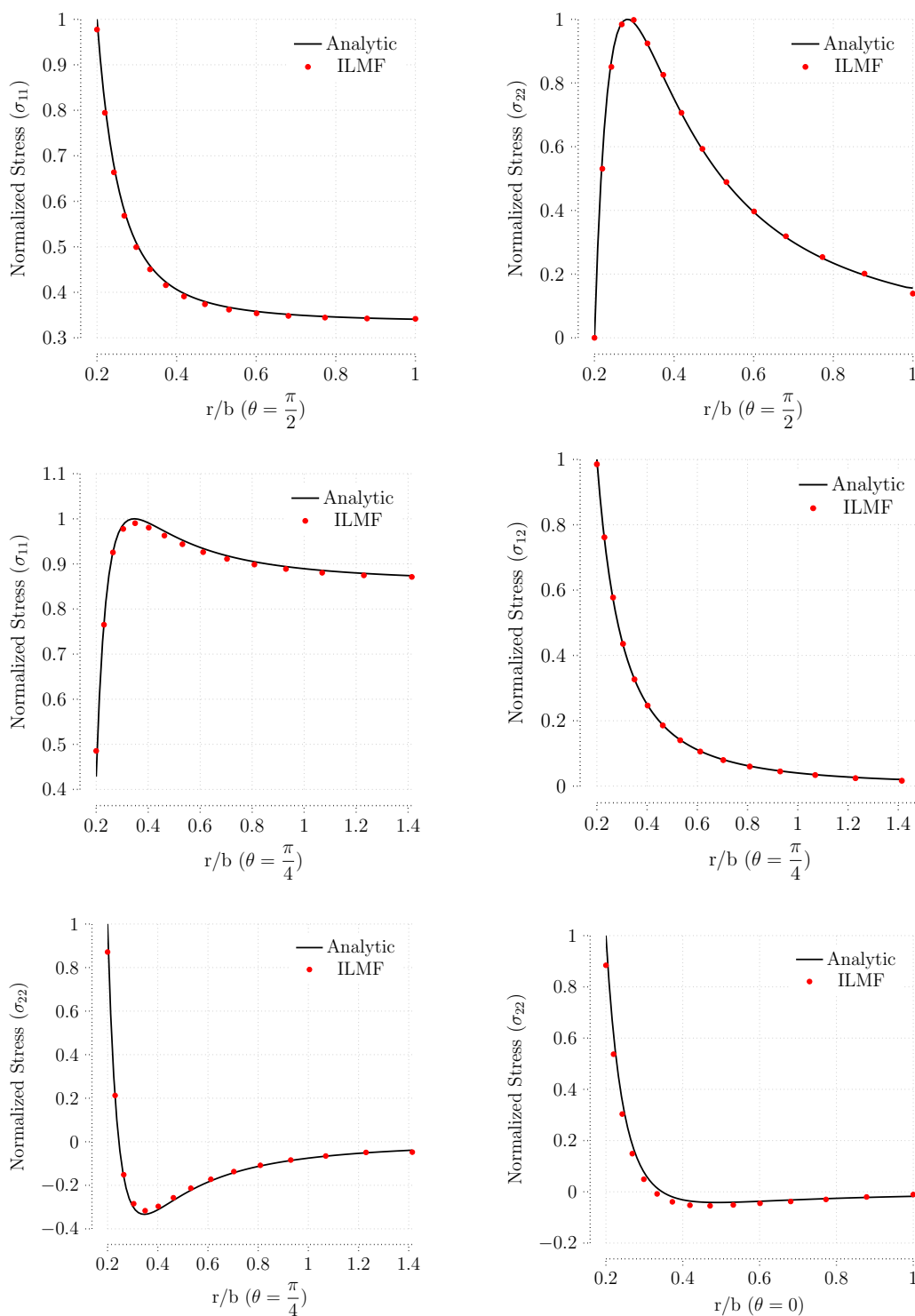
Figure 37: Stress distribution of the plate with circular hole for $\theta = 0, \frac{\pi}{4}, \frac{\pi}{2}$

.
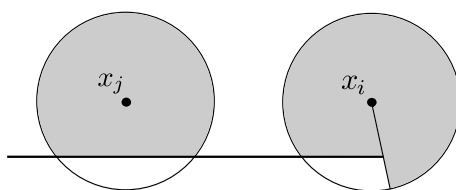
Figure 38: The visibility criterion, originally introduced by Belytschko et al. [1994a].

Figure 39: Square plate with a single edge crack under mode-I loading (h/w = 0.5).
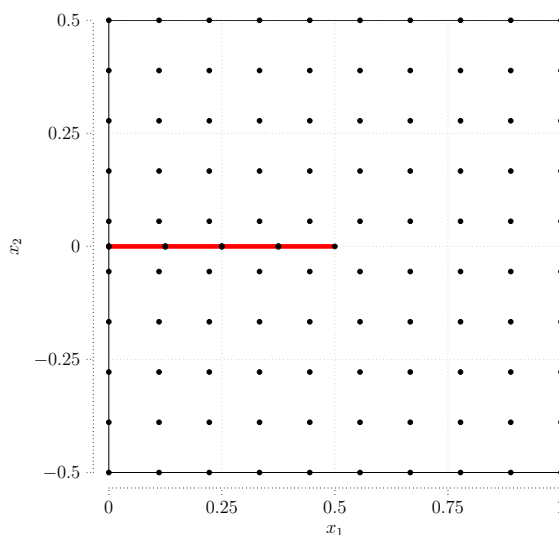
Figure 40: Discretization of the plate with a regular nodal distribution, for a/w = 0.5. The red line represents the crack faces.

of $10 \times 10 = 100$ nodes, with additional overlapping nodes on the crack faces. For all the five cases of crack length, only the nodal distribution of the crack faces was modified, adding more nodes for longer lengths, always without any refinement of the discretization around the crack tip.

Results obtained are presented in Table 11, where ILMF correspond the values obtained in this

Table 11: Square plate with a single edge crack under mode-I loading.

a/w	$K_I/(\bar{t}\sqrt{\pi a})$			% Error	
	ILMF	**J-DBEM**	**Reference**	**ILMF**	**J-DBEM**
0.2	1.520	1.495	1.488	0.0216	0.005
0.3	1.967	1.858	1.848	0.0647	0.005
0.4	2.413	2.338	2.324	0.0387	0.006
0.5	2.973	3.028	3.010	0.0122	0.006
0.6	3.991	4.184	4.152	0.0387	0.008

analysis, J-DBEM represents the values obtained with the J-integral implemented in the DBEM, published by Portela and Aliabadi [1993], and reference represent the values published by Civelek and Erdogan [1982]. Percentage errors are calculated from the values of reference. The results clearly show that ILMF have a good agreement with J-DBEM and the reference values. Since this is a mode-I loading crack problem, the SIF values of the mode-II are always below 10^{-7}. The plate deformed configuration is schematically represented in Figure 41.
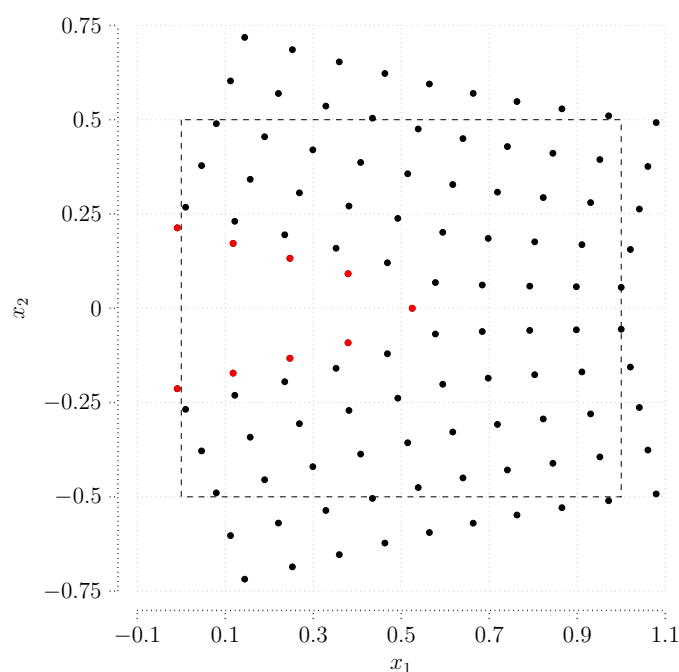
Figure 41: Deformed configuration of the plate, for a/w = 0.5, under mode-I loading.

8.3.2   Mode-II Loading

Now, consider a square edge-cracked plate, as presented in Figure 42. The crack length is denoted by a and $h/w = 0.5$ is considered. The uniform traction $\bar{t}$ is applied anti-symmetrically at the plate sides, parallel to the crack. This is a very complex and difficult problem, for which there are
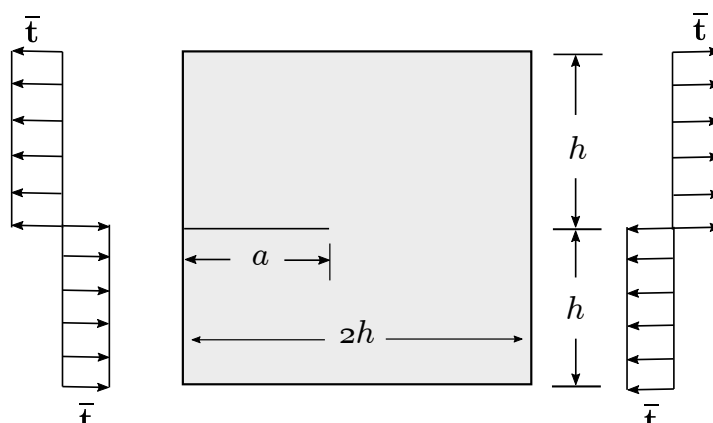
Figure 42: Square plate with a single edge crack under mode-II loading (w = 2h).

no published benchmark results. Hence, the results provided by J-DBEM are used as reference for this problem. Five cases are presented, for $a/w = 0.2, 0.3, 0.4, 0.5$ and 0.6. The nodal distribution used in the analysis is represented in Figure 43, with a regular nodal distribution of $16 \times 16 = 256$
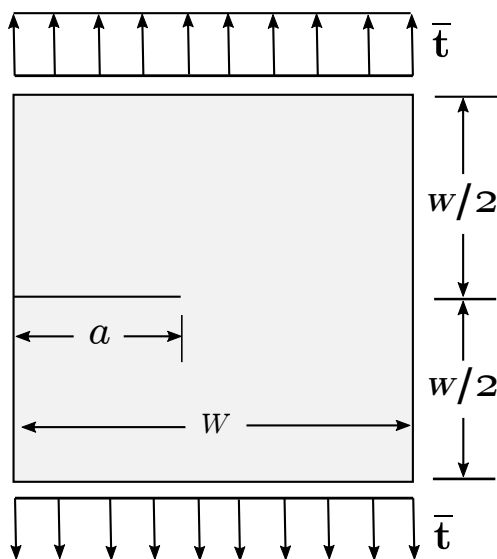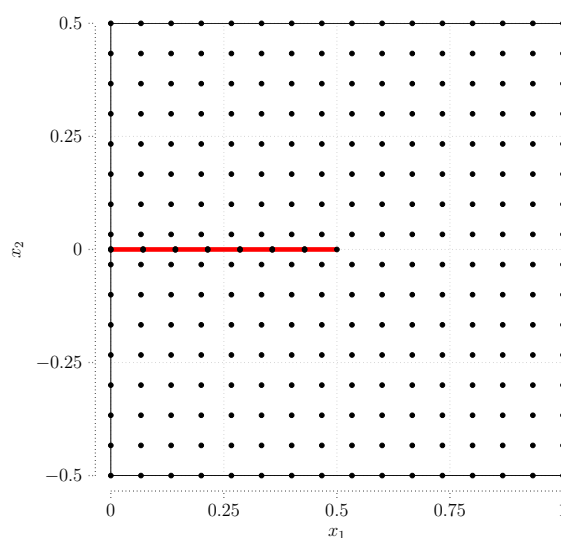

Figure 43: Discretization of the plate with a regular nodal distribution, for $a/w = 0.5$. The red line represents the crack faces.

nodes, with additional overlapping nodes on the crack faces. For all the five cases of crack length, only the nodal distribution of the crack faces was modified, adding more nodes for longer lengths, always without any refinement of the discretization around the crack tip.

Results obtained are presented in Table 12, where percentage errors are calculated from the values of J-DBEM. For this problem, the SIF values obtained for the mode-I are always below 10^{-3}, since this is a typical mode-II crack problem. Figure 44 shows the deformed configuration of the plate.

Table 12: Square plate with a single edge crack under mode-II loading.

a/w	$\mathbf{K_{II}/(\bar{t}\sqrt{\pi a})}$		
	ILMF	**J-DBEM**	**% Error**
0.2	0.416	0.435	0.0436
0.3	0.338	0.358	0.0532
0.4	0.296	0.304	0.0261
0.5	0.248	0.262	0.0522
0.6	0.218	0.223	0.0218
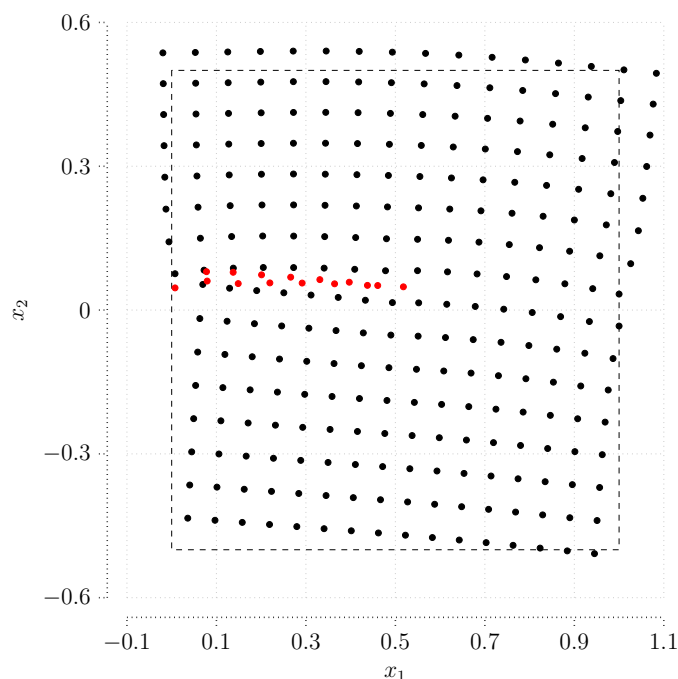
Figure 44: Deformed configuration of the plate, for $a/w = 0.5$, under mode-II loading.

8.3.3   Mixed-Mode Loading

Consider now a plate with an edge slant crack, as showed in Figure 45, in mixed-mode deformation derived from a remote stress σ. Three cases are presented, for $a/w = 0.2, 0.4$ and 0.6 with $\alpha = 30^o$; and two cases, for $a/w = 0.2$ and 0.4 with $\alpha = 60^o$. This problem was analyzed with the nodal distribution represented in Figure 46; with a regular nodal distribution of $16 \times 16 = 256$ nodes, with additional overlapping nodes on the crack faces. For all cases of crack length, only the nodal distribution of the crack faces was modified, adding more nodes for longer lengths, always without any refinement of the discretization around the crack tip.

Tables 13 and 14 show, respectively, the values of $K_I/(\sigma\sqrt{\pi a})$ and $K_{II}/(\sigma\sqrt{\pi a})$, as well as the percentage relative to the difference between the appropriate values published by Murakami [1987b], used as reference, and ILMF results; as a function of a/W and for $\alpha = 30^o$. Tables 15 and 16 present the values of $K_I/(\sigma\sqrt{\pi a})$, $K_{II}/(\sigma\sqrt{\pi a})$ and the percentage relative to the difference between the appropriate values published by Murakami [1987b] and ILMF; as a function of a/W, for $\alpha = 60^o$. Once more, the results obtained for this problem are in agreement with those obtained with the J-DBEM and those published in references, provided by Murakami [1987b] and Tada [2000]. It is important to remark the high level of accuracy obtained in all cracked plate problems, always considering coarseness nodal distributions, without any refinement around the
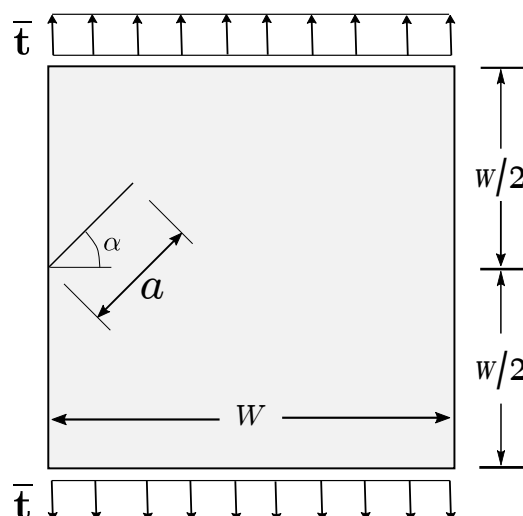
Figure 45: Square plate with an edge slant crack, under remote stress σ loading.
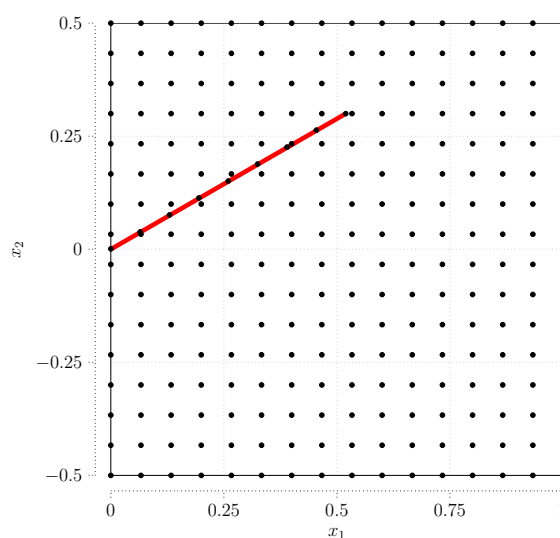

Figure 46: Discretization of the plate with a regular nodal distribution, for $a/w = 0.5$. The red line represents the crack faces.

Table 13: Stress intensity factor $K_I/(\sigma\sqrt{\pi a})$ for the edge slant crack $(\alpha = 30°)$.

a/W	$K_I/(\sigma\sqrt{\pi a})$			% Difference	
	ILMF	J-DBEM	Reference	ILMF	J-DBEM
0.2	1.164	1.082	1.100	0.058	0.016
0.4	1.513	1.545	1.550	0.024	0.003
0.6	2.732	2.572	2.550	0.071	0.009

crack tip.

The deformed configuration of the plate is show in Figure 47.

Table 14: Stress intensity factor $K_{II}/(\sigma\sqrt{\pi a})$ for the edge slant crack ($\alpha = 30°$).

a/W	$K_{II}/(\sigma\sqrt{\pi a})$			% Difference	
	ILMF	J-DBEM	Reference	ILMF	J-DBEM
0.2	0.325	0.351	0.350	0.071	0.003
0.4	0.471	0.474	0.470	0.002	0.009
0.6	0.580	0.700	0.700	0.171	0.000

Table 15: Stress intensity factor $K_{I}/(\sigma\sqrt{\pi a})$ for the edge slant crack ($\alpha = 60°$).

a/W	$K_{I}/(\sigma\sqrt{\pi a})$			% Difference	
	ILMF	J-DBEM	Reference	ILMF	J-DBEM
0.2	0.543	0.495	0.500	0.086	0.010
0.4	0.603	0.592	0.600	0.055	0.013

Table 16: Stress intensity factor $K_{II}/(\sigma\sqrt{\pi a})$ for the edge slant crack ($\alpha = 60°$).

a/W	$K_{II}/(\sigma\sqrt{\pi a})$			% Difference	
	ILMF	J-DBEM	Reference	ILMF	J-DBEM
0.2	0.327	0.356	0.360	0.092	0.011
0.4	0.439	0.413	0.420	0.045	0.017
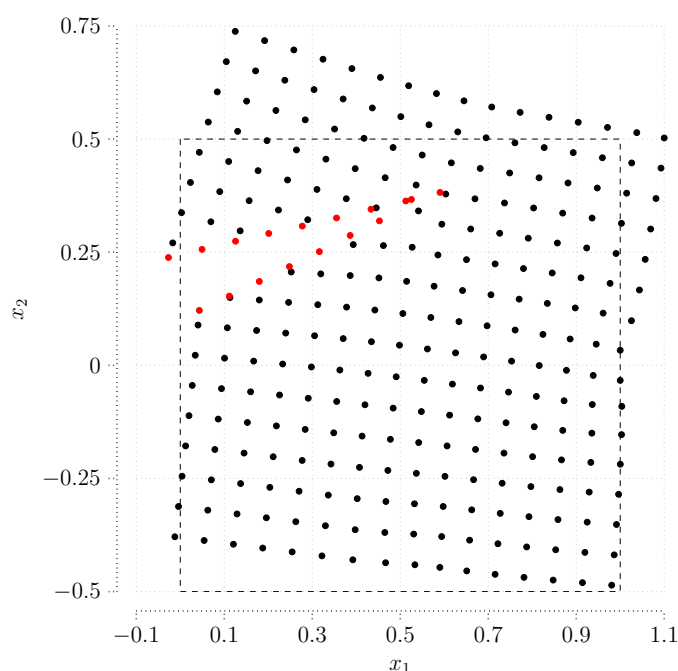
Figure 47: Deformed configuration of the plate, for $a/w = 0.5$, under mixed-mode loading.

8.4   Benchmark Problem 4 – Central Cracked Plate

For practical applications, albeit curved in most cases, can be effectively modeled as piece-wise flat, when the path of a crack is concerned. As reported by Caicedo and Portela [2015], the Williams' fields can be locally used at each crack tip, as a particular solution of an arbitrary piece-wise flat crack. Hence, to deal with several cracks simultaneously, superposition is used in SST strategy in a way that, in the proximity of each crack tip, the Williams' field is locally used in the

regularization procedure. As a direct consequence, the central cracked plate can be considered as a multi-cracked plate, with two distinct crack tips.

Consider a rectangular plate with a central slant crack, as show in Figure 48. The uniform
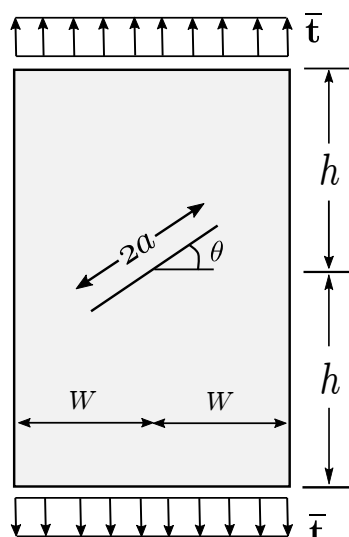
Figure 48: Rectangular plate with a central slant crack, under uniform traction.

traction $\bar{t}$ is applied symmetrically at the ends. The ratio between the height and the width of the plate is given by $h/w = 2$. The crack length is $2a$ and form an angle of $\theta = 45^o$ with the horizontal direction. The results published by Murakami [1987a] are used as reference. Three cases are presented, for $a/w = 0.2, 0.4$ and 0.6. For this particular case, discretization parameters were considered as $\alpha_s = 5 \sim 8$ and $\alpha_q = 0.5$. The discretization was performed with the nodal distribution, as show in Figure 49; with a regular nodal distribution of $7 \times 12 = 84$ nodes, with additional overlapping nodes on the crack faces. For all three cases of crack length, only the nodal distribution of the crack faces was modified, adding more nodes for longer lengths, always without any refinement of the discretization around the crack tip.

Tables 17 and 18 demonstrate the results obtained, for the values of $K_I/(\bar{t}\sqrt{\pi a})$ and $K_{II}/(\bar{t}\sqrt{\pi a})$, as well as comparisons with the appropriate values of the reference presented by Murakami [1987a], as a function of a/W. The results obtained clearly demonstrate the excellent accuracy

Table 17: Stress intensity factor $\mathbf{K_I}/(\bar{t}\sqrt{\pi a})$ for the central slant crack ($\theta = 45°$).

a/W	$\mathbf{K_I}/(\bar{t}\sqrt{\pi a})$			% Difference	
	ILMF	J-DBEM	Reference	ILMF	J-DBEM
0.2	0.519	0.521	0.518	0.002	0.006
0.4	0.575	0.576	0.572	0.005	0.007
0.6	0.626	0.666	0.661	0.053	0.001

of this new formulation of the ILMF numerical model that is an efficient tool for the mixed-mode deformation analysis of cracked plates.

The deformed configuration of the plate is presented in Figure 50.
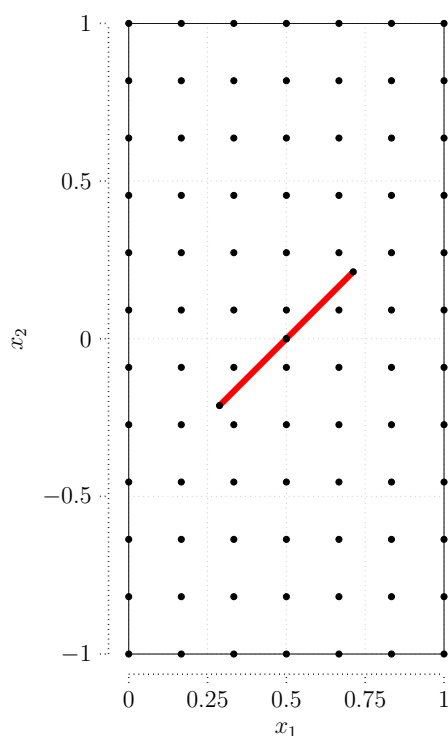
Figure 49: Discretization of the plate with a regular nodal distribution for $a/w = 0.6$. The red line represents the crack faces.

Table 18: Stress intensity factor $K_{II}/(\bar{t}\sqrt{\pi a})$ for the edge slant crack ($\theta = 45°$).

	$K_{II}/(\bar{t}\sqrt{\pi a})$			% Difference	
a/W	ILMF	J-DBEM	Reference	ILMF	J-DBEM
0.2	0.529	0.508	0.507	0.043	0.002
0.4	0.532	0.529	0.529	0.005	0.001
0.6	0.585	0.569	0.567	0.032	0.003
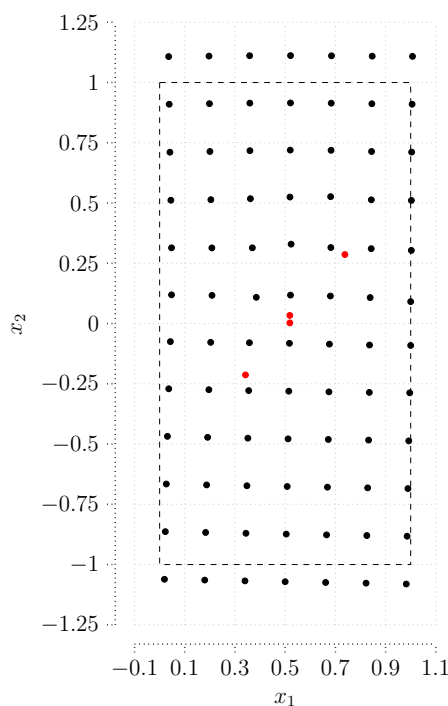
Figure 50: Deformed configuration of the plate for $a/w = 0.6$, under uniform traction.

9   Concluding Remarks

The local mesh free method for solving linear elastic and fracture mechanics problems were presented on this chapter. The method is derived from the work theorem, where the formulation leads to a weak form of the weighted residual statement of a statically admissible stress field, kinematically formulated with a rigid-body displacement. The node-by-node discretization considers the MLS approximation and implements a reduced numerical integration.

In a nodal discretization, the size of the compact support and the size of the local integration domain of each node are parameters directly linked to the accuracy and efficiency of local mesh free methods. In this paper, both discretization parameters are automatically defined through a multi-objective optimization process based on genetic algorithms and symbiotic organism search algorithm.

Benchmark test problems were analyzed in order to assess the accuracy and efficiency of the local mesh free method. Both regular and irregular nodal distributions can be considered. For irregular nodal distributions, the combination of stable results and a high accuracy are obtained, even for severe irregular distributions. The optimization scheme defined on this chapter is very efficient, from a computational point of view, and do not require any analytical solution to be performed. Therefore, the local mesh free method proved to be a reliable and robust formulation for solving linear elastic problems.

Linear elastic fracture mechanics problems using the local mesh free method are performed through the singularity subtraction technique (SST), which regularizes the elastic field, before the numerical solution, thus introducing the stress intensity factors (SIF) as additional primary unknowns of the problem. This strategy result in a direct computation of the SIF and does not require a refined discretization to obtain accurate results. The high efficiency of this model strategy can be seen in the numerical results, for simple coarse nodal distributions, without any refinement around crack tips. Therefore, the reliability and robustness can also be extend for solving fracture mechanics problems.

This chapter shows that the local mesh free method, along with optimization processes, could provide stable and accurate solutions for linear elastic and fracture mechanics problems, without most known setbacks, contributing to a mainstream use of mesh-free numerical methods in the near future. For the next research projects, the local mesh free method, with the SST implementation and optimization, will be extended for the analysis of multiple crack growth problems, nonlinear plates and dynamic problems.

References

M. Aliabadi, D. Rooke, and D. Cartwright. An improved boundary element formulation for calculating stress intensity factors: Application to aerospace structures. *J. Strain Analysis*, 22(4): 1–5, 1987.

S. Atluri and S. Shen. The meshless local petrov-galerkin (mlpg) method: A simple and less-costly alternative to the finite element and boundary element methods. *CMES: Computer Modeling in Engineering and Sciences*, 3(1):11–51, 2002.

S. Atluri and T. Zhu. A new meshless local petrov-galerkin (mlpg) approach in computational mechanics. *Computational Mechanics*, 22(2):117–127, 1998.

S. Atluri and T. Zhu. New concepts in meshless methods. *International Journal for Numerical Methods in Engineering*, 47:537–556, 2000.

S. Atluri, Z. Han, and A. Rajendran. A new implementation of the meshless finite volume method through the mlpg mixed approach. *CMES: Computer Modeling in Engineering and Sciences*, 6:491–513, 2004.

A. Bagheri, R. Ehsany, M. Mahmoodabadi, and G. Baradaran. Optimization of meshless local petrov-galerkin using genetic algorithm for 3d elasto–static problems. *International Journal of Engineering*, 24(2):143–153, 2011.

G. Baradaran and M. Mahmoodabadi. Optimal pareto parametric analysis of two dimensional steady–state heat conduction problems by mlpg method. *International Journal of Engineering*, 22(4):387–406, 2009.

P. Basu, A. Jorge, S. Badri, and J. Lin. Higher-order modeling of continua by finite-element, boundary-element, meshless, and wavelet methods. *Computers and Mathematics with Applications*, 46(1):15–33, 2003.

K. Bathe. *Finite Element Procedures*. Prentice Hall, 2014.

S. Beissel and T. Belytschko. Nodal integration of the element-free galerkin method. *Computer Methods in Applied Mechanics and Engineering*, 139(1–4):49–74, 1996.

T. Belytschko, L. Gu, and Y. Y. Lu. Fracture and crack growth by element-free galerkin methods. *Modelling and Simulation in Materials Science and Engineering*, 2(3A):519–534, 1994a.

T. Belytschko, Y. Y. Lu, and L. Gu. Element-free galerkin methods. *International Journal for Numerical Methods in Engineering*, 37(2):229–256, 1994b. ISSN 1097-0207.

T. Belytschko, Y. Guo, W. Liu, and S. Xiao. A unified stability analysis of meshless particle methods. *International Journal for Numerical Methods in Engineering*, 48(9):1359–1400, 2000.

S. Bordas, T. Rabczuk, and G. Zi. Three-dimensional crack initiation, propagation, branching and junction in non-linear materials by an extended mesh free method without asymptotic enrichment. *Engineering Fracture Mechanics*, 75(5):943–960, 2008.

J. Brahtz. Stress distribution in a reentrant corner. *Transactions of the American Society of Mechanical Engineers*, 55:31–37, 1933.

J. Caicedo and A. Portela. Cracked plate analysis with the dual boundary element method and williams eigenexpansion. *J. of Engineering Analysis with Boundary Elements*, 52:16–23, 2015.

A. Carpinteri, G. Ferro, and G. Ventura. The partition of unity quadrature in element-free crack modeling. *Journal of Computers and Structures*, 81:1783–1794, 2003.

M.-Y. Cheng and D. Prayogo. Symbiotic organisms search: A new metaheuristic optimization algorithm. *Computers & Structures*, 139(15):98–112, 2014.

M. Civelek and F. Erdogan. *Crack problems for a rectangular plate and an infinite strip*, volume 19. 1982.

R. C. Eberhart and Y. Shi. *Computational Intelligence: Concepts to Implementations*. Elsevier, 2007.

M. Ebrahimnejad, N. Fallah, and A. Khoei. Adaptive refinement in the meshless finite volume method for elasticity problems. *Computers & Mathematics with Applications*, 69(12):1420–1443, 2015.

G. Fichera. *Linear Elliptic Differential Systems and Eigenvalue Problems*. Springer, 2006.

B. Finalyson. *The Method of Weighted Residuals and Variational Principles*, volume 87. Academic Press, 1972.

M. Fleming, Y. Chu, B. Moran, and T. Belytschko. Enriched element free galerkin methods for crack tip fields. *Int. J. for Numerical Methods in Engineering*, 40:1483–504, 1997.

M. Gen and R. Cheng. *Genetic Algorithms and Engineering Optimization*. Wiley, 2000.

J. H. Holland. *Adaptation in Natural and Artificial Systems*. MIT press, 1975.

C. Hwang and A. Masud. *Multiple Objectives Decision Making Methods and Applications*. Springer, 1979.

V. Kelner and O. Leonard. Application of genetic algorithms to lubrication pump stacking design. *Journal of Computational and Applied Mathematics*, 168(1):255–265, 2004.

G. Kirchhoff. Uber das gleichgewicht und die bewegung einer unendlich diinnen elastischen stabes. *J. Reine Angew. Math.*, 56(1):285–313, 1859.

G. Liu. Mesh free methods - moving beyond the finite element method. 2003.

G. Liu and Y. Gu. A local point interpolation method for stress analysis of two-dimensional solids. *Structural Engineering and Mechanics*, 11(2):221–236, 2001.

G. Liu, L. Yan, J. Wang, and Y. Gu. Point interpolation method based on local residual formulation using radial basis functions. *Structural Engineering and Mechanics*, 14:713–732, 2002.

G. Liu, G. Zhang, Y. Wang, Z. Zhong, G. Li, and X. Han. A nodal integration technique for meshfree radial point interpolation method (ni-rpim). *International Journal of Solids and Structures*, 44(11:12):3840–3860, 2007.

W. Liu, J. Ong, and R. Uras. Finite element stabilization matrices – a unification approach. *Computer Methods in Applied Mechanics and Engineering*, 53(1):13–46, 1985.

W. Liu, S. Jun, and Y. Zhang. Reproducing kernel particle methods. *International Journal for Numerical Methods in Engineering*, 20:1081–1106, 1995.

W. Liu, Y. Chen, S. Jun, J. Chen, T. Belytschko, C. Pan, R. Uras, and C. Chang. Overview and applications of the reproducing kernel particle methods. *Archives of Computational Methods in Engineering State of the Art Reviews*, 3(1):3–80, 1996.

X. Liu, Q. Xiao, and B. Karihaloo. Xfem for direct evaluation of mixed mode stress intensity factors in homogeneous and bi-materials. *Int. J. for Numerical Methods in Engineering*, 59:1103–1118, 2004.

J. McCall. Genetic algorithms for modelling and optimisation. *Journal of Computational and Applied Mathematics*, 184(1):205–222, 2005.

A. Moussaoui and T. Bouziane. Comparative study of the effect of the parameters of sizing data on results by the meshless methods (mlpg). *World Journal of Mechanics*, 3(1):82–87, 2013.

Y. Murakami. *Linear Elliptic Differential Systems and Eigenvalue Problems*. Pergamon Press, 1987a.

Y. Murakami. *Stress intensity factors handbook, 1st edition, vol 2*. Pergamon Press, 1987b.

B. Nayroles, G. Touzot, and P. Villon. Generalizing the finite element method: Diffuse approximation and diffuse elements. *Computational Mechanics*, 10:307–318, 1992.

N. T. Nguyen, T. Q. Bui, M. N. Nguyen, and T. T. Truong. Meshfree thermomechanical crack growth simulations with new numerical integration scheme. *Engineering Fracture Mechanics*, 235(5):107–121, 2020.

T. Oliveira and A. Portela. Weak form collocation – a local meshless method in linear elasticity. *Engineering Analysis with Boundary Elements*, 73(1):144–160, 2016.

A. Portela and M. Aliabadi. Crack growth analysis using boundary elements – software. 1993.

L. Qingbo, X. Nengxiong, W. Weifeng, and L. Yazhe. Modeling of shear crack propagation in rock masses using mesh-free lrpim. *Advances in Civil Engineering*, 2021(1):1–13, 2021.

T. Rabczuk and T. Belytschko. A three-dimensional large deformation mesh free method for arbitrary evolving cracks. *Computer Methods in Applied Mechanics and Engineering*, 196(29–30):2777–2799, 2007.

J. Ringuest. *Multiobjective Optimization: Behavioral and Computational Considerations*. Kluwer, 1992.

Y. Sawaragi, H. Nakayama, and T. Tanino. *Theory of Multiobjective Optimization*. Academic Press, 1985.

R. Steuer. *Multiple Criteria Optimization: Theory, Computation, and Application*. Wiley, 1986.

G. Symm. Integral equation methods in potential theory, ii. *Proceedings of Royal Society*, A275: 33–46, 1963.

H. Tada. *The stress analysis of cracks handbook*. ASME Press, 2000.

P. Wen and M. Aliabadi. Applications of meshless method to fracture mechanics with enriched radial basis functions. *Durability of Structures and Health Monitoring*, 3:107–119, 2007.

M. Williams. Stress singularities resulting from various boundary conditions in angular corners of plates in extension. *Journal of Applied Mechanics*, pages 526–528, 1952.

L. Xanthis, M. Bernal, and C. Atkinson. The treatment of the singularities in the calculation of stress intensity factors using the integral equation method. *Comp. Meth. in Applied Mechanics Engineering*, 26:285–304, 1981.

T. Zhu, J. Zhang, and S. Atluri. A local boundary integral equation (lbie) method in computational mechanics and a meshless discretization approach. *Computational Mechanics*, 21:223–235, 1998.

O. Zienkiewicz and R. Taylor. *Finite Element and Approximation*. John Wiley & Sons, 1983.

Chapter 24

Meshless smoothed point interpolation methods for damage modelling

Meshless smoothed point interpolation methods for damage modelling

Lapo Gori[1*]

[1]Department of Structural Engineering, Federal University of Minas Gerais, Brazil.
E-mail: lapo@dees.ufmg.br

*Corresponding author

Abstract

Damage models represent an important tool for the analysis of the degradation of quasi-brittle media and, due to their continuous formulation, present certain advantages with respect to other modelling strategies. However, they also exhibit a number of issues when combined with the standard finite element method, like mesh-objectivity and mesh-bias, that can significantly affect the results of a simulation. Due to their nature, meshless techniques are a valid candidate to deal with such issues. The lack of an element-like connectivity between the meshless nodes can allliviate the mesh-bias in damage propagation, while the intrinsic nonlocality of meshless approximation functions can act as a regularisation technique at the numerical level. The present work aims to review the application of a specific class of meshless methods, the smoothed point interpolation methods (SPIMs) to the problem of damage modelling.

Keywords: meshless methods; smoothed point interpolation methods; damage mechanics; strain localisation

1 Introduction

In order to solve the system of partial differential equations (PDEs) governing a problem of continuum mechanics (or any other continuum problem representable in terms of PDEs), the finite element method (FEM) *discretises* the problem domain with a *mesh* (see, e.g. Bathe [1996] or Zienkiewicz and Taylor [2000]), in the following manner:

> "
> 1. The continuum is separated by imaginary lines or surfaces into a number of "finite elements".
>
> 2. The elements are assumed to be interconnected at a discrete number of nodal points situated on their boundaries and occasionally in their interior.
>
> "[Zienkiewicz and Taylor, 2000, pag. 18]

The unknown parameters of the problem are then represented by the nodal values of the field variable (e.g. the displacement field in a solid mechanics problem). The choice of proper approximation functions within each element allows to mount a system of linear equations for the solution of the problem. On the other hand:

> "The meshfree method is used to establish a system of algebraic equations for the whole problem domain without the use of a predefined mesh, or uses easily generable meshes in a much more flexible or "freer" manner. Meshfree methods essentially use a set of nodes scattered within the problem domain as well as on the boundaries to represent the problem domain and its boundaries. The field functions are then approximated locally using these nodes."[Liu, 2009, pag. 14]

As pointed out by Liu in his book [Liu, 2009], the standard finite element method suffers for a number of limitations. Among them there are:

- the need for a quality mesh, that reduces the automation in mesh generation;

- the "overly stiff" behaviour, resulting from the full compatibility in the assumed displacement field, and leading to locking and poor solutions in gradient/derivatives;

- the loss of accuracy due to element distorsions in problems with large deformations;

- the mesh bias in problems like crack growth and phase transformations;

- the difficult simulation of breakage and fragmentation problems;

- the costly adaptive and remeshing approaches;

- the availability of solely a "lower bound" to the exact solution.

An examination of this list reveals that most of the mentioned issues are due to the "heavy and rigid reliance on the use of quality elements that are the building blocks of FEM " [Liu, 2009, pag. 17], and to the predefined connectivity required by such elements.

The basic idea of meshless methods is then to mitigate these issues by eliminating or reducing the reliance on a mesh[1]. Among the most common meshless methods there are the *smoothed particle hydrodynamics* (SPH) method [Gingold and Monaghan, 1977], the *element-free Galerkin*[2] (EFG) method [Belytschko et al., 1994], the *reproducing kernel particle method* (RKPM) [Liu et al., 1995], the family of *point interpolation methods* (which the smoothed point interpolation methods discussed in this manuscript belong to), and the *meshless local Petrov-Galerkin* (MLPG) method [Atluri and Zhu, 1998]. Despite a computational cost that is, in general, higher than in the standard FEM, meshless methods exhibit a number of important features. Among them, the following can be highlighted [Liu, 2009]:

- easy automatic mesh generation using triangulation strategies;

- absent or limited mesh alignment sensitivity;

- no need for remeshing operations, especially in problems with large deformations or moving discontinuities;

---

[1]Though meshless discretisations are not based on a conventional mesh as intended in the standard FEM, the term "mesh" will still be used in the following to indicate such discretisations.

[2]Based on the *diffuse elements method* (DEM) originated by Nayroles et al. [1992].

- construction of shape functions of any desired order of continuity.

Regarding physically nonlinear problems, and especially the problem of *continuum damage mechanics* discussed in this manuscript, the standard FEM suffers for other issues besides the aforementioned ones. The presence of damage indeed, results in a *strain-softening* behaviour. Numerical simulations of strain-softening problems, where *localisation* occours, performed with the standard finite element method (FEM), are usually affected by certain pathological behaviours, such as *strong mesh-dependency*, *premature fracture initiation*, and *instantaneous perfectly-brittle fracture* [de Borst et al., 1993, Peerlings et al., 2002]. These pathological effects are due to the fact that, at a certain load level, the continuum boundary value problem may become *ill-posed* (the so-called loss of ellipticity of the equilibrium equations), resulting in an infinite set of solutions (discontinuous bifurcation), from which the numerical method selects the one corresponding to the smallest energy dissipation. This approximated solution strongly depends on the mesh; at mesh refinement it tends to a failure with zero energy dissipation, and then to a *nonphysical* behaviour.

It has been pointed out that the pathological behaviours that may affect the numerical simulations where localisation occours are due to the *local* representation offered by the classic continuum theory, in contrast with the *nonlocal* nature of phenomena like damage and plasticity [Bažant, 1991]. The main aim of the proposed solutions to this problem (the so-called regularisation techniques) is the introduction of an *internal length* in the continuum model, allowing to recover the nonlocal character of the phenomenon; an interesting overview on the different regularisation methods can be found in the papers by de Borst et al. [de Borst et al., 1993] and by Bažant et al. [Bažant and Jirásek, 2002].

Some classes of meshless methods have been shown to be capable to deal with the aforementioned localisation issues, due to their intrinsic nonlocal character. As pointed out in a paper by Chen et al. [Chen et al., 2000], the nonlocality of these methods is due to the fact that their approximation functions are not constructed locally as in the finite element method, because of the use of basis and weighting functions with support size greater than the nodal spacing. In the same paper the authors pointed out the analogy between MLS/RK approximations and gradient-enhanced models, and also showed the beneficial effects on localisation associated to the use of an assumed strain method where the nonlocal equivalent strain measure is directly approximated in terms of displacement parameters. Moreover, the use of a meshless method allows, in general, to overcome the problem of mesh orientation bias, that may appear in damage propagation problems. Among the methods that have been shown to possess certain regularisation effects in localisation problems there are *moving least square* (MLS) and *reproducing kernel* (RK) approximations, as well as methods based on *strain smoothing* techniques [Liu et al., 1999, Chen et al., 2000, Li et al., 2000, Chen et al., 2004, 2007, Wang and Li, 2012, Pozo et al., 2014]. As strain smoothing methods, also the *smoothed point interpolation methods* (SPIMs) discussed in this manuscript have been shown to exhibit regularisation properties, as illustrated by Gori et al. [Gori et al., 2019b], both alone as well as when combined with other regularisation strategies, like the micropolar continuum theory [Gori et al., 2019a,c]. Particle methods, like the SPH, have also been shown to be capable to deal with strain-softening problems [Vignjevic et al., 2014].

One of the main issues in the most common meshfree approaches is the lack of the Kronecker delta property, which requires a special treatment for the imposition of essential boundary conditions, like the use of the well-known *Lagrange multipliers* and *penalty* methods or other procedures [Chen and Wang, 2000, Wu and Plesha, 2002, Fernández-Méndez and Huerta, 2004]. The smoothed point interpolation methods discussed in this manuscript [Liu, 2009, 2010a,b, Liu and Zhang, 2013] allow for a more simple imposition of boundary conditions, since they are based on shape functions constructed with the *point interpolation method* (PIM), which guarantee the Kronecker delta property. The price for a more simple imposition of the boundary conditions is the presence of *incompatible* shape function, which may present discontinuities in the problem

domain, requiring the use of a so-called *weakened-weak* form of the continuum problem [Liu, 2010a,b] based on a *strain smoothing technique* [Liu, 2008]. Regarding the field of continuum mechanics, these methods have been applied to linear elasticity [Liu, 2010b] and elasto-plasticity [Zhang et al., 2015]. The smoothing operation which these methods are based on is a sort of generalisation of the *Stabilised Conforming Nodal Integration* (SCNI) technique originally proposed by Chen et al. [Chen et al., 2001].

1.1   Outline

The outline of this manuscript is organised as follows. In the first section after this introduction (Section 2), the fundamental aspects of meshless methods, like discretisation, field variables approximation, and numerical integration, are reviewed, and compared with the approach of the standard FEM. Section 3 is the core of the manuscript; it discusses in details the main aspects of smoothed point interpolation methods, and their application to problems of continuum damage mechanics (more specifically, to problems with scalar damage). Section 4 briefly discusses the issue of localisation in strain-softening problems, and the different regularisation strategies that can be applied to scalar damage problems and to other problems where localisation may occour. Finally, Section 5 illustrates some numerical results obtained with SPIM stategies applied to damage problems, while Section 6 presents some concluding remarks.

1.2   Notations and tools

Some standard notations used in the body of the manuscript are summarised here. The symbol $\mathbf{D} \subset \mathbf{E}$ indicates the domain of a body embedded in the three-dimensional Euclidean space $\mathbf{E}$, and $\mathbf{D}_k^S \subset \mathbf{D}$ one of its subsets, referred to as *smoothing domain*. *Vectors* are indicated as $\bar{\boldsymbol{x}} \in \bar{\mathbf{E}}$, with $\bar{\boldsymbol{x}} = x_i \, \bar{\boldsymbol{e}}_i$, where $\bar{E}$ is the vector space associated to $\mathbf{E}$, and $(\bar{\boldsymbol{e}}_i)$ a basis in $\mathbf{E}$. *Second-order* and *fourth-order* tensors are indicated, respectively, by $\underline{\boldsymbol{x}} \in \bar{\mathbf{E}} \otimes \bar{\mathbf{E}}$, with $\underline{\boldsymbol{x}} = x_{ij} \, \bar{\boldsymbol{e}}_i \otimes \bar{\boldsymbol{e}}_j$, and by $\hat{\mathbf{x}} \in \bar{\mathbf{E}} \otimes \bar{\mathbf{E}} \otimes \bar{\mathbf{E}} \otimes \bar{\mathbf{E}}$, with $\hat{\mathbf{x}} = x_{ijk\ell} \, \bar{\boldsymbol{e}}_i \otimes \bar{\boldsymbol{e}}_j \otimes \bar{\boldsymbol{e}}_k \otimes \bar{\boldsymbol{e}}_\ell$. The symbol "·" denotes the standard dot product between vectors and the one index contraction between tensors (or between a tensor and a vector) like, for example, $\bar{\boldsymbol{x}} \cdot \bar{\boldsymbol{y}} = x_i \, y_i$ and $\underline{\boldsymbol{x}} \cdot \bar{\boldsymbol{y}} = x_{ij} \, y_j \, \bar{\boldsymbol{e}}_i$, while the symbol ":" denotes the double contraction between tensors like, for example, $\hat{\mathbf{x}} \cdot \underline{\boldsymbol{y}} = x_{ijk\ell} \, y_{k\ell} \, \bar{\boldsymbol{e}}_i \otimes \bar{\boldsymbol{e}}_j$ and the other possible combinations. With the symbol "$\otimes$", the standard tensor product, as $\bar{\boldsymbol{x}} \otimes \bar{\boldsymbol{y}} = x_i \, y_j \, \bar{\boldsymbol{e}}_i \otimes \bar{\boldsymbol{e}}_j$ or $\underline{\boldsymbol{x}} \otimes \underline{\boldsymbol{y}} = x_{ij} \, y_{k\ell} \, \bar{\boldsymbol{e}}_i \otimes \bar{\boldsymbol{e}}_j \otimes \bar{\boldsymbol{e}}_k \otimes \bar{\boldsymbol{e}}_\ell$, is indicated. In some applications the Voigt notation will be used to represent second-order and fourth-order tensors; once a certain coordinates system has been fixed, a generic second-order tensor with dimension three $\underline{\boldsymbol{x}}$ can be represented by means of an *array* with nine components, indicated with the symbol $\{\underline{\boldsymbol{x}}\}$. In an analogous way, a fourth-order tensor with dimension three $\hat{\mathbf{x}}$ can be represented by means of a 9×9 matrix, indicated as $[\hat{\mathbf{x}}]$. It should be noted that the provided dimensions refer to a general three-dimensional case; in different situations (e.g. plane-strain or plane-stress states, or peculiar symmetries), the size of arrays and matrices in Voigt representation is minor, in general. The same symbols $\{\cdot\}$ and $[\cdot]$ are also used to indicate, respectively, arrays and matrices in numerical equations. The numerical implementations of the strategies discussed in this paper, as well as the numerical simulations, have been performed in the open-source program **INSANE**[3]. The triangular background cells used for the construction of the meshfree discretisations, as well as the contour plots of the results obtained with the meshfree models, have been generated with the program **Gmsh** [Geuzaine and Remacle, 2009].

---

[3]More information on the project can be found at `https://www.insane.dees.ufmg.br/`

2   Fundamentals of meshless methods

Before presenting the fundamentals of meshless methods it's worth it to briefly illustrate the main aspects of the finite element method (FEM); these will be used later to introduce the meshless approach, serving as a basis for the reader that is familiar with the FEM. Given a domain $\mathbf{D}$, an FEM model is contructed as a tesselation of this domain using a finite number of *elements* $\mathbf{D}_e$ that don't overlap and don't leave gaps in the domain (Figure 1); this tesselation is commonly referred to as *mesh*. Finite elements may present different geometrical shapes, depending on the size of the domain of the problem; straight lines and curves in one-dimensional domains, polygons in two-dimensional domains, and polyhedra in three-dimensional domains. Regardless of the peculiar shape of an element, each one of its vertices is a so-called *node* (Figure 1).
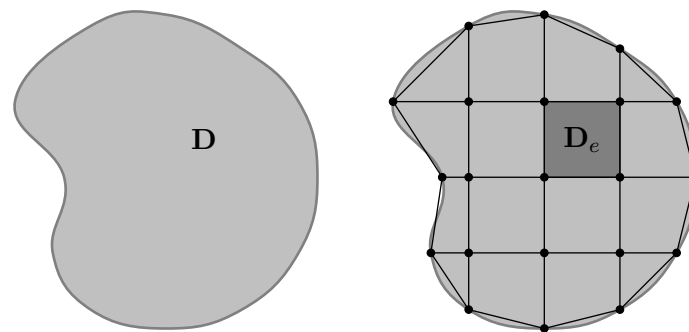
Figure 1: Two-dimensional FEM mesh

The role of the nodes is to discretise the field variables of the problem. A generic continuous problem characterised by the field variable $u(p)$, with p being a point in the domain $\mathbf{D}$, is transformed into a discrete one, where the field variable is only sampled at a finite number of points p_i in the domain, corresponding to the nodes, $u_i = u(p_i)$. Regarding the discretisation of a problem, the elements have a double task. Firstly, they serve as units for the interpolation of the field variables. Once the field variables are known at the nodes of a model, their values can be interpolated inside each element using the so-called shape functions $\mathcal{N}_i$ of the element (Figure 2):

$$u(p) \simeq u^h(p) = \sum_{i=1}^{N} \mathcal{N}_i(p)\, u_i, \qquad p \in \mathbf{D}_e \tag{1}$$
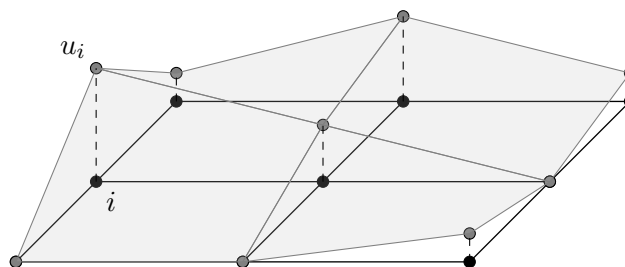
Figure 2: Two-dimensional FEM interpolation

The second task of the elements is to allow the numerical integration of the weak form that describes the behaviour of the problem at hand. Regardless of the kind of problem, a weak form usually requires to perform an integration over the problem domain. In this sense, the tesselation of the domain allows to build a quadrature rule, where the integral is performed considering a

certain number of integration points within each element (Figure 3); such points are also referred to as *Gauss points*, since the Gauss quadrature rule is the one usually adopted in the FEM.
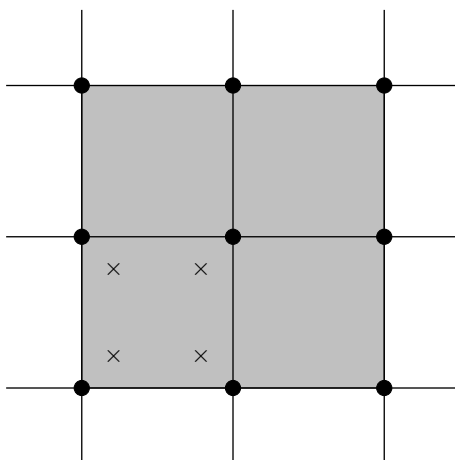
Figure 3: Two-dimensional FEM integration points

Meshless methods still need to perform the aforementioned tasks, i.e. the field variables interpolation and the numerical integration of the weak form. However, while in the FEM these tasks are performed using a single object, the finite element, in meshless methods there are usually two distinct objects, the *support domain*, that allows to perform the interpolation (or approximation), and the *integration domain*, that allows to perform the numerical integration.

2.1   Field variables interpolation/approximation

As pointed out in Section 2, in the FEM the field variables interpolation is element-based, i.e. it's defined within each finite element. In meshless methods on the other hand, the interpolation (or approximation, as it will be pointed out later) is *node-based*, i.e. it only uses the nodes scattered on the domain, without any information about their connectivity. Many meshless methods still use some sort of mesh-like grid for different purposes, but this grid is not stricly needed for the interpolation of the field variables.

As mentioned before, the object responsible for the interpolation is the *support domain*. A support domain S_d (Figure 4) is defined at each interest point $p \in \mathbf{D}$ where the field variables must be interpolated, and is composed by the set of nodes (the so-called *support nodes*) in the neighbourhood of the point p.
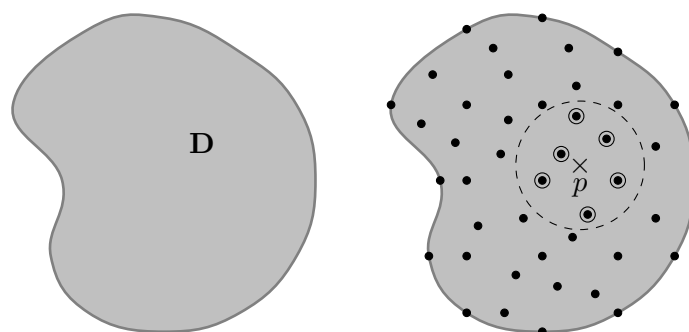
Figure 4: Meshless support domain

Given a point $p \in \mathbf{D}$, the interpolation of a generic field variable $u(p)$ is built using the nodes belonging to the support domain at p:

$$u(p) \simeq u^h(p) = \sum_{i \in S_d(p)} \phi_i(p)\, u_i \qquad (2)$$

In the summation above, the terms $u_i = u(p_i)$ are the values of the field variable at the support nodes, and the functions ϕ_i are the shape functions. Unlike FEM shape functions, there isn't always a closed form expression for meshless shape functions; the shape functions for a certain support domain are usually evaluated with a numerical procedure that involves a matrix inversion, resulting in a higher computational cost.

While the concept of support domain is the same for the different meshless method, each method is characterised by it's own strategy for the construction of shape functions[4]. Among the different strategies there are[5]:

- the moving least square (MLS) method;

- the point interpolation method (PIM);

- the radial point interpolation method (RPIM);

- the radial point interpolation method with polynomial reproduction (RPIMp).

In the present section the terms interpolation and approximation have been mentioned; while many meshless shape functions possess the delta Kronecker property, resulting in an interpolation of the field variables, many other shape functions, like the ones obtained with the MLS, don't possess such a property and are only capable to provide an approximation of the field variables.

2.2   Numerical integration

Just like the FEM many meshless methods are based on the weak form of a certain problem (or a weakened-weak form, like for the SPIM strategy discussed in Section 3), that requires a numerical integration over the problem domain. While in the FEM the integration is performed using a quadrature rule within each element, meshless methods perform this operation making use of the so-called *integration domains*. Together with the kind of shape function, the specific type of integration process is a characteristic of each meshless method.

In the present section, the concept of numerical integration for meshless methods is illustrated using the procedure adopted in the EFG method [Belytschko et al., 1994], also similar to the one adopted in the MLPG method [Atluri and Zhu, 1998] and in the PIM [Liu and Gu, 2001]. In these methods the numerical integration is performed in a way that is similar to the FEM integration. As illustrated in Figure 5, the domain is tesselated into integration domains, that may form a regular or an irregular grid. Each integration domain is endowed with integration points, where the approximation functions are evaluated. The main difference with the FEM integration is that in the FEM all the integration points of the same element are supported by the same nodes (i.e. the nodes of the element), while in a meshless method each integration point usually has its own support domain, that may vary from point to point even in the same integration domain (Figure 5).

As it will be shown in Section 3, SPIM strategies are based on a different approach to the numerical integration process, due to the presence of a smoothing operation; the resulting integration

---

[4]Shape functions construction will be discussed with more details in Section 3.1, for the case of smoothed point interpolation methods.

[5]A comprehensive account on the different strategies for the construction of the most common meshless shape functions can be found in Liu [2009]
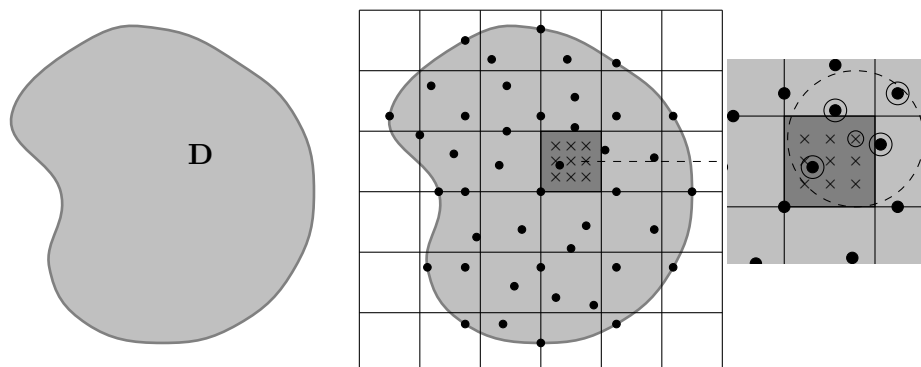
Figure 5: Meshless grid-like integration domains

is similar to the one of the stabilised conforming nodal integration (SNCI) proposed for the EFG method by Chen et al. [2001].

3   Meshless Smoothed Point Interpolation Methods (SPIMs)

Smoothed point interpolation methods, like other meshfree methods, rely on a set of nodes scattered in the problem domain, usually obtained through a triangulation operation. In a smoothed point interpolation method the field variable of the boundary value problem in linear elasticity, i.e. the displacement field $\bar{\boldsymbol{u}}(p)$ at each point $p \in \mathbf{D}$, is approximated as [Liu, 2009]

$$\bar{\boldsymbol{u}}(p) \simeq \sum_{i \in S_d} [\phi_i(p)]\{d_i\} \tag{3}$$

where the index i indicates a node p_i in the *support domain* S_d, i.e. the set of nodes in the neighbourhood of the point $p \in \mathbf{D}$ usually selected using a *T-scheme* [Liu, 2009], $[\phi_i(p)]$ is the nodal matrix of approximation functions, and $\{d_i\}$ is an array containing the nodal parameters of the field variable, i.e. its values $\bar{\boldsymbol{u}}(p_i)$ at each node p_i.

The shape functions, in this class of methods, are usually generated using the *point interpolation method* [Liu and Gu, 2001] (PIM), or the *radial point interpolation method* with or without polynomial reproduction [Wang and Liu, 2002b] (RPIM and RPIMp), and are characterised by the following properties: they are linearly independent, posses the Kronecker delta property, form a partition of unity, posses the linear reproducing property, present compact support, and are *not compatible*. The first meshfree methods based on these shape functions were proposed by Liu and his co-authors in Liu and Gu [2001] and Wang and Liu [2002b], as an alternative to existent meshfree methods. Indeed, due to their *delta Kronecker* property they allowed a more simple imposition of essential boundary conditions, with respect to other meshfree methods.

As pointed out above, however, the price for the delta Kronecker property is a lack of compatibility of the shape functions, meaning that the approximated fields may exhibit *discontinuities* when passing from a support domain to another. This makes such shape functions unable to satisfy the requirement of *square integrable first derivatives* needed for the formulation of standard weak forms. In order to overcome this issu, Liu [Liu, 2010a,b] proposed the use of a *weakened-weak form* of the elastic problem, based on a *smoothing operation*[6] [Liu, 2008] applied to the gradi-

---

[6] As mentioned by Liu (see, e.g. the introduction of Liu [2010a]) such smoothing technique [Liu, 2008] is analogous to the one adopted in other contextes like non-local continuum mechanics [Zhang et al., 2006, Eringen and Edelen, 1972], SPH methods [Liu and Liu, 2003, Lucy, 1977, Liu et al., 2008, Monaghan, 1982], hybrid FEM [Quarteroni and Valli, 1994], for the regularisation of spatial instabilities in nodal

ents involved in the formulation, that allows to reduce the continuity requirement of the shape functions.

The combination of the smoothing technique with point interpolation functions allowed to obtain different smoothed meshfree methods[7][8], like the *node-based smoothed point interpolation* (NS-PIM) method [Liu et al., 2005, Zhang et al., 2007], the *edge-based smoothed point interpolation* (ES-PIM) method [Liu and Zhang, 2008], and the *cell-based smoothed point interpolation method* [Liu and Zhang, 2009]. In order to deal with the presence of incompatible shape functions and smoothing operations, Liu developed a new theoretical framework, establishing two novel concepts: the *G-space theory* and the *weakened-weak form* (W^2) formulation (see, e.g. Liu [2010a,b], Liu and Zhang [2013]). These concepts were later extended to the case of the micropolar continuum theory by Gori et al. [2019c].

3.1 Shape functions

As pointed out above, three types of shape functions are commonly used in SPIMs strategies: PIM, RPIM and RPIMp. The present section focuses on shape functions obtained with the radial point interpolation method with polynomial reproduction, since they are the ones adopted in the numerical simulations of Section 5. Furthermore, the formulation of RPIMp shape function is more general and PIM and RPIM shape functions can be obtained as special cases.

The RPIMp approximation of a function u is expressed by

$$u(q) \simeq u^h(q) = \sum_{i=1}^{n} R_i(q)a_i + \sum_{j=1}^{m} p_j(q)b_j = \{R(q)\}^T\{a\} + \{p(q)\}^T\{b\} \tag{4}$$

where the terms $R_i(q)$ are a set of radial functions evaluated at q, constituting a radial basis, n is the number of support nodes in the local support domain at the point q, the terms $p_j(q)$ constitute a polynomial basis, and m is the number of monomials composing the polynomial basis. The number of monomials should be sufficient to guarantee, at least, the linear reproduction (e.g. in a two-dimensional domain three monomials are sufficient to pass the standard patch test, the constant term and the two linear terms in the coordinates x and y). The approximation of Equation 4 is characterised by two sets of unknown coefficients:

$$\{a\} = \left(a_1, \ldots, a_n\right)^T, \quad \{b\} = \left(b_1, \ldots, b_m\right)^T \tag{5}$$

which can be evaluated imposing the interpolation condition

$$u_k = \sum_{i=1}^{n} R_i(q_k)a_i + \sum_{j=1}^{m} p_j(q_k)b_j, \quad k = 1, \ldots, n \tag{6}$$

and the following additional condition [Golberg et al., 1999]:

$$\sum_{i=1}^{n} p_j(q_i)a_i = 0, \quad j = 1, \ldots, m \tag{7}$$

---

integrated meshfree methods Chen et al. [2001], and for the regularisation of material instabilities [Chen et al., 2000].

[7]The smoothing technique has been also applied by Liu and his co-authors to the standard FEM, obtaining the so-called *smoothed finite element method* (see, e.g. Liu et al. [2007] and Liu et al. [2009]).

[8]As pointed out in Liu and Zhang [2013], the smoothed point interpolation methods belong to the more general class of *strain constructed* methods, which still relies on point interpolation function, but with a different strategy for the treatement of the gradients.

that can be recast in the following compact form:

$$
\begin{cases}
\{U\} &= [R_q]\{a\} + [P_m]\{b\} \\
\{0\} &= [P_m]^T\{a\}
\end{cases}
\rightarrow
\begin{pmatrix} [R_q] & [P_m] \\ [P_m]^T & [0] \end{pmatrix}
\begin{pmatrix} \{a\} \\ \{b\} \end{pmatrix}
= \begin{pmatrix} \{U\} \\ \{0\} \end{pmatrix}
\tag{8}
$$

where the matrix $[R_q]$ with dimension $n \times n$ is the *moment matrix*, each line of which is composed by the radial basis function evaluated at a support node, while the matrix $[P_m]$ with dimension $n \times m$ has its lines formed by the polynomial basis evaluated at the support nodes:

$$
[R_q] = \begin{pmatrix} \{R(q_1)\}^T \\ \vdots \\ \{R(q_n)\}^T \end{pmatrix}, \quad
[P_m] = \begin{pmatrix} \{p(q_1)\}^T \\ \vdots \\ \{p(q_n)\}^T \end{pmatrix}
\tag{9}
$$

After some manipulations of the involved equations (see, e.g. Liu [2009]), the unknown coefficients can be evaluated as

$$
\{a\} = [S_a]\{U\}, \quad \{b\} = [S_b]\{U\}
\tag{10}
$$

where the matrices $[S_a]$ and $[S_b]$ are represented by

$$
[S_a] := [R_q]^{-1} - [R_q]^{-1}[P_m][S_b]
\tag{11}
$$

$$
[S_b] := \left([P_m]^T[R_q]^{-1}[P_m]\right)^{-1} [P_m]^T[R_q]^{-1}
\tag{12}
$$

resulting in the approximation

$$
u^h(q) = \left(\{R(q)\}^T[S_a] + \{p(q)\}^T[S_b]\right)\{U\} = \{\phi(q)\}^T\{U\}
\tag{13}
$$

where each *shape function* $\phi_i(q)$ is given by

$$
\phi_i(q) = R_j(q)[S_a]_{ji} + p_j(q)[S_b]_{ji}
\tag{14}
$$

The *radial functions* $R_i(p)$ appearing in Equation 4 defined for each node i in the support domain, depend only on the distance r_i between the point $p \in \mathbf{D}$ at which they must be evaluated and the node i. In the numerical simulations presented in Section 5 the following *exponential* (EXP) function was adopted:

$$
R_i(r_i) = \exp\left(-cr_i^2\right)
\tag{15}
$$

depending on the shape parameter c [Wang and Liu, 2002b]. Investigations on the choice of optimal shape parameters for the accuracy of the approximation can be found in Wang and Liu [2002b] and Wang and Liu [2002a], for example. However, as pointed out in Liu [2009], in presence of polynomial terms as in the RPIMp, and when smoothing techniques are adopted, the reliance of the accuracy on the shape parameters is significantly reduced.

By neglecting the polynomial term $\{p(q)\}^T\{b\}$ appearing in Equation 4 it's possible to obtain the formulation of of RPIM shape functions. PIM shape functions, on the other hand, can be obtained by neglecting the same term $\{p(q)\}^T\{b\}$ and by replacing the radial functions R_i with polynomial functions.

3.1.1   Shape functions properties

As already pointed out, the main advantage of PIM, RPIM and RPIMp shape functions over other common meshless shape functions is the delta Kronecker property, that allows a more simple imposition of boundary conditions. This property is obtained at the price of possible discontinuities of the shape functions over the domain, resulting in incompatible shape functions. According to

Liu [2009], these discontinuities are due to the absence of a *smooth transition* between support domains. When passing from an integration point to another, with different support domains, the shape function for a node changes suddenly, resulting in a discontinuity at that point. This doesn't happen, for example, in the *moving least square* (MLS) method [Liu, 2009], where the presence of weight functions allows for a smooth transition between support domains; MLS shape functions indeed, are compatible, in general.

PIM, RPIM and RPIMp shape functions require a matrix inversion operation in order to be evaluated at each interest point, and may suffer from singularity issues. PIM functions are more prone to the singularity of the moment matrix, that may occour due to peculiar alignments of the support nodes [Liu, 2009]. The moment matrix of RPIM and RPIMp, in general, is not singular and, as pointed out by Liu [2009], the construction of an RPIMp approximation is possible as long as the matrix $[P_m]^T [R_q]^{-1} [P_m]$ appearing in Equation 12 is invertible; the invertibility of such matrix is guaranteed, in general, as long as $n \geq m$.

Despite being more complex, RPIMp shape functions are usually preferred over the two other strategies, because of the singularity issues of PIM interpolations and because RPIM functions lack of consistency, in the sense that they don't exhibit polynomial reproduction of any order, meaning that they cannot pass the standard *patch test*.
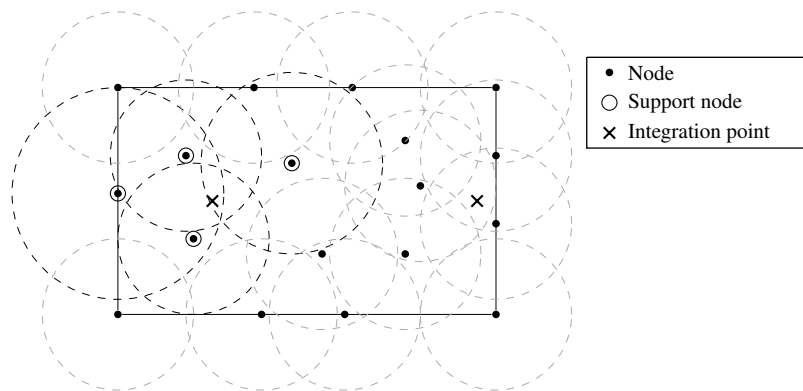
3.1.2   Support nodes selection strategies

In order to construct a meshless approximation at a certain point q of the problem domain it is necessary to use a number of n *support nodes*, composing the so-called *support domain* at the point q. In order to compose the support domain by selecting proper nodes in the neighbourhood of the point q, two different strategies have been adopted in this work: the selection via *influence domains* and via *T-schemes*[9].

The selection of support nodes via *influence domains* is a standard approach adopted in a number of meshfree methods. Each node is endowed with an *influence domain*, characterised by a *shape* and its *dimensions*. For example, in Figure 6, each node possesses a *circular* influence domain, characterised by a certain radius which may vary from node to node. For each integration point, the corresponding support domain is generated adding all the nodes which influence domains contain the selected integration point. In the example depicted in Figure 6, the support domain at the selected integration have been marked with an hollow circle. The number of nodes in each support domain is controlled by the ratio between the size of the influence domains and the mean nodal distance. While this method works well for MLS and RPIM shape functions, when applied to PIM shape functions it may lead to a singular moment matrix, in case of peculiar nodal alignments.

An alternative is represented by the so-called *T-schemes* [Liu, 2009]. Such methods perform the support nodes selection making use of *background triangular cells*, constructed as a triangulation of the scattered nodes of the discrete model. In general, there is no need to construct such set of cells specifically for the application of the T-schemes. A triangulation indeed, could have been already constructed during the discretisation of the domain, at the moment of the nodes generation. Furthermore, in smoothed point interpolation methods, like the ones considered in

---

[9]Another strategy, that hasn't been considered in this treatise but that could improve the performances of this class of meshfree methods, especially in case of large models, is the support nodes selection via *K-Nearest Neighbor* (KNN) algorithms, that could also be useful as an alternative to the methods considered in this treatise for the investigation of the regularisation properties related to the non-locality of PIM and RPIM approximations. As pointed out in 3.1.3, the use of the influence domains strategy tends to affect the sparseness of the stiffness matrix in a negative way; in this case, KNN strategies should introduce a non-locality analogous to the one of the influence domains strategy, with a reduced effect on the sparseness of the stiffness matrix.

Figure 6: Support nodes selection via influence domains

this treatise, a set of background cells is necessary for the construction of the *smoothing domains* (Section 3.2); hence, the triangular cells are already available for nodes selection. In the examples presented in Section 5, two kind of T-schemes have been considered: the *T3-scheme* and the *T6/3-scheme*, which, as pointed out by Liu [Liu, 2009], allow to obtain invertible moment matrices with both PIM and RPIM shape functions[10]. For an integration point belonging to a certain cell, the T3-scheme selects as support nodes the three nodes at the vertices of the cell (Figure 7(a)). The T6/3-scheme distinguishes between *interior* and *boundary* cells. The former are cells which have no one of their edges on the boundary of the problem domain, while the latter are cells with at least an edge on the boundary of the domain. For a boundary cell, the three nodes at the vertices of the cell are selected as support nodes, like in the T3-scheme. On the other hand, in case of an interior cell, a total number of six nodes is selected: the three nodes located at the vertices of the cell, and three nodes located at the remote vertices of the three neighbouring cells (Figure 7(b)).

(a) T3-scheme

(b) T6/3-scheme
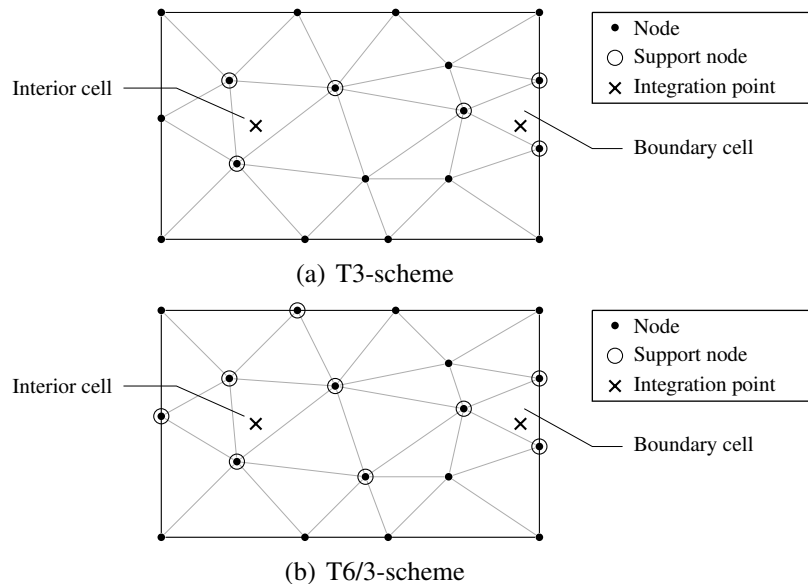
Figure 7: Support nodes selection via T-schemes

---

[10]As pointed out in Liu [2009], two further methods based on triangular background cells are available, the so-called T6 and T2L schemes, which selects, in general, a larger number of nodes with respect to the T-schemes already mentioned in this section. However, the example discussed in Section 5 focused only on the two T-schemes discussed in this section.

3.1.3　T-schemes vs influence domains

It has been mentioned that T-schemes are useful to guarantee the invertibility of the moment matrix in the PIM strategy. As pointed out by Liu [2009], they are also important to obtain a *sparse* stiffness matrix, which eases the solution of the linear system of equations. The sparseness of the stiffness matrix results from the *compact* character of the support domains generated with the T-schemes. Another interesting feature is that they also allow to know *a priori* the parts of the domain where the approximation functions may exhibit discontinuities, which is important for the node- and edge-based methods presented in Section 3.2.2. The influence domains strategy on the contrary, depending on the size of the influence domains, tends to destroy the sparseness of the stiffness matrix. Furthermore, when using the influence domains strategy, the positions of the shape functions discontinuities is not known *a priori*. Despite these disadvantages, this strategy was adopted in the simulations of Section 5.1 in order to investigate the non-local effects of the PIM and RPIM meshfree methods.

3.2　Smoothing domains creation and weakened-weak form

As pointed out in the beginning of Section 3, the use of *incompatible* approximation functions led Liu and his co-authors to the introduction of a novel theoretical structure, constituted by the *G-space theory* and the *weakened-weak form* (W^2) formulation (see, e.g. Liu [2010a,b] and Liu and Zhang [2013]), which will be briefly recalled here. First, the concept of weak form in classic elasticity is briefly recalled. Then, the novel formulation introduced by Liu and his co-authors is recalled, focusing on the following points:

- smoothing domains generation;

- smoothing operation;

- G-spaces;

- weakened-weak form.

3.2.1　Weak form in classic elasticity

For a problem of classic elasticity, characterised by the unknown field variable $\bar{u}$ defined over the problem domain $\mathbf{D}$, by the essential boundary condition $\bar{u} = \bar{u}^*$ at $\partial\mathbf{D}_e$, by the natural boundary condition $\bar{n} \cdot \underline{\sigma} = \bar{t}$ at $\partial\mathbf{D}_n$, and subjected to volume forces $\bar{b}_V$ defined over the whole domain $\mathbf{D}$, the weak form of the problem can be expressed as in the following: find the field $\bar{u} \in \mathcal{V}(\mathbf{D})$ such that

$$\int_{\mathbf{D}} \underline{\varepsilon}(\bar{w}) : \left(\hat{\mathbf{E}} : \underline{\varepsilon}(\bar{u}) \right) \, \mathrm{d}\mathcal{V} - \int_{\partial\mathbf{D}_n} \bar{w} \cdot \bar{t} \, \mathrm{d}\mathcal{S} - \int_{\mathbf{D}} \bar{w} \cdot \bar{b}_V \, \mathrm{d}\mathcal{V} = 0, \quad \forall \bar{w} \in \mathcal{V}^0(\mathbf{D}) \tag{16}$$

where $\underline{\varepsilon}(\bar{u}) = (u_{i,j} + u_{j,i})/2 \, \bar{e}_i \otimes \bar{e}_j$, and where $\mathcal{V}(\mathbf{D})$ and $\mathcal{V}^0(\mathbf{D})$ are, respectively, the spaces of *trial* and *test* functions, defined as

$$\mathcal{V}(\mathbf{D}) := \left\{ \bar{u} \in \left(\mathcal{H}^1(\mathbf{D}) \right)^n \mid \bar{u} = \bar{u}^* \text{ at } \partial\mathbf{D}_e^u \right\} \tag{17}$$

$$\mathcal{V}^0(\mathbf{D}) := \left\{ \bar{w} \in \left(\mathcal{H}^1(\mathbf{D}) \right)^n \mid \bar{w} = 0 \text{ at } \partial\mathbf{D}_e^u \right\} \tag{18}$$

where $\left(\mathcal{H}^1(\mathbf{D}) \right)^n$ is the space of square integrable n-dimensional vector fields with square integrable first derivatives over the domain $\mathbf{D}$. The weak form of Equation 16 can be recast in a compact for as

$$a(\bar{w}, \bar{u}) = f(\bar{w}), \quad \forall \bar{w} \in \mathcal{V}^0(\mathbf{D}) \tag{19}$$

where the *bilinear form* $a(\bar{\boldsymbol{w}}, \bar{\boldsymbol{u}})$ and the *linear functional* $f(\bar{\boldsymbol{w}})$ have been introduced, defined as

$$a(\bar{\boldsymbol{w}}, \bar{\boldsymbol{u}}) := \int_{\mathbf{D}} \underline{\boldsymbol{\varepsilon}}(\bar{\boldsymbol{w}}) : \left(\hat{\mathbf{E}} : \underline{\boldsymbol{\varepsilon}}(\bar{\boldsymbol{u}})\right) \, d\mathcal{V} \tag{20}$$

$$f(\bar{\boldsymbol{w}}) := \int_{\partial \mathbf{D}_n} \bar{\boldsymbol{w}} \cdot \bar{\boldsymbol{t}} \, d\mathcal{S} + \int_{\mathbf{D}} \bar{\boldsymbol{w}} \cdot \bar{\boldsymbol{b}}_V \, d\mathcal{V} \tag{21}$$

It is worth it to note that the requirement $\bar{\boldsymbol{u}}, \bar{\boldsymbol{w}} \in \left(\mathcal{H}^1(\mathbf{D})\right)^n$ is necessary to bound from above the value of the bilinear form[11].

Introducing the Voigt notation for a plane stress case, the components of the weak form of Equation 19 can be recast as

$$a(\bar{\boldsymbol{w}}, \bar{\boldsymbol{u}}) := \int_{\mathbf{D}} \left([L]\{\bar{\boldsymbol{w}}\}\right)^T [\hat{\mathbf{E}}] \left([L]\{\bar{\boldsymbol{u}}\}\right) \, d\mathcal{V} \tag{22}$$

$$f(\bar{\boldsymbol{w}}) := \int_{\partial \mathbf{D}_n} \{\bar{\boldsymbol{w}}\}^T \{\bar{\boldsymbol{t}}\} \, d\mathcal{S} + \int_{\mathbf{D}} \{\bar{\boldsymbol{w}}\}\{\bar{\boldsymbol{b}}_V\} \, d\mathcal{V} \tag{23}$$

where the derivative operator $[L]$ is such that

$$\{\underline{\boldsymbol{\varepsilon}}(\bar{\boldsymbol{u}})\} = [L]\{\bar{\boldsymbol{u}}\} \rightarrow \begin{pmatrix} \varepsilon_{xx} \\ \varepsilon_{yy} \\ \varepsilon_{xy} \end{pmatrix} = \begin{pmatrix} \partial_x & 0 \\ 0 & \partial_y \\ \partial_y & \partial_x \end{pmatrix} \begin{pmatrix} u_x \\ u_y \end{pmatrix} \tag{24}$$

Within the FEM approach the weak form of Equation 19 is discretised by replacing the trial and test functions $\bar{\boldsymbol{u}}$ and $\bar{\boldsymbol{w}}$ with the approximations $\bar{\boldsymbol{u}}^h \in \mathcal{V}_h(\mathbf{D})$ and $\bar{\boldsymbol{w}}^h \in \mathcal{V}_h^0(\mathbf{D})$, where $\mathcal{V}_h(\mathbf{D})$ and $\mathcal{V}_h^0(\mathbf{D})$ are the *discretised* spaces of trial and test functions such that

$$\mathcal{V}_h(\mathbf{D}) := \left\{ \bar{\boldsymbol{u}} \in \left(\mathcal{H}_h^1(\mathbf{D})\right)^n \mid \bar{\boldsymbol{u}} = \bar{\boldsymbol{u}}^* \text{ at } \partial \mathbf{D}_e^u \right\} \tag{25}$$

$$\mathcal{V}_h^0(\mathbf{D}) := \left\{ \bar{\boldsymbol{w}} \in \left(\mathcal{H}_h^1(\mathbf{D})\right)^n \mid \bar{\boldsymbol{w}} = 0 \text{ at } \partial \mathbf{D}_e^u \right\} \tag{26}$$

where $\left(\mathcal{H}_h^1(\mathbf{D})\right)^n$ is the space of square integrable n-dimensional *discretised* vector fields (i.e. constructed with approximation functions in terms of a set of nodal parameters) with square integrable first derivatives over the domain $\mathbf{D}$. The discretisation results in a matrix system of the kind

$$[K] \{X\} = \{R\} \tag{27}$$

where $[K]$ is the global stiffness matrix of the system, $\{X\}$ the nodal parameters vector collecting all the nodal parameters $\{d_i\}$, and $\{R\}$ the vector of nodal forces. In a FEM model, the stiffness matrix $[K]$ would be evaluated through the contribution of each finite element:

$$[K]_{el} = \int_{\mathbf{D}_{el}} [B(p)]^T [\hat{\mathbf{E}}(p)][B(p)] \, d\mathcal{V} \tag{28}$$

where the symbol $\int_{\mathbf{D}_{el}}$ indicates the integral over an element, and where the matrix $[B(p)]$ is composed by the submatrices $[B_i(p)]$ as $[B(p)] = ([B_1(p)] \ldots [B_i(p)] \ldots [B_N(p)])$, such that

$$\{\underline{\boldsymbol{\varepsilon}}(p)\} = \sum_{i=1}^{N} [B_i(p)]\{d_i\} = \begin{pmatrix} \partial_x N_i(p) & 0 \\ 0 & \partial_y N_i(p) \\ \partial_y N_i(p) & \partial_x N_i(p) \end{pmatrix} \begin{pmatrix} d_{xi}^u \\ d_{yi}^u \end{pmatrix} \tag{29}$$

---

[11]Taking into account the analogy between the bilinear form and the total strain energy of a body it is possible to emphasise that this requirement is necessary to bound from above the strain energy.

The requirement of the approximated field variable to belong to the discretised space $\left(\mathcal{H}_h^1(\mathbf{D})\right)^n$ is satisfied when the approximation is constructed with FEM shape functions, which exhibit a piecewise continuous first derivative that is *bounded in an integral sense*. This requirement however, poses a limitation on the use of the meshless shape functions generated with the PIM and RPIMp strategies. Since such shape functions are, in general, *incompatible*, also the resulting approximation of the field variable will be *incompatible*, i.e. it will present *discontinuities*. Hence, if the trial and test functions $\bar{\boldsymbol{u}}$ and $\bar{\boldsymbol{w}}$ are replaced by the approximations $\bar{\boldsymbol{u}}^h$ and $\bar{\boldsymbol{w}}^h$ obtained with PIM or RPIM shape functions, the requirement on the square integrable first derivative won't be satisfied anymore.

3.2.2 Smoothing domains creation

G-spaces are defined for discrete models, where the field variables are expressed in terms of approximation functions and nodal parameters, like the space $\left(\mathcal{H}_h^1(\mathbf{D})\right)^n$ containing the approximated field variables of an FEM model as pointed out in the previous section. Before recalling the definition of G-spaces is then necessary to present the peculiar discretisation strategy which they rely on.

As pointed out in Liu [2010a], the domain $\mathbf{D}$ is discretised with a set of N_e non-overlapping *background cells* $\mathbf{D}_i^C$, with $i = 1, \ldots, N_e$, which vertices correspond to a set of N_n scattered nodes; these cells are, in general, triangular. It is worth it to note that, if one of the T-schemes illustrated in Figure 7 is adopted, the boundaries $\partial \mathbf{D}_i^C$ of the cells represent parts of the domain where the approximation functions may be discontinuous. A further tessellation of the domain is performed, introducing a set of N_S non-overlapping *smoothing domains* $\partial \mathbf{D}_k^S$, with $k = 1, \ldots, N_S$. When generating this second subdivision, the following *no-sharing rule* must be considered: the boundaries $\partial \mathbf{D}_k^S$ of the smoothing domains must not share any finite portion with the boundaries $\partial \mathbf{D}_i^C$ of the background cells, i.e. they may share at most a finite number of points with the parts of the domain where the approximation functions may be discontinuous. The reason for this requirement is to guarantee the possibility to perform the integration of the approximation functions along the boundary of the smoothing domains.

In this treatise, two different strategies for the creation of smoothing domains are considered:
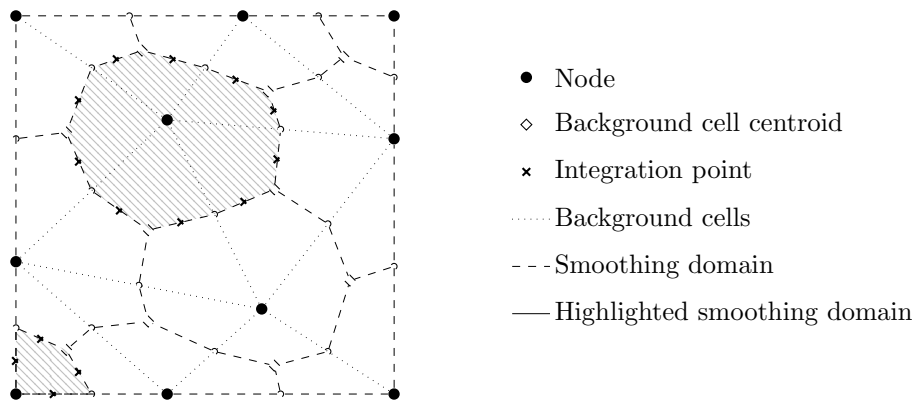
- the *node-based smoothed point interpolation method* (NS-PIM), and

- the *edge-based smoothed point interpolation method* (ES-PIM).

The *node-based smoothed point interpolation method* (NS-PIM) was originally proposed by Liu and his co-authors in Liu et al. [2005], Liu and Zhang [2007], and Zhang et al. [2007] as a meshfree method based on *point interpolation* shape functions with a *nodal integration procedure*[12], and was later shown to belong to the more general class of methods obtained with a *gradient smoothing technique* [Liu, 2008]. Such method relies on the weakened-weak form presented in Section 3.2.5 and, as anticipated by its name, on smoothing domains based on the scattered nodes of the discrete model. Despite it could be used also for one- and three-dimensional problems, in the following attention is focused on the two-dimensional case. The generation of smoothing domains with the *equally-shared smoothing domains strategy*[13] (see, e.g. Liu and Zhang [2013]) is depicted in Figure 8, for an *internal* and a *boundary* domains. The generic smoothing domain $\mathbf{D}_k^S$ at the node k is generated using the surrounding triangular cells, by connecting sequentially, the midpoints of

---

[12]In the cited papers the method was originally called *linearly conforming point interpolation method* (LC-PIM).

[13]The equally-shared smoothing domain strategy is the most common in the NS-PIM. However, as pointed out in Liu and Zhang [2013], for example, also Voronoi cells can be used as smoothing domains, as done in Chen et al. [2001] for the nodal integration strategy in the EFG method.

the cells edges containing the node k with the centroids of the cells. With this strategy, the number of smoothing domains is equal to the number of nodes ($N_S = N_n$), which satifies the minimum number requirement discussed in Liu [2008]. From Figure 8 it can be observed that these domains also satisfy the requirements presented in Section 3.2.2, since they are *non-overlapping* and they respect the *no-sharing rule*; indeed, the boundary $\partial \mathbf{D}_k^S$ of a generic smoothing domain doesn't share any finite portion with the edges of the surrounding cells, where the approximation functions may be discontinuous, but share only the midpoint of their edges.

- • Node
- ◇ Background cell centroid
- ✕ Integration point
- ······ Background cells
- - - - Smoothing domain
- —— Highlighted smoothing domain

Figure 8: Node-based smoothing domain

The *edge-based smoothed point interpolation method* (ES-PIM) was introduced by Liu and his co-authors in Liu and Zhang [2008] in order to correct the excessive *softnening* effect of the NS-PIM, which resulted in temporally unstable dynamic problems. As pointed out in Liu and Zhang [2013], the ES-PIM exhibits a stiffer behaviour with respect to the NS-PIM, is both spatially and temporally stable, and is capable to produce much more accurate results compared to the NS-PIM and the standard FEM.

The difference between the NS-PIM and the ES-PIM relies in the strategy for the generation of the smoothing domains, which in the latter, as anticipated by the name of the method, is based on the *edges* of the background cells instead of the nodes. As illustrated in Figure 9, the smoothing domain associated to aninternal edge is constructed by connecting the two nodes at the ends of the edge with the centroids of the two triangular cells that share the edge. For a boundary edge the procedure is the same, except for the fact that also the edge belongs to the boundary of the smoothing domain. As pointed out in Liu [2009], also this strategy satisfies the requirement on the minimum number of smoothing domains, is *non-overlapping*, and respect the *no-sharing* rule.

- • Node
- ◇ Background cell centroid
- ✕ Integration point
- ······ Background cells
- - - - Smoothing domain
- —— Highlighted smoothing domain
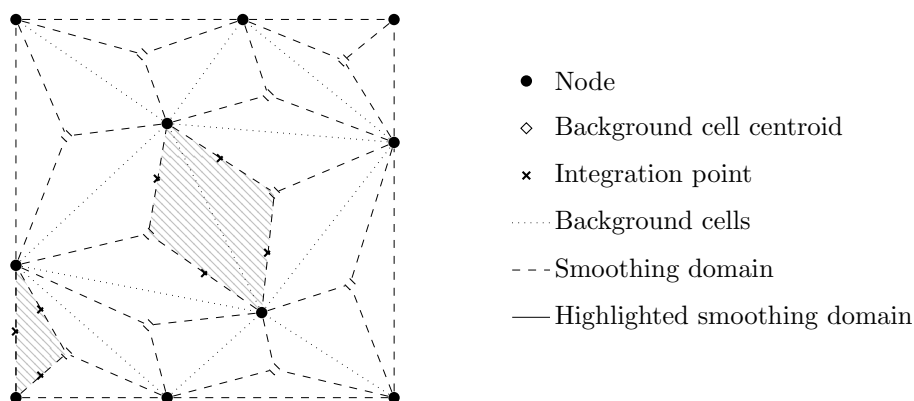
Figure 9: Edge-based smoothing domain

3.2.3   Smoothing operation

The smoothing operation illustrated in this section was introduced by Liu (see, e.g. Liu [2008]) in order to reduce the requirement of continuity of the field variable appearing in the weak form expressed by Equation 16. Such smoothing operation is based on the domain tessellation discussed in Section 3.2.2, assuming the tessellation to be *stationary*[14] during the analysis. Within this approach, the derivative $\mathrm{grad}(\bar{\boldsymbol{u}}) = u_{i,j}\,\bar{\boldsymbol{e}}_i \otimes \bar{\boldsymbol{e}}_j$ of the field variable $\bar{\boldsymbol{u}}$ at a certain point $p \in \mathbf{D}_k^S$ is replaced inside the smoothing domain $\mathbf{D}_k^S$ by the *smoothed derivative* $\widetilde{\mathrm{grad}}(\bar{\boldsymbol{u}}) = \widetilde{u_{i,j}}\,\bar{\boldsymbol{e}}_i \otimes \bar{\boldsymbol{e}}_j$, where

$$u_{i,j}(p) \simeq \widetilde{u_{i,j}}(p_k) := \int_{\mathbf{D}_k^S} u_{i,j}(\xi)\,\widetilde{W}(p_k - \xi)\,\mathrm{d}\mathcal{V}, \quad p \in \mathbf{D}_k^S \tag{30}$$

is *constant* within a smoothing domain. In the equation above, $\widetilde{W}$ is a *smoothing function*, and p_k is the centre of the smoothing domain. If the field variable $\bar{\boldsymbol{u}}$ is continuous, the Green's divergence theorem can be applied, resulting in

$$\widetilde{u_{i,j}}(p_k) = \int_{\partial \mathbf{D}_k^S} \left(u_i(\xi) \otimes n_j^{(k)}(\xi) \right) \widetilde{W}(p_k - \xi)\,\mathrm{d}\mathcal{S} - \int_{\mathbf{D}_k^S} u_i(\xi) \otimes \widetilde{W}_{,j}(p_k - \xi)\,\mathrm{d}\mathcal{V} \tag{31}$$

where $\bar{\boldsymbol{n}}^{(k)}$ is the unitary outward normal vector field on the boundary $\partial \mathbf{D}_k^S$. A common choice for the smoothing function $\widetilde{W}$ is the following Heaviside-type function

$$\widetilde{W}(p_k - \xi) := \begin{cases} 1/A_k & \xi \in \mathbf{D}_k^S \\ 0 & \xi \notin \mathbf{D}_k^S \end{cases} \tag{32}$$

where $A_k = \int_{\mathbf{D}_k^S} \mathrm{d}\mathcal{V}$, which results in

$$\widetilde{u_{i,j}}(p_k) = \frac{1}{A_k} \int_{\partial \mathbf{D}_k^S} u_i(\xi) \otimes n_j^{(k)}(\xi)\,\mathrm{d}\mathcal{S} \tag{33}$$

As pointed out by Liu and Zhang:

> "The "smoothed derivatives" defined in Equation (2.67) [Equation 33 in this treatise] is a generalized concept. It is NOT "the derivative obtained by smoothing the derivatives of the function", because such a gradient does not in general exist, as the function may not be continuous! Rigorously speaking, the "smoothed derivative" is the outward flux of the function across the smoothing domain boundary $\Gamma_{\mathbf{x}}^s$ [$\partial \mathbf{D}_k^S$ in in this treatise]. The smoothed derivative of a function can be approximated using only the function values, and no differentiation is needed. Hence the consistency requirement on the function is reduced, if only the approximate derivative is required." [Liu and Zhang, 2013, pag. 67]

As emphasised in the quoted text, the smoothing operation consists into replace the derivative of the field variable with the smoothed derivative illustrated in Equation 33. This substitution is assumed to be valid whether the field variable is continuous or not, i.e. whether the application of the Green's theorem in Equation 31 is licit or not. As pointed out in Liu [2008], though not rigorous in theory, this operation is possible to implement, since Equation 33 require no differentiation of the field variable, opening the possibility to use PIM and RPIM *incompatible* functions for the approximation of the field variable.

---

[14]The stationarity requirement was originally adopted in Liu [2010a]; however, other *smoothed* methods don't rely on this assumption (see, e.g. Liu and Zhang [2013]).

3.2.4 G-space theory

A general treatement on the G-space theory can be found in Liu [2010a] and Liu and Zhang [2013], and its application to classic elasticity in Liu [2010b]. Briefly, the G-space[15] $\mathcal{G}_h^1(\mathbf{D})$ is defined as the following space of functions $u(p)$ *discretised* in terms of approximation functions $\phi_j(p)$ and nodal parameters d_j

$$
\mathcal{G}_h^1(\mathbf{D}) := \Big\{ u \mid u(p) = \sum_{j=1}^{N_n} \phi_j(p) d_j, \ u \in \mathcal{L}^2(\mathbf{D}),
$$
$$
\sum_{k=1}^{N_S} \left(\int_{\partial \mathbf{D}_k^S} u(\xi)\, n_i^{(k)}(\xi)\, \mathrm{d}\mathcal{S} \right)^2 > 0 \Leftrightarrow u \neq c \in \mathbb{R}, \ i = 1, \dots, d \Big\} \tag{34}
$$

where $c \in \mathbb{R}$ is a constant, d the dimension of the space $\mathbf{D}$, and $\mathcal{L}^2(\mathbf{D})$ the *Lebesgue* space of square integrable functions. When n-dimensional vector fields are considered, the following space can be introduced

$$
\left(\mathcal{G}_h^1(\mathbf{D}) \right)^n := \left\{ \bar{\boldsymbol{u}} = u_i\, \bar{\boldsymbol{e}}_i \mid u_i \in \mathcal{G}_h^1(\mathbf{D}), \ i = 1, \dots, n \right\} \tag{35}
$$

This space is endowed with the following *inner product*

$$
< \bar{\boldsymbol{u}}, \bar{\boldsymbol{w}} >_{\mathcal{G}^1} = \underbrace{\int_{\mathbf{D}} (\bar{\boldsymbol{u}} \cdot \bar{\boldsymbol{w}})\, \mathrm{d}\mathcal{V}}_{< \bar{\boldsymbol{u}}, \bar{\boldsymbol{w}} >_{\mathcal{L}^2}} + \underbrace{\int_{\mathbf{D}} \left(\widetilde{\mathrm{grad}}(\bar{\boldsymbol{u}}) : \widetilde{\mathrm{grad}}(\bar{\boldsymbol{w}}) \right) \mathrm{d}\mathcal{V}}_{< \widetilde{\mathrm{grad}}(\bar{\boldsymbol{u}}), \widetilde{\mathrm{grad}}(\bar{\boldsymbol{w}}) >_{\mathcal{L}^2}}, \quad \bar{\boldsymbol{u}}, \bar{\boldsymbol{v}} \in \left(\mathcal{G}_h^1(\mathbf{D}) \right)^n \tag{36}
$$

with induced *norm* $\| \cdot \|_{\mathcal{G}^1}^2$ and *semi-norm* $| \cdot |_{\mathcal{G}^1}^2$ expressed as combination of norms in the Lebesgue space $\mathcal{L}^2(\mathbf{D})$

$$
\| \bar{\boldsymbol{u}} \|_{\mathcal{G}^1}^2 = \| \bar{\boldsymbol{u}} \|_{\mathcal{L}^2}^2 + | \bar{\boldsymbol{u}} |_{\mathcal{G}^1}^2, \quad \bar{\boldsymbol{u}} \in \left(\mathcal{G}_h^1(\mathbf{D}) \right)^n \tag{37}
$$

$$
| \bar{\boldsymbol{u}} |_{\mathcal{G}^1}^2 = \left\| \widetilde{\mathrm{grad}}(\bar{\boldsymbol{u}}) \right\|_{\mathcal{L}^2}^2, \quad \bar{\boldsymbol{u}} \in \left(\mathcal{G}_h^1(\mathbf{D}) \right)^n \tag{38}
$$

As it can be observed in Equation 34, the shape functions must be (i) *linearly independent*, in order to form a basis, (ii) *bounded*, i.e. square integrable, and (iii) must verify the following *positivity condition*:

$$
\sum_{k=1}^{N_S} \left(\int_{\partial \mathbf{D}_k^S} u(\xi)\, n_i^{(k)}(\xi)\, \mathrm{d}\mathcal{S} \right)^2 > 0 \tag{39}
$$

The two last requirements, as pointed out by Liu [Liu, 2010a], are necessary to guarantee the stability and convergence of the numerical models built upon the weakened-weak formulation based on G-spaces.

The main difference between the space $\mathcal{G}_h^1(\mathbf{D})$ and the space $\mathcal{H}_h^1(\mathbf{D})$ usually adopted in FEM applications (i.e. the discretised space of square integrable functions with square integrable first derivative), is the fact that the latter requires both the function and its first derivative to be square integrable ($\| \bar{\boldsymbol{u}} \|_{\mathcal{L}^2(\mathbf{D})}^2 < \infty$ and $\| \mathrm{grad}(\bar{\boldsymbol{u}}) \|_{\mathcal{L}^2(\mathbf{D})}^2 < \infty$) in order to ensure an upper bound to the strain energy (aka the bilinear form), while in the former only the function is required to be square integrable since, as it will be discussed in the following section, the bilinear form of the weakened-weak form depends only on the function and not on its first derivative. While in the weakened-weak form the strain energy is automatically bounded from above once the functions are

---

[15]The more general case of spaces $\mathcal{G}_h^m(\mathbf{D})$ with $m > 1$ is not considered here.

square integrable, a lower bound must be explicitly imposed, with the aforementioned positivity condition; in the standard weak form, as pointed out in Liu [2010a], an explicit lower bound is not necessary, since the condition $\|\mathrm{grad}(\bar{\boldsymbol{u}})\|_{\mathcal{L}^2(\mathbf{D})}^2 = 0$ is attained only if the function is zero everywhere, due to the Poincare-Friedrichs inequality[16] [Liu, 2009]. The reduced order of continuity required by the space $\mathcal{G}_h^1(\mathbf{D})$ opens the possibility to use PIM and RPIM shape functions as a basis to generate its elements. The main characteristics of G-spaces needed to guarantee the existence and uniqueness of the solution of the weakened-weak formulation discussed in the following Section 3.2.5 have been widely discussed by Liu and his co-authors in a number of papers and books (see, e.g. Liu [2010a,b, 2009] and Liu and Zhang [2013]) and won't be recalled here.

3.2.5   Weakened-weak form of the classic elasticity problem

The weakened-weak form in classic elasticity have been presented in Liu [2010b]. As discussed in the mentioned paper, such formulation can be obtained by replacing the strain tensor $\underline{\boldsymbol{\varepsilon}}$ appearing in the bilinear form of Equation 20 with its *smoothed* version $\widetilde{\underline{\boldsymbol{\varepsilon}}}$, resulting in the *smoothed bilinear form*

$$\widetilde{a}(\bar{\boldsymbol{w}}, \bar{\boldsymbol{u}}) = \int_{\mathbf{D}} \widetilde{\underline{\boldsymbol{\varepsilon}}}(\bar{\boldsymbol{w}}(p_k)) : \left(\hat{\mathbf{E}} : \widetilde{\underline{\boldsymbol{\varepsilon}}}(\bar{\boldsymbol{u}}(p_k)) \right) \, \mathrm{d}\mathcal{V} \tag{40}$$

where the smoothed strain tensor $\widetilde{\underline{\boldsymbol{\varepsilon}}}$ is obtained considering the smoothing derivatives of Equation 33

$$\widetilde{\varepsilon}_{ij} = \frac{1}{2} \left(\widetilde{u_{i,j}} + \widetilde{u_{j,i}} \right) \tag{41}$$

In plane stress case, the strain tensor assumes the following matrix expression:

$$\{\widetilde{\underline{\boldsymbol{\varepsilon}}}(\bar{\boldsymbol{u}}(p_k))\} = \frac{1}{A_k} \int_{\partial \mathbf{D}_k^S} [\widetilde{L_n(\xi)}] \{\bar{\boldsymbol{u}}(\xi)\} \, \mathrm{d}\mathcal{S} \tag{42}$$

$$\begin{pmatrix} \widetilde{\varepsilon}_{xx} \\ \widetilde{\varepsilon}_{yy} \\ \widetilde{\varepsilon}_{xy} \end{pmatrix} = \frac{1}{A_k} \int_{\partial \mathbf{D}_k^S} \begin{pmatrix} n_x^{(k)}(\xi) & 0 \\ 0 & n_y^{(k)}(\xi) \\ n_y^{(k)}(\xi) & n_x^{(k)}(\xi) \end{pmatrix} \begin{pmatrix} u_x(\xi) \\ u_y(\xi) \end{pmatrix} \mathrm{d}\mathcal{S} \tag{43}$$

Recalling that the smoothed derivatives are *constant* within each smoothing domain defined in Section 3.2.2, and also assuming the constitutive operator $\hat{\mathbf{E}}$ to be constant within each smoothing domain, the integral $\int_{\mathbf{D}}$ may be replaced with a summation over the smoothing domains, resulting in

$$\widetilde{a}(\bar{\boldsymbol{w}}, \bar{\boldsymbol{u}}) = \sum_{k=1}^{N_S} A_k \left(\widetilde{\underline{\boldsymbol{\varepsilon}}}(\bar{\boldsymbol{w}}(p_k)) : \left(\hat{\mathbf{E}} : \widetilde{\underline{\boldsymbol{\varepsilon}}}(\bar{\boldsymbol{u}}(p_k)) \right) \right) \tag{44}$$

The *weakened-weak form* of the classic elasticity problem recalled in Section 3.2.1 consists then into find the field $\bar{\boldsymbol{u}} \in \mathcal{V}(\mathbf{D})$ such that

$$\widetilde{a}(\bar{\boldsymbol{w}}, \bar{\boldsymbol{u}}) = f(\bar{\boldsymbol{w}}), \quad \forall \bar{\boldsymbol{w}} \in \mathcal{V}^0(\mathbf{D}) \tag{45}$$

where $\mathcal{V}(\mathbf{D})$ and $\mathcal{V}^0(\mathbf{D})$ are, respectively, the spaces of *trial* and *test* functions, defined as

$$\mathcal{V}(\mathbf{D}) := \left\{ \bar{\boldsymbol{u}} \in \left(\mathcal{G}_h^1(\mathbf{D}) \right)^n \mid \bar{\boldsymbol{u}} = \bar{\boldsymbol{u}}^* \text{ at } \partial \mathbf{D}_e^u \right\} \tag{46}$$

$$\mathcal{V}^0(\mathbf{D}) := \left\{ \bar{\boldsymbol{w}} \in \left(\mathcal{G}_h^1(\mathbf{D}) \right)^n \mid \bar{\boldsymbol{w}} = 0 \text{ at } \partial \mathbf{D}_e^u \right\} \tag{47}$$

---

[16]As pointed out in Liu [2009], the Poincare-Friedrichs inequality is represented by $c\|\bar{\boldsymbol{w}}\|_{\mathcal{H}^1}^2 \leq |\bar{\boldsymbol{w}}|_{\mathcal{H}^1}^2$, $\forall \bar{\boldsymbol{w}} \in \left(\mathcal{H}_0^1(\mathbf{D}) \right)^k$, with $c \in \mathbb{R}$ and $c > 0$, and expresses an equivalence between the norm and the seminorm for k-dimensional vector fields in the space $\mathcal{H}_0^1(\mathbf{D})$ of square integrable k-dimensional vector fields with square integrable first derivative with prevented *rigid-body* motions.

Discussions on the properties of the weakened-weak form of Equation 45, as well as on the conditions that ensure the existence and uniqueness of the solution $\bar{\boldsymbol{u}} \in \mathcal{V}(\mathbf{D})$ can be found in Liu and Zhang [2008] and Liu [2010b].

The absence of derivatives in the smoothed bilinear form (Equation 44) allows to express both the trial and the test functions in terms of PIM and RPIM shape functions $\phi_i(p)$, since they are well suited to form a basis for the space $\left(\mathcal{G}_h^1(\mathbf{D})\right)^n$, resulting (for the trial functions) in

$$\{\bar{\boldsymbol{u}}(p)\} = \sum_{i \in S_d} [\phi_i(p)]\{d_i\} \tag{48}$$

where $\{d_i\}$ is the array collecting the nodal parameters at the node i, and where S_d is the support domain of the point $p \in \mathbf{D}$. The smoothed strains can be expressed in terms of the smoothed strain-displacement matrix $[\widetilde{B}_i(p_k)]$ as

$$\{\widetilde{\underline{\varepsilon}}(\bar{\boldsymbol{u}}(p_k))\} = \sum_{i \in S_d} [\widetilde{B}_i(p_k)]\{d_i\} \tag{49}$$

where $[\widetilde{B}_i(p_k)]$, in a plane stress state, is represented by

$$\begin{aligned}
[\widetilde{B}_i(p_k)] &= \frac{1}{A_k} \int_{\partial \mathbf{D}_k^S} [\widetilde{L_n}(\xi)][\phi_i(\xi)] \, \mathrm{d}\mathcal{S} \\
&= \frac{1}{A_k} \int_{\partial \mathbf{D}_k^S} \begin{pmatrix} n_x^{(k)}(\xi)\,\phi_i(\xi) & 0 \\ 0 & n_y^{(k)}(\xi)\,\phi_i(\xi) \\ n_y^{(k)}(\xi)\,\phi_i(\xi) & n_x^{(k)}(\xi)\,\phi_i(\xi) \end{pmatrix} \, \mathrm{d}\mathcal{S} \\
&= \begin{pmatrix} \widetilde{\phi}_{i,x}(p_k) & 0 \\ 0 & \widetilde{\phi}_{i,y}(p_k) \\ \widetilde{\phi}_{i,y}(p_k) & \widetilde{\phi}_{i,x}(p_k) \end{pmatrix}
\end{aligned} \tag{50}$$

where the terms $\widetilde{\phi}_{i,l}(p_k)$ are the *smoothed* derivatives of the shape functions, expressed by

$$\widetilde{\phi}_{i,l}(p_k) := \frac{1}{A_k} \int_{\partial \mathbf{D}_k^S} n_l^{(k)}(\xi)\,\phi_i(\xi) \, \mathrm{d}\mathcal{S}, \quad l = x, y \tag{51}$$

The smoothed shape functions appearing in Equation 51, which allow to evaluate the smoothed bilinear form, are calculated performing a numerical integration along the boundary $\partial \mathbf{D}_k^S$ of each smoothing domain. Since the boundary of each smoothing domain is composed by a set of linear segments, the integration can be expressed as a sum of Gaussian quadratures over each segment, resulting in

$$\widetilde{\phi}_{i,l}(p_k) = \frac{1}{A_k} \sum_{m=1}^{n_{seg}} \frac{L_m}{2} \left(\sum_{n=1}^{n_{gp}} W_n^{gp}\,\phi_i(p_{m,n})\,n_{l,m}^{(k)} \right), \quad l = x, y \tag{52}$$

where n_{seg} is the number of segments, L_m the length of the *m-th* segment, n_{gp} the number of integration points of each segment, $p_{m,n}$ the *n-th* integration point of the *m-th* segment with associated weight W_n^{gp}, and $n_{l,m}^{(k)}$ the component in the direction l of the unit normal to the *m-th* segment of the *k-th* smoothing domain.

Finally, the discretisation results in the same algebraic system expressed in Equation 27, where now the stiffness matrix $[K]$ is evaluated in terms the contribution of each *smoothing domain*

$$[K(p_k)]_{Sd} = A_k[\widetilde{B}(p_k)]^T[\hat{\mathbf{E}}(p_k)][\widetilde{B}(p_k)] \tag{53}$$

where, as in the FEM, the matrix $[\widetilde{B}(p_k)]$ is composed by the submatrices $[\widetilde{B}_i(p_k)]$ as:

$$[\widetilde{B}(p_k)] = \left([\widetilde{B}_1(p_k)] \ldots [\widetilde{B}_i(p_k)] \ldots [\widetilde{B}_N(p_k)] \right) \tag{54}$$

where N is the number of nodes in the support domain S_d at the point p_k.

Due to the peculiar domain tessellation and to the adoption of the smoothing operation, SPIM models exhibit different properties when compared to the standard FEM. In Liu and Zhang [2007] and Liu [2008], the authors pointed out that the smoothed bilinear form is capable to provide *softer* results with respect to the standard weak form, when the same approximation functions are used $(\widetilde{a}(\bar{\boldsymbol{w}}, \bar{\boldsymbol{w}}) \leq a(\bar{\boldsymbol{w}}, \bar{\boldsymbol{w}}), \bar{\boldsymbol{w}} \in \mathcal{V}_h^0(\mathbf{D}))$. They also showed that it is also capable to provide an *upper bound* approximation to the exact solution. This last characteristic however, depends on both the kind of approximation functions that are being adopted, and on the peculiar strategy used for the generation of the smoothing domains.

3.3 SPIMs for damage modelling

The first application of SPIM strategies to the modelling of damage problems was proposed by Gori et al. [2019b], where the authors also pointed out the regularisation properties induced by the SPIM approach; later, in Saliba et al. [2021], a strategy was proposed to analyse damage models with a coupled SPIM-FEM model. Some of the results discussed in Gori et al. [2019b] are recalled in this section.

Here, attention is focused on the case of *scalar-isotropic damage models* in a geometrically linear context. Such models belong to the more general class of elastic-degrading models, and are expressed in terms of a *secant* stress-strain relation $\underline{\boldsymbol{\sigma}} = \hat{\mathbf{E}}^S : \underline{\boldsymbol{\varepsilon}}$, where $\hat{\mathbf{E}}^S$ is the *secant* constitutive operator, which components depend both on the *initial* constitutive tensor $\hat{\mathbf{E}}$ and on a *scalar damage variable* D, assuming values from 0 to 1. When the damage is assumed to be *isotropic* the secant constitutive operator is represented by the well-known expression $\hat{\mathbf{E}}^S(D, \hat{\mathbf{E}}) = (1-D)\,\hat{\mathbf{E}}$. In such models the loading process is represented in terms of a loading function which is usually expressed as the following additive decomposition:

$$f(\underline{\boldsymbol{\varepsilon}}, D) = \varepsilon_{eq}(\underline{\boldsymbol{\varepsilon}}) - K(D) \leq 0 \tag{55}$$

where $\varepsilon_{eq}(\underline{\boldsymbol{\varepsilon}})$ is a function depending only on the strain tensor, usually indicated as *equivalent deformation*, that represents the loading condition of the continuum, while $K(D)$ is a *historical parameter* that depends only on the damage variable and that is representative of the maximum level of deformation reached during the loading process. The rate of the previous secant relation, $\underline{\dot{\boldsymbol{\sigma}}} = \hat{\mathbf{E}}^S : \underline{\dot{\boldsymbol{\varepsilon}}} + \dot{\hat{\mathbf{E}}}^S : \underline{\boldsymbol{\varepsilon}}$, can be recast in the *tangent* relation $\underline{\dot{\boldsymbol{\sigma}}} = \hat{\mathbf{E}}^t : \underline{\dot{\boldsymbol{\varepsilon}}}$ between the stress and the strain rates, where $\hat{\mathbf{E}}^t$ is the tangent constitutive operator expressed by Carol et al. [1994]

$$\hat{\mathbf{E}}^t = (1-D)\,\hat{\mathbf{E}} - \frac{1}{H^*}\,(\underline{\boldsymbol{m}}^* \otimes \underline{\boldsymbol{n}}^*) \tag{56}$$

where

$$\underline{\boldsymbol{m}}^* := -\hat{\mathbf{E}} \cdot \underline{\boldsymbol{\varepsilon}}, \qquad \underline{\boldsymbol{n}}^* := \frac{\partial \varepsilon_{eq}}{\partial \underline{\boldsymbol{\varepsilon}}}, \qquad H^* := \frac{\partial K(D)}{\partial D} = \left(\frac{\partial D(\varepsilon_{eq})}{\partial \varepsilon_{eq}} \right)^{-1} \tag{57}$$

The function $D(\varepsilon_{eq})$ is a prescribed damage evolution law; in the numerical examples of Section 5, the following exponential damage law was considered:

$$D(\varepsilon_{eq}) = 1 - \frac{K_0}{\varepsilon_{eq}} \left(1 - \alpha + \alpha e^{-\beta(\varepsilon_{eq} - K_0)} \right) \tag{58}$$

In the expression above, K_0 is a threshold value for the equivalent deformation, representing the onset of damage, and where α and β are parameters that define, respectively, the maximum allowed damage level and the damage evolution intensity. Different scalar damage models can be obtained choosing a peculiar equivalent deformation; in the numerical examples of Section 5, the following equivalent deformation by *Mazars* [Mazars, 1984, de Borst and Gutiérrez, 1999] was adopted:

$$\varepsilon_{eq} = \sqrt{\left[\sum_{k=1}^{3} \left(< \varepsilon^{(k)} >_+\right)^2\right]} \tag{59}$$

where $\varepsilon^{(k)}$ the k-th eigenvalue of the strain tensor, and $< \varepsilon^{(k)} >_+ = (\varepsilon^{(k)} + |\varepsilon^{(k)}|)/2$ its positive part.

As discussed by Gori et al. [2019b], the main issue for the application of SPIM strategies to elastic-degradation is the transition from Eq. 40 to Eq. 44, i.e. the passage from a smoothed bilinear form expressed in terms of the domain integral $\int_{\mathbf{D}}$ to a smoothed bilinear form expressed as a summation over the number of smoothing domains, that relies on the assumption of a linear elastic constitutive operator $\hat{\mathbf{E}}$ *constant* within a smoothing domain. In a physically linear problem, since the material properties are independent on the state of the body, this assumption is verified both in case of homogeneous and heterogeneous materials; an eventual heterogeneous distribution of the material properties indeed, could be easily considered with the attribution of different material properties at each smoothing domain, constant over the same smoothing domain.

When dealing with elastic-degrading models, the initial elastic constitutive operator $\hat{\mathbf{E}}$ appearing in the smoothed bilinear form (Eq. 40) must be replaced with the *secant* operator $\hat{\mathbf{E}}^S$, which depends on the state of the body, and which varies during the loading process:

$$\widetilde{a}(\bar{\boldsymbol{w}}, \bar{\boldsymbol{u}}) = \int_{\mathbf{D}} \widetilde{\underline{\varepsilon}}(\bar{\boldsymbol{w}}(p_k)) : \left(\hat{\mathbf{E}}^S(\underline{\varepsilon}(\bar{\boldsymbol{u}})) : \widetilde{\underline{\varepsilon}}(\bar{\boldsymbol{u}}(p_k))\right) \, \mathrm{d}\mathcal{V} \tag{60}$$

In order to obtain an expression similar to the second one of Eq. 44, a *smoothed* constitutive operator $\widetilde{\hat{\mathbf{E}}}^S(p_k)$, *constant* over the smoothing domain $\mathbf{D}_k^S$, must be introduced, resulting in

$$\widetilde{a}(\bar{\boldsymbol{w}}, \bar{\boldsymbol{u}}) = \sum_{k=1}^{N_S} A_k \left(\widetilde{\underline{\varepsilon}}(\bar{\boldsymbol{w}}(p_k)) : \left(\widetilde{\hat{\mathbf{E}}}^S(p_k) : \widetilde{\underline{\varepsilon}}(\bar{\boldsymbol{u}}(p_k))\right)\right) \tag{61}$$

Regarding how to obtain such smoothed constitutive operator it can be observed that the secant operator depends on the state of the body at each point $\xi \in \mathbf{D}_k^S$, i.e. on the current strain tensor $\underline{\varepsilon}(\bar{\boldsymbol{u}}(\xi))$ which depends on the displacement field. In NS-PIM and ES-PIM procedures, the displacement field is calculated at the point p_k of each smoothing domain $\mathbf{D}_k^S$, resulting in a smoothed strain tensor $\widetilde{\underline{\varepsilon}}(\bar{\boldsymbol{u}}(p_k))$ which is constant within a smoothing domain. The smoothed constitutive operator can then be approximated with the secant operator generated using the smoothed strain as

$$\widetilde{\hat{\mathbf{E}}}^S(p_k) \simeq \hat{\mathbf{E}}^S(\widetilde{\underline{\varepsilon}}(\bar{\boldsymbol{u}}(p_k)) \tag{62}$$

resulting in

$$\widetilde{a}(\bar{\boldsymbol{w}}, \bar{\boldsymbol{u}}) = \sum_{k=1}^{N_S} A_k \left(\widetilde{\underline{\varepsilon}}(\bar{\boldsymbol{w}}(p_k)) : \left(\hat{\mathbf{E}}^S(\widetilde{\underline{\varepsilon}}(\bar{\boldsymbol{u}}(p_k)) : \widetilde{\underline{\varepsilon}}(\bar{\boldsymbol{u}}(p_k)))\right)\right) \tag{63}$$

In the specific case of a scalar-isotropic damage models the secant constitutive operator depends on the scalar damage variable D which, according to Eq. 58, can be expressed as a function that depends on the current strain state of the body through an equivalent strain measure, $D = D(\varepsilon_{eq})$

with $\varepsilon_{eq} = \varepsilon_{eq}(\underline{\varepsilon}(\bar{u}(p)))$. In this case, the smoothed constitutive operator will depend on the smoothed damage variable $\widetilde{D}(p_k)$, depending on the smoothed equivalent strain measure $\widetilde{\varepsilon}_{eq}$ as

$$\widetilde{\hat{\mathbf{E}}}^S(p_k) = (1 - \widetilde{D}(p_k))\,\hat{\mathbf{E}}, \quad \widetilde{D}(p_k) = D(\widetilde{\varepsilon}_{eq}), \quad \widetilde{\varepsilon}_{eq} = \varepsilon_{eq}(\underline{\widetilde{\varepsilon}}(\bar{u}(p_k))) \tag{64}$$

3.4   Linearisation of the weakened-weak form

In presence of damage, the algebraic systems of Eq. 27 must be recast as the following nonlinear system:

$$[K^S]\,\{X\} = \{R\} \tag{65}$$

where $[K]^S$ is the global secant stiffness matrix of the discrete model, resulting from the discretisation of the smoothed bilinear form of Eq. 63. This nonlinear system can be solved with an incremental-iterative strategy based on the *Newton-Raphson* method, which requires the *linearisation* of Eq. 65, as in the standard nonlinear FEM [Wriggers, 2008].

The first step for the linearisation within the Newton-Raphson method consists in the introduction of a space of *admissible variations* $\delta\mathcal{V}(\mathbf{D})$, associated with the space of trial functions $\mathcal{V}(\mathbf{D})$, defined as

$$\delta\mathcal{V}(\mathbf{D}) := \left\{ \delta\bar{u} \in \left(\mathcal{G}_h^1(\mathbf{D})\right)^n \,\middle|\, \delta\bar{u} = \bar{\mathbf{0}} \text{ at } \partial\mathbf{D}_e^u \right\} \tag{66}$$

The admissible variations $\delta\bar{u}$ allow to obtain a set of *perturbed* configurations $\mathcal{V}_\varepsilon(\mathbf{D})$, whose elements $\bar{u}_\varepsilon = \bar{u} + \varepsilon\,\delta\bar{u}$ satisfy the kinematical boundary conditions of the problem prescribed at $\partial\mathbf{D}_e^u$. The weakened-weak form of Eq. 45 can be recast as

$$G(\bar{w},\bar{u}) := \widetilde{a}(\bar{w},\bar{u}) - f(\bar{w}) = 0, \quad \forall\bar{w} \in \mathcal{V}^0(\mathbf{D}) \tag{67}$$

with the introduction of the functional $G(\bar{w},\bar{u})$. In order to obtain a linearisation of such functional, a *perturbed* configuration $G(\bar{w},\bar{u}_\varepsilon)$ near the *known* equilibrium configuration $G(\bar{w},\bar{u})$ (which satisfies Eq. 67) is introduced; such perturbed configuration must satisfy the condition

$$G(\bar{w},\bar{u}_\varepsilon) = \widetilde{a}(\bar{w},\bar{u}_\varepsilon) - f(\bar{w}) = 0, \quad \forall\bar{w} \in \mathcal{V}^0(\mathbf{D}) \tag{68}$$

The vector field $\delta\bar{u}$ which allows to reach the new equilibrium configuration can be calculated with the linearisation $G(\bar{w},\bar{u}_\varepsilon) \simeq L\left[G(\bar{w},\bar{u}_\varepsilon)\right]$, resulting in

$$L\left[G(\bar{w},\bar{u}_\varepsilon)\right] = G(\bar{w},\bar{u}) + DG(\bar{w},\bar{u})\cdot\delta\bar{u} = 0, \quad \forall\bar{w} \in \mathcal{V}^0(\mathbf{D}) \tag{69}$$

where the terms $DG(\bar{w},\bar{u}_\varepsilon)\cdot\delta\bar{u}$ is the following *directional* (or *Fréchet*) derivative

$$DG(\bar{w},\bar{u})\cdot\delta\bar{u} = \left.\frac{\partial G(\bar{w},\bar{u}_\varepsilon)}{\partial\varepsilon}\right|_{\varepsilon=0} \tag{70}$$

that can be shown to be expressed by

$$\begin{aligned}
DG(\bar{w},\bar{u})\cdot\delta\bar{u} &= \sum_{k=1}^{N_S} A_k\left(\underline{\widetilde{\varepsilon}}(\bar{w}(p_k)) : \left(\hat{\mathbf{E}}^t(\underline{\widetilde{\varepsilon}}(\bar{u}(p_k)) : \delta\underline{\widetilde{\varepsilon}}(\bar{u}(p_k)))\right)\right) \\
&= \sum_{k=1}^{N_S} A_k\left(\underline{\widetilde{\varepsilon}}(\bar{w}(p_k)) : \left(\hat{\mathbf{E}}^t(\underline{\widetilde{\varepsilon}}(\bar{u}(p_k)) : \dot{\underline{\widetilde{\varepsilon}}}(\bar{u}(p_k)))\right)\right)
\end{aligned} \tag{71}$$

where the admissible variation of the smoothed strain tensor $(\delta\underline{\widetilde{\varepsilon}})$ coincides with its rate $(\dot{\underline{\widetilde{\varepsilon}}})$, and where the tangent constitutive operator $\hat{\mathbf{E}}^t$ is the one defined in Eq. 56 (see Gori et al. [2019b] for

further details). The linearised weakened-weak form can then be recast into: find the *increments* $\delta\bar{\boldsymbol{u}} \in \delta\mathcal{V}(\mathbf{D})$ such that

$$DG(\bar{\boldsymbol{w}}, \bar{\boldsymbol{u}}) \cdot \delta\bar{\boldsymbol{u}} = -G(\bar{\boldsymbol{w}}, \bar{\boldsymbol{u}}), \quad \forall\bar{\boldsymbol{w}} \in \mathcal{V}^0(\mathbf{D}) \tag{72}$$

The right hand side of Eq. 72 is known, since it depends on the displacement field $\bar{\boldsymbol{u}}$ of a known equilibrium configuration, and is expressed as

$$G(\bar{\boldsymbol{w}}, \bar{\boldsymbol{u}}) = \widetilde{a}(\bar{\boldsymbol{w}}, \bar{\boldsymbol{u}}) - f(\bar{\boldsymbol{w}}) = \sum_{k=1}^{N_S} A_k \left(\widetilde{\bar{\boldsymbol{\varepsilon}}}(\bar{\boldsymbol{w}}(p_k)) : \widetilde{\bar{\boldsymbol{\sigma}}}(\bar{\boldsymbol{u}}(p_k))\right) - f(\bar{\boldsymbol{w}}) \tag{73}$$

Introducing PIM or RPIM approximation functions into Eq. 72, for both the test functions $\bar{\boldsymbol{w}}(p)$ and the increments $\delta\bar{\boldsymbol{u}}(p)$:

$$\{\bar{\boldsymbol{w}}(p)\} = \sum_{i \in S_d} [\phi_i(p)]\{d_i^w\}, \quad \{\delta\bar{\boldsymbol{u}}(p)\} = \sum_{i \in S_d} [\phi_i(p)]\{\delta d_i\} \tag{74}$$

the following algebraic system can be obtained

$$[K^t]\{\Delta X\} = \{N\} \tag{75}$$

where $[K^t]$ is the global *tangent* stiffness matrix of the discrete model, $\{\Delta X\}$ the nodal parameters vector collecting all the nodal parameters $\{\delta d_i\}$, and $\{N\}$ an array containing the discretisation of the right hand side of Eq. 72. The matrix $[K^t]$ is evaluated through the contribution of each *smoothing domain*

$$[K^t(p_k)]_{Sd} = A_k[\widetilde{B}(p_k)]^T[\hat{\mathbf{E}}^t(\widetilde{\bar{\boldsymbol{\varepsilon}}}(\bar{\boldsymbol{u}}(p_k)))][\widetilde{B}(p_k)] \tag{76}$$

where as in the linear SPIM, the matrix $[\widetilde{B}(p_k)]$ is composed by the submatrices $[\widetilde{B}_i(p_k)]$ as $[\widetilde{B}(p_k)] = \left([\widetilde{B}_1(p_k)] \dots [\widetilde{B}_i(p_k)] \dots [\widetilde{B}_N(p_k)]\right)$, where N is the number of nodes in the support domain S_d at the point p_k, and where $[\hat{\mathbf{E}}^t(\widetilde{\bar{\boldsymbol{\varepsilon}}}(\bar{\boldsymbol{u}}(p_k)))]$ is the matricial expression of the tangent constitutive operator of Eq. 56.

4 Regularisation strategies for damage models

As already stated in Section 1, the objective of this manuscript is to discuss the application of SPIM strategies to the analysis of damage models, taking advantage of the regularisation effects provided by the intrinsic nonlocal character of such formulations. Damage models and other strain-softening models are characterised by the phenomenon of *localisation*, and when analised with the standard FEM they may exhibit certain pathological behaviours such as *strong mesh-dependency*, *premature fracture initiation*, and *instantaneous perfectly-brittle fracture* [de Borst et al., 1993, Peerlings et al., 2002], as already discussed in Section 1. As pointed out in the literature (see, e.g. the paper by Bažant [Bažant, 1991]), these pathological behaviours are due to the *local* representation offered by the classic continuum theory, in contrast with the *nonlocal* nature of phenomena like damage and plasticity. The main aim of the proposed solutions to this problem, the so-called *regularisation* techniques, is the introduction of an *internal length* in the continuum model, allowing to recover the nonlocal character of the phenomenon.

Regularisation techniques may act on two different levels: at the *formulation* level, i.e. directly in the continuum description, or at the *numerical* level, i.e. within the discretisation method. Among the different alternatives for regularisation at the formulation level there are: *nonlocal* and *gradient-enhanced* models [Bažant and Lin, 1988, Pijaudier-Cabot and Bažant, 1987, de Borst and Mühlhaus, 1992, Peerlings et al., 1996, 2001, 2002, Badnava et al., 2016], *viscous* models

[Needleman, 1988], *cohesive zone* models [Dugdale, 1960, Barenblatt, 1962], methods based on the *fracture energy approach* [Bažant and Oh, 1983], *phase-field* models [Frémond and Nedjar, 1996, Miehe et al., 2010, 2016], and the *micropolar* theory [de Borst, 1991, de Borst and Sluys, 1991, Dietsche et al., 1993, Iordache and Willam, 1998, Xotta et al., 2016, Gori et al., 2017b,a, Gori, 2018]. The micropolar theory has been used in combination with the SPIM approach in the numerical simulations of Section 5.3, in order to obtain a two-levels regularisation strategy (for more details on the application of the micropolar theory to damage models and it's combination with the SPIM strategy refer to the papers by Gori et al. [Gori et al., 2017a,b, 2019c]).

Regularisation techniques at the numerical level can be based on the FEM or on other discretisation methods. Among the various solutions based on the finite element method there are, for example, the use of elements with embedded discontinuities [Ortiz et al., 1987], able to represent various kind of weak and strong discontinuities, or element with embedded localisation zones [Pietruszczak and Mróz, 1981, Belytschko et al., 1988]. Meshless methods have also been shown to be capable of providing certain regularisation effects. One of the first works devoted to the investigation of the regularisation properties of meshless methods is a paper by Chen et al. [Chen et al., 2000], where the authors, focusing on *moving least square* and *reproducing kernel* approximations, pointed out that these methods posses an *intrinsic nonlocality* due to the presence of weight functions whose support size is greater than the nodal spacing. They also emphasised that a further regularisation effect can be introduced when an assumed strain method based on the direct discretization of a nonlocal equivalent strain measure is adopted. Recently, in a paper by Wang and Li [Wang and Li, 2012], also the SCNI technique [Chen et al., 2001] have been shown to be able to provide regularisation effects in localisation problems.

SPIM strategies present some analogies with the aforementioned methods and are also capable to provide regularisation effects, as pointed out by Gori et al. [Gori et al., 2019b]. Despite the absence of weight functions (which are present in MLS approximations), also PIM and the RPIM approximations embed a certain nonlocality, due to the use of support domains with a size larger than the nodal spacing. As discussed by Chen et al. [Chen et al., 2000], the MLS approximation functions are capable to introduce a length scale which can be considered an *intrinsic* length, "since it resides in the approximation but is independent of the degree of discretization refinement" (Chen et al. [Chen et al., 2000], p. 1320). This independence on the discretisation is due to the use *influence domains* which allows to obtain support domains which size is independent on the nodal spacing. As it will be pointed out in Section 5.2, PIM strategies based on T-schemes for the support nodes selection can't be rigorously considered as *intrinsically* nonlocal, since the size of the support domains, though larger than the nodal spacing for certain selection schemes, depends on the refinement of the discretisation. However, a stronger nonlocal character, like the one of MLS shape functions, can be recovered by combining SPIM strategies with the influence domain technique for the selection of support nodes (Section 5.2). Another analogy with the discussion of Chen et al. [Chen et al., 2000] is the presence of the smoothing operation in SPIM strategies that, in the NS-PIM coincides with the nodal integration scheme adopted by Chen et al. [Chen et al., 2001] and by Wang and Li [Wang and Li, 2012].

5   Numerical results

5.1   Mesh objectivity

The purpose of this section is to illustrate the mesh objectivity properties induced by the intrinsic nonlocality of the SPIM approach. As it will be pointed out, SPIM strategies are capable to provide better results with respect to the standard FEM regarding mesh objectivity issues in simulations with damage models. This quality of the SPIM strategies is illustrated through the simulation

performed by Gori et al. [2019b] of the plain concrete L-shaped panel depicted in Figure 10, investigated experimentally and numerically by Winkler et al. [2004]. While in each plot the experimental results obtained by Winkler et al. [2004] have also been represented, it's important to emphasise that the aim of this section wasn't to exactly reproduce the experimental results, but to illustate the capability of the adopted strategies to reproduce the general behaviour of the experimental test due to their regularisation properties. A more detailed comparison with the experimental results would have required accurate calibrations of the damage laws and, possibly, the use of damage models more complex than a simple scalar one, able to better capture the physical behaviour of the sample.
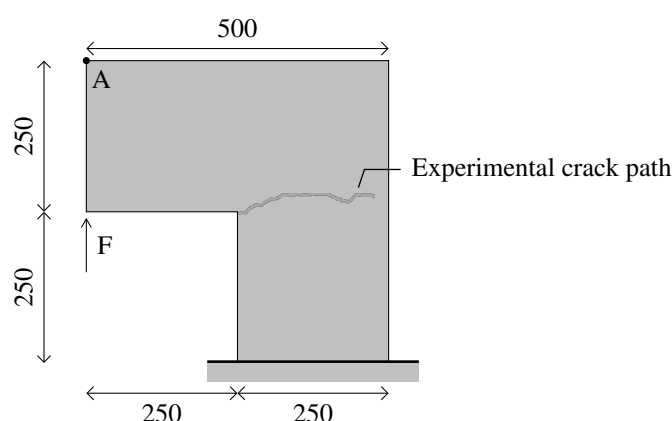
Figure 10: L-shaped panel by Winkler et al. [2004] - Geometry (measures in mm)

The concrete investigated by Winkler et al. [2004] was characterised by a Young's modulus E = 25850 N/mm^2, a Poisson's ratio ν = 0.18, tensile and compressive uniaxial strengths f$_t$ = 2.7 N/mm^2 and 4.0 N/mm^2, a fracture energy G$_c$ = 0.065 N/mm^2, and a characteristic length of the material h = 28 mm; in the following simulations its behaviour was reproduced adopting the *Mazars* scalar damage model (Equation 59), with the following parameters for the exponential damage law, α = 0.950, β = 1100 and K$_0$ = 1.12 $\times 10^{-4}$.
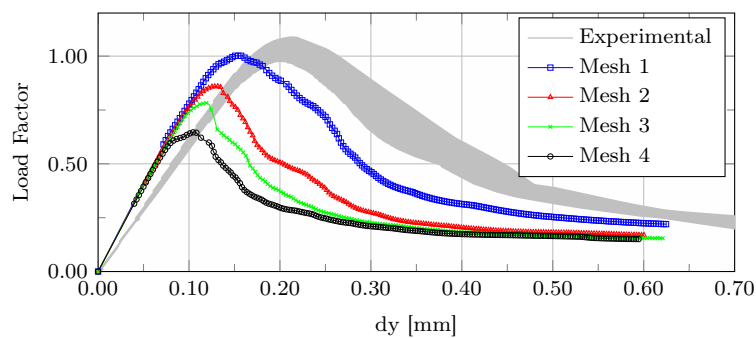
5.1.1 FEM simulations

The sample of Figure 10 was first investigated with the FEM, using four different discretisations (Figure 11), each one composed by three-node triangular elements in a plane-stress state, with a thickness of 100 mm. The four meshes were characterised by a different mean nodal spacing near the concave corner, equal to 25 mm, 15 mm, 10 mm, and 5 mm, while it was equal to 50 mm elsewhere. The analyses were performed adopting a loading process driven by the *generalized displacement control method* [Yang and Shieh, 1990], assuming a reference load F = 7000 N, an initial loading factor increment of 0.005, and a tollerance for convergence in relative displacement of 1×10^{-4}. The simulations discussed in this section were performed considering the tangent approximation of the constitutive operator, except for some of the meshfree simulations with influence domains discussed later which, due to convergence issues, required a secant approximation.

The results of the FEM analyses are illustrated in Figure 12, where the values of the vertical displacement at the point A of Figure 10 are plotted against the load factor, together with the experimental results presented by Winkler et al. [2004]. As it can be observed, the results obtained with the coarsest mesh were in good agreement with the experimental results, both in terms of peak value of the load factor and shape of the softening branch, except for an initial stiffness higher than the one observed in the experiment; this issue however, is common to other simulations

(a) Mesh 1　　　(b) Mesh 2　　　(c) Mesh 3　　　(d) Mesh 4
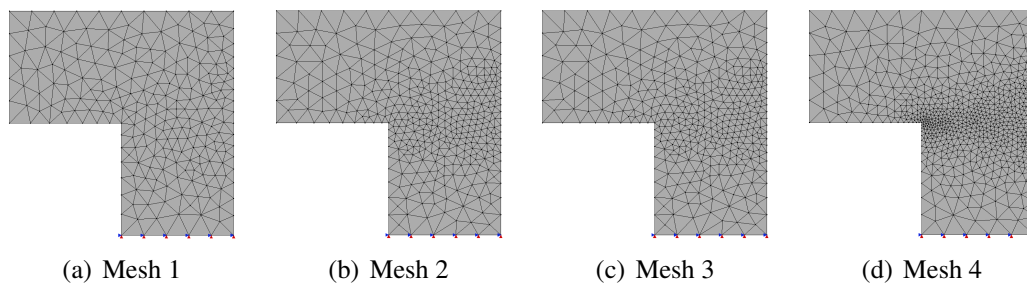
Figure 11: L-shaped panel - FEM meshes

of such a test that can be found in the literature, and it can be observed also in the simulations performed by Winkler et al. [2004]. However, the problem appeared to be strongly dependent on the discretisation, since the analyses performed with the other meshes showed sensibly lower peak values of the load factor. The presence of mesh dependency is also pointed out by the contour plots of the scalar damage variable illustrated in Figure 13. Indeed, despite their shape was compatible with the experimental cracking path depicted in Figure 10, the most refined meshes exhibited a narrower width.

Figure 12: L-shaped panel - FEM - Equilibrium paths

(a) Mesh 1　　　(b) Mesh 2　　　(c) Mesh 3　　　(d) Mesh 4
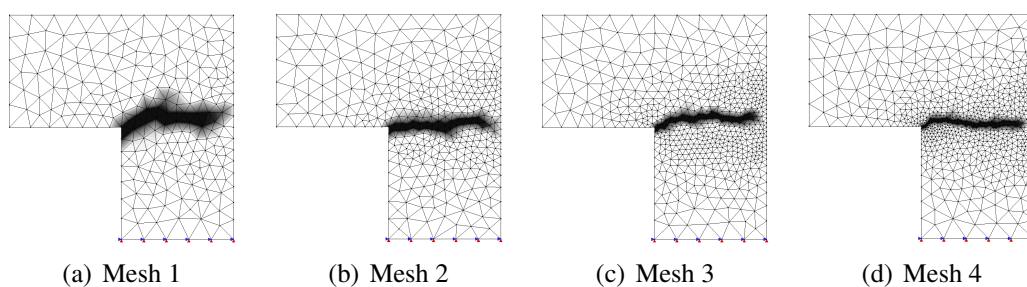
**Figure 13: L-shaped panel - FEM - Damaged configurations**

5.1.2　SPIM simulations

Node- and edge-based discretisations were constructed according to the same procedure discussed in Section 3.2.2, i.e. using the triangular finite elements illustrated in Figure 11 as background cells, resulting in the meshes depicted in Figures 14 and 15, maintaining the same nodal distributions adopted in the FEM simulations.

(a) Mesh 1   (b) Mesh 2   (c) Mesh 3   (d) Mesh 4
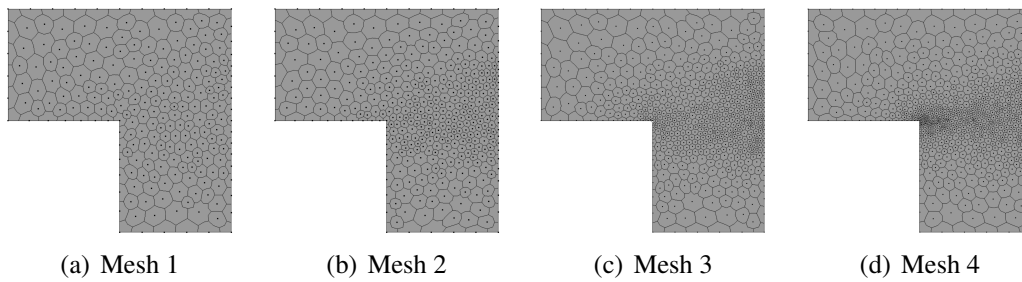
Figure 14: L-shaped panel - NS-RPIM meshes

(a) Mesh 1   (b) Mesh 2   (c) Mesh 3   (d) Mesh 4
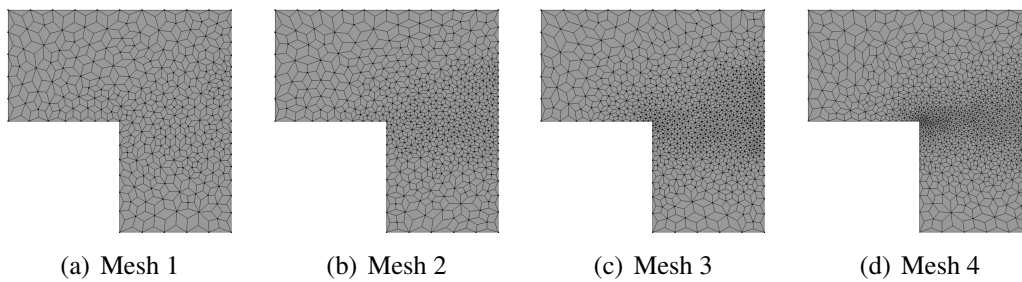
**Figure 15: L-shaped panel - ES-RPIM meshes**

At each integration point, the support domains were generated using both the T3 and the T6/3 schemes, while the shape functions were constructed with the radial point interpolation method with polynomial reproduction, using the exponential radial function with c = 0.002, and adopting 3 polynomial terms. The analyses were performed adopting the same loading process of the FEM simulations. The results of the analyses performed with the NS-RPIM in terms of equilibrium paths are illustrated in Figure 16, while the contour plots of the damaged configurations are depicted in Figures 17 and 18. As it can be observed, due to the upper bound approximation [Liu and Zhang, 2007], the NS-RPIM produced solutions with peak values higher than the ones obtained with the FEM. However, they exhibited the same mesh dependency issues of the finite element solutions. It is interesting to note that both the T3 and the T6/3 schemes produced almost the same results, both in terms of equilibrium paths and damage distributions.

(a) T3   (b) T6/3
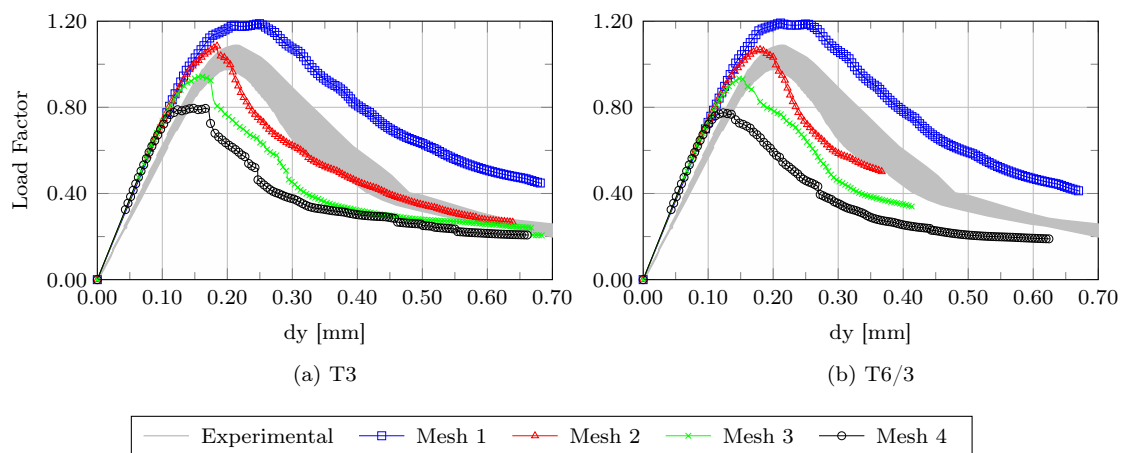
Figure 16: L-shaped panel - NS-RPIM - Equilibrium paths

(a) Mesh 1 (b) Mesh 2 (c) Mesh 3 (d) Mesh 4
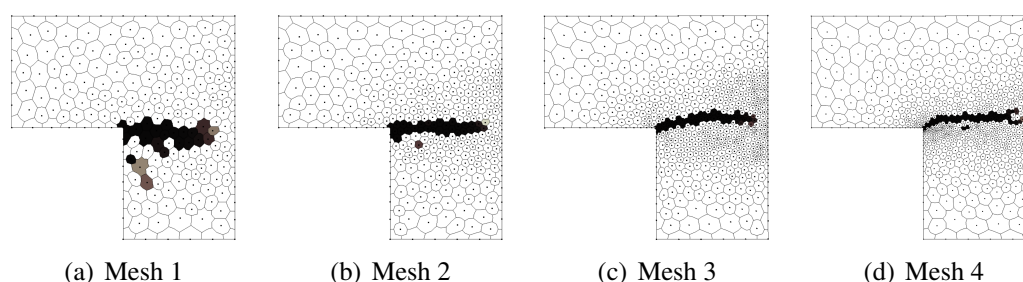
Figure 17: L-shaped panel - NS-RPIM T3 - Damaged configurations


(a) Mesh 1 (b) Mesh 2 (c) Mesh 3 (d) Mesh 4
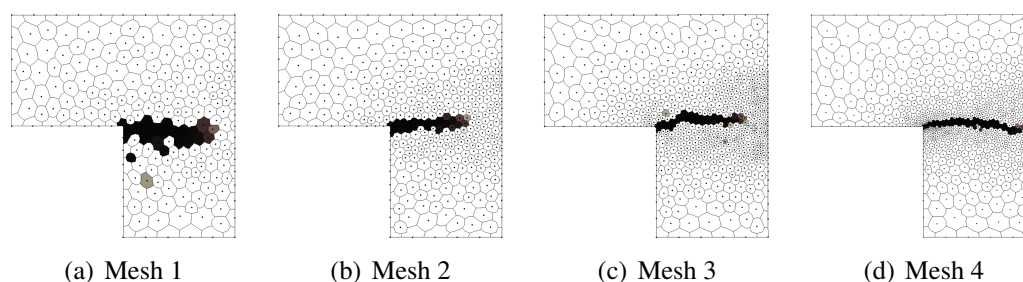
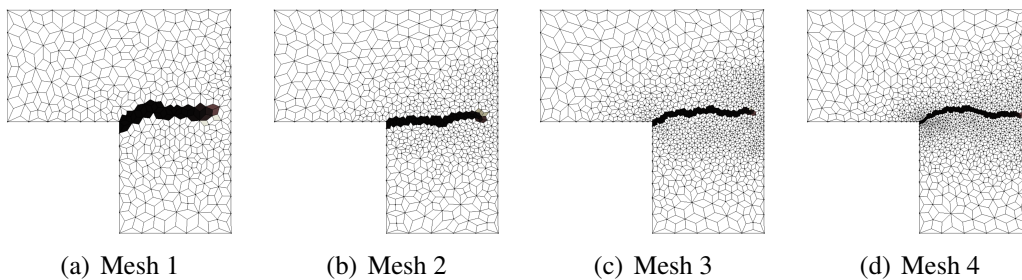**Figure 18: L-shaped panel - NS-RPIM T6/3 - Damaged configurations**

As expected from the known properties of the edge-based scheme [Liu, 2009], the equilibrium paths obtained with the ES-RPIM (Figure 19) exhibited values that were intermediate between the ones of the FEM and the ones of the NS-RPIM. Regarding the equilibrium paths obtained with the T6/3 scheme it is interesting to note that while they still presented different peak values depending on the discretisation, they were characterised by less dispersed results with respect to the ones obtained with the T3 scheme. The effect of the T6/3 scheme was more evident in the meshes 2, 3, and 4, which exhibited a considerable growth of the peak values; the coarsest mesh instead, manifested almost the same peak values with the two schemes, though the post-peak branch presented a reduced decay with the T6/3 approach. The fact that the results obtained with the T6/3 scheme were less dispersed is also emphasised by the contour plots of the scalar damage variable depicted in Figures 20 and 21. While the damaged zones obtained with the T3 scheme Figure 20 presented a considerably narrower width as the discretisation was refined, the ones obtained with the T6/3 scheme appeared to be more uniform.

## 5.2   SPIM with influence domains

The improved results, in terms of mesh objectivity, obtained with the T6/3 scheme with respect to the T3 scheme in the ES-RPIM simulations seems to corroborate again the hypothesis that this class of methods, like other meshfree methods, are characterised by a certain degree of nonlocality embedded in their formulation, as commented in Section 4. As discussed by Gori et al. [2019b], this nonlocality can be further exploited using a different approach for the support nodes selection, switching from the T-schemes strategy to the *influence domains strategy* commonly adopted in the Element-Free Galerkin method and other meshfree methods. As discussed in Section 4, when T-schemes are being used a method can't be rigorously considered as *intrinsically* nonlocal in the sense given by Chen et al. [2000], since the spatial size of the support domain, and hence the induced internal length, depends on the discretisation. On the contrary, if the support nodes are selected using the influence domains strategy, it is possible to obtain support domains with a spatial size that is independent on the discretisation refinement. The SPIM strategy with

(a) T3

(b) T6/3
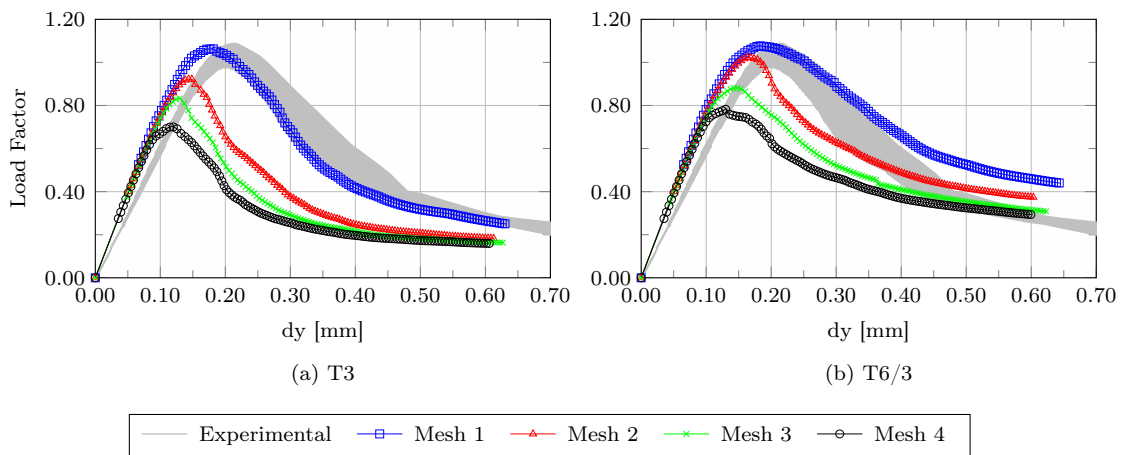
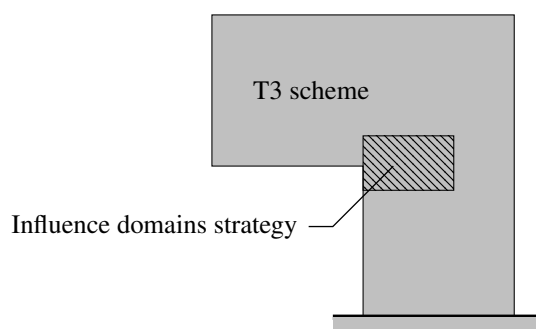Figure 19: L-shaped panel - ES-RPIM - Equilibrium paths

(a) Mesh 1   (b) Mesh 2   (c) Mesh 3   (d) Mesh 4

Figure 20: L-shaped panel - ES-RPIM T3 - Damaged configurations

(a) Mesh 1   (b) Mesh 2   (c) Mesh 3   (d) Mesh 4
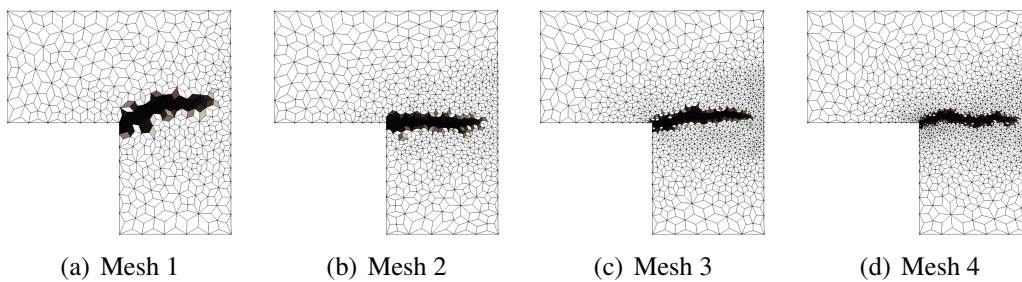
Figure 21: L-shaped panel - ES-RPIM T6/3 - Damaged configurations

influence domains presented in this section is similar to the *two-level regularisation method* proposed by Chen et al. [2000]. In the cited paper the authors showed the regularisation effects of RK discretisations in damage problems, while in case of elasto-plastic problems with more pronounced softening they adopted the aforementioned two-level regularisation, consisting in the use of a smoothing operation for the strain measure and an assumed strain method for the weak form. Despite some similarities in the approach, the strategy presented in this section differs from the one of the mentioned paper regarding the kind of shape functions, weak form and integration strategy.

The L-shaped panel was then further investigated assuming a different approach for the support nodes selection: in the zone near the concave corner (the hatched area in Figure 22), the support domains were constructed using the *influence domains strategy*, while in the other parts of the problem domain the T3 scheme was maintained. The adopted influence domains were circular, and the analyses were performed with three different values for their radius, 20 mm, 25 mm, and 30 mm. This approach was applied only to the meshes 2, 3, and 4, while for the mesh 1 the results obtained with the T3 scheme were maintained. As already stated, the idea of this approach was to try to improve the nonlocality of the SPIM strategy by using support domains larger than the ones obtainable with the sole T6/3 scheme.


Figure 22: L-shaped panel - Area with support nodes selection via influence domains

As it can be observed in Figure 23, when circular influence domains with radius R = 20 mm were adopted, the meshes 3 and 4 exhibited almost the same equilibrium path, with a slight discrepancy in the softening branch. For the values R = 25 mm and R = 30 mm the two discretisations still manifested the same peak value, though with larger differences in the post-peak branch. Furthermore, it should be noted that to higher radii corresponded higher peak values. Considering the results obtained for the mesh 2, it is interesting to observe that as the radius of the influence domains was increased, the difference in terms of peak-values between the mesh 2 and the meshes 3 and 4 tended to decrease, emphasising the behaviour obtained with the T6/3 scheme and observed in Figure 19.

On the other hand, despite a better agreement on the value of the peak load factor, the softening branches still presented different paths. This behaviour can be ascribed, at least partially, to the fact that, as pointed out by Figure 22, the influence domains stategy was applied only near the damage initiation zone. In the other zones interested by damage propagation, that have an influence on the shape of the post-peak branch, the approximation was constructed using the T3 scheme, without the introduction of further nonlocal effects. This fact seems to be confirmed also by the contour plots illustrated in Figures 24, 25 and 26. Indeed, as it can be observed, as long as the damage developed in the area subjected to nodes selection by influence domains, the width of the damaged zones was almost the same among the three discretisations. As it started to grow outside of that area, the damaged zones became mesh dependent again.

(a) R = 20 mm

(b) R = 25 mm

(c) R = 30 mm
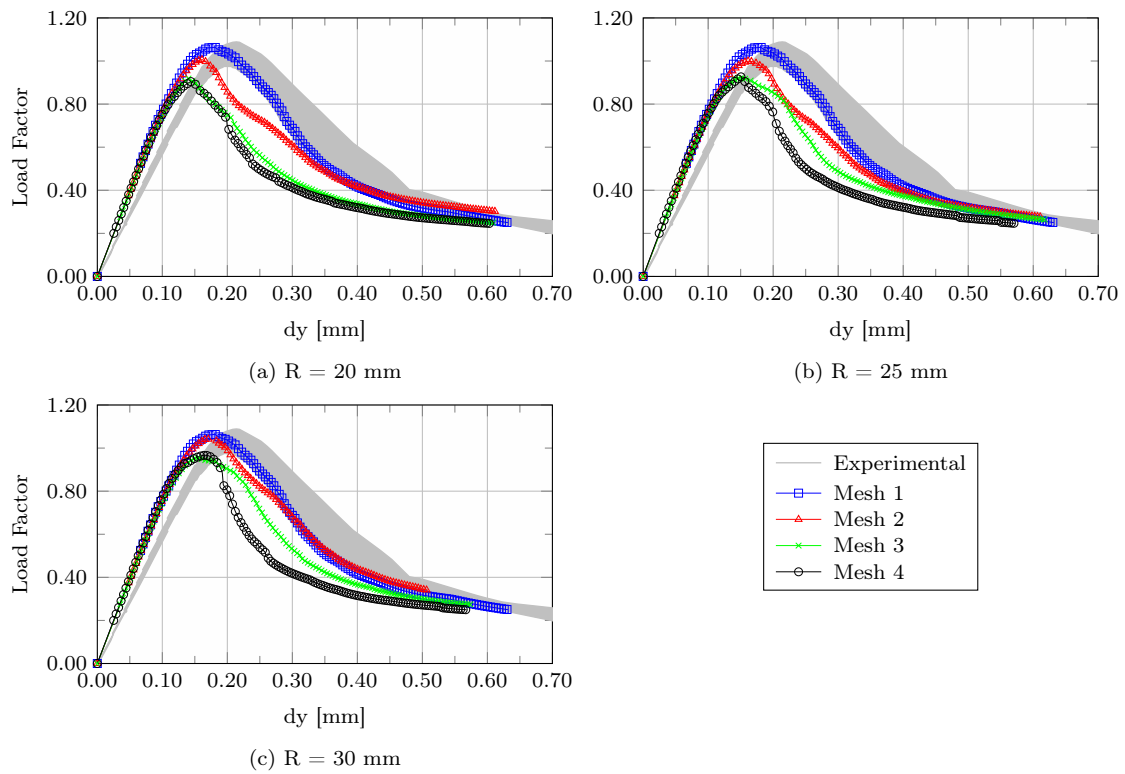
Figure 23: L-shaped panel - ES-RPIM with influence domains strategy - Equilibrium paths

(a) Mesh 2

(b) Mesh 3

(c) Mesh 4
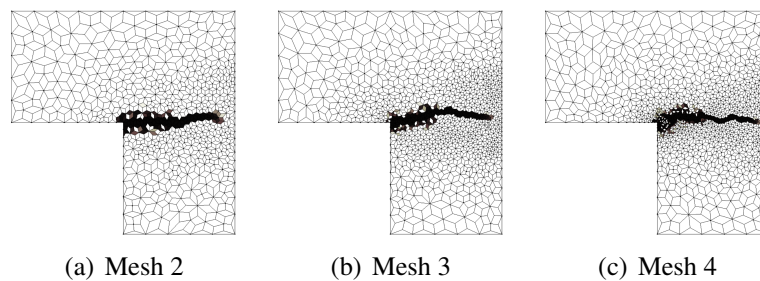
Figure 24: L-shaped panel - ES-RPIM with influence domains strategy - R = 20 mm - Damaged configurations

(a) Mesh 2

(b) Mesh 3

(c) Mesh 4
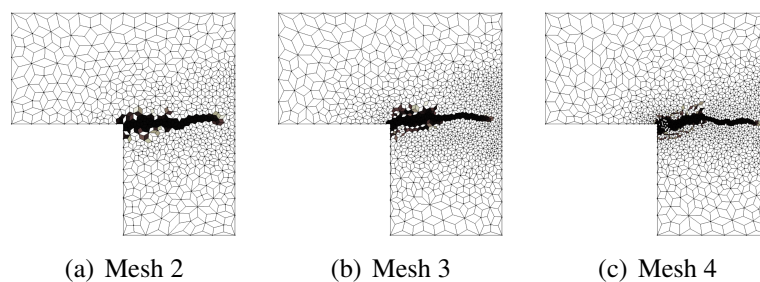
Figure 25: L-shaped panel - ES-RPIM with influence domains strategy - R = 25 mm - Damaged configurations

| (a) Mesh 2 | (b) Mesh 3 | (c) Mesh 4 |
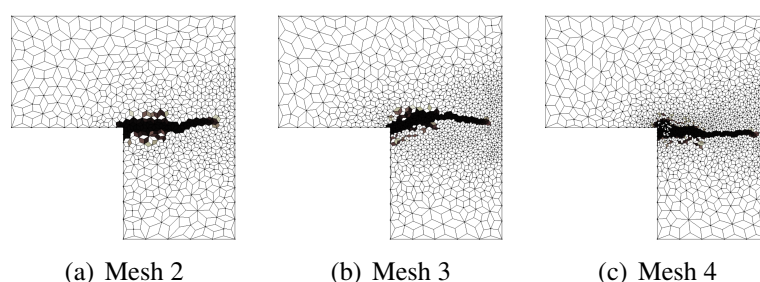
Figure 26: L-shaped panel - ES-RPIM with influence domains strategy - R = 30 mm - Damaged configurations

5.2.1 Drawbacks of the influence domains strategy

While the application of the influence domains strategy to PIM and RPIM shape functions exhibited certain beneficial effects concerning mesh objectivity, it also presents three main drawbacks. The first one is related to the efficiency of the numerical method. The influence domains strategy indeed, tends to generate support domains with a larger number of nodes with respect to the T-schemes, affecting the *sparseness* of the stiffness matrix of the discrete model, increasing the computational cost for the solution of the model. The effects of this issue however, may be reduced by limiting the application of such strategy to specific parts of the problem domain, as done in Figure 22 where it was applied in the area interested by damage propagation.

The second issue is related to the convergence of the iterative process for the solution of the nonlinear problem. As discussed before, while most of the simulations were performed considering the tangent approximation of the constitutive operator, the most refined mesh combined with the influence domains strategy required a *secant* approximation of the constitutive operator, in order to attain convergence. The application of the influence domains strategy to the most refined mesh resulted in support domains with a considerable number of nodes, which led to a bad conditioning of the moment matrix used for the generation of the shape functions, and then to a bad conditioning of the stiffness matrix with respect to the other situations, as illustrated in Table 1, affecting the stability of the iterative process. It is necessary to emphasise that the analysis of the most refined mesh with the influence domains strategy also required an adjustment of the shape parameter of the radial function which was modified to 0.003, since the initial value of 0.002 led to a singular stiffness matrix.

| Mesh	T3	T6/3	R = 20 mm	R = 25 mm	R = 30 mm
2	1.7310×10^4	4.1281×10^4	3.1798×10^4	2.7123×10^4	3.3014×10^4
3	2.2411×10^4	6.7891×10^4	6.0680×10^4	6.2369×10^4	8.2492×10^4
4	2.5352×10^4	1.1324×10^5	4.5255×10^{16}	1.6335×10^{13}	2.3189×10^{13}

Table 1: Condition number of the initial stiffness matrix

The third and final issue is the possibility to obtain a singular moment matrix for the integration points near the domain boundary. As discussed by Liu [2009], PIM shape function suffer from singularity issues in presence of peculiar support nodes alignments, like the one that may arise when a large number of support nodes is selected on a straight domain boundary; the same issue may appear also with RPIM and RPIMp shape functions. While nodes alignments are naturally avoided with T-schemes, when using an influence domains strategy there is no such control over possible alignments.

These issues point out that the use of the influence domains strategy as a mean for improving the regularisation properties of the SPIM approach still need further investigations to guarantee a more general applicability.

5.3   Mixed-mode fracture in concrete

The previous section pointed out the mesh objectivity properties induced by the intrinsic nonlocality of the SPIM approach. In a number of situations however, such properties are not sufficient to completely regularise a simulation and further tools are needed. The purpose of the present section is then to show that the SPIM approach can be combined with other regularisation strategies, in this case the micropolar continuum theory, to provide a stronger regularisation effect. This quality of the SPIM is illustrated with the simulation performed by Gori [2018] and Gori et al. [2019a] of the four-point shear test of the plain concrete beam depicted in Figure 27, investigated experimentally by Arrea and Ingraffea [1982]; this test has been widely used in the literature as a benchmark for numerical investigations on concrete behaviour. The beam is characterised by a mixed-mode loading, with an high shear gradient between the fixed constraint and the applied load P. The failure corresponds to a curved crack path, going from the top of the notch to the point of application of the load P. Due to its characteristics, the simulation of such test is difficult with scalar-isotropic damage models, and usually requires more complex approaches, like discrete cracking methods (see, e.g. Oliver et al. [2002], Rabczuk and Belytschko [2004], de Borst et al. [2004] and Fang et al. [2008]), or special treatments for scalar damage models like the non-local approach (see, e.g. Jirásek [2007]), for example. As it will be shown in the present section, analyses performed with classic scalar damage models were not able to reproduce the experimental results of the four-point shear test, due to instabilities in the loading branch of the equilibrium paths. On the other hand, it was possible to reproduce the behaviour of the experimental test by providing the SPIM approach with a further level of regularisation, using the micropolar approach (Section 4). This result was expected for this peculiar loading condition since, in presence of high values of shear stresses, couple-stresses usually arise, leading to the activation of the internal bending length, and to the regularisation effects of the micropolar formulation.
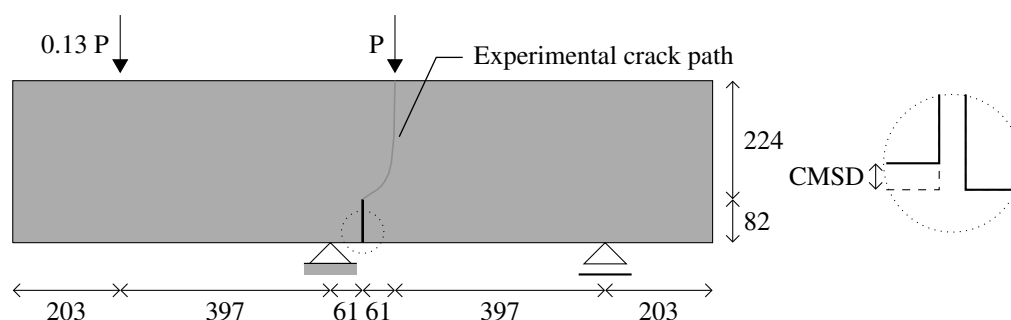

Figure 27: Four-point shear test by Arrea and Ingraffea [1982] - Geometry (measures in mm)

The concrete used by Arrea and Ingraffea [1982] in the experimental test was characterised by a Young's modulus $E = 24800$ N/mm^2, Poisson's ratio $\nu = 0.20$, tensile uniaxial strength between 2.8 N/mm^2 and 4.0 N/mm^2, and fracture enegy between 0.10 N/mm^2 and 0.14 N/mm^2; these characteristics were reproduced in these simulations adopting the *Mazars* scalar damage model (Equation 59), with the following parameters for the exponential damage law (Equation 58), $\alpha = 0.950$, $\beta = 1000$ and $K_0 = 1.6 \times 10^{-4}$.

5.3.1   FEM simulations

The analyses with the finite element method were performed considering meshes composed by three-node triangular elements in a plane-stress state, with a thickness of 156 mm. Three discretisations were adopted (Figure 28), with mean nodal spacing of 30 mm, 20 mm, and 10 mm between the notch and the point of application of the load P, and 70 mm elsewhere. The notch was represented as sharp, with an initial opening of 5 mm.

(a) Mesh 1   (b) Mesh 2

(c) Mesh 3
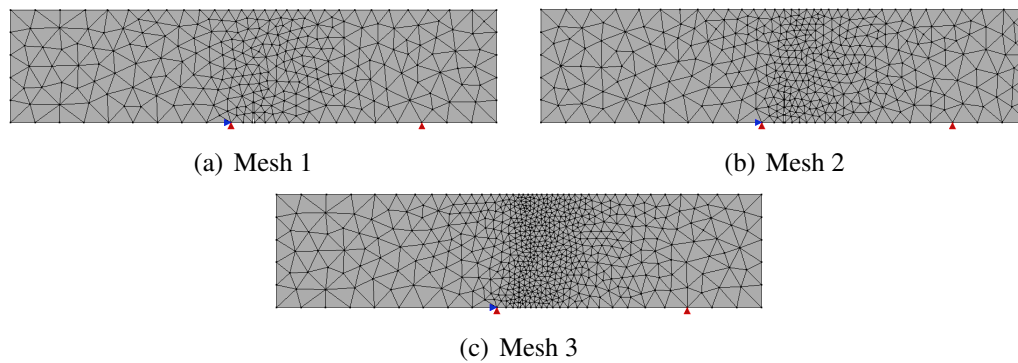
Figure 28: Four-point shear test - FEM meshes

The FEM analyses were performed adopting a loading process driven by a *cylindrical arc length* control method, assuming a reference load P = 130000 N, an initial loading factor increment of 0.0125, and a tollerance for convergence in relative displacement of 1×10^{-4}. All the simulations presented in this section were performed considering the tangent approximation of the constitutive operator. The results of the analyses performed with the classic medium, in terms of *crack mouth sliding displacement* (CMSD) plotted against the load factor are illustrated in Figure 29, together with the experimental results obtained by Arrea and Ingraffea [1982]. As it can be observed, no one of the three meshes was able to describe the behaviour of the beam; the meshes 1 and 2 exhibited an elastic unloading once the peak value of the load factor was reached, while the third mesh lost convergence before the maximum load factor value.
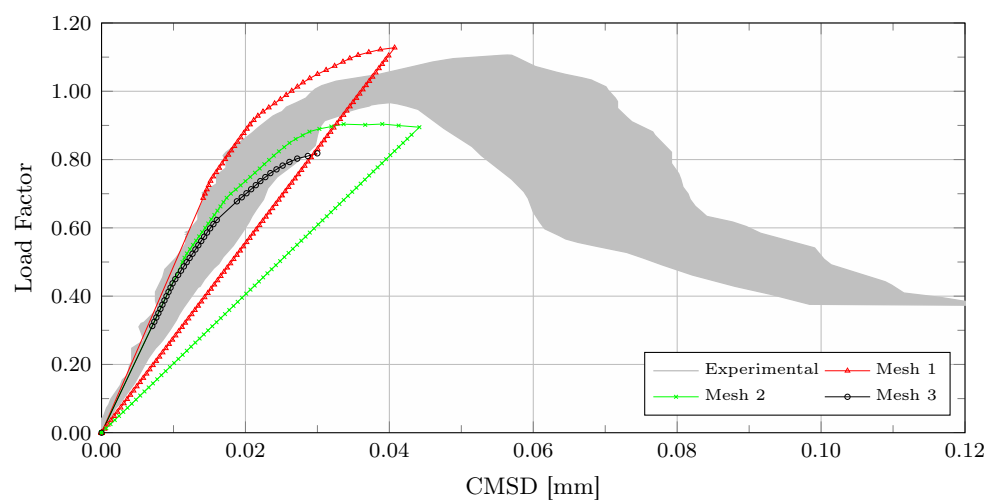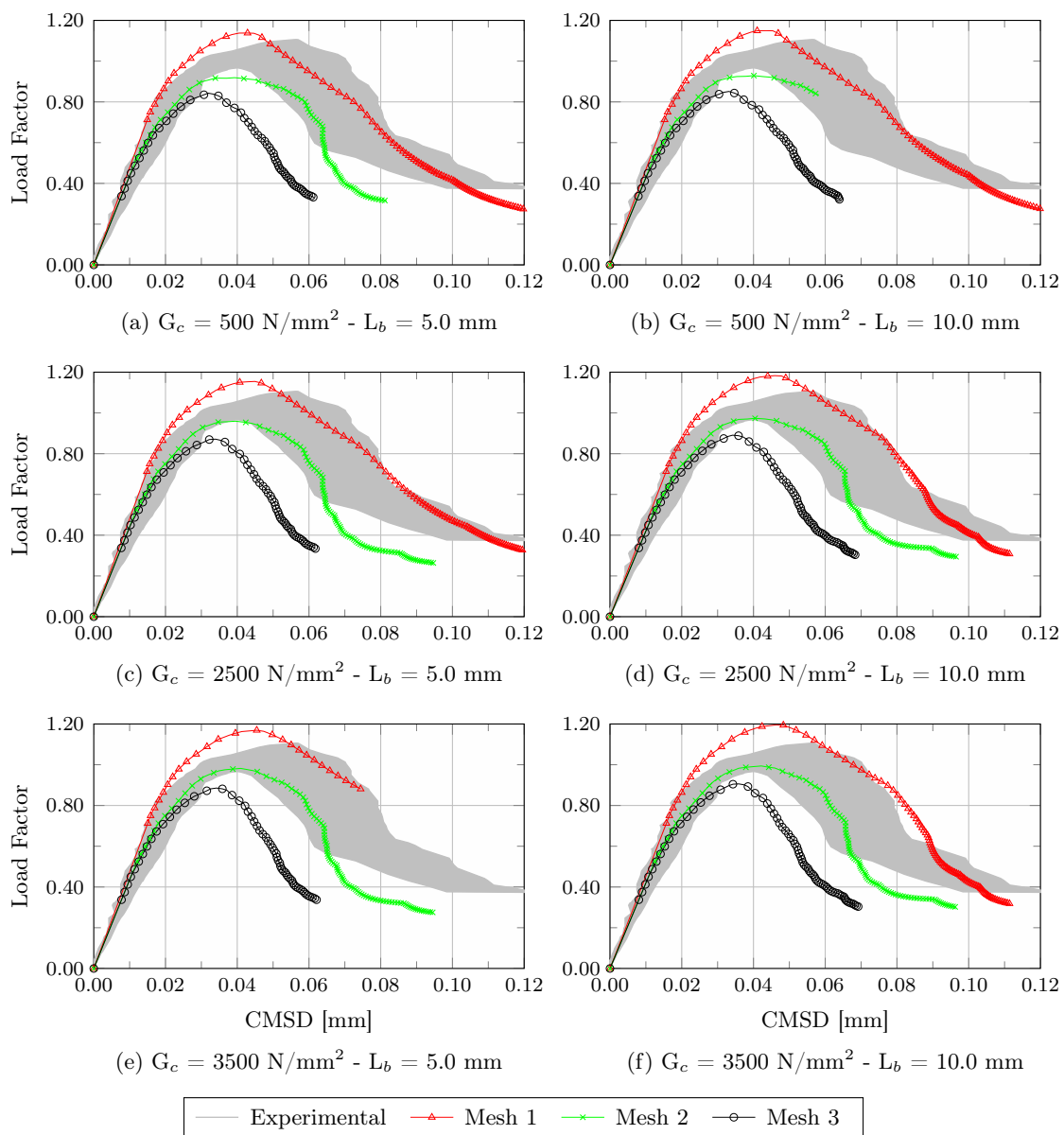

**Figure 29: Four-point shear test - FEM - Equilibrium paths**

The analysis of the four-point shear test was repeated for the three discretisations using the micropolar medium, with six different combinations of the additional material parameters, adopt-

ing the values 500 N/mm^2, 2500 N/mm^2, and 3500 N/mm^2 for the Cosserat's shear modulus G$_c$, and the values 5.0 mm and 10.0 mm for the internal bending length L$_b$. The results are collected in the plots of Figure 30. As it can be observed, the use of the micropolar medium with a simple scalar damage model allowed to investigate also the post-peak branch of the equilibrium paths, which were affected by both the additional material parameters; specifically, to higher values of G$_c$ and L$_b$ corresponded higher peak values of the load factor. Despite the fact that, on the contrary of the classic medium, the micropolar one allowed to reproduce the softening phase of the loading process, it can be observed that the solutions depicted in Figure 30 strongly depended on the discretisation, with lower peak values obtained with the most refined meshes. This fact is emphasised also by the damaged configurations illustrated in Figure 31. The damaged zones obtained with the three meshes were compatible with the expected cracking path (Figure 27); however, it can be observed that to a finer mesh corresponded a narrow damaged zone, pointing out the mesh dependency of the problem, which wasn't mitigated by the micropolar formulation.


Figure 30: Four-point shear test - Micropolar FEM - Equilibrium paths

(a) Mesh 1   (b) Mesh 2

(c) Mesh 3
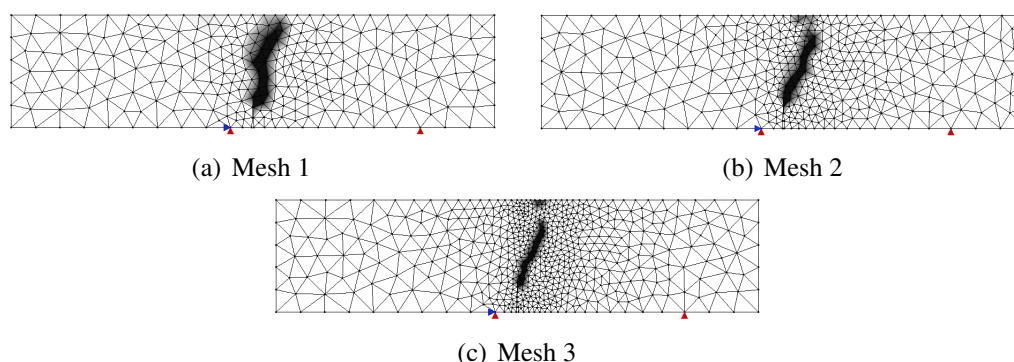
Figure 31: Four-point shear test - Micropolar FEM - G_c = 2500 N/mm^2 - L_b = 10.0 mm - Damaged configuration

5.3.2   ES-RPIM simulations

The beam of Figure 27 was investigated using also the ES-RPIM, with the discretisations depicted in Figure 32, each one obtained constructing the edge-based smoothing domains using as background cells the triangular finite elements of Figure 28, hence maintaining the same nodal distributions of the finite element meshes[17].

(a) Mesh 1   (b) Mesh 2

(c) Mesh 3
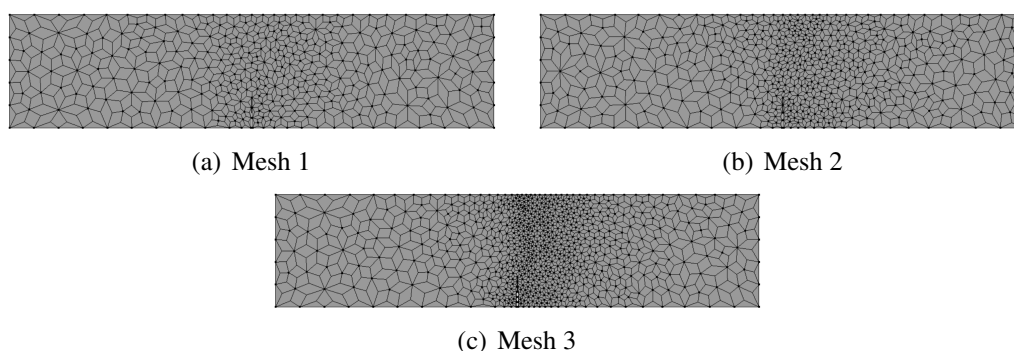
Figure 32: Four-point shear test - ESRPIM meshes

Regarding the generation of the support domains, both the T3 and the T6/3 schemes were adopted. The shape functions were constructed with the *radial point interpolation method with polynomial reproduction*, using the exponential radial function (15) with c = 0.002, and adopting 3 polynomial terms. As for the finite element analyses, the nonlinear simulations were performed adopting a loading process driven by a *cylindrical arc length* control method, assuming a reference load P = 130000 N, an initial loading factor increment of 0.0125, and a tollerance for convergence in relative displacement of 1×10^{-4}, considering the tangent approximation of the constitutive operator. The results of the analyses performed with the classic medium are illustrated in Figure 33. As it can be noted, in this case the behaviour of the ES-RPIM was similar to the finite element method (Figure 29); in all the simulations the models lost convergence already in the

---

[17]The simulation of the four-point shear test was performed using also node-based smooting domains. Both polynomial and radial basis functions were tested, as well as both the selection schemes T3 and T6/3. However, neither with the classic nor with the micropolar medium it was possible to obtain satisfactory results, since damage initiated long before the expected threshold and the analyses arrested soon after the onset of damage. Hence, only the results obtained with the edge-based method are presented in this section.
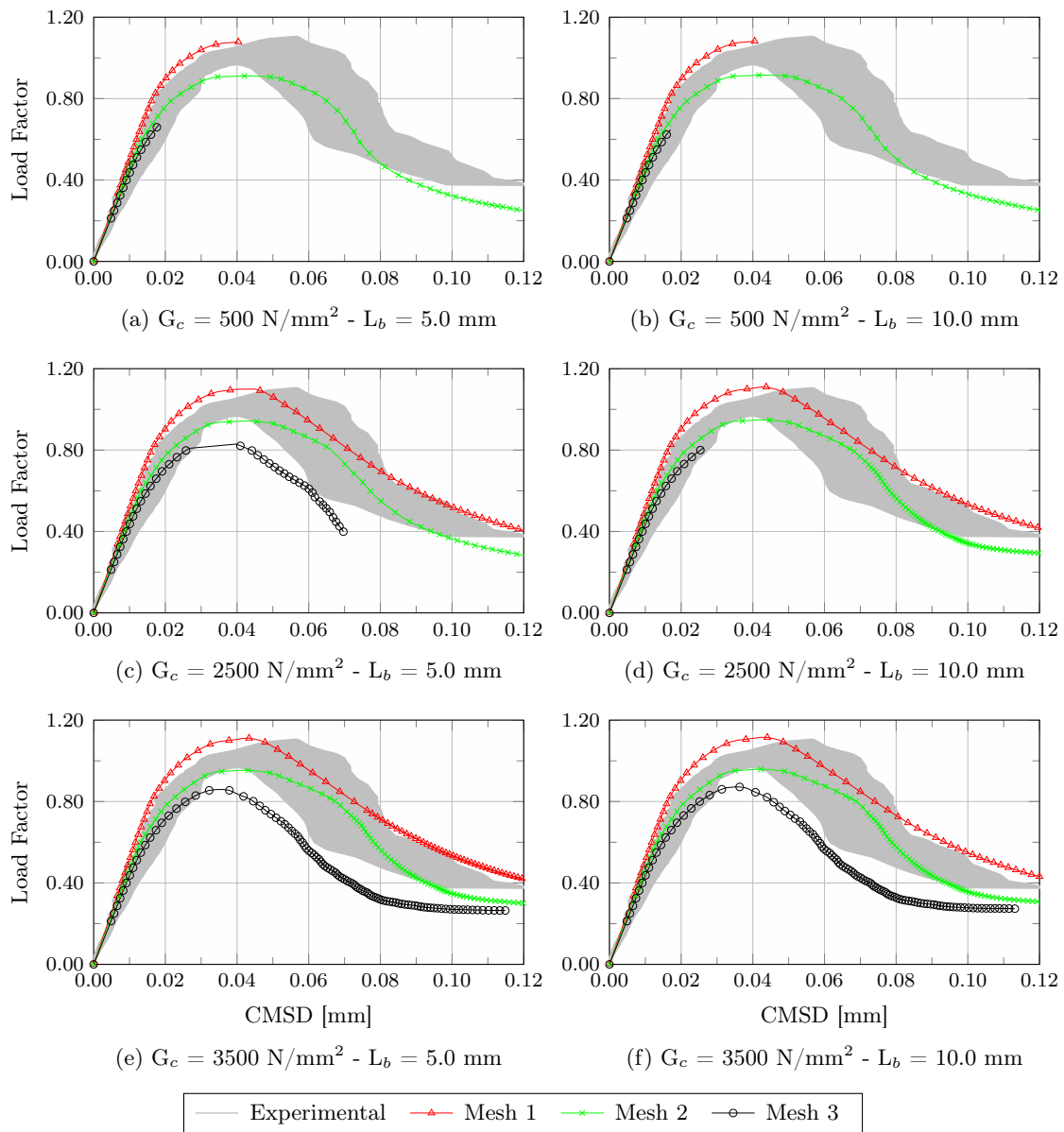
loading path, except for the mesh 1 with the T3 scheme, which manifested an elastic unloading along the original loading path once the peak value was attained.
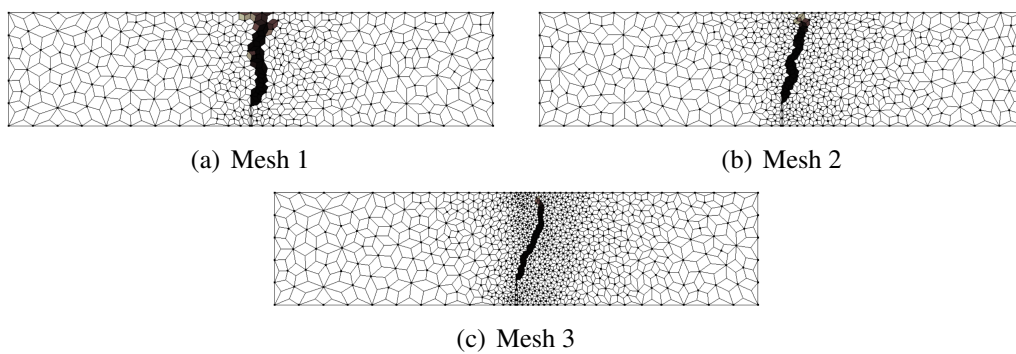

(a) T3

(b) T6/3
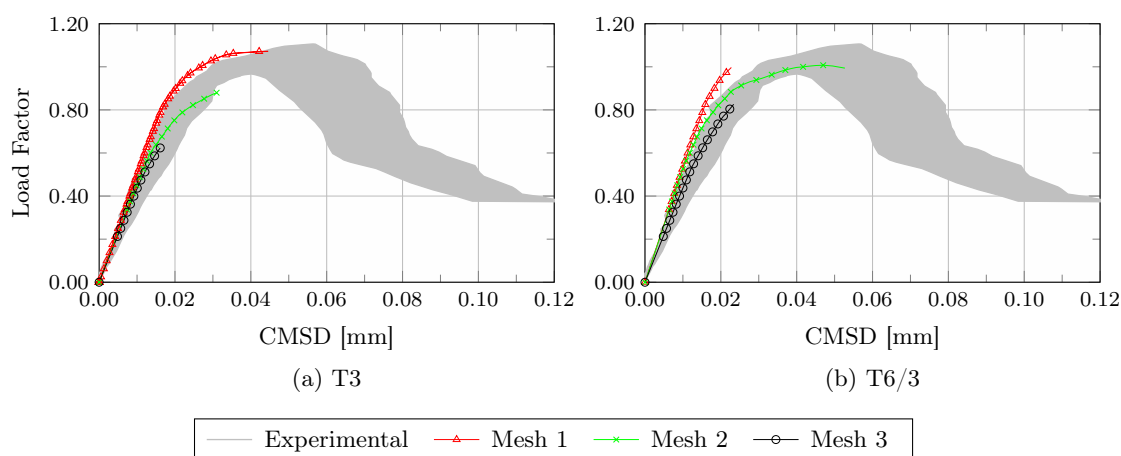
Figure 33: Four-point shear test - ES-RPIM - Equilibrium paths

Like in the case of the finite element method, the analyses with the micropolar medium gave significantly better results. Adopting the T3 scheme it was possible to investigate the softening phase of the loading process, except for the combinations with G_c = 500 N/mm^2, which exhibited instabilities with the meshes 1 and 3, and for the mesh 3 with the combination G_c = 2500 N/mm^2 and L_b = 10.0 mm, which also lost convegence in the loading phase, as it can be observed in Figure 34. Figure 35 illustrates the damaged configurations obtained for the three discretisations with the combination G_c = 3500 N/mm^2 and L_b = 10.0 mm, showing damaged zones compatible with the expected crack path depicted in Figure 27. However, observing the results illustrated in Figures 34 and 35 it is worth it to note that also in this case, as previously observed for the finite element method, the analyses were strongly dependent on the discretisation, with lower peak values and narrower damaged zones in the finest meshes.
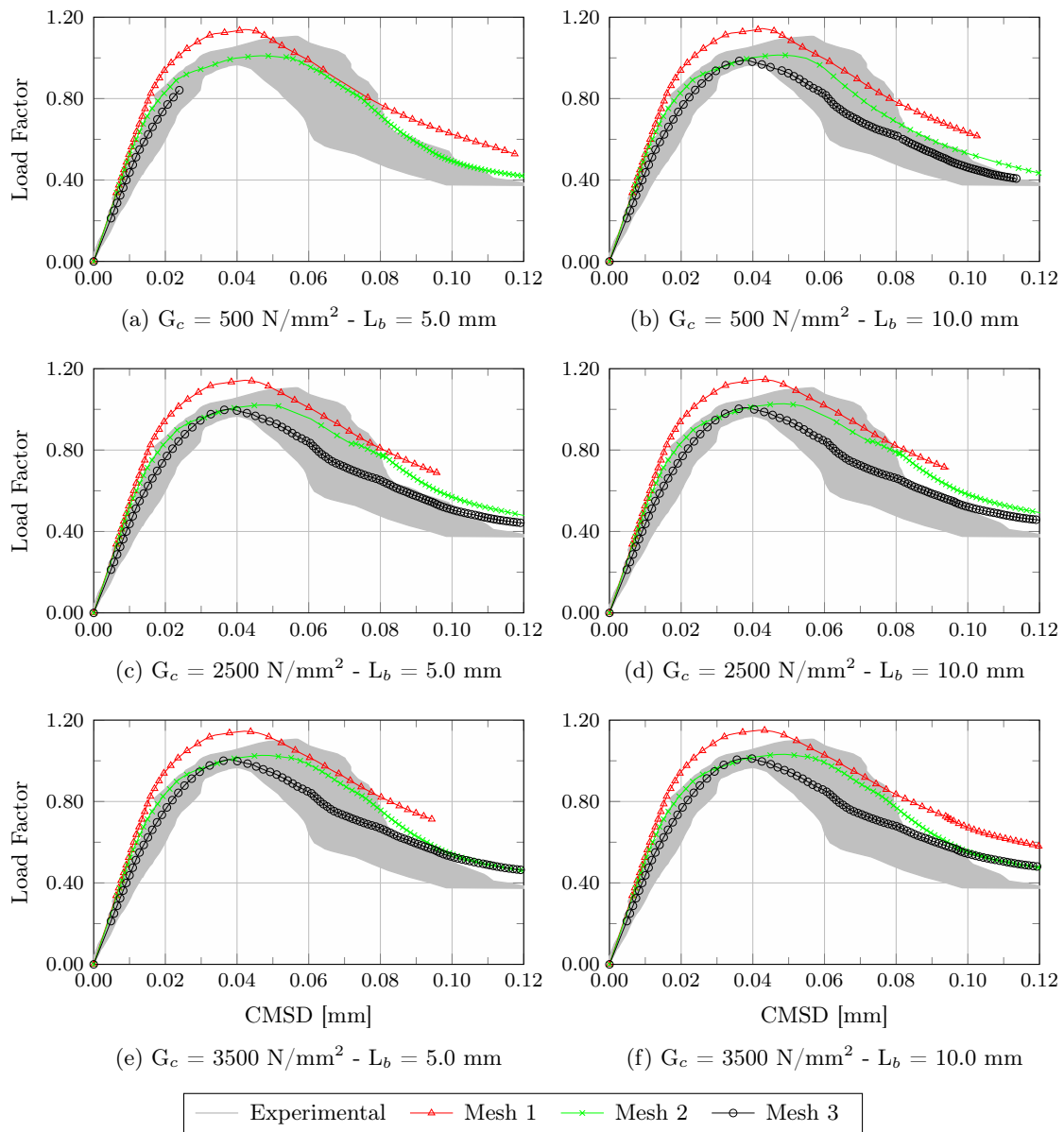
The adoption of the T6/3 selection scheme in the ES-RPIM simulations led to an improvement of the results. Observing the equilibrium paths of Figure 36 it can be noted that more stable analyses were obtained, also with the combinations with G_c = 500 N/mm^2, which were characterised by instabilities in the case of the T3 scheme. Furthermore, while the simulations with the coarsest discretisation led to results well above the experimental ones, both the meshes 2 and 3 produced results that fell in the experimental rage. The most interesting result however, is that a certain mesh objectivity was observed adopting this scheme. Indeed, observing the equilibrium paths of the meshes 2 and 3 it can be noted that they exhibited similar results in terms of peak value, and were almost coincident in the final part of the softening branch, especially for the combinations with G_c = 3500 N/mm^2, with some discrepancies in the middle of the post peak branch. This result is emphasised also by the contour plots of the scalar damage variable depicted in Figure 37. Comparing Figure 37(b) with Figure 37(c) it can be observed that the two discretisations with the T6/3 scheme produced damaged zones with a similar width, while with the T3 scheme the difference in width was considerably higher (see Figures 35(b) and 35(c)).

(a) $G_c = 500$ N/mm^2 - $L_b = 5.0$ mm

(b) $G_c = 500$ N/mm^2 - $L_b = 10.0$ mm

(c) $G_c = 2500$ N/mm^2 - $L_b = 5.0$ mm

(d) $G_c = 2500$ N/mm^2 - $L_b = 10.0$ mm

(e) $G_c = 3500$ N/mm^2 - $L_b = 5.0$ mm

(f) $G_c = 3500$ N/mm^2 - $L_b = 10.0$ mm

Experimental — Mesh 1 — Mesh 2 — Mesh 3

Figure 34: Four-point shear test - Micropolar ES-RPIM T3

(a) Mesh 1

(b) Mesh 2

(c) Mesh 3

Figure 35: Four-point shear test - Micropolar ESRPIM-T3 - G_c = 3500 N/mm^2 - L_b = 10.0 mm - Damaged configuration

(a) $G_c = 500$ N/mm^2 - $L_b = 5.0$ mm

(b) $G_c = 500$ N/mm^2 - $L_b = 10.0$ mm

(c) $G_c = 2500$ N/mm^2 - $L_b = 5.0$ mm

(d) $G_c = 2500$ N/mm^2 - $L_b = 10.0$ mm

(e) $G_c = 3500$ N/mm^2 - $L_b = 5.0$ mm

(f) $G_c = 3500$ N/mm^2 - $L_b = 10.0$ mm

| Experimental | Mesh 1 | Mesh 2 | Mesh 3 |

Figure 36: Four-point shear test - Micropolar ESRPIM-T6/3

(a) Mesh 1

(b) Mesh 2

(c) Mesh 3
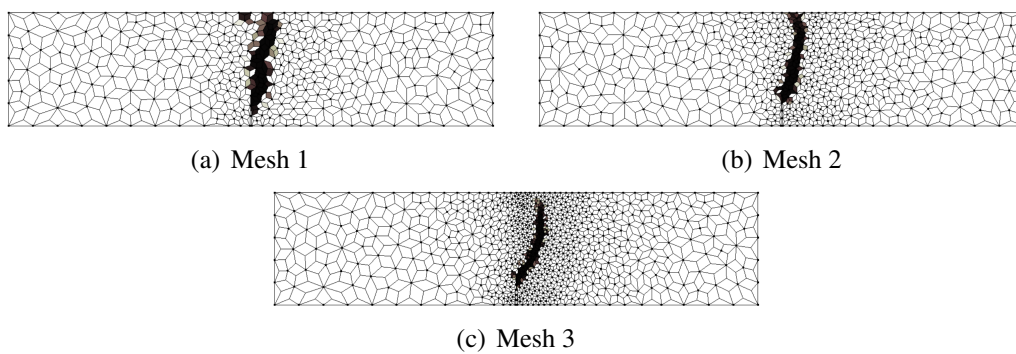
Figure 37: Four-point shear test - Micropolar ESRPIM-T6/3 - $G_c = 3500$ N/mm^2 - $L_b = 10.0$ mm - Damaged configuration

6   Concluding remarks

The main aim of this paper was to review the main aspects of the application of smoothed point interpolation methods, a family of meshless methods, to the problem of damage modelling. It has been clearly pointed out that this class of meshless methods is a valid alternative to deal with constitutive models that exhibit a strain-softening behaviour, such as the scalar damage model considered in the paper. Different levels of regularisation can be obtained, depending on how the meshless method is used. It has been shown that, when used as the sole regularisation strategy, SPIM techniques are not capable to provide a sufficient level of regularisation in certain situations. Whenever this occours, SPIM techniques can be combined with other regularisation strategies, like the micropolar continuum theory considered in this paper, in order to obtain a stronger regularisation effect. The paper also briefly discussed other existing results regarding regularisation effects provided by other meshless methods. Despite the promising results reviewed in this paper, further investigations seems to be necessary to truly point out the potential of meshless methods when applied to damage modelling and to other nonlinear phenomena. Among the possible studies there are:

- the evaluation of the influence of different kind of shape functions on the regularisation effects provided by SPIM strategies;

- the investigation of regularisation effects provided by other meshless methods like the MLPG, for example;

- the evaluation of the optimal size of the support domain to give a good trade-off between regularisation effects and the sparseness of the stiffness matrix;

- the association of meshless methods with other regularisation techniques.

References

M. Arrea and A. R. Ingraffea. Mixed mode crack propagation in mortar and concrete. Technical report, Departement of Structural Engineering, Cornell University, Ithaca, USA, 1982.

S. N. Atluri and T. Zhu. A new meshless Local Petrov-Galerkin (MLPG) approach in computational mechanics. *Computational Mechanics*, 22(2):117–127, 1998.

H. Badnava, M. Mashayekhi, and M. Kadkhodaei. An anisotropic gradient damage model based on microplane theory. *International Journal of Damage Mechanics*, 25(3):336–357, 2016. doi: 10.1177/1056789515586072.

G. Barenblatt. The mathematical theory of equilibrium of crack in brittle fracture. *Advances in Applied Mechanics*, 7:55–129, 1962. doi: Lastaccessed:14/04/2016.

K. J. Bathe. *Finite element procedures*. Prentice Hall, New Jersey, 1996.

Z. Bažant and F.-B. Lin. Non-local yield limit degradation. *International Journal for Numerical Methods in Engineering*, 26(8):1805–1823, 1988. doi: 10.1002/nme.1620260809.

Z. Bažant and B. Oh. Crack band for fracture of concrete. *Matériaux et Constructions*, 16:155–177, 1983.

Z. P. Bažant. Why continuum damage is nonlocal: Micromechanics arguments. *Journal of Engineering Mechanics*, 117(5):1070–1087, 1991. doi: 10.1061/(ASCE)0733-9399(1991)117:5(1070).

Z. P. Bažant and M. Jirásek. Nonlocal integral formulations of plasticity and damage: Survey of progress. *Journal of Engineering Mechanics*, 128(11):1119–1149, 2002. doi: 10.1061/(ASCE)0733-9399(2002)128:11(1119).

T. Belytschko, J. Fish, and B. Engelmann. A finite element with embedded localization zones. *Computer Methods in Applied Mechanics and Engineering*, 70:59–89, 1988.

T. Belytschko, Y. Y. Lu, and L. Gu. Element-free Galerkin methods. *International Journal for Numerical Methods in Engineering*, 37(2):229–256, 1994.

I. Carol, E. Rizzi, and K. J. Willam. A unified theory of elastic degradation and damage based on a loading surface. *International Journal of Solids and Structures*, 31(20):2836–2865, 1994.

J.-S. Chen and H. Wang. New boundary condition treatments in meshfree computation of contact problems. *Computer Methods in Applied Mechanics and Engineering*, 187:441–468, 2000. doi: 10.1016/S0045-7825(00)80004-3.

J.-S. Chen, C.-T. Wu, and T. Belytschko. Regularization of material instabilities by meshfree approximations with intrinsic length scales. *International Journal for Numerical Methods in Engineering*, 47:1303–1322, 2000.

J.-S. Chen, C.-T. Wu, S. Yoon, and Y. You. A stabilized conforming nodal integration for Galerkin mesh-free methods. *International Journal for Numerical Methods in Engineering*, 50:435–466, 2001. doi: 10.1002/nme.338.

J. S. Chen, X. Zhang, and T. Belytschko. An implicit gradient model by a reproducing kernel strain regularization in strain localization problems. *Computer Methods in Applied Mechanics and Engineering*, 193:2827–2844, 2004.

J. S. Chen, W. Hu, M. Puso, and X. Zhang. Strain smoothing for stabilization and regularization of Galerkin meshfree. In M. Griebel and M. A. Schweitzer, editors, *Meshfree Methods for Partial Differential Equations III*, volume 57, pages 57–75. Springer Berlin Heidelberg, Berlin, Germany, 2007.

R. de Borst. Simulation of strain localization: a reappraisal of the Cosserat continuum. *Engineering Computations*, 8:317–332, 1991. doi: 10.1108/eb023842.

R. de Borst and M. A. Gutiérrez. A unified framework for concrete damage and fracture models including size effects. *International Journal of Fracture*, 95(1-4):261–277, 1999.

R. de Borst and H.-B. Mühlhaus. Gradient dependent plasticity: formulation and algorithmic aspects. *International Journal for Numerical Methods in Engineering*, 35:521–539, 1992. doi: 10.1002/nme.1620350307.

R. de Borst and L. Sluys. Localization in a Cosserat continuum under static and dynamic loading conditions. *Computer Methods in Applied Mechanics and Engineering*, 90:805–827, 1991. doi: 10.1016/0045-7825(91)90185-9.

R. de Borst, L. Sluys, H.-B. Mühlhaus, and J. Pamin. Fundamental issues in finite element analyses of localization of deformation. *Engineering Computations*, 10:99–121, 1993. doi: 10.1108/eb023897.

R. de Borst, M. a. Gutiérrez, G. N. Wells, J. J. C. Remmers, and H. Askes. Cohesive-zone models, higher-order continuum theories and reliability methods for computational failure analysis. *International Journal for Numerical Methods in Engineering*, 60:289–315, 2004. doi: 10.1002/nme.963.

A. Dietsche, P. Steinmann, and K. Willam. Micropolar elastoplasticity and its role in localization. *International Journal of Plasticity*, 9:813–831, 1993.

D. Dugdale. Yielding of steel sheets containing slits. *Journal of the Mechanics and Physics of Solids*, 8:100–104, 1960. doi: 10.1016/0022-5096(60)90013-2.

A. C. Eringen and D. G. B. Edelen. On nonlocal elasticity. *International Journal of Engineering Science*, 10:233–248, 1972. doi: 10.1016/0020-7225(72)90039-0.

X.-J. Fang, F. Jin, and Q.-D. Yang. Extended finite-element analysis of fractures in concrete. *Engineering and Computational Mechanics*, 161(EM4):187–197, 2008. doi: 10.1680/eacm.2008.161.4.187.

S. Fernández-Méndez and A. Huerta. Imposing essential boundary conditions in mesh-free methods. *Computer Methods in Applied Mechanics and Engineering*, 193:1257–1275, 2004. doi: 10.1016/j.cma.2003.12.019.

M. Frémond and B. Nedjar. Damage, gradient of damage and principle of virtual power. *International Journal of Solids and Structures*, 33(8):1083–1103, 1996. doi: 10.1016/0020-7683(95)00074-7.

C. Geuzaine and J.-F. Remacle. Gmsh: a 3D finite element mesh generator with built-in pre- and post-processing facilities. *International Journal for Numerical Methods in Engineering*, 79(11):1309–1331, 2009. doi: 10.1002/nme.2579.

R. A. Gingold and J. J. Monaghan. Smoothed particle hydrodynamics: theory and applications to non-spherical stars. *Monthly Notics of the Royal Astronomical Society*, 181:375–389, 1977.

M. Golberg, C. Chen, and H. Bowman. Some recent results and proposals for the use of radial basis functions in the BEM. *Engineering Analysis with Boundary Elements*, 23:285–296, 1999. doi: 10.1016/S0955-7997(98)00087-3.

L. Gori. *Failure analysis of quasi-brittle media using the micropolar continuum theory, elastic-degrading constitutive models, and smoothed point interpolation methods*. Phd thesis, Universidade Federal de Minas Gerais (UFMG), 2018.

L. Gori, S. Penna, and R. Pitangueira. An enhanced tensorial formulation for elastic degradation in micropolar continua. *Applied Mathematical Modelling*, 41:299–315, 2017a. ISSN 0307904X. doi: 10.1016/j.apm.2016.08.025.

L. Gori, S. Penna, and R. Pitangueira. Discontinuous failure in micropolar elastic-degrading models. *International Journal of Damage Mechanics*, 27(10):1482–1515, 2017b. doi: 10.1177/1056789517731137.

L. Gori, S. S. Penna, and R. L. d. S. Pitangueira. Damage modelling with smoothed point interpolation methods. In *Proceedings of the XL Ibero-Latin American Congress on Computational Methods in Engineering*, Natal, RN, Brazil, 2019a.

L. Gori, S. Silva Penna, and R. L. da Silva Pitangueira. Smoothed point interpolation methods for the regularization of material instabilities in scalar damage models. *International Journal for Numerical Methods in Engineering*, 117(7):729–755, 2019b. doi: 10.1002/nme.5974.

L. Gori, S. Silva Penna, and R. L. da Silva Pitangueira. G-space theory and weakened-weak form for micropolar media: Application to smoothed point interpolation methods. *Engineering Analysis with Boundary Elements*, 101:318–329, 2019c. doi: 10.1016/j.enganabound.2019.01.013.

M.-M. Iordache and K. Willam. Localized failure analysis in elastoplastic Cosserat continua. *Computer Methods in Applied Mechanics and Engineering*, 151:559–586, 1998. doi: 10.1016/S0045-7825(97)00166-7.

M. Jirásek. Nonlocal damage mechanics. *Revue Européenne de Génie Civil*, 11(7-8):993–1021, 2007. doi: 10.1080/17747120.2007.9692974.

S. Li, W. Hao, and W. K. Liu. Mesh-free simulations of shear banding in large deformation. *International Journal of Solids and Structures*, 37:7185–7206, 2000. doi: 10.1016/S0020-7683(00)00195-5.

G. Liu. A generalized gradient smoothing technique and the smoothed bilinear form for Galerkin formulation of a wide class of computational methods. *International Journal of Computational Methods*, 5(2):199–236, 2008. doi: 10.1142/S0219876208001510.

G. Liu. *Meshfree Methods: Moving Beyond the Finite Element Method*. CRC Press - Taylor & Francis Group, New York, USA, 2009.

G. Liu. A G space theory and a weakened weak (W^2) form for a unified formulation of compatible and incompatible methods: Part I theory. *International Journal for Numerical Mehods in Engineering*, 81:1093–1126, 2010a. doi: 10.1002/nme.2719.

G. Liu. A G space theory and a weakened weak (W^2) form for a unified formulation of compatible and incompatible methods: Part II applications to solid mechanics problems. *International Journal for Numerical Methods in Engineering*, 81:1127–1156, 2010b. doi: 10.1002/nme.2720.

G. Liu and Y. T. Gu. A point interpolation method for two-dimensional solids. *International Journal for Numerical Methods in Engineering*, 50:937–951, 2001.

G. Liu and M. B. Liu. *Smoothed Particle Hydrodynamics - A mesh free particle method*. World Scientific, Singapore, 2003.

G. Liu and G. Zhang. Upper bound solution to elasticity problems: a unique property of the linearly conforming point interpolation method (LC-PIM). *International Journal for Numerical Mehods in Engineering*, 74:1128–1161, 2007. doi: 10.1002/nme.2204.

G. Liu and G. Zhang. A normed G space and weakened weak (W^2) formulation of a cell-based smoothed point interpolation method. *International Journal of Computational Methods*, 6(1):147–179, 2009. doi: 10.1142/S0219876209001796.

G. Liu and G. Y. Zhang. Edge-based smoothed point interpolation methods. *International Journal of Computational Methods*, 5(4):621–646, 2008. doi: 10.1142/S0219876208001662.

G. Liu and G. Y. Zhang. *Smoothed Point Interpolation Methods - G Space Theory and Weakened Weak Forms*. World Scientific, 2013.

G. Liu, G. Y. Zhang, and K. Y. Dai. A linearly conforming point interpolation method (LC-PIM) for 2D solid mechanics problems. *International Journal of Computational Methods*, 2(4):645–665, 2005. doi: 10.1142/S0219876206001132.

G. Liu, K. Y. Dai, and T. T. Nguyen. A smoothed finite element method for mechanics problems. *Computational Mechanics*, 39:859–877, 2007. doi: 10.1007/s00466-006-0075-4.

G. Liu, T. Nguyen-Thoi, H. Nguyen-Xuan, and K. Lam. A node-based smoothed finite element method (NS-FEM) for upper bound solutions to solid mechanics problems. *Computers and Structures*, 87:14–26, 2009. doi: 10.1016/j.compstruc.2008.09.003.

M. B. Liu, G. R. Liu, and Z. Zong. An overview on smoothed particle hydrodynamics. *International Journal of Computational Methods*, 5(1):135–188, 2008.

W. K. Liu, S. Jun, and Y. F. Zhang. Reproducing kernel particle methods. *International Journal for Numerical Methods in Fluids*, 20(8-9):1081–1106, 1995.

W. K. Liu, S. Hao, T. Belytschko, S. F. Li, and C. T. Chang. Multiple scale meshfree methods for damage fracture and localization. *Computational Materials Science*, 16:197–205, 1999. doi: 10.1016/S0927-0256(99)00062-2.

L. B. Lucy. A numerical approach to the testing of the fission hypothesis. *The Astronomical Journal*, 82(12):1013–1024, 1977.

J. Mazars. *Application de le Mécanique de l'endommagement au comportement non lineaire et à la rupture du béton de Structure*. PhD thesis, Université Pierre et Marie Curie - Laboratoire de Mécanique et Technologie, Paris, France, 1984. (in french).

C. Miehe, F. Welschinger, and M. Hofacker. Thermodynamically consistent phase-field models of fracture: Variational principles and multi-field FE implementations. *International Journal for Numerical Mehods in Engineering*, 83:1273–1311, 2010. doi: 10.1002/nme.2861.

C. Miehe, S. Teichtmeister, and F. Aldakheel. Phase-field modelling of ductile fracture: a variational gradient-extended plasticity-damage theory and its micromorphic regularization. *Philosophical Transactions of the Royal Society A: Mathematical, Physical and Engineering Sciences*, 374(2066), 2016. doi: 10.1098/rsta.2015.0170.

J. Monaghan. Why particle methods work. *Journal on Scientific and Statistical Computing*, 3(4):422–433, 1982.

B. Nayroles, G. Touzot, and P. Villon. Generalizing the finite element method: Diffuse approximation and diffuse elements. *Computational Mechanics*, 10(5):307–318, 1992.

A. Needleman. Material rate dependence and mesh sensitivity in localization problems. *Computer Methods in Applied Mechanics and Engineering*, 67:69–85, 1988. doi: 10.1016/0045-7825(88)90069-2.

J. Oliver, a. E. Huespe, M. D. G. Pulido, and E. Chaves. From continuum mechanics to fracture mechanics: The strong discontinuity approach. *Engineering Fracture Mechanics*, 69:113–136, 2002. doi: 10.1016/S0013-7944(01)00060-1.

M. Ortiz, Y. Leroy, and A. Needleman. A finite element method for localized failure analysis. *Computer Methods in Applied Mechanics and Engineering*, 61(2):189–214, 1987.

R. Peerlings, R. de Borst, W. Brekelmans, and J. de Vree. Gradient enhanced damage for quasi-brittle materials. *International Journal for Numerical Methods in Engineering*, 39:3391–3403, 1996. doi: 10.1002/(SICI)1097-0207(19961015)39:19⟨3391::AID-NME7⟩3.0.CO;2-D.

R. Peerlings, M. Geers, R. de Borst, and W. Brekelmans. A critical comparison of nonlocal and gradient-enhanced softening continua. *International Journal of Solids and Structures*, 38: 7723–7746, 2001. doi: 10.1016/S0020-7683(01)00087-7.

R. H. J. Peerlings, R. De Borst, W. A. M. Brekelmans, and M. G. D. Geers. Localisation issues in local and nonlocal continuum approaches to fracture. *European Journal of Mechanics, A/Solids*, 21:175–189, 2002. doi: 10.1016/S0997-7538(02)01211-1.

S. Pietruszczak and Z. Mróz. Finite element analysis of deformation of strain-softening materials. *International Journal for Numerical Methods in Engineering*, 17:327–334, 1981.

G. Pijaudier-Cabot and Z. Bažant. Nonlocal damage theory. *Journal of Engineering Mechanics*, 113(10):1512–1533, 1987. doi: 10.1061/(ASCE)0733-9399(1987)113:10(1512).

P. L. Pozo, A. Campos, S. Lascano, S. Oller, and A. Rodriguez-Ferran. A finite points method approach for strain localization using the gradient plasticity formulation. *Mathematical Problems in Engineering*, 2014, 2014.

A. Quarteroni and A. Valli. *Numerical Approximation of Partial Differential Equations*. Springer-Verlag Berlin Heidelberg, 1994.

T. Rabczuk and T. Belytschko. Cracking particles: a simplified meshfree method for arbitrary evolving cracks. *International Journal for Numerical Methods in Engineering*, 61:2316–2343, 2004. doi: 10.1002/nme.1151.

S. S. Saliba, L. Gori, and R. L. da Silva Pitangueira. A coupled finite element-meshfree smoothed point interpolation method for nonlinear analysis. *Engineering Analysis with Boundary Elements*, 128:1–18, 2021. doi: 10.1016/j.enganabound.2021.03.015.

R. Vignjevic, N. Djordjevic, S. Gemkow, T. De Vuyst, and J. Campbell. SPH as a nonlocal regularisation method: Solution for instabilities due to strain-softening. *Computer Methods in Applied Mechanics and Engineering*, 277:281–304, 2014. doi: 10.1016/j.cma.2014.04.010.

D. Wang and Z. Li. A two-level strain smoothing regularized meshfree approach with stabilized conforming nodal integration for elastic damage analysis. *International Journal of Damage Mechanics*, 22(3):440–459, 2012. doi: 10.1177/1056789512455938.

J. Wang and G. Liu. On the optimal shape parameters of radial basis functions used for 2-d meshless methods. *Computer Methods in Applied Mechanics and Engineering*, 191:2611–2630, 2002a. doi: 10.1016/S0045-7825(01)00419-4.

J. G. Wang and G. R. Liu. A point interpolation meshless method based on radial basis functions. *International Journal for Numerical Methods in Engineering*, 54:1623–1648, 2002b. doi: 10.1002/nme.489.

B. Winkler, G. Hofstetter, and H. Lehar. Application of a constitutive model for concrete to the analysis of a precast segmental tunnel lining. *International Journal for Numerical and Analytical Methods in Geomechanics*, 28:797–819, 2004. doi: 10.1002/nag.362.

P. Wriggers. *Nonlinear Finite Element Methods*. Springer-Verlag Berlin Heidelberg, 2008. doi: 10.1007/978-3-540-71001-1.

C.-K. C. Wu and M. Plesha. Essential boundary condition enforcement in meshless methods: Boundary flux collocation method. *International Journal for Numerical Methods in Engineering*, 53:499–514, 2002. doi: 10.1002/nme.267.

G. Xotta, S. Beizaee, and K. Willam. Bifurcation investigation of coupled damage-plasticity models for concrete materials. *Computer Methods in Applied Mechanics and Engineering*, 298:428–452, 2016.

Y.-B. Yang and M.-S. Shieh. Solution method for nonlinear problems with multiple critical points. *AIAA Journal*, 28(12):2110–2116, 1990. doi: 10.2514/3.10529.

G. Zhang, Y. Li, X. Gao, D. Hui, S. Wang, and Z. Zong. Smoothed point interpolation method for elastoplastic analysis. *International Journal of Computational Methods*, 12(4), 2015. doi: 10.1142/S0219876215400137.

G. Y. Zhang, G. R. Liu, Y. Y. Wang, H. T. Huang, Z. H. Zhong, G. Y. Li, and X. Han. A linearly conforming point interpolation method (LC-PIM) for three-dimensional elasticity problems. *International Journal for Numerical Mehods in Engineering*, 72:1524–1543, 2007. doi: 10.1002/nme.2050.

Y. Q. Zhang, G. R. Liu, and X. Han. Effect of small length scale on elastic buckling of multi-walled carbon nanotubes under radial pressure. *Physics Letters A*, 349:370–376, 2006. doi: 10.1016/j.physleta.2005.09.036.

O. C. Zienkiewicz and R. L. Taylor. *The finite element method - Volume 1*. Butterworth Heinemann, Oxford, 2000.

Chapter 25

A New Non-Iterative Reconstruction Method for Solving a Class of Inverse Problems

A New Non-Iterative Reconstruction Method for Solving a Class of Inverse Problems

Antonio André Novotny

Laboratório Nacional de Computação Científica (LNCC), Coordenação de Métodos Matemáticos e Computacionais, Av. Getúlio Vargas 333, 25651-075 Petrópolis - RJ, Brasil. E-mail: novotny@lncc.br

Abstract

Several classes of inverse reconstruction problems are written in the form of over-determined boundary value problems. The general idea consists in rewriting them as an optimization problem. Therefore, a cost functional measuring the misfit between observed and predicted data is minimized with respect to a set of admissible solutions, leading to a non-iterative second order reconstruction algorithm. As a result, the reconstruction process becomes very robust with respect to noisy data and independent of any initial guess. In particular, we are interested in the spatial reconstruction and characterization of (micro-) seismic events via joint source location and moment tensor inversion from pointwise boundary measurements.

Keywords: Topological derivative method, non-iterative reconstruction method, full-waveform inversion, seismic moment tensor, multiple micro-seismic events.

1 Introduction

The topological derivative has been specifically conceived to provide a precise information on the sensitivity of a given shape functional with respect to topological domain perturbations. It appears in the first term of the asymptotic expansion of the shape functional with respect to a small parameter measuring the size of the perturbation under consideration, typically a hole, an inclusion, a source-term, or a crack. See, for instance, the books by Novotny and Sokołowski [2013, 2020].

The origin of the topological derivative method in optimal design can be dated to the work by Schumacher [1995] on the optimal location of holes within elastic structures. It is nevertheless worth mentioning prior related mathematical developments on the asymptotic behaviour of solutions to singularly perturbed boundary value problems and on the notions of polarization and capacity matrices. These objects are essential ingredients in the formulation of topological derivatives. The first mathematical justifications for topological derivatives in the framework of partial differential equations are due Sokołowski and Żochowski [1999] and Garreau et al. [2001], in the context of the Poisson equation and the Navier system for Neumann and Dirichlet holes.

In the last decade, the topological sensitivity analysis has become a rich and fascinating research field that combines the modern theory of calculus of variations, partial

differential equations, differential geometry, numerical analysis, physics, engineering and computational mechanics. The field grew up rapidly to develop many extensions and address a variety of physical and industrial problems. The topological derivative method has applications in shape and topology optimization [Novotny et al., 2007, Amstutz and Novotny, 2010], inverse problems [Canelas et al., 2015, Ferreira and Novotny, 2017], image processing [Auroux et al., 2007, Amstutz et al., 2014], multi-scale material design [Amstutz et al., 2010, Giusti et al., 2010] and mechanical modelling, including damage [Allaire et al., 2011] and fracture [Xavier et al., 2017] evolution phenomena. See, for instance, the book by Novotny et al. [2019a] and the special issue on the topological derivative method and its applications in computational engineering recently published in the Engineering Computations Journal [Novotny et al., 2022], covering various topics ranging from new theoretical developments [Amstutz, 2022, Baumann and Sturm, 2022, Delfour, 2022] to applications in structural and fluid dynamics topology optimization [Kliewe et al., 2022, Romero, 2022, Santos and Lopes, 2022], geometrical inverse problems [Bonnet, 2022, Canelas and Roche, 2022, Fernandez and Prakash, 2022, Louër and Rapún, 2022a,b] synthesis and optimal design of metamaterials [Ferrer and Giusti, 2022, Yera et al., 2022], fracture mechanics modelling [Xavier and Van Goethem, 2022], up to industrial applications [Rakotondrainibe et al., 2022] and experimental validation of the topological derivative method [Barros et al., 2022].

In this chapter, we are interested in the spatial reconstruction and characterization of (micro-) seismic events via joint source location and moment tensor inversion from pointwise boundary measurements. Seismic and micro-seismic source characterization is a keen area of research in geophysics, engineering, hydrocarbon production, and materials science due to its central role in the understanding of earthquake and faulting processes [Shearer, 2009]; monitoring of mines, highway bridges, and offshore platforms [Koerner et al., 1981]; tracking the progress of hydraulic fracturing [Baig and Urbancic, 2010], and investigating the failure of brittle materials [Grosse and Ohtsu, 2008]. Generally speaking any (micro-) seismic source, interpreted as a sudden material failure, can be characterized by its spatial support, temporal variation, and the underpinning failure mechanism. In situations when the extent of a material failure is small relative to the remaining length scales in the problem (e.g. seismic wavelengths and source-receiver distances), the seismic source can be interpreted as a point source [Scruby et al., 1985, Jost and Herrmann, 1989]; a hypothesis that is implicitly assumed hereon. In this setting, the accepted continuum mechanics description of a seismic source is given by a linear combination of force dipoles [Aki and Richards, 2009] whose weights are specified in terms of the so-called *seismic moment tensor* [Gilbert, 1973]; a second-order tensorial quantity whose accurate reconstruction from remote wavefield measurements is the key point of seismic source characterization.

In contrast to the classical approaches to moment tensor inversion in laboratory [Scruby et al., 1985] and geophysical [Jost and Herrmann, 1989] environments that rely on prior knowledge of the source location and possibly other simplifying assumptions (e.g. far field hypothesis), recent attempts at seismic source characterization are increasingly based on the full waveform analysis of multi-axial seismic observations [Cesca and Dahm, 2008]. In general, the latter can be pursued either via time- or frequency-domain approaches. As an example of the former class of inverse solutions, the paper by Song and Toksöz [2011] deploys grid search for the source location – aiming to minimize the misfit

between the observed and synthetic waveforms, followed by a least-squares solution for the moment tensor that relies on an *a priori* premise of the source time function. In the paper by Sjögreen and Petersson [2014], on the other hand, the investigators pursue simultaneous inversion for the source location, moment tensor, and two-parameter source time function via nonlinear minimization of the germane waveform misfit, aided by adjoint-field sensitivity estimates. In recent years, studies by Bazargani and Snieder [2015] and Kawakatsu and Montagner [2008] have demonstrated the utility of time reversal methods as a viable (time- or frequency-domain) alternative for exposing the seismic source location. With the latter information at hand, a full-waveform reconstruction of the moment tensor, including the underpinning source time function, can be conveniently pursued in the frequency domain [Cesca and Dahm, 2008] by solving the underpinning linear system of equations.

A common thread to the above and related inverse source analyses entails (i) the fundamental premise of a *synchronous seismic source*, where all components of its moment tensor share the same time dependence (given by the source time function); and (ii) the assumption of *a single* seismic (point) source, precluding the possibility that two events – originating from distinct locations – may overlap in time. To provide an alternative to the foregoing analyses that is free of such impediments, this work deals with spatial reconstruction and characterization of micro-seismic events in the frequency domain from pointwise wavefield measurements, where the associated moment tensors are fully reconstructed. Since the inverse problem at hand is (as expected) ill-posed, the idea is to rewrite it as an optimization problem in which a functional measuring the misfit between synthetic and observed waveforms is minimized with respect to a set of admissible point sources representing the hidden faults. The necessary optimality conditions are derived in the spirit of the topological derivative method as proposed by Novotny et al. [2019b] which, in this context, consists in exposing the perturbation of the functional as a quadratic function of the germane moment tensor components. Then, the resulting expansion is trivially minimized with respect to the sought source parameters, leading to a non-iterative reconstruction algorithm that is initial guess-free and robust with respect to perturbations of sensory data. We test the proposed technique via numerical experiments designed to examine its performance under a variety of source, sensing, and uncertainty scenarios.

The chapter is organized as follows. The germane (frequency-domain) forward problem and affiliated inverse problem, targeting the locations and moment-tensor "strengths" of micro-seismic events from the observed acoustic emission data, are described in Section 2. In Section 2.1 the germane cost functional, measuring the misfit between the synthetic and sensory data, is expanded with respect to the set of admissible source densities. The resulting expansion is used to devise a novel reconstruction algorithm presented in Section 2.2. A set of numerical experiments examining the effectiveness of the proposed reconstruction algorithm is provided in Section 3. Finally, the chapter ends with some concluding remarks presented in Section 4.

2   Full-Waveform Inversion of Seismic Moment Tensors

Following the original ideas presented in the paper by Amad et al. [2020], let us consider an open and bounded domain $\Omega \subset \mathbb{R}^2$ representing an elastic body. Its boundary is denoted as $\partial\Omega$, such that $\Gamma_N \subset \partial\Omega$ and $\Gamma_D = \partial\Omega \setminus \Gamma_N$ denote respectively the parts of $\partial\Omega$

subjected to homogeneous Neumann and Dirichlet boundary conditions. In this setting, we are interested in the inverse source problem of reconstructing the source density f^* such that

$$
\begin{cases}
-\operatorname{div}\sigma(u) - \rho\omega^2 u &=& f^* & \text{in} & \Omega, \\
u &=& u^* & \text{on} & \Gamma_m \subset \Gamma_N, \\
u &=& 0 & \text{on} & \Gamma_D, \\
\sigma(u)n &=& 0 & \text{on} & \Gamma_N,
\end{cases}
\tag{1}
$$

where $u : \Omega \to \mathbb{R}^2$ is the elastodynamic displacement field; ω denotes the frequency of wave motion; ρ is the density; n is the unit outward normal on $\partial\Omega$; $\Gamma_m \subset \Gamma_N$ is the measurement surface; and u^* are the acoustic emission data from which we aim to resolve f^*. See Fig. 1. In addition, $\sigma(u) = \mathbb{C}(\nabla u)^s$ is the Cauchy stress tensor, with $\mathbb{C}$ the elasticity tensor and $(\cdot)^s$ the symmetric part of a second order tensor $(\cdot)$. Without loss of generality, we assume the elastic body Ω to be homogeneous and isotropic, in which case the elasticity tensor reads

$$
\mathbb{C} = 2\mu\,\mathbb{I} + \lambda(\mathrm{I} \otimes \mathrm{I}),
\tag{2}
$$

where λ and μ are the Lamé moduli, and $\mathbb{I}$ and I are the fourth and second order identity tensors, respectively. The source density $f^* \in C_\delta(\Omega)$ to be reconstructed is given by a superposition of a finite number of dipoles, where

$$
C_\delta(\Omega) = \left\{ f : \Omega \to \mathbb{R}^2 \mid f(x) = \sum_{i=1}^{N} M_i \nabla_{x_i} \delta(x - x_i) \right\}.
\tag{3}
$$

Here, $\delta(\cdot)$ is the two-dimensional Dirac delta function; N denotes the number of point sources located at $x_i \in \Omega$ ($i = 1, 2, \ldots, N$), and $M_i \in \mathbb{R}^2 \times \mathbb{R}^2$ is a symmetric seismic moment tensor characterizing the i-th point source. For completeness, we recall from the continuum mechanics definition [Aki and Richards, 2009] that a generic seismic moment tensor is represented as

$$
M = a\,\mathbb{C}(\llbracket u \rrbracket \odot \eta),
\tag{4}
$$

where a is the area of a newly created micro-fracture (giving rise to the acoustic emission) whose unit normal is denoted by η, and $\llbracket u \rrbracket$ is the average displacement jump across the micro-fracture. Finally, $u \odot v$ denotes the symmetric tensor product between the vectors u and v, namely $u \odot v = \frac{1}{2}(u \otimes v + v \otimes u)$. On the basis of (3), we write the sought source density satisfying (1) as
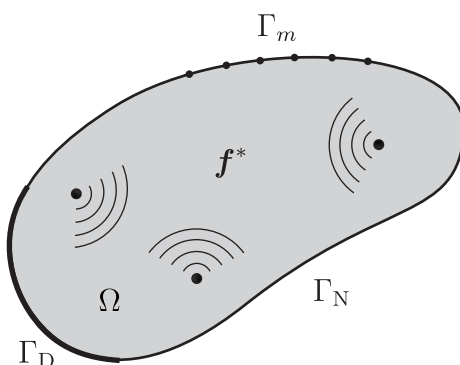
$$
f^*(x) = \sum_{i=1}^{N^*} M_i^* \nabla_{x_i^*} \delta(x - x_i^*).
\tag{5}
$$

Now, let us rewrite the inverse problem (1) as an optimization problem. The associated functional to be minimized in $C_\delta(\Omega)$ is given by

$$
\mathcal{J}(u) := \frac{1}{2} \int_{\Gamma_m} \|u - u^*\|^2,
\tag{6}
$$

where $u : \Omega \to \mathbb{R}^2$ solves the boundary value problem

$$
\begin{cases}
-\operatorname{div}\sigma(u) - \rho\omega^2 u &=& f & \text{in} & \Omega, \\
u &=& 0 & \text{on} & \Gamma_D, \\
\sigma(u)n &=& 0 & \text{on} & \Gamma_N,
\end{cases}
\tag{7}
$$

Γ_m

f^*

Γ_N

Ω

Γ_D

Figure 1: Problem setting.

for a trial source term $f \in C_\delta(\Omega)$. In this setting, the relevant optimization problem can be stated as

$$\underset{f \in C_\delta(\Omega)}{\text{Minimize}} \; \mathcal{J}(u), \; \text{subject to (7).} \tag{8}$$

2.1   Sensitivity Analysis

The next step is to minimize the misfit functional (6) with respect to the set of admissible solutions (3). In order to evaluate the germane sensitivities of this functional, the idea is to perturb the trial source term $f \in C_\delta(\Omega)$ in (7) by a fixed number N of point sources with arbitrary locations x_i and generic moment tensors M_i as

$$f_\delta(x) = f(x) + \sum_{i=1}^{N} M_i \nabla_{x_i} \delta(x - x_i), \tag{9}$$

where $M_i \in \mathbb{R}^2 \times \mathbb{R}^2$ are symmetric. On the basis of (7) and (9), we can introduce the forward solution $u_\delta : \Omega \to \mathbb{R}^2$ as that solving

$$\begin{cases} -\text{div}\sigma(u_\delta) - \rho\omega^2 u_\delta &=& f_\delta & \text{in} & \Omega, \\ u_\delta &=& 0 & \text{on} & \Gamma_D, \\ \sigma(u_\delta)n &=& 0 & \text{on} & \Gamma_N, \end{cases} \tag{10}$$

which gives rise to the perturbed cost functional

$$\mathcal{J}(u_\delta) = \frac{1}{2} \int_{\Gamma_m} \|u_\delta - u^*\|^2. \tag{11}$$

Assuming a sufficient number of micro-seismic source locations x_i ($i = 1, 2, \ldots, N$), we are interested in obtaining the variation of (6) with respect to the components of the moment tensor M_i at each location. To facilitate the analysis, one may decompose M_i into its Cartesian components using Einstein summation notation over repeated indexes $k, l = 1, 2$, namely

$$M_i = M_i^{kl}(e_k \otimes e_l), \tag{12}$$

where e_k and e_l are the unit vectors of the reference Cartesian frame, and M_i^{kl} are the components of M_i. With such definitions, the solution of (10) can be conveniently de-

composed as

$$u_\delta(x) = u(x) + \sum_{i=1}^{N} M_i^{kl} p_i^{kl}(x), \tag{13}$$

where $p_i^{kl} : \Omega \to \mathbb{R}^2$ solve the canonical boundary value problems of the form

$$\begin{cases} -\mathrm{div}\sigma(p_i^{kl}) - \rho\omega^2 p_i^{kl} &= (e_k \otimes e_l)\nabla_{x_i}\delta(x - x_i) & \text{in} & \Omega, \\ p_i^{kl} &= 0 & \text{on} & \Gamma_D, \\ \sigma(p_i^{kl})n &= 0 & \text{on} & \Gamma_N, \end{cases} \tag{14}$$

for $k, l = 1, 2$. Here it is useful to note that, thanks to ansatz (13), canonical problems (14) are independent of the components M_i^{kl} of the moment tensor M_i in (12). Now we have all elements needed to evaluate the variation of functional (6) with respect to M_i^{kl}. Specifically, on substituting (13) in (11), we obtain

$$\mathcal{J}(u_\delta) = \mathcal{J}(u) + \sum_{i=1}^{N} M_i^{kl} \int_{\Gamma_m} p_i^{kl} \cdot (u - u^*) + \frac{1}{2}\sum_{i=1}^{N}\sum_{j=1}^{N} M_i^{kl} M_j^{mn} \int_{\Gamma_m} p_i^{kl} \cdot p_j^{mn}, \tag{15}$$

assuming implicit summation over repeated indexes $k, l, m, n = 1, 2$.

For a systematic treatment of (15), we next introduce the vector of trial source locations

$$\xi = (x_1, x_2, \ldots, x_N) \in \mathbb{R}^{2N} \tag{16}$$

and the affiliated strength vectors

$$\alpha = (\alpha_1, \alpha_2, \ldots, \alpha_N)^\top \in \mathbb{R}^{3N}, \tag{17}$$

collecting the respective components of M_i, where

$$\alpha_i = (M_i^{11}, M_i^{22}, M_i^{12} = M_i^{21})^\top.$$

With such definitions, the residual in (15) can be rewritten more compactly as

$$\Psi(\alpha) \quad := \quad \mathcal{J}(u_\delta) - \mathcal{J}(u) \tag{18}$$

$$= \quad h \cdot \alpha + \frac{1}{2} H \alpha \cdot \alpha. \tag{19}$$

Here, vector $h \in \mathbb{R}^{3N}$ and matrix $H \in \mathbb{R}^{3N} \times \mathbb{R}^{3N}$ are respectively defined as

$$h := \begin{pmatrix} h_1 \\ h_2 \\ \vdots \\ h_N \end{pmatrix}, \quad \text{and} \quad H := \begin{pmatrix} H_{11} & H_{12} & \ldots & H_{1N} \\ H_{21} & H_{22} & \ldots & H_{2N} \\ \vdots & \vdots & \ddots & \vdots \\ H_{N1} & H_{N2} & \ldots & H_{NN} \end{pmatrix}, \tag{20}$$

whose entries are given by

$$h_i := \begin{pmatrix} h_i^1 \\ h_i^2 \\ h_i^3 \end{pmatrix}, \quad \text{and} \quad H_{ij} := \begin{pmatrix} H_{ij}^{11} & H_{ij}^{12} & \ldots & H_{ij}^{13} \\ H_{ij}^{21} & H_{ij}^{22} & \ldots & H_{ij}^{23} \\ H_{ij}^{31} & H_{ij}^{32} & \ldots & H_{ij}^{33} \end{pmatrix}, \tag{21}$$

where

$$h_i^1 := \int_{\Gamma_m} p_i^{11} \cdot (u - u^*), \quad h_i^2 := \int_{\Gamma_m} p_i^{22} \cdot (u - u^*), \quad h_i^3 := \int_{\Gamma_m} (p_i^{12} + p_i^{21}) \cdot (u - u^*),$$

and

$$H_{ij}^{11} := \int_{\Gamma_m} p_i^{11} \cdot p_j^{11}, \quad H_{ij}^{12} := \int_{\Gamma_m} p_i^{11} \cdot p_j^{22}, \quad H_{ij}^{13} := \int_{\Gamma_m} p_i^{11} \cdot (p_j^{12} + p_j^{21}),$$

$$H_{ij}^{21} := \int_{\Gamma_m} p_i^{22} \cdot p_j^{11}, \quad H_{ij}^{22} := \int_{\Gamma_m} p_i^{22} \cdot p_j^{22}, \quad H_{ij}^{23} := \int_{\Gamma_m} p_i^{22} \cdot (p_j^{12} + p_j^{21}),$$

$$H_{ij}^{31} := \int_{\Gamma_m} (p_i^{12} + p_i^{21}) \cdot p_j^{11}, \quad H_{ij}^{32} := \int_{\Gamma_m} (p_i^{12} + p_i^{21}) \cdot p_j^{22},$$

$$H_{ij}^{33} := \int_{\Gamma_m} (p_i^{12} + p_i^{21}) \cdot (p_j^{12} + p_j^{21}).$$

2.2 Reconstruction Algorithm

For each fixed pair (N, ξ), we seek α that minimizes Ψ according to (19). Since Ψ represents a quadratic form with respect to α, sufficient optimality condition

$$\langle D_\alpha \Psi(\alpha), \delta\alpha \rangle = 0, \quad \forall \, \delta\alpha \in \mathbb{R}^{3N}, \tag{22}$$

lead to the linear system

$$H\alpha = -h. \tag{23}$$

In this setting, the solution α of (23) is implicitly a function of the vector (16) of source locations ξ, namely $\alpha = \alpha(\xi)$. On substituting (23) into (19), the optimal vector of source locations $\xi^\star$ can be trivially obtained via combinatorial search over a prescribed grid, X, of $M \geqslant N$ trial source locations geared toward solving the minimization problem

$$\xi^\star = \underset{\xi \subset X}{\mathrm{argmin}} \left\{ \Psi(\alpha(\xi)) = \frac{1}{2} h \cdot \alpha(\xi) \right\}. \tag{24}$$

On resolving $\xi^\star$, the components of N reconstructed moment tensors $M_i^\star$ are then given by the optimal strength vector $\alpha^\star = \alpha(\xi^\star)$. The associated optimal value of the objective function is denoted as $\Psi^\star := \Psi(\alpha^\star)$. We remark that when the true number of micro-seismic sources, $N^\star$, is less than N, numerical simulations show that a number $N - N^\star$ of components $\alpha_i^\star$, in the solution set $\alpha^\star$, take near-trivial values.

To complete the analysis, we next introduce a second-order optimization algorithm that synthesizes the process of obtaining $\xi^\star$ and $\alpha^\star$ from the computational point of view. The input of the algorithm is listed below:

- Upper bound N on the number of (micro-seismic) point sources.

- Grid X of $M \geqslant N$ trial source locations.

- Canonical solutions p_i^{kl} for each grid point $x_i \in X$.

Algorithm 1: Micro-seismic source reconstruction

---

      input : N, X, $p_i^{kl}\ \forall x_i \in X$

1 Initialization: $\xi^\star \leftarrow 0$; $\alpha^\star \leftarrow 0$; $\Psi^\star \leftarrow \infty$; $M \leftarrow \mathrm{card}(X)$

2 **for** $i_1 \leftarrow 1$ **to** M **do**

3   **for** $i_2 \leftarrow i_1 + 1$ **to** M **do**

         $\vdots$

4   **for** $i_N \leftarrow i_{N-1} + 1$ **to** M **do**

5            $h \leftarrow \begin{bmatrix} h_{(i_1)} \\ h_{(i_2)} \\ \vdots \\ h_{(i_N)} \end{bmatrix}$; $H \leftarrow \begin{bmatrix} H_{(i_1 i_1)} & H_{(i_1 i_2)} & \cdots & H_{(i_1 i_N)} \\ H_{(i_2 i_1)} & H_{(i_2 i_2)} & \cdots & H_{(i_2 i_N)} \\ \vdots & \vdots & \ddots & \vdots \\ H_{(i_N i_1)} & H_{(i_N i_2)} & \cdots & H_{(i_N i_N)} \end{bmatrix}$

6            $\alpha \leftarrow -H^{-1}h$; $\Psi \leftarrow \frac{1}{2}h \cdot \alpha$

7            $\mathcal{I} \leftarrow (i_1, i_2, \ldots, i_N)$; $\xi \leftarrow \Pi(\mathcal{I})$

8   **if** $\Psi < \Psi^\star$ **then**

9               $\xi^\star \leftarrow \xi$; $\alpha^\star \leftarrow \alpha$; $\Psi^\star \leftarrow \Psi$

10   **end if**

11   **end for**

12   **end for**

13 **end for**

14 **return** $\xi^\star$, $\alpha^\star$, $\Psi^\star$

The algorithm returns the optimal set of source locations $\xi^\star$ and respective moment tensor components given by $\alpha^\star$. The above procedure, originally developed in the paper by Canelas et al. [2014] in the context of inverse potential problems, is shown in Algorithm 1 using pseudo-code format. Therein, $\Pi : \{1, 2, \ldots, M\}^N \mapsto X$ maps the vector of source indices $\mathcal{I} = (i_1, i_2, \ldots, i_N)$ to the corresponding vector of source locations $\xi \subset X$. For further applications of this algorithm, we refer to the paper by Novotny et al. [2019b].

In Algorithm 1, optimal source locations $\xi^\star$ are obtained through a combinatorial search over M trial points sampling the set of admissible locations X. As a result, the computational complexity $\mathcal{C}(M, N)$ of the algorithm can be evaluated by the formula

$$\mathcal{C}(M, N) \approx \binom{M}{N} N^3 = \frac{M!}{N!(M-N)!} N^3.$$

In Fig. 2, the graphs of $N \times \log_{10}(\mathcal{C}(M, N))$ for $M = 100$ and $M = 400$ are plotted as solid and dashed lines, respectively. As can be seen from the display, the computational cost of the algorithm may become prohibitive for a large N, with $N \approx M/2$. In the ensuing numerical examples (Section 3), we set $N \ll M$, so that Algorithm 1 runs in a few seconds for all examples.
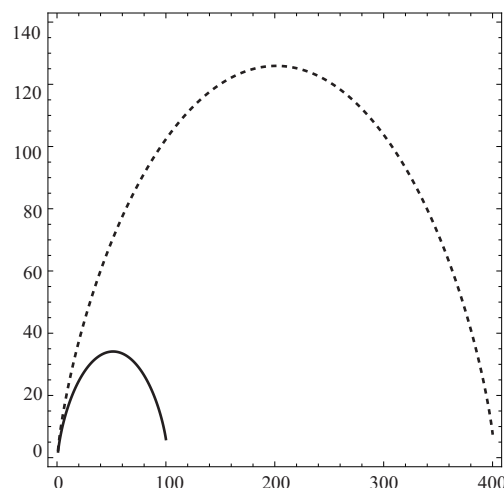
Figure 2: Complexity order of Algorithm 1: $N \times \log_{10}(\mathcal{C}(M, N))$ **for** $M = 100$ **(solid) and** $M = 400$ **(dashed).**

3   Numerical Results

Thanks to the fact that the moment tensor $M_i \in \mathbb{R}^2 \times \mathbb{R}^2$ is symmetric, its eigenvalues can be conveniently written as

$$m_i^{1,2} := \frac{1}{2}\left(\operatorname{tr}(M_i) \pm \sqrt{M_i^D \cdot M_i^D}\right) \tag{25}$$

in terms of the volumetric $\operatorname{tr}(M_i)$ and deviatoric M_i^D components of M_i, with

$$M_i^D = M_i - \frac{1}{2}\operatorname{tr}(M_i)\mathrm{I}. \tag{26}$$

In the sequel, we denote the affiliated eigenvectors by $v_i^{1,2}$.

   For the purposes of source inversion, we next consider three types of micro-seismic events given by the moment tensors $M_i^* \in \mathbb{R}^2 \times \mathbb{R}^2$ ($i = 1, \ldots, N^*$) featuring [Aki and Richards, 2009]: (i) real amplitude $\gamma_i \in \mathbb{R}$, (ii) unit normal to the micro-crack $\eta_i \in \mathbb{R}^2$ (when applicable), and (iii) Lamé moduli μ and λ of the background solid. Specifically, when generating the synthetic data u^* according to (1) and (5), we allow for
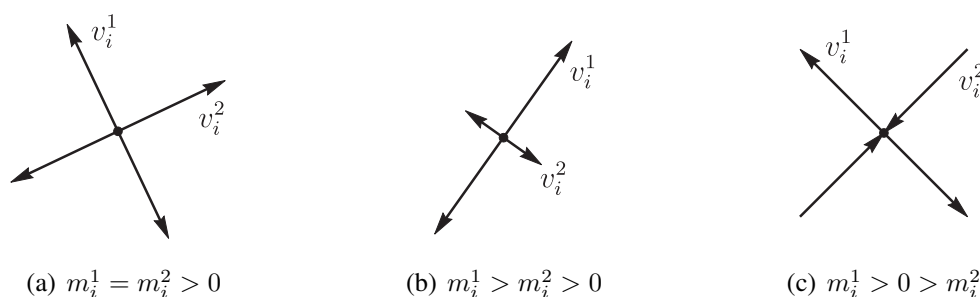
1. Cavitation:
$$M_i^* = 2\gamma_i(\mu + \lambda)\mathrm{I} \quad \Rightarrow \quad m_i^{1,2} = 2\gamma_i(\mu + \lambda); \tag{27}$$

2. Mode I crack:
$$M_i^* = \gamma_i(2\mu(\eta_i \otimes \eta_i) + \lambda\mathrm{I}) \quad \Rightarrow \quad m_i^1 = \gamma_i(2\mu + \lambda),\ m_i^2 = \gamma_i\lambda; \tag{28}$$

3. Mode II crack:
$$M_i^* = \gamma_i\mu(\eta_i^\perp \otimes \eta_i + \eta_i \otimes \eta_i^\perp) \quad \Rightarrow \quad m_i^{1,2} = \pm\gamma_i\mu. \tag{29}$$

(a) $m_i^1 = m_i^2 > 0$ (b) $m_i^1 > m_i^2 > 0$ (c) $m_i^1 > 0 > m_i^2$

Figure 3: Representation of the moment tensors in terms of their eigenvalues and eigenvectors: (a) cavitation, (b) mode I crack, and (c) mode II crack.

For future reference, the moment tensors given by (27)–(29) are depicted graphically in Fig. 3.

The elastic body Ω used for numerical simulations is taken as an $\ell \times \ell$ block of rock with mass density ρ and Lamé moduli $\lambda = \mu$ (Poisson's ratio $\nu = 0.25$), fixed at the bottom corners. The pointwise motion sensors are assumed to be distributed along the boundary $\partial\Omega$ with various densities and apertures as described in the sequel. The dimensionless frequency of acoustic emission is taken as

$$\bar{\omega} = \frac{\omega\,\ell}{\sqrt{\mu/\rho}} = 10\pi,$$

resulting in the specimen-size-to-shear-wavelength ratio of $\ell/\lambda_s = 5$. With reference to (4), (9) and (27)–(29), we also introduce the dimensionless coordinates $y = \ell^{-1}x$; we consider the dimensionless source strength $\bar{\gamma} = \ell^{-3}\gamma$, and we specify the unit normal to the micro-crack as $\eta = (\cos\theta, \sin\theta)$, where θ is the angle measured counterclockwise from the horizontal axis. The forward elastodynamic problem is solved via standard Galerkin finite element method. To handle the germane wave propagation with sufficient accuracy, domain Ω is first subdivided into a uniform 10×10 grid of square subdomains. Then, each subdomain is discretized via 4^n triangular finite elements with $n = 7$. Next, the set of admissible source locations X is taken as the union of vertices of like triangles with $n = 1$, giving $M = 221$ in Algorithm 1. Finally, the dipoles are represented by a Gaussian distribution of the form

$$\delta(x - x_i) = \lim_{\varepsilon \to 0} \frac{1}{2\pi\varepsilon^2} \exp\left(-\frac{\|x - x_i\|^2}{2\varepsilon^2}\right). \tag{30}$$

The gradient of $\delta(x - x_i)$ with respect to x_i can be obtained as follows

$$\nabla_{x_i}\delta(x - x_i) = \lim_{\varepsilon \to 0} \frac{x - x_i}{2\pi\varepsilon^4} \exp\left(-\frac{\|x - x_i\|^2}{2\varepsilon^2}\right), \tag{31}$$

where the parameter $\varepsilon = 10^{-2} \times h^e$ for the numerical purposes, with h^e used to denote the size of the finite element.

To illustrate the performance of the inversion algorithm, we adopt the graphical representation of moment tensors introduced in Fig. 3, and we denote the true (resp. reconstructed) sources by thick red (resp. thin blue) arrows. Finally, the pointwise sensors are represented by black dots.

3.1   Example 1

In this example, we pursue reconstruction of one, two and three micro-seismic sources representing: (i) cavitation, (ii) mode I and mode II cracks and (iii) cavitation, mode I and mode II cracks. More precisely, in Fig. 4 there are: (a) $\bar{\gamma}_1 = 0.02$; (b) $\bar{\gamma}_1 = 0.04$ and $\theta_1 = 20°$, $\bar{\gamma}_2 = 0.01$ and $\theta_2 = 15°$; and (c) $\bar{\gamma}_1 = 0.01$, $\bar{\gamma}_2 = 0.03$ and $\theta_2 = 20°$, $\bar{\gamma}_3 = 0.02$ and $\theta_3 = 15°$. As sensory data, we consider the biaxial motion measurements captured by one, two and three pairs of sensors, respectively. As expected, the sources reconstructions shown in Fig. 4 are nearly exact in all cases.

(a) single micro-fault   (b) two micro-faults   (c) three micro-faults
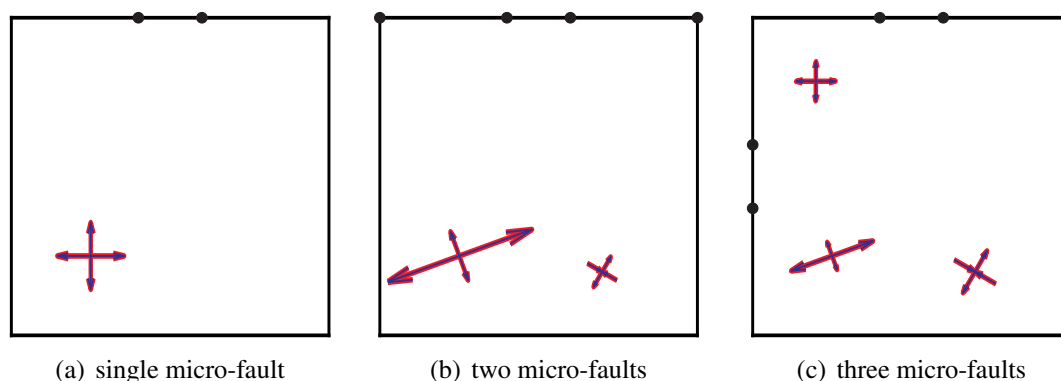
Figure 4: Reconstruction of one, two and three micro-faults using different configurations of biaxial motion sensors.

At this point, it is worth noting that the reconstruction fails if a smaller-than-featured number of sensors is deployed in each of the foregoing examples. Qualitatively speaking, this suggests the use of at least two sensors per (micro-seismic) source. When using S sensors in a laboratory setting, one should accordingly expect to reliably reconstruct up to $S/2$ simultaneous sources. In situations where the reconstruction algorithm consistently exposes more than $S/2$ contemporaneous events, the above result suggests either (i) deploying additional motion sensors, or (ii) retaining only the "strongest" $S/2$ events, as quantified e.g. in terms of Frobenius norm of the moment tensors M_i, $i = 1, 2, \ldots, N$. For completeness, we note that in conventional acoustic emission (AE) testing [Grosse and Ohtsu, 2008], micro-seismic events are reconstructed one at a time, which precludes the existence of contemporaneous sources.

3.2   Example 2

In this second and last example, we examine the robustness of the reconstruction algorithm with respect to random modeling errors. To this end, we assume the true material parameters to be corrupted with White Gaussian Noise according to

$$\mu_\tau = \mu(1 + \tau\varphi), \quad \lambda_\tau = \lambda(1 + \tau\varphi) \quad \text{and} \quad \rho_\tau = \rho(1 + \tau\varphi), \quad (32)$$

where $\varphi : \Omega \mapsto (0, 1)$ is a random variable and τ specifies the amplitude of fluctuations. The domain Ω is subdivided into 10×10 subregions. To have a meaningful representation of material heterogeneities, each subregion is discretized by 4^4 triangular elements where the corrupted material parameters are evaluated according to (32). In this way, the average

heterogeneity size d_h can be computed as $d_h/\lambda_s = (5/10)/4^2 \simeq 0.03$, i.e. 3% of the shear wavelength. For consistency, such material distribution is then projected onto a finer mesh with 4^7 triangular elements per subregion, leading to a finite element discretization that is commensurate with those in the former example. As before, the reconstruction algorithm assumes a homogeneous background model with Lamé parameters $\lambda = \mu$ and mass density ρ. The perturbation function $(1 + \tau\varphi)$ is plotted in Fig. 5 with $\tau = 1$. For completeness of discussion, we next introduce the effective noise level in the data due to (32) as

$$\tau^\star := \frac{\|u_0 - u_\tau\|_{L^2(\Omega)}}{\|u_0\|_{L^2(\Omega)}}, \tag{33}$$

where $u_0 = u_{\tau|_{\tau=0}}$ and u_τ is the acoustic emission field due to exact source distribution (5) computed assuming (32) for the background solid.
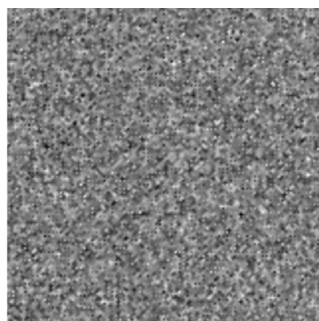
Figure 5: Corrupted background with White Gaussian Noise.

In this scenario, let us reconstruct a single mode II event with $\bar{\gamma}_1 = 0.05$ and $\theta_1 = 15°$ using the six sensors shown in Fig. 6. We assume that the number of faults is not known, and we set $N = 2 > N^* = 1$. The results of source reconstruction for 0.5%, 1.0% and 2.0% are shown in Fig. 6. For $\tau = 0.0\%$, the reconstruction is nearly exact and thus the result is not reported. For $\tau = 0.5\%$ ($\tau^\star = 10\%$), the reconstruction is still good, but there is a minuscule artifact in the form of a *phantom* second event as permitted by the premise $N = 2$. This type of solution degradation continues to grow for $\tau = 1.0\%$ ($\tau^\star = 21\%$) and $\tau = 2.0\%$ ($\tau^\star = 51\%$) as can be seen from the respective displays.

(a) $\tau = 0.5\%$ ($\tau^\star = 10\%$)   (b) $\tau = 1.0\%$ ($\tau^\star = 21\%$)   (c) $\tau = 2.0\%$ ($\tau^\star = 51\%$)
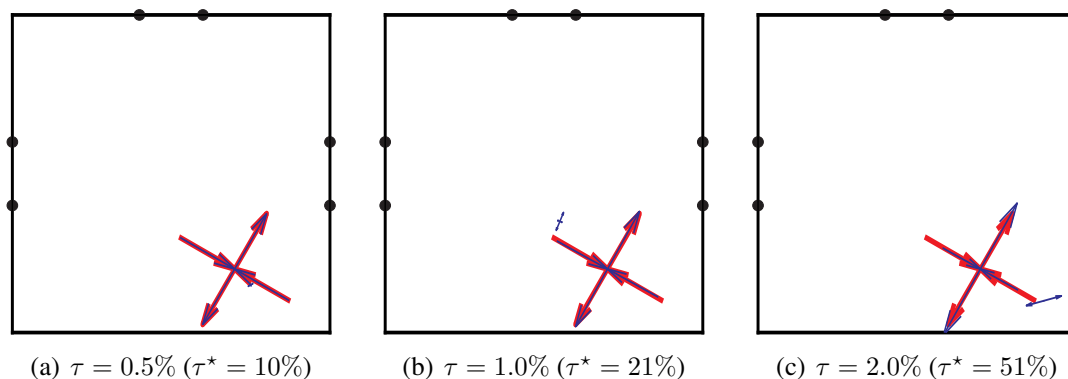
Figure 6: Reconstruction of a single micro-fault under varying levels of noise.

4   Concluding Remarks

In this study, we propose an algorithm for the frequency-domain reconstruction of micro-seismic events using full-waveform analysis of the acoustic emission data. The inversion approach integrates a combinatorial grid search for source locations with the sensitivity analysis in terms of moment tensor components to arrive at an effective algorithm that simultaneously returns both micro-seismic source coordinates and respective tensorial strengths. We investigate the performance of the algorithm, assuming pointwise waveform observations, via numerical examples that include both isolated and multiple point sources. Under ideal testing conditions, the results suggest that two point receivers per acoustic emission source may provide sufficient information for accurate moment tensor inversion. For generality, we also investigate the micro-seismic source reconstruction under the adverse condition of randomly perturbed background medium, whose local fluctuations are unavailable as prior information. The results show a significant resilience of the reconstruction algorithm to this type of modeling errors.

Acknowledgements

References

K. Aki and P. Richards. *Quantitative Seismology*. University Science Books, Sausalito, California, 2009.

G. Allaire, F. Jouve, and N. Van Goethem. Damage and fracture evolution in brittle materials by shape optimization methods. *Journal of Computational Physics*, 230(12): 5010–5044, 2011.

A. Amad, A. Novotny, and B. Guzina. On the full-waveform inversion of seismic moment tensors. *International Journal of Solids and Structures*, 202(1):717–728, 2020. doi: 10.1016/j.ijsolstr.2020.06.012.

S. Amstutz. An introduction to the topological derivative. *Engineering Computations*, 39 (1):3–33, 2022.

S. Amstutz and A. Novotny. Topological optimization of structures subject to von Mises stress constraints. *Structural and Multidisciplinary Optimization*, 41(3):407–420, 2010.

S. Amstutz, S. Giusti, A. Novotny, and E. de Souza Neto. Topological derivative for multi-scale linear elasticity models applied to the synthesis of microstructures. *International Journal for Numerical Methods in Engineering*, 84:733–756, 2010.

S. Amstutz, A. Novotny, and N. Van Goethem. Minimal partitions and image classification using a gradient-free perimeter approximation. *Inverse Problems and Imaging*, 8 (2):361–387, 2014.

D. Auroux, L. J. Belaid, and M. Masmoudi. A topological asymptotic analysis for the regularized greylevel image classification problem. *ESAIM Mathematical Modelling and Numerical Analysis*, 41:607–625, 2007.

A. Baig and T. Urbancic. Microseismic moment tensors: A path to understanding frac growth. *The Leading Edge*, 29:320–324, 2010.

G. Barros, J. Filho, L. Nunes, and M. Xavier. Experimental validation of a topological derivative-based crack growth control method using digital image correlation. *Engineering Computations*, 39(1):438–454, 2022.

P. Baumann and K. Sturm. Adjoint-based methods to compute higher-order topological derivatives with an application to elasticity. *Engineering Computations*, 39(1):60–114, 2022.

F. Bazargani and R. Snieder. Optimal source imaging in elastic media. *Geophysical Journal International*, 204:1134–1147, 2015.

M. Bonnet. On the justification of topological derivative for wave-based qualitative imaging of finite-sized defects in bounded media. *Engineering Computations*, 39(1):313–336, 2022.

A. Canelas and J. Roche. Shape and topology optimal design problems in electromagnetic casting. *Engineering Computations*, 39(1):147–171, 2022.

A. Canelas, A. Laurain, and A. Novotny. A new reconstruction method for the inverse potential problem. *Journal of Computational Physics*, 268:417–431, 2014.

A. Canelas, A. Laurain, and A. Novotny. A new reconstruction method for the inverse source problem from partial boundary measurements. *Inverse Problems*, 31(7):075009, 2015. doi: 10.1088/0266-5611/31/7/075009.

S. Cesca and T. Dahm. A frequency domain inversion code to retrieve time-dependent parameters of very long period volcanic sources. *Computers & Geosciences*, 34:235–246, 2008.

M. Delfour. Topological derivatives via one-sided derivative of parametrized minima and minimax. *Engineering Computations*, 39(1):34–59, 2022.

L. Fernandez and R. Prakash. Imaging of small penetrable obstacles based on the topological derivative method. *Engineering Computations*, 39(1):201–231, 2022.

A. Ferreira and A. Novotny. A new non-iterative reconstruction method for the electrical impedance tomography problem. *Inverse Problems*, 33(3):035005, 2017. doi: 10.1088/1361-6420/aa54e4.

A. Ferrer and S. Giusti. Inverse homogenization using the topological derivative. *Engineering Computations*, 39(1):337–353, 2022.

S. Garreau, P. Guillaume, and M. Masmoudi. The topological asymptotic for PDE systems: the elasticity case. *SIAM Journal on Control and Optimization*, 39(6):1756–1778, 2001.

F. Gilbert. Derivation of source parameters from low-frequency spectra. *Philosophical Transactions of the Royal Society of London. Series A, Mathematical and Physical Sciences*, 274:369–371, 1973.

S. Giusti, A. Novotny, and E. de Souza Neto. Sensitivity of the macroscopic response of elastic microstructures to the insertion of inclusions. *Proceeding of the Royal Society A: Mathematical, Physical and Engineering Sciences*, 466:1703–1723, 2010.

C. Grosse and M. Ohtsu. *Acoustic Emission Testing*. Springer Science & Business Media, 2008.

M. Jost and R. Herrmann. A student's guide to and review of moment tensors. *Seismological Research Letters*, 60:37–57, 1989.

H. Kawakatsu and J. Montagner. Time-reversal seismic-source imaging and moment-tensor inversion. *Geophysical Journal International*, 175:686–688, 2008.

P. Kliewe, A. Laurain, and K. Schmidt. Shape optimization in acoustic-structure interaction. *Engineering Computations*, 39(1):172–200, 2022.

R. Koerner, W. McCabe, and A. Lord. Overview of acoustic emission monitoring of rock structures. *Rock Mechanics*, 14:27–35, 1981.

F. L. Louër and M. Rapún. Topological sensitivity analysis revisited for time-harmonic wave scattering problems. Part I: The free space case. *Engineering Computations*, 39(1):232–271, 2022a.

F. L. Louër and M. Rapún. Topological sensitivity analysis revisited for time-harmonic wave scattering problems. Part II: Recursive computations by the boundary integral equation method. *Engineering Computations*, 39(1):272–312, 2022b.

A. Novotny and J. Sokołowski. *Topological derivatives in shape optimization*. Interaction of Mechanics and Mathematics. Springer-Verlag, Berlin, Heidelberg, 2013. doi: 10.1007/978-3-642-35245-4.

A. Novotny and J. Sokołowski. *An introduction to the topological derivative method*. Springer Briefs in Mathematics. Springer Nature Switzerland, 2020. doi: 10.1007/978-3-030-36915-6.

A. Novotny, R. Feijóo, E. Taroco, and C. Padra. Topological sensitivity analysis for three-dimensional linear elasticity problem. *Computer Methods in Applied Mechanics and Engineering*, 196(41–44):4354–4364, 2007.

A. Novotny, J. Sokołowski, and A. Żochowski. *Applications of the topological derivative method*. Studies in Systems, Decision and Control. Springer Nature Switzerland, 2019a. doi: 10.1007/978-3-030-05432-8.

A. Novotny, J. Sokołowski, and A. Żochowski. Topological derivatives of shape functionals. Part III: Second order method and applications. *Journal of Optimization Theory and Applications*, 181(1):1–22, 2019b.

A. Novotny, S. Giusti, and S. Amstutz. Guest Editorial: On the topological derivative method and its applications in computational engineering. *Engineering Computations*, 39(1):1–2, 2022.

L. Rakotondrainibe, G. Allaire, and P. Orval. Topological sensitivity analysis with respect to a small idealized bolt. *Engineering Computations*, 39(1):115–146, 2022.

A. Romero. Optimum design of two-material bending plate compliant devices. *Engineering Computations*, 39(1):395–420, 2022.

R. Santos and C. Lopes. Topology optimization of structures subject to self-weight loading under stress constraints. *Engineering Computations*, 39(1):380–394, 2022.

A. Schumacher. *Topologieoptimierung von bauteilstrukturen unter verwendung von lochpositionierungkriterien*. Ph.D. Thesis, Universität-Gesamthochschule-Siegen, Siegen - Germany, 1995.

C. Scruby, G. Baldwin, and K. Stacey. Characterisation of fatigue crack extension by quantitative acoustic emission. *International Journal of Fracture*, 28:201–222, 1985.

P. Shearer. *Introduction to Seismology*. Cambridge University Press, 2009.

B. Sjögreen and N. Petersson. Source estimation by full wave form inversion. *Journal of Scientific Computing*, 59(1):247–276, 2014.

J. Sokołowski and A. Żochowski. On the topological derivative in shape optimization. *SIAM Journal on Control and Optimization*, 37(4):1251–1272, 1999.

F. Song and M. Toksöz. Full-waveform based complete moment tensor inversion and source parameter estimation from downhole microseismic data for hydrofracture monitoring. *Geophysics*, 76:WC103–WC116, 2011.

M. Xavier and N. Van Goethem. Brittle fracture on plates governed by topological derivatives. *Engineering Computations*, 39(1):421–437, 2022.

M. Xavier, E. Fancello, J. Farias, N. Van Goethem, and A. Novotny. Topological derivative-based fracture modelling in brittle materials: A phenomenological approach. *Engineering Fracture Mechanics*, 179:13–27, 2017.

R. Yera, L. Forzani, C. Méndez, and A. Huespe. A topology optimization algorithm based on topological derivative and level-set function for designing phononic crystals. *Engineering Computations*, 39(1):354–379, 2022.

About the Editors

Ariosto Bretanha Jorge (Book Series Leading Editor)

Visiting Professor at Post-Graduate Program - Integrity of Engineering Materials, University of Brasilia, Brazil

Research interests include: helicopter technologies, mechanical vibrations, computational mechanics, numerical methods, optimization, reliability, aircraft structures, fracture mechanics, inverse problems.

More info: lattes.cnpq.br/3558866397613277, orcid.org/0000-0002-8631-1381

✉ ariosto.b.jorge@gmail.com, ariosto.jorge@unb.br

Carla Tatiana Mota Anflor

Professor at Post-Graduate Program - Integrity of Engineering Materials, University of Brasilia, Brazil

Research interests include: optimization, boundary element method, mechanical vibrations and solid mechanics

More info: lattes.cnpq.br/0526742760439036, orcid.org/0000-0003-3941-8335

✉ ctanflor@gmail.com; anflor@unb.br

Guilherme Ferreira Gomes

Professor at Mechanical Engineering Institute, Federal University of Itajubá, Itajubá, Brazil.

Research interests include: structures, vibration and modal testing, structural health monitoring, composite structures, optimization and applied artificial intelligence

More info: guilherme.unifei.edu.br, lattes.cnpq.br/4963257858781799, orcid.org/0000-0003-0811-6334

✉ guilhermefergom@gmail.com; guilhermefergom@unifei.edu.br

Sergio Henrique da Silva Carneiro

Collaborating Professor at Post-Graduate Program - Integrity of Engineering Materials, University of Brasilia, Brazil.

Research interests include: modal testing, structural analysis, finite element method, dynamics, fracture mechanics and damage detection.

More info: lattes.cnpq.br/6280300531787552, orcid.org/0000-0001-6669-2255

✉ shscarneiro@gmail.com, shscarneiro@unb.br

Book Series in Discrete Models, Inverse Methods, & Uncertainty Modeling in Structural Integrity

VOLUME I

MODEL-BASED AND SIGNAL-BASED INVERSE METHODS

VOLUME II

Fundamental Concepts and Models for the Direct Problem

VOLUME III

Uncertainty Modeling: Fundamental Concepts and Models

This book series is an initiative of the Post Graduate Program in Integrity of Engineering Materials from UnB, organized as a collaborative work involving researchers, engineers, scholars, from several institutions, universities, industry, recognized both nationally and internationally. The book chapters discuss several direct methods, inverse methods and uncertainty models available for model-based and signal based inverse problems, including discrete numerical methods for continuum mechanics (Finite Element Method, Boundary Element Method, Mesh-Free Method, Wavelet Method). The different topics covered include aspects related to multiscale modeling, multiphysics modeling, inverse methods (Optimization, Identification, Artificial Intelligence and Data Science), Uncertainty Modeling (Probabilistic Methods, Uncertainty Quantification, Risk & Reliability), Model Validation and Verification. Each book includes an initial chapter with a presentation of the book chapters included in the volume, and their connection and relationship with regard to the whole setting of methods and models.

The Book Series is an initiative supported by:

UNIVERSITY OF BRASILIA - UnB
www.unb.br

With the kind encouragement of:

BRAZILIAN ASSOCIATION OF COMPUTATIONAL METHODS IN ENGINEERING - ABMEC
www.abmec.org.br

BRAZILIAN SOCIETY OF MECHANICAL SCIENCES AND ENGINEERING – ABCM
www.abcm.org.br

LATIN AMERICAN JOURNAL OF SOLIDS AND STRUCTURES - LAJSS
www.lajss.org